

~~A11105 853181~~

NAT'L INST. OF STAND & TECH R.I.C.

A11105 853181



A11103 072153

NAT'L INST OF STANDARDS & TECH R.I.C.



A11103072153

Symposium on the Sci/The science of cera
QC100 .U57 NO.562, 1979 C.2 NBS-PUB-C 19



NBS SPECIAL PUBLICATION 562

U.S. DEPARTMENT OF COMMERCE / National Bureau of Standards Admin. Bldg.

National Bureau of Standards

OCT 1 1981
191083

QC
100
.U57

The Science of Ceramic Machining and Surface Finishing II

QC
100
U57
o.562
1979
c.2

NATIONAL BUREAU OF STANDARDS

The National Bureau of Standards¹ was established by an act of Congress on March 3, 1901. The Bureau's overall goal is to strengthen and advance the Nation's science and technology and facilitate their effective application for public benefit. To this end, the Bureau conducts research and provides: (1) a basis for the Nation's physical measurement system, (2) scientific and technological services for industry and government, (3) a technical basis for equity in trade, and (4) technical services to promote public safety. The Bureau's technical work is performed by the National Measurement Laboratory, the National Engineering Laboratory, and the Institute for Computer Sciences and Technology.

THE NATIONAL MEASUREMENT LABORATORY provides the national system of physical and chemical and materials measurement; coordinates the system with measurement systems of other nations and furnishes essential services leading to accurate and uniform physical and chemical measurement throughout the Nation's scientific community, industry, and commerce; conducts materials research leading to improved methods of measurement, standards, and data on the properties of materials needed by industry, commerce, educational institutions, and Government; provides advisory and research services to other Government agencies; develops, produces, and distributes Standard Reference Materials; and provides calibration services. The Laboratory consists of the following centers:

Absolute Physical Quantities² — Radiation Research — Thermodynamics and Molecular Science — Analytical Chemistry — Materials Science.

THE NATIONAL ENGINEERING LABORATORY provides technology and technical services to the public and private sectors to address national needs and to solve national problems; conducts research in engineering and applied science in support of these efforts; builds and maintains competence in the necessary disciplines required to carry out this research and technical service; develops engineering data and measurement capabilities; provides engineering measurement traceability services; develops test methods and proposes engineering standards and code changes; develops and proposes new engineering practices; and develops and improves mechanisms to transfer results of its research to the ultimate user. The Laboratory consists of the following centers:

Applied Mathematics — Electronics and Electrical Engineering² — Mechanical Engineering and Process Technology² — Building Technology — Fire Research — Consumer Product Technology — Field Methods.

THE INSTITUTE FOR COMPUTER SCIENCES AND TECHNOLOGY conducts research and provides scientific and technical services to aid Federal agencies in the selection, acquisition, application, and use of computer technology to improve effectiveness and economy in Government operations in accordance with Public Law 89-306 (40 U.S.C. 759), relevant Executive Orders, and other directives; carries out this mission by managing the Federal Information Processing Standards Program, developing Federal ADP standards guidelines, and managing Federal participation in ADP voluntary standardization activities; provides scientific and technological advisory services and assistance to Federal agencies; and provides the technical foundation for computer-related policies of the Federal Government. The Institute consists of the following centers:

Programming Science and Technology — Computer Systems Engineering.

¹Headquarters and Laboratories at Gaithersburg, MD, unless otherwise noted; mailing address Washington, DC 20234.

²Some divisions within the center are located at Boulder, CO 80303.

NOV 30 1979

The Science of Ceramic Machining and Surface Finishing II

QC 100
US
10.30
1979
C.F.

Proceedings of a Symposium
held at the National Bureau of Standards,
Gaithersburg, Maryland,
November 13-15, 1978

Edited by

B. J. Hockey

Center for Materials Science
National Measurement Laboratory
National Bureau of Standards
Washington, D.C. 20390

and

R. W. Rice

Naval Research Laboratory
Washington, D.C. 20390

Sponsored in part by

Air Force Office of Scientific Research
American Ceramic Society
Office of Naval Research



Special pub. 562

U.S. DEPARTMENT OF COMMERCE, Juanita M. Kreps, Secretary

Luther H. Hodges, Jr., Under Secretary

Jordan J. Baruch, Assistant Secretary for Science and Technology

NATIONAL BUREAU OF STANDARDS, Ernest Ambler, Director

Issued October 1979

Library of Congress Catalog Card Number 79-600149

National Bureau of Standards Special Publication 562

Nat. Bur. Stand. (U.S.), Spec. Publ. 562, 524 pages (Oct. 1979)

CODEN: XNBSAV

U.S. GOVERNMENT PRINTING OFFICE
WASHINGTON: 1979

For sale by the Superintendent of Documents, U.S. Government Printing Office, Washington, D.C. 20402
Stock No. 003-003-02122-9 Price \$9.
(Add 25 percent additional for other than U.S. mailing)

FOREWORD

Machining and surface finishing operations play a vital role in the production and reliable use of ceramics. It is essential, therefore, that the full scope of this technologically important subject be periodically reviewed and evaluated. One of the most effective ways of accomplishing this is through meetings, such as this Second Symposium on Ceramic Machining and Surface Finishing. These meetings provide the necessary forum for the direct exchange and discussion of new data, recently developed techniques, and advances in our understanding of underlying principles.

This Symposium, in particular, has focused on both the scientific and technological advances in ceramic machining and related topics. The interaction that has occurred at this meeting between science and technology will provide many direct benefits and, hopefully, will act as a stimulus for further progress. Through publication of these proceedings, the information presented at this symposium, together with any derived benefits, can be shared with the scientific and industrial community at large.

The National Bureau of Standards is pleased to be responsible for this publication, and to have joined with the Air Force Office of Scientific Research, the Office of Naval Research, and the American Ceramic Society in sponsoring the symposium.

John D. Hoffman

Director
National Measurement Laboratory
National Bureau of Standards

PREFACE

The first Symposium on Ceramic Machining and Surface Finishing was held eight years ago at the National Bureau of Standards. That meeting covered, for the first time, various topics on the scientific and technological efforts that represent the full scope of ceramic machining and surface finishing. It was, thus, largely responsible for the development of what is now known as the Science of Ceramic Machining and Surface Finishing. The resulting publication¹ continues to be a useful reference on the subject.

The present volume records the proceedings of the Second Symposium on Ceramic Machining and Surface Finishing held at the National Bureau of Standards, Gaithersburg, Maryland on November 13-15, 1978. Attendance at this meeting, augmented by attendees to the concurrently held Fall meeting of the Basic Science Division of the American Ceramic Society, numbered over two hundred and included representatives from seven countries including the USA.

The primary purpose of this meeting was the same as that of the previous meeting, namely: "To survey the developing science of ceramic machining and to stimulate further progress by discussion of current problems and research."

In keeping with this theme, the meeting provided not only a timely review of subsequent research on the mechanisms and techniques of machining, surface characterization, and the effects of finishing on material properties, but also incorporated data on recently developed materials and information gained from related research efforts. As an example, new insights into the mechanisms of material removal during multipoint, fixed abrasive machining have been gained from recent indentation and solid particle impact studies. Significant advances in the technology of machining and surface finishing have also been achieved, in particular, through the application of single-point diamond machining to ceramics. Current results for this technique are doubly encouraging in that they suggest that still further advances are possible. Similarly, advances have taken place in the rapidly developing area of non-destructive evaluation, and the initial application of techniques such as acoustic surface wave emission shows considerable promise in the rapid evaluation of machining-induced flaws. In addition, the proceedings of this meeting record continuing efforts to better define the nature of machined or polished surfaces, the effects of gaseous and liquid environments, and quite importantly, the effects of machining on the various properties and reliability of ceramics. Also presented are a number of specific examples which illustrate the technological progress made in machining and finishing ceramics for important commercial applications, such as turbine components, laser windows, and electronic substrates. These examples clearly reflect the benefits derived from the interaction between technology and science, and, hopefully, will provide the justification for further research on machining.

¹The Science of Ceramic Machining and Surface Finishing, S. J. Schneider, Jr. and R. W. Rice, eds., National Bureau of Standards Special Publication 348, 1972.

Looking to the future, it is hoped that several avenues of research and development are stimulated by this latest conference and its proceedings. Although significant progress has been made in understanding the general aspects of traditional abrasive machining together with the flaws that are produced, possible new developments might include: 1) further improvements in machining technology that lead to substantial reduction in the cost of finished products (most specifically, in ceramic turbine components); 2) further improvements in the detection and characterization of flaws (e.g., cracks) and other damage produced by machining; and, 3) a more detailed understanding of the correlation between the nature and distribution of machining flaws and the properties (mechanical, optical, dielectric, etc.) of ceramics. With regard to the latter, mechanical reliability for example, may be improved by not only limiting the maximum flaw size, but also by deliberately increasing the density of subcritical flaws. Through multiple flaw interactions, the effectiveness of any single flaw may well be limited and resistance to further surface damage improved. In addition it is felt that the potential suggested by current results on single point diamond and laser, or laser assisted machining – as well as other non-conventional techniques – should certainly encourage further research.

Finally, a few comments on the organization of these proceedings are in order. For the most part, we have attempted to follow the outline of the symposium program; however, some changes were deemed necessary to better reflect the content of the papers. Also, as is often the case, many papers could be placed equally well in different sections and, hence, section headings should be regarded as general guidelines. Discussions of the papers have been included, and in every case were transcribed from handwritten notes obtained during the meeting. In most cases, these comments were returned to those involved to verify their accuracy.

Roy W. Rice
Bernard J. Hockey

ACKNOWLEDGMENT

The editors wish to acknowledge several organizations and individuals for their aid in conducting the Symposium and in the publication of these proceedings. In particular, financial support was received from the Air Force Office of Scientific Research, the Office of Naval Research, and the National Bureau of Standards. The additional sponsorship and organizational assistance of the American Ceramic Society is also acknowledged. Similarly, we wish to acknowledge Dr. A. M. Diness, Office of Naval Research; Major Will Simmons, Air Force Office of Scientific Research; Mr. Charles Bersch, Naval Air Systems Command; Dr. John B. Wachtman, Jr., National Bureau of Standards; and, Dr. Benjamin Wilcox, National Science Foundation, for their roles in developing the Symposium program. Further, it should be noted that this symposium was held in conjunction with the Fall meeting of the Basic Science Division of the American Ceramic Society. Accordingly, we wish to thank Dr. Nancy Tighe, National Bureau of Standards, who as program chairperson for the American Ceramic Society, assisted in coordinating the scheduling of the two meetings.

Finally we wish to acknowledge the much needed assistance provided during the symposium and in the preparation of these proceedings by Mrs. Pellechehia and Mrs. Craig of the Naval Research Laboratory and Mrs. Salpino and Mrs. Stang of the National Bureau of Standards. Special thanks are due to Rosemary Maddock of the National Bureau of Standards for her extensive efforts and guidance in preparing this volume for publication.

ABSTRACT

This volume presents the proceedings of the Second Symposium on the Science of Ceramic Machining and Surface Finishing held at the National Bureau of Standards in Gaithersburg, Maryland, on November 13-15, 1978. The symposium was jointly sponsored by the Air Force Office of Scientific Research, the American Ceramic Society, the Office of Naval Research, and the National Bureau of Standards. The purpose of the symposium was to review recent progress by discussion of current problems and research efforts. The proceedings contain forty of forty-three research papers, together with floor discussions, presented at the Symposium. Specific topics covered include: 1) mechanisms of abrasive machining and surface finishing; 2) technology of machining and surface finishing; 3) characterization of machined surfaces; and 4) effects of machining on the properties of ceramics. Also included is an edited discussion on hardness and its relation to machining.

Key words: Abrasion; ceramics; ceramic machining; effects of machining on ceramic properties; hardness; surface characterizations; surface finishing.

CONTENTS

	Page
Foreword	iii
Preface	iv
Acknowledgment	vi
Abstract	vii
Session I: Mechanisms of Abrasive Machining and Surface Finishing	
Abrasive Wear in Ceramics: An Assessment A. G. Evans	1
Nucleation of Median and Lateral Cracks Around Vickers Indentations in Soda-Lime Glass J. T. Hagan, M. V. Swain, and J. E. Field	15
Fragmentation and Damage Penetration During Abrasive Machining of Ceramics H. P. Kirchner, R. M. Gruver, and D. M. Richard	23
Single-Point Scratches as a Basis for Understanding Grinding and Lapping A. Broese van Groenou, N. Maan, and J. B. D. Veldkamp	43
Experiments on High-Speed Grinding of Ferrites and Glasses A. Broese van Groenou and R. Brehm	61
Effect of Workpiece Properties on Grinding Forces in Polycrystalline Ceramics B. G. Koepke and R. J. Stokes	75
Glass Grinding Mechanisms and Influence on the Finished Surface and Strength S. Malkin and M. Huerta	93
The Fine Grinding of Glass and Ceramic Material Using Conventional Grinding Wheels E. D. Doyle and S. K. Dean	107
Some Observations on Environmental Effects when Diamond Drilling G. A. Cooper	115
The Effect of Chemical Environments on the Fracture of Ceramic Surfaces R. E. Cuthrell	139
Some Results on the Wear of a Bronze-Bonded Grinding Wheel A. Broese van Groenou	147
New Concepts on Surface Finishing and Its Application to Ceramics — Recent Progress in Ultra-Fine Finishing in Japan O. Imanaka and M. Okutomi	157

Mechanism and Application of the "Mechanochemical Polishing Method Using Soft Powder"	171
N. Yasunaga, N. Tarumi, A. Obara, and O. Imanaka	
Extended Discussion: Hardness and Its Relation to Machining	185
R. W. Rice and A. G. Evans	
Session II: Technology of Machining and Surface Finishing	
Optimization of Multistage Grinding Operations: The Choice of Consecutive Removal Rates	191
A. Broese van Groenou	
Grinding Stone, Concrete and Ceramics with Coated Abrasives	201
R. C. Lokken and E. J. Duwell	
Turbine Component Machining Development	209
D. W. Richerson and M. W. Robare	
Machinability Studies on Macor TM Glass-Ceramic	221
D. G. Grossman and D. L. Taylor	
Effects of Various Polishing Media and Techniques on the surface Finish and Behavior of Laser Glasses	231
R. L. Landingham, A. W. Casey, and R. O. Lindahl	
The Fabrication of Alumina Tooth Roots by Diamond Contour Grinding	247
G. L. Messing, L. G. McCoy, and C. R. Hassler	
Simultaneous Finishing of Both Surfaces of Hemispherical Domes	255
R. Gentilman, F. Cooke, and P. Miles	
Abrasionless Machining Methods for Ceramics	261
R. F. Firestone	
Shaping Silicon Compound Ceramics with a Continuous Wave Carbon Dioxide Laser	283
S. M. Copley, M. Bass, and R. G. Wallace	
Optical and Surface Physical Characteristics of Diamond-Machined Infrared Windows	293
D. L. Decker, D. J. Grandjean, and J. M. Bennett	
Electrochemical Grinding and Surface Damage for Cemented Carbides	305
S. Malkin and R. Levinger	
A New Ultra-Fine Polishing Technique for Sapphire	317
T. Sugita, S. Kawakami, and O. Imanaka	
Fine Polishing of Sapphire Crystals	325
M. Ikeda, A. Yamada, Y. Kokaji, S. Kimura	

Session III: Characterization of Machined Surfaces

Surface Characterization of Optical Materials	337
H. E. Bennett	
The Nature of Strength Controlling Machining Flaws in Ceramics	351
R. W. Rice and J. J. Mecholsky, Jr.	
Acoustic Surface Wave Measurements of Surface Cracks in Ceramics	379
B. T. Khuri-Yakub, A. G. Evans, and G. S. Kino	
Characterization of Surface Damage in Ceramics Using Selected Area Electron Channeling	395
J. Lankford and D. L. Davidson	
Y-Deflection Modulated Secondary Electron Images in the Evaluation of Ceramic Surface Finish	407
L. P. Cook, E. N. Farabaugh, and C. D. Olson	
Latent Scratches on Optical Glasses that Appear After Cleaning	417
T. Izumitani, E. Miyade, S. Adachi, and S. Harada	

Session IV: Effects of Machining and Surface Finishing
on Ceramic Properties

Machining Flaws and the Strength Grain Size Behavior of Ceramics	429
R. W. Rice	
Surface Machining Effects on the Strength Distributions of Aluminas	455
T. E. Easler, T. A. Counterline, R. E. Tressler, and R. C. Bradt	
Effect of Surface Finish on the Strength of Hot Pressed Silicon Nitride	463
C. A. Andersson and R. J. Bratton	
The Effect of Surface Finishing on the Strength of Commercial Hot Pressed Silicon Nitride	477
C. Cm. Wu and K. R. McKinney	
Surface Condition and Strength of Silicon Carbide- Silicon Materials	483
T. J. Whalen and L. L. Turner	
The Effect of Grinding and Polishing on the Strength of Annealed Soda-Lime Silica Glass	489
R. Bowles	
Surface Flaw Effects on Crack Propagation from Subsonic Water Drop Impact	501
Y. M. Ito and M. Rosenblatt	

Surface Characteristics of Diamond-Machined Ceramic Surfaces Evaluated by High Fluence Diagnostics	513
M. J. Soileau, J. O. Porteus, and D. L. Decker	
Symposium Attendees	519
Author Index	529
Subject Index	530

Session I

Mechanisms of Abrasive Machining and Surface Finishing

Session Chairmen

A. Diness, Office of Naval Research

B. Wilcox, National Science Foundation

ABRASIVE WEAR IN CERAMICS: AN ASSESSMENT

A. G. Evans

University of California
Berkeley, CA 94720

The mechanisms of material removal during abrasive wear have been examined, and preliminary analyses presented. Primary emphasis has been placed on the lateral fracture mechanism, in an attempt to elucidate both its realm of importance and the concomitant material removal rates. Thermal stresses induced by plastic penetration have also been shown to be a potential source of material removal, especially at low levels of the normal force.

Key Words: Abrasive wear; ceramics; fracture, plastic penetration; thermal stresses

1. Introduction

The abrasive wear of ceramics has been the subject of extensive empirical investigation [1].¹ For example, material removal rates have been measured on various materials as functions of the normal force, P_n , the horizontal (frictional) force, P_ℓ , the wheel speed, etc. However, the detailed mechanisms of material removal have only been cursorily explored. Yet, some understanding of mechanisms is an essential prerequisite to optimization (especially for complex processes such as abrasive wear). The intent of the present paper is to examine possible mechanisms of abrasive material removal, as a prelude to suggesting research studies that should elucidate details of the various removal processes.

Several investigators [2-4] have recently recognized the important role of lateral fracture in abrasive material removal. This mechanism of wear is explored in some detail, to determine both its realm of importance and the parameters that might influence the removal rate. Other potential mechanisms of material removal are then examined to assess their significance as alternative or superposed influences.

2. Lateral Fracture Mechanisms

2.1 Regime of influence

Studies of indentation conducted under quasi-static [4], sliding [2,3] and impact conditions have indicated a threshold for lateral crack formation. A definition of this threshold is of great significance, because it defines the lower limit of pertinence of the lateral fracture mechanism of abrasive wear. A transition to another mechanism may also obtain under very severe grinding conditions [2]. However, this regime could be just

¹ Figures in brackets indicate the literature references at the end of this paper.

another manifestation of lateral cracking (perhaps involving a multiplicity of lateral cracks as observed during projectile impact [5]); consequently, this "transition" is not afforded specific consideration in the present analysis.

During "steady-state" grinding conditions, a ceramic will contain a distribution of microcracks, formed as a consequence of the stresses produced by the penetration of the grinding particles. These pre-existent microcracks are considered to be the sources of lateral fracture. The pre-existent microcracks will develop into lateral cracks when the grinding stresses attain the requisite level. The tensile stresses that induce lateral cracks develop primarily during load removal [6,7] (i.e. residual stresses), and exhibit a maximum either within the plastic zone (in work hardening materials) or at the elastic/plastic interface (in non-hardening materials). It has recently been demonstrated [8] that elastic/plastic indentation fields can be approximated in the immediate vicinity of the plastic zone by the elastic/plastic solution for a spherical cavity,² and remote from the indentation by the elastic solution for a half-space: the intermediate stresses being obtained by interpolation. This procedure also provides estimates of the residual tensile stress, σ_{zz}^R , obtained by subtracting the elastic unloading stresses from the elastic/plastic stresses at peak load. In particular, the residual stresses in the elastic zone (the zone of primary interest for fracture analysis [4]), are obtained at zero load by matching the elastic stress at the indenter interface, $\hat{\sigma}_{zz}^e$, to the equivalent elastic/plastic stress at peak penetration, a , (i.e. to the hardness H), viz;

$$\hat{\sigma}_{zz}^e = - \left(\frac{3H}{2} \right) \left(\frac{z}{\sqrt{u}} \right)^3 \left[\frac{\hat{a}^2 u}{u^2 + \hat{a}^2 z^2} \right] \quad (1)$$

where

$$2u = r^2 + z^2 - \hat{a}^2 + \sqrt{(r^2 + z^2 - \hat{a}^2)^2 + 4a^2 z^2}$$

and then subtracting this stress from the elastic/plastic stress, σ_{zz}^p ;

$$\left(\sigma_{zz}^p = - \frac{\sigma_y}{6} \right) \left(\frac{r_p}{\sqrt{z^2 + r^2}} \right)^3 \left[1 + 3 \left(\frac{z^2 - r^2}{z^2 + r^2} \right) \right] \quad (z > 0) \quad (2)$$

By noting that, $\sigma_y \sim H/3$ [4,6,10], and that, $r_p \sim \hat{a}$ [4,5], the residual stress σ_{zz}^R at zero load becomes;

$$\sigma_{zz}^R \equiv \left(\sigma_{zz}^p - \hat{\sigma}_{zz}^e \right) \approx \left(\frac{H\hat{a}^2}{2} \right) \left\{ \frac{3z^2}{\sqrt{u}(u^2 + \hat{a}^2 z^2)} - \frac{\hat{a}}{9(z^2 + r^2)^{3/2}} \left[1 + 3 \left(\frac{z^2 - r^2}{z^2 + r^2} \right) \right] \right\} \quad (3)$$

²With the obvious exception of σ_{zz} stresses near the surface, which are poorly predicted by the spherical cavity solution.

The peak axial value of this stress,

$$\hat{\sigma}_{ZZ}^R \approx H/2$$

occurs at the elastic/plastic interface, and is appreciably larger than the peak stress at maximum penetration [8] ($\sim H/12$). Note, however, that $\hat{\sigma}_{ZZ}^R$ decreases rapidly as the relative plastic zone size increases, e.g. $\hat{\sigma}_{ZZ}^R = 0.27H$ at $r_p = 2a$.

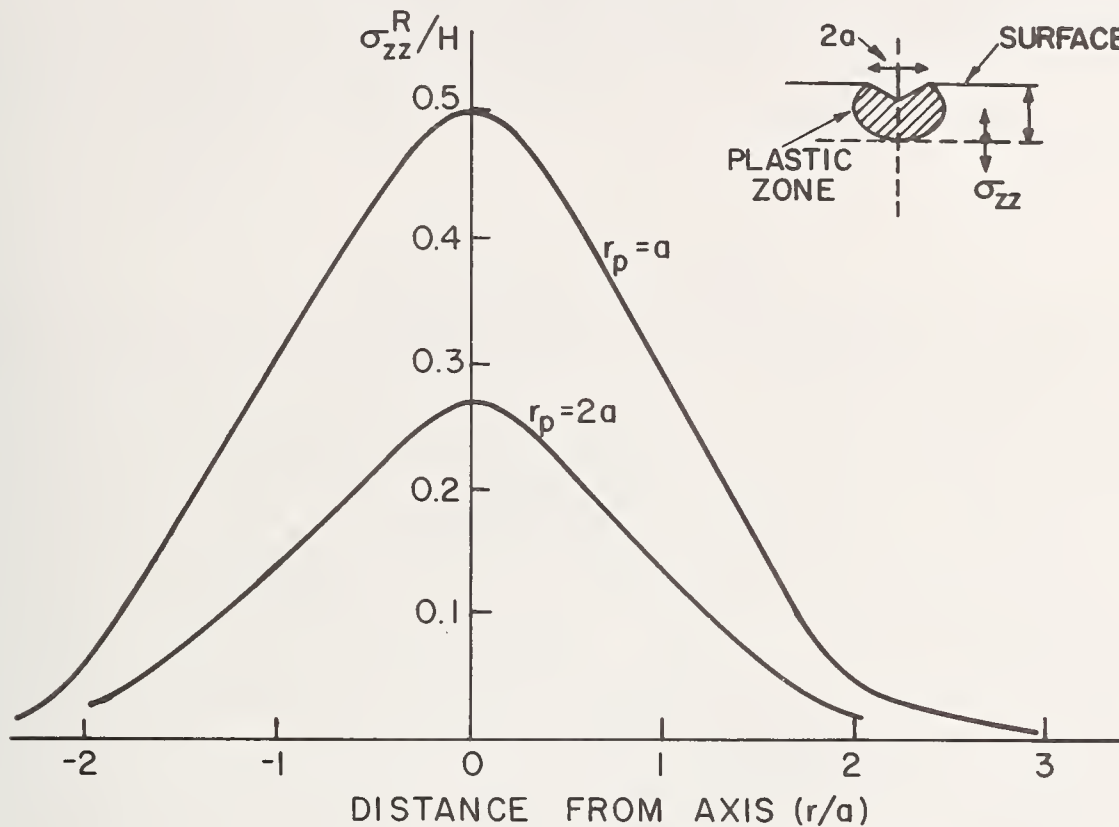


Fig. 1 The spatial dependence of the residual tensile stress along a plane through the intersection of the plastic zone with the penetration axis: the stresses were estimated from an analytic elastic/plastic solution for a spherical cavity and an elastic solution for a half space.

The spacial variation of the stress along a plane through the location of maximum tension is plotted in Fig. 1. The stresses can be approximated by

$$\sigma_{ZZ}^R \approx \sigma(1 - r/2a) \quad (r < 2a) \quad (5)$$

$$\sigma_{ZZ}^R = 0 \quad (r > 2a)$$

where $\hat{\sigma}$ is the peak stress. A stress-intensity factor solution for an axisymmetric crack located in such a linearly varying stress field has recently been derived by Lawn and Evans [11]. This solution demonstrates the existence of an absolute minimum P^* in the normal force required for crack activation. For the stress field represented by eq. (5), P^* is given by

$$P^* = 14\xi^4 \beta K_C^4 / H^3 \quad (6)$$

where K_C is the toughness of the material, β is a parameter related to the shape of the indenting particle [11] (e.g. $\beta = 2/\pi$ for a Vickers indenter) and $\xi = H/\hat{\sigma}$. In a material that contains a wide size distribution of pre-existent microcracks, there will be a relatively high probability of lateral crack nucleation at P^* . However, more generally, P^* will need to be exceeded: by an amount related to the size range of microcracks in the vicinity of the indentation. The parameter K_C^4/H^3 in the expression for P^* is considered to afford a reasonably accurate relative measure of the influence of the material variables on the fracture threshold, as indicated by recent observations on radial fracture [12]. However, the magnitudes of the coefficients - being strongly dependent on the value of the peak stress - could be appreciably in error and should only be regarded as order of magnitude estimates.

2.2 Material removal rates

The amount of material removed by the passage of each abrasive particle that exceeds the fracture threshold force P^* is determined (in part) by the extent of the lateral fracture. Most observations of lateral fracture indicate that the fracture extent is related to the extent of the prior radial fracture (4,5); but the generality of this result has not been substantiated. Nevertheless, the present analysis of material removal rates will assume a relationship between lateral crack extension and the more extensively characterized radial crack extension, C . The average depth of the lateral cracks, $\langle h \rangle$, also influences the material removal (Fig. 2a). The only available analysis of lateral crack depths indicates that $\langle h \rangle$ is proportional to the plastic zone radius r_p . This relationship will also be assumed in the present analysis.

The maximum volume \hat{V}_i of material that could be removed by the passage of an abrasive particle is (Fig. 2);

$$\hat{V}_i \approx 2 \langle h \rangle C_i \ell_i \quad (7)$$

where ℓ_i is the distance of motion. This expression will be the basis for estimating variations in the material removal rate.

The plastic zone radius r_p is related to the plastic contact radius a , under both dynamic [5] and quasi-static [4] conditions. We will use the direct proportionality, $r_p \propto a$, so that,

$$\langle h \rangle \approx \psi a \quad (8)$$

where ψ is a constant ≈ 1 . However, the radial crack extension C differs appreciably under quasi-static and dynamic conditions [5]: being more extensive (for the equivalent contact area) under dynamic conditions. For typical abrasive wear situations, both quasi-static and dynamic conditions can obtain. A preliminary analysis that embraces both quasi-static and dynamic influences is attempted herein. The analysis considers the exten-

³A tenuous rationale for this observation is that the presence of the radial cracks enhances the stress intensity factor at lateral cracks toward the limit of their extension, by relaxing the circumferential constraint and permitting additional z-displacements.

sion of the lateral cracks normal to the motion of the abrading particle (Fig. 2a), since this distance defines the width of the potential material removal zone. The situation to be modelled is defined in Fig. 2b; it consists of an abrasive particle subjected to normal force P_n , moving with a prescribed lateral velocity v_ℓ .

If the velocity v_ℓ is very low, the consequences of the lateral motion can be approximated by a quasi-static lateral force $P_\ell \equiv \mu P_n$ (where μ is a friction coefficient). Although this condition is rarely encountered, it is instructive to examine the influence of the lateral force, vis-a-vis the normal force. The normal force dictates the penetration according to the normal hardness relation [11];

$$H = P_n / \beta \pi a^2 \quad (9)$$

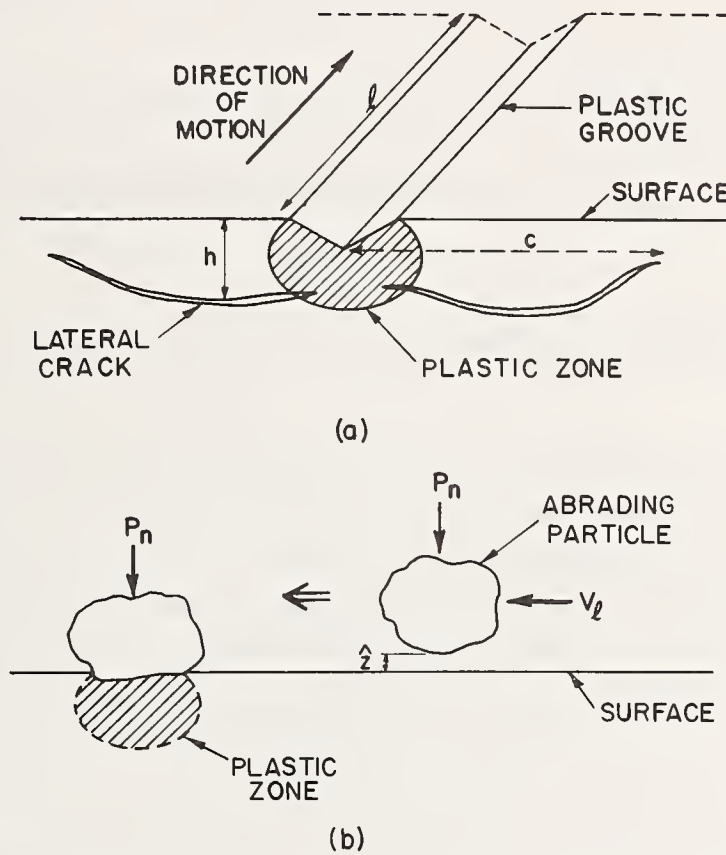


Fig. 2 a) A schematic indicating the nature of the lateral cracking that leads to material removal
 b) A schematic indicating typical conditions that apply to an abrading particle during abrasive wear.

Both the lateral and normal forces are expected to influence the stress field. By analogy with the equivalent elastic problem [13], it is anticipated that the lateral force will tend to rotate the stress field in the direction of P_ℓ , in the sense that the tension is enhanced behind the contact zone and suppressed ahead of the contact. But, there should be no appreciable influence on the stresses contained in the plane normal to P_ℓ . The latter have the primary effect on the lateral crack extension normal to the motion of the abrading particle. It is thus concluded that under quasi-static conditions, the width of the lateral fracture zone should be relatively insensitive to the magnitude of the lateral

force. The zone width may, therefore, be approximately characterized by a relation similar to that obtained for radial cracks under conditions of normal penetration; viz., for a Vicker's indenter [14],

$$C/a = F_1 \left[(K_c/H\sqrt{a}), (H/E) \right] \quad (10a)$$

where F_1 is a function, which for $c/a \gtrsim 2$ reduces to;

$$F_1 \approx 0.29 \left(\frac{K_c}{H\sqrt{a}} \right)^{-2/3} \quad (10b)$$

giving;

$$C = \frac{0.29}{(\pi\alpha)^{2/3}} \left(\frac{\hat{P}}{K_c} \right)^{2/3} \quad (10c)$$

Combining equations (7), (8) and (10c) yields the quasi-static material removal rate;

$$\hat{V}_i^E = \left[\frac{0.58\psi}{(\pi\beta)^{7/6}} \right] \frac{(P_n)^{7/6} i}{(K_c^{2/3} H^{1/2})} \ell_i \quad (11)$$

More generally, the lateral motion of the abrading particle will lead to dynamic effects. These dynamic effects arise both from the prescribed motion v_ℓ of the particle, and from local instabilities. The instabilities occur following a fracturing event and result in an abrupt increase in the local particle velocity. They are manifested as the lateral force oscillations typically observed in studies of the motion of abrading particles. The impact events that result from the instabilities are likely to have impulse components both normal and parallel to the surface. The normal component will affect the penetration, but both components will influence the dynamic stress field. We will assume that, as in the quasi-static case, the lateral component of velocity does not generate stresses that significantly influence lateral crack extension in the direction of present interest (Fig. 2a). The effect of the normal particle velocity v_n can then be assessed from experimental results obtained for projectile impact [5];

$$C \approx \lambda \left[r_p^2 v_n^2 / K_c \right]^{2/3} \quad (12)$$

where r_p is the radius of the projectile and λ is a constant. The normal component of the velocity acquired by the abrading particle depends on the magnitude of the normal force P_n and the height \hat{z} that the particle rises above the surface during the instability (Fig. 2b);

$$v_n^2 = 2P_n \hat{z} / m \quad (13)$$

Where m is the mass of the grinding wheel. The height \hat{z} will be influenced by the detailed character of the instability, the imposed lateral velocity v_ℓ and the friction coefficient μ . The influence of normal velocity on the extent of the fracture will be assumed in the present analysis to be equivalent to that found for projectile impact. This assumption is based on the premise that the stresses which influence the fracture relate to the conditions that prevail soon after initial contact:⁵ as dictated by the impedance, the initial velocity mismatch and the dynamic hardness. Clearly, experimental studies of the velocity dependence of C are needed to assess the utility of this assumption. The crack extension obtained from eq. (12) is then;

$$C = \left[\frac{P_n \hat{z}(v_\ell, \mu)}{K_C} \right]^{2/3} F(r_p, m) \quad (14)$$

where F is an undetermined function. It is interesting to note that the dependence on the normal force is identical to that obtained for quasi-static indentation (eq. 11). Now, assuming that eq. (9) still affords a reasonable estimate of the contact radius, equations (7), (9), and (14) can be combined to give;

$$\hat{V}_i^d = \left[\frac{2 F(r_p, m)}{(\pi\beta)^{1/2}} \right] \left[\frac{(P_n)_i^{7/6}}{H^{1/2}} \right] \left[\frac{\hat{z}(v_\ell, \mu)}{K_C} \right]^{2/3} \ell_i \quad (15)$$

This result is quite similar to the quasi-static result except that influences of the lateral velocity and the friction coefficient emerge, through the instability height \hat{z} . No information is presently available concerning the magnitude of the instability; this is clearly an important parameter for future study.

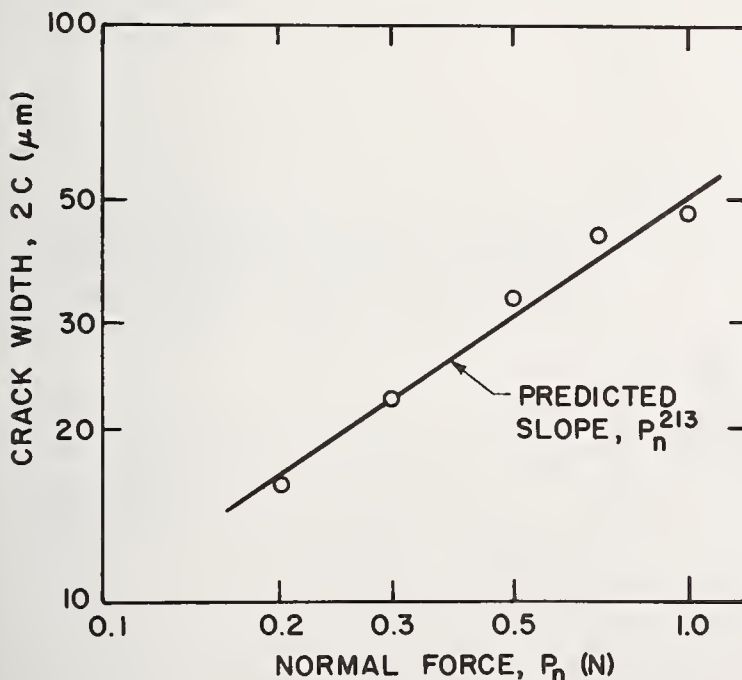


Fig. 3 A plot of the lateral crack width as a function of the normal force [3], indicating the $P_n^{2/3}$ relation.

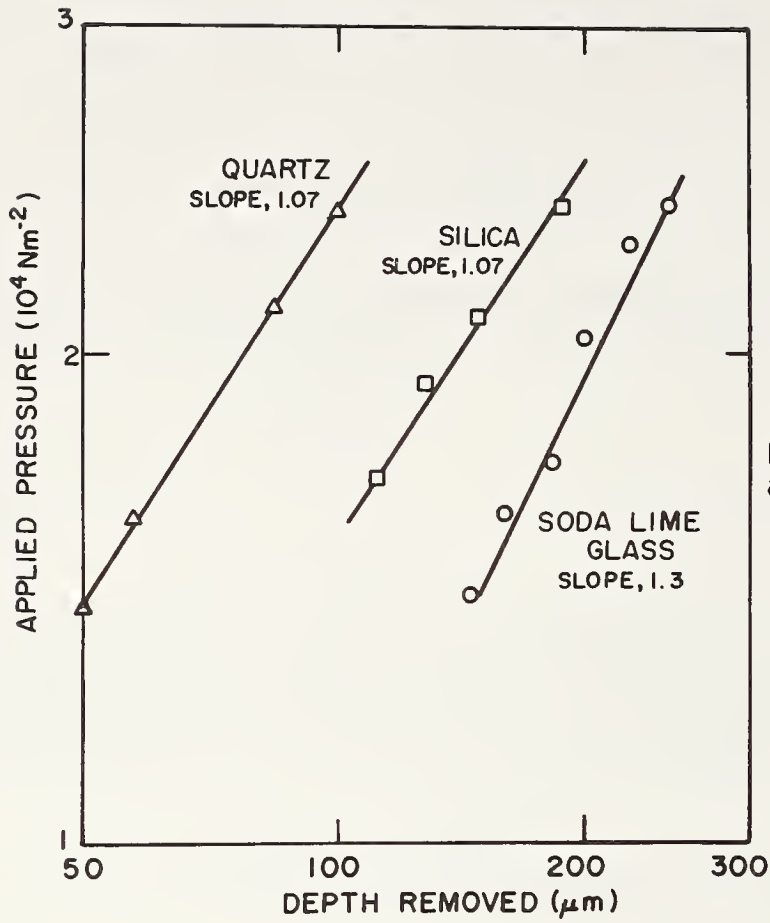


Fig. 4 A plot of the material removed as a function of the applied force [15].

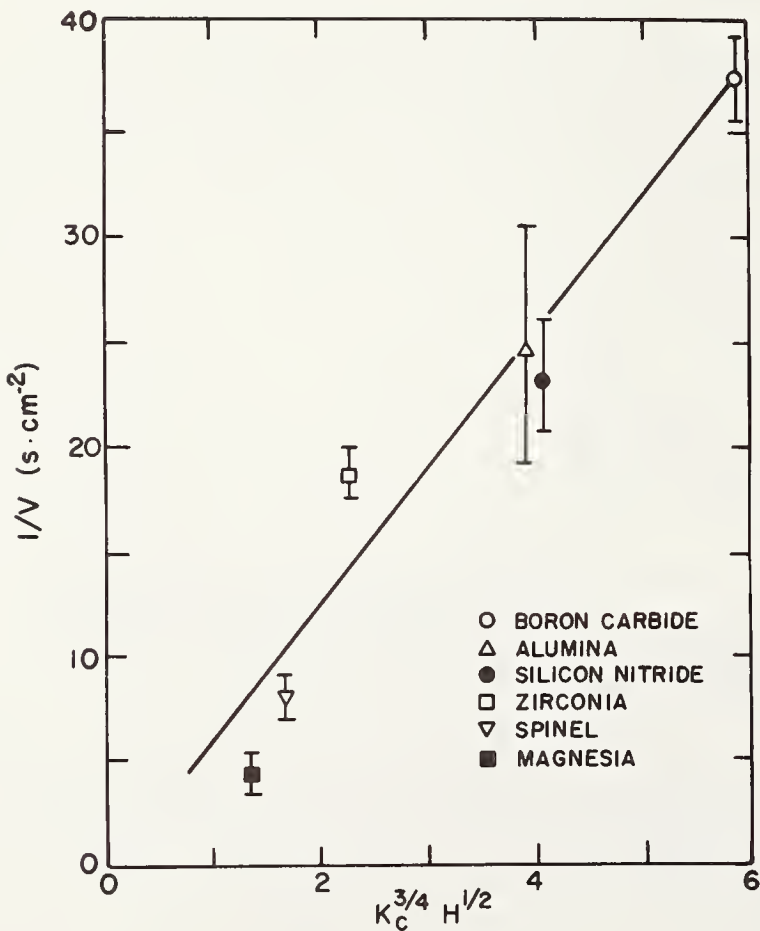


Fig. 5 A plot of the inverse of the material removal against the material dependent parameter $K_C^{2/3} H^{1/2}$ predicted by the lateral fracture analysis.

A comparison of the predictions of the present simplified analysis with available results should provide a basis for assessing the merits of this approach to abrasive material removal. The dependence of the lateral crack width on the normal force has previously been examined by Veldkamp et al [3] in MgZn ferrite, and shown to approximately conform with the predicted $P_n^{2/3}$ relation (Fig. 3). The dependence of the material removal on the normal force has been explored by Hartley and Wilshaw [15] (Fig. 4). A non-linear force dependence with an exponent ranging between 1.07 and 1.3 was found, similar to the predicted dependence of $P^{7/6}$. The important dependence on the material properties K_C and H can be ascertained from the study of Rice and Speronello [16]. A comparison of their results with the predicted material dependent quantity, $H^{1/2} K_C^{2/3}$, reveals a consistent trend (Fig. 5). However, variations of the instability height with the material type have not been incorporated in the comparison, and these could account for some of the residual trends in the experimental results.

The reasonably good correlation of the available abrasive wear results with the lateral cracking model encourages further study. These studies would include the characterization of lateral cracking under conditions that simulate abrasive wear, and estimations of the zone of material removal vis-a-vis the zone of lateral fracture.

3. Other Mechanisms

3.1 Thermal stresses

It is widely recognized that heat is generated during a grinding operation. This heat derives primarily from the plastic work expended by the penetration of the abrading particles. An upper bound (adiabatic) estimate of the thermal stresses that develop as a consequence of the heat generation is derived in this section. The potential influence of the thermal stresses upon material removal are then assessed.

The plastic work W_p expended during indentation can be estimated from the macroscopic force-penetration curve, (Fig. 6) as;

$$W_p = \int_0^{\hat{p}} P d\delta_p \quad (16)$$

where δ_p is the plastic penetration. The plastic penetration is directly related to the contact diameter $2a$ through the profile of the penetrator. For a penetrator of fixed profile (Fig. 6);

$$\delta_p = a \cot\theta \quad (17)$$

The penetration pressure (i.e. the hardness, H) for a fixed profile indenter is independent of the penetration. Hence, for an axisymmetric penetrator, combining equations (9), (16) and (17) and integrating gives;

$$W_p = \frac{\cot\theta}{3(\beta\pi)^{1/2}} \left[\frac{\hat{p}^{3/2}}{H^{1/2}} \right] \quad (18)$$

It is interesting to note the inverse dependence on the hardness. This arises because the plastic penetration decreases more rapidly with the increase in hardness than the

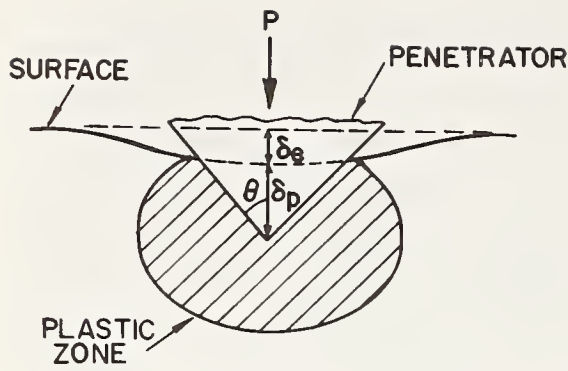
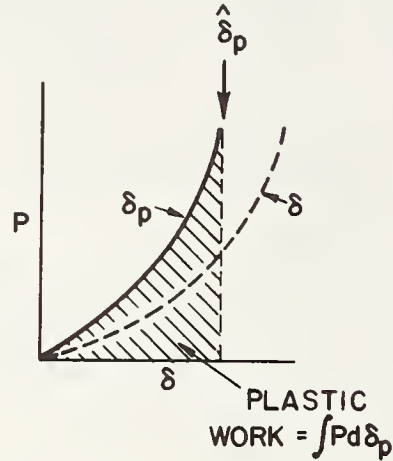


Fig. 6 A schematic indicating the elastic δ_1 and plastic δ_p penetrations by a fixed profile indenter.



concomitant increase in the penetration force.

The work expended during a lateral traverse of an abrading article depends very sensitively on the details of the traverse. In the presence of instabilities in the lateral motion, individual impacts will occur at various sites along the traverse. The plastic work at each impact site will be given approximately by eq. (18). Under adiabatic conditions, if all of the plastic work is converted into heat, the temperature T generated within the plastic zone at each impact site is;

$$T \approx W_p \left[(4\pi/3)r_p^3 \rho c_p \right]^{-1} \quad (19)$$

where c_p is the specific heat and ρ is the density. Setting $r_p \approx a$ and combining with eq. (9) then gives;

$$T = \left(\frac{3 \beta \cot \theta}{4} \right) \left(\frac{H}{\rho c_p} \right) \quad (20)$$

Note that the temperature rise is independent of the applied force. Heat flow during penetration will clearly reduce this temperature, as dictated by the differential equation;

$$\frac{d^2 T}{dr^2} = \rho \frac{c_p}{k} \left(\frac{dT}{dt} \right) \quad (21)$$

where k is the thermal conductivity.

The local increase in temperature will generate thermal stresses.⁴ By assuming the plastic zone to be a spherical enclave in an infinite body (Fig. 7), the thermal stresses are analogous to the stresses that develop due to thermal expansion mismatch [17], viz,

$$\left. \begin{aligned} \sigma_{rr} &= -\frac{2E\alpha T}{3(1-\nu)} \left(\frac{r_p}{r}\right)^3 \\ \sigma_{\theta\theta} &= \frac{E\alpha T}{3(1-\nu)} \left(\frac{r_p}{r}\right)^3 \end{aligned} \right\} \quad (r > r_p) \quad (22)$$

$$\sigma_{rr} = \sigma_{\theta\theta} = -\frac{2E\alpha T}{3(1-\nu)} \quad (r < r_p)$$

where r is the distance from the center of the plastic zone. An upper bound value for the tensile stress generated by the local plasticity, obtained from eqs. (20) and (22) is thus;

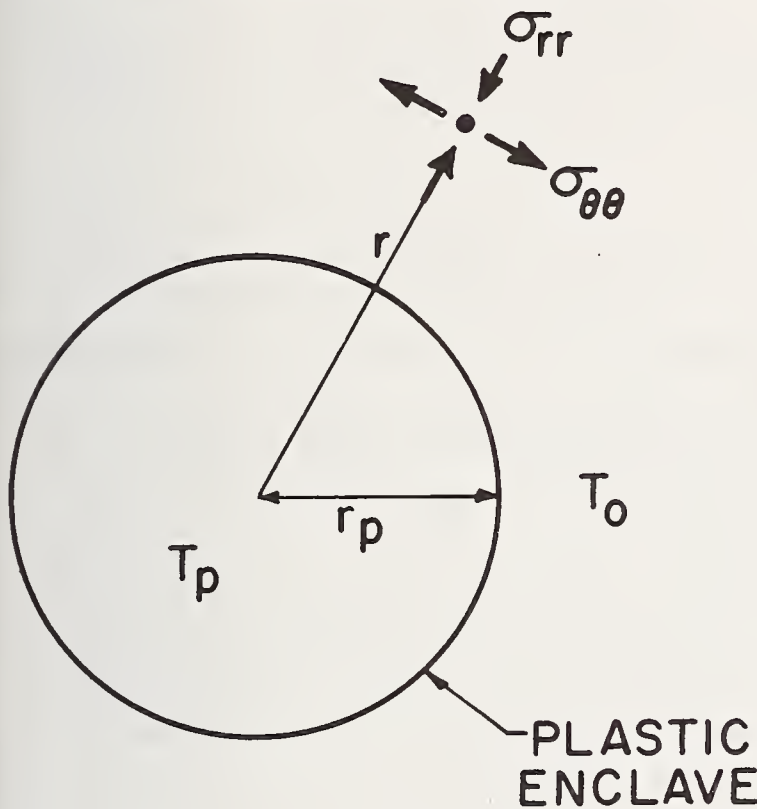


Fig. 7 A plastic enclave in an elastic matrix indicating the stresses developed by heat generation in the plastic zone.

$$\hat{\sigma}_{\theta\theta} = \frac{\beta \cot\theta}{4(1-\nu)} \left(\frac{\alpha H E}{\rho c_p}\right) \quad (23)$$

Inserting some typical values for E , ρ , c_p and α into eq. (23) yields values of $\hat{\sigma}_{\theta\theta}$ in the range $\sim 10^{-2}$ to $10^{-1}H$. These stresses approach the stresses that result from plastic penetration (eq. 4). Thermal stresses should thus be regarded as a possible source of material removal, particularly in materials with large values of thermal expansion coefficients, elastic modulus and hardness, and low values of specific heat. Since the thermal

⁴An elastic solution is not strictly valid, because the thermal shear stresses, which are a maximum at r_p , superimpose on the penetration stresses and extend the plastic zone.

stresses are independent of the normal force, the thermal influences should be particularly effective at low force levels. The thermal stresses could either enhance the lateral fracture just above the threshold force P^* , or perhaps, provide an independent mechanism of material removal below P^* .

3.2 Elastic stress pulses

Impact events can, in certain situations, lead to the generation of Rayleigh waves [18]. The Rayleigh wave can produce large amplitude, short duration tensile pulses, which introduce circumferential cracks that link together to cause material removal [19]. A similar mechanism could apply in abrasive wear, under analogous circumstances, e.g., the wear of very hard materials at low force levels. An important feature of this mechanism is that crack development is impeded by large values of the elastic wave velocity.

4. Summary

Some mechanisms of material removal during abrasive wear have been assessed. A preliminary lateral fracture model has been developed. The model indicates that a minimum force is required to initiate lateral fracture. The threshold force is determined primarily by the fracture toughness and the hardness.

The material removal that occurs by lateral fracture above the threshold has been estimated to depend on the normal force, the hardness and toughness as well as on the lateral velocity and friction coefficient (through local instabilities caused by the fracture process). A comparison of the predictions that emerge from the preliminary model with available data indicates encouraging correlations. Further development of lateral fracture models thus appear to be a promising course for future studies of abrasive wear.

An upper bound estimate of the thermal stresses that result from plastic grooving indicates that these stresses can be appreciable. The stresses are, to a first approximation, independent of the normal force, suggesting that the thermal stresses are likely to be most important at low force levels, i.e., when the lateral fracture mechanism is least effective. The thermal stresses are enhanced by large values of the thermal expansion coefficient, elastic modulus and hardness and small values of the specific heat. Thermal effects are most likely to emerge in materials with these properties. Thermal stresses can either enhance the extent of lateral fracture just above the threshold, or provide an alternate material removal mechanism.

Finally, one other mechanism has been suggested, by analogy with impact problems. It entails the growth of cracks by elastic tensile stress pulses generated by deformable particles. However, no specific estimates of the realm of importance of this mechanism have yet been obtained.

ACKNOWLEDGEMENT

This work was supported in part by the Office of Naval Research and in part by the Division of Materials Sciences, Office of Basic Energy Sciences, U.S. Department of Energy.

REFERENCES

- [1] Gielisse, P. J. and Stanisloa, J., The science of ceramic machining and surface finishing, NBS Special Technical Publication, [348], 5, (1972).
- [2] Swain, M. V., Fracture mechanics of ceramics (Ed. Bradt, R. C., Hasselman, D.P.H. and Lange, F. F.), Plenum, NY, 3, 257, (1978).
- [3] Veldkamp, J.D.B., Hattu, N. and Snyders, V.A.C., Fracture mechanics of ceramics, 3, 273, (1978).
- [4] Evans, A. G. and Wilshaw, T. R., Acta Met., [24], 939, (1976).
- [5] Evans, A. G., Gulden, M. E. and Rosenblatt, M., Proc. Royal Soc., [A361], 343, (1978).
- [6] Lawn, B. R. and Wilshaw, T. R., Journal of Mater. Sci., [10], 1049, (1975).
- [7] Swain, M. V., and Hagan, J. T., Jnl. Phys., [9], D, 2201, (1976).
- [8] Evans, A. G., ASTM Special Technical Publication, in press
- [9] Perrott, C.M., Wear, [45], 293, (1977).
- [10] Tabor, D., Hardness of Metals, Oxford: Clarendon Press, (1951).
- [11] Lawn, B. R. and Evans, A. G., Jnl. Mater. Sci. [12], 2195, (1977).
- [12] Lankford, J., to be published.
- [13] Hamilton, G. M., and Goodman, L. E., Jnl. Appl. Mech., [33], 371, (1966).
- [14] Evans, A. G. and Charles, E. A., Jnl. Amer. Ceram. Soc., [59], 371, (1976).
- [15] Wilshaw, T. R. and Hartley, N.E.W., (Proc. Third European Symposium on Comminution), Chemia GMBH, Weinheim/Bergstrasse, (1972).
- [16] Rice, R. W. and Speronello, B. K., Jnl. Amer. Ceram. Soc., [59], 330, (1976).
- [17] Selsing, J., Jnl. Amer. Ceram. Soc., [44], 419, (1961).
- [18] Evans, A. G., Treatise on materials science and engineering, (Ed. Preece, C.M.), Academic Press, in press.
- [19] Adler, W. F., Jnl. Mater. Sci., [12], 1253, (1977).

Discussion

CHOUDRY

- 1) The superposition of the compressive stress (which occurs during loading) and the tensile stress (which occurs during unloading) could be questioned since these two are operational at different times.
- 2) The calculation of temperatures through the integration of the 'Adiabat' is again to be looked from the time point of view, i.e. during compression σ & ϵ (strain) increase giving the adiabat; which you integrated; however during the tensile relaxation (which is a part of your treatment)

the adiabat would reverse itself (in the absence of internal friction etc.) completely and the heat dissipation (area between the two curves) would be Zero. In any case i.e. even in the presence of internal friction etc, the adiabat integral of your paper would grossly overestimate the temp.

EVANS

1) In elastic/plastic problems, the residual stresses are obtained by subtracting the elastic stresses associated with unloading from the elastic/plastic stress at peak load (See Hill's book on plasticity). This is standard procedure.

2) The thermal stresses calculated in this paper refer to the heat generation in the plastic zone during penetration. This heat results directly from the plastic work (the irreversible component of the penetration) expended during penetration. The unloading, as noted above, is elastic and therefore does not contribute to the heat generation, nor can it absorb the heat generated during penetration. The heat generation does influence the local plastic flow properties, through the temperature dependence of the constitutive equations. The appropriate hardness is thus the 'adiabatic' hardness which may be lower than the isothermal hardness.

M. SRINIVASAN

1. What are the mechanisms by which the lateral cracks curve toward the surface after propagating a distance c ?

2. In such a situation will Mode I critical stress intensity factor alone be sufficient?

EVANS

The residual stress calculations indicate principal tensile stress trajectories that initiate within the plastic zone and progress gradually toward the surface. The conventional wisdom would then anticipate crack development along these trajectories. However, some crack surface interaction should be expected in this case, causing the cracks to approach the surface before the principal tensile stress trajectory reaches the surface. Crack propagation is exclusively Mode I.

S. W. FREIMAN

Based on your analysis of the formation of lateral cracks during machining could you also not calculate the sizes of the radial cracks formed? Shouldn't you then be able to calculate the strength of the workpiece after machining?

EVANS

The radial crack sizes can indeed be characterized according to a similar scheme. The prediction of the strength after machining would also require that the residual stress distribution be known. This could be estimated using the methods described in the paper and then used to predict the strength.

NUCLEATION OF MEDIAN AND LATERAL CRACKS AROUND
VICKERS INDENTATIONS IN SODA-LIME GLASS

J.T. Hagan, M.V. Swain and J.E. Field

Physics and Chemistry of Solids
Cavendish Laboratory
Cambridge/England

The median, radial and lateral cracks that form around Vickers indentations in soda-lime glass have been studied. Cross sections of the plastic indentations have revealed a system of intersecting flow lines in the deformed zone directly beneath the indenter; these flow lines lie close to the elastic shear trajectories beneath a pointed indenter and also around a radially expanding cylinder. It is suggested that the nucleation of both the median (radial) and lateral cracks arise from the inhomogeneous nature of the subsurface deformation. The nucleation of the bulk median crack occurs at the intersection point of two limiting flow lines and is therefore similar to crack nucleation from a pile of dislocations at an obstacle, or the interaction of dislocations on two intersecting slip planes. The radial cracks are nucleated from the interaction of similar flow lines that develop on the sample surface and around the indentation. The lateral cracks appear to form as shear cracks along the flow lines and are propagated by the unloading residual stresses. The interaction of the flow lines may also be responsible for the powdering or crushing of material that occurs at high indenter loads.

Key Words: Fracture; plastic indentations; crack nucleation; median, radial and lateral cracks; shear flow lines; residual stresses.

1. Introduction

When blunt or sharp indenters are loaded slowly or impacted on brittle solids, the extensive cracking - median, (radial) and lateral cracks - that forms around the contact can lead to erosion, wear and strength degradation. These cracks are also basic to such processes like abrasion, machining and drilling since all these processes may be regarded as the summation of damage at all contact sites. The relevance of these cracks to a better understanding of the above processes demands a proper study of the origins of the various cracks that develop around blunt (elastic) and sharp (plastic) indentations.

The case of the radial, median and lateral cracks around blunt contacts during impact has been treated by Chaudhri and Walley [1] and it will not be considered here; they, however, suggest that the radial and lateral cracks, that develop during elastic impact, arise from purely frictional effects between the newly created fracture surfaces as they are brought together during overloading.

Of more interest, however, are the median, radial and lateral cracks that form around plastic indentations; this is because they form at loads as low as 0.5N. This paper is, therefore, concerned primarily with the origins of the median, radial and lateral cracks that develop around plastic pyramidal indentations.

These cracks are illustrated in figure 1. The median (radial) cracks, pp, form across the major diagonals of the plastic indentation; the lateral cracks are subsurface cracks that give rise to the halo, h, around the plastic indentations. Within the plastic zone itself and extending from the edge of the indentation is an annular ring of cracks, cz; these are clearer in figure 1b which shows a Vickers indentation in toughened soda-lime glass. The cross-sectional views are illustrated schematically in figure 2. The median crack is a semi-circular crack, npn, with the deformed zone (the hatched region) at its origin; pp is the section of the other orthogonal crack. The radial cracks, rc, are

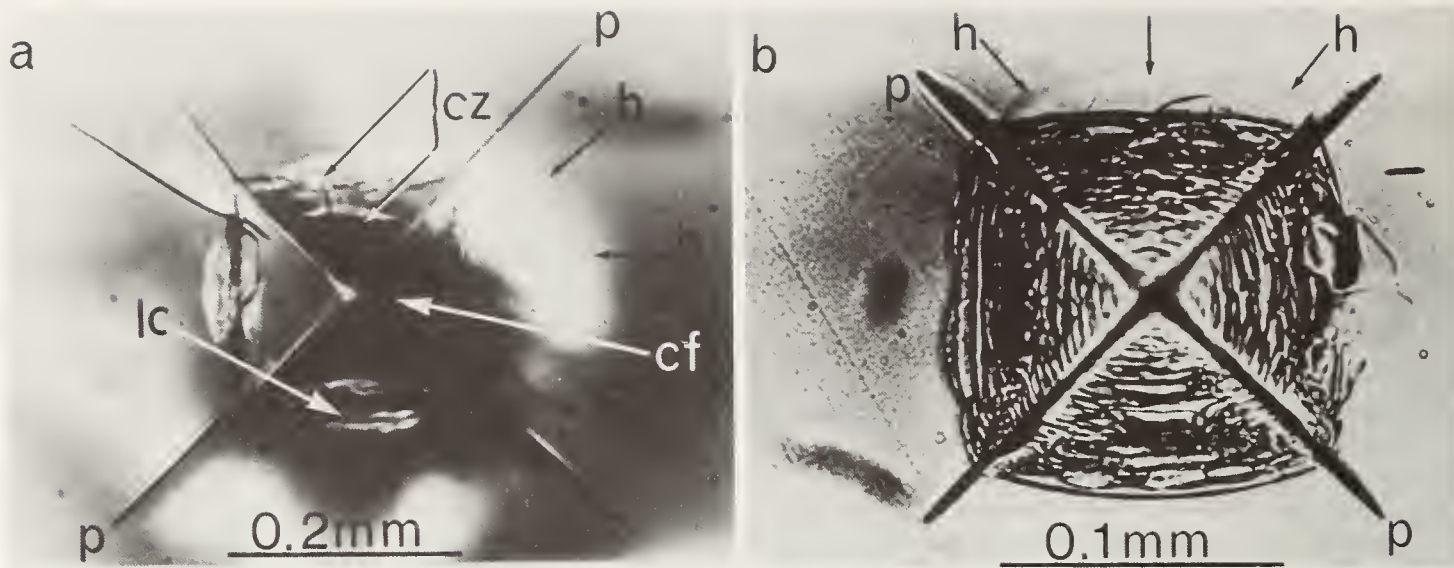


Figure 1. Vickers indentations in annealed and toughened soda-lime glasses respectively.

shallow surface cracks which emanate from the edge of the deformed zone: the different situations which give rise to radial rather than median cracks are discussed later. The lateral cracks, lc, develop from the bottom of the deformed zone and extend in saucer-like fashion to the specimen surface [fig. 2]. (See Lawn and Swain [2], Swain and Hagan [3] and Hagan and Swain [4] for a full description of these cracks).

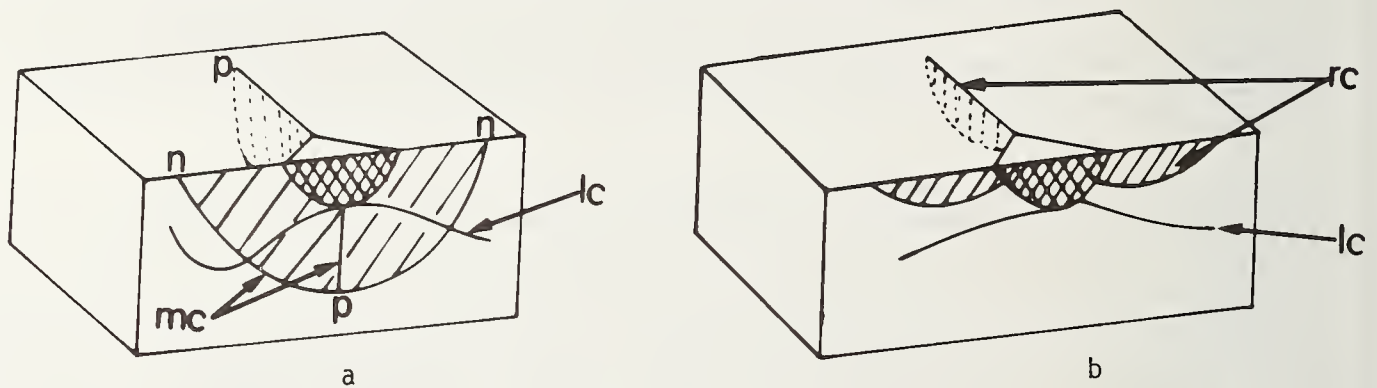


Figure 2. Schematic of median, lateral and radial cracks, mc, lc, rc, respectively around sectioned Vickers indentations. The oval-hatched zone marks the extent of the deformed zone.

The propagation of these cracks, especially of the median cracks, is fairly well understood and there are standard fracture mechanics expressions to describe the propagation (Lawn and Fuller [5], Evans and Charles [6]). The more important problem of the initiation of these cracks has not been treated. The initiation process is often complicated by the fact that the material may be crystalline or amorphous and material properties like grain size, d , hardness, H , and the critical stress intensity factor K_{IC} would be expected to influence the nucleation process. Lawn and Evans [7] have recently suggested a model for the nucleation of the median crack in glasses. Their model relies on the existence of subsurface fortuitous flaws of the right critical dimensions in the vicinity of the elastic-plastic boundary where the tensile stresses are highest. In this paper we present a new model for the origins of the median and lateral cracks around plastic indentations in soda-lime glass. Details of this model have been published by Hagan and Swain [4].

2. Experiments

Since the median and lateral cracks are associated with the plastic deformation under the indentation, the study of the origins of these cracks requires examination of cross-sectional views of the plastic indentations. The indentations were sectioned by making the indentation on and near the tip of a pre-existing crack. Similar sectioning technique has been employed by Peter [8] and Mulhearn [9].

3. Results

A summary of the observations are illustrated with figures 3 and 4; figures 3 and 4 show the surface and sub-surface damage around and under Vickers indentations in soda-lime glass, at indenter loads of 2N and 50N respectively. Figures 3a, and b illustrate surface traces of the radial or median cracks around the plastic indentation on the specimen surface. The halo, h, around the plastic indentation in figure 3b is reflected light from the sub-surface lateral cracks. The sub-surface view consists of a deformed zone, dz, directly beneath the indenter, and the lateral cracks, lc, which emanate from the bottom of the deformed zone. At such low indenter loads, there is no evidence of the trace of the median crack in the bulk. The traces on the specimen surface are therefore shallow radial cracks confined to narrow regions of the specimen surface and are propagated by unloading residual stresses. In most cases the radial cracks could be watched propagating after the load has been taken off completely.

At the higher indenter load of 50N (fig.4) the surface damage consists of traces of the characteristic radial/median and lateral cracks. There are also some shallow cracks, cz, in figure 4a, that occur within the surface of the plastic indentation itself. Similar observations have been reported by Müller[10]for Vickers indentations in phenolic resin. The sub-surface deformation consists of a deformed zone and traces of both the median and lateral cracks, mc and lc respectively, as in figure 4b. The deformed zone is made up of a series of intersecting inhomogeneous flow lines which are characteristic of materials undergoing radial flow (Peter, [8] and Nadai [11]). These flow lines are clearer in

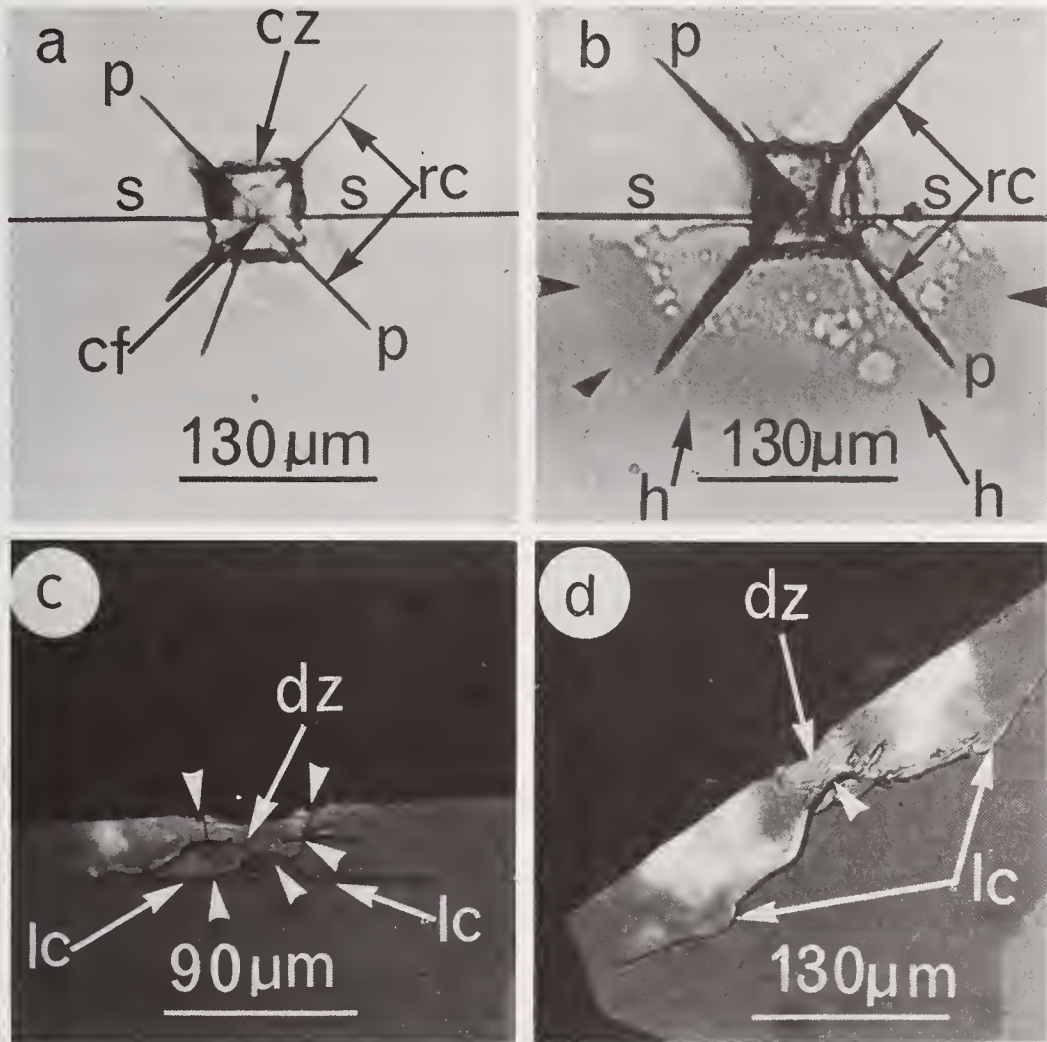


Figure 3 (a), (b) show 2N Vickers indentations on a pre-existing crack, ss. The sub-surface views (c) and (d) show no evidence of median cracks and are dominated by the lateral cracks.

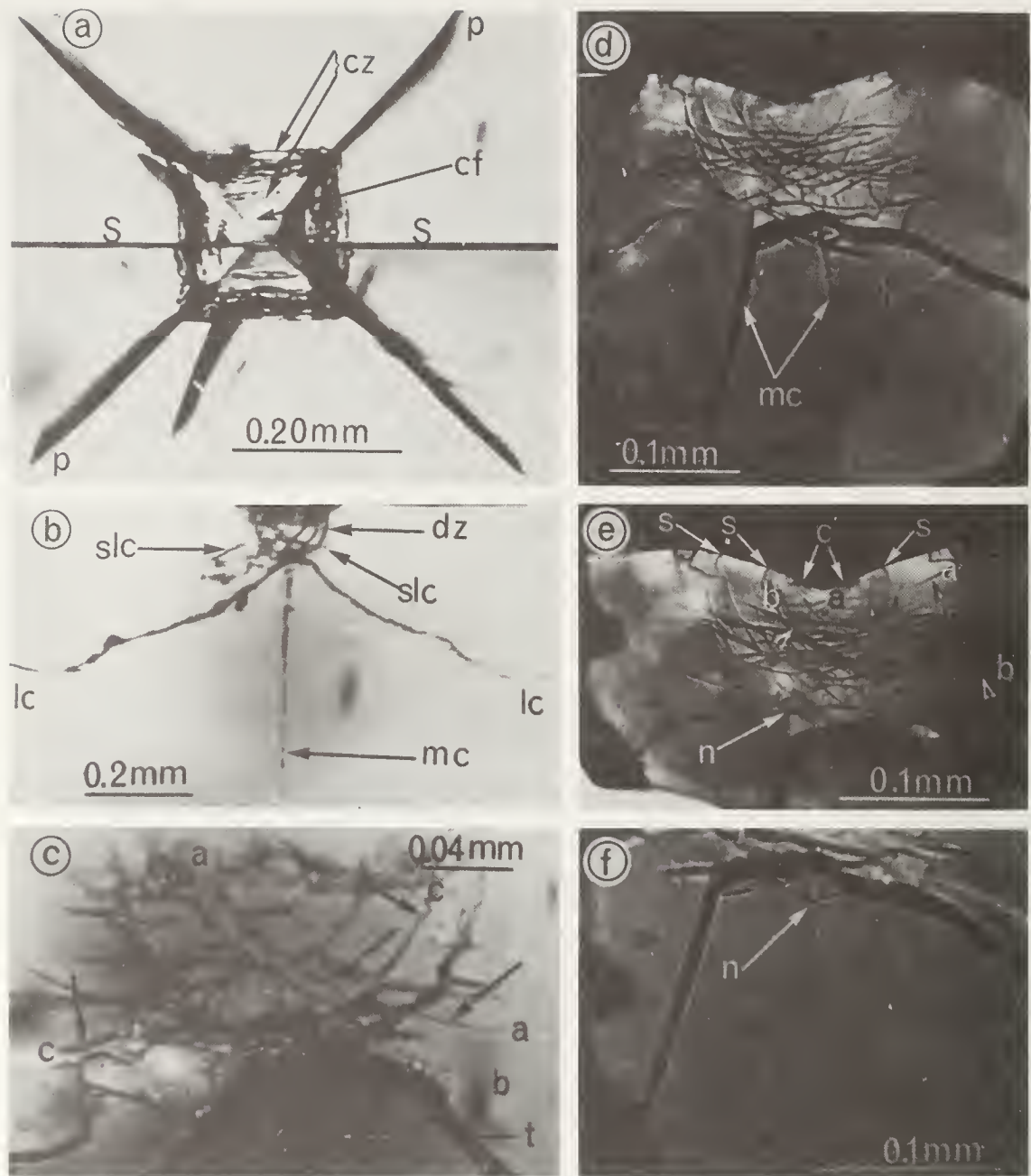


Figure 4 (a), (b) and (c) are surface and sub-surface views of a 50N Vickers indentation. Sub-surface deformed zone, dz, consists of network of flow lines aa,bb and cc as in (c); (d), (e) and (f) show sub-surface damage of another 50N indentation.

figures 4d-f which are sub-surface deformation of another 50N load indentation. Some of the flow lines, arrowed in figure 4d, appear to degenerate into lateral cracks outside the plastic contact; they also coincide with the short shallow cracks, ss, within the surface of the plastic indentation. The dominant lateral cracks, lc, again emanate from the bottom of the deformed zone (figure 4b). The trace of the median cracks appears at the bottom of the deformed zone at t and n the intersection points of two of the flow lines in figure 4.

At higher indenter loads, extensive crushing of the material within the deformed zone occurs and the flow lines become unresolvable. Such entanglement of shear flow lines and the subsequent break up of material within the deformed zone may constitute the early stages of the crushing of the material within the contact zone.

4. Discussion

From the sub-surface deformation, it is obvious that the radial, median and lateral cracks are nucleated as a result of the inhomogeneous nature of the deformation beneath the indenter.

It appears that the lateral cracks are nucleated as a result of the special nature of shear deformation in glassy materials; shear deformation in glassy materials in the absence of any long range order is non-constructive, and the overstraining of atomic bonds leads to bond breakage and the degeneration into shear cracks. These cracks, however, do not propagate under load because of the compressive stresses that exist across the prospective crack path. The driving force for the propagation of these lateral cracks is provided by the unloading residual stresses that develop around the indentation as the load is taken off.

The nucleation of the median cracks at the points of intersection or blocking points on a flow line is similar to crack nucleation from the interaction of dislocations on two intersecting flow lines or the pile up of edge dislocations against an obstacle (see Zener [12], Stroh [13]). The nucleation and propagation of the median crack is therefore by the wedging action of the deformed zone beneath the indenter and not by the indenter itself as is commonly believed and on which most analyses are based; this is, however, only true for wide angle (blunt) wedge for which the deformation is radially from the indenter faces.

The shallow radial cracks confined to the specimen surface are probably nucleated by the interaction of similarly occurring flow lines that develop on the surface of the specimen (Peter [8]). These radial cracks may also form to accommodate displacement of material in two orthogonal directions from the indenter faces.

The shallow surface cracks, c_z (figure 3a) within the plastic indentation may be traces of the sub-surface flow lines on the surface. They are more probably formed by the large component of elastic stresses which are associated with wide angle indentations in highly elastic solids (Hirst and Howes, [15]). These cracks are therefore similar to ring cracks associated with Hertzian elastic contacts except that they do not reflect the symmetry of the indenter (Hagan and Swain [4], Hagan [16]).

5. Conclusions

It has been established that the cracks that develop around plastic indentations in solids arise from the inhomogeneous nature of the sub-surface deformation. This has been confirmed by recent studies of sub-surface deformation of indentations in LiF and NaCl. It is also obvious that the median and radial cracks would be mainly responsible for the strength degradation of materials. The propagation of the lateral cracks from the bottom of the deformed zone in a saucer-like manner to the specimen will remove material with it as it propagates; these lateral cracks will therefore enhance the erosion of the brittle materials. For efficient grinding and polishing, however, the dominant median crack should be avoided by using low polishing loads but high enough for sub-surface lateral cracks to extend to the surface. The interaction of the shallow radial cracks with the sub-surface lateral cracks would be responsible for material removal without introducing the strength degrading median cracks.

The authors are grateful to Dr. M.M. Chaudhri for useful discussions and comments on the paper. This work was supported by the Ministry of Defence (Procurement Executive) and the Science Research Council.

References

- [1] Chaudhri, M.M. and Walley, S.M., Damage to glass surfaces by the impact of small glass and steel spheres, *Phil. Mag.* Vol. 37, 2, 153-65 (1978)
- [2] Lawn, B.R. and Swain, M.V. Microfracture beneath point indentations in brittle solids, *J. Mater. Sci.*, 10, 113-22, (1978)
- [3] Swain, M.V. and Hagan, J.T., Indentation plasticity and ensuing fracture of glass, *J. Phys. D: Appl. Phys.* 9, 2201-14, (1976)
- [4] Hagan, J.T. and Swain, M.V., The origin of median and lateral cracks around plastic indents in brittle materials, *J. Phys. D: Appl. Phys.* 11, 2091-202, (1978)
- [5] Lawn, B.R. and Fuller, E.R., Equilibrium penny-like cracks in indentations, *J. Mater. Sci.* 10 [1], 113-22 (1975)
- [6] Evans, A.G. and Charles, E.A., Fracture toughness determination by indentation, *J. Am. Ceram. Soc.* 59 [7-8] 371-2, (1976)
- [7] Lawn, B.R. and Evans, A.G., A model for crack initiation in elastic/plastic indentation fields, *J. Mater. Sci.*, 12, 2195-9, (1977)
- [8] Peter, K.W., Densification and flow properties of glass in indentation experiments, *J. Non. Cryst. Solids*, 5, 103-15 (1970)
- [9] Mulhearn, T.O., The deformation of metal by Vickers-type pyramidal indenters, *J. Mech. and Phys. of Solids*, 7, 85-96, (1959)
- [10] Muller, K., Determination of Vickers hardness under load - a method considering viscoelastic behaviour of plastics. The science of hardness testing and its research applications, J.H. Westbrook and H. Conrad eds, pp.291-9, (ASM, Metals Park, Ohio, 1973)
- [11] Nadai, A., *Plasticity* (McGraw Hill - N.Y., 1931)
- [12] Zener, C, *Fracturing of metals* pp. 3-31 (Cleveland, Ohio; Am. Soc. Metal 1948)
- [13] Stroh, A.N., A theory of the fracture of metals, *Advances in Physics*, 6, 418-65 (1957)
- [14] Hirst, W. and Howse, M.G.J.W., The indentation of materials by wedges, *Proc. Roy. Soc. A311*, 429-44, (1969)
- [15] Hagan, J.T., unpublished work, (1978)

Discussion

GIELISSE

Would, under continued loading, the lateral cracks continue to go downwards, as initially divested or come up to the surface? Have you followed crack extension under continued loading experimentally in time?

HAGAN

We have not followed the lateral crack extension during continual loading; this has, however, been done for the median crack though. The main

driving force for the propagation of the lateral cracks is provided by the unloading residual stresses. Continued loading will, however, provide an overloaded system and it is possible for the flow lines to break through the specimen surface outside the contact area. Note that the flow lines are not just directed downwards, but they follow logarithmic spiral trajectories and there is a tendency for them to turn towards the surface.

HOCKEY

Did you notice the formation of cone cracks beneath sharp indenters in glass?

HAGAN

No, we did not observe any cone cracks around Vickers indentations in soda-lime glass. However, the shallow cracks, CA, in Fig 16 probably arise from the large elastic radial tensile stresses which develop on the surface of the specimen for Vickers indentations in highly elastic solids. These cracks are, therefore, similar to the collar on the 'skirt' of cone cracks. In fact, for Vickers indentations in fused silica glass, the dominant cracks are the cone cracks.

FRAGMENTATION AND DAMAGE PENETRATION DURING ABRASIVE MACHINING OF CERAMICS

H. P. Kirchner, R. M. Gruver, and D. M. Richard

Ceramic Finishing Company
State College, PA 16801

Mechanisms of fragmentation and damage penetration during abrasive machining of ceramics were investigated using indentation fracture mechanics. Specimens of glass and hot pressed silicon nitride were damaged by controlled scratching and single point diamond grinding. Vertical and horizontal forces acting on the material were measured for various diamond shapes, set depths and wheel speeds. The damage was characterized by optical and scanning electron microscopy. Cracks, similar to those formed by static contact and particle impact, were observed. The vertical forces were correlated with the extent of damage yielding results consistent with those expected based on indentation fracture mechanics.

Initially, the penetration of damage was analyzed in terms of point contact loading. This analysis resulted in improved understanding of the effect of diamond shape on the variations of the forces and damage penetration which were manifested by variations in the dimensionless contact constant χ . Subsequently, the results were analyzed in terms of line contact loading which allowed the results for hot pressed silicon nitride and various diamond shapes to be represented by a single value of χ .

Key Words: Abrasive machining; grinding; ceramics; glass; silicon nitride; impact; contact stress; stress intensity factor; fracture mechanics; fragmentation; damage penetration; strength.

1. Introduction

Empirically developed processes are used for abrasive machining¹ of ceramics despite several efforts to establish a more scientific basis for these processes [1-7]. It is highly desirable to develop methods to control fragmentation, to minimize penetration of subsurface damage and to increase the efficiency of material removal. To aid in accomplishing these objectives, it is necessary to have improved understanding of the fracture mechanisms. Based on extensive studies of mechanisms of localized impact damage [8-20], there has been a growing conviction that the methods of indentation fracture mechanics can be applied to aid in understanding of ceramic machining. This approach is the basis of the present investigation.

The various types of damage occurring during localized impact are sketched in figure 1. These include Hertzian cone cracks, lateral vent cracks, and radial cracks [8,14]. In addition, crushing is frequently observed. Hertzian cone cracks are formed by static contacts or low velocity impacts with blunt objects such as spheres or punches. Impact velocities during abrasive machining are in this low velocity range (10-100 ms⁻¹). Even though there are many similarities between the damage resulting from "static" contact loading and that from impact loading, there are also significant differences. One such difference is that, in impact loading, there is less subcritical crack growth so that fractures originate at higher stresses. In the case of Hertzian cone cracks, the ring

¹Abrasive machining includes grit blasting, free abrasive machining and other processes, as well as grinding.

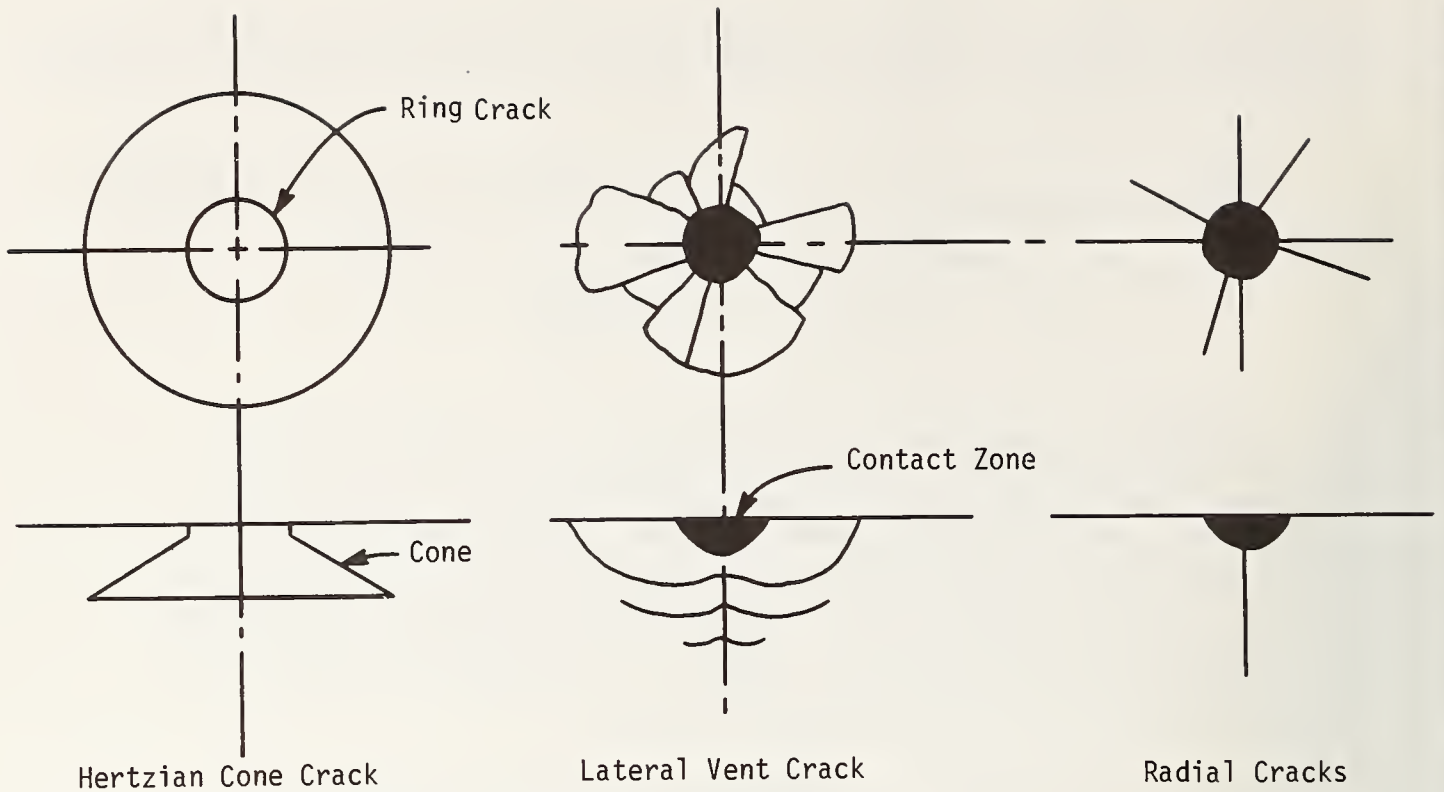


Fig. 1. Types of cracks formed by localized impact.

cracks formed at the surface may branch at regular intervals which are determined by the fracture stress and the crack branching stress intensity factor of the target material [16]. The wedge-shaped fragments formed by this crack branching mechanism may subsequently be subject to material removal.

Impacts by either sharp objects or blunt objects at relatively high velocities cause radial and lateral vent crack formation. Radial cracks may be perpendicular to the surface, radiating from the impact site as shown in the top right hand view in figure 1, but also may occur at other angles to the surface. Radial cracks arise because, as indentation increases, the tensile stresses tangential to the contact area increase and the radial stresses decrease, causing a shift from ring cracks to radial crack formation.

Lateral vent cracks are saucer shaped cracks that form mainly parallel to the surface but that tend to come to the surface at the periphery. These cracks form, as the load is released, by reaction of the elastically deformed material against the permanently deformed material in the contact zone. Because these cracks form after the radial cracks, they are frequently separated into segments extending between the radial cracks. When the cracks extend to the surface at the periphery, these segments are frequently removed as chips or fragments. Because of this tendency toward material removal by lateral vent crack formation, Lawn and Wilshaw [8] and others have suggested that this mechanism is responsible for material removal during abrasive machining processes such as grit blasting or grinding.

The depth of penetration of surface damage and its subsequent subcritical crack growth are the principal factors controlling the strength and integrity of ceramics intended for use in structural applications. This surface damage may be induced when the part is machined during the original manufacturing process or subsequently during use. Clearly, for optimum performance, the ceramics should leave the manufacturing process with minimum surface damage. Penetration of surface damage and the effect of surface damage on the remaining strength were investigated previously for scratched and indented specimens [21-24]. Since that time, the new information from impact investigations has become available making possible new approaches to understanding abrasive machining processes.

The depth of damage induced by contact stresses can be estimated by the following equation [25]

$$K_{IC} = \chi \frac{P}{C^{3/2}} \quad (1)$$

in which K_{IC} is the critical stress intensity factor for the particular material, P is the contact force or load, C is the crack depth, and χ is a dimensionless contact "constant" that incorporates the effects of uncertain geometrical factors, interface friction, etc. χ can be determined in special cases from the theory of hardness indentations but is usually determined by experiment. Appropriate subscripts can be used with χ and C to designate the symbols related to various types of cracks such as Hertzian cone cracks, lateral vent cracks and radial cracks. The analysis assumes that the crack propagation in the far field is independent of the conditions (indenter shape, surface roughness) in the contact zone. However, experience has shown that many important cases fall in a less severe damage range.

One objective of this research was to investigate the applicability of eq. (1) to damage caused by abrasive machining. This included characterization of the various types of damage and determination of appropriate values of χ for these types of damage and abrasive machining conditions. The effects of variables such as abrasive grain shape, set depth, and wheel speed (impact velocity) were investigated.

The remaining strengths of ceramics with subsurface damage were estimated using

$$K_{IC} = Y \sigma_F C^{1/2} \quad (2)$$

in which σ_F is the fracture stress and Y is a dimensionless constant determined by crack shape and proximity to the surface. Values of Y have been determined by fracture mechanics techniques for a wide variety of cases [26,27]. Equations (1) and (2) can be combined and solved for the remaining strength (σ_F) by eliminating the crack length (C) yielding

$$\sigma_F = \frac{K_{IC}^{4/3}}{Y \chi^{1/3} P^{1/3}} \quad (3)$$

It has been common to use eq. (3) to describe the effect of surface damage on the strength of ceramics without verifying that the cracks do grow to the predicted dimensions. In the present investigation, the surface damage was introduced by scratching and single point grinding and care was taken to characterize the cracks to assure that the crack dimensions were properly accounted for by the above equations.

2. Procedures

2.1. Materials

Several criteria were used to select materials for this investigation. Perhaps the most important criterion was the ease with which cracks and other damage could be observed. This criterion was the principal reason for the selection of soda-lime-silica glass² and hot pressed (H.P.) silicon nitride³. Other factors considered were the potential importance of the materials as structural ceramics, availability and cost.

2.2. Techniques for material removal

Two techniques were used to remove material from ceramic surfaces; scratching and single point diamond machining. For scratching tests, a microtome which consists of a

²Float glass, Centre Glass, Inc., State College, PA, thickness 6 mm.

³NC-132, Norton Company, Worcester, MA, grain size 1-2 μ m.

massive carriage sliding very smoothly on metal ways was modified to provide a means to press a loaded diamond point against a ceramic plate specimen mounted on the carriage while the carriage was pulled past the diamond point at approximately constant speed by means of a weight acting on a cord running through a pulley. The diamond points, which were 75° coned wheel dressers were loaded with various weights to form scratches of various depths [23].

The single point diamond machining was done using an apparatus located at the Department of Chemical Engineering, University of Rhode Island. The equipment consists of a high speed milling machine⁴ with pressure cylinders arranged to drive the table under the tool at a constant speed of 0.017 ms⁻¹. A dynamometer, mounted on the table was used to measure the vertical and horizontal forces transmitted from the tool to the specimen. The forces were converted to electrical signals by Kistler quartz load cells (Model 504A) and displayed on a Tektronix Type 564 storage oscilloscope. In most cases, the traces were photographed to provide a permanent record of the forces experienced by the specimen (Fig. 2).

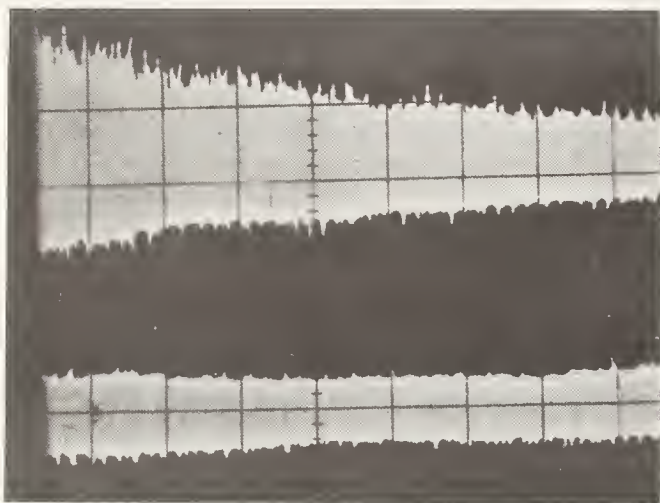


Fig. 2. Load traces for single point grinding of H.P. Si₃N₄, top trace is vertical force (50 μm flat, 25 μm set depth, wheel speed 8000 rpm).

The forces were calibrated using a pendulum falling from known heights. This apparatus was used to construct calibration curves giving the actual vertical and horizontal forces in terms of the nominal forces determined taking into account the transducer range, vertical scale setting of the oscilloscope, etc. Usually, the vertical forces were larger than the horizontal forces. The results were analyzed in terms of the vertical forces because this is the principal factor controlling penetration of surface damage.

The diamond points used in these experiments were single crystals ground to form 120° cones. Normally, the tip radii were about 40 μm. In some cases flats were ground on the tips to form truncated cones. These flats were 50 or 100 μm in diameter. The diamond points were fastened to the periphery of a two and one-half inch diameter wheel which rotated at speeds ranging from 4,000 to 12,000 rpm.

A typical test was performed as follows:

1. The height of the diamond was adjusted so that it would traverse the specimen at the desired depth beneath the surface.
2. The wheel speed was adjusted to the desired value using a stroboscope (General Radio 1531-AB).
3. The horizontal trace on the oscilloscope was adjusted so that the load was recorded just as the diamond point entered the specimen and recording stopped when the specimen had traversed the entire distance under the diamond point. The vertical traces represent the load calibrated in arbitrary units.

⁴Precise Milling Machine, Model II.

4. The trace on the oscilloscope was photographed.
5. The diamond point was examined for possible damage using a magnifier.

All of the present tests were performed using down grinding; that is, the table and the diamond point were moving in the same direction during contact.

2.3. Characterization

Standard nomenclature for describing the features formed by the diamond points was previously adopted [23]. The term "scratch" refers to the entire result of scratching or single point grinding and includes both surface and subsurface effects. The "track" is the path formed by the diamond point in the surface. The individual striations in the track are called "grooves."

The damage was characterized by optical and scanning electron microscopy (SEM). Various methods were used to expose the subsurface damage. In some cases, the specimens were beveled through the track (1-2° bevel). The beveling was done by holding the specimens at the desired beveling angle on a lap rotating from the edge of the bevel back toward the track. This direction of rotation was used to avoid extending the subsurface damage. The effect of beveling is to expose the subsurface damage along the beveled surface. In other cases the specimens were notched from the surface opposite that containing the track. Then, the specimens were fractured back from the notches toward the tracks, thereby avoiding propagation of the machining damage. The swarf and the changes in the diamond points were also characterized.

The remaining strengths of the damaged specimens were measured in flexure by three point loading on a one inch span at a loading rate of 20 Ns⁻¹.

3. Results and Discussion

3.1. Scratching experiments

Glass plates, approximately 10.7 x 4.3 x 0.6 cm, were scratched using various loads. In each case the specimen was scratched lengthwise along the center of the large face. Then, the plates were cut crosswise to form bars and a large fraction of the bars were fractured to measure the remaining strength after scratching. Thus, the scratches were parallel to the fracture surfaces. In almost all cases the fractures originated at the scratches. The depths of damage were measured by viewing the damage through the sides of glass bars using a microscope with a scale in the eyepiece. At a low load (9N) a very smooth track was formed. At higher loads the tensile stresses behind the diamond point generated characteristic U-shaped cracks. At the highest load (38N) lateral cracks were formed on both sides of the track.

The loads (P) were plotted vs. the depth of damage raised to the three halves power as suggested by eq. (1), in figure 3. Taking the slope as K_{IC}/χ with $K_{IC} = 0.8 \text{ MNm}^{-3/2}$ [28] yielded $\chi = 0.053$. This estimate is higher than a previous value obtained by impact tests [17]. The data are too sparse to prove that the depth of damage varies with load as predicted by eq. (1) but the results are consistent with this possibility.

The variation of the average fracture stresses with the inverse square root of the depth of damage was plotted based on eq. (2) and compared with theoretical curves for semi-circular and edge notch flaws (fig. 4). The slope indicated by the data is close to that for edge notch flaws, perhaps indicating that the scratches act as edge notches. The average remaining strengths are plotted vs. the load on the diamond point in figure 5. Six to 10 results were averaged for each load. Results for a total of two specimens in which the fractures did not originate at the scratches and three specimens that yielded unusually high values were omitted from the averages. The fracture stress decreases with increasing load on the diamond point as expected. The average remaining strengths are plotted vs. $P^{-1/3}$, as suggested by eq. (3), in figure 6. Although the range of the data is limited, the results are consistent with a straight line through the origin.

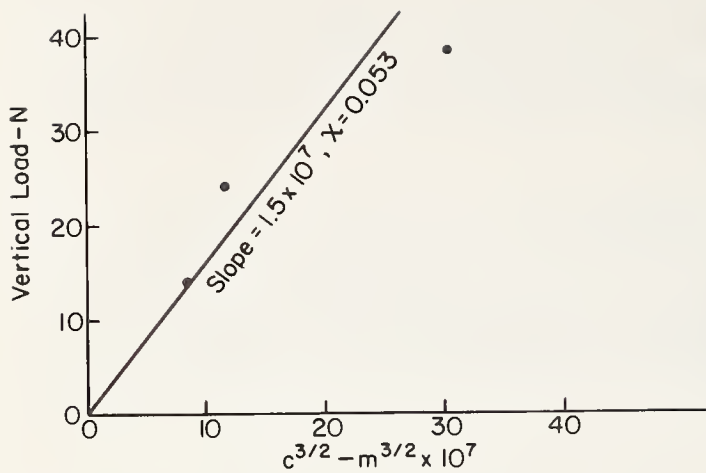


Fig. 3. Vertical load vs. $c^{3/2}$ for glass scratched by a diamond point.

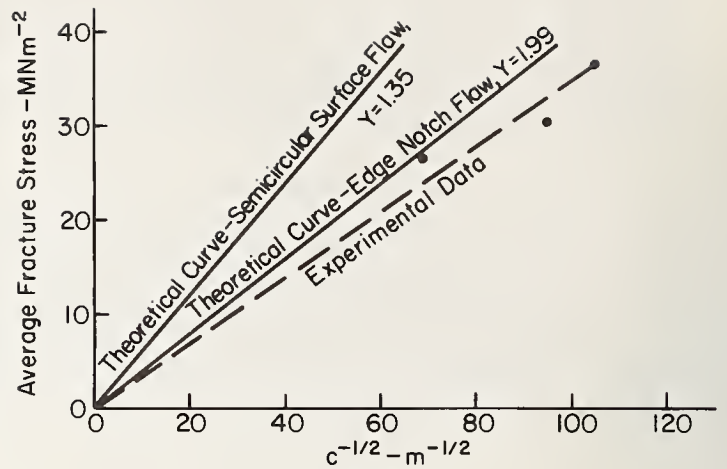


Fig. 4. Average fracture stress vs. $c^{-1/2}$ for glass scratched various loads.

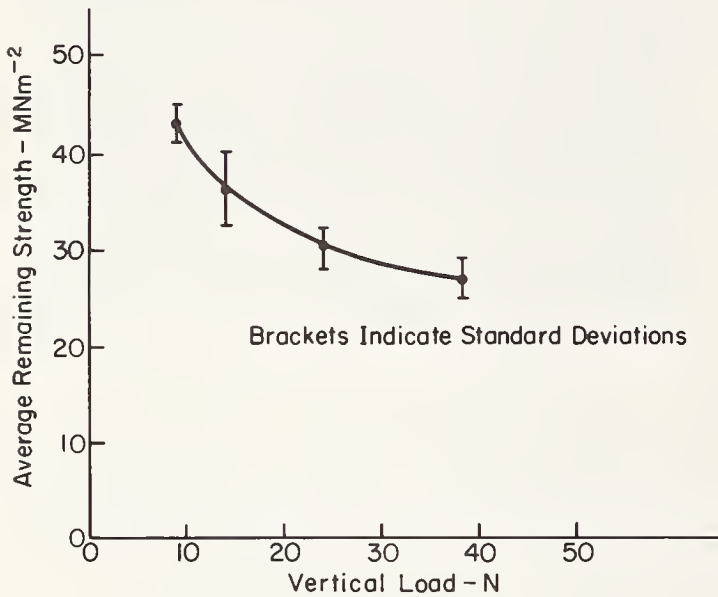


Fig. 5. Average remaining strength vs. vertical load for scratched glass plates.

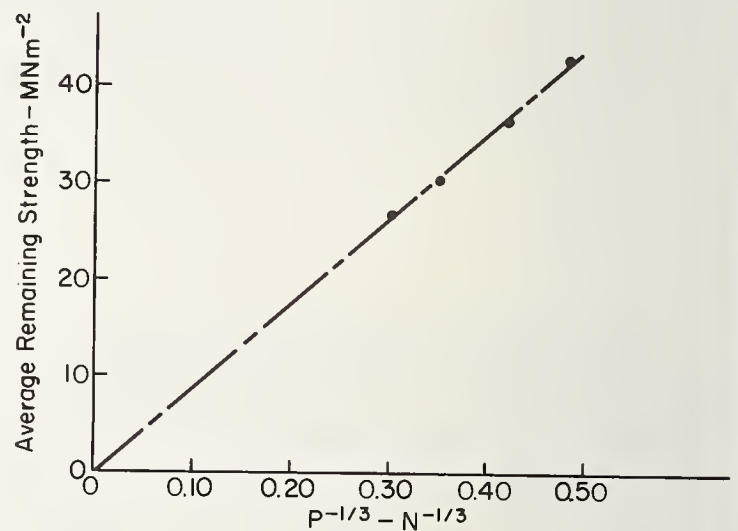


Fig. 6. Average remaining strength vs. $p^{-1/3}$ for scratched glass plates.

H.P. silicon nitride plates (4 x 14 x 0.3 cm) were ground and lapped. Then, the plates were carefully scratched lengthwise by a diamond point under various loads and cut crosswise to form bars. The depths of scratch damage were measured. As shown in figure 7, the tracks do not contain deep grooves. The smoothness along the track may indicate microplastic flow under the diamond point. A crack projects downward from the track. Examination of a 1° bevel through a track shows that there has been considerable loosening of the individual grains in the material under the track. This loosening led to frequent pull out of the grains as the bevel was lapped.

The variation of the crack depth (C) with load on the diamond point is illustrated in figure 8. The load is approximately linear with $C^{3/2}$ as expected based on eq. (1) although it appears that a somewhat better fit would result from using a lower exponent. Taking $K_{IC} = 4.7 \text{ MNm}^{-3/2}$ [29], the value of χ was calculated from the slope of the curve in figure 8, yielding a value of 0.20.

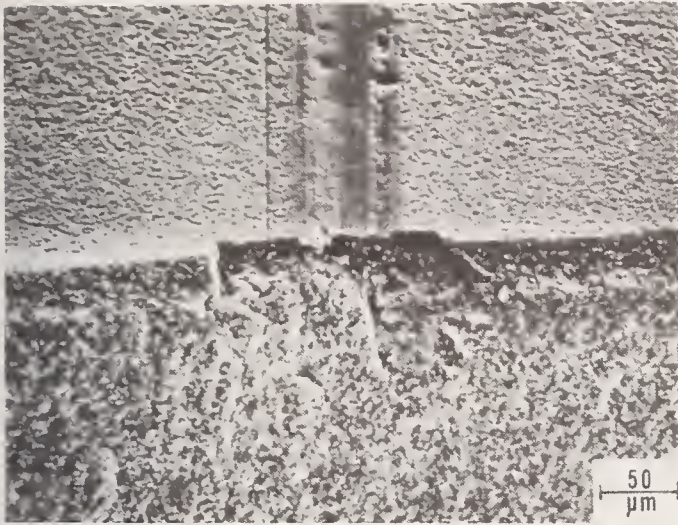


Fig. 7. Track and subsurface damage in H.P. silicon nitride (vertical load 38 N).

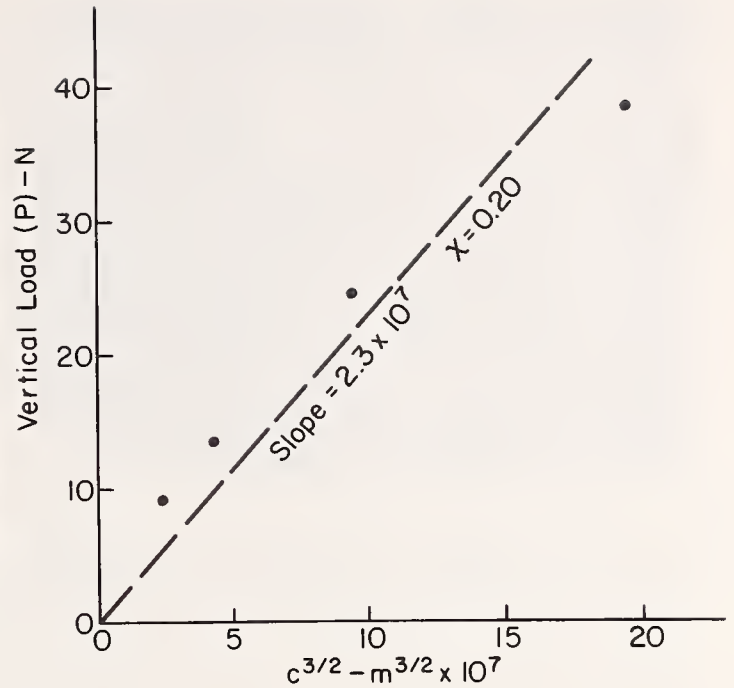


Fig. 8. Vertical load vs. (Crack Depth)^{3/2} for H.P. Si₃N₄ scratched with a diamond point.

3.2. Single point grinding experiments

3.2.1. Glass

Glass was machined by single point grinding in two series of experiments. In the first series, the set depth (the depth to which the diamond is set to penetrate the glass) was varied from 25-100 μm , using "sharp" diamonds. Examination of the results gave the impression that the observed damage was too severe to be realistic in terms of practical applications. Therefore, in the second series smaller set depths, 13 and 25 μm , were used. Also, the sharpness of the diamond points was varied by using both sharp diamonds and diamonds in which the tips were blunted to form flats 50 or 100 μm in diameter.

The impact causes fragmentation of glass in the track and crack formation under and alongside the track. The fragments have a bimodal size distribution. Large numbers of very fine particles (1-5 μm) are produced in the grooves by crushing. Frequently, these particles are packed against the sides of the grooves as the diamond point passes. Smaller numbers of large fragments (40-400 μm) form by chipping of material at lateral cracks alongside the track. The shapes of these cracks and the resulting fragments are similar to those of lateral vent cracks observed to result from impact and "static" indentation. Although investigators of machining damage have referred to these cracks by several other names, they will be referred to as lateral or lateral vent cracks in this investigation. The damage under the tracks was studied. Blunt diamonds form wider tracks than those formed by sharp points. Figure 9 shows the damage under a track formed by a 100 μm flat diamond at 25 μm set depth and 6000 rpm. The wide track formed by this diamond and the wide separation of the radial cracks under the track are characteristic of the damage due to blunt diamonds. Voids caused by removal of chips formed by lateral cracks are shown on both sides of the track.

In some cases the forces at the start of the scratch were greater than those farther along in the scratch. Apparently, the initial impact was sufficient to induce vibrations in the wheel, shaft and mounting which resulted in these higher forces which were damped

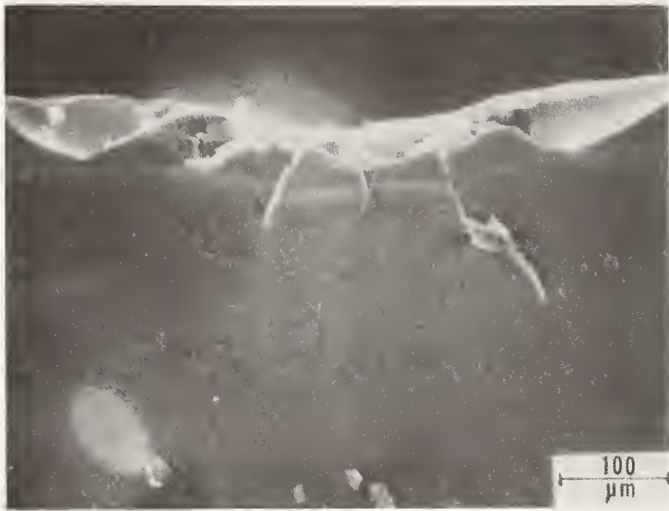


Fig. 9. Subsurface damage in glass ground with 100 μm flat diamond with 25 μm set depth, 6000 rpm.

out as the grinding continued. The forces increased with increasing set depth, as expected. When the specimens were not quite flat, or were mounted not quite parallel to the table travel, the depth of cut varied during the traverse with corresponding variation in the forces. One might expect that, at constant table speed, increasing the wheel speed would decrease the volume of material swept out by the diamond point on each rotation and thus decrease the forces but this decrease in forces was not observed consistently with glass. The forces increase with decreasing sharpness of the diamond point as expected; that is, the forces increased in the series sharp point \rightarrow 50 μm diameter flat \rightarrow 100 μm diameter flat.

In order to learn more about the variation of force with groove depth⁵ and to explain some of the observations in the previous section, the groove depths were measured at intervals along some of the tracks yielding interesting results. The increase in groove depth with vertical load is illustrated in figure 10. The variations of the groove depths for tracks made at 4000 and 12000 rpm are shown in figure 11. Groove depths are, with few exceptions, much greater than the set depths and the differences between groove depths and set depths are greater at 12000 rpm than at 4000 rpm. This latter observation indicates why the forces do not decrease consistently with increasing wheel speed. Evidently, the extra force necessary to remove the added depth at higher wheel speed is offset to some degree by the decrease in the horizontal distance swept out so that whether there is an increase or decrease in the force in a particular case depends on the balance of these opposing effects.

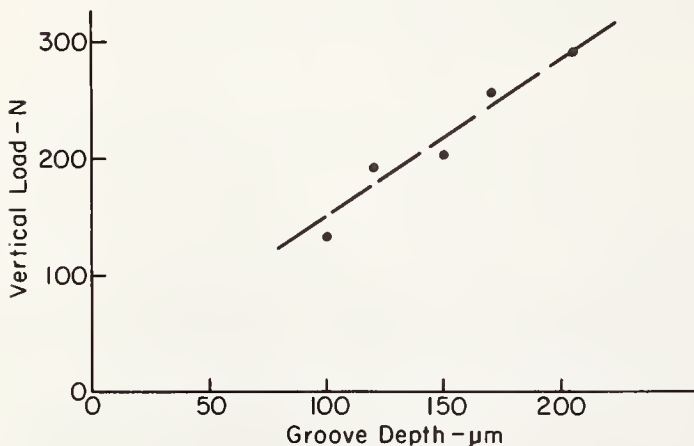


Fig. 10. Vertical load vs. groove depth for single point grinding of glass (set depth 50 μm , 4000 rpm, track no. 14).

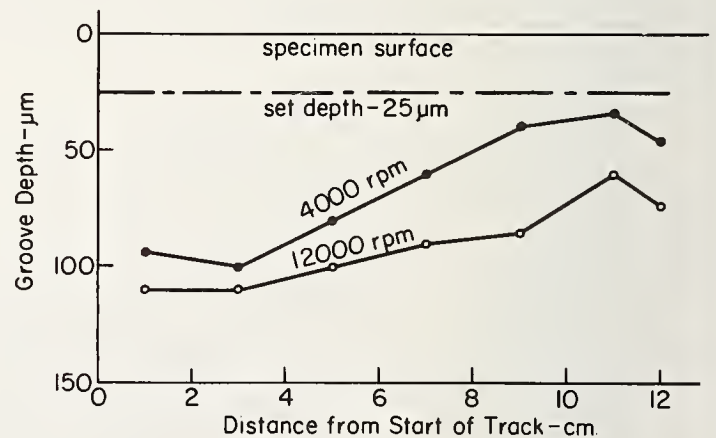


Fig. 11. Groove depth vs. distance from start of track for single point grinding of glass (set depth 25 μm , tracks 3 and 4).

⁵It is important to remember that the groove depth is measured only to the bottom of the track and does not include the subsurface damage.

For single point grinding with sharp diamond points the lateral crack lengths increase with increasing set depth and wheel speed and, therefore, with increasing force. Because the lengths of lateral cracks vary substantially even within short distances along a particular track, it is difficult to find an accurate way to represent the above variation. Therefore, it was decided to compare the lengths of the largest lateral cracks observed for various grinding conditions. The results of this comparison are given in figure 12. The increases in lateral vent crack length with set depth and wheel speed, shown in the figure, occur as a result of the increases in forces that occur with increases in these variables.

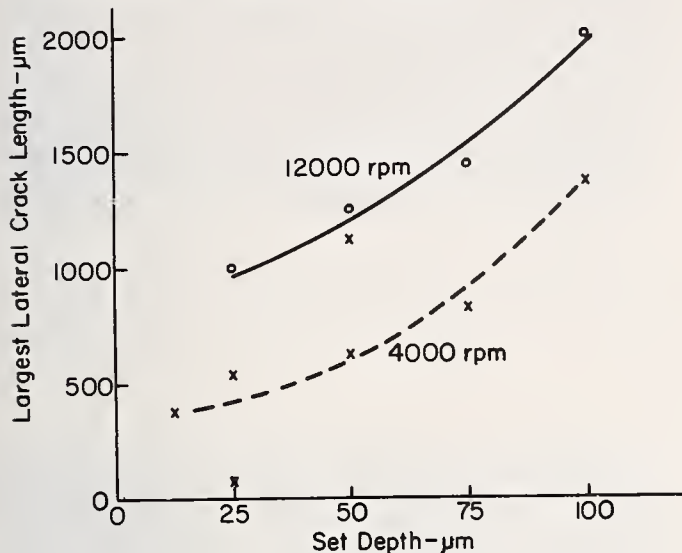


Fig. 12. Largest lateral crack length vs. set depth for single point grinding of glass (sharp diamond points, 4000 and 12000 rpm).

At 6000 rpm and 13 μm set depth, the largest lateral crack length decreased with decreasing sharpness of the diamond point as follows: sharp point, 420 μm ; 50 μm flat, 290 μm ; 100 μm flat, 150 μm . This suppression of lateral crack propagation with decreasing sharpness of the diamond points was unexpected.

The penetration of damage was measured in glass subjected to single point grinding with sharp diamond points at various wheel speeds and relatively large set depths. The variation of the maximum crack depth raised to the three halves power with the vertical

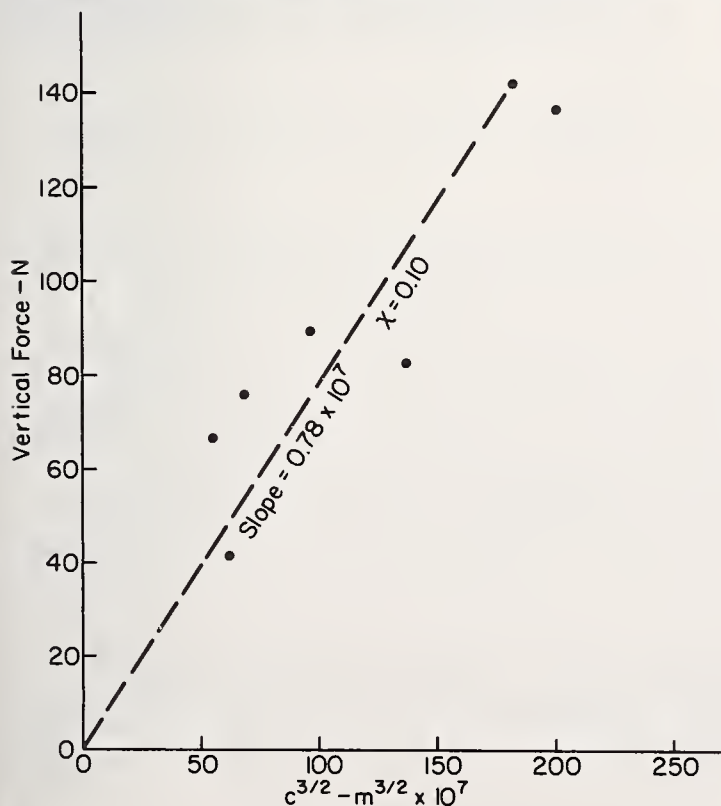


Fig. 13. Vertical force vs. (crack depth)^{3/2} for single point grinding of glass with sharp diamond points at various set depths and wheel speeds.

force is plotted in figure 13 which shows that the depth of damage increases with vertical force as expected and that the relationship is approximately linear with $C^{3/2}$. The value of χ was calculated and found to be 0.10 which is about twice the value determined from the scratching tests. This difference is attributed mainly to the fact that the diamond points used for single point grinding had smaller tip radii than the points used for scratching.

In a later experiment at smaller set depths the variations in forces and depths of damage for sharp and 50 μm flat diamonds were investigated with the results shown in figure 14. The forces were higher for the 50 μm flat diamond but the damage penetration averaged slightly less than for the sharp point. The values of χ were estimated and found to be 0.14 for the sharp point and 0.038 for the 50 μm flat.

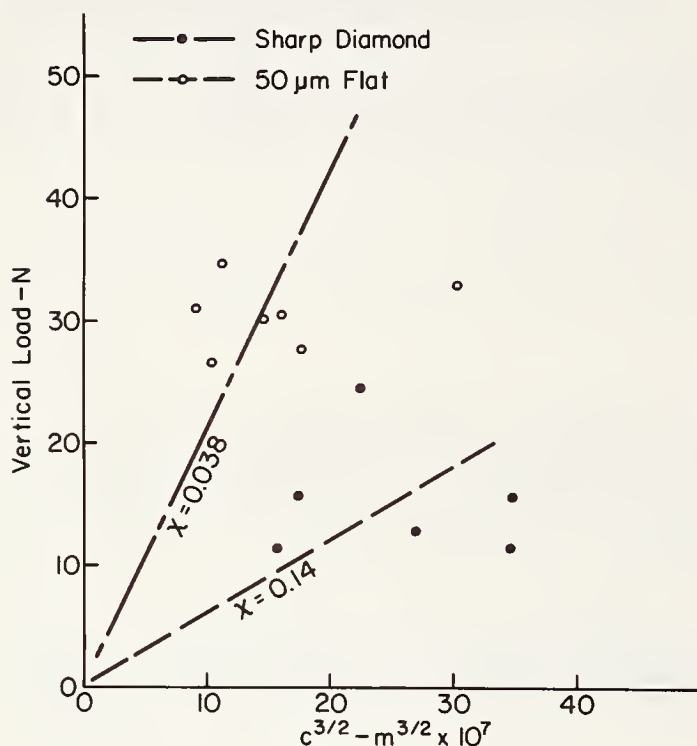
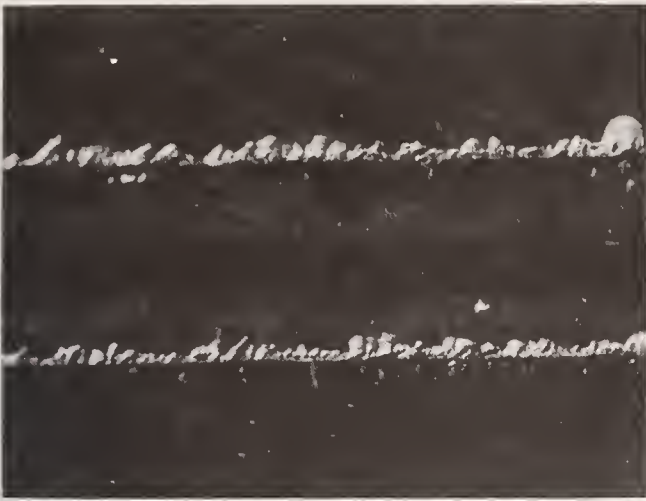


Fig. 14. Vertical load vs. (crack depth)^{3/2} for single point grinding of glass with sharp and 50 μm flat diamond points at various set depths and wheel speeds.

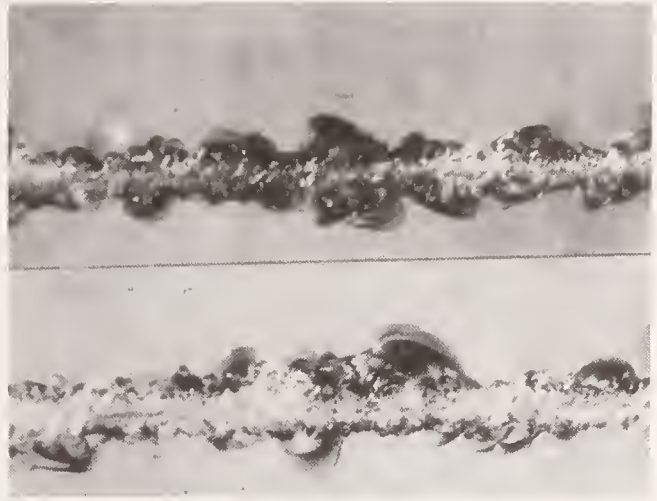
3.2.2. H.P. silicon nitride

There are significant differences in fragmentation and crack formation of glass and H.P. Si_3N_4 . The higher K_{IC} of H.P. Si_3N_4 tends to restrict fragmentation and crack formation compared with that in glass but this is partially offset by the greater forces required to drive a diamond point through the H.P. Si_3N_4 . The differences in crack formation are illustrated by the pictures of the tracks in figure 15. With sharp diamonds, the tracks in glass and H.P. Si_3N_4 are similar in appearance but the scale of the lateral cracking in H.P. Si_3N_4 is much smaller than that in glass. With blunt diamonds, at small set depths and low wheel speeds the tracks in H.P. Si_3N_4 are very smooth and there is little or no chipping (lateral crack formation) alongside the track. As the scale of the damage becomes smaller the response of the material tends to become less brittle, as expected.

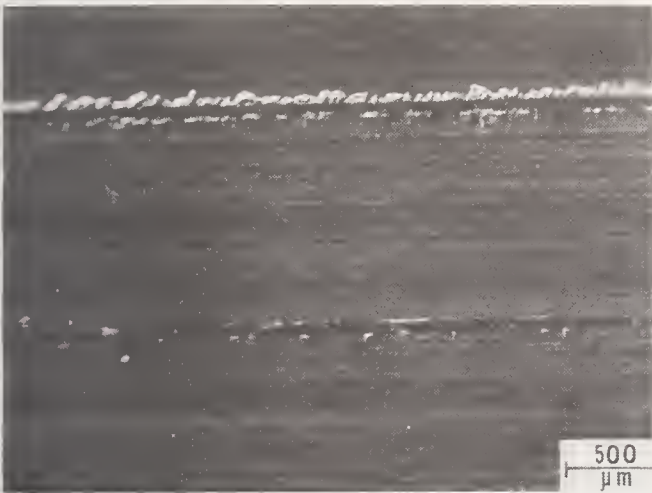
The total volume of silicon nitride fragments formed is much smaller than that of glass. The fragments have a bimodal size distribution which consists of fine powder formed by crushing and larger fragments formed by chipping. The shapes of the fragments formed by chipping are similar to those observed in glass.



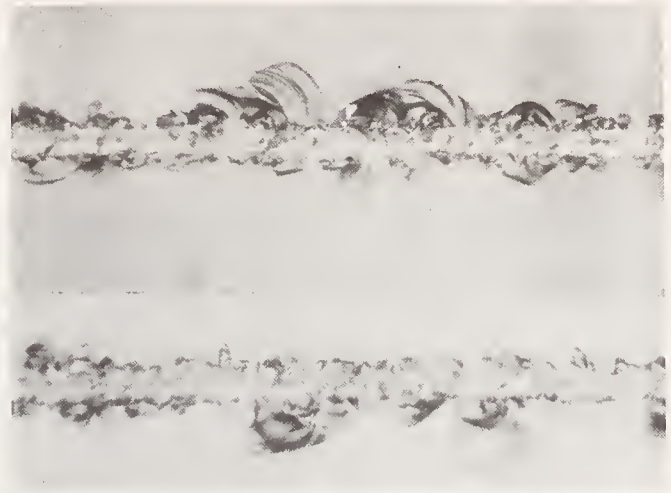
A. H.P. Si_3N_4 , sharp diamond point, top-wheel speed 8000 rpm, bottom-wheel speed 4000 rpm.



B. Glass, sharp diamond point, top-wheel speed 8000 rpm, bottom-wheel speed 4000 rpm.



C. H.P. Si_3N_4 , 50 μm flat diamond, top-wheel speed 8000 rpm, bottom-wheel speed 4000 rpm.



D. Glass, 50 μm flat diamond, top-wheel speed 8000 rpm, bottom-wheel speed 4000 rpm.

Figure 15. Comparisons of tracks formed in H.P. Si_3N_4 and glass (set depth 13 μm).

The groove depths in the H.P. Si_3N_4 specimens varied along their lengths as they did in glass. At the initial impact site the groove depths were always much greater than the set depths. As the midpoint of the track was approached, the groove depth became almost equal to the set depth. In this respect, this case is different from glass in which the groove depth was always substantially greater than the set depth. The groove depths increased with increasing vertical force as shown in figure 16. Comparisons for sharp, 50 μm flat and 100 μm flat diamond points show decreasing slope with decreasing sharpness. The spacings between the curves are roughly equal to the differences in the set depths.

Gielisse, Kim and Choudry [30] have shown that grinding forces decrease with increasing wheel speed, pass through a minimum, and then increase at high wheel speeds. Lateral crack formation responds to these variations in forces as shown in figure 17 for sharp diamond points. As expected, the maximum lateral crack lengths decrease with increasing wheel speed, pass through a minimum and then increase.

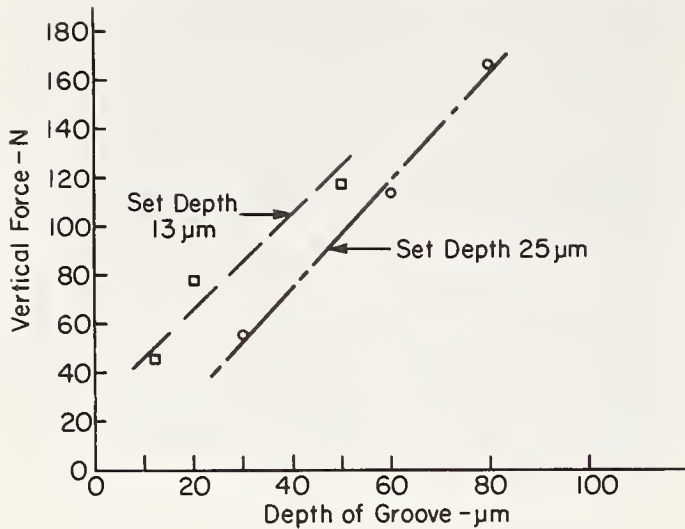


Fig. 16. Vertical force vs. depth of groove for single point grinding of H.P. Si_3N_4 using 50 μm flat diamond, wheel speed 8000 rpm.

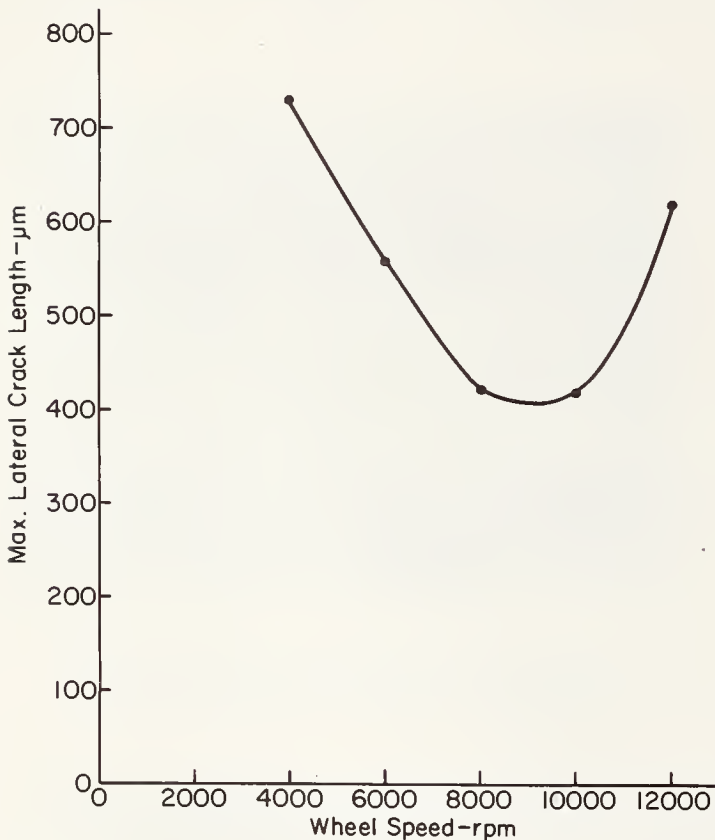


Fig. 17. Maximum lateral crack length vs. wheel speed for single point grinding of H.P. Si_3N_4 (sharp diamond point, set depth 50 μm).

The maximum lateral crack lengths (C_1) for diamonds of varying sharpness were determined for various grinding conditions. Then, the vertical force at each such lateral crack was estimated from the oscilloscope trace and plotted vs. the maximum crack length to the three halves power as shown in figure 18. The principal result is that these lateral crack lengths fall in the same range for the diamond points of varying sharpness despite the large variations in load from one type of point to another. This result indicates that the variations in χ for the various geometries roughly offset the effect of the variations in force for the three degrees of sharpness.

Substantial differences in the morphologies of subsurface cracks were observed in H.P. Si_3N_4 ground with points of varying sharpness as shown in figure 19. The pictures show cross-sections formed by fracturing the specimens back toward the tracks. The shapes of the grooves accurately reflect the shapes of the diamonds. The depths of penetration increase with increasing sharpness and wheel speed. For sharp points, the most penetrating

damage usually consisted of a radial crack perpendicular to the surface and directly under the groove. For flat diamonds, cracks usually radiated from the corners of the grooves. In many cases these cracks were the deepest damage.

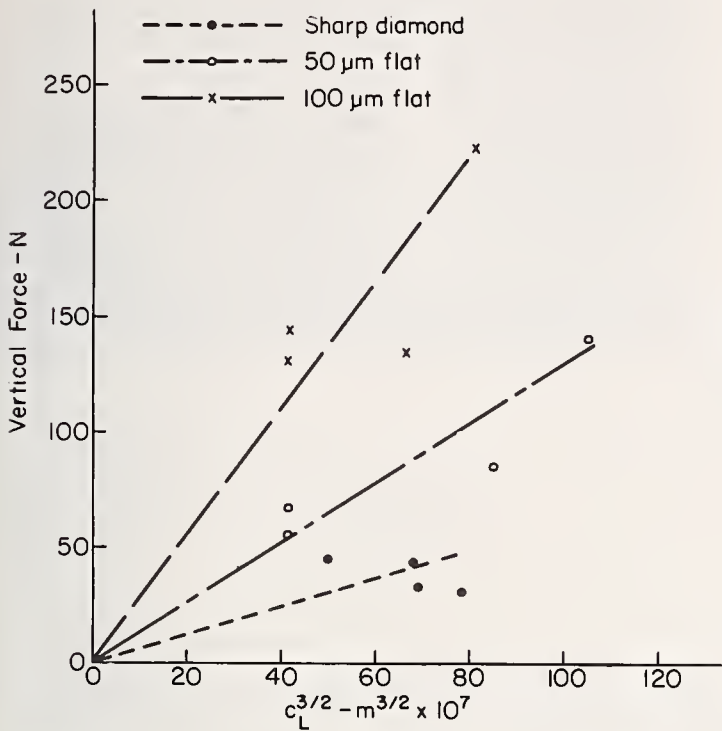
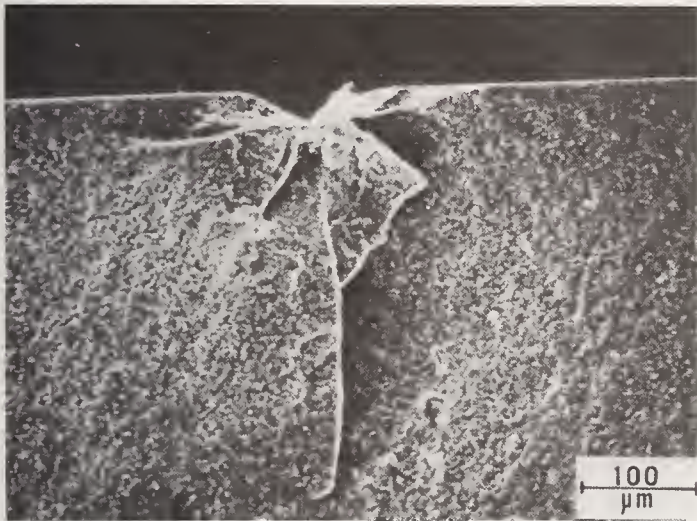
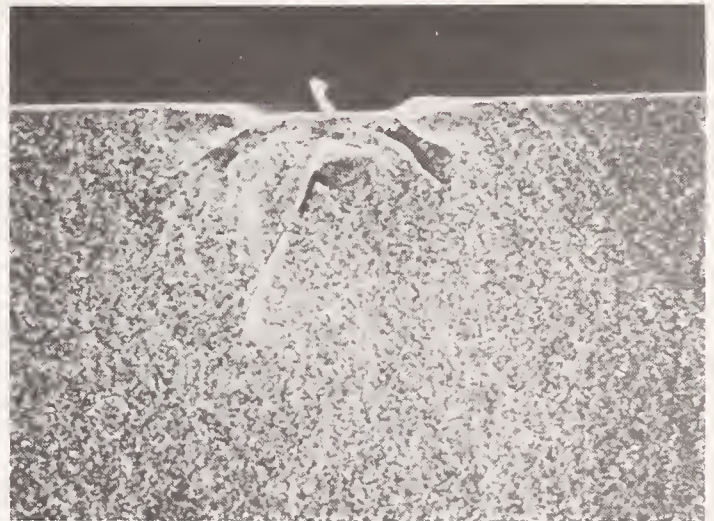


Fig. 18. Vertical force vs. (max. lateral crack length)^{3/2} for single point grinding of H.P. Si₃N₄ with diamond points of varying sharpness.



A. Sharp diamond, 8000 rpm.



B. 100 μm flat, 8000 rpm.

Fig. 19. Variations in subsurface damage with diamond shape and wheel speed; H.P. Si₃N₄, set depth 13 μm.

In addition to radial and lateral cracks, two other types of cracks were observed in specimens ground with flat diamonds. Surfaces of fractures parallel to the track contain a succession of small conical (Hertzian cone crack) surfaces, one of which is shown in figure 20. The cone crack continues under the track from the exposed conical surface. The second type of crack was usually observed in fracture surfaces perpendicular to the tracks and has a bulbous appearance (fig. 21). No explanation for the formation of these bulbous cracks is available.



Fig. 20. Evidence for Hertzian cone crack damage in H.P. Si_3N_4 ground with $100\ \mu\text{m}$ flat diamond ($25\ \mu\text{m}$ set depth, 8000 rpm).

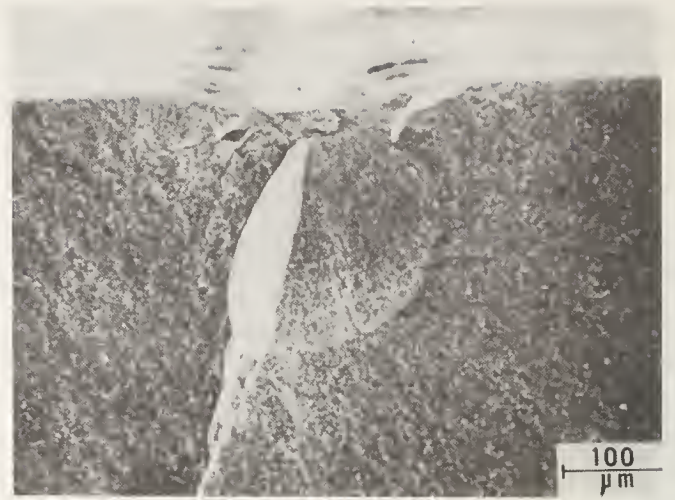


Fig. 21. Bulbous crack formed under tracks in H.P. Si_3N_4 ($50\ \mu\text{m}$ flat diamond, $25\ \mu\text{m}$ set depth, 4000 rpm).

Composite photographs of the beveled portions of tracks formed in H.P. Si_3N_4 by diamond points of varying sharpness were presented previously [31]. The increasing track width with decreasing sharpness of the diamonds was clearly shown. The groove depth decreased with decreasing sharpness of the diamonds. This decrease was observed by noting the depths of the smooth portions of the track that are formed by shearing of material at the bottom of the track. The results were $26\ \mu\text{m}$ for the sharp point, $23\ \mu\text{m}$ for the $50\ \mu\text{m}$ flat and $12\ \mu\text{m}$ for the $100\ \mu\text{m}$ flat. Arc-like cracks were observed on the beveled surface under the track. These cracks are believed to be associated with the conical or bulbous cracks noted previously. The horizontal intervals between these arc-like cracks were estimated and were found, on the average, to correspond to the distance traveled by the table between revolutions of the diamond. Thus, the material responds to the individual impacts as originally hypothesized.

The vertical force vs. the depth of damage to the three halves power was plotted with the results shown in figure 22. This figure shows strikingly that χ in eq. (1) varies with the sharpness of the diamond point. It is clear from this figure that, in practical applications, in which diamond points or abrasive grains become less sharp during use, the tendency toward damage penetration decreases despite the increased load on the diamond point as it wears. Busch and Prins [32] have shown that, in multipoint grinding of a hard ceramic, initially sharp diamonds are rapidly dulled. In view of the reduction in damage penetration, further investigation of the use of dull diamonds for grinding ceramics, is justified. The values of χ were estimated for the three sets of data with the following results: sharp diamond, $\chi = 0.46$; $50\ \mu\text{m}$ flat, $\chi = 0.13$; $100\ \mu\text{m}$ flat, $\chi = 0.065$. These data show that χ depends strongly on sharpness.

It is not uncommon for diamond points to break, especially when used at large set depths and low wheel speeds. Therefore, one might question whether or not the diamond points maintained their integrity in these tests. Perhaps the most important tests were those involving the points of varying sharpness, so one set of these points, exposed to lengths of cut ranging from 56-73.5 cm at set depths of 13 and $25\ \mu\text{m}$ was characterized. The points were examined under the optical microscope with reflecting light perpendicular to the points. The reflecting areas were photographed and the dimensions of the flats were measured on the photographs. The 50 and $100\ \mu\text{m}$ diameter flats remained close to their original dimensions. A firmly adhering layer of silicon nitride that obscures much of the surface of each of the diamonds was observed by SEM. As indicated by the

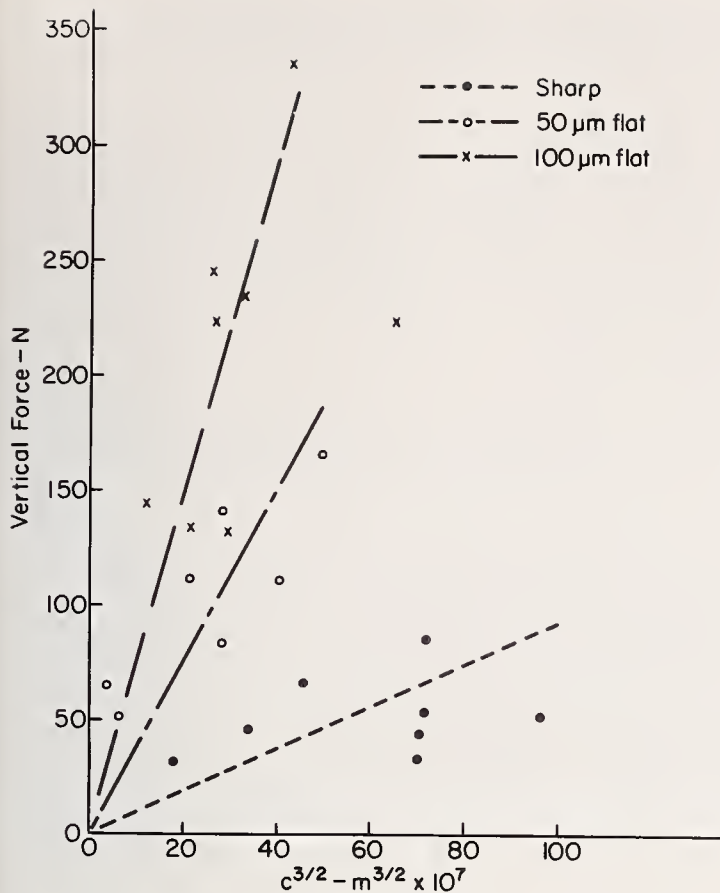


Fig. 22. Vertical force vs. (crack depth)^{3/2} for H.P. Si₃N₄ ground with diamond points of varying sharpness (combined data 4000 and 8000 rpm, 13 and 25 μm set depth).

intense white light emitted from the contact zone, high temperatures are generated by the single point grinding [33]. The silicon nitride contains a low melting magnesia and silica rich intergranular phase that would be expected to melt at these temperatures. The presence of this viscous material may account for the adhesion of the silicon nitride to the diamonds. Despite the fact that the surfaces are obscured, it is clear that the diamonds have retained their original shapes. Therefore, it can be concluded that, at least for moderate set depths, the diamonds maintain their integrity in machining H.P. Si₃N₄.

4. General Discussion

For diamond scratches in glass, the depth of damage increased with increasing load as expected. Although the results are sparse so that a definite relationship cannot be specified, the variation of the depth of damage (C) with load (P) is consistent with the C^{3/2} dependence expected based on eq. (1). The remaining strength increases with C^{-1/2} as expected based on eq. (2) and the slope of the curve was close to that expected if the scratch acts as a notch. Looking at the overall phenomenon, the remaining strength increases with P^{-1/3} as expected based on eq. (3).

For diamond scratches in H.P. Si₃N₄, the depth of damage also increases with increasing load, as expected. The results were plotted assuming the C^{3/2} dependence but it appears that a better fit could be obtained with a lower exponent.

In single point grinding of glass, the damage increased with increasing load on the diamond point. Groove depths were measured and were found to increase strongly with wheel speed. Therefore, the forces do not depend simply on the volume swept out by the diamond point on each revolution. Instead, the force depends in a complex way on the volume swept out by the diamond point which decreases with increasing wheel speed and the extent of damage outside this swept out volume which increases with increasing wheel speed. These opposing effects offset each other to some degree so that the variation of the force depends on the balance of these effects in a particular case. At low wheel

speeds the volume swept out is the dominant effect so that the force decreases with increasing wheel speed. At higher wheel speeds the extent of damage outside this swept out volume becomes dominant so the force passes through a minimum and increases at high wheel speeds.

The extent of damage reflects the factors discussed above. The lateral crack lengths increase with increasing set depth and wheel speed and, therefore, with increasing force. The depth of penetration of damage under the track increased with force on the diamond point, as expected. The variation is approximately $P \propto C^{3/2}$ as in eq. (1). The forces increase with decreasing sharpness of the diamond point but the damage penetration does not increase correspondingly. The effect of this is that the values of χ decrease to compensate for the lack of the expected increase in $C^{3/2}$.

In single point grinding of H.P. Si_3N_4 , the groove depth also increased with the vertical force as it did for glass. However, near the midpoint of the track, after the vibrations due to the initial impact have decayed, the set depth and groove depth were very nearly the same in most cases.

The extent of the damage increased with the vertical force, as expected, for both the lengths of lateral cracks and penetration of damage under the track. For individual diamond points the variation in the extent of damage was consistent with $P \propto C^{3/2}$ based on eq. (1). The vertical forces increased with decreasing sharpness of the diamond and, again, this increased force was not accompanied by a corresponding increase in $C^{3/2}$. The damage under the tracks formed by the 50 and 100 μm flats differed somewhat from that due to sharp diamonds in that the radial cracks frequently emanated from the corners formed by the edges of the flats. In addition, there was evidence of two other types of cracks; Hertzian cone cracks and what we have called bulbous cracks. The frequencies of occurrence of these cracks are consistent with formation of the cracks in response to the individual impacts of the diamond points.

The values of χ for penetration of damage under the track are given in table I for various materials and test conditions. The strong dependence of χ for single point grinding on the sharpness of the diamond is evident for both glass and H.P. Si_3N_4 . The differences observed in values of χ from scratching and single point grinding tests are also consistent with the differences in the diamond point radii used for the two methods.

Table I. Estimated values of χ for various materials and test conditions.

	Glass	H.P. Si_3N_4
Scratching Test		
Sharp ($\sim 150-300 \mu m$ tip radius)	0.053	0.20
Single Point Grinding		
Sharp ($\sim 40 \mu m$ tip radius)	0.10, 0.14	0.46
50 μm Flat	0.038	0.13
100 μm Flat	---	0.065

The values of χ for H.P. Si_3N_4 are consistently about four times the comparable values of χ for glass. This consistent difference indicates that some factor that is important for abrasive machining was not taken into account in the derivation of eq. (1). The principal difference in the response of glass and H.P. Si_3N_4 to abrasive machining seems to be the more extensive crushing of the glass. It seems reasonable that, if the diamond point acts through a layer of crushed material, it will act as though it is less sharp than would otherwise be the case. The lower values of χ observed for glass are consistent with this explanation. Decreased penetration of damage in the presence of crushing was observed previously in a study of damage due to impacts by spheres [14]. This earlier observation is also consistent with the proposed explanation.

The consistent decrease in χ with decreasing sharpness of the diamond point suggested that it might be possible to find an explanation for the variations in χ . The principal damage to be accounted for is the radial cracks which are extended in increments parallel to the track with each rotation of the diamond. Physically, this situation is somewhat different from that for which eq. (1) was derived. Lawn and Marshall [34], derived an equation for an idealized straight-crack model for indentation induced failure. It was assumed that once a straight crack was developed, it is driven by essentially localized, mouth-loading forces representing effective wedging components of the applied load. The result for straight cracks is

$$K_{IC} = \chi_L \frac{P_L}{c^{1/2}} = \chi_L \frac{P}{L c^{1/2}} \quad (4)$$

where $P = P_L L$ is the load on an indenter of length L and χ_L is again a dimensionless contact constant which incorporates uncertain geometrical and frictional factors. In our case the contact lengths of the flat diamonds were taken as the diameters of the flats. There was fractographic evidence of the contact width of the sharp diamond points in the tracks formed by single point grinding. This width is determined by the combined effect of elastic and microplastic deformation under the diamond point. The contact was assumed to be symmetrical so that the length of contact could be taken equal to the width. The widths of the smooth contact regions in a small number of specimens were examined. On the basis of these measurements a contact length of $20 \mu\text{m}$ was selected. The results of these calculations are plotted in figure 23 which shows that the assumption of line contact loading as described above allows the data to be represented roughly by a single line with a value of $\chi_L = 0.030$.

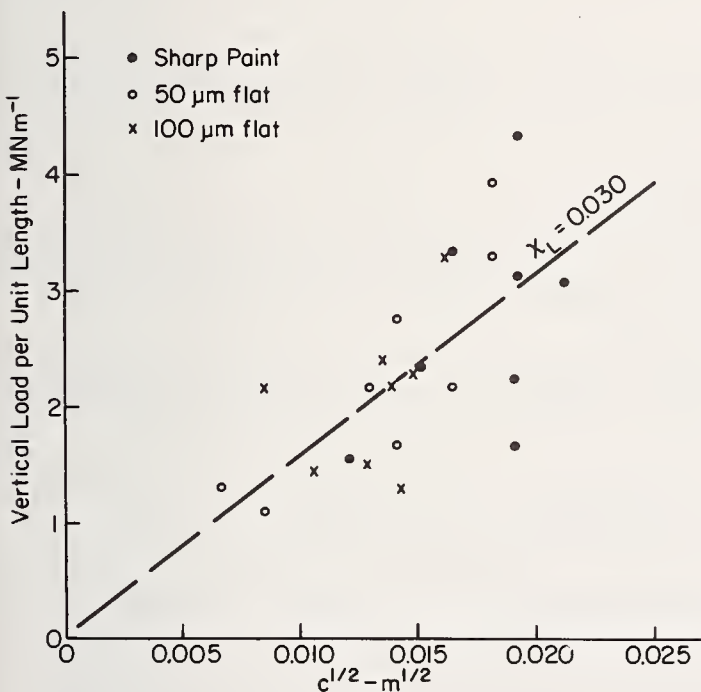


Fig. 23. Vertical load per unit contact length vs. $(\text{depth of damage})^{1/2}$ for single point grinding of H.P. Si_3N_4 with diamonds of varying sharpness.

5. Conclusions and Recommendations

The types and extent of damage observed in this investigation depended strongly on the diamond shape, set depth and wheel speed. Sharp diamonds induced radial cracks perpendicular to the surface and lateral cracks. Flat diamonds induced radial cracks emanating from the edges of the contact zone and lateral cracks which usually were shorter than those induced by sharp diamonds. In addition, Hertzian cone cracks and so-called bulbous cracks were observed in several cases in tracks formed by flat diamonds. As the grinding conditions became less severe and the contact zones were smaller, there was

evidence that the response of the materials became less brittle.

The penetration of the damage was analyzed initially in terms of eq. (1) and it was found that the values of χ decreased with decreasing sharpness of the diamond point. Subsequently, it was assumed that the mechanism of damage penetration involved line contact loading which was represented by eq. (4). This assumption allowed the results for H.P. Si_3N_4 to be represented by a single value of χ .

The penetrations of damage in H.P. Si_3N_4 and glass were compared. The values of χ for glass were approximately a factor of four smaller than those of H.P. Si_3N_4 indicating that the K_{IC} does not account for all of the differences between the materials. Therefore, the mechanism of damage penetration in glass must be somewhat different from that in H.P. Si_3N_4 . One obvious difference is that glass crushes much more extensively than H.P. Si_3N_4 . Therefore, the diamonds may act to wedge open the cracks through a layer of crushed glass making each diamond act somewhat less sharp than otherwise expected. The differences in χ between glass and H.P. Si_3N_4 are consistent with such an explanation.

It is highly desirable to investigate less severe grinding conditions, multipoint grinding and other materials. Use of less severe grinding conditions may yield a better description of the role of microplastic processes in abrasive machining. Further advances should make it possible to predict the penetration of surface damage for each set of abrasive machining conditions. This information would be very useful for prediction of the strengths of machined ceramics and for the development of machining processes in which each successive step is designed to remove the damage of the preceding step so that machining time required using fine-grained abrasives can be minimized.

Acknowledgment

The authors are pleased to acknowledge the advice and assistance of Professor P. J. Gielisse and Mr. Ray McLaughlin of the University of Rhode Island and the sponsorship of the National Science Foundation.

References

- [1] The Science of Ceramic Machining and Surface Finishing, S. J. Schneider and R. W. Rice, eds. NBS Special Publication 348 (1973).
- [2] Gielisse, P. J. and Stanislao, J., Mechanical methods of ceramic finishing, Reference 1, pp. 5-35.
- [3] Oh, H. L., Oh, K. P. L., Vaidyanathan, S., and Finnie, I., On the shaping of brittle solids by erosion and ultrasonic cutting, Reference 1, pp. 119-132.
- [4] Gielisse, P. J., Kim, T. L., Goyette, L. F. and Nagarkar, R. V., Fundamental and practical evaluation of the ceramic finishing process, U. of Rhode Island Final Technical Report, Contract N00019-72-C-0202 (1974).
- [5] Mecholsky, J. J., Jr., Freiman, S. W., and Rice, R. W., Effect of grinding on flaw geometry and fracture of glass, J. Amer. Ceram. Soc. 60 [3-4] 114-117 (1977).
- [6] Rice, R. W. and Speronello, B. K., Effect of microstructure on rate of machining of ceramics, J. Amer. Ceram. Soc. 59 [7-8] 330-333 (1976).
- [7] Rice, R. W., Machining of ceramics, in Ceramics for High Performance Applications. J. J. Burke, A. E. Gorum and R. N. Katz, eds., pp. 287-343 (Brook Hill Publishing Co., Chestnut Hill, Mass., 1974).

- [8] Lawn, B. and Wilshaw, R., Indentation fracture: principles and applications, *J. Mater. Sci.* 10 1049-1081 (1975).
- [9] Wiederhorn, S. M. and Lawn, B., Strength degradation of glass resulting from impact with spheres, *J. Amer. Ceram. Soc.* 60 [9-10] 451-458 (1977).
- [10] Evans, A. G., Strength degradation by projectile impacts, *J. Amer. Ceram. Soc.* 56 [8] 405-409 (1973).
- [11] Evans, A. G. and Wilshaw, T. R., Quasi-static solid particle damage in brittle solids, I. Observations, analysis and implications, *Acta Met.* 24, 939-956 (1976).
- [12] Evans, A. G. and Wilshaw, T. R., Dynamic solid particle damage in brittle materials: an appraisal, *J. Mater. Sci.* 12, 97-116 (1977).
- [13] Adler, W. F. and Hooker, S. V., Impact damage in single crystals, Effects Technology Report No. TR 77-49, Contract N00014-76-C-0744 (1977).
- [14] Kirchner, H. P. and Gruver, R. M., Localized impact damage in glass, *Mater. Sci. and Eng.* 28, 153-160 (1977).
- [15] Kirchner, H. P. and Gruver, R. M., Localized impact damage in stressed members, *Mater. Sci. and Eng.* 28, 249-255 (1977).
- [16] Kirchner, H. P. and Gruver, R. M., Branching of Hertz Cracks, from *Fracture 1977*, Vol. 3, D. M. R. Taplin, ed. pp. 959-964, (University of Waterloo Press, Waterloo, Ontario, 1977).
- [17] Kirchner, H. P., Analysis of localized impact damage in biaxially stressed glass plates, *J. Amer. Ceram. Soc.* 61 [3-4], 161-163 (1978).
- [18] Kirchner, H. P. and Gruver, R. M., The effect of localized damage on energy losses during impact, *Mater. Sci. and Eng.* 33, 101-106 (1978).
- [19] Kirchner, H. P. and Gruver, R. M., Localized impact damage in stressed Al_2O_3 and Si_3N_4 , *Mater. Sci. and Eng.* 34, 25-31 (1978).
- [20] Kirchner, H. P. and Gruver, R. M., Localized impact damage in a viscous medium (glass), from *Fracture Mechanics of Ceramics*, Vol. 3, R. C. Bradt, D. P. H. Hasselman, and F. F. Lange, eds., pp. 365-377 (Plenum, New York, 1978).
- [21] Kirchner, H. P., Gruver, R. M., and Walker, R. E., Strength Effects Resulting from Simple Surface Treatments, Reference 1, pp. 353-363.
- [22] Gruver, R. M. and Kirchner, H. P. Effect of surface damage on the strength of Al_2O_3 ceramics with compressive surface stresses, *J. Amer. Ceram. Soc.* 56 [1] 21-24 (1973).
- [23] Gruver, R. M. and Kirchner, H. P., Effect of Environment on penetration of surface damage and remaining strength of Al_2O_3 , *J. Amer. Ceram. Soc.* 57 [5] 220-223 (1974).
- [24] Marshall, D. B., Lawn, B. R., Kirchner, H. P., and Gruver, R. M., Contact-induced strength degradation of thermally treated alumina, *J. Amer. Ceram. Soc.* 61 [5-6] 271-272 (1978).
- [25] Lawn, B. R. and Fuller, E. R., Equilibrium penny-like cracks in indentation fracture, *J. Mater. Sci.* 10, 2016-2024 (1975).
- [26] Tada, H., Paris, P., and Irwin, G., *The Stress Analysis of Cracks Handbook*, (Del Research Corporation, Hellertown, PA 1973).
- [27] Smith, F. W., Emery, A. F., and Kobayashi, A. S., Stress intensity factors for semi-circular cracks, Part 2, semi-infinite solid, *J. Appl. Mech.* 34, Series E, 453-959 (1967).

- [28] Wiederhorn, S. M., Subcritical crack growth in ceramics, from Fracture Mechanics of Ceramics, Vol. 2, R. C. Bradt, D. P. H. Hasselman and F. F. Lange, eds. (pp. 613-646, Plenum Press, New York, 1974).
- [29] Petrovic, J. J., Jacobson, L. A., Talty, P. K., and Vasudevan, A. K., Controlled surface flaws in hot pressed Si₃N₄, J. Amer. Ceram. Soc. 58 [3-4] 113-116 (1975).
- [30] Gielisse, P. J., Kim, T. J., and Choudry, A., Dynamic thermal aspects of ceramic processing, University of Rhode Island Final Technical Report, Contract N00019-71-C-0244 (1971),
- [31] Kirchner, H. P., Gruver, R. M., Richard, D. M., Fragment formation and damage penetration during machining of ceramics, Ceramic Finishing Company Technical Report, Contract NSF-C-APR77-19818 (1973).
- [32] Busch, D. M. and Prins, J. F., A basic study of diamond grinding of alumina, Reference 1, pp. 73-87.
- [33] Gielisse, P. J., Kim, T. J., Choudry, A., Short, J. F., and Turker, E. J., Force and wear analysis in ceramic processing, University of Rhode Island Final Technical Report, Contract N00019-72-C-0202 (1972).
- [34] Lawn, B. R. and Marshall, D. B., Contact fracture resistance of physically and chemically tempered glass plates: theoretical model, Phys. Chem. Glasses 18 [1] 7-18 (1977).

SINGLE-POINT SCRATCHES AS A BASIS FOR UNDERSTANDING GRINDING AND LAPPING

A. Broese van Groenou, N. Maan and J.B.D. Veldkamp
Philips Research Laboratories
5600 MD Eindhoven, The Netherlands

Considering grinding as a multi-scratch process we have used single-point, low-speed, scratch experiments with pyramidal diamonds in an attempt to understand such quantities as the force ratio and the specific energy in terms of the shape of the diamond and of the properties of the workpiece, here ferrites, glasses and various oxides. The force ratio is found to be dominated by the geometry of the diamond, while the interface friction is small. The specific energy for groove formation is determined by the Vickers hardness. A depth dependence ("size effect") occurs with the harder materials. Moreover, scratch experiments yield information on the resistance of cracking on a microscopic scale and therefore give some idea of the relative strength of the grain boundaries with respect to the grains.

A liquid environment of e.g. n-alcohols does not have a pronounced influence on the force ratio and the specific energy for grooving, in contrast to water. Experiments made with a loose particle between a binder material (brass, pitch, steel) and an oxide or a metal shows that the particle motion depends on its shape and on the hardness of the two materials. Rolling occurs where the hardness values are about equal. For a spherical particle a high load favours rolling, deforming both materials to a moderate extent. Sharp particles behave in an irregular manner and scratch both materials. Finally, scratching is a useful means of testing the homogeneity of materials.

Keywords: Ceramics; chipping; crack formation; fracture toughness; friction; hardness; liquid softening; oxides; scratching; size effect; specific energy.

1. Introduction

Grinding, lapping and abrasive polishing of brittle materials like ceramics and glass are often necessary but complicated processes. One essential element of the grinding system is the interaction between the abrasive particles and the workpiece: here the material removal takes place and here the residual deformation is formed. This can be seen in an experiment in which a slightly tilted workpiece is ground: where the wheel first touches the sample many scratches are seen, which at greater depth influence each other (fig. 1). The basis for understanding grinding is therefore the scratching action of sharp points, and a model may be built on the phenomena caused by a single point. In our study such scratches were made at a low speed (less than 1mm/s). Apart from making experiments somewhat easier, this speed range is expected to give simpler results than when scratching at speeds used in grinding, e.g. 30 m/s, where heat generation may in any case cause complications. The low-speed experiments provide a basis for the high-speed problems, which must be tackled separately. In this paper attention is focussed on the behaviour of various materials - glass, crystals, polycrystals - under the action of a sharp pyramidal point. Experimental details are given in the next section.

Two modes of deformation are of interest in scratching: the plastic deformation underneath and the brittle fracture around the point, as can be seen in the figure. For both phenomena it appears that the scratching speed is important, at the low speeds used here. For the plastic deformation it should be kept in mind that a sharp point causes a considerable strain rate, of the order of $\dot{\epsilon} = v_s/b$. This is in the range from 0.1 to 10^3 sec^{-1} for a scratching speed v_s of $1-10^3 \text{ } \mu\text{m/s}$ and a scratch width b of several microns.

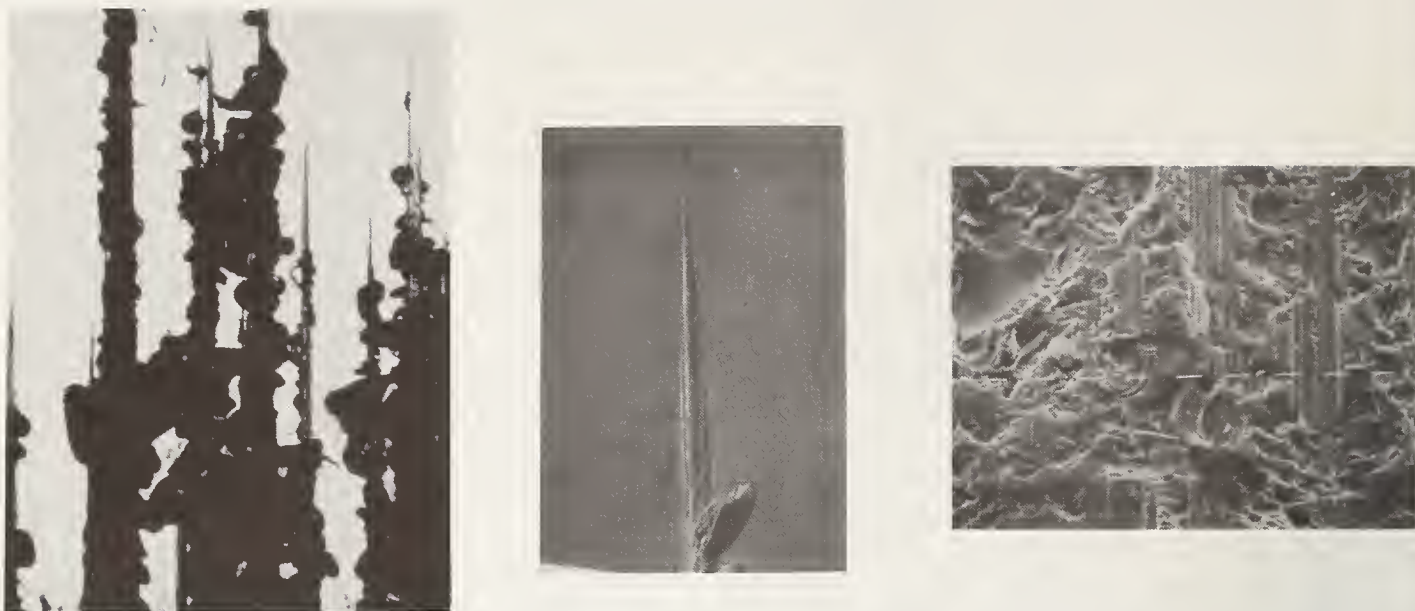


Fig. 1. Photograph of scratches on polycrystalline $\text{Mn}_{0.57}\text{Zn}_{0.35}\text{Fe}_{2.08}\text{O}_4$ made by a number of diamonds on an electroplated wheel, running at 75 m/s. Since the sample was slightly tilted, the start of the scratches could be made visible.

A slow-scratch apparatus therefore allows the investigation of plastic behaviour over a reasonable range of $\dot{\epsilon}$, although the deformation is limited to small volumes. This speed range is also of interest for the second mode of deformation, crack propagation, because for low stresses slow crack growth has been observed in glass and Al_2O_3 [1-4]¹.

Returning now to high-speed grinding, the connection with scratching is found in that both processes remove material and both need a certain mechanical action, expressible in force and energy. The characteristic quantities are usually taken to be the force ratio, i.e. the ratio of the force component parallel and normal to the surface, and the energy necessary for removing a unit volume (for that reason it is called the specific energy) [5-7]. Low-speed scratching may clarify the precise meaning of these quantities; for example, what is the relation between force ratio and the Coulomb friction in the interface between particle and workpiece? Does the type of abrasive particle influence the process? And is the specific energy typical of a material or of a grinding system? For the last question it is important to realize that the specific energy depends closely on the mode of deformation: removing material by plastic deformation requires a much higher energy than by brittle fracture (section 3). This is one reason for the interest shown in the types of cracking that accompany a scratch; another reason is that the presence of microscopic cracks weakens a product. Cracking during scratching in glass was studied by Peter [8], who noted that the "median" crack extended further not only at a higher load but also at a lower speed. For other types of cracks, to be classified in section 4, load-speed diagrams can be given [9,10]. Two types of cracks have recently been investigated theoretically: fracture near an indentation [11,12] and around a scratch [9]. It appears that the propagation of cracks on a microscale allows a description with reasonable accuracy, in spite of the unknown stress field around a pyramidal indenter.

Scratching may also be useful in the study of the possible influence of water and other liquids on material behaviour, leading to better insight into their role in the creation of surface damage. It is well known from the work of Westbrook [13] and Westwood [14] that the hardness of a number of materials (e.g. LiF, MgO, Al_2O_3 , glass) varies with time in a suitable liquid environment. A scratching experiment allows much shorter observation times (Westwood used 1000 sec.) and moreover it is possible to verify a lubricating action at the contact between particle and workpiece from the value of the force ratio (section 5). The action of water on the propagation of slow cracks in glass is well known [1]; in the

¹ Figures in brackets indicate the literature reference at the end of this paper.

same speed range scratches can be made [8] and slow crack growth observed. Although such low speeds are not directly relevant to grinding, they may influence the residual damage in a ground surface. Also, for slower processes such as lapping, liquids may play a role. Lapping is a process where material is removed by loose particles. How "loose" these particles really are is also a subject that can be investigated in a single-point scratching apparatus. A variety of lapping materials can thus be investigated (section 6). Leaving aside the other applications of a scratching apparatus, we discuss the relevance of scratching data to grinding in section 7.

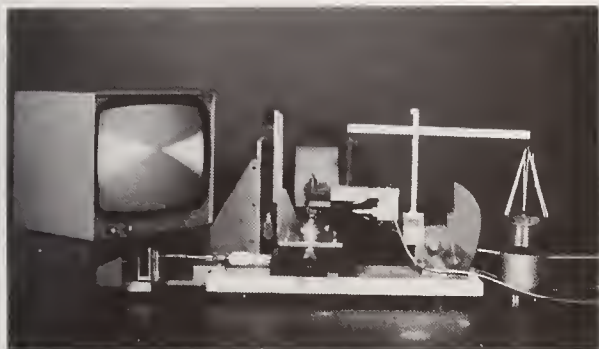


Fig. 2. Scratching apparatus

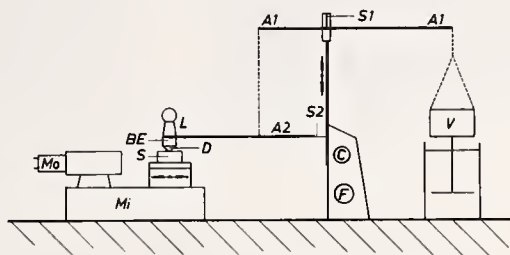


Fig. 3. Schematic drawing of the scratching apparatus. A1, A3: upper arms, A2: lower arm; S1, S2: leaf springs; V: counter weight and damper; C, F: coarse and fine vertical adjustments; L: load; D: diamond; BE: bending element used for force measurements; S: sample; Mo: motor; E: x-y and rotation stages; Mi: micromanipulator.

2. Experimental

Scratches were made by moving a polished sample under a vertically loaded diamond. During the motion the horizontal force on the diamond was recorded. Afterwards the depth and width of the scratch were measured under a microscope. (Details have been given in ref. 15.) The apparatus, shown in fig. 2 and 3, contains a balance to enable scratching to be carried out at loads as low as 0.01 N. The maximum load is about 3N. The sample-holder is driven by a motor at speeds in the range from 0.4 to 400 $\mu\text{m/s}$. The diamonds were ground into square pyramids of about 4 mm size, with apex angles of $2\theta = 100^\circ$, 120° and 136° . The radius of curvature of the tips was better than $0.3 \mu\text{m}$ as can be checked in a dark-field microscope. A tungsten carbide indenter was ground to the same shape ($2\theta = 120^\circ$), but could only be made with a radius of curvature of about $1 \mu\text{m}$, owing to its microstructure. During scratching in air the point and its reflection in the surface were observed with the aid of a microscope connected to a TV monitor.

Scratches were made in a liquid environment by surrounding the diamond with a droplet. The same apparatus could be used for observing loose particles by replacing the diamond holder by a flat plate.

The standard three-point bend test was used in order to determine the critical stress intensity factor, K_{Ic} . The double torsion test was used for determining the crack speed dependence of K_{Ic} .

A range of polycrystalline ceramic materials was used (various ferrites, ZnO , Al_2O_3) as well as crystals of MgO , ZnO and lead-hexaferrite. A number of glasses were also investigated. All samples were highly polished with diamond abrasives. For the etching of the MgO crystals Stokes' recipe was followed [16].

3. Grooves

3.1. Force ratio

Examples of scratches on a MnZn ferrite are shown in figure 4, for various loads, at a speed of 400 $\mu\text{m/s}$ and an apex angle of 136° .

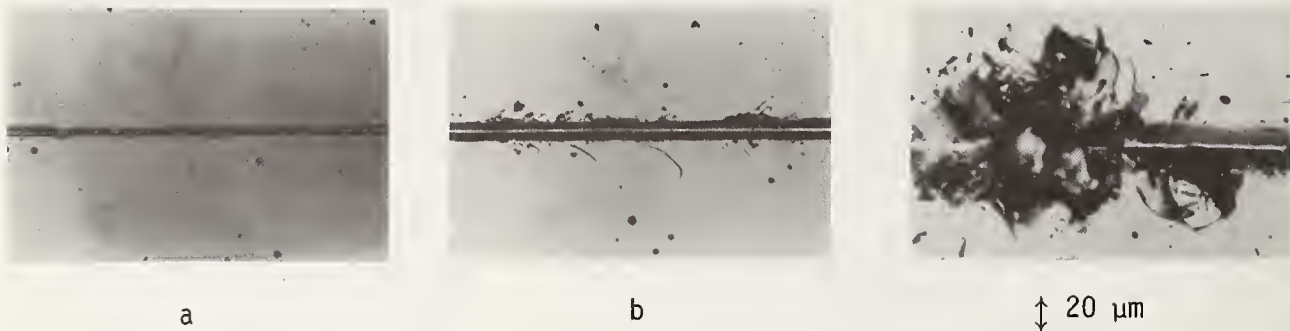


Fig. 4: Influence of load on the presence of crack types in crystalline materials. View from above of scratches made on Mn Zn ferrite. Scratching speed: 400 $\mu\text{m/s}$. Loads: 0.1 (a), 0.7 (b) and 3 N (c). Incident light, bright field.

Grooves are found at all loads, whereas cracks become visible at higher loads. During scratching the horizontal force is recorded (fig. 5). At low loads a much smoother curve is found than at higher loads. The average value of F_t can be used to calculate the force ratio

$$f = F_t / F_n \quad (1)$$

f values have been determined for three pyramids and six materials [15]. The results allow a simple presentation in a $f - \cot \theta$ plot, where 2θ is the apex angle of the pyramidal particle (fig. 6). Independent of load or material, f is equal

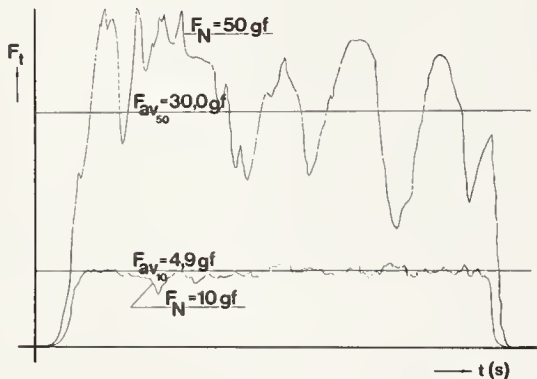


Fig. 5. Recording of horizontal force component, F_t , for a load of 0.1 N (bottom) and 0.5 N (top) on MnZn ferrite.

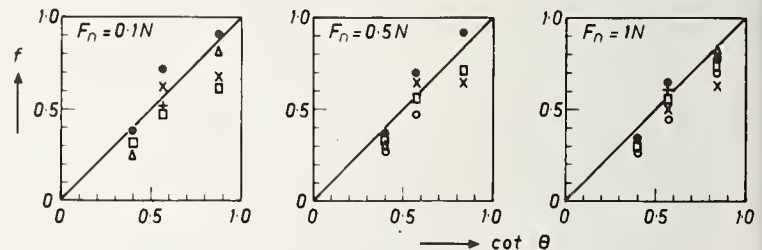


Fig. 6. Force ratio $f = F_t / F_n$ as a function of $\cot \theta$ for various loads on the diamond. All materials are included (from ref. [15]).

to $\cot \theta$ in a good approximation. The same result has been obtained for a number of metals [17].

The significance of this result can be seen from the directions of the force components on the contact plane between diamond and workpiece (fig. 7). The vertical load F_n and the horizontal component F_t combine to give the total force F_{tot} (we consider scratching by a leading plane, so there is no resultant component in the third direction). The components of F_{tot} along the contact plane $F_{//}$ and perpendicular to it, F_{\perp} can be determined for a known value of θ . The experimental results show that $F_{//} / F_{\perp}$, i.e. the friction coefficient on the contact plane, is much smaller than the force ratio, F_t / F_n . Denoting $F_{//} / F_{\perp}$ by

$\mu = \tan \alpha$, we can write f as

$$f = \cot(\theta + \alpha) = \frac{\cot \theta - \mu}{1 + \mu \cot \theta} \quad (2)$$

The μ values are 0.1 or smaller. For large θ , i.e. blunt particles, the μ value is more important since $\cot \theta$ is small. In the limit of a sphere, at very shallow penetration, $f = \mu$. For deeper sphere-scratches a correction is needed [17,18].

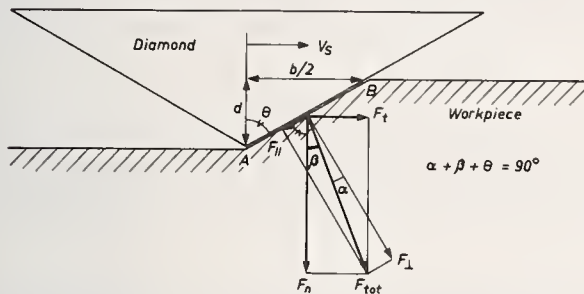


Fig. 7. Diamond geometry showing the contact area AB. The load, F_n , and the measured tangential force, F_t , are combined to form the total force F_{tot} . The components perpendicular (F_{\perp}) and (F_{\parallel}) to the contact area can easily be deduced. The force ratio f equals $\tan \beta$. The friction coefficient is $\mu = \tan \alpha$.

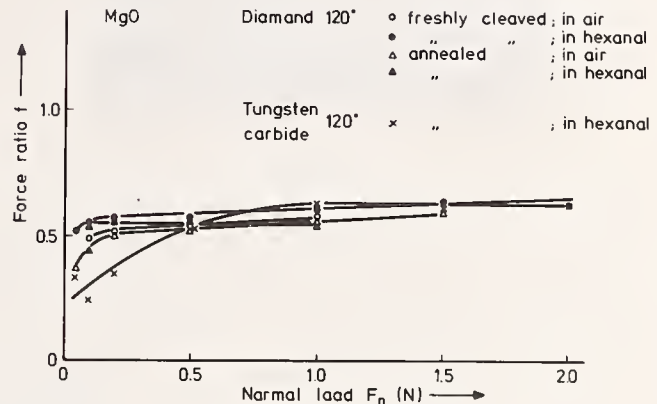


Fig. 8. Force ratio versus load for two pyramid materials, diamond and tungsten carbide, for scratches on MgO crystals.

The geometry of the scratching point is not only important for a diamond pyramid. For a tungsten carbide point with $2\theta = 120^\circ$ similar results are found, e.g. on MgO (fig. 8). Below a certain load the force ratio depends on the load, i.e. on depth of penetration. This effect corresponds to the larger tip radius of the tungsten carbide point, which has a varying θ value and therefore an increasing f until the depth is larger than the radius. With our diamond tips such an f -load variation has frequently been an indication of wear on the tip. After regrinding the load dependence had disappeared. Experiments with rounded-off cones, as used in gramophones, are not suitable for a simple interpretation for this reason. The influence of rounding-off has also been noticed by Prins [6].

The horizontal force, as given in figure 5, shows an increasing number of fluctuations with increasing load. Part of these are due to irregularities in the workpiece material, such as pores or grain boundaries. The load dependence is due to the occurrence of various cracks in and around the grooves, which will be discussed below. First the type of deformation will be treated and a quantitative characterization given.

3.2. Deformation

During scratching the diamond moves through the material (cf. fig. 7) and pushes the debris up in front, as can be seen on the microscope picture. In exceptional cases the debris is still fastened to the groove [7] (fig. 9), in most cases it consists of short pieces of material and lies around the groove. The groove itself is a highly deformed area. From its depth d and width b , as determined under a microscope after scratching, the groove cross-section is found to be congruent with the diamond pyramid [15]; for grooves on some metals, however, the depth/width ratio was too low [17]. A slight pile-up of material along the groove has been found in the softer ceramics.

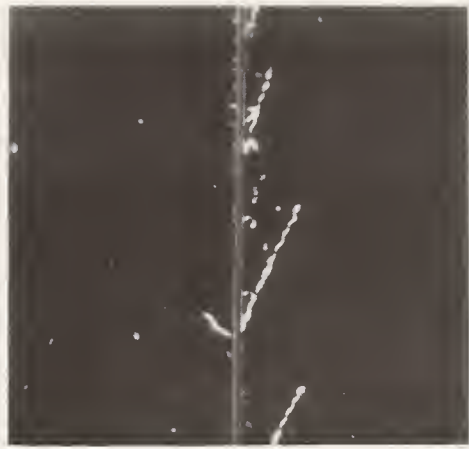


Fig. 9. Glass curls fastened to groove.



Fig. 10. Dislocation pattern on cleaved MgO, perpendicular to scratch ($2\theta = 136^\circ$; $F_n = 0.2N$); etched; horizontal and vertical cracks under the groove.

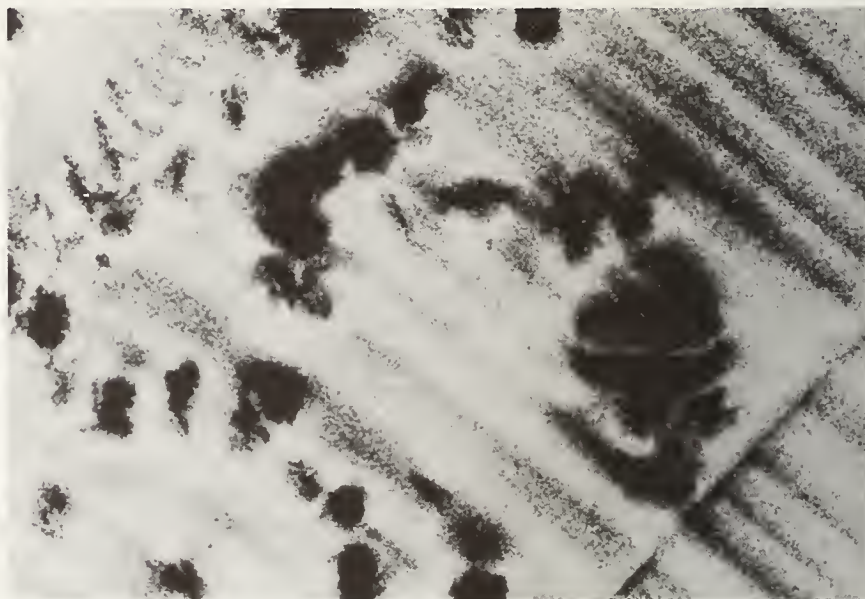
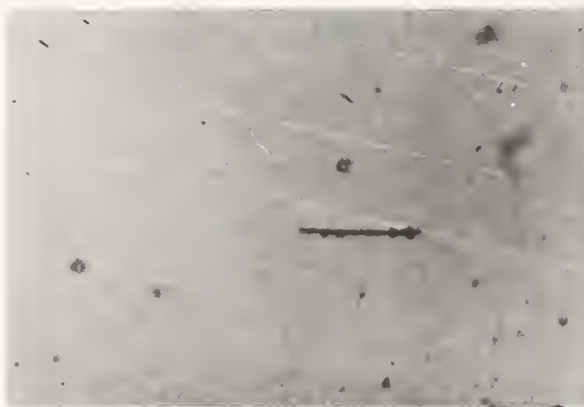


Fig. 11. Scratch on $Gd_3 Ga_5 O_{12}$ crystal ($F_n = 0.05N$). Scratch length is $100 \mu m$. On the left a microscope picture of the scratch, on the right an X-ray topograph of the same area.

The high pressure on the contact plane leads to dislocation generation and movement. Dislocations are found deep under the surface of crystalline samples; an example is given in figure 10 for MgO. This result was obtained after cleaving perpendicular to the scratch and etching; the dislocations along $[110]$ extend down to $100 \mu m$ for a load on the diamond of $0.1 N$. Even further from the scratch one can detect the stress field corresponding to the plastic deformation near the groove by means of X-ray topography (fig. 11). In polycrystalline materials the deformation on cleaved surfaces has never been found at large depths, presumably because the grain boundaries formed a barrier.

3.3. Scratching hardness, specific energy

More quantitative statements can be made about grooving from the measured depth and width and the force components, by introducing the scratching hardness,

$$H_s = \frac{4F}{b^2} \quad (3)$$

and the specific energy,

$$e = \frac{2F_t}{bd} \quad (4)$$

In the "ploughing" model [15, 19, 20] these quantities are related to the contact stress σ , derived from the total force and the contact area (AB in fig. 7), and the friction coefficient μ by

$$e = \sigma(1 - \mu \tan \theta) \quad (5)$$

$$H_s = \sigma(1 + \mu \cot \theta). \quad (6)$$

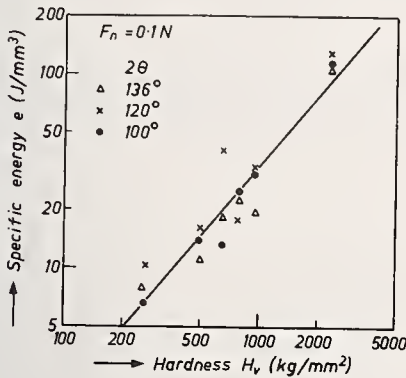


Fig. 12. Specific energy values for a range of materials as a function of their Vickers hardness ($1 \text{ kg/mm}^2 = 10^7 \text{ N/m}^2$). Load: 0.1 N; three pyramids have been used [15].

In our experiments the μ and θ values are such that the second terms are only minor corrections. This is confirmed by the experimental result that, within our accuracy, e and H_s are equal. The results for a number of ceramic materials are given for a low load, $F_n = 0.1 \text{ N}$, in fig. 12 as a function of the Vickers hardness, measured on these materials. A good correlation is found, the slope being about 2.5. This indicates that the formation of a scratching groove is closely related to the plastic yield that occurs in indentation.

3.4. Size effect

The specific energy values do not depend on the shape of the pyramid, but on load, or, which is more interesting, on depth. Such a size effect is well known in grinding metals [21] and occurs also in grinding ceramics [22-24]. Experimental data for low-speed scratching are given in figure 13a for some ceramics and in 13b for several ferrites

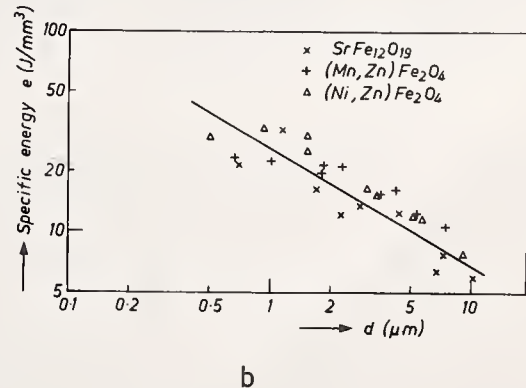
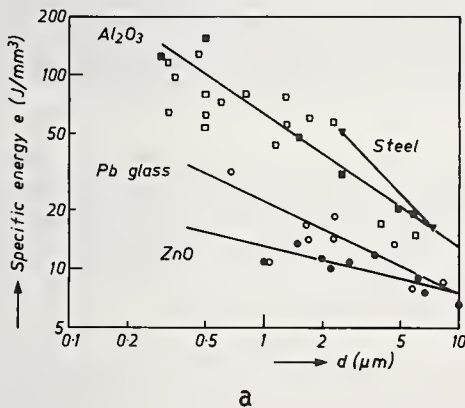


Fig. 13. Specific energy, e , versus depth of scratch, d , for all apex angles. For clarity of presentation the white ceramics are shown in (a) separate from the black ceramics (b). The values labelled steel (\blacktriangledown)(a) have been taken from grinding results of Brecker and Shaw ([21]). The black squares for Al_2O_3 refer to measured d values, the open squares have d calculated from b.

It is remarkable that the decrease of e with d is greater for harder materials. The porous ZnO sample ($H_V = 2 \cdot 10^9 \text{ N/m}^2$, $p = 8\%$) shows a small size effect; this is not due to porosity, because for a crystal with $H_V = 10 \cdot 10^9 \text{ N/m}^2$ we found a small size effect too.

The influence of the scratching speed has been determined for a MnZn ferrite, MgO and a number of glasses. The results show a clear increase of scratching hardness and specific energy with speed in the range between 0.1 and 400 $\mu\text{m/s}$ (fig. 14). For metals a similar increase has been found [17]

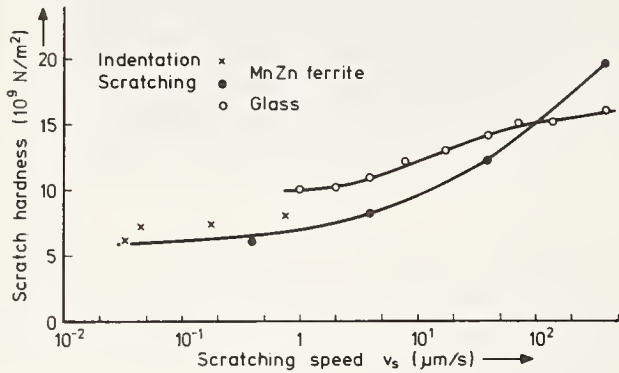


Fig. 14. Scratching hardness as a function of scratching speed (v_s) for glass and MnZn ferrite.

4. Cracking

4.1. Glass

Cracks of various kinds occur along and underneath a scratch. Examples have already been given for a MnZn ferrite (fig. 4) and for MgO (fig. 10). Before returning to these materials, some attention will be given to the glass-like materials, which are simpler (no anisotropy, no grain boundaries). Surface cracks (fig. 15) and sub-surface cracks (fig. 16) in a NaCa glass allow the following inventory:

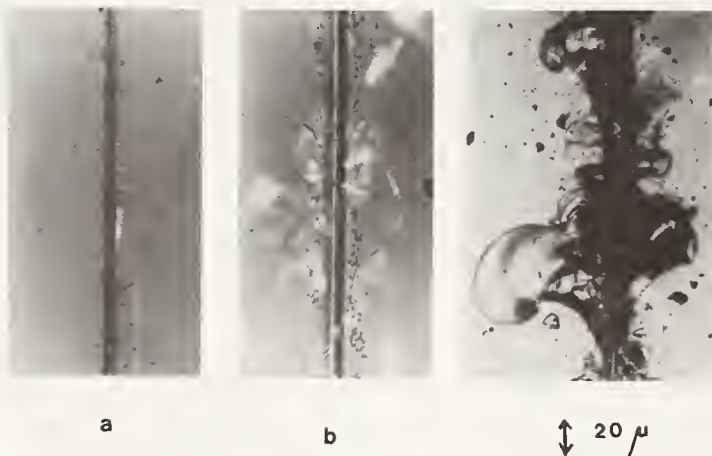


Fig. 15: Influence of load on the presence of crack types in glass. Views from above of scratches made on SF58 glass, scratching speed 400 $\mu\text{m/s}$. Loads: 0.1(a), 0.5(b) and 3 N(c). Incident light, bright field.



Fig. 16: Cross-section of a scratch in glass. The median crack is clearly shown. The open space is bounded by lateral and sub-surface cracks. Load 0.5 N scratching speed 400 $\mu\text{m/s}$. Incident light, bright field.

1. *On the surface* cracks run from the groove at an angle of about 30° . These cracks, which are lateral with respect to the scratching direction, start in front of the scratching pyramid and move away from the groove while the pyramid continues its motion. The "lateral" cracks show some resemblance to the horseshoe shapes found around scratches made by spheres [25] and to the cracks [11,12] underneath a static pyramidal indenter. In a film on scratching made by Busch [26] the speed of propagation of the lateral cracks is about the same as that of the scratching particle. Quite often there is a correlation in the length of neighbouring lateral cracks: the second one is shorter than the first and the third smaller again (fig. 15b).

2. *Underneath the surface* a vertical crack starts out just underneath the top of the pyramid [9] (fig. 16). This "median" crack occurs especially when the pyramid is used in the leading edge position [9]. A minimum load seems necessary before the extent of the stress field is large enough to nucleate this type of crack. In Peter's extensive work ([8], see also Dick [27]) the extent of cracking is found to depend on the load and on the speed of scratching.

3. *On the surface*, especially at higher loads, and at lower speeds two lateral cracks are seen to combine to form chips (fig. 15c). The second crack thereby takes a curved path and ends up about perpendicularly to the first crack [9]. For a theoretical treatment the complex stress field seems forbidding. The chips are particularly interesting for the mechanism of material removal. For one scratch the chips often remain connected to the surface and a second scratch seems necessary to harvest the loose material. At the end of section 4.2. we shall return to this question. In the microscope the chips are seen to be formed behind the scratching point.

4. *Subsurface cracks*, propagating parallel to the surface (fig. 16), are easily seen on the glass surface from their optical effects (fig. 15b). These cracks are formed behind the scratching particle (as observed in the film by Busch [26]) and are similar to the cracks that start on the unloading of a hardness indenter [12].

The cracks described start near the scratching particle, i.e. in the complex stress field of a pyramid. The chips and subsurface cracks are formed behind the point where the residual stress due to the groove adds up to the field from the point itself. To some extent similar complexities occur for the median and the lateral cracks, as long as these are short. To add to the difficulties of an analytical treatment, the cracks are formed in a material that already contains a number of cracks. This may be responsible for the 1-2-3 effect in the lengths of subsequent lateral cracks (fig. 15b). It may also be relevant for the formation of a groove, i.e. the specific energy may be lower in a cracked material, because the effective hardness will be somewhat lower due to a lower effective stiffness. A similar effect is seen in the widening of a groove when it reaches the end of a sample.

The analytical treatment of the extent of cracking for a given load on an indenting particle was first given by Roesler [28] for the cone crack and by Lawn [11] and Swain [12] for the median and penny-shaped crack. From the known stress field it is possible to deduce when the stress intensity factor K_I reaches the critical value for crack propagation K_{IC} . At a large distance from the loaded point the derivation is simple: for a load F_n the stress at a distance r is $\sigma = F_n/\pi r^2$. If r is also the crack length, the K_I value is $K_I = \sigma\sqrt{r}$, which immediately leads to

$$r = (F_n/\pi K_I)^{2/3} \quad (7)$$

For small cracks, however, the presence of the groove cannot be disregarded. Since the details of the stress field are unknown, one can use the experimental results on lateral cracking to find a correction term. Veldkamp [9] found a satisfactory description of the experiments with the relation

$$F_n = a K_I r(r+6b)^{1/2} \quad (8)$$

where a is a constant and b is the width of the groove. The K_I values deduced from (7) and (8) agree reasonably well with values found from the double torsion test [9] for the propagation of slow cracks. The effects are illustrated in figure 17, where the decrease of r with increasing speed is shown.

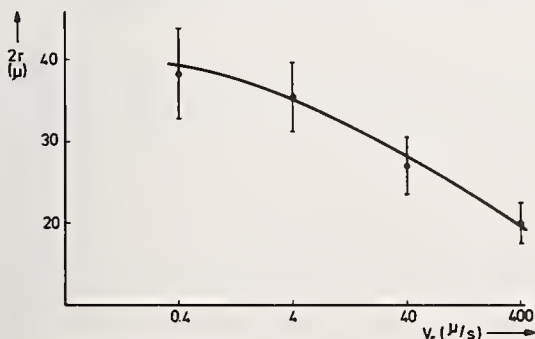


Fig. 17. Crack length taken on both side of a scratch, ($2r$) as a function of scratching speed (v_s) for MgO.

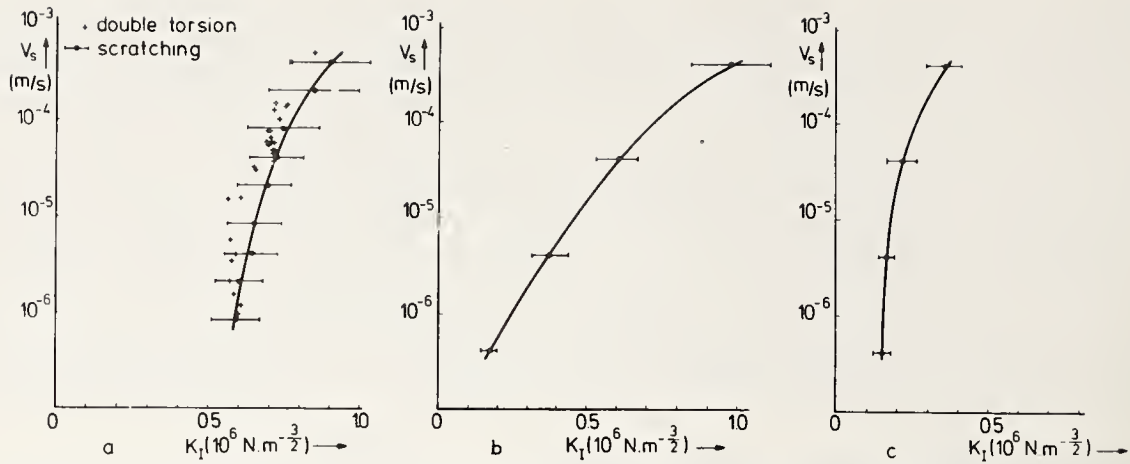


Fig. 18. Speed dependence of K_I as determined from scratching experiments on glass (left), MnZn ferrite (middle) and a MgO crystal (right). K_I values from a double torsion experiment have been added for the glass [9].

By using eq.(8) the results can be presented as a v_s - K diagram, as so often is used in stress-corrosion cracking of glass [1-4] (fig. 18). The appearance of a given type of crack is also a function of scratching speed, and a diagram can be made that combines the effects of speed and load (fig. 19). Grooves are observed at all loads and speeds, but the various cracks are found in a limited region only.

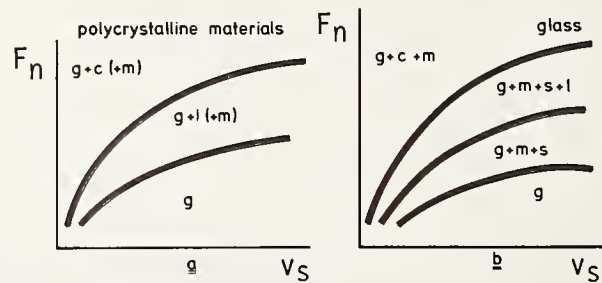


Fig. 19 Regions in a load (F_n)-speed (v_s) diagram where the various types of cracks occur, for a polycrystalline MnZn ferrite (left) and a glass (right). Grooves (g), lateral cracks (l), median cracks (m), subsurface cracks (s) and chips (c) are found in these materials.

4.2. Crystalline materials

Anisotropic materials often show the same types of crack as glass but the direction of cracking may be quite different for materials with pronounced cleavage planes. An example is the surface of a scratched MgO crystal (fig. 20) where the planes of easy cleavage show up clearly. In the cross-section shown in figure 10, horizontal and vertical cracks were visible; the horizontal crack extends over the length of the scratch [29]. The case of cracking makes it difficult to determine the groove dimensions. The extent of cracking in MgO shows a speed dependence (fig. 17).



Fig. 20. View from above of scratch made on (010) plane in the [100] direction of MgO single crystal, load 0.1 N, scratching speed 40 $\mu\text{m/s}$. Incident light.

Median cracks have also been observed in a MnZn ferrite, scratched by a pyramid with a leading edge (fig. 21). The surface cracks are of the lateral type, accompanied by chips (figs. 3 and 22). Here too, speed effects have been found [9,10] and the types of cracks can be given in a load-speed diagram, as was done for glass (fig. 19), but now the subsurface cracks are missing.



Fig. 21. Cross-section of a scratch in Mn Zn ferrite. Clearly shown is the median crack. Load 1 N, speed 400 $\mu\text{m/s}$. Incident light, bright field.



Fig. 22. Scratch made on MnZn ferrite. The two types of chip are marked with I and II. Load 0.2 N, scratching speed 4 $\mu\text{m/s}$. Scanning electron microscope.

In a polycrystalline material it can easily be shown by scratching where cracking takes place, along the grain boundaries as in fig. 23 or through the grains (fig. 24). The example in fig. 24 has exceptionally strong grain boundaries; one chip is seen to contain even three boundaries. As in glass, the large chips have been observed to crack open after the passage of the scratching pyramid.



Fig. 23. Scratch on NiZn ferrite, fired at 1230°C; load 1 N; width of picture: 150 μm .

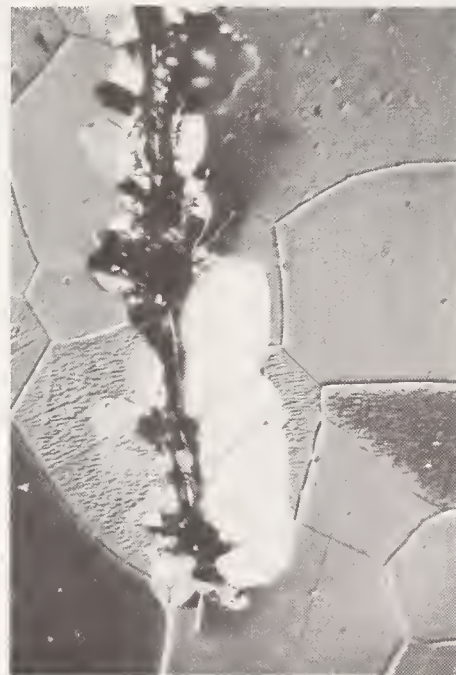


Fig. 24. Scratch on NiZn ferrite, after hot isostatic pressing at 1300°C; load 0.5 N; scratched after thermal etching; width of picture: 150 μm .

Notice that the chips remain fastened to the surface. A greater removal of material is expected to occur when a second scratch interferes with the chips of the first one. An example of this effect has been found on a MnZn ferrite that shows large chips. The following experiment was done: scratches were made at various distances (fig. 25) and the

material that was removed was determined by weighing. A pronounced increase was found below a certain distance that still depends on load (fig. 26).



Fig. 25. Photographs of parallel scratches on MnZn ferrite at various distances between the scratches: 250, 175, 200 and 125 μm .

Another item of interest in the context of material removal is the number of lateral cracks and chips per unit length of the scratch. Both increase with increasing load; the chips remain smaller until at higher loads the lateral cracks have disappeared in the area with large damage and a few large chips remain, as shown schematically in figure 27.

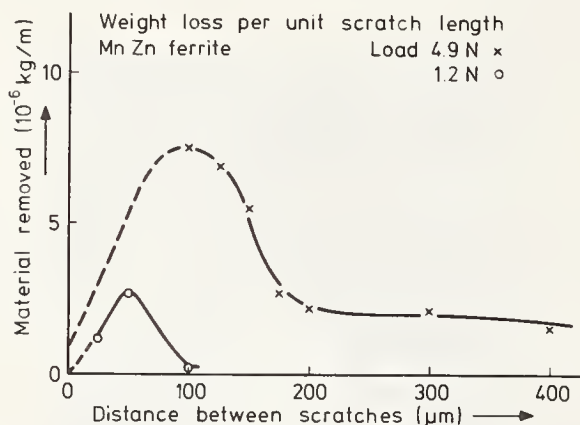


Fig. 26. The effect of the distance between parallel scratches, at constant load, on the weight of the material that was removed. Weight per unit scratch length vertical, interscratch distance horizontal. Material Mn Zn ferrite ($2\theta = 136^\circ$ $v_s = 50 \mu\text{m/s}$).

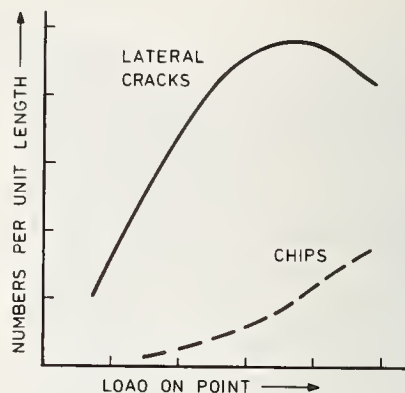


Fig. 27. The number of lateral cracks per unit scratch length, as measured on a MnZn ferrite, and, schematically, the number of chips, both as a function of load ($v_s = 400 \mu\text{m/s}$).

5. Liquids

In ferrites the effects of water are similar to those in glass. Scratching with a pyramid in a droplet of water the results of figure 28 were obtained: a slow scratch in normal, humid, air has a cracked groove, whereas a faster one is smooth. The influence of water on the strength of ferrites has been noticed before by Lessoff [30] .

Liquids on the surface of an oxide may have a softening effect as well as an influence on crack propagation. We used a variety of liquids during the scratching of MgO crystals, such as n-alcohols, di-methyl-formamide (DMF), di-methyl-sulfoxide (DMSO) and a 40-60% mixture of the latter two. Neither force ratio nor the scratching hardness were found to be influenced. Underneath the surface, however, the dislocation pattern extends farther for hexanol than it does for methanol or ethanol, in agreement with Westwood's findings

[14], taken by indentation at much longer times than in scratching. Two other experiments also gave negative results for a possible influence on the force ratio: one on quartz crystals in the presence of dodecyl-trimethyl-ammonium-bromide (DTAB) and one on a barium titanate in DMF and DMSO. The latter combination of a piezoelectric material with a liquid having a high dielectric constant looked promising, but gave no result. A real lubricant, DDDS - dioctadecyl-disulfide-, was used on a glass ceramic, dissolved in di-ethyl-ether and in ethanol; neither in solution nor after the evaporation of the solvent was there any change in the force ratio (fig. 29). The lubricating action during grinding, however, is in fact present, because when the solution is sprayed on a grinding wheel, the grinding force drops to a low (friction) level and material removal stops!

The lubricating effects of alcohols etc. on oxides have been investigated by Wiederhorn [31], using a spherical indenter; a sphere allows a more direct determination of the friction coefficient (cf. eq. (2)). Again no effect was found. The only positive result is the softening of MgO in hexanol, but only after the samples had been annealed. A possible influence of alcohols on the ease of crack propagation was investigated by Freiman [3,4]



Fig. 28. Scratches on $\text{SrFe}_{12}\text{O}_{19}$ under various circumstances: slow ($v_s = 50 \mu\text{m/s}$) and dry (left); fast ($750 \mu\text{m/s}$) and dry (middle); slow and wet (right). Load 5 N.

A slightly higher crack speed is only found for hexanol.

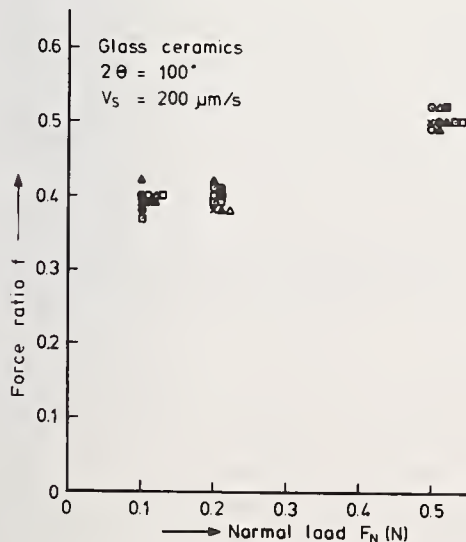


Fig. 29. Force ratio f versus load for scratching on a glass ceramic with and without DDDS (see text).

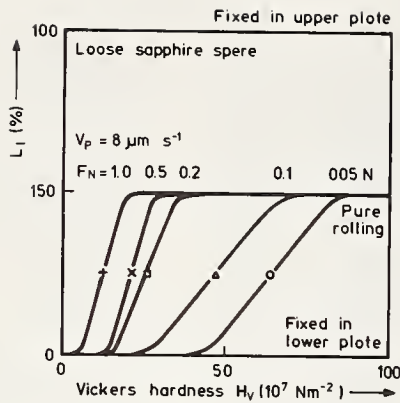


Fig. 30. Scratch length on lower metal divided by total scratch length, the rolling fraction, as a function of the hardness of the lower metal for various loads; $v_s = 8 \mu\text{m/s}$; brass upper plate; sapphire sphere.

6. Rolling

Scratches were made with a loose particle between a brass plate on top and a variety of materials underneath. For a sapphire sphere (0.1 or 0.2 mm diam.) some of the results are simple. On soft metals (In, Sn, Pb, Al, Zn, Cd, Cu) a transition occurs between fixation in the soft metal and rolling. This transition depends on load (fig. 30), the harder substrates needing less load for rolling to occur. On harder metals, like annealed and quenched steels or soft cast iron, rolling and fixation in the upper or the lower metal plate occurred in one scratch. The effect of increasing scratching speed is also confusing in that fixation and rolling seem to happen irrespective of the circumstances. At high speeds, however, rolling seemed to be the dominant phenomenon.

For a sharp diamond grain of about $250 \mu\text{m}$, the degrees of freedom include that of rotation around several axes, as can be seen in the pictures taken successively during a scratch (fig. 31). The trace left on the workpiece surface gives the impression of a periodic but random walk (fig. 32). We conclude that, although scratching with a fixed pyramid seems to present a number of problems, a loose particle is much worse. The inefficiency of lapping with loose particles is clearly visible in these single-point loose-scratching experiments.

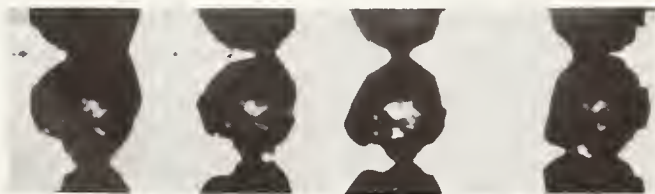


Fig. 31. Subsequent photographs of rolling diamond ($250 \mu\text{m}$ diam.) and its two images in the upper and lower plate (brass). During the motion of the lower plate the particle rotates around a horizontal and the vertical axis. Load 0.5 N ; $v_s = 8 \mu\text{m/s}$.



Fig. 32. Track on $\text{SrFe}_{12}\text{O}_{19}$ after a rolling diamond has passed over its surface. Load 0.2 N ; upper plate: brass.

6. Discussion

Scratching experiments are a source of information on three types of problems: what happens during scratching, what can be learned about the material and in how far can grinding behaviour be predicted?

1. The problems of single-point scratching can be summarized as follows:
 - a. Can one ever expect a detailed description of the stress field around the point and of the deformation? Electron-microscopy (Hockey, Lawn [32]) provides an enormous amount of interesting information, but it is qualitative in nature with respect to a description of the deformation.
 - b. From the groove dimensions under a known total force, characteristic average stresses have been derived (e and H_g) which are related to the indenter hardness. The hardness values show a dependence on depth, the "size effect". It is especially large in Al_2O_3 and rather small in ZnO (fig. 13). The same result was found for the soft polycrystalline ZnO ($H_v = 2.10^9$ N/m²) as for the harder ZnO crystal ($H_v = 10.10^9$ N/m²).

We consider two possible explanations for the size effect: one is based on a reduced stiffness, the other uses the speed dependence of the hardness. The first argument notices an important difference between the extreme cases of ZnO and Al_2O_3 : the number of cracks in ZnO is much smaller. A cracked material has a larger compliance; similarly, a scratching particle at the end of a sample encounters a more compliant material. A lower resistance to bending may lead to wider grooves and a lower hardness. This argument might also be used to understand the variation in length of consecutive cracks along the scratch (fig. 15b).

A quite different explanation of the size effect relies on the speed dependence of the hardness (fig. 14), relating it to an effect of the strain rate, $\dot{\epsilon} = v_s/d$ and giving equal weight to a change in speed v_s as to depth d . This model could be checked by careful measurements of the size effect at various scratching speeds.

- c. A third problem is the sign of the interface friction coefficient μ in eq. (2). The sign depends on the material [15, 17] for scratching with a leading plane, and it is rather large for the case of a leading edge. The difficulty is to predict the relative motion of the pyramid and the material that is emerging from the upper layer of the workpiece.

- d. Cracks are formed on the surface and underneath the scratching point. Some cracks (median, lateral) are formed in the contact area between indenter and material, others are formed (subsurface, chips) after the point has passed. All cracks propagate in the combined stress field of the loaded point and the groove that was just made. Since the groove region is highly deformed this is a complicated problem. Correct analytical expressions are not expected.

2. Scratching provides an easy way to obtain the following information about a material.

- a. The scratch hardness can be determined, similar to the indenter hardness; it can be used as a test of homogeneity as well.
 - b. The extent of cracking is an indication of the fracture resistance of the material and by using eqs. (7,8), K_{IC} can be derived. In a polycrystalline material the strength of the grain boundaries can be tested qualitatively; the same holds for the possible weakening effects of second phases and pores.
 - c. Speed-dependent fracture phenomena can be studied on a microscopic scale by direct observation. The influence of special environments is easily studied. The problem, however, is that scratching is no more than a handy mechanical device, but cannot provide details of the mechanisms involved.
 - d. A minimum load F_{min} can be derived from eq. (8) below which the cracks are confined to the groove [9]. F_{min} is proportional to K^4/H^3 and may be used in considerations about lapping, for example.

3. Scratching can be used as a basic model for grinding and lapping by comparing equivalent quantities such as the specific energy and the force ratio [5,6,22]. For some materials the agreement is quite good, for others the extent of cracking must be considered, because

that was omitted in calculating the groove energy from eq. (4). The experiments with parallel scratches at various distances have shown that cracking plays an important role at the higher loads (fig. 26). Damage made by grinding can be studied in detail by scratching, where especially the depth of cracking is relevant.

7. Conclusions

Scratching has proved to be a useful basis for understanding qualitatively the deformations that are encountered in grinding and other abrasive processes. The experiment allows detailed investigations of the dependence on load, speed and environment for those quantities that characterize a scratch. The results are as follows.

1. The force ratio is independent of load, material, speed and environment; it is determined by the geometry of the point. The interface Coulomb friction is a minor correction for pyramidal points, whereas it is the major effect for a sphere.
2. The specific energy depends on the material and is proportional to the Vickers hardness. No dependence on environment was found, but for several materials its value depends on the load, the so-called "size effect", and on the speed, at least in the present range of (low) scratching speeds.
3. The type of cracking depends heavily on the type of material. In glass, four types have been found; in crystalline materials, three. The extent of cracking depends on load according to eqs.(7 and 8), which contain the material-dependent fracture toughness K_{I} . Especially in humid environments containing water the extent of cracking in several materials becomes speed-dependent.

The link with grinding parameters, such as the force ratio, the specific energy, the surface roughness and the depth of damage, can now be made.

References

- [1] Charles, R.J., Static fatigue of glass, *J.Appl.Phys.* 29, 1549-1560 (1958).
- [2] Davidge, R.W. and Tappin, G., Strength of polycrystalline aluminas, *Proc. Brit. Cer. Soc.*, 15, 47-60 (Jan. 1970).
- [3] Freiman, S.W., Effect of environment on fracture of ceramics, 2, [3] , 111-118 (1976).
- [4] Freiman, S.W., Mulville, D.R. and Mast, P.W., Crack propagation studies in brittle materials, *J. Mater. Sci.* 8, 1527-1533 (1973).
- [5] Gielisse, P.J., Kim, T.J., Goyette, L.F. and Nagarkar, R.V., Fundamental and practical evaluation of the ceramic finishing process, Report (Univ. of Rhode Island), Kingston R.I., 1975.
- [6] Prins, J.F., A study of single diamond particle interaction on alumina, *Ind. Diamond Rev.*, 497-503 (Dec. 1971).
- [7] Busch, D.M. and Prins J.F., A basic study of the diamond grinding of alumina, (*Proc. Symp. Science of Ceramic Machining and Surface Finishing, Gaithersburg, Md., November 2-4, 1970*), pp. 73-87 (NBS Spec. Publ. 348).
- [8] Peter K., Sprödbbruch und Mikroplastizität von Glas in Eindruckversuchen, *Glastechn. Ber.*, 37, [7] , 333-345 (July 1964).
- [9] Veldkamp J.D.B., Hattu N., and Snijders, V.A.C., Crack formation during scratching of brittle materials, in *Fracture Mechanics of Ceramics*, Vol. 3, R.C. Bradt, D.P.H. Hasselman and F.F. Lange, eds., pp. 273-301 (Plenum Publ. Corp. 1978).
- [10] Veldkamp, J.D.B., Crack formation during scratching, (*Proc. 9th. Int. Conf. on Science of Ceramics, Noordwijkerhout, November 13-16, 1977*), Book, *Science of Ceramics*, 9, K.J. de Vries ed., pp. 438-446 (Nederlandse Keramische Vereniging, 1977).
- [11] Lawn, B.R. and Fuller, E.R., Equilibrium penny-like cracks in indentation fracture, *J. Mater. Sci.* 10, 2016-2024 (1975).
- [12] Swain M.V. and Hagan J.T., Indentation plasticity and the ensuing fracture of glass, *J. Phys. D.: Appl. Phys.*, 9, 2201-2214 (1976).
- [13] Westbrook, J.H. and Jorgensen, P.J., Effects of water desorption on indentation microhardness anisotropy in minerals, *The Am. Mineral.*, 53, 1899-1909 (Nov. 1968).
- [14] Westwood, A.R.C., Control and application of environment-sensitive fracture processes, *J. Mater. Sci.* 9, 1871-1895 (1974).

- [15] Broese van Groenou A., Maan N., and Veldkamp, J.D.B., Scratching experiments on various ceramic materials, Philips Res. Repts., 30, 320-359 (1975).
- [16] Stokes, R.J., Johnston, T.L. and Li, C.H., Crack formation in magnesium oxide crystals, Phil. Mag., 3, 718-725 (1958).
- [17] Maan, N. and Broese van Groenou, A., Low speed scratch experiments on steels, Wear, 42, 365-390 (1977).
- [18] Hisakado, T., On the mechanism of contact between solid surfaces, Bull. JSME, 13, [55], 129-139 (1970).
- [19] Bowden, F.P., and Tabor, D., The friction and lubrication of solids (Clarendon Press, Oxford, 1954).
- [20] Bowden, F.P. and Tabor, D., Friction, lubrication and wear: a survey of work during the last decade, Brit. J. Appl. Phys., 17, 1521-1544 (1966).
- [21] Shaw, M.C., Fundamentals of grinding, in New Developments in Grinding, M.C. Shaw, ed., pp: 220-258 (Carnegie Press, Pittsburgh, Pa, 1972).
- [22] Broese van Groenou, A., Veldkamp J.D.B. and Snip, D., Scratching and grinding parameters of various ferrites, J. de Physique, C1, 285-289 (1977).
- [23] Broese van Groenou, A., Experiments on grinding of ceramic ferrites, see ref. 9, pp. 486-493.
- [24] B.G. Koepke and R.J. Stokes, Grinding forces and the machining of magnesium oxide crystals, J. Mater. Sci. 7, 485-493 (1972).
- [25] Lawn, B.R., Partial cone crack formation in a brittle material loaded with a sliding spherical indenter, Proc. Roy. Soc. (London) 299A, 307-316 (1966).
- [26] Busch, D.M., Verformen von Glas mit Ritzwerkzeugen, Films 1328-1330, Inst. Wiss. Film., Göttingen 1967.
- [27] Dick, E., Plastische Verformung, Anrissbildung und statische Ermüdung bei Ritzversuchen an Tafelglas, Glastechn. Ber., 46 [6], 120-128 (1973).
- [28] Roessler, F.C., Brittle fractures near equilibrium, Proc. Phys. Soc. B69, 981-992 (1956).
- [29] Sugita, T., Suzuki, K. and Kinoshita, S., Wear characteristics of magnesium oxide single crystals on steel, Wear 45, 57-73 (1977).
- [30] Lessoff, H., Effect of moisture on strength of ferrite memory cores, J. Am. Cer. Soc., 54, [7], 353 (1971).
- [31] Witherhorn, S.M. and Roberts, D.E., Influence of normal alcohols on the abrasive wear of glass, Wear 32, 51-72 (1975).
- [32] Hockey, B.C., and Lawn, B.R., Electron microscopy of microcracking about indentations in aluminium oxide and silicon carbide, J. Mater. Sci. 10, 1275-1284 (1975).

Discussion

BENNETT

Did you investigate scratch behavior for increasingly light loading? Your slide on the force ratio seemed to indicate the beginning of a deviation from a constant value for light loading. Our results on much softer materials suggest that this deviation would continue to increase as the loading decreases and is not simply a result of the error in shape of the diamond point.

VAN GROENOU

Our experience is the following: every time we found such a decrease in force ratio on decreasing the load, we looked at the diamond under high magnification (dark-field) and found something suspicious at the point, usually a tiny flat spot. After regrinding the pyramid the force ratio was found to be increased.

CHOUDRY

The tangential force (F_t) for high speed grinding in your model is strictly governed by the geometrical volume removed and this volume is calculated by the geometry of the tool (a), depth of cut (d) and the ratio of the work-

piece speed (V_w) & wheel speed (V_s); all of which are experimentally adjusted parameters and do not depend on the elastic (or materials) property of the workpiece. Does it mean that for a given set of a , d , V_w , V_s , one would always get the same F_t irrespective of the workpiece material be it diamond or marble. On the other hand the dynamic elasticity of the impact would inescapably generate a force which among other variables depends on the materials properties. Is there a need in your model to take this into account?

VAN GROENOU

In the paper the specific energy is introduced by the relation power = $e \cdot Z$, also power = $F_t \cdot V_s$ from which follows $F_t = e \cdot Z / V_s$. The material properties relevant for grinding are contained in the factor e .

EXPERIMENTS ON HIGH-SPEED GRINDING OF FERRITES AND GLASSES

A. Broese van Groenou and R. Brehm

Philips Research Laboratories

5600 MD Eindhoven, The Netherlands

At wheel speeds of 60-100 m/s measurements have been made on a horizontal-spindle grinder with a nickel-plated diamond wheel. The grinding force components are unique functions of the continuum chip thickness $h_{eq} = av_w/v_s$, over a large range of the depth of cut a , the workpiece speed v_w and the given range of wheel-speed v_s . The v_s dependence is different for those glasses where melting occurs. Where a specific energy can be determined, it shows a dependence on the depth of diamond penetration. This "size effect" is strong in the case of low-toughness materials. The energy data are compared with those obtained for grooving in low-speed scratching experiments. Deviations occur where groove formation is accompanied by heavy chipping. Finally, for brittle materials, the requirements of a grinding model are considered, with emphasis on the amount of chipping and the diamond distribution on the grinding wheel. In this model the specific energy is a characteristic of the grinding system and not of the workpiece alone.

Keywords: Chipping; ferrites; glass melting; grinding; grinding model; high-speed grinding; pyrex; size effect.

1. Introduction

The first meeting on "Ceramic Machining and Surface Finishing" [1]¹ showed clearly that grinding is a complicated process, in which many components take part. Macroscopically one finds: motor, grinding wheel, frame, workpiece, cooling. On a microscopic scale: diamonds, wheel and workpiece microstructure, frame displacements and wheel unroundness. This complexity stimulated us to set up experiments and collect data in order to find a description of the process on both a large and a small scale. Medium hard materials, ferrites and glasses, have been studied in some detail. The results will be reviewed in this paper; some of the results have been published elsewhere [2-4].

A macroscopic quantitative description considers the components F_t and F_n , rate of volume removal, Z , the power W , the force components F_t and F_n , the workpiece-wheel contact width b , the depth of cut a , the workpiece feed v_w , the wheel speed v_s and the contact length l_c (fig.1). For horizontal surface grinding the following relations are useful [5]:

$$Z = a \cdot b \cdot v_w \quad (1)$$

$$W = F_t \cdot v_s \quad (2)$$

$$= e \cdot Z \quad (3)$$

$$Z = F_t \cdot v_s / e \quad (4)$$

$$= F_n \cdot v_s / H_g \quad (5)$$

$$f = F_t / F_n \quad (6)$$

¹Figures in brackets indicate the literature references at the end of this paper.

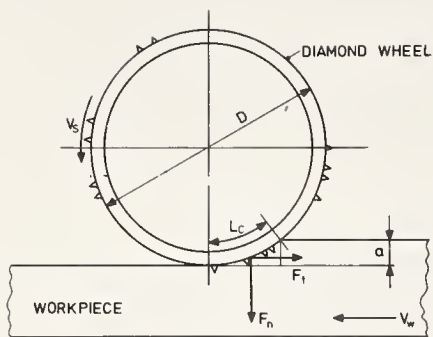


Fig. 1. Schematic view of grinding wheel in horizontal surface grinding.

where, by analogy with the grinding of metals [5], the force ratio f , the specific energy e and the grinding hardness H_g were introduced. Both have the dimensions of a stress, or of an energy per unit volume. Together with the wheel wear and the surface damage, e.g. expressed in terms of c.l.a. roughness, these quantities usually characterize a grinding operation. In grinding steel a useful quantity is the continuum chip thickness, h_{eq} , defined by [6,7]

$$Z = b \cdot v_s \cdot h_{eq} \quad (7)$$

which, together with eqs. (4) and (5), gives

$$F_t = b \cdot e \cdot h_{eq} \quad (8)$$

$$F_n = b \cdot H_g \cdot h_{eq} \quad (9)$$

It would be a considerable simplification if these relations were to hold for grinding ceramics and glass. If that were the case, different grinding machines could be compared, although used at different values of a , v_w and v_s . In grinding steel [5] the linear relation between force and rate of removal that is suggested by eqs. (8) and (9) is not found. The deviations are usually described by having e and H_g vary with, for example, h_{eq} . Such a "size effect" has also been found in grinding MgO [8] and forms an important part of the discussion on the present results for several ferrites (sections 3.1 and 3.2) and glass (section 3.3). From eqs. (4) and (5) the advantages of using high-wheel speeds are obvious, as long as the specific energy is independent of v_s . A comparison between e values found in grinding steel at 20-30 m/s [5] and low-speed scratching at 0.4-400 mm/s [9] shows that the high-speed e values are higher and show a stronger size effect. The experiments to be described were done at 60 to 100 m/s (section 2) in order to see whether such discrepancies are also found in oxides; where possible the results obtained at 5 m/s will be included [2]. The corresponding scratching experiments have been described in refs. [10,11]. Some high-speed grinding experiments were done on a number of glasses, one of which, a borosilicate glass, will be treated here because of its deviating behaviour.

The reason for comparing grinding data with scratching becomes clear when the processes are compared on a microcopic scale. At the beginning of contact between a grinding wheel and a slightly tilted sample (e.g. 1:100) one observes first a fine scratch at the start of the tracks made by the diamonds; then, the track widens and chips appear, which finally merge with the deformation made by neighbouring particles (fig. 2).

From the figure another complication is clear: different diamonds touch the tilted sample at various places. This makes it impossible to speak about the depth of cut for every particle and statistical considerations are necessary for any grinding model [12,13]. Figure 2 also shows the two basic features of the grinding models that have been proposed, grooves and cracks. The grooves have led to the ploughing type of models [5], which give the resistance to grinding or lapping as proportional to the hardness of the workpiece, in agreement with experiments on lapping of glass [14,15] and ceramics [16].



Fig. 2. First contact between grinding wheel and slightly tilted sample of MnZn ferrite ($v_s = 75$ m/s).

The cracks and chips have been used in models that are based on the fracture underneath a statically loaded spherical indenter, where ring and cone cracks are formed. These ideas have been applied to erosion [17] and lapping [18]. A difficulty is estimating the volume removed by a single indentation, and opinions vary considerably [12, 17, 18]; it seems essential to take into account the interaction between cracks made by different indenters because no material is loosened from the surface by a single indentation [18]. One result of this model is a dependence on the fracture strength, which agrees with Gielisse's results on grinding various types of alumina [19]. Figure 2, however, does not show separate indentations but long scratches. A grinding model based on the phenomena around a scratch has been given by Veldkamp [2] and we will return to such models in the discussion. First a description is given of the experimental set-up; results for two ferrites and one glass are given in section 3. The relevance of the continuum chip thickness is discussed in section 4, followed by considerations about grinding temperatures, the size effect and the requirements for a grinding model for brittle materials.

2. Experimental

The measurements were made on a flat bed grinder using a horizontal axis motor², running at 20000 to 36000 r.p.m., with a nickel-plated diamond wheel³ (diamond size 220 μm). The horizontal traversing carriage is hydrostatically supported and hydraulically driven. The oil unit is separate from the grinder (fig. 3). The following values were used: the feed v_w from 0.1 to 60 mm/s, the depth of cut a up to 500 μm , the wheel speed v_s from 58 to 102 m/s (in continuous operation, lower values were obtained upon starting the motor), the sample length 10 to 40 mm and the contact width b from 2 to 5 mm. Mist cooling was applied. The apparatus and a detail are seen in figure 3. The force components were measured by means of a piezoelectric transducer⁴ and the necessary electronics, including a multichannel tape recorder⁵ for the data on force components, speed v_s and radial vibrations⁶.

The apparatus was carefully balanced. The amplitude of the vibrations of various parts of the grinder was measured as a function of frequency, both by external excitation and with the motor running. The amplitude u during grinding remained constant at 330 Hz ($v_s = 58$ m/s), increased at 495 Hz (86 m/s) and decreased at 550 Hz (96 m/s) with respect to the amplitude before contact (fig. 4).

² SJF-HE 40, Fischer, Herzogenbuchsee, FRG

³ Techno Diamant, Amsterdam

⁴ Kistler 9259, Winterthur, Switzerland

⁵ Analog 7, Philips

⁶ PM 6431, Philips

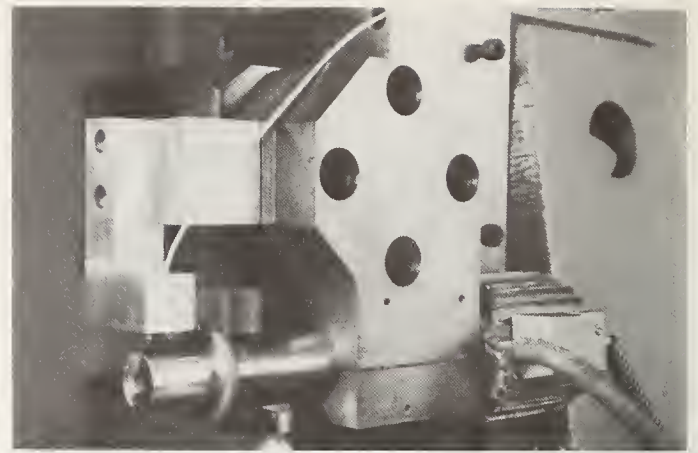


Fig. 3. Grinding apparatus: electronics (left, grinder and oil-and mist supply right. Detail showing wheel, motor and the contactless vibration transducer above the extended shaft

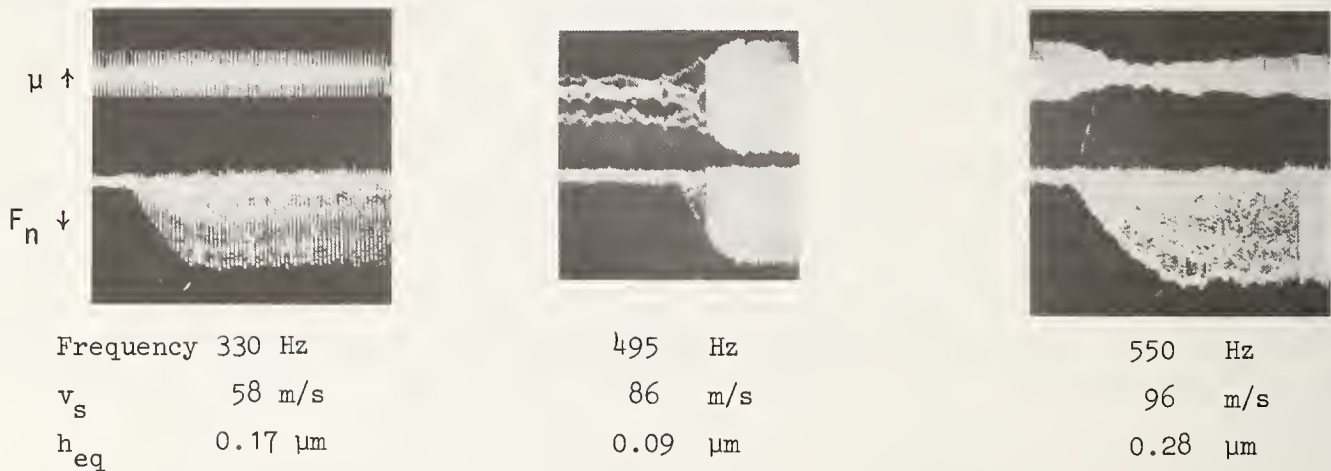


Fig. 4. Amplitude of axial vibration u and normal force F_n as a function of time, showing the changes upon the start of grinding.

From such results we have the impression that vibrations do not contribute much to the force level during grinding. More important is the finding (also on other grinders we have used) that the force level is pulsed, with a repetition time equal to the period of the wheel (fig. 5). This was due to the unroundness of the wheel. During about 18 months of experimenting the wheel showed very little wear, as measured by making replicas of those parts that had a slightly larger radius. This was known from a roughness measurement, done by rolling a small cylinder over the wheel surface. From the roughness plot the distribution of the heights of the diamonds was obtained.

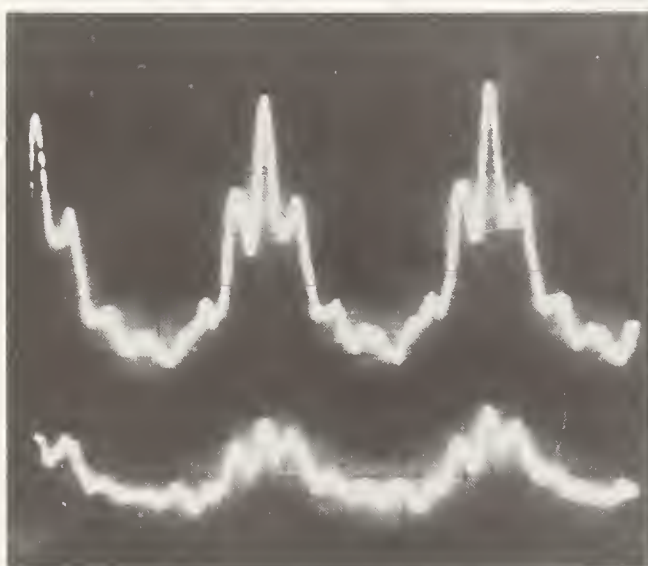


Fig. 5. Force pulses during several revolutions of the grinding wheel; frequency 330 Hz, $v_s = 58$ m/s, $v_w = 60$ mm/s, $h_{eq} = 0.84$ μm ; 20 N/div vert, 1 ms/div horizon; material: $\text{SrFe}_{12}\text{O}_{19}$.

The following samples were used:

- SrFe₁₂O₁₉, a hexagonal ferrite, polycrystalline, porosity 8%, aligned, grain size about 5 μm,
- (Mn, Zn, Fe) Fe₂O₄, a cubic ferrite, polycrystalline, porosity 8%, grain size about 15 μm,
- A borosilicate glass with an ASTM softening point of 800°C.
- Quartz glass.

3. Results

3.1. SrFe₁₂O₁₉

The results for three wheel speeds are given in figure 6 for the normal force component F_n as a function of the volume rate of removal Z ; both quantities have been reduced to unit width of contact. The whole range of variation for a and v_w were used. The three v_s ranges show clearly different curves. From eqs. (7 and 9) a single curve is expected if $h_{eq} = Z/bv_s$ is plotted along the abscissa. For both F_t and F_n this is indeed the case (fig. 7); there is no longer any systematic variation with v_s . This result means that one combination of the machine parameters, a , v_w en v_s , is sufficient to describe the grinding force for this material. The same holds true for the (c.l.a.) roughness, which shows a relatively small variation, from 0.7 to 1.5 μm, over the h_{eq} range in fig. 7. The force ratio, $f = F_t/F_n$, varies from 0.1 to 0.3 over the same h_{eq} range.

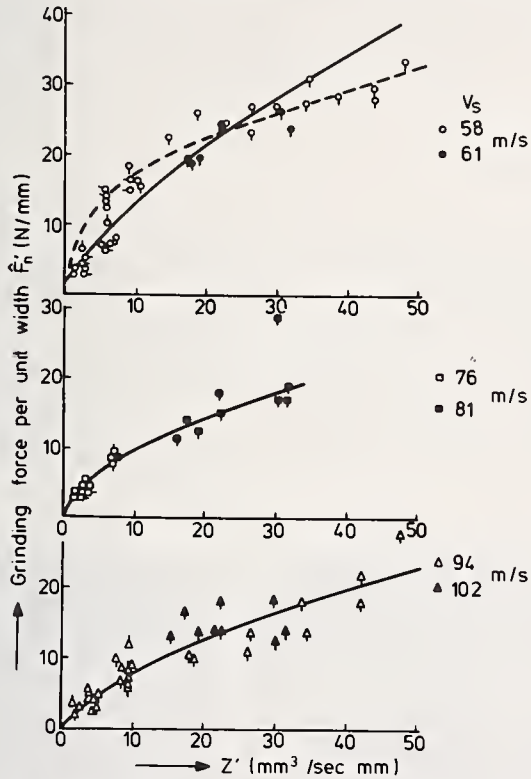


Fig. 6. Normal component of grinding force F_n as a function of rate of removal Z , both per unit width of contact zone. Three ranges of wheel speed v_s are shown; material: SrFe₁₂O₁₉.

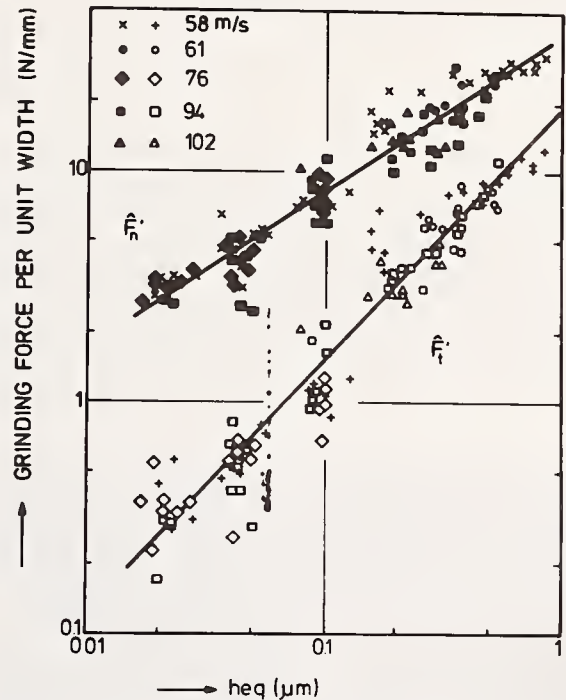


Fig. 7. Grinding force components, F_n and F_t , versus continuum chip thickness h_{eq} ; data from fig. 6.

In these results the peak values of the force components were used, whereas Z from eq. (1) and h_{eq} from eq. (7) are average values. For the calculation of the specific energy and the grinding hardness from eqs. (8) and (9) a factor of three was used to change from peak to average values. The results are shown in figure 8, where data from ref. [2] taken at $v_s = 5$ m/s are shown too. The slope in the $\log F - \log h_{eq}$ plot of fig. 7 was less than one for F_n and just above one for F_t , which corresponds in fig. 8 to a decrease of H_g and a slight increase of e with h_{eq} .

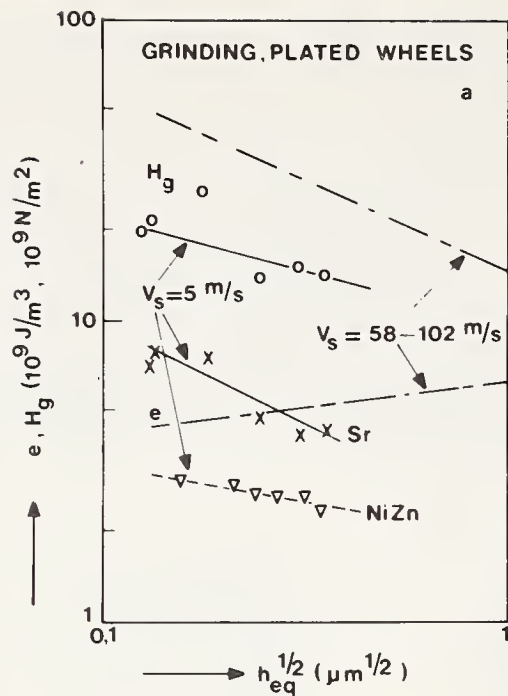


Fig. 8. Specific energy e and grinding hardness H_g versus h_{eq} for $SrFe_{12}O_{19}$ at $v_s = 5$ m/s ([2,3] and at high v_s values.

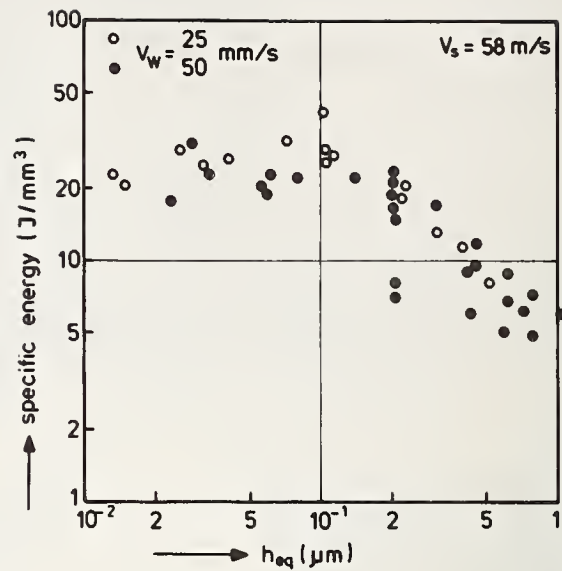


Fig. 9. Specific energy for MnZn ferrite at 58 m/s, versus h_{eq} .

3.2. $(Mn,Zn,Fe)Fe_2O_4$

The data on this cubic ferrite show the same independence of wheel speed when the grinding force is plotted versus h_{eq} as for the hexagonal ferrite. The force ratio is about 0.2 over a large range of h_{eq} values. The specific energy data show a marked decrease at h_{eq} larger than $0.1 \mu m$ (fig. 9). We shall return to this size effect in section 4.3.

A qualitative check was made on the behaviour of some materials as a function of wheel speed. Again using the first contact with the diamonds on a tilted sample, of the same MnZn ferrite, the photographs of fig. 10 were obtained, giving the grooves due to the same group of diamonds. There seems to be more variation due to local differences in the material than due to the fivefold increase in v_s .



Fig. 10 Start of grooves on MnZn ferrite, as observed on a tilted sample. From left to right: $v_s = 22, 58, 81$ and 104 m/s.

When the grooves become deeper, more chips appear along the scratches, which finally merge with those from neighbouring scratches. We have studied this interaction between parallel scratches at low speed in a single-point apparatus by varying the distance in between. The smaller the distance, the more damage is found and the weight of the material removed is a strong function of distance [11] .

3.3. Glasses

Quartz glass behaves in the same way as the ferrites at these high speeds. The grinding hardness decreases from 40 to 30 $\cdot 10^9/\text{Nm}^2$, the specific energy from 15 to 7 $\cdot 10^9\text{J}/\text{m}^3$ when h_{eq} increases from 0.1 to 0.6 μm . The data for $v_s = 58$ and 94 m/s are equal within the scatter. The e values are about a factor 3-5 larger than Huerta and Malkin's results at $v_s = 19$ m/s [20] .

The borosilicate glass, however, deviates in several respects when $v_s = 94$ m/s is used. The time dependence of the force during the passage across the workpiece is an example. Normally the force increases upon contact and quickly reaches a constant value; at low h_{eq} this is indeed found (fig. 11a). At higher h_{eq} it takes much longer to reach a constant value (fig. 11b). The damage changes too, from a normal, rough, surface to a shining surface with dikes of molten material, cracking and sometimes large holes where big lumps have disappeared (fig. 12). In spite of this, the F_n-h_{eq} plot is quite normal (fig. 13a). The tangential force, however, is completely irregular at high v_s ; at all h_{eq} values above 0.2 μm melting occurs and the correlation between F_t and h_{eq} is lost (fig. 13b) For a molten surface the continuum chip thickness is no longer a useful parameter to describe grinding; the same holds for the specific energy. At lower wheel speeds, up to 40 m/s, Huerta and Malkin [20] found a normal $F - Z$ behaviour, as in our results at 58 m/s in fig. 13.

4. Discussion

4.1. Significance and use of h_{eq}

For the results on the grinding of ferrite, shown above, and a number of other materials, the continuum chip thickness is a valuable parameter. It can be calculated from the machine settings with eq. (7) and is a direct measure of the grinding forces for a given material, i.e. for given e and H_g values (eqs. 8 and 9). Measurements on dry grinding of MgO reported by Koepke [8] can be presented in a simpler way by using h_{eq} . It is also a measure of the thickness of the debris layer that would be left on the grinding wheel if no cleaning were used; in fact, this is where h_{eq} got its name of continuum chip thickness [6,7]. In this application h_{eq} should be compared with the height of the abrasive particles above the binder level. If the wheel is clogged after a small number of revolutions, each of which add a layer of h_{eq} , the cleaning action should be improved. For small diamonds or a large contact area this is sometimes solved by segmenting the grinding wheel, e.g. by using pellets. One should distinguish between h_{eq} and the average depth of cut of the diamonds, which will be discussed in the next section.

The surface roughness is only a weak function of h_{eq} , much weaker than the force. Since grinding force and workpiece damage are certainly related, this result is surprising at first sight. Two reasons, however, may be given. Firstly, as mentioned before, h_{eq} is not a direct measure of the depth of cut of the average diamond; it can even be shown that for a distribution of heights of the diamonds, its value depends only weakly on the depth of cut of the outermost diamond. Secondly, referring to figure 1, the maximum depth of cut for each diamonds occurs at the end of the contact length (at the beginning for down-grinding); this area, however, is removed to a depth a by the action of the following diamonds. This probably leaves the damage at first contact (last contact for down-grinding) as the main contribution to the roughness. This part of the contact zone, however, hardly contributes to Z or h_{eq} and certainly not to the peak value of the grinding force. It is therefore not surprising that roughness and h_{eq} (or F_n) are not strongly correlated.

4.2. Melting

For several glasses a quite different result has been obtained: at high wheel speeds melting occurs and h_{eq} is no longer a useful parameter. The heat input q into the workpiece can be derived from the power in eq.(2) and the ratio of the thermal "impedances" of wheel and workpiece [21-24],

$$\frac{q_{wheel}}{q_{workpiece}} = \left[\frac{(k\rho c)_{wheel}}{(k\rho c)_{workpiece}} \right]^{\frac{1}{2}} \quad (10)$$

where k is the heat conductivity, ρ is the density and c the heat capacity per unit mass. For a steel wheel on a ceramic workpiece 6 to 8% of the total heat generated enters the workpiece, the rest goes into the wheel and the cooling water. The temperature at a depth y can be calculated from a model where the heat source, $W=F_t v_s$, moves over the surface at a speed v_w ; the result is [21-23]

$$T(y) = T(o)\exp(-y/y_o). \quad (11)$$

In this expression $T(o)$ and y_o are functions of $l_c v_w / \alpha$, where α is the thermal diffusivity $\alpha = k/\rho c$; the contact length l_c is given by $l_c = (\alpha D)^{\frac{1}{2}}$ for horizontal surface grinding (fig. 1), where D is the wheel diameter. Without going into further details, it can now be seen that the equivalence of depth of cut a and feed v_w , which was present in eqs.(1) to (9), is lost when the temperature affects the behaviour of the material. In the most extreme circumstances of our grinding apparatus the surface temperature is calculated to be $10^4 K$, and at a depth of cut of $400 \mu m$ the borosilicate glass reaches its ASTM softening point ($800^\circ C$). The appearance of glass surface can thus be understood in a qualitative way. As in the roughness problem discussed earlier, not all of the damage due to melting and cooling will be present on the surface afterwards.

If melting or, less severe, softening occurs, a shear deformation of the hot surface material must be considered. The necessary shear stress τ probably contributes more to F_t than to F_n , which agrees with the normal behaviour of the $F_n - h_{eq}$ curve (fig. 13). With the viscosity of the flowing material, τ is given by

$$\tau = \eta \frac{dv_x}{dy} \approx \eta \frac{v_s}{y_o} \quad (12)$$

τ is related to F_t by

$$F_t = \tau l_c b. \quad (13)$$

The specific energy is derived from (4), (12) and (13),

$$e = F_t v_s / Z = \eta v_s^2 l_c b / y_o Z \quad (14)$$

In this simplified model a strong influence of v_s on e is therefore expected. This may account for the relatively high e values found here at high v_s , even in quartz glass, in comparison to Huerta's results at 19 m/s [20]. The increase of e with the softening temperature [20], is also in agreement with the η dependence in eq. (14).

4.3. Size effect

The specific energy depends on the rate of removal Z , or, as in figs. 8 and 9, on h_{eq} . This "size effect" is usually attributed to the behaviour of the material and must then

be considered on a microscopic scale, where the depth of cut of each diamond, d , is used as a relevant variable [5,8]. To derive d from Z or h_{eq} one assumes that each of the active diamonds (total instantaneous number N_d , speed v_s) makes a groove with cross-section A_d ,

$$Z = N_d A_d v_s. \quad (15)$$

For pyramidal particles (apex angle θ) the grooves are triangular. In horizontal axis grinding the groove starts at a point and widens over the contact length l_c . The cross-section, averaged over l_c , is

$$A_d = d_{max}^2 / 3 \cot \theta \quad (16)$$

where d_{max} is the depth at the end of the groove. With eqs.(7), (15) and (16), d_{max} is given by

$$d_{max} = (3 \cot \theta h_{eq} \cdot b / N_d)^{1/2}. \quad (17)$$

For groove formation at low scratching speeds [9, 10] the force ratio f equals $\cot \theta$; an estimate of $\cot \theta$ at high speeds can also be made by using f . A number of methods are known for obtaining the N_d value [25]; here we used a roughness measurement by a roller over the circumference of the wheel. The result conforms with what the figures 2 and 10 already indicated, i.e. a distribution of heights of the diamond type must be used. Introducing the probability density $N(y)$, A_d is given by

$$A_d = \frac{1}{3 \cot \theta} \int_0^{d_{max}} (d_{max} - y)^2 N(y) dy \quad (18)$$

where y runs from the outermost diamond tip to the depth d_{max} . In the roughness experiment a discrete distribution was obtained, counting the number of peaks at intervals of $\Delta y = 5 \mu m$ (no shadow correction was applied [26]). The integral in eq.(15) was evaluated as a sum for d_{max} up to $60 \mu m$. Together with eqs.(7) and (15) a numerical relation between d_{max} and h_{eq} is found which replaces eq.(17). The specific energy can now be taken from figures 8 and 9 and replotted as a function of d_{max} (figs. 14 and 15). For the hexagonal ferrite we have added data taken from measurements at

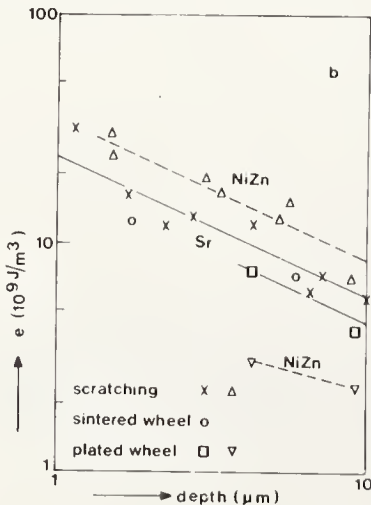


Fig. 14 Specific energy as a function of calculated grit depth for $SrFe_{12}O_{19}$ and $(Ni,Zn)Fe_2O_4$.

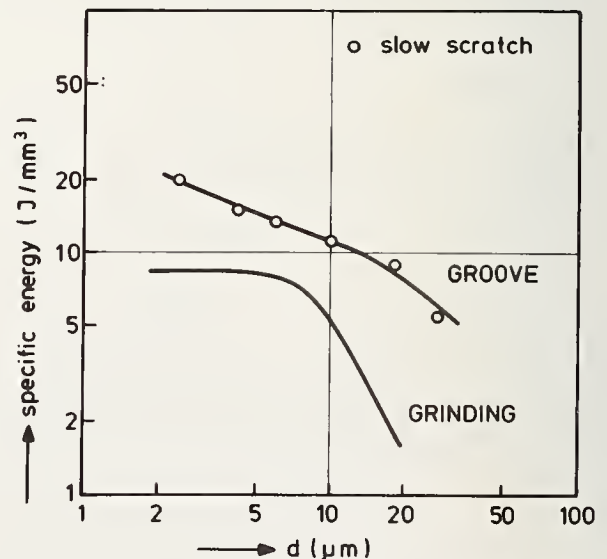


Fig. 15. As Fig. 14 for $(Mn,Zn)Fe_2O_4$.

$v_s = 5$ m/s (an average N_d was used [2]) and from low-speed scratching [10,11]. The agreement is remarkably good. For the cubic ferrite the results show again the strong decrease of the specific energy at the larger depths of cut, much more than found upon scratching the same material (fig. 15). It should be remembered, however, that the value of the specific energy for scratching has been derived from the groove parameters only, disregarding the chips that were made and may still be fastened to the surface. In grinding the chips are loosened too and must be included in the volume removed. This, however, has not been taken into account in the derivation of eqs. (16-18). Formally, one could introduce a wider groove by using a lower value for $\cot \theta$. The result is an even stronger decrease of e with increasing d . On the other hand, the agreement between e values from grooving and scratching for $\text{SrFe}_{12}\text{O}_{19}$ (fig. 14) should correspond to the absence of large-scale chipping in this material. Such is indeed the case: when the extent of cracking and chipping in the hexagonal ferrite is compared with that in the MnZn ferrite one finds that the latter is much larger. By analogy with the half-penny crack model [27] the extent of chipping can be expressed in terms of the fracture toughness value, K_{I} , by

$$c \propto (F_n / \pi K_{\text{I}})^{2/3} \quad (19)$$

where F_n is the load on the scratching diamond. The K_{I} values obtained from a three-point bend test [2], are

$$\begin{array}{ll} \text{SrFe}_{12}\text{O}_{19} & K_{\text{I}} = 2.1 \times 10^6 \text{ N/m}^{2/2} \\ (\text{Mn, Zn}) \text{Fe}_2\text{O}_4 & K_{\text{I}} = 1.1 \times 10^6 \text{ N/m}^{3/2}. \end{array}$$

We conclude that the different chipping of these materials may be responsible for the different size effects. A grinding model for brittle materials should therefore include the consequences of fracture on a microscopic scale.

4.4. Grinding models

Characteristic quantities for grinding are the force ratio, the depth of damage and the specific energy. The force ratio has a simple meaning for scratching at low speeds: $f = \cot(\theta + \alpha)$, where 2θ is the apex angle of the scratching pyramid and $\tan \alpha$ is the Coulomb friction on the interface between diamond and workpiece [9,10]. At high speeds heat is developed that may modify the material: softening for metals [28], melting in glass; the simple "ploughing" relation between f and θ is then no longer valid. The force ratio seems to be a good measure of the sharpness of the abrasive particles, which need not be the same when the wheel is used in fine and coarse grinding, because more and different particles are active in the latter case.

The depth of damage, as measured by the surface roughness, R_a , does not allow a simple interpretation as was argued in section 4.1. Compared with the d_{max} values derived from h_{eq} in section 4.3., R_a is much smaller. A much better description of damage would be given by the subsurface cracking, but this requires much more experimental work and is suitable for laboratory investigations only.

The specific energy, the third characteristic quantity of grinding, measures the resistance to material removal. Under the action of the diamonds the material is heavily deformed and grooves, cracks and chips are formed. The groove is found at all loads on the diamonds, but cracks appear outside the groove at a force level that is given by [29],

$$F_{\text{min}} \propto K_{\text{I}}^4 / H_v^3. \quad (20)$$

For a grinding force below this value one could speak of light grinding. Apparently, this definition depends on the material: for metals no chips are formed, while for a ceramic

where A_{ch} is the volume removed per unit length of scratching, as plotted in fig. 16. In view of the distribution of heights and distances (the Z- and X-distributions of ref. 13) A_{ch} is a sum over curves as shown in fig. 16. The power W necessary for the removal rate in eq. (21) is mainly determined by the formation of the groove, because cracking requires little energy and can be ignored:

$$W = e_{gr} Z_{gr}. \quad (22)$$

The specific energy follows

$$e = \frac{W}{Z} = \frac{e_{gr} Z_{gr}}{Z_{gr} + Z_{ch}} = \frac{e_{gr} A_{gr}}{A_{gr} + A_{ch}}. \quad (23)$$

With increasing depth of cut, A_{ch} increases sharply for two reasons: firstly, the chip volume increases and secondly, the interaction between chips increases (fig. 16). If this interpretation of the size effect in fig. 15 is correct, this means that fairly detailed information about the grinding wheel is needed. In that case the specific energy is not a material property, as in groove formation, but a property of the grinding system.

5. Conclusions

Grinding experiments at wheel speeds of 60-100 m/s have shown that the force components are unique functions of the continuum chip thickness, h_{eq} , defined by eq. (7). For a quick comparison of grinding operations h_{eq} is useful (e.g. $h_{eq} = 0.01 \mu\text{m}$ for light grinding, $h_{eq} = 1 \mu\text{m}$ for coarse grinding). Problems are encountered when melting occurs, as in the borosilicate glass at $v_s = 100 \text{ m/s}$. Depth of cut and feed are then no longer equivalent and h_{eq} loses its meaning.

For microscopic details, however, more information is necessary. The surface quality as measured by the c.l.a. roughness, is a weak function of h_{eq} . This may be related to the variation of the grinding force over the contact length, the maximum damage being removed, the minimum being left behind (sect. 4.1.). It would be better, but more cumbersome, to measure the subsurface damage, especially cracking. This is also relevant for the matching of subsequent stages in a grinding operation.

The specific energy has been derived from the data and considered in some detail. The dependence of e on the grit depth d_{max} is found to be rather weak in a hexagonal ferrite. The e values are in good agreement with those found at a lower grinding speed and in scratching at very low speeds. This material shows small chips only, and the groove energy is a good measure of the grinding energy.

Quite a different behaviour was found in a (Mn,Zn,Fe) ferrite, where a strong size effect is found. This material shows large chips, and arguments have been presented that the interaction of neighbouring scratches is responsible for the increase in removal.

A grinding model that goes beyond simple grooving must be based on the workpiece behaviour, i.e. the extent and frequency of chipping and the more or less random interaction between neighbouring scratches. It seems that multiscratching experiments can provide the necessary information. The model cannot avoid rather detailed information about the diamond distribution on the grinding wheel. The height distribution is needed for the number of active diamonds at a given depth of cut, while the transverse distribution (pairwise) allows the scratch interaction to be treated. For brittle materials of the second kind the specific energy, especially the size effect, is a property of several components of the grinding system.

The authors wish to thank a number of colleagues for their contributions to this work: J.C.G. Teunissen and M.A. Brebels for their help in building the grinding apparatus; G.F.M. Gasseling for his contributions to the experimental results and D. Snip for many discussions during several years of close cooperation on the grinding of ceramics.

References

- [1] Proc. Symp. on Ceramic Machining and Surface Finishing, Gaithersburg, Md., November 2-4 1970, Book, The science of ceramic machining and surface finishing, S.J. Schneider Jr. and R.W. Rice eds. (NBS Spec. Publ. 348, 1972).
- [2] Veldkamp, J.D.B. and Klein Wassink, R.J., Grindability of brittle materials, Philips Res. Repts., 31 153-189 (1976).
- [3] Broese van Groenou, A., Veldkamp J.D.B. and Snip, D., Scratching and grinding parameters of various ferrites, J. de Physique, C1, 285-289 (1977).
- [4] Broese van Groenou, A., Experiments on grinding of ceramic ferrites, (Proc. 9 th Int. Conf. on Science of Ceramics, Noordwijkerhout, November 13-16, 1977), Book, Science of Ceramics 9, K.J. de Vries, ed., pp. 486-493 (Nederlandse Keramische Vereniging, 1977).
- [5] Shaw, M.C., Fundamentals of grinding, in New Developments in Grinding, M.C. Shaw, ed., pp. 220-258 (Carnegie Press, Pittsburg, Pa., 1972).
- [6] Snoeys, R., The mean undeformed chip thickness as a basic parameter in grinding, Annals C.I.R.P., 20[2], 183-186 (1971).
- [7] Snoeys, R., Peters, J. and Decneut, A., The significance of chip thickness in grinding, Annals C.I.R.P., 23[2], 227-237 (1974).
- [8] Koepke, B.G. and Stokes R.J., Grinding forces and the machining of magnesium oxide crystals, J. Mater. Sci. 7, 485-493 (1972).
- [9] Maan, N. and Broese van Groenou, A., Low speed scratching experiments on steels, Wear 42, 365-390 (1977).
- [10] Broese van Groenou, A., Maan, N. and Veldkamp J.D.B., Scratching experiments on various ceramic materials, Philips Res. Repts, 30, 320-359 (1975).
- [11] Broese van Groenou, A., Maan, N., and Veldkamp, J.D.B., Single-point scratches as a basis for understanding grinding and lapping (Proc. Conf. Ceramic Machining and Surface Finishing II, 1978).
- [12] Vaidyanathan, S. and Finnie I., The grinding of brittle solids, in New Developments in Grinding, M.C. Shaw, ed., pp. 813-831 (Carnegie Press, Pittsburgh, Pa., 1972).
- [13] Law, S.S., Wu, S.M. and Joglekar, A.M., J. Eng. Ind. (Trans ASME), B95, 983-991 (1973).
- [14] Izumitani, T., and Harada, S., Polishing mechanism of optical glasses, Glass Techn., 12[5], 131-135 (Oct. 1971).
- [15] Izumitani, T. and Suzuki, I. Indentation hardness and lapping hardness of optical glass, Glass Techn. 14[2], 35-41 (Apr. 1973).
- [16] Broese van Groenou, A., Grinding of ferrites, some mechanical and magnetic aspects, IEEE Trans. on Magn., MAG-11[5], 1446-1451 (Sept. 1975).
- [17] Oh, H.L., Oh, K.P.L., Vaidyanathan, S. and Finnie I., On the shaping of brittle solids by erosion and ultrasonic cutting, see ref. 1 of this paper, pp. 119-132.
- [18] Wiese, G.E. and Wagner, R.E., Physical model for predicting grinding rates, Appl. Optics, 3[11]2719-2722 (Nov. 1974).
- [19] Gielisse, P.J., Kim T.J., Goyette L.F., and Nagarkar, R.V., Fundamental and practical evaluation of the ceramic finishing process, Report, Univ. of Rhode Island, Kingston, R.I., 1976.
- [20] Huerta, M. and Malkin, S., Grinding of glass: the mechanics of the process, J. Eng. Ind. (Trans. ASME), 459-467 (May 1976).
- [21] Gielisse, P.J., and Stanislaos, J. Mechanical methods of ceramic finishing, ref. 1 of this paper, pp. 5-35.
- [22] Takazawa, K., Thermal aspects of the grinding operation, Ind. Diamond Rev., 143-149 (Apr. 1973).
- [23] Maris, M. and Snoeys, R., Heat affected zone in grinding operations, (Proc. 14th Conf. on Mach. Tool Design and Research, Manchester 1973), paper 604.
- [24] Maris, M., Thermische aspecten van de oppervlakteintegriteit bij het slijpen, Thesis Univ. of Leuven, Belgium, 1977 (in Dutch).
- [25] Horn, K., Überblick über moderne Verfahren der In-Prozess-Messung in der Fertigungstechnik, Annals C.I.R.P., 24, 257-262, (1975).
- [26] Tigerström, C.L., A model for the determination of the number of active grinding edges in various grinding processes, Annals C.I.R.P., 24, 271-275 (1975).
- [27] Lawn, B.R. and Fuller, E.R., Equilibrium penny-like cracks in indentation fracture, J. Mater. Sci. 10 2016-2024 (1975).
- [28] Broese van Groenou, A., The high speed size effect in grinding: the role of heat generation, Wear 44[2], 203-211 (1977).
- [29] Veldkamp, J.D.B., Hattu, N. and Snijders, V.A.C., Crack formation during scratching of brittle materials, in Fracture Mechanics of Ceramics, Vol. 3, R.C. Bradt, D.P.H. Hasselman and F.F. Lange, eds., pp. 273-301 (Plenum Publ. Corp. 1978).

EFFECT OF WORKPIECE PROPERTIES ON GRINDING FORCES IN POLYCRYSTALLINE CERAMICS¹

B. G. Koepke and R. J. Stokes

Honeywell Corporate Material Sciences Center
10701 Lyndale Ave. S.
Bloomington, MN 55420

Grinding forces have been measured on a number of polycrystalline ceramics and correlations between the forces and workpiece properties have been attempted in an effort to gain insight into mechanisms of chip formation. The closest correlations were with a parameter related to the indentation fracture characteristics of each workpiece. This suggests that a major mechanism of chip formation during multipoint abrasive machining of ceramics is fracture resulting from the plastic indentation of the workpiece by the abrasive grains. Grinding forces during up and down grinding were different but both correlated with the indentation fracture parameter when the comminution characteristics of the chips during down grinding were accounted for.

Key Words: Chip formation; grinding forces; surface condition; surface grinding.

1. Introduction

The quality and usefulness of a precision ceramic component may depend entirely on the abrasive machining operations used to shape and finish its surfaces. Yet it has been noted that abrasive surface finishing is still an "art based on experience" [1,2]². There are good reasons for this comment. First, the mutual interactions between the components of a surface finishing system (e.g., machine, tool, workpiece, environment, etc.) are complex and not well defined[2]. Second, the mechanisms whereby material is removed are not completely understood. For example, finish surface grinding causes chip formation on an extremely fine scale at high rates under conditions of stress and temperature that are difficult to measure [2,3].

Nevertheless considerable progress has been made since the first Symposium on the Science of Ceramic Machining and Surface Finishing [4]. It is now known that significant plastic flow may accompany chip formation during grinding of even the most brittle ceramics [5-8]. Scratch test studies [9,10] and work using model grinding systems employing single point diamonds mounted on a grinding wheel [2,11] have clearly shown that the mechanism of material removal depends on the normal force on the abrasive grain or, equivalently, on the depth of cut. At low loads material is removed by plastic flow, as the load increases cracking occurs and finally chips with dimensions larger than the abrasive grain form [10]. In a multipoint cutting process such as surface grinding, the subsurface interaction of the fractures due to chipping represent a major mechanism of material removal[10]. Single point grinding studies have further shown that chips can form in front of and behind the abrasive grain [3,8], the latter presumably due to relaxation of stored elastic energy.

In view of the complexity of the situation the question arises as to whether there is any physical property or combination of physical properties which can be related to the forces involved in machining a particular ceramic. From the scratch test and single point grinding work it is recognized that the resistance to plastic flow and to fracture must both be included in any model of chip formation [2, 7-9]. Low speed scratch tests have

¹Work carried out under Contract N00014-69-C-0123 to Office of Naval Research.

²Figures in brackets indicate the literature references at the end of this paper.

shown that the forces vary with hardness when plastic flow is the dominant mode of material removal [9]. Giessel et al. [11] have demonstrated in single point grinding that the forces vary as $\sigma^2/2E$, where σ is the fracture stress and E Young's modulus, when brittle fracture is the dominant mode of material removal.

Recent analyses of the relation of material properties and chip formation during ceramic machining have benefited from the indentation fracture theories of Lawn and co-workers [12,13]. Evans and Wilshaw [13] have modelled abrasive machining as a series of sliding parallel indenters and have shown that the chip volume, V , is $V \sim P^{5/4} H^{-1/2} K_c^{-3/4}$ where P is the vertical load on the abrasive grain, H is the hardness and K_c is the fracture toughness. Sawing rate data of Rice and Speronello [14] fit this relation well. Kirchner et al. [15] have measured the depth of damage, c , introduced in Si_3N_4 during single point diamond grinding and have shown it to be related to the vertical grinding force, P , according to a relation derived by Lawn and Marshall [16] based on indentation fracture theory $P \sim K_c c^{1/2}$. Thus, studies using single point abrasive systems and analyses incorporating the relatively new indentation fracture theories have both led to an improved understanding of the important physical parameters determining material removal during abrasive machining of ceramics. Whether these results can be directly applied to multi-point machining operations such as surface grinding is questionable. The simultaneous interaction of adjacent abrasive grains during chip formation will alter the relative amounts of plastic flow and fracture and thus the resulting forces. Which dominates and under what conditions are not clear.

In this paper we attempt to establish correlations by examining the effects of workpiece properties on forces generated during the surface grinding of a number of different ceramics. It was our hope that a clear correlation would establish the predominant mechanism of material removal under given conditions. Correlations are attempted between the forces and the workpiece properties to determine, at least, what properties most affect the mechanism of chip formation.

2. Experimental Procedure

2.1 Grinding

Grinding was carried out using a DoAll Model D618-7 high speed precision surface grinder with a fixed spindle speed of 3540 rpm. A 100 grit resinoid bond diamond wheel³ 15.2 cm (6 inches) in diameter and 1.32 cm (1/8 inch) wide was used for all measurements. The cutting point density on the wheel face was 480 cm^{-2} and the mean width to depth ratio for a groove made by a single abrasive grain, as determined by techniques described by Backer et al. [17] was 1.6. Grinding forces were measured with a strain gauge dynamometer based on a design of Cook et al. [18]. The dynamometer is similar to those used by others [2] and will not be discussed. With a sample mounted on the dynamometer, the horizontal and vertical grinding forces induced in the workpiece during a grinding pass can be measured independently. The elastic stiffness of the dynamometer is $1.2 \times 10^5 \text{ gm/cm}$ in the horizontal direction and $4.5 \times 10^5 \text{ gm/cm}$ in the vertical direction. The sensitivity of the instrument is 3 gm in both directions. Grinding was carried out both with the cutting face of the wheel moving in the same direction as the workpiece (down or climb grinding) and with the wheel moving in the opposite direction (up grinding). Different parts of the same workpiece were used for each case, i.e. one part of the surface was up ground and a separate part was down ground. Samples were ground at feed rates of 0.042, 0.21, and 0.42 cm/sec (1, 5 and 10 inches/min). The depth of cut was $25.4 \mu\text{m}$ (10^{-3} inches) except in one case where it was half this value. At least 5 passes were made at each feed rate and each sample was always ground at increasing rates of material removal. The wheel was dressed by grinding the face of the wheel with a silicon carbide wheel before each sample was ground at the lowest rate of material removal.

The theoretical chip geometry (i.e. chip length and maximum chip thickness) [17] for the grinding conditions used here are listed in table 1.

³DoAll Type. D1A1-Md100N/IDoB1/4B3

From table 1 we note first that the grit depths of cut, t , are small and are on the order of 10^{-4} of the chip lengths. An indentation made by an abrasive grain on a ceramic workpiece is, therefore, no more than a long thin scratch [5,9] provided material is removed by plastic flow. As noted above, however, if brittle fracture takes place during chip formation the actual chip geometry may in no way resemble the dimensions in table 1. Note also that the small grit depth of cut indicates the advisability in many instances of using small wheel depths of cut. Otherwise a large amount of the binder in the wheel face may contact the workpiece.

Table 1. Theoretical maximum chip thickness, t , and chip length, l , for the 100 grit diamond wheel at the machine settings used in this study.

Wheel	Depth of cut	Feed Rate (in/min)	t (μm)	l (mm)
100 grit	25.4 μm	.042 cm/sec	.32	2.0
		.21 cm/sec	.71	2.0
		.42 cm/sec	1.0	2.0

Samples used for grinding were approximately 25.4 x 6.4 x 3.2 mm (1 x 1/4 x 1/8 inches). Grinding was carried out on the 25.4 x 6.4 mm side in the short (6.4 mm) direction. All grinding was carried out dry.

2.2 Characterization of the Ground Surface

Both optical and scanning electron microscopy were used for routine characterization of the surfaces produced by grinding. Most observations were made after the last pass at the highest feed rate of 0.42 cm/sec.

2.3 Workpiece Materials

The materials machined in this study are listed in table 2. Also included in the table are the supplier, method of manufacture and grain size.

Table 2. Materials used for Grinding Force Measurements

Material	Supplier	Manufacturing Method	Approximate Grain Size (μm)
PZT	Honeywell	Cold Pressed and Sintered	3
MgO	IITRI	Cold Pressed and Sintered	18
Ferrite NiZn	Honeywell	Hot Pressed	13
Ferrite NiZn	Honeywell	Hot Pressed	3
Silicon Nitride ^a "β"	Westinghouse	Hot Pressed	2
Silicon Nitride ^a	Norton	Hot Pressed	1
Silicon Nitride ^a "α"	Westinghouse	Hot Pressed	1
Lucalox Alumina	G.E.	Cold Pressed and Sintered	38
Alumina ^b	AVCO	Hot Pressed	2
AD 999 Alumina	Coors	Cold Pressed and Sintered	2
Boron Carbide ^b	AVCO	Hot Pressed	8

^aCourtesy Dr. F. F. Lange

^bCourtesy Dr. J. Niesse

The Westinghouse silicon nitrides listed in the table differ as follows [19,20]. "β" Si₃N₄ was fabricated from powders containing 90% β-phase Si₃N₄ and 10% α-phase Si₃N₄. "α" Si₃N₄ was fabricated from powders containing 90% α-phase and 10% β-phase powder. All three materials were β phase after hot pressing. The three different Si₃N₄ materials are interesting because, as noted later, they exhibit measurably different properties.

3. Experimental Results

3.1 Grinding Force Measurements

In order to conserve space the results are presented in tabular rather than graphical form although a few curves will be presented for illustrative purposes. The grinding force measurements are listed in the Appendix. Each value of force is normalized by the width of the cut, *b*, and is the average of five passes made at the depths of cut and feed rates indicated. Some brief comments concerning the force measurements are given below.

Grinding forces on PZT, MgO and the ferrites were extremely low and without exception increased with rate of material removal. The forces measured during up and down grinding were about equal. The vertical forces measured on the smaller grained ferrite exceeded those measured on the larger grained material. The horizontal forces measured on both ferrites were not a function of grain size.

The forces measured on Si₃N₄ during 25.4μm cuts were the highest measured in the series. In order to minimize damage to the dynamometer or wheel, measurements of the effect of rate of material removal on grinding forces were made using a cut of 12.2μm. We note here that in a number of cases the vertical forces measured during down grinding exceeded those measured during up grinding in contrast to results on other hard ceramics such as B₄C and AVCO Al₂O₃. Examples of this behavior are shown in figure 1 in which the grinding forces for the Westinghouse "α" Si₃N₄ are plotted as a function of feed rate during cuts of 12.2μm.

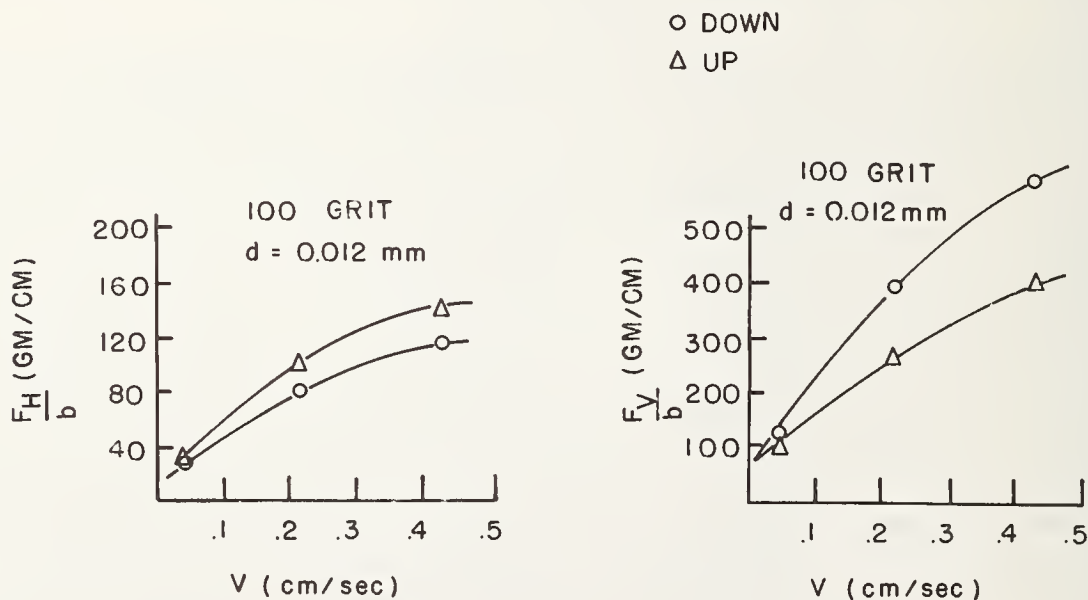


Figure 1. Horizontal, F_H/b , and vertical, F_V/b , grinding forces measured on Westinghouse "α" Si₃N₄ during up and down grinding plotted as a function of workpiece feed rate. *b* is the width of the cut. The depth of cut, *d*, is 12.2μm (0.0005 inch).

The forces measured on alumina depended on fabrication. Sintered material such as Lucalox and Coors AD 999 showed low grinding forces at low feed rates but the forces increased rapidly with feed rate. AVCO hot pressed alumina on the other hand sustained a relatively high force level at all feed rates as indicated in figure 2. The low

sensitivity to feed rate during down grinding is not understood but may be related to the comminution characteristics of the chips as they travel between the wheel and the workpiece. This point is discussed later.

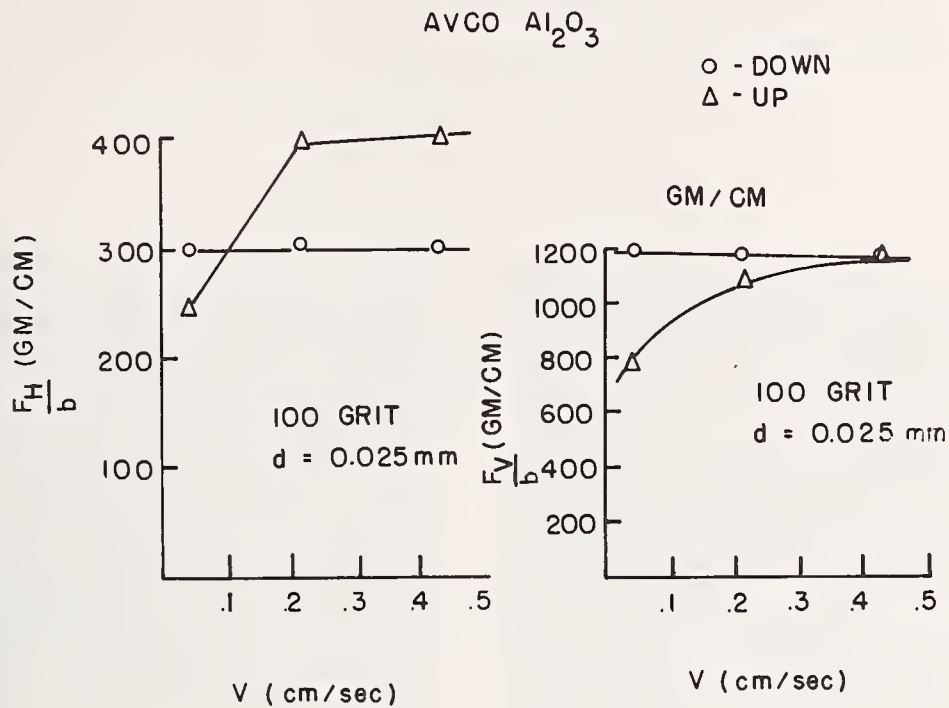


Figure 2. Horizontal, F_H/b , and vertical, F_V/b , grinding forces measured on AVCO hot pressed Al_2O_3 during up and down grinding plotted as a function of workpiece feed rate. b is the width of the cut. The depth of cut, d , is $25.4\mu m$ (0.001 inch).

At the lowest feed rate the forces on B_4C during down grinding were greater than those during up grinding. This behavior reversed at the higher feed rates.

3.2 Examination of the Ground Surfaces

The ground surfaces of every sample were examined following the last grinding force measurement which, as noted earlier, was made at the highest feed rate used in this work, 0.42 cm/sec. The nature of the surfaces will be commented on and illustrated in a few cases with scanning electron micrographs.

The ground surfaces of PZT were smooth and severely burnished. This accounts for the high grinding forces measured on this relatively soft ceramic.

The MgO surfaces were similar to the ferrite surfaces and contained plastically flowed regions and regions where material had been removed by brittle fracture. These surfaces are similar to those examined in an earlier study [6].

The large grained ferrite showed more intergranular fracture than plastically flowed material. The fine grained ferrite showed large flowed regions with some patches where material was removed by intergranular fracture. Examples of these surfaces are shown in figure 3. Recall that the grinding forces on the fine grained material were slightly higher at the highest feed rate.

Without exception all silicon nitride surfaces were quite smooth and burnished and consisted mainly of plastically flowed regions. Patches where material was removed by what appeared to be intergranular fracture were seen scattered over every surface.

The sintered aluminas had surface features resembling the Si_3N_4 samples. A typical example is shown in figure 4(a) for Coors AD 999 alumina down ground, 0.42 cm/sec. The irregular patches are where material has been removed by intergranular fracture. In contrast, the hot pressed alumina showed fewer burnished regions as shown in figure 4(b). Most material has been removed by transgranular fracture. The B_4C surfaces were similar to those of Si_3N_4 and the sintered aluminas and contained regions of plastically flowed material and patches where material had been removed by brittle fracture. Due to a large amount of debris on the surfaces the nature of the fractures could not be assessed.

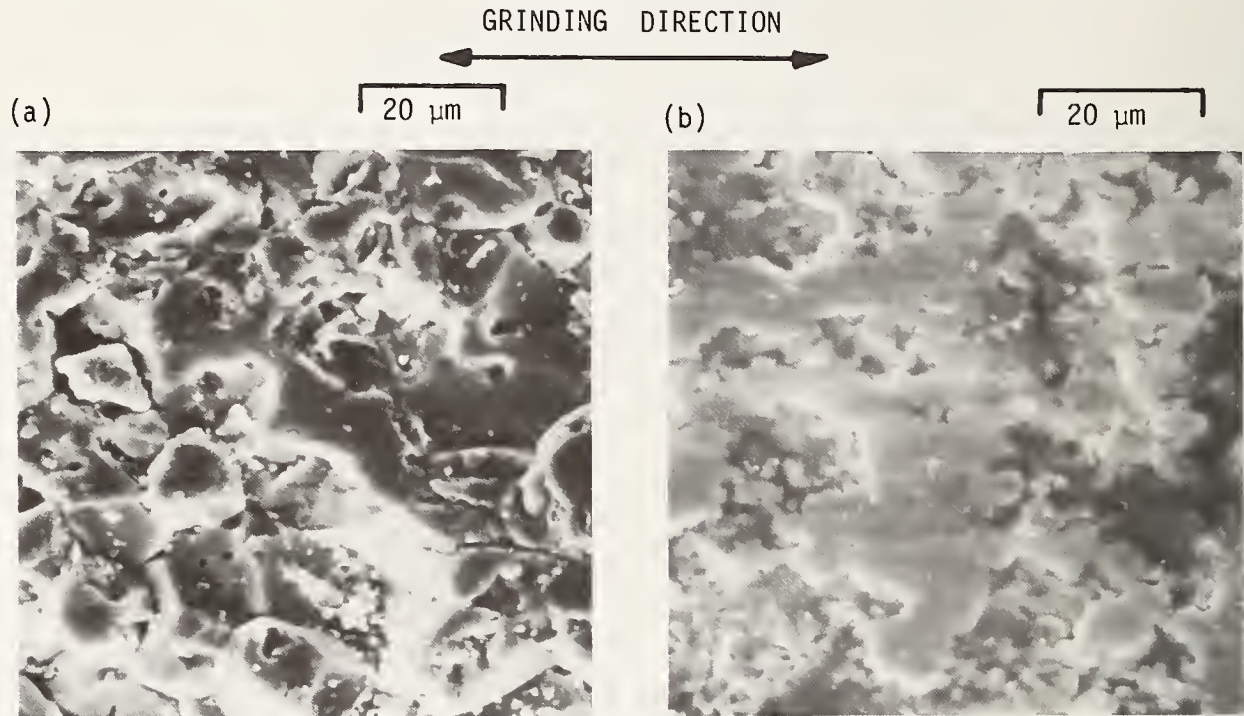


Figure 3. Scanning electron micrographs of the ground surfaces of NiZn ferrite with mean grain sizes of (a) 3 and (b) 13 μm.

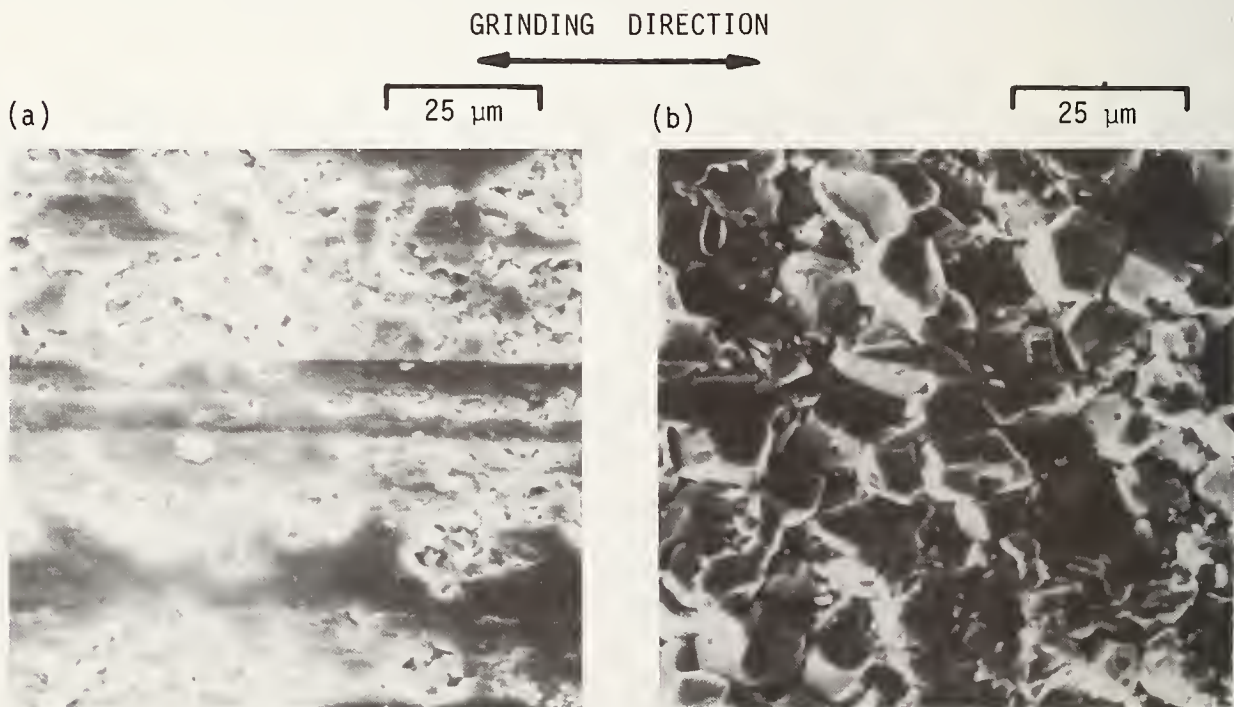


Figure 4. Scanning electron micrographs of the ground surfaces of (a) Coors AD 999 alumina and (b) AVCO hot press.

A few general comments concerning the nature of the ground surfaces are appropriate at this time. First, no significant differences were noted between surfaces produced by up and by down grinding. This was unexpected in view of the differences in forces observed. Second, all surfaces contained significant amounts of plastic flow. The large grained ferrite and hot pressed alumina contained less plastic flow than the others. Finally, it must be cautioned that the conditions observed here may not be identical to those obtained in actual practice. The samples were ground dry and were mounted on a dynamometer whose compliance is significantly greater than that of the machine table itself. Both dry grinding and a lower compliance may enhance burnishing.

4. Grinding Force Correlations

The properties used for the correlations are listed in table 3. Note that many of the values in the table were not measured directly on the material used in this study, but were taken from the literature or supplied by individuals noted in the references to the table. In all cases the vertical and horizontal grinding forces measured during both up and down grinding during a 25.4 μ m cut at a workpiece feed rate of 0.21 cm/sec were used for correlations.

Table 3. Representative physical and mechanical properties of ceramics.

Material	Crain Size (μ m)	Melting Point ($^{\circ}$ C)	Knoop Hardness ^a (kg/mm ²)	Bend Tensile Strength (MN/m ²)	Polycrystal-line Young's Modulus (CN/m ²)	K _{IC} (MN/m ^{3/2})
PZT	3	1300	200 *	55 ^b	83 ^b	.75 ^h
MgO	18	2850	400 *	28 ^c	303 ^c	2.5 ⁱ
NiZn Ferrite	13	1660	550 #	166 ^d	200 ^g	-
NiZn Ferrite	3	1660	650 #	124 ^d	200 ^g	-
" β " Si ₃ N ₄	2	Sublimes at 1870	1450 *	375 ^c	307 ^e	3.1 ^e
Norton Si ₃ N ₄	1	Sublimes at 1870	1500 *	676 ^c	307 ^e	5.1 ^e
" α " Si ₃ N ₄	1	Sublimes at 1870	1550 *	656 ^c	307 ^e	6.5 ^e
Lucalox Al ₂ O ₃	38	2050	1800 *	440 ^c	400 ^c	4.1 ^{j,k}
AVCO Al ₂ O ₃	10	2050	1850 *	407 ^f	400 ^c	6.5 ^l
AD999 Al ₂ O ₃	2	2050	2000 *	469 ^c	400 ^c	4.0 ^m
B ₄ C	8	2350	2600 *	448 ^f	448 ^c	4.2 ⁿ

- a. All values measured in this laboratory. (# 100gm load, * 500gm load).
 b. Honeywell data sheet.
 c. Engineering Properties of Selected Ceramic Materials, American Ceramic Society, Columbus, Ohio (1966).
 d. M. Braitburg, Honeywell Inc. private communication (1972).
 e. F. F. Lange, Journ. Amer. Ceram. Soc., 56, 518 (1973).
 f. AVCO data sheet.
 g. J. Smit and H. P. Wijn, Ferrites, Wiley & Sons, New York (1959) p. 225.
 h. J. G. Bruce, et al. Fracture Mechanics of Ceramics, Vol. 4, R.C. Bradt et al. ed., Plenum, N.Y. (1978) p. 696.
 i. P. Gutshall and G. Cross, Eng. Fract. Mech., 1, 463 (1969).
 j. R. F. Pabst, Fracture Mechanics of Ceramics, Vol. 2, R. C. Bradt et al. ed., Plenum N.Y. (1974) p. 557.
 k. S. W. Freiman et al. ibid p. 666.
 l. Measured in this laboratory by hardness indentation technique of Evans and Charles, Journ. Amer. Ceram. Soc., 59, 371 (1976).
 m. L. M. Barker, Fracture Mechanics of Ceramics, Vol. 4, R. C. Bradt, et al. ed., Plenum, N.Y. (1978) p. 490.
 n. G. Gazza, Army Research Center, Watertown, MA., private communication (1972).

4.1 Melting Point

No obvious correlations with melting point were noted.

4.2 Hardness

Since hardness is an indication of resistance to plastic flow an examination of the relation between grinding forces and hardness is warranted. The horizontal and vertical forces measured during down grinding are shown as a function of workpiece hardness in figure 5. There is a trend toward increasing vertical grinding forces with hardness but the horizontal forces drop in the harder materials. In both cases the highest grinding forces are those measured on ceramics exhibiting intermediate values of hardness. Similar trends were observed during up grinding but the forces measured on ceramics with intermediate hardnesses were lower than those shown in figure 5.

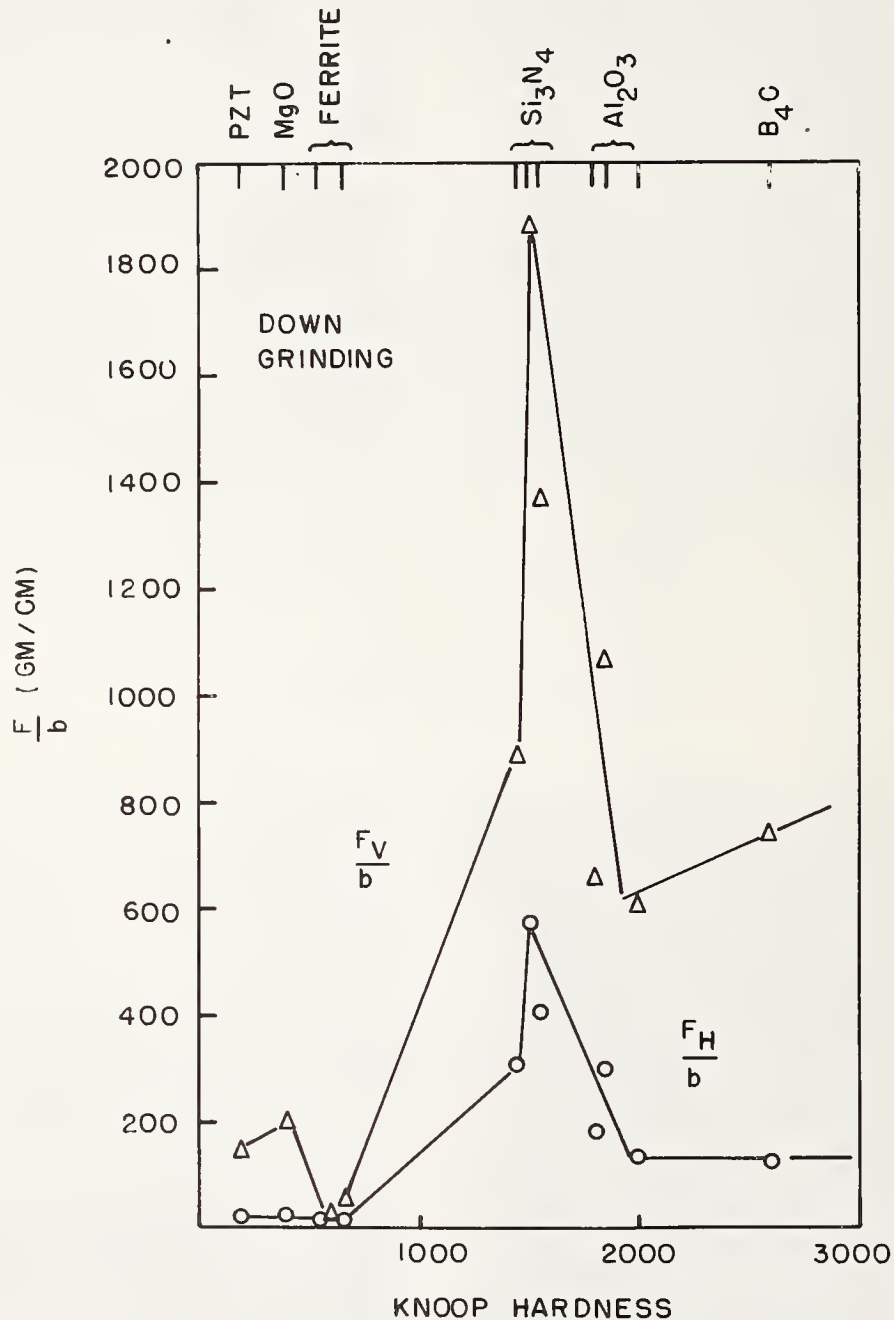


Figure 5. Horizontal, F_H/b and vertical, F_V/b , grinding forces measured during down grinding on different ceramics plotted as a function of workpiece hardness. The depth of cut and feedrate were $25.4\mu\text{m}$ and 0.21 cm/sec respectively.

4.3 Tensile Strength

Grinding forces measured during down grinding are shown as a function of tensile strength in figure 6. There is a trend for the forces to increase with strength but again the forces measured on materials with intermediate strengths are high. Similar behavior is observed when the forces measured during up grinding are plotted versus tensile strength.

4.4 Polycrystalline Young's Modulus

No correlations were noted but again the forces were highest on materials with intermediate values of modulus eg. Si_3N_4 .

4.5 Strain Energy Density, $\sigma^2/2E$

In single point diamond grinding studies on alumina workpieces Gielisse et al. [11] obtained excellent correlation between grinding forces and the strain energy density, $\sigma^2/2E$, where σ is the tensile strength and E is Young's modulus. No correlations were noted when the grinding forces measured in this work were plotted versus $\sigma^2/2E$.

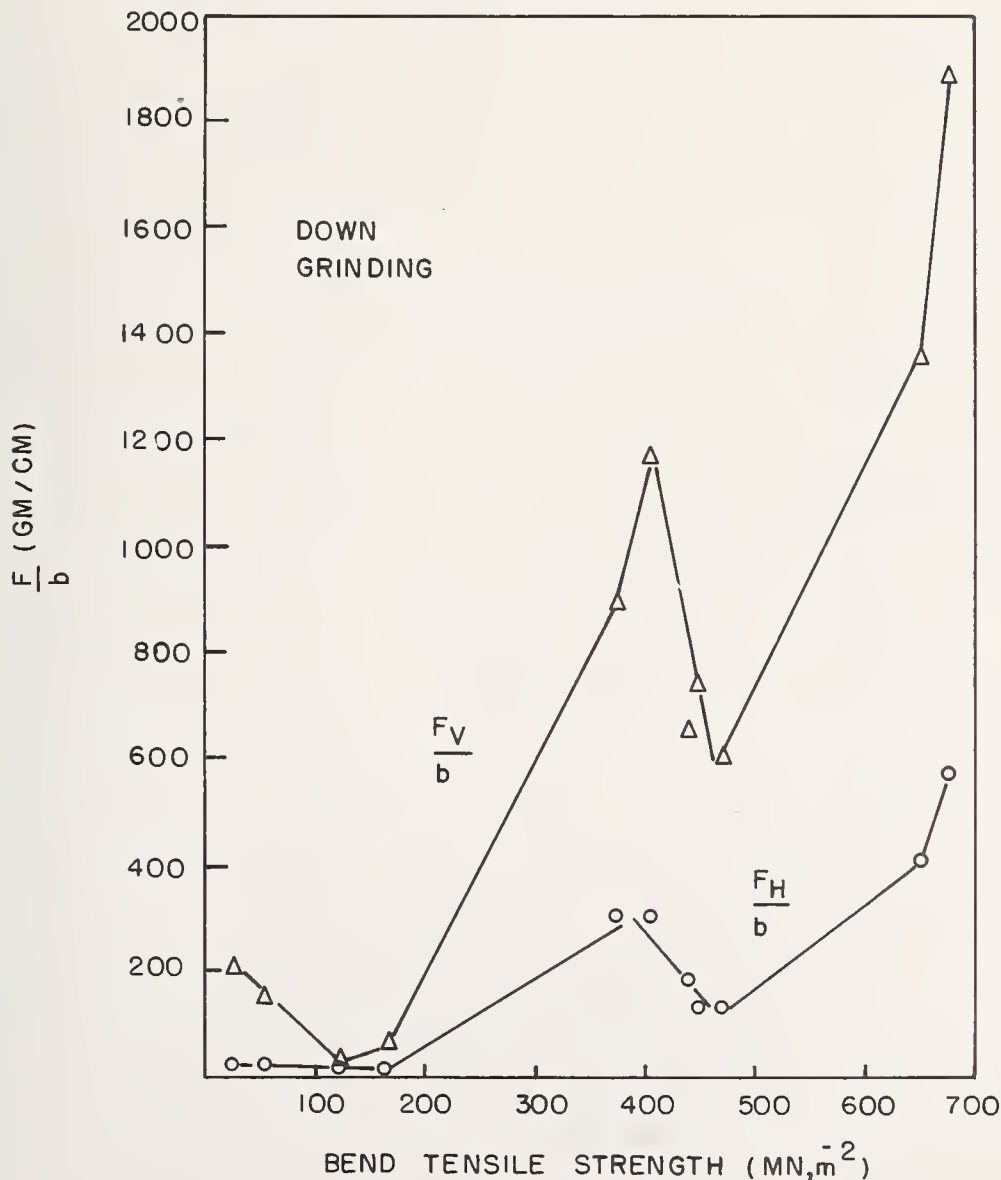


Figure 6. Horizontal and vertical grinding forces measured on different ceramics plotted as a function of the bend tensile strength of the workpiece materials. The depth of cut and feedrate were $25.4\mu\text{m}$ and 0.21 cm/sec respectively.

4.6 Fracture Toughness

It can be argued that, if a major mechanism of material removal during grinding is the initiation and/or propagation of brittle cracks, then grinding forces should correlate with fracture toughness. Figure 7 shows that the grinding forces measured during up grinding do increase with the fracture toughness, but not linearly.

The grinding forces measured on Lucalox were low with respect to the other aluminas particularly during up grinding. The vertical forces measured on Lucalox are indicated on the plot. The low forces are attributed to the large grain size of this material. Gielisse et al. [11] have noted a similar sharp decrease in forces during single point grinding of aluminas when the grain size exceeded about 20 μ m.

No conclusions between grinding forces measured during down grinding and K_{IC} were obtained.

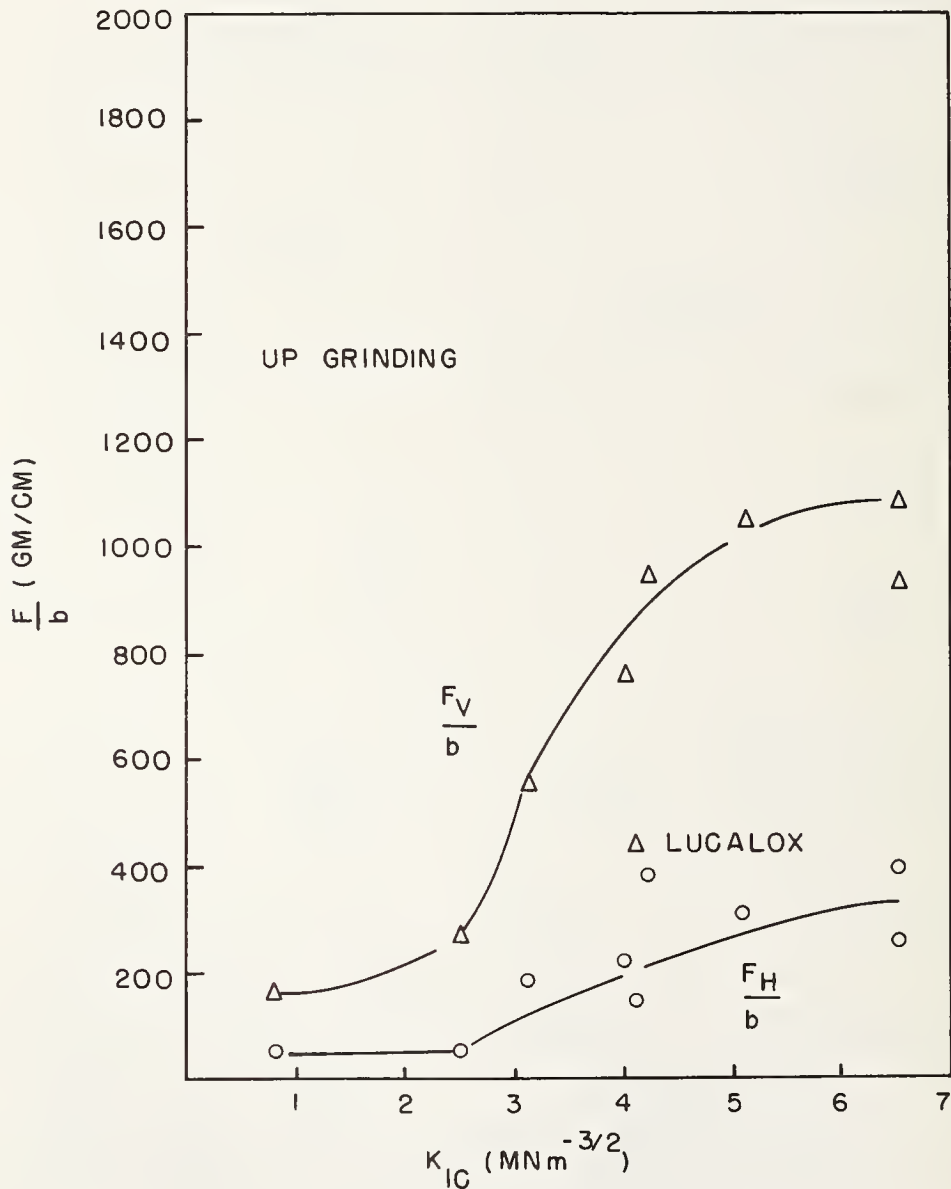


Figure 7. Horizontal and vertical grinding forces measured during up grinding on different ceramics plotted as a function of the fracture toughness, K_{IC} , of the workpiece materials. The depth of cut and feedrate were 25.4 μ m and 0.21 cm/sec respectively.

4.7 Indentation Fracture Parameter

As noted in the Introduction, recent theories of plastic indentation fracture of brittle materials have led to increased understanding of the mechanisms of material removal during the high speed impact of ceramics. A major result of the plastic indentation of a brittle solid with a sharp indenter is the formation of subsurface lateral cracks lying roughly parallel to the surface. When these cracks intersect the surface or other fractures a chip is formed and material is removed. The volume of material removed is proportional to the size of these cracks which, in turn, is governed by the vertical force on the particle, P , the hardness, H , and the fracture toughness, K_{IC} . When material removal during abrasive machining is assumed to take place by a parallel array of sliding indenters, Evans and Wilshaw [13] have shown the upper limit for the volume removed to be $V \sim P^{5/4} K_{IC}^{-3/4} H^{-1/2}$. Thus, under conditions of a fixed rate of material removal (ie. fixed feed rate and depth of cut) the grinding forces are expected to be close to a linear function of $K_{IC}^{3/4} H^{1/2}$. Figure 8 shows this to be the case for data taken during up grinding. The low data point represents the large grained Lucalox data discussed above. The high point is Norton Si_3N_4 . Figure 8 represents by far the best correlation we have found between material properties and grinding force measurements.

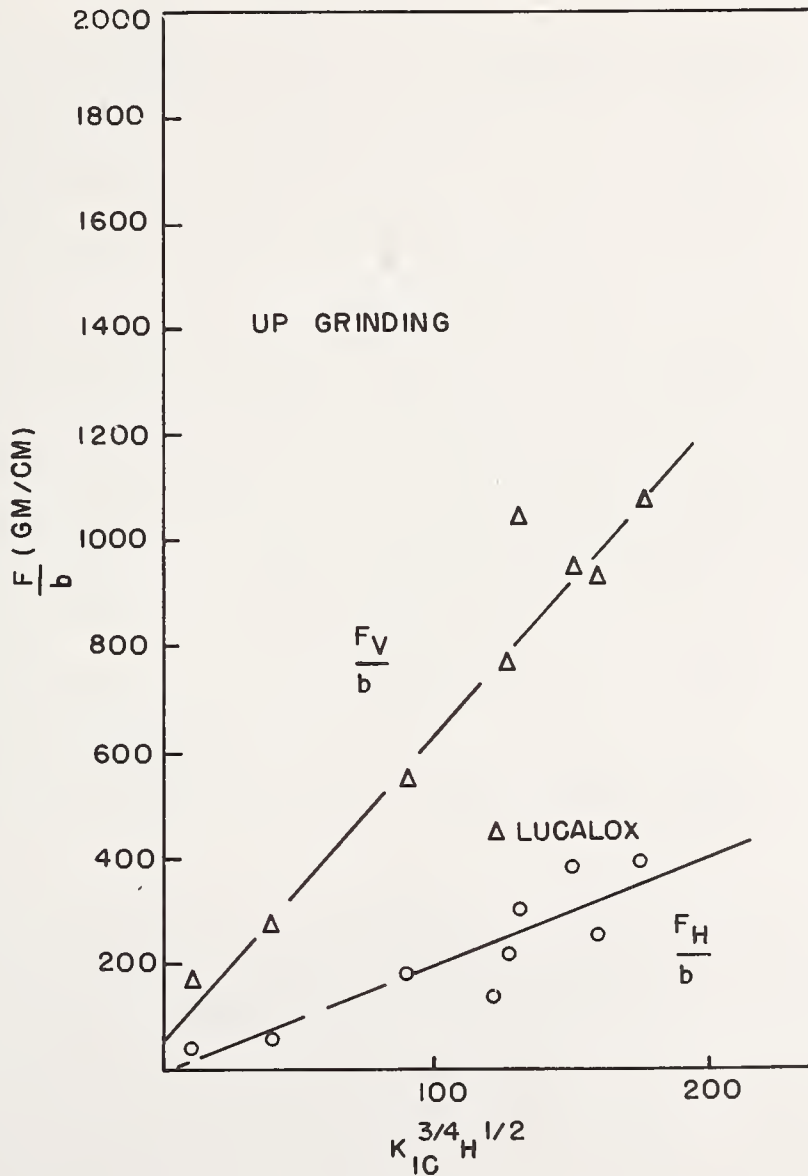


Figure 8. Horizontal and vertical grinding forces measured during up grinding on different ceramics plotted as a function of an indentation fracture parameter derived by Evans and Wilshaw [13]. K_{IC} is the fracture toughness and H is the Knoop hardness. The depth of cut and feedrate were $25.4\mu m$ and 0.21 cm/sec respectively.

When the grinding forces measured during down grinding are plotted in a similar fashion, no correlation is obtained. In what follows we attempt to rationalize this lack of correlation by considering a basic difference in the mode of material removal during up and down surface grinding of ceramics on a dynamometer. During up grinding chips are formed at the leading edge of the contact area between the wheel and workpiece and are immediately ejected from the system. During down grinding the chips formed at the leading edge of the wheel-workpiece interface must first travel between the workpiece and the wheel to the back edge of the contact area before they can be ejected. The initial chip size in both cases is larger than the theoretical chip size and is presumably determined by the indentation fracture characteristics of the workpiece and the cutting point geometry on the wheel surface as discussed by Evans and Wilshaw [13]. During up grinding the vertical grinding forces measured by the dynamometer depend mainly on the forces necessary to form the chips. During down grinding, on the other hand, the measured vertical grinding forces must also be related to the impact fracture or comminution characteristics of the isolated chips. If the chips break up readily as they travel between the wheel and the workpiece the vertical grinding forces will be reduced. If the chips do not break up readily, high vertical grinding forces

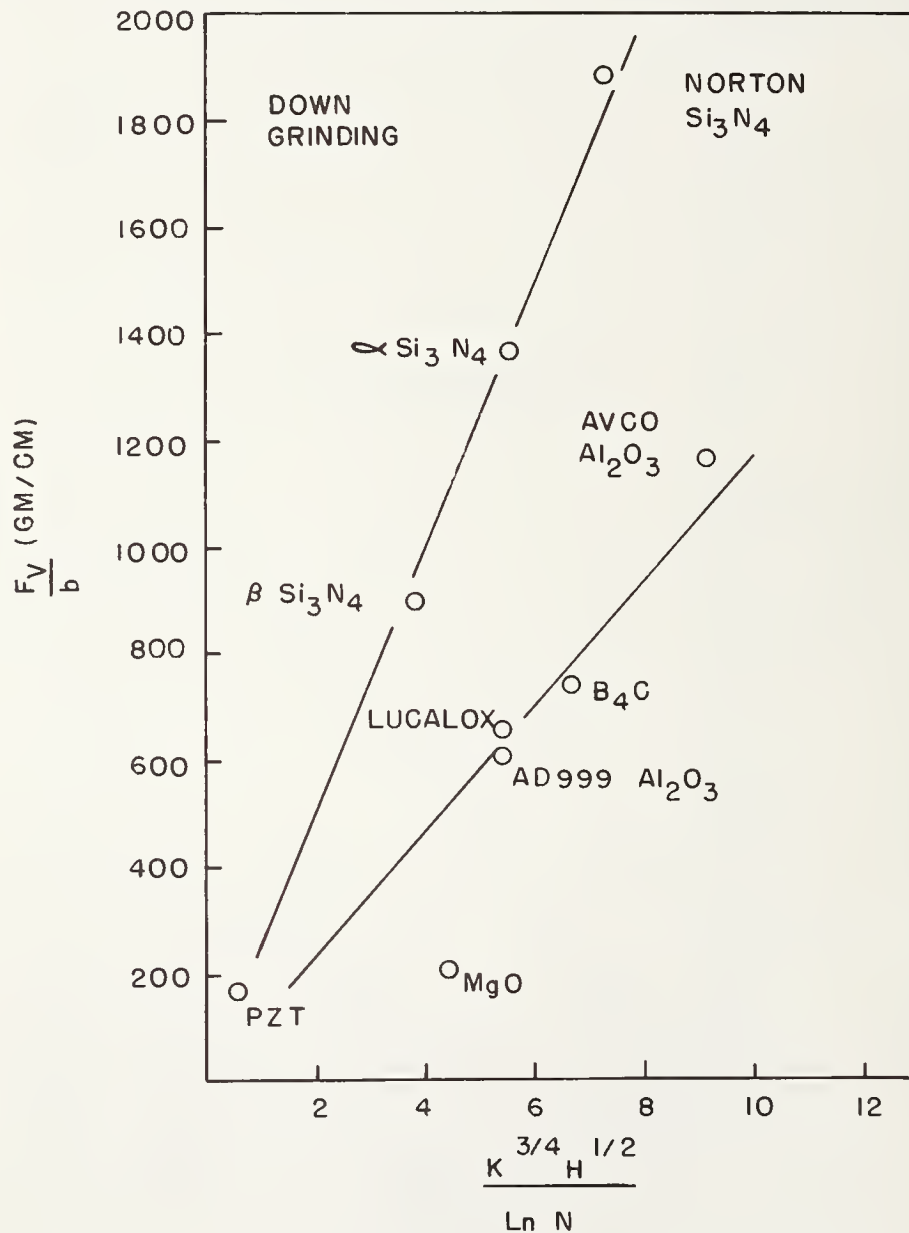


Figure 9. Vertical grinding forces measured during down grinding on different ceramics plotted as a function of the indentation fracture parameter of Evans and Wilshaw [13] divided by a toughness parameter suggested by Clarke et. al [21] that can be related to the comminution characteristics of the chips.

are expected. A parameter relating to the ability of a ceramic to resist impact fracture has been suggested by Clarke et. al. [21]. The number of pieces a cubic centimeter of material would break up into under the influence of an elastic-energy density, $2W$, is $N \sim (W/6\gamma)^3$ where γ is the fracture surface energy and W can be approximately by $\sigma^2/2E$. σ is the fracture strength and E is Young's modulus. Clarke et. al. [21] suggested that a suitable toughness parameter is $-\ln N$. If N is large the chips break up readily and their effect on the vertical grinding forces should be small. By relating this concept to surface grinding we suggest that the vertical grinding forces measured during down grinding vary according to $F_v \sim K^{3/4} H^{1/2} / \ln N$. This relationship is shown plotted in figure 9. Note first that a correlation is obtained indicating that the comminution characteristics of the chips do affect the vertical grinding forces measured during down grinding. Note also that the data are in two distinct groups. The data of figure 9 suggest that a major reason for the large difference in grinding forces measured during down and up grinding on Si_3N_4 is that once formed, the chips break up only with much difficulty and cause high forces during down grinding. The other group of data including the aluminas and B_4C also show good correlation. MgO is low presumably because the chips are easily deformable [5] and do not cause high vertical grinding forces. No correlations were noted when the forces measured during up grinding were plotted in this manner.

5. Conclusions

A number of points concerning multipoint abrasive machining of ceramics have emerged from this work. First, grinding forces were highest on ceramic workpieces with intermediate values of hardness. Secondly, in materials exhibiting high grinding forces, the forces measured during down grinding exceeded those measured during up grinding. The highest grinding forces measured were on hot pressed Si_3N_4 and the lowest were on softer ceramics such as $NiZn$ ferrite and MgO . Furthermore, the general features of most ground surfaces were similar. The surfaces contained regions of highly deformed material and regions where material had been removed by brittle intergranular and transgranular fracture.

The grinding force correlations strongly suggest that initial chip formation occurs by indentation fracture. If this is the case then the highly deformed regions on the ground surfaces presumably occur after the leading edge of the wheel passes. This is a plausible argument because as the wheel depth of cut decreases (ie. approaches the theoretical chip thickness) the abrasive grains have more of a tendency to remove material by plastic flow. This situation is enhanced by the burnishing action of swarf moving between wheel and workpiece, high vertical grinding forces and by the increased compliance of the dynamometer. We should point out, however, that we have observed the surfaces of ceramics ground on stiff tables to be very similar to those discussed here. Major differences are usually in the relative amounts of plastic flow and fracture rather than in the absence of one or the other.

Based on the correlations of grinding forces and workpiece properties discussed in this paper, we conclude the following:

1. Chip formation during up and down surface grinding of hard ceramics occurs initially by indentation fracture due to the impact of the abrasive grains on the wheel on the workpiece.
2. The grinding forces during up grinding correlate with workpiece properties according to the indentation fracture theories of Lawn et al. [12,13]. In particular the forces vary linearly with a parameter derived by Evans and Wilshaw [13] according to $F \sim K_c^{3/4} H^{1/2}$ where K_c is the fracture toughness and H is the hardness.
3. Grinding forces during down grinding differ from those during up grinding because the chips formed at the leading edge of the wheel-workpiece interface must travel between the wheel and workpiece before being ejected from the system. This results in an increased vertical force that can be accounted for in different ceramics by considering the comminution characteristics of each material.
4. In every case the ground surfaces contained regions that were plastically flowed and regions where material had been removed by brittle fracture. It is suggested that a large amount of deformation occurred after the leading edge of the wheel had passed.

5. Because of the complexity of the cutting point geometry on a grinding wheel, grinding force measurements can only be used in a qualitative manner to examine mechanisms of material removal. Possibly a better and more direct approach is to measure the rates of material removal on different materials at constant force settings.

6. Acknowledgements

The authors are indebted to D. Woodward for carrying out the experiments during the course of this work. The continued interest of Dr. A. Diness, Office of Naval Research is gratefully acknowledged.

7. References

1. Ceramic Processing, Publication 1576 (National Academy of Sciences, Washington, D.C., 1968) p. 145.
2. Gielisse, P.J. and Stanislaw, J., Mechanical methods of surface finishing, in The Science of Ceramic Machining and Surface Finishing, S.J. Schneider and R.W. Rice, eds. pp. 5-35 (Special Publication 348, National Bureau of Standards, Washington, D.C., 1972).
3. Imanaka, O., Fugino, S. and Mineta, S., direct observation of material removal process during grinding of ceramics by micro-flash technique, *ibid* pp. 37-43.
4. The Science of Ceramic Machining and Surface Finishing, S.J. Schneider and R.W. Rice, eds. (Special Publication 348, National Bureau of Standards, Washington, D.C., 1972).
5. Koepke, B.G. and Stokes, R.J., Grinding forces and the machining of magnesium oxide crystals, *Journ. Mater. Sci.*, 7, [3], 485-493 (1972).
6. Koepke, B.G., An assessment of surface and subsurface damage introduced in ceramics by semifinish grinding operations, pp. 317-332 in Reference 4.
7. Hockey, B.J., Observations by transmission electron microscopy on the subsurface damage produced in aluminum oxide by mechanical polishing and grinding, *Proc. Brit. Ceram. Soc.*, 20, 95-115 (1972).
8. Becher, P.F., Ceramic machining and surface finishing, in Treatise on Materials Science and Technology, Vol. 9. Ceramic Fabrication Processes, F.F.Y. Wang ed., pp. 217-226. (Academic Press, New York, N.Y., 1976)
9. Broese van Groenou, A., Maan, N. and Veldkamp, J.D.B., Scratching experiments on various ceramic materials, *Phillips Res. Rep.*, 30, [5], 320-359 (1975)
10. Broese van Groenou, A. and Veldkamp, J.D.B., Scratching and grinding parameters of various ferrites, *Journ. Phys. (Paris)*, *Colloq.* [1] 285-289 (1977)
11. Gielisse, P.J., Kim, T.J. and Choudry, A., An experimental investigation of the dynamic and thermal characteristics of the ceramic stock removal process, in Materials Science and Research, Vol. 7. Surfaces and Interfaces of Glass and Ceramics, V.D. Frechette, W.C. LaCourse and V.L. Burdick eds. pp. 137-148 (Plenum Press, New York, N.Y. 1974).
12. Lawn, B. and Wilshaw, R., Indentation fracture: principles and applications, *Journ. Mater. Sci.*, 10 [6], 1049-1081 (1975)
13. Evans, A.G. and Wilshaw, T.R., Quasi-static solid particle damage in brittle solids-I. observations, analysis and implications, *Acta Met.*, 24, [10] 939-956 (1976)
14. Rice, R.W. and Speronello, B.K., *Journ. Amer. Ceram. Soc.*, 59, [7-8], 330-333 (1976)
15. Kirchner, H.P., Gruver, R.M. and Richard, D., Fragment formation and damage penetration during abrasive machining of ceramics, these proceedings.

16. Lawn, B.R. and Marshall, D.B., Contact fracture resistance of physically and chemically tempered glass plates, a theoretical model, *Phys. Chem. Glasses*, 18, [1], 7-18 (1977)
17. Backer, W.R., Marshall, E.R. and Shaw, M.C., The size effect in metal cutting. *Trans. Amer. Soc. Mech. Eng.*, 74, [1], 61-72 (1952)
18. Cook, N.H., Loewen, E.G. and Shaw, M.C., Machine - tool dynamometers: a current appraisal. *Amer. Mach.*, 98, [10], 125-129 (1954)
19. Lange, F.F., Relation between strength, fracture energy and microstructure of hot-pressed Si_3N_4 , *Journ. Amer. Ceram. Soc.*, 56, [10], 518-522 (1973)
20. Lange, F.F., Strong, high-temperature ceramics, in Annual Review of Materials Science, Vol. 4, R.A. Huggins, R.H. Bube and R.W. Roberts, eds. pp. 365-390 (Annual Reviews Inc., Palo Alto, CA, 1974)
21. Clarke, F.J.P., Tattersall, H.G. and Tappin, G., Toughness of ceramics and their work of fracture, *Proc. Brit. Ceram. Soc.*, [6], 163-172 (1966)

Discussion

CHOUDRY

There is a geometrical difference between the undeformed chips in up and down grinding. Have your results, showing the differences between the two modes (up and down), been already corrected for this difference, i.e., is the difference between up and down grinding (under identical wheel and workpiece velocity and depth of cut) more than what is warranted by the geometry?

KOEPKE & STOKES

The grinding forces reported in this paper have not been corrected for differences in the undeformed chip geometry obtained during up and down grinding. We argue that when chip formation occurs by relatively long-range cracking the actual chip shape bears little resemblance to the theoretical shape of an undeformed chip. The formation of lateral cracks that are large with respect to the widths of scratches made by single abrasive grains during diamond surface grinding has been clearly shown on a ceramic workpiece that was tilted slightly with respect to the table of a grinding machine by van Groenou et al., (1). The correlation in our paper of grinding forces measured during up grinding with the indentation fracture parameter derived by Evans and Wilshaw (2) is taken as further evidence that a major mechanism of chip formation during grinding is the intersection of lateral vent cracks. During down grinding these chips must travel between the wheel and workpiece before being ejected from the system, thus the vertical grinding forces measured during down grinding should exceed those measured during up grinding. This was found to be the case for most of the harder ceramics examined in this work.

GIELISSE

In one of your figures you showed that you found no dependence of grinding force on hardness of the material. In subsequent slides you show that there is an apparent correlation between grinding force and a compound evaluation parameter in which this hardness is again featured. We do note further that there still remains the need to differentiate between up grinding and down grinding and subsequently between Si_3N_4 and "other ceramics." Do your researches indicate that evaluation of the grinding process in terms of derived quantities such as hardness carry physical significance, i.e., are fundamentally justifiable?

KOEPKE & STOKES

The physical significance implied by a correlation of grinding forces and the indentation fracture parameters of Lawn, Evans, and Wilshaw (2,3) relates to the mechanism of material removal during chip formation. Correlation of grinding forces measured during up grinding with the parameter derived by Evans and Wilshaw (2) argues that chips form, at least in part, by the intersection of lateral vent cracks formed as a result of the plastic indentation of the workpiece by adjacent abrasive grains on the wheel surface. The difference between grinding forces measured during down grinding on silicon nitride and the other materials emphasizes that during down grinding the comminution characteristics of the chips contribute to the measured grinding forces.

MALKIN

Could you please explain your conclusion that deformation occurs after the leading edge of the wheel has passed? Do you mean to imply that plastic deformation during abrasive-workpiece interaction occurs after chip formation by fracture? If so, this is contrary to our observations on grinding of glass, as seen in our paper in this conference.

KOEPKE & STOKES

The correlations shown in this paper, the results of Evans (4) and Evans and Wilshaw (2) and the particularly revealing photographs of van Groenau et al., (1) and Veldkamp et al., (5), all argue that chip formation during abrasive machining of ceramics occurs at least in part by the interaction of lateral cracks resulting from the elastic-plastic indentation of the workpiece by an abrasive grain. Thus, the chip size at the leading edge of the wheel-workpiece interface is greater than the theoretical plastic-chip size. At the trailing edge of the wheel-workpiece interface, however, the wheel depth of cut approaches the grit depth of cut and chip formation by plastic deformation becomes more realistic. During down grinding plastic flow in this region is further enhanced by the burnishing action of the swarf moving between the wheel and workpiece (6). Thus we suggest that a large amount of the observed deformation occurs after the leading edge of the wheel has passed.

LEE

I found the good correlation between some of the monitored parameters and the hardness of materials Dr. Koepke and also the previous speaker Dr. Evans reported to be very interesting. However, I am troubled somewhat by the term hardness used. In view of the complexity of determining hardness of a brittle solid, I will appreciate it if the speaker could clarify the point further.

KOEPKE & STOKES

The hardness values used in this work were, as noted in Table 3, measured with a Knoop indenter under a 100 gm load following accepted procedures (7). We agree that the "hardness" of a brittle solid is a complex quantity but suggest that it is measurable and is related to the elastic and plastic mechanical properties of the workpiece (8,9). This point is discussed in detail by Rice and Evans in this conference (see p. 185)

8. Appendix

Horizontal, F_H/b , and vertical, F_V/b , grinding forces measured on a number of ceramics during down (wheel moving with workpiece travel) and up (wheel moving against workpiece travel) surface grinding with a 100 grit diamond wheel as a function of feed rate, b is the width of cut. The workpiece materials are listed in order of their hardness.

Material	Depth of Cut (mm)	Feed Rate (cm/sec)	Down Grinding		Up Grinding	
			$\frac{F_H}{b}$	$\frac{F_V}{b}$	$\frac{F_H}{b}$	$\frac{F_V}{b}$
			(gm/cm)	(gm/cm)	(gm/cm)	(gm/cm)
PZT	.025	.042	12	74	17	72
		.21	25	153	40	165
		.42	42	220	59	236
MgO	.025	.042	6	79	11	93
		.21	24	208	51	265
		.42	44	268	74	312
NiZN Ferrite (13 μ m g.s.)	.025	.042	6	14	6	14
		.21	11	31	16	38
		.42	15	49	23	52
NiZN Ferrite (3 μ m g.s.)	.025	.042	8	27	9	30
		.21	14	66	20	74
		.42	16	88	27	101
"β" Si ₃ N ₄	.025	.21	306	895	183	551
		.042	31	106	34	106
	.012	.21	87	311	84	271
		.42	128	429	125	399
Norton Si ₃ N ₄	.025	.21	574	1883	312	1046
		.042	56	361	100	370
	.012	.21	84	493	126	505
		.42	113	562	153	659
"α" Si ₃ N ₄	.025	.21	409	1362	254	934
		.042	26	124	30	103
	.012	.21	80	396	101	263
		.42	114	590	143	408
Lucalox Al ₂ O ₃	.025	.042	15	120	25	139
		.21	185	654	145	431
		.42	176	620	172	498
AVCO Al ₂ O ₃	.025	.042	299	1184	249	775
		.21	303	1167	397	1071
		.42	293	1159	404	1156
Coors Al ₂ O ₃	.025	.042	91	413	136	315
		.21	132	605	220	762
		.42	227	1005	311	1068
B ₄ C	.025	.042	73	523	43	154
		.21	129	740	386	942
		.42	152	838	415	1257

Re
R.
Pr

inv
wor
for
bil
inv
lar
abr
scr
loa

fac
in
pro
was
str
exp

ren
ism
gic
the
The
str

1
F

GLASS GRINDING MECHANISMS AND INFLUENCE ON THE FINISHED SURFACE AND STRENGTH

S. Malkin

Faculty of Mechanical Engineering
Technion-Israel Institute of Technology
Haifa, Israel

M. Huerta

Sandia Laboratories
Albuquerque, New Mexico

Mechanisms for grinding of glass were investigated and related to the finished surface morphology and fracture strength. The abrasive-glass interaction was found to involve flow into chips for grinding with silicon carbide abrasive, and flow followed by concoidal fracture for grinding with diamond abrasive. Much less energy was required for grinding with diamond, since much less of the material being removed is deformed. Grinding conditions causing more flow were generally found to give less surface damage and higher fracture strengths after grinding.

Key Words: Glass, grinding; strength; surface damage.

1. Introduction

Machining of glass is generally performed by grinding. Grinding is a complex process involving the interaction of numerous abrasive cutting points on the wheel surface with the workpiece material. For metals, material removal by grinding is known to occur by shear deformation into chips. For glass the situation appears to be more complex due to the possibility of both irreversible flow of the glass and brittle fracture. Although a number of investigations imply glass removal during grinding by fracture [1-6], flow can also occur at large hydrostatic compressive stress conditions [7] such as developed in the vicinity of the abrasive cutting edges. Such hydrostatically induced flow is obtained by indentation and by scratching of glass surfaces, the flow followed by localized fracture at sufficiently large loads [8-12].

An important consequence of the grinding process for glass is the condition of the surface which is produced. The strength of glass is sensitive to the surface condition which, in turn, is a direct consequence of the mechanisms of abrasive-glass interactions during processing. One illustration of the influence of processing conditions on fracture strength was provided by Shand [13] who found for sandblasting of glass rods a decrease in fracture strength for higher blasting pressure. The parameters of the grinding process can also be expected to have a significant influence on the strength of glass.

The present paper reviews the results of an investigation into the mechanisms of material removal for grinding of glass and their influence on the finished materials [14, 15]. Mechanisms of the grinding process were assessed from measurements of the grinding forces and energies for a number of glasses over a wide range of operating conditions, from the nature of the particles removed by grinding, and from examination of individual grinding scratches. These findings were subsequently related to the ground surface morphology and fracture strength after grinding.

¹ Figures in brackets indicate the literature references at the end of this paper.

2. Experimental

Plunge grinding was performed on a straight surface grinder as illustrated in figure 1. During grinding, the force components F_t and F_n were measured using a semiconductor strain gage dynamometer. A fundamental parameter obtained from the force measurements is the specific grinding energy u , which is the energy expended per unit volume of material removed:

$$u = \frac{F_t V}{bvd} \quad (1)$$

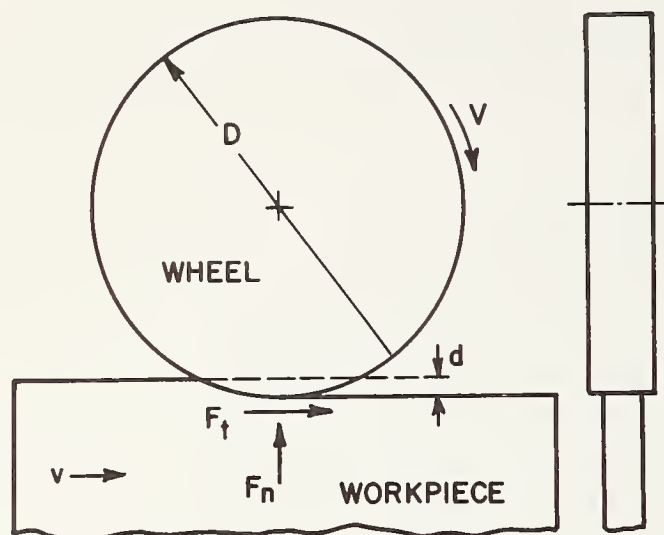


Figure 1. Illustration of plunge surface grinding

Any proposed mechanism of material removal must be consistent with the magnitude of the specific grinding energy and its dependence on the grinding parameters.

Table 1. Glasses and their Compositions

GLASS*	Weight Percents													α	T_s
	SiO ₂	Al ₂ O ₃	B ₂ O ₃	CaO	BaO	8aNO ₃	MgO	K ₂ O	Na ₂ O	PbO	ZnO	TiO ₂	LiO		
8429 Borosilicate	72	1	14					13						60	834
8390 Lead	30							2		65		3		77	583
1723 Aluminosilicate	57	15	5	10	3	3	7							46	908
7906 High Silica	96													7.5	1500
7913 High Silica	96													7.5	1500
9616 Aluminosilicate	67	21					2				1	5	4	36	919
8871 Potash Lead	35							7		58				102	525
0329 Aluminosilicate	65	20	2	Plus 4 PbO · Pb ₃ O ₄			2				2	5	4	39	880
8463 High Lead	5	3	10							78				83	377
Soda Lime	70			10			4		13					92	710
9617 Pyroceram				Same as parent glass 9616										12	
0330 Pyroceram				Same as parent glass 0329										12	

*Numbers refer to Corning glass code.
 α = coefficient of thermal expansion, $\times 10^7 \text{ }^\circ\text{C}^{-1}$
 T_s = softening temperature, $^\circ\text{C}$

The numerous workpiece materials used in this investigation are listed in table 1 together with the manufacturer's identification code. The specimens were typically 50mm long and 6mm wide. Grinding experiments were performed with one type of vitreous bonded silicon car-

bide wheel (37C 801-K8V) of 8in (200 mm) nominal diameter and four different metal bonded diamond wheels (MD100-N50M, MD100-N100M, MD180-N50M, and MD180-N100M) of 7in (175mm) diameter giving two grain sizes (100 and 180 mesh) and two diamond concentrations (50 and 100). The silicon carbide wheel was dressed prior to each test with a pyramidal diamond tool taking a radial depth per pass of 0.001 in. (25.4 μ m) and a dressing lead across the wheel of 70 μ m per wheel revolution. The diamond wheels trued using a silicon carbide dressing wheel (37C60MV) mounted in a brake-controlled device at a radial depth of from 25 μ m to 38 μ m and a crossfeed of 80 μ m per wheel revolution. Grinding fluid applied during grinding consisted of a commercial soluble oil (Cimcool S2) mixed with water in a concentration of 1:25.

Scratch tests were run using the method developed by Thompson and Malkin [16] to observe the grinding action by individual cutting points against a glass workpiece. This method consists of taking a single grinding pass across the workpiece with a relatively slow wheelspeed ($V = 4.1$ m/s) and fast workspeed ($v = 46$ cm/s) so that the scratches generated on the workpiece do not overlap.

Fracture strength after grinding was measured for 1723 aluminosilicate and soda lime glass specimens using the four-point loading arrangement illustrated in figure 2 with the ground edge of the specimen in tension. Prior to testing, ten grinding passes were taken along each specimen at the given test condition except for the largest depth of cut ($d = 51$ μ m) in which case only six passes were taken.

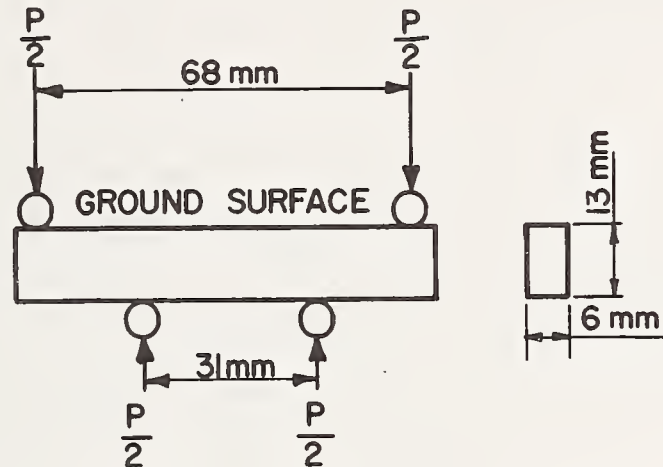


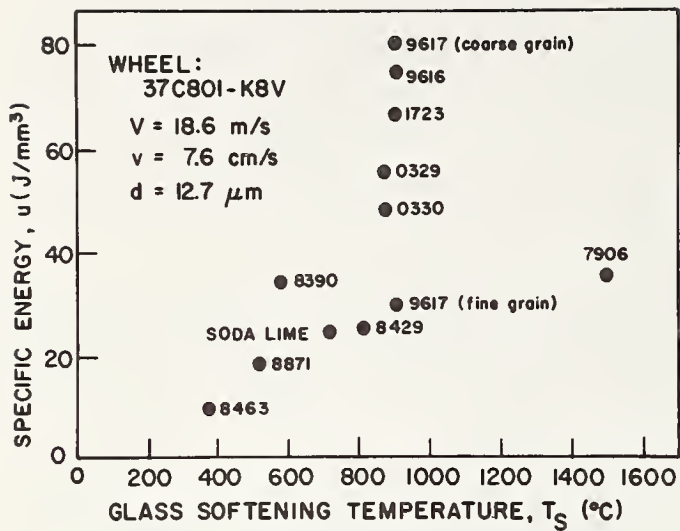
Figure 2. Four-point loading arrangement for measuring fracture strength.

3. Grinding Tests

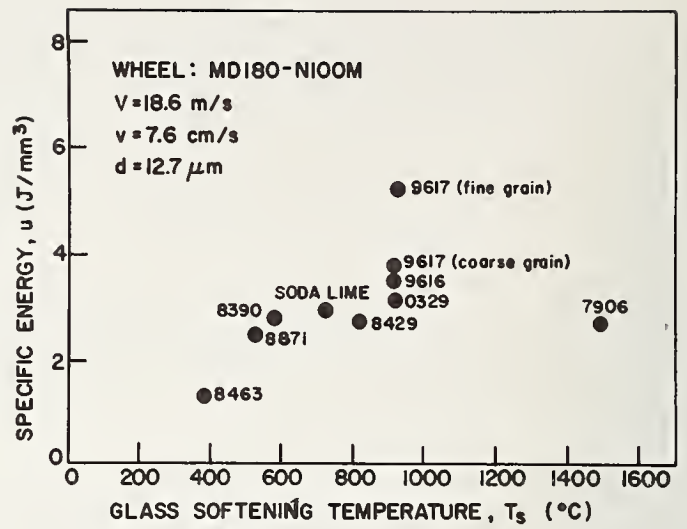
Numerous grinding tests were performed on the various glasses and a few glass-ceramics with the different grinding wheels over a wide range of operating conditions. The results to be presented here illustrate the main effects which were found.

A comparison of the specific grinding energies for the various glasses and a few glass-ceramics is shown as a plot of specific energy versus softening temperature for a silicon carbide wheel in figure 3a and for a diamond wheel in figure 3b. Both series of tests using the different wheels were run at the same wheel velocity, workpiece velocity, and wheel depth of cut. Similar behavior was found for both wheels with the specific energy tending to be bigger for higher softening temperatures. However, the specific energy for grinding with the diamond wheel was approximately an order of magnitude less than for grinding with the silicon carbide wheel, as the ordinate in figure 3a is a factor of ten bigger than in figure 3b.

The effects of wheel depth of cut and workpiece velocity on specific grinding energy is shown in figures 4 and 5. Increasing the removal rate by raising either of these parameters generally reduces the specific energy for both the silicon carbide and diamond wheels in a similar way, although this effect is much more sensitive to wheel velocity.

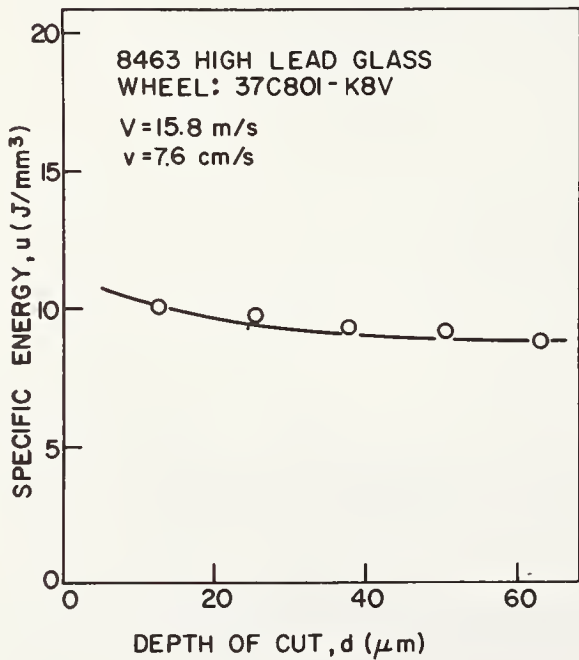


(a)

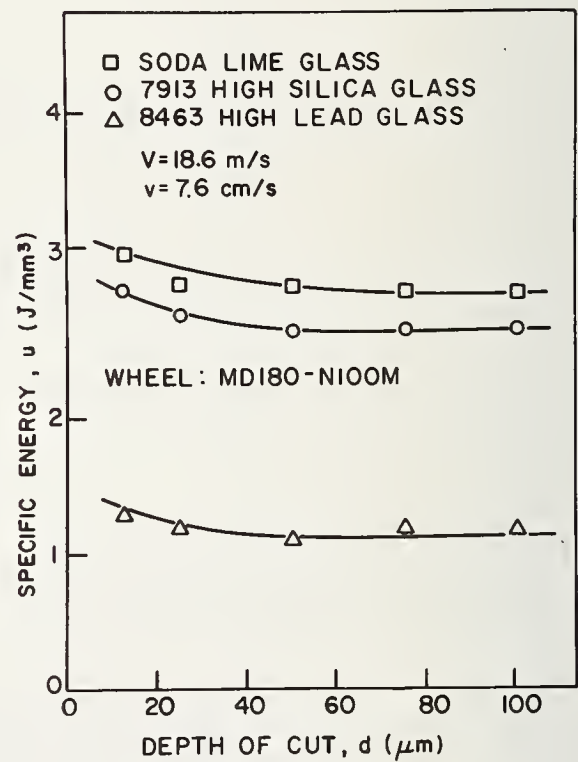


(b)

Figure 3. Specific grinding energy versus softening temperature for (a) silicon carbide wheel and (b) diamond wheel.



(a)



(b)

Figure 4. Specific grinding energy versus wheel depth of cut for (a) silicon carbide wheel and (b) diamond wheel.

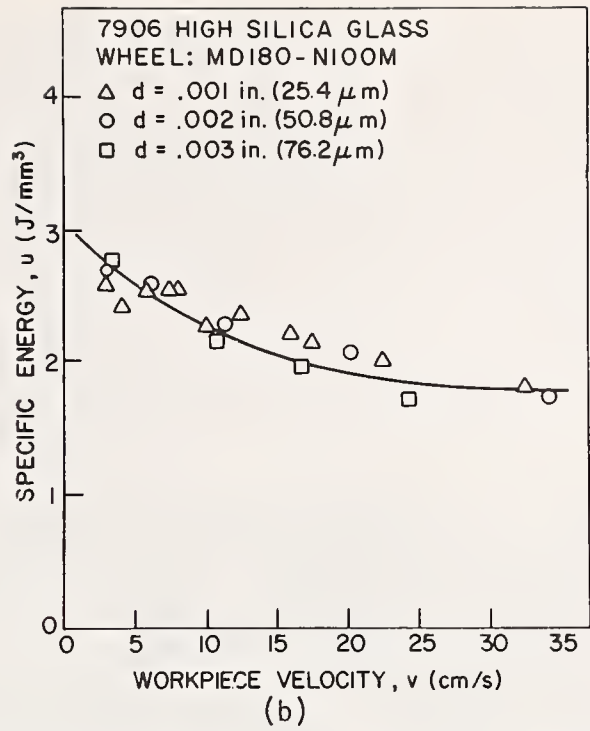
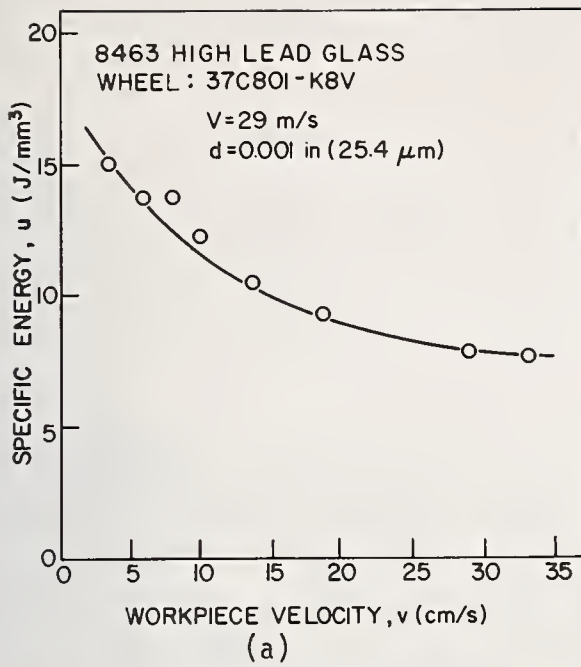


Figure 5. Specific grinding energy versus workpiece velocity for (a) silicon carbide wheel and (b) diamond wheel.

The influence of diamond wheel composition is shown in figure 6 where the specific energy is plotted versus the number of diamond grains per unit area of wheel surface measured by counting exposed grains with the aid of a microscope. These results imply that the increase in specific energy observed with finer diamond grains and higher concentration can be attributed to having more grains on the diamond wheel surface. The relative influence of diamond grain size and concentration can be seen in terms of their influence on the number of grains per unit area of a cube plane for diamond grains arranged with simple cubic packing. Approximating the diamond grains as spheres of diameter a , and noting that the concentration number M in the wheel specification is four times the volume percentage of diamond, the number of grains per unit area of cube face can be shown to be [14]:

$$C = \frac{0.022 M^{2/3}}{a^3} \quad (2)$$

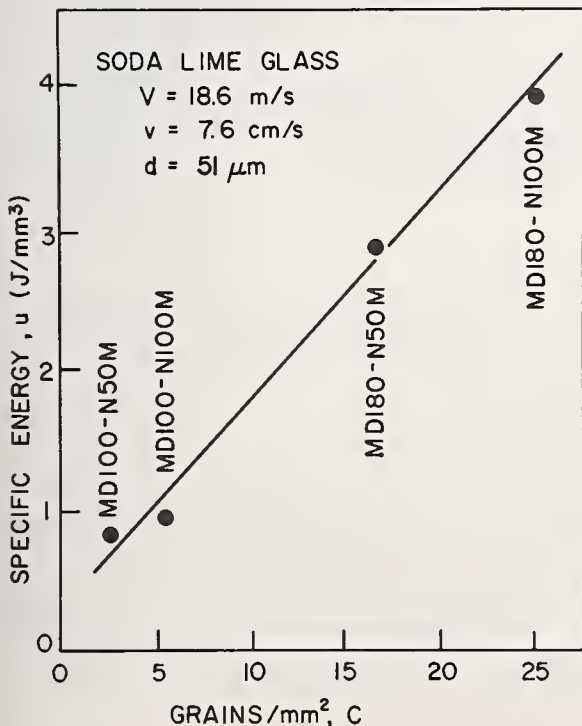


Figure 6. Specific grinding energy versus number of diamond grains per unit area on the wheel surface.

Non-cubic packing or non-spherical diamond particles would alter the value of the constant in eq. (2). The relative influence of grain size and concentration on the measured values of C was found to correlate closely with eq. (2) although the calculated values were approximately twice the measured ones with $a = 210\mu\text{m}$ for the wheels with 100 mesh diamond and $a = 80\mu\text{m}$ for those with 180 mesh diamond.

In order to provide some additional information as to the grinding mechanisms, particles removed during grinding were collected and examined by scanning electron microscopy (SEM). Two examples of what was found are shown in figure 7. When grinding with a silicon carbide wheel, the grinding particles consisted mostly of flow-type chips as in figure 7a whereas the diamond grinding tended to give mainly brittle fracture particles as in figure 7b. The striking difference in the nature of these particles would suggest that the much higher energies required for grinding with silicon carbide than with diamond (see fig. 3) is due to material removal by flow rather than by fracture.

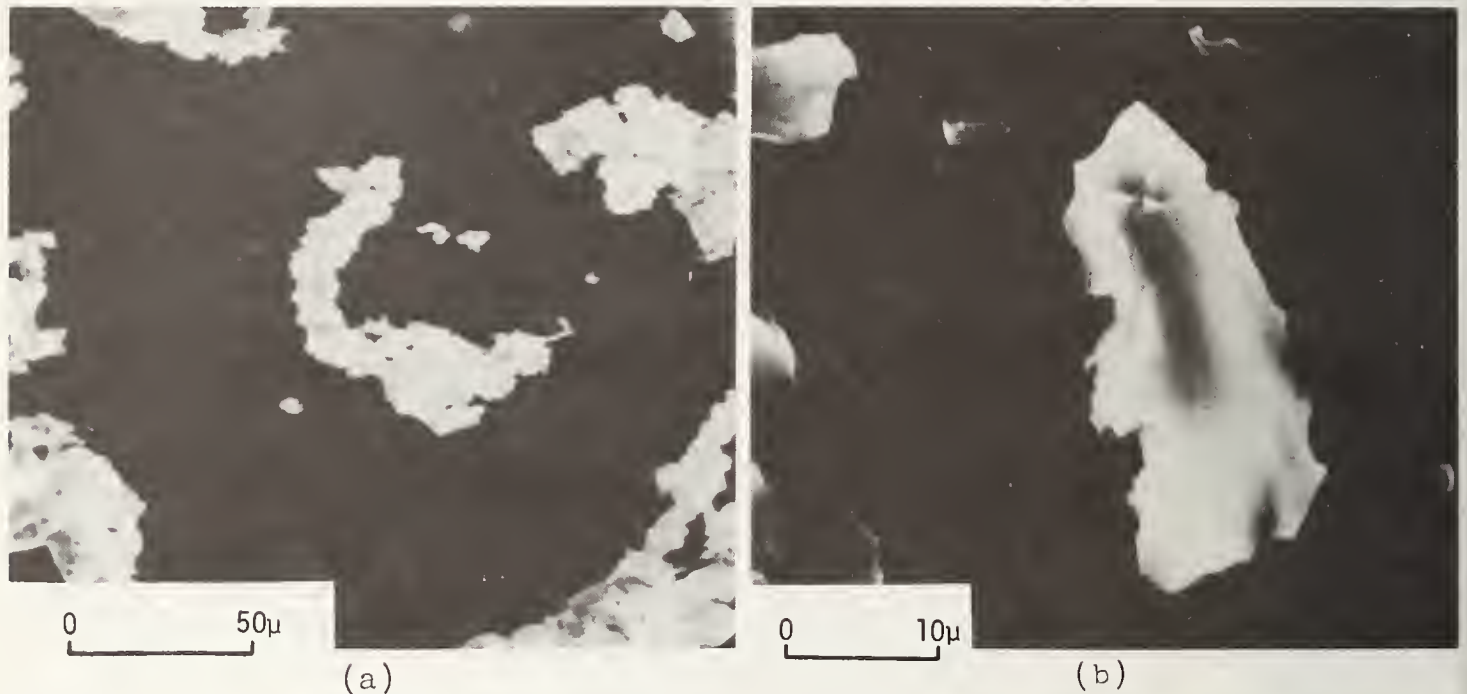


Figure 7. SEM micrographs of grinding detritus: (a) silicon carbide wheel, 8463 glass, $V = 18.6 \text{ m/s}$, $v = 7.6 \text{ cm/s}$, $d = 63.5\mu\text{m}$; (b) diamond grinding wheel MD180-N50M, soda lime glass, $V = 18.6 \text{ m/s}$, $v = 7.6 \text{ cm/s}$, $d = 12.7\mu\text{m}$.

4. Scratch Tests

Grinding scratches were generated on soda lime glass specimens by taking a single pass with a slow wheel velocity and fast workpiece velocity, as described above. Optical micrographs of typical scratch patterns produced in this way are shown in figure 8a for a silicon carbide wheel and in figure 8b for a diamond wheel. Scratch lengths were found to be more uniformly distributed for the silicon carbide than for diamond wheels, which indicates more uniform radial distribution of cutting points on the silicon carbide wheel surface. With both types of abrasive, the scratches appear to have been formed by flow of the glass, which is followed by concoidal fracture for the diamond wheel mainly in the longer scratches made by grains protruding further out from the wheel and penetrating deeper into the glass. This would imply that initial deformation of the glass by diamond grains is followed by concoidal fracture if the penetration is sufficiently deep. No concoidal fractures were observed with the silicon carbide wheel. Concoidal fractures appear to be caused by the formation of lateral vent cracks similar to those observed by Lawn and Swain [12] for indentation. Numerous measurements were made on individual scratches to determine their cross-sectional shape using the method previously developed [16]. Both silicon carbide and diamond wheels were found to produce very similar trapezoidal scratch cross sections with the width at the bottom of the scratch typically about $1\mu\text{m}$ and included angle between the scratch sides of about 150 deg . SEM examination of scratches for silicon carbide and diamond grinding in figure 9 also reveal regularly spaced crevices or cracks extending down below the scratches normal to the grinding direction.

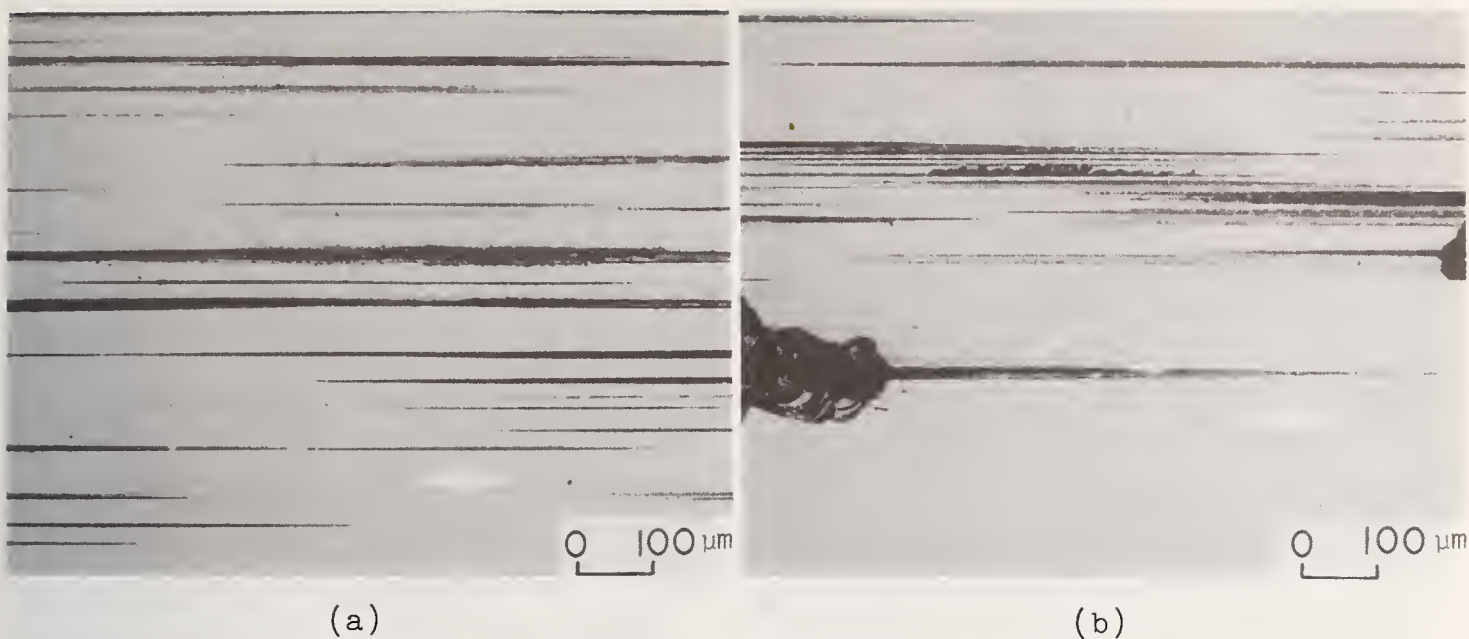


Figure 8. Optical micrographs of scratches for (a) silicon carbide wheel and (b) diamond wheel MD180-N50M. The arrows indicate grinding direction.

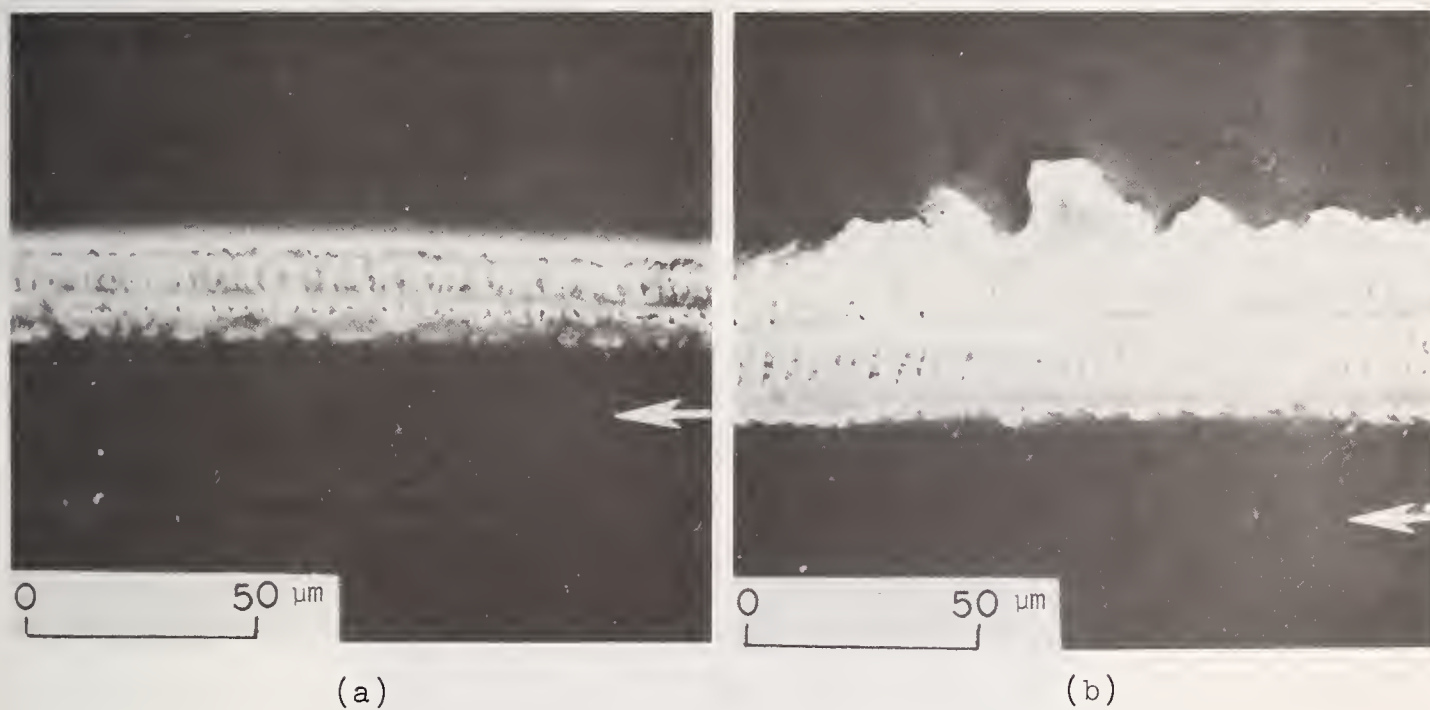


Figure 9. SEM micrographs of scratches for (a) silicon carbide wheel and (b) diamond wheel MD180-N50M.

5. Surface Morphology

SEM micrographs of finished surfaces are shown in figure 10 for silicon carbide grinding of soda lime and 7906 high silica glasses using a slow workpiece velocity and fine wheel depth of cut. In these micrographs and the others to follow, the grinding direction is from top to bottom. The surfaces for these two different glasses appear very similar, with striations running along the grinding direction indicative of extensive plastic flow. This flow is evident in figure 10b which shows a portion of the high silica glass surface at higher magnification. Grinding of other glasses under the same conditions gave similar surfaces.

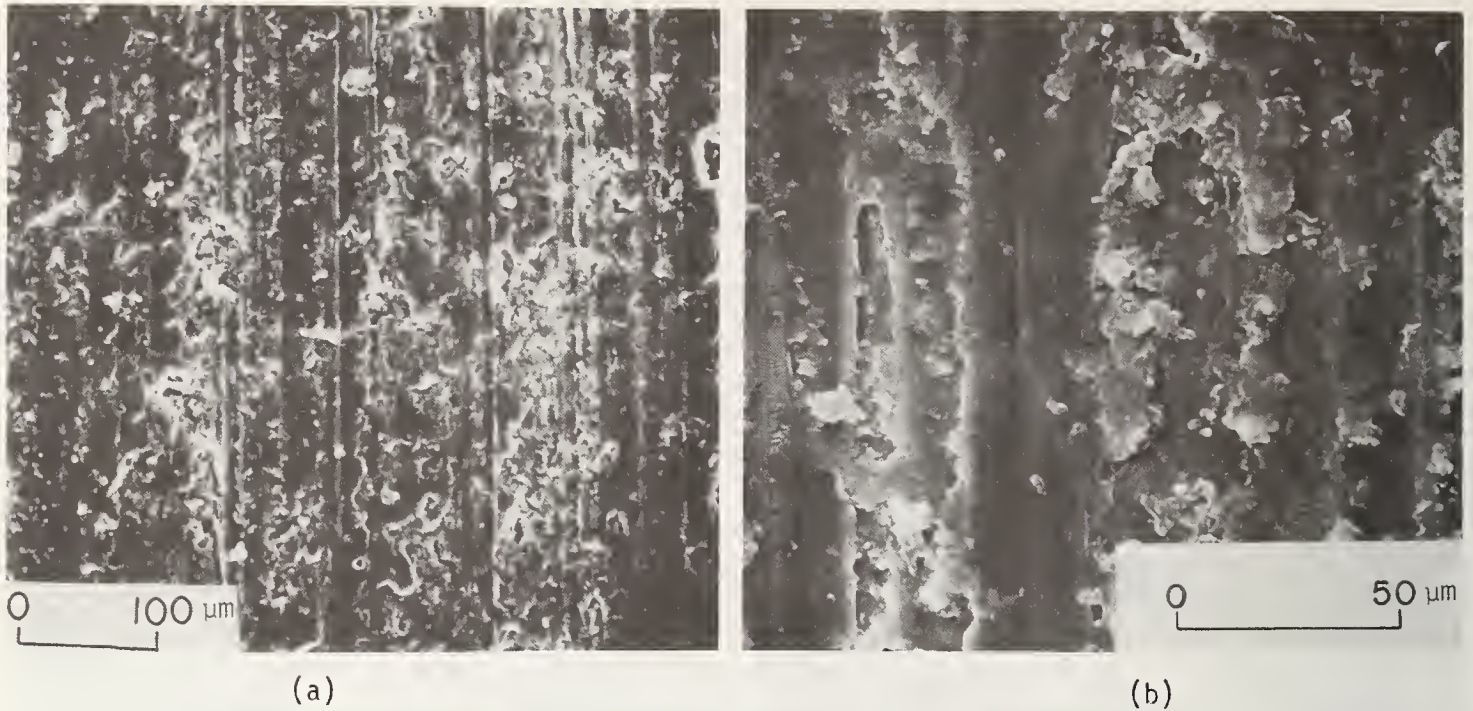


Figure 10. SEM micrographs of surfaces ground with silicon carbide wheel 6 with $V = 18.6$ m/s, $v = 7.6$ cm/s, and $d = 12.7\mu\text{m}$: (a) soda lime glass; (b) 7906 high silica glass.

Additional SEM observations of surfaces ground with the silicon carbide wheel were made in order to observe the effect of wheel depth of cut and workpiece velocity. Increasing the wheel depth of cut was found to have little noticeable effect on ground surface morphology, except for spalling which was observed beyond a certain point. For 8390 leaded glass and soda lime glass, the limiting wheel depth of cut without spalling was 0.0015 in. ($38\mu\text{m}$). Increasing the workpiece velocity tended to give a much rougher surface with less flow. This can be seen in figure 11 where a 7913 high silica glass surface is shown for a much faster workpiece velocity than in figure 10. Both microcracks and localized regions of flow can be seen on the surface.

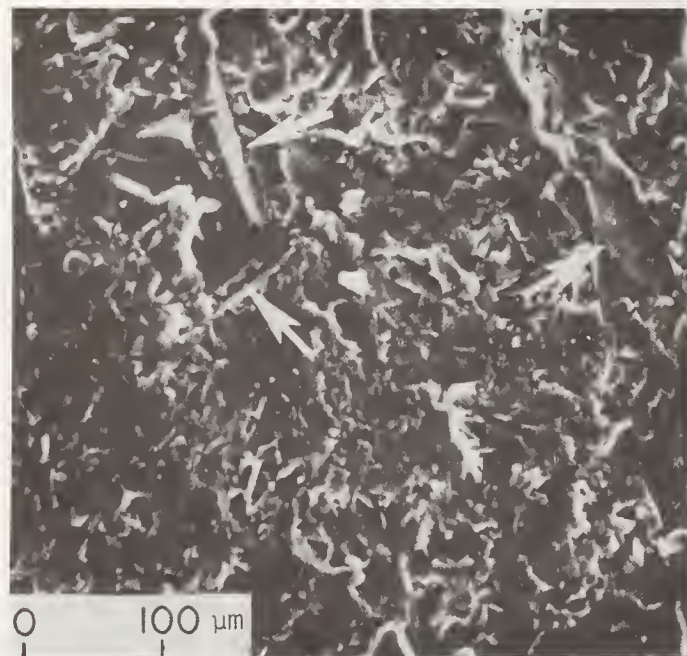


Figure 11. SEM micrograph of 7913 high silica glass ground with silicon carbide wheel with fast workpiece velocity: $V = 18.6$ m/s, $v = 30.5$ cm/s, and $d = 12.7\mu\text{m}$. Arrows show microcracks on the surface.

Surfaces produced by diamond grinding appear markedly different from those ground with silicon carbide. Comparing the diamond ground surfaces in figures 12 with those in figure 10 for silicon carbide grinding at the same operating parameters, it can be seen that grinding with diamond results in a rougher fragmented surface with much less flow. As with silicon carbide grinding, increasing the wheel depth of cut had little effect on the surface appearance, but increasing the workpiece velocity causes a much rougher surface as shown in figure 13. A few striations can be seen in figure 13, although most of the surface is fragmented.

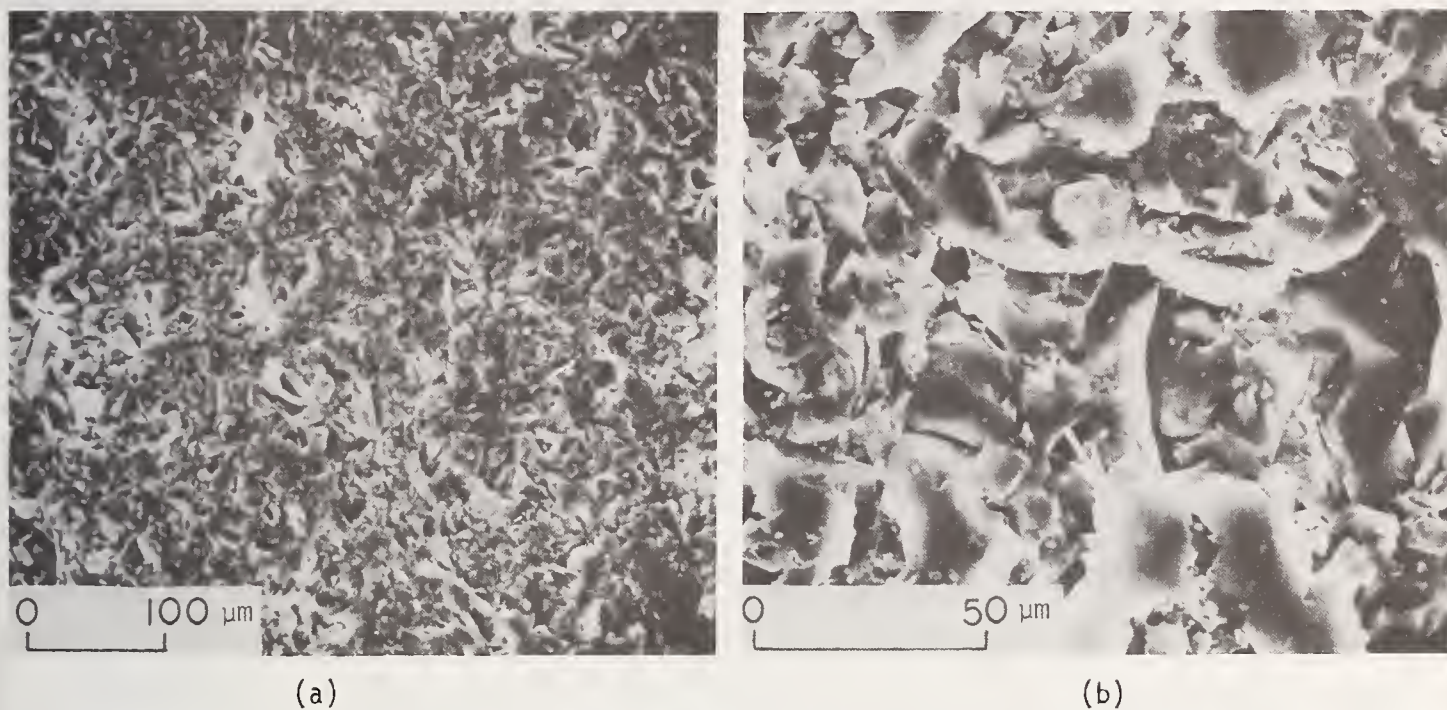


Figure 12. SEM micrographs of surfaces ground with MD180-N100M diamond wheel at $V = 18.6$ m/s $v = 7.6$ cm/s and $d = 12.7\mu\text{m}$: (a) 1723 aluminosilicate glass; (b) soda lime glass.

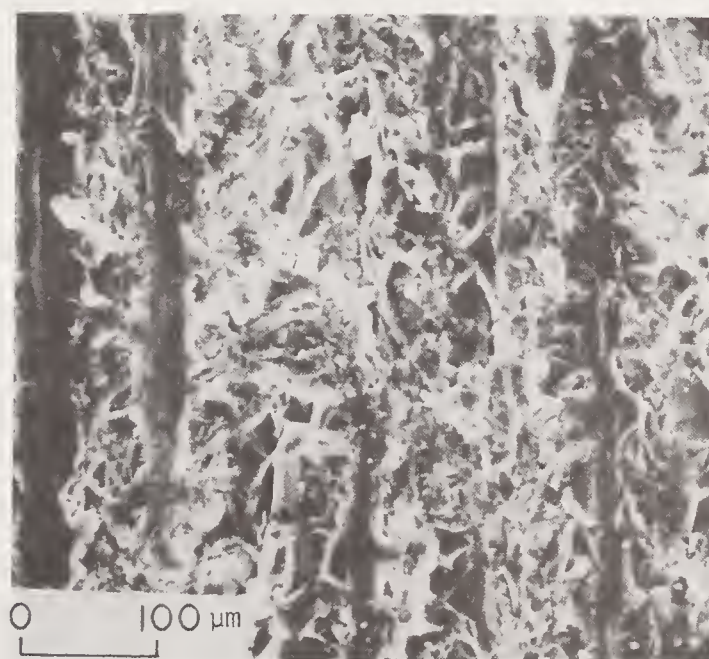


Figure 13. SEM micrograph of 1723 aluminosilicate glass ground at fast workpiece velocity with MD180-N100M diamond wheel: $V = 18.6$ m/s, $v = 41$ cm/s, and $d = 51\mu\text{m}$.

The SEM micrographs in figures 12 and 13 were all for the same diamond wheel with the finer grain size and higher concentration. Reducing the number of diamond grains on the wheel surface by using the coarser grained wheel produced a more highly fractured surface with little evidence of plastic flow as seen in figure 14. With the coarser grained wheel, the fractured areas are more distinct, and some brittle fracture hackle markings can be seen at the higher magnification in figure 14.

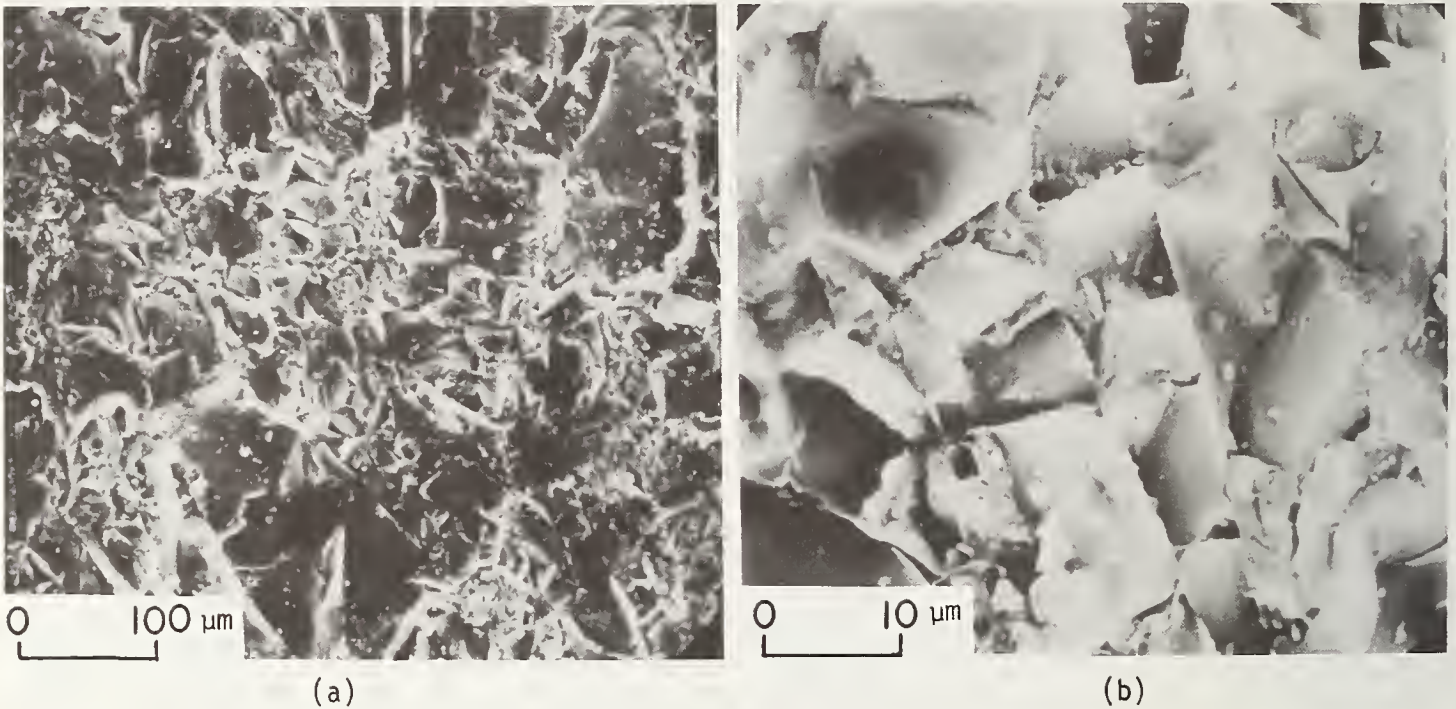


Figure 14. SEM micrographs of soda lime glass ground with coarser grained diamond wheel: $V = 18.6\text{m/s}$, $V = 7.6\text{ cm/s}$, $d = 12.7\mu\text{m}$, MD100-N100M wheel.

6. Fracture Strength

Fracture tests were carried out on 1723 aluminosilicate and soda lime glass specimens for various grinding conditions. The results are summarized in table 2 which gives the mean strength σ and standard deviation based on a minimum of five data points obtained for each test condition. Relatively little scatter was found in fracture strengths for each test condition, the standard deviation being typically about 10% of the mean.

Table 2. Fracture Strengths

Test Condition	Wheel	v (cm/s)	d (μm)	σ (N/mm^2)	
				1723 aluminosilicate	soda lime
1	37C801-KV	7.6	13	77.2 ± 7.9	91.8 ± 8.8
2	MD180-N100M	7.6	13	71.0 ± 8.4	65.1 ± 5.0
3	MD180-N50M	7.6	13	63.9 ± 4.5	70.1 ± 4.8
4	MD100-N100M	7.6	13	44.2 ± 2.4	46.4 ± 3.7
5	MD130-N100M	7.6	51	69.3 ± 6.3	76.1 ± 2.3
6	MD180-N50M	7.6	51	—	71.6 ± 3.6
7	MD100-N100M	7.6	51	42.1 ± 3.2	46.0 ± 4.8
8	MD180-N100M	40.6	13	—	64.0 ± 6.9
9	MD180-N100M	40.6	51	46.7 ± 6.6	69.8 ± 5.5

The fracture strength results follow a similar pattern for both glasses. The highest fracture strengths for each material were obtained with the silicon carbide wheel (test condition 1). The strengths for diamond grinding with the same operating parameters (test conditions 2-4) were significantly lower. With both glasses, the lowest strengths with these operating parameters were obtained with the coarser grained wheel, and comparable strength reduction with the coarser grained wheel was also found with tests carried out at bigger wheel depths of cut (test conditions 4 and 7). Raising the removal rate by taking a bigger depth of cut can be seen to have had almost no effect on fracture strength, but the effect of the increasing removal rate by taking a faster workpiece velocity is not clear. For the soda lime glass, the faster workpiece velocity had relatively little effect on fracture strength as seen by comparing test conditions 8 and 9 with test conditions 2 and 5, respectively. For the aluminosilicate glass, however, a comparison of test condition 9 with test condition 5 shows a big drop in fracture strength with a faster workpiece velocity.

7. Discussion

Grinding of glass is done with either silicon carbide or diamond wheels. It is apparent that the grinding process and the nature of the ground surfaces depend on which type of abrasive is used. The grinding energy requirements for silicon carbide are much greater than for diamond. SEM observations of the grinding detritus (fig.7) suggest that these differences in grinding energy can be attributed to material removal by flow-type chip formation with silicon carbide as opposed to concoidal fracture for diamond. These same differences appear again in scratch test micrographs (fig. 8), although the observations here also show evidence of irreversible flow with diamond prior to fracture. The SEM micrographs of the ground surfaces showing extensive flow with silicon carbide and fracture and localized flow with diamond are consistent with these observations.

It can therefore be concluded that grinding of glass occurs by flow-type chip formation for silicon carbide, and a combination of flow and fracture with diamond. Although most of the actual material removal with diamond occurs by fracture, the energy required for particle removal by brittle fracture can be shown to be only a negligible portion of the total grinding energy [14]. Therefore, virtually all the energy for grinding of glass, whether with silicon carbide or diamond wheels, is expended by irreversible flow. Much more material is deformed with silicon carbide than with diamond, which accounts for the differences in magnitude of the specific energy.

When comparing the grinding behavior of various glasses, a general trend was found of increasing specific energy for higher softening temperature both for silicon carbide and diamond grinding. This behavior would appear to be a direct consequence of the adiabatic constrained flow situation at the abrasive grain cutting edges. At the rapid strain rates imposed during grinding, the deformation takes place under adiabatic conditions so that all irreversible work of deformation heats up the material being deformed without time for heat to be conducted away. Very large strains are required during the deformation in order to accommodate the severe flow constraint arising from the highly negative rake angles at the abrasive grain cutting edges. Under these conditions, the energy input during the deformation process can become a limiting factor in the process. When grinding metals, for example, the shearing energy of the metal can be approximated as the energy required to take the metal from ambient conditions to the melting state [17]. As the limiting energy is approached during adiabatic deformation, the shear resistance of the material being deformed decreases rapidly, with a corresponding drop in the energy input rate with continued deformation. For glass, the softening temperature may approximate the relative energy limit for adiabatic deformation, insofar as it also provides an indication of the energy input to reduce the shear resistance (viscosity) to some very low value.

The influence of grinding conditions was observed by varying the wheel composition and operating parameters. For diamond grinding, higher diamond concentration and finer grain size were found to provide more grains per unit area wheel surface. The linear increase of specific grinding energy with the number of grains per unit area (fig.6) suggests that each grain, on the average, expends a certain amount of deformation energy prior to concoidal fracture. With fewer grains on the surface, the amount of material removed by fracture would have to be bigger, thus accounting for the more highly fractured appearance of the ground surface with a coarser grained wheel (fig.14). The diamond concentration has much less effect on grain density than grain size (see eq.2), so that its effect on ground surface morphology is also much less.

The decrease in specific energy with faster workpiece velocities and bigger wheel depths of cut is similar to what occurs when grinding metals, although the effect of depth of cut is much less sensitive for glass. With metals, this behavior has been attributed to increased plowing and sliding energy as the removal rate is decreased [17]. This same explanation may be applicable to glass grinding with silicon carbide which gives flow-type chips as in the case of metals. For diamond grinding, one possible explanation to account for the variation of specific energy with v and d can be developed by returning to the idea that each diamond grain expends a given amount of energy per encounter with the workpiece. When either the workpiece velocity or wheel depth or cut is increased by itself, there are proportionally fewer diamond grain encounters with the workpiece for removing a given volume of material. On this basis, the specific energy should vary inversely with both v and d , which is a stronger dependence than observed especially for wheel depth of cut.

Additional insight into the effect of operating parameters for diamond grinding can be gained by referring to the cutting geometry in the grinding zone as illustrated in figure 15. As an abrasive grain enters the grinding zone, it initially cuts into the workpiece at an interference angle β . After initial deformation, material removal occurs by concoidal fracture. Now the size of the particles removed by concoidal fracture are typically much smaller than the length of the grinding zone, so the abrasive grain repeats this cutting event a number of times during a single traverse through the grinding zone. In figure 15 it can be seen that a faster workpiece velocity increases the initial interference angle β , whereas a bigger wheel depth of cut extends the length of the grinding zone but has no effect on this angle. Assuming that the amount of material removed by each concoidal fracture increases with β , fewer cutting events each consisting of flow followed by fracture would occur with a larger interference angle, resulting in less flow. This could account for the decrease in specific energy and the more highly fractured surfaces obtained with a faster workpiece velocity. The slight decrease in specific energy with increased depth of cut may be due to the progressive increase in interference angle for the successive cutting events during a single traverse of a grain through the grinding zone. Because of the longer grinding zone with bigger depths of cut, the interference angle averaged over all the cutting events becomes slightly larger. Since the initial interference angle is independent of wheel depth of cut, the ground surface morphology also does not depend on this parameter.

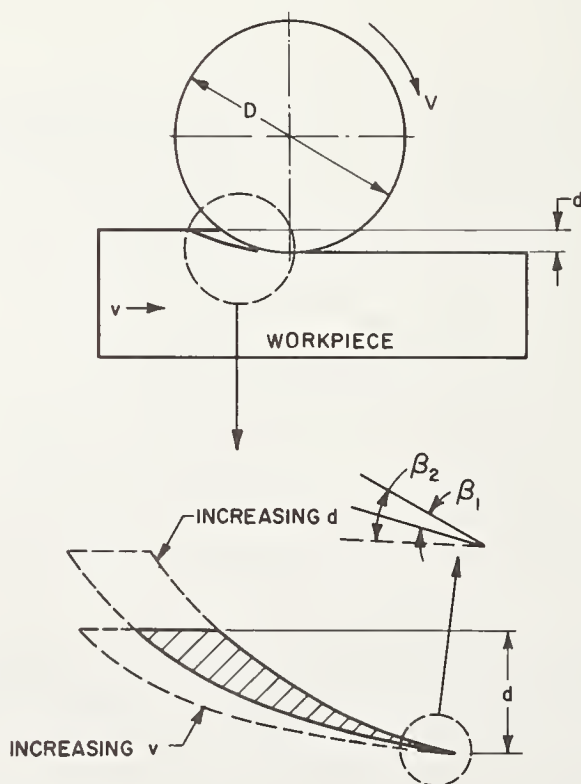


Figure 15. Illustration of influence of workpiece velocity and depth of cut on grinding geometry.

The fracture strength after grinding appears to be a direct consequence of the relative amounts of flow and fracture of the grinding process. The highest strengths were obtained by silicon carbide grinding where extensive surface flow during grinding produces a relatively smooth surface. The more fragmented surfaces obtained by diamond grinding apparently provide more favorable sites for unstable crack initiation at lower stresses. Coarser grained wheels lead to more highly fragmented surfaces with less flow, and much lower strength. Increasing the workpiece velocity had a similar effect on surface morphology, giving a lower strength as expected for the 1723 aluminosilicate glass, but not with the soda lime glass. The diamond concentration had little effect on surface morphology and insignificant influence on fracture strength. Both the surface morphology and fracture strength were also unaffected by wheel depth of cut.

These results have some immediate practical implications for grinding of glass. The use of silicon carbide wheels would appear to be preferable to diamond wheels for obtaining a higher strength. However, the removal rate with silicon carbide will be limited by spalling of the glass at larger depths of cut, and increasing the removal rate by taking a faster workpiece velocity can be expected to have an adverse effect on fracture strengths. Silicon carbide wheels also wear more than diamond wheels, which can make it more difficult to maintain any required geometrical form. Diamond grinding offers the possibility of taking much larger wheel depths of cut without degradation in strength. The fracture strength is enhanced with finer grain size and much less sensitive to concentration. Since the diamond wheel cost depends primarily on the diamond content, it should be possible to obtain good fracture strength with inexpensive wheels having a fine grain size and low concentration. Just how far one can go with large depths of cut, fine grain size, and low concentrations for grinding with diamond remains to be seen.

The research was supported by a grant from Corning Glass Works.

References

- [1] Newton, I., Opticks, 1695, from Holland, L., The Properties of Glass Surfaces, p.16 (Chapman and Hall, London, 1964).
- [2] Hooke, R., Micrographia, from Holland, L., The Properties of Glass Surfaces, p.16 (Chapman and Hall, London, 1964).
- [3] French, J.W., More notes on glass grinding, Opt. Soc. Trans. 8, 8-48 (1917).
- [4] Fielden, J.H. and Rubenstein, C., The grinding of glass by a fixed abrasive Glass Technology, 10, [3], 73-83 (1969).
- [5] Vaidyanathan, S., and Finnie, I., Grinding of brittle solids, New Developments in Grinding, Proceedings of the International Grinding Conference, M.C. Shaw, ed., pp. 813-831 (Carnegie Press, Pittsburgh, Pa, 1972).
- [6] Pahlitzsch, E., Recent results of research into sawing of glass, Proceedings of the Industrial Diamond Conference, p.221-244 (Oxford, England, 1966).
- [7] Bridgman, P.W. and Simon, I., Effects of very high pressure on glass, J. Appl. Phys., 24, [4], 405-413 (1953).
- [8] Ryskewitch, E., Die plastisch Deformierbarkeit sproder Korper, Glasstechn. Ber., 20, [6], 166-174 (1942).
- [9] Joos, P., Uber die Mikrohartete von Glass Oberflachen, Z.F. Angew, Phys. 9, 556-562 (1957)
- [10] McClintock, F.A. and Argon, A., Mechanical Behavior of Materials, p. 495 (Addison-Wesley, Reading, MA., 1966).

- [11] Marsh, D.M., Plastic flow in glass, Proc. Roy. Soc. Lond., 279A, 420-435 (1963).
- [12] Lawn, B.R. and Swain, M.V., Microfracture beneath point indentations in brittle solids, J. Mater. Sci., 10, 113-122 (1975).
- [13] Shand, E.B., Experimental study of fracture of glass: 1, the fracture process, J. Amer. Ceram. Soc., 37, [2], 52-60 (1954).
- [14] Huerta, M., and Malkin, S., Grinding of glass: the mechanics of the process, J. Eng. Ind., Trans. ASME, 98, [2], 459-467 (1976).
- [15] Huerta, M., and Malkin, S., Grinding of glass: surface structure and fracture strength, Trans. ASME 98, [2], 468-473 (1976)
- [16] Thompson, D., and Malkin, S., Grinding wheel topography and undeformed chip shape, Proc. International Conf. on Production Engineering, pp. 727-732 (Japan Society of Precision Eng., Tokyo, 1974)
- [17] Malkin, S., Specific energy and mechanisms in abrasive processes, Proceedings Third North American Metalworking Research Conf., M.C. Shaw, ed., pp. 453-465 (Carnegie Press, Pittsburgh, Pa., 1975).

Discussion

GIELISSE

You showed a difference of about one order of magnitude in specific grinding energy between vitrefied SiC wheels (about $25 \text{ J}/\mu\text{m}^3$) and metal banded diamond wheels (about $2.5 \text{ J}/\mu\text{m}^3$) grinding. Should not a comparison between a metal bonded SiC wheel and an metal bonded diamond wheel with all other factors equal, have been better? In any case, why do we have this big difference between the two wheels.

MALKIN

The experiments were carried out with vitrefied SiC and metal bonded diamond wheels because these are the types normally used in practice. We found significant differences in specific grinding energy, surface morphology, and fracture strength. One possible explanation to account for these differences is related to the radial distribution of cutting points on the wheel. With SiC, the distribution is more uniform giving fewer deep scratches where material removal is by concoidal fracture.

THE FINE GRINDING OF GLASS AND CERAMIC MATERIAL USING CONVENTIONAL GRINDING WHEELS

E.D. Doyle and S.K. Dean

Materials Research Laboratories, Defence Science and
Technology Organization, Maribyrnong, Victoria 3032,
Australia

The fine grinding of glass and ceramic material, using standard silicon carbide and aluminium oxide grinding wheels was studied.

Transparent glass surfaces were produced by both grinding wheels using wheel depths of cut of less than 1 μm . Electron microscopy of the glass grinding debris produced with the silicon carbide wheel showed that the glass was removed by a chip-formation process, leaving a finely grooved surface. On the other hand, the aluminium oxide wheel removed glass by a ploughing process, whereby the appearance of the ground surface on a micro-scale was relatively rough. Surface quality of fine ground glass was found to be dependent on the type of cutting fluid used.

The silicon carbide grinding wheel produced a smooth surface finish on an alumina workpiece. The mechanism of material removal was predominantly by chip formation. Some wear debris was also produced as a result of a chemical reaction between the wheel and the workpiece in the region of rubbing contact. Alumina workpieces could not be ground with aluminium oxide grinding wheels due to high frictional interactions.

Key Words: Abrasive machining; chip formation; fine grinding; glass; ceramics; material removal.

1. Introduction

Optical glass components are normally ground approximately to shape and finished by a polishing operation to correct the shape and to achieve the required surface quality. Sometimes, particularly with aspheric surfaces, they are ground accurately to shape and then polished with great care to obtain a high-quality surface without changing the shape. In both cases the polishing is time-consuming and laborious but is necessary as the surface finish normally obtained in grinding is rough because of the formation and propagation of cracks in the ground glass surface. The present study was, in the first instance, aimed at providing a better understanding of the mechanism of fine grinding of glass (i.e., by keeping the wheel depth of cut down to about 50 nm (2 μin)) with the use of conventional grinding wheels, and thus introduce the possibility of obtaining high-quality glass surfaces of controlled geometry.

The success of the results on glass also led to a preliminary study of the fine grinding of ceramic materials. To facilitate presentation of the findings, the fine grinding of glass and the fine grinding of a ceramic material are presented separately in the following two sections.

2. Fine Grinding of Glass

2.1. Experimental

Glass workpieces were prepared by fixing steel end pieces to cylinders of borosilicate crown glass (30 mm (1.2 in) diameter x 40 mm (1.6 in) long) with epoxy resin adhesive, and machining centre-holes in the steel end pieces. The glass workpieces were ground on a cylindrical grinding machine (254 mm (10 in) x 610 mm (24 in)) fitted with a stepless,

temperature-stable, magnetostriction actuator [1]. The actuator was mounted on the upper slide of the machine to give small, precise wheel position adjustments in addition to the normal fine movements available by means of the existing screw mechanism on the lower slide. To reduce stick-slip on the upper slide, strips of PTFE were cemented to the sliding surfaces. During grinding, the workpiece was rotated on fixed centres at 7.5 rev/s and was traversed at 1.5 mm/s (0.06 in/s).

Tests were made with aluminium oxide (38A320JVG) and silicon carbide (37C180HVK) wheels (305 mm (12 in) diameter x 19 mm (3/4 in) wide) using a wheel speed of 29 rev/s. Sharp cutting edges were produced on the abrasive grits by utilizing a wheel dressing technique which has previously been described for this purpose [2]. This involved taking a series of dressing cuts with a cluster diamond dresser, each cut being half the depth of the preceding cut. For the aluminium oxide wheel the final dressing cut was about 50 nm (2 μ in) but, as described previously [2], the grits of freshly dressed wheels had smooth flat tops. These flats were broken up by taking a 50 nm (2 μ in) grinding cut on a workpiece of hardened steel. The high quality of the surface ground on the steel (12 nm (0.5 μ in) CLA) demonstrated the good cutting condition of the grits. With silicon carbide wheels, however, the flats could not be satisfactorily broken up by grinding steel and so, to avoid their formation, the dressing cuts were not reduced below 250 nm (10 μ in). Four different cutting fluids were used, viz, water-based sodium nitrite, distilled water, kerosene (40 ppm water) and an air jet.

To take an initial grinding cut, the glass workpiece surface was painted with a blue spirit-based dye and the grinding wheel was advanced until the glass just appeared through the dye, indicating that the wheel was just touching the workpiece. When the workpiece arrived at the end of a traversing stroke, the wheel was advanced for a cut. The workpiece was first tried by taking a series of cuts of diminishing size down to a wheel advance of about 1 μ m (40 μ in). The wheel was then redressed as before and from 10 to 20 finishing cuts on the workpiece were taken with wheel advances of down to 50 nm (2 μ in).

When grinding with liquid cutting fluids, glass debris from the grinding process was collected for examination by transmission electron microscopy. The technique used involved separating the debris from the cutting fluid by centrifuging, taking it up on a cellulose acetate film softened in acetone and coating it with carbon. The sandwich of debris between the cellulose acetate and carbon was then cut into 3 mm (1/8 in) squares, placed on copper grids and put in a still with acetone vapour which dissolved away the cellulose acetate leaving the carbon film holding the glass debris on the copper grids. The grids were inserted into a 100 kV electron microscope for examination of the debris.

2.2. Results

Both aluminium oxide and silicon carbide wheels produced transparent surfaces (see fig. 1), the degree of transparency varying considerably with the type of wheel and cutting fluid used.

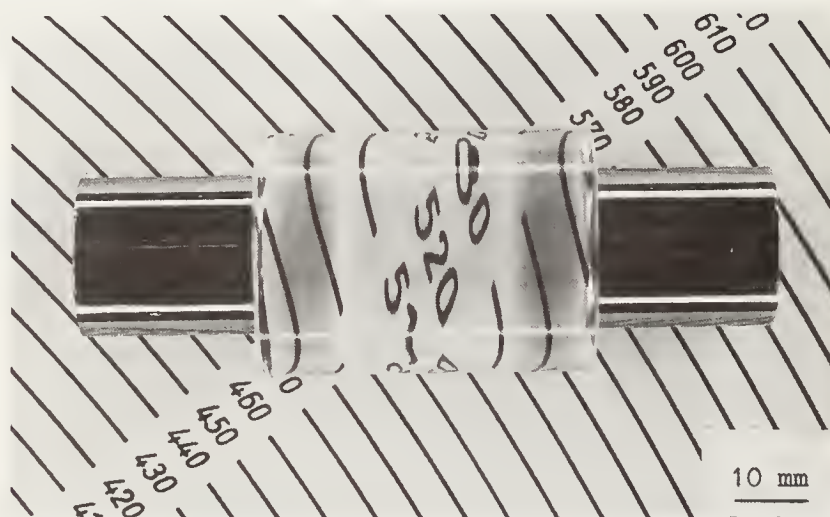


Figure 1. Photograph of a glass workpiece showing the high degree of transparency achieved by wheel fine grinding (silicon carbide wheel with jet of air as cutting fluid).

2.2.1. Grinding With The Aluminium Oxide Wheel

Examination of the surface ground, prepared using either the sodium nitrite solution or distilled water as cutting fluid, showed it to have numerous rounded projections resulting in a rough appearance on a micro-scale (fig. 2) with occasional surface pits of the type shown in figure 3. The glass grinding debris was in the form of individual rods (fig. 4) of similar dimensions to the rounded projectiles seen on the ground surface in figure 2. A much smoother surface was produced by using kerosene as cutting fluid, the surface then being similar to that shown in figure 5. The glass debris, however, was again in the form of rods. When grinding was carried out with only a jet of air directed into the cutting zone, the surface quality quickly deteriorated and grinding was stopped. It was apparent from handling the workpiece that a significant temperature rise had occurred during grinding.

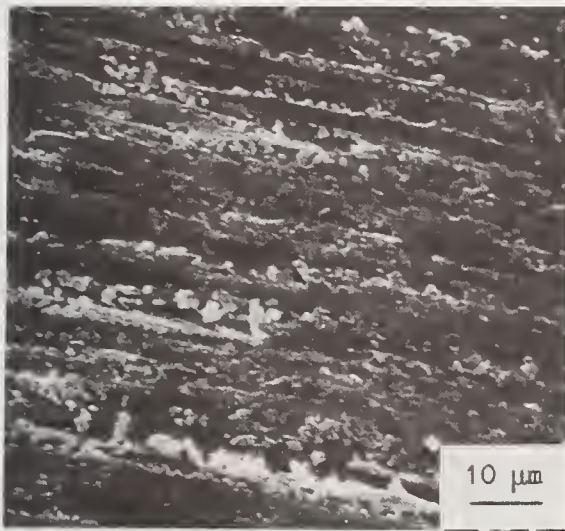


Figure 2. Scanning electron micrograph of a ground surface produced with an aluminium oxide wheel (water as cutting fluid), showing the micro-scale roughness due to numerous rounded projections.



Figure 3. Scanning electron micrograph of a ground surface produced with a silicon carbide wheel, showing the nature of the surface pitting.



Figure 4. Transmission electron micrograph of glass grinding debris produced with an aluminium oxide wheel (water as cutting fluid), showing the debris to be in the form of rod-like particles.

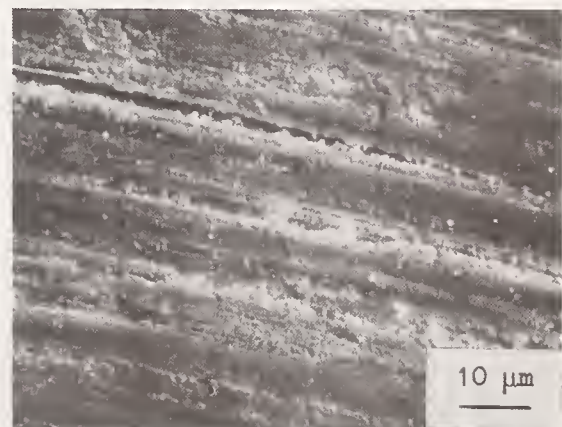


Figure 5. Scanning electron micrograph of a ground surface produced with a silicon carbide wheel (water as cutting fluid), showing that the surface consists of fine grinding grooves with very small rounded projections.

2.2.2. Grinding With The Silicon Carbide Wheel

In comparison with the surfaces obtained for the aluminium oxide wheel, surfaces ground with the silicon carbide wheel using the same cutting fluids were of higher quality (fig. 5). When using water or water-based cutting fluids, the surfaces consisted of fine grinding grooves with small rounded projections and occasional pits. The glass debris was of particular interest because the particles were in the form of segmented chips similar to those formed in some metal removal processes (fig. 6). When kerosene was used as cutting fluid an even better surface was obtained (fig. 7); very fine grooves were present and no rounded projections were evident. The debris particles were again in the form of segmented chips. A similar high-quality surface was produced when an air jet was the only cutting fluid and, in this case, no temperature rise was detected.



Figure 6. Transmission electron micrograph of glass grinding debris produced with a silicon carbide wheel, showing a segmented chip.

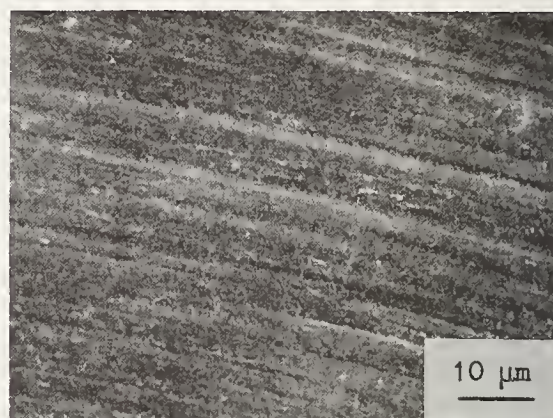


Figure 7. Scanning electron micrograph of a ground surface produced with a silicon carbide wheel (kerosene as cutting fluid), showing that the surface consists of very fine grooves without any evidence of rounded projections (cf. figs. 2 and 5).

2.2.3. Discussion

The most striking feature emanating from the present study is that, by fine grinding with a comparatively coarse-grit grinding wheel, glass can be ground to give a clear surface free from pits. This means that, in the manufacturing of optical components, the wheel grinding stage can incorporate the polishing stage, thereby eliminating much of the time-consuming effort of polishing.

The results indicate that a critical aspect of glass removal in an abrasive finishing operation is that the normal grey surface finish, which is associated with a series of pits formed by conchoidal fractures, gives way to a clear transparent surface as the grit depth of cut is reduced. In the case of grinding with a silicon carbide wheel, the glass removal process occurs by chip formation, while for the aluminium oxide wheel it seems to be associated with a ploughing process, as evidenced by the grinding debris being in the form of rod-like particles.

The importance of the depth of interaction between a grinding grit and a brittle solid is highlighted by comparing the present findings with those of Huerta and Malkin [3]. They investigated the comparatively coarse-grinding of glass, operating in a range of wheel depths of cut from 15 μm (0.0005 in) to 65 μm (0.0025 in) using a silicon carbide wheel. Their ground surface produced by grinding at a wheel depth of cut of 15 μm (0.0005 in) exhibited surface fracture and was much rougher than that shown in figure 7.

The occurrence of both a chip formation and ploughing process when grinding with small depths of cut is consistent with the recent observations made by Lawn and Swain [4] on the micro-fracturing of brittle solids beneath point indentations. The essential features of the indentation process may be described as follows: Initially, the point indenter induces

a zone of irreversible deformation about the contact point, the size of the zone increasing with load. At some critical indenter load a crack, termed the median vent, initiates below the contact point where the stress concentration is greatest. On initial unloading the median vent begins to close, but not heal, and relaxation of the deformed material within the contact zone just prior to removal of the indenter superimposes intense residual tensile stresses upon the applied field. Sideways-extending cracks, termed lateral vents, begin to appear. These lateral vents continue to extend and may cause chipping. It is important to note that micro-fracturing depends on the sharpness of the indenter [5] and upon the magnitude of the load.

Brose Van Goenou et al. [6] also showed that the load was important by demonstrating that, when lead glass was scratched with the point of a diamond pyramid (apex angle 136°), a smooth groove was produced with a normal load of 0.1 N but considerable chipping occurred with a normal load of 1.0 N. Grinding is more complex, but it may be described as an indentation process followed by a short translation in the direction of grinding. Clearly the exact depth of interaction of any one grit on the wheel is unknown because of the uncertainty of the number of grits within the cutting zone and of the elasticity of the machine-workpiece system [2]. In this regard, fine grinding in the present study refers to cylindrical traverse grinding with wheel in-feeds in the range of 50 nm (2 μ in) to a maximum of 250 nm (10 μ in).

Referring to the description of point indentation of brittle solids by Lawn and Swain [4], one would expect that the grinding grit indentations are within the zone of irreversible deformation and that the short translation in the direction of grinding leads to glass removal by ploughing or segmented chip formation. The generally inferior surface finish obtained when using an aluminium oxide wheel can be explained by the higher friction conditions due to the greater chemical affinity between the glass and the aluminium oxide than between the glass and silicon carbide [7]. This explanation is further supported by the fact that the glass workpiece suffered a marked increase in temperature when ground in air using the aluminium oxide wheel, but no temperature rise was detected when the silicon carbide wheel was used. The fact that silicon carbide is relatively inert to glass means that, as each chip segment is formed, it is free to move up the rake face of the grit. However, with aluminium oxide the glass adheres to the grit preventing a chip segment from forming. The glass is then pushed to one side, and this process can be considered similar to a ploughing mechanism. Adhesion could explain why, with both wheels, the presence of water as cutting fluid in place of kerosene led to a deterioration in the surface finish.

3. Fine Grinding Of A Ceramic Material

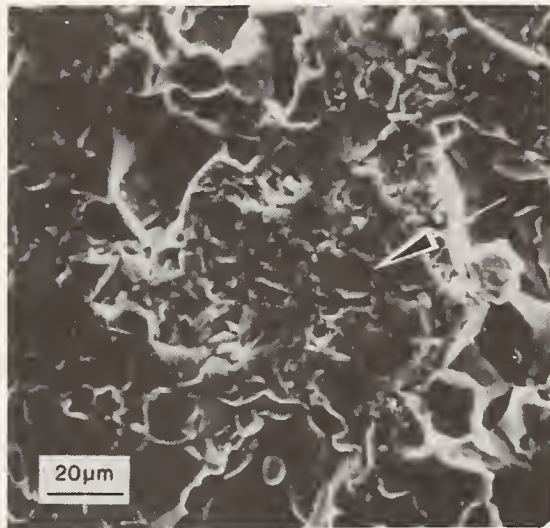
3.1. Experimental

The ceramic material chosen for the present investigation was recrystallised alumina because it was readily available. The workpieces were prepared by fixing hollow cylinders of recrystallised alumina to steel rods with epoxy resin adhesive, centre holes being machined in the ends of the steel. The workpiece dimensions were similar to the glass workpieces (fig. 1). The grinding conditions were the same as those outlined previously for the fine grinding of glass. For the fine grinding of alumina, however, only distilled water was used as a grinding fluid, but the method of extraction and examination of the grinding debris was identical to that outlined above for glass.

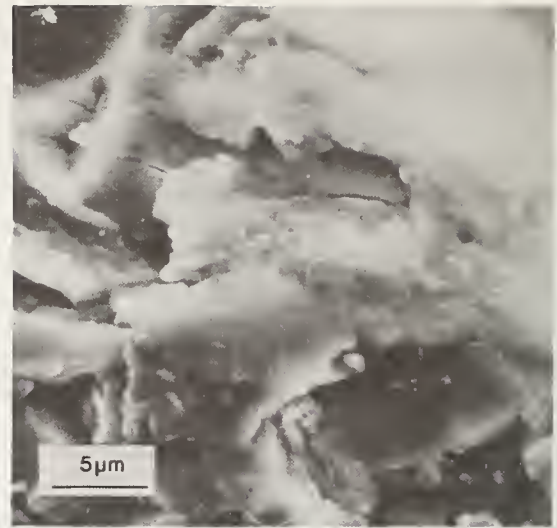
3.2. Results

3.2.1. Fine Grinding With An Aluminium Oxide Wheel

It was evident from the dull appearance of the alumina workpiece that the aluminium oxide wheel had failed to produce a smooth surface finish. Examination of the surface using the SEM revealed that the fine-ground areas had a rough torn appearance, as shown in figure 8. The intercrystalline facets evident in figure 8(a) were present on the unground workpiece. Examination of the grinding debris particles in the transmission electron microscope was uninformative as they were too thick to allow transmission of the electrons.



(a)



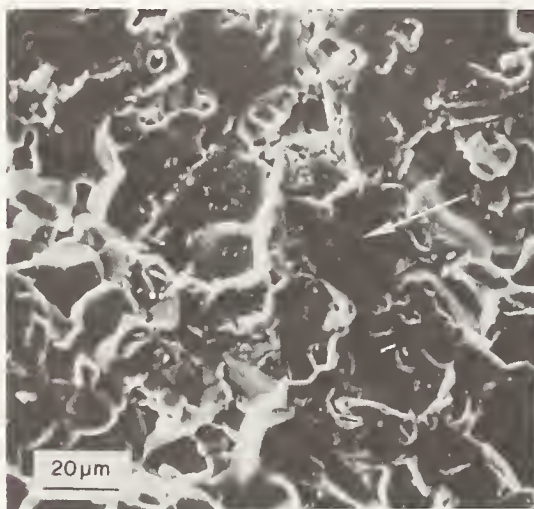
(b)

Figure 8. Scanning electron micrographs of a ground surface of alumina produced with an aluminium oxide wheel showing

- (a) that the surface has a rough torn appearance (arrowed). The intercrystalline facets were present on the unground surface.
- (b) detail of the rough area in (a) above at higher magnification.

3.2.2. Fine Grinding With A Silicon Carbide Wheel

The appearance of the alumina workpiece, fine-ground with a silicon carbide wheel, was much brighter and smoother than that produced with the aluminium oxide wheel. Figure 9(a) is a scanning electron micrograph showing that the alumina grains had smooth flat tops. The latter is shown in figure 9(b) at high magnification showing these smooth areas to be essentially featureless at this level of magnification. The intercrystalline facets again evident in figure 9(a) were present on the unground workpiece. Examination of the fine grinding debris by transmission electron microscopy revealed that two distinct types of grinding debris were produced. The first type of grinding debris, shown in figure 10(a),



(a)



(b)

Figure 9. Scanning electron micrographs of a ground surface of alumina produced with a silicon carbide wheel showing

- (a) that the alumina grains have smooth flat tops (arrowed). The intercrystalline facets were present on the unground surface.
- (b) detail of the smooth area in (a) above at higher magnification.



Figure 10. Transmission electron micrographs of alumina grinding debris produced with a silicon carbide wheel showing

- (a) an alumina chip characterized by a fine lamellar structure. The continuous ring electron diffraction pattern is indicative of the chip having a very small grain size.
- (b) wear debris the electron diffraction pattern of which is again indicative of wear particles having a small grain size. The diffraction pattern most closely indexed to aluminium silicon carbide.

was in the form of a chip with a fine lamellar structure. The lamellar structure was much finer than that observed in the glass chips, and more closely resembled the lamellar structure of chips produced from the fine grinding of a hardened steel [2]. The diffraction patterns obtained from the alumina chips were composed of continuous rings, the d-spacings of which corresponded to α - Al_2O_3 . This indicates that the grain size of the alumina chips was extremely small. The second type of grinding debris, shown in figure 10(b), was quite different, there being no characteristic shape or lamellar structure. These particles also gave fine-ringed electron diffraction patterns, the d-spacings of which indexed most closely to aluminium silicon carbide.

3.2.3. Discussion

As with glass, it is possible to produce a smooth surface finish on alumina with a silicon carbide wheel, providing that the wheel depth of cut, and therefore the grit depth of cut, is kept small. Again the observations of Lawn and Swain [4] appear to be relevant, that is, that indentations of small depth produce zones of irreversible deformation rather than fracture and, from the present study, it seems that translation in the direction of grinding of the grinding grits at small depths of indentation can lead to the removal of material by chip formation.

Further important aspects of the present results relate to the grinding debris produced by fine grinding with the silicon carbide wheel. For example, the chip-like debris shown in figure 10(a) had an extremely fine grain size, as evidenced by the continuous ring electron diffraction pattern. Aghan and McPherson [8] also observed chip-like material of fine grain size produced from slow speed fine abrasion of rutile. The large difference in cutting speed between abrasion and grinding appears to have little effect on the microstructural changes and the mechanism of material removal; this feature is also common to the abrasion and fine grinding of hard metals [9]. The question on the origin of the fine-grain structure has not been resolved beyond the suggestion [9] that it may be a recrystallization process, resulting from the very high stresses encountered when the deformation is confined to very small volumes of material.

Another important aspect of the results is the evidence of a chemical reaction between the wheel and the workpiece. The diffraction pattern of the grinding debris shown in figure 10(b) most closely indexed to aluminium silicon carbide, which presumably is formed by the rubbing contact between the wheel and the workpiece. This must then constitute a form

of grinding wheel wear. When grinding with the aluminium oxide wheel the frictional interaction would appear to be so strong that it prevents chip formation and results in a rough torn surface finish as indicated in figure 8(b).

4. Conclusions

4.1. Fine Grinding Of Glass

(a) Clear transparent ground glass surfaces were produced by fine grinding with standard silicon carbide and aluminium oxide grinding wheels with wheel depths of cut less than 1 μm . The best surfaces were obtained by grinding with a silicon carbide wheel using air or kerosene as cutting fluid.

(b) When grinding with a silicon carbide wheel the surface finish on a micro-scale consisted of multiple fine grooves and the mechanism of glass removal was by segmented chip formation.

(c) When grinding with an aluminium oxide wheel the surface finish on a micro-scale was very rough, and the presence of glass debris in the form of rod-like particles suggested the operation of a ploughing mechanism for glass removal.

(d) With both wheels the quality of the glass surface finish was found to be critically dependent on the type of cutting fluid used.

4.2. Fine Grinding Of Ceramic Material

(a) A smooth surface finish can be produced on alumina workpieces by fine grinding with a conventional silicon carbide grinding wheel. The mechanism of material removal is predominantly by chip formation. Some wear debris is also formed as a result of a chemical reaction between the wheel and workpiece in the region of rubbing contact.

(b) Alumina workpieces could not be ground with aluminium oxide grinding wheels. It is concluded that the high frictional interaction between the two materials impedes chip formation and produces a rough surface finish.

5. References

- {1} Dean, S.K., Cylindrical grinding to very accurate dimensions, *Microtecnic*, 20, 198-200 (1966).
- {2} Dean, S.K. and Doyle, E.D., Mechanisms in fine grinding, *Proc. Int. Conf. Production Engineering, Japan, Part 1*, 655-658 (1974).
- {3} Huerta, M. and Malkin, S., Grinding of glass: surface structure and fracture strength *Proc. General Engineering Conference, Baltimore, U.S. 1975* (ASME Paper No 75/Prod-2, 1975).
- {4} Lawn, B.R. and Swain, M.V., Microfracture beneath point indentations in brittle solids *J. Materials Science* 10, 113-122 (1975).
- {5} Lawn, B.R. and Wilshaw, T.R., Indentation and fracture: principles and applications *ibid* 10, 1049-1081 (1975).
- {6} Brose Van Goenou, A., Naan, N. and Veldkamp, J.D.B., Scratch experiments on various ceramic materials *Philips Research Reports* 30, 320-359 (1975).
- {7} Mairlot, H., Texture of ground glass surfaces, *Industrial Diamond Review*, 61-66 (1972).
- {8} Aghan, R.L. and McPherson, R., Mechanism of material removal during abrasion of rutile *American Ceramic Society* 56, 46-47 (1973).
- {9} Doyle, E.D. and Aghan, R.L., Mechanism of metal removal in the polishing and fine grinding of hard metals, *Metall. Trans.* 6B, 143-147 (1975).

SOME OBSERVATIONS ON ENVIRONMENTAL EFFECTS WHEN DIAMOND DRILLING

G. A. Cooper

Institut CERAC SA
CH-1024 Ecublens, Switzerland

During the forties, the Russian scientist P. A. Rehbinder presented evidence to show that when drilling in rock, the addition of certain chemicals to the flushing liquid had the effect of markedly increasing the rate of penetration. He explained the effect by supposing that the rock was softened or made more brittle by the additive, and hence was more easily drilled.

Results which have been published subsequently have been contradictory and have shown that, *inter alia*, the rock may be either hardened or softened by the additive. It is significant that even though the original work dates from thirty years ago, there has as yet been no commercial exploitation of the so-called Rehbinder effect.

The present report describes an investigation of the effects of some additives recommended in the literature on the speed of diamond drilling in marble and granite. It is found that at the speeds of penetration common in commercial practice, none of the additives has any effect on the rate of penetration. By contrast, however, they have a very significant effect on the rate of wear of the diamonds. It is this effect which is now thought to be at the root of Rehbinder's observations, and it may well explain the conflicting results obtained by different groups of workers.

Having established this explanation, one then asks how the environment influences the wear of the diamonds. The process is almost certainly chemical, rather than mechanical, and related to frictional heating. Three possible effects of the environment are then possible: 1) the heat generated during cutting is reduced by the environment, 2) the efficiency by which it is carried away is improved, or 3) the chemical nature of the additive can influence the wear of the diamond. Work described shows that any or all of these influences can be significant.

Key Words: Rehbinder effect; drilling; diamond drilling; drilling additives; wear; surface chemistry; rock fracture.

1. Introduction

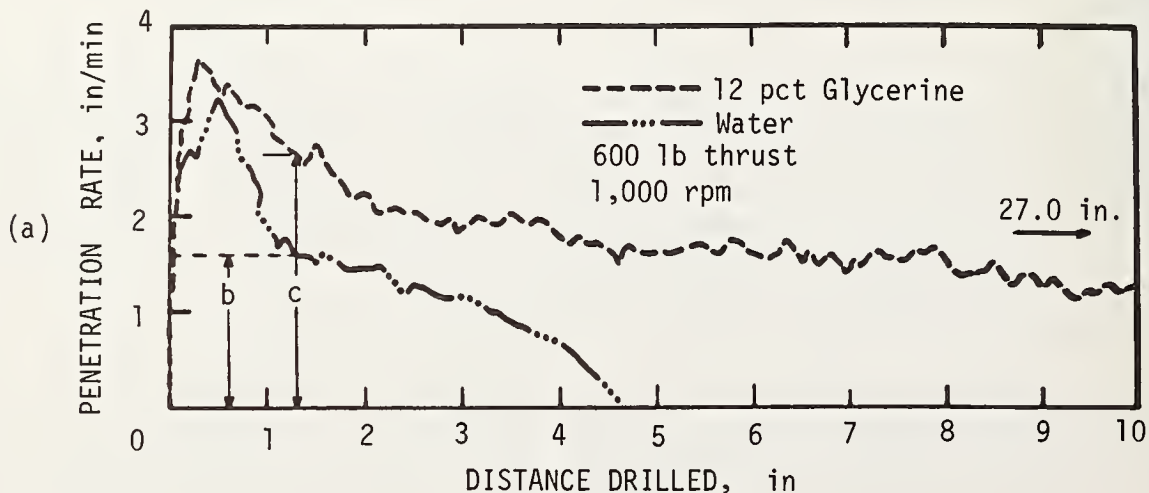
Interest in the effect of the environment on drilling in rocks dates from the publication in the forties of work by Rehbinder and co-workers [1] showing substantial increases in the rate of penetration of hard rocks by the addition of small quantities of common inorganic chemicals. The results were interpreted by supposing that the additive aided the formation of cracks by reducing the fracture surface energy of the material being drilled. An alternative hypothesis, that the additive acts to reduce the wear of the drill bit, was never examined, possibly because of Rehbinder's interest in the action of liquids on metals [2], where the phenomenon of stress-corrosion is of great importance.

There is considerable evidence that a liquid environment can influence the elastic-plastic properties of a variety of rocks. Boozer et al [3], in a comprehensive series of tests, showed that fluids which were strongly absorbed onto the rock surface tend to reduce the fracture strength of sandstone and limestone under conditions where the confining pres-

sure was sufficient to induce plastic deformation, but not when the failure was intrinsically brittle. These results were confirmed by the work of Robinson [4] who again found decreases in the plastic yield stress, but no effect on the failure under "brittle" conditions, on exposure of the rock to an active chemical environment. Robinson's work included drilling tests with cone and drag bits, in which it was found that those additives which produced increases in the drilling rate with one of the bits produced decreases with the other, and the differences were most marked in the case of the drag bit. This tool removes rock by a shearing action, and thus can clearly be aided by a decrease in the plastic yield stress of the rock. In the case of the cone bit, however, where the rock removal mechanism is essentially one of crushing and chipping, one can argue that an increase in the plasticity of the rock will be unfavourable. These observations will be seen to have considerable significance to the work of Westwood and co-workers (discussed below). In any event, it is clear that, as Robinson himself notes, these observations are in direct conflict with Rehbinder's hypothesis, which would have predicted little influence of the environment on the plastic yield stress, but a large effect on the brittle failure behaviour.

Selim et al. [5] investigated the effect of ethylene glycol, glycerine and an anionic detergent on the rate of diamond drilling in quartzite, following the suggestion of Joris and McLaren [6] that additives which lower the surface tension of the flushing fluid will improve the cooling of the diamonds, and hence decrease the rate of wear. In addition, such compounds will also improve the efficiency of removal of the cuttings. The results of Selim et al. have several interesting features. A typical result from their work is shown in Figure 1, which shows, above, the variation of penetration rate, and, below, the apparent friction coefficient for the drilling of quartzite in water or 12% glycerine solution respectively. After an initial settling-in period the penetration curves show a steady decrease in penetration rate with time, as the diamonds wear, and this is accompanied by a reduction in the "friction coefficient". Selim et al. were looking for evidence of the "Rehbinder effect" and so, to reduce their data, they compared the instantaneous rates of penetration after drilling to a certain depth (that at which the penetration rate in water was half its peak value). This gave, in the case being discussed, an improvement of c/b (see Figure 1). Such an improvement would have led the authors to conclude in favour of the "Rehbinder effect" but for the fact that the "friction coefficient" was greater in the presence of the additive than without, and in fact calculations showed more energy to have been consumed per drill meter in the presence of the additive than without. Unfortunately, Selim et al. did not make the critical experiment, which was to use the same bit and drill alternately in the presence of the additive and in pure water. This would have shown whether the improved drilling performance was caused by softening the rock, or by the bit retaining its sharpness better.

Similar results to those of Selim et al. were obtained by Engelmann, Unger and Snowden [7] on surface set bits drilling in granite. Rates of penetration up to 35% greater were obtained in some circumstances, coupled with reduced rates of wear. Again, however, the critical experiment of taking the same bit and changing back and forth between the additive and pure water, to distinguish between the phenomena of rock softening and diamond wear, was not done.



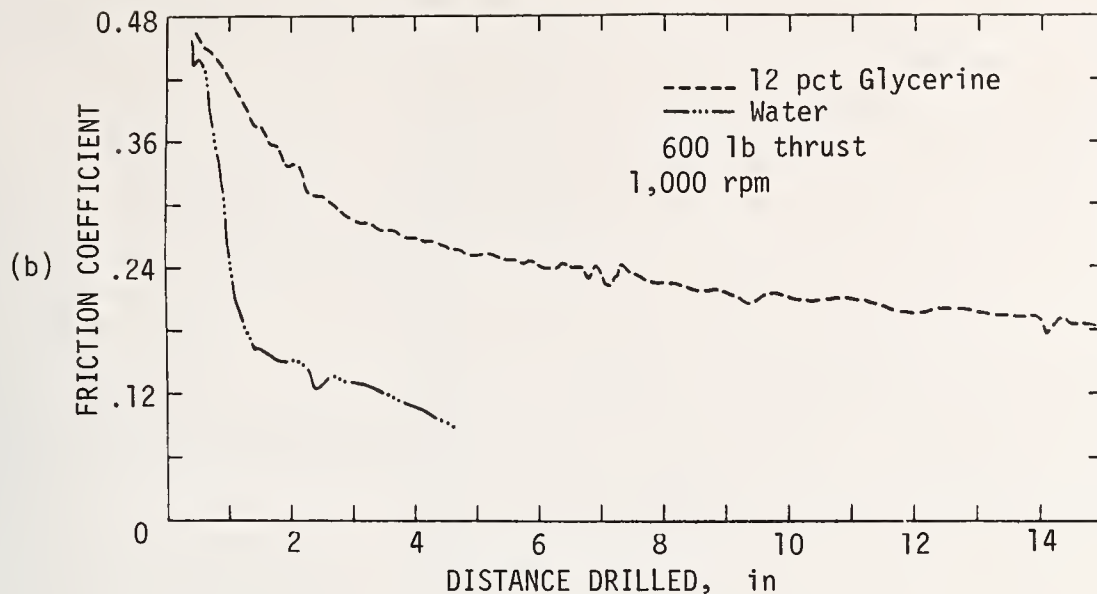


Figure 1. (a), penetration rate in quartzite as a function of distance drilled, and (b), "coefficient of friction". From Selim et al. [5]. Note: the "coefficient of friction" was derived directly from the torque on the shaft of the drill.

At this point, it is worth reviewing what is known of the influence of the environment on the behaviour of ceramic substances on the atomic scale. The subject has been fully reviewed by Westwood and Macmillan [8], and will not be discussed exhaustively here.

It is, however, beyond doubt that a surrounding environment can have a significant effect upon the mechanical behaviour of the near surface regions of a variety of materials. Not only are chemical environments effective, but also light and electric fields, under certain circumstances. Of the various explanations put forward, the original surface energy argument of Rehbinder has been shown to be suspect, since in some circumstances, the environment can cause increases in the strength. This would require that, following Rehbinder, a species which is spontaneously absorbed onto the solid surface can cause an increase in its surface energy. Such a proposition is thermodynamically unreasonable, and in addition, it has been shown that for certain materials such as MgO [9, 10] and soda-lime glass [11] certain environments which markedly influence the hardness have little or no effect on the cleavage fracture energy, at least for reasonably rapid crack growth.

An alternative explanation, due to Hanneman and Westbrook [12] that the additive acts in some way as a lubricant (to aid in the penetration of an indenter) has been shown to be untenable, at least in the case of calcium fluoride, since not only was the penetration of a diamond into the material aided by the environment, but also the recovery of the deformation upon removal of the load [13].

The final explanation is that the environment directly affects the near surface flow behaviour of the solid it contacts. This implies that for crystalline materials at least, chemisorbtion on the crystal surface influences dislocation mobility in the crystal to a depth of a few microns or so. This explanation has been championed by Westwood and co-workers, and much data has been collected to support it. The evidence is particularly clear in the case of non-metallic ionic solids, and includes such materials as silver bromide and iodide, alumina, calcite, and magnesia, in a variety of environments [14].

It has further been shown that many of these effects may be correlated with the ζ -potential, which is a measure of the state of electric charge of the solid surface. In particular, it is observed that dislocation mobility is a minimum when the ζ -potential is zero (fig. 2), and this minimum can be shown to coincide with a maximum in the measured hardness of the crystal.

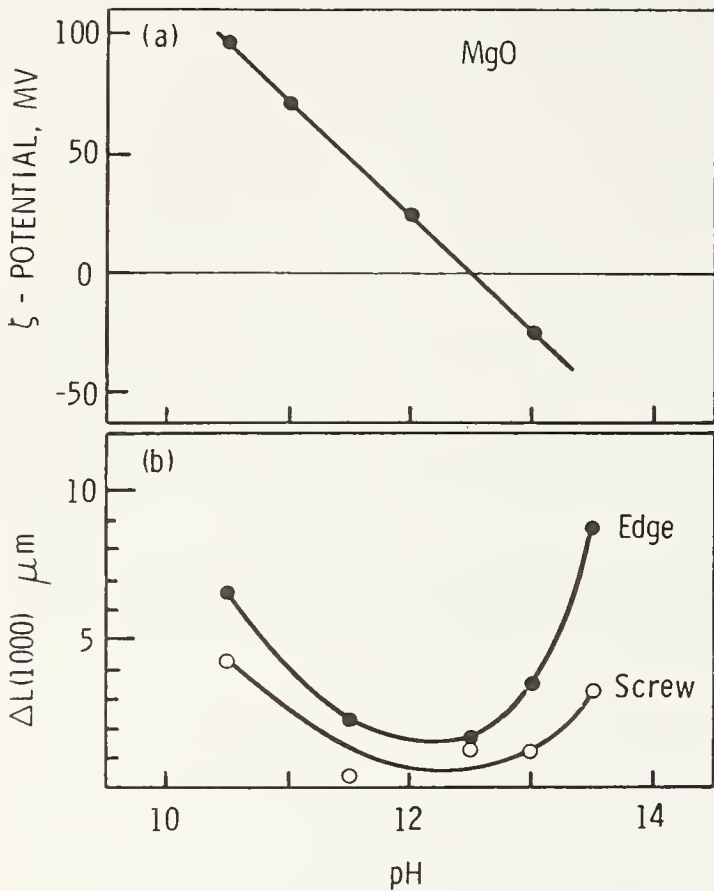


Figure 2. Variation with pH of (a) ζ -potential and (b) dislocation mobility parameter $\Delta l(1000)$ for MgO in 10^{-2} aqueous NaOH. Dislocation mobility is least, i.e., the crystal is hardest, when $\zeta = 0$. From Westwood and Macmillan [8].

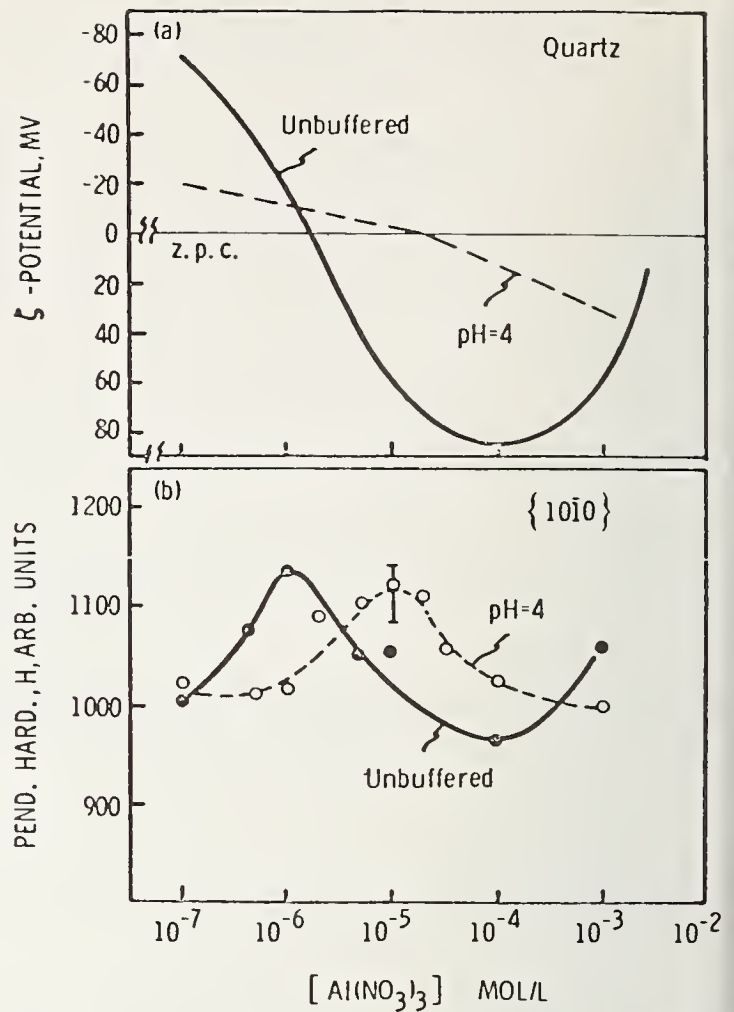


Figure 3. Variation of ζ -potential and pendulum hardness respectively for (0001) surface of single crystal quartz in buffered and unbuffered aqueous $\text{Al}(\text{NO}_3)_3$ solutions. From Westwood and Macmillan [8].

Why this should be so is not, however, known in detail, since there is no theoretical correlation between dislocation mobility and the state of surface charge of the material being deformed. More puzzling is why the same correlation exists with soda-lime glass [8] and more significantly in the present case, with quartz (fig. 3), since dislocations as such are not known in glass, and, to the author's knowledge (with the possible exception of work by Payne [A. Ball, private communication]), dislocation movement in quartz has never been observed at room temperature.

Whatever the connection between the phenomena, however, there is considerable evidence to connect the ζ -potential with drilling rates. Figure 4, for example, shows this correlation for alumina, and similar data have been obtained for magnesium oxide, calcite, and glass [8, 14]. One of the most puzzling aspects of this work is, however, the observation that, in the three latter cases quoted above, the same material when drilled in the same environment with a tungsten-carbide-tipped twist drill gave the opposite behaviour to that obtained when diamond drilling; an example is shown in figure 5, and the reader's attention is drawn to the similarity of these results to those of Robinson [4] discussed earlier.

Various explanations have been put forward to account for this behaviour, generally based upon supposed differences in the cutting mechanism for the two types of bit [4, 14, 17]. Specifically, it is claimed that the carbide spade bit operates by a ploughing action, and hence works best when the material is soft, whereas the diamond bit operates either by an impacting mechanism [8] or by opening tensile cracks in the wake of the diamonds as they

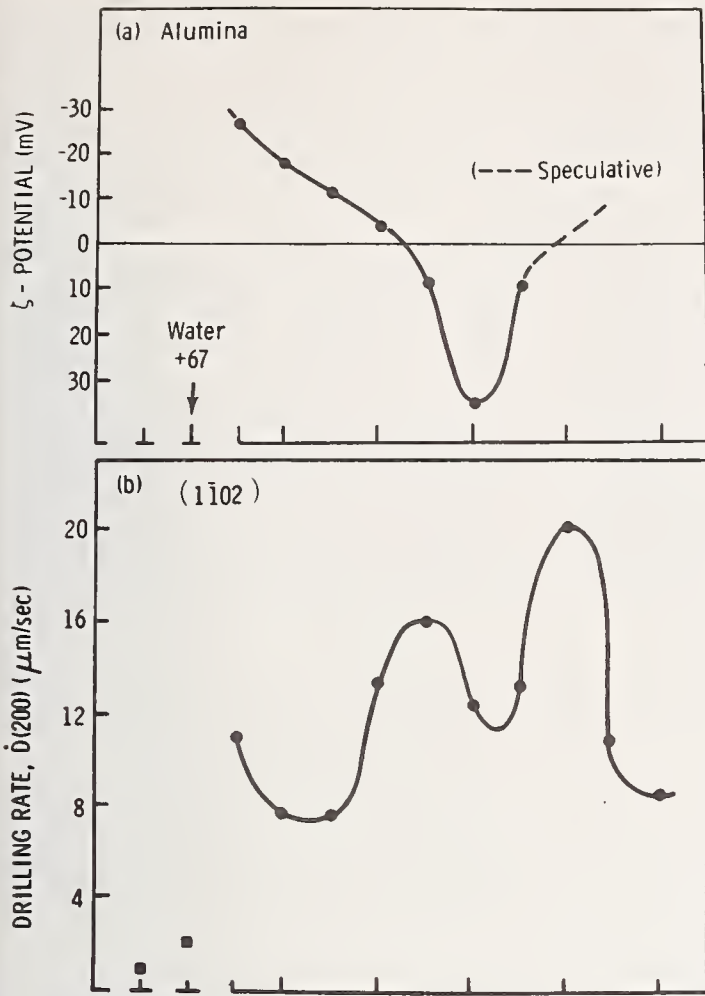


Figure 4. (a) ζ -potential, and (b) rate of core bit drilling for alumina using toluene, water and n-alcohol environments [15]. Note the maximum hardness and drilling rate at zero ζ -potential. N_C is the number of carbon atoms in the alcohol molecule.

pass over the material being drilled [14]. The diamond bit thus works at its best when the material to be drilled is hard and brittle. Why the two tools should function in a different manner is, however, not at all clear. Even more confusing is the observation that for those conditions where the diamond drilling of alumina is a maximum, the rate of cutting by a diamond-impregnated wheel is a minimum [18]. Here again, it is difficult to understand how the cutting mechanism can be so different as to generate results which are diametrically opposed.

Westwood and his group have also investigated the effects of surfactants on the drilling of rocks. Figure 6 shows results obtained with a diamond drill on Westerly Granite. In this earlier work, it was consistently shown that the maximum rate of penetration was obtained at zero ζ -potential, and that this coincided with the conditions of maximum hardness. At first sight, the improvements in drilling rate are very spectacular - greater than a factor of four in the present case -, but it should be emphasised that the absolute rates of penetration obtained in these laboratory scale experiments were very low. Taking the data of figure 6, for example, the best rate obtained was some 4.8 mm/minute, compared with that in water of 1 mm/minute. These values may be compared with the peak values reported by Selim et al. [5] in quartzite (a harder rock) of 90 and 80 mm/minute with 12% glycerine and pure water, respectively (see fig. 1). Results obtained at CERAC using pure water were typically in the range of 50 mm/minute at 1000 rpm, and up to 120 mm/minute at 3000 rpm (0.47 and 1.42 metres per sec. linear cutting speed, respectively).

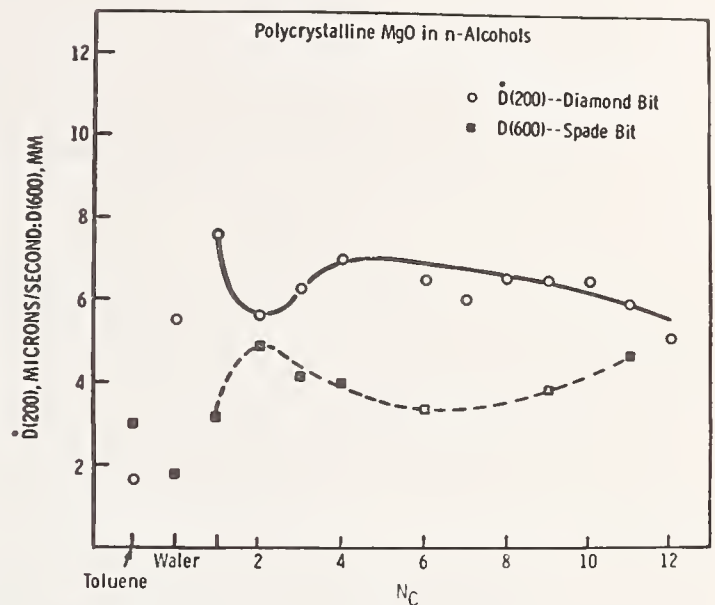


Figure 5. Influence of n-alcohol environments and type of bit on efficiency of drilling polycrystalline MgO. After Westwood and Latansion [16].

The subsequent results of Westwood and co-workers, at larger scale, will be discussed below, and compared to data obtained by the present author.

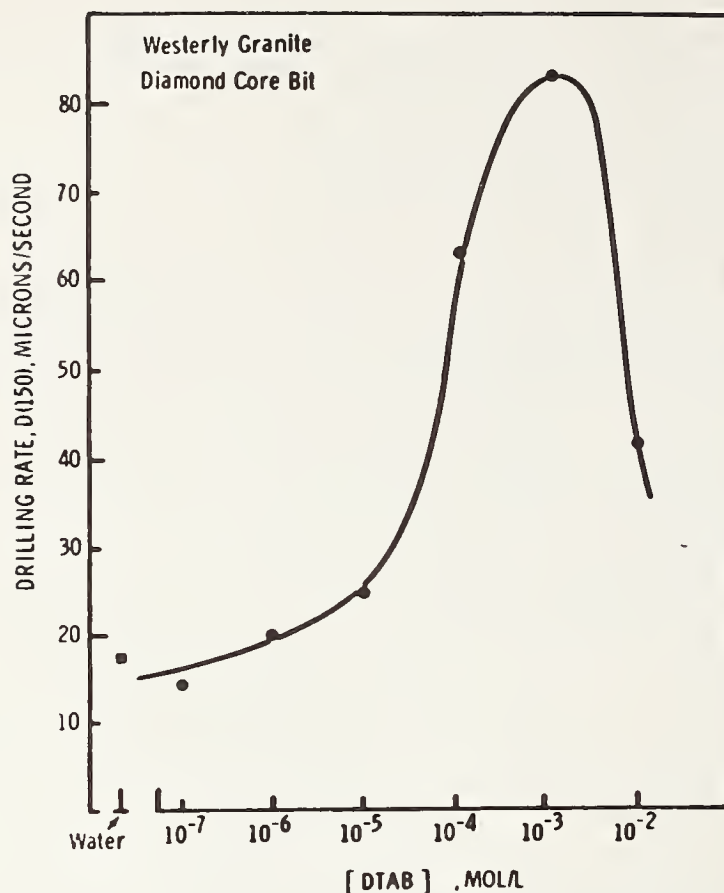


Figure 6. Variation of D(150) (rate of drilling after 150 seconds) for Westerley granite in aqueous DTAB (dodecy trimethyl ammonium bromide). Diamond core bit, room temperature. After Macmillan et al. [19].

2. Results obtained at CERAC

Work at CERAC was confined to the area of diamond drilling, using impregnated core bits. These drills contain diamonds distributed throughout the volume of a bronze matrix, and in commercial operation, conditions are adjusted so that the bronze wears away at approximately the same rate as the diamonds are blunted. Hence, due to periodic loss of the worn diamonds, and exposure of new ones, a steady drilling performance can be obtained. In the laboratory, however, conditions can be adjusted to produce steady-state drilling, as above, or, if the wear of the bronze matrix is reduced, conditions similar to those experienced with "surface-set" bits may be obtained. ("Surface-set" bits have one layer of larger diamonds cast into the surface of the bit. When these are worn, the bit must be returned to the maker for re-setting the stones.)

Experiments were made at small scale, but great attention was paid to the scaling so as to reproduce similar feed pressure per unit area of bit, and similar cutting speeds to those used in commercial practice. Accordingly, experiments were carried out using diamond-impregnated core drills of 10 mm O.D., x 8 mm i.d. The diamonds were of type de Beers MDA-S, of 70-80 mesh (U.S.), present at a concentration of 19 volume percent in a bronze matrix. The drills were used in a bench-mounted drill press having a co-axial water flushing system provided with flow and pressure-measurement systems, and a continuously-variable rotation speed in the range 500 to 3500 rpm. At 3000 rpm, the mean cutting speed of the diamond in our drill was 1.42 m/sec, which should be compared with the following values common in large scale drilling*: surface-set bits: 1-2 m/sec, impregnated bits:

* Anders Odèn, Craelius Diabor, private communication.

2-5 m/sec, saws, 30-50 m/sec. It will be seen that our cutting speeds were somewhat lower than those used in the field. The feed pressures recommended for impregnated bits range from 2 to 10 N/mm² of bit surface, depending upon whether the material is soft and abrasive (sandstone, concrete) or hard and non-abrasive (taconite, granite). As will be seen below, we have ourselves established the optimum feed pressure required for our drill in different rocks, and the values are found to lie within these limits.

Experiments were made on two rocks, a pure white marble from Lasa, Ticino, Switzerland, and the well-known pink granite from Bohus, Sweden. The marble was chosen since it is well-known that calcite can deform plastically at room temperature, and hence if dislocation effects are important to the mechanism of the Rehbinder effect, this is a likely material in which to observe them. The granite was chosen for the opposite reason, since dislocation movement is not known to occur in quartz at room temperature, and because granite is itself a very widespread and commercially significant rock. The experimental programme carried out was first to investigate the performance of the core drill in each of these rocks in the presence of pure water alone, in order to establish the basic performance envelope of the drill, and then, having found certain "standard conditions", to investigate the effect of a number of additives recommended in the literature.

2.1. Drilling in marble: establishment of drill performance

The variable parameters when diamond drilling are: the rotation speed, the feed force, and the water flushing pressure. Penetration speed increases with the first two provided that the loads do not become so great that the drill is destroyed, and provided that adequate flushing is maintained to remove the rock debris and prevent overheating of the drill.

When drilling in marble, it was observed that the rate of wear of both diamonds and matrix was very low, and it therefore proved possible to carry out a large number of experiments with the cutting capacity of the drill essentially constant.

To establish the drilling performance envelope, therefore, tests were made at rotation speeds of 500, 1000, 2000 and 3000 rpm, and the drilling rate was measured as a function of water flushing pressure for different feed pressures. Typical results, for a rotation speed of 500 rpm are shown in figure 7. In this figure, it will be seen that, for a given feed force, the penetration rate decreases slowly with flushing water pressure. This is simply because of the upthrust on the drill column exerted by the water pressure. More interestingly, it will be seen that there is a region at low water pressures where drilling is not possible due to choking. This occurs, particularly at high feed forces (when there are large quantities of cuttings produced and the drill is forced deeply into the rock), when the liquid flow is not sufficient to remove the cuttings as fast as they are produced. Under these conditions, the viscosity of the slurry of cuttings increases, the flow rate further decreases, and eventually the drill is completely choked. Then, unless the feed force is immediately released and the liquid flow re-established, the heat generated will be sufficient to melt the bit within a few seconds. The required flushing water pressure to prevent choking increases with the feed force, as is evident from figure 7. A simple theoretical description of the choking process [20] indicates that the line separating choked from free-flushing conditions should be of the form: $P \propto R^3$, where P is the minimum flushing pressure, and R is the rate of advance. The dashed line in figure 7 has the form

$$P_{(at)} = 2 \cdot 10^{-5} R^3 \text{ (mm} \cdot \text{min}^{-1}\text{)}$$

which appears to describe the observed data quite well.

Using the data obtained in these and other tests, it was decided that a feed force of 150 N and a flushing pressure of 3 bars would give satisfactory drilling performance in the speed range investigated, and these were therefore adopted as the "standard conditions" for

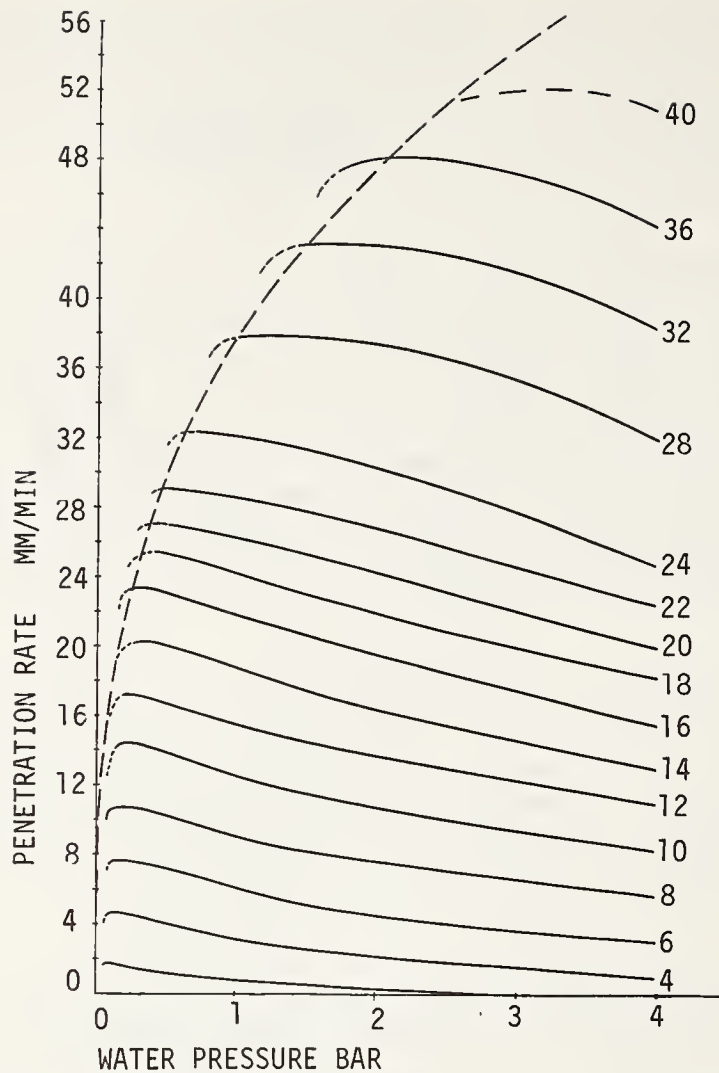


Figure 7. Marble: penetration rate as a function of flushing water pressure for different feed loads at 500 rpm.

the tests with different environments.

2.2. Drilling in marble: effect of additives

Using the standard conditions at different rotation speeds in the range 1000 to 3300 rpm, tests were made with a variety of additives in aqueous solution in the flushing fluid. These were:

- Al Cl₃ 0.5, 0.75 and 1%
- Na₂CO₃ 0.2, 0.33, 0.5 and 1%
- Na OH 0.025, 0.05, 0.1 and 0.25%
- "Quat 316" (dodecyl ethyl dimethyl ammonium bromide) 10⁻³ and 10⁻² mole/litre
- CWS liquid soap, containing 21% salts of fatty acids and 5% sulphonated compounds as its active constituents, diluted to 0.25 and 0.5%.

All of these compounds have been recommended by various authors as improving the rate of drilling in calcareous rocks.

The results obtained are shown in figure 8: mean results only are given for the additives, while a scatter band indicates the 95% confidence limits for the rates obtained with pure water. An examination of the data shows, as might be expected, that the penetration

rate increases approximately linearly with drill rotation speed. Apart from this, there is no systematic trend in the data which separates one environment from any other. One must therefore conclude that, at least for marble under our standard conditions, none of the recommended additives causes a measurable increase in the drilling speed. In the face of this surprisingly consistent negative result, experiments on drilling in marble were abandoned.

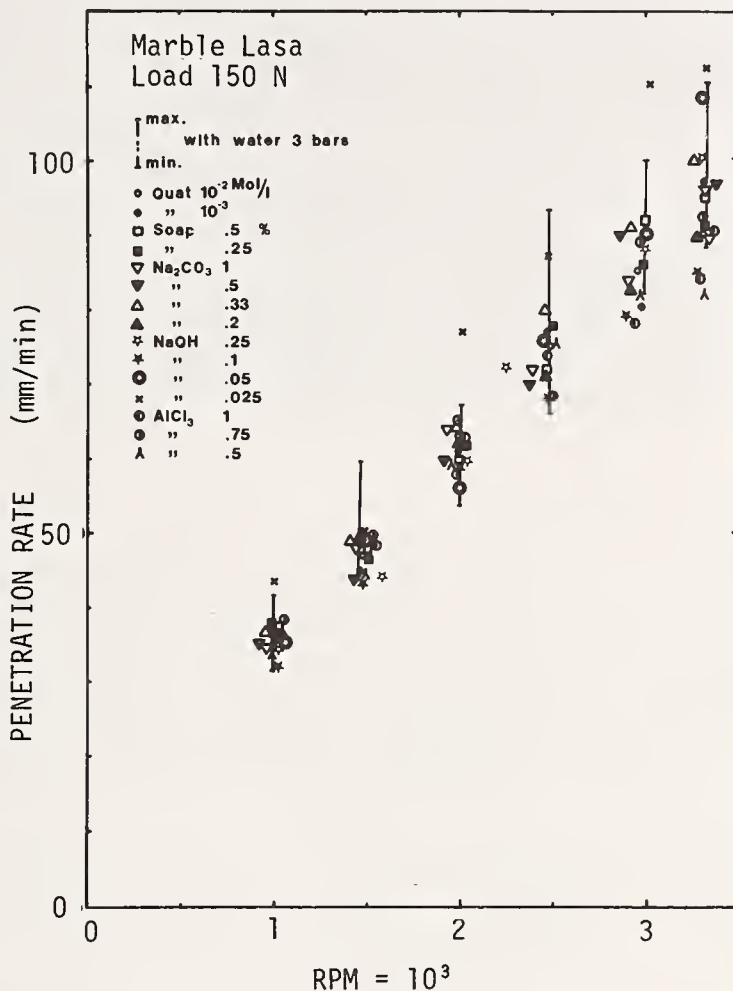


Figure 8. Marble: penetration rate as a function of drill rpm for various additives in aqueous solution. "Standard conditions" of 15 kg. feed load and 3 bars flushing pressure. From ref. [21].

2.3. Drilling in granite: establishment of drill performance

When diamond drilling in quartz-containing rocks including granite, it is observed that there is a continuous wear of the diamonds. This effect may be more or less masked by the simultaneous wear of the matrix material, leading to the periodic loss of worn diamonds and the exposure of new ones on the drill surface. These three interacting wear mechanisms are shown schematically in figure 9. The drill bit we have used for our studies had a bronze matrix which would be considered somewhat too hard for successful commercial drilling in granite, since when drilling with pure water as the flushing medium, the abrasive wear of the matrix did not, in general, keep up with the wear of the diamonds. Thus, if one measured the penetration distance as a function of time over a wide range of conditions, an approximately exponential curve was obtained, with the rate of penetration of the bit decreasing continuously to zero. Under commercial conditions, such a performance would not be considered to be satisfactory, since the bit would have to be periodically removed from the hole for re-sharpening (for example, by drilling for a short distance in a weak but very abrasive material: fire brick is commonly used for this purpose). On the other hand, such a bit was ideal for our purposes since it allowed us to separate out to some extent the phenomena of the wear of the diamonds and the wear of the matrix.

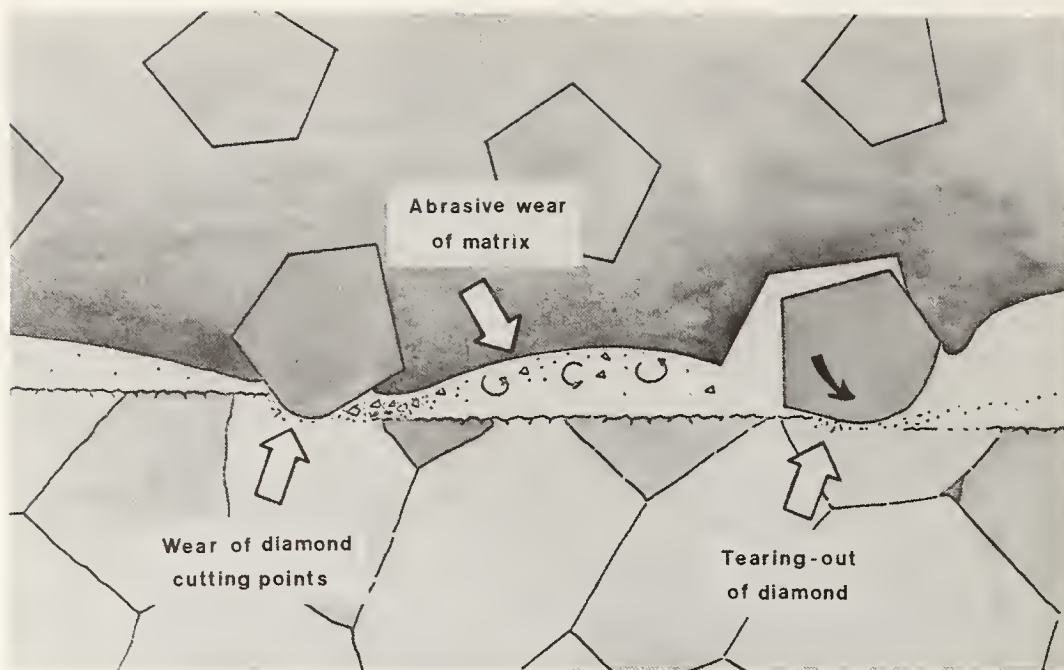


Figure 9. Schematic view of the drilling process, showing the three possible wear mechanisms (after Cooper, ref. [22]).

Although the penetration-time curve for our bit in granite was nearly always exponential, the asymptote (i.e. the total distance drilled) varied very greatly. Examples are shown in figure 10 for two feed forces at 1000 rpm and 3 bars flushing pressure, and these are by no means extreme values. Depending principally upon the feed force, we have observed total lives varying from less than five mm to more than three metres. The range of drilling conditions we have investigated lies between the following limits: flushing pressure 3 or 6 bars, feed forces 100-600 N, and rotation speeds 500-3000 rpm.

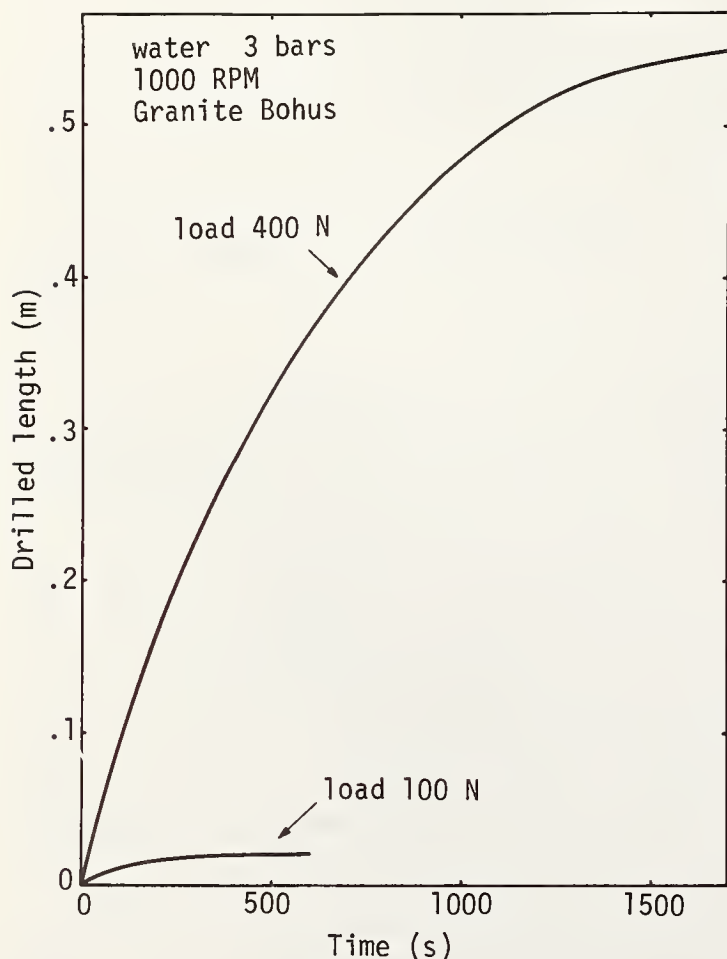


Figure 10. Granite: distance drilled as a function of time for two different load conditions (from ref. [21]).

Under most circumstances, provided that the drill is not operating in "self-sharpening" mode, the wear process produces a decrease in performance which is exponential, and a measure of drill performance may then be obtained by calculating the diamond half-lives, and, by multiplying by the rotation speed, obtaining the total distance travelled by the diamond over the rock in this period. Such data are presented for a variety of conditions in figure 11, plotted against the feed force. It will be seen that the life of the diamond is strongly dependent upon the feed force, but not, apparently, upon either the rotation speed or the flushing water pressure. It would be tempting to conclude that the relationship was approximately linear if it were not for a group of data lying in the upper right-hand corner of the figure. These values, however, come almost exclusively from tests in which the steady degradation of cutting performance is interspersed with sudden, irregular increases. These are almost certainly associated with the loss of worn diamonds, by erosion of the supporting matrix, and the exposure of new, sharp diamonds.

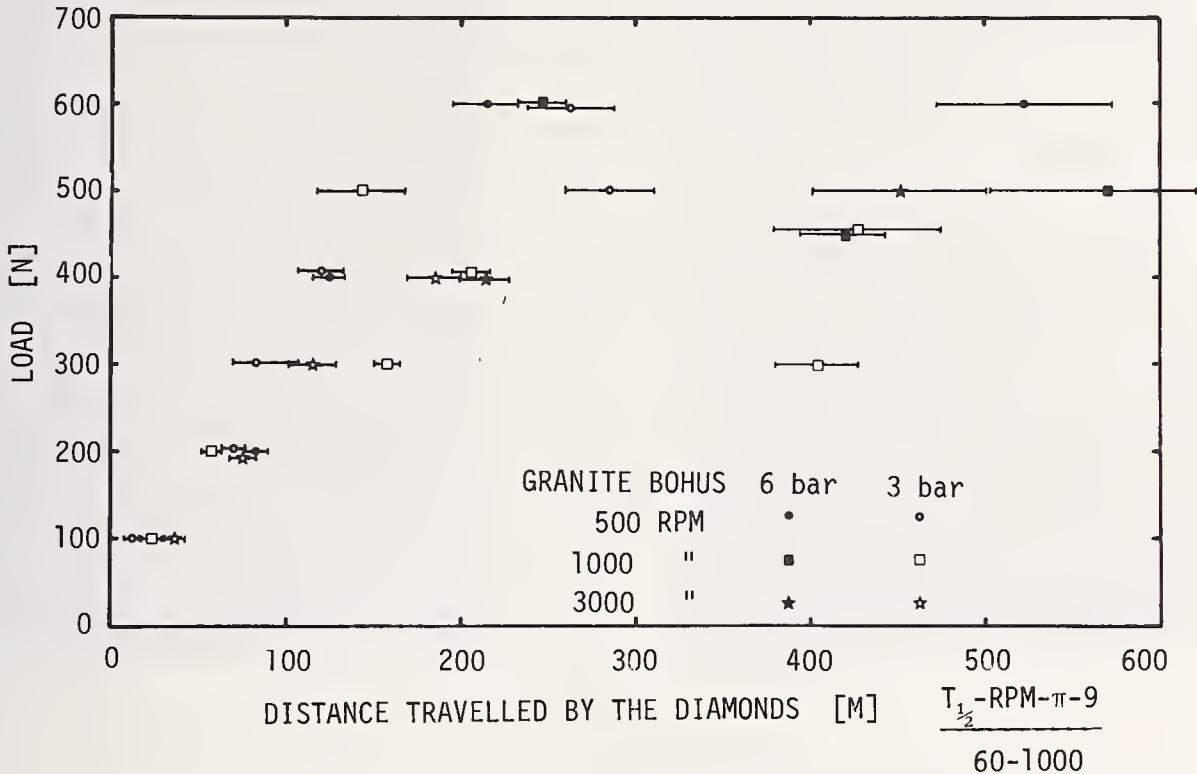


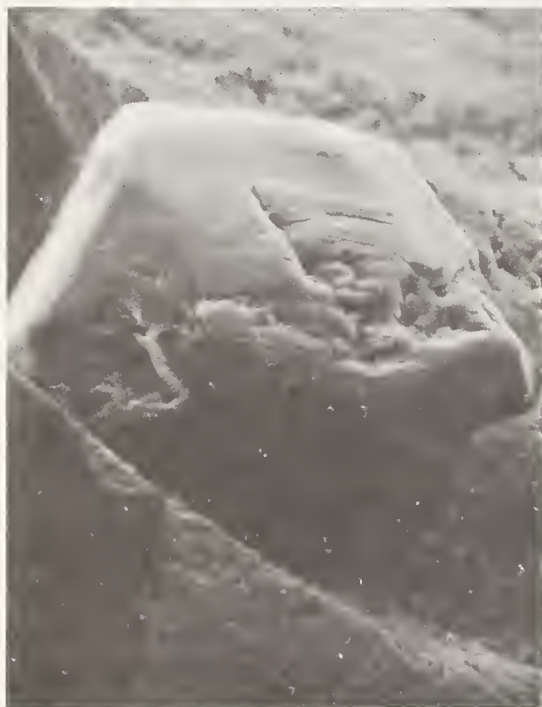
Figure 11. Granite: relationship between the feed force and the distance travelled by the diamond over the rock up to its half life.

At first sight, the observation that the life of the diamonds is less under low feed forces is surprising. The following hypothesis is, however, proposed to explain this phenomenon. Firstly, we note that the diamond is very much harder than the hardest phase present in the rock being drilled (the quartz), and therefore even if the latter is supported by its surroundings, it is extremely unlikely that the diamond can be caused to flow plastically by the stresses imposed on it by the rock.

In addition, we observe that the half life of the diamond (in distance travelled) appears to be independent of the traversing speed, and hence of the strain rate applied to the rock. This would argue in favour of a brittle failure mechanism in the rock which does not depend upon thermal activation of, for example, dislocations for deformation to occur. In consequence, it is reasonable to believe that an increase in the feed force applied to the drill will not result in increased contact stresses at the diamond-rock interface, since the latter is already at its failure stress and this is strain-rate independent. Instead, it is rather to be expected that the diamonds will be pressed more deeply into the rock and that the total contact surface will increase rather than the contact stress. This indeed appears to be the case, as it has been shown that under conditions of drilling with a sharp bit, the initial penetration distance per rotation is linearly proportional to the feed load and essentially independent of rotation speed or flushing water

pressure [20]. Since the total load carried by each diamond must necessarily increase with the feed force, the internal, rather than the surface stresses will increase. In the limit, the diamonds may be cracked, broken or torn out of the matrix at very high feed loads, but we did not attain such conditions in our experiments because choking of the drill occurred beforehand. In commercial practise, however, such damage can easily be obtained (Anders Odén, Craelius Diabor, private communication).

Microscopic observations of the drill bit tend to support these arguments. Figure 12 shows two S.E.M. photographs of diamonds in a worn bit. The wear is normally characterised by a rounding of the sharp crystal edges, and various patterns of striae or grooves on the crystal surface, suggestive of an ablative wear process, can be seen.



a



b

Figure 12. Scanning electron micrographs of diamonds in a worn drill bit. a) mag 400x, b) mag 700x.

If, as seems likely, mechanical deformation is not responsible for the wear of the diamonds, some chemical transformation may be involved. Two possible candidates are oxidation or graphitisation, both occurring as a consequence of frictional heating of the diamonds. Oxidation would be expected to be a strictly surface phenomenon, resulting in a steady ablation of the diamond surface, and with the production of rather rounded wear forms. In the case of graphitisation, however, it is possible that, in view of the high thermal conductivity of diamond, graphitisation will occur not only on the surface, but also in the interior of the diamond. This would result in a general weakening of the diamond throughout its volume (although of course most markedly in the hotter regions near the cutting edge), and it is possible that this would lead to failure by progressive fracture of the weakened regions. At present, it is not possible to say whether this reasoning is correct, to distinguish whether both mechanisms are operative, or to say if one is dominant. Some further evidence will, however, be presented below in the section on environmental effects.

Whatever the mechanism of the wear process, however, the microscopic evidence shows that wear occurs principally by a progressive ablation and rounding-off of the cutting edges of the diamond. In addition, we have seen that changing the feed force probably results in the diamonds being forced more or less deeply into the rock, rather than changing the contact stresses. The wear process under high or low feed forces is then envisaged to

occur as follows: Starting from an initial condition with a sharp diamond, and applying a high feed force, the diamond will be forced deeply into the rock. The stress-field associated with the indentation will be large, and a large volume of rock will be fractured as the diamond sweeps over the rock surface. As wear occurs, the cutting edge of the diamond will be progressively worn away, until a large wear flat has been produced and the diamond ceases to cut. Contrast the case of a bit in which the feed force is low. Here, the diamond points penetrate only a little way into the rock, and, since the feed force is low, only a small quantity of diamond must be worn away before the surface of the wear flat is sufficiently large to transmit the feed force to the rock without it fracturing under the diamond. We now make use of our assumption that since, during cutting, the rock is at its fracture stress, the surface stresses on the diamond where it contacts the rock will be the same in the two cases. Since, in addition, we presume the wear to occur as a consequence of frictional heating at the rock-diamond interface, we suppose that the rate of ablation of the cutting edges will also be the same in the two cases. It is thus clear that since a greater depth of diamond must be worn away in the case of the high feed force, the life expectancy of the drill will be correspondingly greater in these conditions.

We have made one simple experiment to check whether the wear mechanism proposed is plausible. We started with a newly-sharpened drill, and ran it at 1000 rpm, with three bars flushing pressure and a feed force of 400 N. At this feed force, the drill had a long life and cut well. Reference to fig. 13 shows an initial drilling rate of 60 to 90 mm per minute in the first 200 seconds. After 6000 seconds, the rate of penetration had fallen to 2 mm per minute. At this point, we imagined the diamonds to have been worn down very

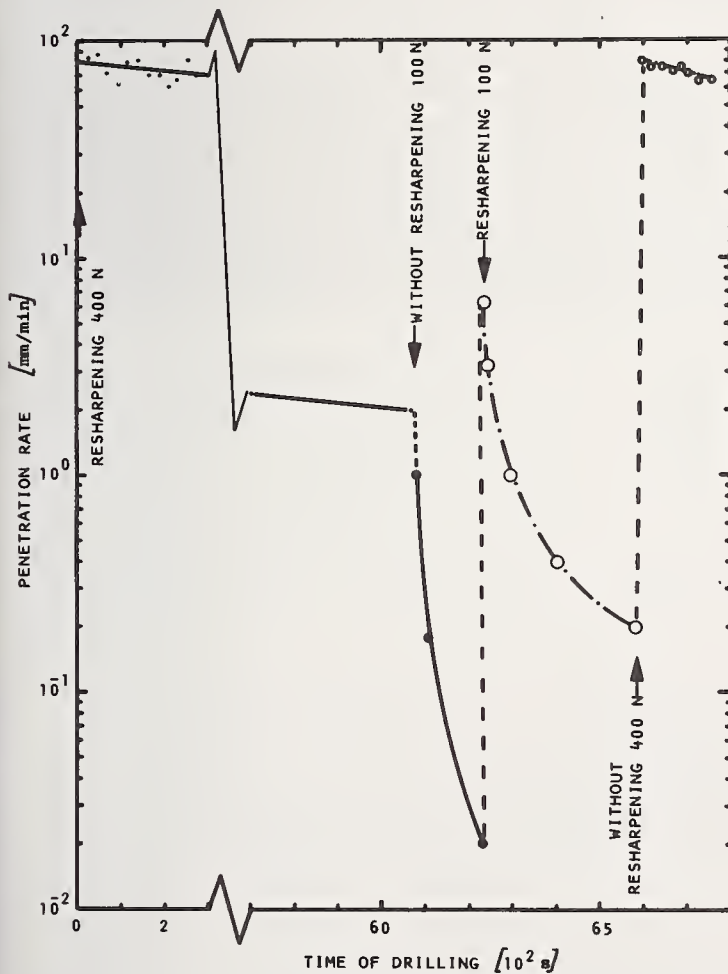


Figure 13. Granite: experiment on drill wear: speed of penetration as a function of time for various drilling conditions.

considerably, and to have developed large wear flats. When the feed force was subsequently reduced to 100 N, therefore, it was not surprising to find that the rate of penetration was only 1 mm per minute, and that this dropped rapidly to 0.02 mm per minute after a further 150 seconds. The drill was then removed from the rock and re-sharpened. It was thereafter returned to the rock again and made to drill under a feed force of 100 N, as had been used

previously. Under these conditions the initial rate of penetration was 6.3 mm per minute, which, as expected, was better than the performance after drilling for 6000 seconds at 400 N. On the other hand, the rate of penetration dropped below this value after only 60 seconds, and after a total of 350 seconds it had fallen to 0.2 mm per minute, at which time the experiment was stopped. The feed force was then increased to 400 N, and drilling was re-started without re-sharpening the bit. As will be seen from figure 13, the drilling rate at this higher load lay between 60 and 90 mm per minute, which is almost the same as had been measured at the beginning of the experiment with the newly-sharpened drill. To summarise this series of tests, therefore, we find that a drill which has been worn at high feed loads has a low initial rate of penetration and thereafter blunts very rapidly when worked at a lower load, but that a drill which has been worn at a lower load is still capable of cutting as well as a newly-sharpened drill when the feed load is increased. These observations are completely consistent with the wear model we have proposed.

2.4. Drilling in granite: effect of additives

In view of what had been learned about the behaviour of our drill in granite, we chose as "standard conditions" to work at 1000 rpm, 3 bars flushing pressure, and a feed force of 400 N. Because of the continued wear of the drill, it was not possible to make straight-forward comparative tests of the different flushing fluids as had been done with marble, but it was necessary to change back and forth between water and the environment in order to allow for the effects of wear. We therefore present the results in this section as the speed of drilling as a function of distance drilled, taking a measurement of the average rate of penetration during each successive advance of 25 mm.

The first group of tests was concerned with the series of pure straight-chain aliphatic alcohols belonging to the homologous series $\text{CH}_3(\text{CH}_2)_n\text{OH}$ between methanol and decanol inclusive, since these have been reported by Westwood and co-workers as improving the rate of penetration in quartz-containing rocks [19]. The first results obtained are shown in figure 14. Here we have taken an initially sharp drill, and have drilled with each successive alcohol, alternating with pure water. There are several striking features in these results. Firstly, as would be expected, we see a generally decreasing rate of penetration with time, which presumably results from the progressive wear of the diamonds. Secondly, it is quite

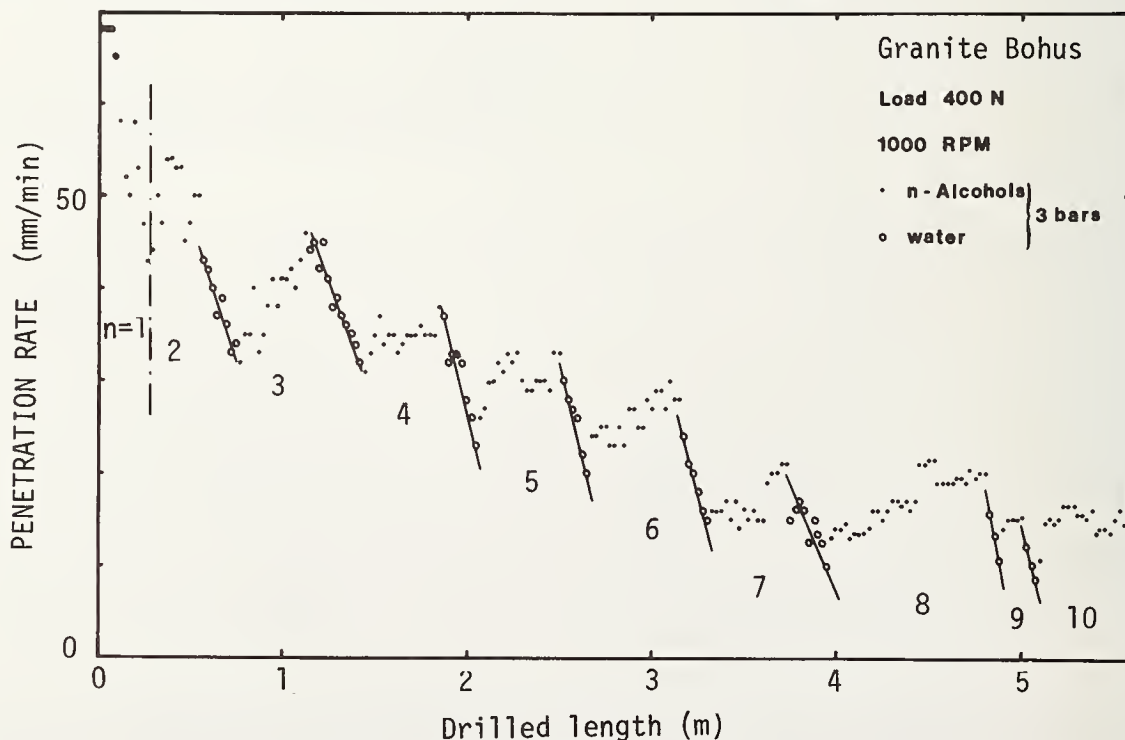


Figure 14. Granite: rate of penetration as a function of distance drilled using the normal alcohols of the series $\text{CH}_3(\text{CH}_2)_n\text{OH}$ alternating with water as the flushing fluid. From ref. [21]

clear that, with the possible exception of methanol, the rate of wear of the diamonds is much greater when water is used as the flushing medium, than when any of the alcohols is used. Thirdly, there is in general no sharp change in the instantaneous rate of penetration when changing from alcohol to water or vice-versa. Together, these observations throw an interesting light on the "Rehbinder effect" in drilling. In essence, they suggest that the principal effect of the additive is not to increase the instantaneous rate of penetration of the drill, but to decrease the rate of wear of the diamonds. This conclusion may go a long way towards explaining the confusing and often conflicting results which have been previously reported in the literature. If, for example, we had conducted our experiments by taking a sharp drill each time, and measured the time taken to drill, say, 500 mm, we would have obtained striking differences in these times, and might have been led to conclude that, since the average penetration rates were different, then the rock had been made harder or softer by the additive. Indeed, with hindsight, one can look back at the results of other workers (eg. Selim et al., figure 1) and find exactly the same behaviour as we have found in the present work.

At certain points in figure 14, one can find evidence of an increase in the rate of penetration (see, for example, results obtained with propanol, pentanol and octanol). It is thought that these are evidence of a spontaneous re-sharpening of the drill. As was mentioned above, we believe that our "standard conditions" for drilling are not far from those necessary for steady-state re-sharpening to occur. Admitting our hypothesis that the additive influences the rate of wear of the diamonds rather than the resistance of the rock, and having in mind the three wear processes active in the drill (see figure 9), we suggest that with water, the rate of wear of the diamond is dominant, whereas with the alcohols it is much reduced. In the former case, as the diamonds wear, the rate of production of rock cuttings decreases, and hence, therefore, so does the abrasive wear of the matrix. This has the consequence that a decreasing number of worn diamonds will be lost from the face of the drill, until, finally, a steady-state condition is reached where all the diamonds in the drill face are blunt, and both the penetration rate of the drill and the rate of replacement of the diamonds drop to zero. When one of the alcohols is used as the flushing agent, however, the diamonds are blunted more slowly and the rate of production of rock cuttings is maintained. Thus the abrasive wear of the matrix is maintained, with consequent loss and renewal of the diamonds on the working face, and the rate of penetration of the drill is maintained or can even increase.

To be sure that there was no undetected systematic error in our previous set of observations, we made another series of tests where we changed at random between the different alcohols. The results obtained were consistent with those reported above: in no case did we find instantaneous changes in the rate of drilling when changing between water or any of the alcohols, but a clear difference in the rates of wear of the drill [20].

We next tested a range of different chemicals which have variously been recommended as drilling additives in the literature. These included:

Sodium Hydroxide, NaOH, 0.1%, 0.5%
Sodium Chloride, NaCl, 0.1%, 0.5%
Sodium Carbonate, Na₂CO₃, 0.1%, 0.3%
Aluminium Chloride, AlCl₃, 0.02%, 1%
CWS liquid soap (see above), 0.5%
"Quat 316" (see above), 10⁻³ Mol/litre,

all in aqueous solution.

Of these various solutions, the inorganic salts showed no influence on either the instantaneous rate of penetration of the drill, or on its rate of wear, while the soap and the quaternary ammonium compound showed no influence on the rate of penetration, but a reduction in the rate of wear. Results from the latter group of tests are shown in figures 15 and 16, respectively. Inspection of figure 15 shows that of the three dilutions of soap used, a concentration of 0.2% does not appear to be very effective, but at concentrations of either 0.5 or 2%, the rate of wear is definitely reduced. In the case of the "Quat 316"

(fig. 16), the evidence is less clear cut. The tests with a concentration of 10^{-4} Mol/litre show a rate of wear comparable with that of water, while those at 10^{-3} Mol/litre show a high rate of wear in the first test, but a rate of penetration oscillating irregularly about 70 mm/minute in the second. At a concentration of 10^{-2} Mol/litre, only one group of tests was made, at the beginning of the experiment, immediately after re-sharpening. There is a fairly rapid fall from 85 to near 65 mm/minute at first, but the rate of penetration

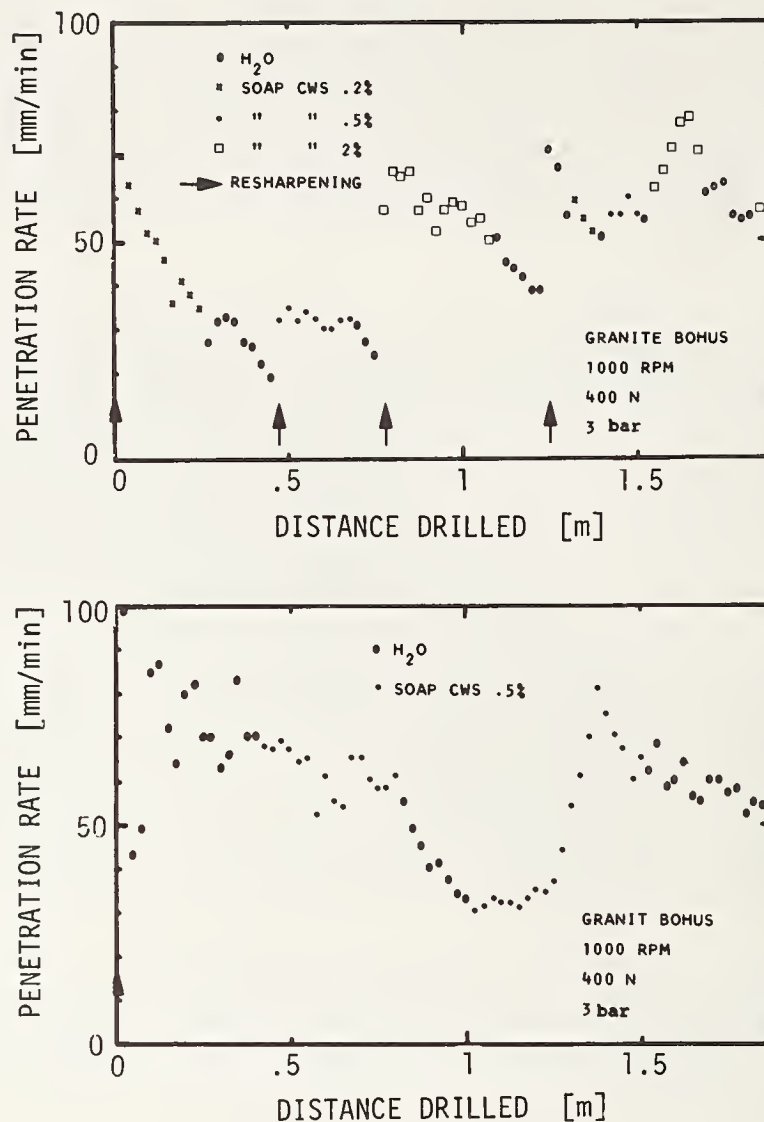


Figure 15. Granite: rate of penetration as a function of distance drilled using water or various concentrations of CWS liquid soap as flushing liquids.

appears to stabilise near this value before falling away again as the concentration of the additive was reduced.

Our conclusion from the tests using either the aliphatic alcohols or various additives in aqueous solution must therefore be that certain environments indeed affect the drilling process. On the other hand, all the evidence points to the conclusion that the environment affects the rate of wear of the diamonds, but does not modify the properties of the rock.

There is recent evidence from other workers to support this view. Figure 17, taken from the work of Mills [23] shows very similar results to our own, but comparing the performance of the quaternary ammonium compound D.T.A.B. and water. Other data obtained by the same authors are shown in figure 18, and should be compared with those of figure 1: the similarity is quite striking, and they are clearly both evidence of the same effect.

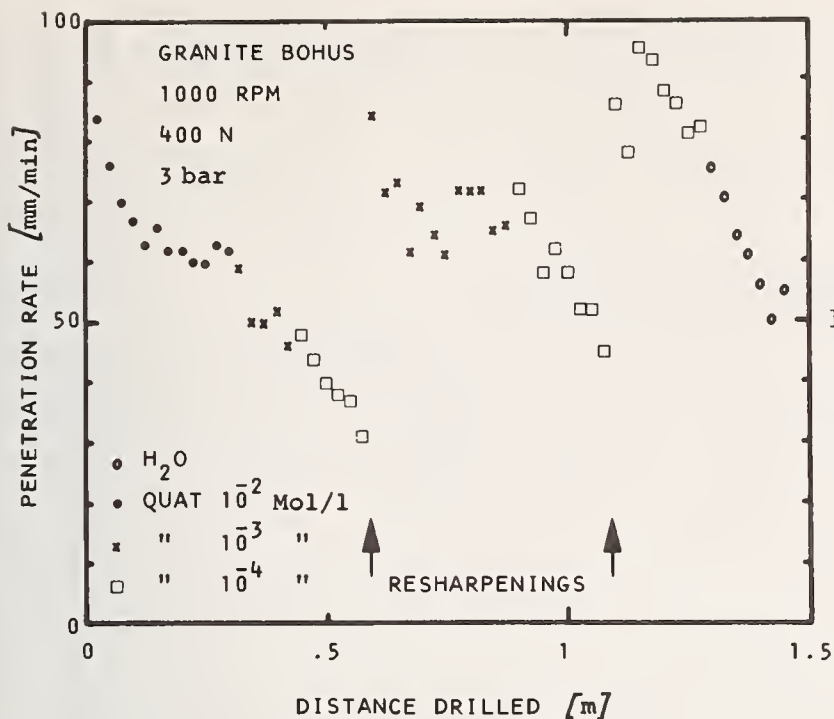


Figure 16. Granite: rate of penetration as a function of distance drilled using different concentrations of "Quat 316" in water as the flushing fluid.

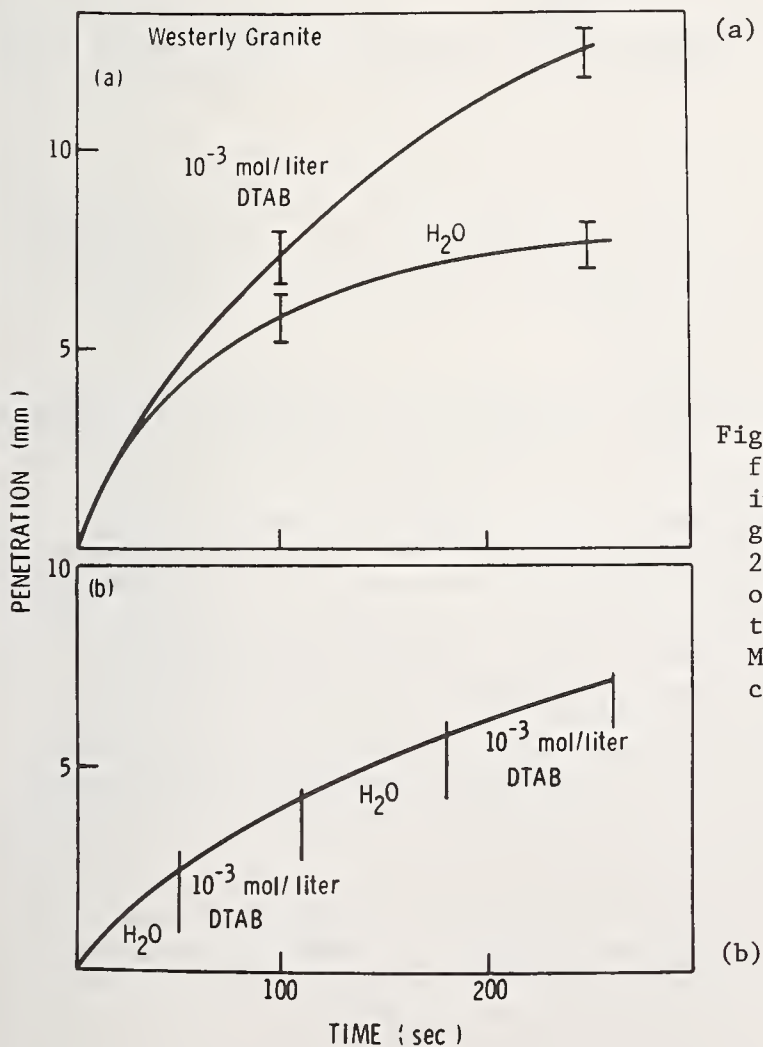


Figure 17. (a) Penetration vs time curves for freshly redressed, 0.6 cm o.d. diamond-impregnated bits drilling into Westerly granite under water or 10^{-3} M D.T.A.B. 2000 rpm. 40 N thrust. (b) Similar data for one freshly dressed bit. Note, however, that on changing from water to the 10^{-3} M D.T.A.B. environment, no significant change in slope occurs. After Mills (Ref. 21).

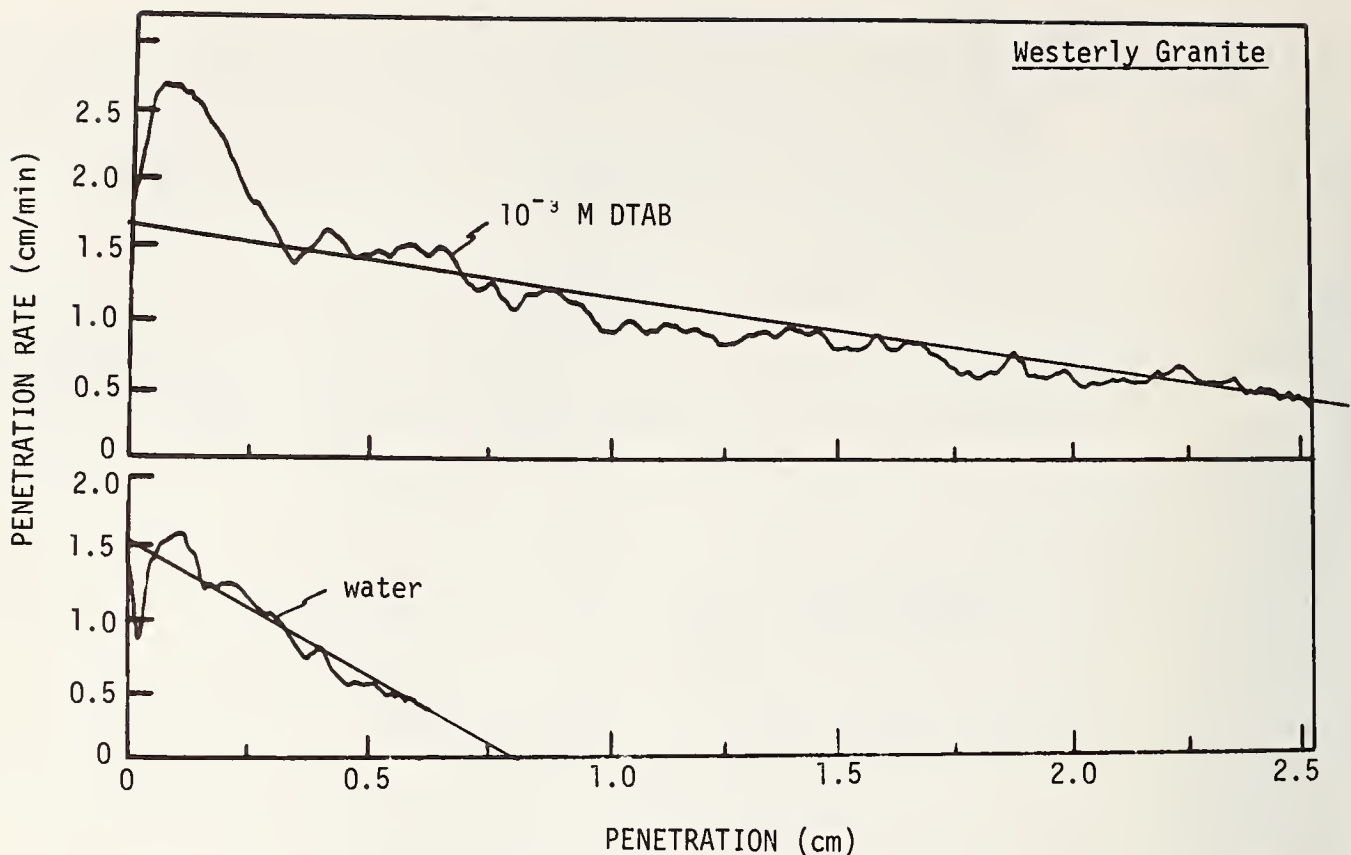


Figure 18. Penetration rate vs penetration distance data for Westerly granite drilled with a 0.95 cm o.d. diamond-impregnated core bit under a) 10^{-3} M aqueous D.T.A.B. and b) water. The thrust was 60 N, and the bit rotation speed 5000 rpm. From Mills [21].

2.5. The wear process and the effect of the additive

In view of the evidence presented above, it can be accepted that, at least for rates of penetration which are of interest commercially (some tens of millimetres per minute), the dominant influence of the additive is in reducing the rate of wear of the diamonds. Why this should be so, however, remains to be answered.

We have discussed above the different possible wear mechanisms of the diamond, and have arrived at the tentative conclusion that wear occurs by physico-chemical rather than purely mechanical means. Of the different possibilities, either graphitisation or oxidation are likely candidates, and either will be aided by the heat generated during drilling. Mills and Westwood [24] have argued that the quantity of heat generated, and hence the wear of the diamonds, depends upon the coefficient of friction between the two materials, and that this in turn is influenced by the environment, since the latter acts to harden or soften the rock by the mechanisms discussed in section 1. An essential question then must be answered before this hypothesis can be accepted: If the rate of wear is affected principally by changes in the hardness of the rock, why then does the instantaneous rate of penetration not change also? In none of our experiments have we found differences in the rate of penetration which could be attributable to changes in the hardness of the rock: this was particularly disappointing in the case of marble, since dislocation motion in calcite is easily possible at room temperature, and the influence of the environment on its plasticity has been documented previously [3, 4, 15].

In the present state of uncertainty, however, it would appear unwise to exclude *a priori*, any possible mechanism, and the following would seem to be worth consideration:

- 1) The quantity of heat generated at the cutting points during drilling is affected by the environment. The cause could be related to the chemomechanical effect, lubrication, or changes in the flow characteristics of the slurry of rock debris in the flushing fluid.

- 2) The efficiency of heat removal from the diamonds is changed; the effectiveness of heat transfer from hot diamond to the flushing fluid could be affected, either directly, or through the rheological properties of the rock debris slurry.
- 3) The environment has a direct chemical effect (corrosive or protective) upon the degradation of the diamond.

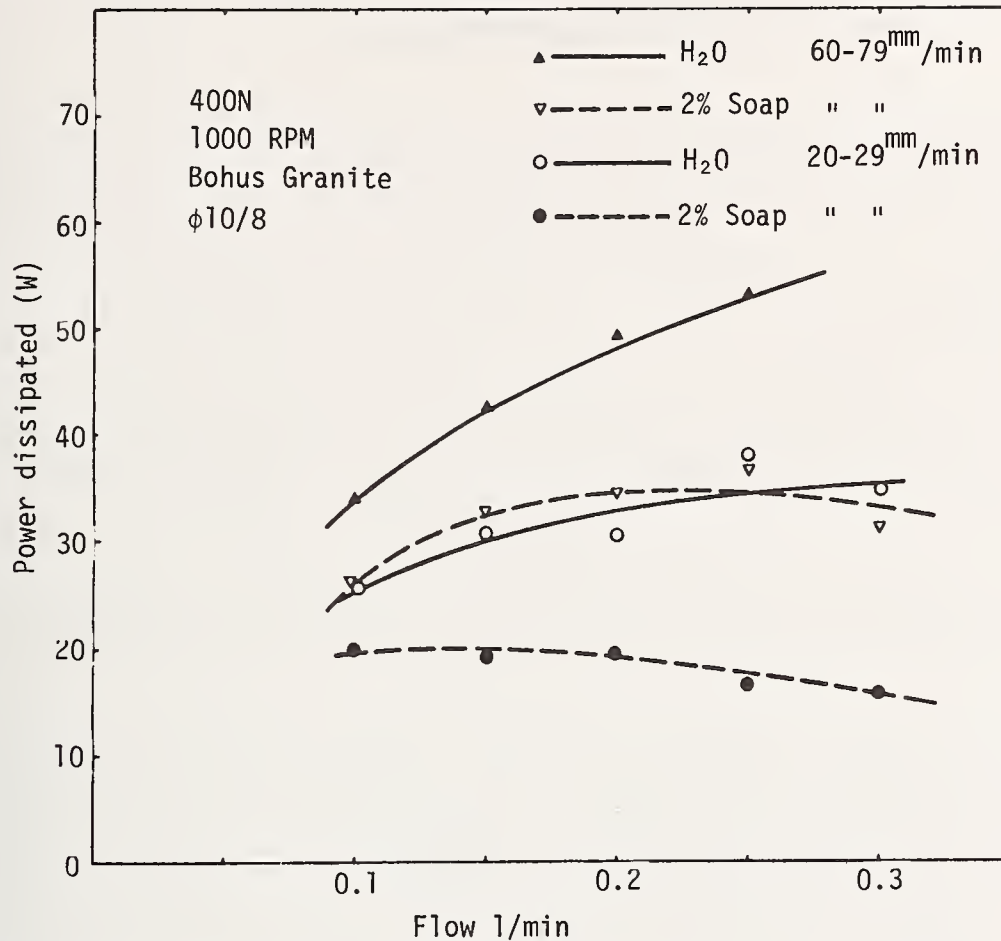


Figure 19. Granite: apparent power dissipated during drilling at different rates, in the presence or absence of an additive.

We have made some experiments to try to clarify the situation, as follows: In the first experiment, we have used a differential thermocouple to measure the heat generated during drilling in the presence or absence of the soap used in previous tests (fig. 19). In such work, it is important to eliminate spurious effects such as the heat generated from the turbulent stirring of the flushing liquid [25], and these deductions have been made in preparing figure 19. Several observations may be made from this data:

- 1) More power is dissipated at higher rates of penetration than at low. This is reasonable, in view of the greater quantity of rock which is broken.
- 2) The addition of soap produces a lower power dissipation than water alone under all drilling conditions. This must be seen as direct confirmation of the first hypothesis above, since if less power is dissipated, the diamonds will in all probability run cooler. Whether the effect is due to the hardening or softening of the rock, or is attributable to a lubricative effect, however, cannot be deduced from the present data.
- 3) The power levels lie in the range 20-50 watts, for a 10 mm O.D. drill bit, having a projected cutting surface area of about 28 mm². The concentration of diamonds in the bit was 19 %/o. If we suppose the heat to have been dissipated into the liquid over

the exposed surface of the diamonds, we obtain values from $20/(28 \times 0.19) = 3.8 \text{ MW m}^{-2}$ to $50/(28 \times 0.19) = 9.4 \text{ MW m}^{-2}$. This is not an exact calculation: some of the diamond will be in intimate contact with the rock, and will not be well cooled, and some heat will be conducted away through the supporting metal of the bit. Nonetheless these are extremely high power levels to be carried over a solid-liquid interface. We suggest, therefore, that under these conditions, the temperature of the diamonds may easily exceed 100°C , and thus any discussion of the cooling process must include the possibility of boiling heat transfer. (Indeed, it is commonly observed that if one drills within a few millimetres of the free surface of a translucent rock such as quartzite or granite, red and orange streaks can be seen which are thought to be individual diamonds at red heat.)

We would agree with the opinion of Mills and Westwood [24] that the presence of small concentrations of additives will not significantly affect thermal transport properties such as the specific heat or conductivity of the flushing fluid, but a possible role could easily be for the additive to influence the transition from nucleate to film boiling. Such an effect would not require the additive to be present in large quantities: Rhodes and Bridges [26] boiled water on the surface of a heated tube. They found that film boiling can be aided by making the surface less wettable, as for example by coating it with wax or by adding very small quantities of oleic acid or mineral oil to the water. On the other hand, inorganic salts such as sodium carbonate or chloride tended to promote nucleate boiling with correspondingly increased heat transfer. In our experiments, we have found soaps to be effective as drilling additives, and these are, of course, designed to have good wetting properties. Rehbinder and other workers have claimed that simple inorganic salts are effective also [1], and the quaternary ammonium compounds used by ourselves and Westwood and co-workers are well-known mineral-dressing additives. It would seem, therefore, that this hypothesis is worth testing further. Finally, the influence of the additive on the rheological properties of the suspension of rock cuttings should not be forgotten, and it could be that if the surfactant significantly changes the viscosity of the slurry around the bit, the cooling could be much improved. There is some evidence to support this view; Clarke [27] has investigated the rheology of suspensions of glass and quartz particles of various shapes in the size range of 20 to 200μ , following the work of Schack et al. [28] and Moreland [29], and has demonstrated that at concentrations as low as 0.6% a common anionic detergent can reduce the effective viscosity of a 30% solids quartz suspension by 50%. Further indirect evidence is available in the work of Haydon [30] who investigated the effects of several additives recommended by Rehbinder and co-workers on the efficiency of grinding quartz in a ball mill. Here it was found that the major part of the change in milling efficiency could be attributed to changes in the viscosity of the milling medium caused by the additive, and that when this was subtracted out, the residual change in efficiency was at best less than 3% (using sodium sulphonaphenate). This is very much less than the 80% or so claimed by Rehbinder as the increase of drilling rate obtainable with this additive.

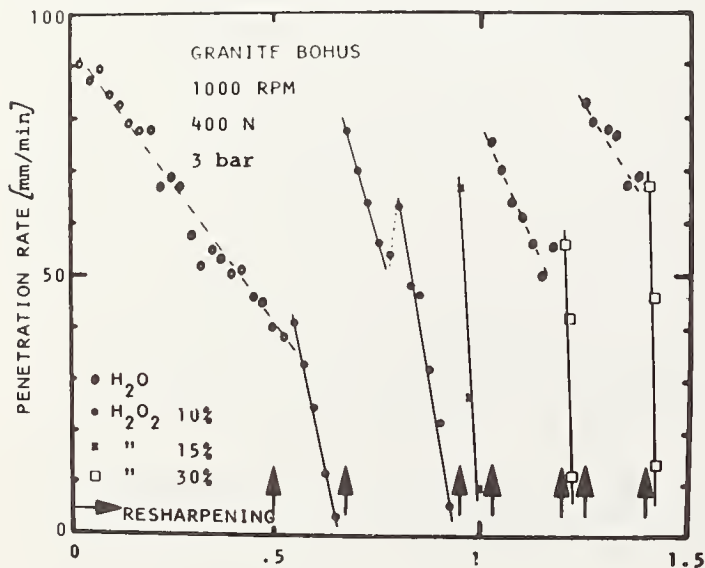


Figure 20. Granite: rate of penetration as a function of distance drilled using water, or 10, 15 or 30% hydrogen peroxide solution.

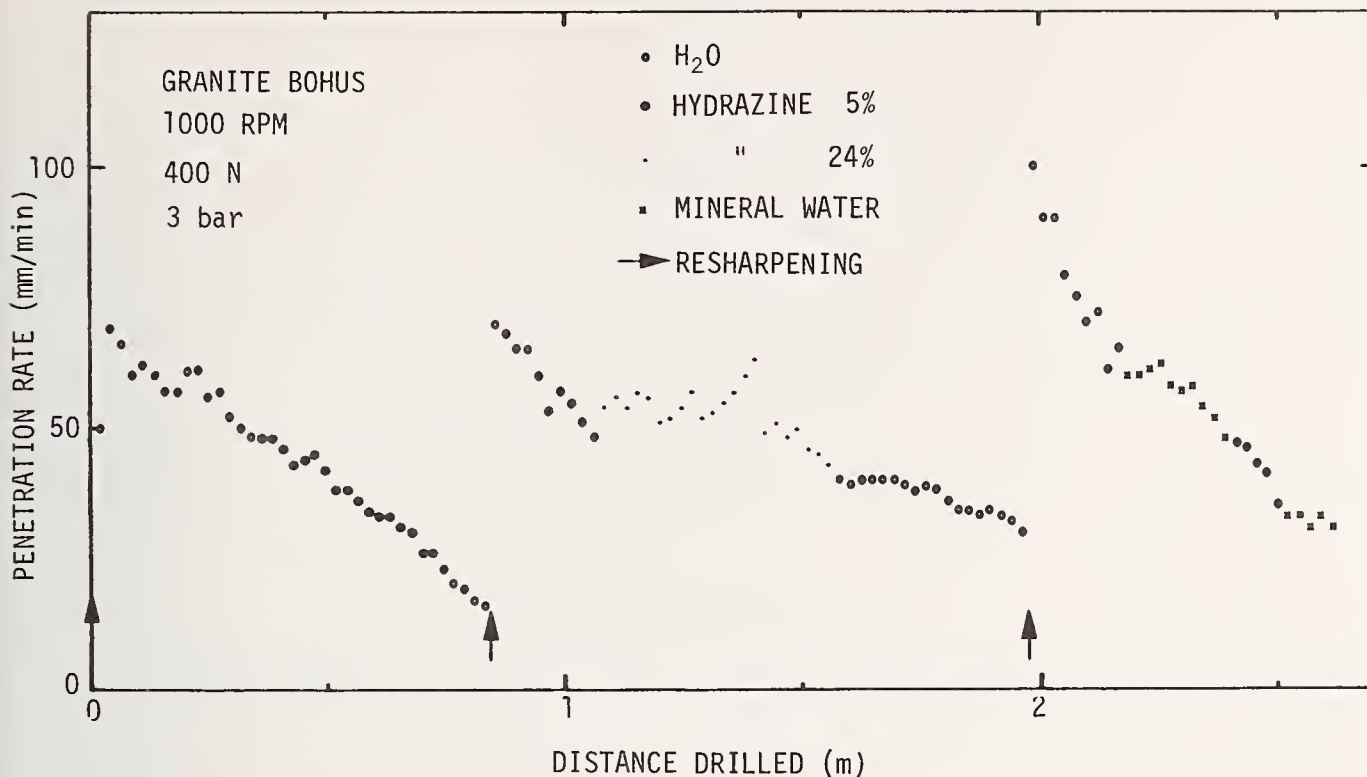


Figure 21. Granite: rate of penetration as a function of distance drilled using water, soda water or hydrazine solutions.

To investigate the third parameter of possible importance, namely that the additive can have a direct chemical effect on the wear of the diamonds, we have drilled in the presence of hydrogen peroxide. The results of these tests are shown in figure 20, where the damaging effects of this powerful oxidising agent are immediately obvious. Unfortunately, the complementary experiment, to drill with a reducing agent such as hydrazine (fig. 21) proved disappointing for the drill performance was not perceptibly improved. The figure also shows results of one final experiment connected with the work on hydrogen peroxide. It had been imagined that a possible cause for the rapid degradation of the drill was that the oxygen bubbles liberated during drilling could interfere with the heat-transfer process. The author is grateful to Professor Nabarro for a suggestion to drill with soda-water, which shows this not to be the case (fig. 21).

3. Conclusions

The conclusions to this study may be summarised as follows:

- 1) When diamond drilling in marble, no additive has been found which increases the instantaneous rate of penetration of the drill. Because the rate of wear of the drill is very low, however, it was not possible to determine whether this parameter was affected or not.
- 2) In granite, again, no additive has been found which increases the instantaneous rate of penetration of the drill. On the other hand, there are numerous additives which can either increase or decrease the rate of wear of the diamonds.
- 3) The wear of the diamond appears to be caused by physico-chemical rather than mechanical means. Oxidation or graphitisation, both thermally activated, are possible mechanisms, and we have obtained evidence of the former when drilling with hydrogen peroxide.

- 4) How the additive affects the wear of the diamond in general is not clear. We have suggested three possible mechanisms, as follows:
- A) The additive affects the quantity of heat generated during drilling. There is direct evidence for this, although we have not determined how it is achieved.
 - B) The additive affects the efficiency of heat removal from the diamond. It is suggested that the most probable way for the additive to act in small concentrations is to promote wetting and hence nucleate rather than film boiling heat transfer at the coolant-diamond interface.
 - C) The additive has a direct chemical effect on the diamond. This has been shown to be the case for a strong oxidising agent, which is deleterious, but improvements have not been obtained with reducing agents.

Finally, the relative importance of these different mechanisms remains to be established in any given situation, without excluding the possibility of additional unexpected influences.

References

- [1] Rehbinder, P.A., Schreiner, L.A. and Zhigach, S.F., Hardness reducers in rock drilling (Academy of Science USSR, Moscow, 1944) (CSIRO Translation, Melbourne, 1948).
- [2] Rehbinder, P.A. and Schchukin, E.D., Surface phenomena in solids during deformation and fracture processes, in Progress in Surface Science 3, [2] (Pergamon Press, Oxford, 1972).
- [3] Boozer, G.D., Miller, K.H. & Serdengecti, S., Effects of pore fluids on the deformation behaviour of rock subject to triaxial compression (Fifth Symposium on Rock Mechanics, University of Minnesota, May 1962).
- [4] Robinson, L.H., Effect of hardness reducers on failure characteristics of rock, Soc. Pet. Eng. J., 295-300 (Sept. 1967).
- [5] Selim, A.A., Schultz, C.W. & Strebis, K.C., The effect of additives on impregnated diamond bit performance, Soc. Pet. Eng. J., 2, 425 (1969).
- [6] Joris, A.C.T. and McLaren, G., Mining and Mineral Engineering, 3, [5], 190 (May 1967).
- [7] Engelmann, W.H., Unger, H.F. and Snowden, B.S., Diamond drilling with surfactants in upper Michigan amygdaloidal basalts using surface-set bits, Trans. S.M.E.-AIME, 285, 185 (Sept. 1975).
- [8] Westwood, A.R.C. and Macmillan, N.H., Environment-sensitive hardness of non-metals (5th Technical Report to ONR. Contract No. N00014-70-C-0330. Nr. 032-524, April 1972).
- [9] Shockey, D.A. and Grooves, G.W., J. Am. Ceram. Soc., 51, 299 (1968).
- [10] Shockey, D.A. and Grooves, G.W., J. Am. Ceram. Soc., 52, 82 (1969).
- [11] Westwood, A.R.C., Parr, G.H., Jr. and Latanision, R.M. in Amorphous Materials, R.W. Douglas and B. Ellis, eds., pp. 533- (Wiley, London, 1972).
- [12] Hanneman, R.E. and Westbrook, J.H., Phil. Mag., 18, 73 (1968).
- [13] Westwood, A.R.C. and Goldheim, D.L., J. Appl. Phys., 39, 3401 (1968).
- [14] Westwood, A.R.C., J. Mat. Sci., 2, [11], 1971 (1974).

- [15] Westwood, A.R.C., Macmillan, N.H. and Kolyoncu, R.S., J. Am. Ceram. Soc., 56, 258 (1973).
- [16] Westwood, A.R.C. and Latanision, R.M. in Science of Ceramic Machining and Surface Finishing, NBS monograph, S.P. 348, p. 141 (NBS, Washington, 1972).
- [17] Westwood, A.R.C. and Latanision, R.M., Surface and environmentally sensitive mechanical behaviour - some current issues (Proc. 4th Int. Conf. on the Strength of Metals and Alloys, Nancy, 1976, to be published).
- [18] Swain, M.V., Latanision, R.M. and Westwood, A.R.C., J. Am. Ceram. Soc., 58, 372 (1975).
- [19] Macmillan, N.H., Jackson, R.E. and Westwood, A.R.C., Proc. 15th IRSM Symp. on Rock Mechanics (Sept. 1973 - to be published).
- [20] Cooper, G.A., CERAC Report No. 403:5 (May 1977).
- [21] Cooper, G.A. and Berlie, J., J. Mats. Sci., 11, 1771 (1976).
- [22] Cooper, G.A., The Civil Engineer in South Africa, 19, [10], 238 (Oct. 1977).
- [23] Mills, J.J., Final report on N.S.F. Contract APR 73-07787 (Feb. 1978).
- [24] Mills, J.J. and Westwood, A.R.C., J. Mats. Sci., in press.
- [25] Cooper, G.A. and Berlie, J., J. Mats. Sci., in press.
- [26] Rhodes, F.H. and Bridges, C.H., Trans. Amer. Inst. Chem. Eng., 35, 73 (1939).
- [27] Clarke, B., Trans. Inst. Chem. Engrs., 45, T. 251 (1967).
- [28] Schack, C.M., Dean, K.C. and Molloy, S.M., U.S. Bureau of Mines, Report of Investigation No. 5334 (1957).
- [29] Moreland, C., Can. J. Chem. Eng., 41, 24 (1963).
- [30] Haydon, B.C., Report on tests for the Rehbinder effect (Imperial College Internal Report, July-November 1966). Kindly communicated to the author by Dr. J.A. Kitchener, Royal School of Mines.

Discussion

FIRESTONE

Does the additive reduce the blunting of the diamonds or does it soften or weaken the bond so the diamonds fall out more easily and fresh diamonds are more rapidly exposed?

COOPER

As far as I know, the additive has no effect on the strength of the diamond - matrix bond.

WILCOX

When the diamonds wear, do they get rounded or just fracture and chip off?

COOPER

They are normally rounded, often with striae and ripple patterns reminiscent of ablative erosion. See, however, the text of the paper. There are two micrographs included.

CHOUDRY

The environment acts on all the three components; namely, the work-piece (rock in this case), tool (diamond) and the matrix (bronze). Effects on the rock (classical Rehbinder effect) could have been independently checked by scratch or single cut experiments on rocks soaked and not soaked in the liquid. Was the 'hardness' of the rock checked as a function of the liquid by methods other than the drilling tests?

COOPER

We made no measurements of the hardness of our rocks, by scratch, indentation, or other tests. Such experiments have been carried out by many other workers, and have shown the hardness to be affected at the low strain rates used in such work. Whether the environment affects the hardness at high strain rates, we do not know; what we observe is that the instantaneous rate of penetration is not affected by the presence or absence of the environment (which is difficult to square with supposed differences in the hardness of the rock), and that the rate of wear of the diamonds is changed. The main contention of our paper is not that the Rehbinder effect does not exist, but that the most important effect of the environment is on the rate of wear of the diamond.

KIRCHNER

We have shown* that greater damage penetration occurs in environments with zeta potential close to zero compared with similar Al_2O_3 specimens scratched in environments with higher zeta potentials. However, low zeta potential implies clean surfaces so that cracks can heal. Therefore, the specimens scratched in low zeta potential environments were stronger instead of weaker than the others showing that these experiments do not always have the expected results. It seems likely that Westwood's results are correct but that, at the high drilling rates reported in the present paper, the high temperatures and other factors have altered the conditions so that comparable results were not observed.

* R. M. Gruver and H. P. Kirchner, "Effect of Environment on Penetration of Surface Damage and Remaining Strength of Al_2O_3 ," J. Amer. Ceram. Soc. 57 (5) 220-223 (1974).

THE EFFECT OF CHEMICAL ENVIRONMENTS ON THE FRACTURE OF CERAMIC SURFACES¹

Robert E. Cuthrell

Sandia Laboratories²
Albuquerque, New Mexico 87185

Environmental effects on the deformation and fracture of a variety of materials during drilling/grinding and four point bending to failure have been traced to embrittlement by hydrogen. The extent of embrittlement is determined by the availability of hydrogen in the drilling fluid or in the gaseous environment in an ultrahigh vacuum chamber (10^{-10} Torr). The hydrogen availability is in turn dependent on its binding in liquids (ionic, covalent, ion paired in media of low dielectric constant) or by the blocking effect of adsorbed carbon monoxide in the vacuum chamber. These hydrogen effects were shown in drilling rates, maximum strain to fracture, acoustic emission amplitude (energy) distributions accompanying fracture, and scanning electron microscope photomicrographs of the fractured surfaces. The embrittling effect appears to be universal, affecting in varying degree the behavior of ceramics, glasses, single crystal minerals, polycrystalline materials, semiconductors, refractory coatings, rocks, and metals containing brittle phases (organic solids may be exceptions).

Key Words: Acoustic emission; chemomechanical effects; environmental effects; fracture of brittle materials; hydrogen embrittlement; Rebinder effects, Westwood effects.

1. Introduction

Rebinder demonstrated that adsorbed surface-active species could affect the microhardness of certain minerals [1].³ These and other manifestations of the effects of chemical environments on mechanical behavior are often termed Rebinder effects.

The influence of several chemical environments on the microhardness of a large number of ionic and ceramic crystals was investigated by Westbrook and Jorgensen [2], following earlier work by Mitsche and Onitsch [3] and Walker and Demer [4]. The anelastic behavior of glass fibers [5,6], the Vickers microhardness and indentation creep of fused silica and alkali glass [7], the pendulum hardness of soda-lime glass [8,9] and quartz [10], and the drilling rates in calcium fluoride [11], magnesium oxide [11], Pyrex glass [12], soda-lime glass [9], aluminum oxide [13], gray granite [13], and Westerly granite [13] are all known to be strongly dependent on the chemical environment. Possibly the most significant contribution to understanding these Rebinder effects was made by Westwood, et. al. [13], on interpreting the correlation between the maximum in the hardness of materials and the zero in the surface charge (zeta potential) which is produced by ions adsorbed from solution environments.

2. Environmental Effects on Drilling/Grinding Indicated by Acoustic Emission

In brittle polycrystalline materials, crack propagation occurs at an average velocity,

¹This work was supported by the Division of Basic Energy Sciences, U.S. Department of Energy (DOE), under Contract AT(29-1)-789.

²A U.S. DOE facility.

³Figures in brackets indicate the literature references at the end of this paper.

\bar{v} , determined by the applied stress intensity factor, K , [14]; usually,

$$\bar{v} = AK^n \quad (1)$$

where A and n are constants for a specified environment and temperature [15]. Most acoustic emission count rate studies performed on polycrystalline ceramics [15-18] have shown an approximate proportionality between the acoustic emission count rate and the average crack velocity and the dependence of these on the stress intensity factor. It was shown⁴ recently by Cuthrell that the acoustic emission count rates and the peak emission amplitudes⁵ were proportional to the low speed drilling/grinding rates⁵ of brittle materials such as Pyrex glass [19] and soda-lime glass [20] in various liquid environments. Minimum acoustic emission count rates (wear rates) were associated with the zero zeta potential (fig. 1) [19] where the maximum hardness would be expected (as shown by Westwood [13] for a wide variety of materials in various liquid environments). In addition, minimum low speed drilling/grinding rates were found in drilling fluids having maximum binding of monovalent ions as neutral ion aggregates (fig. 2) [19] (a condition which was mathematically predicted [19] using the theories of Bjerrum [21,22] and Fuoss and Kraus [21,23]). It was proposed (1) that the higher drilling/grinding rates were primarily results of the embrittling effects of hydrogen ions from liquid or gaseous environments and (2) that the minima in drilling/grinding rates were results of reduced availability of hydrogen through its aggregation in ion pairs [24].

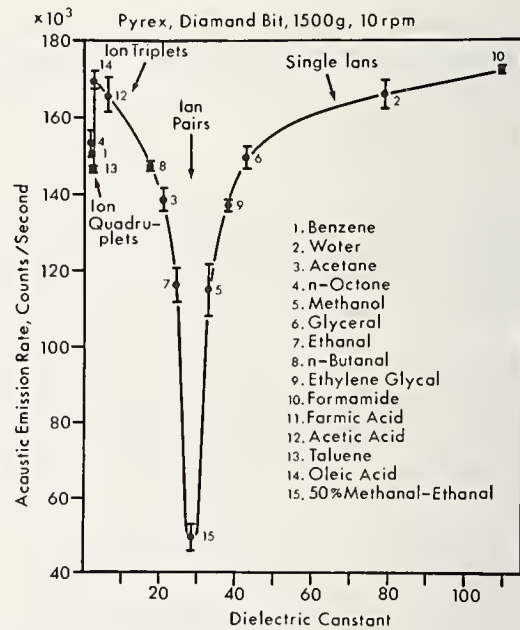
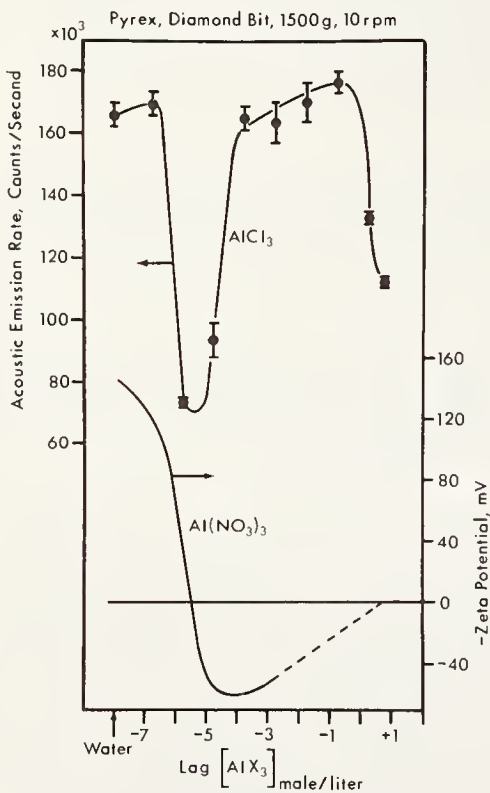


Figure 1. The acoustic emission rate during drilling (upper curve) and the zeta potential (lower curve) of glass as functions of the concentration of trivalent aluminum ions in aqueous solution [19].

Figure 2. The acoustic emission rate during drilling glass as a function of the dielectric constant of the drilling fluid [19].

⁴Acoustic emission was detected over the frequency range 0.125-2 MHz.

⁵Drilling was performed using a spherical-ended diamond studded bit rotated at 10 rpm under a 1500 g load in various drilling fluid environments. Drilling at this very low speed may be more analogous to grinding than to conventional high speed drilling.

3. Embrittling Effects of Hydrogen

In order to test this theory, several drilling experiments were performed under very carefully controlled conditions in an ultrahigh vacuum chamber. Figure 3 [24] shows the acoustic emission rate as a function of drilling time in ultrahigh vacuum (5×10^{-10} Torr), in carbon monoxide (10^{-7} Torr), in a mixture of carbon monoxide (10^{-7} Torr) and hydrogen (680 Torr), and in hydrogen alone (680 Torr). For Pyrex glass the presence of at least 10^{-7} Torr of carbon monoxide appears to inhibit the diffusion of hydrogen into the solid. There is a remarkable change in behavior when the carbon monoxide is differentially pumped out such that the glass is exposed to hydrogen alone. The effect is reversed when the hydrogen is pumped out and the return to the original condition is accelerated by heating to 100°C in vacuo

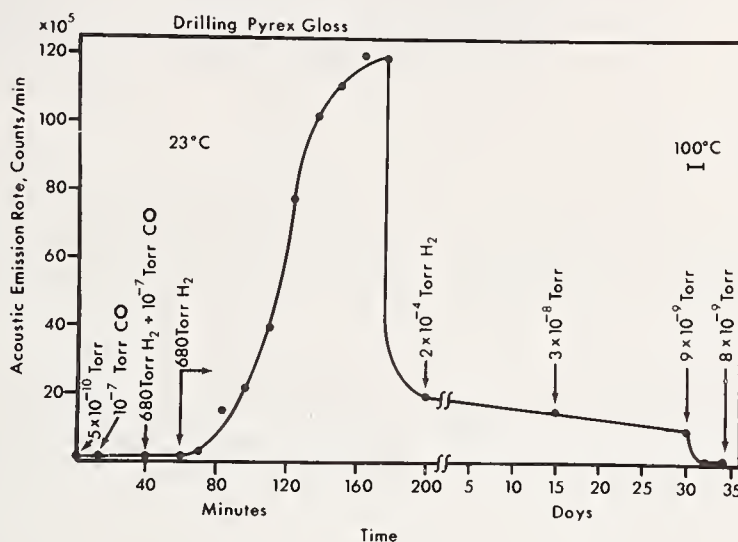
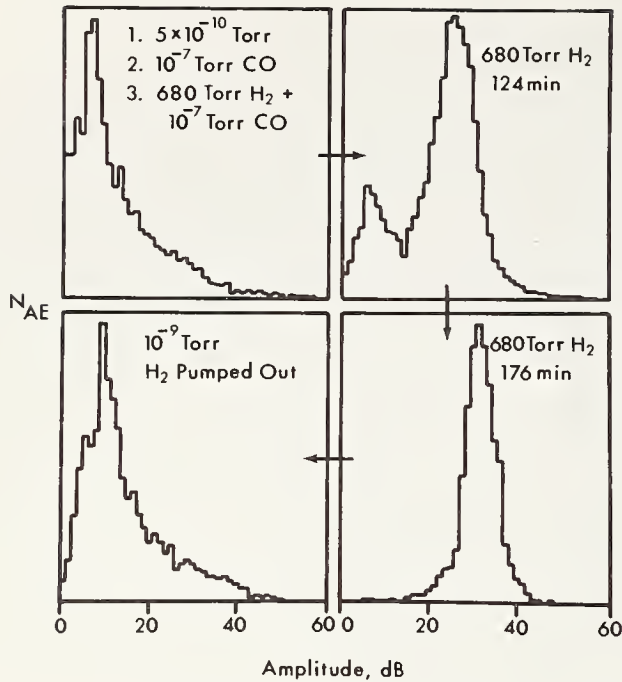


Figure 3. Acoustic emission count rate as a function of drilling time for Pyrex glass in an ultrahigh vacuum chamber. Note that there is no effect of gaseous environment in carbon monoxide nor in hydrogen when the carbon monoxide is present. The time required for the acoustic emission rate to reach a maximum in hydrogen indicates that Rebinder-Westwood effects occur in the near-surface region rather than solely at the surface. The time dependence is also consistent with a hydrogen permeation mechanism for the chemomechanical effect, [24].

Figure 4 [24] shows the shift to higher amplitudes (greater energy release on fracture) of the acoustic emission peak on exposure to hydrogen and reversal of this trend on pumping out the hydrogen. Drilling in air or under water environments results in acoustic emission amplitude distributions very similar to the lower right, figure 4, as shown in figure 5 [24]. Apparently sufficient hydrogen is available from water vapor in air or the liquid water to produce the embrittling effect. As shown in figure 5, the results obtained for drilling under liquids follow the same trend observed for hydrogen in the gaseous state, i.e., a shift to low amplitude for drilling in a hydrogen free liquid (carbon tetrachloride) and a higher amplitude distribution for drilling in a hydrogen bearing liquid (water). Peaks of intermediate amplitude were produced for drilling under hydrocarbons in which hydrogen is covalently bound and is thus less available than in a partially ionized aqueous environment [24].

Figures 6 and 7 show similar results for polycrystalline alumina [25] and for silicon [20] (the intermediate amplitude for drilling alumina under carbon tetrachloride may be a result of moisture trapped in cracks, crevices, and pores in the sintered solid). The changes from peaks at higher amplitudes in hydrogen bearing environments to progressively lower amplitudes in drilling fluids containing less hydrogen were found to be time dependent and thus consistent with a hydrogen diffusion mechanism for embrittlement. Figure 8 shows that drilling silicon under carbon tetrachloride, a hydrogen free liquid, produces primarily ductile fracture in the near surface layer (ductile plowing in smooth grooves which follow the drill rotation) while primarily brittle fracture (with some ductile plowing) occurs under water, a source of hydrogen, for the same sample surface.

Drilling Pyrex Glass



Drilling Pyrex Glass

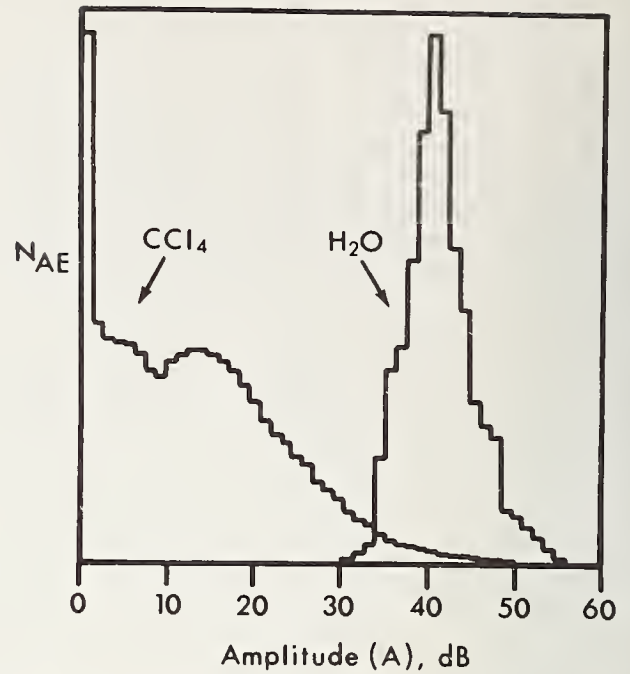
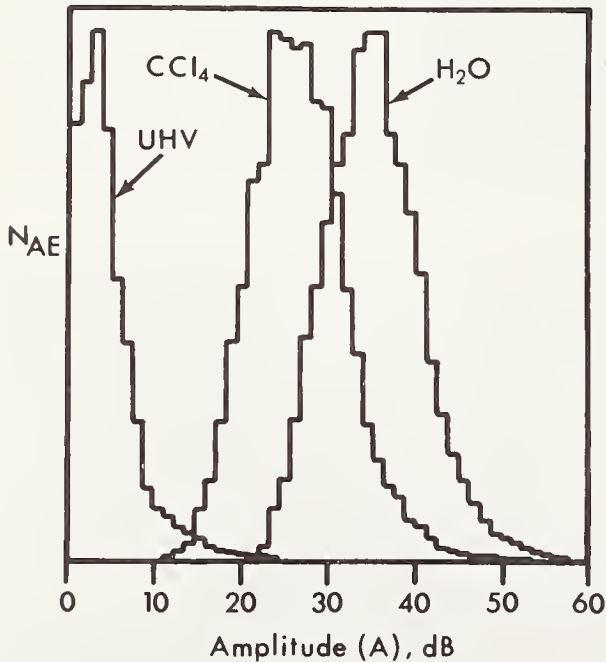


Figure 4. Acoustic emission amplitude distributions for the drilling of Pyrex glass. The upper left curve is typical of each of the three conditions listed. The drilling times correspond to the abscissa in figure 3 [24].

Figure 5. Acoustic emission amplitude distributions for the drilling of Pyrex glass under carbon tetrachloride (a hydrogen free liquid) and under water (a source of hydrogen) [24].

Drilling Polycrystalline Alumina



Drilling Silicon

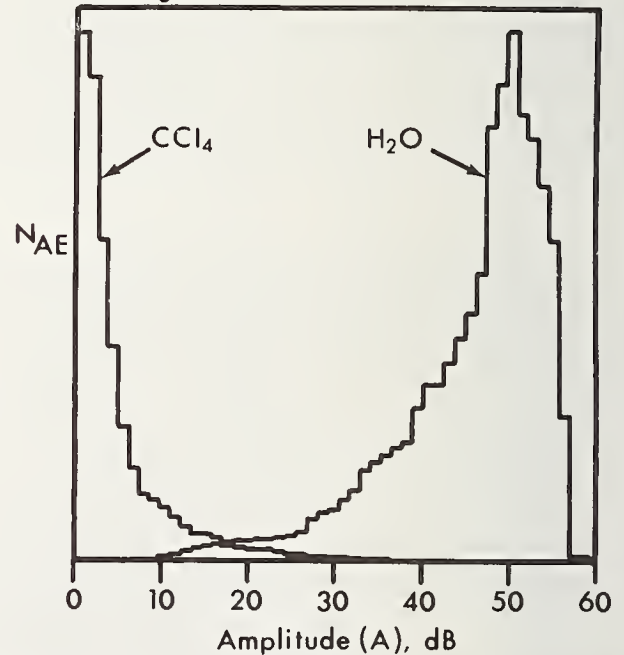


Figure 6. Acoustic emission amplitude distributions for the drilling of polycrystalline alumina in vacuo, under carbon tetrachloride, and under water. The intermediate amplitude for drilling alumina under carbon tetrachloride may be a result of moisture trapped in cracks, crevices, and pores in the sintered solid [25].

Figure 7. Acoustic emission amplitude distributions for the drilling of the (111) plane of single crystal silicon under carbon tetrachloride and under water [20].

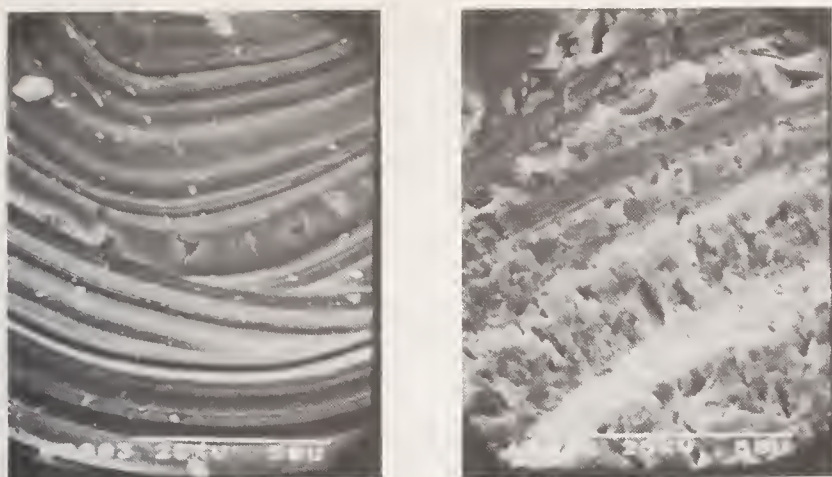


Figure 8. Scanning electron microscope photographs of the surface of a silicon sample showing the ductile fracture (left) when drilled under a hydrogen free liquid (carbon tetrachloride) and the brittle fracture (right) when drilled under a hydrogen bearing liquid (water) [20].

4. Ductile, Brittle, More Brittle

The assignment of "ductile" or "brittle" designations for acoustic emission amplitude distributions was based on the observation that curves decreasing asymptotically to the abscissa were obtained for the drilling of a wide variety of metals which were known to be ductile, whereas peaks at higher amplitudes were obtained without exception for the drilling of brittle materials. The effect on the acoustic emission amplitude distributions of changing from a ductile to a brittle condition in the same sample (Ferrovac E iron) without changing structure or composition was shown (fig. 9) by drilling above and below the ductile-to-brittle transition temperature (about -73°C) in vacuo (10^{-10} Torr, to avoid ice, condensation, or oxidation) [20]. These data, obtained under very carefully controlled conditions, confirm the assignment of "ductile/brittle" designations for acoustic emission amplitude distributions and show that acoustic emission measurements may be used to distinguish between these two fracture modes. Figures 4-7 and 9 show "brittle" peaks which occur at different amplitudes for different materials under the same conditions and for the same material under different conditions. In order to facilitate comparison, the concept of "degrees of brittleness" is introduced. Thus a material for which an acoustic emission peak at higher amplitude is obtained on fracture may be said to be more brittle under the particular experimental conditions. Initial results of a study of the environmental dependence of slow crack growth in glass indicate that higher acoustic emission amplitudes during drilling may be correlated with lower stress intensity factors for crack propagation in the same environment [27].

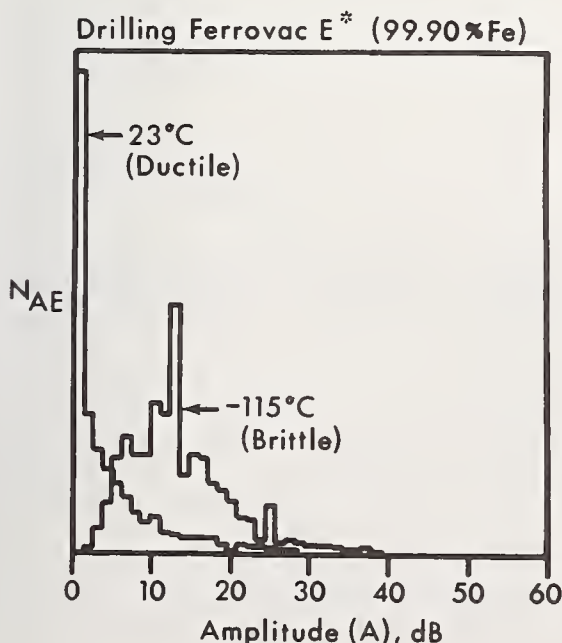


Figure 9. The drilling of Ferrovac E iron at 23°C produces an acoustic emission amplitude distribution which is typical of ductile materials. Drilling the same sample at -115°C (well below its ductile-to-brittle transition temperature of about -73°C) produces a peaked acoustic emission distribution at higher amplitudes which is typical of brittle materials [20].

5. Conclusions

The results presented indicate that the embrittling effect of hydrogen is one of the origins of the environment-dependence of the deformation and fracture of the near surface region of solids (the Rebinder-Westwood effect). It was indicated that the results for drilling solids under hydrogen bearing liquids were the same as those for drilling in a well-controlled gaseous hydrogen environment except that the availability of the hydrogen in the liquid case depends on its bonding (covalent, partially ionized, or bound as ion aggregates). The time dependence of the chemomechanical effect is consistent with a hydrogen permeation process.

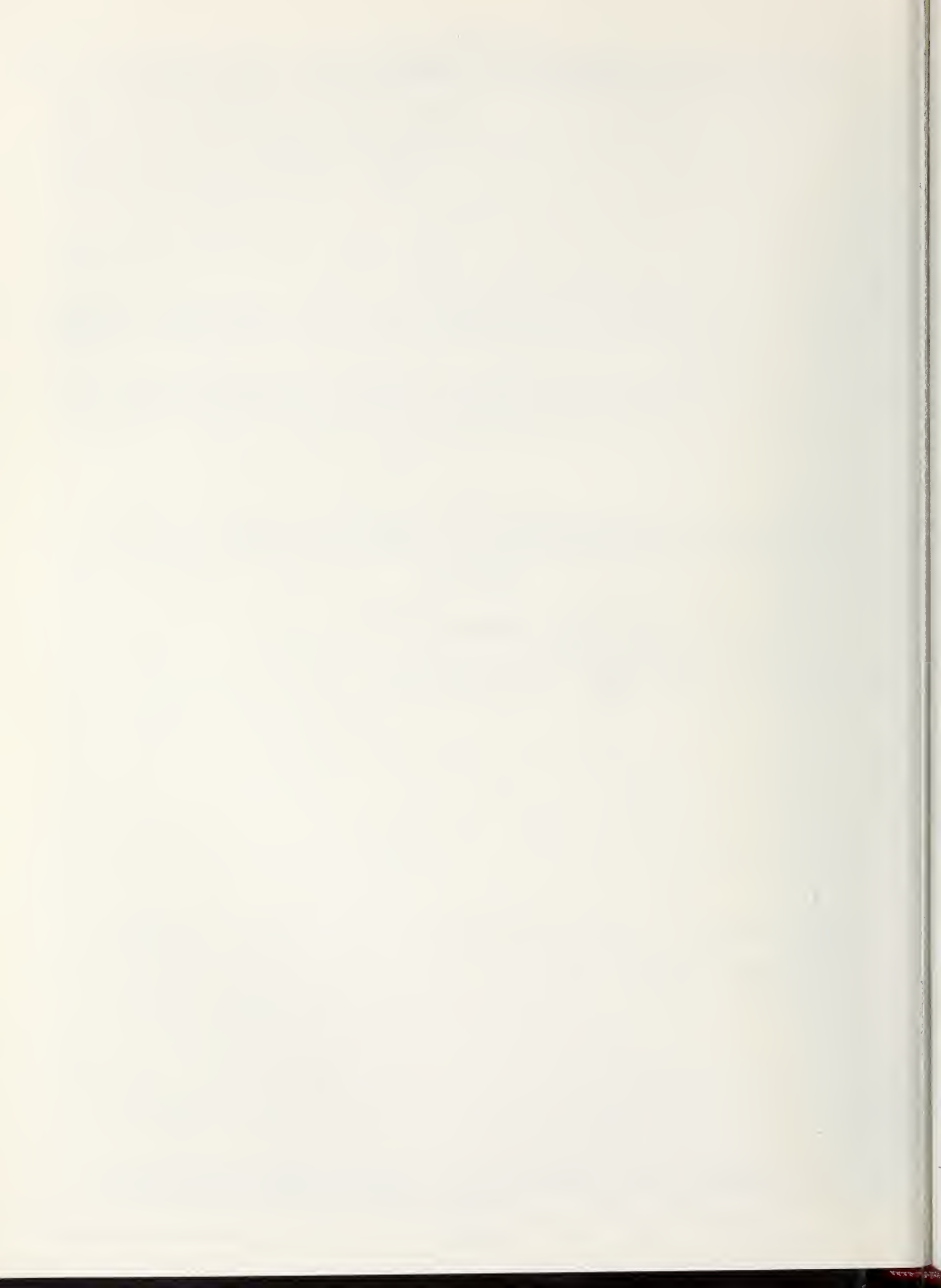
Although silicon exhibits one of the largest observed hydrogen-dependent changes in mechanical properties, similar effects have now been observed in many quite different materials (Pyrex glass [19,24], soda-lime glass [20], silicon [20], fused silica [25], quartz [25], polycrystalline alumina [25], calcite [25], fluorite [25], sierra white granite [25], Texas pink granite [25], hot pressed boron carbide (B_4C) [25], hot pressed titanium diboride [25], type 02 tool steel [25], 1080 steel [25], and 440C stainless steel [26]). It is proposed that embrittlement by hydrogen is a universal effect (organic solids may be exceptions) which would be expected to affect other materials and other forms of wear in addition to low speed drilling (such as high speed drilling, erosion, grinding, polishing, comminution, machining, and cutting). It is also proposed (1) that the environmental effects on slow crack growth or fatigue in brittle materials, which have been previously attributed to water, may be attributable to hydrogen from the water, and (2) that embrittlement by hydrogen may be the origin of the Rebinder-Westwood chemomechanical effects.

The author wishes to thank D. M. Mattox for suggesting acoustic emission techniques for this investigation, E. Randich for fruitful discussions and metallurgy contributions, and V. D. Nogle for sample preparation.

References

- [1] Rebinder, P. A., Proc. 6th Physics Conf., Moscow, 1928 (unpublished).
- [2] Westbrook, J. H. and Jorgensen, P. J., Trans. Metall. Soc. AIME 233, 425 (1965).
- [3] Mitsche, R. and Onitsch, E. M., Mikroskopie 3, 257 (1957).
- [4] Walker, W. W. and Demer, L. J., Trans. Metall. Soc. AIME 230, 613 (1964).
- [5] Aslanova, M. S., C. R. (Dokl.) Acad. Sci. URSS 95, 1215 (1954).
- [6] Aslanova, M. S. and Rebinder, P. A., C. R. (Dokl.) Acad. Sci. URSS 96, 299 (1954).
- [7] Hanneman, R. E. and Westbrook, J. H., Philos. Mag. 18, 73 (1968).
- [8] Westwood, A. R. C., Parr, G. H., Jr., and Latanision, R. M., in Amorphous Materials, edited by R. W. Douglas and B. Ellis (Wiley, London, 1972), p. 533.
- [9] Westwood, A. R. C. and Huntington, R. D., in Mechanical Behavior of Materials (Society for Material Science, Japan, 1972), Vol. IV, p. 383.
- [10] Westwood, A. R. C. and Huntington, R. D., (unpublished).
- [11] Westwood, A. R. C. and Goldheim, D. L., J. Am. Ceram. Soc. 53, 142 (1970).
- [12] Westwood, A. R. C. and Latanision, R. M., Natl. Bur. Stand. (U.S.) Spec. Publ. 348, 141 (1972).
- [13] Westwood, A. R. C. and Macmillan, N. H., in The Science of Hardness Testing and Its Research Applications, edited by J. H. Westbrook and H. Conrad (American Society for Metals, Metals Park, Ohio, 1973), p. 377.

- [14] Wiederhorn, S. M., in Fracture Mechanics of Ceramics, edited by R. C. Bradt, F. F. Lange, and D. P. H. Hasselman (Plenum, New York, 1974), p. 613.
- [15] Evans, A. G. and Linzer, M., *Ann. Rev. Mater. Sci.* 7, 179 (1977).
- [16] Evans, A. G. and Linzer, M., *J. Am. Ceram. Soc.* 56, 575 (1973).
- [17] Evans, A. G., Linzer, M., and Russell, L. R., *Mater. Sci. Eng.* 15, 253 (1974).
- [18] McKinney, K. R., Chaskelis, H. H., and Freiman, S. W., *Bull. Am. Ceram. Soc.* 53, 618 (1974).
- [19] Cuthrell, R. E., *J. Appl. Phys.* 49, 432 (1978).
- [20] Cuthrell, R. E., The Influence of Hydrogen on the Deformation and Fracture of the Near Surface Region of Solids — Proposed Origin of the Rebinder-Westwood Effect, *J. Mater. Sci.*, in press.
- [21] Harned, H. S. and Owen, B. B., The Physical Chemistry of Electrolytic Solutions (Reinhold, New York, 1958), p. 70.
- [22] Bjerrum, N., *K. Dan. Vidensk. Selsk. Mat.-Fys. Medd.* 7, (No. 9), (1926).
- [23] Fuoss, R. M. and Kraus, C. A., *J. Am. Chem. Soc.* 55, 2387 (1933); 57, 1 (1935).
- [24] Cuthrell, R. E., Near Surface Embrittlement of Solids by Hydrogen — The Origin of the Rebinder-Westwood Chemomechanical Effects, *J. Appl. Phys.*, in press.
- [25] Cuthrell, R. E. and Randich, E., (unpublished).
- [26] Cuthrell, R. E., Surface Effects in Crystal Plasticity, edited by R. M. Latanision and J. T. Fourie (Noordhoff, Leyden, 1977), p. 773.
- [27] Marion, R. H. and Cuthrell, R. E., (unpublished).



SOME RESULTS ON THE WEAR OF A BRONZE-BONDED GRINDING WHEEL

A. Broese van Groenou

Philips Research Laboratories
5600 MD Eindhoven, The Netherlands

Abstract

Small parts of a diamond grinding tool have been investigated in a grinding apparatus where the tool is fixed whereas the workpiece material, here a MnZn ferrite, moves at 20 m/s. The wear of the bronze binder and of the diamonds can be measured on plastic replicas. Apart from an estimate of the average G value it is also possible to study locally the erosion of the binder and the wear of the diamonds. Two areas of erosion are distinguished: the region between the diamonds and the zone in front of a diamond. For a dozen diamonds it is found that the average erosion rate is proportional to the removal rate of the workpiece, whereas the local rate of increase of zone depth is about twice as fast. For this type of wheel the conditions for self-sharpening can be formulated. For a nickel-plated wheel the wear was too small to be measureable.

Key words: Bronze binder; diamonds; erosion; grinding; wear.

1. Introduction

As part of a program on the grinding of ceramics and glass some aspects of the wear of a grinding wheel have been studied. Usually the wear is characterised by the G value, G being defined as the ratio of the volume of material removed by grinding to the loss of grinding wheel volume. For grinding steel with alumina wheels [1]¹ and carbide tools with diamond wheels [2] G is between 100 and 1000. Much higher values ($10^4 - 10^5$) are found in the grinding of ceramics and glass with diamond wheels. The correspondingly long life of the wheels allows the grinding of a cubic metre of ceramic. If one is not satisfied with this performance, one may ask: why not a longer life? Which wheel should one choose? Can dressing be avoided? In view of the large number of wheel variables the answers are not readily available. Rate of workpiece removal Z and rate of wheel wear are related. For high Z values the grinding force increases and so does the force F_d exerted on a diamond. Introducing the grinding hardness H_g one has for a given workpiece material

$$F_d = H_g Z / v_s N_d \quad (1)$$

where v_s is the wheel speed and N_d the number of diamonds in action. The depth of cut of a single diamond is of the order of a micron or less. Moreover, the height of the diamond tips above the binder varies over half the size of the particles, e.g. 50 to 100 μm . Not even on this scale is the radius of a grinding wheel constant, which implies that even a slight unroundness has a pronounced influence on N_d . In order to study wear it is therefore necessary to locate the site of action with some precision. The apparatus to be described has been designed especially with this requirement in mind.

Wheel wear involves the diamonds and the binder. Diamond wear may not contribute much to the loss of volume because of the small particle volume, but it does influence binder wear if it is true that "the diamond protects the matrix" [3]. A detailed study of the wear of diamonds is not possible on a grinding wheel, because the unequal protrusion of the particles above the binder, even when it is flat, means that the force on each particle

¹ Figures in brackets indicate the literature references at the end of this paper.

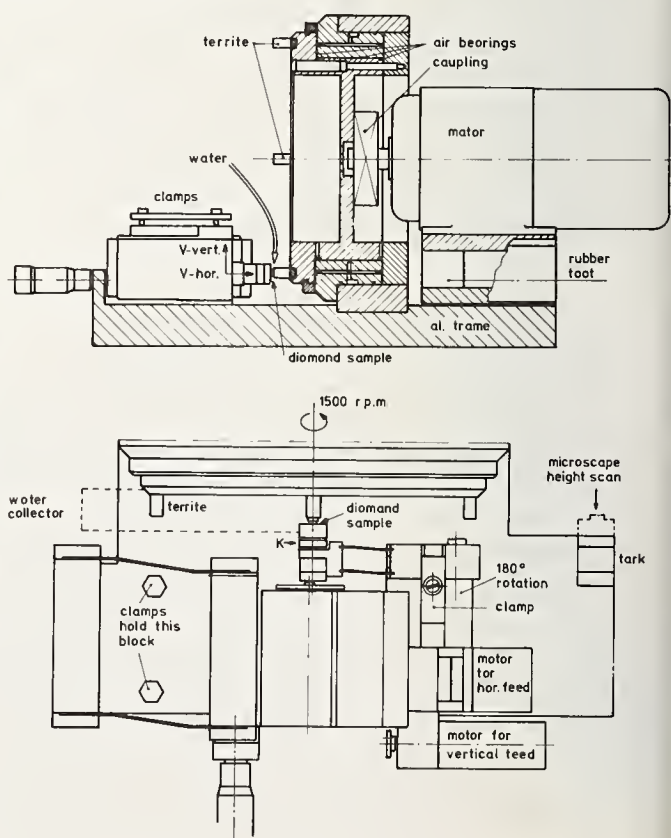
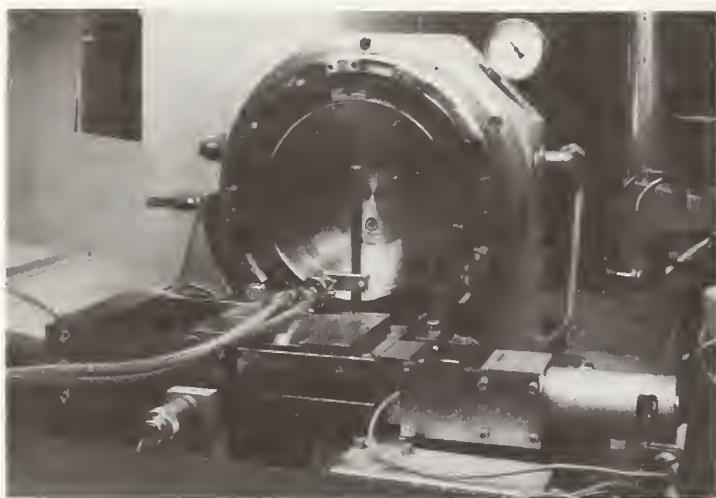
is very uncertain. Single diamond studies are more appropriate [4]. In the present paper the wear of the binder has been measured quantitatively, enabling the G values to be determined. It was also possible to determine the number of diamonds in action, especially the changes in this number due to diamond loss and "birth". This is of interest, because it gives information on the "sharpness" of a wheel. It is important that a wheel remains sharp, since the continuity of the grinding operation is essential in manufacturing and corrections by dressing are very costly. Sharpness is therefore more important than the G value, for only after a continuous operation has been realised, can G be used to calculate the wheel contribution to the cost of grinding.

This paper describes a wear apparatus where the grinding "wheel" is fixed and the workpiece moves at a relative velocity of 22 m/s. The grinding tool is moved into the samples at a speed v_w . Normally, every abrasive particle acts once during a wheel revolution. Such intermittent action was imitated here by interrupting the contact with the workpiece: twelve samples were used. During the interruption the diamond tool is cleaned and cooled by a mist beam of water and air. The force on the tool and the volume removed from the workpiece are measured. The detailed behaviour of the diamonds and the binder is determined by observing replicas of the tool. The apparatus is described in the next section. Data on the combination of a MnZn ferrite ceramic and a bronze-bonded diamond tool are given in section 3. Other binders were investigated, especially a nickel-plated tool, but the small amount of wear could not be measured. Wear details are given in section 4, and in section 5 we return to the question of the wheel sharpness in the discussion.

2. Experimental

a. Workpiece wheel

The apparatus consists of a wheel containing twelve workpiece samples and a mechanism feeding the diamond tool. The wheel is connected via a flexible coupling to a 1.5 kW motor running at 1400 r.p.m. The wheel is supported by air bearings (240 mm i.d., 300 mm o.d., 70 mm high) fed by an air supply at 7 atm. Two-stage air filtering is used. In the axial and radial directions the running inaccuracy is less than 0.5 μ m. The workpiece samples are fastened on the face of the wheel (figs. 1 and 2) and not on the circumference because a flat wear plane was preferred to a curved one. The sample speed is 22 m/s, which makes the contact time 0.45 ms for a sample width of 10 mm. The sample blocks, 9x10x11 mm³, are glued in steel blocks in a 4 mm deep recess. The apparatus was carefully balanced. For this purpose the wheel was provided with balancing blocks.



Figures 1 and 2: Photograph and schematic cross-section of the grinding and wear apparatus.

b. Tool motion

The diamond tool is a block, 20x10 mm, cut from a grinding wheel. It is held in a brass holder, together with the dynamometer² for the measurement of up to three force components. The holder is subject to a horizontal and a vertical (fig. 2) motion. The first one is parallel to the axis of the wheel: it consists of a coarse motion by hand over 20 mm and a fine motion by motor over 1 mm. In order to increase the stiffness of the feeding construction, a wedge is used (held in cylinder bearings) which is moved by a spindle and motor. The feed rate v_w was given the values $v_w = 19, 43$ and $56 \mu\text{m/s}$, which correspond to a depth of cut of $a = v_w T_s = 0.76, 1.71$ and $2.22 \mu\text{m}$, where T_s is the motor period. The rate of material removal Z , is given by $Z = abv_s$ with $b =$ sample width; introducing the equivalent chip thickness h_{eq} by $Z = h_{eq} b v_s$, one has $a = h_{eq}$ for this apparatus. The Z values follow from v_w : $Z_1 = 166, Z_2 = 376$ and $Z_3 = 489 \text{ mm}^3/\text{s}$.

The second motion of the tool is in the vertical direction, in order to avoid the diamonds repeating the same grooves on the ferrite samples. By means a second d.c. motor and an eccentric a vertical amplitude of 0.8 mm is obtained with a period of 0.44 sec. This motor moves the wedge, its bearings, the tool and the first motor against the counteraction of two horizontal springs.

c. Samples

The ceramic samples were cut from blocks of MnZn ferrite (commercial grade, porosity 8%), taking care that all twelve samples were the same height when fastened on the wheel. The diamond tool was cut from an L-bronze wheel³, containing nominally 80 μm diamonds in a concentration 40 (10% volume concentration). The Vickers hardness of the binder was about 300 kg/mm^2 ($3 \cdot 10^9 \text{ N/m}^2$).

The experiments were performed as follows: for each Z value several runs were made; in each run about half of the heights of the ferrite blocks, i.e. about 6 cm^3 in total, was ground away. After a run the tool was inspected, the blocks were replaced and a new run was started. Five runs were made in the first stage (Z_1), three in the second (Z_2) and third (Z_3). The data will be characterized by the cumulative volume of ferrite removed at the end of the run and by the removal rate (Z) used in the run.

Before every run the tool was observed under a microscope and scanned by a rolling wheel as used in a roughness measurement. This procedure was found to be less satisfactory than making a permanent replica and measuring the wear there. Such replicas were made by pouring a mixture of powder and liquid⁴ on the diamond sample, which had first been surrounded by a plasticine dike. With some care air bubbles can be avoided. On the various replicas the individual diamonds could be followed as well as the details of the binder.

3. Results

a. Grinding force

The output of the dynamometer showed twelve pulses per revolution of the wheel, as expected for the same number of samples. Superposed is a slower modulation (period 0.44 s) due to the vertical motion. The force values, averaged over the modulation, showed no significant change with time due to wheel wear (with a much softer wheel we did observe such changes). The average normal and tangential force components increase with increased feed v_w , from which the grinding hardness ($20 \cdot 10^9 \text{ N/m}^2$) and the specific energy ($4 \cdot 10^9 \text{ J/m}^3$) can be deduced. These values correspond to $a = h_{eq} = 1 \mu\text{m}$. At higher h_{eq} the specific energy decreases strongly, as found before at wheel speeds of 60 to 100 m/s in a horizontal axis surface grinder [5].

2. Kistler, 9251 A.

3. Diamant Boart, Brussels

4. Technovite 5071.

On the successive replicas the amount of wear was measured with a microscope, using a conspicuous diamond as a reference. This particular diamond, a rectangle, was present in all replicas. Because of its uneven surface it was possible to measure the wear of the top - about 5 μm over the whole range of experiments - but this was negligible compared with the amount of wear of the binder as will be shown below. By scanning the replicas over a fixed line through this diamond, the profile was measured at 21 equally spaced points (fig. 3). The steeply rising parts at the ends of the profile are caused by the parts of the tool which did not show wear because the sample is less wide than the tool. The fluctuating data in figure 3 have been averaged over the active area. As can be seen in figure 4, the averaged results are linear in the amount of ceramic that was removed. From these data the G ratio can be calculated, taking into account that wear occurred on about half of the tool surface. The G values range from 29000 at low Z ($h_{eq} = 0.76 \mu\text{m}$) to 11000 at high Z ($h_{eq} = 2.2 \mu\text{m}$).

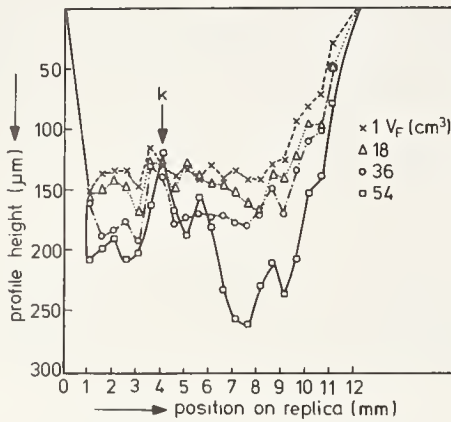


Fig. 3. Profile depths measured over the length of the replicas; the arrow points to the fixed reference diamond (k). Replica depth increases with tool wear. Data for various amounts of ferrite ground away (V_f).

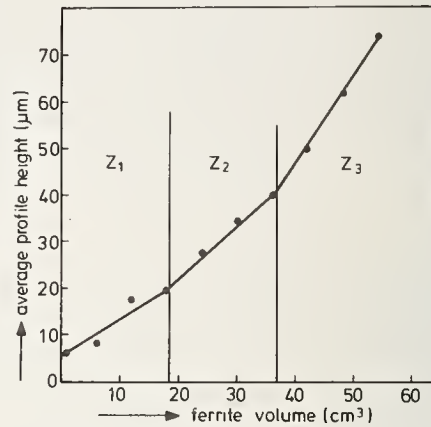


Fig. 4. Average profile height deduced from figure 3 versus ground volume. The three regions of different Z values are indicated. The zero point of the vertical axis has been shifted with respect to that of figure 3.

On the replicas the number of visible diamonds per unit area can be determined. At low Z the number is about 7 diamonds per mm^2 , independent of the ferrite volume. Loss of diamonds is apparently balanced by the emergence of new ones. At the highest Z value a decrease is observed to 5 per mm^2 (fig. 5). The details of this process will now be considered.

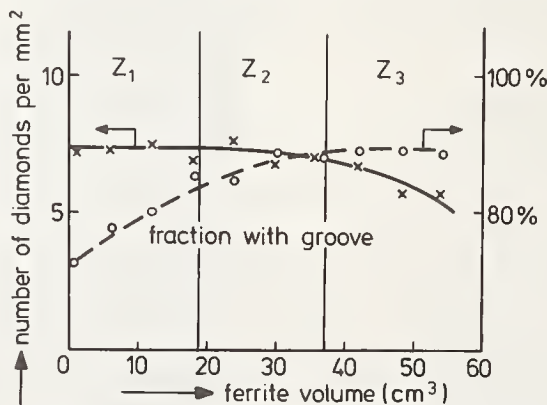


Figure 5. Number of diamonds per unit area, visible on replicas of the active part of the tool (full line), and the fraction of diamonds with a groove (broken line, right-hand scale), both as a function of the volume removed by grinding.

4. Details of wear

Comparing the same area on consecutive replicas one can observe the life and times of the various diamonds. Figure 6 shows a number of particles where all wear phenomena can be

seen. The diamond on the right (to be labelled j) is already active after 6 cm^3 has been ground; it shows wear flats, a widening groove in front and on both sides, and a hill behind it, which disappears as soon as the particle itself is lost (for this particle after grinding 42 cm^3). A second diamond (to be labelled e) appears on the left side of j and quite near to a square diamond. No wear is visible on e, and it is uncertain whether this particle contributed to the removal of ferrite. In the centre two diamonds become visible after 12 cm^3 , the upper one (to be labelled a) shows a nice groove after 42 cm^3 , whereas the binder in front of the lower one seems to be protected, although this particle is subject to some wear.



(a)



(b)



(c)



(d)

Figure 6. Diamonds a, e and j after grinding various amounts of ferrite. Photo (a): $V_F = 6 \text{ cm}^3$ diamond j on the right, a and e just emerging; (b): $V_F = 12 \text{ cm}^3$, a's edge above the middle, just right of a lost diamond, e is next to the white square on the right, both on the left of j; (c): 24 cm^3 , all diamonds quite well visible, a groove is forming around a and the white square; (d): 42 cm^3 , a has a deep groove and e's two neighbours have vanished, j's groove is nearly gone.

The fraction of diamonds with a groove on three of its sides increases from 30% at low Z to 70% at Z_3 , where it flattens off (fig. 5). In contrast to the G value, which is constant for each Z, the number of diamonds per unit area and the fraction with a groove still varies in the constant Z ranges.

We noted that a groove appears when the diamond emerges above the binder over a distance of 10 to $15 \mu\text{m}$. The groove in front is narrow, where the diamond has an edge, and wide where it has a flat plane. The groove on the side becomes longer with increasing grinding time.

The hill behind the particle seems to be a passive zone, since it appears only when the side groove makes it visible. A schematic view of the groove and hill is shown in figure 7.

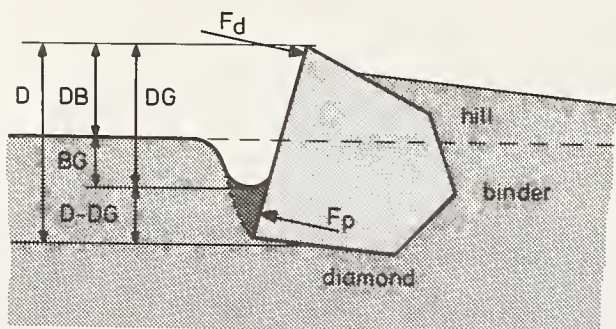


Figure 7. Schematic cross-section of diamond in binder, indicating the distances DG, DB and BG, the forces F_d (due to grinding) and F_p (ploughing the binder near the groove). D is the diamond size.

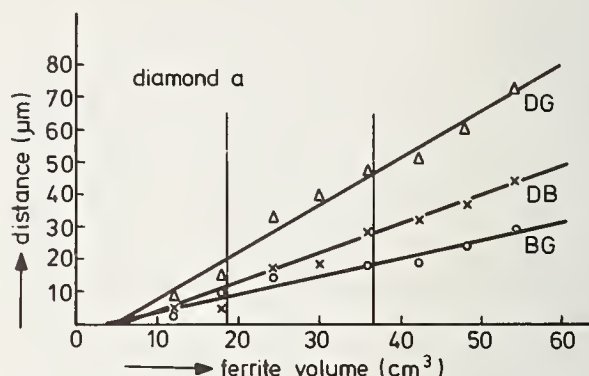
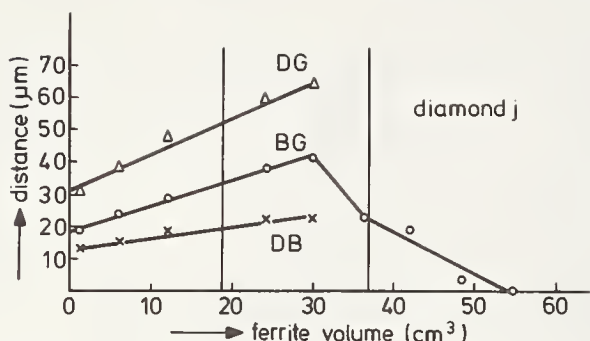


Figure 8. Measured values of the distance between top of diamond and binder (DB), diamond and groove-bottom (DG) and binder to groove (BG) for diamonds j and a. The three ranges of Z are shown. Along the abscissa is the volume ground away. After loss of diamond j the groove erodes away rather quickly (BG).

Table I. Data on selected diamonds of various shapes and with or without neighbours.

Name	Shape	Start run(stage)	Loss	DG(μm) max.	Erosion slopes ($\mu\text{m}/\text{cm}^3$)			Neighbour	Wear	Remarks	
					DB	BG	DG width				
a		3(I)	-	73	0.96	0.52	1.48	1.76	yes	no	
b		1(I)	8(II)	81	0.86	1.36	2.22	1.76	no	yes	fractured flat
c		4(I)	9(III)	61	0.70	0.46	1.16	2.31	no	yes	chipped
d		5(I)	-	75	0.72	1.01	1.73	0-1.7	yes(2)	yes	flat
e		3(I)	-	64	0.65	0.45	1.10	2.12	yes(j,a,o)	no	
f		1(I)	9(III)	66	0.53	1.01	1.54	1.79	no	yes	flat
g		7(III)	-	59	0.98	2.17	3.15	2.08	no	-	
h		5(I)	10(III)	65	1.37	0.72	2.08	2.33	yes(i)	yes	chip
i		2(I)	10(III)	45	0.38	0.20	0.58	0.60	yes(h)	yes	chip
j		1(I)	8(II)	65	0.34	0.74	1.08	-	yes(e)	yes	flat
k		1(I)	-	74	0.57	0.69	1.25	1.53	no	yes	flat
average erosion slope					0.73	0.85	1.58				
standard deviation					0.30	0.54					

Table I. Data on selected diamonds of various shapes and with or without neighbours. The run of first appearance is given under Start, the last run before loss is given under Loss. The runs are labelled 1-5 (I), 6-8 (II) and 9-11 (III), where the roman numerals refer to the Z values. The erosion slopes were determined from plots such as in figure 8. The definition of DG etc. is given in figure 7.

Quantitative data were obtained on eleven diamonds during the grinding of 54 cm^3 of ferrite. The rate of erosion of the binder far from the diamonds was measured from the distance between the top of the selected diamond and the level of the binder: diamond-binder data (DB) are shown in figure 8 for the diamonds e and j of the previous figure. Also shown are the distance between the average binder level and the deepest part of the grooves (BG) and the sum, that is the distance diamond-groove (DG). The geometric meaning of DB, BG and DG is shown in figure 7. All distances increase linearly with the volume of ferrite removed V_f . The slopes of the lines are given in table I, together with information about the shape of the particles, the presence of wear, the stage where the particle became visible and where it had disappeared, the corresponding maximum DG value and the presence of other particles nearby. No systematic variation is seen with shape, amount of wear or the presence of neighbours. After the particle has disappeared, e.g. diamond j in figure 6, the groove gradually disappears (fig. 8), where the hill vanishes within 6 cm^3 of ferrite volume. The DG value at loss is 65 to 80 μm , the BG value is about half this value.

5. Discussion

a. Binder erosion

In the previous sections three modes of wear were reported: diamond wear, loss of diamonds and binder erosion. The first two are unimportant in terms of volume and therefore of no direct consequences for the G ratio. The grinding action, of course, takes place where the diamonds are, which reduces the relevance of G as a grinding characteristic to a quantity that determines cost, once the wheel grinds, but does it? The capabilities of a wheel must be described by the details of the interplay of diamonds and binder together. The life of the particles in the case of the bronze-bonded wheel which we used consists of the following stages:

1. The diamonds emerge because the binder wears away; the rate of change of the number of diamonds visible on a unit area N is related to the change in the binder level and thus to the change in the distance DB by

$$\frac{dN}{dt} = N \left[\frac{d}{dt} \text{DB} \right] / L = NAZ/L \quad (2)$$

where L is the interparticle distance, A is the slope of the DB-ferrite volume V_f line in figure 8 and $Z = dV_f/dt$. From a count of the number of diamonds (Fig. 5) L is calculated to be 0.4 mm, which is a factor two more than expected on the basis of diamond size D (80-100 μm) and concentration C (10% by volume).

2. A groove is formed when the top of the particle is about 15 to 20 μm above the binder. The groove first forms in front of the particle, then also on the sides, leaving a passive area behind it; this grows into a hill, because of the groove getting deeper. Where the particle has an edge in front, the width of the groove is smaller than where it shows a plane face. Groove depth and width increase with time, just as the length and height of the hill.

3. At a given moment the diamond is lost. It may be that this happens because the distance DG between the top of the particle and the bottom of the groove has reached a critical value, between 50 and 80 μm . The hill disappears very quickly, the grooves take longer to disappear. In this stage the change in binder-groove distance, BG, is faster than the binder erosion itself, given by DB (fig. 8).

From these observations one can state precisely what is meant by "the diamond protects the matrix" [3]: If there is no diamond, the matrix (i.e. the binder) wears away, whereas if there is a diamond, part of the matrix wears away much quicker (the groove), part does not wear at all (the hill), until the diamond is lost. The latter process does not contribute much to the G value, at least for the Z values used here, because diamond loss is a relatively rare event. A "background" value of binder loss is given by the change in the height DB, taken far from a diamond; as in eq.(2) the rate of change equals $A \cdot Z$; from table I, $\frac{d}{dt} \text{DB} = 0.73 Z$, which gives a G value of 55000 independent of Z. The G values reported here are smaller and do depend on Z. The reason is the formation of grooves near the diamond: their width, depth and length all increase with Z, their volume thus increases stronger than proportional to Z.

The presence and the shape of the grooves near the place where the grinding debris is formed suggest that the binder wear is an erosion process, caused by the hard ceramic particles, probably in combination with the cooling water. The wear on the flat binder is less than near the diamonds. This resembles the results of Thomas and Brunton [6] in their study on erosion of metals by water jets at speeds up to 125 m/s. They found that on a flat surface hardly any wear occurs, whereas a disturbance, e.g. a groove, has a considerable effect. This may also be relevant for the faster binder wear near the groove when the diamond has disappeared. The rate of change of the binder height can be discussed in terms of the well-known relation between rate and pressure,

$$\frac{dh}{dt} = k P v_s / H_b \quad (3)$$

where H_b is the binder hardness, k a constant and P the unknown pressure exerted by the particle responsible for the material removal. From the average values of the rate of change of DB and DG in table I and the Z values, kP is calculated from eq.(3) to be of the order of 100 N/m^2 . For a free particle erosion [7,8] P is expected to be of the order of $\frac{1}{2} \rho v^2$, where ρ is the particle density (here about $5 \cdot 10^3 \text{ kg/m}^3$) and v the particle velocity. If v equals v_s , the P value would be 10^6 N/m^2 , which makes k about 10^{-4} .

One reason for this low value may be that the horizontal motion of the water in the gap between workpiece and binder disturbs the vertical motion of the debris that is generated at the top of the diamond and moves along the leading plane downwards to the foot of the diamond. The water moves near the top at $v_s = 22 \text{ m/s}$ and is presumably turbulent (this raises the question of whether more viscous liquids would show less binder wear). For smaller diamonds the high water speed would be more effective. Another reason for low wear rate near the diamond might be that perpendicular erosion [7,8] on metals is much less effective than when the particles impinge under an angle of $10\text{-}20^\circ$. The latter case may apply to the wear of the flat part of the binder, as measured by DB in table I.

The experimental data are limited to one combination of binder (H_b), wheel speed (v_s) and diamond size (D). In the erosion model one would expect higher wear rates for softer binders, higher wheel speeds and smaller diamonds. The present results are too limited to check this.

b. Diamond loss

The lifetime of a diamond, from its emergence to its loss, plays an important part in the choice of a binder for a given work-piece. The short duration of the present experiment did not allow the quantitative determination of the life for a single Z value. In the following model a crude estimate of the lifetime t_c can be made from the grinding force on the one hand and on the other from the "holding force" of the binder at a given groove, DG. One finds (see appendix)

$$t_c = \frac{(DG)_{\max}}{BZ} = \frac{D}{BZ} \left[1 - \left(\frac{H_w}{H_b} \right) \frac{Z}{v_s D^2 N_d} \right] \quad (4)$$

where B is the slope of the DG - ferrite volume line (Fig. 8), H_w is the grinding hardness of the workpiece and N_d the number of diamond in contact.

When the lifetime of the diamonds is too long and the particles become blunt, the expressions (1) and (4) can be used to determine which factor (H_b , D , v_s , Z , C) should be changed. Although a number of rules found in the literature agree with this equation [3, 9, 10], it is obvious that the limited extent of the present experiments is not sufficient to prove their validity.

6. Conclusions

An apparatus has been described which allows the measurement of the wear of small parts of a grinding tool, as well as the grinding force. With the aid of replicas of the tool made at regular intervals, the details of the diamond and binder wear could be followed. Apart from some diamond blunting, the formation of grooves near the diamond was observed. Loss of diamond occurred when a certain groove depth (here $50\text{-}80 \mu\text{m}$ for $80\text{-}100 \mu\text{m}$ diamonds) had formed. The life of the diamonds is determined by the erosion of metal

binder, which is presumably caused by the action of the debris particles. Although detailed results were recorded, which allowed some conjectures about diamond loss and the need for dressing, the experiment was limited to one binder, one workpiece material, one wheel speed and one diamond size and concentration. Obviously more data are necessary for an accurate prediction of the behaviour of the combination of workpiece, diamond and binder.

The author is indebted to a number of colleagues for discussions about the principle of the investigated wear tester, to P. Merkelbach for the design of the apparatus and to M.A. Immerix for his dedication in testing the apparatus and performing the experiments.

References

- [1] Malkin S. and Cook N.H., The wear of grinding wheels, J. Eng. Ind. (Trans. ASME) 93, B4, 1120-1133, (Nov. 1971).
- [2] Freeman J.P., Some aspects of the evaluation of diamond wheels in dry grinding (Proc. Int. Ind. Diamond Conf., Oxford 1966), Book, Science and Technology of Industrial Diamonds II, J. Burls, ed., pp. 263-271 (Ind. Diam. Inf. Bur., London, 1967).
- [3] Thomas D.M., Some aspects of wheel formulation in ceramic grinding, Ind. Diam. Rev., pp. 504-507 (Dec. 1971).
- [4] Gielisse P.J., Kim T.J., Choudry A., Short J.F. and Turker E.J., Force and wear analysis in ceramic processing, Report, pp. 35 ff. (Univ. Rhode Island), Kingston R.I. (1972).
- [5] A. Broese van Groenou, Grinding experiments on ceramics, (Proc. 9th Int. Conf. on Science of Ceramics, Noordwijkerhout, November 13-16, 1977), Book, Science of Ceramics Vol. 9, K.J. de Vries ed., pp. 486-493 (Nederlandse Keramische Vereniging, 1977).
- [6] Thomas G.P. and Brunton, J.H. Drop impingement erosion of metals, Proc. Roy. Soc. London, A314, 549-565 (1970).
- [7] Oh, H.L., Oh K.P.L., Vaidyanathan, S. and Finnie, I., On the shaping of brittle solids by erosion and ultrasonic cutting, (Proc. Symp. Science of Ceramic Machining and Surface Finishing, Gaithersburg, Md, 2-4 Nov. 1970) pp. 119-132 (NBS Spec. Publ. 348).
- [8] Engel, P.A., Impact wear of materials, pp. 106-110 Elsevier Scient. Publ. Cy, Amsterdam, (1976).
- [9] Reed, J.R., Applying metal bond diamond blades - art or science? Ind. Diamond Rev., pp. 291-296 (Aug. 1973).
- [10] Decneut, A. And Aerents R., Etude théorique et pratique du comportement des meules diamantées et à base de nitrure de bore cubique, (Preprints Intergrind 76, Nov. 1976, Västermik, Sweden).

Appendix

The lifetime of a diamond

The following model takes into account the presence of a groove in front of the diamond and the grinding force which tries to rotate the particle against the resistance offered by the binder. The binder is assumed to yield when the stress near the groove exceeds the yield stress of the metal. The shaded area in figure 7 is removed by a "ploughing" force,

$$F_p = H_b b (D-DG) \quad (A1)$$

where $b \approx D$ is the width of the diamond and H_b the stress necessary for the ploughing. The grinding force F_d is given in eq.(1). As soon as F_d exceeds F_p the particle rotates and is lost. This occurs when at time t_c the distance DG has reached its maximum value $DG_{max} = BZ t_c$:

$$F_p = H_b D(D-BZ t_c) = F_d = H_w Z/v_s N_d \quad (A2)$$

This leads to eq.(4). The ratio H_w/H_b may be about 10; this is multiplied by a term of the order of d^2/D^2 . Since in heavy grinding the depth of cut for one diamond, d , may be an appreciable fraction of its size D , the second term in t_c is by no means negligible.

CHOUDRY

Could not the formation of the 'hill' and the 'groove'; behind the diamond grain; be interpreted as the process in which the diamond grain acts on both the workpiece and the bronze matrix. The latter is plastically deformed forward in the 'plowing' mode forming the 'hill' whereas the 'groove' is just cavitation due to the the motion of the grain. In this manner, one does not have to invoke the erosion of the bronze matrix by the workpiece debris, and the process would thus be dominated by the plastic yield strength of the matrix.

VAN GROENOU

Would this mechanism not depend on the force exerted on the diamond - or on the workpiece? The force would increase from zero at no contact until a maximum value when the diamond is lost. We have found that the grooves start rather early in the life of a diamond, when it protrudes about 15 to 20 μm above the binder. I am not sure that such a particle is taking part in the grinding. Moreover, the rate of change of depth of the groove seems to be linear in ferrite volume rate, i.e. force, and not be increasing the more the particle cuts into the workpiece. The proposed mechanism also raises the question, why the groove extends behind the particle, sometimes even in a symmetric warp. Would not the distance between a not-yet active diamond and an active diamond increase, if the latter is pushed into the binder? We did not notice this.

GIELISSE

Might there be anything unique about your results on ferrites in as much as there are many examples to quote in which diamonds in wheel-applications do show considerable wear before pull out? In any case, thank you for a very nice piece of work.

VAN GROENOU

The apparatus can be used for many other combinations of binder - diamond-workpiece. The wear that was found here for a ferrite is only moderate, for harder workpiece materials different results are expected. As regards to self-sharpening of the wheel, the present combination seems to be a good one.

NEW CONCEPTS ON SURFACE FINISHING AND ITS APPLICATION TO CERAMICS
----- RECENT PROGRESS IN ULTRA-FINE FINISHING IN JAPAN -----

Osamu Imanaka

Department of Precision Engineering, Kanazawa University
Kodatsuno, Kanazawa, Ishikawa 920, Japan

Mamoru Okutomi

Electrotechnical Laboratory, MITI
Mukodaimachi, Tanashi, Tokyo 188, Japan

This paper outlines the ultra-fine finishing techniques developed in Japan. First, mechanical behavior of a crystal is considered in connection with the "working unit", that is, a bit of stock removal or the range of stress field induced in the working zone. Since the defects pre-existing in the stressed part affect the microscopic deformation or fracture of the material, importance of the working unit as a basic concept in machining or fine finishing should be emphasized. As an attempt to realize ultra-fine finishing by minute elastic fracture of the lattice size order, the study on "Elastic Emission Machining" is described. Chemical phenomena in abrasive machining process are also dealt with; these have led the development of mechanochemical finishing techniques, e.g., "mechanochemical polishing of a hard crystal with a softer powder", and "hydration polishing". Polishing characteristics for the latter method are somewhat detailed. Additionally, fine finishing techniques of ceramics by electron beams and ion beams are reviewed.

Key Words: Damaged layer; "elastic emission machining"; environmental effect; hydrate; hydration polishing; mechanochemical polishing with soft powder; pre-existing defect; sapphire; solid state reaction; "working unit"; water vapor.

1. Introduction

Material processing could be defined as the procedure which makes a material "memorize" or fix certain desired information by supplying the working energy to it. The desired information to be fixed is usually the dimensional accuracy or surface roughness. In some cases, e.g. in manufacturing electronic and opto-electronic devices, physical perfectness of the finished surface is increasingly needed. As to integrated circuits in the electronics field, the surface of silicon wafers, for example, have to be finished to a high grade of flatness, onto which very thin films of precise thickness are coated and some impurities are doped to precise depths. This is the reason that the crystallographically undisturbed surface, free from chemical contamination is necessitated. This kind of ultra-fine finishing or machining is required in processing of laser elements, crystal and ceramic oscillators, and so on. Moreover, in manufacturing mechanical parts of high precision machines, endeavor is being made to obtain not only geometrical accuracies but also high grade surfaces with the minimum deteriorated layers.

It would be a new trend in precision machining to attain surfaces of higher dimensional accuracy without vitiating the original function of the material. From the emergent needs based on these industrial requirements, new techniques have been investigated and developed in Japan with substantial results. In this paper, some of these are outlined. Their background, conception and development are also considered.

2. Mechanical behavior of material in connection with the range of stress field

In finishing or machining processes of materials, mechanical behavior of the materials

is an important factor that affects the surface texture generated. In abrasive machining, for instance, the material removal and the surface finish are brought out by a sum of microscopic deformation or fracture at the point where an abrasive grain acts at the working instant. The mechanism of machining would vary according to the size of stress field induced in the working zone. The size of the stress field is hereafter called "working unit".

Yoshikawa [1]¹ theoretically studied the effects of the working unit upon the material behavior, and gave the basis to select the finishing method which is optional for the surface property required. He classified the working unit into four domains as shown in figure 1 [1]. Each domain is characterized by the lattice defects which preexist or have been generated by processing. Investigation of the operating predominance of lattice defects for each domain revealed the following distinct behavior of crystals when impressed by an indenter.

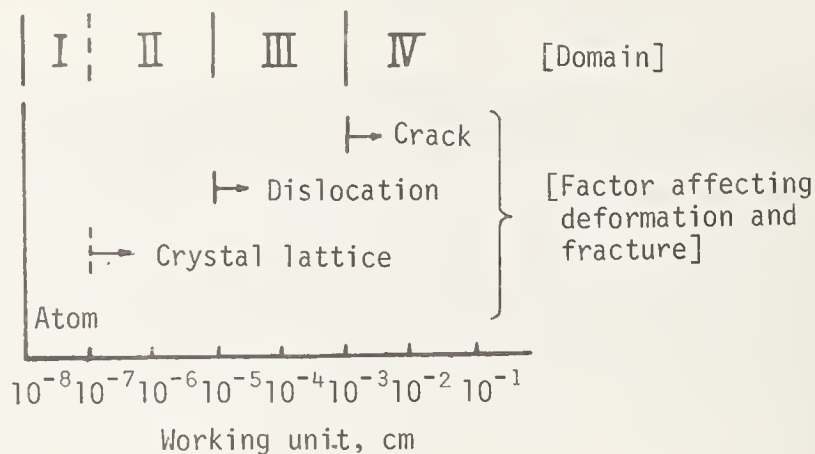


Figure 1. Factor affecting deformation and fracture.

In domain I, material removal of the order of atoms or molecules has been done generally by chemical decomposition, electrolytic decomposition, evaporation, and ion sputtering processes. Material removal of this order could not occur by purely mechanical means. Chemical action activated by mechanical stress may play a role in material processing in this domain.

In domain II, where no dislocations and no cracks exist, a crystal should behave mechanically as an ideal crystal. Theoretical consideration proved that the impressing of an indenter upon a crystal surface in this domain gives rise to generation of dislocations prior to brittle fracture. After dislocations have generated, a crystal is thought to behave as in domain III.

In domain III with only dislocations, plastic deformation occurs first, some amount of which allow cracks to nucleate in the deformation zone. In domain IV, the crack defect is the dominant factor. This can be realized by the indentation onto glass surface using indenters with different tip radii. Contrary to the case where a ball indenter with relatively large radius produces ring cracks on the glass surface, a sharp indenter at relatively light load yields a plastic indentation mark. The breaking tensile stress to cause the ring crack is estimated at about $10 \sim 50 \text{ kg/mm}^2$, and the shearing stress under the plastic indentation at about $400 \sim 800 \text{ kg/mm}^2$. The brittle fracture of glass is caused, as is well known, by pre-existing surface cracks, which are intrinsically distributed with a density of the order of $10^8/\text{cm}^3$ (mean distribution pitch = $10 \mu\text{m}$). Therefore, if the indentation area becomes smaller than about $10 \mu\text{m}$, brittle fracture caused by tensile stresses can no longer occur. Figure 2 also shows an example of a relatively large working unit which causes brittle fracture in high strength material at relatively low stress. Here, the alumina ceramic specimen was attacked by a water jet of 0.15 mm diameter at exit pressure of 10 kbar [2].

¹ Figures in brackets indicate the literature references at the end of this paper.



Figure 2. Fracture of alumina ceramics caused by water jet of 0.15mm diameter at 10kbar.

The concept of the above-mentioned working unit might establish some general rules for selection of machining methods or conditions. In rough machining of ceramic materials, a comparatively large working unit should be adopted to obtain efficient removal rates. Rough lapping with coarser grains at higher pressure, for instance, is the case, where the vertical load acting on each grain is higher and the material removal proceeds by micro-fracturing. In the aspect of working energy, a large working unit was proved to be efficient [3].

In fine finishing, the working unit smaller than the distribution of crack defects has been selected from experience. Polishing with finer grains on soft polishers demonstrating elastic or viscoelastic behavior at lighter pressures are the examples. To achieve ultra-fine finishing mechanically, the working unit should be at least smaller than the dislocation level.

3. Ultra-fine finishing by utilizing minute elastic fracture

Tsuwa, Osaka University, and his colleagues [4, 5, 6, 7] have examined the possibility of mechanically machining on the order of lattice dimensions to obtain finished surfaces which are not only of mirror quality but are crystallographically and physically undisturbed. The fundamental concept is that the collision of fine powder particles with the work surface, if the size of stress field becomes smaller than the distance between the pre-existing defects, may cause the elastic fracture of the order of the lattice size and may not leave a plastically deformed surface layer. The density of pre-existing dislocations has a certain limit and is of the order of $10^8/\text{cm}^2$. Thus, the distance between them is of the order of $1\ \mu\text{m}$. The crystal structure and the strength of material between the defects can be assumed as the ideal ones. If the fracture is introduced mechanically in the minute ideal crystal parts between defects, and if the pre-existing defects do not act, elastic fracture may occur which destroys the ideal binding of atoms. This conception led the new finishing method named as "Elastic Emission Machining" (EEM). The principle of EEM is schematically shown in figure 3 [4].

In this case, a doubt may arise on the feasibility of EEM, that is, when powder particles collide with the ideal crystal parts, new dislocations and cracks may be induced. However, the emergence of dislocations and cracks in these ideal crystal parts may mean that the tensile or shear fracture is overcoming the ideal strength. This suggests that ideal elastic tensile fracture or shear fracture of the order of the lattice size can be introduced by controlling the magnitude, shape and orientation of stress field, for example, by shooting the powder particles almost parallel to the work surface.

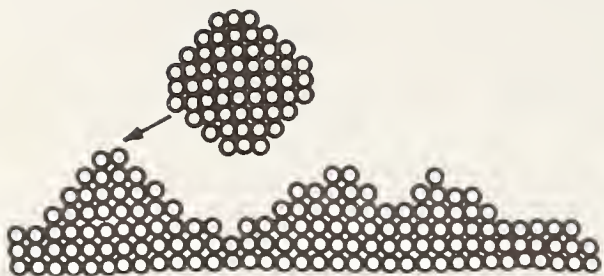


Figure 3. Model of elastic emission machining.

The collision of powder particles with the work surface was done in the following way: vibratory collision (fig. 4 [5]), circulatory collision using rotary disk (fig. 5 [4]), circulatory collision using gas stream (fig. 6 [4]), and charged particle collision using electrostatic acceleration (fig. 7 [7]). Factors governing the machining characteristics of EEM are the density of pre-existing defects in the material, their mobility, elastic properties and binding energy of the material and so on. As for powder particles, the factors are size, angle of collision, kinetic energy and so on.

In figure 4, powder particles are loaded on the workpiece in a container. Horizontal vibration of the container (frequency 30 Hz, amplitude 4mm) gives the mutual displacement of the workpiece and powder particles. The surface of the workpiece is intended to be finished by the collision with powder particles in the horizontal direction. The vertical load can be taken as the weight of each particle itself. Mean kinetic energy given to a single particle is calculated to be 4.3×10^{-3} , 2.6×10^{-4} and 4.0×10^{-6} erg for alumina particles of 20, 8 and $2 \mu\text{m}$ diameter, respectively. Assuming that the kinetic energy is converted to the surface energy at the time of fracture, and that the surface energy is of the order of 10 erg/cm^2 , it becomes possible to fracture the area of 200, 13 and $0.2 \mu\text{m}^2$, respectively. It was proven that the electron diffraction image of a Si single crystal surface finished with $2 \mu\text{m}$ particles is composed of clear spots and Kikuchi lines.

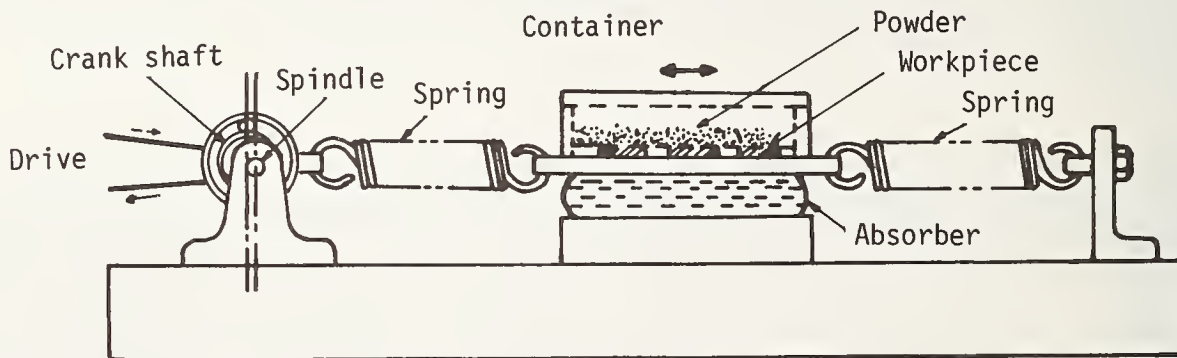


Figure 4. Schematic diagram of vibratory EEM Apparatus.

Figure 5 shows an apparatus made for ductile materials. In the figure, rotation of the disk accelerates the powder and N_2 gas in the container. Experiments were done with $0.1 \mu\text{m}$ zirconia at 50 m/s peripheral speed of the disk. Aluminum single crystal was reported to be finished fairly successfully.

In Figure 6, particles are enclosed in a closed circuit and circulated with air by means of a blower. From the electron diffraction patterns of the finished Si surfaces with zirconia powder of 0.1 and $0.6 \mu\text{m}$ diameter at the collision angle (α) of 20° , 30° , and 45° , it became evident that the smaller the particle size is and the smaller the collision angle, the better crystalline property is retained. Namely, the extent of stress field and its direction at the time of collision are related to the quality of finished surface.

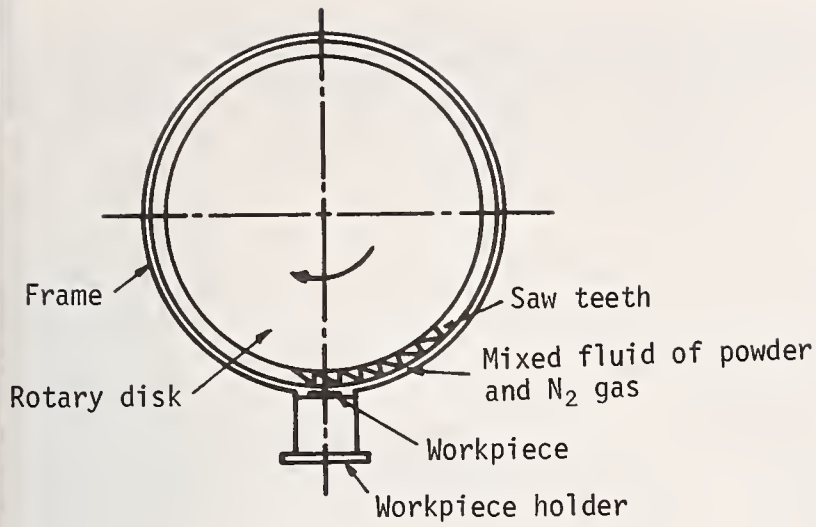


Figure 5. Schematic diagram of rotary EEM apparatus.

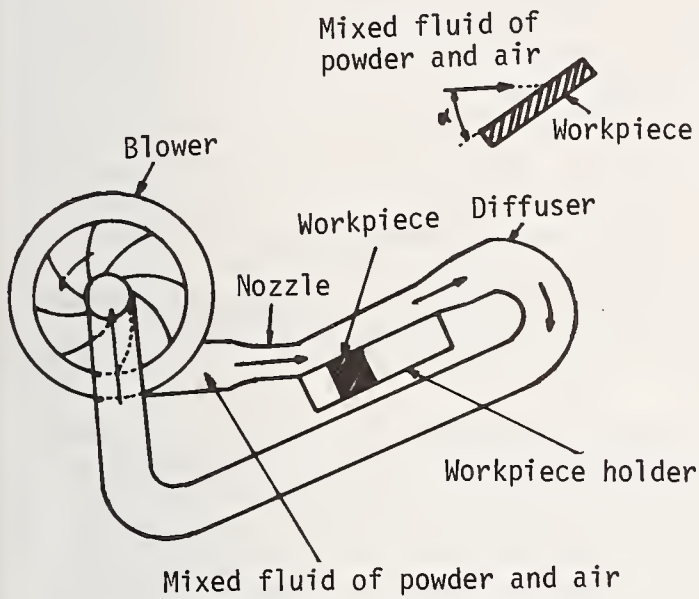


Figure 6. Schematic diagram of EEM apparatus using blower.

To realize EEM using electrostatic acceleration, a new type of powder particle beam gun was developed [6,7]. The apparatus shown in Figure 7 was reported to accelerate the tungsten particles of 5 μm diameter to the velocity of 570 m/s at the accelerating voltage of 100 kV. The beam density of 10^9 particles/s.cm² was obtained.

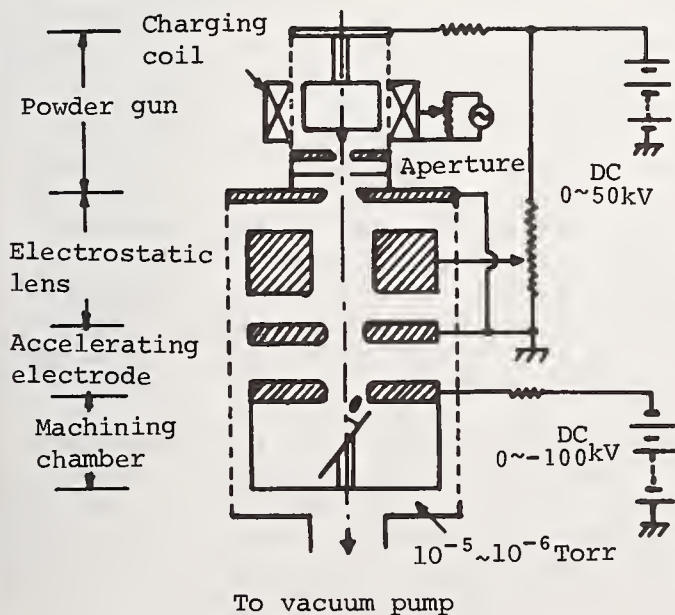


Figure 7. EEM apparatus using electrostatic acceleration.

Recently Suzuki and Watanabe [8], Musashino Electric Communication Laboratory, Nippon Telegram and Telephone Public Corporation, have developed a surface polishing machine utilizing the principle shown in figure 5. As shown in figure 8, workpieces are floating on a rotating annular disk. Slurry lying between them collides with the work surface. Adding some chemical agents in the slurry, chemo-mechanical polishing is also done.

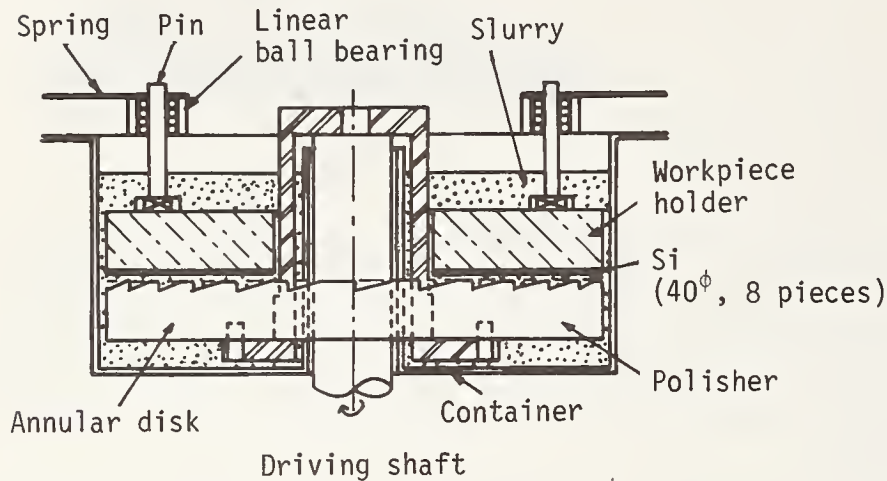


Figure 8. EEM apparatus modified from figure 5.

4. Chemical phenomena in abrasive machining

As the background of the development of new finishing methods described in the next section, this section briefly deals with chemical interactions between the work materials, grain and machining environments.

When thread-grinding a glass bobbin for a standard inductor to be used in the absolute measurement of electric resistance, one of the authors experienced the importance of chemical phenomena in abrasive machining [9]. At that time, the wear rate of alumina grains on the grinding wheel used was recognized to be higher than anticipated, in spite of the facts that Al_2O_3 is much harder than the glass. The wear was dependent on grinding environment. The same tendency was also observed in grinding steel. Thorough investigation confirmed that the chemical phenomena at the interface played a significant role in the wear of hard materials. That led to the development of the mechanical polishing method, [10,11]. This novel surface finishing technique will be detailed in the next paper in this symposium.

For fundamental understanding of the effect of machining environment or of fluid on the fracture behavior of abrasive grains, the fracture strength of alumina grain was measured by quasi-static loading and by repeated impact loading in various environments [12]. Main results obtained were as follows: The strength of the grain may be lowered with the increase of surface tension and dipole moment of surrounding liquid medium. This can be explained mainly by the lowering of the surface free energy of the grain by adsorption of surrounding fluid on their surface or their surface being wetted by the liquid. As to the effect of superheated water vapor in a stress field, as shown in figure 9 [12], water vapor lowers the fracture strength as its temperature is raised. This effect can not be explained by physical adsorption, for, in physical adsorption, the amount adsorbed which must be related to the strength of the specimen, becomes smaller as the temperature is raised. The prior exposure of a specimen to superheated steam under an unstressed condition (aging) caused an irreversible change in its fracture strength, which suggests that a structural change of the specimen surface has occurred. In fact, x-ray analysis of finer powder aged in superheated steam for a considerable time showed the formation of alumina hydrates.

As an example of the formation of alumina hydrates under a stressed condition for a short time duration, Figure 10 [13] is given, where the grinding wheel used was WA46N-nV and the temperature of water vapor sprayed, 100 °C. Under grinding environments containing water vapor, various diffraction lines of alumina hydrates (gibbsite, boehmite, and diaspore) are seen. The formation of alumina hydrates can be considered as the reaction between the activated alumina surfaces and water vapor molecules. On the worn alumina grain, surface

deposits and metallic layers were not observed; the smooth wear surface was found. Moreover, the hydrates were also identified from the x-ray analyses of the ground chips collected. These results inspired the development of the "Hydration Polishing" method to be mentioned in the next section.

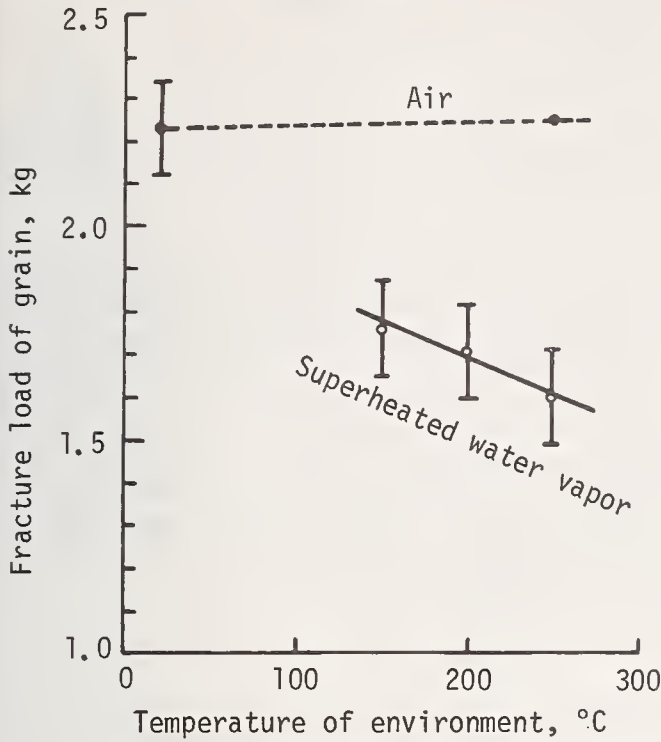


Figure 9. Effect of superheated water vapor on fracture load of Al_2O_3 grains.

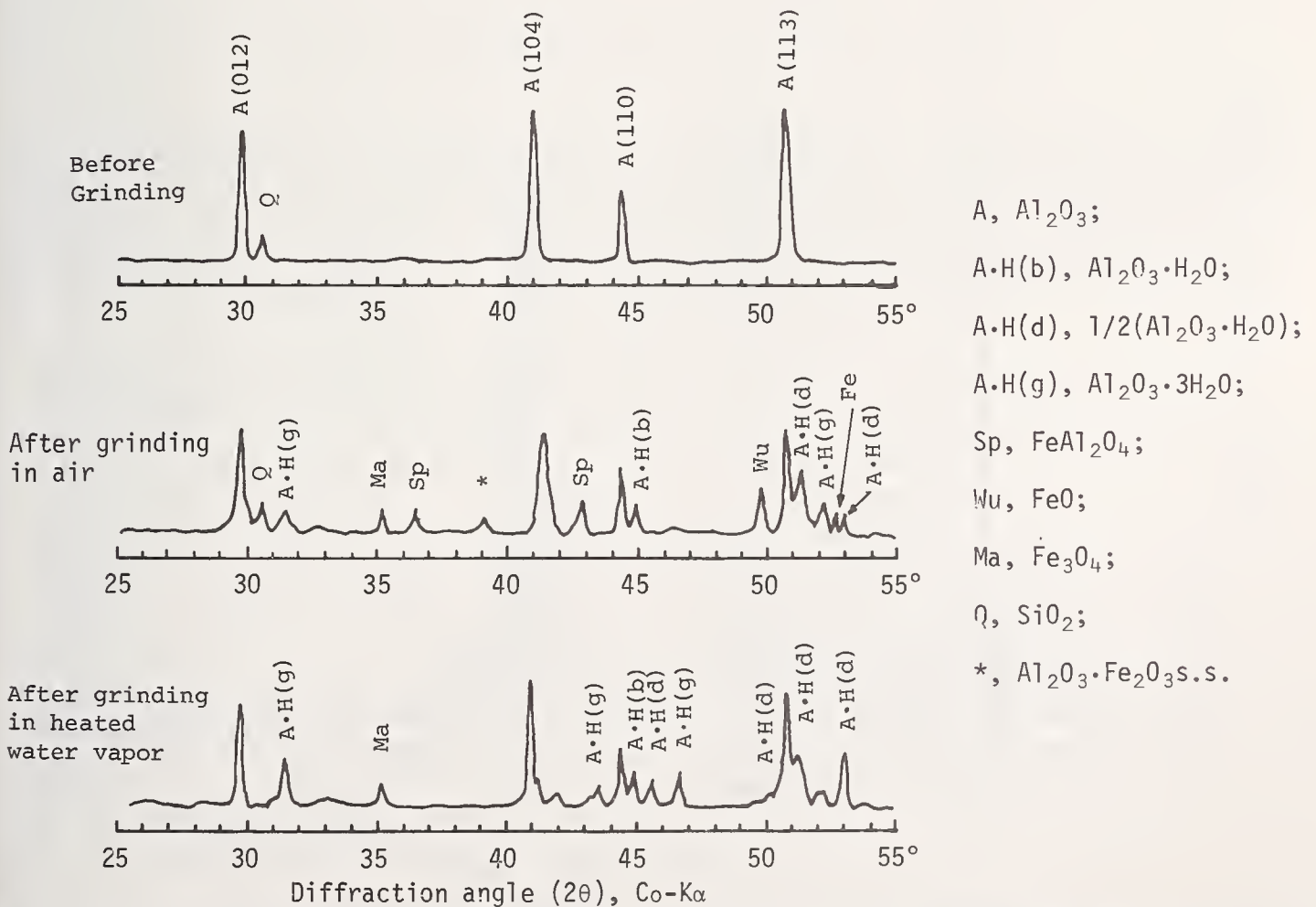


Figure 10. X-ray diffraction patterns of Al_2O_3 wheel surface after grinding mild steel. Grinding distance was 33.6m.

collected. These results inspired the development of the "Hydration Polishing" method to be mentioned in the next section.

5. Ultra-fine finishing by utilizing mechanochemical phenomena

5.1 Mechanochemical polishing with soft powder

This newly developed finishing technique [10,11] is based on mechanochemical reactions at real contact points between the work and powder, which is mechanically softer than the materials to be worked, and can react chemically with them. The mechanism and application of this technique will be detailed in the next paper in this symposium.

In addition, Namba and Tsuwa of Osaka University [14] have recently reported the surface characteristics of sapphire finished with various soft powders on a tin polisher. Ion microprobe analysis revealed the existence of iron atoms or ions on the sapphire surface finished with Fe_2O_3 powder as shown in figure 11 [14], where ions of carbon and hydrogen are contaminations. Figure 12 [14] gives the depth profile of $^{56}\text{Fe}^+$. The curve does not show the exact chemical composition due to the characteristics of this analysis, but shows that iron exists in the first few monolayers of the finished sapphire surface. In the case of finishing with LiF powder, the first few atomic layers (less than 10\AA) on the finished surface were proved to contain atoms constituting the used powder. These results may suggest the occurrence of solid state reaction between the work material and the powder.

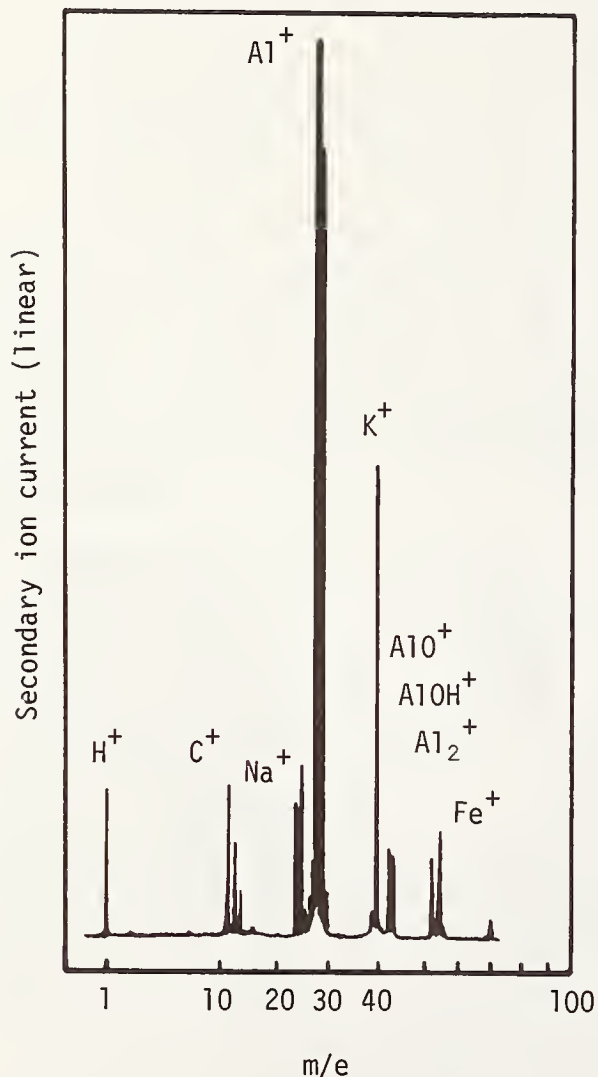


Figure 11. Ion microprobe analysis of sapphire surface finished with Fe_2O_3 powder.

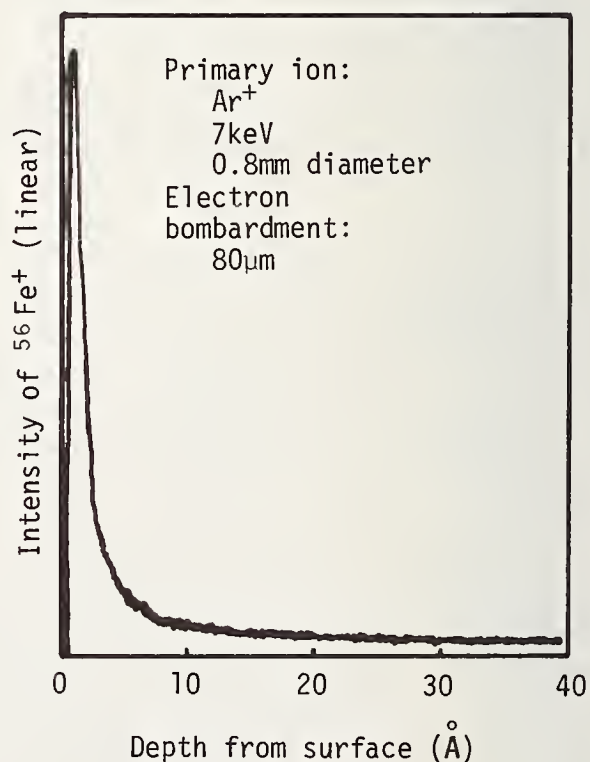


Figure 12. Depth profile of $^{56}\text{Fe}^+$ on sapphire surface finished with Fe_2O_3 powder, obtained by ion microprobe analysis.

5.2 Hydration polishing

This surface finishing method has been developed on the basis of hydration phenomenon, occurring by the action of water vapor molecules on the stressed surface of the hydrophilic material to be polished [15,16]. Its feature is to use neither powder nor chemical etchants. Polishing is done in the environment containing superheated water vapor. Hydrates formed on the activated surface are rubbed off by the friction of the polisher. If the hydration occurs only at the true contact point between the work and the polisher, and if only the hydrates are removed from the work surface, this method may fulfill the ultra-fine finishing of the order of molecular size and yield the surface with the least possible defects.

Figure 13 shows the apparatus used in the experiment. A lapping machine is enclosed in an electric furnace. To the apparatus, saturated water vapor can be introduced from autoclave. The temperature of the introduced steam can be equalized by heaters to a certain desired value from 100 to 200°C. The specimens used were mainly synthetic sapphire, which were lapped with SiC abrasives of #4000 grit size prior to every polishing test.

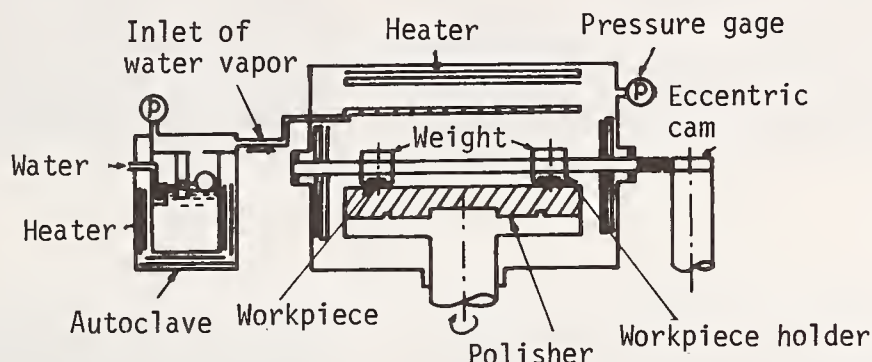


Figure 13. Schematic diagram of hydration polishing apparatus.

The polishing rate of sapphire is shown in figure 14, where the polisher materials used were straight-grained cedar wood (H_V , 100 ~ 210 kg/mm², average width of annual rings, 4 mm) and carbon for electric use (H_V , 380 kg/mm²). Polisher materials in hydration polishing are desired to be inert to water vapor and to be undeformable under hydrothermal conditions. In the figure, the polishing rates with carbon polisher are seen to be higher in the lower temperature range than those with cedar wood polisher. This would be due to the difference of the hardness between the polishers.

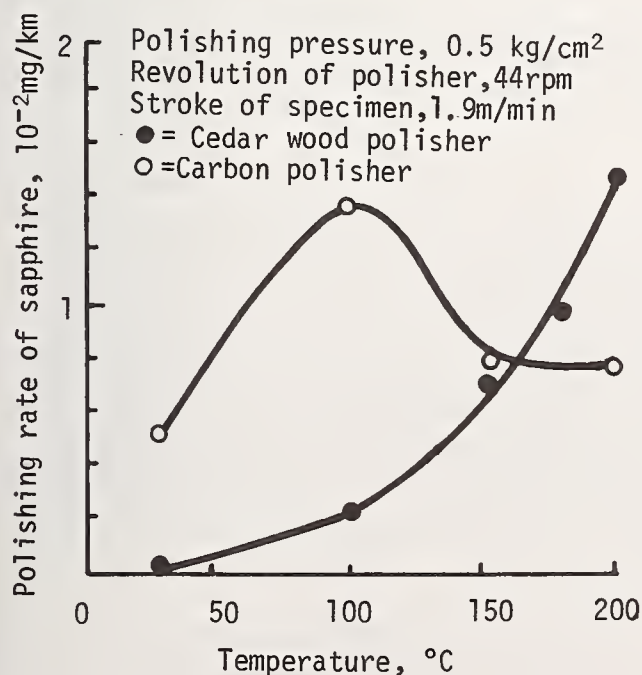


Figure 14. Effect of water vapor temperature on polishing rate of sapphire.

The surfaces obtained with the different polishers are shown in figure 15. The surface with cedar wood polisher is very smooth and free from scratches. In the case of carbon polisher, carbon layers were observed to adhere to some sites on the polished surface in the high temperature range. The adhesion would affect the polishing rate. On the surface with mild steel and silica glass polisher, are seen small scratches (fig. 15-b) and many deposits which may be considered as the fine debris removed from the polisher during processing (fig. 15-c). Mechanical polishing with diamond paste leaves the deep scratches on the surface as shown in figure 15-d.

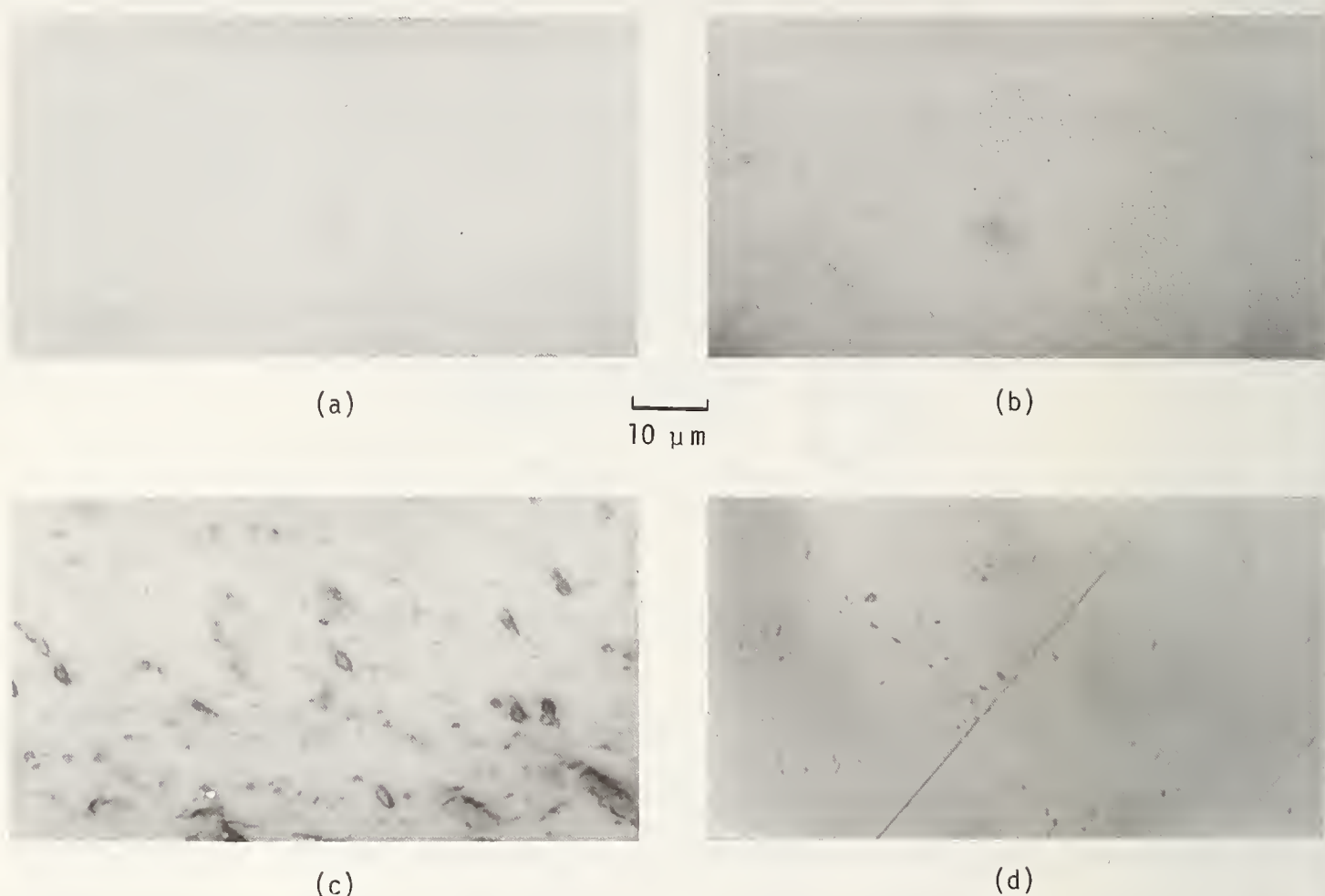


Figure 15. Sapphire surface finished by different processes: (a) hydration polishing with cedar wood polisher, (b) hydration polishing with mild steel polisher, (c) hydration polishing with silica glass polisher, (d) conventional diamond polishing at room temperature.

Figure 16 shows the sapphire surfaces reacted under a controlled partial pressure of water vapor. The analysis of the aged specimen and the hydration-polished surface by means of Raman spectroscopy (with reflected Ar laser) revealed the following: The spectra of H-O is seen in the range of $3000 \sim 4000 \text{ cm}^{-1}$ on the aged surface, as shown in figure 17. On the polished surface, the H-O spectra were not identified, but appearance of fluorescence scattering was found. The results obtained with ESCA proved that the hydration polished surface of sapphire shows little chemical shift in Al levels. From the results mentioned above, it might be concluded that the sapphire surface hydration polished is clean from the hydrates and hydroxyl groups and shows little disorder of crystal lattice. These phenomena would be the minimal effect of the hydroxyl group coordinate bond to the Al_2O_3 surface. The present technique could also be applied to final polishing of hydrophilic crystals.



10 μ m

Figure 16. Reaction products on the sapphire surface aged in water vapor at 135°C, 2.5kg/cm² for 20hr.

6. Surface finishing by non-traditional methods

6.1 Ion beam sputter-machining

Ion beam sputtering is basically a knocking-out of atoms composing the work material due to bombardment of inert gas ions with high kinetic energy. That is, the bombarding ion makes sequential elastic collisions with atoms in the target material and knocks out the atom from its surface layer. Therefore, the sputtering is essentially a non-thermal process, and can remove the stock of the work material by the order of atomic size.

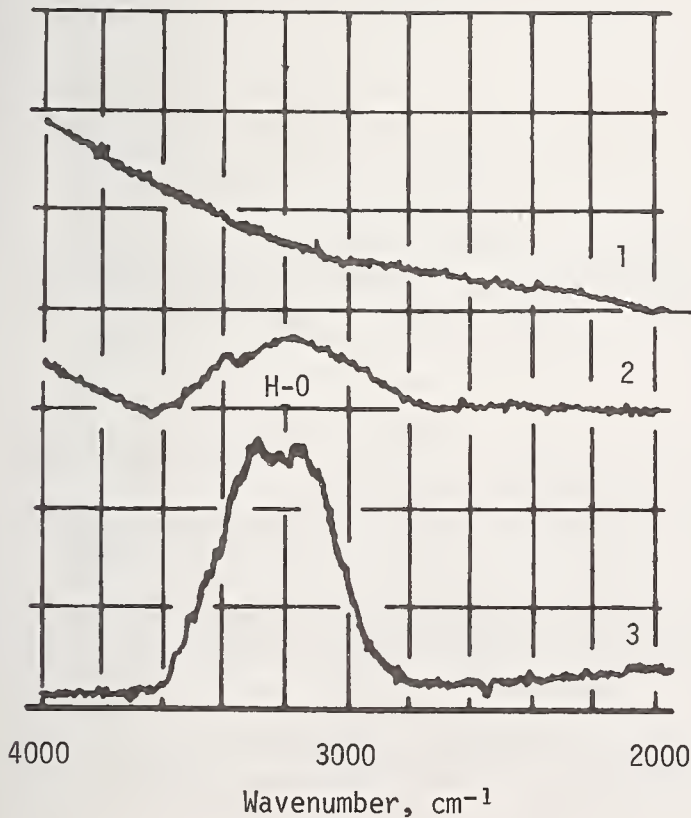


Figure 17. Observation of sapphire surface by Raman spectroscopy.

1. Polished surface
2. Aged surface with water vapor
3. Water

From this point of view, Taniguchi² and Kanekama, the Institute of Physical and Chemical Research, started the study on ion beam sputter-machining [17] and developed an ion sputter-machining apparatus for aspherical surface lens [18]. A duo-plasmatron type ion gun was used as the ion source. The position and the incident angle of the ion beam to the work were set with mechanical devices by sliding, rotating, and swinging mechanisms. The surface roughness of the lens obtained was reported to be of the order of $\lambda/100$ (λ , wavelength of mercury lamp).

6.2 Finishing of sintered ceramics by electron beam.

In mechanical lapping of sintered ceramics, fine finishing is not possible due to the micro pores existing in the materials. Abrasive grains would be left in the pores. In order to solve these problems, Taniguchi [19] examined the thermal finishing of ceramics of high melting point by using an electron beam of a relatively wide diameter. Surfaces of beryllia ceramics were finished to below $1\mu\text{m}$ roughness under the following conditions: the accelerating voltage, 12kV (max); mean beam current, 10mA (max); spot diameter of beam, 0.2mm.

7. Conclusion

Higher integration density of electronic and opto-electronic devices has characterized the trends of "electronic age" in the world. This has constantly called for higher precision processing in machining technology. Ultra-fine finishing to attain the surface of high dimensional accuracy without vitiating the original function of the material, is considered as one of the most important problems in this field.

The techniques introduced in the present paper, being developed very recently, cannot claim to be firmly established as a generally-accepted technology. However, a higher grade of surface finishing, unattainable by the conventional methods, is expected to be accomplished through further investigation on the basis of these novel techniques.

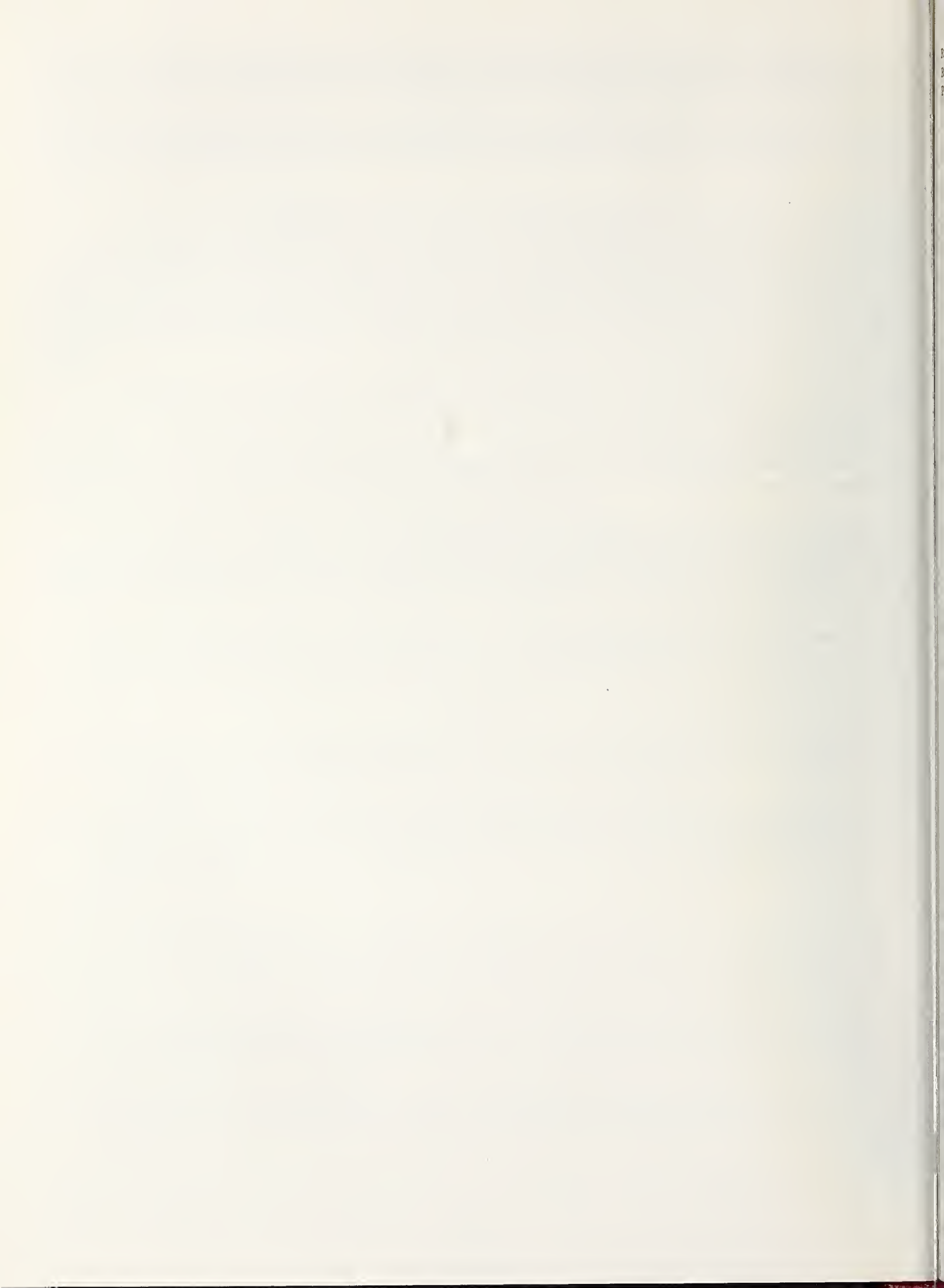
Additionally, new techniques have been often developed in the course to solve some troubles. The proverb "Turn a misfortune into a blessing" is thought to be true.

References

- (1) Yoshikawa, H., Brittle-ductile behavior of crystal surface in finishing, J. Japan Soc. Precision Engg. 35 (10), 662-667 (Oct. 1967). In Japanese.
- (2) Imanaka, O., Fujino, S., Shinohara, K., and Kawate, Y., Experimental study of machining characteristics by liquid jets of high power density up to 10^8W cm^{-2} , Proc. 1st Intern. Symp. Jet Cutting Technology, pp. G3/25-35, Univ. Warwick, England, April 5-7, 1972.
- (3) Taniguchi, N., Analysis of mechanism of various material-workings based on the concept of working energy, Sci. Papers Inst. Phys. Chem. Res. 61, (3), 79-91 (Sep. 1967).
- (4) Tsuwa, H. and Aketa, Y., Elastic emission machining as an ultra-fine finishing method, Proc. Intern. Conf. Production Engg., Pt. II, pp. 33-38, Tokyo, Aug. 26-29, 1974.
- (5) Mori, Y., Tsuwa, H., and Sugiyama, K., EEM (elastic emission machining) (1st Report) Concept of EEM and its feasibility _____, J. Japan Soc. Prec. Engg. 43, (5), 542-548 (May 1977). In Japanese.
- (6) Tsuwa, H., Aketa, Y., and Ide, T. Studies on powder particle beam machining by electrostatic acceleration (1st Report), *ibid.* 38, (8), 659-666, (Aug. 1972). In Japanese.

² Now, at Tokyo Science University

- (7) Ikawa, N., Mori, Y., and Ide, T., Studies on powder particles beam machining by electrostatic acceleration (2nd Report), *ibid.* 43, (3), 542-548 (March 1977). In Japanese.
- (8) Suzuki, J. and Watanabe, J., Study on polishing without contacting between work and polisher, Preprint at Annual Meeting of Japan Soc. Prec. Engg. pp. 213-214 (Oct. 1977). In Japanese.
- (9) Imanaka, O., et al., Precision machining of standard inductor bobbins (1), *Bull. Electrotechnical Lab.* 19, (10), 736-742 (Oct. 1955). In Japanese.
- (10) Yasunaga, N., Obara, A., and Imanaka, O., Mechanochemical polishing of single crystals with soft powders, *Proc. Intern. Conf. Production Engg., Pt. I*, pp. 32-37, Tokyo, Aug. 26-29, 1974.
- (11) Yasunaga, N. and Imanaka, O., A new polishing technique using the mechanochemical phenomenon, *Technocrat* 8, (9), 15-21 (Sept. 1975).
- (12) Imanaka, O., Fujino, S., and Shinohara, K., Effect of environments on fracture strength of aluminum oxide grain, *Bull. Japan Soc. Prec. Engg.* 2, (1), 22-30 (April 1966).
- (13) Okutomi, M. and Imanaka, O., Chemical phenomena in grinding process, *Proc. 3rd Intern. Conf. Prod. Engg.*, pp. 296-301, Kyoto, July 14-16, 1977.
- (14) Namba, Y. and Tsuwa, H., Ultra-fine finishing of sapphire single crystals, Paper presented at 27th General Sssembly of CIRP (New Delhi, Aug. 1977).
- (15) Okutomi, M. and Imanaka, O., "Hydration polishing" of sapphire, *Bull. Japan Soc. Prec. Engg.* 10, (4), 156-158 (Dec. 1976).
- (16) Okutomi, M. and Imanaka, O., A novel finishing technique using hydration phenomenon, *Proc. Intern. Conf. Prod. Engg. Vol. 2.* vi 79-86, New Delhi, Aug. 1977.
- (17) Taniguchi, N. and Kanekama, N., Ion-beam sputter machining of glass, *Annals CIRP* 22, (1), 69-70 (1973).
- (18) Taniguchi, N. and Kanekama, N., On the ion beam sputter-machining of aspherical surface lens, *Bull. Japan Soc. Prec. Engg.* 7, (1), 29-30 (March 1973).
- (19) Taniguchi, N., Surface finishing by electron beam, Preprint at Annual Meeting of Japan Soc. Prec. Engg., pp. 159-160 (April 1963). In Japanese.



MECHANISM AND APPLICATION OF THE "MECHANOCHEMICAL POLISHING METHOD USING SOFT POWDER"

Nobuo Yasunaga, Noboru Tarumi, Akira Obara
Electrotechnical Laboratory, MITI, Mukodaimachi,
Tanashi, Tokyo 188, Japan

Osamu Imanaka
University of Kanazawa, Japan

Polishing mechanisms of the mechanochemical polishing method using soft powders are discussed by estimating the reaction rates at interfacial contact points from static reaction experiments of mixed powder. Considering the case of polishing sapphire by SiO_2 powder, reaction process of $\alpha\text{-Al}_2\text{O}_3\text{-SiO}_2$ powder was examined at high pressures (36, 50 kbar) and high temperatures (630~1230°C) which were supposed to be generated at real contact points in polishing operation. The following are the main results obtained. (1) Reaction rates for kyanite formation at high pressures were much higher than those for mullite formation at atmospheric pressure. (2) The theoretical polishing rate estimated from these reaction rates approximately coincides with the one measured in the actual processing of sapphire by SiO_2 powder. (3) Polishing of sapphire could proceed only by mechanochemical reactions at contact points.

Mechanochemical polishing of Si single crystals and quartz crystals were tried in order to extend the applicability of this surface finishing method to other hard materials besides sapphire. It was disclosed that damage-free mirror surface could be obtained by mechanochemical polishing using powders such as BaCO_3 , CaCO_3 etc. for Si single crystals and Fe_3O_4 , MgO etc. for quartz crystals.

Key words: High pressure; high temperature; mechanochemical polishing; quartz crystal; sapphire; Si single crystal.

1. Introduction

High precision surface finishing technologies have been required especially in the electronic industry. The "Mechanochemical polishing method by soft powders" developed by the authors is ideal for this purpose, because very flat and damageless mirror surface can be easily obtained by using this new technique, which can be carried out in the same way as conventional mechanical lapping and polishing methods. The main distinction of this surface finishing method is to use powders which are mechanically softer than the materials to be polished and chemically reactable with them, for example, SiO_2 , iron oxides, MgO powder etc. for polishing sapphire. As the soft "abrasive" powders neither mechanically indent nor scratch the material surface, smooth and scratch-free finished surface of hard crystals can be obtained, even if powders of large grain sizes and relatively rigid polishers are used.

The conception of this polishing method was derived from the investigation on wear mechanisms of sapphire sliding on softer materials. The wear experiments of sapphire sliding on a rotating quartz glass ring have revealed that amorphous mullite was produced at the real contact points between the sapphire surface and glass debris. In the wear tests of sapphire against steel ring, solid solutions of $\text{FeAl}_2\text{O}_4\text{-Fe}_3\text{O}_4$ and $\alpha\text{-Al}_2\text{O}_3\text{-Fe}_2\text{O}_3$ formed. In both cases the worn sapphire surface was so smooth that the wear of sapphire was understood to proceed fundamentally in consequence of the exfoliation of very small reacted parts at the real contact points. The positive usage of these wear mechanisms yielded the new mechanochemical polishing method.

The evaluations of machining efficiencies and surface observations have been made in detail about sapphire polishing(1)¹. It is, however, very difficult to detect reaction products and to determine the reaction processes in the actual polishing operation. In this report, material removal processes at the polishing interface are estimated by means of reaction experiments of mixed powder at high pressures and high temperatures which are supposed to be generated at the real contact points. Application experiments of this machining technique to other crystals such as Si single crystals and quartz crystals are also described.

2. Experimental

Polishing experiments were carried out using a lapping apparatus schematically shown in figure 1. In a round holder A which rotates independently of the polishing plate, 3 specimens are mounted. Using holder B, unidirectional polishing tests with an oscillation of about 20 mm in the radial direction are done for a single specimen. Before polishing experiments, every specimen oriented by X-ray back reflection Laue method, was lapped with fine abrasives and furthermore etched by 360° C H_3PO_4 for sapphire and CP-6 ($\text{HNO}_3\text{:HF:CH}_3\text{COOH}=2\text{:1:6}$) for Si single crystals in order to eliminate the surface damage produced by the mechanical lapping.

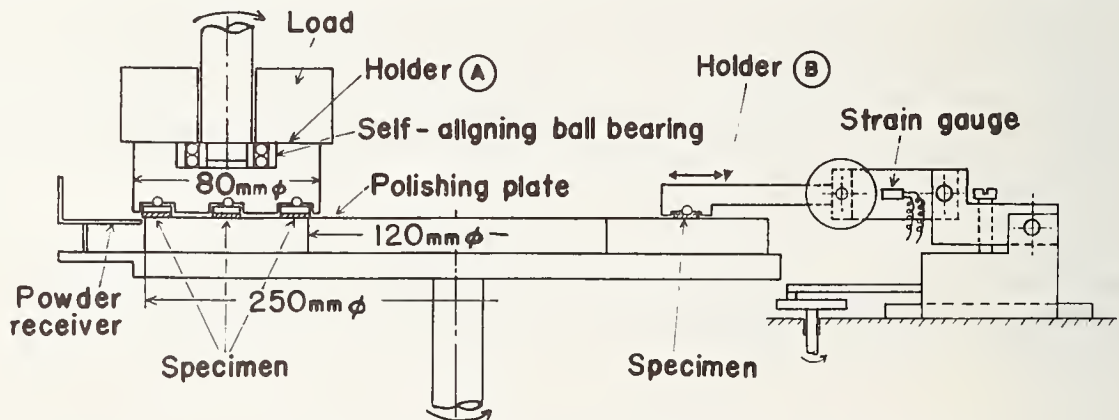


Figure 1 Schematic diagram of polishing apparatus.

For reaction experiments of mixed powders, a girdle-type high pressure apparatus was used, which is capable of generating up to 80 kbar at room temperature and up to 50 kbar at 1000° C. The schematic arrangement is shown in figure 2. In consideration of the polishing of sapphire by SiO_2 powder, mixed powder of $\alpha\text{-Al}_2\text{O}_3$ (average grain size 2 μm) and SiO_2 (0.5 μm) was prepared for reaction experiments (the mole ratio was 1:1). The powder sample was heated in a graphite tube. The temperature of the every sample was measured by a thermocouple (Pt-13%PtRh, 0.5 mm ϕ). The pressure generated in the sample was previously calibrated with the BiI- $\bar{\text{I}}$, TlI- $\bar{\text{III}}$, BaI- $\bar{\text{II}}$ and BiV- $\bar{\text{VII}}$ transitions. After the reaction experiments, the samples were milled and analyzed by means of X-ray diffraction method.

¹Figures in brackets indicate the literature references at the end of this paper.

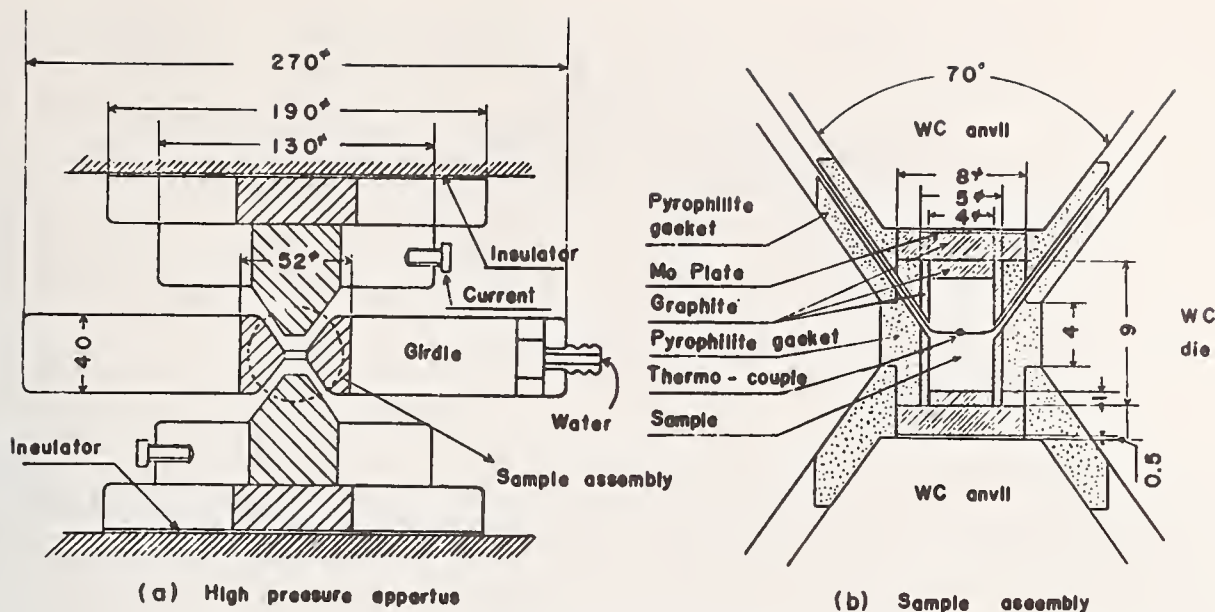
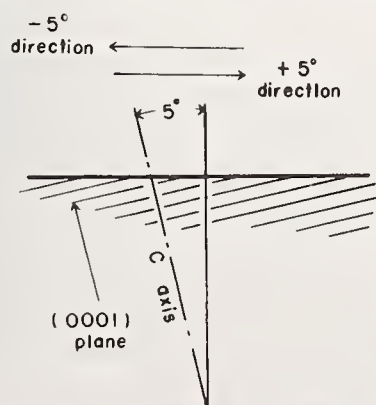


Figure 2 High pressure apparatus and sample assembly

3. Mechanism of Mechanochemical Polishing of Sapphire

3.1. Polishing rate of sapphire by SiO₂ powder.

In wear experiments of sapphire sliding on fused quartz glass ring, which was conducted in order to investigate what kind of reactions would occur at the interface and how the products would be removed, the following results have been obtained [2]. The wear rate of sapphire strongly depends on crystallographic orientation as shown in figure 3. Especially in the (0001)+5° direction the wear rate is high, whereas very low in the opposite (0001)-5° direction of the same slide surface and other sliding direction. This peculiarity is the same as Duwell has already reported [3]. The wear debris collected was amorphous to X-ray for all sliding condition and crystallized to form mullite when heated above ca.950°C as listed also in figure 3. From X-ray measurements of the grain size of the crystallized mullite and of the reaction process of the debris at higher temperatures than that of crystallization, fig 4 was proposed as the appropriate removal model at the contact points [2]. In the (0001)+5° high wear direction a small region of sapphire where basal sheets could easily slip toward the surface is rubbed off, being joined to the thin reaction layer (fig. 4(a)). In the other directions, where sapphire could hardly deform, only the reacted part (of which size was estimated to be under several tens Å) exfoliates as seen in figure 4 (b).



Sliding direction	Wear rate (mg/km)	Products in wear debris after heat treatment (980°C)
(0001)+5°	5.75	mullite + δ-Al ₂ O ₃
(0001)-5°	0.55	mullite
(10 $\bar{1}$ 2)<12 $\bar{1}$ 0>	0.50	mullite
(1 $\bar{2}$ 10)<10 $\bar{1}$ 0>	0.09	mullite

Sliding condition ; Load 0.5kg , Sliding speed 24^m/min
Relative humidity 100%

Figure 3 Wear characteristics of sapphire sliding on quartz glass

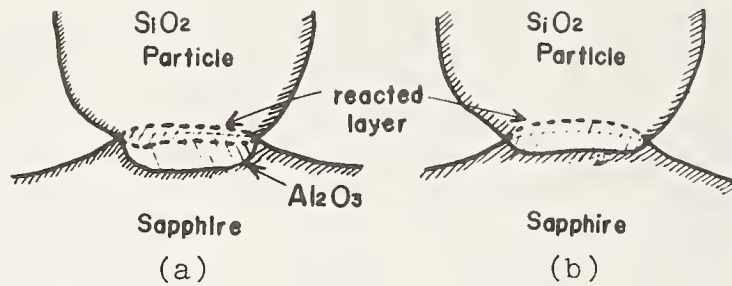


Figure 4 Removal model of wear debris

It is technically very difficult to detect the interfacial reaction products in the actual polishing operation. As an expedient for confirming the possibility of mechanochemical reactions during polishing, a wear experiment of sapphire sliding on a quartz glass disk (polisher) was carried out on the same sliding condition as in the actual polishing operation, i.e. at the load of 0.5 kg and the sliding speed of 20 m/min under water lubrication. In the (0001)+5° direction the debris collected was also amorphous and the same phase transition that had been seen in the wear experiments mentioned above was observed (fig. 5). This fact means that even in the actual polishing process mechanochemical reaction could occur at real contact points.

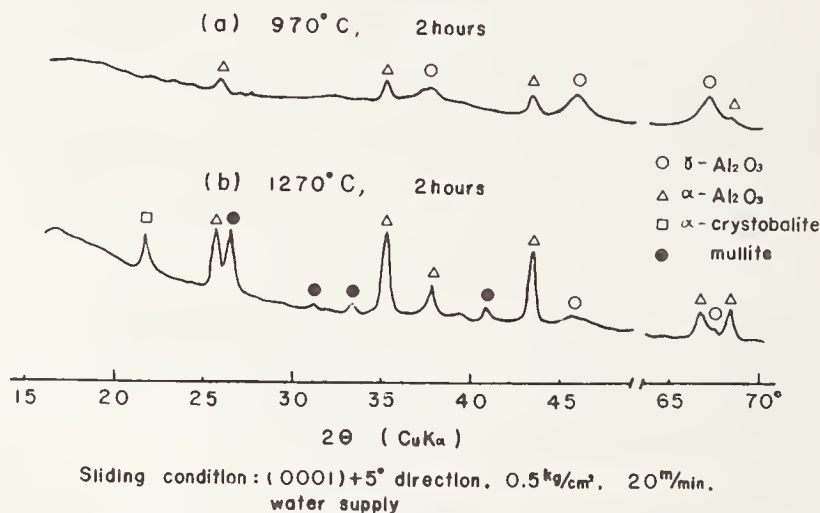


Figure 5 X-ray diffraction patterns of heat-treated wear debris

In this mechanochemical polishing, the machining efficiency is much higher in dry conditions (without fluid) than in wet conditions, because chemical and thermal activities at the contact interface are expected to be higher in dry conditions. Figure 6 shows polishing rates in (1210)<1010> direction which is known as the most undeformable direction of sapphire (holder B was used for this experiment). Higher reactivity at the contact interface at 20 m/min would have resulted in the higher polishing rate than at 10 m/min. Figure 7 shows, the orientation dependence of polishing rates. The highest polishing rate is obtained on the (0001) plane which most easily deforms plastically and the lowest rate on the plane where the machining is supposed to proceed ideally based on the removal mechanism of figure 4 (b).

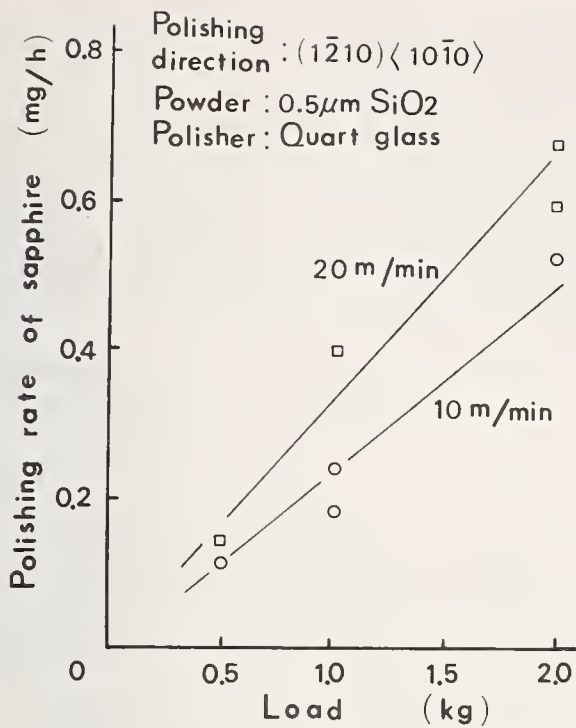


Figure 6 Polishing rates of sapphire in dry condition

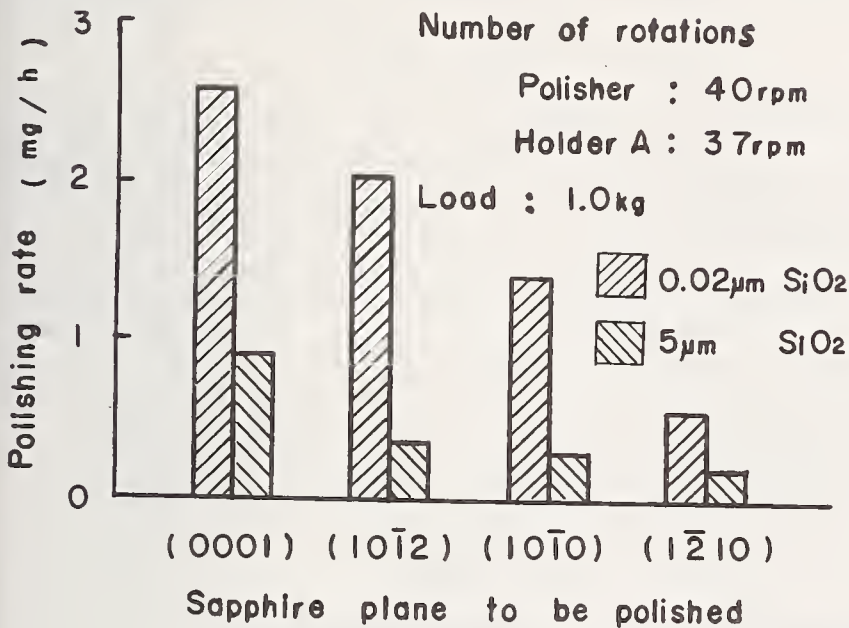


Figure 7 Polishing rates of sapphire polished with holder A

3.2. Reaction rates of mixed powder at high temperatures and high pressures.

It is very important to measure the reaction rates at contact points in polishing operation, in order to verify the contribution of chemical reactions to this mechanochemical polishing. For this purpose, reaction experiments of mixed powder were conducted on the same conditions (temperatures and pressures) which would have been generated at the real contact points between sapphire surface and SiO_2 powder.

The plastic flow pressure p_m at a real contact point would be nearly equal to the hardness H_v of the softer material at that temperature. The pressure generated at a contact point between sapphire surface and SiO_2 powder is therefore estimated from the hardness of quartz glass. The p_m is for example about 38 kbar at 800°C and 50 kbar at 600°C . In this report, reaction experiments were done on some of these "critical conditions" and on some of higher conditions than the critical ones.

Figure 8 shows the X-ray diffraction patterns of α - Al_2O_3 - SiO_2 mixed powder after 10 sec reaction at 1030°C and 36 kbar. As seen, a reaction product formed kyanite which is the stable phase of Al_2O_3 - SiO_2 system in the high pressure region. The amorphous SiO_2 changed to coesite in this condition. The relation between the fraction α of kyanite produced and the time of reaction at 36 kbar is shown in figure 9. It is notable that very high α (0.3~0.5) was obtained even by rapid cooling just after rapid heating to 1230°C (the existing time above 1000°C was about 2 sec). In comparison with the very low reaction rates of this system at the atmospheric pressure (products were little observed even after 10 hours heating at 1200°C), the rate at a high pressure is extremely high.

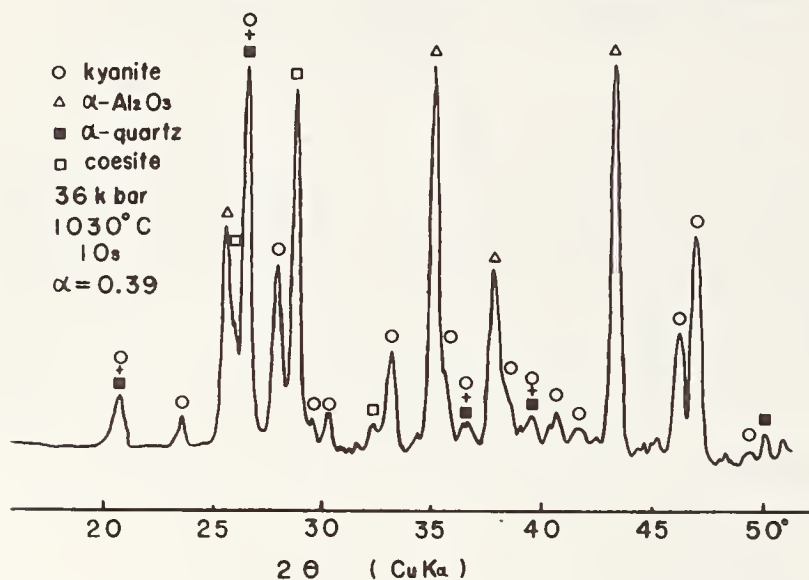


Figure 8 X-ray diffraction pattern of SiO_2 - α - Al_2O_3 mixed powder after the reaction at 36 kbar

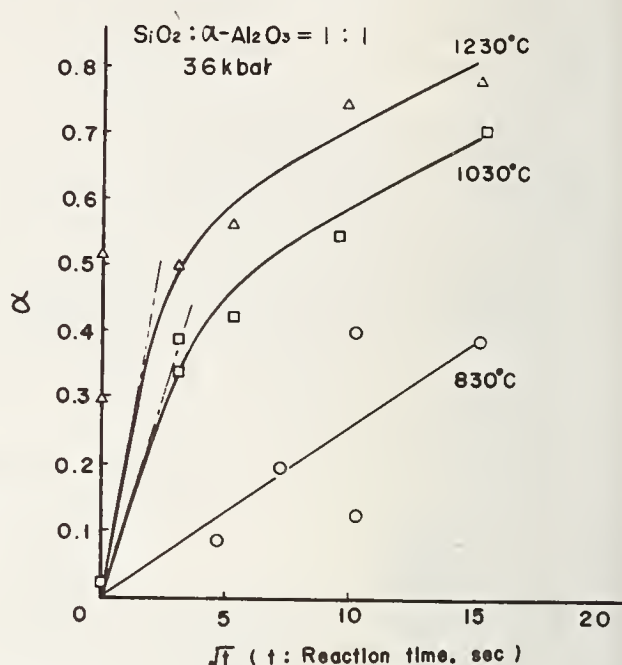
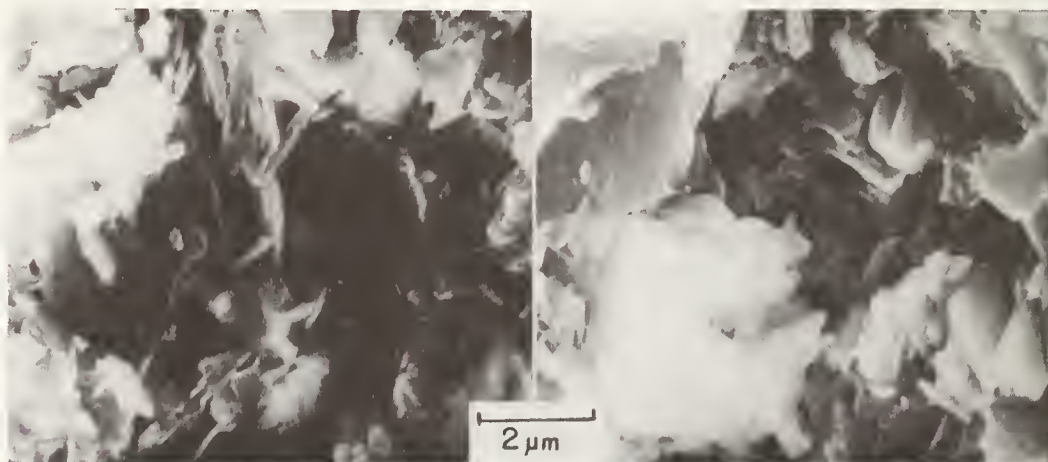


Figure 9 Fraction α of kyanite formation related to \sqrt{t}

The SEM image of the as-reacted powder reveals that the kyanite grows to columnar and plate-like structure (fig.10). As a suitable contact model of the individual spherical powder for such a reaction form, the partial contact model like figure 11(a) should be adopted instead of the one of whole surface contact like figure 11(b). It is known that the thickness ρ of the reacted layer and the reaction time t can be connected by the parabolic law



(a) 36 kbar, 830°C, 20s
 $\alpha = 0.095$

(b) 36 kbar, 1030°C, 900s
 $\alpha = 0.79$

Figure 10 SEM image of mixed powder in the as-reacted state

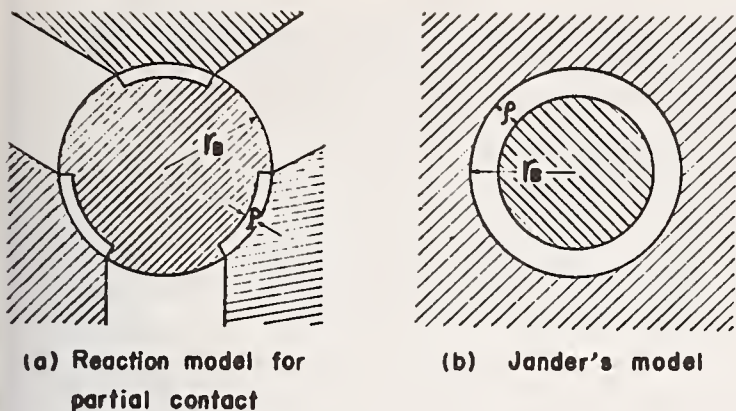


Figure 11 Reaction model of mixed powder

$$\rho^2 = K't \quad (1)$$

where K' is rate constant. If the fraction of the contact area to the total surface area is represented by f , for small ρ/r_B (r_B is the radius of the larger particle) α is given by

$$\alpha = 4\pi r_B^2 \cdot f \cdot \rho / \frac{4}{3}\pi r_B^3 = 3f\rho/r_B \quad (2)$$

From equations (1) and (2)^a is given by

$$\alpha^2 = K''t \quad (3)$$

where $K'' = 9f^2 K'/r_B^2$. When $F=1$ and $\alpha \ll 1$, the equation (3) agrees approximately with the Jander's equation $\{1 - (1 - \alpha)^{1/3}\}^2 = K't/r_B^2$. In figure 10, the relation of α to \sqrt{t} can be regarded as linear up to $\alpha = 0.3 \sim 0.4$. The K'' in the equation (3) can be obtained from the initial gradient (the broken line) of the each curve. The values of K'' for each temperature at 36 kbar and 50 kbar are listed in figure 12(a). Then, the time t' necessary for formation of reaction layer of 50 Å was calculated assuming $F=1/3$ and r_B (of $\alpha\text{-Al}_2\text{O}_3$ particle) = 2 μm . The results are shown in figure 12(b).

(a) K'' for kyanite formation ($\alpha^2 = K''t$)

Pressure Temperature	36 k bar	50 k bar
630°C	—	2.9×10^{-6}
780°C	—	7.2×10^{-4}
830°C	6.3×10^{-4}	1.7×10^{-3}
1030°C	1.1×10^{-2}	—
1230°C	9.8×10^{-2}	—

(b) t' corresponding to $\rho/r_B = 0.005/2$ (in the case of $f=1/3$)

Pressure Temperature	36 k bar	50 k bar
630°C	—	2.2
780°C	—	8.6×10^{-3}
830°C	1.0×10^{-2}	3.7×10^{-3}
1030°C	5.7×10^{-4}	—
1230°C	6.4×10^{-8}	—

Figure 12 Reaction rates of $\text{SiO}_2\text{-}\alpha\text{Al}_2\text{O}_3$ mixed powder at high pressures and high temperatures

Connecting these results with the polishing process, the following interpretation would be possible. Assuming the temperature generated at a contact point to be 830°C , the pressure generated there would be about 36 kbar. Assuming further that the reaction layer is rubbed off from the surface when the thickness ρ reaches 50 \AA (the actual reaction layer at the contact points is presumed to be thinner than 50 \AA), the time required from the beginning of contact till rubbing off should be about 1×10^{-2} sec.

3.3. Estimation of the polishing rate from the reaction experiments.

The actual contact points in a polishing operation are considered to be fresh and chemically very active, compared with the surface of the powders contacting in the static reaction experiments. Besides, the value of f/R_b in K'' of the equation (3) is supposed to be smaller in an actual reaction than in the assumption adopted for the above calculation. Taking these circumstances into consideration, the actual contacting time could be shortened to about one-tenth of the t' in figure 12 (b).

A polishing rate would be now estimated on the assumption that a temperature of ca. 830°C and a pressure of ca. 36 kbar arise at the sliding contact points, and reaction layers 50 \AA thick are produced and rubbed off within 1×10^{-3} sec. The volume v of each exfoliated part is given by

$$v = W \cdot h / p_m \quad (4)$$

Where W is the load, p_m is the plastic flow pressure of SiO_2 and h is the thickness of exfoliated layer. If the volume v is rubbed off in every time t' , the polishing rate \dot{w} per unit time is

$$w = d \cdot v / t' = d \cdot W \cdot h / p_m \cdot t' \quad (5)$$

Where d is the density of the reaction product. When $w = 1.0 \text{ kg}$, $p_m = 36 \text{ kbar} = 360 \text{ kg/mm}^2$, $h = 50 \text{ \AA} = 50 \times 10^{-7} \text{ mm}$, $t' = 1 \times 10^{-3} \text{ sec}$ and $d = 3.7 \text{ mg/mm}^3$, the \dot{w} is calculated at 0.18 mg/h . This value is nearly equal to the average polishing rate on the least deformable (1210) plane (fig. 6 and 7), where polishing would proceed approximately on the basis of the simple model discussed above. The fact that the polishing rate estimated from the static reaction experiments would approximate to the actual rate proves that sapphire can be only polished by solid state reaction.

It is known that kyanite is unstable under the atmospheric pressure and changes to mullite phase above 1325°C . Kyanite also easily changes mechanochemically to amorphous and mullite phase by light milling in a mortar [2]. It would, therefore, be reasonable to conclude that kyanite forms first at the sliding contact points, and then it changes to amorphous phase by receiving frictional stresses.

4. Application of the Mechanochemical Polishing Method for Si Single Crystals and Quartz Crystals.

4.1. Polishing characteristics of Si single crystals.

As it is the substance of this new mechanochemical polishing method to use powders softer than the material to be worked and reactable with it, this technique should be applicable for polishing other hard crystals besides sapphire. So, as an example, the possibility of polishing Si single crystals by this method was investigated.

It is known that the crystal surface of Si is apt to oxidise easily, so that "solid state reactions between the softer powder and the oxide film

formed on Si surface" would be the foundation of Si polishing. In this investigation, polishing experiments using BaCO_3 , CaCO_3 and Fe_3O_4 powders was tried. All of these materials, which are softer than Si and its oxide film, are expected to have mechanochemical effect on Si polishing.

The holder A in figure 1 was used for polishing experiments. 3 specimens of 12 mm by 12 mm by 2 mm thick were polished at the number of polisher rotations 20 rpm and at the nominal pressure 120 g/cm². The polishing rates obtained on the (111) plane are shown in figure 13. It is noticeable that the polishing rate by BaCO_3 powder in dry condition (without any fluid) is high enough, when compared with that of the conventional polishing by SiO_2 and CeO_2 powders. BaCO_3 is reactable with SiO_2 even at a relatively low temperature of about 850°C [4]. High reactivity like this would have brought about the efficient polishing. Figure 13 also shows that mechanochemical polishing by BaCO_3 and Fe_3O_4 in dry conditions gives much higher polishing rate than in wet conditions (water supply). This feature which has been also seen in the case of sapphire polishing indicates that high activity at the contact points in dry conditions brings high machining efficiency in the mechanochemical polishing.

Powder	Grainsize (μm)	Polisher	Environment	Polishing rate ($\mu\text{m}/\text{h}$)
BaCO_3	3 ~ 10	Cloth	Dry	1.16
		Cloth	Wet	0.17
	2 ~ 4	Bakelite	Dry	2.60
		Bakelite	Wet	0.30
Fe_3O_4	10 ~ 20	Cloth	Dry	0.68
		Cloth	Wet	0.28
CaCO_3	4 ~ 7	Cloth	Dry	0.59
	2 ~ 3	Cloth	Dry	0.97
SiO_2	2 ~ 3	Bakelite	Wet	1.30
		Cloth	Dry	1.00
	0.5	Cloth	Wet	0.85
		Cloth	Dry	1.91
0.01 0.02	Cloth	Dry	1.91	
	Cloth	Wet	1.05	
CeO_2	2 ~ 3	Bakelite	Wet	0.91
Diamond	1	Cloth	Dry	2.2~4.2

Figure 13 Polishing rates on Si (111) plane

4.2. Observation of polishing surface

Etched surfaces of the polished Si (111) plane were observed by a differential interference microscope (fig. 14). It is evident that little worked damage remains on the Si surface polished by coarse BaCO_3 powder, while cracks and scratches are seen on the surface mechanically polished by CeO_2 and SiO_2 powders.

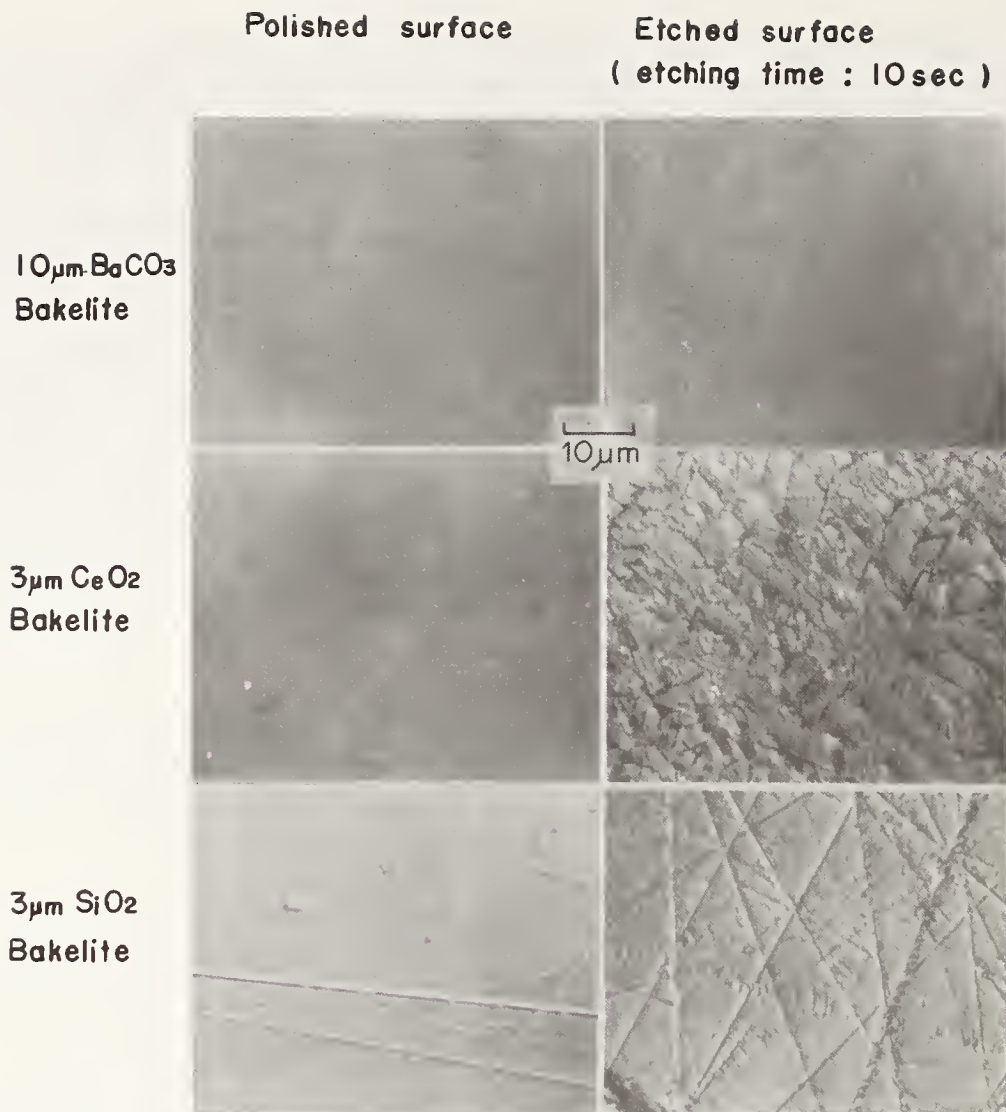


Figure 14 Si surface polished in wet condition

The electron diffraction patterns (fig. 15) show that no detectable defects are remaining on the surface polished by BaCO₃, whereas no detectable crystalline structures are observed on the surface polished by diamond paste. Figure 16 shows ESCA spectra of Si2p (binding energy $E_b=99$ eV) and O1s ($E_b=532$ eV) on the polished surfaces. The peak at $E_b=103$ eV means the chemical shift of Si2p caused by surface oxidation. The figures

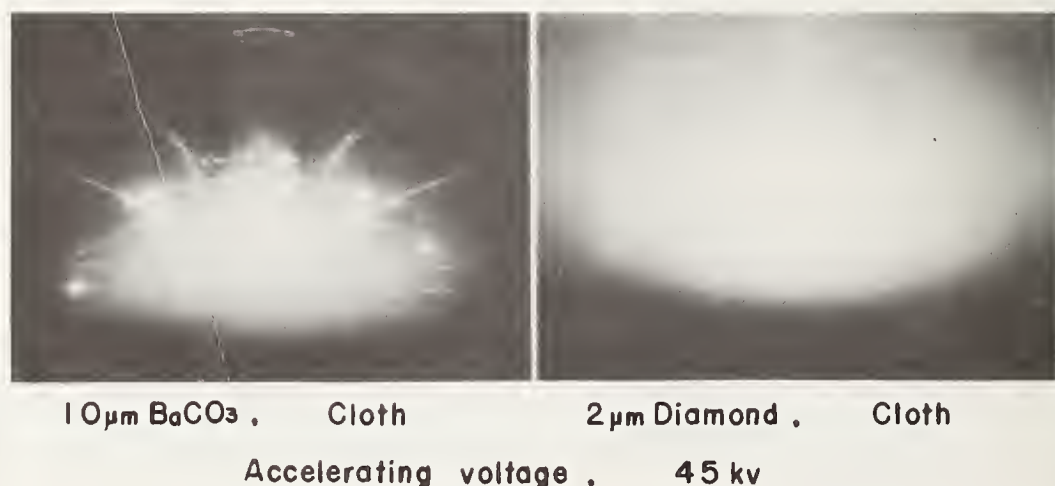


Figure 15 Electron diffraction pattern of Si surface polished in dry

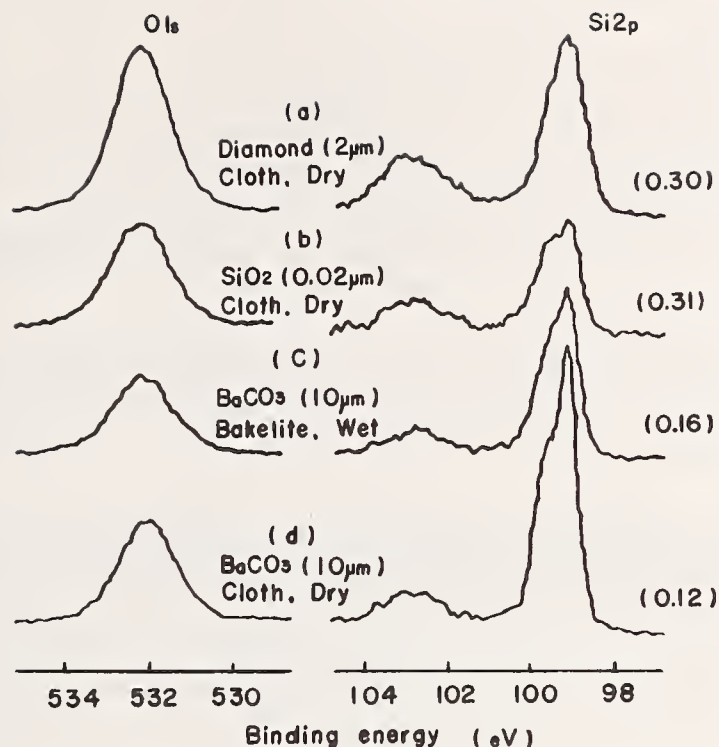


Figure 16 ESCA spectra on polished surface of Si (111) plane

in () on the right side of figure 16 represent peak height's ratios of the shifted Si2p peaks ($E_b=103$ eV) to the proper Si2p peaks ($E_b=99$ eV). It can be qualitatively said that the smaller these figures are, the less the surface oxidation is. Figure 16 indicates that mechanochemical polishing by $BaCO_3$ powder brings less surface oxidation than mechanical polishing by fine diamond and SiO_2 powders. From the ESCA analysis in the low binding energy region the worked layer was estimated as under about 20 Å.

4.3. Polishing of quartz crystals

This mechanochemical polishing method was also applied to surface finishing of quartz crystals. It was found that powders such as Fe_3O_4 , MgO , MnO_2 etc. are useful for high precision polishing of quartz crystals. Especially, polishing by Fe_3O_4 powder in dry condition brings as high machining efficiency as conventional polishing by CeO_2 and Fe_2O_3 powders does. Furthermore, a damage-free surface with high flatness is obtainable by using a relatively rigid polisher like one made of copper.

5. Conclusion

Reaction experiments at high pressures and high temperatures have shown that chemical reactivity at contact points is the fundamental factor which controls the polishing rate. In order to improve the polishing efficiency, it should therefore be considered how to increase the interfacial reactivity, namely; it should be investigated what kind of powders and environments could give the highest polishing rates. This polishing method is fundamentally applicable to various kinds of hard materials as discussed in 4.. Selection of powders and machining conditions suitable for polishing of the respective materials would be very important.

References

- { 1 } Yasunaga, N., Obara, A. and Imanaka, O., Mechanochemical polishing of single crystals with soft powders (Proc. 1st Intern. Conf. Production Engg., pp. 32-37 Tokyo, August 26-29, 1974).
- { 2 } Yasunaga, N., Obara, A. and Tarumi, N., in Study of mechanochemical effect on wear and its application to surface finishing, pp. 73-76 (Researches of the Electrotechnical Laboratory No 776, 1977).
- { 3 } Duwell, E. J., Friction and wear of single crystal sapphire sliding on steel, J. Appl. Phys. 33, 9, 2691-2697 (1962).
Duwell, E. J., and H. C. Butzke, The effect of interface composition on the wear rate of sapphire, ASLE Trans., 2, 101-108 (1964).
- { 4 } Yamaguchi, T., Fujii, H. and Kuno, H. Kinetic studies of the solid state reaction involving intermediate phases system BaCO₃-SiO₂, J. inorg. nucl. 34, 2739-2745 (1972).

Discussion

GIELISSE

In the case of BaCO₃ on Si is the actual chemo mechanical mechanism known? Are we getting a reaction between the two components to give a reaction product or does BaCO₃ break down followed by subsequent oxidation of Si? We have noticed that the amount of "breakdown oxygen" available on the interface influence the reaction rate. Are you getting similar results?

YASUNAGA & TARUMI & OBARA

Since the Si surface is apt to oxide easily, the mechanochemical reactions are considered to occur at the interface between the powder and the Si oxide film. Yamaguchi et al* have showed that BaCO₃ reacts easily with SiO₂ to form BaSiO₃ and Ba₂SiO₄ above 850°C. So, it can be inferred that "breakdown" and rubbing off of these reaction products formed at the real contact points lead to the fine machining of Si surface.

*Ref. 4 in text.

NOVAK

1. If no cooling is used in the experimental apparatus, why doesn't the clot or bakelite thermally degrade in a very short time period?
2. What pH was used during the polishing conditions listed in the slide as wet?
3. Is the powder continually replenished on the wear surface?

YASUNAGA

1. In these experimental conditions, apparent temperatures generated on the polishers are not high enough to degrade their function, although at small real contact points very high temperatures would be generated in each short contact time.

2. In our experiments water from the pipe was directly supplied and no pH adjustment was carried out. As Gutsche and Moody* indicated, pH of the polishing fluid might be a important factor. In our further investigation this point will be taken into consideration.
3. As the polishing machine was designed so that the powder does not "get away", replenishment of powder is not always necessary even in dry polishing.

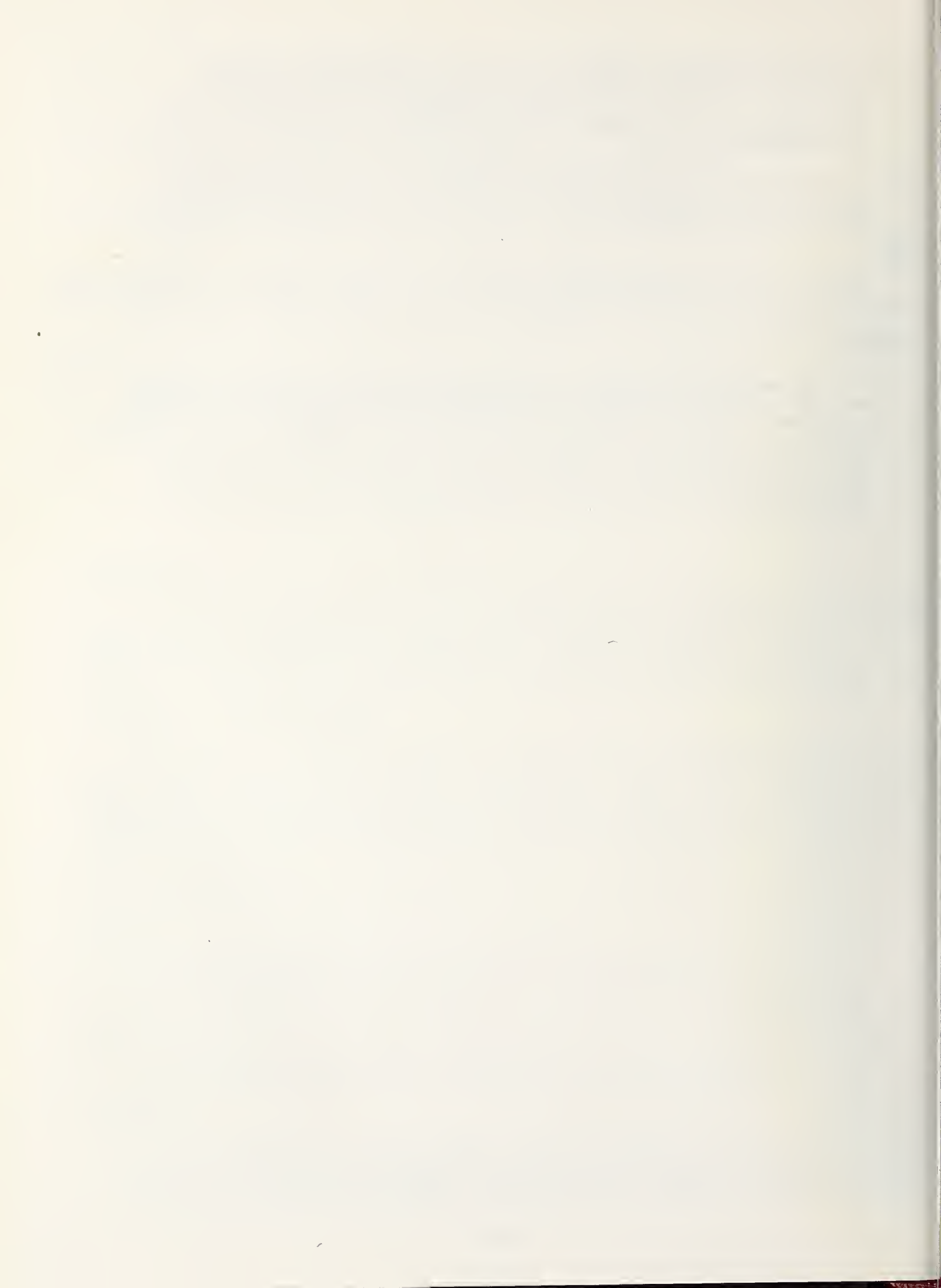
LEE

In your high pressure reaction study, how did you control the temperature for the short reaction time you need.

YASUNAGA

In these high pressure experiments the mass of the mixed powder samples is small (4mm ϕ x7mm). By supplying the graphite tube heater an electric current under 200A at about 4V, the sample can be rapidly heated and cooled. In this experiment by manual control, rapid heating from room temperature to 1230^oC was realized within a few seconds. Preparation of automatic control system would make it possible to realize more rapid and precise control of the reaction times and temperatures.

* H.W. Gutsche · J.W.Moody: J.Electrochem. Soc., 125, 1(1978)136.



EXTENDED DISCUSSION: HARDNESS AND ITS RELATION TO MACHINING

R. W. Rice

Naval Research Laboratory
Washington, DC 20390

A. G. Evans

University of California
Berkeley, CA 94720

During the conference, a number of questions arose about hardness and its relation to machining. As a consequence, time was set aside for a general discussion; A. G. Evans volunteered to present some specific considerations on this subject as an aid in focusing this discussion. The following note, subsequently prepared by R. W. Rice and A. G. Evans, represents a summary of both his specific considerations and the general group discussion. Basically, three issues were addressed: 1) the meaning and technique of hardness measurements; 2) the appropriate hardness/load values to use in machining considerations; and, 3) the relevance of hardness to multipoint machining.

1. The first topic, the meaning and technique of hardness measurements, is an old and complex topic because of the many factors that can affect hardness and its measurement. These factors can largely be classified into the following three main categories:

a. Load Application Factors - Of these, major importance is ascribed to the dependence of hardness on load; the effect of translational motion; and, the effect of loading rate.

Several factors give an apparent or real dependence of hardness on load. Actual errors in measurement of the true indentation dimensions can occur. Typically, the dimensions are undermeasured by a constant factor, and hence, the errors are more serious for small indentations, i.e., harder materials and lighter loads. Another long known factor giving an apparent load dependence is elastic relaxation on unloading. It is generally accepted that elastic relaxation results in a fixed shortening of indentation dimensions and, thus, again becomes a serious effect for low loads and hard materials. Since elastic relaxation also increases with Young's modulus (E), the effect is more properly described in terms of the ratio H/E , with the extent of elastic recovery increasing with H/E . In this regard, it is important to note that ceramics, in comparison with metals, are characterized by relatively large H/E values.

Finally, work hardening of the surface due to machining or abrasive lapping has been shown to produce an intrinsic load effect [1]. At low loads the indentation deformation occurs primarily within a work hardened surface layer, while at higher loads only a fraction of the deformation occurs within the work hardened layer. This again leads to an increase in measured hardness with decreasing load. For most ceramic materials, these effects (both real and apparent) become negligible for loads above a few hundred grams. During machining operations, normal loads in excess of this range are exerted on the workpiece, so that any correlation between machining rate and hardness should not be influenced by these effects. This may not be true for correlations between hardness and fine abrasive surface finishing operations.

The second consideration, namely the effect of translational motion, is extremely pertinent to machining applications. Since translational motion is

involved in machining operations, it would appear that scratch hardness is a more relevant parameter than the commonly used indentation hardness. Nevertheless, while detailed comparisons of scratch and indentation hardness are not known, the relative ranking of materials by both techniques is expected to be similar. Several authors have, in fact, shown good correlations between the Moh scratch hardness scale and indentation hardness [2,3].

The effect of loading rate on hardness is also pertinent to machining considerations. Again, while only limited information on the effect of loading rate is available, the relative ranking of materials obtained under typical quasi-static conditions is not expected to be significantly altered. For ceramics, the phenomena of indentation creep has been observed and appears limited (primarily to relatively soft ceramics) though not extensively documented. Another indication that loading rate is not a significant factor is the successful use of punch testing (i.e., impact hardness) on metals [4]. Furthermore, the static hardness of ceramics appears to be a factor of three, and possibly less, times the dynamic yield stress (i.e., the shock yield stress as obtained under ballistic impact) [3,7]. Accordingly, little difference between quasi-static and dynamic hardness is expected, and may be minimal for materials of high H/E values.

b. Material Factors - Two material factors that effect hardness are microstructure and the propensity for cracking. The latter depends on material properties, microstructure, and on load, i.e., cracking usually commences above a threshold load and becomes more severe at higher loads. However, observations on cracking indicate that the effect on hardness is generally small. Since cracking that occurs during the indenting process, i.e., during loading, is confined to a region outside of the plastic zone (the stresses within the plastic zone are compressive) the effect of such cracking on hardness should be small. Cracking that occurs during unloading can, and often does, extend into the indentation. This should have little effect since it normally results in minimal distortion of the indentation or in the accuracy of determining its dimensions. Some effect of cracking might occur, however, if cracking is extensive enough to change the effective compliance and hence elastic restraint of the material around the indentation (e.g., crushing beneath the indenter).

Microstructure, i.e., grain size and the size and distribution of any second phases or pores, also affects hardness [8]. The extent of the effects generally depends on the scale of the indentation relative to the scale of the microstructural features. Of the microstructural parameters, grain size is the variable of greatest pertinence to the relatively pure and dense materials discussed at this conference. For small indentations, or very large grains, single crystal values of hardness apply, but should probably reflect an average over all crystal orientations. For larger indentations or smaller grain sizes, the polycrystalline value should be appropriate. This may be smaller than, but is often larger than, the single crystal value. However, for hard ceramics, grain size effects do not appear to be very pronounced [8].

c. Environmental Effects - Chemomechanical effects have also been found to affect hardness, mainly at quite low loads, and are at best of uncertain pertinence to machining processes [9,10]. Lubrication effects of coolants under the dynamic conditions of machining are also not well understood, but appear to be limited. Local temperature excursions due to abrasive particle-workpiece interaction apparently can be quite substantial [10]. Although hardness decreases substantially at the temperatures indicated, the volume of material with substantial temperature rise should generally be much smaller than the volume of materials deformed in machining so that any local temperature effect should be fairly limited.

2. In the context of the preceding discussion, the second major topic, the selection of appropriate loads in hardness determinations, can be addressed directly; generally, high loads in the kilogram range are considered more

appropriate in machining considerations. This can be seen by recalling the typical hardness formulas:

$$H = \frac{\alpha P}{L^2} \quad (1)$$

where α = a constant determined by indenter geometry, P = load, and L = characteristic dimensions, e.g., indentation diagonal, and

$$L = \beta d \quad (2)$$

where d = depth of the indentation and β = another constant determined by indenter geometry. The hardness value pertinent to machining should generally be that value representing similar depths of penetration of the hardness indenter and the abrasive particles. One easily obtains the load in terms of the penetration (depth, d):

$$P = \left(\frac{\beta^2}{\alpha}\right) H d^2 \quad (3)$$

Thus, if one assumes that abrasive particles will penetrate a reasonable fraction of their diameter (e.g., $\approx 1/4$) during a machining operation, one can calculate the load required for comparable penetration during indentation. As an example, consider Al_2O_3 ($H \approx 2000$ kg/mm²) abraded by a 325 grit (dia. ≈ 40 μ m); taking $d = 10$ μ m, the appropriate Vickers indentation ($\alpha = 1.854$; $\beta = 7$) load from eq. 3 is: $P \approx 5.3$ kg. Thus, one can readily see that even for smaller abrasive grits (with correspondingly smaller penetrations) and for softer materials, loads of the order of a kilogram or more are required. At such loads, the major load-dependent effects are minimal and hardness is nearly insensitive to load. One notable exception is the possible effect of surface work hardening from prior machining steps or prior passes with the same abrasive. Generally, the full depth of slip, D , produced by a given finishing processes varies roughly as $1/H$ [11]. For Al_2O_3 , ground with a 325 grit wheel, D is found to be of the order of 10 μ m. Since this is comparable to the estimated depth of penetration (see above), the effect of work hardening is difficult to determine. However, for MgO , $D \approx 40$ μ m, and hence the effect of work hardening can be of consequence. The effect of work hardening should be of greatest importance during the early stages of each step in sequential finishing operations, since the smaller particles must penetrate initially into the residual damage layer of the preceding step. One of the uncertainties is the extent of work hardening in the deformed layer; a fair portion of this zone may represent slip on only one or two systems. Also, transient temperature effects, noted earlier will be greatest at the surface, i.e., in the region of extensive deformation, and may offset some of the effect of work hardening.

3. The final major topic, which is concerned with the relevance of hardness to multipoint machining, has two aspects. The first is the good correlation between indentation fracture and the primary mode of natural removal during machining. In both cases, lateral cracking occurs about a central plastic compression (or groove), and expressions for material removal can be derived from consideration of the extent of lateral cracking. These expressions invariably involve hardness because of the nearly direct relationship between depth of lateral fracture and depth of penetration [12].

The second aspect of the relevance of hardness to multipoint machining is the direct correlation of the process and its effects with hardness. For example, the rates of both sawing and grinding directly correlate with hardness [11,13] as does the depth of slip, D , discussed earlier. Also, in some earlier studies the rate of lapping was used as an extension of, or replacement for, the familiar Moh hardness scale [14].

In summary, it appears clear that hardness is a basic factor in the machining of ceramics. Further, although there are many second order effects,

some of them such as work hardening possibly being significant, the major trends and implications of hardness for machining seem fairly well outlined by present work. Thus, while hardness depends on a number of variables (such that some may question calling it a material property), it is fortunate that most of the inherent problems are not significant at the higher (i.e., kg) load values that are generally implied for relating hardness and machining. Further work is important to define in much more detail the hardness-machining relationships, but a sound foundation on which to build is fairly well developed.

References

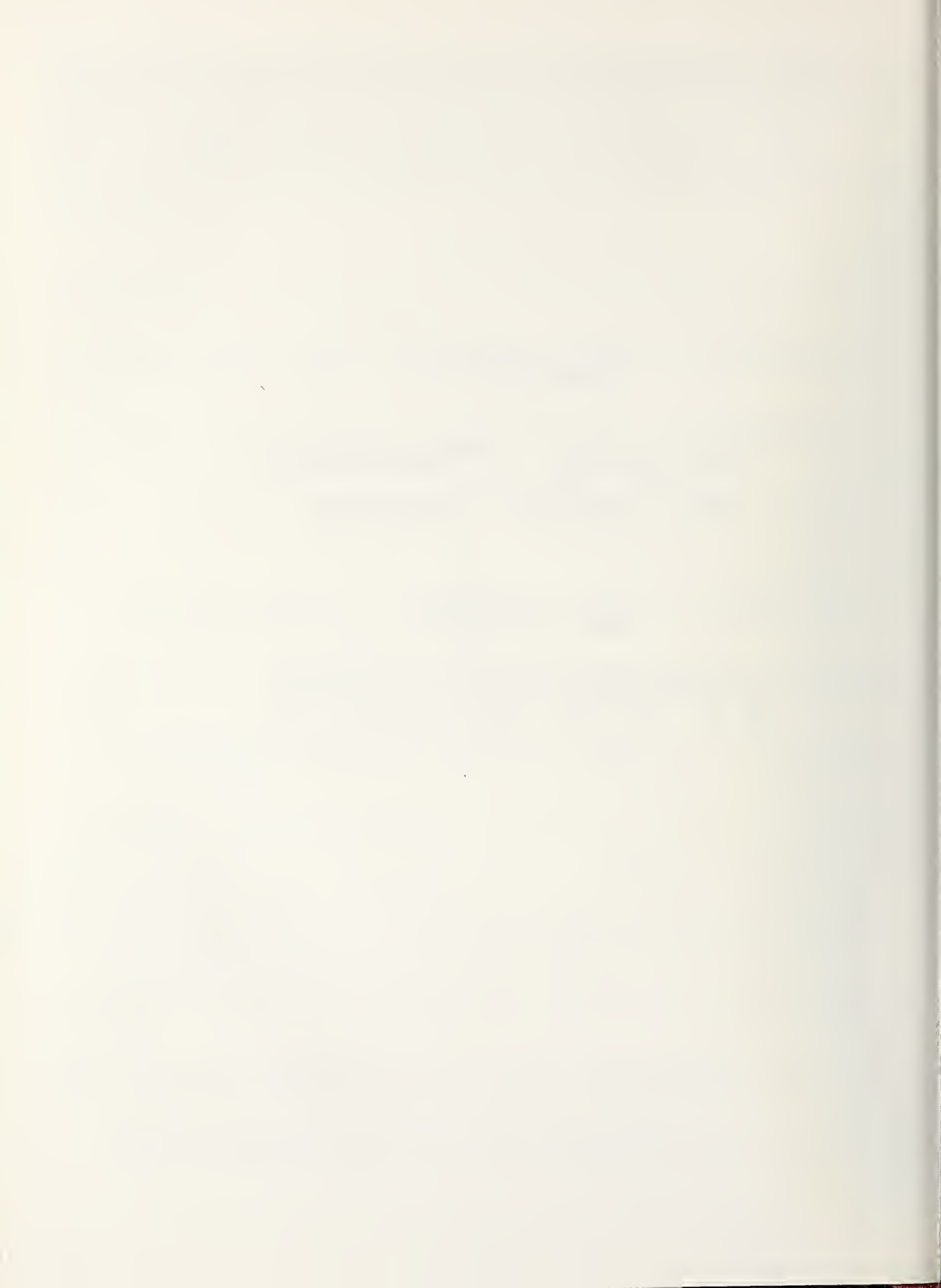
- [1] Becher, P. F., Surface Hardening of Sapphire and Rutile Associated with Machining, J. Am. Ceram. Soc., [57] 2 (1974).
- [2] Rice, R. W., Discussion in The Science of Hardness Testing and Its Hardness Testing and Its Research Applications, J. H. Westbrook and H. Conrad, eds., 72-73 (1973).
- [3] Gilman, J. J., Hardness - A Strength Microprobe, in The Science of Hardness Testing and Its Research Applications, J. H. Westbrook and H. Conrad, eds., 51-72 (1973).
- [4] Li, C. H. and Enos, G. M., Punch Hardness Testing: Theory and Uses, Ibid, 300-310.
- [5] Shaw, M. C., The Fundamental Basis of the Hardness Test, Ibid, 1-11.
- [6] Rice, R. W., The Compressive Strength of Ceramics, in Ceramics in Severe Environments, W. W. Kriegel and H. Palmour, III, eds., 195-227, Proceedings of 6th University Conference on Ceramic Science, North Carolina State University at Raleigh (1970).
- [7] Gilman, J. J., Relationship Between Impact Yield Stress and Indentation Hardness, J. Appl. Phys. [46] 4, 1435-1436 (1975).
- [8] Rice, R. W., Microstructure Dependence of Mechanical Behavior of Ceramics, in Treatise on Materials Science and Technology, R. K. MacCrone, ed., 199-381 (1977).
- [9] Cooper, G. A., Some Observations on Environmental Effects When Diamond Drilling (these proceedings).
- [10] Gielisse, P. F., Choudry, A., and Ida, I., The Effects of Abrasive Finishing Processes on Materials (oral presentation, this proceedings).
- [11] Rice, R. W., Machining of Ceramics, in Ceramics for High Performance Applications, J. J. Burke, A. E. Gorum, and R. N. Katz, eds., 287-343, Proceedings of 2nd Army Materials Technology Conference, Hyannis, Massachusetts (1973).
- [12] Evans, A. G., Abrasive Wear Damage in Brittle Materials (these proceedings).
- [13] Rice, R. W. and Speronello, B. K., Effect of Microstructure on Rate of Machining of Ceramics, J. Am. Ceram. Soc. [59] 7-8, 330 (1976).
- [14] Wooddell, C. E., Method of Comparing the Hardness of Electric Furnace Products and Natural Abrasives, J. Electrochem. Soc. [68], 111-130 (1935).

Session II

**Technology of Machining
and Surface Finishing**

Session Chairmen

C. Bersch, Naval Air Systems Command
R. W. Rice, Naval Research Laboratory



OPTIMIZATION OF MULTISTAGE GRINDING OPERATIONS:
THE CHOICE OF CONSECUTIVE REMOVAL RATES

A. Broese van Groenou

Philips Research Laboratories,
5600 MD Eindhoven, the Netherlands

The optimum choice of removal rates is determined in a model for multistage grinding on the basis of remedying the damage introduced in the previous stage. A set of second order difference equations is derived from the relation between the depth of damage d and removal rate Z , written in the form $d = \alpha Z^m$. The boundary conditions are the shape error in the workpiece d_0 and the final, acceptable, depth of damage d_e . The solution shows that the minimum total time is achieved when the number of stages increases; more than three or five stages are ineffective both as regards the constant duration of each stage and the optimum duration. In contradistinction to normal practice, the first stage - to be optimum- should ensure a high removal rate over a short period of time. The following rates are one order of magnitude smaller and last longer. A map with time contours is given for three-stage grinding; a shallow minimum is found which allows wide margins for choosing removal rates.

Key Words: Grinding; grinding damage; lapping; polishing; polishing times.

1. Introduction

Grinding and lapping are used to shape a given workpiece correctly and obtain the required surface quality. Shaping is the main aim of a grinding operation, but it leaves a damaged surface. This is then lapped and polished until the degree of damage is acceptable. These stages are interdependent: the higher the removal rate, the greater the damage and the longer the final operation. Where economy is important, the rough grinding rate must be balanced against the time spent in removing the damage by a finer treatment. Various examples of such multistage operations have been described in the literature, e.g. for glass [1,2,3]¹, where two to four stages are used. In preparing samples for microscopic observation five or more stages may be necessary. In such laboratory work the duration of the various stages need not be controlled, in contrast to a production process where the time for each stage is often equal [2,3]. In view of these variations in grinding and lapping procedures, it is worthwhile to know how many stages give an optimum result and how the subsequent times and removal rates should be chosen. A useful approach has been described by Mushardt [4] and Scherf [5] who combine on-line measurements of the volume rate of removal and the surface roughness with numerical control of the grinder. They include wheel wear and sparking out in their analysis and obtain workpieces with the roughness required. Roughness, however, is not always a good measure of the damage in the workpiece. In ground metals there is a zone of considerable depth where the material has been modified by plastic deformation and the heat generated [6]; also, in glass and ceramics, deep cracks may be masked by a smeared surface [7]. For a high quality surface such layers must be removed.

The present treatment optimizes the total time of the multistage operation by considering for each stage the time required to remove the depth of the damaged layer created by the previous stage. This approach leads to a set of equations that can be solved when the initial shape error and the final, acceptable, depth of damage are given. To achieve this, the relation between the rate of removal Z (mm^3/s) and the depth of damage d must be known for each stage. It is possible to start from Preston's

¹Figures in brackets indicate the literature references at the end of this paper.

equation [8,9,10] between Z and force F,

$$Z = F v_s / H_g \quad (1)$$

where v_s is the wheel speed and H_g the grinding hardness. Because of the force a damaged layer is present. A quantitative relation between its thickness d and F can be given in a few cases:

1. $d \propto F^2 / H_g^2$ when groove formation [10] occurs as in low-speed grinding in metals and in fine grinding of glass and ceramics; H_g is then proportional to the Vickers hardness.
2. $d \propto F^{2/3} / K^{2/3}$ when cracking and chipping occur as in rough grinding of brittle materials [11,12]; K is then proportional to the fracture toughness K_{Ic} . Generalising from these two cases it seems appropriate to assume a power law between d and F : $d \propto F^m$. For practical purposes it is more useful to relate the damage to the rate of removal by writing

$$d = \alpha Z^m \quad (2)$$

using one value of m for a range of finishing processes. This has the added advantage over using F that eq. (2) includes deviations from (1) - the "size effect" which is so often found in grinding metals [13,14] and ceramics [15,16]. In this form the treatment becomes fairly general and may be applied to a wide range of finishing operations. An example of a relation such as eq.(2) is shown in figure 1 for glass grinding with three rates of removal. The damage was made visible by sawing through the grinding tracks and polishing away the damage due to the sawing. The length of the biggest cracks are given in the figure.

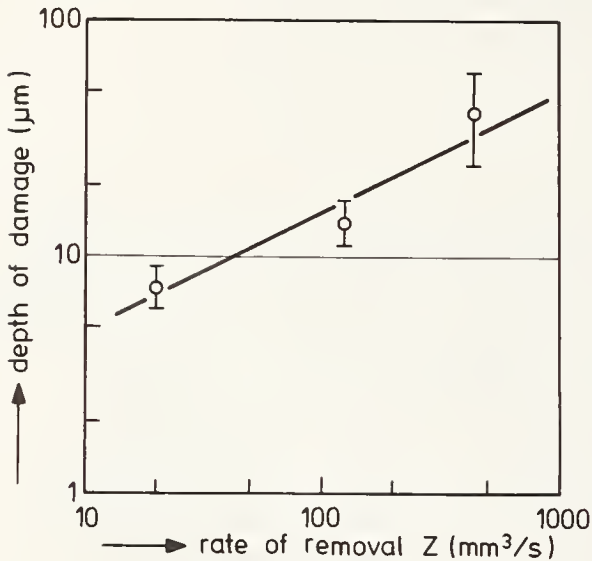


Figure 1. Depth of damage in glass after grinding on various machines with different rates of removal Z. The line drawn has a slope of 0.5

In the next section the optimization procedure for a two-stage situation is considered which is extended to k stages in section 3. The applicability of the model is discussed in section 4.

2. Two-stage optimization

Consider the example of a horizontal axis surface grinder which is used for two stages of finishing. The shape errors of thickness d_0 must be removed; the final surface damage must be smaller than a given thickness d_e . In the first stage no more than d_0 is removed, in the second stage no more than the damage that results from the first stage, d_1 . In total a thickness $d_0 + d_1$ is removed, which should be acceptable in view of the tolerance on the final dimensions. The depth of cut a and the workpiece speed v_w must be chosen for each of the two stages. For a sample of width b the volume rate of removal Z equals

$$Z = a \cdot b \cdot v_w \quad (3)$$

For a sample length l the volume to be removed in the first stage is $d_o \cdot l \cdot b$; the grinding time is then

$$T_1 = d_o \cdot bl / Z_1 \quad (4)$$

where the index 1 denotes the first stage. For a given Z_1 the damaged layer is known from eq.(2), $d_1 = \alpha Z_1^m$; this layer is removed in the second and last stage by using a removal rate Z_2 . This leaves damage over a thickness $d_2 = \alpha Z_2^m$, which should be the known required surface damage d_e . Z_2 is therefore known from eq.(2),

$$Z_2 = (d_e / \alpha)^{1/m} \quad (5)$$

The grinding time for the second stage is $T_2 = d_1 bl / Z_2$ and the total time becomes

$$T = T_1 + T_2 = \left(\frac{d_o}{Z_1} + \frac{d_1}{Z_2} \right) \cdot bl \quad (6)$$

Here d_o is given, Z_2 follows from eq. (5) and d_1 is related to Z_1 by eq.(2). Two choices for Z_1 will be considered, the equal-time case and the minimum-time case. In the first one, the times for the two stages are taken equal, $T_1 = T_2$ and thus $d_o / Z_1 = d_1 / Z_2$, thus $d_o Z_2 = d_1 Z_1$, or using eq.(2),

$$d_o Z_2 = \alpha Z_1^{1+m} \quad (7)$$

from which Z_1 can be solved. The total time becomes

$$T = 2T_1 = 2 \left(\alpha d_o^m / Z_2 \right)^{\frac{1}{m+1}} \cdot bl \quad (8)$$

In the second case the duration of the two stages is not taken as equal, but Z_1 is varied to minimize T . In eq.(6) a minimum occurs when

$$d_o Z_2 = m \alpha Z_1^{1+m} \quad (9)$$

which gives a higher Z_1 value than eq.(7). From eq.(9) follows that $d_o / Z_1 = m(\alpha Z_1^m / Z_2) = m(d_1 / Z_2)$, or using eq.(4),

$$T_1 = mT_2 \quad (10)$$

The first stage takes a shorter time than the second, it is also shorter than in the equal-time case. The total time is now 5.5% lower than in eq.(8). A further reduction in total time is possible by using more stages.

3. k stages

The extension from 2 to k stages does not essentially change the minimization problem. As before, the initial shape error d_o and the final depth of damage d_e are given. The rate of removal during the last stage is then found from eq.(2)

$$Z_k = (d_e / \alpha)^{1/m} \quad (11)$$

The two cases considered before - equal times for all stages and minimum total time - can be calculated now (see the Appendix for details). For equal times the total time T is given in figure 2a as a function of the number of stages used, for various values of m and a fixed value of (d_o / d_e) . From the minimum in the $T(k)$ curve it follows that, for equal times, the number of stages should not be increased above a certain k that still depends on the material behaviour, i.e. m .

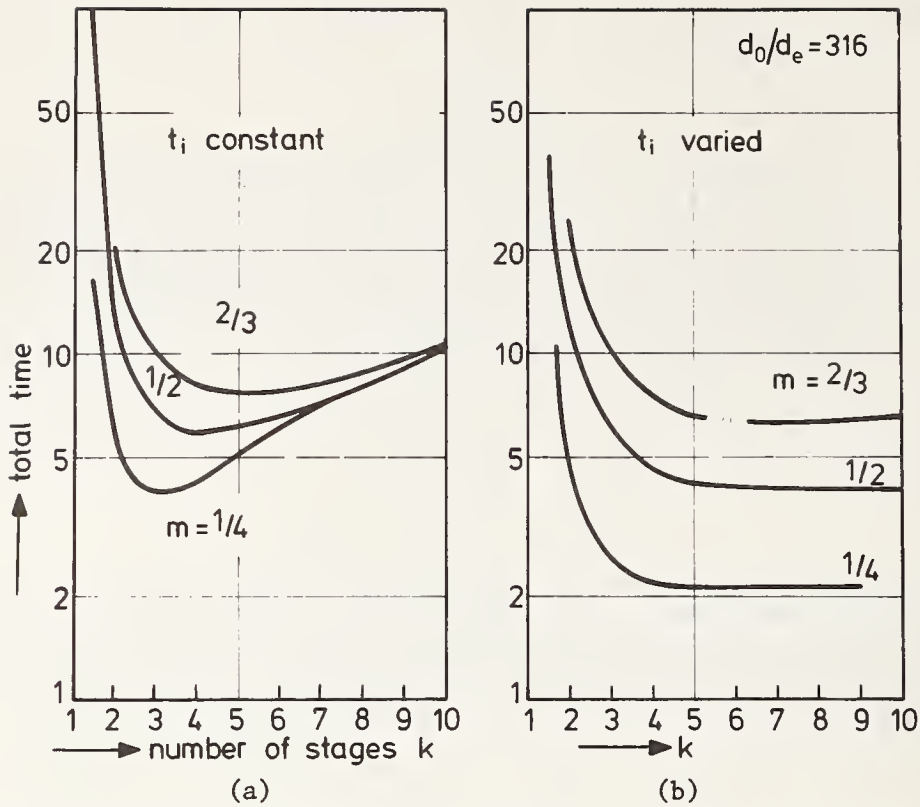


Figure 2. Total time needed for grinding in k stages as a function of k . On the left the result for the case when the duration of the stages is equal; on the right the times are not equal and the optimum total time is shown. m is exponent in eq.(2), d_0 is the initial shape error, d_e is the final depth of damage. The unit of time is given in the Appendix.

For the case of minimum total time the result is given in figure 2b. Again a minimum time occurs, now at higher k than in the first case and the minimum is very shallow.

For five stages of grinding the results have been worked out in greater detail. The removal rates in the subsequent stages are shown in figure 3 for $m = 1/2$ and $(d_0/d_e)^2 = 10^5$. The constant-times case has lower Z values, but takes longer than the optimum where the times were varied. Here higher Z values are found, especially in the first stages; these higher removal rates, however, act during a shorter time!

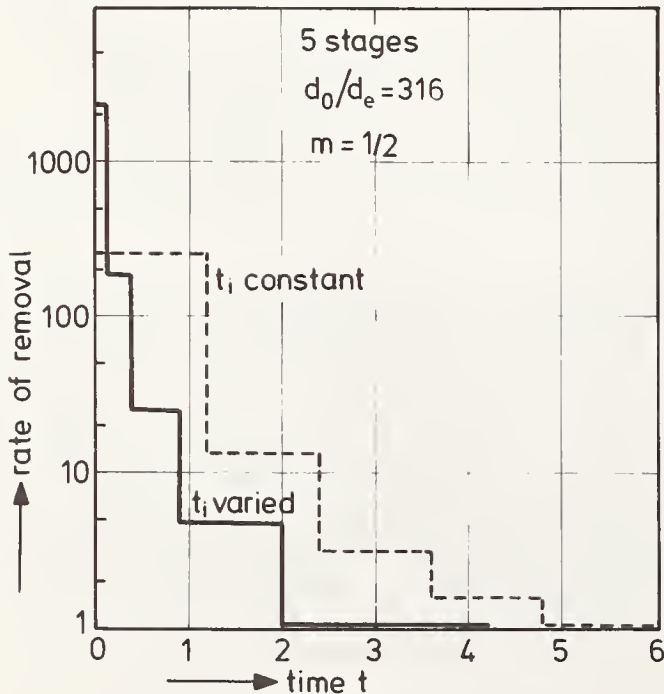


Figure 3. The removal rates during subsequent grinding stages as a function of time for five stages. Equal duration of each stage is shown by the broken line, optimum: full lines.

For three stages, e.g. grinding, lapping and polishing, a simple representation is possible. The total time is given by

$$T = \{d_0/Z_1 + d_1/Z_2 + d_2/Z_3\} b_1 \quad (12)$$

As before, the starting shape error d_0 and the final depth of damage d_e are given. With eq.(11) the final removal rate Z_3 is then known. This makes T a function of Z_1/Z_3 and Z_2/Z_3 only. For every possible operation where these ratio's are known, it is possible to indicate the T value on a graph where Z_1/Z_3 and Z_2/Z_3 are plotted along the axes (fig.4). From the model presented here T values have been calculated and plotted as contours of constant time in the figure; $m = \frac{1}{2}$ and $d_0/d_e = 316$ were used for this case. The two standard cases are indicated too: for constant duration of the three stages the time (in certain units) is 6.94; if the times are allowed to vary, the total time has a minimum of 5.92. The margin around the minimum is seen to be quite large (notice the logarithmic scales for both axes). Near the $T_1 = T_2 = T_3$ point the hatched area in the figure corresponds to a variation in T_1/T_2 and T_2/T_3 by $\pm 20\%$.

The influence of the choice of d_0/d_e on the optimum time T is not very strong: for $m = \frac{1}{2}$, T is proportional to $(d_0/d_e)^{1/12}$, for $m = \frac{1}{4}$ the exponent is $1/84$. The dashed line in figure 4 indicates the locus of T when d_0/d_e is varied. There is hardly any effect on the Z_2/Z_3 value, but rather more on the abscissa Z_1/Z_3 . For lower m values the minimum of T as a function of Z_1/Z_3 and Z_2/Z_3 becomes even more shallow than the one shown in figure 4.

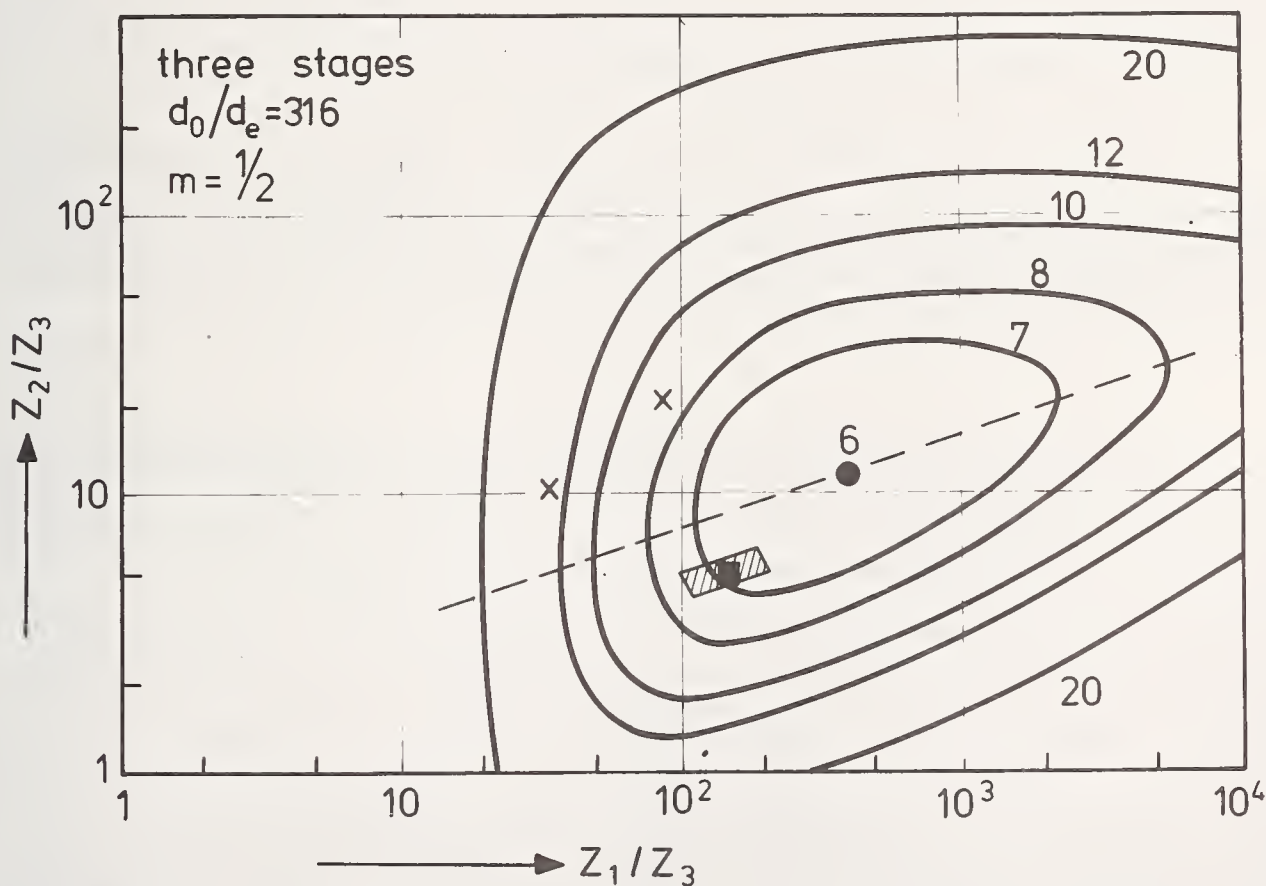


Figure 4. For a three-stage operation the total time is shown as contours in a graph where the removal rates Z_2 and Z_1 (normalized on the last rate Z_3) are plotted along the axes. The round dot is the optimum choice, the square corresponds to constant duration of the stages (the hatched area refers to 20% variations in t_1 and t_2). The lines are calculated for $m = \frac{1}{2}$ and d_0/d_e . For other d_0/d_e values the optimum shifts along the broken line. The crosses are examples of a practical operation taken from [1].

4. Discussion

The requirements for the application of the model described above are twofold: firstly, the depth of damage after an operation with a known volume rate of removal must be known; this $d(Z)$ relation supplies the values for α and m in eq.(2). Techniques for measuring d are available [6,7]. Secondly, the starting conditions (d_0) and the acceptable damage (depth d_e) must be known. The recipe for all stages follows from $d_0/d_e = f_0^m$ and the equations given. It should be pointed out that the $d(Z)$ data are to be taken on the grinding machine as it operates, e.g. at constant wheel speed and with the same abrasive, at the concentration and grain size to be used in practice and at the same wheel width. The results of the calculation show a minimum time for the total operation, but the minimum is fairly shallow (fig. 4). With an increasing number of stages the rate of removal in the initial stages rises considerably, although the duration of these stages is short (fig. 3). Apparently the model favours boldness, in contrast to the approach used in current practice. For example, in Balai's paper [1] a three-stage grinder (t_i is constant) is described with consecutive depths of cut of 0.7 - 2.5 mm, 0.2 - 0.7 mm and 0.02 - 0.03 mm. Assuming constant workpiece feed these data are included in figure 4. Z_1 is about three times Z_2 whereas figure 4 shows a Z_1 value that is about 25 times higher for constant duration of the stages. The total time is not far from the optimum for this value of d_0/d_e (where no damage data were available, m and d_0/d_e need not be correct for this example). No notice was taken of the time required for handling the workpieces between the stages; this is expected to lead to a sharper minimum in figure 1. The minimization procedure for the total grinding time that was reported here, is of economic use when the grinding costs are taken proportional to grinding time. Other contributions to the total costs, such as wheel wear and the resultant cost of dressing, were disregarded, but can be incorporated where quantitative data are available, e.g. in the grinding of metals [4-6]. High Z_1 values (and thus high wheel wear) are expected to be penalized and the optimum in figure 4 will shift to the left.

Sparking out as a last stage in grinding improves the surface quality; the relieve of the elastic deformation of the machine is easier to measure than predict [4,5]. Might it perhaps be possible to control sparking out and thereby eliminate many of the k stages? The geometric progression in t_i suggests a continuous grinding operation where Z decreases with time as a power law, $Z \propto t^{-n}$ (n is about 2 for the data in figure 3). Numerical control of feed or depth of cut would be necessary.

5. Conclusions

-A model has been given for the optimization of a multistage grinding operation. The duration of each stage need not be larger than the time required for removing the damage caused by the previous stage. In combination with the shape errors that must be removed and the acceptable damage at the end of the operation, a complete method has been worked out for the choice of removal rates in the various stages.

- The basis of the calculation is the relation between the depth of damage in a given operation and its volume rate of removal. An example was given for grinding glass.
- The total finishing time shows a minimum for the proper choice of the consecutive removal rates and the duration of the stages. The minimum time improves as the number of stages increases (fig. 2). Depending on the behaviour of the workpiece, three to five stages are sufficient. If the various stages are of constant duration the total process takes longer. Variation of the removal rates around the optimum values shows that the curve representing the total time has a rather shallow minimum (fig. 4).
- The removal rate during the initial stages increases sharply with the number of stages, but the duration decreases (fig. 3). In practice, however, the ratio of consecutive removal rates is much smaller than predicted here. Improvement seems possible.
- For a three-stage operation a convenient method of presentation is to plot the reduced removal rate during the first stage versus that of the second, both divided by that of the third stage (fig. 4).
- On the assumption that the depth of damage has been determined for the range of removal rates that is of interest, the calculations may be applied to any multistage grinding operation, be it on metals, glass or ceramics. By using data on wear, dressing and handling, the model may be extended to cover those situations as well.

References

- [1] Balai, V.V., Method, technology and automated equipment for diamond polishing of optical prisms, Sov. J. Opt. Techn. 43, [8], 481-483 (Aug. 1976).
- [2] Ardamatskii, A.L. and Vorontsova, N.M., The polishing of optical components with a diamond tool, Sov. J. Opt. Techn. 43, [12], 756 (Dec. 1976).
- [3] Bohache, J.J., Chen, G.H. and Moore, D.T., Design of a high speed optical production line, Opt. Eng. 15, 416-423 (Sept. 1976).
- [4] Muschardt, H., Optimierung des mehrstufigen Schleifprozesses, Techn. Mitteil. 69, 418-420 (July 1976).
- [5] Scherf, E., ACO-Pilotanlage für den mehrstufigen Schleifprozess, Techn. Mitteil. 69, 421-424 (July 1976).
- [6] Peters, J., Snoeys, R. and Maris, M., Oberflächenspannungen beim Einsteichschleifen, Techn. Mitteil., 69, 338-342 (July 1976).
- [7] Rupp, W., Surface Structure of fine ground surface, Opt. Eng. 15 [5] 392-397 (May 1976).
- [8] Preston, W.J., The Theory and design of plate glass polishing machines, J. Soc. Glass Techn., 11, 214-256 (1927).
- [9] Kumanin, K.G., Generation of optical surface (The Focal Library, London, 1962)
- [10] Rabinowicz, E., in Friction and wear of materials, p. 168 (J.Wiley, New York, N.Y. 1966).
- [11] Lawn B.R., Fuller E.R. and Wiederhorn, S.M., Strength degradation of brittle surfaces: sharp indenters, J. Am. Cer. Soc., 59 [3] 193-197 (May 1976).
- [12] Veldkamp J.D.B., Crack formation during scratching, (Proc. 9th Int. Conf. on Science of Ceramics, Noordwijkerhout, November 13-16, 1977), Book, Science of Ceramics, 9, K.J. de Vries ed., pp. 438-446 (Nederlandse Keramische Vereniging, 1977).
- [13] Bacher, W.R., Marshall, E.R. and Shaw, M.C., The size effect in metal cutting, Trans. ASME, 74, 61-72 (Jan. 1952).
- [14] Shaw, M.C., Fundamentals of grinding, Book, New Developments in Grinding, M.C. Shaw, ed., pp. 220-258 (Carnegie Press, Pittsburgh, Pa., 1972).
- [15] Broese van Groenou, A., Veldkamp, J.D.B., and Snip, D., Scratching and grinding parameters of various ferrites, J. de Physique, C1, 285-289 (1977).
- [16] Broese van Groenou, A., Grinding experiments on ceramics, see ref. 12, pp. 486-493.

Appendix

k stages

As in the two-stage problem in section 2 the initial shape error d_o , the final depth of damage d_e and, from eq.(2), the rate of removal during the last(k^{th}) stage, $Z_e = (d_e/\alpha)^{1/m}$, are given. Using these a number of useful dimensionless quantities can be introduced. The removal rate Z_i during stage i ($i = 1$ to k) can be normalized by introducing reduced removal rates $f_i = Z_i/Z_e$. The rate f_i is a decreasing function of i and satisfies a number of equations which will be derived below. In the last stage, for $i = k$, $f_k = 1$. It is also useful for the following calculation to introduce f_o for $k = 0$; f_o is related to d_o by $d_o = \alpha Z_e^m f_o^m$; also

$$f_o^m = d_o/d_e \quad (A1)$$

The duration of stage i is determined by the damage in stage $i-1$, d_{i-1} , and Z_i . By analogy with eq.(4) T_i can be written

$$T_i = d_{i-1} b l / Z_i = \alpha Z_{i-1}^m b l / Z_i = (\alpha Z_e^{m-1} b l) (f_{i-1}^m / f_i) \quad (A2)$$

The first factor in the last expression is convenient for introducing a reduced time, t_i ; consequently, by definition,

$$t_i = f_{i-1}^m / f_i \quad (A3)$$

The total reduced time g for k stages is given by

$$g(k) = \sum_{i=1}^k t_i = \sum_{i=1}^k f_{i-1}^m / f_i \quad (A4)$$

As before, two approaches are possible: 1. t_i is constant and 2. t_i is allowed to vary.

t_i is constant

Each grinding stage has now the same duration, which we will call t , so $t_i = t$. The rate f_i ($i = 1$ to k) can be derived from eq.(A3) taking the logarithm,

$$\ln t_i = \ln t = m \ln f_{i-1} - \ln f_i \quad (A5)$$

or

$$\ln f_i = m \ln f_{i-1} - \ln t \quad (A6)$$

After elimination of $\ln t$ this becomes a set of second order difference equations in $\ln f_i$ with boundary conditions for $i = 0$ (f_0 is known) and $i = k$ ($f_k = 1$). The solution is

$$\ln f_i = \ln f_0 \{S(k) - S(i)\} / \{S(k) - 1\} \quad (A7)$$

$$\ln t = m^k \ln f_0 / S(k-1) \quad (A8)$$

where

$$S(k) = 1 + m + \dots + m^k = (1 - m^{k+1}) / (1 - m) \quad (A9)$$

The total time given by eq.(A4) is now known, $g(k) = kt$. Figure 2 gives g as a function of k for various values of m and for $f_0^m = 316$. The value of f_i can be calculated from eqs.(A6) and (A8).

t_i varies

When f_i is varied in eq.(A4) to minimize the total time $g(k)$, two terms contribute, namely t_i and t_{i+1} ; after differentiating to f_i and putting the result equal to zero, we find

$$m f_i^{m+1} = f_{i-1}^m f_{i+1} \quad (A10)$$

t_i can now be expressed in t_{i+1} by

$$t_i = f_{i-1}^m / f_i = m f_i^m / f_{i+1} = m t_{i+1} \quad (A11)$$

as in eq.(10). This can be continued for $i+1, i+2 \dots$ to $k-1$: $t_i = m t_{i+1} = \dots = m^{k-i} t_k$:
Hence

$$g(k) = \sum_{i=1}^k t_i = t_k \sum_{i=1}^k m^{k-i} = t_k S(k-1) \quad (A12)$$

Also from eq.(A10), by taking the logarithm,

$$\ln m + m \ln (f_i / f_{i-1}) = \ln (f_{i+1} / f_i) \quad (A13)$$

This is again a second order difference equation in f_i , with the same boundary conditions as before. The solution is similar to eq. (A7), with an extra term containing $\ln m$,

$$\ln f_i = \left\{ \frac{S(i)-1}{S(k)-1} k - i \right\} \frac{\ln m}{m-1} + \left\{ \frac{S(k)-S(i)}{S(k)-1} \right\} \ln f_0 \quad (A14)$$

t_k follows from eq. (A3), $t_k = f_{k-1}^m$; f_{k-1} follows from eq.(A14) and $g(k)$ from eq.(A12).

Figure 2b gives $g(k)$ for $f_0^m = 316$ and for various values of m .

List of symbols

a	depth of cut	t_i	normalized duration of stage i
b	width of workpiece	v_s	wheel speed
d_o	shape error before operation	v_w	workpiece speed
d_e	depth of residual damage after operation	F	grinding force
d_i	depth of damage after stage i	H_g	grinding hardness
f_i	$= Z_i / Z_e$, reduced removal rate	H	Vickers hardness
f_o^m	from $d_o / d_e = f_o^m$	K	fracture toughness
g	normalized total time	S	sum of powers of m
i	integer	T_i	duration of stage i
k	number of stages	T	total time
l	length of workpiece	Z	volume removal rate (m ³ /sec)
m	exponent in eq. 2	Z_e	removal rate in last stage
n	exponent	Z_i	removal rate in stage i
		α	proportionality factor

Discussion

NARKEN

1. In the abrasion process, regarding the normal and tangential force vectors (F_N, F_T) when considering the machine stiffness, the machine will yield in some degree to both vector components (or resultant). The yield to F_T is probably of little consequence. However, the yield to F_N (perpendicular to grinding surface) affects the resultant flatness and also (probably) the median crack depth (or surface damage). If these problems are of concern then it should be considered that the abrasion process should be designed (wheel and machine parameters) to minimum F_N .

2. Regarding the optimization of consecutive removal rates

$$T_A = \frac{d_o}{Z_1} + \frac{d_1}{Z_2} + \dots + \frac{d_n}{Z_{n+1}}$$

It is implied that the total depth of surface removed is $D_A = d_0 + d_1 + \dots + d_n$. Ideally it appears that a more efficient approach would be

$$T_B = \frac{d_0 - d_1}{Z_1} + \frac{d_1 - d_2}{Z_2} + \dots + \frac{d_n - d_{n+1}}{Z_{n+1}}$$

because here $D_B = d_0$ and therefore $D_B < D_A$. If the same Z_1, Z_2, Z_n is assumed (and respective d_0, d_1, d_n) then $T_B = \frac{D_B}{D_A} T_A$ and it may be expected that $T_{\min_B} \approx \frac{D_B}{D_A} T_{\min_A}$

clearly, the more steps involved in the process, the more significant is the effect.

VAN GROENOU

1. A frequency dependence of the compliance is known to lead to chattering and an uneven surface (in steel grinding the wheel is the most compliant part of the system, metal-bonded wheels are much stiffer). A yielding machine leads to a lower grinding force and a lower removal rate. It is therefore possible to do fine grinding by mounting the workpiece on a piece of rubber, with the risk of chattering.

2. This seems to be a good idea.

MALKIN

You have assumed that the depth of damage depends on the removal rate Z . This is contrary to our results which show for plunge grinding of glass that increasing the removal rate by taking a bigger depth of cut has almost no influence on surface damage and transverse rupture strength, whereas increasing the removal rate by taking a faster workpiece velocity causes more damage and reduces transverse rupture strength. This would completely alter the nature of your optimization problem.

VAN GROENOU

If the depth of damage is only a function of the workpiece velocity V_w and independent of the depth of cut, a , it is clearly advantageous to use large V_w values. The total time can then be minimized with respect to the various V_w values, that can be chosen for the consecutive grinding stages. Apart from factors that contain the ratio's of the subsequent depths of cut the results will be similar as those given in the paper.

RICE

On your log - log plot of depth of damage (d) vs. removal rate (Z) you had three points through which you drew a straight line. However, these points would also suggest an initially slower increase of depth of damage (d) with removal rate (Z) with d becoming progressively greater as Z increases in contrast to your linear log - log plot. Have you other information to clarify the possible distinction between these two trends? Our data suggests the second of the above trends i.e. even more non-linear than a straight line on a log - log plot.

VAN GROENOU

I have no other information. The power law, $d \propto Z^m$, was chosen because of ease of computation. I think the extension to other relations should not be difficult.

GRINDING STONE, CONCRETE AND CERAMICS WITH COATED ABRASIVES

R. C. Lokken and E. J. Duwell

Industrial Abrasives Div., 3M Co.
St. Paul MN 55101

Silicon carbide coated abrasives grind stone or ceramics most efficiently when run dry and at high speeds. This high energy process appears to heat the surface layer of the workpiece to temperatures which make "chip formation" easy. However, neither the ground surface of the workpiece nor the coated abrasive is thermally damaged to any significant degree. Dry dust collection may be an attractive alternative to the removal of wet debris in water lubricated operations.

Key Words: Abrasives; ceramics; coated abrasives; grinding; stone.

1. Introduction

Ceramics are generally regarded as "hard-to-grind" materials. This may be caused by their hardness, or perhaps by their inability to deform plastically to form continuous chips as metals do. Chemical interactions may also affect the grinding process. Quartz, for example, is undoubtedly difficult to grind because of its hardness ($KHN = 820 \text{ kg/mm}^2$), which is twice that of a fully hardened high carbon steel. However, it may also react with abrasives like aluminum oxide to form alumina-silicates at the grinding interface. Thus, hard oxides are usually abraded with hard carbides such as silicon carbide or diamond. Water floods are generally used to minimize thermal or chemical damage to the abrasive in the grind interface.

This project was started with the objective of using wide abrasive belts to machine or finish large concrete or ceramic surfaces. Although wet grinding does not adversely affect the mechanics of using an abrasive belt, the problems associated with the control and removal of wet debris were a strong incentive to include an investigation of dry grinding conditions. Granite was chosen as a workpiece, mainly because it is readily available in our area in large pieces of uniform composition that were found to give grinding data of excellent reproducibility. Granite is composed largely of quartz and feldspar, but the exact composition varies considerably depending on location of the deposit.

The method to be described in this paper involves the utilization of coated abrasive belts under dry conditions and at high belt speeds and high horsepower levels. Grinding debris is collected in a high velocity air stream and deposited in dry dust collection equipment. Although the early development work was done on granite, marketing efforts have led to use of the process in the concrete block industry for dimensioning and face-grinding block [1]. Grinding concrete block to accurate dimensions permits the use of thin-line adhesives and rapid lay-up procedures, while face-grinding imparts an attractive terrazzo-like appearance to the surfaces of the concrete block [1].

To date this process has not been applied to the machining of any other ceramic or stone composites. The purpose of this paper is to offer additional data on the performance of coated abrasives for dry grinding of other ceramics, and to relate, as far as possible, the grinding process to the properties of the workpiece being ground. backing before the mineral is electrostatically drawn up to the backing. This procedure serves to orient the mineral grain so that elongated particles have their long axis perpendicular to the backing. A second adhesive layer, or size coat, is deposited over

2. Structure and Evaluation of Coated Abrasives

A coated abrasive consists of essentially one layer of abrasive grain on a flexible backing (Figure 1). A first adhesive layer, called the make coat, is deposited on the

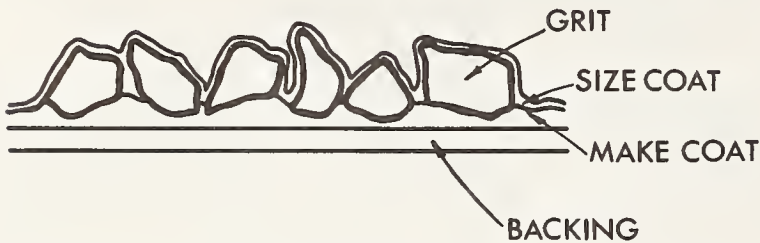


Figure 1. Schematic diagram of the cross section of a coated abrasive.

the mineral to provide further anchorage to the abrasive grain. The coated abrasive material is converted to belts for use in this process.

Both the cost and stock removal capability of an abrasive belt tend to be closely related to the surface area of the belt. A belt 160 inches long will in general remove twice as much stock as a belt 80 inches long, while doubling the width will result in another two fold increase if the workpiece is correspondingly wider. It is, therefore, convenient to define two terms which can be combined to give a measure of belt efficiency:

- Cut: The total volume of workpiece material removed.
- Path: The area of coated abrasive actually used to remove stock.
- Efficiency: $\text{Cut (in}^3\text{)}/\text{Path (in}^2\text{)}$ when the abrasive belt is no longer capable of removing stock at a satisfactory rate or when the horsepower requirement exceeds the capability of the machine.

A simple schematic of a belt grinding operation is shown in Figure 2. Because the belt is generally wider than the workpiece, some attention must be given to distribution of wear across the belt. Uneven belt wear detracts from belt efficiency and also limits the dimensional tolerance that can be produced in the workpiece. If the belt is substantially wider than the workpiece and the workpiece is not uni-dimensional in the grinding direction, uniform belt wear can be achieved by staggering the entry point of the workpiece, or by oscillating the belt [2]. Belt oscillation can be controlled through deflection of the idler drum (fig. 2).

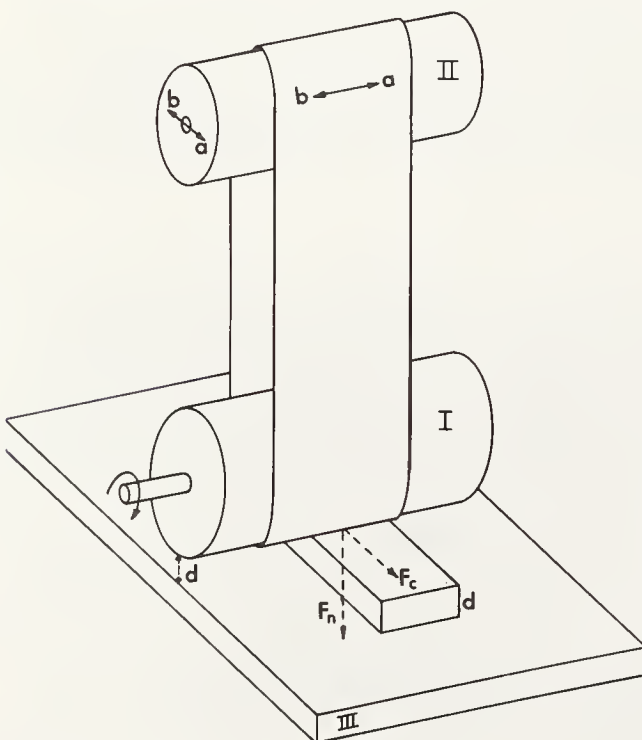


Figure 2. Simple schematic of a belt grinding operation. Belt can be oscillated in directions a and b by appropriate deflection of idler. Spindle is generally driven, and for dimensioning is at some fixed distance (d) from conveyor bed (III). Load on bed (F_n) and cutting force (F_c) increase as belt wears. Specific energy of grinding ($E_s = \text{hp-min/in}^3$) is independent of F_n but is proportional to F_c .

Power requirements depend on depth of cut, belt speed, workpiece infeed velocity, state of wear of the abrasive belt, and on the "grindability" of the workpiece.¹ It is usually expressed as horsepower per inch of workpiece width (HP/in) and does not include the no-load power requirement of the machine. Rate of cut, R , is also normalized with respect to the width of belt actually used ($\text{in}^3/\text{min}/\text{in}$). Belt efficiency (cut/path) is a good indication of workpiece grindability, as is the energy (E_s) required to grind up a unit volume of workpiece ($\text{HP}\cdot\text{min}/\text{in}^3$). E_s is obtained from the relationship $E_s = P(\text{HP}/\text{in})R(\text{in}^3/\text{min}/\text{in})$.

3. Grinding Granite

Using Dakota granite, a wide range of machine conditions were used with coated abrasives made with silicon carbide (SiC), boron carbide (B_4C) and aluminum oxide (Al_2O_3). Grade 24 minerals were used since the objective was to remove stock rapidly as a result of large downfeeds, high belt speeds, or large throughfeeds. Both dry and water-flooded experiments were performed. The investigation showed that by far the greatest belt efficiencies were obtained with the following conditions:

- (1) Silicon carbide mineral
- (2) Dry grinding
- (3) A hard non-elastic backing to carry the mineral
- (4) A smooth steel contact wheel
- (5) High belt speeds (≥ 9000 ft/min), (≥ 2743 m/min)
- (6) High throughfeeds (300-100 ft/min), (9-30 m/min).

Decrease in belt caliper, belt wear, and power requirement are plotted as a function of stock removed in figure 3. The power consumption is noted to level off and the rate of

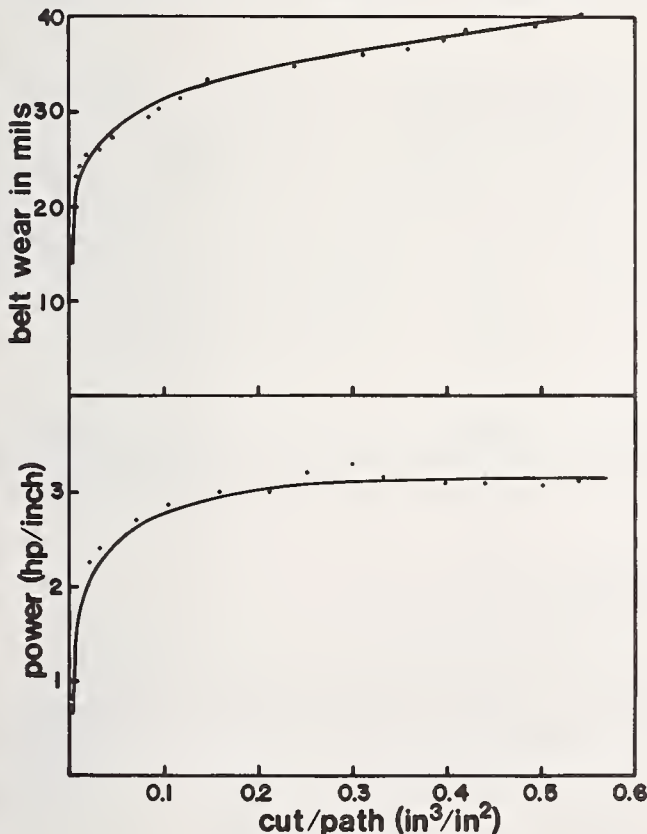


Figure 3. Belt wear and horsepower requirements for grinding Dakota granite as a function of stock removal. A 24-mesh silicon carbide belt was run at 7800 ft/min over a smooth steel contact wheel. Infeed was 10 ft/min, downfeed was 0.01 in/pass.

¹Since the machine settings and abrasive tool dimensions are in English units, these units will be used in this paper. For reference, a belt speed of 10,000 ft/min = 305 m/min; a rate of cut of 1.0 $\text{in}^3/\text{min}/\text{in}$ = 6.45 $\text{cm}^3/\text{min}/\text{cm}$; a cut/path of 1.0 in^3/in^2 = 2.54 cm^3/cm^2 ; 1.0 $\text{HP}\cdot\text{min}/\text{in}^3$ = .653 Kcal/cm^3 .

belt wear becomes linear after the initial sharp rise in both variables. This initial sharp increase is believed to accompany the fracture and loss of a small population of sharp grains that rise above the general level of the abrasive coating. Under the same conditions, the introduction of water results in an increase of 50% in power consumption and a substantial loss in belt efficiency. Use of an aluminum oxide belt of the same grade resulted in a decrease in belt efficiency of approximately 95%. B₄C performed even more poorly, failure appearing to be a result of catastrophic mineral fracture.

Although belt speeds of 3000-6000 ft/min commonly give optimum belt performance on metals, higher speeds are definitely better for grinding granite (fig. 4). Grinding

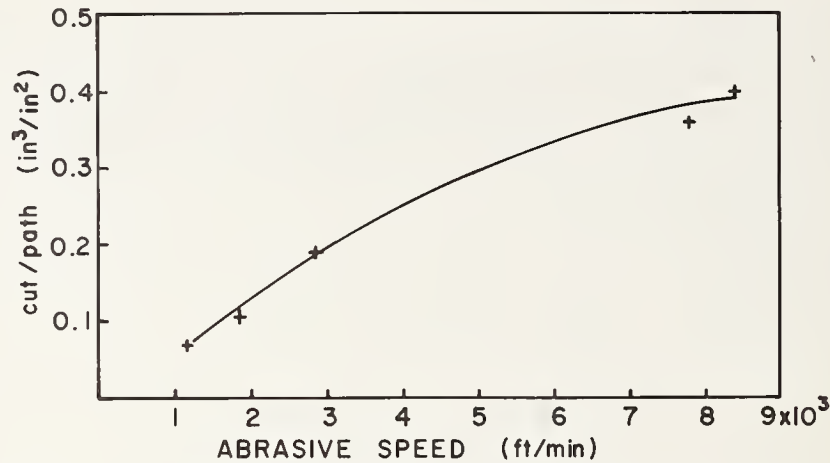


Figure 4. Cut/path as a function of belt speed for granite grinding with 24-mesh silicon carbide belts. All data was taken at a belt speed of 7800 ft/min over a smooth steel contact wheel. Infeed speed was 10 ft/min, downfeed was 0.010 in/pass.

granite dry at 9000-12000 ft/min produces highly incandescent grinding debris, while the belt and the ground surface remain relatively cool (the surface is slightly warm to the touch). Thus, it appears that grinding energy leaves the grind interface almost entirely in the chips being formed. The situation appears to be improved by increased through-feeds, and throughfeeds of 50-100 ft/min are now commonly used for grinding concrete block (there are no commercial applications of this method in the stone industry). Since these materials do not increase in temperature as a result of air oxidation, as is the case with metals, it must be concluded that the conversion of mechanical energy to heat energy in the grind interface increases the temperature of the surface layer being removed to possibly 1000°C or higher.

Not surprisingly, examination of the ground surface and the swarf (grinding debris) indicates that some of the particulates are globular and apparently became molten during the process. However, angular particles are also present, indicating chipping or spalling.

From the data in figure 3, it can be calculated that

$$E_s \approx 3.1 \text{ (HP/in)} / 1.76 \text{ (in}^3\text{/min/in)} = 1.76 \text{ HP-min/in}^3 \text{ (= 1.15 Kcal/cm}^3\text{)}.$$

Based on the constituents of granite, a specific heat (C_p) of 0.20 can be reasonably assumed. Thus, the heat generated can be expected to increase the temperature (T) as follows:

$$T = \frac{E_s}{C_p \rho} \times 1000 = \frac{1.15 \times 1000}{0.20 \times 2.75} = 2090^\circ\text{C.} \quad (\rho = \text{density})$$

Although some heat is certainly lost in the abrasive belt, to the atmosphere, and into the remaining surface, it is not surprising that the swarf temperature is increased to the melting point of the constituents in the stone.

4. Grinding Other Ceramic Materials

A porous alumina fire brick and a dense magnesite fire brick were abraded under the high speed, dry conditions, used for granite. The porous alumina brick offered such little resistance to stock removal that power measurements could not be determined with any degree of accuracy. The magnesite brick offered much less resistance to abrasion than granite, and was effectively ground under the conditions recorded in table I. Belt efficiencies were not determined for all conditions, but based on data generated for granite for which the specific energy of grinding is greater (~ 1.75 HP-min/in³), belt efficiencies (cut/path) probably exceed 3 in³/in². The magnesite bricks displayed distinct grind lines on the abraded surface, indicating the possible existence of a chip forming process by plastic deformation.

Table I - Grinding Data for Magnesite Fire Brick
Belt Speed: 8650 ft/min, Infeed: 10 ft/min

<u>Depth of Cut</u> (mils)	<u>Rate of Cut</u> (in ³ /min/in)	$\frac{E_s}{}$ (HP-min/in ³)
10	1.2	0.358
20	2.4	0.333
30	3.6	0.327
40	4.8	0.329
50	6.0	0.331

Although the aluminum oxide firebricks were easily abraded, dense forms of this compound are not easily ground, as evidenced by the data in table II. Dense, fused aluminum

Table II - Grinding Data for Fused and Natural Corundum (Al₂O₃)
Belt Speed: 8650 ft/min

<u>Workpiece</u>	<u>Depth of Cut</u> (mils)	<u>Rate of Cut</u> (in ³ /min/in)	$\frac{E_s}{}$ (HP-min/in ³)
Fused Al ₂ O ₃ *	10	1.26	2.1
"	15	1.89	1.3
"	20	2.52	0.91
Corundum**	10	0.6	1.35
"	20	1.2	1.11
"	30	1.8	1.00
"	40	2.4	0.93
"	50	3.0	0.91
"	60	3.6	1.10

* at 10.5 ft/min infeed rate

** Corundum in terrazzo composite - at 5.0 ft/min infeed

oxide for the preparation of abrasive grain was somewhat more difficult to grind than natural corundum in a terrazzo matrix. In both bases, examination of the swarf or ground surface failed to reveal evidence of melting, but rather indicated a material removal process by chipping and spalling.

More recently, alumina has been co-fused with zirconia at or near the eutectic composition to form mechanically tough, thermally stable structures. Grinding of this material produced specific energy values far in excess of that noted for any other fused ceramic (table III). As in the case of fused Al₂O₃, higher cut rates appear to result

Table III - Grinding Data for Fused Eutectic Alumina-Zirconia
Belt Speed: 8650 ft/min, Infeed: 10.5 ft/min

<u>Depth of Cut</u> (mils)	<u>Rate of Cut</u> (in ³ /min/in)	$\frac{E_s}{(HP\text{-min/in}^3)}$
2	0.25	10.20
3	0.38	6.64
5	0.63	3.69

in lower specific energy of grinding. For this material, chip formation appeared definitely to involve plastic deformation or melting. The ground surface was metallic and shiny in appearance with well defined grind lines. The chips exhibited the curl shapes noted in metal swarf.

Quartz was ground both as a synthetic single crystal and in its natural polycrystalline form (flint). It was apparent that the grindability of the single crystal depended on crystal orientation (table IV). From the limited data obtained, the flint

Table IV - Grinding Data for Quartz
Belt Speed: 8650 ft/min

<u>Workpiece</u>	<u>Rate of Cut</u> (in ³ /min/in)	$\frac{E_s}{(HP\text{-min/in}^3)}$
Crystal*	2.52	0.23
Crystal**	2.52	0.42
Flint	2.52	0.71

* grinding parallel to a axis
** grinding parallel to c axis

was more difficult to grind than single crystal quartz, although it is possible that some crystal orientations may result in far greater resistance to chip formation. No evidence was found of plastic chip formation, with all workpieces exhibiting extensive chipping and thermal spalling.

5. Discussion of Results

High belt speeds, high infeeds, and dry grinding conditions appear to create a material removal process in which the energy of grinding is removed from the grind interface almost entirely by the chips. Composite workpieces such as granite, fused alumina-zirconia, or concrete, appear to resist spalling and fracturing, with the result that the chips are formed plastically or by actual melting of the surface layer being ground away. A survey of specific heat values [3] for the materials under consideration indicates that between 100°C and 1500°C, specific heat values generally rise from 0.2 cal/g/°C to 0.3 cal/g/°C. (ZrO₂ has a specific heat range of 0.11 to 0.18, but its density is also greater than the rest of the material studied). The greatest values for E_s were noted for the alumina-zirconia eutectic. This ceramic has a density (ρ) of 4.7. For an E_s of 5.0, and assuming an average specific heat of 0.15 for alumina-zirconia, the increase in temperature is calculated to be at least 1800°C (to melting point) with about 2000 cal/g left over for fusion (assuming, of course, that all energy goes into the chips). Thus, as in the case of granite, the swarf is noted to be incandescent as it leaves the grind interface. By contrast, ΔT for magnesite is calculated to be 288°C and no incandescent chips are observed during grinding. Various architectural marbles yield similar values for E_s , and also did not exhibit incandescent grinding debris.

It should be noted that E_s generally tends to decrease with an increase in depth of cut. This is probably caused by material removal as a result of sub-surfacing cracking, and less chip formation by deformation processes. It should be noted that the energy losses in the machine at higher rates of cut will increase, this tending to be a factor contributing an error which would result in lower values for E_s than are calculated assuming the no-load horsepower reading.

Whether chip formation is induced by fracture or by plastic processes, it is apparent that high stock removal rates by grinding can be achieved at high belt speeds and under dry conditions with silicon carbide coated abrasives. Commercially, concrete blocks are being ground with belt efficiencies (cut/path) of 1.0 - 5.0 in³/in². At current coated abrasive prices, this represents a tool cost of generally less than \$0.01 for each cubic inch of workpiece removed.

References

- [1] Lokken, R. C., McDonald, W. J., and Duwell, E. J., Grinding Stone and Concrete with Coated Abrasives, Am. Cer. Soc. Bull., 53, [a], 646-649 (1974).
- [2] McGibbon, T. R., Amundson, S. E., and Lokken, R. C., CAMOS: A Computer Aided System for Establishing Optimal Parameters for Achieving Uniform Abrasive Wear During High Rate Grinding, Wear, 37, [1], pp. 1-14 (1976).
- [3] International Critical Tables, Vol. II, p. 85.

Re
R.
Pr

in
m
th

tu
Pr

ite

me
in
rec
fab
var
ow

sta
eng
ter
the
eos

TURBINE COMPONENT MACHINING DEVELOPMENT

D. W. Richerson and M. W. Robare

AiResearch Manufacturing Company of Arizona
Phoenix, Arizona 85010

Various machining methods that have been evaluated to produce ceramic turbine components from high-strength ceramic materials are discussed. These machining methods are compared in terms of economics, dimensional tolerances, surface finish, and strength of the resulting product. Special emphasis is on the machining methods developed for fabrication of rotor blades from hot-pressed silicon nitride (Si_3N_4).

Key Words: As-machined material strength; dimensional tolerances; profile grinding; silicon nitride; ultrasonic machining.

1. Introduction

The majority of chapters in this Proceedings discuss the basic theory of machining with respect to interactions of a tool and a ceramic workpiece. This chapter will discuss the application of basic machining theory to fabrication of complex gas turbine components and the effects of the machining on the strength of the material.

The examples and data that will be described were obtained during fabrication development of turbine components conducted under the DARPA/NAVY/AiResearch Ceramic Engine Demonstration Program. Three types of configurations were involved:

- (1) "Green machining" of silicon vanes, shrouds, and other static hardware.
- (2) Finish machining of reaction-bonded Si_3N_4 stator vanes.
- (3) Individual rotor blades of hot-pressed silicon nitride (Si_3N_4) requiring machining of an airfoil, a platform, and a dovetail attachment.

Items 1 and 2 will be discussed briefly, item 3 in detail.

2. Green Machining

Green machining refers to machining of a ceramic part prior to final densification while the material consists of compacted, loosely-bonded powder. Such material is much softer than the ceramic in its final densified condition and can be machined much more economically since diamond tooling is not required. However, the material is relatively fragile, and great care is necessary in the design and fabrication of the tooling and fixturing so that the parts can be accurately and uniformly held during the various shaping operations. In addition, the machining parameters must be carefully controlled to avoid over-stressing the fragile material and producing chips, cracks, breakage or poor surface.

Reaction-bonded silicon nitride (RBSN) is presently an important material being evaluated for static hardware (stator vanes, shrouds, transition liners, pilot cylinders, combustors, etc.) in gas turbine engines. It is prepared by reacting a compact of silicon particles in a nitrogen atmosphere at high temperature under controlled conditions to achieve densification. This material is relatively unique in that no significant dimensional change occurs during this nitriding operation. Thus, to achieve minimum cost, it is advisable to conduct all shaping operations on the silicon compact prior to nitriding.

Prior to green machining, the silicon-compact is either partially nitrided or presintered to provide adequate strength for handling and fixturing. This is a critical step, because insufficient prenitriding or presintering will leave the part too fragile and an excess will increase the difficulty of machining.

Holding of the presintered silicon for machining is typically accomplished with a combination of bee's wax and precision metal fixtures. The part must be held rigidly, but with no distortion or stress concentration. Metal fixturing should normally be located either on the outer diameter or the face of the part. This is to avoid expansion of the metal fixture into the ceramic causing breakage when heat is applied to soften the wax during removal of the machined part from the fixture. If there is no way to locate the part except on the inside diameter, special care must be taken to heat the ceramic rapidly while keeping the metal cool.

Once a ceramic part has been secured rigidly in a fixture, machining can be conducted by a variety of methods — turning, milling, drilling, form wheel grinding, and profile grinding. Machining can be accomplished either dry or wet. In either case, the silicon compact is abrasive and results in tool wear. As little as 0.005-inch wear land on the cutting edge will result in a buildup of the cutting pressure and damage to the ceramic.

It is possible to machine silicon compacts with high-speed, steel cutting tools, but this is not recommended for critical gas turbine components. The tools dull so rapidly that extreme care is necessary to avoid damage to the workpiece. Figure 1 summarizes a study of other cutting tool materials using a 5-degree positive rake and 10-degree clearance angle. The GE compact diamond costs about 10 times as much as the tungsten carbide but results in a significant cost savings in terms of increased life, less time changing inserts, and reduced risk of damage to the workpiece from a dull tool.

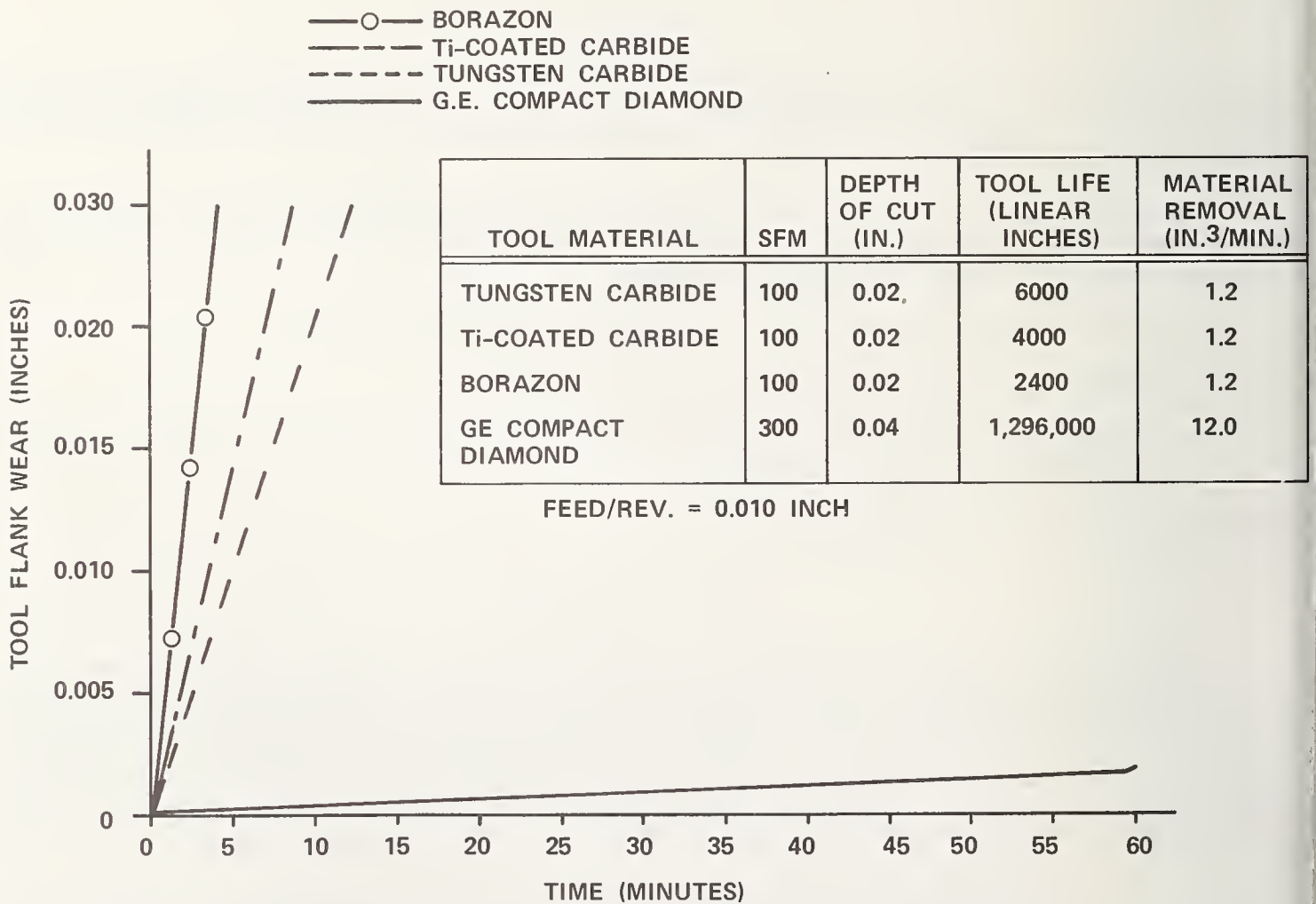


Figure 1. Tool Wear During Machining of Pre-Sintered Silicon.

The above study was conducted with single-point turning on an engine lathe. Milling with a two-flute end mill at 200 surface feet per minute (SFM) with GE compact diamond inserts showed the same life characteristics.

As a portion of the DARPA/Navy/AiResearch Program, Norton Company and Jarvis Company [1]¹ have teamed to develop the capability to produce complex stator vane configurations by green machining isostatically pressed, presintered silicon compacts. Most of the grinding steps were conducted with form-grinding wheels manufactured by the Norton Process E, which utilizes a very accurately formed steel substrate coated with a single layer of carefully sized diamond particles. Formed wheels with 120-grit diamond were used to shape a blank having appropriate shroud contours and dimensions. The airfoil was then profile ground using a 1/8-inch diameter spindle-mounted, diamond-coated wheel. A finished Si_3N_4 vane from Norton is shown in figure 2. No machining was required after nitriding. Typical material strength in the as-nitrided condition was 44 KSI, compared to about 35 KSI for similar vanes made by other processes (slip casting or injection molding).

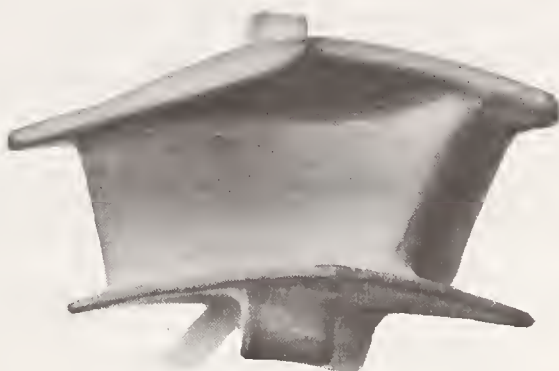


Figure 2. A Finished Si_3N_4 Vane.

3. Machining After Nitriding

The loosely bonded silicon compact that could easily be machined with a variety of tooling is converted to strongly-bonded silicon nitride during the nitriding operation. The resulting reaction-bonded silicon nitride (RBSN) is about 85 percent of theoretical density with high hardness and a strength typically over 35 KSI. It can only be machined effectively with diamond tooling.

Cost analyses have shown that it is important to make the RBSN part as close to net shape as possible since even small amounts of post-nitriding machining can dominate the cost of the part. When machining is required, however, the same type of careful procedures as for the previous silicon compact machining are necessary. Holding is accomplished with rigid metal fixtures and bee's wax. Machining is typically done with resinoid-bonded diamond wheels operating at 6000 to 7000 SFM with a water-soluble coolant. To avoid edge-chipping or other damage to the part, downfeed is restricted to about 0.0005 to 0.001 inch per pass.

4. Rotor Blade Machining Development

Norton Company NC-132 hot-pressed silicon nitride (HPSN) was selected as the rotor blade material to be machined from solid blocks into individual rotor blades for insertion into a metal rotor hub. The final engine blade design was not available at the start of the program; therefore, a preliminary attachment design (fig. 3) and an airfoil design (fig. 4) were selected so that machining process development could be initiated. The attachment design was selected to permit subsequent spin-

¹

Figures in brackets indicate the literature references at the end of this paper.

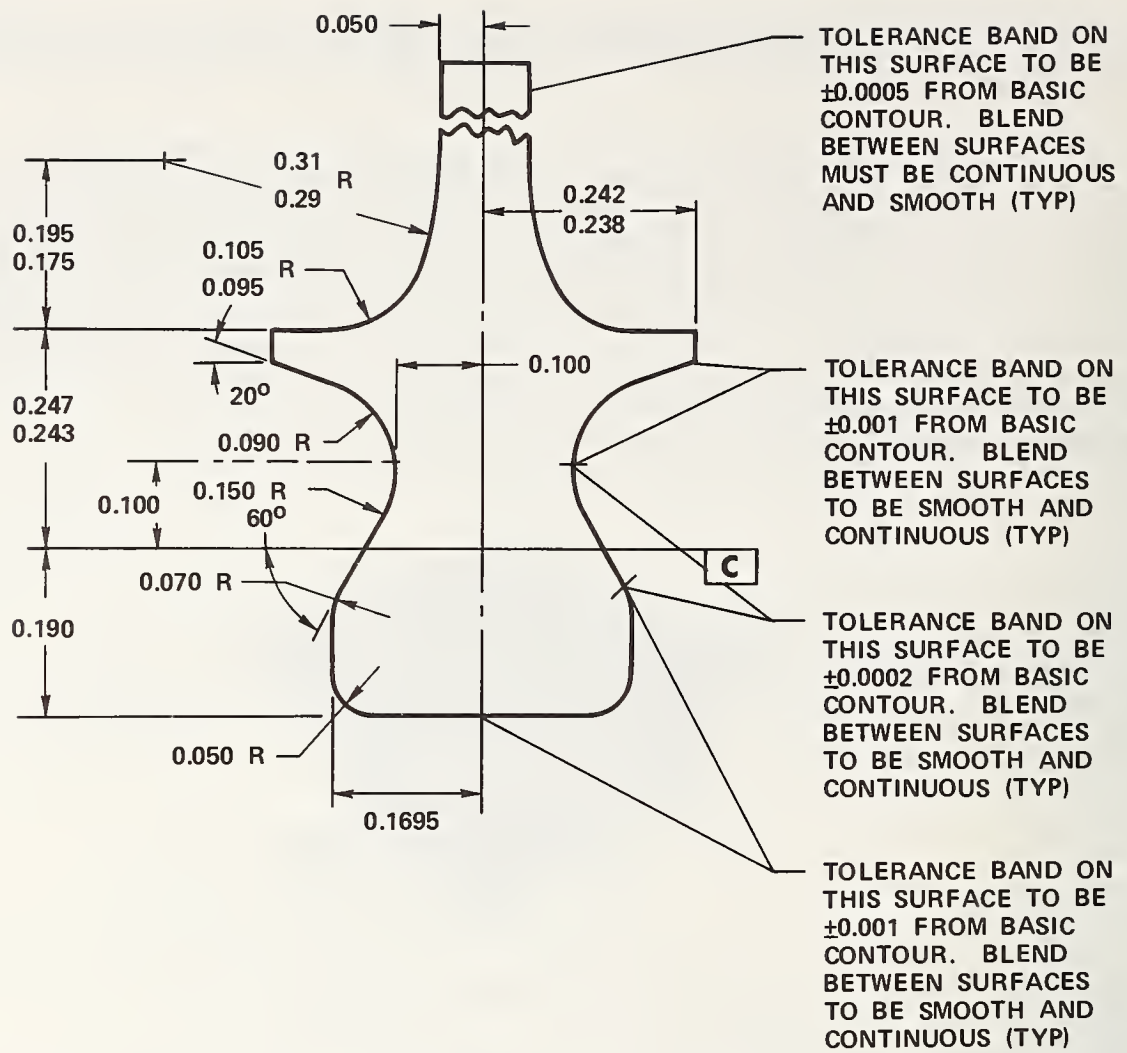


Figure 3. Attachment Configuration for Machining Development.

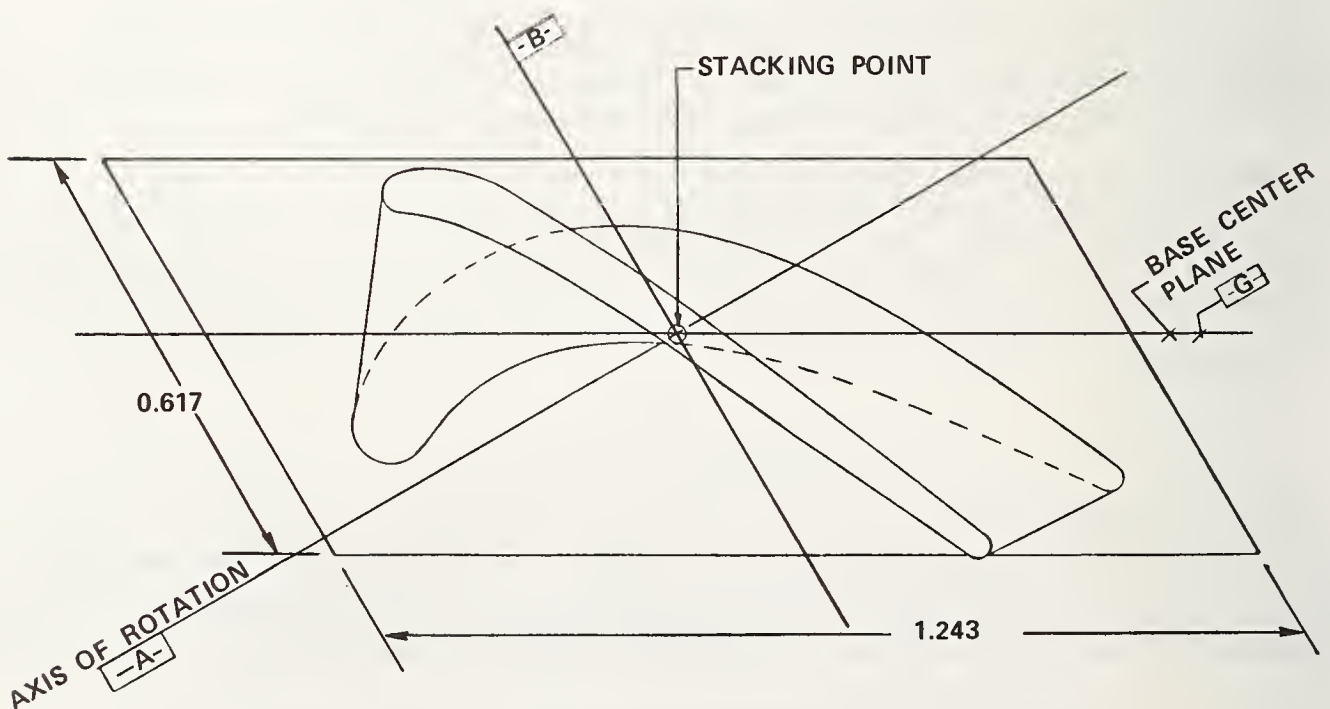


Figure 4. Airfoil Configuration for Machining Development.

testing of the machined specimens to assess the as-machined component strength for comparison with previous strength data for NC-132 generated with simple test bars. The selected airfoil configuration was highly twisted and tapered to make certain that it would be at least as difficult to machine as the final engine configuration.

Since machining of such complex airfoil configurations with tight tolerances had not previously been demonstrated for ceramics, a variety of approaches and sources were evaluated. Efforts conducted at AiResearch included Pantograph profile grinding, ultrasonic machining, and lapping. Efforts conducted by Norton Company included contour grinding, formed-wheel grinding, cam grinding, profile grinding, and lapping. Efforts at Western Gold and Platinum Co. (WESGO) included profile grinding and lapping. The key evaluation criteria for these machining development studies included dimensional tolerances, surface finish, orientation of grinding damage, and as-machined strength.

Since the importance of orientation of grinding damage may not be readily obvious to the reader, it will be explained with respect to a turbine-rotor blade. Peak stresses in an inserted rotor blade occur in the neck region of the attachment perpendicular to the radial direction. The strength of a machined ceramic is greatest parallel to the direction of grinding (subsequently referred to as the longitudinal direction) and weakest perpendicular to the direction of grinding (the transverse direction) [2]. For NC-132 HPSN surface-ground with 320-grit diamond and tested in quarter-point bending with a 0.125-by-0.250-inch cross section over a 1.5-inch outer span, the longitudinal strength is typically 100 KSI \pm 15 KSI and the transverse strength is 62 KSI \pm 5 KSI. To achieve optimum strength for a rotor blade, therefore, the highly stressed attachment region should be machined in the radial direction. Since this is not possible by most of the machining approaches, the damage resulting from machining must be minimized by using finer grit diamond for the final machining passes, followed by lapping.

The following sections describe the techniques that have been evaluated for rotor-blade machining.

4.1 Attachment contour grinding

Contour grinding of the blade attachment was conducted at Arthur Crafts Company (ARCO) under the AiResearch subcontract to Norton Company. A schematic of the contour grinding technique is illustrated in figure 5. In this technique, a manual machine is equipped with a shadow lamp, which projects an enlarged image of the work piece and grinding wheel on a screen. With the aid of this projection, the operator is able to manipulate the machine to produce the proper shape. A very high degree of accuracy may be obtained by a skilled operator. Typically, blade attachment specimens are rough machined at a down-feed rate of 0.0005 inch per pass, and finish machined at a rate of 0.0002 inch per pass using a finer grit diamond wheel.

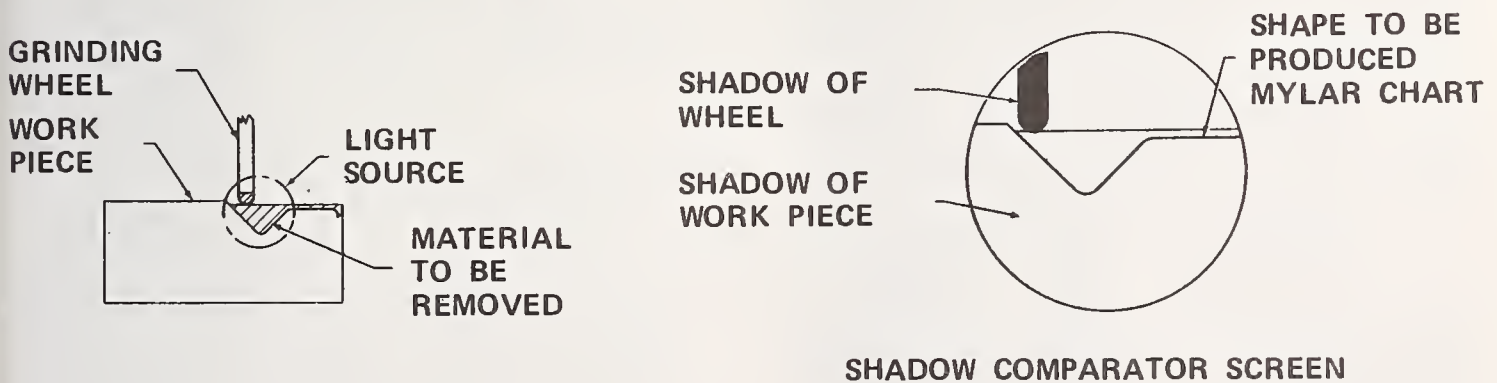


Figure 5. Contour Grinding.

The contour grinding process uses very small amounts of diamond, since dressing and reshaping of the wheel are not as necessary as in some other techniques. However, contour grinding is still a very expensive approach since an operator must be present continuously. An additional disadvantage of contour grinding is that all the grinding grooves are aligned in the axial direction of the blade and are thus perpendicular to the axis of maximum tensile stress. This is comparable to 4-point flexure test specimens machined in the transverse direction.

The contour grinding approach has produced rotor blade attachments to the required tolerances which, after lapping, have survived 130-percent design-speed spin testing.

4.2 Attachment formed-wheel grinding

Formed-wheel grinding is performed on a surface grinding machine using a diamond wheel that has the exact mirror image of the shape to be produced. Typically, for a shape such as the blade attachment, a series of formed wheels are used, with each subsequent wheel having a configuration closer to the final shape and a finer grit size to achieve an improved surface finish.

The initial cost of formed wheels is high because they must be precision shaped, and during machining they require frequent reshaping. In spite of these difficulties, formed-wheel configurations and grit sizes can be chosen to allow very rapid stock removal to produce an overall low-cost machining operation. As with contour grinding, formed-wheel grinding produces grinding grooves in the axial direction of the blade, which is transverse to the principal stresses. This results in reduced material strength. Lapping is required to minimize the strength degradation.

Acceptable blade attachments have been produced by formed-wheel grinding, and the cost projections are very encouraging.

4.3 Attachment profile grinding at WESGO

WESGO has machined the attachment sections on both spin-test specimens and turbine blades using a combination of form-wheel grinding and profile grinding. The attachment specimens were first ground to within 0.010 inch of net size using a formed wheel. Final machining was accomplished on a single-spindle, numerically controlled, profile-grinding machine, resulting in orientation of grinding grooves in a radial direction. The surfaces were then lapped and polished. Spin-test specimens and blades were within required tolerances and have survived the 130-percent design speed spin testing.

4.4 Airfoil cam grinding

Initial airfoil fabrication studies by Norton Company were conducted at Excello using cam grinding techniques that had been successfully used to fabricate a large ceramic airfoil configuration for Westinghouse. However, machining was more difficult for the rotor blades of this program because of their complex geometry, small size, and thin trailing edges.

A schematic of the basic cam grinding setup is shown in figure 6. This was not successful in achieving the required geometry. Support of the airfoil at the tip severely limited the size and angle of approach of the grinding wheel. This prevented grinding the base of the airfoil to tolerance. The set-up was modified, removing the blade-tip support and machining the blade cantilevered. This permitted a smaller angle of attack of the grinding wheel, eliminating the initial restrictions. Excello demonstrated the feasibility of airfoil machining but chose not to continue further.

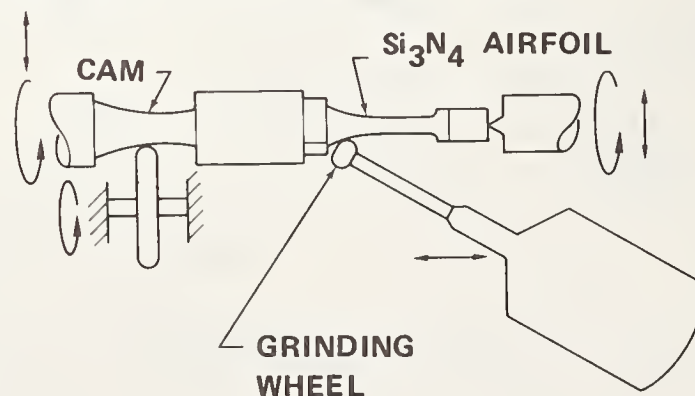


Figure 6. Schematic of Cam Grinding Technique.

4.5 Airfoil profile grinding at Jarvis

Norton Company teamed with Jarvis Company to machine airfoils after Excello chose not to continue. Jarvis used a two-spindle automatic profile grinding machine. Rough grinding was conducted

with a 2-inch diameter diamond wheel followed by final grinding with a 0.5-inch diameter wheel. Airfoils were successfully machined onto attachments supplied by Arthur Crafts, and the complete blades were successfully spin tested to the required 130-percent of design speed.

4.6 AiResearch rotor blade machining

AiResearch has conducted process-development studies of both attachment and airfoil machining using a Gorton P-2-3 Pantograph Profile Grinder. The setup is shown schematically in figure 7 for airfoil machining and pictorially in figure 8 for attachment machining. In both cases an 8:1 master is used to achieve the required close tolerances.

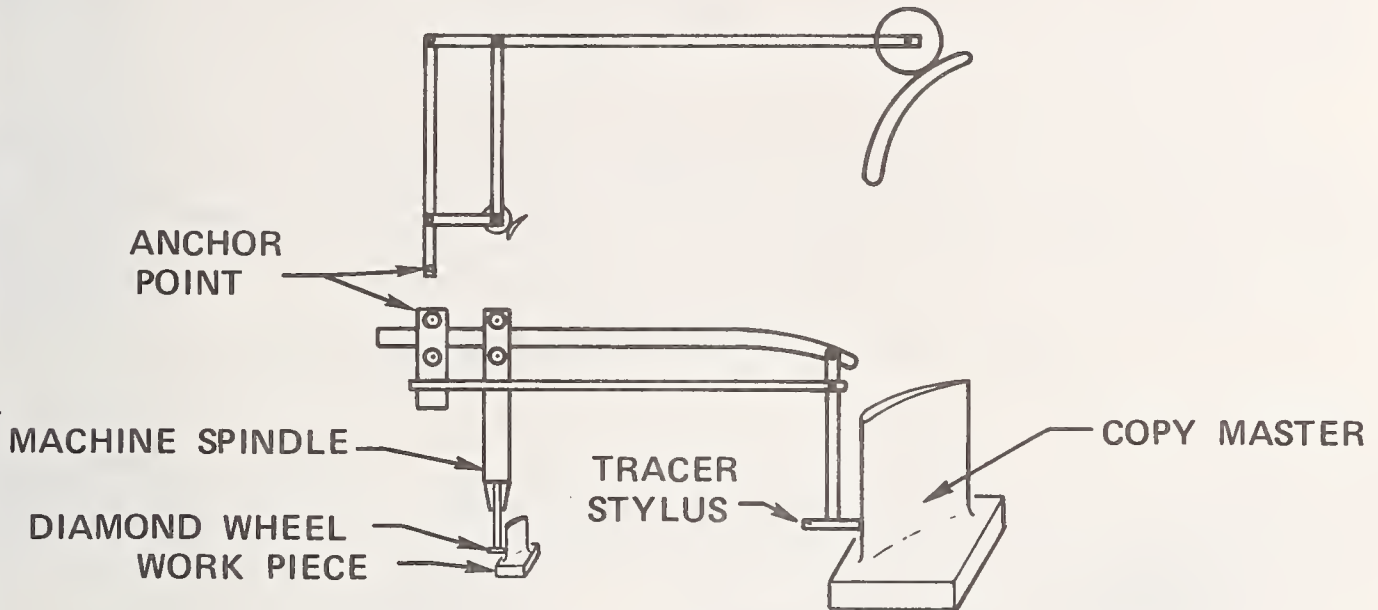


Figure 7. Schematic of Pantograph Profile Grinding Setup for Airfoil.

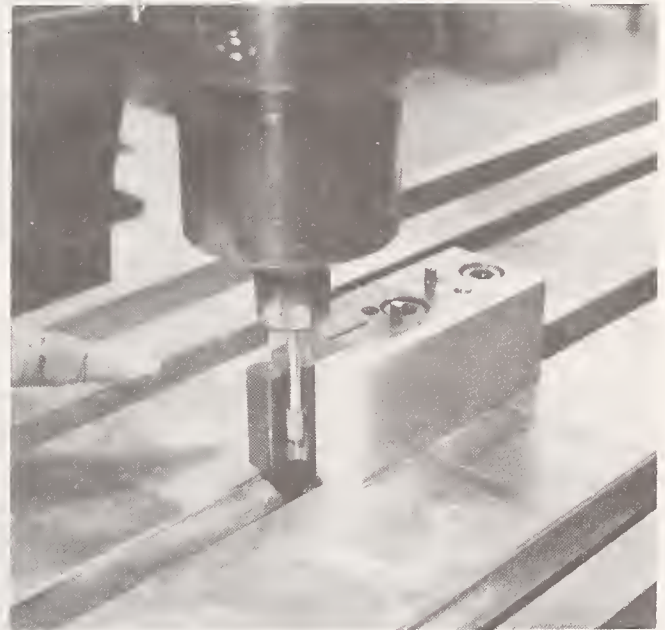
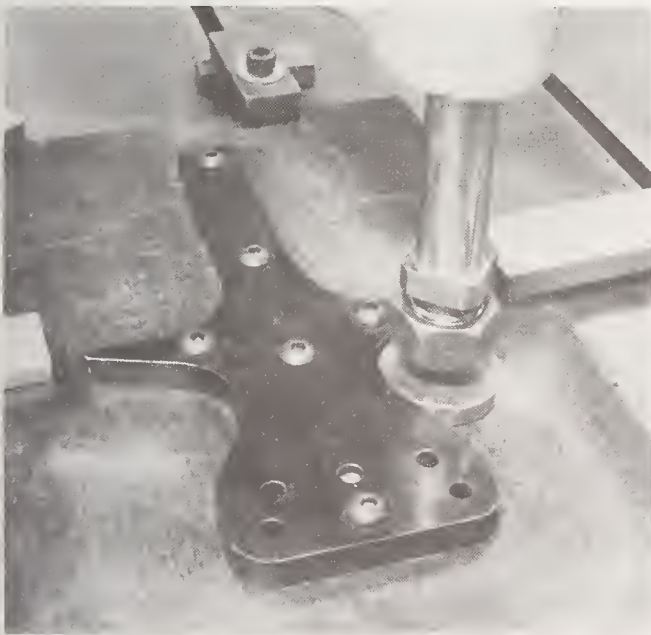


Figure 8. Pantograph Setup for Grinding Blade Attachment.

A major advantage of the Pantograph approach is the capability of aligning all the grinding grooves radially in the attachment region. This results in the major tensile stresses being parallel to the grinding grooves during engine operation. As previously discussed, this represents the condition that will have the least detrimental effect on the material strength.

To evaluate the strength achieved by Pantograph profile grinding and to help define techniques to improve the strength, 4-point bend-test specimens were machined with the Pantograph, simulating the same surface finish and orientation as in the blade attachment region. Initial specimens were machined with a 60,000 rpm spindle varying the final diamond grit size. A 220-grit finish resulted in an average strength (in the longitudinal direction) of 73 KSI. A 320-grit finish resulted in an average strength of 84.5 KSI. Both of these strengths were lower than typically measured for specimens prepared by standard surface grinding using comparable diamond grit size. This indicated that the Pantograph procedure was producing more severe surface damage. The equipment was modified to permit a spindle speed of 100,000 rpm, resulting in an average strength of 98.8 KSI, comparable with standard surface grinding. Slight further improvements occurred as the Pantograph operators became more experienced, and as the diamond tooling was optimized. Additional significant strength improvement (>110 KSI) was achieved by a post-machining oxidation treatment which either blunted or removed surface cracks resulting from machining [3, 4].

Initial-blade attachment specimens were machined by a multi-step approach. A blank was cut from a 9-inch-diameter billet and rough-machined on a surface grinder to remove as much stock as possible. The remaining stock was then removed by Pantograph machining using 220-grit wheels for rough passes and 320-grit for finishing. This procedure was slow and expensive. Table 1 summarizes material removal rates for these various machining operations. Removal rates are extremely low for the profile grinding operations, which is mostly due to the small size of the diamond wheel and the minimal area of contact with the workpiece.

TABLE I. MATERIAL REMOVAL RATES AND OPERATIONS.

OPERATION	MACHINE USED	TOOL USED	WHEEL AND/OR GRIT SIZE	IN. ³ /HR
GRIND BILLET TO THICKNESS	SURFACE GRINDER	DIAMOND WHEEL	1/2 X 6 IN. - 150 GRIT	2.4
SLICE BILLET	SURFACE GRINDER	DIAMOND WHEEL	0.050 X 6 IN. - 150 GRIT	1.2
FORM-GRIND ATTACHMENT	SURFACE GRINDER	FORMED DIAMOND WHEEL	1/2 X 6 IN. - 150 GRIT	1.4
PROFILE-GRIND ATTACHMENT (ROUGH)	PANTOGRAPH	MOUNTED DIAMOND WHEEL	1/4 X 1/4 IN. - 150 GRIT	0.040
PROFILE-GRIND ATTACHMENT (FINISH)	PANTOGRAPH	MOUNTED DIAMOND WHEEL	1/4 X 3/16 IN. - 320 GRIT	0.005
TREPAN AIRFOIL SHAPE	ULTRASONIC	SHAPED TUBE	320 GRIT B ₄ C SLURRY	1.4
ROUGH-GRIND AIRFOIL	PANTOGRAPH	MOUNTED DIAMOND WHEEL	1/8 X 5/8 IN. - 150 GRIT	0.02
FINISH-GRIND AIRFOIL	PANTOGRAPH	MOUNTED DIAMOND WHEEL	1/8 X 7/16 IN. - 320 GRIT	0.01

Ultrasonic trepanning was developed to remove stock that could not be removed by conventional diamond grinding, and thus reduce the stock removal required by profile grinding. A schematic of the ultrasonic system is shown in figure 9.

Trepanning is analogous to cookie-cutting in that a thin-walled tool produces the cut, avoiding the necessity of grinding away the adjacent material. Figure 10 shows the trepanning tool used to ultrasonically machine a blade-attachment spin-test specimen directly from a solid HPSN billet in a single step to within 0.010 inch of the required tolerance. This resulted in a significant cost reduction by reducing machine time and operator time. In addition, tooling cost was reduced because the cutting was done with boron carbide (B₄C) abrasive which is much less expensive than diamond tooling grit-abrasive.

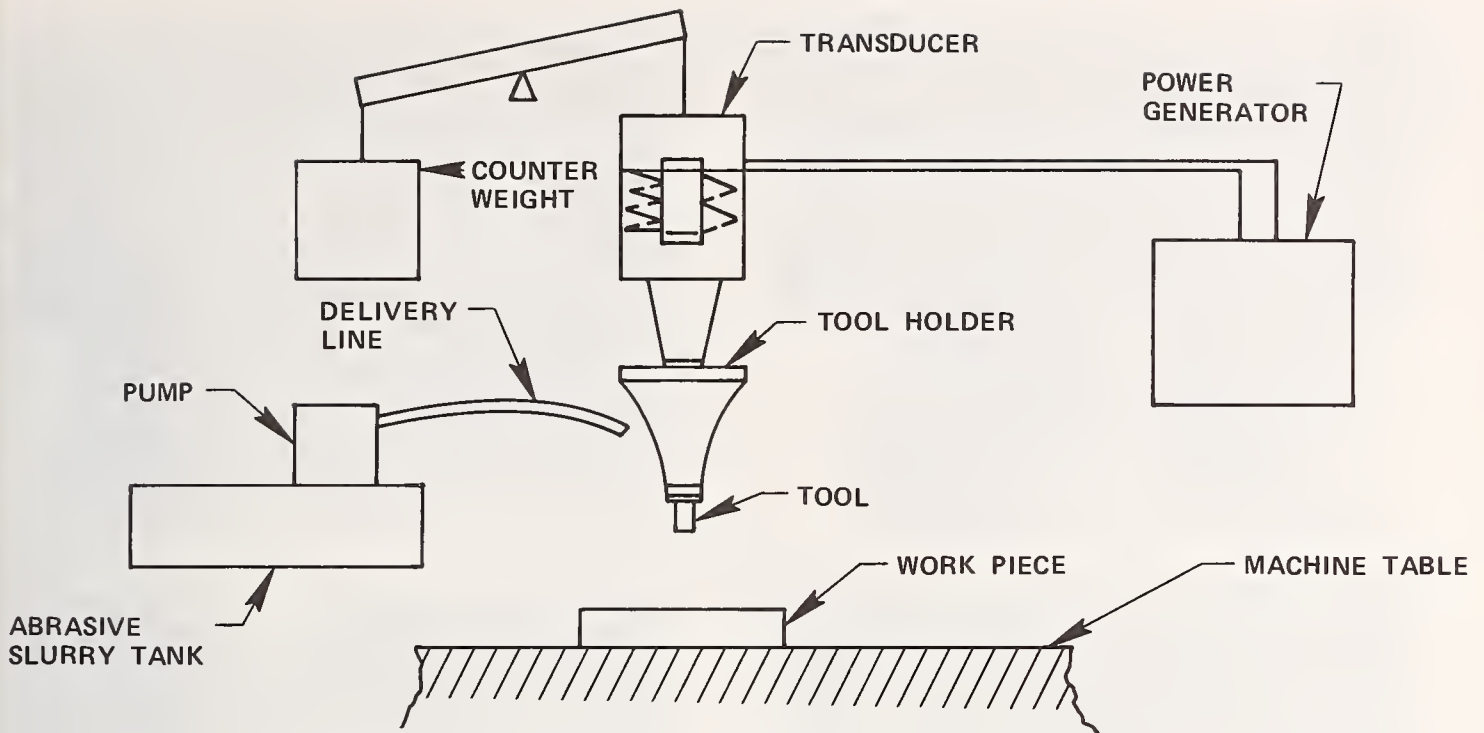


Figure 9. Ultrasonic Machining System.

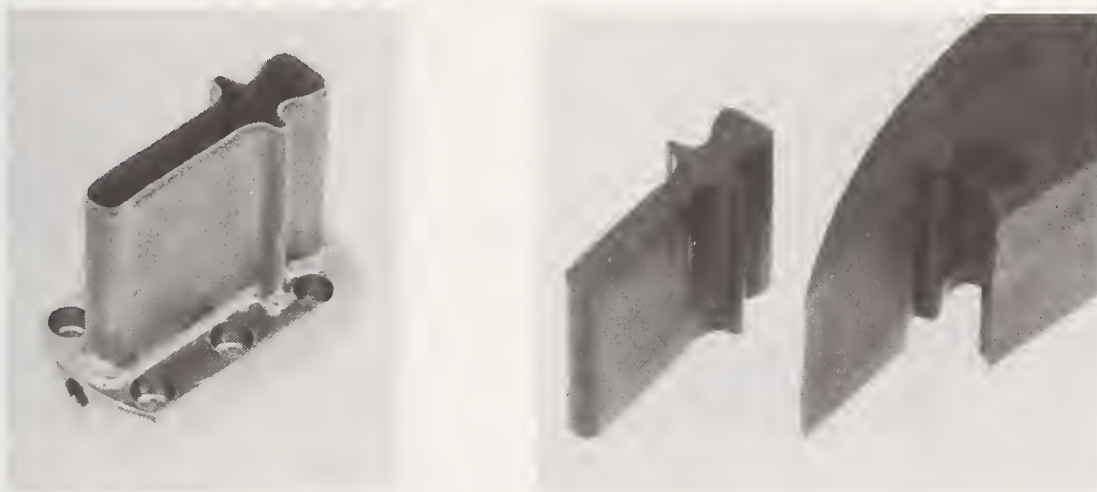


Figure 10. Ultrasonic Trepanning Tool and Blade Attachment Machined by Ultrasonic Trepanning.

Ultrasonic trepanning has been further refined to significantly decrease the time and cost of machining complete rotor blades. The steps are shown in figure 11. First, ultrasonic trepanning produces a blank containing the attachment to within about 0.010 inch, plus adequate stock from which the airfoil and platform can be machined. An airfoil envelope is then ultrasonically trepanned to the proper depth 90 degrees to the initial cut. A thin diamond slicing wheel is then used to cut in from the sides and intersect the bottom of the trepanning cut. This removes a large amount of stock without grinding, and thus yields a shaped blank that requires relatively little finishing by profile grinding. The completed blade is shown in step 4.

As part of the machining process development, the strength of an ultrasonically machined 4-point bend specimen was evaluated. Two different ultrasonic tool motions were evaluated, one referred to as transverse (as would occur in trepanning) and one referred to as frontal. Surfaces machined ultrasonically had a nondirectional surface texture compared to the highly directional surface produced by diamond surface grinding. This is clearly visible with a scanning electron microscope as shown in figure 12. Figure 13 compares the strength of ultrasonically machined HPSN with specimens prepared by

standard surface grinding in the longitudinal and transverse directions, and by profile grinding in the longitudinal direction. Based upon this and other data, the strength of the ultrasonically-machined HPSN appears unaffected by grinding direction, and is comparable to longitudinal grinding by the other approaches.



1
ATTACHMENT
BLANK
ULTRASONICALLY
TREPANNED



2
AIRFOIL
ENVELOPE
ULTRASONICALLY
TREPANNED

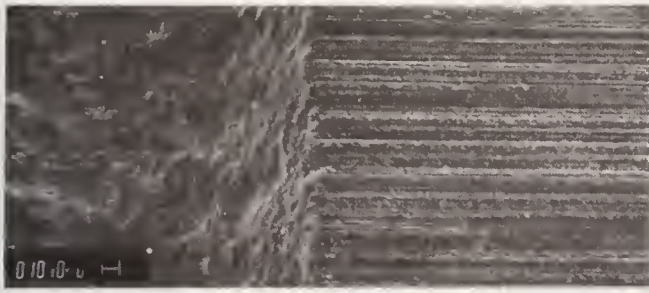


3
SHELL
SEPARATED
WITH DIAMOND
SLICING WHEEL



4
BLADE FINISH-
GROUND BY
PANTOGRAPH

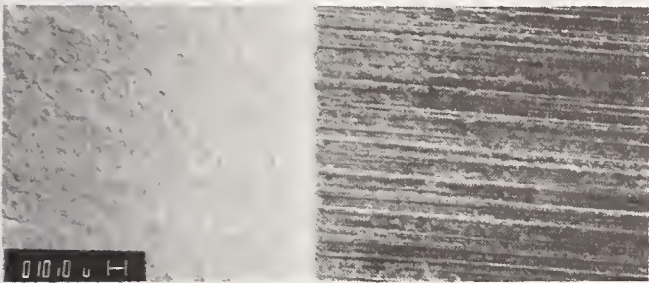
Figure 11. Reduced-Cost Blade Machining Using Ultrasonic Trepanning and Pantograph Profile Grinding.



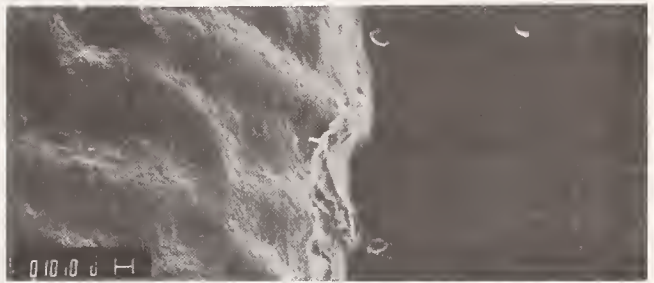
TRANSVERSE ULTRASONIC ON LEFT
(320-GRIT BORON CARBIDE)
CONVENTIONAL 320- GRIT DIAMOND
GRINDING ON RIGHT



FRONTAL ULTRASONIC ON LEFT
(320-GRIT BORON CARBIDE)
CONVENTIONAL 320-GRIT DIAMOND
GRINDING ON RIGHT



TRANSVERSE ULTRASONIC ON LEFT
(600-GRIT BORON CARBIDE)
CONVENTIONAL 320-GRIT DIAMOND
GRINDING ON RIGHT



ULTRASONIC EDGE-WASH OCCURRING
DUE TO UNOPTIMIZED TOOLING
AND PROCEDURES
320-GRIT BORON CARBIDE

Figure 12. Typical Surfaces Prepared by Conventional Diamond Grinding and by Ultrasonic Machining.

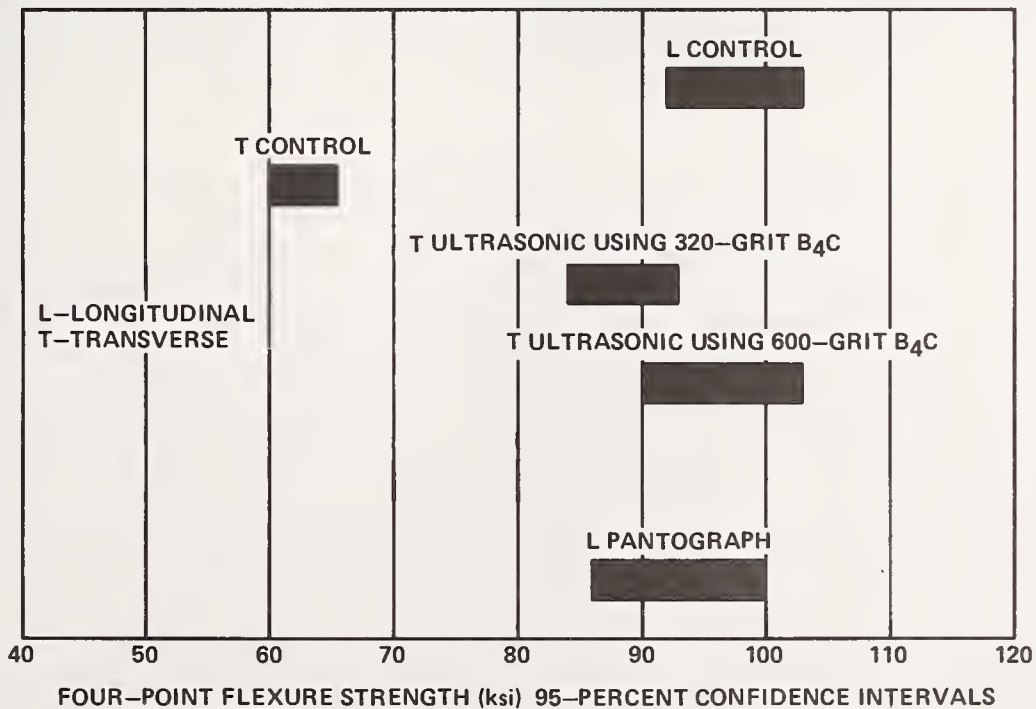


Figure 13. Strength Versus Machining Technique.

5. Conclusions

Machining of complex rotor blades to the required close tolerances has been successfully accomplished at AiResearch and other sources. Fabrication time and costs have been significantly reduced by development of formed-wheel grinding and ultrasonic machining techniques.

Material strengths resulting from the various machining techniques have been measured, and the data has been used to modify the machining procedures to achieve improved strength. Pantograph profile grinding results have been significantly improved by this iterative procedure.

The HPSN ceramic rotor blades resulting from this machining process development effort have been successfully tested with high yield at 130-percent of design speed for the intended engine application.

The authors wish to thank the Defense Advanced Research Projects Agency for supporting this effort.

References

- [1] Torti, M. L., Baker, S.H., Tuffs, S. and Olson, B.A., Norton process optimization studies for hot pressed silicon nitride blades and reaction sintered silicon nitride stator and static components, Proceedings of the 1977 DARPA/NAVSEA Ceramic Gas Turbine Demonstration Engine Program Review, MCIC-78-36 pp. 341-363 (March 1978).
- [2] Mecholsky, J. J., Freiman, S. W. and Rice, R. W., Effect of grinding on flaw geometry and fracture stress of glass, J. Am. Ceram. Soc. 60 3-4 pp. 114-117 (1977).
- [3] Richerson, D. W. and Yonushonis, T. M., The effect of surface condition on the strength of hot pressed silicon nitride, presented at the fall meeting of the American Ceramic Society, San Francisco, California, (November 1, 1976).
- [4] Richerson, D. W., Schuldies, J. J., Yonushonis, T. M., and Johansen, K. M., ARPA/Navy ceramic engine materials and process development summary, in Ceramics for High Performance Applications—II, ed. by John J. Burke, et al., pp. 625-650 (Brook Hill Publishing Co., Chestnut Hill, MA, 1978).

MACHINABILITY STUDIES ON MACOR™ GLASS-CERAMIC

D. G. Grossman and D. L. Taylor

Research and Development Laboratories
Corning Glass Works, Corning, N. Y., 14830

MACOR™ glass-ceramic is a class of ceramic material which lends itself to conventional machining tools and equipment. This machinability is attributed to the unique microstructure which consists of a highly interlocked array of plate-like mica crystals dispersed in a glassy matrix. The machining of this material is unlike machining ductile metals and this paper makes some comparisons of the energy requirements, cutting forces and tool wear in turning and drilling operations.

Key words: Corning code 9658; glass-ceramic; machinable; MACOR™

1. Introduction

The word machinable as applied to a ceramic material most often connotes the use of abrasive techniques such as grinding. With MACOR™ machinable glass-ceramic, parts are mostly shaped by single point turning, milling, drilling, sawing, etc. using metal-working tools. Evaluation of this material in these operations is made through comparisons with metals and plastics for, even though MACOR™ is a brittle ceramic, its unique microstructure allows it to be shaped with the ease of conventional machining. Furthermore, it is ready for immediate use after machining because it does not require the subsequent firing needed by ceramic materials that are machinable in the "green" or unfired state.

MACOR™ glass-ceramic is distinguished from most other ceramics by its microstructure, which consists of an interlocked array of plate-like mica crystals dispersed throughout a glassy matrix. A description of the microstructural development has been previously described through a series of photomicrographs [1].¹ The "house of cards" microstructure is the key to MACOR's™ machinability. Like natural mica sheet, it is difficult to propagate fractures through the thin, flat mica crystals. Typically, fractures follow the glass-mica interfaces and cleavage planes of the mica as revealed in figure 1. The microscopic fractures are repeatedly deflected, branched and blunted - in effect, turned around and arrested. Since the fractures are localized, MACOR™ glass-ceramic does not sacrifice strength or hardness for the sake of its machinability.

Evaluation of machinability can be made using the following considerations: energy (forces, temperature) tool life (wear) and work result (stock

¹ Figures in brackets indicate literature references at the end of this paper.

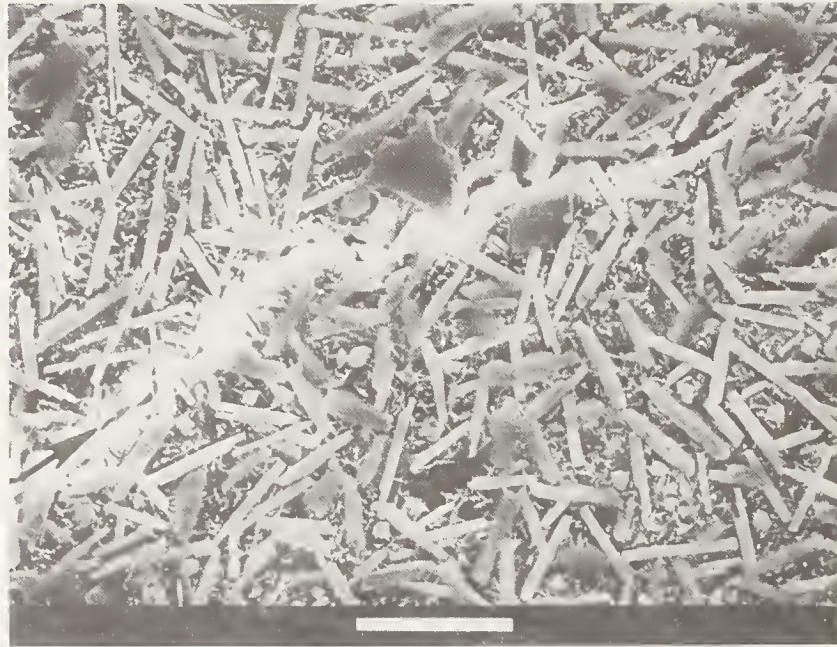


Figure 1. Crack deflection by mica crystals in MACOR™ glass-ceramic. White marker = 10 μm .

removal rate, precision, surface quality). Since MACOR™, Corning Code 9658, machinable glass-ceramic is a relatively new material, particular emphasis was given to tool design in an effort to establish the optimum machining conditions under various operations.

2. Power and Energy Requirements

The unit power required to remove a specific volume of material was measured using a drill dynamometer which simultaneously monitored the torque and thrust imparted to the work piece through two sets of strain gages mounted on the shank of the test stand. The arrangement is shown in figure 2. A split collet specimen holder is joined to the base by a hollow torque tube of 5/8 inch O.D. and 1/2 inch I.D. A pair of two-element 90° torque sensitive strain gages is mounted so that they face each other diametrically on the tube. A second pair of two-element gages is mounted in the same plane at 90° and respond respectively to the axial strain and circumferential (Poisson) strain. Both sensors act as four-arm bridges. Calibration for both torque and thrust was accomplished using certified weights. The cross-sensitivity between torque and thrust outputs was determined to be less than 1%. The output signals from the strain gage conditioning system were fed to a datalogger.²

The unit power requirements, P , for drilling can be calculated from the following equation [2]:

²Autodata Nine datalogger with VISIG II signal conditioning system, Acurex Autodata, Mountain View, California.

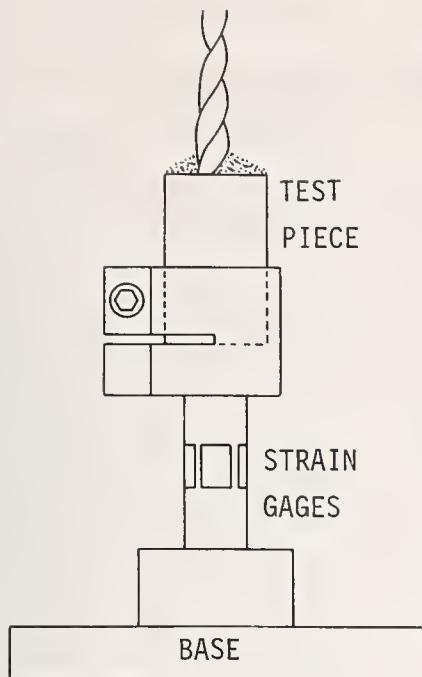


Figure 2. Drill dynamometer.

$$P = \frac{T}{50,000 d^2 f}$$

where

P = Unit power requirements in drilling, hp/in³/min.

T = Torque, in-lb.

d = Diameter of drill, in.

f = Feed, in/rev.

Note that only the torque enters the power equation since the horsepower due to thrust accounts for a small percent of the total power developed [3].

The test stand was accurately located on the center line of a Bridgeport drill press equipped with a variable feed rate. The drill speed was held constant at 300 rpm or 20 fpm using 1/4 inch diameter drills.

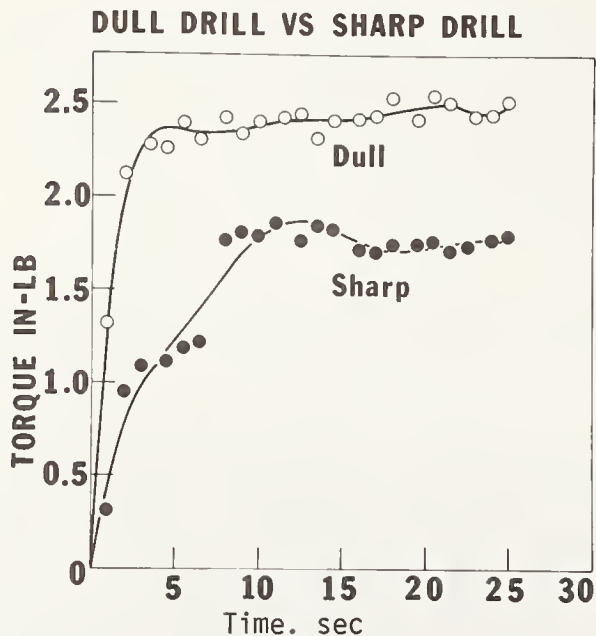
A number of different drill styles including high-speed steel, solid-carbide, carbide-tipped, masonry, etc. were compared using the torque and thrust data shown in table 1. A somewhat surprising result was that masonry drills designed for brittle materials performed poorly on MACOR™ glass-ceramic. This new machinable ceramic responded particularly well to ordinary high-speed steel twist drills. Where wear or tool life is a problem, the carbide-tipped twist drills also developed low forces at the point of the drill.

Drill sharpness was also investigated to examine both the effect of wear and whether grabbing with a sharp drill is a problem as is the case when drilling brass. Figure 3 indicates less torque is imparted to the stock by a sharp drill but in both conditions, stability was attained after the drill penetrated the glass-ceramic. Figure 4 indicates no particular benefit in reduction of force from lubrication during drilling. Water-soluble coolants have been shown useful in other operations, such as turning, particularly to trap the loose powder which is released.

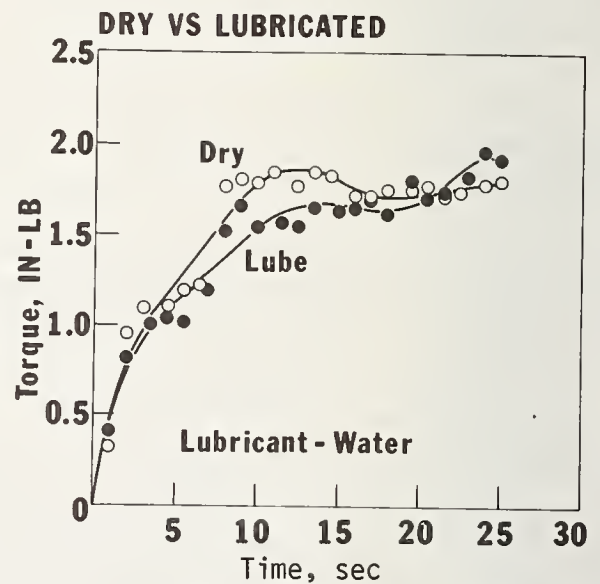
Table 1.

Torque and Thrust at 20 Second Drill Time

MATERIAL	DRILL STYLE	TORQUE in-lb	THRUST lb
MACOR™	#917 High-speed steel surface treated	1.65	27.5
	#924 Plastics	1.8	19.
	#957 Hi-Helix	1.5	24.
	#960 Lo-Helix	1.5	24.
	#4947 Cotter pin w/135° split point	3.5	36.
	#77653 CID style carbide tipped	1.75	28.
	Style 400 solid-carbide twist drill	1.5	24.
	Style HD straight flute	6.5	65.
	Style KK masonry	8.	64.



Cleveland 1/4" High Speed Drill
118° Point Angle #917
6 Mil/Rev Feed Rate, 300 RPM



Cleveland 1/4" High Speed Drill
118° Point Angle #917
6 Mil/Rev Feed Rate, 300 RPM

Figure 3. Effect of drill sharpness.

Figure 4. Effect of lubrication.

To examine the effect of point angle, a series of high-speed drills was ground with angles from 90° to 140°. The forces at the point of the drill remained fairly constant over this range; therefore, it was unnecessary to

apply a special point angle for a particular drill.

The form of the torque, T and thrust, B, equations are [4]:

$$T = Cf^k d^\ell$$

$$B = Kf^m d^n$$

where C and K are constants, the values of which depend on the material, drill and cutting fluid; f is the feed per rev; d is drill diameter; and k, ℓ , m and n are exponents the values of which depend primarily on the material being drilled. For most steels the value of $k = 0.78$ and the value of $\ell = 1.8$. For cast iron, $k = 0.60$ and $\ell = 1.7$. A series of drilling experiments varying the feed rate and drill diameter for MACOR™ glass-ceramic gave exponents which more closely follow the brittle metals as shown in table 2. The slopes of the lines for torque and thrust are much lower for the machinable glass-ceramic. Figures 5 and 6 show the torque as a function of feed rate and drill diameter, respectively, for MACOR™ machinable glass-ceramic.

Table 2

Constants for Torque and Thrust Equations

MATERIAL	EXONENTS				CONSTANTS	
	k	ℓ	m	n	C	K
MACOR™ Code 9658	0.66	1.67	0.71	0.60	39.4	2,305
Leaded brass screwstock	0.73	1.9	0.60	1.0	418.	6,938
S.A.E. 33 aluminum	0.83	1.9	1.1	1.2	646.	75,030
Cast iron	0.60	1.7	0.73	-	370.	160,000
S.A.E. 1020 steel	0.78	1.8	0.87	-	2,186	906,000
Carbon tool steel, annealed	0.78	1.8	0.87	-	2,089	933,000

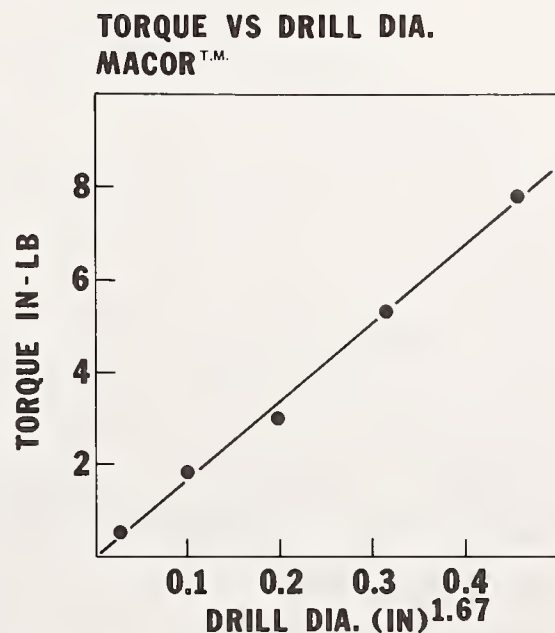
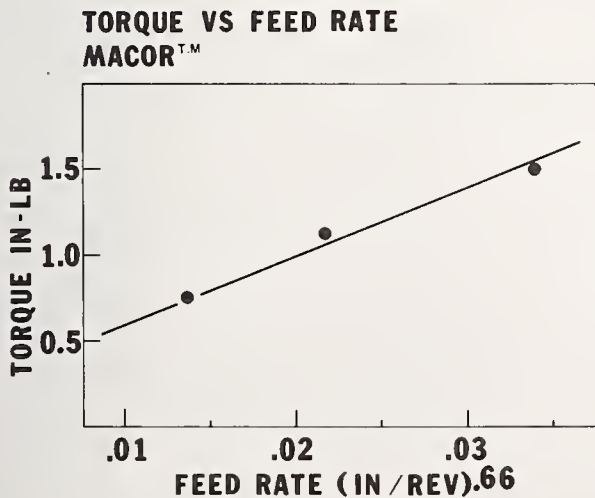


Figure 5. Torque-feed rate relationship for MACOR™ glass-ceramic.

Figure 6. Torque-drill diameter relationship for MACOR™ glass-ceramic.

The average power consumed during drilling can be compared for a number of machinable materials by the bar graph shown in figure 7. Note that all the materials were drilled using high-speed drills at a feed rate of 6 mil/rev and a speed of 300 rpm. It is interesting to compare these results with tests of stock removal rate described in an earlier publication [1] as "Machinability Index". The test measures the cut depth using a weighted hacksaw for a given number of strokes. The values are arbitrarily scaled against that of a standard, namely cold-rolled 1018 steel, assigned a value of 111 on the scale. The scale is such that the index value increases as the difficulty of machining increases. The machinability index values are compared to the unit power consumed in drilling in table 3. The correlation between these values indicates that the tool's efficiency does not vary widely over the range of materials investigated.

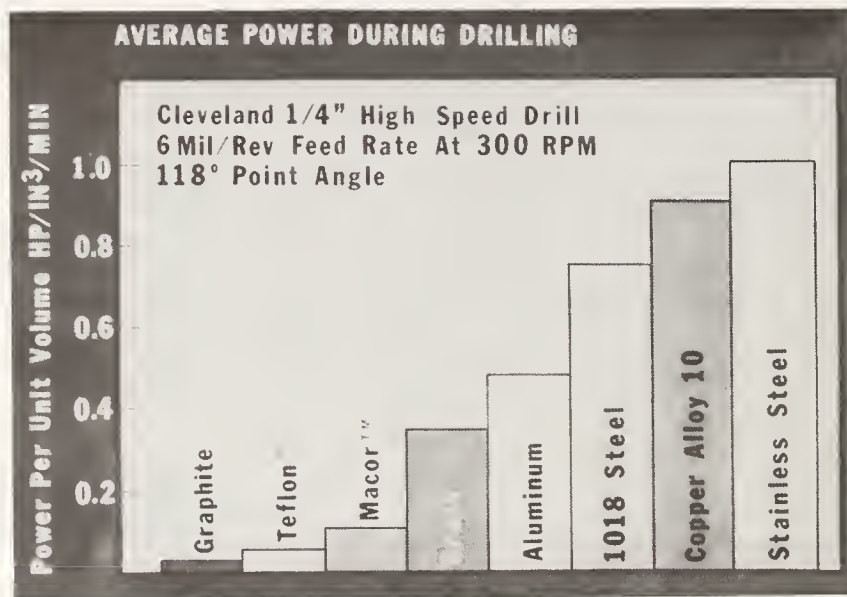


Figure 7. Average power during drilling for various materials.

Table 3

Power, Torque and Thrust at 20 sec. Drill Time

MATERIAL	POWER hp/in. ³ /min	TORQUE in-lb	THRUST lb	MI*
Graphite	0.03	0.5	5.	1.
Teflon® TFE	0.06	1.	7.5	2.5
MACOR™ Code 9658	0.11	2.	40.	25.
Brass-free machining alloy 2024	0.35	6.5	52.	36.
Aluminum T-4	0.48	9.	90.	50.
1018 Steel cold-rolled	0.75	14.	122.	111.
Copper alloy 10	0.92	17.	168.	97.
#304 Stainless steel	1.00	19.	260.	229.

*Machinability Index is an arbitrary unit and increases with difficulty of machining.

3. Tool Life

Frequently the machinability of a material is assessed by how hard it is on the tool, for example, number of holes completed per drill bit or inches of work travel per milling tooth or simply the time taken to produce a set amount of wear on the face of the tool. Tool life does affect production economics through tool costs and change time. However, for MACOR™ machinable glass-ceramic, tool life is not the limiting factor in machining. Instead, surface finish requirements set constraints on speeds and feed rates.

In single point turning, for example, feeds and speeds that produce acceptable surface finishes do not cause excessive wear on either high-speed steel or carbide tools. The wear on the tool body was measured under deliberately harsh conditions for both high-speed steel (fig. 8) and carbide (fig. 9) tools.

How long a tool will last depends on factors other than just the material being machined; tool design and parameters are also important. This effect is shown dramatically by altering the side cutting-edge angle using C2-carbide tooling. Figure 10 shows that the allowable cutting speed, that is, the maximum surface speed before the onset of chipping, may be increased markedly with higher side cutting-edge angles.

Another factor in tool life is lubrication. The use of water-soluble coolants such as Supercut S67, Johnsons Cold Stream or Quaker 103 is strongly recommended not only to prolong tool life but also to achieve better results. These materials improve the cutting action and also trap and wash away the loose powder produced during machining.

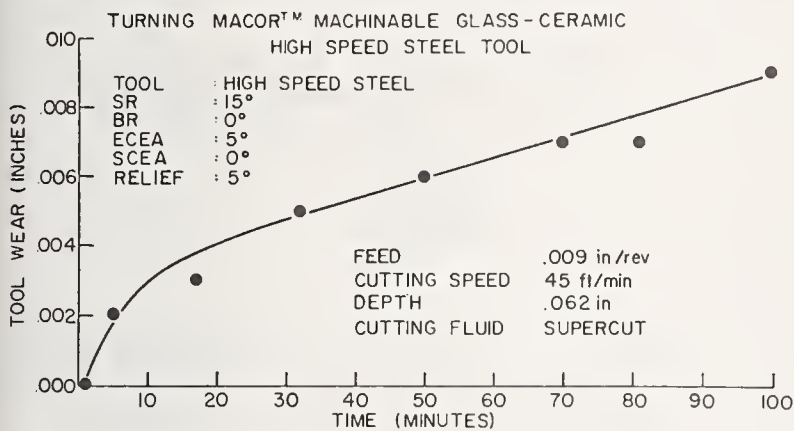


Figure 8. High-speed steel tool wear in turning under deliberately harsh conditions.

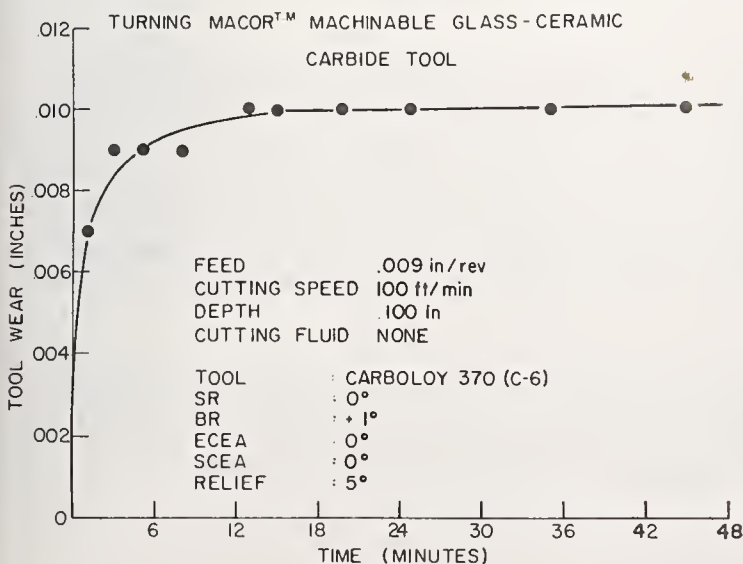


Figure 9. Carbide-tool wear in turning under deliberately harsh conditions.

4. Work Results

The effect on surface roughness was investigated for a variety of machining parameters in single point turning. The surface quality is simultaneously controlled by the feed rate, depth of cut and cutting velocity. The manner of material removal can be divided into two classes: Mode I results from lower cutting forces; under dry machining conditions it occurs when the velocity ≤ 400 sfpm, depth of cut ≤ 0.100 in. and the feed ≤ 0.0035 ipr. This form of material removal results in a surface quality represented by the measured profile shown in figure 11(a). Mode II results when the cutting forces exceed a given value.

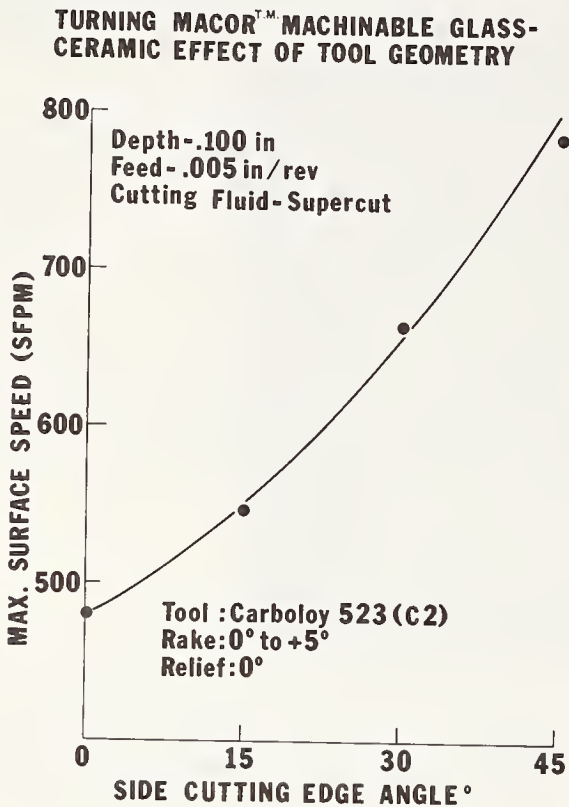


Figure 10. Effect of tool geometry in turning MACOR™ machinable glass-ceramic.

SURFACE ROUGHNESS OF MACOR™ MACHINABLE GLASS-CERAMIC

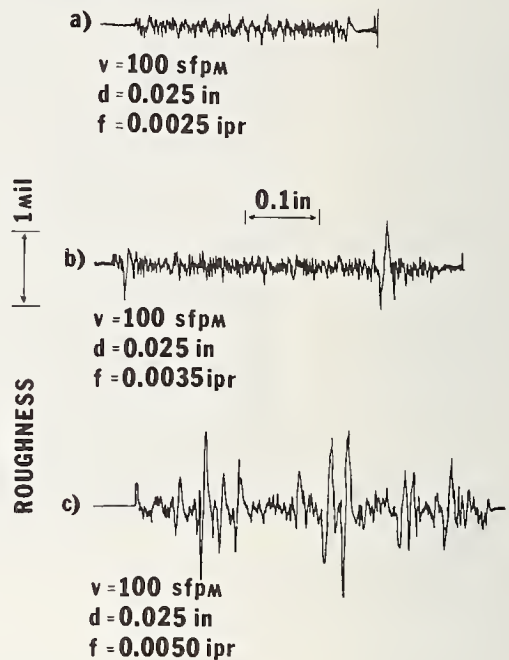


Figure 11. Effect of machining parameters on the surface quality of MACOR™ glass-ceramic in turning.

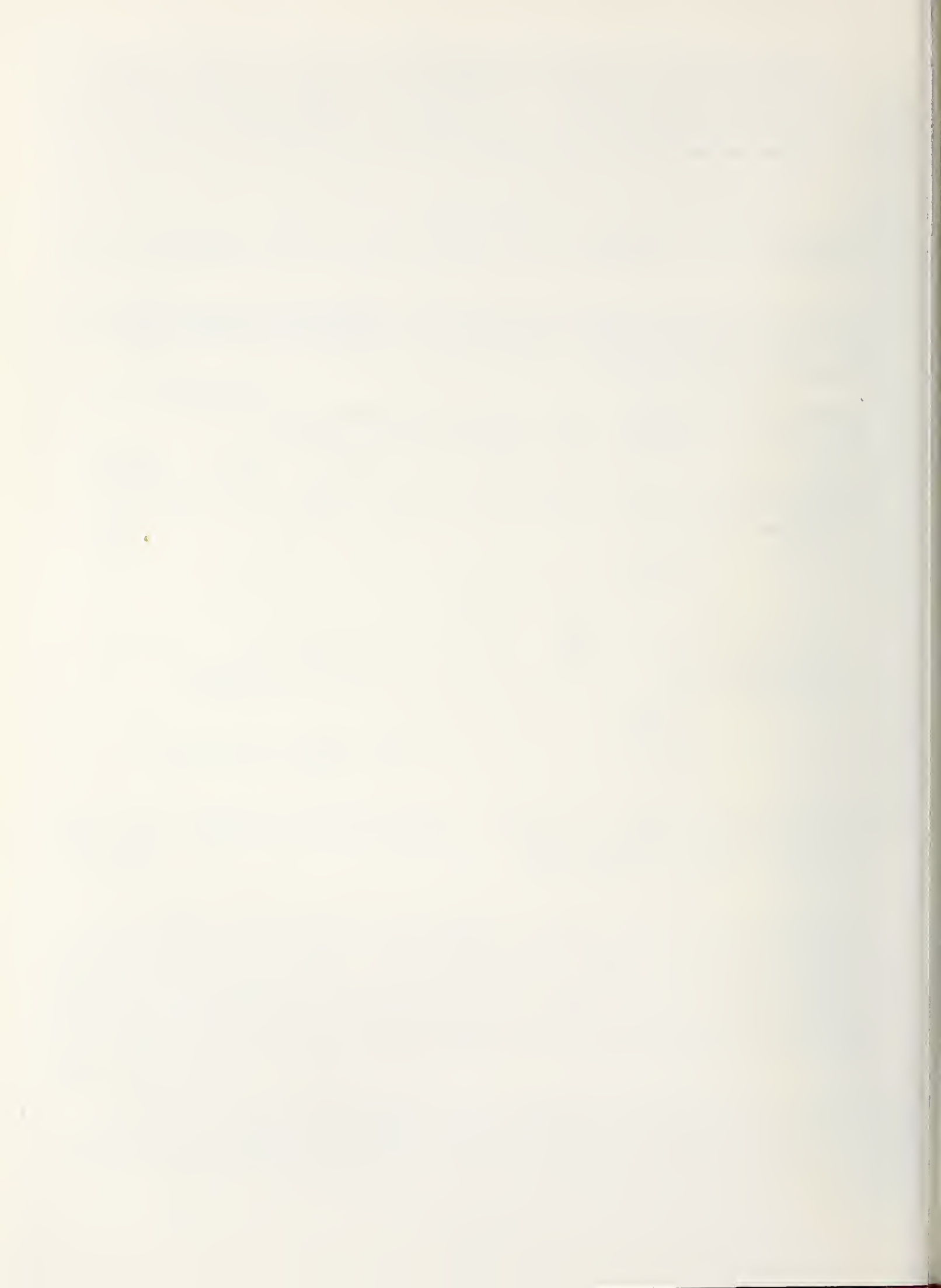
With higher cutting forces, random but densely populated imperfections are produced on the surface. The onset of this condition for dry machining is depicted in figure 11(b). The population of these imperfections increases with still higher cutting forces as shown in figure 11(c). The two modes of material removal operating simultaneously at higher cutting forces result in a bimodal distribution of the collected chips. The ratio of the number of small chips to the number of large chips is definitely related to the machining parameters.

The use of a wet environment during turning allows for greater speeds and feed rates without sacrificing surface quality. It is quite probable that the Mode II material removal mechanism is thermal-shock related.

The authors wish to acknowledge the assistance of E. G. Turker of the Industrial Engineering Department, Cleveland State University who conducted the surface roughness experiments. We should also like to thank the members of the Machine Shop at Technical Staffs Services of Corning Glass Works who helped us with the drilling experiments.

References

- [1] Grossman, D. G., Machining a machinable glass-ceramic, Vacuum 28, 55-61 (1978).
- [2] Anon., Power requirements and coefficient of friction in machining, Machining Characteristics of High Strength Thermal Resistance Materials, pp. 129-137 (AMC Technical Report 60-7-532, Curtiss-Wright Corp., Cincinnati, Ohio, 1960).
- [3] Boston, O. W., Power required in drilling, Metal Processing, pp. 268-280 (John Wiley & Sons, Inc., New York, N.Y., 1941).
- [4] Marks, L. S., Torque, thrust, and power in drilling, Mechanical Engineers Handbook, 4th Ed., pp. 1828-9 (McGraw Hill Inc., New York, N.Y., 1941).



EFFECTS OF VARIOUS POLISHING MEDIA AND TECHNIQUES ON THE SURFACE FINISH AND BEHAVIOR OF LASER GLASSES*

Richard L. Landingham, Alton W. Casey and Roy O. Lindahl

Lawrence Livermore Laboratory
Livermore, California 94550

The advance of high-power laser technology is dependent on the rate of advancement in laser glass forming and surface preparation. The threshold damage of glass surfaces continues to be a weak link in the overall advancement of laser technology. Methods were developed and used in the evaluation of existing glass surface preparation techniques. Modified procedures were evaluated to reduce surface contamination and subsurface defects. Polishing rates were monitored under controlled polishing conditions (purity, pH, particle size distribution, particle concentration, etc.). Future work at LLL for this ongoing investigation are described.

Key Words: Laser glass; surface preparation; polishing compounds; particle characterization; surface contamination; and subsurface defects.

1. Introduction

High-power lasers are used to implode D-T targets at LLL. Results from such implosions demonstrate the feasibility of generating electrical power by inertial confinement fusion. The 30-TW SHIVA laser (the world's most powerful laser) was designed and built at LLL for this purpose. This first design used neodymium-doped oxide glass as the amplifying medium. A typical laser chain (50-m long) is shown in figure 1. Large increases in laser power are anticipated by using fluoride-base laser glass instead of oxide-base glass in the next upgrade: 200- to 300-TW NOVA solid-state laser design. Such improvements are possible because fluoride amplifiers will have high gain and low nonlinear refraction index. High gain is achieved with optimum balance between emission cross section of the lasing ion and duration of the laser pulse. A smaller cross section is generally needed with increasing pulse width. The emission cross section is host-dependent.

The nonlinear refractive index is most important to the performance of short-pulse high-power lasers. Glasses with low linear refractive index will also have lower nonlinear index coefficients. Glasses with low coefficients propagate laser beams with less distortion. Classes of glasses in order of decreasing index are silicates, phosphates, fluorosilicates, fluorophosphates, and fluorides (BeF_2 is the lowest). The advanced laser designs will need these fluoride glasses, which are now under intense development. Both passive components (lenses and windows) and active components (amplifiers and Faraday-rotation media) of the fluorophosphate glasses (LG-810, E-181, LHG-10, etc.) are being developed commercially for the NOVA design. Scaleup problems similar to those encountered in scaling up the silicate glasses for the large high-power lasers are anticipated.

A more persistent problem common to these glasses is their low resistance to laser damage at their surfaces. This low damage threshold is reduced further when these surfaces are coated. Properly controlled laser damage tests generally confirm that the damage threshold decreases in the following order: bulk glass (highest), bare entry surface, bare exit surface, coated entry surface, and coated exit surface (lowest). Laser pulse duration and wavelength can affect this order[1]. The lower damage threshold of the exit surface as compared to the entrance surface is attributed to a greater optical electric-field strength

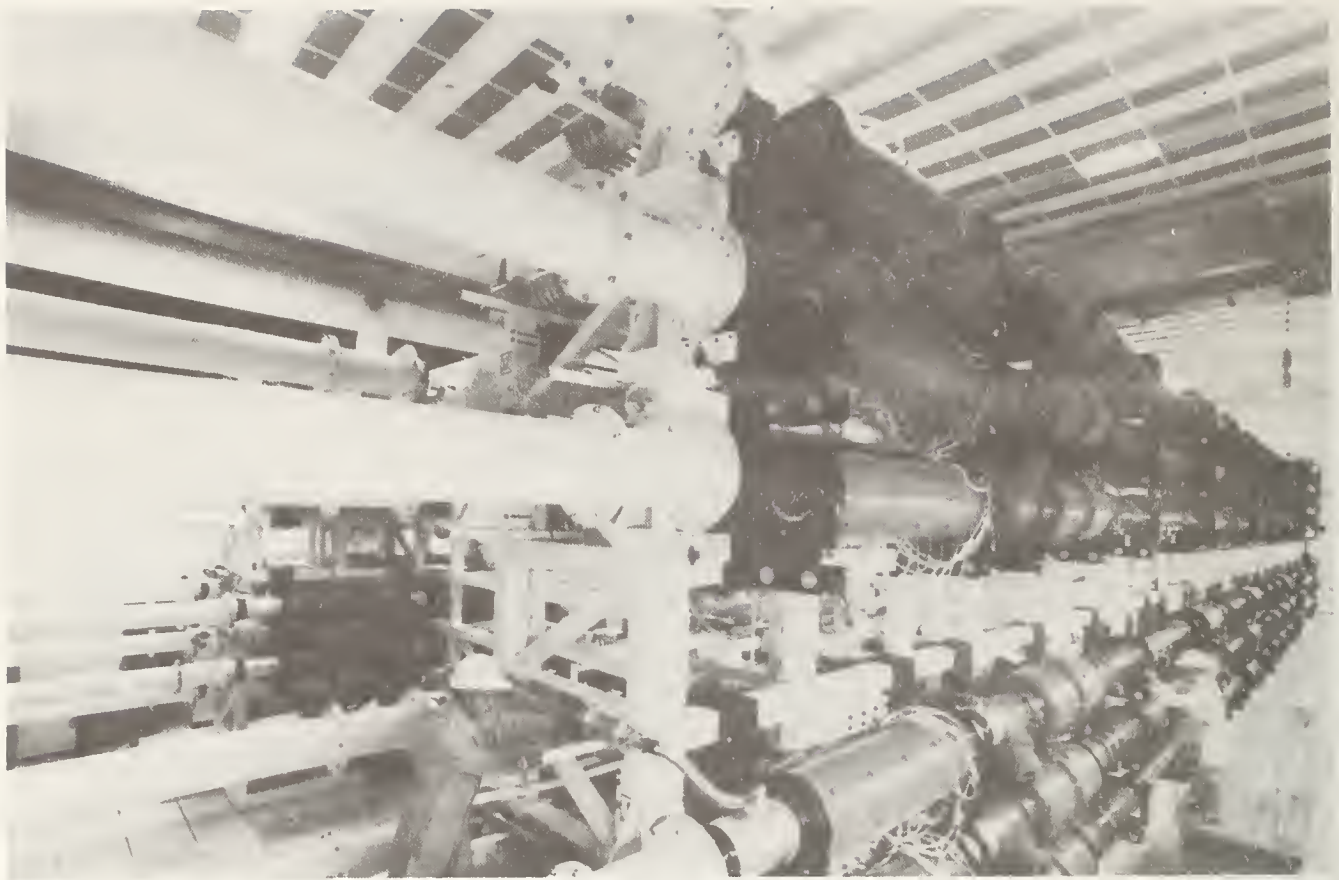


Fig. 1. The installation of components in the Shiva laser system at the Lawrence Livermore Laboratory.

at the exit surface[2]. Conflicting results and lack of consistent evidence still prevent adequate explanation of the lower damage threshold for bare and coated surfaces as compared to their bulk glass damage threshold. Surface damage is generally attributed to surface finish and various techniques have been tried to obtain imperfection-free surfaces[3]. No improvement in damage threshold is anticipated after achieving surface roughness (rms) of $<100 \text{ \AA}$ [4]. Surface damage threshold could also be affected by a variety of other surface related features as dust particles, surface films, embedded polishing particles, subsurface scratches and cracks, and residual stresses[4-7].

An investigation was initiated this summer at LLL to evaluate the polishing procedures used to prepare our laser glass components. In this document, we report some of our findings on polishing compounds, subsurface defects, surface chemistry of the polished glass, and techniques developed to evaluate glass surfaces. Since this is an ongoing study, we will also comment on the direction being taken as a result of existing data.

2. Procedure

This investigation is divided into three parts; (1) evaluation of existing processes, (2) laboratory-scale experiments on modified processes, and (3) development of techniques to analyze the glasses prepared by these processes. Effort is ongoing in all three areas.

The proprietary nature of most processes used in preparing the surfaces of laser glass hampers our direct correlation of surface conditions with processing stages. The surface conditions from well-established grinding and polishing practices are being evaluated by preparing these surfaces in our Optics Laboratory from glass provided by the laser glass suppliers. Suprasil-II¹ silica disks (50 mm diam, 10 mm thick) are being evaluated

¹ Reference to a company or product name does not imply approval or recommendation of the product by the University of California or the U. S. Department of Energy to the exclusion of others that might be suitable.

first. The surface damage introduced by coarse grinding and polishing operations is being monitored quantitatively by the Ernsberger technique[9]. The surface from each state of preparation is polished on cloth laps with fine polishing compound ($< 1 \mu\text{m}$ diam TiO_2) to remove the surface roughness without introducing more deep subsurface defects. Ion exchange or etching techniques are used to expose these subsurface defects and the concentration of defects per mm are determined by image analysis with a Model 720 Imanco image analyzer. Alternate fine polishing and etching steps are used to determine the depth of the defects to within a few micrometers.

The polishing compounds affect the degree of subsurface damage and surface impurity level. The characterization of these compounds includes particle size distribution, surface area, true density, particle shape, phase identification, composition, and impurity level. Impurity levels of other potential contamination sources (carrier solution, anti-foam and dispersion agents, wheel pitch, dressing blocks, etc.) are also checked. The impurity level of the polishing medium is monitored during and after polishing the glass. The impurity levels of the glass are determined to establish the lowest attainable impurity level on the polished surface.

Several analytical techniques were compared to establish a method of monitoring the surface impurity level after the finer polishing and finishing stages. Ion microprobe, Auger electron spectroscopy (AES), energy dispersive system (EDS), electron spectroscopy for chemical analysis (ESCA), atomic absorption spectrometry, and atomic emission spectroscopy techniques were evaluated.

The characterization of the final surface will include roughness and flatness determinations, laser damage threshold tests, surface impurity analyses, and/or subsurface defect tests. A unique laser damage facility has been developed at LLL to provide rapid and reliable damage threshold results to accelerate the development of laser glass components [1].

We have begun applying some of the experience gained in preparing the Suprasil-II silica surfaces to the preparation of fluorophosphate glasses. The pH level in a high-purity polishing slurry was controlled to determine its effect on polishing rate.

3. Results and Discussion

Various final polishing compounds were characterized because most of the contamination and defects on the surface of the glass should come from this final polishing stage (see table I). The particle size distribution was larger than desired in every case although the mean particle size was $\leq 3 \mu\text{m}$. The large particles were primarily bonded agglomerates, which should breakdown if recycled in the final polishing stage. The subsurface damage



a. Single large particles in MgO (Code 920) b. Large agglomerate particles in SnO(AV-116)

Fig. 2. Photomicrograph of typical large particles discovered in final polishing compounds by scanning electron microscopy.

caused by hard agglomerates is difficult to polish out in this final stage. Neither large single particles nor agglomerates (see figure 2) should be present in the final polishing stage. We have removed such particles by three methods: (1) allowing large particles to settle out in a liquid and decanting off smaller particles for polishing, (2) continuous-centrifugation of the polishing solution to remove large particles during polishing and (3) filtering the polishing solution to remove large particles.

Table I. Glass Polishing Compounds.

Compound	Density, g/cm ³	Phases detected by x-ray diffraction	Surface area, m ² /g	X-ray fluorescence ^f	Particle size range, μm
MgO (Code 920)	3.58	Cubic + unident lines	26.84		0.01-15 ^a
SnO (AV-116)	6.45	Tetrga SnO ₂ + Sn ₃ O ₄	11.27		0.01-10
ZnO (HSA)	4.84	Hexag. + unident lines	50.79		0.01-30
TK68	6.77	Ce ₆ WO ₁₂ Type ^b	2.82	Ce(s), La(s), W(vvw)	0.03-10
Rhodite 15	6.20	CeO ₂ (s) CeOF(w)	3.42		0.01-15
Rhodite 50	5.91	CeO ₂ (s) CeF ₃ (w)	12.49	Ce(s), Ca(m), W(vvw)	0.01-20 ^a
Rhodite 76	6.38	CeO ₂ (s) CeOF(w)	6.21		0.01-20
ZOX CE89	6.05	Ce ₆ WO ₁₂ Type ^b	16.36		0.01-10
ZOX E	5.78	ZrO ₂ ¹	14.59		0.01-10
Cerium 85	6.603	Ce ₆ WO ₁₂ (s) Type ^b + CeCO ₃ F(w)	29.01	Ce(s), La(s), W(vvw)	0.01-7
Lustrox 1200	4.97	ZrO ₂ (s) ^d + ZrO ₂ (w) ^c	20.32	Zr(s)	0.01-12
Lustrox PG	3.41	ZrO ₂ ^c	27.78	Zr(s)	0.01-20
ZnO ^e	5.61	Hexag. (5-660)	7.18		0.02-15

^a Large particles are solid and not agglomerates of smaller particles as determined for other powders listed.

^b Ce₆WO₁₂ crystal type structure but La replaces W.

^c (13-307) ZrO₂ monoclinic (variable brown to colorless) Baddeleyite.

^d (14-534) ZrO₂ Tetragonal.

^e Reagent grade powder (8832).

^f Relative intensities; s-strong, m-medium, vvw-very very weak.

No direct correlation between surface area and particle size distribution was observed (see table I). The surface area of powders is primarily affected by the relatively small amount of fines ($< 1 \mu\text{m}$) in the powder.

The densities of these powders varied both above and below the theoretical density of the supposed major phase. Multiple phases or impurities generally contributed to these types of shifts. Multiple phase compounds make the control of the polishing operation more difficult unless the same ratio of phases can be obtained and behavior of both are understood during polishing operations. Impurities can alter polishing conditions and contaminate the surface of the glass. We determined impurity levels of several compounds being used to polish LLL laser glasses (see table II). Table II includes impurity levels

Table II. Impurities in polishing compounds as determined by emission spectrometry.

Impurity levels in polishing compounds,^a ppm

Impurity elements	MgO Code 920	SnO AV-116	Liquid 85 ^b	ZOX CE-89	Al ₂ O ₃ Microgrit 30T	Al ₂ O ₃ Microgrit 9T	Reagent grade ZnO
Al	300	< 5000	nd	nd	major	major	< 100
Cu	6	1	10	10	4	nd	3
Si	600	1000	nd	nd	1 Wt%	1 Wt%	< 2
Fe	200	600	≥ 1000	1000	1000	1000	nd
Ca	3000	100	2000	20	3000	3000	< 2
Zn	< 30	100	nd	< 1	< 30	< 30	major
Ni	10	60	nd	< 1	5	5	< 3
Cr	< 10	30	nd	1000	< 10	< 10	< 10
Ag	< 1	< 1	nd	nd	< 1	3	< 1
Sr	10	< 1	≥ 1000	1000	100	1000	< 1
V	< 10	< 10	nd	nd	40	20	< 30
Pb	< 10	< 10	600	60	< 30	< 30	< 10
La	nd	nd	nd	≥ 10 Wt%	nd	nd	nd
Ba	< 100	< 10	≥ 1 Wt%	5000	< 30	< 30	< 100
Nb	< 30	< 30	≥ 1000	300	< 30	< 30	< 100
Mn	10	< 1	30	20	5	5	< 10
Mg	nd	nd	≥ 1000	10	500	500	< 1
Na	< 300	nd	100	3000	3000	nd	nd
Ti	10	nd	nd	800	800	nd	< 10
Ga	nd	nd	nd	30	30	nd	nd
Zr	< 10	nd	≥ 1000	nd	nd	nd	nd

^a nd means not detected.

^b Y and Th level at 100-1000 according to x-ray fluorescence.

of two coarser polishing compounds also being used. The impurity levels of other potential sources of contamination are shown in table III. These impurity levels should be compared with those in the bulk of the glass (see table IV) before selecting polishing materials. The impurity levels of all these polishing materials are above those of the bulk glasses so we can expect contamination of the surface and/or difficulty in getting reproducible polishing conditions.

The surfaces of Suprasil-II silica disks were analyzed after final polishing with Liquid 85¹ by a commercial vendor or with ZOX CE-89 in our Optics Laboratory. Surfaces polished with Liquid 85 were highly contaminated with Ce, Pb, Na, Al, K, and Ca. Trace amounts of Be, B, Mg, Ti, and La were also detected by ion microprobe analyses at depths under the surface of < 150 Å. Ion microprobe analysis is not sensitive for P, Sc, and Fe in the presence of Si molecular ions. Auger electron spectroscopy (AES) could only detect C, P, S, Cl, Ca, and N within 10 Å of the surface. Photoelectron spectroscopy (PES) was able to detect Ce, Sn, Ca, N, and C at the same depth. Trace quantities of Al, Pb, and water were detected at greater depths (≤ 3200 Å). As expected, none of these surface impurities could be detected by the energy dispersive system (EDS) in the scanning electron microscope (SEM). Embedded particles of > 0.1 μm could be identified by SEM and analyzed by EDS when exposed at the surface.

The interpretation and turn-around time prevent the use of electron spectroscopy for chemical analysis (ESCA) on routine surfaces. The sensitivity level for several elements of interest is too low to use induction-coupled-plasma (ICP) with direct-reading spectrometry (DRS), flame atomic absorption, or furnace atomic absorption techniques. Evaluation of these surfaces are still in progress by secondary ion mass spectrometry (SIMS).

Table III. Other sources of contamination during laser glass polishing operation.

Impurity elements	Pitch			Ever-Flo Solution
	64°C melt	73°C melt	82°C melt	
Al	3	2	2	1
Cu	0.1	0.1	0.1	<1
Si	10	2	2	2
Fe	3	10(60) ^a	7	1
Ca	3	1	2	2
Zn	< 1	< 1(5) ^a	7	< 1
Ni	7	6(10) ^a	2	< 1
V	10	10(20) ^a	7	< 1
Pb	< 1	< 1(5) ^a	< 1	2
Mg	1	0.6	0.7	< 2
Na	< 6	< 6	< 6	25
Ti	2	< 0.3	< 0.3	< 1
K	nd	nd	nd	25

^aX-ray Fluorescence Analysis (xx)

(Note: nd means element was not detected)

¹ Reference to a company or product name does not imply approval or recommendations of the product by the University of California or the U. S. Department of Energy to the exclusion of others that might be suitable.

Table IV. Impurities in laser glasses as determined by emission spectrometry^a

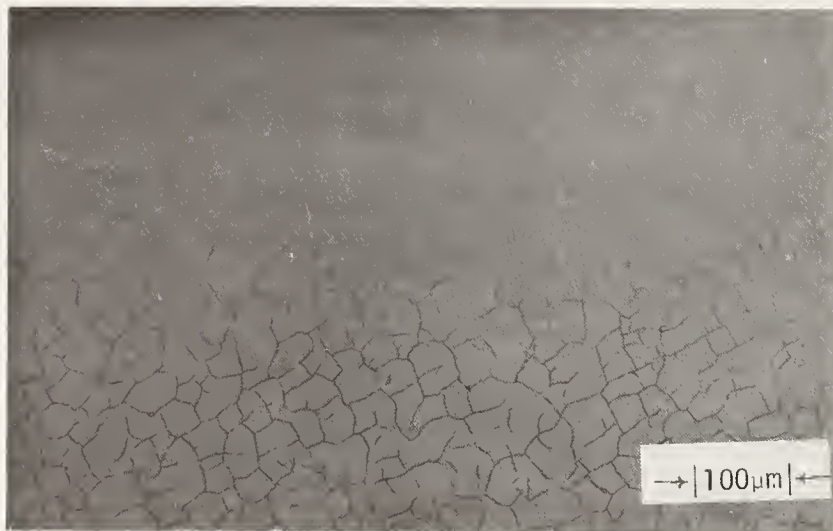
Impurity elements	Impurities, ppm		
	BK-7	Laser glasses LG-812	ED-2
Mg	100	major	10
Mo	200	2000	1000
Ba	major	1000	60
Si	major	20	major
Cu	3	6	3
Sr	60	major	major
B	major		100
Sn	< 30	< 10	30
Ti	200	< 10	< 3
As	1000	< 30	300

a Major = additives or major elements of glass composition; blanks mean not detected.

We have developed a rapid and more quantitative method to detect impurities on these surfaces. We attach teflon fixture to the surface of a glass to contain an etchant ($\sim 2\%$ HF) within a 13 mm diameter area on the surface. Etchant time and temperature is controlled to dissolve the desired depth of glass (≤ 3000 Å) for subsequent analysis. The actual etch-out depth is profiled with a Det Tak surface analyzer (background threshold of approximately 200 Å). The solution of dissolved glass is evaporated and analyzed by emission spectroscopy. Three surfaces polished with ZOX CE 89 were analyzed by etching to depths of 1200, 2000, and 2600 Å, respectively. Surface impurities detected by this method include Na, Al, Ca, Cu, Mg, Fe, Ti, Ba, Ni, Pb, Cr, Mn, Sr, Zr, and Zn. No Ce was detected although CeO_2 was used to final polish these surfaces. This analytical method is not as sensitive to Ce as the ion microprobe method. The bulk glass is contaminated with Al. Additional analyses and development of standards are in progress to improve the accuracy of this method.

A second feature of the above method is that the etched region can be examined optically. Surface and near-surface flaws are revealed by etching or ion exchange techniques[9]. The deep microcracks caused by rough surface removal operations (blanchard grinding, diamond saw cuts, etc.) have patterns similar to those in figure 3. The shallow defects of the coarser polishing operations (30 and 9 μm Al_2O_3 polish) used to remove the previous defects are shown in figure 4. If proper amounts of the surface are removed during each stage of polishing, these deep defects will not be observed after etching a surface polished with fine ($\leq 1 \mu\text{m}$) polishing compounds. Etching such a finely polished surface does expose the polish scratches previously filled in and/or covered over by a surface film (see figure 5). The concentration of scratches and defects can be determined by image analysis and compared with laser damage results to establish a quantitative correlation. Such information would be useful in establishing inspection limits on surfaces before coating or bare-surface use.

The laboratory scale polishing unit (305 mm diam wheel) was set up to final polish the Suprasil-II silica disks with high-purity polishing slurries. We stopped using pitch on this wheel after we observed that the pitch reacted with the polishing slurry and was picked up on the glass. Nylon covered wheels allowed better monitoring of polishing rates and impurity levels. Evaluation of surfaces suitable for commercial polishing applications will be investigated after the questions about impurity effects have been resolved.



a. Defect pattern in diamond saw cut surface



b. Defect patterns in blanchard ground surface

Fig. 3. Surface defects revealed on Suprasil-II silica surfaces after etching with dulite HF

The characterization results are given in table V and VI for the high-purity powders used on the laboratory-scale polishing studies. These powders were used on the final polishing stage to remove the defects of the two previous coarse stages (Al_2O_3 microgrit 30% and 9% in table II). To date, we have polished Suprasil-II silica disks (51 mm diam) with MgO , CeO_2 (B-1407), and both Al_2O_3 powder and a fluorophosphate glass (ZG-812) disk (25 mm diam) with the ZnO powder. The adjusted polishing parameters and polishing rates for these initial studies are listed in Table VII. Polishing with MgO was discontinued because additives would be required to control excessive foaming. High polishing rates with CeO_2 powder were obtained after the coarse particles ($> 5 \mu\text{m}$ diam) were removed while maintaining a constant concentration of particles ($< 5 \mu\text{m}$ diam) in the polishing slurry.



as-polished

etched

a. Coarse polish with 30 μm Al_2O_3 compounds



as-polished

etched

b. Coarse polished with 9 μm Al_2O_3 compounds

Fig. 4. Surface defects revealed on Suprasil-II silica surface after etching with dulite HF

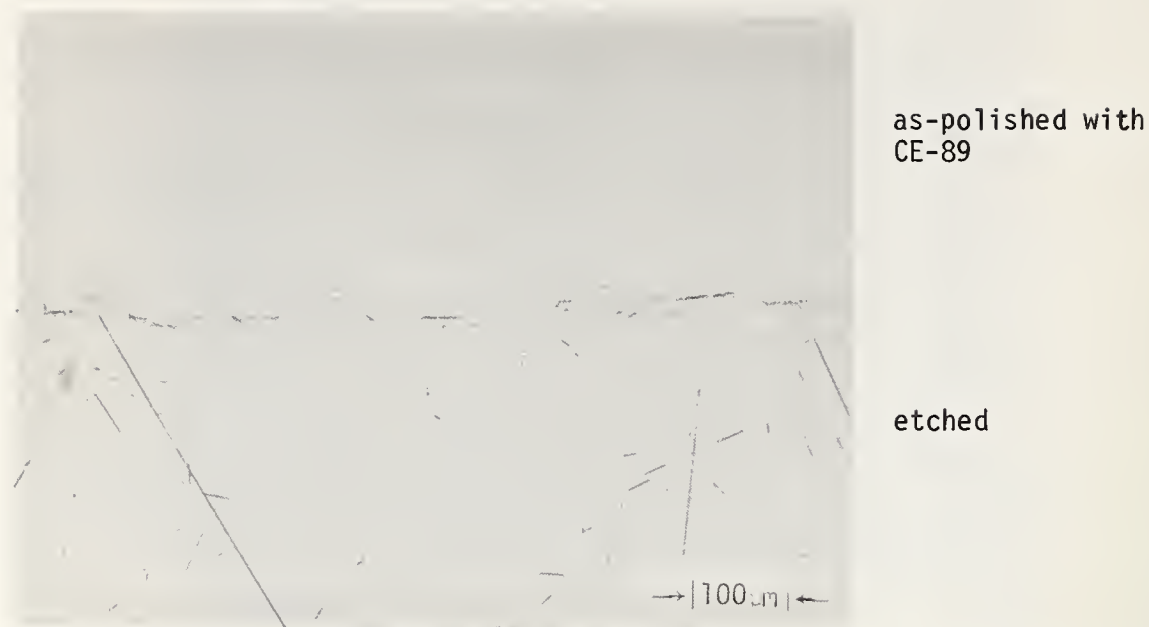


Fig. 5 Surface scratches on Suprasil-II silica are apparent after etching with HF.

Table V. Material characterization of high-purity powders under evaluation as polishing compounds.

Powder type	Density, g/cm ³	Phases detected by x-ray diff.	Surface area, (m ² /2)	Particle size ranges, μm	Status of large particles ^a
ZnO (Code 8832)	5.61	Hexag.	7.2	.02-15	A
MgO(100m)	3.58	Cubic + Moderate Mg(OH) ₂	76.6	.01-25	A
CeO ₂ B-1407	7.03	F.C.C.	1.4	.05-20	A
CeO ₂ B-1408	7.09	F.C.C.	1.2	.05-20	A
CeO ₂ B-1409	7.58 ^b	F.C.C.	6.6	.05-25	A
Al ₂ O ₃ ERC	3.97	Alpha Al ₂ O ₃ +Unknown lines	7.4	.03-20	A
Al ₂ O ₃ Lot 4071	3.93	Alpha Al ₂ O ₃ +Unknown lines	9.6	.03-18	A

^a S = single particle, and A = agglomerate.

^b After vacuum bakeout at 230°C this density dropped to 7.13 g/cm³, but the particle size range remained the same.

*** Unknown = unknown lines also detected.

Table VI. Impurities in high-purity powders under evaluation as polishing compounds (as determined by emission spectrometry)^a

Impurity elements	Impurities, ppm						
	ZnO 8832	MgO 100m	CeO ₂ B-1407	CeO ₂ B1408	CeO ₂ B-1409	Al ₂ O ₃ ERC-HP-DBM	Al ₂ O ₃ 4071
Cu	3	10	≤ 10	nd	nd	4	1
Mg	< 1	nd	6	6	≤ 2	100	100
Si	< 2	100	nd	nd	nd	110	100
Ca	< 2	3000	1000	nd	nd	25	30
Fe	< 10	300	15	≤ 5	≤ 5	30	30
Ga	nd	< 3	nd	nd	nd	100	20
Mn	< 10	30	10	≤ 1	nd	< 1	3
B	< 3	300	100	nd	nd	< 3	< 3
Ba	< 100	< 100	100	nd	nd	< 30	nd
Pb	< 10	< 10	2	2	2	< 30	< 30
Al	nd	200	nd	nd	nd	major	major
Sr	nd	30	nd	nd	nd	< 1	nd

^a nd mean not detected.

Polishing with Al₂O₃ (ERC-HP-DBR) powder was stopped because of excessive foaming. This foaming action was attributed to the Mg doping agent in this hot press powder. Satisfactory polishing rates were obtained with the Al₂O₃ (4071 powder, but subsurface scratches persisted after 35 h of polishing with the same slurry. Starting with a finer agglomerate size (< 5 μm diam) Al₂O₃ slurry and continuously removing large agglomerates (> 5 μm diam) from the slurry reduced subsurface scratches. Preliminary evidence indicates a rapid buildup (snowballing) of agglomerates comprised of Al₂O₃ particles and silica from the glass (see figure 6). This buildup was also observed by determining the particle distribution size of the slurry before and after polishing. Further evaluation of this buildup mechanism is in progress because it could account for the common belief that Al₂O₃ is "too hard" to polish glass.

Our first attempt to polish fluorophosphate glass was made with ZnO (8832) powder with controlled pH slurry (see table VII). At lower pH values (< 7.0), the foaming was not excessive, and a maximum polishing rate was observed at 6.5 pH. Fewer subsurface scratches were observed with ZnO on the fluorophosphate glass than observed with Al₂O₃ on the silica glass. Additional polishing studies are in progress on both glasses.

Table VII. Results vs adjusted parameters of laboratory scale polishing with high purity powders.

Polishing compound	Polishing pH*	Polishing time, h	Glass Removal Rate		Remarks
			Wt, $\mu\text{g/h}$	Thickness, $\mu\text{m/h}$	
MgO (100m)	9.8-9.7	27.5	250	0.11	Excessive Foaming
CeO ₂ (B-1407) as received	8.3-6.8	27.5	990	0.44	
CeO ₂ (B-1407) as received	6.8-7.2	27.5	3,900	0.48	Control pH
CeO ₂ (B-1407) -5 μm fraction	8.9-7.5	34.5	4,600	2.06	
Al ₂ O ₃ ERC HP-DBM	8.0-7.7	17.5	1,800	0.82	Excessive foaming
Al ₂ O ₃ (4071) as received	9.0-7.9	35	1,600	0.71	
Al ₂ O ₃ (4071) -5 μm fraction	8.3-7.4	24.5	760	0.34	Decreasing Al ₂ O ₃ conc. (50%) due to decant of large particles (> 5 μm dia).
ZnO (8832) as received	5.9-5.8	13	420	1.80	Control pH
ZnO (8832) as received	6.5-6.6	13	780	3.32	Control pH
AnO (8832) as received	9.0-8.5	13	500	2.15	Control pH. Excessive foaming.

* pH values before and after polishing

Laser damage tests have begun to establish the threshold damage of Suprasil-II silica surfaces after various polishing and etching procedures. A separate report will be prepared when we have sufficient results to show a direct relationship between specific impurity levels, defects, and surface threshold damage.

4. Conclusions and Recommendations

The rapid advance of high-power lasers for fusion applications requires advances in glass fabrication, glass surface preparation, and glass coating techniques, to sustain laser stability and durability. Since the laser threshold damage of glasses seems to be the weakest link, we examined existing surface preparation procedures as well as evaluated alternate methods to reduce surface contamination and subsurface defects. Analytical techniques were developed to quantitatively determine surface impurities and subsurface defects. The origin of many of these impurities and defects were identified.

Closer control of final polishing compounds is needed to assist opticians in meeting the increasing constraints on surface finishes. Characterization of polishing compounds should at least include impurity content, phase content, particle size distribution, and nature of large particles and/or agglomerates. Such information could prevent problems in subsequent polishing operations, which might trigger unwanted changes in those procedures.

The contamination of the polished surface by the polishing slurry has been confirmed. Efforts to maintain a low contamination level in this slurry should improve polishing operations as well as laser threshold damage. The chemical reactions at the glass-slurry interface seem to control polishing rates as well as polishing particle breakdown or growth (snowballing) rates. More work in this area is in progress at LLL.

5. Acknowledgements

This investigation was initiated and supported by Norman Brown of the Optics Laboratory and Howard Lowdermilk and Lee Smith of the Laser Damage Group at LLL. Their assistance

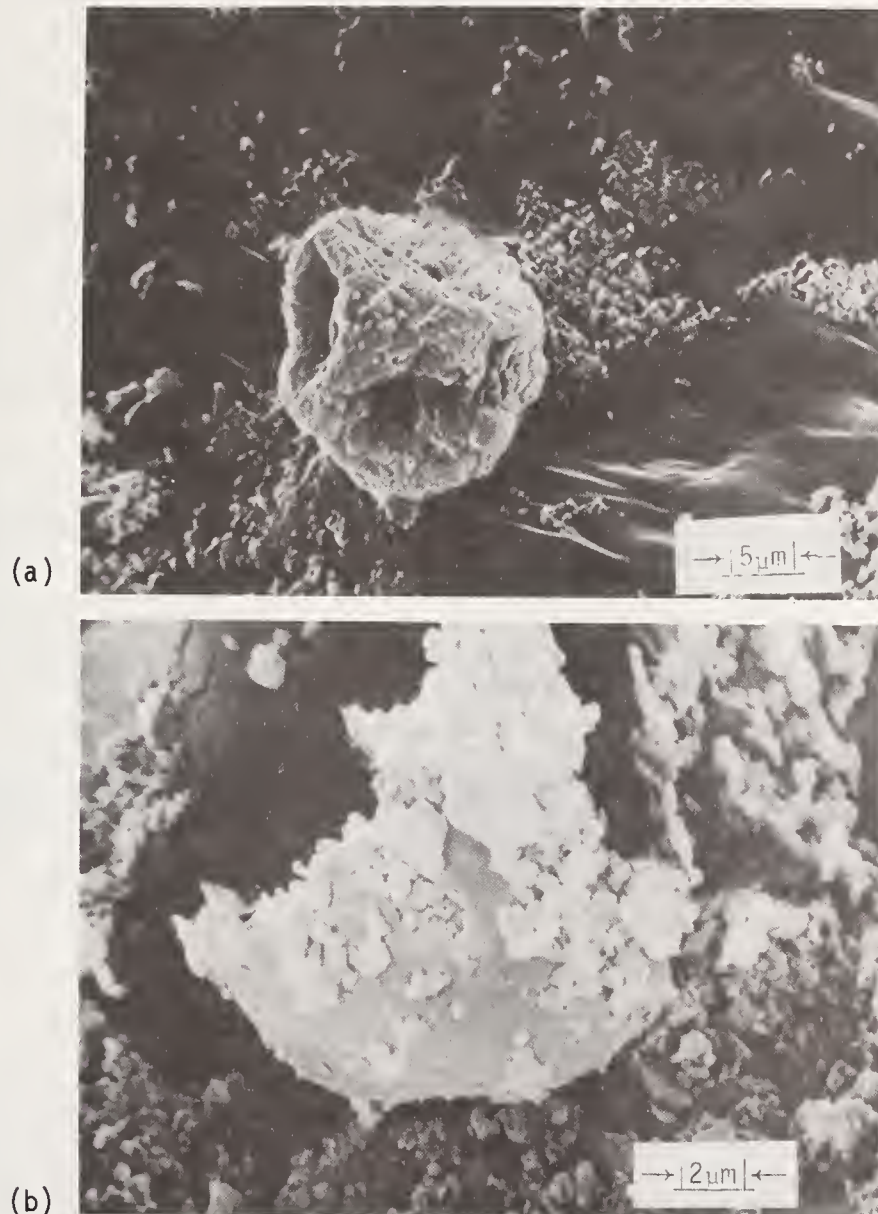


Fig. 6. Buildup (Snowballing) of large agglomerates in the final polishing slurry were photographed in the SEM and analyzed by EDS. These agglomerates were made up of aluminum, silicon, and oxygen and formed during final polish of silica glass with Al_2O_3 polishing compounds.

and guidance made this report possible. Dave Milam of the Laser Damage Group has been most helpful in directing us in matters relating to and evaluation of laser damage tests. Al Ulrich has prepared and evaluated many of the glass surfaces by metallographic techniques. Charlie Farrell developed the procedures used to detect impurities and defects on the surface of these glasses. The unique support of Carol Weaver and Chuck Slettevold was needed in the characterization of all the polishing compounds.

6. References

- [1] Milam, D., "Laser-induced Damage at 1064 nm, 125 psec", *Applied Optics*, Vol. 16, May 1977, pp. 1204-1213.
- [2] Crisp, M. D., Boling, N. L., and Dubé, G., "Importance of Fresnel Reflections in Laser Surface Damage of Transparent Dielectrics", *Appl. Phys. Lett.*, Vol. 21, No. 8, October 15, 1972, pp. 364-366.
- [3] Fradin, D. W. and Bass, M., "Comparison of Laser-Induced Surface and Bulk Damage", *Appl. Phys. Lett.* Vol. 22, No. 4, February 15, 1973, pp. 157-159.
- [4] Milam, D., Smith, W. L., Weber, M. J., Genter, A. H., House, R. A., and Bettis, J. R., "The Effects of Surface Roughness on 1064-nm, 150 ps Laser Damage", in Laser Induced Damage in Optica, A. J. Glass and A. H. Guenther, eds., Nat. Bur. Stand. (U.S.) Spec. Publ. 509, pp. 166-173.
- [5] House, R. A., Guenther, A. H., and Bennett, J. M., "Surface Roughness Statistics of Fused Silica as a Function of Surface Preparation and Treatment", in Laser Induced Damage in Optical Materials: 1977, A. J. Glass and A. H. Guenther, eds. Nat. Bur. Stand. (U.S.) Spec. Publ. 509, pp. 157-165.
- [6] Bloemberg, N., "Role of Cracks, Pores, and Absorbing Inclusions on Laser Induced Damage Threshold at Surfaces of Transparent Dielectrics", *Applied Optics*, Vol. 12, No. 4, April, 1973, pp. 661-664.
- [7] Ringlien, J. A., Boling, N. L., and Dubé, G., "An Acid Treatment for Raising the Surface Damage Threshold of Laser Glass", *Applied Physics Letter*, Vol. 25, No. 10, November 25, 1974, pp. 598-600.
- [8] Boling, N. L., Ringlien, J. A., and Dubé, G., "Q-Switched Laser Inducted Surface Damage at 1.06 Microns", in Laser Induced Damage in Optical Materials: 1974", edited by A. J. Glass and A. H. Guenther, Nat. Bur. Stand. (U.S.) Spec. Publ. 414, December, 1974, pp. 119-130.
- [9] Ernsberger, F. M., "Origin and Detection of Microflows in Glass", Fracture Mechanics of Ceramics, Volume I, Fractography, edited by R. C. Bradt, D. P. H. Hasselman, and F. F. Lange, Plenum Press, N.Y. - London, 1974.

Discussion

BENNETT

The industry has a good feeling, I believe, for the depth of subsurface damage introduced by various finishing techniques but not for the depth of the impurity level added. If most of the impurities are only a few hundred angstroms below the surface, perhaps they could be removed after final polishing by a weak etch or by light sputter etching. We have succeeded in removing several thousand angstroms of fused SiO₂ by sputter etching without adversely affecting surface roughness, for example, although BK 7 glass does roughen using this technique. Would such an approach reduce the need for high purity polishing compounds?

LANDINGHAM

The major amount of contamination was within the first 150 Å of the surface for quartz glass polished with CE 89 (CeO₂). This contamination layer will vary with polishing conditions (material^s being polished.) In general, improvements have been observed in surface damage threshold when the surface is etched. We are testing material that has been etched to confirm this improvement. If impurities are the main problem and we can remove them without causing other defects (like stress corrosion of defects), the improvement in high-purity polishing may not be needed. I would expect some intermediate solution between both approaches will be necessary.

JOHNSON

Comment on the results of coolant pH - hydrogen ion effect in relation to the previous paper results. One paper said No enhancement; the other paper said, Yes, there is and it is H ion increasing brittle behavior.

LANDINGHAM

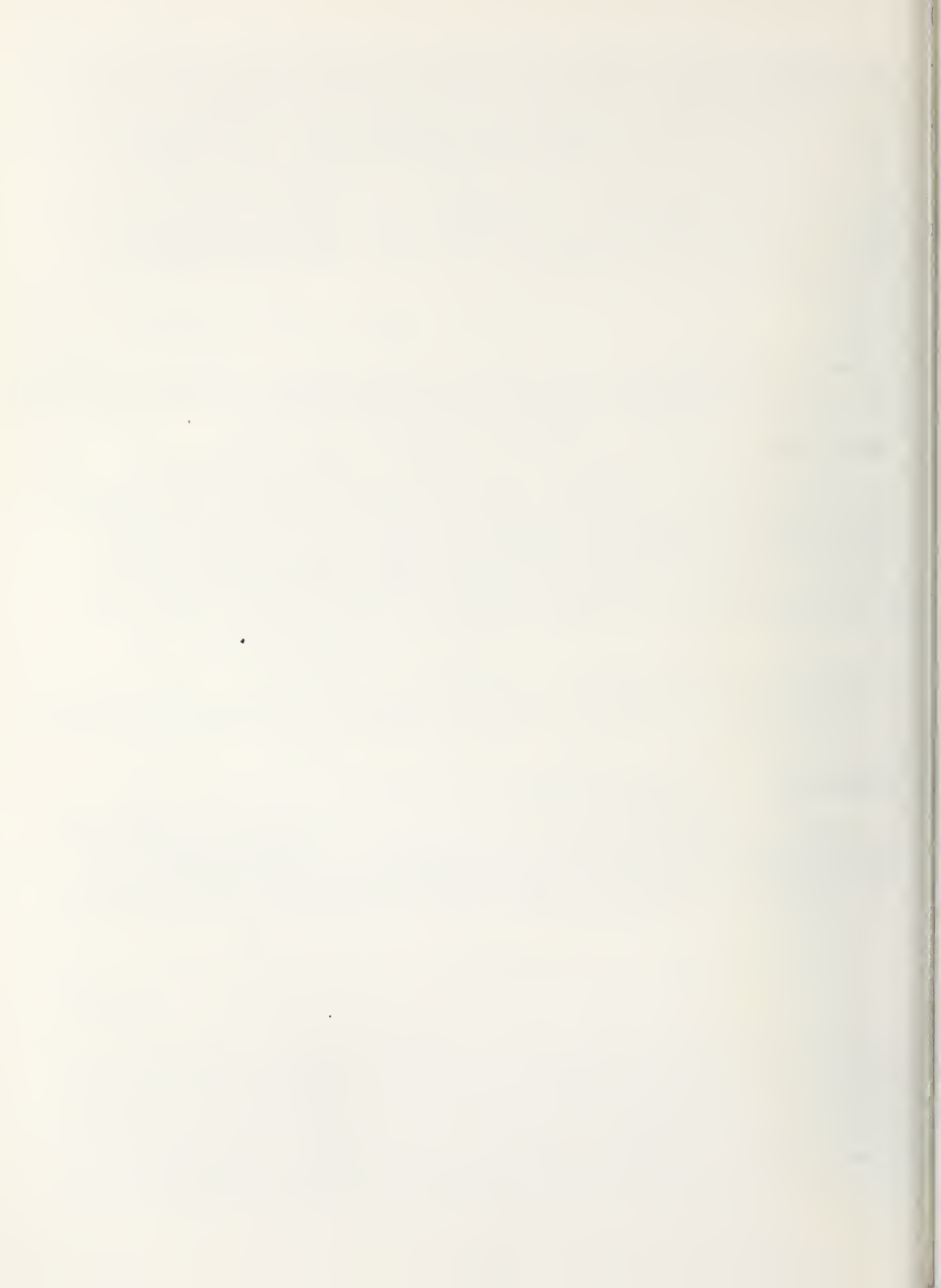
The interaction of the coolant with the surface of a workpiece is dependent on many conditions (pressure, temperature, time, etc). The previous speakers are working in very different environments and observe different behaviors. We are polishing at relatively low rates and pressures with relatively chemical active surface so pH variations can influence our results. At higher polishing rates with higher temperatures and pressure, other parameters may become more important. We plan to investigate these parameters.

BOWLES

Has variation in surface quality been observed in polishing with media at different pH?

LANDINGHAM

Under our present polishing conditions, the fluorophosphate glasses are significantly affected by small shifts in pH. Such pronounced affects on polishing rate will also alter the surface quality in some manner. The affect is not independent of other polishing parameters and requires specific attention to the system (glass, polishing compounds, carrier, solution, etc.) of interest.



THE FABRICATION OF ALUMINA TOOTH ROOTS BY DIAMOND CONTOUR GRINDING

G. L. Messing, L. G. McCoy, and C. R. Hassler

BATTELLE
Columbus Laboratories
505 King Avenue
Columbus, Ohio 43201

To determine if the process of fabricating alumina tooth roots by diamond contour grinding significantly reduces the strength of the tooth root, flexure strengths were determined for four different grinding conditions. The grinding conditions studied were grinding direction (longitudinal or transverse) and the sintered state of the alumina during grinding (bisque or fully sintered). Only for one condition (transversely ground, sintered alumina), did the grinding process lead to the strength-limiting flaw. For the other conditions the strength limiting flaw was entirely intrinsic (i.e., pores) or an interaction of a pore with surface damage from grinding.

Key Words: Alumina; diamond contour grinding; flexure strength; prosthetic device; serrated surface design; tooth roots.

1. Introduction

In the past 10 years there has been considerable interest in the possibility of replacing missing teeth with a new generation of implant designs. In ceramics, the implant is characteristically an alumina-based root structure designed to accept a precious metal or composite porcelain crown. Alumina is used because of its established biocompatibility and good strength behavior *in vivo*. Artificial tooth roots had been fabricated in earlier studies by slip casting [1]¹, but because it is difficult to maintain current design details, this process has been replaced by diamond contour grinding [2]. Diamond contour grinding is a process whereby either a sintered, bisque, or green preform is ground with a diamond tool that has the negative contour of the desired design. Contour grinding can be cost and efficiency advantageous over other processes, such as injection molding, when small lots of tooth roots, having a variety of sizes and shapes, are required.

At Battelle, a three-component prosthetic system was designed using an alumina root as the implanted component. The root has a serrated surface designed for stress distribution. After implantation the serrations are filled with and stabilized by ingrown bone. In implant studies using a baboon model, only a single failure due to implant fracture has occurred out of ~100 implanted roots. To assess the cause of the failure and to assure the viability of this process for fabrication of human implants, it is necessary to establish whether the grinding operation significantly flaws the tooth root surface. It has been well demonstrated in the literature [3] that the presence of surface grinding flaws can be strength-limiting in ceramics. This could be a significant effect as is apparent in Figure 1 which shows the flawed surface of the serration in a contour ground root. Furthermore, with the recent advent of a clinical study at The Ohio State University College of Dentistry using BCL-designed and fabricated implants, it is necessary to demonstrate that tentative ASTM standards [4] for high-density alumina implants could be met. These standards require a flexural strength in three-point loading of 58 ksi (400 MNm⁻²).

¹Figures in brackets indicate the literature references at the end of this paper.



Figure 1. Scanning electron micrograph of surface damage (both uniform and non-uniform) on ground serration of a tooth root

2. Tooth Root Design and Fabrication

Before describing the grinding operation, it is informative to first describe the design of the tooth root. The tooth root is either elliptical or rectangular in cross section with a tapered, serrated surface (Figure 2). The depth of the serrations is 1.5 mm to maximize the horizontal area available to support occlusal loads. To avoid a stress riser, the inside of the serration is rounded. A 5-degree taper of the tooth structure permits easier fitting into the vacant site. The top of the tooth root is recessed 2 mm and a hole is drilled into the tooth root to a depth of 7 mm. A combination gold post and core is investment cast to fit each implant and is cemented to the tooth root 3 months after it has been implanted. This initial 3-month period allows for bone ingrowth into the serrations and stabilization of the root structure. A gold crown is then fitted to the post and core to provide correct occlusion.

Contour grinding was chosen as the process for fabricating this design because it gives detail definition, structural reproducibility, and size and shape flexibility. The process of contour grinding is used extensively in the ceramic industry to fabricate precision electrical insulator components. However, since the cross-sectional shape of the tooth root is either elliptical or rectangular, a machining operation more involved than a simple lathe operation is required. For this purpose, a computer-controlled milling machine is used. To generate the elliptical and rectangular shapes, the alumina rod stock blank is supported on an indexed rotary table. Variations in shape are generated by moving the cutting tool relative to the x-y plane of the rotary table. Thus, it is a simple matter to generate a tooth root having either an elliptical or rectangular cross section of varying size.

To fabricate a tooth root, high-purity alumina powder² with 0.025 percent MgO is hydro-pressed at 345 MNm^{-2} and bisque fired at 1120 C for 2 hours. The bisqued alumina rod is preground to a solid truncated cone having a 5-degree taper on each side, so that only a minimal amount of material (i.e., 2 to 2.5 mm) needs to be removed during contour grinding. The serrations are ground in water with a 200-grit diamond-coated tool which has the negative relief of the tooth root. The feed rate is approximately 12.7 cm/min with a

²Reynolds' Alumina RC-HP-DBM

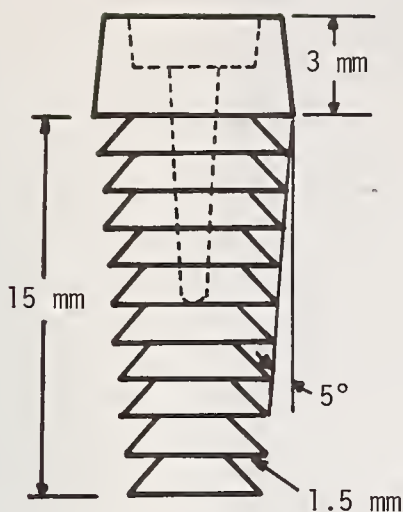


Figure 2. Design details of a rectangular tooth root

maximum depth per pass of 0.5 mm. Consequently, the number of passes required to grind the full depth of the serration is either 4 or 5, depending on the cross-sectional shape. A high-speed (23,000 rpm), air-driven³ chuck is required to attain a machining rate of 1,828 surface m/min (6,000 surface ft/min) with the present tool. There is a minimal loss in speed if the tool is sharp and appropriate feed rates are maintained. To finish the tooth root, which is ground 15 percent oversize to allow for sintering shrinkage, the recessed top is ground with a conical diamond tool and a post hole is drilled. The tooth root is then sintered for 1 hour at 1538°C. The density of the tooth root is ~99.5 percent of theoretical and the average grain size is 3 to 4 micrometers.

3. Experimental

To determine whether the described grinding process and sintering procedure affects the mechanical properties of the implants, rectangular test bars were prepared for four-point flexure experiments. All of the test bars were prepared by the same two-step sintering cycle described above. Half of the test bars were ground to size after the bisque sinter and the other half were ground after the final sinter. Half of the bars in each group were ground transversely (i.e., perpendicular to the tensile axis) to reflect the processing conditions and the other half were ground longitudinally to simulate a control condition. The four grinding conditions are:

- (1) Bisque, transversely ground (BT)
- (2) Bisque, longitudinally ground (BL)
- (3) Sintered, transversely ground (ST)
- (4) Sintered, longitudinally ground (SL).

To simulate the contour grinding operation, the test bars were ground in water with a 200-grit diamond-coated grinding wheel⁴. The edges on the tensile side of the finished test bars were rounded and polished with 320-grit diamond to reduce corner fractures.

Fracture stresses were determined in air with a special four-point bend test fixture [5] at a stressing rate of 6.9 MNm⁻²/sec. The specimens had an outer span of 3.17 cm and an inner span of 1.9 cm. After the samples were fractured, optical and scanning electron microscopy were used to identify the fracture origin.

To determine whether the four-point bend strengths yield an average three-point bend strength of 400 MNm⁻², the procedure of Davies [6] was used. This calculation takes into account the Weibull modulus, stress distribution, and specimen geometry. These data were calculated with the Weibull moduli presented in Table 1 and are given in parentheses.

The surface roughness due to grinding was characterized using a Talysurf IV profilometer with a 2.5-micron-diameter diamond stylus drawn perpendicular to the grinding direction. The center-line average of the roughness profile was determined for each of the grinding/sintering combinations.

³Starlite Industries, Inc.

⁴Norton SD200-R75B56-1/8.

Table 1. Bend Strengths of Al_2O_3

	No. of Observations	Average Strength, (MNm^{-2})	Std. Dev.	m
ST	8	218 [276]	24	7.4
SL	8	414 [493]	32	12.2
BT	9	359 [416]	26	15.9
BL	9	361 [457]	48	7.1

4. Results and Discussion

4.1. Grinding of Bisqued Alumina

The strength data obtained for the bisqued alumina bars are plotted in Figure 3 and additional information is given in Table 1. These data indicate that the grinding direction has no apparent effect on the strength of the bisqued, ground alumina. A comparison of the standard deviations with the statistical F-test at the 95 percent confidence level demonstrates that there is a significant difference in the variability of the data. This could be explained by assuming that flaws are generated during grinding which are oriented normal to the tensile direction. As a consequence, these flaws have a more common character and/or orientation than those generated by grinding in the longitudinal direction. This, of course, would explain the higher Weibull modulus of the BT samples. However, fractographs of representative samples do not substantiate this claim. Instead, BT and BL samples fracture because of apparent intrinsic flaws (Figure 4) such as porous regions (50 to 100 μm) or large grain areas. The porous regions probably arise from agglomerates in the original powder which were not compacted during hydropressing.

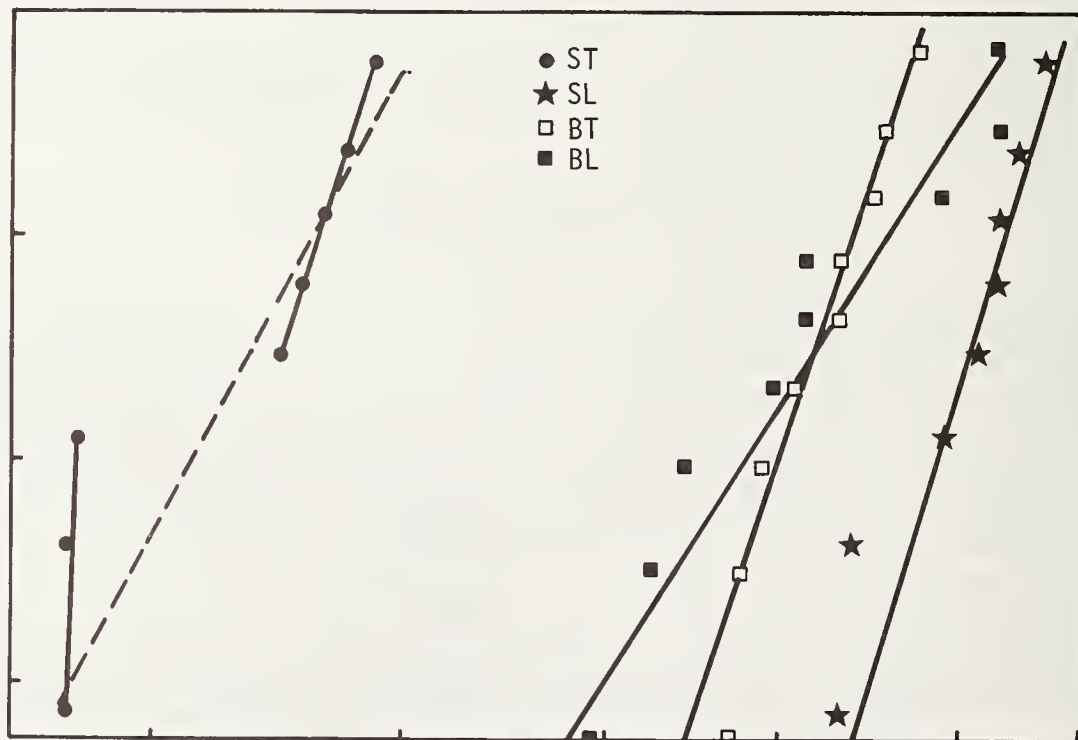


Figure 3. Stress-failure probability curves for test bars ground transversely in sintered state (ST), longitudinally in sintered state (SL), transversely in bisque state (BT), and longitudinally in bisque state (BL).

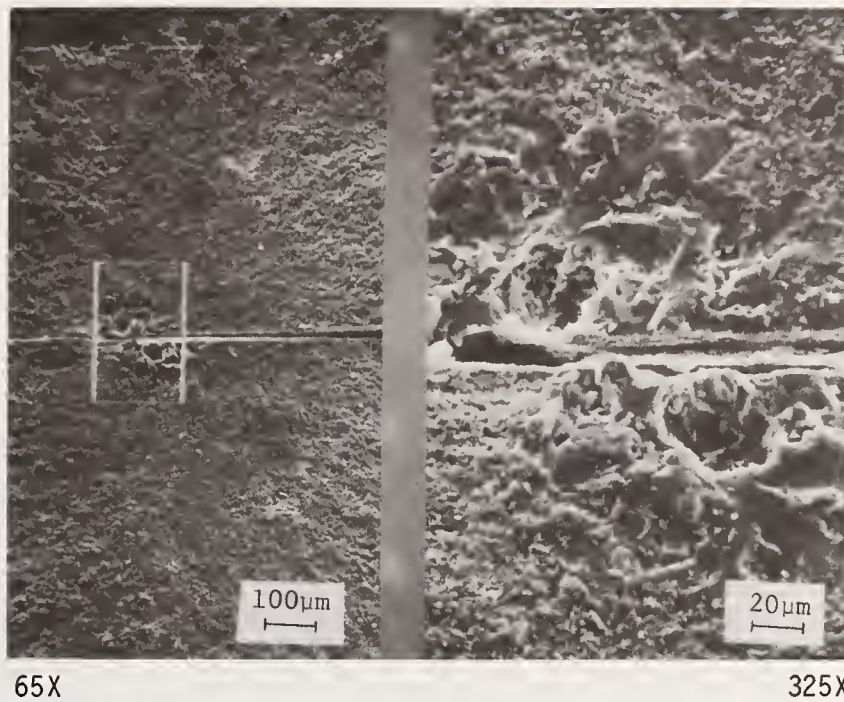


Figure 4. Scanning electron micrograph of internal pore fracture site for a BT test bar.

4.2. Grinding of Sintered Alumina

The average strengths and standard deviations obtained from SL and ST samples are given in Table 1 and plotted in Figure 3. It is apparent that samples ground transversely have a significantly lower strength than those ground longitudinally. This would be the expected result if one assumes that microcracking is associated with diamond grinding of dense alumina. Then for transverse grinding, the potentially critical flaw would be oriented normal to the tensile axis, and would essentially be larger [7] than that produced when the microcrack is aligned parallel to the tensile axis. In fractographs of ST samples (Figure 5), a small region of transgranular fracture near the surface is seen to depths of 20 to 30 μm and lengths of 0.7 to 1.0 mm and the remaining fracture is intergranular.

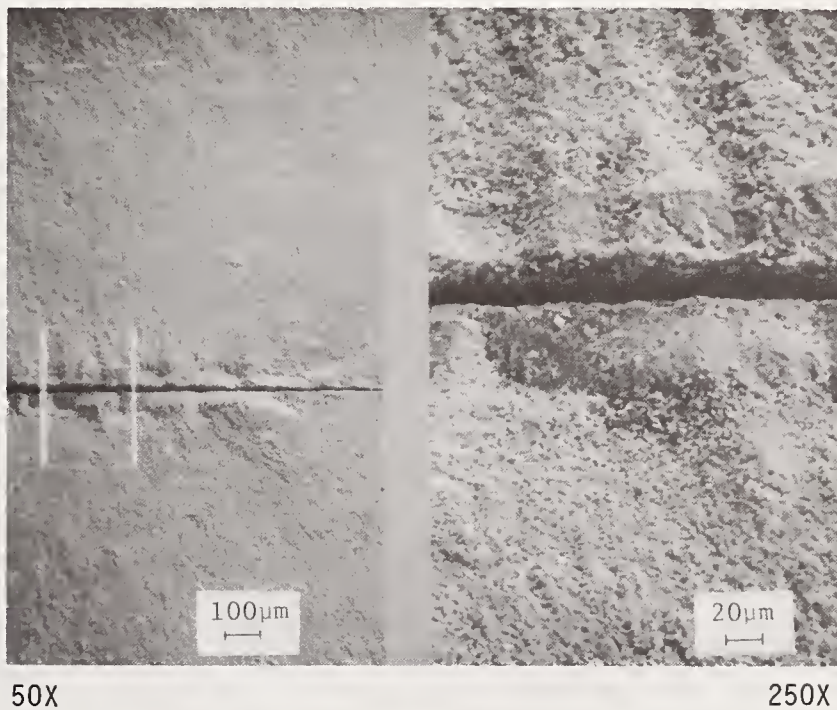


Figure 5. Scanning electron micrograph of transgranular fracture region which originated during machining and acted as the fracture origin site (ST sample).

The existence of this type of fracture surface with the ST samples demonstrates that microcracking is the predominant flaw type for these samples. The particular significance of the orientation effect is demonstrated by the fact that the fracture origins for SL samples were intrinsic in nature, i.e., pores and large grains (Figure 6). While in this particular case the mean strengths were sufficient to indicate a difference due to grinding one would also expect a significant difference to be demonstrated by comparing the Weibull moduli (i.e., standard deviations). In Figure 3 the data for the ST samples indicate that there may really be two different flaw populations instead of one. But, because of the small population size, it is not possible to discern these differences with any degree of reliability.

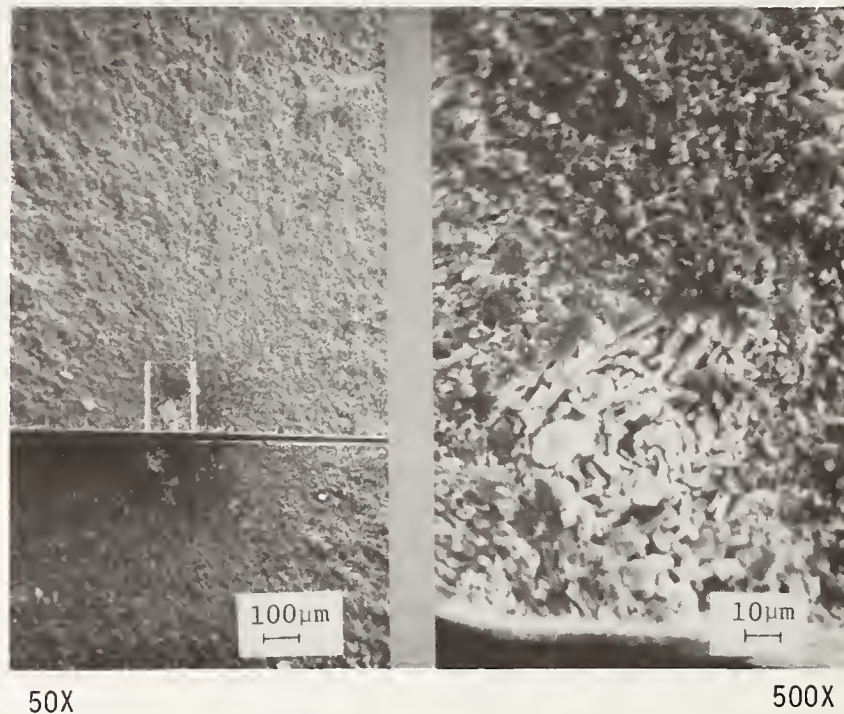


Figure 6. Scanning electron micrograph of internal pore fracture site for an SL test bar

When the sintered ground (SL) strength is compared with the bisque ground strengths (BT and BL), it becomes apparent that the SL process results in the least effect on the strength of the alumina. Because all test bars were fabricated at the same time and failed by the same mechanism, this would indicate that the BT and BL samples have been flawed to some degree during grinding. By comparing the surface roughness generated during the grinding operation (Figure 7) it is apparent that the bisque ground surface both before and after sintering is appreciably rougher than the sintered ground surface. This difference is attributed to the mechanism of material removal which is chipping for the dense alumina and a plowing or smearing process for the relatively soft, bisqued alumina. This surface roughness can easily coincide with the surface pore to yield an effectively large flaw than for a pore only. This increase in flaw size would account for the observed strength differences noted above. This could also explain the directionality seen in the bisqued alumina data.

One might conclude that the SL sintering/grinding operation is the best fabrication process. But, it must be remembered that significant microcracking is associated with material removal. The propagation of these cracks is strongly orientation dependent and susceptible to subcritical crack growth *in vivo*. Therefore, for a tooth root, which is used under multiaxial stresses rather than simple uniaxial stress, grinding of the tooth root from dense alumina is less desirable than grinding from a bisqued alumina because of the possibility for failure after implantation. While most of the stresses are compressive, there is considerable stress generated at the serrations, which makes breakage a real possibility.

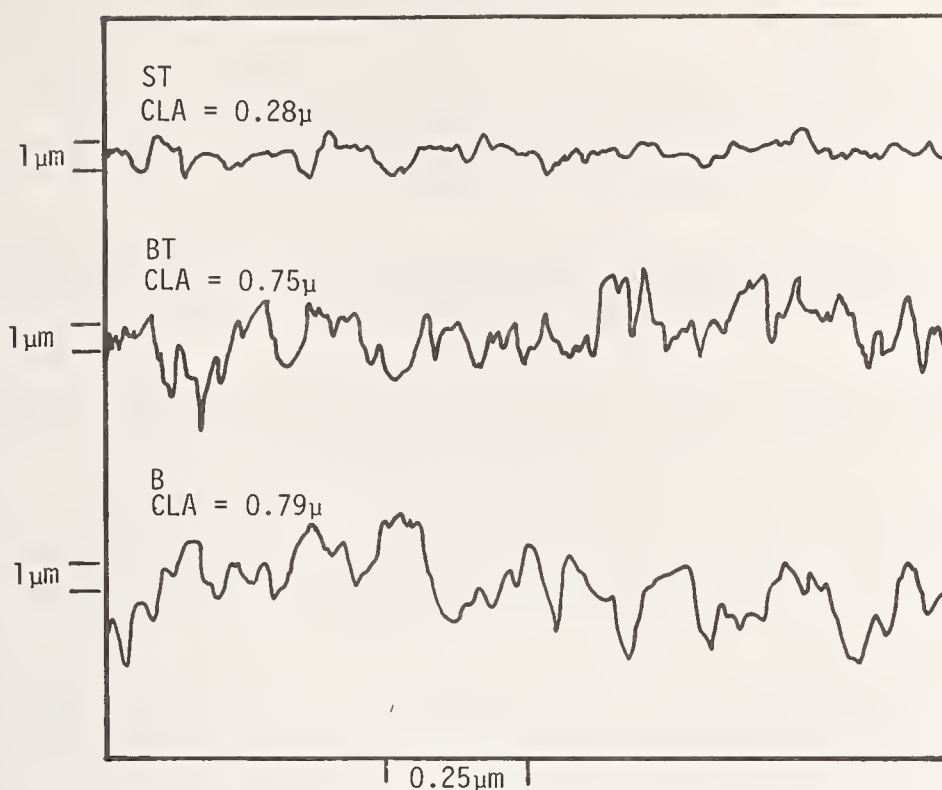


Figure 7. Surface stylus traces of surfaces machined with alumina in sintered state (ST), bisque state, then sintered (BT) and bisque state only (B).

From the above results, it is apparent that porosity is the main intrinsic flaw. Therefore, to significantly improve the strength of the tooth roots, a milling operation is needed to eliminate the agglomerates within the powder. With a significant reduction of this type and size of flaw, and improved intrinsic strength, it might be expected that grinding flaws would have a greater effect on the strength.

5. Conclusion

It has been shown that the main strength-limiting flaw for three of the test conditions was related to intrinsic flaws (pores) rather than to the grinding operation. But, the grinding operation does lead to some reduction in strength for the bisque ground material and to a significant reduction in strength for the sintered ground material, depending on orientation. Thus, the strength of the ground alumina can be increased by powder processing to eliminate agglomerates, after which it is suggested that flaws associated with the grinding operation could be the strength-limiting flaw type.

Assistance of Battelle staff members J. Van Bibber, R. Higgins, and A. Skidmore respectively in diamond contour grinding, testing and fractography is greatly appreciated. Helpful discussions with G. Bansal and W. Duckworth contributed to this work.

References

- [1] Driskell, T. D., O'Hara, M. J., and Niesz, D. E., "Surgical Tooth Implants, Combat and Field", Report No. 2, Contract No. DADA 17-69-C-9181 (April, 1973).
- [2] Hassler, C. R. and McCoy, L. G., "Surgical Tooth Implants, Combat and Field", Report No. 7, Contract No. DADA 17-69-C-9181 (October, 1976).
- [3] Rice, R. W., "The Effect of Grinding Direction on the Strength of Ceramics", The Science of Ceramic Machining and Surface Finishing, S. J. Schneider and R. W. Rice (Eds.), NBS Special Publication 348, Washington, D. C.: Government Printing Office, pp 365-76 (1972).
- [4] Tentative ASTM Standard F4·XXX, "High Density Alumina for Surgical Implants", American Society of Testing Materials, Philadelphia, Pennsylvania (1976).
- [5] Hoagland, R. G., Marschall, C. W., and Duckworth, W. H., "Reduction of Errors in Ceramic Bend Tests", J. Am. Ceram. Soc., 59 [5-6] pp. 89-92 (1976).
- [6] Davies, D. G., "Statistical Approach to Engineering Design in Ceramics", Proc. Br. Ceram. Soc. No 22, pp 429-52 (1973).
- [7] Bansal, G. K., "Effect of Flaw Shape on Strength of Ceramics", J. Am. Ceram. Soc., 59, [1-2], pp. 87-88 (1976).

SIMULTANEOUS FINISHING OF BOTH SURFACES OF HEMISPHERICAL DOMES¹

R. Gentilman

Raytheon Research Division
Waltham, MA 02154

F. Cooke

Frank Cooke, Inc.
North Brookfield, MA 01535

P. Miles

Raytheon Missile Systems Division
Bedford, MA 01730

The high cost of finishing durable oxide materials is the major factor limiting their use as infrared domes for future missiles. A novel technique has been developed for lapping and polishing both surfaces of hemispherical domes simultaneously. The technique, which halves finishing time and costs, has been successfully demonstrated for sapphire and glass.

Key Words: Dome finishing; finishing technique; hemispherical domes; oxides, sapphire, two-surface lapping, two-surface polishing.

1. Introduction

More durable materials are being considered for domes for infrared air-to-air missiles. In addition to optical transparency in the 3 to 5 micron wavelength band, increased resistance to thermal shock, mechanical abrasion, rain erosion, and handling damage is desired. Magnesium oxide, sapphire, and spinel ($MgAl_2O_4$) are among the candidate materials being considered.

The actual domes are hemispherical sheets approximately 75 mm diameter and 3 mm thick. Because it acts as a lens in the optical system which guides the missile, the dome must be finished to within specific tolerances of sphericity and concentricity in addition to being optically polished.

The conventional procedure involves generating the two spherical surfaces by grinding followed by lapping and polishing one surface at a time. Unfortunately, the cost of finishing domes composed of these hard oxide materials is high. In fact, finishing costs can be as much as twice the cost of raw materials and blank fabrication combined. This is the major factor which may limit the use of more durable domes on future systems.

Reported herein are preliminary results using a novel technique for grinding and polishing both surfaces of hemispherical domes simultaneously. Finishing both surfaces at once is expected to halve finishing time and costs, and simplify the optical test procedure, thus reducing the total product cost to a more acceptable value.

¹This work is supported by the Air Force Materials Laboratory, Wright-Patterson AFB, OH 45433 under Contract No. F33615-77-C-5007.

2. Conventional Lapping and Polishing Techniques

After a hemispherical blank has been generated by cutting and grinding, the dome is cemented on a fixture and the inside spherical surface is lapped and then polished with successively finer abrasive slurries (Figure 1-A). A pitch or metal lap is used with either alumina, silicon carbide, or diamond abrasive. When finishing the inside dome surface, the bottom lap rotates while the mounted dome undergoes a reciprocating motion during which it is free to rotate about its axis in response to varying frictional forces.

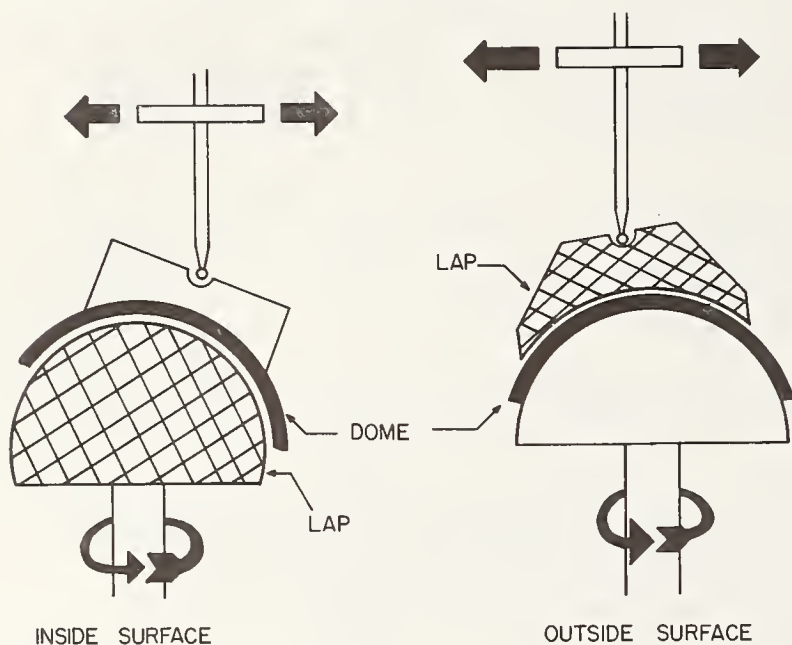


Figure 1. The conventional finishing of domes requires separate operations for the (a) inside and (b) outside surfaces.

The accuracy of the surface is checked against a spherical reference test plate, and, if necessary, changes are made in the lapping motion to correct for errors. The final operations produce a polished surface which is required to eliminate light scattering at the surface.

After the inside surface has been finished, the dome is remounted on the bottom spindle and the outside surface prepared by similar procedures (Figure 1-B). The accuracy of the second surface is checked independently. Then, when the dome is fully polished and unmounted, the concentricity of the two surfaces is checked.

Unlike optical glass or the common infrared materials such as germanium, zinc selenide, or magnesium fluoride, the durable dome candidate materials require extended machine time of several tens of hours for lapping and polishing, much of it with expensive diamond abrasives. Rework of domes which do not meet specifications also requires correspondingly long times.

3. The Two-Surface Finishing Technique

The two-surface lapping and polishing technique for domes is based, in part, on the highly effective technique first introduced near the turn of the century by C. E. Johansson for the production of high precision gauge blocks, and used recently for the fabrication of multiple, high precision laser window elements. In this process, five or more blanks are mechanized to execute a planetary movement between two counter-rotating annular lapping surfaces [1]. The proper choice of speed of the planetary motion and of the absolute and relative lapping speeds produces twin polished surfaces that are flat and parallel to a high degree of precision.

Two-surface finishing of a hemispherical dome is shown schematically in Figure 2. The dome workpiece is placed onto the inside lap, and the outer lap then placed atop the dome. An oscillating support ring causes the dome to rock back and forth between the two counter rotating spherical laps. In order to avoid contact with either of the laps, the thickness of the support ring is less than that of the dome. The bottom lap is on a conven-

tional spindle while the top lap is driven by means of an off-axis ball-and-socket joint. The top drive axis can be fixed at an arbitrary angle or made to swing through a range of angles relative to the axis of the bottom spindle.

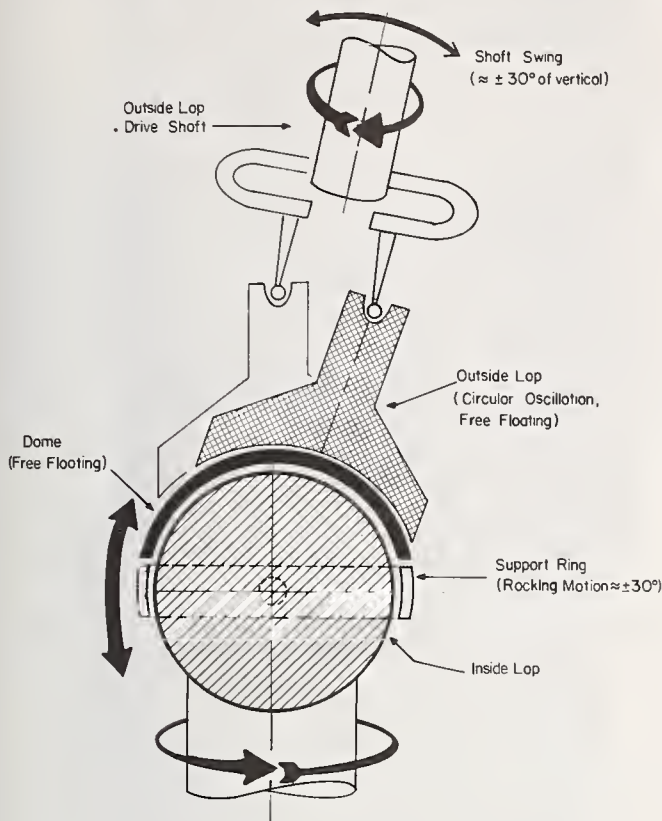


Figure 2. Schematic description of the simultaneous two-surface dome lapping and polishing machine.

Figure 3-A shows the inner lap and the support ring removed from the machine. In Figure 3-B, the dome blank is shown being placed onto the inner lap. With the top lap in place (Figure 3-C), the two-surface finishing process can commence.

Because both the blank and the laps are mechanized to execute four different movements, the dome is carried over a large fraction of each lapping surface and through a wide combination of positions of the lapping surfaces. These movements ensure a symmetry in the optical working of the dome as a function of dome azimuth and, with suitable adjustment of relative movements, uniformity of material removed as a function of dome angle.

The speeds of the four machine movements - top and bottom lap rotation, support ring oscillation, and optional top drive shaft swing - are controlled independently with variable speed motors. The relative rotation rates of the two laps are adjusted so that there is little or no net rotation of the dome. In this way, lapping or polishing occurs simultaneously on both surfaces.

4. Results and Discussion

Domes of glass and sapphire have been successfully lapped and polished using the two-surface technique. As discussed below, optical quality of these domes is equivalent to others finished by the conventional single surface technique. It should be noted, however, that finishing of sapphire domes by either single surface or two-surface techniques has presented problems resulting not only from the hardness of the material but also from its anisotropic machining characteristics, as described by Becher [2].

Diamond impregnated metal laps have been used for the initial lapping operations. Abrasive slurries are used for polishing. Lead foil covered pitch laps have given the best results for polishing the spherical surfaces.



A) Inside lap and support ring



B) Dome blank being placed on inside lap



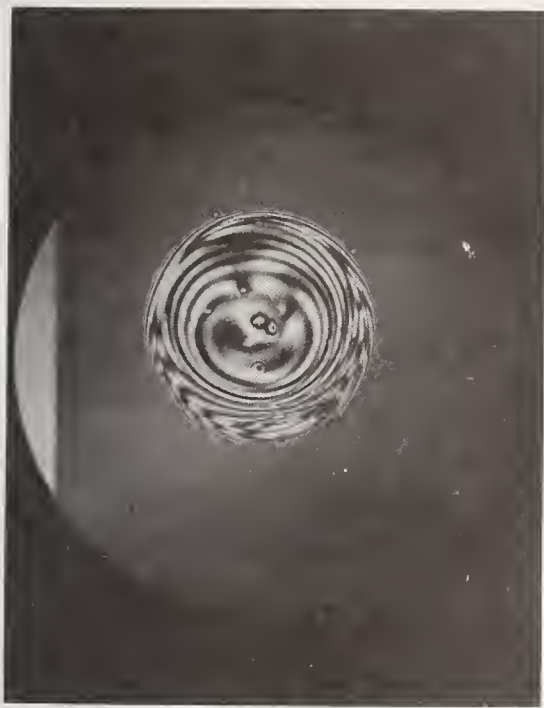
C) Polisher loaded. Free floating outside lap atop dome.

Figure 3. Photographs of Two-Surface Dome Polisher.

For domes, which are transmissive elements, the control of optical thickness over the dome is more important than the control of the optical figure of each individual surface. In conventional dome fabrication, tolerances on the local sphericity of each surface are held to very tight tolerances to attempt to ensure acceptable control of transmitted wavefronts. The simultaneous two-surface technique, because of continual free access to the dome, allows the dome figure to be observed in transmission, as well as the individual surfaces to be spot checked. The degree of perfection of the transmitted wavefront can be observed in a conventional interferometer using a correction lens to compensate for the inherent power and spherical aberration of the dome. Thus the optical quality of the dome can be determined directly from the transmission interferogram at any time in the polishing sequence.

To date, two sapphire domes have been fabricated using the two-surface polishing technique, with encouraging results. Both were cut from single crystal boules such that the dome axis lies close to the crystal c-axis. The design thickness of the domes was 2.540 mm. Actual measurements of the better of the two gave a value of 2.527 mm at the zenith as compared to 2.500 ± 0.03 mm around the lip of the dome.

The optical quality of each dome was examined in transmission by placing it, along with the precision correction lens, in a Zygo interferometer set up in the Fabry Perot mode with plates adjusted to near exact parallelism. The resultant interferogram for the better dome, taken at 6328 Å, is reproduced in Figure 4-A. The fringe pattern results from a double pass through the dome and shows some 10 fringes of irregularity, corresponding to a single pass optical path difference of some $3 \mu\text{m}$ over the 5 cm aperture of the system. While by no means perfect, this degree of uniformity is very close to that achieved in similar c-axis domes polished by conventional techniques, where the best result of several attempts produced a dome with a zenith thickness of 2.522 mm and lip thicknesses of 2.510 ± 0.005 mm. The transmission fringe pattern of this dome is shown in Figure 4-B.



(a)



(b)

Figure 4. Two-pass interferograms of the best domes produced by (a) the two-surface technique and (b) conventional single surface techniques.

In a related set of experiments, the spreading of a line image was measured in an optical system capable of $< 25 \mu\text{radian}$ image spread in the absence of the dome-lens pair. With the dome-lens pair placed in an otherwise parallel light beam, the observed focal line spreads were $75 \mu\text{rads}$ for the best conventionally polished dome and $88 \mu\text{rads}$ for the best two-surface polished dome. It is clear that further improvement is needed in the technique, but already domes can be produced that give image spreads of less than $100 \mu\text{rads}$, a value approaching aperture limited resolution for infrared radiation beyond $3 \mu\text{m}$ wavelength.

5. Summary

A new technique has been demonstrated for lapping and polishing both sides of hemispherical domes simultaneously. The optical quality of domes produced to date approaches aperture limited resolution at mid-infrared wavelengths. This technique gives free access to the workpiece permitting optical evaluation in transmission at any stage of the finishing process. When perfected, the technique will halve finishing time and cost of domes made of durable oxide materials.

References

- [1] Cooke, Frank, "About Flats and Parallels," *Applied Optics* 5 (7) 1104 (1966).
- [2] Becher, Paul F., "Abrasive Surface Deformation of Sapphire," *J. Am. Ceram. Soc.* 59 (3-4) 143 (1976).

Discussion

DECKER

Do you continuously add diamond abrasive during your final polishing operation?

GENTILMAN

At the present time, the abrasive slurry is applied manually. Lead foil covered laps appear to extend the useful life of the diamond, but it must be recharged periodically.

REMPER

You mentioned extensive time for polishing, can you be specific?

GENTILMAN

I do not have the time on the two-side technique, but it requires forty hours per side with conventional single side polishing.

SCHMID

For zero degree sapphire domes, (domes whose axis is aligned with the C axis) you state that the area on the top surface of dome polishes easier than near the sides. You suggest that this is due to easy polishing of the top zero degree material as opposed to the sides that is about 60° from zero.

I suggest that this is a mechanical problem. We have found that zero degree material is hardest to polish. The dome is probably not polishing well on the sides because of the polishing set-up. The pitch has give and therefore there is insufficient pressure on the sides of the dome for adequate polishing.

ABRASIONLESS MACHINING METHODS FOR CERAMICS

R. F. FIRESTONE

IIT Research Institute
Chicago, Illinois 60616

Abrasionless machining methods for ceramic materials are reviewed with extensive references to the recent literature. These methods offer significant advantages over traditional abrasive machining methods since they are not limited by the hardness of the ceramic and easily machine delicate or complex parts.

Key Words: Ceramics; chemical milling, electric discharge machining; electron beam machining; glass; hydrodynamic machining; ion beam machining; water jet cutting.

1. Introduction

Ceramics are the hardest and potentially the strongest of all materials. Many applications require them to be machined to complex shapes with precision, turbine blades for example. The hardness of ceramics makes traditional abrasive machining slow and expensive, especially for complex shapes. Abrasionless machining methods circumvent the limitations of traditional abrasive machining.

2. Background

Ceramic machining is traditionally accomplished by mechanical abrasion, an art whose methods have been developed empirically and whose origins disappear into the mists of pre-history. Six thousand years ago the Egyptians were cutting blocks of granite for obelisks using copper saws set with emery teeth, dressing the surface with dolerite balls and polishing with fine emery power [1]. In these processes, one can recognize the precursors of the modern diamond saw, grinding wheel and polishing lap. Advances on these ancient techniques have been made by improving the abrasives, e.g., diamond instead of natural emery, and substituting power machinery for the sweating fellaheen. But the basic processes for shaping hard materials by abrasion remain the same.

Abrasion is the most widely used and highly developed machining method for ceramics. Hard abrasive grains are pressed against the workpiece to introduce cracks and remove stock by controlled fracture. The cracks can shatter fragile parts, reduce the strength and provide nexus for delayed failure. The rate of stock removal depends upon the ratio of the hardness of the abrasive to the hardness of the ceramics. Machining hard ceramics such as alumina, silicon carbide, silicon nitride, etc. is slow and costly even with diamond, the hardest abrasive. The cost of machining can compose from 50% to 90% of the cost of the finished part [2].

Abrasive machining methods, being mechanical, are generally restricted to simple parts that are flat, or have axial or radial symmetry. Machining complex or asymmetrical parts may be nearly impossible and prohibitively expensive. Thus, ceramics which are not formed to final shape tend to have simple geometrical shapes, a severe limitation on their use.

¹Numbers in square brackets indicate the literature references at the end of the paper.

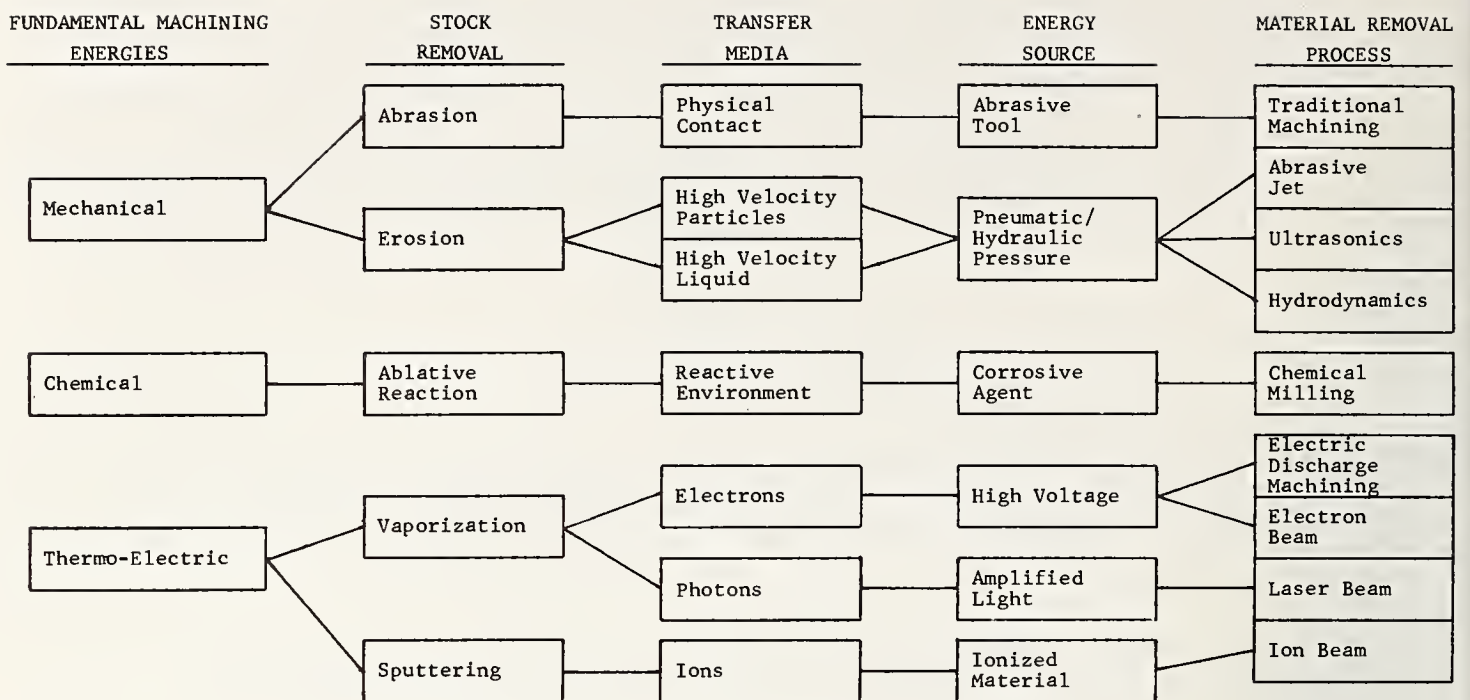


Figure 1. Ceramic machining processes

The objective of this paper is to survey the most important abrasionless machining methods for ceramics. The principles of each method will be discussed and the advantages and disadvantages compared with abrasive machining will be pointed out. The literature, mainly since 1970, will be reviewed. References to earlier literature can be found the proceedings of the first ceramic machining symposium [3].

3. Abrasionless Machining Methods

Abrasionless machining methods do not have the limitations of abrasive methods which require solid-to-solid contact. The hardness of the ceramic is not a factor in determining stock removal rate. Some of the abrasionless methods produce ceramic parts without cracks or flaws which are therefore stronger than as-fired or abrasive machined parts; allow asymmetrical, three dimensional shapes to be produced to close tolerances; or have cubic centimeter per second stock removal rates. Because of the advantages, abrasionless methods are finding increasing application to ceramics.

Machining is the application of energy to the workpiece to remove stock. The fundamental sources of machining energy can be separated into: mechanical, chemical and thermo-electric. The relation of these sources to the machining processes is shown schematically in figure 1 after Springborn [4]. This diagram includes traditional abrasive machining, two non-traditional abrasive methods, and the six major abrasionless machining methods.

Mechanical energy is the oldest energy source applied to machining. It is used for both traditional abrasive machining; non-traditional abrasive machining: abrasive jet and ultrasonics; and for abrasionless machining: hydrodynamic machining (HDM). Chemical energy is used for chemical milling (CM), the oldest abrasionless machining method, and for its hybrid with the thermo-electrical energy, electro-chemical machining (ECM). Thermo-electric is the final category and includes four recent abrasionless methods: electric discharge machining (DM), electron beam machining (EBM), laser beam machining (LBM) and ion beam machining (IBM). The applications of these methods to metals have been recently reviewed [5].

Machining methods may be described by the process by which the workpiece is shaped. The generation process focuses energy onto an area of the workpiece and by relative movement generates a new free surface of desired configuration. Hydrodynamic machining, electron beam machining and laser beam machining use this process which may be numerically controlled. The transfer process uses a pattern or model to direct energy from a diffuse source. Chemi-

cal machining and electric discharge machining use this process which is analogous to printing. Ion beam machining is unique since it can use either process.

The material properties and environment which are required for the use of abrasionless methods are listed in table 1. Hydrodynamic machining and laser beam machining are the most flexible methods since they can be used to machine any material under ambient conditions. Hydrodynamic machining is the most portable since it was originally developed as a field method. The other four methods require immersion of the workpiece in a liquid or a vacuum.

Table 1. Conditions for abrasionless machining methods

<u>MACHINING METHOD</u>	<u>MATERIAL</u>	<u>ENVIRONMENT</u>
Hydrodynamic (HDM)	Any	Ambient
Chemical (CM)	Non-crystalline	Reagent
Electric Discharge (EDM)	Electrically conductive ^a	Dielectric
Electron Beam (EBM)	Any	Vacuum
Laser Beam (LBM)	Any	Ambient
Ion Beam (IBM)	Any	Vacuum

^aResistivity less than 300 ohm-cm.

The applications and results of abrasionless machining methods in the present state of development are listed in table 2. Hydrodynamic machining (HDM) is best for rapid cutting of large holes, slots and grooves in porous materials. Chemical milling (CM) is good for transferring patterns of shallow holes and slots. Electric discharge machining (EDM) drills small holes well but is unexcelled for pocketing, i.e., making cavities with straight sides and flat bottoms, and contouring surfaces. Electron beam machining (EBM) and laser beam machining (LBM) are excellent for drilling small holes. Ion beam machining (IBM) can be used either as a focused energy source for drilling and contouring or as a diffuse source for pattern transfer. Ceramics that have been ion beam machined are usually stronger and never weaker than as-fired or abrasive machined parts. Chemical machining and laser beam machining may also increase the strength of ceramics.

All abrasionless machining processes, with the exception of chemical milling, are capital intensive compared to abrasive machining. Minimum cost of equipment ranges from approximately \$10,000 for electric discharge machining up to \$1,000,000 for high powered lasers. Specially trained personnel are required and operating costs are usually higher. However, for many applications, the total cost of machining a ceramic part is less than abrasive machining.

3.1 Hydrodynamic Machining

Hydrodynamic machining uses a high velocity fluid jet to erode material [6]. The fluid is commonly plain water and the method is often called water jet machining. There are three types of jets: pulsed jets which are used to fracture material, cavitating jets which are used primarily underwater, and continuous jets which are the subject of this section.

The water jet is a nonwearing tool with no frictional drag in the cut and virtually no forces at right angles to the jet. The kerf is insensitive to dwell of the jet which allows contours to be accurately controlled. It is as versatile as a jigsaw on wood and is, indeed, used to cut wood and other organic materials.

The equipment for a continuous jet is simple and robust (fig. 2). It consists of a fluid reservoir, a hydraulic intensifier to produce high pressure, a pump to drive the intensifier surges, pressure and flow control systems, and a nozzle. A relatively low flow of fluid is required for cutting, only 1 to 10 l/m which is less in fact than the normal coolant flow for diamond grinding.

Table 2. Comparison of abrasionless machining methods for ceramics
METHOD

	<u>HDM^a</u>	<u>CM</u>	<u>EDM</u>	<u>EMB</u>	<u>LBM</u>	<u>IBM</u>
<u>APPLICATION</u>						
<u>Holes:</u>						
Standard (>.005")	Good ^b	Poor	Fair	Poor	Fair	Poor
Small (.005-.001")	N.A. ^b	Good	Fair	Good	Good	Fair
Micro (<.001")	N.A.	N.A.	N.A.	Fair	Good	Good
Shallow (L/D < 20) ^c	Good	Good	Fair	Fair	Fair	Fair
Deep (L/D > 20)	Fair	N.A.	Fair	Poor	Poor	N.A.
<u>Through Cutting:</u>						
Shallow (L/D > 20)	Good	Good	Poor	Good	Good	Fair
Deep (L/D < 20)	Fair	N.A.	N.A.	Fair	Fair	N.A.
<u>Contouring</u>	Poor	N.A.	Fair	N.A.	N.A.	Good
<u>Pocketing</u>	Fair	Poor	Good	N.A.	N.A.	Fair
<u>Through Cavities</u>	Good	Good	Good	Poor	Poor	Good
<u>RESULTS:</u>						
Maximum Precision (in)	.005	.001	.0005	.001	.001	.000001
Best Finish (μ -inch rms)	100-1000	5-1000	10-500	20-100	20-50	1-20
Effect on Strength	D ^d	M ^e	D	D	M	I ^f

^aSee text for meaning of acronyms.

^bNot applicable.

^cLength to diameter ratio.

^dDecrease in strength of abrasive machined ceramic.

^eMay either increase or decrease strength of abrasive machined.

^fIncrease in strength of abrasive machined ceramic.

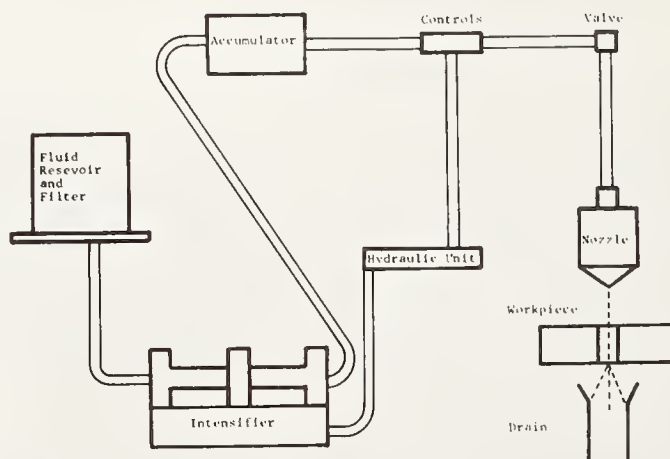


Figure 2. Hydrodynamic machining (HDM) apparatus

The process parameters are pressure (50 to 1000 MPa), nozzle diameter (0.01 to 1 mm), standoff distance between nozzle and workpiece (2 to 25 mm), jet angle (usually normal incidence, 90°) and traverse rate (0.1 to 10 m/s). The power requirements are related to the pressure and nozzle diameter. The cutting rate is a complex function of the process parameters and the workpiece properties. In general, it increases with increasing pressure and decreasing nozzle diameter and standoff distance. The hardness of the workpiece is not a major factor but weak, porous materials cut more rapidly than dense, strong ones. The jet may be augmented with abrasives to increase the cutting rate in some materials. The abrasive may be either inspired by the nozzle or placed on the surface of the workpiece to be driven in by the jet.

The depth of cut in ceramic materials varies from 0.1 to 100 mm for a single pass of a simple jet using plain water. Multiple passes of the jet in the same kerf will increase the depth of cut by a factor of two approximately. The depth produced by multiple passes is limited since the standoff distance increases with each pass. By using a penetrating nozzle which descends into the kerf to maintain constant standoff distance, deep holes may be drilled and multiple passes may be used to cut grooves and slots. The depth to kerf ratio may be 150 to 1 or greater and the depth may be 3000 mm or more being limited only by the length of the nozzle.

The kerf is a function of nozzle diameter and material grain size. For small nozzle diameters and fine grain material, the kerf may be only 0.5 mm greater than the nozzle diameter. For coarse grain materials, it may be as large as the nozzle diameter plus two grain sizes. Since the jet spreads as it leaves the nozzle, the kerf is slightly larger at the bottom than at the top. This may be reduced by using water to which has been added long chain polymers, such as polyethylene oxide. Penetrating nozzles cut wider kerfs to accommodate the nozzle as it descends into the cut. The minimum kerf for a penetrating nozzle is dependent on the depth of cut but can be less than 5 mm.

Water jets have been used to cut metal, rock [8], composites, concrete [9], and many softer materials such as wood, cloth and paper [10]. Their use on ceramics is just beginning. Some of the preliminary results on the use of a water jet to cut refractory bricks by the author are shown in table 3. The values are averages for each class of brick. The surface exposure rate (m^2/s) is the depth of cut multiplied by the traversing rate.

Table 3. Water jet cutting of refractory bricks

<u>Refractory</u>	<u>Depth of Cut (mm)</u>	<u>Surface Exposure Rate (m^2/s)</u>
Insulating Firebricks	90	90×10^{-3}
Porous Bricks, Al_2O_3 & SiC	25	25×10^{-3}
Dense Firebricks	15	15×10^{-3}
Fusion Cast Bricks	1	1×10^{-3}

CONDITIONS: Nozzle Diameter: 0.5 mm
 Pressure: 480 MPa
 Traverse Rate: 1 m/s
 Fluid: Plain water
 Jet Incidence: Normal
 Standoff Distance: 10 mm

The results indicate that the porosity and tensile strength of a material is more important than the hardness in determining the cutting rate. The alumina and silicon carbide bricks are very hard and abrasion resistant but quite porous. Rough calculations show that for the same power input, the water jet cuts these bricks five times more rapidly than a diamond saw. The silicon carbide bricks will abrade the firebricks but the firebricks are denser and stronger and so do not cut as rapidly. Fusion cast bricks are very strong and non-porous. The cutting rate is very slow. Increasing the pressure shatters the brick

rather than increase the cutting rate. Future work may result in a more exact correlation of these parameters.

The effect of hydrodynamic machining on strength is similar to abrasive machining. However, since it works best on porous materials which are inherently weak and in which the pores tend to serve as crack stoppers, the strength loss is minimal.

3.2 Chemical milling

Chemical milling is the controlled solution of the workpiece by a chemical reagent. The areas to be milled are defined by a chemical resistant, strippable mask. Since solution proceeds radially from the opening in the mask, the resulting undercutting limits the process to shallow cuts. Undercutting control on deeper cuts or contour milling may be accomplished by successively stripping masks as the cutting progresses. The amount of material removed, i.e., the depth of cut, is controlled by the length of time the workpiece is left in the reagent and the temperature.

Although there are reagents which will dissolve almost all ceramics, chemical milling is restricted to glass by the lack of suitable reagents which will dissolve polycrystalline ceramics uniformly and at low temperatures where masking can be used economically. For chemical milling glass (glass etching), the reagents are based on hydrofluoric acid and the mask is traditionally wax through which the pattern is scratched, although polymers and photoresists are now also used. For an abrasionless machining method, glass etching is very old, beginning shortly after K.S. Scheele prepared hydrofluoric acid in 1771, and rapidly supplanting copper wheel engraving of glass [11]. Much of the technique was developed empirically but there has been some scientific study [12].

A special proprietary photosensitive glass has been developed by Corning Glass Works which is self-masking [13]. When exposed to ultraviolet light, the glass records a latent image which is developed by heating. There is a pronounced difference in solubility between the exposed and unexposed areas so that the image in the glass can be etched out with hydrofluoric acid. Any pattern may be produced with resolution of 25 μm . Further heat treatment after etching can change the glass into a crystalline glass-ceramic.

A variation on chemical milling which can only be applied to conductive ceramics, such as carbides, is electro-chemical machining (ECM). The electric field supplies the additional energy which allows polycrystalline ceramics to be dissolved uniformly at room temperature. There is an extensive literature which was reviewed in 1974 [14]. Recent work on the process for carbides has been done in Japan [15] and Russia [16]. A detailed description of the process has been given by Wilson [17].

Chemical milling need not decrease the strength of ceramics. Glass etching, if done under proper conditions, can eliminate surface flaws and restore glass to its pristine strength [18].

3.3 Electric discharge machining (EDM)

Electric discharge machining is the controlled melting and vaporization of the workpiece by multiple arcs between the workpiece and tooling to form a three-dimensional reverse image of the tooling. The components required are: a pulse generator to deliver either DC bipolar pulses 200 to 500,000 times a second at 50 to 100 volts; a tool, usually graphite, copper or tungsten; a dielectric, usually oil or deionized water; a pump to circulate the dielectric; and a feed control to maintain a constant standoff, usually 10-500 μm , between the tool and workpiece (fig. 3). The workpiece must have an electrical resistivity of less than 300 ohm-cm unless a conductive electrolyte is used in place of a dielectric.

An excellent review of electric discharge machining up to 1968 was made by Bucklow and Cole [19], who point out that it has developed broad applications "by virtue of its special abilities to sink any profile, however elaborate, into a workpiece in one basic operation, to machine any electrically conductive substance irrespective of hardness, and to remove metal without exerting any appreciable force on the workpiece." There are no other articles

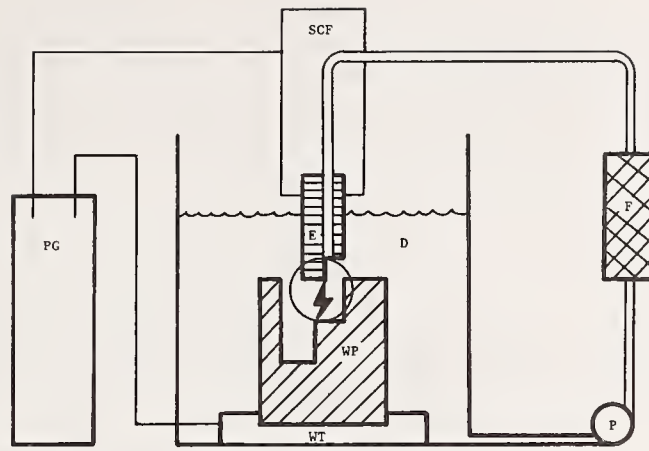


Figure 3. Electric Discharge Machining (EDM) Apparatus. PG, pulse generator; SCF, servo controlled feed; E, electrode; D, dielectric; WP, workpiece; WT, work table; F, filter; P, dielectric pump.

which: treat the physics of the process [20]; compare electric discharge machining with electrochemical machining [21,22] and with laser beam machining [23]; and analyze the cracks produced in cemented tungsten carbides which propagate through the cobalt phase [23,24].

Since electric discharge machining causes melting of the material, there is a thermally affected zone (recast layer) beneath the machined surface which produces residual stress and cracks. In fact, this method is often used to introduce automatically sharp cracks into fatigue specimens. Electric discharge machining decreases the strength of cemented carbides. In applications, such as tool inserts, where high strength is required, the material is diamond ground rather than electric discharge machined. For hot pressed silicon carbide, the author's experiments on flexure bars show that the room temperature strength is reduced by half after electric discharge machining 100 μm from the tensile side. However, the machining conditions were not optimized.

3.4 Electron Beam Machining

A beam of electrons is focused to produce an energy density of 10^5 to 10^8 watts per square millimeter on a part of the workpiece which causes it to melt and evaporate. The components required are: electron gun, a high voltage supply (50 to 150 kV), a vacuum chamber (10^{-5} to 10^{-6} Torr) and beam deflecting coils (fig. 4). The beam positioning is very fast since it is electrical and can be computer controlled. For example, holes may be drilled in ceramic substrates at the rate of 12,000 per second and the beam may be traversed at 10 m/s [25].

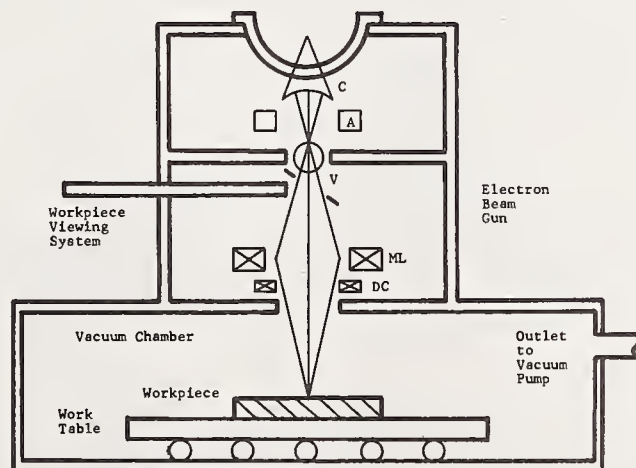


Figure 4. Electron Beam Machining (EBM) Apparatus. C, cathode; A, anode; V, valve; ML magnetic lens; DC, deflection coils.

Electron beam machining is particularly good for drilling small, deep holes. Hundreds of holes 0.1 to 1 millimeter in diameter can be generated in seconds. The process is not affected by the kind of material being drilled or its hardness [26]. Not only cylindrical holes can be drilled but also tapered holes and holes with irregular cross-section. The holes may be drilled at normal incidence or at an angle to the workpiece surface. For drilling very small holes in ceramics, beam focusing must compensate for the space charge on the surface and above the ceramic [25,27].

Since electron beam machining is essentially a thermal process, there is a melted zone around the cut and residual stresses and cracks are introduced into the ceramic. While thin (.040 in. thick) substrates can be cut by perforation, thicker ceramic pieces must be heated before machining to avoid shattering. Another approach is to machine unfired ceramics, the binder volatiles which removes excess heat and firing heals any cracks [28].

3.5 Laser Beam Machining (LBM)

Laser beam machining uses a laser to form an intense beam of light which focused on the workpiece causing it to melt and vaporize due to the intense heating [29]. The components required are a laser with controls, a means of focusing the beam and workpiece positioner (fig. 5). Beam positioning is mechanical so it is neither as fast nor as precise as electron beam machining, a process with which it directly competes. On the other hand, machining is done under ambient conditions which gives the process greater flexibility.

Laser are of two types: continuous (C.W.) and pulsed, and the pulsed are further divided into normal and Q-switched. The pulse duration of these types is tabulated below.

Laser Type	Pulse Duration
Continuous (C.W.)	10^{-1} seconds to infinity
Normal Pulsed	10^{-6} seconds
Q-switched	10^{-9} seconds

The wavelength of the light emitted depends upon the lasing material of which Nd-glass at $1.06 \mu\text{m}$ and CO_2 at $10.6 \mu\text{m}$ are, perhaps, the most common.

Laser beam machining is not limited by the hardness of the material. For example, graphite and diamond are cut with almost equal rapidity and, indeed, lasers are used for commercial production of holes in diamond wire drawing dies [30-33]. Lasers may be used to drill, groove and cut ceramics and are nearly as versatile as an end mill on metal.

The rate of laser beam machining is controlled by the rate at which material is removed which is melted and vaporized by the beam. This occurs mainly by thermal convection but also by the radiation pressure of the beam [29]. Experiments with metals have shown that the machining rate is greatly increased if a gas jet is used to blow the melted material away [34].

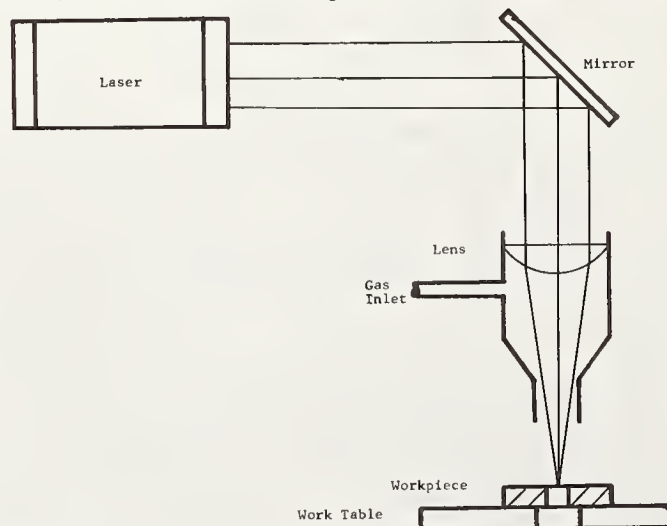


Figure 5. Laser beam machining (LBM) Apparatus

The thermal gradients produced in the material around the focus of the laser beam produce stresses which can cause cracking and fracture [23,35-38]. Laser damage is a complex phenomenon which is not well understood. The amount of damage is a function of the laser wavelength and power, the duration of the beam, and the material properties, particularly absorption of the laser light. Combining pulse and continuous laser beams produces enhanced damage in some materials [39]. In spite of the thermal stresses, laser beam machined ceramics can be as strong or stronger than diamond machined ceramics with the proper choice of machining conditions. For example, alumina substrates sawed with a Q-switched Nd-YAG laser (1.06 μ m) were 45% stronger than substrates sawed with a continuous CO₂ laser (10.6 μ m) and 13% stronger than diamond sawed substrates [40].

Damage may be avoided by machining unfired ceramics, by using very short pulses to remove only small amounts of material so the thermal stresses produce only elastic deformation, or by putting the ceramic in compression to suppress cracking. This is done with diamond dies which are mounted in a metal matrix if holes larger than 0.12 mm are to be drilled. Preheating the workpiece before laser beam machining also reduces thermal stresses by decreasing the temperature gradient and making some materials more ductile. This approach has been used to cut sheet glass successfully. A 15 kw CO₂ laser made smooth, damage free cuts through 1.6 mm thick soda lime glass at 250 mm/s and through 3.2 mm thick glass at 75 mm/s after the glass had been preheated to 593°C [41]. At this temperature, the viscosity of soda-lime sheet glass is about 10¹¹ poises so that thermal stresses may have been accommodated by local plastic flow. Efforts by the author to use this method for laser cutting of hot pressed silicon carbide and silicon nitride were not successful. Even when preheated to 1000°C, specimens, 3x6x50 mm, shattered when cut with a 500 watt continuous CO₂ laser beam. Of course, these ceramics are still very strong at this temperature.

Laser beam machining is established in the semiconductor industry where lasers are routinely used for machining thin substrates [42-44], for drilling small holes with precise dimensions [29,45,46] and for scribing grooves in substrates and silicon for controlled breakage [47-49]. For example, a 150 watt CO₂ pulsed laser can scribe a 0.63 mm thick alumina substrate at 230 mm/s, cut it through at 20 mm/s or drill a through hole in 10 ms [50]. Silicon wafers can be scribed with less than 1% yield loss [51]. The lasers which are available for semiconductor [52] and ceramic machining [53] have recently been reviewed. Laser beam machining of larger parts has not been as successful since it is difficult to avoid catastrophic fracture. This can be used as an advantage in removing large volumes of material, as in concrete breaking [54], or in laser assisted machining in which a single point tool is used to remove the laser weakened material [55]. Thermal shock resistant materials such as silica glass [44,56] and porous refractories may easily be laser machined without fracture. The refractories may also be grooved or dimpled with a laser without melting the surface by sintering and densification [44].

A number of studies have been made of laser cutting of silicate glass [41,57-63] and also of laser welding [64]. However, glass which has been laser cut without preheating is weaker than conventionally cut glass. Hot glass may be cut without weakening it, this is inconvenient except immediately after forming. Although laser cutting is fast, it is no faster than glass cutting and much more expensive than this well established process. Because of these factors, laser glass cutting has found few commercial applications. Cemented tungsten carbides have been drilled using lasers [65,66]. However, the drilling initiates cracks which propagate through the cobalt phase [67] as in electric discharge machined carbides [23,24].

Laser beam machining is finding increasing application to ceramics. The use of lasers on ceramics and other inorganic materials has been the subject of several reviews of the process and its applications [68-71] and of the manufacturing technology of computer controlled laser cutting [72,73]. A bibliography through July 1977 on laser applications to non-metals has been compiled [74].

3.6 Ion Beam Machining

Ion beam machining uses a directed stream of ions to sputter material atom-by-atom from the surface of the workpiece [75-79] with minimum damage leaving a surface which is atomically clean [80,81]. Atoms are ejected from the surface by the transfer of momentum from

the incident ions when the transferred energy exceeds the binding energy (~ 10 eV) and the momentum vector of the atom points away from the surface. Atoms whose momentum vector points into the surface are implanted as are some ions of the incident beam. Sputtering has sometimes been called enhanced sublimation but it is not a thermal process and there is very little heating. For example, paper may be machined to nanometer thickness without burning or charring. This behavior of surfaces under ion bombardment has been recently reviewed [82].

A system for ion beam machining is composed of an ion gun, a neutralizer, a workpiece positioner and vacuum chamber (fig. 6). The gun uses a confined plasma discharge to generate ions which are then extracted and accelerated to form a beam of ions which are positive if the usual inert gas is used for the plasma. The neutralizer sprays electrons onto the workpiece to eliminate space charge buildup. The worktable allows translation of the workpiece in three dimensions, variation of the angle of incidence between the beam and the workpiece, and workpiece rotation. Accelerating voltages vary between 500 and 10,000 eV and beam current density is usually from 0.5 to 2 ma/cm. The vacuum chamber pressure during machining is 10^{-4} Torr or less.

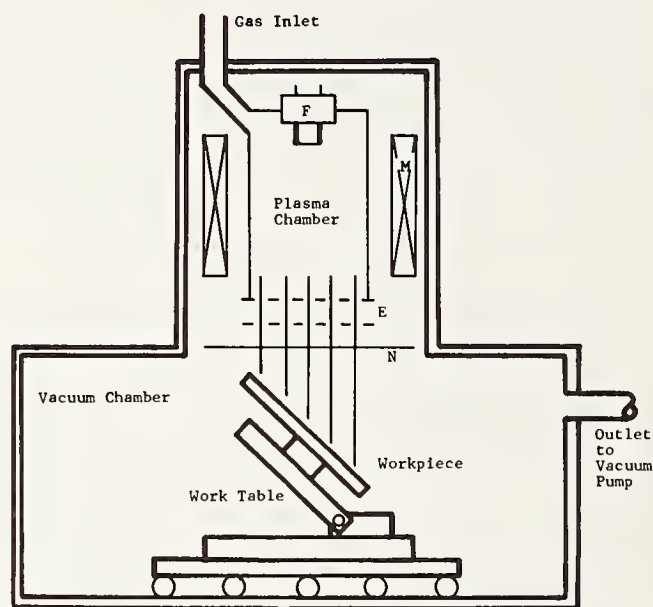


Figure 6. Ion Beam Machining (IBM) Apparatus. E, accelerating electrodes; F, filament; M, magnet; N, neutralizer.

There are two types of ion beam systems: diffuse which is shown in figure 6 and focused. The focused system is similar to the electron beam apparatus shown in figure 4 except an ion gun is used instead of an electron gun and a neutralizer is added. The deflection coils are used to sweep the ion beam across the workpiece surface. The focused ion beam is used for drilling, cutting and surface contouring by computer control.

The diffuse ion beam system uses multiple ion sources to form a uniform ion beam which may be as large as 30 cm diameter [83]. The areas to be machined are defined by openings in a mask which may either be placed on the workpiece as in chemical milling [84] or close to the ion gun and its image projected on the workpiece (fig. 7). The latter method allows multiple images to be projected [85] at up to fifty times demagnification [86] so that very small patterns may be machined.

The ion beam machining rate is determined by the sputtering yield which is defined as the number of sputtered workpiece atoms per incident ion. The sputtering yield depends on the material being machined and its temperature, the ions used and their energy and angle of incidence, the ion beam current density, and, in some cases, the residual gas in the vacuum chamber. The machining rate increases with increasing ion energy and usually saturates above a few kilo-electron volts as penetration of ions into the workpiece increases. Ion penetration is also affected by the angle of incidence since normally incident ions penetrate more

ION APERTURE LENS TECHNIQUE

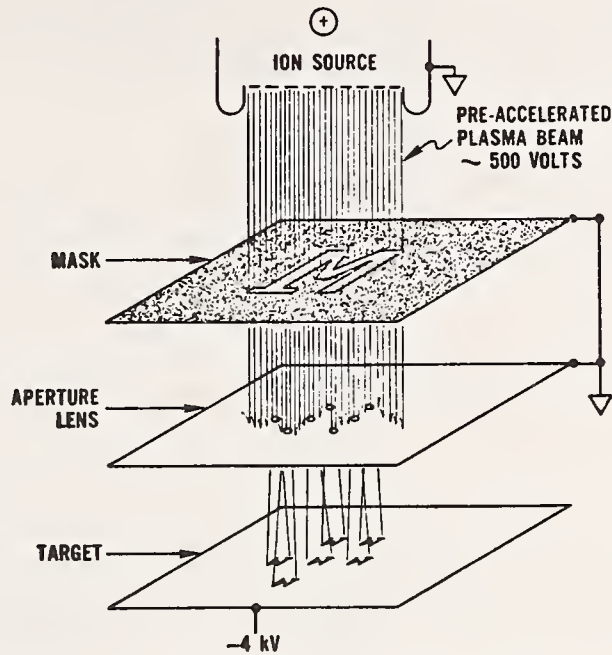


Figure 7. Ion beam projection lithography

deeply into the workpiece and produce fewer workpiece atoms with momentum vectors pointing away from the surface than grazing incidence ions. For most materials, the maximum machining rate occurs at an angle of incidence of about 15° from the workpiece surface. Since the rate is related to the binding energy of the workpiece atoms, reactive gases can change the rate. For example, oxygen absorbed on machined silicon surfaces forms silica and reduces the rate while fluorine forms volatile silicon compounds and increases the rate.

A compilation of ion beam machining rates was published in 1971 [87]. Data from more recent literature and from the author's work are in table 4. The rates are not affected by the hardness of the material, hot pressed silicon nitride and soda lime glass machine at about the same rate, but are dependent on process parameters. Ion beam machining is very slow, the slowest of all ceramic machining processes, but in spite of this it is being used in a number of applications where delicate parts are involved and/or it is necessary to produce a clean, damage free surface of precise dimensions. Ion guns are now being developed which produce intense ion beams with current densities a thousand times or more greater than present systems [89] and which can be used to produce concomitantly greater stock removal rates.

Surface textures may develop during ion beam machining [90] which are similar in appearance to wind erosion features on rock [91] and show characteristic topography such as cones, facets, ridges, pyramids, hollows or even hoodoos. These textures are particularly pronounced on polycrystalline and/or polyphase surfaces but also occur on single crystal and normally clean glass surfaces. Ultra clean single phase glass and most crystalline semiconductors, whose surfaces become amorphous during machining with inert gas ion [92], are the only materials which do not develop texture.

The development of texture is caused by three mechanisms: the sputter yield is different on different crystalline faces [93]; and it depends on the angle of incidence [94]; and some of the sputtered material may redeposit on the higher parts of the surface. Materials which are initially smooth and featureless will develop a stable texture during machining whose specific topography depends on the interaction between the mechanisms. The initial workpiece contour [96] and its angle of incidence to the ion beam also influence topography. The relief of even the most strongly textured surfaces is only a few microns and may be ignored for many applications. It may be minimized by rotating and rocking the workpiece during machining to vary the angle of incidence and by starting with an ultra clean workpiece surface. However, texture development is not always a disadvantage. Some strongly textured surfaces show high light absorptance and have been suggested for solar absorbers [97].

Table 4. Ion beam machining rates

MATERIAL	MACHINING RATE ($\mu\text{m/hr}$) ^a	ION BEAM PARAMETERS ^b			REFERENCE
		ENERGY (eV)	CURRENT (mA/cm ²)	ANGLE	
<u>Polycrystals</u>					
Al	1.8-4.2	500	1	90° ^c	[84] ^d
	4.2	1000	0.5	15°	--
	2.7-4.5	1000	1	90°	[84]
Al ₂ O ₃	0.5	500	1	90°	[84]
	0.8	1000	1	90°	[84]
C (graphite)	3	1000	0.5	15°	--
C (diamond)	120	7500	1	90°	[88]
LiNbO ₃	3.8	1000	1	90°	[84]
Si	1.3-3.0	500	1	90°	[84]
	2.2-4.5	1000	0.5	15°	[84]
SiC (HP) ^f	3.5	1000	0.5	15°	--
SiC (HP)	5.6	1000	0.5	15°	--
<u>Single Crystals</u>					
Al ₂ O ₃ {1102}	0.5	500	1	90°	[74]
Al ₂ O ₃ {1123}	2.2	1000	0.5	15°	--
Si {100}	1.3	500	1	90°	[74]
SiO ₂ {100}	2	500	1	90°	[74]
<u>Glasses</u>					
Silica	3.9	1000	0.5	15°	--
Soda-lime-silica	5.9	1000	0.5	15°	--
	1.2	500	1.0	90°	[74]

^afor milling except where noted.

^bArgon ions.

^cnormal incidence.

^dnumbers in square brackets refer to the literature references at the end of the paper. When no reference is given, the data are the result of the author's research.

^edrilling.

^fHP = hot pressed.

Ion beam machining can implant ions into the workpiece and causes radiation damage in semiconductors and zirconia [98]. Most of these effects can be avoided by using low energy ions at grazing incidence. If damage occurs, it may be eliminated after machining by annealing, often with a laser [99]. However, ion beam machining can also be used to produce desirable changes in the properties of thin semiconductor films [100].

Precision ion beam machining of contours on optical components has been developed into a process of great precision for glass polishing [101-109], figuring of aspherical surfaces [110-116], and grooving and blazing diffraction gratings [76,117,118]. By 1970, computer controlled ion beam machining could remove glass with depth tolerances of 1 nm from 750 mm diameter components and "superpolish" the surface for increased reflection efficiency [119]. Today, even larger components may be ion beam machined.

The advantage of ion beam machining for optical components is the precision with which stock can be removed to form an arbitrary surface and the freedom from the residual stress and deformed layer which are introduced by mechanical abrasion and can cause delayed distortion.

Diffraction gratings are now commercially produced by ion beam machining. A diffuse beam is used and masking is used to define the areas to be machined. X-ray gratings are produced at the National Physical Laboratory, London [116] and blazed holographic gratings and grating couplers are produced at the Institute of Physical and Chemical Research, Japan [117].

Ion beam machining is a rapidly expanding method for producing semiconductor devices, especially since the ion beam can not only be used for machining but for thin film deposition (SID, secondary ion deposition) [120-122]. This is also useful for materials such as sodium chloride which are hygroscopic since they may be machined and then coated with a moisture resistant film before being removed from the vacuum chamber to the ambient air [123]. The first ion beam machined semiconductor devices were made using a modified ion beam thinner for TEM foils with a 1 cm diameter beam [124] but ion sources of 30 cm diameter are now used [83]. The linewidths possible with ion beam machining have decreased from 10^{-4} m [125] since the initial experiments to 10^{-6} m using carbon masks [126] which is much less than is possible with chemical etching [127] to 10^{-7} m using STEM lithography [128]. There are numerous reviews of ion beam techniques for device fabrication [89,124,125] and of production methods and equipment [83,129-132].

The strength of a ceramic which has been ion beam machined is greater than one which has been conventionally abrasive machined and may be greater than the strength of the pristine as-fired ceramic. This is due to the removal of surface flaws by ion beam machining which does not introduce new flaws so that the strength of the ceramic is controlled by processing defects like pores and agglomerates. Ion beam polycrystalline ceramics have been found to be 10 to 60% stronger than diamond machined ceramics [133] and strength increases of over 100% have been reported for silica glass after ion beam machining [134]. However, the strength of the glass was limited by the texturing caused by ion beam machining since the fracture origins were always at the bottom of depressions in the surface. The author's ion beam machined a number of ceramics which had been carefully diamond machined. The strength increases varied from about 50% for a processing immature silicon carbide to over 300% for a processing mature silicon nitride. In all cases, once the damaged surface produced by diamond machining was removed, the strength was controlled by processing flaws.

Because ion beam machining does not introduce damage, it has been used to shape a number of delicate components. Diamond machined sawn-cavity heterostructure lasers rapidly degrade in use but ion beam machined lasers do not [135]. Other components which have been ion beam machined with success are: feedback lasers [136], reflective arrays [137], quartz resonators [138], acoustic transducers [139], pyroelectric vidicons [140], magnetic arrays [141-142], surface acoustic wave devices [143] and grooves, aerodynamic [142] and hydrodynamic [144], for bearings. The literature on ion beam machining and applications is extensive. An incomplete bibliography contains 215 references for the years from 1954 to 1975 [145].

4. Conclusion

Abrasionless machining methods for ceramics offer a variety of techniques which complement conventional abrasion methods. As the requirements for ceramic materials become more stringent or the uses more exacting, the application of these unconventional method will grow.

5. References

- [1] Engelback, R., The Problem of the Obelisks (Fisher Urwin Publishing Co., London, 1923).
- [2] Gielisse, P.J. and Stanislaw, J., Mechanical Methods of Ceramic Finishing, in The Science of Ceramic Machining and Surface Finishing, S.J. Schneider, Jr. and R.W. Rice, eds., pp. 5-36 (Special Publication 348, National Bureau of Standards, Washington, DC, 1972).
- [3] Schneider, S.J. and Rice, R.W., ed., The Science of Ceramic Machining and Surface Finishing (Special Publication 348, National Bureau of Standards, Washington, DC, 1972).
- [4] Springborn, R.K., ed., Nontraditional Machining Processes, (American Society of Tool and Manufacturing Engineers, Dearborn, Michigan, 1967).
- [5] Bellows, G., Nontraditional machining: Where does it stand? Mod. Mach. Shop 48 [11] 85-93 (Apr. 1976), 48 [12] 103-115 (May 1976), 49 [1] 109-116 (June 1976), 49 [12] 79-90 (July 1976).
- [6] Field, J.E. and Lesser, M.B., On the mechanics of high speed liquid jets, Proc. Roy. Soc., London, A.357, 143-162 (1977).
- [7] Maurer, W.C., Novel Drilling Techniques, Pergamon Press, Oxford (1968).
- [8] Farmer, I.W. and Attewell, P.B., Rock penetration by high velocity water jet, Intl. J. Rock. Mech. Min. Sci., 2 [2] 71-77 (1965).
- [9] British Hydromechanics Research Association, Cranfield, Bedford, England, Proceedings of International Symposia on Jet Cutting Technology, various eds., 1st (1972), 2nd (1974), 3rd (1976), 4th (1978).
- [10] Saunders, D.H., "Water as a cutting tool," Engr. (London), 217 [4] 297-301 (1977).
- [11] Angus-Butterworth, L.M., Glass in A History of Technology, C. Singer, E.J. Holmyard, A.R. Hall and T.I. Williams, eds., vol. 4, pp. 358-378 (Oxford Univ. Press, London, 1958).
- [12] Kahlson, W.S., Studies on etching glass, J. Amer. Ceram. Soc. 14 827-832 (1931).
- [13] Thompson, T.J., Glass-new developments-new products, Ceram. Bull. 31 [8] 289-293 (1952).
- [14] Bannard, J., Electrochemical machining, J. Appl. Electrochem. 7 [1] 1-29 (1977).
- [15] Saganuma, E., Fundamental studies on electrochemical machining of cemented carbide alloys, J. Jap. Soc. Precision Engrng., 44 [4] 502-507 (1978).
- [16] Parshutin, V.V., Effect of composition and proportion of carbide and binder phases on the process of anodic dissolution of metaloceram hard alloys, Elek. Obrab Mater. 5 [1] 27-34 (1977).
- [17] Wilson, J.F., Practice and Theory of Electrochemical Machining (John Wiley and Sons, New York, 1971).
- [18] Doremus, R.H., Glass Science (Wiley Interscience, New York, 1973).

- [19] Bucklow, I.A. and Cole, M., Spark-machining, *Met. Rev.* 14 [135] 103-118 (1969).
- [20] Childs, T.H.C. and Rowe, G.W., Physics in metal cutting, *Rept. Prog. Physics* 36 [3] 223-228 (1973).
- [21] Anon., Non-traditional machining methods - EDM vs. ECM, *Cutting Tool Engrng.* 25 [5-6] 8-11 (1973).
- [22] Anon., Electro-machining in the workshop (Int. Symp. for Electromach., 4th, Bratislava, Czech., Sept. 18-19, 1974).
- [23] Schachrai, A. and Lenz, E., LBM (Laser Beam Machining) and EDM (Electric Discharge Machining) - a comparison on the cracks' behavior, *CIRP Ann. (Switzerland)* 25 [1] 121-123 (1976).
- [24] Lenz, E., Katz, E. Konig, W. and Wertheim, R., Cracking behavior of sintered carbides during EDM (Electric Discharge Machining), *CIRP Ann. (Switzerland)* 24 [1] 109-114 (1975).
- [25] Sturans, M.A. and Koste, W.W., Kinetic focusing requirements for precision e-beam machining of unfired ceramic material, *J. Vac. Sci. Technol.* 15 [3] 1060-1063 (1978).
- [26] Drew, J., Electron beams tackle tough machining jobs, *Mach. Design* 48 [4] 94-98 (1976).
- [27] Koste, W.W. and Bojam, W., Profiling of high powder density electron beams for precision thermal machining (Fifth Int. Conf. on Electron Beam and Ion Beam Sci. and Tech., Bakish, R., ed., Electrochemical Society, Princeton, N.J. 1972).
- [28] Desilets, B.H., Mechanism of cavity formation in unfired ceramic by electron-beam machining, *J. Vac. Sci. Technol.* 15 [3] 1056-1059 (1978).
- [29] Wagner, R.E., Laser drilling mechanics, *J. Appl. Phys.* 45 [10] 4531-4637 (1974).
- [30] Harris, K.D., Laser unit drills diamond in a matter of minutes, *S A Mining Eng.*, 81 [4045] 562-564 (1970).
- [31] Murphy, R. and Ritter, G.J., Interaction of laser and electron beams with diamond surfaces, *Nat'l Phy. Res. Lab.* 30 [354] 174-180 (1970).
- [32] Willis, J.B. and Davis, M.B., Drilling of diamond dies for the production of fine wire using a laser powered drilling machine, *Wire Ind.* 41 [492] 993-998 (1974).
- [33] Gresser, H.D., Laser sawing of diamonds, *SME Tech Pap* MR76-855 (1976).
- [34] Lunau, F.W., Gas-jet cutting of non-metallics with high power CO₂ lasers, *BOC-Murex Welding Res & Dev. Lab.*, [51] 1-6 (1970).
- [35] Deotto, D.R. and Wang, K.K., Theoretical study of laser-induced thermal fatigue of carbide tool materials, (*N. Am. Metalwork Res. Conf.*, 2nd Proc., 88-104, 1974).
- [36] Paek, U.C and Gagliano, F.P., Thermal analysis of laser drilling processes, *IEEE J Quantum Electron* QE-8 [2] 112-119 (1972).
- [37] Schachrai, A. and Lenz, E., LBM (Laser beam machining) and EDM (Electro discharge machining)-A comparison on the cracks behaviour, *Technion-Israel Inst. of Technol. Israel*, 25 [1] 121-123 (1976).
- [38] Bristow, T.J., Packer, M.E. and Gane, N, Surface layer fracture of brittle material by giant laser pulses. *Nature* 222 [5188] 27-29 (1969).
- [39] Spann, J.R., Mecholsky, J.J., Jr., Freiman, S.W., Fox, J.A. and Sluss, E.C., Enhanced failure of ceramics irradiated by combined pulse and c.w. lasers, *J. Mater. Sci.* 14 175-178 (1979).

- [40] Schroeder, D.H. and English, F.L., Comparison of the strength of alumina substrates for different separation techniques, *IEEE Trans. Parts.* PHP-8 [3] 4-6 (1972).
- [41] Chui, G.K., Laser cutting of hot glass, *Am. Ceram. Bull.*, 54 [54] 514-518 (1975).
- [42] Belland, R., Laser scribing and drilling of ceramic substrates, *Electron Pack. Prod.* 15 [1] 56-58 (1975).
- [43] Longfellow, J., Sawing alumina substrates with a CO₂ laser, *Ceram. Bull.* 52 [6] 513-515 (1973).
- [44] Cockayne, B. and Gasson, D.G., The machining of oxides using gas lasers, *J. Mater. Sci.* 6 126-129 (1971).
- [45] Longfellow, J., High speed drilling in alumina substrates with a CO₂ laser, *Ceram. Bull.* 50 [3] 251-253 (1971).
- [46] Hamilton, D.C. and James, D.J., Hole drilling with a repetitively-pulsed TEA CO₂ laser., *J. Phys. D. (Appl Phys)* 9 [4] L41-L43 (1976).
- [47] Lumley, R.M., Controlled separation of brittle materials using a laser, *Ceram. Bull.* 48 [9] 850-854 (1969).
- [48] Kirby, P. Laser scribing of ceramic substrates, *Prod. Eng.* 56 [7-8] 31-32 (1977).
- [49] Balland, R., Scribing ceramic substrates (with lasers), *Electron. Prod. Methods & Equip.* 4 [4] 6 (1975).
- [50] Pasturel, M. and Saunders, R., CO₂ industrial laser machining, *Electro-Opt. Syst. Design.* 23-25 (1976).
- [51] Kobayaski, A., Nagano, Y. and Sumiya, M., Scribing of silicon wafers with a YAG laser. *Jpn. Soc. of Precis. Eng.* 22-25 (1974).
- [52] Hardway, G.A., Applications to microelectronic and silicon wafer dicing, *SME Tech. Paper MR70-522* (1970).
- [53] Spalding, I.J., High power lasers for processing of materials - A comparison of available systems, *Opt. Laser Technol.* 10 [1] 29-32 (1978).
- [54] Jones, J.W. and Scott, B.F., Breaking Concrete by laser, *Build. Res. Pract.* 1 [6] 335-339 (1973).
- 55 Copley, S.M., Bass, M. and Garmire, F., Laser assisted hot spot machining, *Status Rept. 3*, (Univ. of Southern Calif., Los Angeles, 1978).
- [56] Duley, W.W. and Gonsalves, J.N., Interaction of CO₂ laser radiation with solids-drilling of fused quartz, *Can J. Phys.* 50 [3] 216-221(1972).
- [57] Rice, R.W., Arc, laser and electron beam machining of ceramics, in The Science of Ceramic Machining and Surface Finishing, S.J. Schneider, Jr. and R.W. Rice, eds., pp. 193-196 (Special Publication 348, National Bureau of Standards, Washington, D.C., 1972).
- [58] Saunders, R.J. and Pasturel, M., CO₂ laser beam machining of plastics and glass, *SME Tech. Pap.* MR74-958, (1974).
- [59] Schieffer, F., Technological investigations concerning the cutting of glass by means of the carbon-dioxide laser, *Feingeratetechnik.* 27 [2] 61-63 (1978).
- [60] Gruenwald, F., New results in fine processing techniques, *Wiss Z. Tech Hochsch Ilmeau* 23 [2] 69-87 (1977).

- [61] Machulka, G.A., Gur'yanov, V.M., Miratova, L.P., Steklo and Keram, Cutting glass by lasers (including thermal conduction equations), Glass and Ceram., 29 [10] 642-644 (1972).
- [62] Brandt, G., Spengel, B., Van Hulle, J., Cutting with a CO₂ laser, Schweissen Schneider, 23 [2] 56-59 (1971).
- [63] Lambert, J.L., Raes, A., Coopmans, P. and Streydio, J.M., Cutting sheet glass using a CO₂ laser, Silicates Ind., 38 [7-8] 145-147 (1978).
- [64] Rueffler, C. and Guers, K., Cutting and welding using a CO₂ laser, Opt. Laser Technol. 4 [6] 265-269 (1972).
- [65] Zhanov, I.A., Laser equipment for machining small diameter holes, Mach. and Tool, 45 [9] 49-50 (1974).
- [66] Schachrai, A. and Lenz, E., Cemented carbides drilling with a CO₂ laser, GAMI, (Saint-Quen, Fr.)
- [67] Darwish, A.H. and Andersen, S.P., Effect of thermal shocks by laser on carbide tips, Soc. Fr de Metall., Paris (1975).
- [68] Hanson, W. and Lawryk, P., Laser machining is now, Modern Mach. Shop, 92-98 (1978).
- [69] Ulmer, W., Machining of ceramic surfaces by means of laser beam, Sprechsaal Keram. Glas. Email. Silikate, 106 [24] 971-978 (1973).
- [70] Saunders, R.J., New developments in pulsed CO₂ laser applications, SPIE Ind. Appl. of High Power Laser Technol. 86 32-39 (1976).
- [71] Uglov, A.A., Lasers in metallurgy and technology of inorganic materials, Sov. J. Quantum Electron, 4 [5] 564-574 (1974).
- [72] Lawryk, P.Z., Lasercutting system technology, AAMA Apparel Res. J. 171-172 (1977).
- [73] Desforges, C.D., Laser applications, Engr. (London) 217 [10] I-VIII (1977).
- [74] Habercom, G.E. Jr., Laser cutting and machining: Nonmentals: Citations from the engineering index data base, Natl. Tech. Inf. Serv., (1977).
- [75] Gloersen, Per. G., Ion-beam etching, J. Vac. Sci. Technol. 12 [1] 28-35 (1975).
- [76] Somekh, S., Introduction to ion and plasma etching, J. Vac. Sci. Technol. 13 [5] 10003-1007 (1976).
- [77] Kelly, R., Theory of thermal sputtering, Rad. Effects 32 91-100 (1977).
- [78] Winters, H.F., Physical sputtering: A discussion of experiment and theory, Adv. in Chem. [158] (1976).
- [79] Tsong, I.S.T. and Barber, D.J., Review: sputtering mechanisms for amorphous and polycrystalline solids, J. Mater. Sci. 8 123-135 (1973).
- [80] Adams, P.B., Bibliography on clean glass, J. Testing and Eval. 5 [1] 53-60 (1977).
- [81] Roberts, E.W., Generation of clean surfaces in high vacuum, Brit. J. Appl. Phys. 14 537-543 (1963).
- [82] McCracken, G.M., The behaviour of surfaces under ion bombardment, Rep, Prog. Physics 33 241-327 (1975).

- [83] Robinson, R.S., Thirty-centimeter-diameter ion milling source, *J. Vac. Sci. Technol.* 15 [2] 277-280 (1978).
- [84] Melliar-Smith, C.M., Ion etching for pattern delineation, *J. Vac. Sci. Technol.* 13 [5] 1008-1022 (1976).
- [85] Free, B.A. and Meadows, G.A., Projection ion lithography with aperture lenses, *J. Vac.* 15 [3] 1028-1031 (1978).
- [86] Castaigne, J., Ion Beam Machining, (Proc. 2nd Intn'l Conf. Electron and Ion Beam Sci. and Tech., New York, New York, July 1966).
- [87] Fritz, L.L., Sputter etch removal rates of insulators, semi-conductors, and conductors, *Solid State Technol.* 14 [12] 43-48 (1971).
- [88] Spencer, E.G. and Schmidt, P.H., Ion machining of diamond, *J. Appl. Phys.* 43 [7] 43-48 (1971).
- [89] Green, T.S., Intense ion beams, *Rept. Prog. Physics* 37 1257-1344 (1974).
- [90] Tsong, I.S.T. and Barber, D.J., Development of the surface topography on silica glass due to ion-bombardment, *J. Mater. Sci.* 7 687-693 (1972).
- [91] Whitney, M.T. and Dietrich, R.V., Ventifact sculpture by windblown duct, *Geo. Soc. of Amer. Bull.* 84 2561-2582 (1973).
- [92] Witcomb, M.J. Sputter etch profiles of spheres, cylinders and slab-like silica targets, *J. Mater. Sci.* 11 859-864 (1976).
- [93] Wilson, I.H., "Semiconductors", in Ion Surface Interaction, Sputtering and Related Phenomena, R. Behrisch, W. Heiland, W. Poschenrieder, P. Staib and H. Verbeek, eds. p. 217, (Gordon and Beach, London, 1973).
- [94] Hosaka, S. and Hashimoto, S., Influence of sample inclination and rotation during ion-beam etching on ion-etched structures, *J. Vac. Sci. & Technol.* 15 [5] 1712-1717 (1978).
- [95] Liffmark, U and Hofer, W.O., "The influence of surface structure on sputtering: angular distribution and yield from faceted surfaces", *J. Mater. Sci.* 13 2577-2586 (1978).
- [96] Dugdale, R.A. and Ford, S.D., The etching of alumina and fused silica by sputtering, *Trans. Brit. Ceram. Soc.* 65 165 (1966).
- [97] Bansal, G.K. and Heuer, A.H., Radiation damage in ZrO₂ produced by argon ion bombardment, *Jernkont. Ann.* 155 451-453 (1971).
- [99] Anon. Laser annealing of semiconductors, *Laser Focus*, 12-14 (1979).
- [100] Stroud, P.T., Ion bombardment and implantation and their application to thin films, *Thin Solid Films* 11 1-26 (1972).
- [101] Bayly, A.R. and Townsend, P.D., Ion beam processing of glass surfaces, *Opt. Laser Technol.* 2 [3] 117-121 (1970).
- [102] Townsend, P.D., Ion beams in optics, An introduction, *Opt. Technol.* 2 [2] 65-67 (1970).
- [103] Pearson, A.D. and Harsell, W.B., Ion beam polishing glass, *Mater. Res. Bull.* 7 567-572 (1972).
- [104] Franks, A., Materials problems in the production of high quality optical surfaces, *Mater. Sci. Eng.* 19 [2] 169-183 (1975).

- [105] Bayly, A.R. and Townsend, P.D., Ion beam processing of glass surfaces, *Optics and Laser Tech.* 117-121 (1970).
- [106] Bayly, A.R. and Townsend, P.D., Glass machining by ion sputtering, *J. Phys. D. (Appl. Phys)* 5 [11] L103-L104 (1972).
- [107] Perveyev, A.F., Il'in, V.V., and Mikhaylov, A.V., Ion polishing of glass, *Sov. J. Opt. Tech.* 39 [10] 622-624 (1972).
- [108] Tarasevich, M., Ion beam erosion of rough glass surfaces, *Appl. Opt.* 9 [1] 173-176 (1970).
- [109] Taniguchi, N., Kanekama, N., Kondo, M. Matsumoto, T. and Wantanabe, K., Characteristics of sputter-machined surface of BK-7 optical glass, *J. Jap. Soc. Precis. Eng.* 39 [7] 753-759 (1973).
- [110] Meinel, A.B., Bashkin, S. and Loomis, D.A., Controlled figuring of optical surfaces by energetic ionic beams, *Appl. Opt.* 4 [12] P. 1674 (1965).
- [111] Narodny, L.H. and Tarasevich, M., Paraboloid figured by ion bombardment, *Appl. Opt.* 6 [11] p. 2010 (1967).
- [112] Schroeder, J.B., Dieselman, H.D., and Douglass, J.W., Technical feasibility of figuring optical surfaces by ion polishing, *Appl. Opt.* 10 [2] 295-299 (1971).
- [113] Taniguchi, N. and Kanekama, N., Ion-beam sputter machining of glass, *CIRP Ann.* 22 [1] 69-70 (1973).
- [114] Karger, A.M., Figuring miniature aspherics - ion polishing, *Appl. Opt.* 12 [3] 451-454 (1973).
- [115] Taniguchi, N. Kanekama, N. and Miyazaki, T., Ion beam sputter-machining of glass in aspheric lens making, *CIRP Ann.* 23 [1] 47-48 (1978).
- [116] Yasuda, H., Application of ion-milling techniques to microparabolic surface formation, *J. Appl. Phys.* 45 [1] 484-486 (1974).
- [117] Franks, A., Lindsey, K., Bennett, J.M., Speer, R.J., Turner, D. and Hunt, D.J., The theory, manufacture, structure and performance of N.P.L. C-ray gratings, *A Math. & Phys. Sci.* 277 [1271] 503-543 (1975).
- [118] Aoyagi, Y. and Namba, S., Blazed ion-etched holographic gratings, *Optica Acta* 23 [9] 701-707 (1976).
- [119] Tarasevich, M., Machining with ions, *Laser Focus* 24-26 (1970).
- [120] Dugdale, R.A., Material processing with glow discharge beams, *Nature*, 220 [4173] 1179-1182 (1968).
- [121] Wehner, G.K. and Anderson, G.S., in *Handbook of Thin Film Technology*, L.I. Maissel and R. Glang, eds. Chap. 3 (McGraw-Hill, New York, 1970).
- [122] Holland, L., Some characteristics and uses of low pressure plasmas in materials science, *J. Vac. Sci. Technol.* 14 [1] 5-15 (1977).
- [123] Hoffman, R.A. Lange, W.F. and Choyke, W.J., Ion planning and coating of sodium chloride, (Proc, of 7th Symp. on Laser Induced Damage in Optical Materials, 1975).
- [124] Spencer, E.G. and Schmidt, P.H., Ion-beam techniques for device fabrication, *J. of Vac. Sci. and Technol.* 8 [5] S52-S70 (1971).

- [125] Garvin, H.L., High resolution fabrication by ion beam sputtering, *Solid State Tech.* 31-36 (1973).
- [126] Cantagrel, M., Possibilities and limitations of high definition ion beam etching, *J. Vac. Sci. & Technol.* (1975).
- [127] Engemann, J., Improvements in dc-ion milling of semiconductor devices with small dimensions, *Rev. Sci. Instrum.* 47 [7] 881-883 (1976).
- [128] Smith, H.I. Flanders, D.C. and Shaver, D.C., New applications of submicrometer structures in materials science and biology, *Scan. Elect. Micro.* 1 33-40 (1978).
- [129] Laznovsky, W., Advanced in low-energy ion beam technology, *R&D* 26 [8]47-55 (1975).
- [130] Kaufman, H.R., Ion sources for ion machining applications, *AIAA J* 15 [6] 843-847 (1977).
- [131] Bollinger, L.D., Ion milling for semiconductor production processes, *Solid State Technol.* 20 [11] 66-70 (1977).
- [132] Bollinger, L.D. and Robertson, D.D., Ions for production etching, *Ind. R&D* 147-157 (1978).
- [133] Rice, E.W., The effects of sputtering on surface topography and strength of ceramics, in *The Science of Ceramic Machining and Surface Finishing*, pp. 171-188 (Special Publication 348, National Bureau of Standards, Washington, D.C., 1972).
- [134] Mecholsky, J.J., Rice, R.W., Anderson, G.W., and Sigel, G.H., Effect of sputting on the strength of silicate glasses, *J. Appl. Phys.* 47 [7] 2972-2974 (1976).
- [135] Henshall, G.D. and Hinton, R.E.P., Degradation studies of sawn-cavity (GaAl) As/GaAs_s-heterostructure lasers under pulsed operation, *IEEE J Solid State Elect. Dev.* 2 [1] 31-37 (1978).
- [136] Schinke, D.P., Smith, R.G., Spencer, E.G., and Galvin, M.F., Thin-film distributed-feedback laser fabricated by ion milling, *Appl. Phys. Lett.* 21 [10] (1972).
- [137] Smith, H.I., Williamson, R.C. and Brogan, W.T., Ion beam etching of reflective array filters *IEEE Ultrasonics Symposium*, J. Deklenk, ed., 198-201 (1972).
- [138] Vig, J., Wasshausen, H., Cook, C., Katz, M. and Hafner, E., Surface preparation and characterization techniques for quartz resonators (Symp. on Freq. Control, 27th Ann. Proc. Pap. Cherry Hill, N.J. 98-112 June 12-14, 1973).
- [139] Beecham, D., Sputter machining of ferroelectric potassium sodium niobate, *Ceram. Bull.* 52 [5] 454-455 (1973).
- [140] Yamaka, E., Teranishi, A., Nakamura, K. and Nagashima, T. Pyroelectric vidicon with grooved retting of PbTiO₃ ceramics *Jpn. Ferroelectrics* 11 [1-2] (IEEE Symp. on Appl. of Ferroelectric Pt. 2, Alburque, NM, 304-308, 1975).
- [141] Schmidt, P.H. Spencer, E.G. and Wlaters, E.M., Ion milling of magnetic oxide platelets for the removal of surface and nearsurface imperfections and defects, *J. Appl. Phys.* 41 [11] 4740-4742 (1970).
- [142] Spencer, E.G., Schmidt, P.H. and Fischer, R.F., Microstructure arrays produced by ion milling, *Appl. Phys. Ltrs.* 17 [8] 328-332 (1970).
- [143] Murray, R.J., Application of ion-etching of grooves into quartz for surface acoustic-wave devices, *J. Mater. Sci.* 13 [10] p. 2105 (1978).

- [144] Pinegin, S.V., Production technology of manufacturing aerodynamic grooves by ionic etching on steel and ceramic bearing plates, Russ. Eng. J. 56 [2] 52-54 (1972).
- [145] Bulter, A., Generation of hydrodynamic bearing grooving by ion machining, J. Lub. Tech. 334-336 (1975).
- [146] Hawkins, D.T., Ion milling (ion-beam etching), 1954-1975: A bibliography, J. Vac. Sci. Technol. 12 [6] 1389-1398 (1975).

Discussion

RUSSELL

With reference to hydrodynamic machining:

1. Is the unit used portable?
2. What water flow rates and pressures would you use to cut dense alumina brick with 10% porosity?
3. Any special safety precautions.
4. Can this replace the water-cooled diamond blade cut-off saw?
5. Can you give me some idea of the cost of a unit for cutting refractory brick?

FIRESTONE

1. We have two water jet machining units; a stationary laboratory unit and a portable, gasoline powered, field unit. The laboratory unit was used for these experiments.
2. For cutting dense alumina bricks, a 0.5 mm (0.020 in) nozzle and a pressure of 700 MPa (100,000 psig) should be used. This requires a flow rate of 70 cm³/s (4 GPM) and a power of 150 kw (200 HP). The cost of such a unit is about \$100,000.
3. A water jet is as dangerous as a buzz saw and similar safety precautions are necessary.
4. Water jets can replace diamond saws for cutting refractories although I know of no commercial operation. However, it is used commercially for cutting concrete, rock and composites.
5. See answer #2 above.

LANDINGHAM

You indicate that cutting or drilling of high density ceramics was not possible with hydrodynamic machining. I assume you meant on an economical basis. Richard Wesley at the Lawrence Livermore Laboratory has conducted many tests with water jets and drilled holes in large blocks of dense ceramics and dense plates of B₄C, Al₂O₃, sapphire, glass, etc.

FIRESTONE

You're right. It's not economical to consider water jet cutting of fully dense ceramics since the cutting rate is from ten to a hundred or more times slower than for ceramics with open porosity. The rate can not be increased by increasing the pressure because above a certain pressure the ceramic shatters along the cut. My interest in water jet cutting is as a replacement for diamond sawing.

SHAPING SILICON COMPOUND CERAMICS WITH A CONTINUOUS WAVE CARBON DIOXIDE LASER

Stephen M. Copley¹, Michael Bass², and Russell G. Wallace²

¹Department of Materials Science
²Center for Laser Studies
University of Southern California
Los Angeles, CA 90007

Results are presented on the use of a high power continuous wave carbon dioxide laser to shape workpieces of Si_3N_4 , SiAlON and SiC . Several shaping operations have been investigated in the turning configuration including grooving, threading and the production of convex and concave surfaces. A straightforward analysis is presented, which predicts the feed and beam power corresponding to a specific surface roughness grade and effective material removal rate.

Key words: Laser; shaping; silicon compound ceramics.

1. Introduction

The application of the continuous wave carbon dioxide laser to processes such as straight-line cutting and hole drilling is well established [1]. In our work we have employed the CW- CO_2 laser to shape metallic materials [2] and recently ceramics in the turning configuration. In this paper, we present results on the use of a 450 W continuous wave carbon dioxide laser to shape Si_3N_4 , SiAlON and SiC workpieces. A straightforward analysis is presented, which predicts the feed and power corresponding to a specific surface roughness grade and effective material removal rate.

2. Experimental Procedures

The apparatus for laser machining of ceramic materials is shown schematically in figure 1. The laser beam is directed along a path that is parallel to the turning axis of the lathe. It

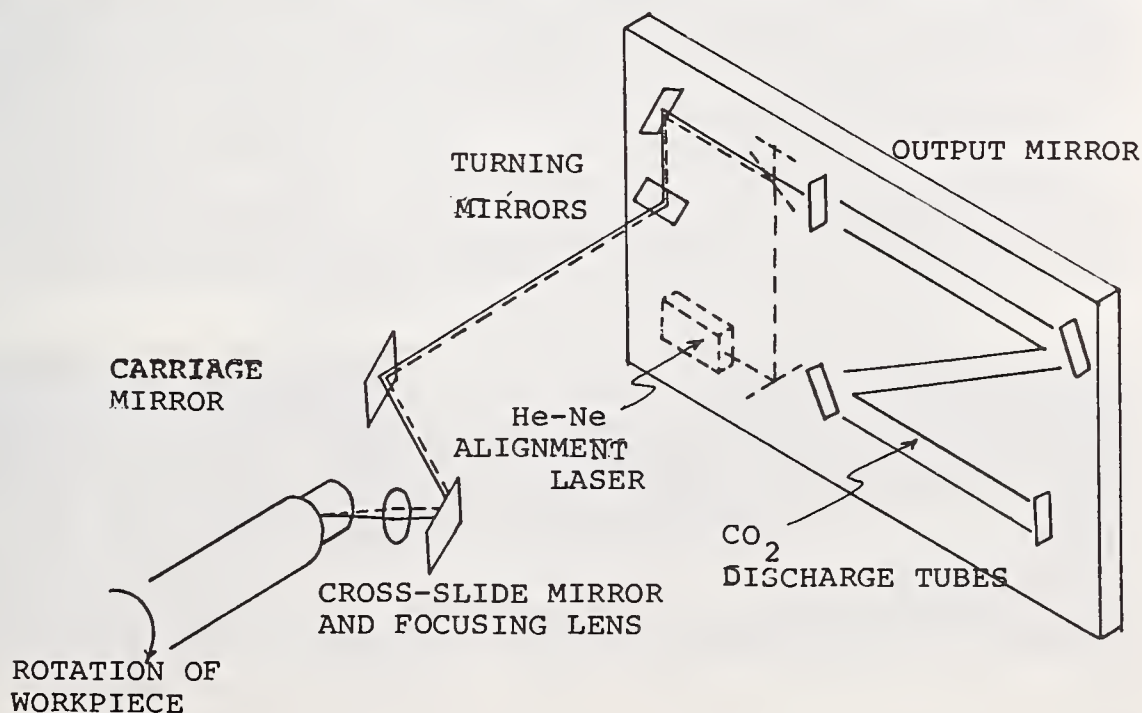


Figure 1 Apparatus for laser machining ceramic materials

is reflected from a mirror mounted on the carriage along a direction perpendicular to the turning axis to a mirror mounted on the cross-slide. After reflection by the cross-slide mirror it is focussed by a ZnSe lens on the workpiece along a radial direction for turning or along the turning axis for facing. Because the direction of motion of the carriage is parallel to the turning axis and the direction of motion of the cross-slide is perpendicular to the turning axis, the angular relationships among the reflected beams remains constant during normal machining operations. A small He-Ne laser is employed for alignment purposes.

In our work, we have employed a 450 W, CW, CO₂ laser ($\lambda = 10.6 \mu\text{m}$) operating in the TEM₀₀ mode (Gaussian spatial distribution of intensity). For the experiments reported in this paper, the beam diameter was 160 μm (1/e² diameter) giving an incident power density of 22.3 GW m⁻².

A description of the materials we have shaped in our experiments is given in Table 1.

Table 1. A description of materials investigated.

Material	Description
SiC	NC 435 (Norton Co.) A sintered SiC containing 20 vol pct free Si.
Si ₃ N ₄	NC 132 (Norton Co.) A hot-pressed Si ₃ N ₄ .
SiAlON	A hot-pressed SiAlON.

3. Results

Figure 2 shows the cross section of the grooves of a laser machined spiral in SiC. The grooves were cut in the facing configuration; the high numbered grooves were closest to the turning axis and thus correspond to the lowest cutting velocities. It is evident that the groove depth increases with decreasing cutting velocity while the groove width decreases slightly, being approximately equal to the beam diameter. In figure 3, the groove depth is plotted as a function of dwell time (θ). The dwell time is given by the equation, $\theta = b/v$, where b is the beam diameter and v is the cutting velocity.

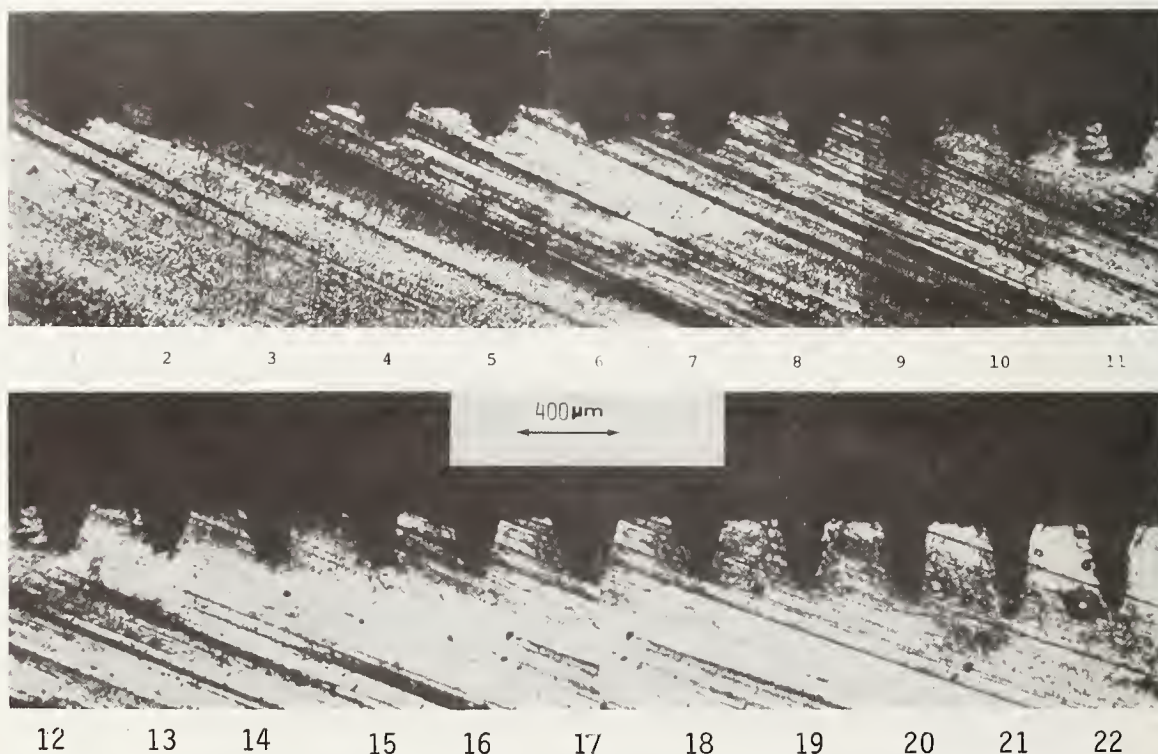


Figure 2: Photomicrographs of laser machined spiral grooves in SiC

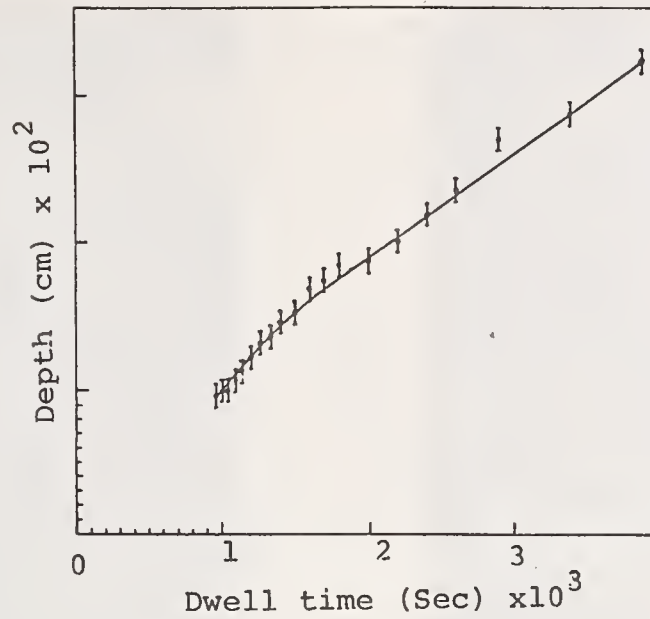


Figure 3: Depth of laser machined grooves in SiC versus dwell time

A major concern in evaluating the potential of shaping with a laser is the quality of the resulting surface. Figure 4 shows the topography of laser machined grooves in SiC. Although no cracks were observed in the grooves of this material or the others examined, deposits suggestive of a condensate or oxide were observed. The mechanical properties of specimens with laser machined surfaces has not yet been investigated.

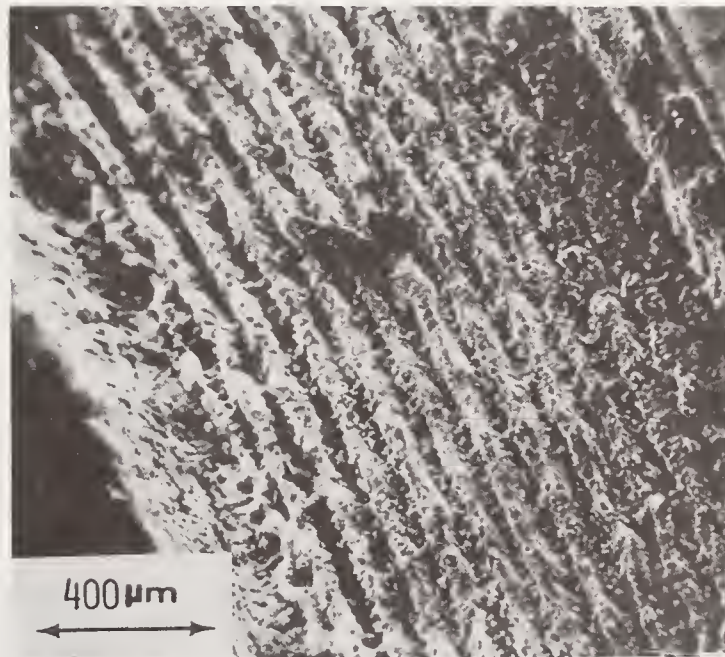


Figure 4: Scanning electron micrograph of laser machined surface in SiC

Figure 5 shows the cross-sections of grooves 2 and 18 at a higher magnification than in figure 2. It appears that their shape is approximately Gaussian. The mechanism of material removal is believed to be evaporation.

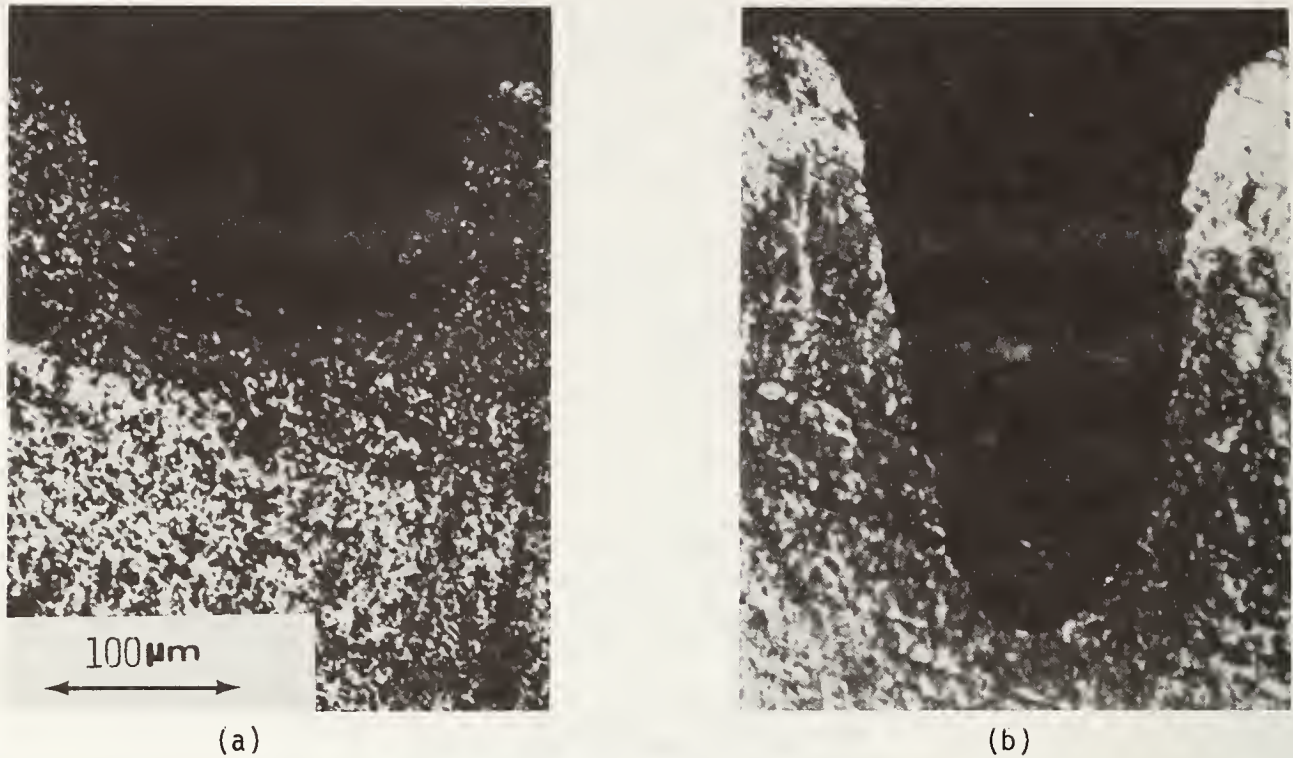


Figure 5: Cross section of laser machined grooves in SiC (a) groove number 2, (b) groove number (18).

4. Analysis of Laser Machining

The shape of the laser machined grooves can be described employing the normal curve

$$D(y) = D_0 \exp\left(-\frac{y^2}{a^2}\right) \quad (1)$$

Tracings of grooves 2 and 18 along with normal curves corresponding to the parameters given in table 2 are shown in figure 6.

The total area under the normal curve is

$$A = D_0 a \sqrt{\pi} \quad (2)$$

The material removal rate is

$$Z = Av \quad (3)$$

and the specific cutting energy neglecting power expanded by the lathe is

$$\rho = \frac{P}{Z} \quad (4)$$

where P is the incident beam power. Values for A , Z and ρ for grooves 2 and 18 are also given in table 1. It is interesting that the cross section of groove 2 is less than that of groove 18 but the material removal rate of groove 2 is the greatest. Since the incident

Table 2. Parameters describing laser machined grooves.

Groove	D_0 (μm)	a (μm)	$A(10^{-8}\text{m}^2)$	$z(10^{-9}\text{m}^3\text{s}^{-1})$	$\rho(\text{GJm}^{-3})$
2	125	100	2.22	3.42	131
18	300	75	3.99	2.19	204

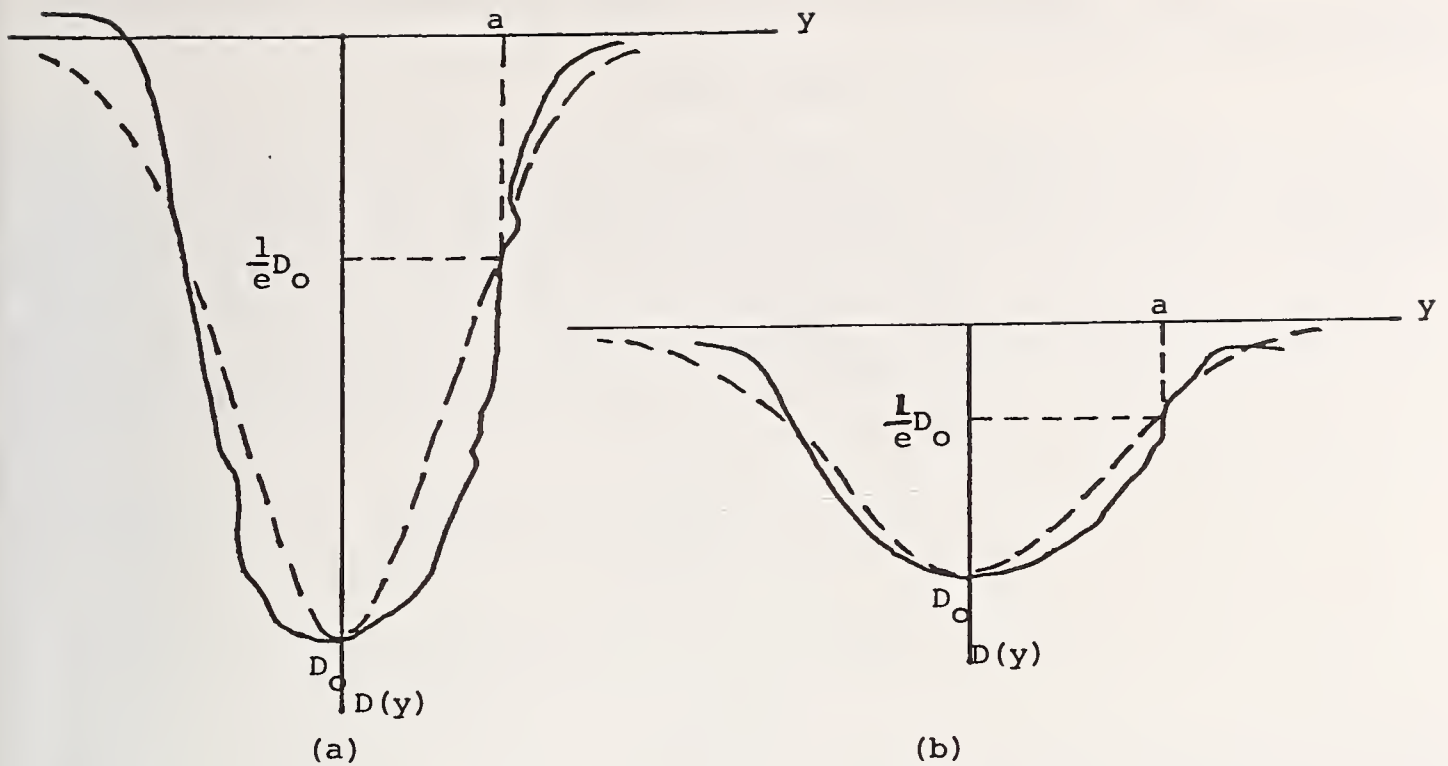


Figure 6; Tracings of laser machined grooves and normal curves based on parameters given in Table 2: (a) groove 18 (b) groove 2.

beam power was the same for both grooves, the specific cutting energy the groove 2 must be the least. Thus, the faster the beam scans the surface, the more efficient becomes the laser machining process. Although the origin of this effect has not been determined, it may be due to lower conductive losses or possibly better coupling of the laser beam to the work-piece at high velocity.

Actual turning or facing involves the partial overlapping of laser machined grooves as shown in figure 7. In the following analysis, we shall assume that the shape of the groove cut by the laser in turning is the same as in figure 2 even though in turning it is cut into the edge of a step. The surface roughness (R), which is equal to the sum of the absolute values of all the areas above and below the mean line divided by the sampling length [3], is given by the equation

$$R = \frac{4abc}{f} \quad (5)$$

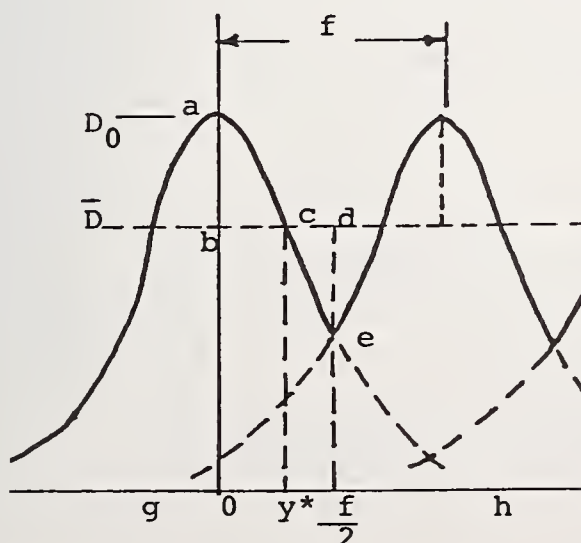


Figure 7: Diagram for calculating surface roughness and effective material removal rate for overlapping laser machined grooves

The effective material removal rate, which is the material removal rate corrected for the overlapping of grooves is given by

$$z' = vD_0 a \sqrt{\pi} - v(\overline{geh}) \quad (6)$$

The areas \overline{abc} , \overline{cde} and \overline{geh} needed to evaluate the surface roughness and the effective material rate can be evaluated with the help of tables giving the ordinates of the normal curve and the areas under the normal curve [4]. Accordingly, the depth of the laser machined groove is given by

$$D(y) = D_0 \sqrt{2\pi} f(z) \quad (7a)$$

$$z = \frac{y\sqrt{2}}{a} \quad (7b)$$

and the area of the laser machine groove is given by

$$\int_0^y D(y) dy = D_0 a \sqrt{\pi} F(z) \quad (8a)$$

$$z = \frac{y\sqrt{2}}{a} \quad (8b)$$

where

$$f(z) = \frac{1}{\sqrt{2\pi}} \exp\left(-\frac{z^2}{2}\right) \quad (9)$$

$$F(z) = \int_0^z f(z) dz \quad (10)$$

The surface roughness can be determined from eq. (5) and is given by

$$R = \frac{4}{f} \left[D_0 a \sqrt{\pi} F\left(\frac{y^* \sqrt{2}}{a}\right) - \bar{D} y^* \right] \quad (11)$$

where y^* is the abscissa value when $D(y)$ equals the mean diameter see figure 7. The mean diameter can be found by equating \overline{abc} (the quantity in brackets in eq. (11)) to \overline{cde} , and solving for \bar{D} , where

$$\overline{cde} = \bar{D} \left(\frac{f}{2} - y^* \right) - \left[D_0 a \sqrt{\pi} F\left(\frac{f \sqrt{2}}{2a}\right) - D_0 a \sqrt{\pi} F\left(\frac{y^* \sqrt{2}}{a}\right) \right] \quad (12)$$

Following this procedure, we obtain

$$\bar{D} = \frac{2D_0 a \sqrt{\pi}}{f} F\left(\frac{f \sqrt{2}}{2a}\right) \quad (13)$$

The parameter y^* can be calculated with the equation

$$y^* = \frac{a}{\sqrt{2}} f^{-1} \left(\frac{\bar{D}}{D_0 \sqrt{2\pi}} \right) \quad (14)$$

The effective material removal rate is obtained from eq. (6) and is given by

$$z' = 2vD_0 a \sqrt{\pi} F\left(\frac{f\sqrt{z}}{2a}\right) \quad (15)$$

Equations (11) and (15) are employed in figure 8 to make a plot of surface roughness and effective material removal rate for a groove cut with incident power density of 22.3 Gw m^{-3} , beam diameter ($1/e^2$) of $160 \mu\text{m}$ and dwell time of $1.05 \times 10^{-3} \text{ s}^{-1}$ (see groove 2, table 2, figure 5). The feeds corresponding to ISO roughness grades N8, N9 and N10 are indicated on the abscissa of figure 8. A feed of 0.05 mm rev^{-1} is normally available on engine lathes. As a rough guide for comparison purposes [3], turning operations in metals normally give surface roughness greater than $1 \mu\text{m}$.

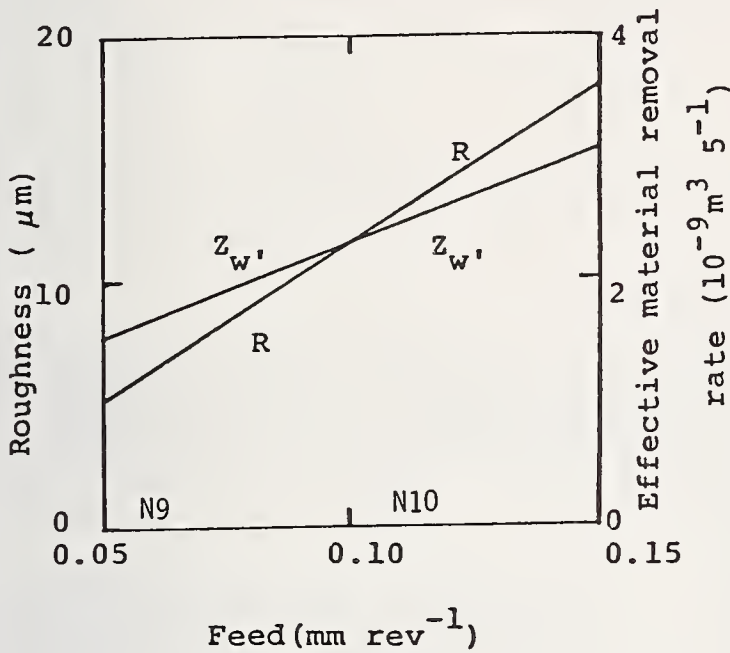


Figure 8: Roughness and effective material removal rate versus feed

It is easiest to understand the meaning of the results given in figure 8 by considering a specific machining task. Consider, for example, the turning of a cylindrical workpiece of SiC 12.5 mm in diameter to the final shape shown in figure 9. The total depth of cut is 1.75 mm; for conditions of cutting corresponding to groove 2, 14 passes of the laser beam would be required. For a dwell time $\theta = 1.05 \times 10^{-3} \text{ s}^{-1}$, $n_w = b/\pi\theta d = 4.6 \text{ s}^{-1}$, where d is $1/2(12.5 + 9.0) \text{ mm}$. If it is assumed that a return time of 2s is required for each pass, then the time for each pass in seconds including the return time is given by the equation $\delta\tau = (L/n_w f) + 2$ where L is the length of the pass (12.5 mm in figure 7). The total machining time $t_m = 14 \delta\tau$.

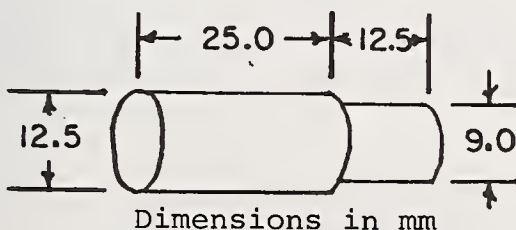


Figure 9: Workpiece for laser machining calculations

Table 3 gives the time for each pass and the total machining time for the workpiece shown in figure 9 for feeds corresponding to roughness grades N8, N9, and N10. The times tabulated in the column marked $P = 450$ W correspond to the irradiation conditions considered in figure 8. The times tabulated in the column marked $P = 1400$ W correspond to machining at a higher velocity or shorter dwell time such that the product $P \theta$ is the same as the previous case. These values are based on the assumption that the shape of the groove depends primarily on the total energy absorbed by a circular area equal in diameter to the spot size. This assumption has not yet been experimentally tested.

Table 3. Time to machine workpiece shown in figure 9 with a specified surface finish for two values of incident beam power.

Roughness	f (mm)	P = 450 W		P = 1400 W	
		δt (s)	t_M (min)	δt (s)	t_M (min)
N8	0.060	47.7	11.1	14.7	3.4
N9	0.083	35.0	8.17	12.6	2.9
N10	0.130	21.1	4.92	8.8	2.0

5. Applications

Figure 10 includes two macrophotographs of a 1/4" x 20" thread turned on Si_3N_4 by laser machining. In figure 10a the rectangular rod from which the threaded section was turned can be seen. Figure 10a also shows a region in which we demonstrate the ability to produce concave surfaces.

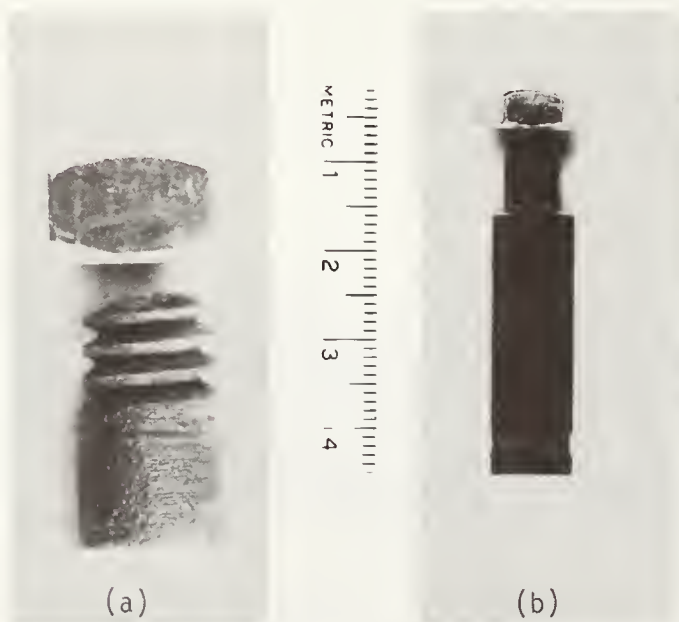


Figure 10: Macrophotographs of laser machined Si_3N_4

The negatively curved surface was made by focussing the laser beam so that it struck the center of the rectangular surface at normal incidence. Thus the corners were out of the focal region and irradiated at near grazing incidence where the light-to-material coupling was less. As a result, more material was removed near the center than near the corners and a concave surface was established. A convex surface (i.e., the round section which was threaded in figure 10) was made by adjusting the focus and angle of incidence so that the corners were near the focus and the light near normal incidence at the corners. This makes the central part of the surface out of the focal region and illuminated at near grazing incidence. Thus more material could be removed near the corners than near the center when the light was so focussed.

When laser machining was used to thread Si_3N_4 the focussed beam was at normal incidence on the cylindrical surface. However, to make a proper thread the position of the focus with respect to the previous spiral groove must be adjusted. This is shown in figure 11 where the sequence of focal positions are sketched.

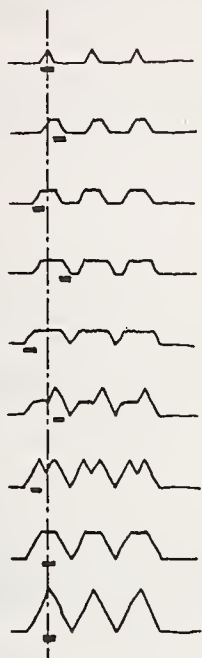


Figure 11: Schematic diagram of the procedure for laser machining screw threads

Figure 11 shows a laser machined piece of SiAlON which originally had the square cross section remaining in the middle of the piece. The maximum peak to valley non-uniformity of the smooth surface is $7.5 \mu\text{m}$ which confirms the potential of laser machining SiAlON to desired surface quality specifications. Figure 12 also shows the $1/2'' \times 13$ screw thread which we laser machined on the other end of the laser turned SiAlON rod.

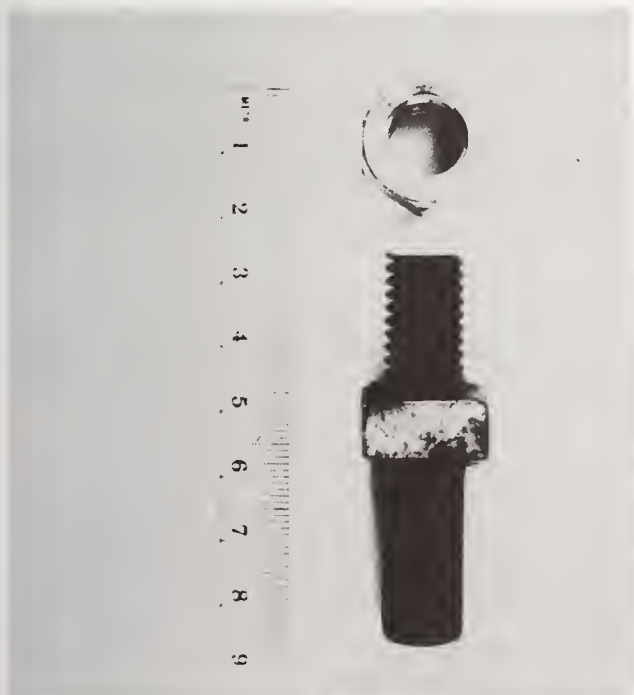


Figure 12: Laser turned and threaded SiAlON

6. Summary

1. A high power CW carbon dioxide laser can be employed to shape workpieces of SiC , Si_3N_4 and SiAlON .

2. The material removal rate increases and specific cutting energy decreases with increasing cutting velocity.
3. For a specific cutting velocity, an analysis is presented, which shows that the maximum feed and the effective material removal rate are limited by the allowable surface roughness.
4. Several shaping operations including grooving, threading and the forming of concave and convex surfaces have been demonstrated in the turning configuration.

Acknowledgments

This research is supported by the Advanced Research Projects Agency under Contract No. 00014-77-C-0478, ARPA Order No. 3421.

The authors wish to thank Dr. E. R. Thompson at United Technologies Research Laboratory and Dr. S. Musicant, General Electric Co. for providing materials used in this investigation.

References

- [1] Duley, W. W., CO₂ Lasers, Effects and Applications (Academic Press, New York, 1976).
- [2] Bass, M., Copley, S. M., and Beck, D., Laser Assisted Machining, in Proceedings of the 4th European electrooptics conference, Utrecht, Netherlands, October 1978.
- [3] Boothroyd, G., Fundamentals of Metal Machining and Machine Tools, p. 134, (McGraw-Hill Book Co., New York, 1975).
- [4] Kennedy, J. B. and Neville, A. M., Basic Statistical Methods for Engineers and Scientists, (Dun-Donnelley Publishing Co., New York, 1976).

Discussion

COOPER

Have you used supplementary lenses to spread out, elongate, or otherwise modify the shape of the spot during machining? If the efficiency is increased at short dwell times, why not spread out the beam normal to the transversing direction?

COPLEY

No, because of diffraction effects you cannot focus the beam to a narrow line perpendicular to the transverse direction that would have as large an average flux density as the Gaussian spot.

RICE

Your work on laser machining of ceramics has apparently been concerned with materials that mainly vaporize without melting. Have you investigated materials that melt such as glass, Al₂O₃, etc., and is the associated use of a diamond tool also not effective with them?

COPLEY

We have investigated laser assisting machining of Al₂O₃ using an Al₂O₃-TiC cutting tool. The tool was not effective in removing material. However, without the tool material, removal was observed by what appeared to be microspalling for conditions such that the surface temperature was less than the melting point.

OPTICAL AND SURFACE PHYSICAL CHARACTERISTICS OF DIAMOND-MACHINED INFRARED WINDOWS¹

D. L. Decker, D. J. Grandjean, and J. M. Bennett
Michelson Laboratories, Physics Division
Naval Weapons Center, China Lake, California 93555

This paper presents the results of the diamond turning of surfaces of a wide range of single-crystal and polycrystalline infrared window materials, including Ge, CaF₂, MgF₂, SrF₂, KCl, and GaAs. These surfaces were obtained from an advanced air-bearing, diamond-turning machine recently brought to an operational state at the Naval Weapons Center. The surface characterization performed includes a wide range of optical and surface physical examination including an analysis of scattered and absorbed light, and a surface microtopographic examination by diamond profilometry, phase contrast interference (Nomarski), and scanning electron microscopy. These data are compared with earlier results and are related to the characteristics of the Naval Weapons Center diamond-turning machine and to the machining parameters. A companion paper at this conference discusses the laser damage resistance of these surfaces with implications for their use in laser applications.

Key Words: Diamond single-point machining; dielectrics; infrared optical components; laser damage; optical properties.

Introduction

Diamond single-point turning or milling as a manufacturing method for precision optics has been demonstrated at a number of laboratories, notably the Energy Research and Development Administration complexes at Livermore, Calif., and at Oak Ridge, Tenn. [1,2].² The advantages of this technology over conventional methods include significant cost savings in many cases but, more importantly, the ability to readily generate aspheric surfaces which would be difficult or impossible otherwise. The materials which are amenable to diamond single-point machining are not limited to metals such as aluminum and copper and many of their alloys, but also include an impressive list of infrared window materials, useful as domes, windows, and lenses (see table 1). Much recent interest in diamond single-point machining is a direct result of the superior optical components for high energy laser application that can reliably be produced by this method. However, there are many low power laser or imaging optics applications for which the method offers significant system performance improvement over what can be done with conventional components [3].

This paper presents surface physical and optical characterization results for dielectric surfaces machined on the Naval Weapons Center (NWC) diamond-turning machine. The optical fabrication criteria outlined in table 2 are given as a reminder of the finishing requirements for a component. This paper is primarily concerned with surface microtopography and the directly related topic of scattered light [4,5]. Most of the previously reported work has been of a qualitative sort, and has not been followed up by detailed optical characterization or optimization of results [6]. This paper presents for the first time data relating to the mechanisms of material removal, and the relationship of these mechanisms to the crystalline orientation of the work surface to the machining geometry.

¹Work supported by Naval Weapons Center Independent Research Funds.

²Figures in brackets indicate the literature references at the end of this paper.

Table 1. List of dielectric materials which have been successfully diamond single-point machined as of 1979.

CaF ₂	NaCl	ZnS
MgF ₂	NaF	ZnSe
SrF ₂	Si	LiNbO ₃
KCl	Ge	GaAs
acrylic plastics		

Table 2. Summary of the fabrication requirements which apply to most optical components.

Optical figure
Surface absorption
Scattered light
Damage threshold

Machining Technique and the Material Removal Process

The basic diamond-machining process discussed here is that of single-point turning or milling of a surface in the fashion of ordinary machine shop fabrication, but using a very precise machine and special diamond tools (fig. 1). The diamonds used are of gem quality and are mounted and polished to a supersharp, highly accurate, radiused cutting edge. The overall view in figure 2 shows the tool and spindle slides of the NWC machine which are arranged in a T-base configuration [7]. The part being turned in this picture is a 6-inch-diameter copper flat which is held on the spindle nose by a vacuum chuck.

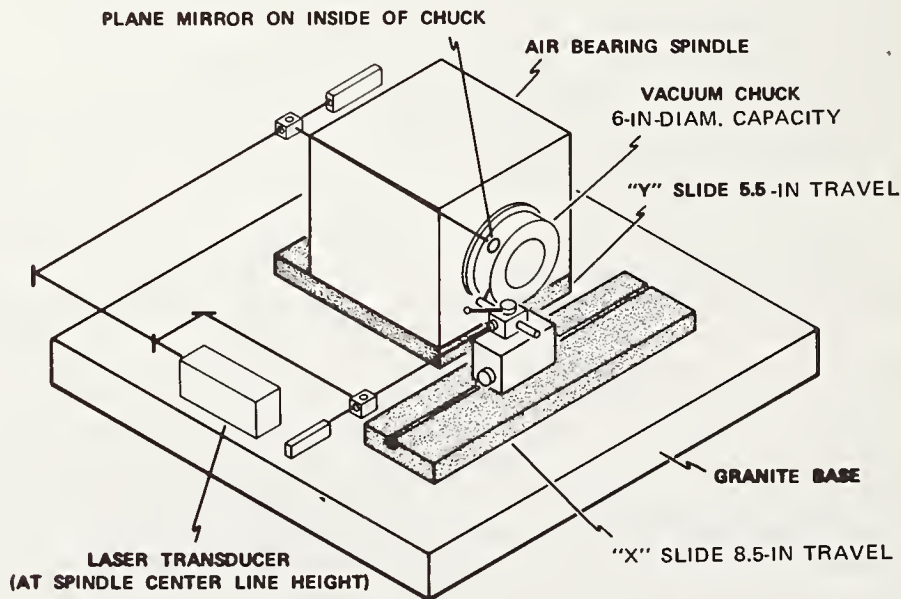


Figure 1. Isometric schematic of the NWC two-axis diamond-turning machine showing the placement of the spindle and tool slides in a T-base configuration. Also shown is a simple interferometer layout for measuring the primary motion of the slides.

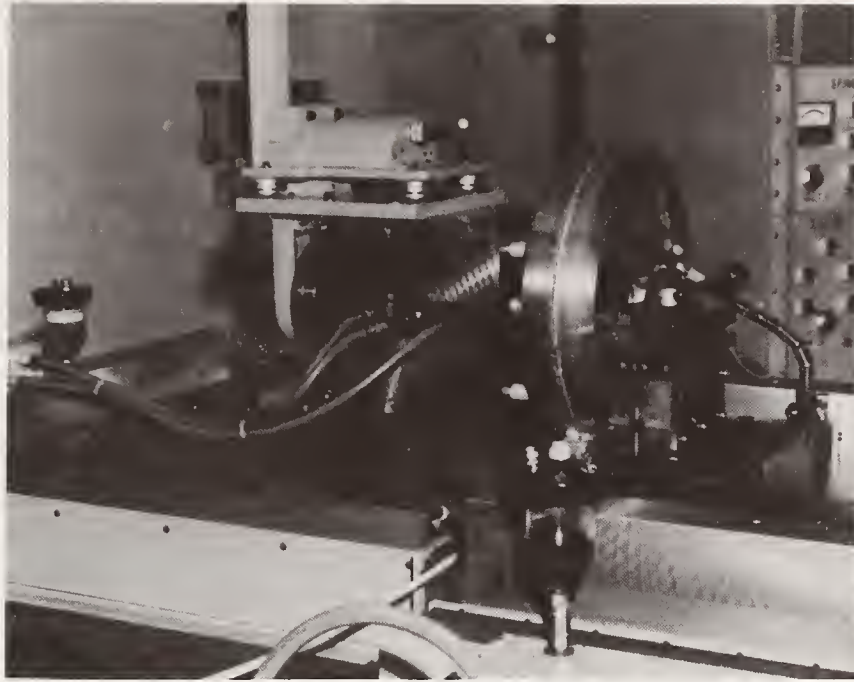
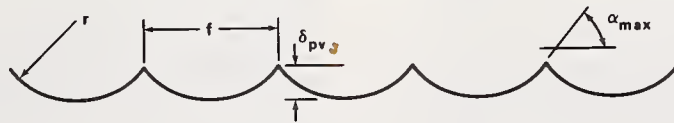


Figure 2. Photograph of the NWC machine showing the tool and spindle slides, the tool post assembly including precision height adjuster, chip/coolant guard, and spindle housing. A 6-inch-diameter copper flat is being machined.

In the case of a metal workpiece, material is removed by the tool in machining by shearing a chip from the surface. The idealized surface profile in a diametral plane perpendicular to the work surface for a turned surface is shown in figure 3. The tool nose radius r is typically 1/8 inch, and the tool feedrate is in the range of 10^{-4} inches per spindle revolution. The theoretical peak-to-valley roughness in this case is 10^{-8} inches. In actual practice, as the feedrate is made smaller, the surface finish does improve as predicted, but approaches an asymptotic roughness, controlled by material imperfection and irregularity in the machining process. The latter effects include very high frequency (10^6 Hz) chip vibration/surface interaction effects which are possibly excited by chip/tool friction [7,8]. Tools and feedrates typically used to machine dielectric surfaces are similar to those used to machine metal surfaces. In contrast with metal machining, there is no strong tool/surface speed dependence to the resulting dielectric surface characteristics.



$$\delta_{pv} \cong f^2/8r \quad \text{ASSUMING THAT } f/r \ll 1$$

$$\alpha_{max} \cong f/2r$$

OR RMS VALUES:

$$\delta_{rms} \cong \delta_{pv}/\sqrt{5}$$

$$\alpha_{rms} \cong \alpha_{max}/\sqrt{3}$$

Figure 3. Ideal finish achieved by machining with a tool of nose radius r and a feedrate f . Both peak-to-valley (pv) and rms values are given.

Material removal from all dielectrics examined in this paper occurs apparently as a consequence of brittle fracture. There is no evidence either on the resulting surface or on the machining debris of plastic deformation. This statement is based upon scanning electron microscopy of the machined surfaces and machining debris. No subsurface examination has yet been made. A pitting effect occurs which is very sensitive to tool geometry and to crystallographic orientation. The location of "clear" and "cloudy" areas on diamond-turned surfaces of several materials is shown in figure 4. The visual effect of a cloudy area is a consequence of light scattering from microscopic pits. When turned on center, single-crystal materials develop a clear/cloudy pattern which will usually have the rotational symmetry of the crystallographic plane exposed by machining. The $[331]$ axis in a cubic lattice is tipped only approximately 20° away from the $[111]$ axis which, of course, has threefold rotational symmetry. Samples a) and b) of CaF_2 have virtually the same orientation, with sample b) showing the expected symmetry, but a) shows curious skewed twofold symmetry. The origin of the effect discovered in sample a) is unknown, and this anomaly was observed only in this case out of several dozen samples of different materials and a variety of orientations which were turned in this study.

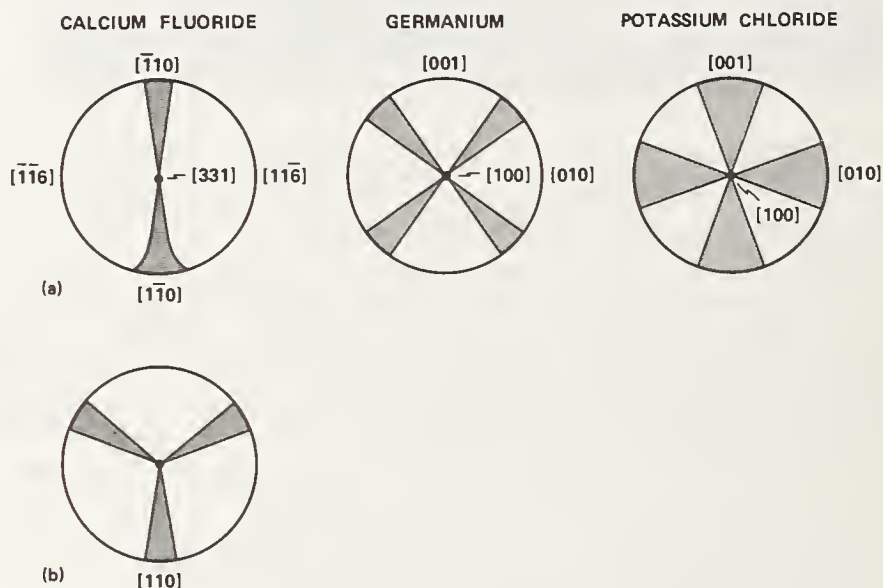


Figure 4. Schematic showing the locations of "clear" and "cloudy" structures resulting from diamond single-point machining relative to crystallographic directions for several different materials and orientations.

It is useful to examine these surfaces microscopically both with a light microscope and by electron microscopy at much higher magnification. Figures 5 and 6 are Nomarski interference contrast micrographs of an Irtran MgF_2 sample and single-crystal CaF_2 sample b). In all cases, the samples were originally polished and were subsequently diamond turned, leaving a central polished spot for direct comparison. As shown in figure 5, the quality of the Irtran surface is substantially limited by voids remaining from processing of the material, both in the polished and diamond-turned areas. In the case of single-crystal CaF_2 (fig. 6), the clear diamond-turned area is indistinguishable from the polished area. The scanning electron micrographs of figure 7 compare CaF_2 b) polished and diamond-turned clear areas at much higher magnification. The polished surface is defined by a superposition of scratches from the polishing grains. Most of the clear diamond-turned area is an extremely smooth, almost featureless, surface. The localized pitted areas often show the effects of multiple tool passes, and a very interesting repetitive nature with a spatial period which varies from slightly less than $1 \mu\text{m}$ down to $0.5 \mu\text{m}$ (fig. 7). This variation is seen to occur even over a very small area and shows no correlation with position on the sample. Figure 8 shows the localized nature of the cloudy areas and a high magnification view of the pits in a cloudy area. There is no qualitative shape or size difference of the pits occurring in clear or cloudy areas--only concentration differences. Often a decrease

POLISHED



1000 μm

DIAMOND TURNED

Figure 5. Nomarski phase contrast interference micrograph of a polished Irtran surface which has been partially diamond machined leaving a polished area for comparison.

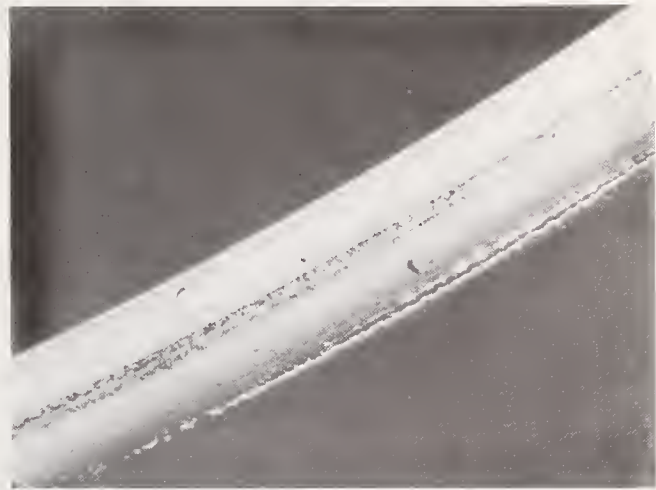
POLISHED



1000 μm

DIAMOND TURNED "CLOUDY"

POLISHED



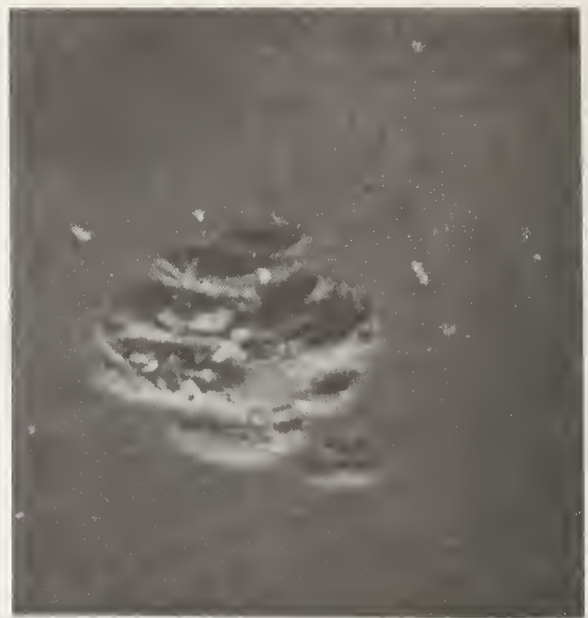
1000 μm

DIAMOND TURNED "CLEAR"

Figure 6. Nomarski phase contrast interference micrograph of a polished single-crystal CaF₂ surface which has been partially diamond machined leaving a polished area for comparison. On the left side is a representative "cloudy" area and on the right a "clear" area.



5 μm
POLISHED AREA



5 μm
CLEAR AREA

Figure 7. Scanning electron micrograph of the same single-crystal CaF_2 surface shown in figure 6. On the left side is a polished area and on the right an area selected from the clear diamond-machined portion showing localized pitting and some debris from turning.



100 μm
CLEAR AND CLOUDY AREAS



5 μm
CLOUDY AREA

Figure 8. Scanning electron micrograph of the same single-crystal CaF_2 surface shown in figures 6 and 7. On the left side is a low magnification view of the localized "cloudy" spoke-shaped area as it is seen near the boundary between the polished and diamond-turned portions. On the right, at much higher magnification, is shown a representative "cloudy" area.

in spatial period can be correlated with a decrease in pit volume, in a sequence of pits. The pit shape is, of course, strongly suggestive of an indentation mark made by the tool tip. However, the relative motion between the surface being turned and the tool tip is a factor of at least 40 smaller than the typical 1- μm -deep pit. A probable explanation is that the pits are produced by spalling as a result of a localized tensile load at the surface which exceeds the material strength following the release of the compressive loading at the cutting edge as the tool passes over the surface. The repetitive nature of the spall pit formation comes from a constructive interaction of the tool loading and a standing acoustic wave in the material which has been excited by the tool. The effect is similar to chatter often observed in an ordinary machine tool, except that it is not a machine structure resonant effect, but an effect in the material itself. The effect is similar to that observed in diamond machining of metal surfaces [7,8]. The standing wave may or may not be a consequence of a resonant effect. However, the temporal frequency of the material "chatter" is approximately 10^6 Hz which is on the order of the resonant frequency of a mass on a spring consisting of a spall fragment connected into the lattice of the work material. In this simple model, the resonant frequency would scale as the square root of the reciprocal of the volume of the spall pit. This relationship is at least qualitatively observed in the decrease in spall pit size and accompanying decrease in spacing. The spall pit sequence on the left of the superposition shown in figure 7 is a clear example of this effect. A resonant explanation thus seems likely.

As the cutting radius increases at constant rotational rate, it has been observed in a number of cases that the spall tendency precipitously can decrease beyond a specific radius (surface speed). This may simply be due to the lack of constructive interaction of the tool and the resonant wave in the material. If so, the tendency to spall should occur in annular bands, depending upon surface speed. This effect has not been observed. Another possible explanation is that spall formation is dependent upon strain rate and hence surface speed. This possibility is further corroborated by the curious fact that although the concentration of spall pits is strongly dependent upon crystallographic orientation, the surfaces defining the shape of the pits are formed by brittle fracture along arbitrary crystallographic planes. There is no evidence either in the pits or on the fragment surfaces of cleavage. Fracture produced in brittle materials at very high strain rates in shock experiments often does not recognize the plane of easy division (cleavage). The tendency towards spall formation can be decreased by two known approaches: 1) higher or lower surface speeds and 2) tool rake angle. By using a tool with a very large negative rake, in the range of 20 to 45°, very uniform surfaces have been turned on several dielectric materials including KCl and CaF₂. However, the success with both surface speed variation and tool geometry are very dependent upon the cutting edge characteristics of the tool being used. Edge sharpness and orientation, and perhaps even the diamond bulk imperfection is involved in the resonant chatter effect.

Optical and Surface Physical Characterization

A diamond stylus profilometer has been used to examine the topography of the several diamond-turned surfaces reported here. The results shown in figures 9 through 12 were obtained from a Talystep profilometer with a 1- μm -radius conical stylus. This instrument yields surface profile data along the track of the stylus with a lateral resolution on the order of a micrometer for the smoother, low slope surfaces examined here, and with a height resolution of 3 Å. The output of the stylus transducer amplifier is digitized and subsequently processed to yield distribution functions for height, slope, and correlation [9]. In figures 9 and 10 unprocessed scans of polished and diamond-turned single-crystal CaF₂ are compared for two different scan lengths, 15 and 600 μm . The diamond-turned clear areas on the CaF₂ sample of figures 9 and 10 are a factor of three smoother than the corresponding polished surface on the same sample, and have much less steeply sloped structure as well. The Irtran MgF₂ surface scans shown in figures 11 and 12 indicate a much rougher surface, the surface being substantially determined by voids still present in the hot pressed material. The diamond-turned surface is uniform and slightly rougher than the polished surface.

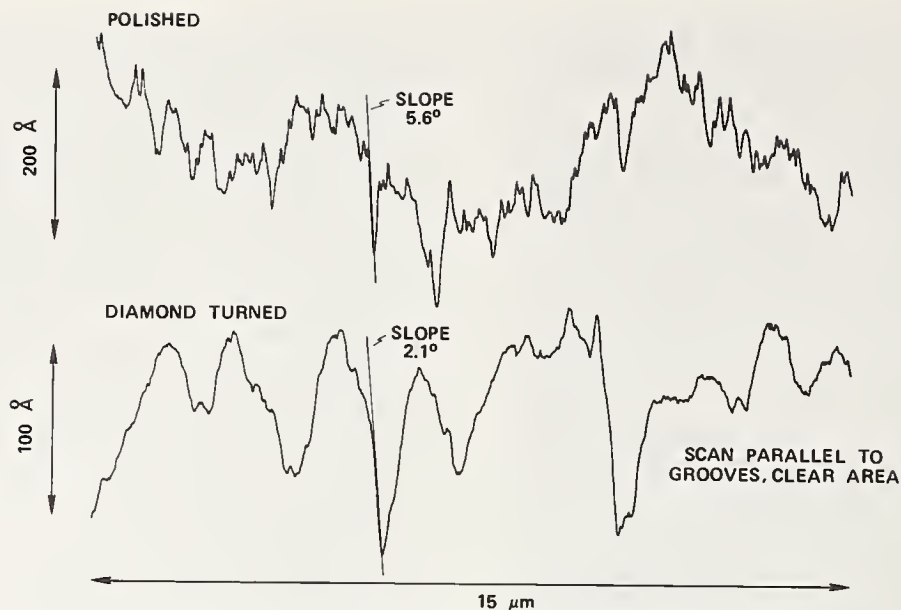


Figure 9. Unprocessed Talystep surface scan of 15- μm length on the CaF_2 sample previously shown in figures 6 through 8. Both polished and diamond-turned "clear" areas are shown.

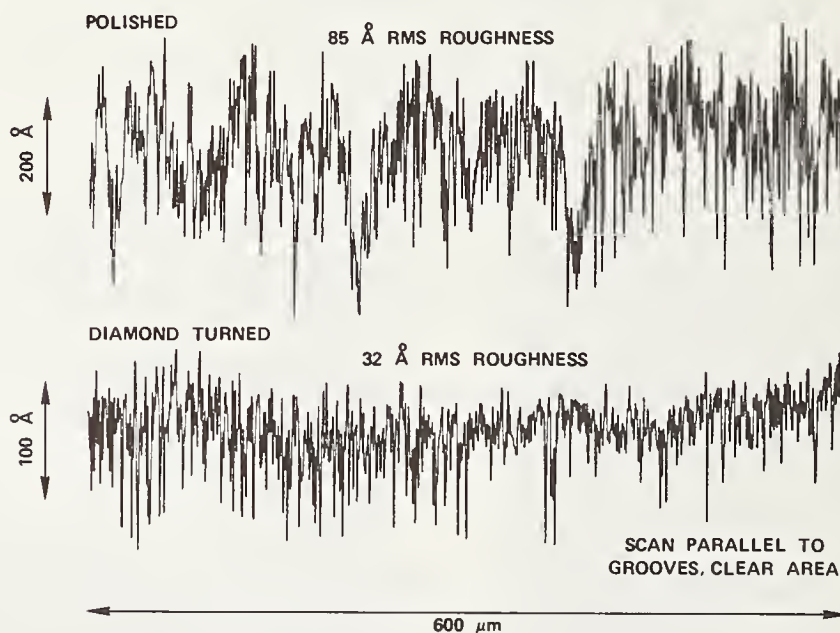


Figure 10. Unprocessed Talystep surface scan of 600- μm length on the CaF_2 sample previously shown in figures 6 through 9. Both polished and diamond-turned "clear" areas are shown.

The surface profiles of the polished and clear diamond-turned areas thus are very similar in distribution of height and slope. Consequently, the light scattering from the two surface types will be similar. The magnitude of the total integrated scattered (TIS) light compared to that light specularly reflected, $\Delta R/R$, can be related to the rms roughness δ

$$\Delta R/R \cong (4\pi\delta/\lambda)^2 ,$$

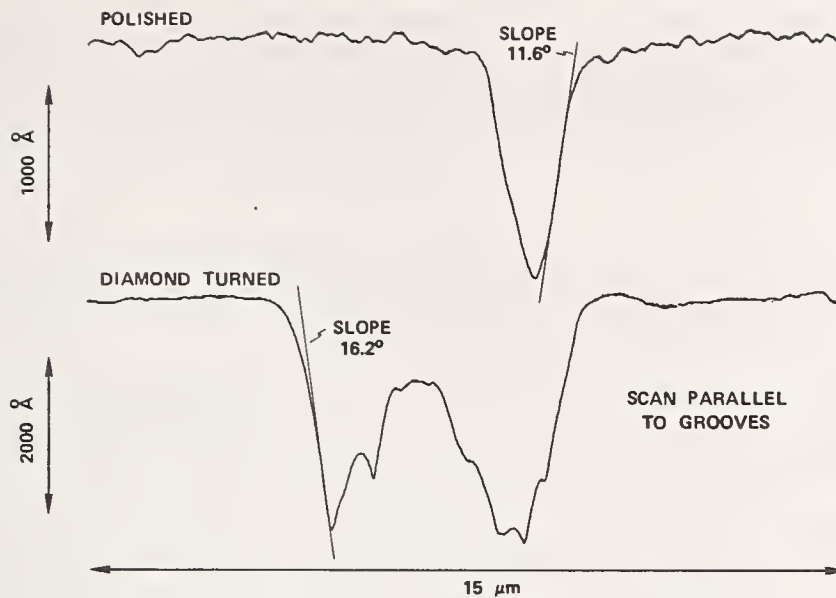


Figure 11. Unprocessed Talystep surface scan of length 15- μm on the polycrystalline MgF_2 previously shown in figure 5. Both polished and diamond-turned areas are shown.

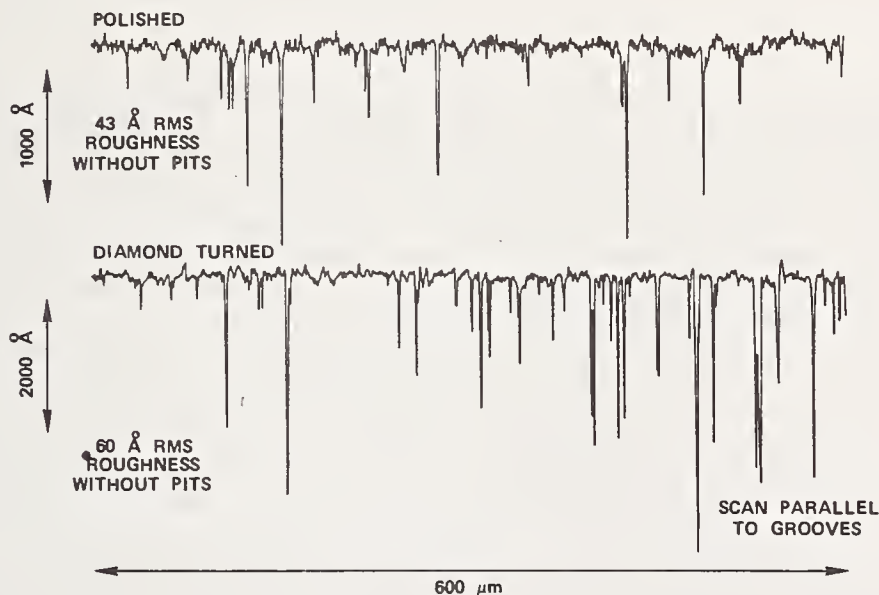


Figure 12. Unprocessed Talystep surface scan of length 600- μm on the polycrystalline MgF_2 previously shown in figures 5 and 11. Both polished and diamond-turned areas are shown.

where λ is the wavelength of the incident light [10]. Table 3 gives values of TIS for Irtran MgF_2 , CaF_2 , and SrF_2 for light in the visible ($0.647 \mu\text{m}$) and in the near infrared ($3.39 \mu\text{m}$). There is little difference in the visible light scatter from the clear diamond-turned polished areas, with the cloudy diamond-turned areas on CaF_2 and SrF_2 scattering a factor of five more light than the clear areas. In the near infrared the differences between polished and clear diamond-turned scattered light is even smaller, with still a factor of roughly five difference between clear and cloudy. From an examination of the CaF_2 diamond-turned surfaces shown in figures 10 and 11, it is obvious that much debris from machining is present even after "cleaning." It is certainly true that much of the scattered light originates from these particles, and that more complete cleaning would materially reduce the TIS, especially in the infrared. The presence of machining debris

also has a negative impact upon the laser damage resistance of the machined surface, especially for short pulse lengths where dielectric breakdown is a predominant damage mechanism [11]. However, in a companion paper at this conference [12], no significant difference in laser damage thresholds for the polished and diamond-turned surfaces described in this paper were discovered for 100- μ sec pulses of 2.7- and 3.8- μ m wavelength laser radiation.

Table 3. Values of TIS at two different wavelengths, 0.647 and 3.39 μ m, for three different materials which were diamond single-point machined in this study. Included is a comparison of polished and diamond-turned "clear" and "cloudy" areas on the same sample.

Material	Wave-length, μ m	Polished	Diamond turned Cloudy	Clear
MgF ₂	0.647	.02	.03	.03
(Irtran)	3.39	.006	.01	.01
CaF ₂	0.647	.0007	.04	.001
	3.39	.00004	.004	.00003
SrF ₂	0.647	.0008	.02	.004
	3.39	.0001	.0006	.0001

Conclusion

The diamond stylus profilometer results from diamond-turned dielectric surfaces are statistically not much different than surfaces produced by conventional grinding and polishing by loose abrasive. As a consequence, the TIS in the visible from a diamond-turned surface can be quite comparable to that of a high quality polished surface, and in some cases even lower. For the materials examined in this paper, Irtran MgF₂, SrF₂, and CaF₂, the diamond-turned surface scattered light at 3.39- μ m wavelength is on the order of that from the corresponding polished surfaces. As was shown, the diamond-turned areas are covered with a significant concentration of debris from turning, even after "cleaning." Much of the measured scattered light certainly originates from these particles. More elaborate cleaning must be accomplished. The scattering from the "cloudy" diamond-turned surfaces is much larger, as a consequence of a much larger concentration of localized spall pitting. A full understanding of the latter effect and its elimination are important to the fully successful application of diamond turning to infrared optics. However, the Irtran MgF₂ results are very interesting and encouraging since this polycrystalline material is often used for low cost infrared optics. There are no preferential cloudy diamond-turned areas on this surface and the diamond-turned surface scatters only slightly more light than the polished area. It is thus demonstrated that under some conditions diamond-turned dielectric surfaces can be quite comparable in optical quality to corresponding polished surfaces. The advantages that diamond single-point machining brings to the production of infrared optical components, high throughput, and ready generation of aspheric surfaces promise to revolutionize infrared optics production.

Acknowledgment

The authors of this paper acknowledge the contributions of many co-workers at NWC, notably Phil Archibald for scattering measurements, Cliff Fountain for x-ray orientation of samples, and Bev Reymore for editorial assistance.

References

- [1] Arnold, J. B., and Steger, P. J., Diamond turning on advanced machine tool prototypes (SME Clinic on Industrial Application of Precision Machining and Gaging, 19-21 November 1974, San Francisco, Calif.) Report Y-DA-5975 (Union Carbide, Inc., Oak Ridge, Tenn., 1975).
- [2] Bryan, J. B., et al., A practical solution to the thermal stability problems in machine tools, Technical Paper MR72-138 (Society of Manufacturing Engineers, Dearborn, Mich., 1972).
- [3] Decker, D. L., Soileau, M. J., Porteus, J. O., and Bennett, J. M., Surface, optical, and laser damage characteristics of diamond turned metal mirrors, in Laser Induced Damage in Optical Materials: 1976, A. J. Glass and A. H. Guenther, eds., pp. 153-164. NBS Spec. Publ. 462 (National Bureau of Standards, Washington, DC, 1976).
- [4] Decker, D. L., Bennett, J. M., Soileau, M. J., Porteus, J. O., and Bennett, H. E., Surface and optical studies of diamond-turned and other metal mirrors, Opt. Engr. 17, [2], 160-166 (Mar/Apr 1978).
- [5] Decker, D. L., and Bennett, J. M., Surface evaluation techniques for optical components (Proc. Society of Photo-Optical Instrumentation Engineers) Optical Coatings II, 140, 32-41 (1978).
- [6] Arnold, J. B., Morris, T. O., Sladky, R. E., Steger, P. J., Machinability studies of infrared window materials and metals (Proc. Society of Photo-Optical Instrumentation Engineers) Advances in Precision Machining of Optics 93, 96-103 (1976).
- [7] Decker, D. L., and Grandjean, D. J., Physical and optical properties of surfaces generated by diamond-turning on an advanced machine, in Laser Induced Damage in Optical Materials: 1978, A. J. Glass and A. H. Guenther, eds., pp. 122-131. NBS Spec. Publ. 541 (National Bureau of Standards, Washington, DC, 1978).
- [8] Decker, D. L., Presented in a paper read before the Society of Manufacturing Engineers, Precision Machining Workshop, 27-29 June 1978, Williamsburg, Va.
- [9] Elson, J. M., and Bennett, J. M., Relation between the angular dependence of scattering and the statistical properties of optical surfaces, J. Opt. Soc. Am. 69, 31 (1979).
- [10] Bennett, H. E., and Porteus, J. O., Relation between surface roughness and specular reflectance at normal incidence, J. Opt. Soc. Am. 51, 123-129 (1961).
- [11] Temple, P. A., and Soileau, M. J., Resonant defect enhancement of the laser electric field, in Laser Induced Damage in Optical Materials: 1976, A. J. Glass and A. H. Guenther, eds., pp. 371-378. NBS Spec. Publ. 462 (National Bureau of Standards, Washington, DC, 1976).
- [12] Porteus, J. O., Soileau, M. J., Faith, W. N., and Jernigan, J. L., Surface characteristics of diamond-machined window surfaces related to 2.7- and 3.8- μm laser damage (this conference).

Discussion

BOWLES

In view of the similarity of the cracks shown in the diamond point surfaced to Hertzian cracks generated by a sliding indenter, might not the "frequency" of spall distribution arise from the flaw population in the surface being worked?

DECKER

It is likely that a spall is located by a flaw, but once initiated it appears that the spatial frequency of additional spall sites is controlled by intrinsic material parameters. Extensive repetitive spalling is observed in the high susceptibility regions which is too regular to be accounted for by extrinsic material properties (flaws).

LANDINGHAM

I have examined a single-point machined fluorophosphate glass which shows spalling in some regions of surface but other regions are very smooth. This coarser spalling seemed to be related to rake angle and tool holder vibrations. Smooth surfaces were examined in an SEM and no submicron spalling cracking could be detected.

DECKER

The tendency to spall in the crystalline materials reported on here is very strongly related to rake angle, tool sharpness, and surface speed. However, I don't believe that tool holder vibration plays a significant role, since the observed temporal frequency of the spall is in the megahertz range and thus is orders of magnitude higher than any resonant frequencies associated with the tool holder assembly.

RICE

1. You noted larger, apparently sporadic surface pits in MgF_2 from processing defects (mainly pores)? Can you estimate the surface density and size range of these to indicate the character and distribution of such processing defects?

2. You stated that the removal mechanism appeared to be by brittle fracture rather than by a deformation process. This is very surprising, especially for several of the materials you have studied. What is your evidence for this statement?

3. Can you elaborate on cost factors, or initial investment and operator skill vs. polishing? Can you comment on possible applicability of single point diamond machining to harder ceramics such as Al_2O_3 or $MgAl_2O_4$?

DECKER

1. The hot pressed MgF_2 used in this study has a defect density of approximately $10^4/MM^2$. These defects are primarily pores of from 0.5 - 3 μm in diameter.

2. It is quite possible that plastic deformation plays a role in spall function, but there is no superficial evidence of plastic flow either associated with the spall pits or with the fragments so produced. For example, there is no upturned edge on any spall pit examined and all fragment edges are very sharp, right to the limit of resolution of the SEM.

3. There is no question that precision single point diamond machining requires a large capital investment, but for high volume production, especially of aspheric or non-standard components, significant cost savings have been demonstrated. The operator skill level required for precision diamond machining is very similar to that required for conventional polishing, involving to a substantial degree technique in handling of optical surfaces. Hardness of the work outlined, per se, is not a criteria for determining the diamond machinability of a material. I have been told by several people that diamond tools have been used to finish Al_2O_3 parts mechanically. It may thus be entirely possible to produce an optical finish by use of a suitable tool and machine.

ELECTROCHEMICAL GRINDING AND SURFACE DAMAGE FOR CEMENTED CARBIDES

S. Malkin and R. Levinger

Materials Processing and Machine Tool Center
Faculty of Mechanical Engineering
Technion-Israel Institute of Technology
Haifa, Israel

The electrochemical grinding process (ECG) for WC-Co cemented carbides is shown to be governed by differences in electrochemical dissolution rates into the two phases. An electrochemical analysis indicates that the initial electrochemical etching rate into the cobalt phase is much faster than into the WC. This facilitates mechanical removal during ECG but produces a damaged surface weakened by partial cobalt depletion. The degree of surface damage is quantitatively measured as the reduction in mechanical grinding resistance as a function of depth below the finished surface.

Key Words: Cemented carbides; electrochemical grinding; grinding; tungsten carbide.

1. Introduction

Electrochemical grinding (ECG) has often been proposed as an alternative to conventional mechanical grinding for machining of cemented carbides. Combined electrochemical and mechanical action in ECG provides faster and more efficient material removal than conventional grinding. However, the resulting surface quality is considered to be inferior, and this has restricted the more widespread use of ECG for machining of cemented carbides.

The conventional analysis of ECG is based upon the assumption that electrochemical and mechanical removal proceed completely independently of each other. While this assumption may be satisfactory for single phase materials, it is unlikely to be valid for cemented carbides which consist of hard carbide particles with a ductile metal binder. With WC-Co cermets, it will be shown that the electrochemical etching rate into the cobalt phase should be much faster than into the WC phase. Selective removal of the binder metal in this way should weaken the cermet and thereby facilitate the mechanical grinding action. However, this same effect may be the cause of poor surface quality after grinding, as the surface produced is likely to be weaker than the bulk material due to a deficiency in cobalt binder selectively removed by electrochemical dissolution.

The present paper reviews the results of a recent investigation of the ECG process for WC-Co cemented carbides with particular consideration of the role of heterogeneous electrochemical dissolution [1, 2]¹. Differential electrochemical etching into the carbide and cobalt phase is analyzed and related to the mechanical grinding energy requirements of the process. Surface damage after grinding is quantitatively measured as the reduction in mechanical grinding resistance of the material in the finished surface layer.

2. Electrochemical Considerations

The electrochemical dissolution process is governed by Faraday's Laws. For a single

¹ Figures in brackets indicate the literature references at the end of this paper.

phase material, the volumetric electrochemical dissolution rate Z_e is proportional to the applied current I :

$$Z_e = \alpha I \quad (1)$$

with the proportionality constant

$$\alpha = \frac{M}{F\omega\gamma} \quad (2)$$

where M is the molecular weight, F is the Faraday constant ($F=96000$ amp), ω is the valency of the electrochemical reaction, and γ is the density. For one-dimensional electrochemical removal normal to a surface of cross sectional area A , the linear removal rate (etching velocity) v_e is obtained by dividing both sides of eq. (1) by A :

$$v_e = \frac{Z_e}{A} = \alpha \frac{I}{A} = \alpha i \quad (3)$$

where i is the current density.

Consider now what happens during electrochemical dissolution of WC-Co cermet, a two-phase material. Let us assume that the WC and cobalt phases behave as parallel electrical conductors near the surface. A portion of the total current normal to the surface will flow through the WC phase and the remainder through the cobalt, the partition of current flow between the two phases depending on the cermet composition and electrical resistivities of each phase. Taking this into account, the corresponding etching velocities into each phase, v_{Co} and v_{WC} , can be obtained by applying eq. (3) to the cobalt and to the WC [1]:

$$v_{Co} = \alpha_{Co} \left(\frac{1 + \epsilon}{1 + \epsilon\beta} \right) i \quad (4a)$$

$$v_{WC} = \alpha_{WC} \left(\frac{1 + \epsilon}{1 + \epsilon\beta} \right) i \quad (4b)$$

where α_{Co} and α_{WC} are the values of α for each material, β is the ratio of electrical resistivity of cobalt to that of WC, and ϵ is the volume ratio of tungsten carbide to cobalt in the cermet. The relevant properties for WC and cobalt are given in table 1 [3]. The ratio of v_{Co} to v_{WC} is:

Table 1. Properties of WC and Cobalt.

	<u>WC</u>	<u>Cobalt</u>
Molecular weight, M	195.92	58.94
Density, γ ($\frac{g}{cm^3}$)	15.7	8.85
Resistivity, ρ (ohm·m)	$18.5-19.2 \times 10^{-8}$	5.8×10^{-8}
Electrochemical constant, α ($\frac{mm^3}{amp \cdot min}$)	0.97	2.08
Valence of electrochemical reaction, ω	8	2

$$\frac{v_{Co}}{v_{WC}} = \frac{\alpha_{Co}}{\beta \alpha_{WC}} \quad (5)$$

which depends only on the properties of the two phases and is independent of cermet composition. Putting in the appropriate properties of WC and cobalt from table 1 gives a velocity ratio $v_{Co} / v_{WC} = 7.2$.

It can therefore be expected that the etching velocity into the cobalt phase will be much faster than into the WC phase, thereby causing selective etching of the cobalt. This is the situation which prevails at the beginning of the electrochemical process. As this process continues, however, the current flow through the cobalt phase will decrease because of the high electrical resistivity of electrolyte filling up the gaps left behind by selective cobalt removal, with a corresponding increase in current through the WC in order to maintain the total applied current. The decreasing current in the cobalt phase will reduce the etching velocity into this phase from its initial value given by eq. (4a), and the increasing current in the WC phase will raise its etching velocity above its initial value given by eq. (4b). Eventually a steady state situation will be reached beyond which the etching velocities into both phases are the same with the cobalt level a fixed depth ahead of the WC level at the surface. The steady state etching velocity is given by [1]:

$$v^* = \alpha^* i \quad (6)$$

where

$$\alpha^* = \frac{\alpha_{Co} \alpha_{WC} (1 + \epsilon)}{\alpha_{WC} + \epsilon \alpha_{Co}} \quad (7)$$

3. Experimental

ECG experiments were conducted using the face grinding arrangement illustrated in figure 1. This type of grinding allows for observing the influence of infeed velocity v_i relative the etching velocities obtained from the electrochemical analysis. The ECG process parameters were the infeed velocity v_i and current density i . During ECG, the force components

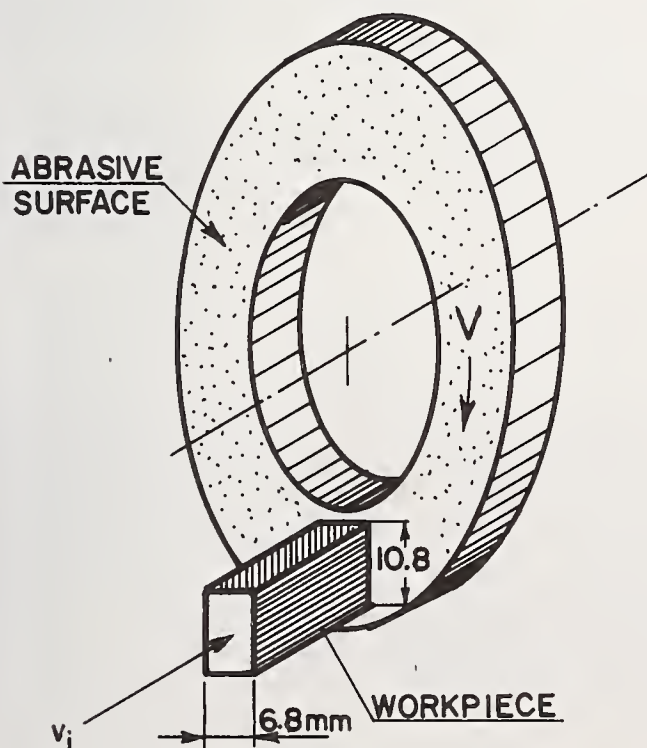


Figure 1. Illustration of face grinding arrangement for ECG.

normal to the wheel surface, F_n , and tangential to the wheel surface parallel to the wheel velocity, F_t , were measured with a semiconductor strain gauge dynamometer. All experiments were performed using the same grinding wheel (Eleform D100) which contained 100 mesh diamond of 100 concentration (4.4 carats/cm³) in a copper binder. The rotational speed of the wheel was fixed at 5000 r/min corresponding to a velocity $V=29.5$ m/s at the mid-point of the grinding area which was located 66/mm down from the wheel axis. During ECG, a commercial electrolyte (ELY-S10) consisting mainly of sodium nitrate and nitrite was supplied to the grinding area at a nominal flow rate of 2 liters/min and temperature of 25°C. Eight commercial grades of WC-Co cemented carbides were used as listed in table 2 together with their composition and properties furnished by their manufacturer.

The weakening of finished surfaces as a consequence of ECG was quantitatively evaluated for some cases from an analysis of the forces obtained during a grinding transient after shutting off the electrical current at the end of the ECG and continuing with mechanical grinding at the same overall infeed velocity v_i [2]. During the transient, the normal grinding force generally increases because the process is no longer electrochemically assisted, thereby causing more of the overall infeed to be taken up by elastic deflection of the grinding system so that the actual infeed velocity drops. Eventually the actual infeed velocity rises again and approaches the steady state value v_i at the end of the transient. From an analysis of the elastic deflection of the system during the transient, the actual infeed velocity and the total infeed depth after switching off the current can be calculated at any time during the transient. Selective electrochemical removal of the cobalt binder prior to shutting off the current should weaken the material below the surface, thereby reducing the grinding resistance of the material removed during the transient. The weakening of the surface layer is expressed as the ratio of the mechanical grinding energy at the calculated depth below the surface after ECG to the normal grinding energy for this material, the comparisons being made at the same actual infeed velocities.

4. ECG Results

ECG experiments were performed on all eight cemented carbides listed in table 2. Illustrative results for two of these materials are presented in figures 2-4 for the supply voltage V_s to maintain the required current, and the grinding force components F_t and F_n as a function of infeed velocity v_i for various values of current density i .

Table 2. Composition and Properties of Cemented Carbides

Material Number	wt. % WC	wt. % Co	wt. % additions		WC grain size (μm)	Vicker's hardness (kg/mm^2)	TRS ^a (N/mm^2)	ϵ
1	93.5	5	1.5	TaC	1.2	1850	2050	10.71
2	91.7	5.8	2.5	TaC	1.8	1700	2200	9.15
3	85	13	2	TaC	1.5	1330	3150	3.77
4	94	6	-	-	2.0	1610	2430	8.83
5	91	9	-	-	2.0	1460	2750	5.70
6	87	13	-	-	2.5	1250	3560	3.77
7	89.7	10	0.2	TaC	3.5	1250	2780	5.07
			0.1	TiC				
8	87	13	-	-	4.0	1090	3100	3.77

^aTRS = Transverse rupture strength

The results for the supply voltage V_s in figure 2 show a linear decrease with faster infeed velocity up to a certain point, beyond which the drop in supply voltage becomes steeper. Since each of these curves is for a fixed current, this means that the electrical resistance across the grinding zone follows a similar relationship. The discontinuity at the start of the steep voltage drop occurs at a faster infeed velocity with a bigger current density.

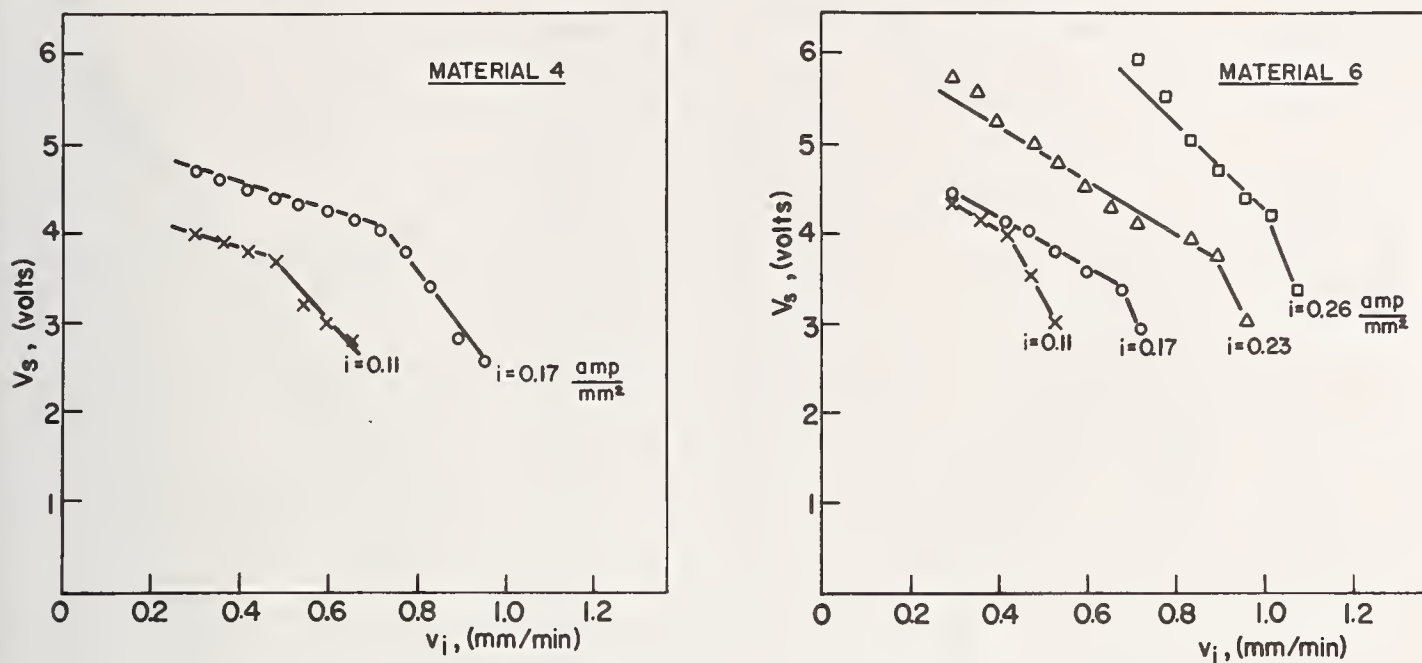


Figure 2. Supply voltage versus infeed velocity at various current densities for Materials 4 and 6.

Both the normal and tangential force components in figures 3 and 4 increase with faster infeed velocity. Discontinuities can be seen in the results in figure 4 for F_t which correspond to those discontinuities in figure 2. Since the tangential force component F_t is proportional to the mechanical grinding power requirements, the decrease in F_t with bigger current densities in figure 4 indicates the effectiveness of electrochemical assistance in reducing the mechanical grinding power. By contrast, the normal force component F_n in figure 3 is much less affected by current density during ECG and in some cases exceeds the normal force for purely mechanical grinding ($i=0$), probably because of pressure from gasses evolved from the electrochemical reactions. Extrapolation of the force components to zero in figures 3 and 4 generally corresponds to a positive infeed velocity except with $i=0$.

One measure of grinding behavior for conventional mechanical grinding is the specific grinding energy input per unit volume of material removal. For ECG, an analogous parameter is the specific mechanical energy u_m , which is the mechanical energy input per unit volume of material removal:

$$u_m = \frac{F_t V}{v_i A} \quad (8)$$

where the numerator is the mechanical power input and the denominator is the volumetric removal rate. The specific mechanical energy results, corresponding to those in figures 2-4, are presented in figure 5. Here it can be seen that for mechanical grinding ($i=0$), the specific mechanical energy decreases as the removal rate is raised by increasing v_i , which is typical for mechanical grinding. With ECG, the opposite trend is observed, the specific mechanical energy being very small at slow infeed velocities and increasing at faster velocities. It is evident from these results that the ECG action is relatively more effective at slower infeed rates. Discontinuities in the results for u_m are observed which correspond to those seen in figures 2 and 4. At infeed velocities beyond the discontinuities, the specific mechanical energy increases at a faster rate coming closer to the results for mechanical grinding ($i=0$).

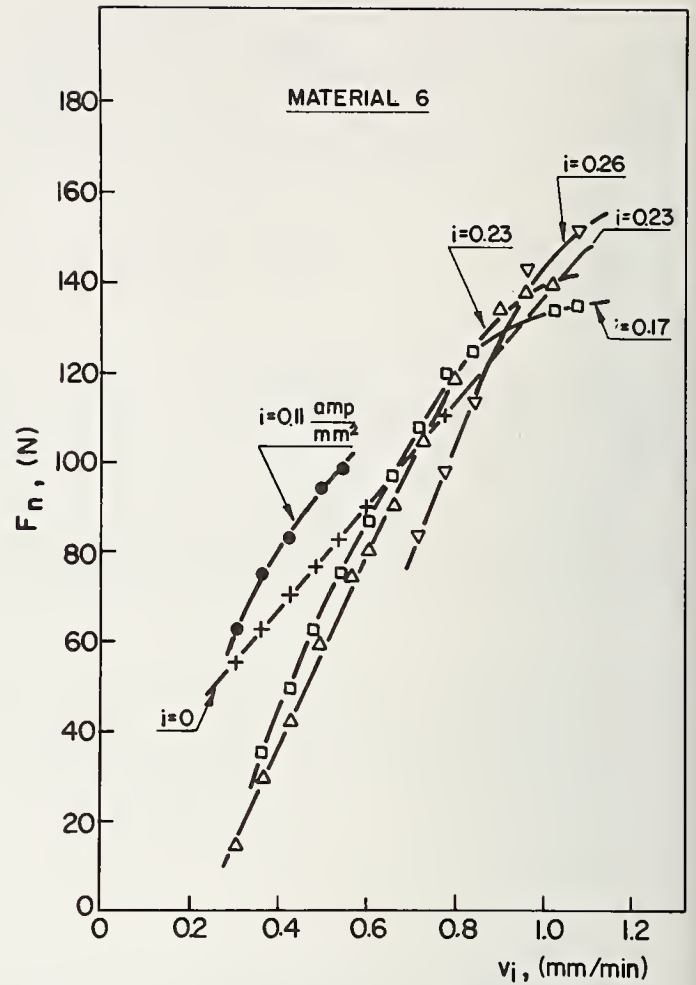
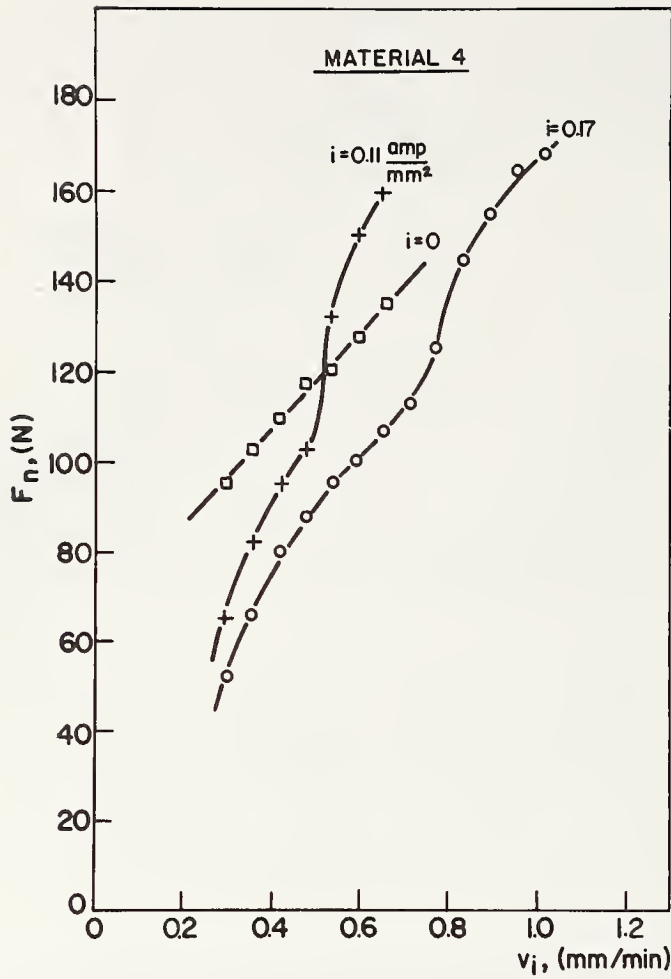


Figure 3. Normal force component versus infeed velocity at various current densities for Materials 4 and 6.

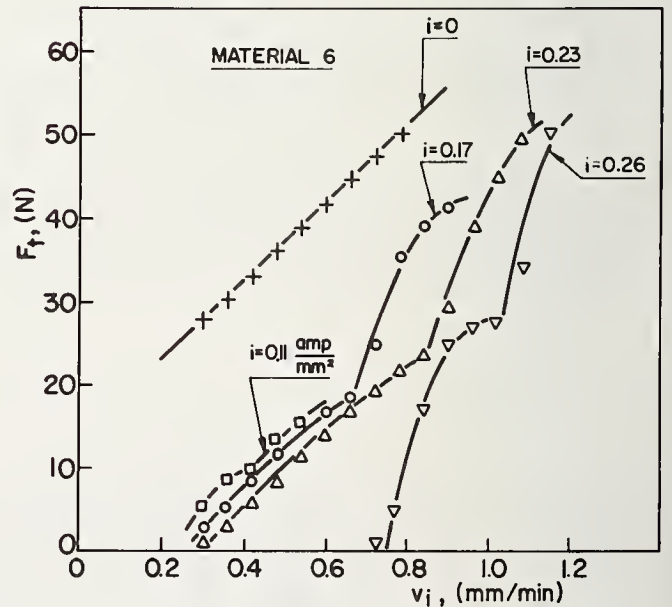
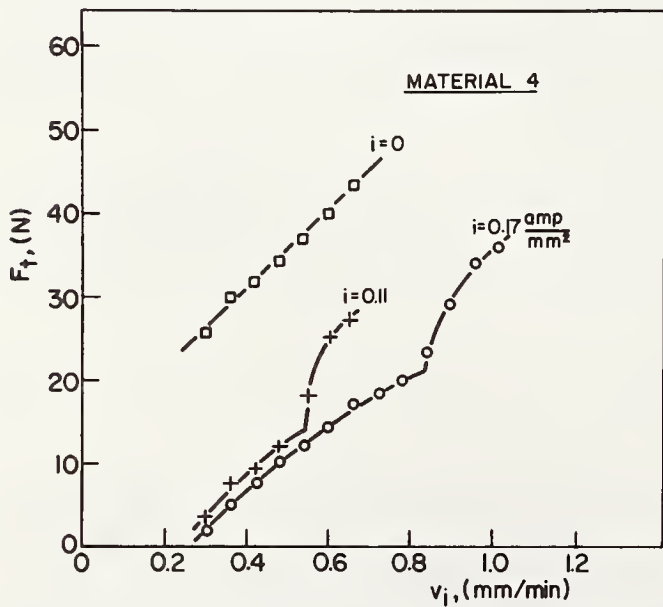


Figure 4. Tangential force component versus infeed velocity at various current densities for Materials 4 and 6.

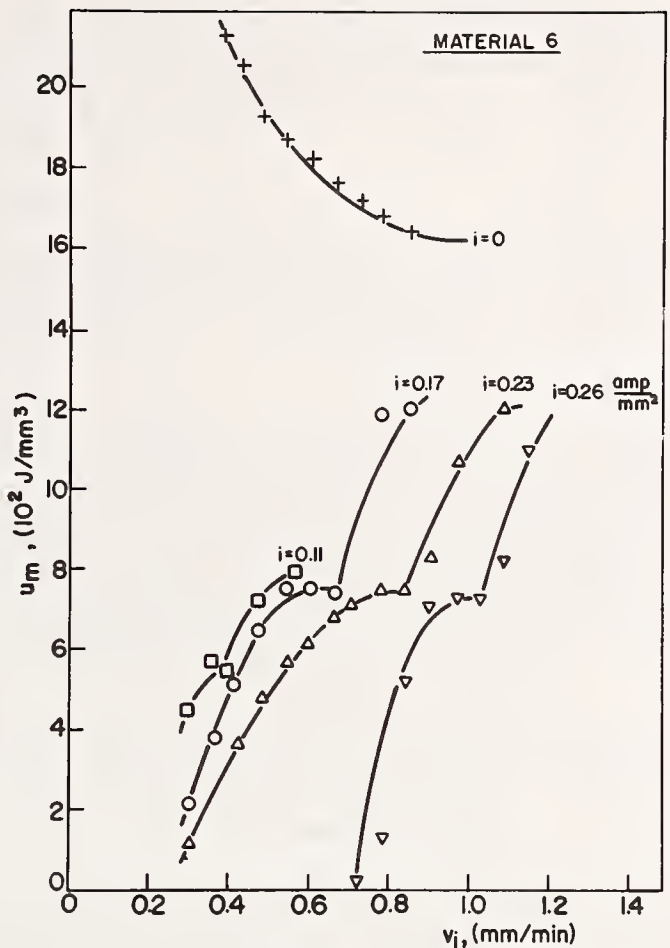
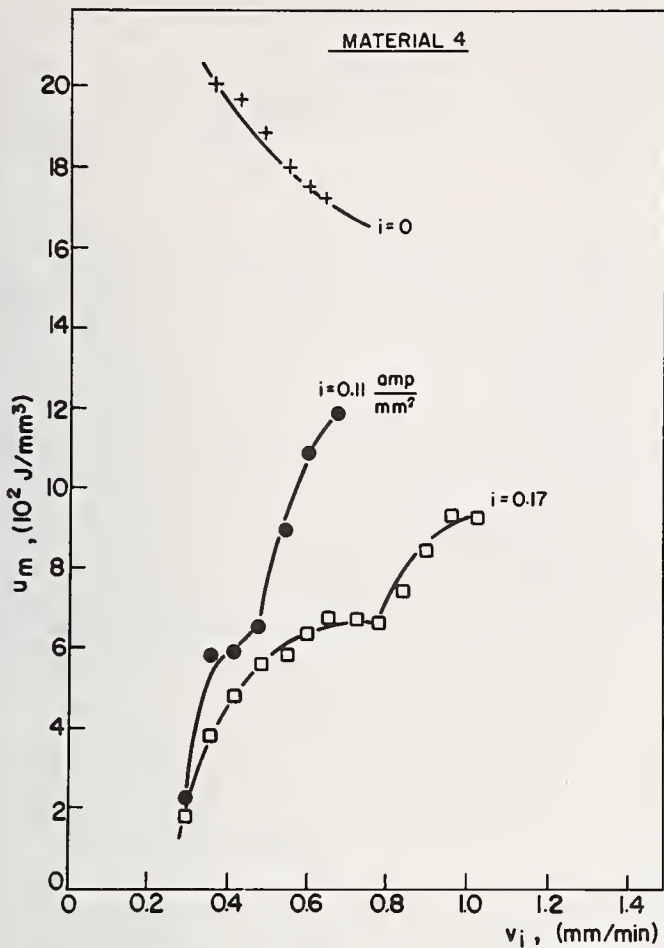


Figure 5. Specific mechanical energy versus infeed velocity at various current densities for Materials 4 and 6.

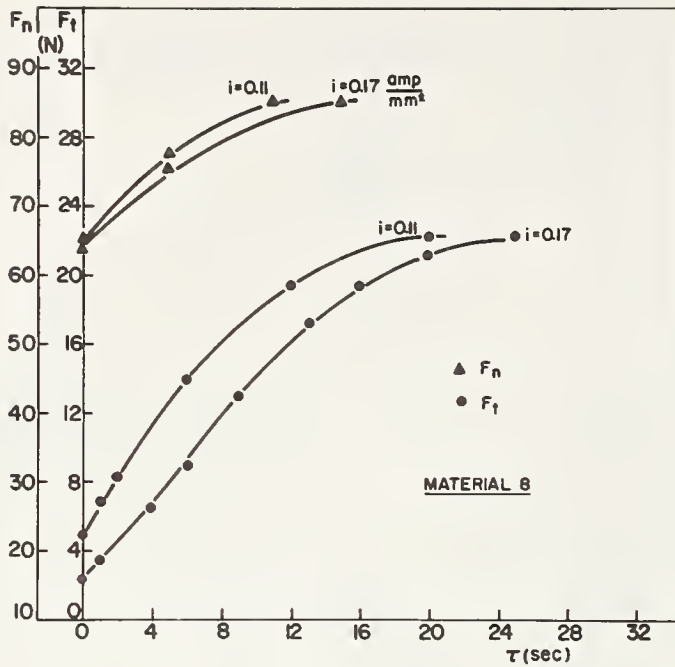
5. Surface Damage

Weakening of the surface due to ECG was determined from the transient grinding behavior after switching off the electrical current, as described above. An example of the force transient obtained after switching off the current is shown in figure 6a for one carbide at two current densities. Both the normal and tangential force components can be seen to increase with time after the start of the transient. Taking into account the elastic deflection of the grinding system as described above, the actual infeed velocity v_t during the transient and the actual depth removed t at any time τ during the transient were computed. The results corresponding to the transient in figure 6a are shown in figure 6b as a plot of v_t versus t . Here it can be seen that the actual infeed velocity drops abruptly from its initial steady state value due to increasing elastic deflection from the growing normal force. This is followed by a subsequent increase in v_t towards its steady state value v_i . The tangential grinding force results from figure 6a are also included in figure 6b.

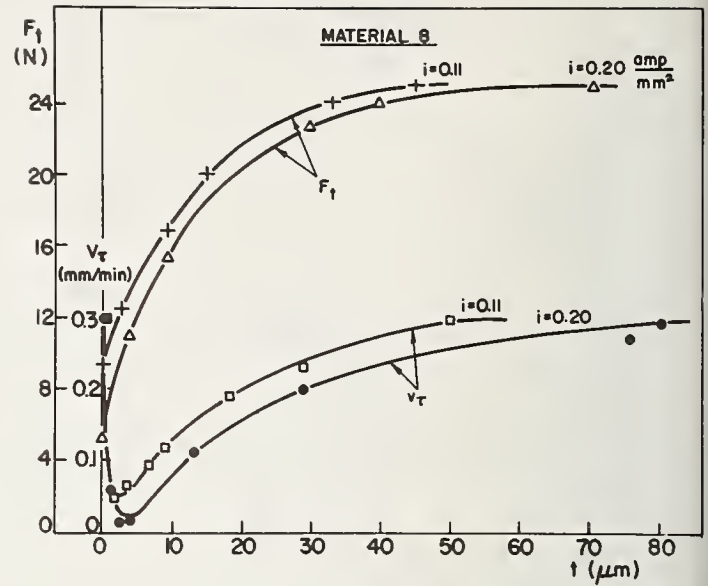
Surface damage caused by ECG is evaluated in terms of the specific grinding energy of the material in the surface layer. From results such as given in figure 6b, the specific grinding energy at depth t can be calculated as:

$$u = \frac{F_t V}{v_t A} \quad (9)$$

where the numerator is the grinding power and the denominator is the instantaneous removal rate. The relative weakness is defined as the ratio ϕ of the specific energy in the surface



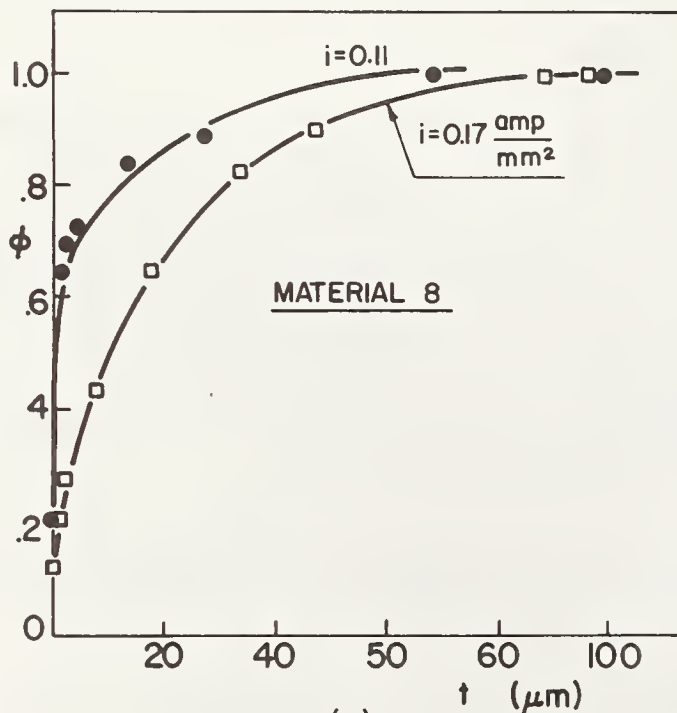
(a)



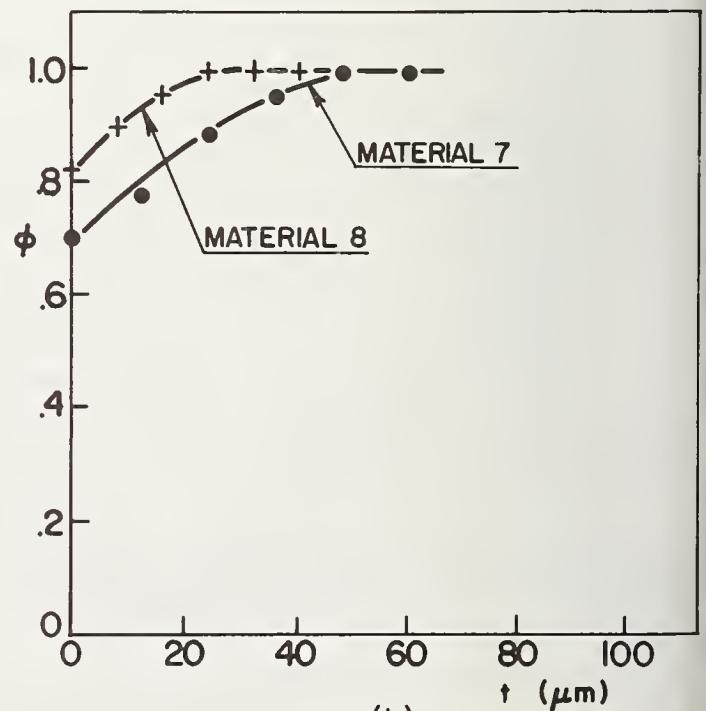
(b)

Figure 6. Results of grinding transient: (a) force components versus time after switching off current; (b) actual infeed velocity and tangential force component versus depth progressed.

layer after ECG to the normal specific energy for mechanical grinding of the same material with the same wheel in a separate series of tests. Damage to the surface by selective etching of cobalt should weaken the material and reduce its specific grinding energy leading to values of ϕ less than unity. The smaller the value of ϕ , the greater the damage. Results obtained in this way for ϕ are shown in figure 7 which includes those for the grinding transient in figure 6. It can be seen in figure 7a that ϕ increases from a very small value at



(a)



(b)

Figure 7. Weakening factor ϕ versus depth below finished surface: (a) $v_i = 0.30$ mm/min; (b) $v_i = 0.48$ mm/min with $i=0.20$ A/mm² for Material 7 and $i=0.17$ A/mm² for Material 8.

the surface to unity at a depth of approximately 50-100 μm , which is the thickness of the surface layer affected by ECG. With the larger current density, the weakness factor at the surface is smaller and the material is damaged to a greater depth. Similar results were obtained with other cemented carbides. With a faster infeed velocity in figure 7b, there is much less weakening at the surface and the ECG affected depth is shallower.

6. Discussion

The electrochemical analysis for WC-Co cermets shows that the initial etching velocity into the cobalt phase is much faster than into the WC phase. It is proposed that selective etching of the cobalt in this way weakens the cermet and facilitates mechanical removal during ECG.

In order for this selective etching phenomenon to occur, it is apparent that the infeed velocity of the ECG process must be slower than the initial etching velocity into the cobalt. If the infeed velocity exceeds this etching velocity, the electrochemical assistance should be much less effective. It may therefore be expected that the steep rise in mechanical power requirements beyond the discontinuities, such as seen in figures 4 and 5, may be due to the infeed velocity exceeding the initial etching velocity into the cobalt. In order to test this hypothesis, the infeed velocity v_i at the discontinuity was plotted versus the initial etching velocity v_{Co} given by eq. (4a) for all eight workpiece materials with various current densities. The results in figure 8 show these two velocities to be almost identical.

The particular effectiveness of ECG on WC-Co cemented carbides can be appreciated by

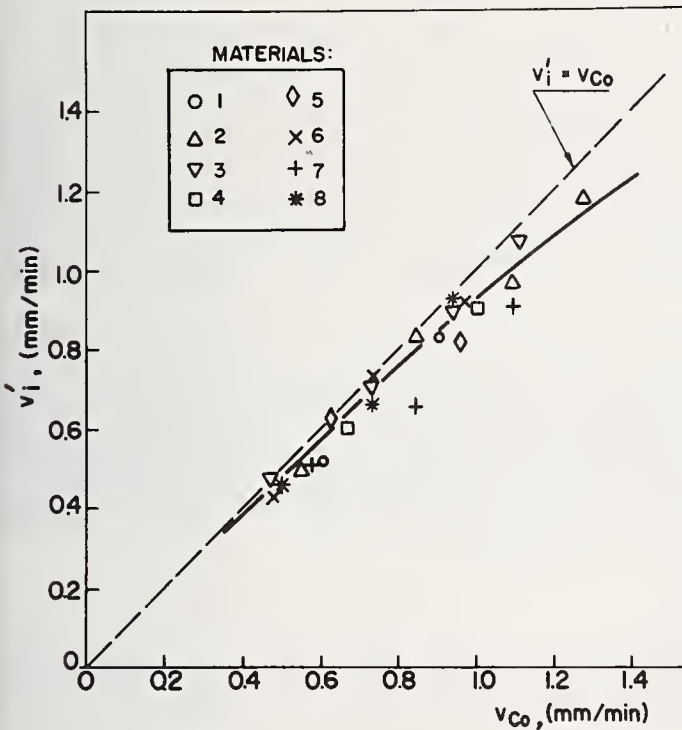


Figure 8. Infeed velocity at discontinuity versus initial etching velocity into cobalt.

applying a conventional type of analysis to the present results [4-6]. The conventional ECG analysis is based upon the assumption that electrochemical and mechanical removal proceed independently, so the total volumetric removal rate is given by:

$$Z = Z_e + Z_m \quad (10)$$

According to this assumption, the relationship between the mechanical power (or force) and mechanical removal rate is the same for both ECG and mechanical grinding with $i=0$. Therefore, for a given relationship between the power and the removal rate for mechanical grinding, the mechanical contribution Z_m during ECG can be estimated by measuring the mechanical power. With this result, the electrochemical efficiency during ECG can be obtained as:

$$\eta = \frac{Z - Z_m}{\alpha I} \quad (11)$$

where the numerator is the electrochemical removal rate obtained by subtracting the estimated Z_m from the total removal rate, and the denominator is the theoretical electrochemical rate according to Faraday's Laws (eqs. 2 and 3). Representative results for the efficiency are shown in figure 9 which were obtained from the results in figures 4 and 5 with $\alpha = \alpha^*$. In all cases, the computed efficiencies were found to exceed the theoretical limit $\eta = 1$.

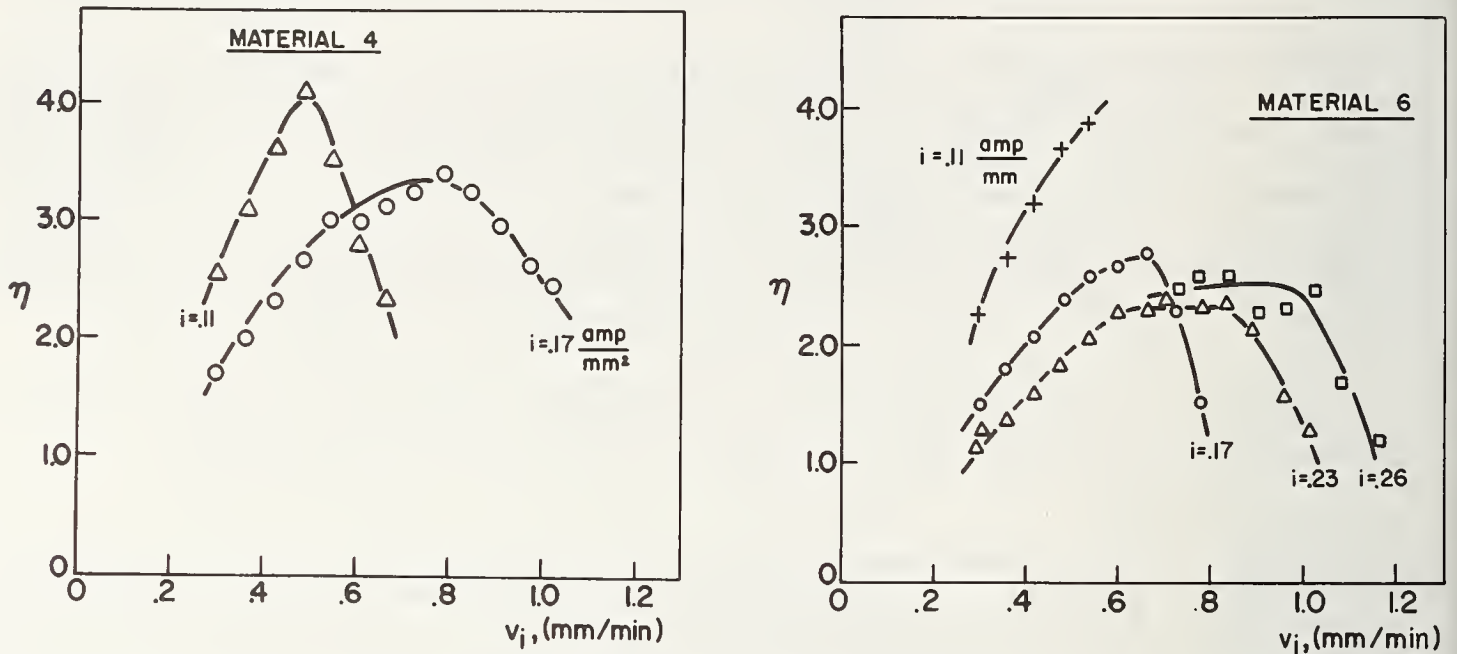


Figure 9. Calculated electrochemical efficiency versus infeed velocity at various current densities for Materials 4 and 6.

Such large calculated values for η are apparently due to selective electrochemical etching of cobalt which weakens the material, thereby reducing the mechanical grinding resistance of the cermets. The degree of weakening obtained in this way can be estimated by applying the conventional ECG analysis setting $\eta = 1$. The value of Z_m is now obtained in a different way by subtracting Z_e , given by eqs. (2) and (3) with $\alpha = \alpha^*$, from the total Z . The specific energy for only mechanical removal during ECG can be obtained as:

$$u = \frac{F_t V}{Z_m} \quad (12)$$

where the numerator is the power and the denominator is the mechanical removal rate. The effectiveness of electrochemical action in reducing the mechanical grinding resistance can be seen by comparing the value of u with specific energy u_0 for grinding with $i = 0$, the comparison being made at the same mechanical removal rate. The specific energy u_0 is the same as the specific mechanical energy u_m when $i = 0$. Representative results for u/u_0 are shown in figure 10 corresponding to those in figure 9. It can be seen that u/u_0 is much less than unity for those materials, especially with slower infeed velocities and larger current densities. Beyond the discontinuities, which correspond to those previously discussed, this ratio increases at a much faster rate toward unity as selective etching should no longer occur.

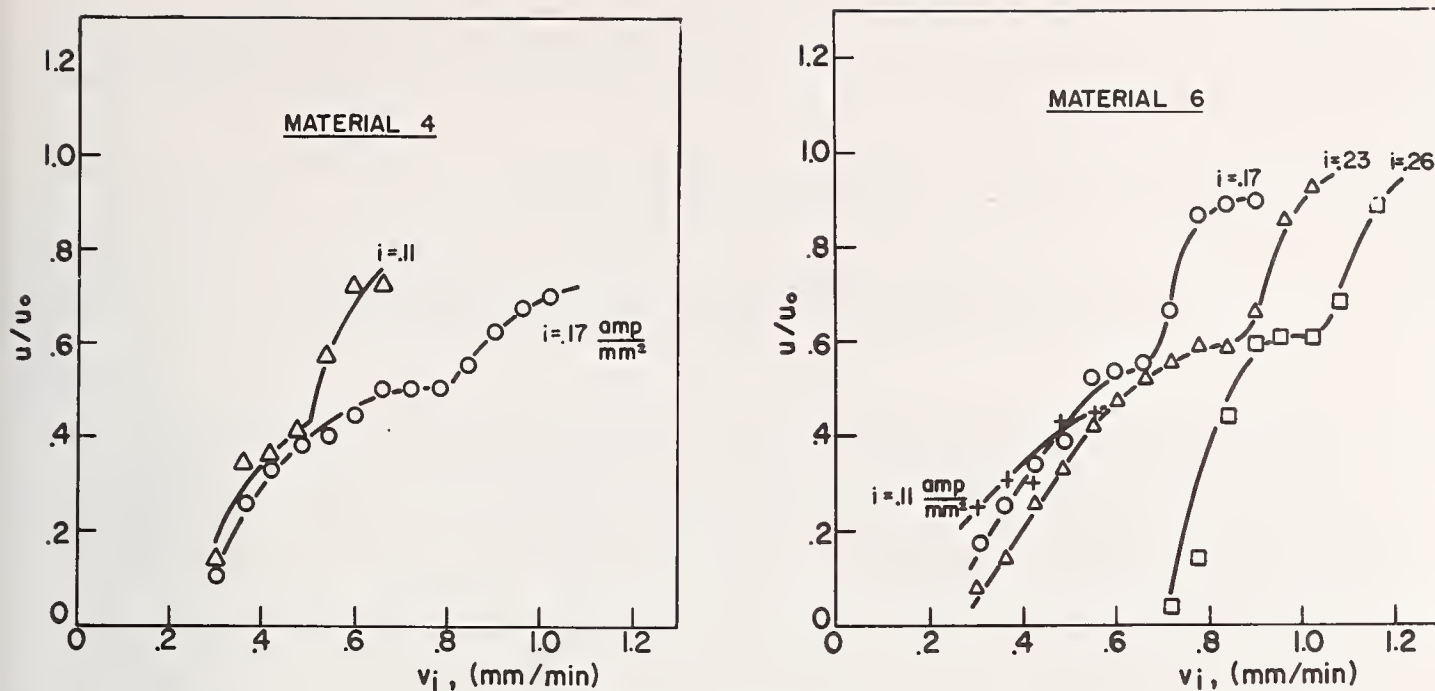


Figure 10. Ratio of specific grinding energy during ECG to specific grinding energy for $i=0$ versus infeed velocity at various current densities for Materials 4 and 6.

In the surface damage experiments, weakening in the finished surface layer was expressed by the parameter ϕ . Weakening of the material during ECG can be expressed by the ratio u/u_0 . Both ϕ and u/u_0 measure the same thing, namely, the reduction in mechanical grinding resistance due to selective electrochemical etching. Therefore, the value of ϕ at the surface ($t=0$) should be equivalent to u/u_0 for the same ECG conditions, as the state of the material below the surface immediately after switching off the electrical current should be the same as that of the material being mechanically ground away during ECG. Indeed, values of ϕ at $t=0$ were found to be very close to corresponding values of u/u_0 .

In summary, the effectiveness of ECG as a material removal process for WC-Co cermets can be attributed to selective electrochemical etching of the cobalt binder. However, this same effect is responsible for poor surface quality. One approach to practically utilize the ECG process would be to begin with a high current density for rough machining followed by a decrease in current density, even to zero, for final grinding to remove the damaged layer and to achieve the required surface integrity. The results of the present study provide a basis for designing appropriate ECG cycles.

References

- [1] Lvinger, R. and Malkin, S., Electrochemical grinding of WC-Co cemented carbides, ASME Paper No. 78/WA/PROD.-26, J. Eng. Ind., Trans. ASME, to appear.
- [2] Malkin, S. and Lvinger, R., Quantitative characterization of surface damage to WC-Cobalt composites by electrochemical grinding, *Wear* **51**, [1], 157-167 (1978).
- [3] Kreimer, G.S., *Strength of Hard Alloys*, p.2 (Consultants Bureau, New York, 1968).
- [4] Backer, W.R. and Dahlin, R.A., The effects of electrolytic assistance in peripheral grinding, ASME, Paper No. 60 WA-4, 1960.
- [5] Cole, R.R., An experimental investigation of the electrolytic grinding process, J. Eng. Ind., Trans. ASME, **83**, 194-201 (1961).
- [6] Kaczmarek, J. and Zachwieja, T., Investigation of the material removal rate by electrochemical grinding of cutting tool materials, *Int. J. Mach. Tool Des. Res.* **6**, [1], 1-13 (1966).



A NEW ULTRA-FINE POLISHING TECHNIQUE FOR SAPPHIRE

Tadaaki Sugita, Seiho Kawakami and Osamu Imanaka
Department of Precision Engineering, Kanazawa University
Kodatsuno, Kanazawa, Ishikawa 920, Japan

A new method of ultra-fine polishing for sapphire oriented with the polishing surface parallel to the (0001) plane is proposed, and the nature of the polished surface is analyzed. Experimental polishing is performed in water using a pin-on-disk machine with a tool disk made of sintered alumina. The sapphire is remarkably polished by friction action causing removal of the surface asperities; the polishing rate is significantly decreased as the smoothed surface is formed. Roughness of the polished surface is less than R_{max} of 200 Å. Behavior of friction is very stable in comparison with specimen worked in air. A high crystallographic integrity of the surface polished in water is confirmed from electron diffraction images. Analyses of the surface with x-ray photoelectron and ion microprobe mass spectrometers indicate the presence of a very thin hydrated layer which acts as an anti-friction agent preventing the damage of the nonhydrated substrate.

Key Words: Crystallographic integrity; electron diffraction images; hydrated layer; ion microprobe mass spectrometer; roughness; sapphire; ultra-fine polishing; water; x-ray photoelectron spectrometer.

1. Introduction

Exact requirements must be considered in the machining of ceramic materials which are to be used as high performance elements in the field of electronics, especially in the production of highly integrated semiconductor circuits. These are high geometrical accuracy, including an ultra-fine surface finish; crystallographic perfection of the worked surface without any damage such as lattice disorder; scratches and cracks; and freedom from chemical contamination which could be caused by the tool material, machining environment and/or chemical etchant. In general, most ceramic materials have been mechanically or chemically polished using a fine hard abrasive, like diamond, or chemical etchants. It is inevitable, however, that mechanical polishing is apt to leave scratches and damages on the polished surface and that chemical contamination occurs in chemical polishing.

In order to obtain such extremely superior surfaces, elastic emission machining using fine hard powder particles [1,2]¹, and mechanochemical polishing with chemically reactive powder particles [3,4] have been developed. These techniques should be considered as novel ultra-fine machining methods. In the elastic emission machining, the intent of the collisions of the fine powder particles with the material surface is to make the size of the stress field smaller than the distance between the pre-existing defects and to verify the feasibility of elastic fracture of the order of atomic size. In mechanochemical polishing, the machining mechanism is based on mechanochemical reactions at real contact points between the work piece and abrasive powder which are softer than the work piece, and easy removal of the chemical reaction compounds from the interface without any surface scratches and damages. These machining methods are expected to be useful for finishing hard electronic crystals.

On the other hand, Imanaka et al. [5,6] have newly developed a hydration polishing technique which is based on the chemical characteristics of a hydration phenomenon occurring by the action of water vapor molecules on the surface of the crystal to be polished. This method uses neither polishing powders nor chemical etchants. Hydrates formed on the activated surface are rubbed off by the friction of the polisher. If the hydration occurs only at the

¹Figures in brackets indicate the literature references at the end of this paper.

true points of contact between the work piece and the polisher, and if only the hydrates are removed from the work piece surface, this polishing method may fulfill the above mentioned exacting and severe requirements for a polished surface.

A new polishing technique to be presented in this paper also utilizes hydration polishing. It is based on the concept that the polished surface would be free from chemical contamination by the polisher material if the same material used as the work piece is selected for the polisher. Also, this polishing technique which removes only the hydrates formed at the real points of contact may be effective in avoiding various surface damages and making an ultra-fine polishing surface because the hydrates are relatively easily removed.

2. Experimental Procedure

Polishing equipment is shown in figure 1. In this figure, the (0001) plane of a Al_2O_3 single crystal (sapphire) is rubbed on a 80 mm diameter rotary disk made of high purity sintered alumina². The sapphire specimen is held at the end of a reciprocating lever with a normal load applied on top of the specimen. The reciprocating lever is attached to a square sliding shaft with a horizontal connecting pin which allows freedom for vertical movement. The rotary disk rotates at 140 r.p.m and the reciprocating lever moves back and forth at 43 cycles per min. Water is always directed on the rotary disk which is in a water tank. Rubbing tests in air are also performed with this machine without using water and keeping the surface of the disk to be dry. Friction forces due to the test environment are measured with strain gauges mounted on the reciprocating lever which remains stationary during such measurements.

The sapphire specimen had a diameter of 3 mm and was oriented with the (0001) basal plane parallel to the polishing face. It was prepared for the polishing test by grinding to a surface roughness of $1 \mu m$ (maximum height of irregularities). The removed volume and the removal rate by polishing was obtained from a change of diameter at the top of another conical specimen, which was only prepared for this test, with an apical angle of 120° . The variable contact pressure in the process of polishing was calculated from a change of the contact area as an average value.

The profile of the polished surface was obtained with a profilometer. The crystalline structure of the polished surface layer was estimated by comparing it with that of the fracture surface using electron diffraction equipment with an accelerating voltage of 100 KV. XPS data which provide information in regard to chemical shifts due to a property change of the material or to chemical contamination of the surface were obtained using an ESCA 650B photoelectron spectrometer, Du Pont, employing $Mg K\alpha$ exciting radiation. Binding energies were corrected to $C_{1S} = 285$ eV for the test samples. The instrument was calibrated by the $Au_{4f_{7/2}}$ peak with a binding energy of 84 eV. The measured binding energies are considered to be accurate to ± 0.3 eV. Elements and compounds in the extreme surface layer of one or two atomic order were detected with an ion microprobe mass spectrometer (Hitachi IMA-2 system, Japan). From these analyses the contaminant elements and compounds on the surface are further identified.

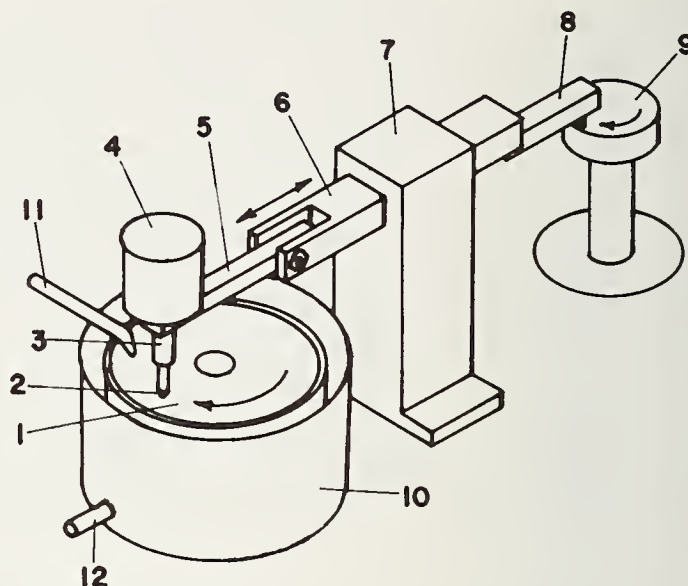


Figure 1. Polishing machine: 1, rotary tool disk(sintered alumina); 2, sapphire specimen; 3,specimen holder; 4, weight; 5, reciprocating lever; 6, sliding shaft; 7, slide bearing; 8, eccentric lever; 9, eccentric cam; 10, water tank; 11, inlet pipe of water; 12, outlet pipe of water.

²Si<30, Mg<10, Na<5, Ca<2, Fe<10, Cu<1 ppm

3. Results and Discussion

3.1 Polishing characteristics

As well known, adhesion occurs easily at the contact interface of two sliding solids when the material in the solids is the same. Therefore, in this study, it is necessary to take this behavior into account in the polishing experiments because the polisher and the work piece have the same structure and composition in order to avoid chemical contamination from the tool material. Figure 2 shows typical friction behaviors in the test environments of water and air. Although the friction obtained by sliding in water is very stable, the friction force in air on a dry disk is changeable and large because of adhesion. The crystalline structure of the surface rubbed in air, as described in following section, becomes disordered. The stable friction in water may be caused by the presence of a water film or hydrate; in the environment of water this friction may be due to shearing the layered aluminum hydroxides at the interface. Thus, the hydrates play the role of anti-friction agents between the solids in moving contact and, moreover, are swept away by the mechanical forces developed in polishing.

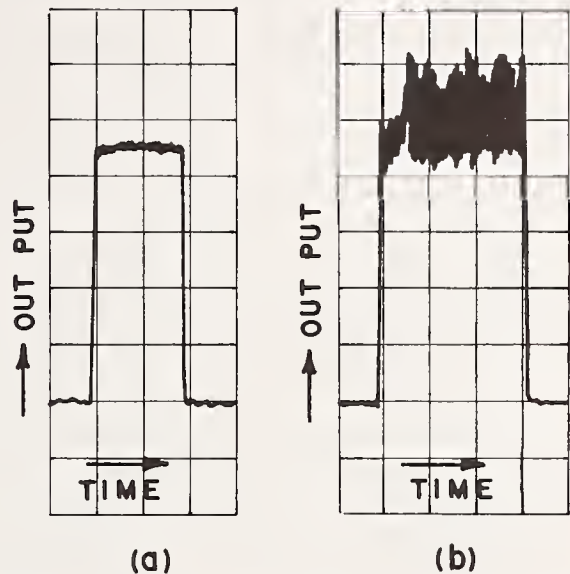


Figure 2. Behavior of friction (a) in water and (b) in air, under a normal load of 0.75 Kg.

Figure 3 shows an exponential relationship between the contact pressure calculated from the change of contact area and the rate of removal. This result was derived from the changes of the removed volume and the average contact pressure during rubbing in water under a load of 1 Kg. The contact pressure is continuously decreased with the increase of wear because the conical specimen with an apical angle of 120° was used in order to measure the removed volume. Sliding distances in Km are shown in parentheses on the figure. It is evident that the removal rate of specimen depends on the change of contact pressure. From the above result, it is suggested that in the polishing test, the polishing rate is relatively high until the asperities formed in the preliminary machining of the specimen are leveled. Also, because of a corresponding increase of contact area, a decrease of the local normal stress must occur which then remains constant. It is expected that the presence of the hydroxide film on the polished surface, because of the continually added water, protects the surface from the damages that would be introduced by the polisher under dry conditions.

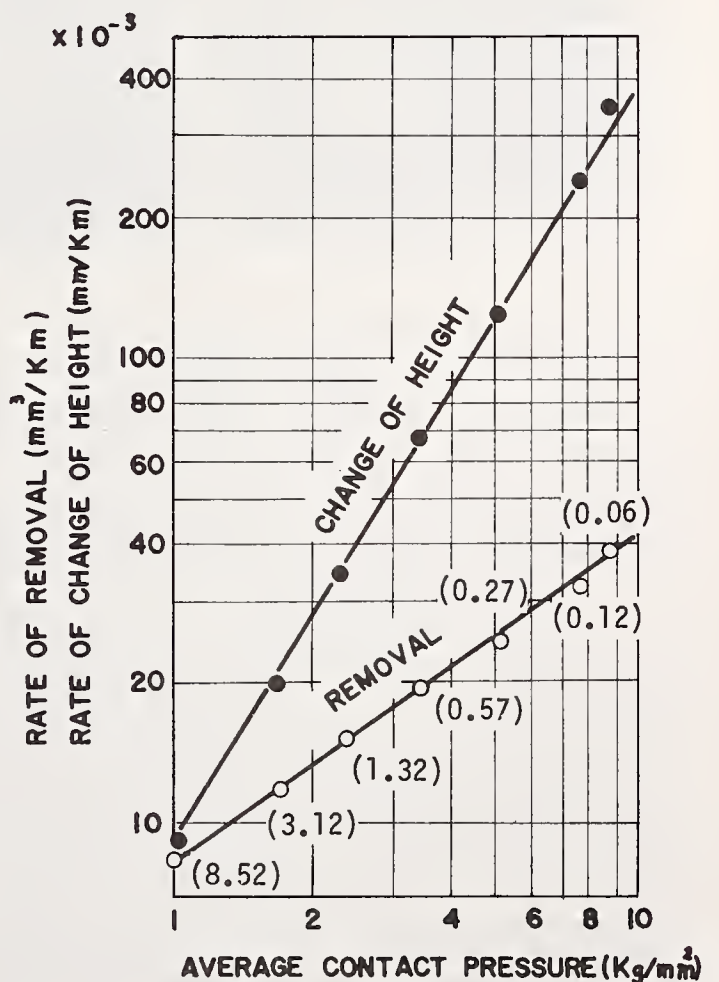


Figure 3. Relationship between rate of removal and contact pressure in rubbing test using a conical specimen with an apical angle of 120° under a load of 1 Kg. Sliding distances in Km are shown in parentheses.

3.2 Analysis of polished surfaces

The profile of a surface polished in water under a normal load of 0.5 Kg is shown in figure 4. The polishing roughness in water is less than R_{max} of 200 Å. In this case, if the measured length is limited to 5 μm , the roughness is approximately R_{max} of 100 Å or less. This result suggests that the thickness of the layered chemical reaction products at the contact interface is less than 100 Å. However, a wide area of the polished surface is difficult to realize because a very heavy load has to be applied to the machine for polishing. This problem will be solved by an improvement of the machine system. The roughness of surface polished in air is about 400 Å because of active adhesion.

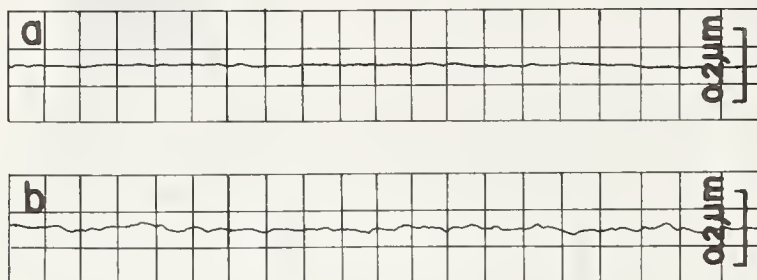


Figure 4. Profiles of polished surface: (a) in water and (b) in air. Load is 0.5 Kg.

Figure 5 shows electron diffraction images for three sapphire surfaces prepared by fracturing and polishing in water and air. The penetration depth of electrons is about 50 Å under the accelerated voltage of 100 KV. Kikuchi lines are clearly observed in the diffraction patterns for the fractured surface and the surface polished in water. This crystallograph evaluation indicates that surface damage, like lattice disorder and/or plastic deformation, were not introduced into the surface polished in water.

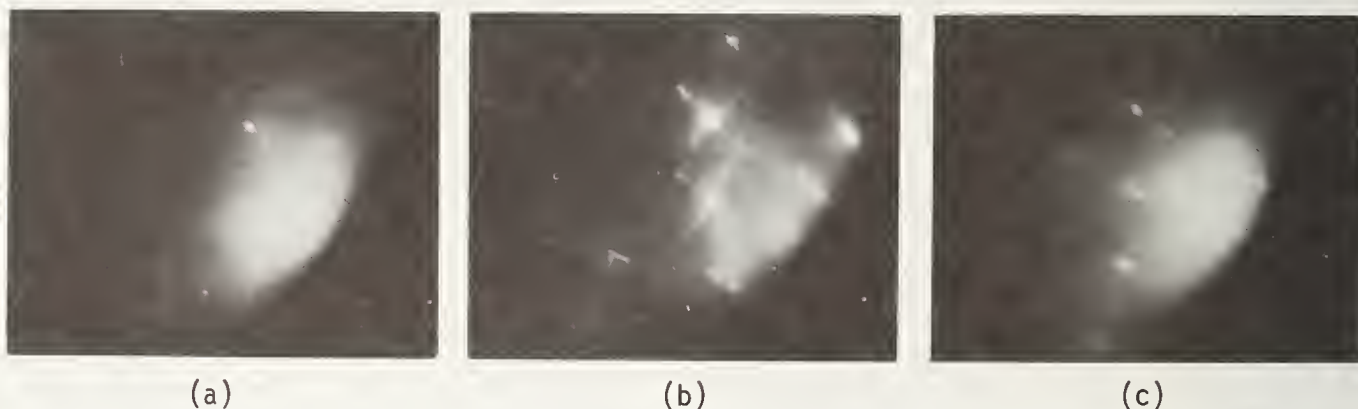


Figure 5. Electron diffraction images: (a) fractured surface, (b) polished surface in water, (c) rubbed surface in air.

Figure 6 shows wide scanned x-ray photoelectron spectra (XPS) for the three sapphire samples. The absolute intensities cannot be used for comparison because the amount of hydrocarbon deposited on the surface varied from sample to sample. The carbon (C_{1s}) electron energy of 285 eV is used to calibrate the spectra. C_{1s} is probably due to the hydrocarbon derived from the vacuum system in the x-ray photoelectron spectrometer. The test environment can easily introduce Na.

Figure 7 shows changes in the photoelectron spectra of Al_{2p} for the fractured surface and the surface polished in water before and after argon ion bombardment: 1 is before ion bombardment, and 2, 3, 4 are after ion bombardment for 10, 30 and 50 seconds, respectively. The corrected Al_{2p} binding energies for the treated sapphire samples and commercial aluminum hydrates are given in table 1. The table data indicate that these specimens are similar suggesting that the exposed fracture surface becomes hydrated and that the hydration layer is very thin since the rate of ion bombardment is approximately 10 Å/min. The chemical shift of about 1 eV in the specimen polished in air can be attributed to a disordered lattice near the surface which is assumed to exist according to the electron diffraction image shown in figure 6(c). The binding energy (75.1 eV) for Al_{2p} in the fractured sample is different from that (76.3 eV) measured by Lindsay et al. This difference may be due to the use of different calibration lines, such as the C_{1s} lines

Table 1. Binding energies of Al_{2p} electrons obtained from experimental surfaces of sapphire, and aluminum hydroxides.

Specimen	Binding energy(eV)	
Fractured surface	1	74.7
	2	74.6
	3	74.8
	4	75.1
Polished surface, in water, (in air)	1	74.3 (73.6)
	2	74.8 (74.7)
	3	74.8 (74.1)
	4	75.0 (74.0)
$\alpha-Al(OH)_3$	74.5	
$\alpha-AlO(OH)$	74.4	

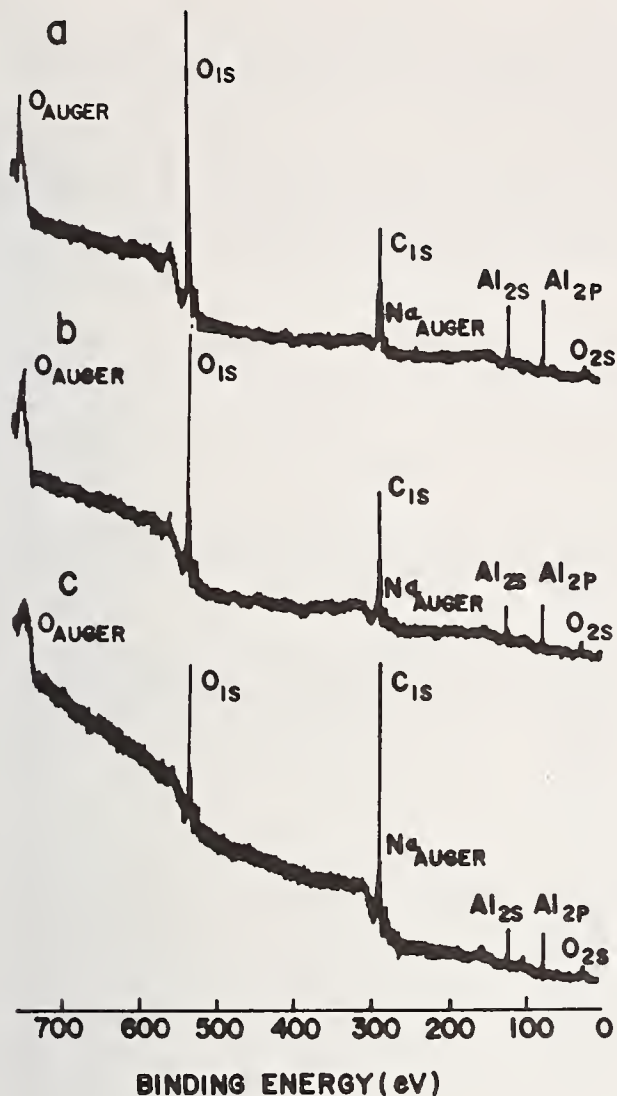


Figure 6. Wide scanned photoelectron spectra for the three sapphire samples used in figure 5: (a) fractured surface, (b) surface polished in water, (c) surface rubbed in air.

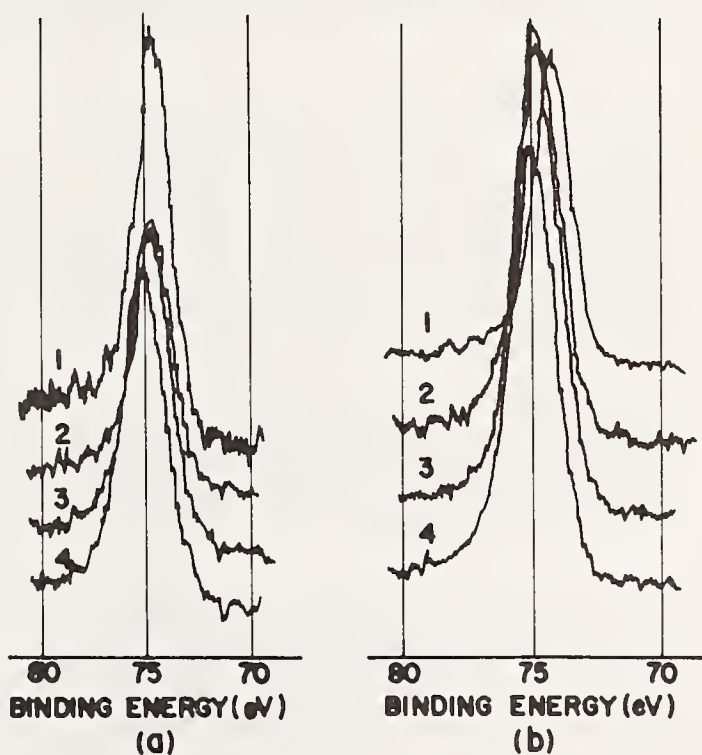


Figure 7. Changes in the photoelectron spectra of Al_{2p} for (a) fractured surface, and (b) the surface polished in water, before and after argon ion bombardment. 1 is before ion bombardment. 2, 3, 4 are after ion bombardment for 10, 30 and 50 seconds, respectively.

in this test and the Au_{4f} line in their test, or to different test materials. It has been shown that the C_{1s} electron line from a hydrocarbon contamination may shift as a function of the type of sample being examined [7], but the data in this analysis are comparable and can be used effectively to compare the test specimens. The hydroxides $\alpha-Al(OH)_3$ and $\alpha-AlO(OH)$ have layered structures with hydrogen bonds joining the layers with a difference in the degree of hydrogen bonding. From the data in table 1 it appears that the indicated hydrates on the surfaces are thin and removed in about 30 seconds of argon ion bombardment. Their structures could not be determined from the photoelectron spectra.

The ion microprobe mass spectrometer (IMA) is useful for analyzing the chemical composition of a surface. Figure 8 is an IMA spectrum of a surface polished in water. While argon gas ions are impinging on the surface at an extremely low current density and sputtering off surface atoms and molecules, the ionized fractions are analyzed with a mass spectrometer. The rate of removal by ion bombardment is 0.2 \AA/s . This spectrum was obtained within 2 min. after the analysis was begun. It indicates that the detected elements and compound units are within about 24 \AA of the surface layer. It is possible that the source of the chemical contaminants K, Na and Ca was the water³ used in polishing. However, the contamination markedly decreased 10 min. after the beginning of the analysis. The amount of aluminum hydroxides may be small as already indicated, but their existence is supported by the presence of the species AlH^+ and AlOH^+ .

4. Conclusions

An ultra-fine polishing technique for sapphire with the use of water^{was} developed, and the nature of the polished surface was analyzed with various surface analyses techniques. The experimental results are summarized as follows:

- (1) The polishing mechanism is due to hydration of the $\alpha\text{-Al}_2\text{O}_3$ surfaces and the mechanical removal of these hydrates without damaging the bulk structure resulting in the removal of the asperities which formed the initial contacts at the interface. The roughness of the polished surface is less than R_{max} of 200 \AA .
- (2) An undisturbed crystalline structure in the water polished surface layer and a damaged structure in the dry polished surface layer are confirmed by electron diffraction images.
- (3) Analyses of the surface of sapphire polished with water with x-ray photoelectron and ion microprobe mass spectrometers support the presence of a hydrated layer on the surface in the range of about $5 - 24 \text{ \AA}$.

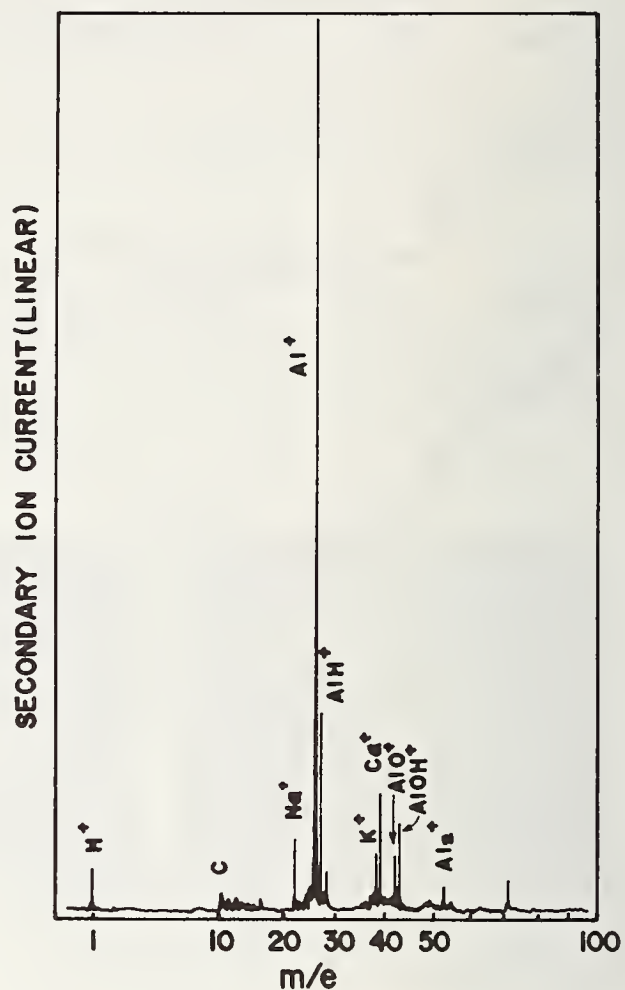


Figure 8. A spectrum for sapphire surface polished in water obtained by ion microprobe analysis; sputtering time, 2 min.

Acknowledgments

The authors express their appreciation to Professor J.A.Pask (Univ. of Calif.) for helpful discussions and advice and to K.Nishikawa for constructing the apparatus. The authors also are grateful to Dr. Y.Namba (Osaka Univ. Japan) for the ion microprobe analysis and to T. Wakabayashi for the x-ray photoelectron analyses.

³Si, Mg, Na, Ca and K were detected from the deposit after vaporizing the water.

References

- [1] Tsuwa, H. and Aketa, Y., Elastic emission machining as an ultra-fine finishing method, Proc. 1st. Inter. Conf. Prod. Engrg. (symposium), pp.33, Tokyo, August, 1974.
- [2] Mori, Y., Ikawa, N., Okuda, T. and Yamagata, K., Numerically controlled elastic emission machining, Tech. Repts. Osaka Univ. 26, [1301], 283 (1976).
- [3] Yasunaga, N., Obara, A. and Imanaka, O., Mechanochemical polishing of single crystals with soft powders, Proc. 1st. Inter. Conf. Prod. Engrg., pp.32, Tokyo, August, 1974.
- [4] Namba, Y. and Tsuwa, H., Ultra-fine finishing of sapphire single crystal, Proc. 27 General Assembly of CIRP, pp.1, New Delhi, August, 1977.
- [5] Okutomi, M. and Imanaka, O., Hydration polishing of sapphire-- A novel finishing technique using hydration phenomenon--, Bull. Japan Soc. Prec. Engrg., 10, [4], 156 (1976).
- [6] Okutomi, M. and Imanaka, O., A novel finishing technique using hydration phenomenon -- Hydration polishing of sapphire --, Proc. 27 General Assembly CIRP, pp. 79, New Delhi, August, 1977.
- [7] Lindsay, J.R., Rose, H.J., Swartz, Jr., W.E., Watt, Jr., P.H. and Rayburn, K.A., X-ray photoelectron spectra of aluminum oxides: Structural effects on the "Chemical shift", Appl. Spectroscopy, 27, [1], 1 (1973).



FINE POLISHING OF SAPPHIRE CRYSTALS

M. IKEDA, A. YAMADA, Y. KOKAJI, S. KIMURA

Electrotechnical Laboratory, MITI
Mukodaimachi, Tanashi, Tokyo 188, Japan

A new method for polishing sapphire crystals has been developed which is based on a chemical reaction at the contact area between surfaces of solids to be polished and a polishing disc. Special features of this method are as follows: (1) A scratch-free and smooth surface is produced on the basis of reaction between silicon oxide and alumina. (2) The worked layer left in a subsurface polished is so thin as not to be detected with a Berg-Barrett method. (3) Use of a rigid polishing disc results in a highly flat finished surface. (4) Since no abrasive particles are used, a clean working environment is maintained.

Key Words: Damaged layer; fine polishing; sapphire; silicon; solid state reaction; wear debris.

1. Introduction

Sapphire single crystal is one of important inorganic electronic materials, as substrates of semiconductor devices. Generally, surfaces of these materials to be used are polished with high geometrical accuracy without residual damage and strain. Many polishing techniques which produce the suitable surface have been studied mainly for semiconductor crystals.

These techniques are concerned with mechanical polishing by using fine, hard abrasives such as diamond, silicon carbide, alumina and plastic or elastic polishing sheets, which leave damaged layers on the finished surfaces. So a final treatments i.e. chemical or electrochemical etching are needed in order to remove such a worked layer at the expense of decreasing geometrical flatness of the surfaces.

The present polishing method is based on the chemical reactions at real contact areas between two surfaces of solids, that is, sapphire crystals worked and a polishing disc. This method can produce fine surfaces which are free of scratches and any damage and have high dimensional accuracy. This paper describes experimental results of the new surface finishing method of sapphire crystal and evaluations of polished surfaces.

2. Background of the polishing method

The concept of this method was derived from the fundamental experiment observing the wearing properties of alumina abrasives against silicon crystals. When a sapphire cone scratches a silicon crystal surface, it was found that the tip of the cone was worn away, and chemical reaction was proved with the X-ray diffraction analysis of the wear debris in sliding tests.

2.1. Scratching Test

Silicon-sapphire contact was examined by scratching test which was performed with a light load scratching equipment specially designed (fig. 1), on a clean surface of silicon single crystal wafer (111) with a sapphire cone whose tip radius was about 5 μm . Then tracks on the wafer and the tip of the cone were observed with a SEM.

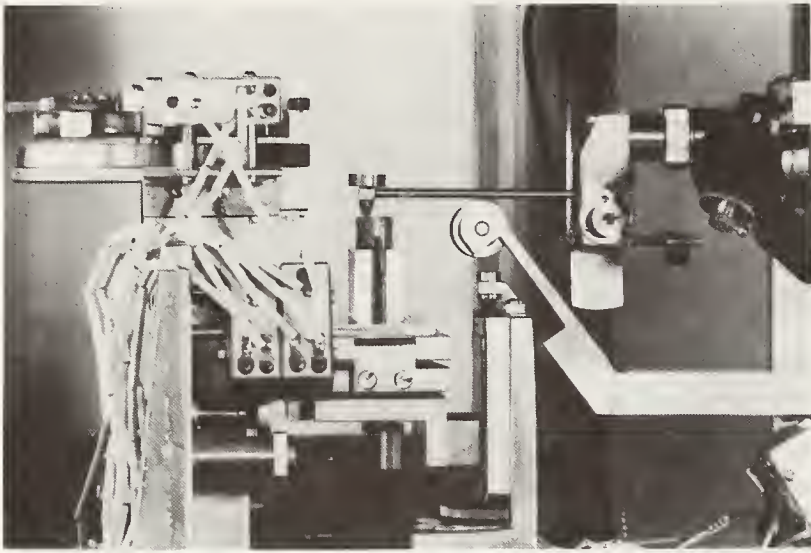


Fig. #1. Scratching apparatus.

Intersecting tracks shown in figure 2 have been formed by scratching in two directions at a speed of 30 mm/min under 7 gram weight load. A series of numerals noted on the diagram in the figure present the order of scratching. Inside of tracks are pellicular and squeezing out scarcely occurs, unlike the tracks scratched with a diamond stylus for example. Broadening of track width with the advancement of scratching length means wear of the sapphire cone. The tip of the cone worn away by scratching test extending through 140 mm (fig. 2) has been flattened to a relatively smooth plane leaving some shallow grooves oriented in scratching direction.

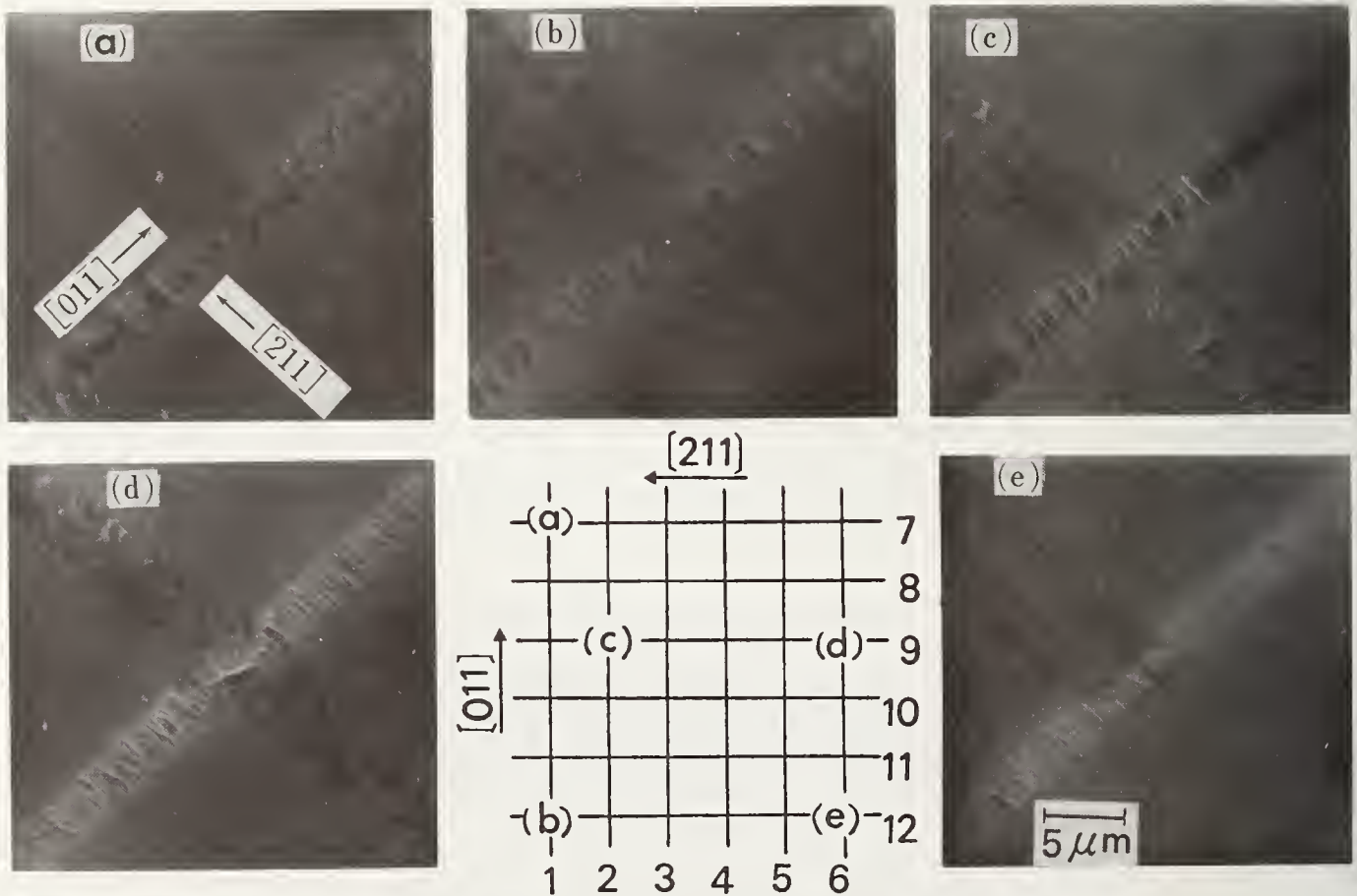


Fig. #2. Tracks on Si crystal surface scratched with a sapphire cone.

Such wear of sapphire seems not to be anticipated because of hardness difference between sapphire and silicon. The mean contact pressure at the interface between a silicon surface and a sapphire cone is estimated to be several million kg/cm^2 , and the temperature at the contact point is considered reasonably high enough because of adiabatic compression and frictional heat occurrence. Thus, the condition is considered to be enough for solid state reaction between two materials.

Anyhow, it is apparently expected that sapphire crystals are able to be polished by silicon without any abrasives.

2.2 Sliding Test

In order to obtain some explanation about the wear of the sapphire cone mentioned above, a sliding test was carried out.

2.2.1 Experimental Set-up

A sapphire specimen (the apparent contacting area $5 \times 4 \text{ mm}^2$) was slid on the end face of a silicon crystal rod (diameter 35 mm, length 70 mm) mounted to a chuck of a lathe. Mean sliding speed was about 7790 mm/min at which chipping of both materials didn't occur. Loads of 250, 600, 1000 g were selected, and they were set dynamically by compression of a coil spring.

The orientation of the silicon rod was [111] and the sapphire specimen surface was about 5° from (0001), which is known to wear most easily (fig. 3). Structure of the wear debris, collected on a sheet of paper, was investigated by X-ray diffraction analysis.



Fig. #3. Tip of sapphire cone.

2.2.2 An analysis of the debris

Figure 4 shows a part of an X-ray diffraction chart ($\text{Cu-K}\alpha$) of the debris produced under 1000 g load. Within the angle of diffraction from 28° to 29° , apparently two peaks are seen. The right one is known as a diffraction peak from a silicon (111) surface, but the left one is a diffraction neither from silicon nor sapphire. It is considered that tiny silicon chips fractured during sliding gave the diffraction peak from silicon [111], since both the occurrence of fragments and the height of the diffraction peak decreases with decreasing load.

The diffraction curve plotted by a scaler method in the angle from 28° to 29° is shown in figure 5. In this case, the debris produced under 600 g was used. Intensity of X-ray diffracted is extremely weak, so the measured values fluctuate a little. No peak is observed at the angle of diffraction from silicon (111), but a peak is seen at the lower diffraction angle which is considered to be diffraction from Kyanite ($\text{Al}_2\text{O}_3 \cdot \text{SiO}_2$). This means that the chemical reaction occurs between SiO_2 covering the silicon crystal surface and Al_2O_3 , and another material; that is, Kyanite is produced during a sliding experiment. Kyanite is generally known as an intermediate reaction product between SiO_2 and Al_2O_3 under relatively gentle conditions.

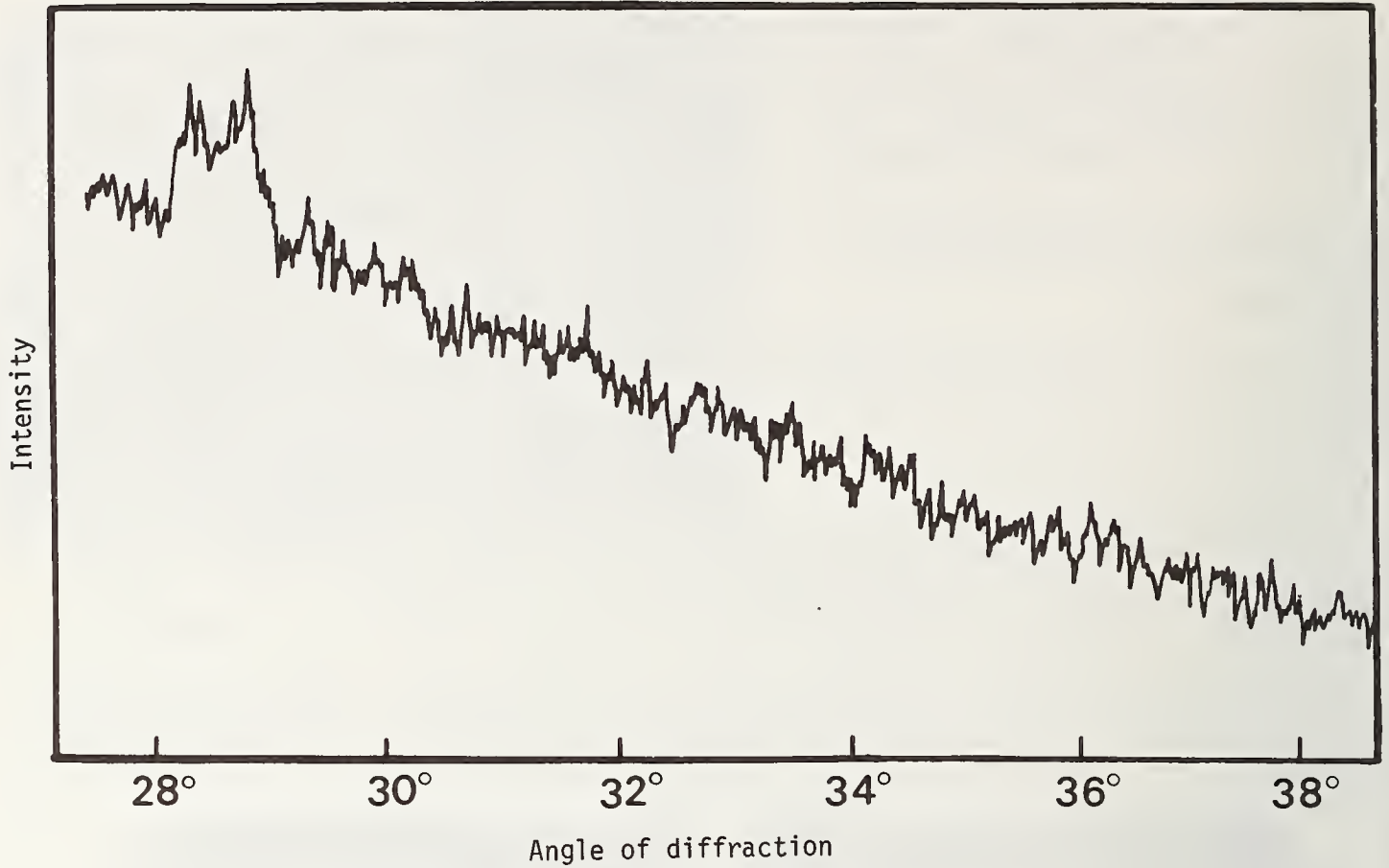


Fig. #4. X-ray diffraction chart of wear debris.

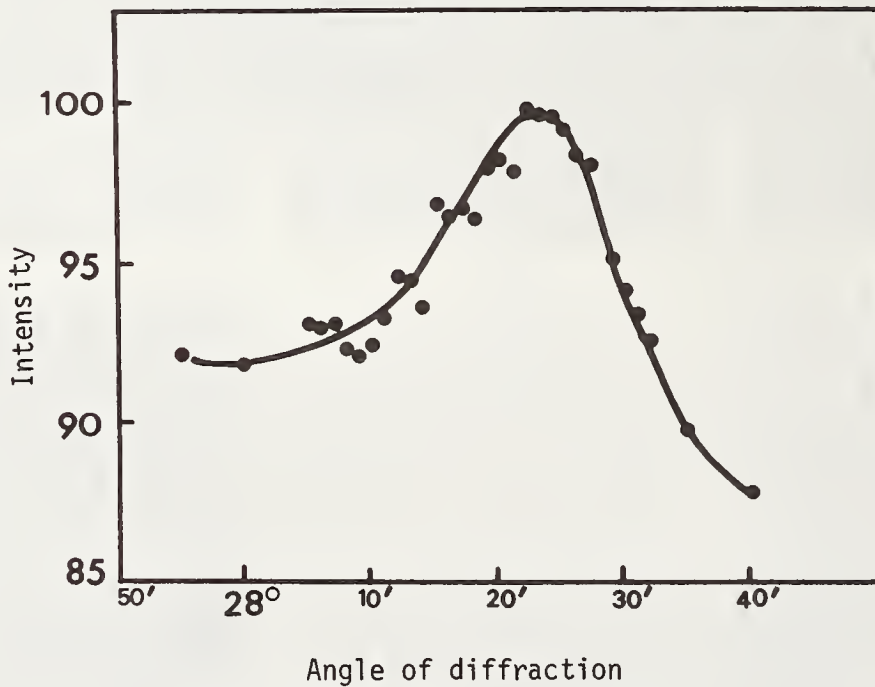


Fig. #5. X-ray diffraction curve of wear debris.

The X-ray diffraction chart also suggests that the amount of crystalline reaction product in the wear debris is extremely small; the major portion of wear debris appears to be amorphous.

3. Polishing Experiment

3.1 Experimental Set-up

Two kinds of polishing discs using silicon were provided for polishing experiments. One of them has been formed as follows, silicon crystals sliced in random orientations were plastered like a mosaic on a steel plate and ground into a flat surface. The other is a similar disc of bonded silicon powder which was crushed from single crystals into about 80 mesh. The disc is set on a polishing machine of particular design and is rotated (fig. 6). Three sapphire specimens (10x10x1.5 mm) mounted to a holder are pressed to the disc and loaded with weight; the holder is forced to rotate on the polishing disc through a synthetic rubber belt driven by a motor. Water (5 cm³/min) was poured into the disc in order to eliminate the refuse formed during polishing. Surfaces of sapphire specimens to be polished were sorted into two classes, one of which was lapped with GC #2000 abrasives and another was ground with a wheel composed of diamond pellets of 1200 mesh. The experimental conditions are described in figure 7.



Fig. #6. Polishing apparatus.

Specimen	Sapphire crystal (1 $\bar{1}$ 02) 10×10×1.5mm
Surface to be polished	Lapped (GC#2000), Ground with diamond pellets (4 μ m)
Polishing disc	Si crystal sliced, Si powder
Polishing time	1~10 hours
Polishing pressure	150~800 g/cm ²
Polishing fluid	Water, 2~5cm ³ /min
Rotating speed	Disc; 100rpm, Specimens; 18rpm

Fig. 7. Experimental conditions.

3.2 Experimental Results and Discussions

3.2.1 Stock Removal

Stock removal of sapphire crystal increases naturally with polishing time as seen in figure 8. The progress rate of the removal is relatively large at early stage of the polishing and it decreases gradually with the lapse of time. It is supposed that the descent of the removal rate results from reduction of the activity at contacting interface with advance of solid state reaction. It must be also taken into consideration that the polishing load at the interface is mitigated owing to increase of real contact area.

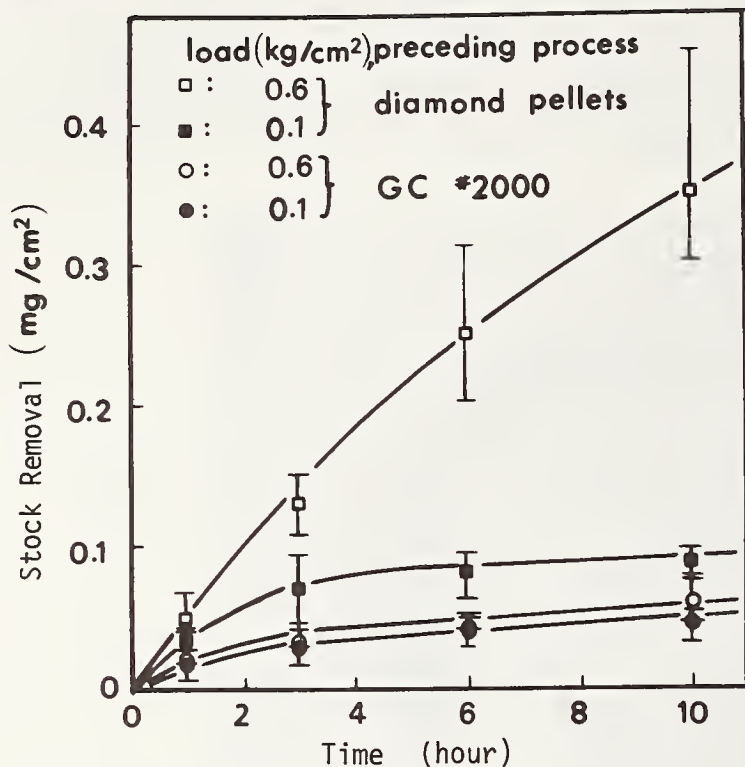


Fig. 8. Stock removal variation with time.

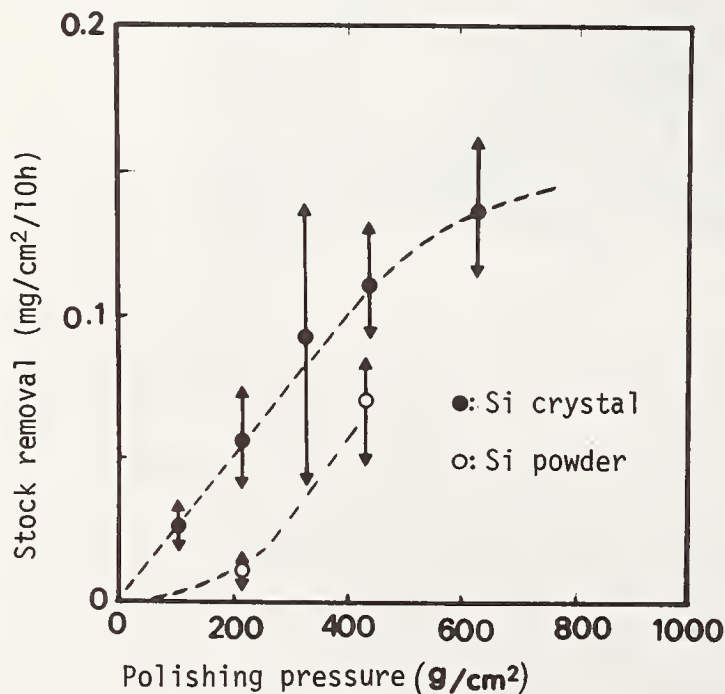


Fig. 9. Pressure dependence of stock removal.

The difference of stock removal among data from different conditions confirms this effect, that is, the surface roughness of specimens ground previously with diamond pellets is about five times as large as those lapped with GC#2000 abrasives. Though the influence of polishing pressure is comparatively large for specimens processed with diamond pellets, it is not so large for the specimens lapped with GC abrasives. This difference is due to sur-

face properties depending on the processes. When the disc made of sliced silicon crystals is used, the stock removal of the sapphire crystal increases in proportion to the polishing pressure below about 500 g/cm^2 and the influence of the pressure lessens gradually at higher pressure (fig. 9). In the case of polishing with the disc formed of silicon powder, stock removal is very small in the lower range of polishing pressure. Under the conditions that the pressure exceeds about 200 g/cm^2 , the influence of the pressure appears to be similar to the mosaic disc. Therefore, it is possible to polish sapphire crystals with any form of silicon. The reason why the stock removal concerning the powder disc is small at low pressure may be that the binder prevents the silicon particles from sufficiently contacting the specimen surfaces.

3.2.2 Characteristics of Polished Surfaces

The surface roughness of sapphire specimens polished for 10 hours under a pressure of 600 g/cm^2 on the sliced-silicon disc was at most, $0.02 \mu\text{m } R_{\text{max}}$. On the polished surface (fig. 10), there are relatively few scratch marks, in contrast to surfaces polished with diamond paste. This contrast shows that the polishing mechanism of the present method is quite different from that of the conventional one with diamond paste that is based on mechanically scraping off. This inference is supported by X-ray Berg-Barrett photographs shown in figure 11 where serious defects are not observed on the polished surface, that is there is little strain present in the crystallographic lattice beneath the surface of the specimen.



Fig. #10. Surface feature of sapphire crystal polished.



Fig. #11 Berg-Barrett photograph of sapphire crystal polished; (a) with pellon cloth and diamond paste; (b) by present method.

Geometrical flatness of the surface polished by present method is excellent and surface curvature at the edge of samples is very small relative to that of samples polished with diamond paste and pella cloth, as seen in figure 12. The ESCA spectra of polished surfaces prove that any reaction product or diffused silicon are not a bit left (fig 13) by comparison with an etched surface.

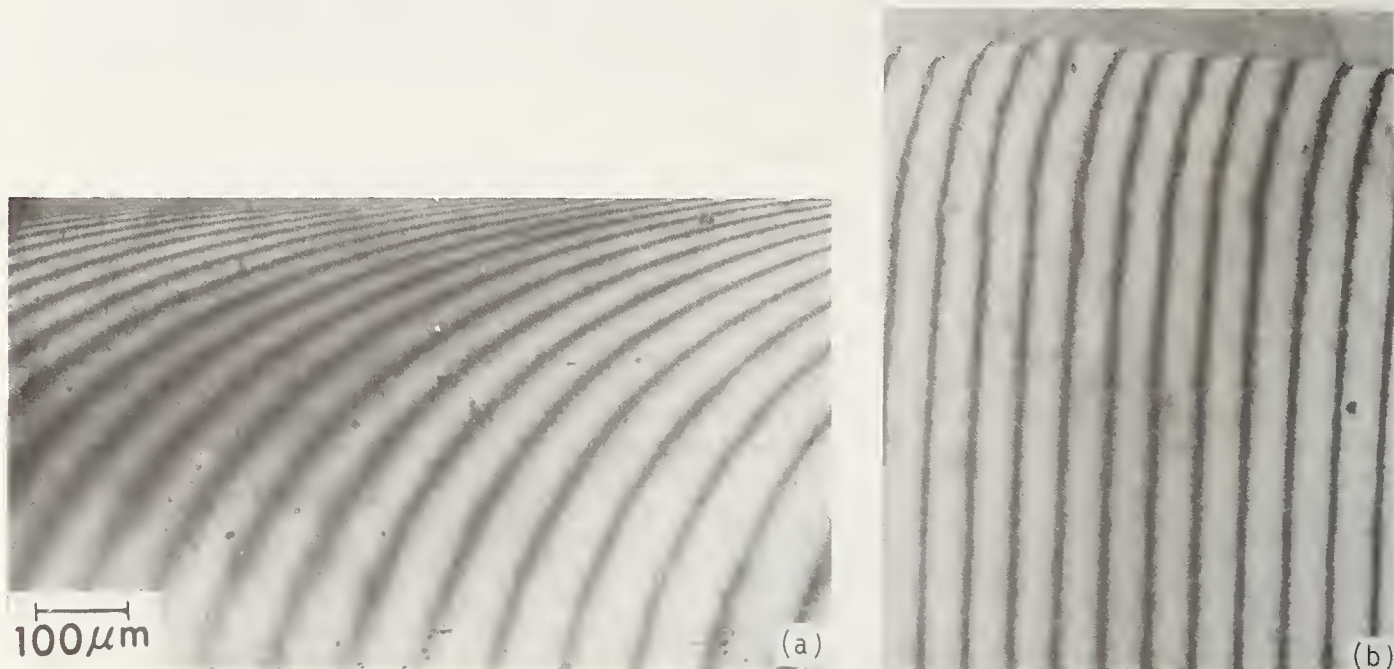


Fig. #12. Interferometric pattern of specimen fringe; (a) with pella cloth and diamond; (b) by present method.

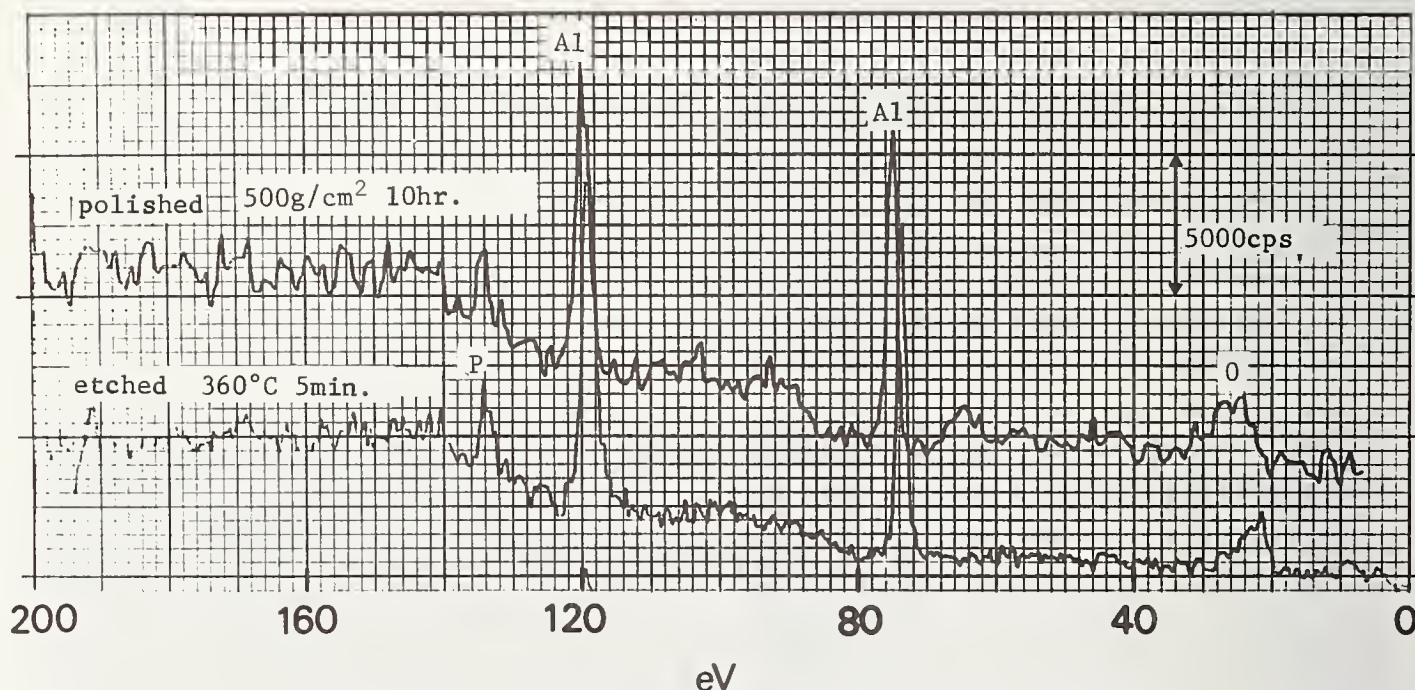


Fig. #13. ESCA spectra on sapphire crystal surface.

4. Conclusions

Experiments show that sapphire crystals are able to be polished with only silicon and water and the method produces sufficiently good surfaces.

(1) By this method which is fundamentally based on the solid state reaction between two surfaces of SiO_2 and Al_2O_3 , a scratch-free and smooth surface (R_{max} 0.02 μm) is produced.

(2) The worked layer left in the subsurface is hardly detected by X-ray Berg-Barrett method.

(3) The use of rigid polishing discs produces a flat surface without curvature at the edge of specimens.

(4) No employment of any abrasives keeps the working environment clean and is convenient to automatic polishing.

In order to apply this method to practical use several problems should be solved, that is, to find out the most suitable surface state to be polished, to keep up the activity of the polishing disc, to prevent the occurrence of cracks at the edge of surface during machining and to increase the stock removal.

Authors wish to thank Mr. M. Okutomi for help of surface observation by ESCA.

References

Main articles presented recently,

Ikeda, M., et al., Polishing of silicon crystals with an elastic wheel, *Annals of CIRP* 23 (1) 103-104 (1974).

Nhar van Huyne, et al., Studies on electrolytic buffing on single crystal silicon, *Seimitsu-kikai*, 43 (6) 650-655 (1977).

Miyake, S., et al., Ferrites precision grinding, *ibid*, 43 (12) 1415-1420 (1977).

Nhar van Huyne, et al. Studies on electrolytic buffing of ferrite single crystal, *ibid*, 43 (4) 421-426 (1977).

Mori, Y., et al., Elastic emission machining, *High Accuracy*, 6 (1) 32-39 (1975), 3 (2) 55-67 (1978).

Yasunaga, N., et al., Mechanochemical polishing of single crystals with soft powders, *Proceedings 1st ICPE*, 32-37 (1974).

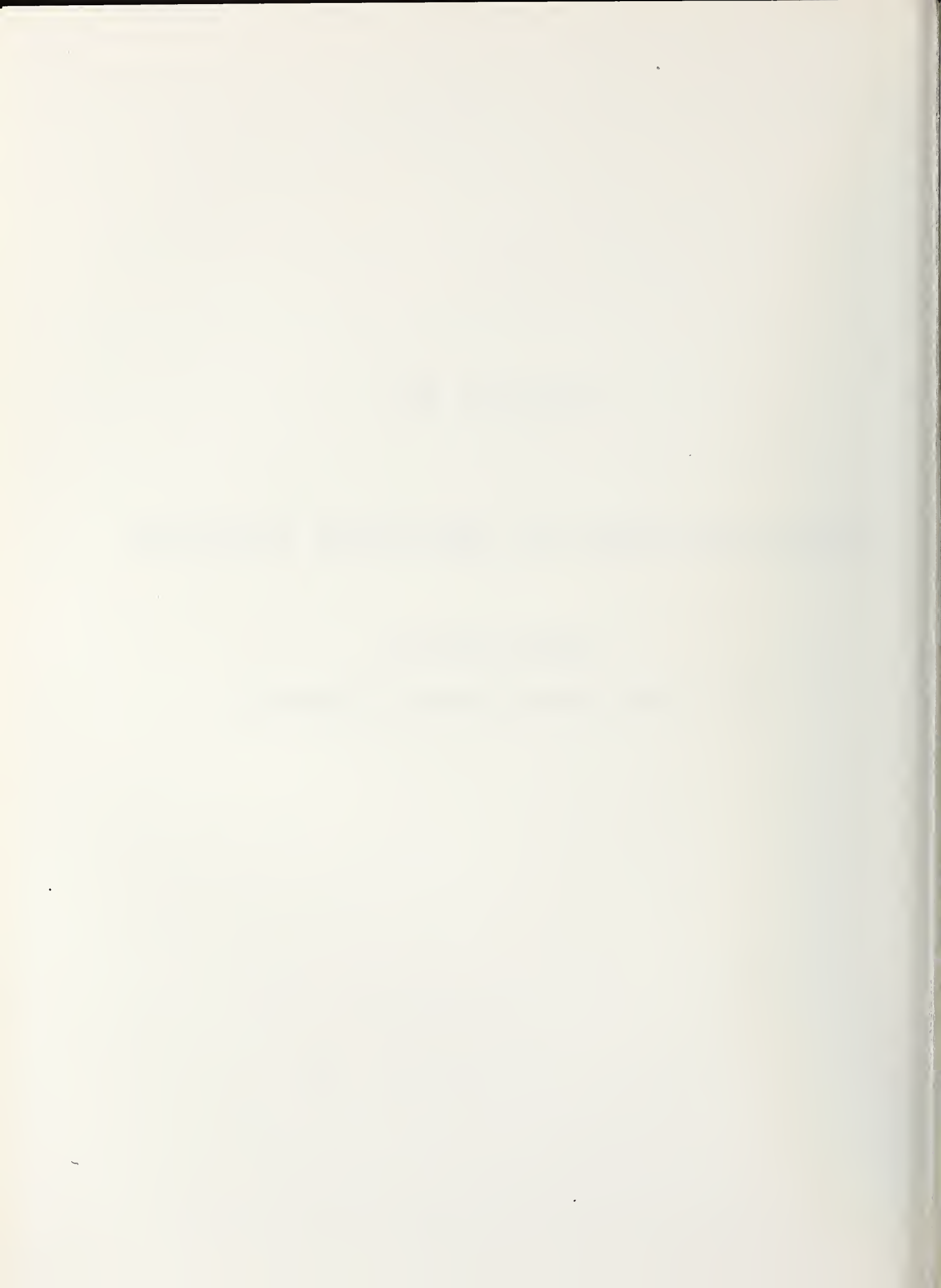


Session III

Characterization of Machined Surfaces

Session Chairman

B. J. Hockey, National Bureau of Standards



SURFACE CHARACTERIZATION OF OPTICAL MATERIALS¹

H. E. Bennett

Michelson Laboratory, Physics Division
Naval Weapons Center, China Lake, CA 93555

A complete description of the surfaces of optical materials involves their topography, presence of particulates, crystallinity and degree of disorder at the surface, impurities in the vicinity of the surface, stoichiometry at the surface, and surface films. The most direct method for observing small surface imperfections is by using electron or optical microscopy. Often transmission electron microscopy using replication has too high a lateral resolution and too low a depth resolution to investigate imperfections of greatest optical interest. Surprisingly, optical interference microscopy has one to two orders of magnitude higher depth resolution than electron microscopy, and techniques such as differential interference contrast, sometimes called Nomarski microscopy, are extremely useful in evaluating surfaces qualitatively. For quantitative results, stylus techniques and interferometry using fringes of equal chromatic order are very useful and give results in good agreement with those obtained by scattered light measurements. Total integrated scattering provides a simple noncontact method for determining the rms height of surface irregularities and may be applied in various surface roughness determinations. Evaluating the roughness of ball bearings is one example.

Surface impurities and stoichiometry at the surface also affect the performance of optical materials. Impurity atoms in concentrations as low as 0.001 monolayer can be detected using Auger spectroscopy. There is a danger however, of disturbing the surface with the high energy electrons required to produce the Auger electrons unless very low electron currents are used. This problem is alleviated by using electron spectroscopy for chemical analysis (ESCA), which depends on photoemission induced by x-ray or vacuum ultraviolet irradiation rather than on electron bombardment. ESCA is also more sensitive to molecular forces than is Auger spectroscopy, so that compounds as well as the atomic constituents can often be detected. Even more sensitive is secondary ion mass spectroscopy. In many cases, surface impurity levels in the 10^{-6} range can be detected using this technique. Surface films also affect the optical properties of materials, often significantly. Their growth can be monitored using ellipsometry, which is insensitive to roughness introduced by the film and is sensitive to changes in average film thickness of a fraction of a monolayer. A new surface evaluation technique being developed is high fluence diagnostics and multithreshold analysis. Most of the techniques discussed are applicable to nonoptical surfaces as well as optical surfaces, and should be used more widely in analyses of surfaces produced by ceramic machining.

Key Words: Auger spectroscopy; corrosion films; ESCA; impurities; microroughness; optical microscopy; polishing defects; scattered light; SIMS; stylus instruments.

¹Work supported by the Naval Air Systems Command, Office of Naval Research, and the Department of Energy.

1. Introduction

Optical surfaces when viewed from the vantage point of common machine shop tolerances are virtually perfect. For example, the flatness of a good $\lambda/4$ optical surface is typically within $0.15 \mu\text{m}$ ($6 \mu\text{in}$) and with more care $0.015 \mu\text{m}$ surfaces can be achieved. The surface roughness of typical optical surfaces is $0.0025 \mu\text{m}$ ($0.1 \mu\text{in}$) rms and values as low as $0.0005 \mu\text{m}$ have been achieved. These values are orders of magnitude smaller than those usually dealt with in machine shop practice, although with the advent of diamond-turning procedures utilizing air bearings they can now be approached using precision machining techniques. Historically optical surfaces have been generated by pitch polishing on machines which are not nearly as accurate as the finished component. The fact that optical surfaces can be produced at all is thus most remarkable and a tribute to the ingenuity of the optician.

A complete description of the surface of an optical material involves its topography, crystallinity and degree of disorder at the surface, impurities in the vicinity of the surface, stoichiometry at the surface, and surface films. Topography of optical surfaces may be divided into long-range deviations from the desired surface, which is referred to as optical figure and is often determined interferometrically, and shorter range imperfections. These short-range imperfections may again be divided into (1) macroscopic imperfections such as scratches, cracks, voids, or bumps and (2) micro-irregularities only a few ten of angstroms in height which cover all well-polished optical surfaces. Optical figure is important since it determines the resolving power of an optical train and also the intensity of light which can be focused at the focal spot of an optical system [1]². The short-range surface imperfections, together with surface particulates, determine the fraction of the incident light which is scattered or, in some cases, absorbed by the surface [2]. They may also be important in nonoptical applications. For example, macroirregularities such as cracks can have a significant effect on the strength of brittle materials. Surface irregularities can also affect the wear properties of surfaces in mechanical contact such as bearings and ways.

In this paper we will first discuss techniques for measuring the surface topography of optical surfaces and implications of these techniques for non optical applications. We will then discuss the detection of surface impurities, stoichiometry, and lattice disorder induced by the surface finishing process. Finally, we will discuss the presence of thin films at the surface and their detection.

2. Surface topography

The topography of an optical surface may be divided into two categories: short-range and long-range. The long-range deviations from an ideal surface, i.e., surface figure, are usually determined either interferometrically, as illustrated in figure 1(a), or by measuring diffraction effects. They can be established with uncertainties as low as $\lambda/80$ to $\lambda/100$ in the best cases (λ is the visible wavelength used in the tests, usually $0.6 \mu\text{m}$ or $24 \mu\text{in}$). Figure 1(a) shows an interference measurement of a good diamond-turned optical surface. Shorter range imperfections in the surface are less commonly measured quantitatively. For optical surfaces used in the visible and ultraviolet regions of the spectrum microirregularities usually contribute most to scattered light, whereas macroscopic irregularities and particulates are the determining topographic features causing scattering in the infrared. All can be readily detected using optical or electron microscopy. Figure 1(b) shows the copper surface whose optical figure was shown in figure 1(a) as viewed using a differential interference contrast (DIC), i.e., Nomarski, microscope. The grooves in this machined surface are only a few hundredths of a micro-

²Figures in brackets indicate the literature references at the end of this paper.

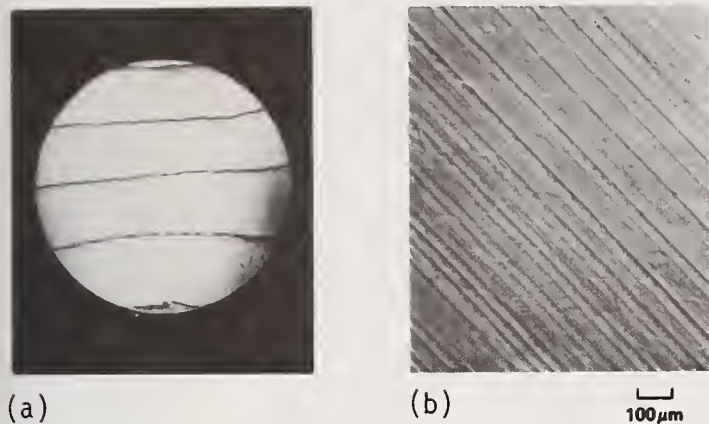
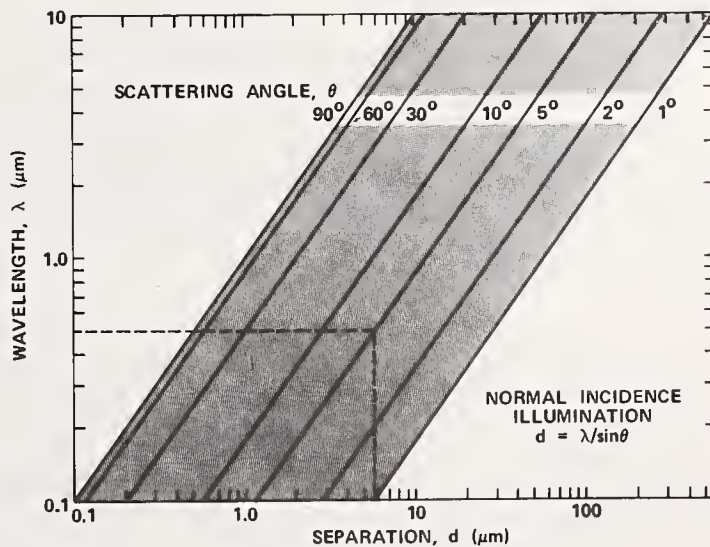


Figure 1. Zygo (Fizeau) interferogram and Normarski micrograph of a diamond-turned copper sample having an excellent figure and low scattering (from ref. 2).

meter in height and would be invisible in an ordinary microscope. The fact that they can be readily observed using an interference microscope causes a curious problem. Such grooves do not appear on conventionally polished optical surfaces and might be cause to reject diamond-turned surfaces for optical applications. A closer investigation, however, shows that these grooves have such a wide spacing that light scattered by them is very close to the specular direction, as illustrated in figure 2, and thus does not affect the optical performance of the surface significantly. At the other extreme, irregularities separated by less than a few tenths of a micrometer (i.e., 20 μin or less) which are regularly spaced will not contribute to scattered light either, since the scattering angle, as seen in figure 2, would be more than 90°. The light averages over such closely spaced irregularities and the sputtered silver film whose micrography is shown on the left in figure 3 will scatter no larger a fraction of the reflected light than the uncoated quartz surface seen on the right. Similarly, the scratch is too narrow to affect optical performance significantly, although it is easily seen using the electron microscope. Electron microscopy, although a very powerful tool in many areas of science, often has too high a lateral resolution and inadequate height sensitivity

Figure 2. Nomogram giving separation of surface features (spatial wavelengths) that produce scattering at a particular angle and wavelength. The dashed lines are an illustrative example (from ref. 3).



to be of great use in optical surface analysis. A comparison of the lateral resolution and height sensitivity of stereo electron microscopy and that obtainable by stylus and interferometric techniques [3] is given in table 1. Scanning electron microscopy has much lower sensitivity than conventional electron microscopy, which has poorer sensitivity to heights than interferometric or stylus techniques. In most investigations of optical surfaces these latter techniques are thus found to be the most useful. Descriptions of interferometric techniques for surface evaluation using fringes of equal chromatic order (FECO) are found in the literature [5,6]. Stylus techniques

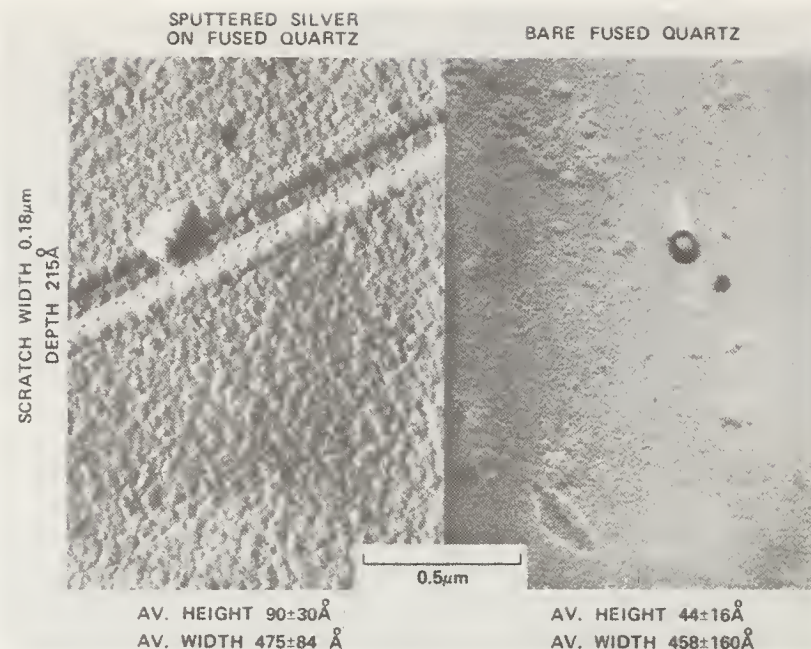


Figure 3. Transmission electron micrographs of surface replicas used in stereo electron microscopy [4]. (a) Sputtered silver film on fused quartz, and (b) bare fused quartz. Average heights and widths of surface features are given.

Table 1. Comparison of statistical methods (from ref. 3).

Instrument	Height sensitivity	Lateral resolution	Maximum length
FECO interferometer	$\sim 3 \text{ \AA}$ rms	$\sim 2.0 \text{ } \mu\text{m}$	1 mm
Talystep profilometer	$\sim 1 \text{ \AA}$ rms	$\sim 0.1 \text{ } \mu\text{m}$	2 mm
Stereo microscopy	$\pm 20 \text{ \AA}$	$\sim 5 \text{ \AA}$	$\sim 1 \text{ } \mu\text{m}$

are equally powerful but are often abused. In order to prevent inelastic deformation of the surface by the stylus, extremely light loadings are required [7]. If loadings in the range of a milligram or less are used, it is possible to study the surfaces of materials even as soft as KCl without introducing scratches [8].

Both microirregularities and more localized nonuniformities such as scratches or cracks can be studied interferometrically or by stylus techniques. Figure 4 shows cracks observed in forged KCl windows when grain boundaries were not removed prior to final forging, as reported by Anderson and Bennett [9]. Such imperfections introduce non-Gaussian height distribution statistics for optical surfaces. In most cases, however, the primary sources of roughness are the microirregularities, and the height distribution function is Gaussian to an excellent approximation [6]. In such cases it is possible to unambiguously specify the microtopography of an optical surface by giving its rms roughness. The range of rms roughnesses found at Michelson Laboratory over the years for various optically polished materials [3] is given in figure 5.

A complete description of an optically polished surface contains both its height distribution function and its autocovariance function [2]. The fraction of the incident light which is scattered into all angles by an optical surface depends almost entirely on its rms roughness, whereas the angle into which it is scattered depends on the autocovariance function [7]. A

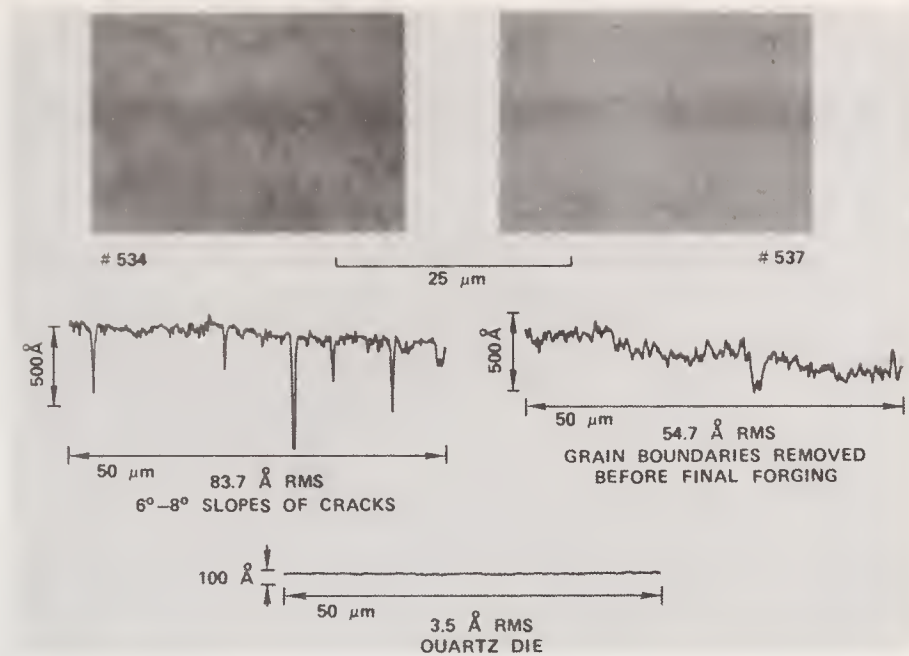


Figure 4. Surface finish on areas of forged KCl windows with and without grain boundary removal before final forging. The bottom trace is the surface finish of the die used to forge the two windows (from ref. 9).

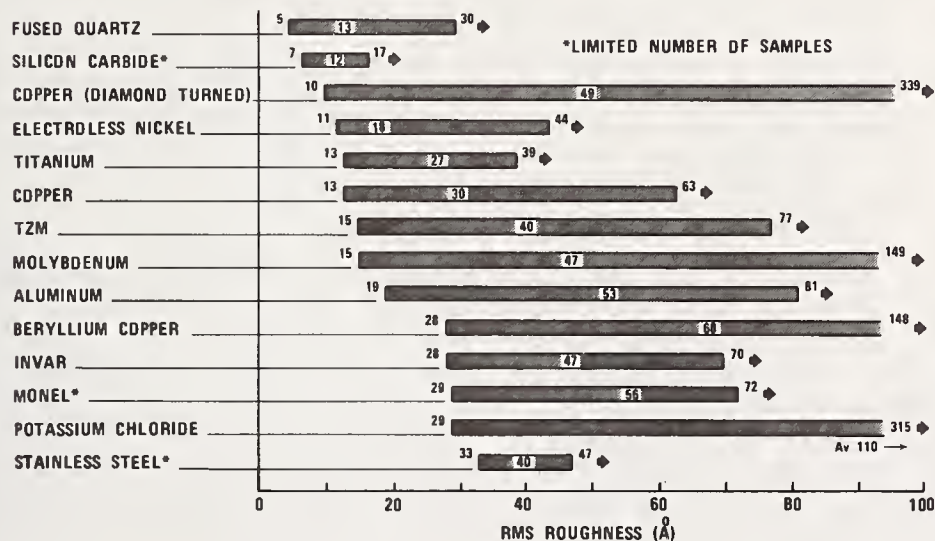


Figure 5. Average rms roughnesses and range of values measured for optical surfaces, as determined from total integrated scattering, interferometric, and stylus measurements (from ref. 3).

simple noncontact method for evaluating surface roughness is thus to measure the total amount of light scattered from it. Such a measurement is often called total integrated scatter (TIS) measurement. Angular scattering measurements, which make it possible to determine the bidirectional reflectance distribution function (BRDF) of the optical surface, are also useful for detecting particulates or other contaminants on an optical surface [10]. If the height distribution function of the surface irregularities is Gaussian and the rms roughness δ is much smaller than the wavelength λ , the relation between the TIS and δ is [2]

$$TIS = (4\pi\delta/\lambda)^2 \quad (1)$$

For typical optical surfaces this relationship holds accurately in the visible and ultraviolet region of the spectrum and begins to deviate only in the infrared [2], as illustrated in figure 6. The deviation is thought to occur because scattering from the microirregularities becomes so small in the infrared that particulates and macroscopic irregularities, whose scattering properties are independent of wavelength, begin to dominate. If the surface microirregularities are somewhat larger, eq. (1) holds in the infrared also, as has been demonstrated for ground surfaces [11].

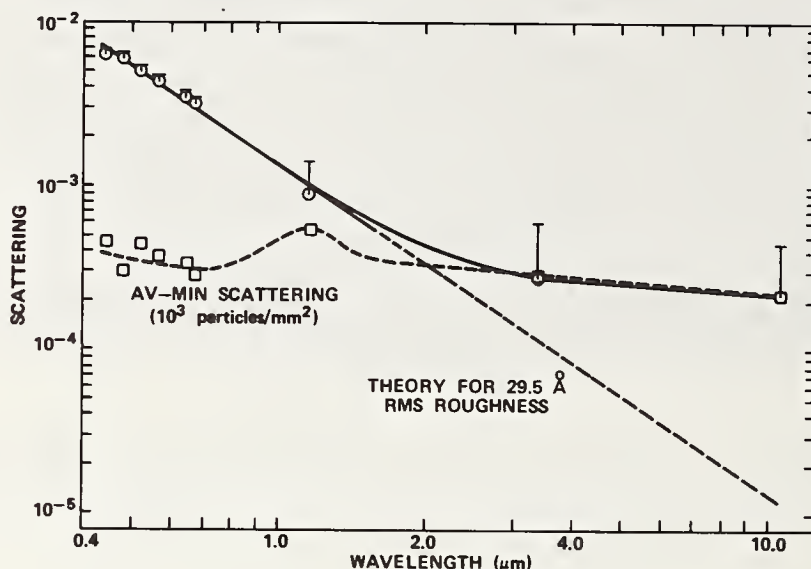


Figure 6. Scattering from an aluminized polished dense flint glass mirror. The diagonal line gives the contribution predicted for microirregularity scattering (eq. (1)) by a 29.5 Å rms roughness surface. Circles indicate the minimum scattering observed, and the bars and squares the difference between the average and minimum scattering levels observed at several points on the surface (from ref. 2).

Since for surfaces with Gaussian height distribution functions there is a unique relation between the rms roughness of the surface and the amount of light scattered from it, light scattering provides a very convenient tool for evaluating surface roughness quantitatively. Figure 7 shows an instrument for making scattering measurements in either reflection or transmission [12]; the optical diagram is given in figure 8. Scattering plots in reflection and transmission made with this instrument in the visible and in the infrared are shown in figure 9 [12]. If a single reflecting surface is measured, such data can be used to determine the surface microroughness.

If average microroughness is the primary object of the scattering measurement, a much simpler arrangement than that shown in figure 8 can be used and the light itself can do the averaging. A possible schematic diagram for such an instrument [14] is shown in figure 10. The light beam from a point source or a coherent source such as a laser is expanded to cover a significant area of the surface to be tested. Light which is specularly reflected falls on a detector; the variation in signal is a measure of the scattered light and hence of the surface roughness. To improve sensitivity, if required, both the specular signal and the scattered light could be recorded. Such a system could be used to evaluate cylindrical or spherical surfaces such as roller bearings or ball bearings as well as flat surfaces, and should be particularly useful as an evaluation technique for production samples. For example, one may visualize a setup for checking the surface roughness of ball bearings in which balls roll down a track and come to rest with the lower part of the ball projecting through a hole. The light reflected from this projecting part of the ball to the detector causes a signal which either indicates accept or

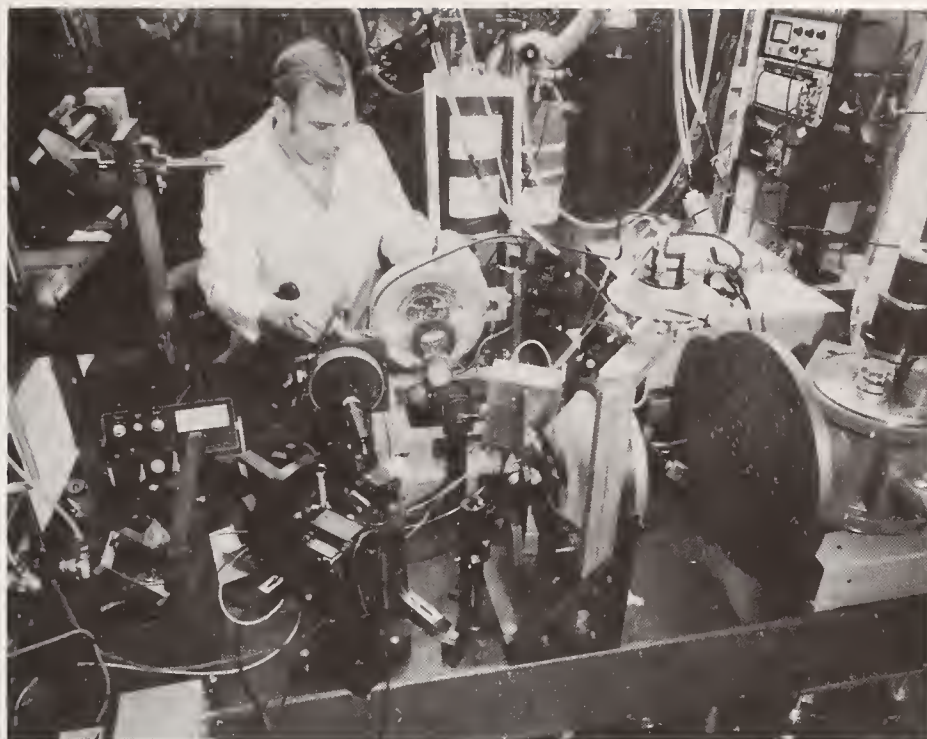


Figure 7. Photograph of the Optical Evaluation Facility used for making total integrated scattering measurements in either reflection or transmission.

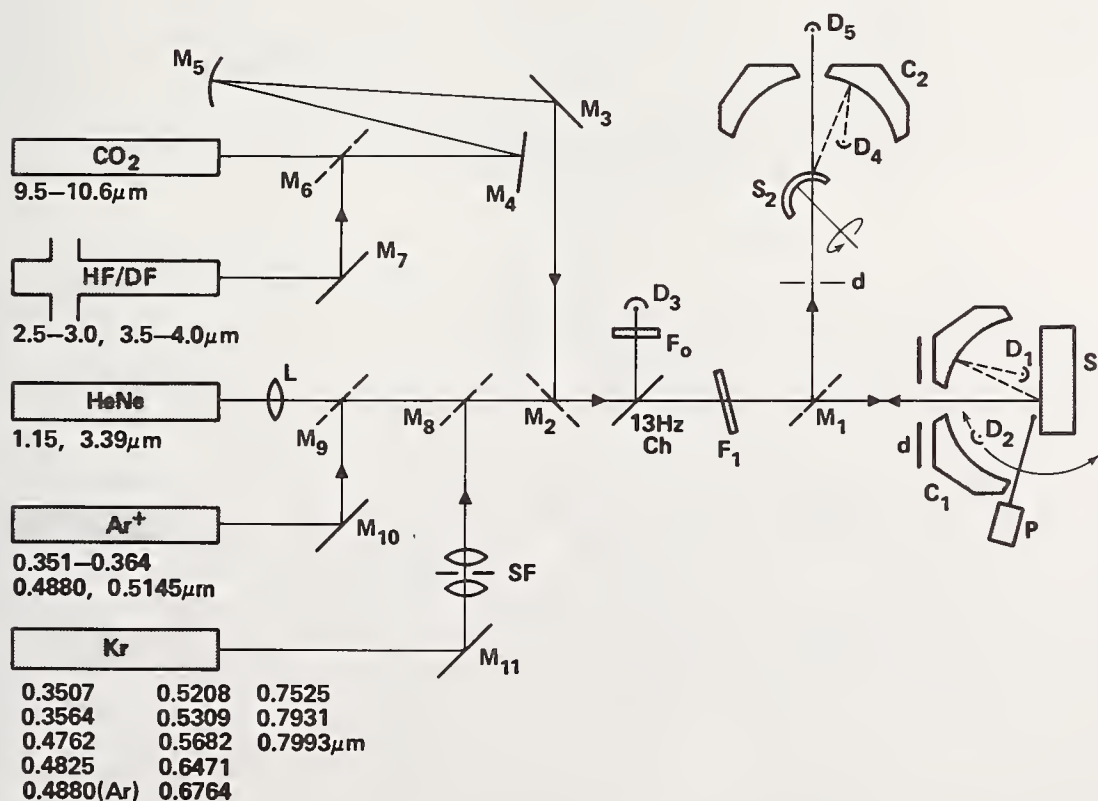


Figure 8. Optical diagram of the Optical Evaluation Facility showing lasers and available laser lines, mirrors M, lens L, spatial filter SF, attenuation filters F, chopper Ch, diaphragm d, Coblentz spheres C, pyroelectric detectors D, and samples S (from ref. 12).

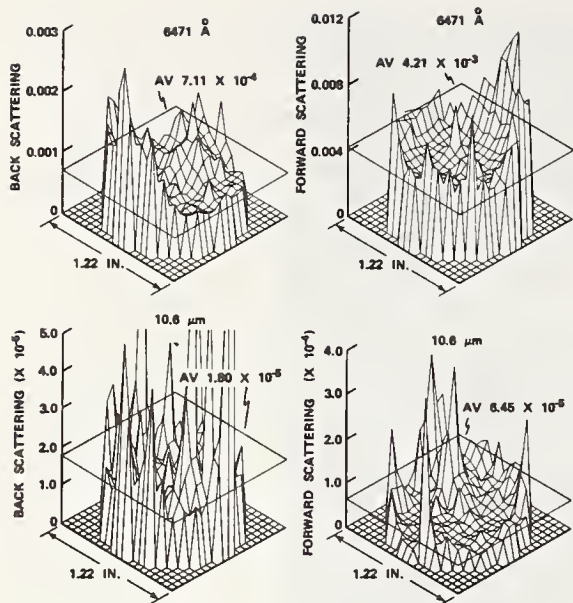


Figure 9. Three-dimensional plots of the scattering in reflection and transmission from a forged KCl window in the visible and infrared (from ref. 13).

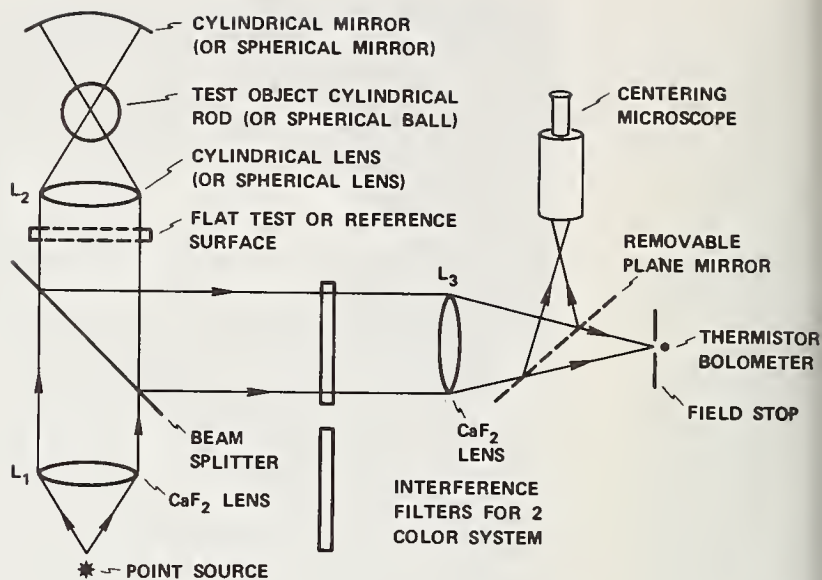


Figure 10. Schematic diagram of an instrument to measure roughness in the 0.4 to μ m range (from ref. 14).

reject. An air jet could rotate the ball if complete coverage was desired. The ball is then ejected and a new ball drops into the hole where the process is repeated. The whole operation is simple, rapid, accurate, and nondestructive. For small roughnesses ($\sim 0.01 \mu\text{m}$) visible light could be used. For larger roughnesses ($\sim 0.1 \mu\text{m}$) infrared light would be necessary since otherwise the roughness would not be small compared to the wavelength and geometrical optics effects would occur. It has been shown experimentally that eq. (1) does hold in the infrared as well as in the visible for appropriately rough surfaces and that the scattered light technique provides a simple method for solving what is otherwise a difficult measurement problem [14].

3. Impurities and surface defects

Other important parameters to characterize on optical surfaces are the presence of impurities and surface stoichiometry. Various techniques using electron spectroscopy are most useful in this regard. For example, figure 11 records a scan made of Auger electrons from a copper surface which was polished using Al_2O_3 powder [15]. The powder has been imbedded in the copper surface; its presence is indicated by the feature at 1400 eV. No feature is seen near 1600 eV, showing that contamination from compounds containing silicon is absent. The sensitivity of Auger spectroscopy varies depending on the sample and experimental conditions, but it is approximately 0.001 monolayer and thus gives us a very sensitive technique for detecting surface contaminants. In most cases, it is insensitive to chemical bonding and hence is used primarily for identifying atomic constituents. Also, the exciting electron beam can easily damage dielectric samples through electron bombardment so that care must be taken to maintain low irradiance levels.

An alternate technique of comparable sensitivity is electron spectroscopy for chemical analysis (ESCA). The surface to be tested is irradiated either with x-rays or with radiation in the vacuum ultraviolet, and the photoemitted electrons are monitored. Since there is no intense electron beam irradiating the surface, the probability of surface damage is minimized by using ESCA instead of Auger spectroscopy. Also, chemical bonding information may sometimes be deduced from ESCA traces. Figure 12 shows an ESCA scan of an evaporated silicon oxide film made using x-ray irradiation. Peaks from Auger

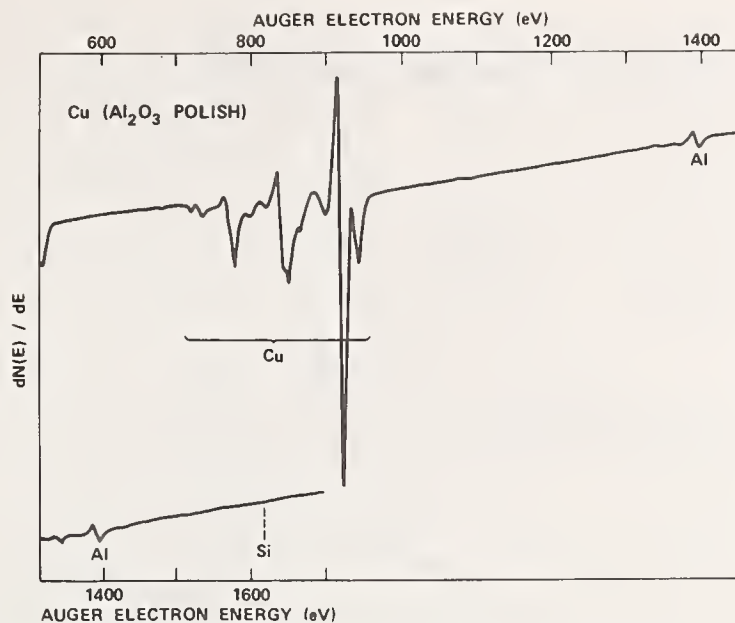


Figure 11. Auger electron energy scan showing the presence of Al₂O₃ polishing compound on the surface of polished copper (from ref. 15).

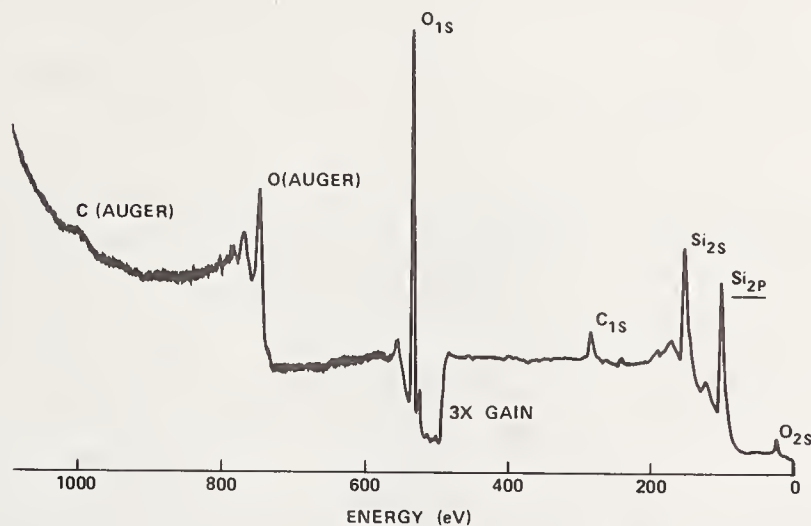


Figure 12. ESCA scan of a SiO₂ film. The energy region around the Si_{2p} peak is expanded in figure 13.

electrons are seen as well as photoemitted electrons [16]. Of particular interest is the Si_{2p} peak, which is shown on an expanded scale in figure 13. The particular sample investigated here, which was produced by reactively sputtering silicon in an oxygen atmosphere, yields a trace which is identical to the trace produced by a fused quartz sample. It is thus stoichiometric, but this sample has a peak which is intermediate between the SiO₂ peak and that produced by pure silicon and is thus not stoichiometric. This example illustrates the advantage ESCA has in making it possible to investigate not only the presence of contaminants but also to some extent the chemical composition and stoichiometry of the surface.

Both ESCA and Auger spectroscopy probe as little as 2-20 Å below the surface, since they depend on the escape depth of the emitted electrons [16]. They can be used to profile the chemical composition of surfaces to much greater depths than this, however, by sputter-etching down through the surface and monitoring one or more emission peaks as a function of depth. This technique makes it possible, for example, to investigate the composition of sur-

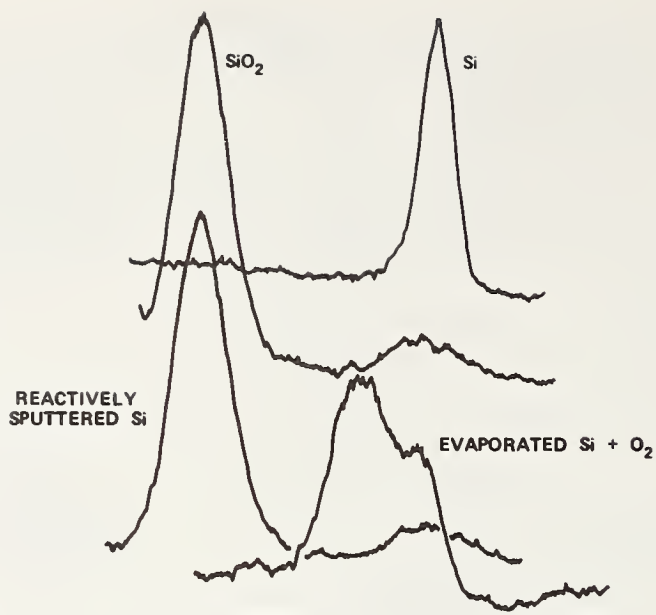


Figure 13. ESCA scan of the Si_{2p} peak on an expanded scale. The upper traces show the difference in energy between silicon in the form of SiO_2 and as free silicon, while the lower traces are for two silicon oxide films prepared under different conditions.

face films, evaluate multilayer coatings, and determine the depth of disturbed surface layers in some cases.

A drawback of both ESCA and Auger spectroscopy is their reduced sensitivity to impurities as compared with bulk analytical techniques. No bulk technique can sample only a few angstroms below the surface, but typical sensitivities of bulk techniques are often in parts per million, as compared to parts per thousand for ESCA and Auger spectroscopy. A solution to this problem is secondary ion mass spectroscopy (SIMS). The surface is bombarded with energetic ions, usually of argon or other rare gases, and the ejected secondary ions are mass analyzed. Both positively and negatively charged ions may be measured with sensitivities approaching those of bulk techniques, i.e., ppm. SIMS is thus a very powerful technique, and although at present it is difficult to extract quantitative data from SIMS measurements, it makes a very useful companion technique to ESCA or Auger spectroscopy. A SIMS trace of a very pure NaF coating [16] is shown in figure 14.

Ellipsometry furnishes another tool for surface analysis. It can be used either in a vacuum chamber or in air, and is particularly useful for studying the growth of thin films or the presence of a polish layer on prepared surfaces. Figure 15 shows the growth of a silver sulfide tarnish layer on a silver film prepared in our laboratory and exposed to air [17]. Note that the film growth is only a few angstroms in average thickness per day, but differences in that growth rate at different times in the day are easily detected ellipsometrically. The arrows indicate mornings. The rate of film growth was significantly larger during the day, when the laboratory was open and being used, than at night. When the film was enclosed in an atmosphere of dry nitrogen, growth virtually stopped. Since ellipsometry depends on phase measurements rather than intensity measurements, it is relatively insensitive to surface roughness, scattered light, or reduction in reflectivity, and hence can be used to monitor film growth which significantly reduces the optical quality of the surface. Silver sulfide is a good example of such a film.

There are many other surface evaluation techniques which could be mentioned. One promising new technique now under active development in our

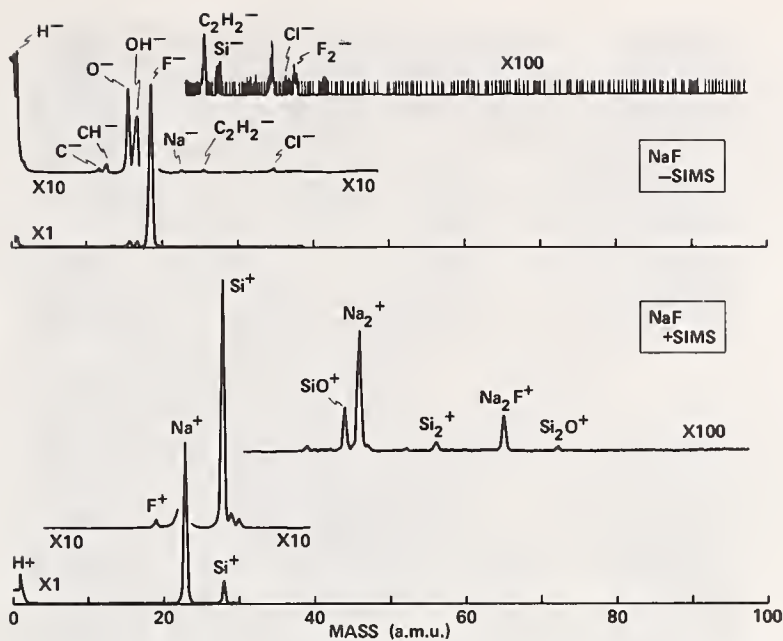


Figure 14. SIMS scan of a very pure NaF film showing the presence of impurities in the parts per million range.

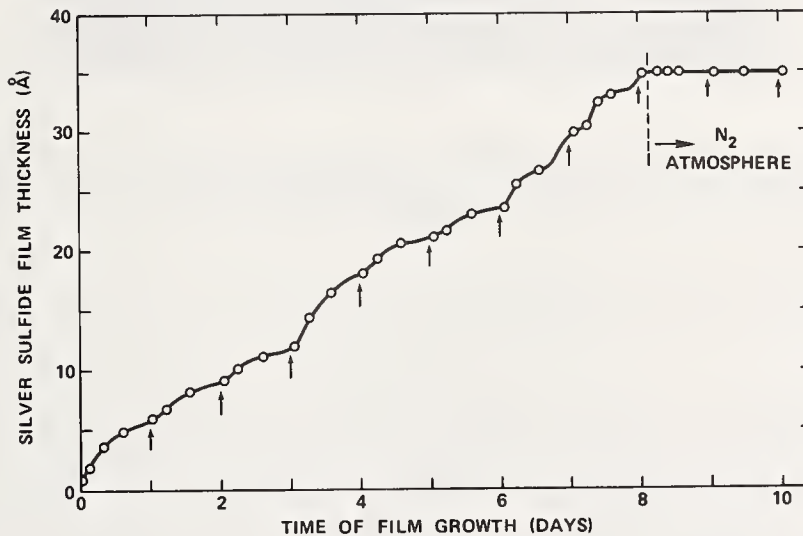


Figure 15. Growth of a silver sulfide tarnish layer on a silver film in room air as measured ellipsometrically. The vertical arrows indicate mornings. After the dashed line on day 8 the sample was enclosed in a nitrogen atmosphere (from ref. 17).

laboratory by Dr. J. O. Porteus and colleagues is high fluence diagnostics [18,19]. The sample is mounted on the ultrahigh vacuum chamber shown in figure 16, which contains various evaluation instruments including an ion collector, visual microscope, scanning electron imager, and Auger analyzer. The sample is irradiated with a high intensity pulsed laser beam, and the thresholds for various processes such as ion emission, plasma formation, change in work function, melting, intergranular slip, pitting, and so on are determined. Significant differences between these various thresholds are found depending on the surface treatment, purity, and grain structure of the samples.

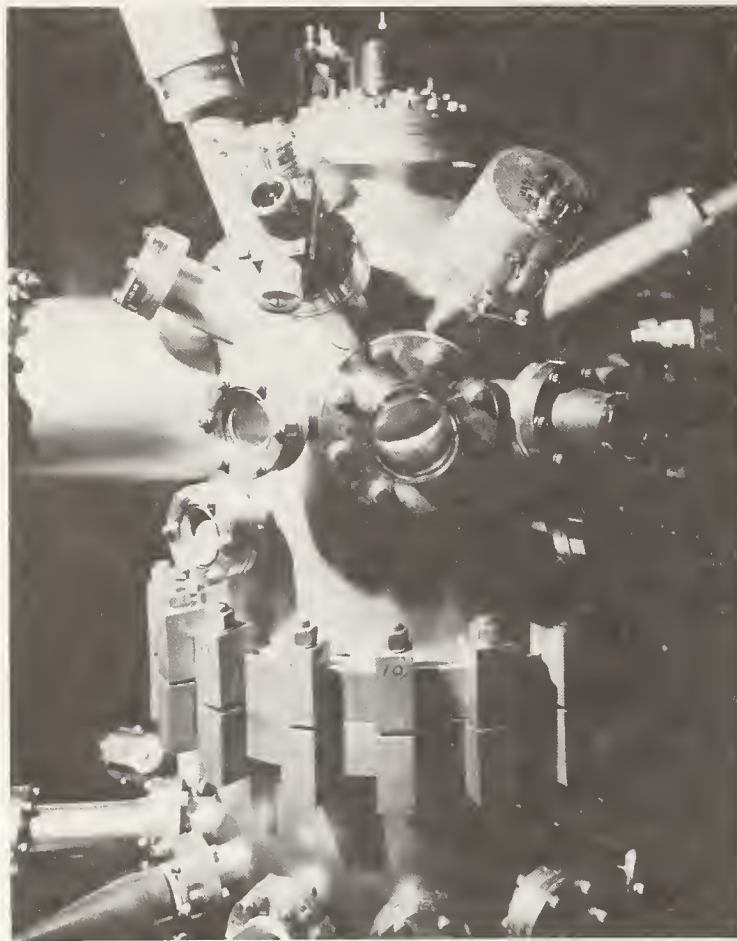


Figure 16. Ultrahigh vacuum laser damage test chamber containing instruments to evaluate effects occurring on the sample during laser irradiation.

4. Conclusion

A complete description of a surface must include its surface topography, structural imperfections, and surface impurities, including the presence of surface films. Although optical surfaces are much more nearly perfect than most surfaces in common experience, they still have the same types of imperfections as other surfaces. Hence, techniques used to explore surfaces used in optical applications may be useful in characterizing other surfaces as well. A prime example as far as surface topography goes is a bearing surface, which for ceramic bearings of materials such as silicon nitride must be finished to nearly optical tolerances. By using techniques such as analysis of scattered light, FECO interferometry, stylus measurements, and DIC microscopy, surface irregularities as small as $5 \times 10^{-4} \mu\text{m}$ in height have been detected on optical surfaces. With some modifications ground surfaces can also be evaluated using some of these techniques. Surface impurities can be detected in the range of parts per thousand in thicknesses of only a few monolayers using ESCA and Auger spectroscopy, and in parts per million using SIMS. The variation in impurity concentration with depth can be determined by sputter-profiling. Non-stoichiometry can also be detected, and by using ellipsometry the growth of thin surface films in air or vacuum can be monitored with a sensitivity of a fraction of an angstrom in average film thickness. New evaluation techniques such as high fluence diagnostics are also under development. These techniques are very powerful and should be more widely used in investigations of ceramic surfaces.

References

- [1] Bennett, H. E., "Thermal distortion thresholds for optical trains handling high pulse powers", in Laser Induced Damage in Optical Materials: 1976, A. J. Glass and A. H. Guenther, eds., National Bureau of Standards, Washington, DC (NBS spec. Publ. 462), pp. 11-24; Bennett, H. E., "Factors limiting the energy transmitted by an optical train", in Laser Damage of Optical Materials, A. J. Glass and A. H. Guenther, eds. (Academic Press, New York, 1979), in press.
- [2] Bennett, H. E., "Scattering characteristics of optical materials", *Opt. Engr.* 17, 480 (1978).
- [3] Bennett, J. M., and Elson, J. M., "Surface statistics of selected optical materials", in Laser Induced Damage in Optical Materials: 1977, A. J. Glass and A. H. Guenther, eds., National Bureau of Standards, Washington, DC (NBS Spec. Publ. 509), pp. 142-155.
- [4] Butler, D. W., "A stereo electron microscope technique for microtopographic measurements", *Micron* 4, 410 (1973).
- [5] Tolanski, S., Multiple-Beam Interferometry of Surfaces and Films (Clarendon Press, Oxford, England, 1948).
- [6] Bennett, J. M., "Measurement of the rms roughness, autocovariance function and other statistical properties of optical surfaces using a FECO scanning interferometer", *Appl. Opt.* 15, 2705 (1976).
- [7] Elson, J. M., and Bennett, J. M., "Relation between the angular dependence of scattering and the statistical properties of optical surfaces", *J. Opt. Soc. Am.*, in press.
- [8] Bennett, J. M., "Surface evaluation techniques for optical components", in Laser Damage of Optical Materials, A. J. Glass and A. H. Guenther, eds. (Academic Press, New York, 1979), in press.
- [9] Anderson, R. H., and Bennett, J. M., "Optical properties of KCl forged between optically polished dies", in Laser Induced Damage in Optical Materials: 1978, A. J. Glass and A. H. Guenther, eds., National Bureau of Standards, Washington, DC, in press.
- [10] Williams, V. L., and Lockie, R. T., "Optical contamination assessment by BRDF measurement", *Opt. Engr.* 18 (1979), in press.
- [11] Bennett, H. E., "Specular reflectance of aluminized ground glass and the height distribution of surface irregularities", *J. Opt. Soc. Am.* 53, 1389 (1963).
- [12] Bennett, H. E., and Stanford, J. L., "Structure-related optical characteristics of thin metallic films in the visible and ultraviolet", *J. Res. Natl. Bur. Stands.* 80A, 643 (1976).
- [13] Anderson, R. H., and Bennett, J. M., "Properties of KCl optical elements forged between optically polished dies", in Proceedings of the High Power Laser Optical Components and Component Materials Meeting, J. S. Harris and C. L. Strecker, eds., (Defense Advanced Research Projects Agency, Arlington, Va., December 1977), pp. 177-186.
- [14] Bennett, H. E., "Measurement of smooth surface finishes", *Industrial Quality Control* 20 [8], 18 (February 1964).

- [15] Bennett, H. E., and Archibald, P. C., "Optical requirements for laser mirrors", in Laser Induced Damage in Optical Materials: 1974, A. J. Glass and A. H. Guenther, eds., National Bureau of Standards, Washington, DC, (NBS Spec. Publ. 414), pp. 23-29.
- [16] Green, A., Naval Weapons Center, private communication, 1978.
- [17] Bennett, H. E., Peck, R. L., Burge, D. K., and Bennett, J. M., "Formation and growth of tarnish on evaporated silver films", J. Appl. Phys. 40, 3351 (1969).
- [18] Porteus, J. O., Jernigan, J. L., and Faith, W. N., "Multithreshold measurement and analysis of pulsed laser damage on optical surfaces", in Laser Induced Damage in Optical Materials: 1977, A. J. Glass and A. H. Guenther, eds., National Bureau of Standards, Washington, DC (NBS Spec. Publ. 509), pp. 507-515.
- [19] Porteus, J. O., Decker, D. L., Jernigan, J. L., Faith, W. N., and Bass, M., "Evaluation of metal mirrors for high power applications by multi-threshold damage analysis", IEEE J. Quantum Electron. QE-14, 776 (1978).

Discussion

VORBURGER

The optical technique for roughness measurement that you discussed is useful for highly polished surfaces only. Are there any possibilities for an optical technique that will be useful for measuring roughnesses on the order of a micrometer?

BENNETT

To measure roughness of the order of a micrometer rms in height one should go to wavelengths of 30-40 μm , i.e., the far infrared. In most applications of which I am aware, however, the roughness values to be measured are much smaller than a micrometer. For example, Dr. Sibley, in his talk on ceramic bearings, concluded that the maximum roughness they could tolerate was about 0.01 μm AA and some balls had roughness as low as 0.004 μm . For evaluating such roughnesses easily and accurately, light scattering is almost ideal and visible wavelengths can be used. For roughnesses of 0.1 or 0.2 μm , one should use infrared wavelengths of 5-10 μm . This is the roughness range which has been of most interest in the past and it is too large to evaluate accurately by light scattering techniques using visible wavelengths. Measurement of light scattering using infrared wavelengths for roughnesses of ~ 0.1 μm or visible wavelengths for roughness ~ 0.01 μm provides us with a very convenient, rapid, noncontact method of determining surface roughness which is particularly attractive for production applications.

THE NATURE OF STRENGTH CONTROLLING MACHINING FLAWS IN CERAMICS

R. W. Rice and J. J. Mecholsky, Jr.¹

Naval Research Laboratory
Washington, D. C. 20375

The nature of machining flaws introduced in a variety of glass, single crystal, and especially polycrystal bodies are reported, based on fractographic determination of such flaws as the source of mechanical failure. Particular attention is given to grinding where the anisotropy of strength due to the direction of grinding relative to the tensile axis is shown to be due primarily to a dual population of flaws of differing shapes. One set of flaws form \sim perpendicular and another \sim parallel to the grinding direction. The latter flaws are typically substantially more elongated and often larger than the former and thus give lower strengths for stressing perpendicular to the direction of grinding. Sawing, sanding, and polishing are also shown to result in similar dual flaw populations. The character of flaws are examined as a function of the type of material and machining, as well as specimen size and shape. The latter suggests a limited strength-size effect due to machining flaws. However, the key findings are that machining flaws do not vary greatly with typical variations of machining or material parameters, e.g. composition, grain size, or hardness.

Key Words: Brittle failure; flaws, flaw populations; fracture origins; fractography; grinding; machining, polishing; sanding; strength-size effects.

1. Introduction

Machining of most glasses, single crystals, and dense polycrystalline specimens is typically assumed to introduce flaws which control their mechanical strength. However, in discussing the evidence for such flaw controlled failure versus dislocation controlled failure, Rice [1]², at the previous Machining Conference, pointed out that there had been little or no direct verification of flaw failure. This paper summarizes and significantly extends recent work on the nature of flaws introduced in a variety of ceramic materials, as a function of various machining and specimen parameters [2-9]. The nature of the two flaw populations that result in the common anisotropy of strength associated with different grinding directions are treated first. Then, more limited studies of other modes of machining are compared with these grinding studies, followed by some discussion of flaw variations and distributions.

¹Present mailing address: Sandia Laboratories, Albuquerque, New Mexico 87185.

²Figures in brackets indicate the literature references at the end of this paper.

2. Experimental Procedure

The grinding observations summarized here cover several years involving several machine operators as well as a variety of materials. Grinding was done predominantly, but not exclusively, with 320 grit diamond wheels, most often either with a vitreous bonded wheel (~ 10 cm dia. operating at ~ 7900 rpm) or a metal bonded wheel (~ 20 cm dia. operating at ~ 1725 rpm). A range of feed rates, commonly of the order of 1 cm/sec, and depths of cut, commonly ~ 0.05 mm, per pass and at least two different sizes and styles of grinding machines have been used [3,10,11]. In addition, some observations are from specimens or components of different materials, sizes, and configurations, ground and tested by at least three other organizations. Thus, the results should have broad applicability.

Diamond sawing was with typical diamond saws, e.g. as described elsewhere [10] with cutting rates of the order of 2 cm²/min for the MgF₂ of this study. Hand sanding was done with 320 or 600 grit SiC paper under dry conditions with finger pressure only. Diamond polishing was typically done to ~ 1 μm grit size on a maple lap with kerosene as a fluid. Some specimens or components were polished and tested in other laboratories.

Mechanical testing was typically by 3 point flexure at ~ 22°C on bars ~ 1.3 x 2.6 mm in cross section on a span of ~ 1.3 cm with a head travel of ~ 1.3 mm/min, but other size and test results are included. Fracture origins were determined on tested samples by optical and scanning electron microscopy using the techniques described by Rice [12].

3. Strength Anisotropy and Flaw Shape as a Function of Grinding Direction

At the previous ceramic machining conference, Rice reported studies showing that an anisotropy of strength resulted in a variety of glasses, single crystal, and polycrystalline flexure bars as a result of stressing relative to the grinding or sanding direction and the bar axis [11]. Characteristically, tensile stresses parallel with the grinding direction, i.e. parallel to the bar axis, gave the highest strength, while tensile stresses perpendicular to the grinding direction gave a lower strength, often by up to 50%. Kirchner also independently reported similar anisotropy of strength relative to the grinding direction of round rods of fine grain Al₂O₃ [13]. Subsequently, other investigators have reported similar anisotropies of strengths especially in hot pressed Si₃N₄ [14] which was also included in Rice's original study.

Rice originally proposed that the cause of this anisotropy of strength was stress concentrations associated with resultant grinding striations or grooves that could be viewed as two facing surface steps, each having a stress concentration associated with it of ~ 1 + 0.7 (h/r) where h is the height of the steps and r is the radius of curvature at the base of the step. Thus, for stressing parallel with the grinding striations there would be no stress concentration while for stressing perpendicular to the direction of grinding the stress being normal to the grinding striations would provide the maximum stress concentrations at the surface steps or grooves. Several subsequent investigators have also generally associated the strength anisotropy with these grinding striations. However, there are two factors which show that these grinding striations are typically not a major factor in the anisotropy of strength associated with stressing relative to the grinding direction.

The first factor showing that the grinding grooves themselves are probably not the predominant factor in the strength anisotropy as a function of the stress direction relative to the grinding direction is a closer eval-

uation of the nature of the grooves themselves and their possible stress concentration. If a grit particle gouged out a simple groove defined by the average upper limit of its protrusion from the grinding wheel, $h \sim r$, it would give an $\sim 70\%$ increase in the component of stress normal to the groove. Thus, if h were of the order of the flaw sizes in ceramics, the $\sim 70\%$ stress concentration would suggest the possibility that the grooves themselves are the source of failure. However, examination of more severe grinding grooves which are typically associated with the flaws causing failure shows that $h/r < 1$, e.g. $\frac{1}{4}$, which is also indicated in the single particle machining experiments of Gielisse et al [15]. This reduces the stress concentration to $\sim 30\%$ or less. While local irregularities in the grooves would locally increase the stress concentrations, these are not likely to extend over a sufficient range to change the situation. Further, the grooves often do not appear to be as deep as typical flaws. Another aspect of the grooves themselves that indicates they are not the predominant cause of strength anisotropy is the fact that they are often not continuous [11], and failure is observed to sometimes occur where grooves have not formed or have been removed by spalling. Note also that correlations between grit particle size and flaw sizes [16-19] do not have to arise from the groove being the flaws. It is quite likely that the different sized grit particles act as different size indentors with larger grit sizes introducing cracks that extend deeper below the surface. Thus, cracks extending in from the surface due to the grooving by the particle may well correlate with particle size. However, because of the increased distance of the crack periphery from the surface steps, the effect of the step stress concentration on the crack would be greatly reduced.

The second, and major factor, showing that the grinding striations themselves are typically not a major factor in the anisotropy of strength as a result of stressing relative to the grinding direction is direct fractographic identification of the nature of flaws from which mechanical failure initiates in specimens. The net result of a substantial amount of study is that there are basically two different sets of flaws extending into the body from the surface generated by grinding (figure 1). Sample fractographs illustrating the difference in shape between the two sets of flaws are shown for fine grain (figure 2), large grain (figure 3), and single crystal bodies (figure 4). Other examples will be shown and discussed later. Additional examples of the two sets of flaws can be seen in references 3-9 and 20-24.

These studies show that one set of flaws form essentially parallel with, and approximately at, the bottom of the grinding groove. The other set of flaws typically form \sim perpendicular to the grinding grooves, apparently due to stick-slip or other dynamic variations in local tensile stresses generated by the machining action \sim parallel with the directions of machining, i.e. of grinding particle motion. Typically, both sets of flaws extend to similar depths. However, the flaws forming along the grinding grooves are characteristically more severe than those forming perpendicular to the grinding grooves consistent with the observed strength anisotropy. The greater severity of the flaws along the grinding grooves is generally due more to their greater length rather than their depth (figures 1-4).

Analysis of extensive observations of the anisotropy in flaw shape between the two sets of flaws on strength is given in table 1. Here the observed anisotropy of strength is compared with the strength anisotropy predicted from the Griffith equation using the observed flaw size and shape parameters. This clearly shows that the anisotropy in flaw shape is typically the overwhelming factor in the strength anisotropy.

In addition to the above more detailed, quantitative studies, a variety of qualitative observations further extend the scope of the observation of strength anisotropy being due to the differences in shape of the two flaw populations associated with machining as indicated in table 2. Thus, for example, in studies of hot pressed Si_3N_4 , limited determinations of machining flaws at fracture origins of bars machined parallel with the tensile (bar)

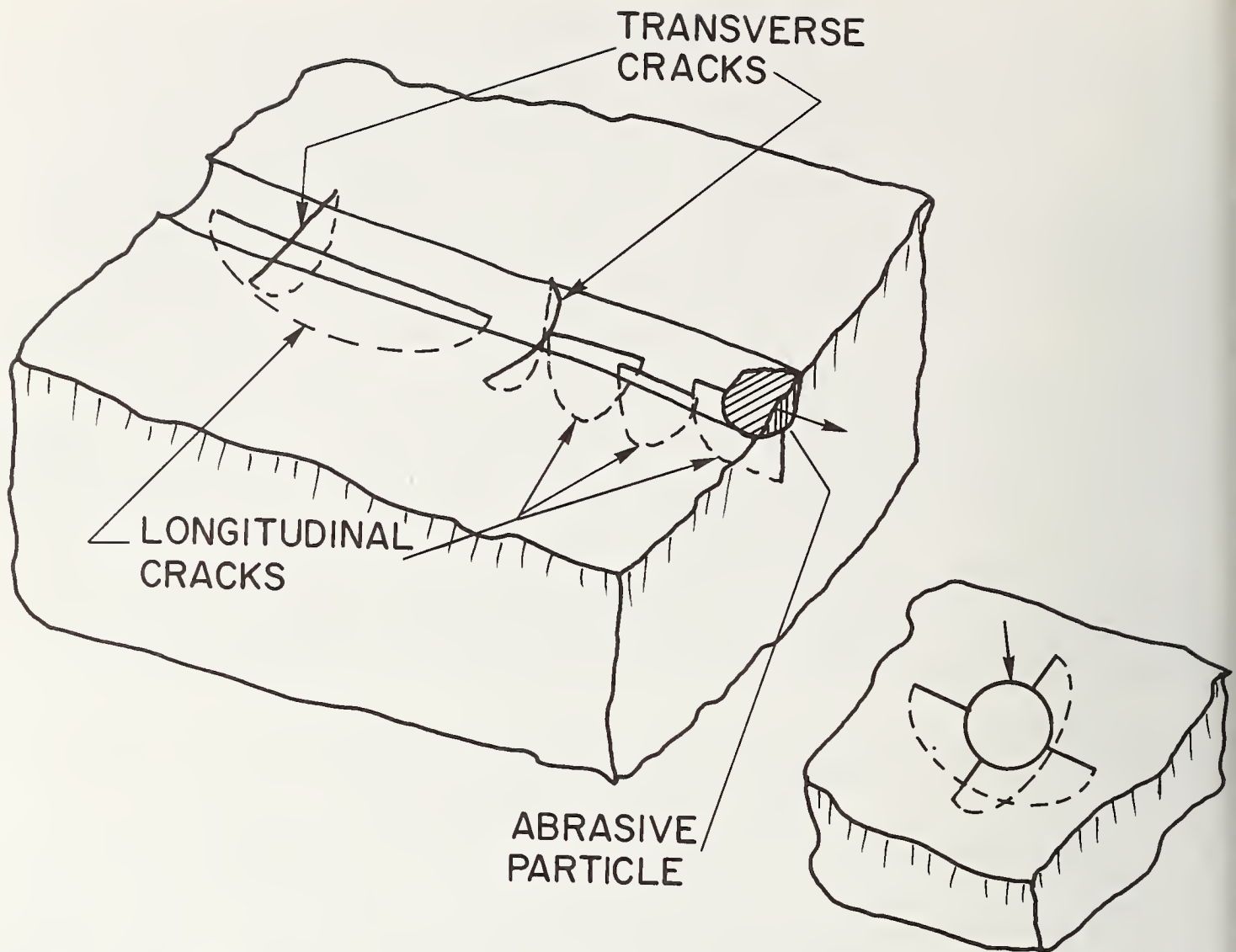


Figure 1. Schematic representation of flaws introduced in scratching a ceramic surface. While the main focus of the schematic is the effect of an abrasive grit particle on the surface of the ceramic, it is also reasonably representative of what commonly happens in a scratch hardness type test. One of the main differences between these two types of scratching operations is that in the abrasive machining operation extensive spalling often occurs along the path of the grit particle which is not shown in order to keep the schematic simple. Such spalling may or may not occur in the scratch hardness type test depending for example on the load and material. This sketch schematically summarizes the basic findings of extensive observations on machining flaws which are also generally consistent with observations made from scratch testing; namely that the motion of particle or an indenter over the surface introduces two sets of flaws extending into the body from the surface. One set of flaws is essentially parallel with the groove. Such flaws are typically reasonably elongated either in a fairly continuous fashion or in a more irregular fashion due to the partial or complete overlap of a number of shorter flaws. The second set of flaws are typically approximately perpendicular to the motion of the particle or point and their periphery often approaches a semi-circle. While some of the second type of flaws may be relatively planar they often have some concavity towards the direction from which the particle or point approached the point where the flaw initiates. The insert to the right schematically illustrates the approximate analogue for a static indentation. While for simplicity, a round particle has been shown from which more than two sets of flaws might well form in a simple indentation test only two have been shown here since this would tend to be more

representative of the angular nature of particles similar to what one obtains with an angular, e.g. Vickers, indenter.

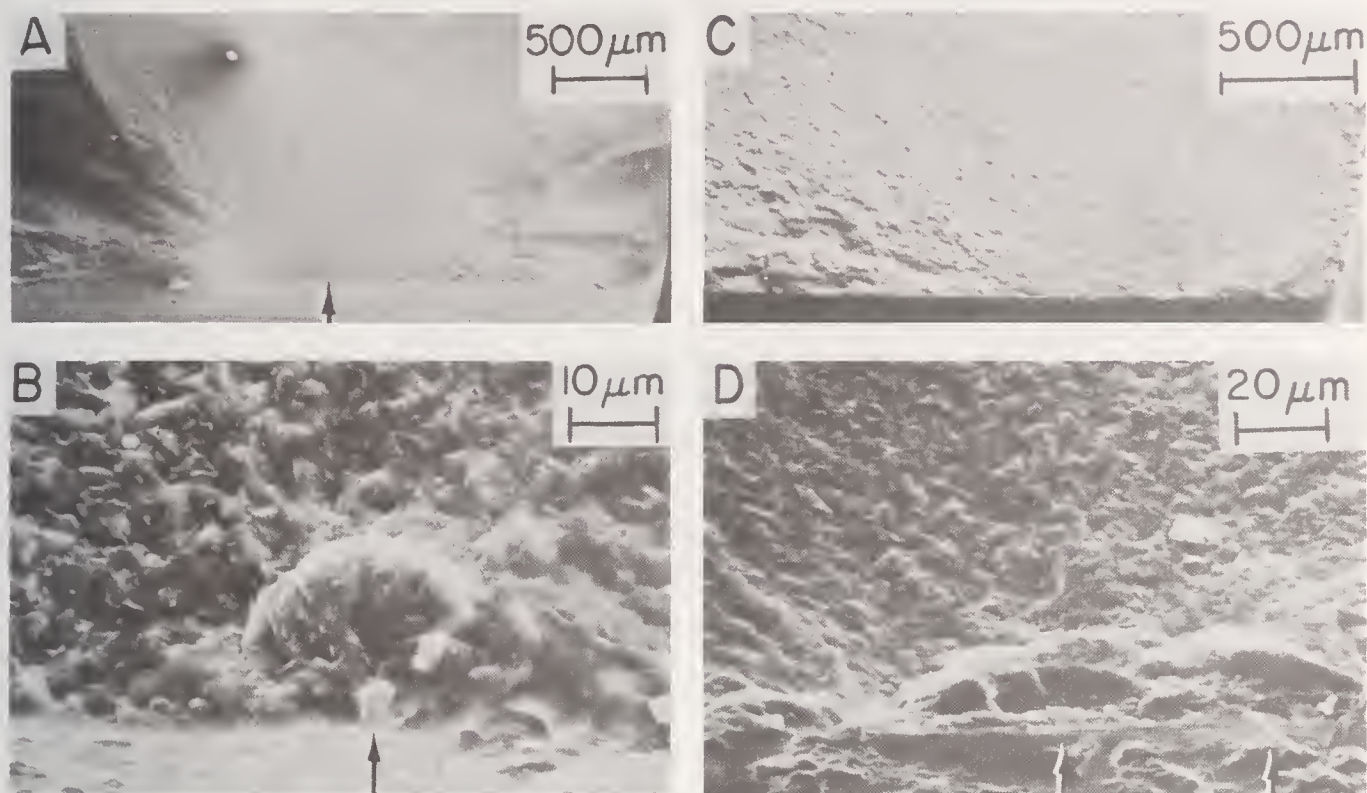


Figure 2. Example of machining flaws at fracture origins in a fine grain ceramic machined parallel and perpendicular to the tensile axis of the bar. A and B represent lower and higher magnification of the fracture origin of a dense, fine grain mullite bar machined parallel with the tensile axis; fracture stress ~ 325 MPa (47,000 psi). Note the nearly semicircular, i.e. half-penny shape of the flaw periphery, but that the flaw has some curvature to it, e.g. its shape is similar to half a clam shell. Figure C and D show fracture surfaces and the fracture origin of a test bar of the same material ground perpendicular to the tensile axis; fracture stress ~ 207 MPa (30,000 psi). Note some difference in depth of the flaws in A-D, the more elongated character of that in C and D, and the fact that the latter consists of at least two partially overlapping segments.

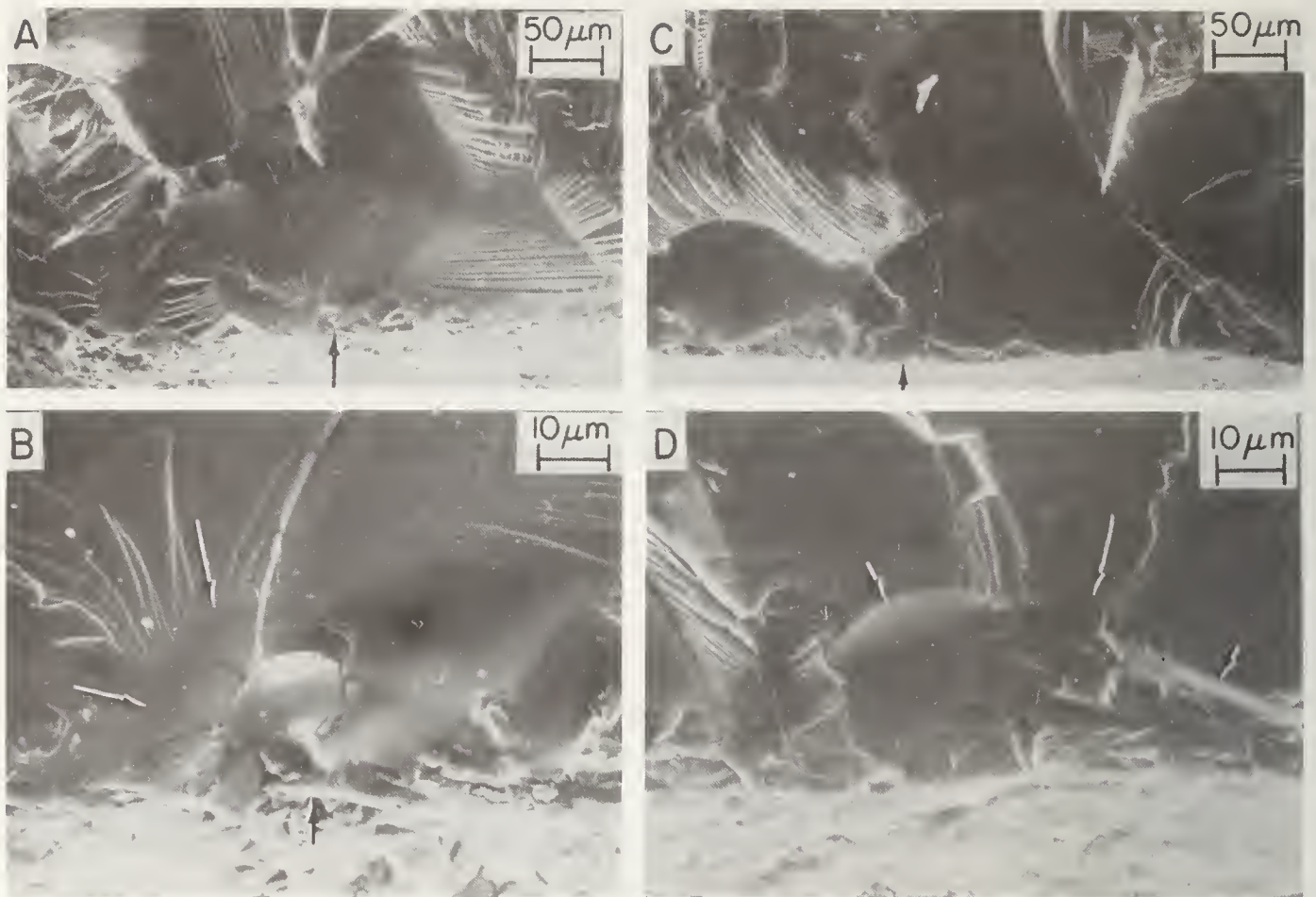


Figure 3. Examples of machining flaws at the fracture origins for parallel and perpendicular machining of a large grain ceramic. A and B show the fracture origin area and the specific failure causing flaw (arrows) as a result of grinding a dense, sintered Y_2O_3 (Yttralox) bar parallel with the tensile axis. Note the nearly semicircular nature of the final flaw boundary and that the flaw is substantially less than the size of the grain in which it formed. C and D show the fracture surface and fracture origin (arrows) of a specimen of the same material ground perpendicular to the tensile axis. Note the more elongated character of the flaw but that it is again substantially smaller than the size of the grain in which it is located.

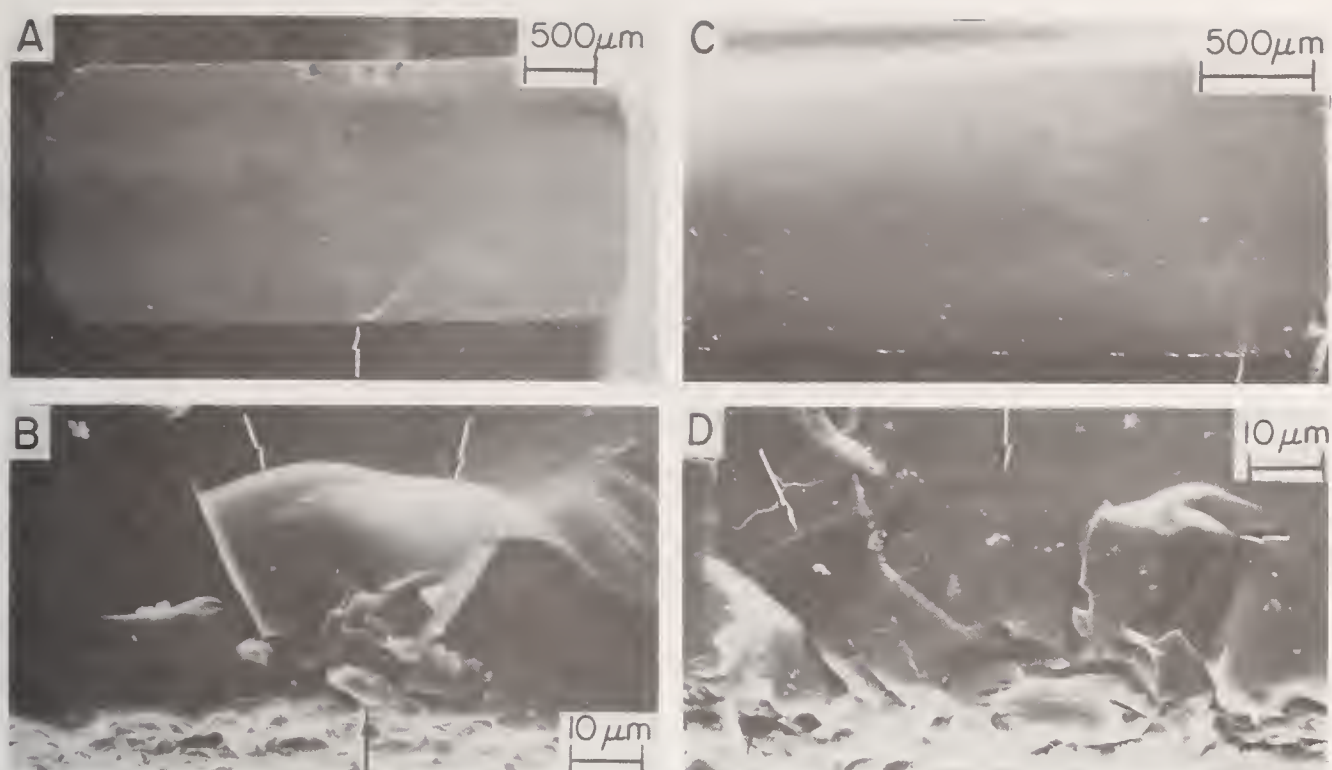


Figure 4. Examples of flaws at the fracture origins in parallel and perpendicular ground MgAl_2O_4 single crystal. A and B show the fracture surface and fracture origin (arrows) of a stoichiometric MgAl_2O_4 crystal ground parallel with the $\langle 100 \rangle$ tensile axis and having a $\{110\}$ tensile surface, fracture stress ~ 145 MPa (21,000 psi). C and D show the fracture surface and origin (arrows) of a sample of the same material and orientation ground perpendicular to the tensile axis; fracture stress ~ 117 MPa (17,000 psi). While the flaw shapes shown here are somewhat more irregular than often observed, the flaw causing failure from machining parallel with the tensile axis is definitely of similar depth but less elongated than that causing failure from machining perpendicular to the tensile axis.

axis show the flaws to commonly approach \sim half penny flaws, while more extensive observations on specimens ground perpendicular to the tensile axis both in the form of flat bars and round tensile specimens clearly show much more elongated flaws [20,21] (see also fig. 18). Similarly, large round tensile specimens of Al_2O_3 which were ground circumferentially [22], i.e. perpendicular to the tensile axis characteristically show more elongated flaws at fracture origins than observed in Al_2O_3 or other materials ground parallel with their tensile axis. Also, limited studies of $\beta\text{-Al}_2\text{O}_3$ bars ground perpendicular to the tensile (bar) axis show more elongated flaws at fracture origins than the \sim penny shaped machining flaws at fracture origins of bars ground parallel with the tensile axis [23]. There are also preliminary indications of strength anisotropy in a cermet (table 2). Finally, Richerson has shown evidence of grinding direction dependent strengths in some denser reaction sintered Si_3N_4 [24] consistent with other observations of machining flaws in such material [20,21].

The observations of this section on two sets of flaws from grinding, one set forming generally parallel with and essentially \sim along the bottom of the grooves generated by the individual grinding particles and the other

TABLE 1

EFFECT OF GRINDING ON FLAW GEOMETRY OF CERAMICS

Material	Orient. ¹ or G.S. (μm)	G.D. ²	No. ³	Fracture Stress (MPa)	c ⁴ (μm)	a/b ^{4,5}	$\sigma_{\perp}/\sigma_{\parallel}$ ⁶	B ⁷
A. Glasses:								
Silica			7	73±10	45±16	1.3±.4	0.84	0.86
		⊥	4	62±8	75±37	1.0±.4		
Alumino- silicate			12	117±10	39±9	1.6±.2	0.68	0.69
		⊥	5	80±7	71±10	0.5±.1		
Borosilicate			3	99±8	35±6	0.9±.3	0.9	0.9
		⊥	4	92±9	39±9	1.1±.3		
Lead Silicate			7	69±3	43±17	1.35±.6	0.86	0.82
		⊥	7	59±17	64±38	1.26±.8		
Soda Lime			25	97±5	28±9	1.6±.2	0.65	0.65
		⊥	16	68±8	67±5	0.5±.2		
Glassy Carbon			10	94±9	40±9	0.9±.3	0.93	1.03
		⊥	9	87±18	35±15	1.2±.6		
B. Crystals:								
TiO ₂	< $\bar{1}10$ >		6	113±7	25	0.7	1.1	0.9
	(110)	⊥	6	120±4	30	0.7		
TiO ₂	< $\bar{1}\bar{1}0$ >		5	113±3	30	1.5	0.7	0.7
	(001)	⊥	5	77±3	70	1.5		
TiO ₂	<010>		6	288±19	--	--	0.83	--
	(100)	⊥	5	239±12	25	1.3		
TiO ₂	<010>		5	108±6	60	1.3	1.0	0.9
	(001)	⊥	5	103±6	70	1.3		
TiO ₂	<001>		8	285±86	10	0.4	0.6	0.5
	(100)	⊥	7	183±36	35	0.18		
MgAl ₂ O ₄	<100>		3	217±28	15±0	0.4±0.6	0.8	0.8
	(110)	⊥	3	165±28	14±7	0.4±0.6		
C. Polycrystals:								
Keatite Glass Ceramic	< 1		6	180±39	16±5	0.9±0.4	0.6	0.5
		⊥	7	102±8	36±15	0.5±0.2		
MgF ₂	< 1		10	87±2	54±21	1.1±.07	0.6	0.6
		⊥	10	53±2	89±20	0.5±.08		
Mullite	1-3		7	319±35	41±23	1.0±0	0.8	1.0
		⊥	6	259±54	24±5	0.4±0.3		
B ₄ C	2-10		5	374±69	19±3	1.0±0	0.6	0.8
		⊥	9	154±24	26±10	0.2±0.07		
B ₄ C	100-200		4	282±228	19±9	0.7±0.5	0.9	0.7
		⊥	6	250±55	23±3	0.3±0.2		
CaF ₂	50-150		3	50±13	23±7	0.7±0.2	0.8	0.8
		⊥	3	40±5	33±7	0.6±0.6		
Yttralox	100-200		6	99±6	36±13	0.8±0.3	0.8	0.9
		⊥	7	77±8	44±20	0.7±0.3		

¹Orientation of single crystals < > gives tensile axis, and () tensile sur-

face. G.S. = grain size.

²G.D. = grinding direction relative to tensile axis.

³No. = number of specimens.

⁴c = smallest flaw dimension (smallest of a or b below).

⁵b = flaw half length along surface; a = flaw depth.

⁶Ratio of fracture stress for perpendicular to parallel grinding.

⁷ $B = \frac{\Phi_{\perp}}{\Phi_{\parallel}} \sqrt{\frac{c_{\parallel}}{c_{\perp}}}$ where c_{\parallel} and c_{\perp} are the smallest flaw dimension for parallel and perpendicular grinding respectively and Φ_{\parallel} and Φ_{\perp} are respective elliptic integrals for the flaw shapes.

TABLE 2

OTHER MATERIALS IN WHICH GRINDING DIRECTION EFFECT HAS BEEN INDICATED¹ BY

<u>Material</u> ²	<u>σ^3</u>	<u>a,b</u> ⁴	<u>Material</u> ²	<u>σ^3</u>	<u>a,b</u> ⁴
Sapphire	x	x	ZrO ₂ -fine grain		
H.P. Al ₂ O ₃	x	x	partially sta-		
S. Al ₂ O ₃	x		bilized	x	x
H.P. Mullite	x	x	H.P. SiC	x	x
H.P. β -Al ₂ O ₃	x	x	H.P. Si ₃ N ₄	x	x
			75% TaC-25 In-		
			conel ⁵ Cermet	x	

¹In studies by the authors.

²S = sintered, H.P. = hot pressed.

³ σ = strength, i.e. strength anisotropy.

⁴a,b = flaw depth and half length, i.e. flaw geometry.

⁵From selection of bars with ~ circular pattern milling or grinding marks ~ \parallel to tensile axis (173 ± 33 ksi) and ~ \perp to tensile axis (140 ± 38 ksi) for 3 spec. each.

set generally forming ~ perpendicular to those grooves, are consistent with cracking patterns observed over a period of years by a variety of investigators for both static hardness impressions and especially dynamic, i.e. scratch, hardness grooves [25-29] including earlier work, Brüche and Poppa [25, 26]. Note also that the flaws ~ perpendicular to the grinding direction have a curvature consistent with that expected for the motion of the grinding particles. Thus, while there are variations in these two sets of flaws, they are a basic aspect of grinding as well as other machining processes as will be discussed later.

Before proceeding with a more detailed description of machining flaws and variables effecting them, it is appropriate to briefly consider the detection of these flaws and their meaning. Typically, the flaws observed are believed to be the original machining flaws for two reasons. The first

of these is based on the fact that cracks typically propagate normal to the tensile stress causing their propagation. Thus, since the orientation of the stress forming the crack during machining can almost never be duplicated by the applied stress causing failure, the crack will be propagated on a somewhat different surface than that on which it originally formed. This change of surface results in a demarcation, which is generally detectable unless failure is nearly or completely intergranular, in which case the demarcation is generally obscured by the grain to grain variation of the crack topography. Since other possible changes in local stress around a crack due to crack velocity effects are much more subtle, if they exist at all, the demarcation between the original flaws and its first subsequent motion for failure are clearly predominant and typically what is observed. This is a major reason why the purely qualitative speculation of Doremus [30] that similar flaws they observed at the fracture origins of machined glass bars represent not the original flaws but some intermediate stage of failure should be rejected.

The second reason that the demarcations seen are attributed to the original flaws rather than some stage of subsequent propagation is due to changes in fracture mode that can occur during some stage of propagation. Mecholsky et al have shown that environmentally induced slow crack growth often proceeds intergranularly in polycrystals, e.g. MgF_2 [31]. Thus, since both the original machining flaws and the subsequent final fast fracture are mainly, or exclusively, transgranular in nature, the slow crack growth region is clearly defined showing the flaws such as those in this paper to typically be the original flaw and not involving some subsequent subcritical growth.

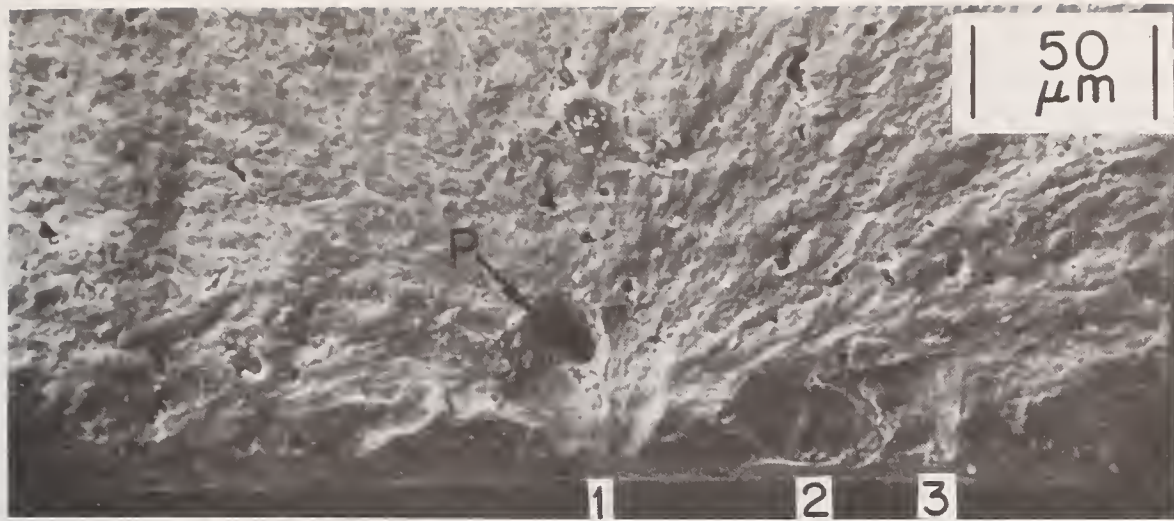
4. Other Aspects of Machining Induced Flaws

4.1 Microstructure, Composition and Machining Flaws from Grinding

Extensive studies of interaction of machining flaws with porosity have not been conducted. However, a number of observations indicate that isolated pores near the surface can be connected to the surface by machining flaws, e.g. figure 5. See also figure 13C and D.

Substantially, more extensive observations have been made on the effect of grain size on machining flaws. The essential result is that over the typical range of grain sizes encountered there is at best a limited decrease in the depth of flaws introduced by machining with decreasing grain size. Thus, for example, note the similarity in flaw sizes of specimens of comparable size for single crystals and polycrystals of $MgAl_2O_4$ of different grain sizes (compare table 1 and figure 4 with figure 3 of reference 22), different grain sizes of B_4C (table 1) and single and polycrystalline flaws in Al_2O_3 [22]. A variety of other more limited, e.g. non-quantitative observations, support this. For example, note the machining flaw at a possible, but uncertain, fracture origin in large grain CVD in figure 6 has ~ the same depth as the typical flaws observed in fine grain hot pressed Si_3N_4 (see references 20 and 21 as well as figure 18).

Further, note in general that there are limited differences in flaw depths and no systematic pattern between materials of different compositions and hence of differing properties such as hardness. Thus, note the typical flaw sizes for the variety of materials of similar specimen size and a common machining direction, do not vary over a significant range (table 1). This further reinforces the limited effect of grain size on the size of machining flaws that control strength (e.g. compare figures 2-4). The ramifications of the observation that there is little or no dependence of the size of machining flaws on grain size of the body being machined, are discussed in another paper [22].



PZT $\sigma_f \sim 15$ KSI

Figure 5. Example of pore-machining flaw interaction as a source of failure. On the fracture surface of this commercial lead zirconate titanate sample, three similar size machining flaws can be seen along the surface. Flaw 1 has connected with a pore, P, somewhat below the surface, to form the primary source of failure. Flaws 2 and 3 indicate two other machining flaws.

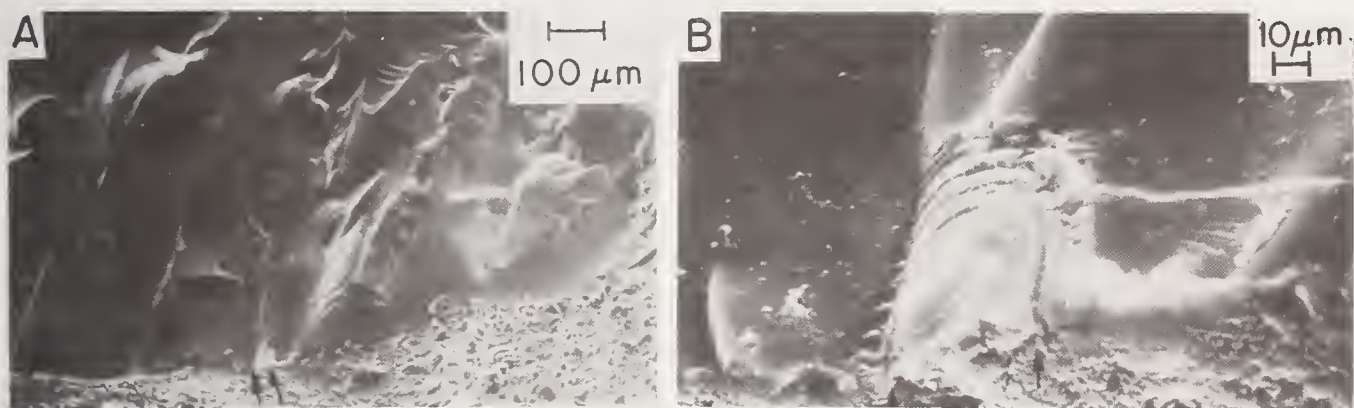


Figure 6. Grinding flaw in large grained Si₃N₄. A and B show respectively lower and higher magnification of a probable fracture origin and probable flaw (arrows) causing failure in this large, columnar grain, CVD Si₃N₄. Note also the two or three nearly concentric markings suggesting progressive stages of flaw development. Such markings with varying spacings are observed fairly frequently with flaws forming approximately perpendicular to the direction of machining. Photo courtesy of Dr. Carl Cm. Wu.

4.2. Machining Flaws from Other Modes of Abrasive Machining

Three other major modes of machining, diamond sawing, hand sanding with abrasive paper, and polishing (with diamond paste) have been studied to varying extent. Consider first diamond sawing. While extensive studies have not been conducted, direct comparisons have been made using optical grade, hot pressed, MgF₂ as shown in table 3. The circular nature of the blade leaves

TABLE 3
FLEXURAL STRENGTH OF AS-DIAMOND SAWN MgF₂*

Bars	No. of Tests	Strength	
		MPa	ksi
0.36 x 0.65 cm 1.9 cm span	10	71 ± 21	10 ± 3
0.23 x 0.55 cm 1.27 cm span	3	100 ± 23	15 ± 3

*Kodak IR window grade tested in 3 point flexure with a 1.27 mm/min head travel rate.

an arc of "sawing" grooves with, in turn, presumably result in a directionality of the strength of diamond sawn specimens if they were tested as a function of such orientation. This has not been explored, most specimens had the sawing grooves at intermediate angles (e.g. ~ 45°) to the tensile axis. The strengths of typical laboratory size bars as a result of such diamond sawing are in the same range but somewhat less than those from diamond grinding. Fractographic studies in this material, which is excellent for such studies, show definitive flaws at fracture origins from diamond sawing. These flaws are very clearly associated with more extreme surface grooves. Again both sets of flaws, i.e. those essentially ~ parallel and ~ perpendicular to the grooves are seen (figs. 7 and 8) with the former tending to dominate failure with the grooves at ~ 45° to the tensile axis.* Both the strengths (table 3) and actual flaw observations (figs. 7 and 8) show similar size flaws from sawing as from the comparable direction of grinding.

Previous studies have shown that stressing relative to the direction of hand sanding results in a similar anisotropy of strength relative to the direction of abrasive particle motion [11]. Thus, hand sanding (dry) with SiC abrasive paper clearly suggests that there are again two populations of flaws, one population forming parallel and the other forming perpendicular to the motion of the abrasive particles. The difference in the shapes of the two sets of such sanding flaws is thus apparently very similar to those of the two sets of flaws from grinding. Again limited, but definitive, observation support this conclusion, e.g. note the character of flaws associated with hand sanding (fig. 9) of very fine grain, high strength SiC resulting from the CNTD[†] process [32]. It should be noted that this similarity suggests that the differences between grinding and sanding, e.g. orders of magnitude difference in abrasive particle velocity have a limited effect

*Such results indicate that much study of mixed mode failure can be done directly with machining flaws by varying the angle of machining relative to the tensile axis, rather than using artificial indent induced flaws.

[†]Essentially a modified chemical vapor deposition process.

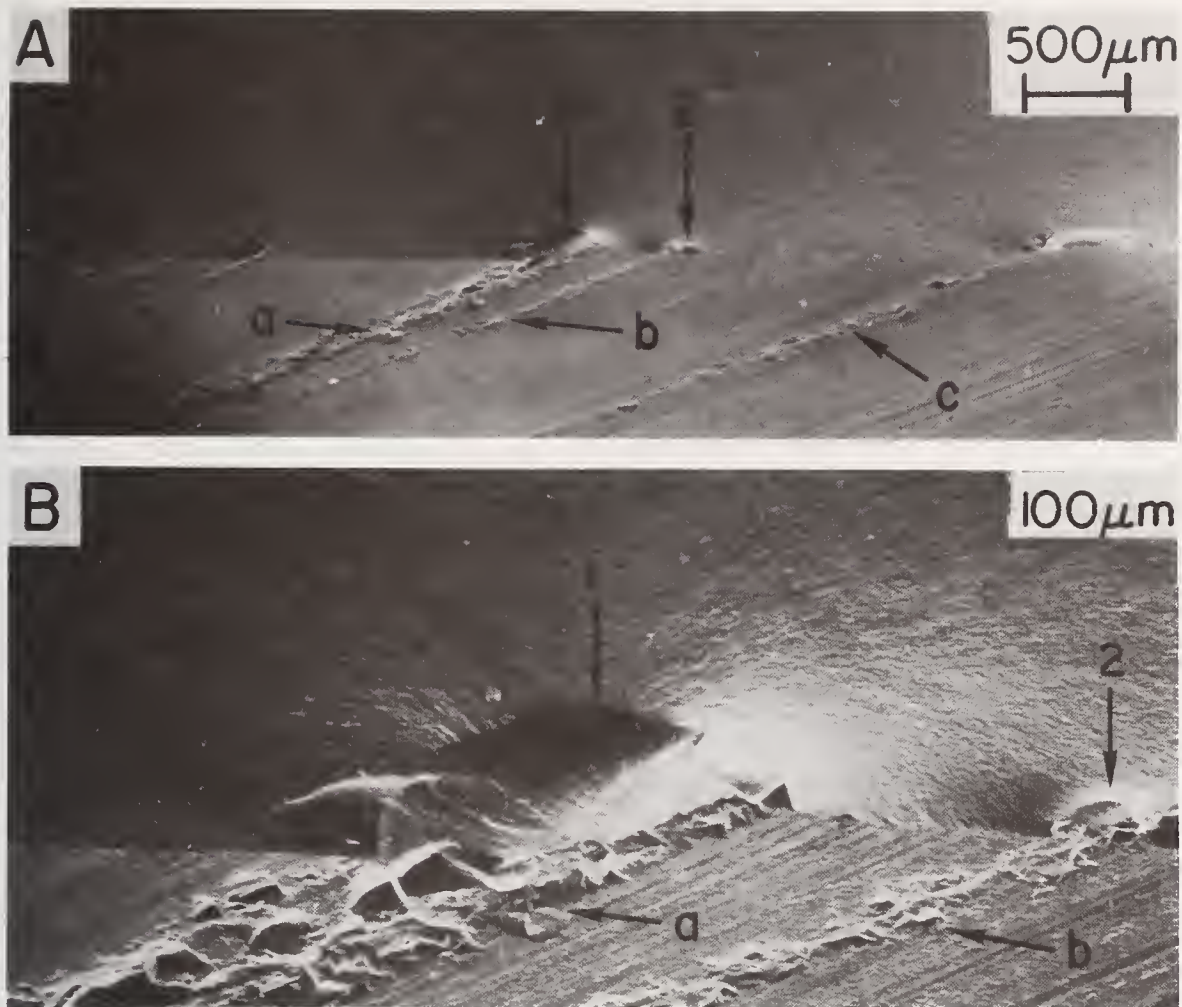


Figure 7. Examples of machining flaws in MgF₂ from diamond sawing. A and B show the fracture surface in the vicinity of the fracture origin (upper part of photos) and part of the machined tensile surface (lower portion of photos) of dense hot pressed optical grade MgF₂. Note the deeper sawing grooves at $\sim 45^\circ$ to the tensile axis and that each of these appears to have a machining flaw associated with it on the fracture surface e.g. note flaws 1 and 2 associated respectively with sawing scratches a and b in both photos. The larger flaw, 1, is clearly the origin of failure. Note that this flaw is somewhat less elongated than average for being \sim parallel with the machining groove. Fracture stress ~ 59 MPa (8,600 psi)

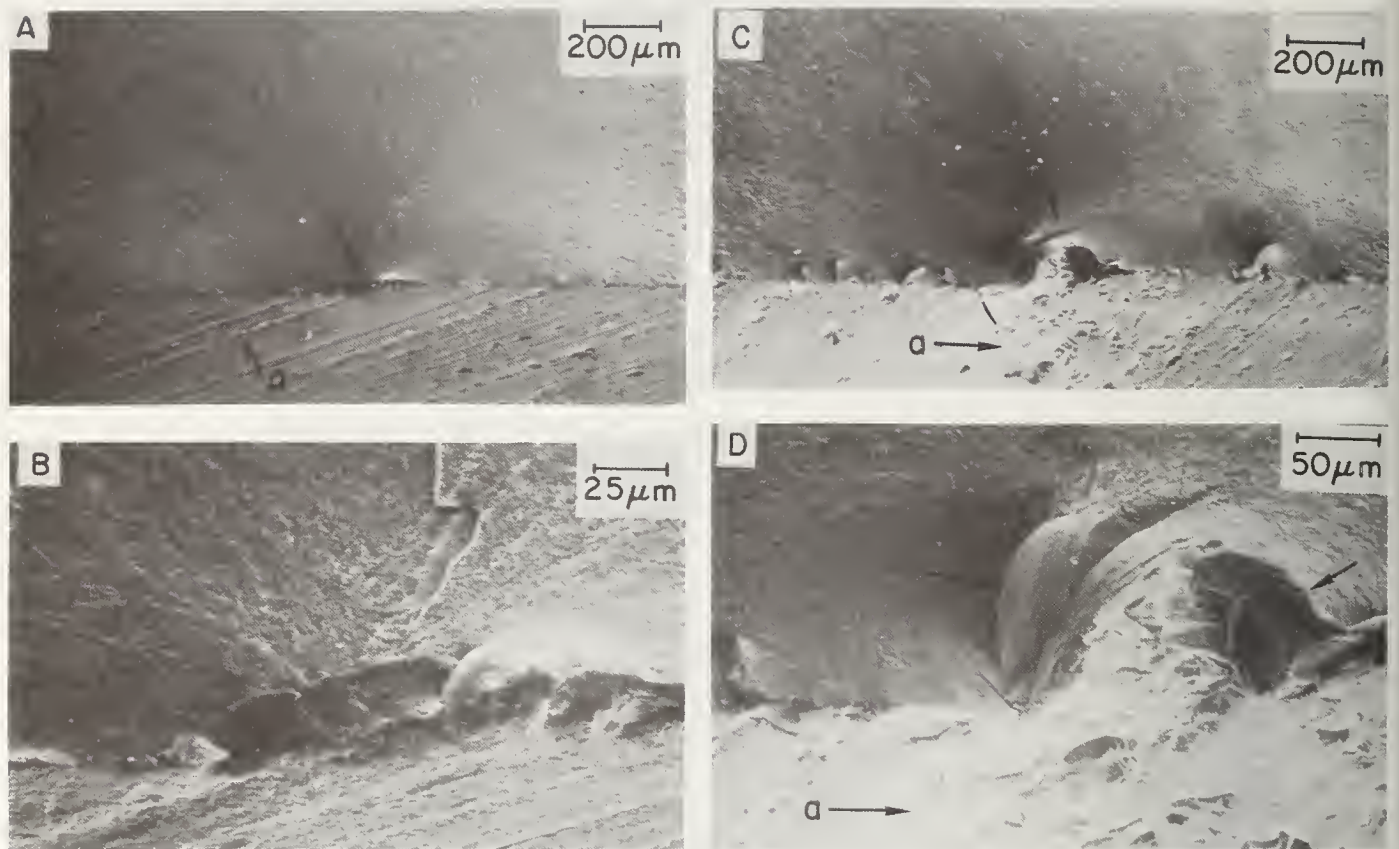


Figure 8. Further examples of flaws from diamond sawing at fracture origins of MgF₂. A and B show another example of an elongated flaw along one of the deeper sawing grooves at $\sim 45^\circ$ to the tensile axis as the source of failure. C and D show another sawn sample of the same hot pressed optical grade MgF₂ failing from sawing flaws where the sawing grooves are \sim parallel with the tensile axis. This illustrates the more complex character of flaws that sometimes can be encountered. Failure appears to have occurred from two flaws; i.e. from part of a flaw parallel to the grinding groove (l in D) and part, or all, of a flaw \sim perpendicular to the grinding groove. The apparent intersection of two such flaws at the fracture origins is rare but illustrates some of the complications that can arise.

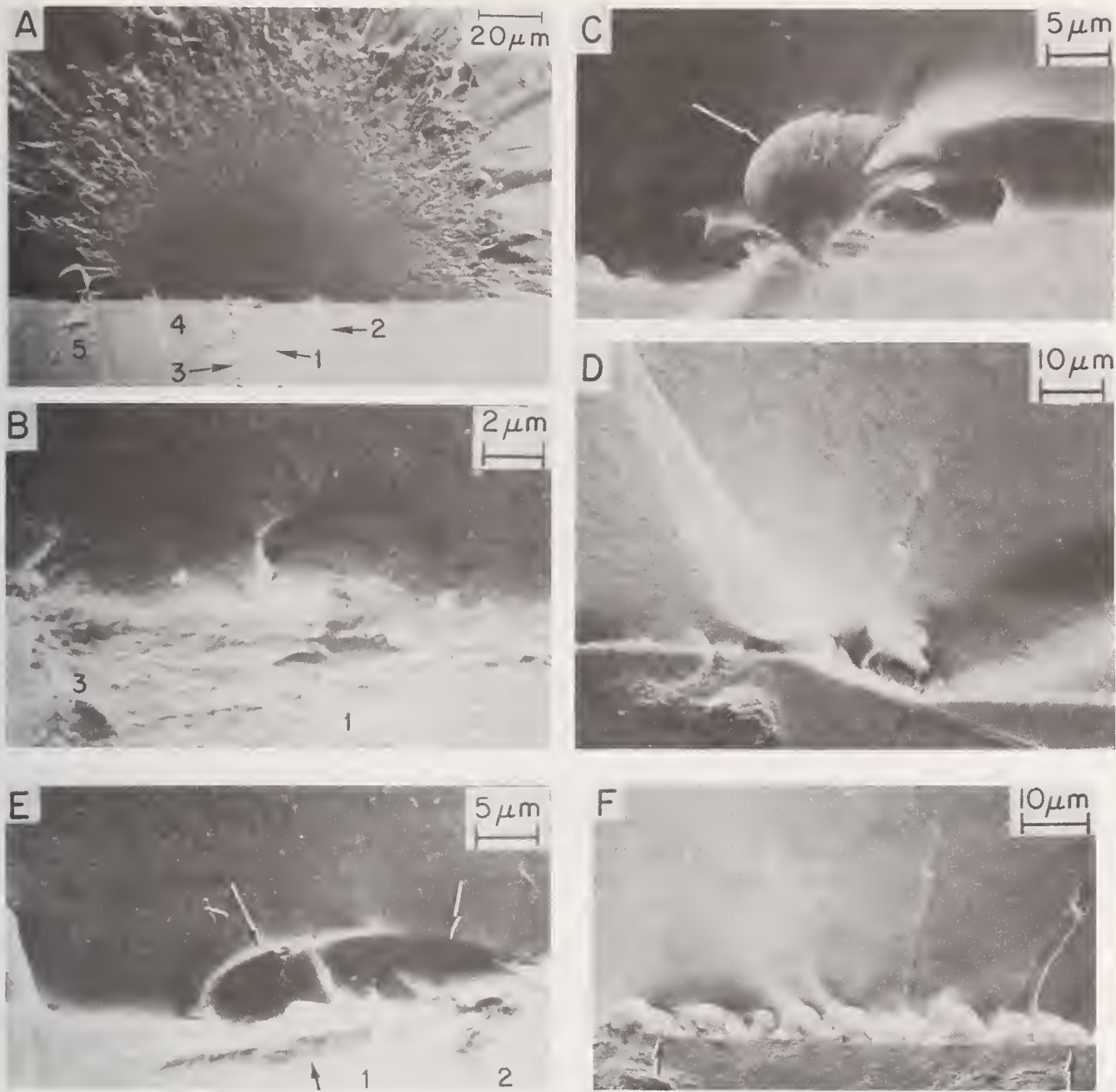


Figure 9. Examples of flaws from sanding CNTD SiC. A and B represent lower and higher magnifications of the fracture origin in a sample sanded ~ parallel with the tensile axis. Note the nearly semi-circular nature of the periphery of the flaw causing failure and its curved character. Note also that it is associated with a somewhat discontinuous sanding groove, (1). Note also that each of the other sanding grooves marked 1 through 5 in A has a flaw associated with them, but smaller than the flaw, F, which caused failure. Note also that some of the other flaws are parallel with the grinding groove, e.g. the flaw associated with scratch 3, and hence results in a short vertical step on the fracture surface. A number of cases of this type of behavior are observed for machining flaws, further reinforcing the concept of the two flaw population observed here. C, D, E, and F are photos of flaws at the origin of different specimens. Note the generally progressively more elongated character of the flaw or portion of the flaw exposed on the fracture surface as the angle of the scratch forming the flaw increases relative to the tensile axis. The much smaller flaw sizes in this material may reflect in part its extremely fine grain size, e.g. $0.2 \mu\text{m}$, but may also be significantly affected by the apparently fairly high residual stress that may exist in these bodies. They, however, provide an excellent opportunity for observing such scratches

and the resultant flaws not only because the fine grain size allows more definitive fractography, but also because they have a near pristine surface to begin with, i.e. producing strengths of the order of up to or exceeding 3,500 MPa (500,000 psi). The failure stress of the specimens were as follows: A, B - 1170 MPa (170,000 psi); C - 986 MPa (143,000 psi); D - 778 MPa (113,000 psi); E - 606 MPa (88,000 psi); F - 220 MPa (32,000 psi).

which is predominately of degree rather than of a kind on the flaws generated.

The third other form of abrasive machining, diamond polishing, has been investigated some. Observations have been made on materials polished in a typical fashion, i.e. with the specimen mounted on a disk which is allowed to rotate while the polishing wheel rotates. This results in a net pattern of abrasive particle motion over the surfaces which is essentially random as sketched in figure 10. Polishing flaws observed at fracture origins of single and polycrystalline materials studied to date are highly elongated flaws, e.g. figures 11 and 12, consistent with all of the above results in the following fashion. As a result of the essentially random motion of the abrasive particle over the surface, one should always have some of the most severe flaws, i.e. those forming parallel with the direction of motion of abrasive particles at or near perpendicularity to the tensile axis of the resultant test bar so that these elongated flaws would dominate failure as observed. It is also consistent with the fact that one has to do rather extensive polishing to obtain significantly higher strengths than can be obtained by diamond grinding parallel with the tensile axis. This results because of differences in the consistency of abrasive particle motion. Although the flaws from the typical polishing operation are somewhat shallower than those from grinding, strengths of polished specimens are typically being controlled by the more severe set of flaws generated by abrasive motion because of the essentially random direction of abrasive across the specimen. On the other hand, specimens ground parallel to the tensile axis have their strength controlled by the less severe population of flaws generated by the consistent motion of abrasive particles across the specimen.

Two factors should be noted about the polishing flaws observed. First, their periphery tends to be much smoother in contrast to the more irregular

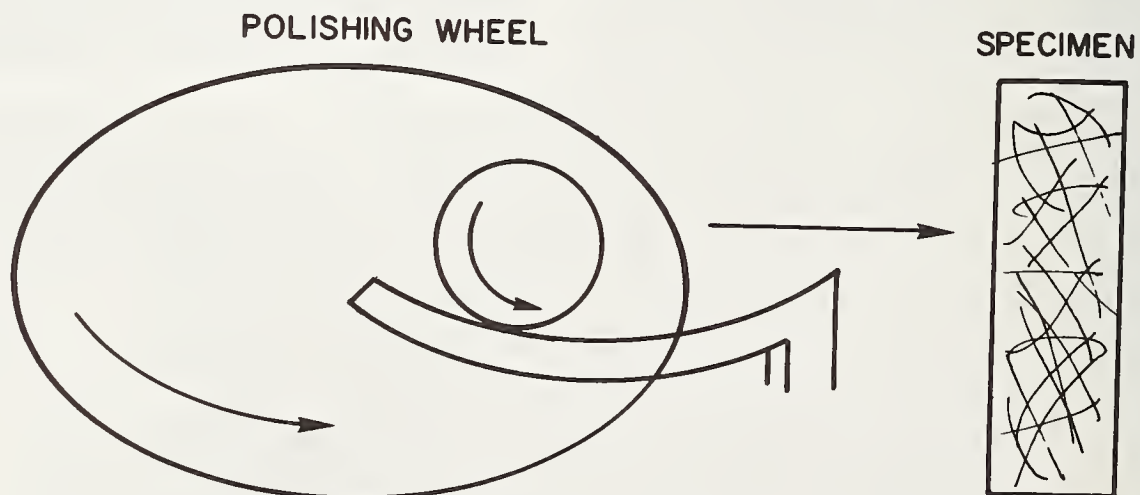


Figure 10. Schematic representation of the common polishing operation and resultant particle and scratch patterns on the surface of the specimen. Typically, these will approach a random pattern; hence the most severe flaws, i.e. those formed essentially parallel with the particles will dominate failure, even in uniaxial stressing.

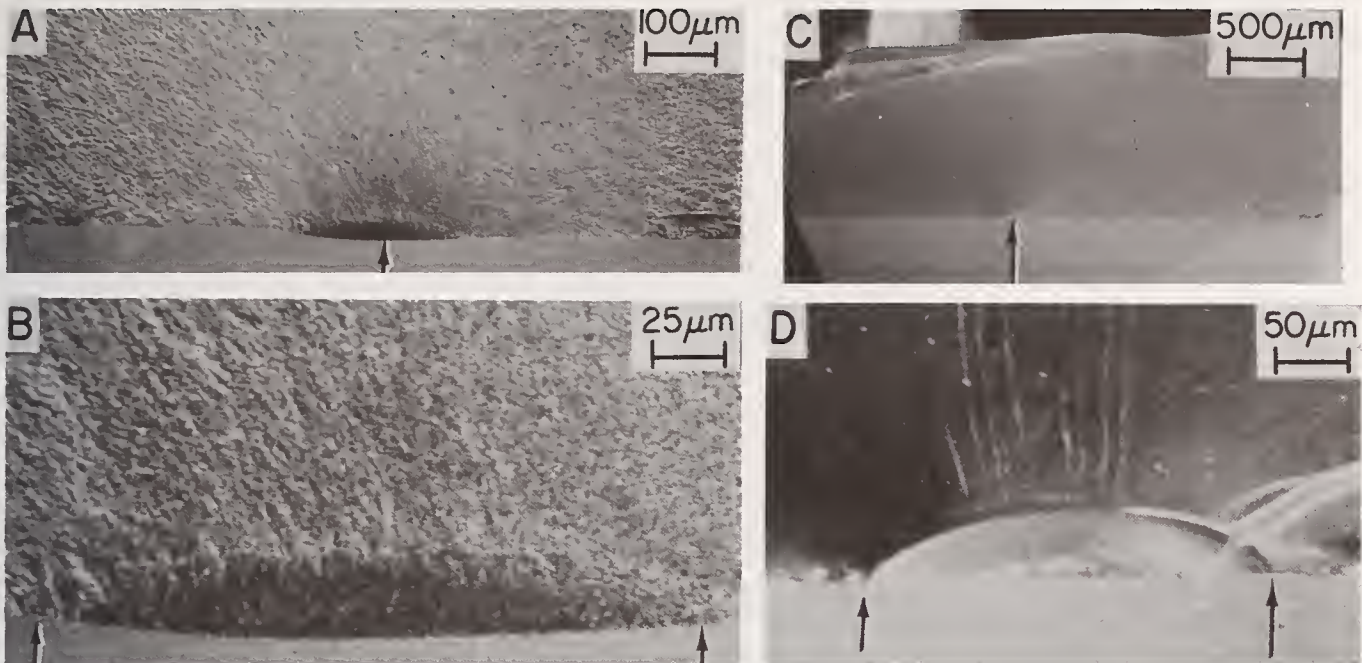


Figure 11. Examples of ceramic polishing flaws. A and B show the area of fracture and the fracture origin (arrows) of a fine grain polycrystalline body (hot pressed, optical grade MgF_2) as a result of polishing. This sample was tested in biaxial flexure, failure stress ~ 91.6 MPa (13,300 psi). Note the elongated character of the flaws as well as their relatively smooth periphery, in contrast to the commonly much more irregular shape of such elongated flaws from grinding. See figure 17 for another similar example. C and D show the fracture origin area and fracture origin (arrows) of a polished specimen of Al_2O_3 -rich $MgAl_2O_4$ (Verneuil) single crystal.

nature of elongated flaws from grinding. As shown in Sections 3 and 4.3, the elongated flaws from grinding are often more irregular, e.g. due to their being made up of a series of smaller flaws of varying degrees of overlapping character. This smoother character of polishing flaws may well represent either, or both of, two aspects of the polishing operations relative to the grinding operation. The much slower motion of the abrasive particles may directly be the cause of the much smoother nature of the flaw periphery due for example to less variation in friction. On the other hand, the slower speed of the abrasive particles may indirectly be effectively allowing more opportunity for stress corrosion or other phenomena to result in a smoother crack periphery during machining flaw formation. Secondly, it should be noted that while there are some differences between grinding and polishing flaws, overall the general nature of the flaws introduced appears to be similar. This again suggests that the velocity and forces associated with different abrasive processes are not a major factor in a character of the flaws that are introduced, but only result in varying degrees of the flaw parameters, e.g. their depth and smoothness.

4.3. Machining Flaw Distributions and Strength-Size Effects

An important set of questions is: 1) how variable are the flaws from machining in terms of size, shape, and orientation; and 2) how do such variations compare with the observed dependence of strength of specimens on their size and shape due to the differences in the amount of surface or volume under significant stress. While much yet needs to be done in terms of detailed studies of the variation and statistical distribution of the different

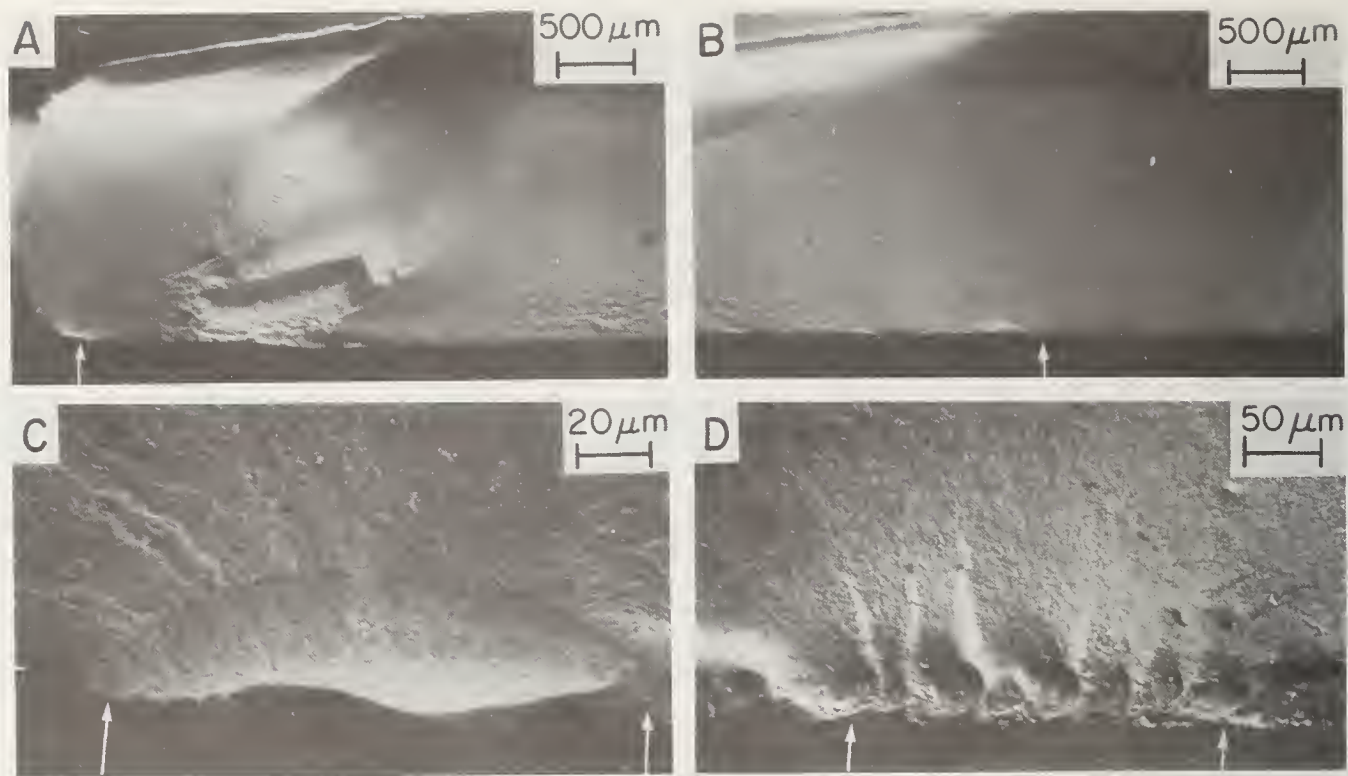


Figure 12. Examples of variation of grinding flaws in hot pressed, optical grade MgF_2 . A and B are fracture photos of the area of origin and the failure causing flaw (arrows) from grinding parallel with the tensile axis, fracture stress ~ 64 MPa (9,300 psi). Note the unusually elongated character for a flaw forming perpendicular to the direction of grinding. This may be in part due to the fact that this flaw is next to the edge of the sample. C and D show the fracture origin and failure causing flaw (arrows) in a sample of the same material ground perpendicular to the tensile axis; failure stress ~ 50 MPa (7,200 psi). This shows a somewhat more exaggerated, but not extreme, example of the type of variation that one can have in flaws forming essentially parallel with the grinding groove.

types of machining flaws, some important observations can be made at this time.

A variety of statistical variations of flaws are observed. One of the most frequent and obviously expected variations of flaws forming parallel and \sim along the bottom of the grinding grooves is their extent and regularity. Basically, these often appear to be not one flaw, but a series of flaws that partially or totally overlap, e.g. see figures 2,3,4,8,9, and 12. For flaws of the type characteristically perpendicular to the grinding grooves, a limited but definite number are observed forming at a variety of angles to the grooves, e.g. figure 13. In finer grain bodies, these angular variations represent sporadic variations of the material or variations of the local machining conditions. However, in larger grain bodies, and single crystals, especially non-cubic ones where planes of the same cleavage system may not be orthogonal, orientation of preferred fracture planes can also be important, figure 13C, D.

Also, some flaws of the type typically forming perpendicular to the grinding grooves may also be wider, i.e. more eccentric than \sim half penny flaws. Again local variations in grinding forces, e.g. a deeper grinding groove or flaw forming between grinding grooves (e.g. see reference 20, 21), as well as local variations in material properties. Another variation, especially with flaws of the type forming perpendicular to the grinding grooves are two to several \sim concentric markings before the final flaw boundaries,

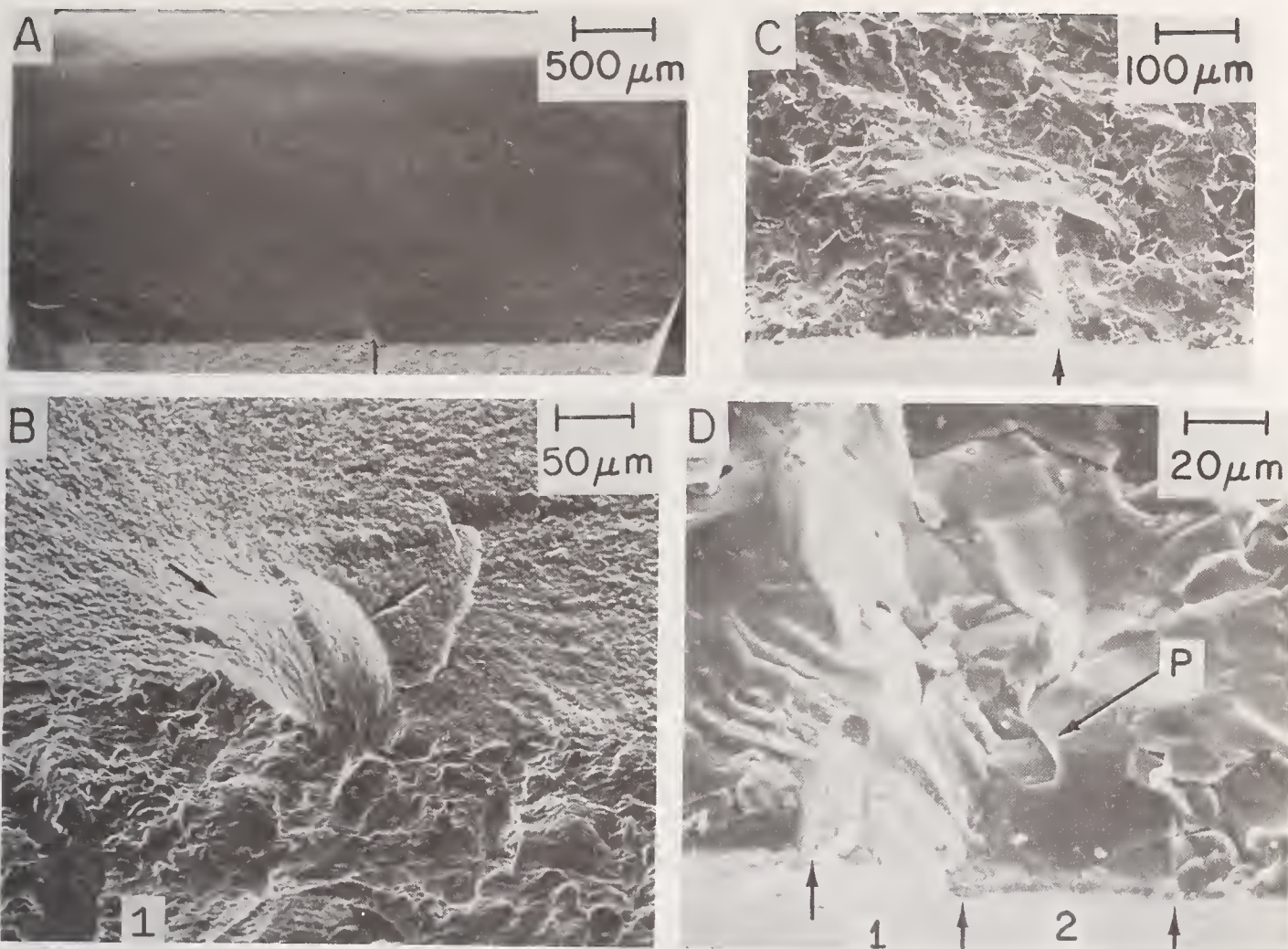


Figure 13. Examples of variation in flaws forming approximately perpendicular to the direction of grinding. A and B are fracture photos of the area of origin and the fracture origin arrows in a specimen of fine grain, dense mullite, fracture stress ~ 206 MPa (30,000 psi). Note that the flaw is at a substantial angle and has substantial curvature relative to the fracture plane and the tensile axis. While some such flaws may actually be the continuation, or a curved end, of a flaw forming parallel with the grinding direction, clearly many of them are not and are simply variations of the angle of flaws forming perpendicular to the direction of grinding. This sample represents an extreme misorientation of such flaws. Note also that there is no obvious deep grinding groove associated with this flaw and that there is a definitive grinding groove to the left of it in B. C and D are photos of the area of fracture origin in dense, hot pressed SiC, failure stress ~ 372 MPa (54,000 psi). While the specific fracture origin and the machining flaws are both less well-defined, 1 is a fairly probable machining flaw and 2 is a possible machining flaw in D. Note that these are \sim equal to the grain size and that neither is associated with obvious grinding grooves. Note also the substantial angle of 1 relative to the direction of grinding and the tensile axis may be as much or more due to the orientation of the grain in which it formed, e.g. due to the orientation of a preferred cleavage plane in that grain, rather than a statistical variation in the machining or material parameters governing the formation of cracks.

e.g. figure 6. Such observations, which are more common than shown in the examples in this paper indicate that the flaws are often formed in stages by some degree of oscillating stresses, or with other vibration.

Another important variation in machining flaws is the formation of edge flaws, such as along the edges of rectangular test bars or edges of components, e.g. trailing edges of turbine blades. While fracture origins from sample edges are generally readily identified, specific flaws are not always evident, e.g. figure 14. However, a substantial number have been identified,

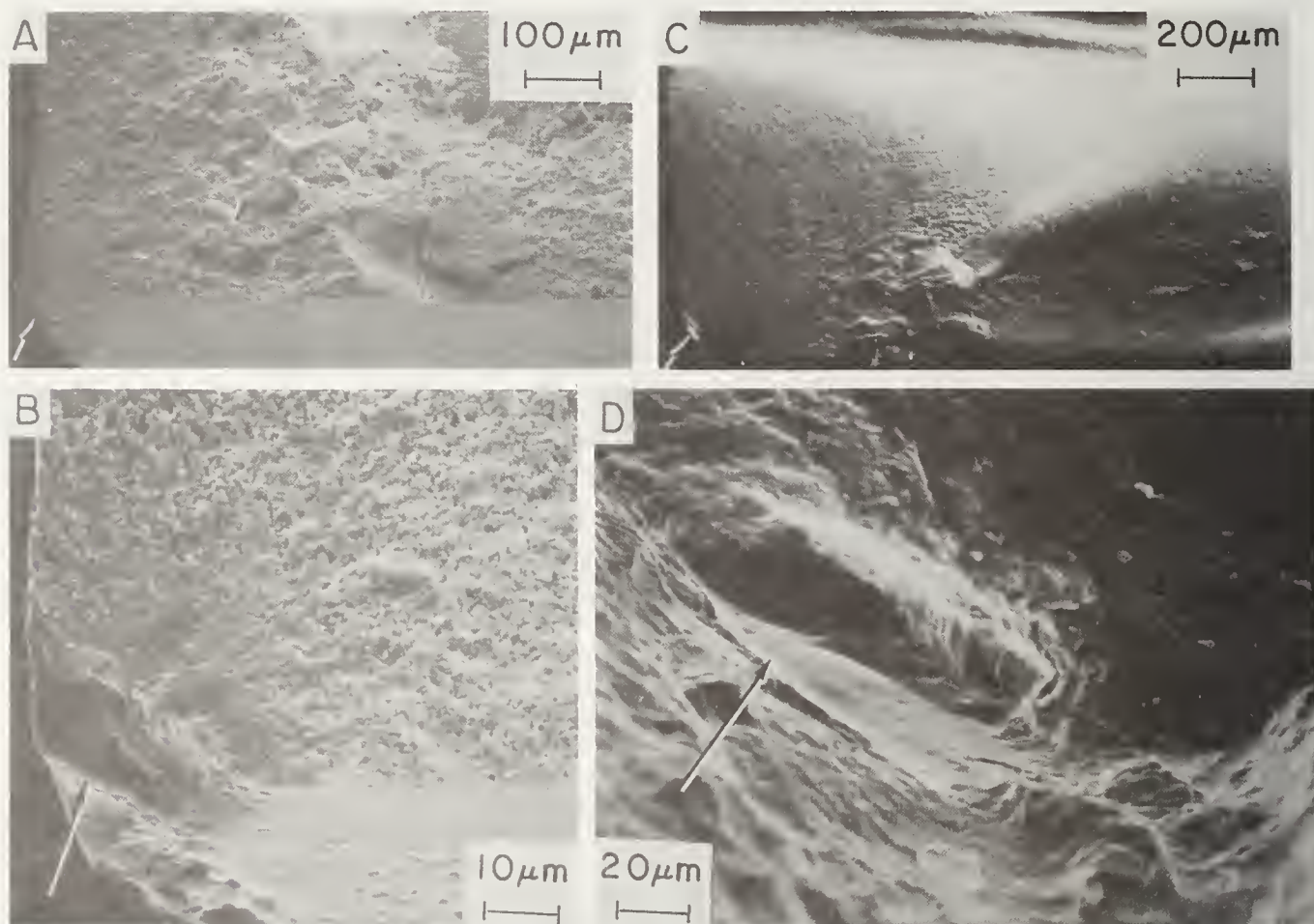


Figure 14. Examples of ill-defined edge flaws at fracture origins in fine grained ceramics. A and B are fracture photos showing the origin of a fine grain ZrO_2 body partially stabilized with 8 w/o Y_2O_3 , fracture stresses 276 MPa (40,000 psi). C and D are similar photos of fine grain, dense mullite, failure stress \sim 296 MPa (43,000 psi). Note that the specimens failed from one of their edges are quite definite and usually fairly readily determined but the specific flaw size and shape often cannot be defined, though first approximation would simply be to use the approximate dimensions of the edge chip in A and B, or lip in C and D as a flaw dimension. Such fracture origins are quite common for specimens failing from edges.

some of which may be close to a quarter ellipse or circle, but there can be a variety of shapes as indicated in figure 15. An example of an edge flaw in hot pressed Si_3N_4 is shown in reference 21. Some indications of the frequency with which such flaws can occur are given elsewhere [4]. It has also been shown that while such edge flaws may be more severe, and hence giving lower strengths, this is clearly not universally so.

An important question is what are the spatial and size distributions of machining flaws. At present, only partial indications of these distributions exist. Thus, for example, fracture surfaces have been examined for machining flaws other than the one from which failure initiated. Such examinations are most definitive in the smooth, fracture mirror, area since machining flaws, especially smaller ones, will generally be partly or totally obscured in the hackle and crack branching regions of fracture [12]. Thus, more area is seen on weaker specimens which could bias the results. However, such observations do give a preliminary idea of flaw distributions, e.g. other machining flaws 10-50% the size of the one causing failure have been reported within $\sim 100\text{-}300\ \mu\text{m}$ along ground surfaces of fine grain MgF_2 and As_2S_3 glass [4]. Similarly note other machining flaws near the fracture origins of specimens in figures 7-9. Finally, one other preliminary indication of flaw distributions are slow crack growth observations in hot pressed Si_3N_4 (HPSN). At elevated temperatures, flaws begin to open up on tensile surfaces of HPSN due to local deformation, presumably predominantly by grain bound-

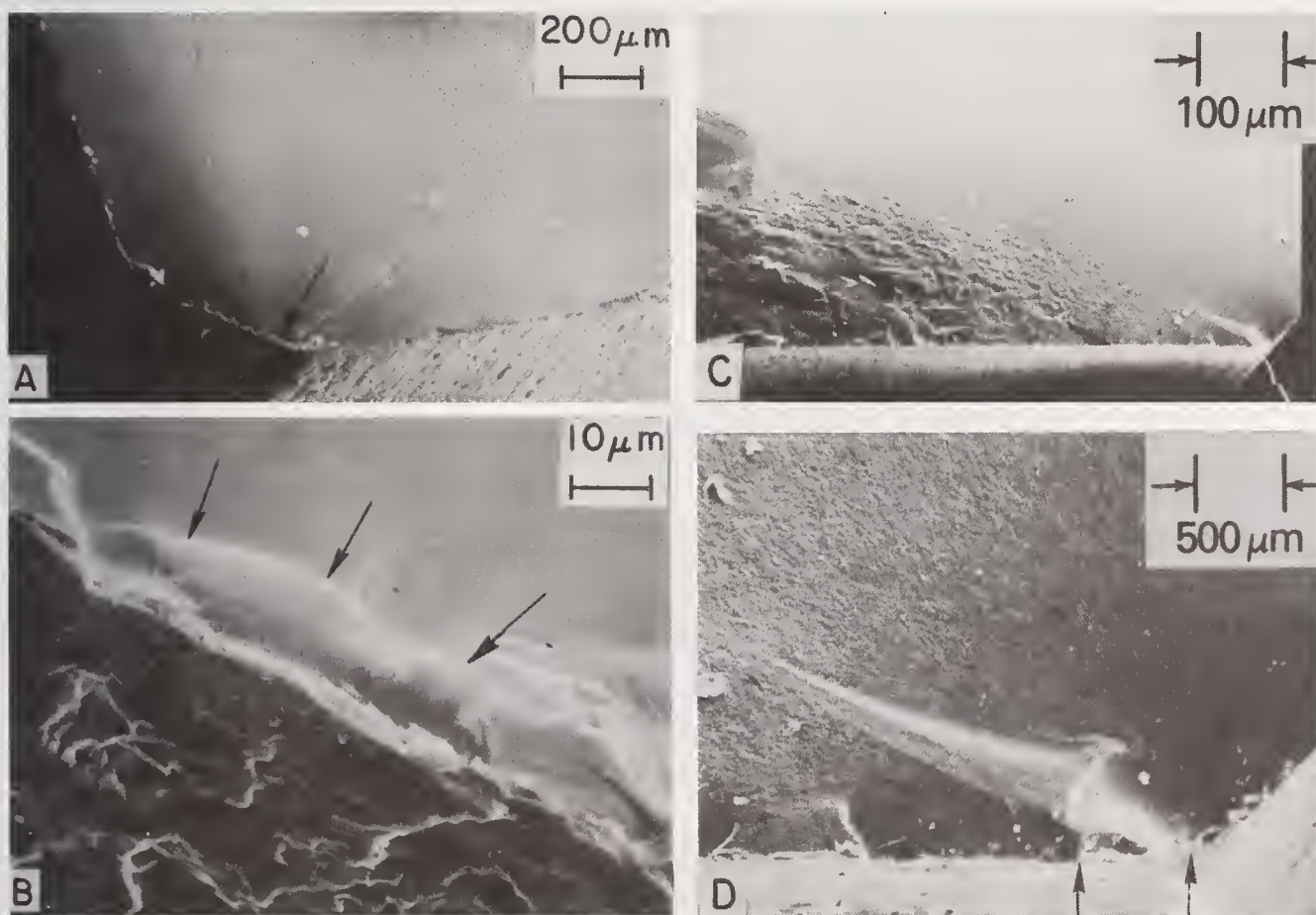


Figure 15. Examples of specific failure causing flaws at specimen edges. A and B are photos of the area of origin and specific fracture origin (arrows) in a single crystal of CaO stabilized ZrO_2 , failure stress 105 MPa (15,300 psi). C and D are fracture photos of the area of origin and actual origin (arrows) of a failure causing flaw at the edge of a hot pressed MgF_2 .

ary sliding. These opening cracks appear to often originate from larger machining flaws (some cases of this have been verified [21]). Therefore, the distribution of these opening cracks gives some idea of the surface density of flaws, e.g. figure 16. While controlled, e.g. side, lighting, or etching

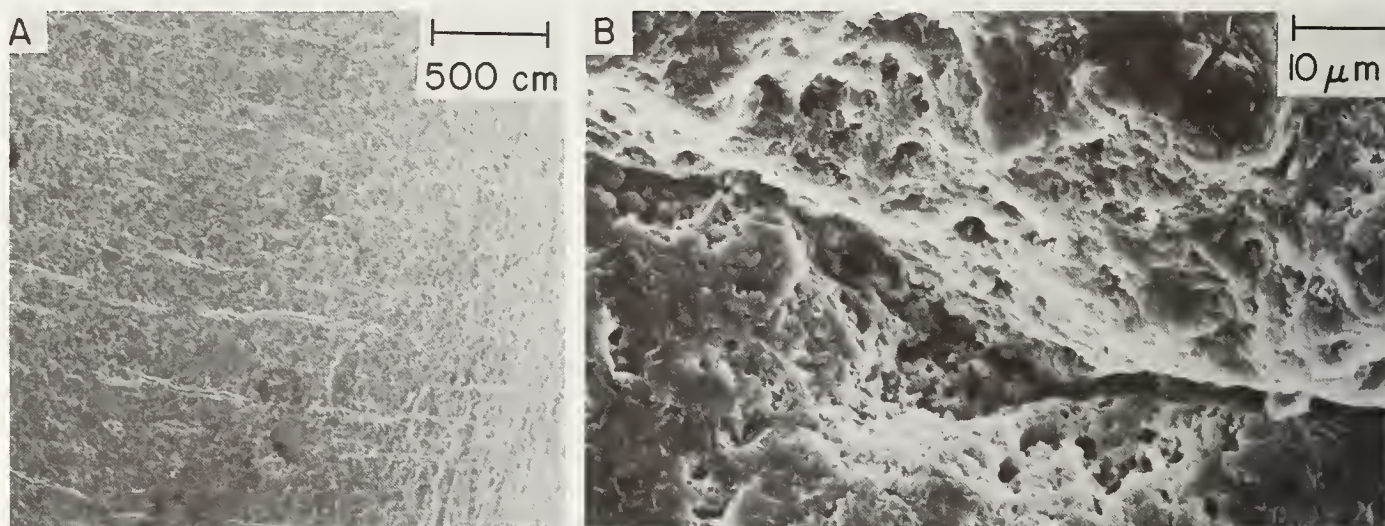


Figure 16. Example of slow crack growth opening of machining flaws. A and B show hot pressed Si_3N_4 (HS-130) tensile creep rupture tested at ~ 87 MPa (12,500 psi) at 1300°C (failure strain $\sim 13.8 \times 10^{-3}$). Note the \sim linear features developing on the surface, shown at higher magnification in B. Machining flaws such as those identified as the source of fracture at lower temperatures (e.g. fig. 18A, B) have been identified as a major source of such flaw growth [21].

of machined transparent bodies, especially of glasses and crystals can be important tools in better defining machining flaw populations, opening of flaws due to slow crack growth may have fairly broad applicability. Thus, a variety of Al_2O_3 and other commercial ceramic bodies, such as crystallized glasses [33] are known, or expected, to exhibit slow crack growth that could be exploited for further definition of machining flaw populations.

The studies thus far of this paper have been made mainly on bars $\sim 1.3 \times 2.6 \times 13$ mm. While much strength-specimen size dependence arises from processing defects [5,6,34,35], the observed size dependence of the strength of ceramic material such as glasses and dense polycrystalline bodies where machining flaws should dominate would suggest that there is a size dependence to the maximum flaw size introduced by machining samples of different sizes. In order to specifically test this, large bars of optical grade, fully dense, hot pressed MgF_2 were ground on one side parallel to the tensile axis and on the other perpendicular, then tested. Sections of these large MgF_2 bars after flexural testing were then cut up into smaller test bars whose tensile surfaces were the original ground surfaces of the large bars so we were testing the same flaw population. The results of these tests along with some data on different sets of B_4C specimens are shown in table 4.

The results of table 4 suggest a possible effect of the specimen size on the size of machining flaws controlling strengths, but several complications occur. First, since the same head travel rate was used, the strain rates were lower for larger bars allowing more slow crack growth to occur; thus strain rate is being held constant in other tests of MgF_2 and SiO_2 based glasses now underway. Second, processing defects (and possibly variations in B_4C) play a larger role in the failure of larger bars, limiting the machining results. Third, both MgF_2 and B_4C have internal stresses due to their non-cubic crystal structures which limit the increases in strength with decreasing flaw size [36]. Thus, while the strength results do not

strongly show a size effect, the flaw observations more strongly indicate such an effect. In order to minimize these complications, additional tests are now under way on SiO₂ based glasses. However, initial results have been complicated by different types of flaws being common sources of failure in many of the large bars. These flaws represent either handling damage (which could be much more severe in larger, i.e. more massive, bars), or a new, much more limited population of machining induced flaws, e.g. from such possible effects such as damage from unusually large swarf particles trapped between the specimen and grinding wheel.* Other indications that a size effect for machining flaws may exist, but may generally be limited, are shown by fracture origins of components or prototypes, e.g. figures 17, 18, and references 5,16,18, and 19. These suggest somewhat deeper flaws than in test bars, but specimen shape may also be a factor. Thus, the data of Bansal and Duckworth on Pyroceram 9606 [34] reporting no size effect of machining is not necessarily at conflict with the preliminary studies. Either their material or machining may have produced limited changes in machining flaw sizes not discernable in the limited number of observations made. (Again, possible effects of internal stresses could limit strength differences between different size bars with different size flaws.)

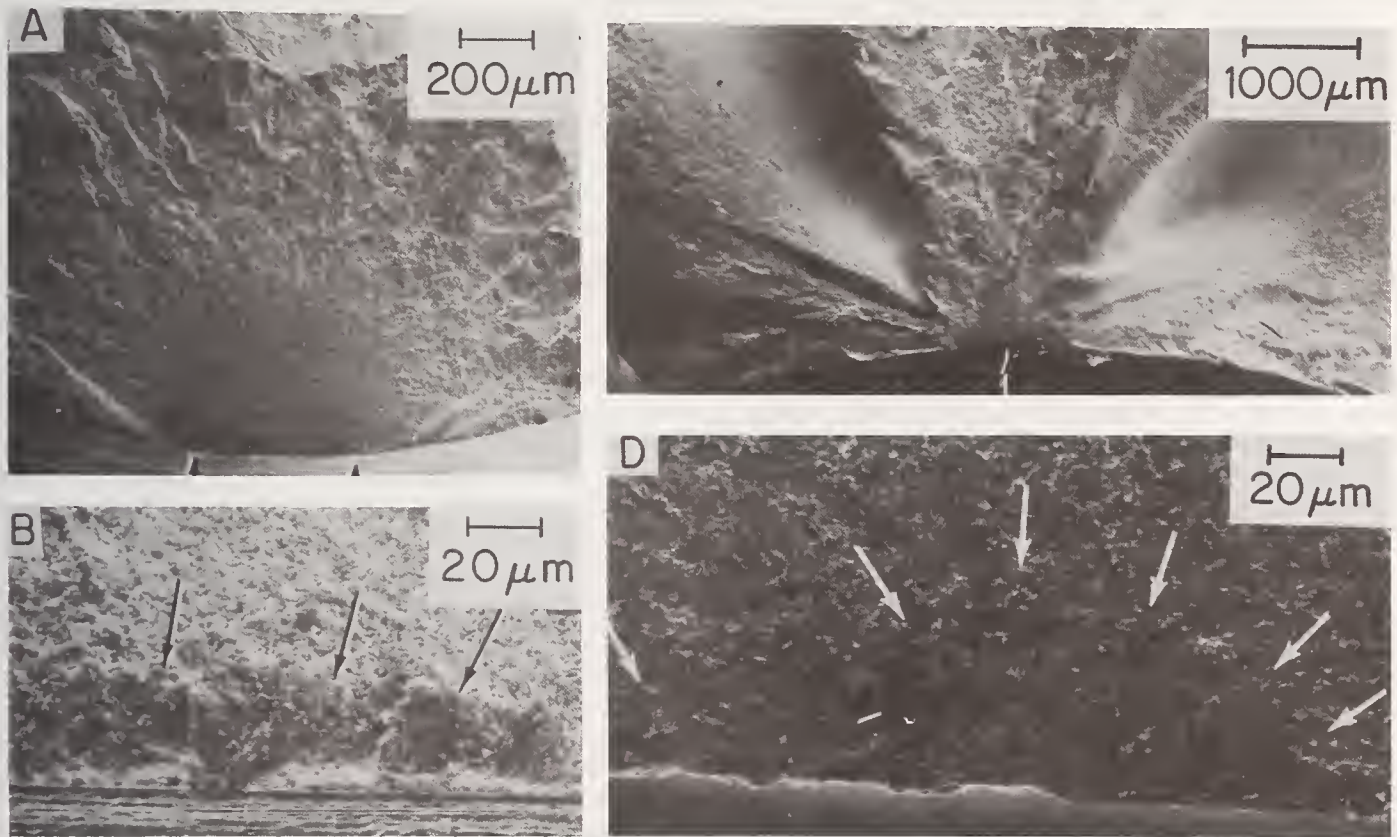


Figure 17. Photos of the area of fracture origin and actual origin (arrows) of a polished, IR dome, MgF₂ failed in a simulated aero-thermal heating test. The failure stress of ~ 69 MPa (10,000 psi) estimated from the observed flaw size and the measured fracture energy and Youngs modulus is in excellent agreement with the failure stress predicted from thermal analysis. Note the similarity in size and shape of this flaw in a polished component to that shown earlier in figure 11 in a polished MgF₂ disk.

* Another possible source of different flaws are those formed at the edge of the grinding wheel on larger bars that are wider than the wheel in contrast to small bars which are narrower than the wheel.

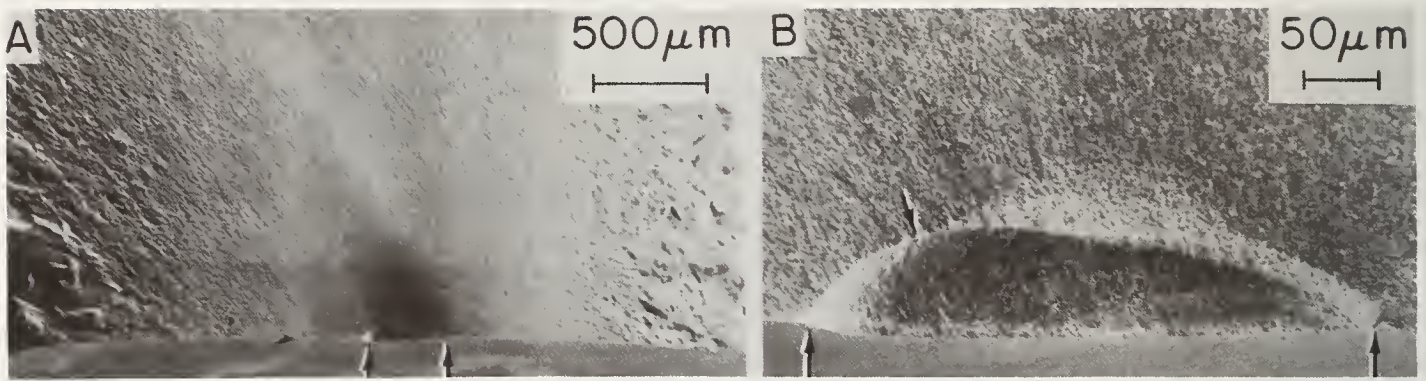


Figure 18. Examples of machining flaws at fracture origins in hot pressed Si_3N_4 (NC-132). A and B are photos of the area of fracture origin and the fracture origin (arrows) of specimen ground circumferentially for true tensile testing; fracture stress 312 MPa (45,300 psi). B shows a portion of the highly elongated flaw which is about average in definition for such flaws in Si_3N_4 . Other clearer examples of these types of flaws can be found in references 20 and 21. C and D show the fracture origin area and fracture origin (arrows) in a simple prototype Si_3N_4 turbine blade spun tested to failure at room temperature. The specimen (courtesy of Mr. Dave Richerson, Garrett Airesearch) failed in the attachment area where stresses are highest and machining is perpendicular to the blade (tensile) axis; failure stress was ~ 483 MPa (70,000 psi). Note the Richerson and Yonushonis [37] have shown similar, clearer examples of such fracture origins in failed turbine blades.

5. Summary and Conclusions

Fractography has been used to identify machining flaws controlling the strengths of a variety of ceramic bodies. This shows that sawing, grinding, sanding, and polishing all introduce predominately two populations of flaws extending in from the surface. One set, those giving the lowest strengths are formed essentially parallel with the machining grooves formed by the grit particles and are generally fairly elongated. The other set of flaws, those typically giving higher strengths, are typically formed perpendicular to the machining grooves and are generally less elongated, often approaching a semi-circular periphery. The differences in size and shape in these two sets of flaws combined with their orientation relative to the direction of machining are the predominate cause of the anisotropy of strength as a function of the stressing direction relative to the direction of machining.

Variations in the depth, shape, and orientation of the above sets of flaws have been observed, as well as effects of composition and microstructure. While some variations in flaw orientation appear to be sporadic in larger grain bodies where flaws are similar to or less than the grain in size, and especially in single crystals, the orientation of preferred cleavage planes can be an important factor. The set of generally elongated flaws that typically form parallel with the machining grooves vary from a continuous flaw to a series of partially overlapping flaws. Flaws forming generally perpendicular to machining grooves often have a fan and curved character, e.g. like half a clam shell. No obvious effect of body composition is seen on the size, i.e. depth, of either set of flaw introduced, and decreasing grain size has at best a limited effect on reducing the size of the strength controlling flaws introduced. Thus, the typical variety of machining processes commonly introduce flaws in the range of 20-50 μm depth for both sets

of flaws in glasses, single crystals, and typical grain size dense polycrystals in most laboratory size test bars. Limited evidence, as well as the statistical nature of machining flaws, both suggest that the size of machining flaws controlling strength increases some with specimen or component size. However, increasing competition from other flaws, e.g. processing flaws or flaws introduced by handling processes limit such machining flaw size-specimen size evaluation.

TABLE 4
SPECIMEN SIZE-STRENGTH¹ AND FLAW SIZE EFFECTS IN GROUND BARS

Ground \perp ²				Ground \parallel ²			
Strength		Flaw ³		Strength		Flaw ³	
ksi	MPa	a (μm)	b/a	ksi	MPa	a (μm)	b/a
<u>MgF₂ (KODAK, HOT PRESSED, ~ 0 POROSITY, GRAIN SIZE ~ 0.5 μm)</u>							
Span 4 cm, cross section 1 x 1.8 cm:							
11 \pm 2 (4)	76 \pm 14	75 \pm 20 (4)	4 \pm 2	12 \pm 2 (3)	80 \pm 14	-	-
Span 1.27 cm, cross section 0.51 x 0.25cm:							
12 \pm 1 (4)	80 \pm 7	42 \pm 3 (3)	~ 4	16 \pm 3 (9)	110 \pm 20	57 \pm 11 (3)	0.8 \pm 0.3
<u>B₄C (NORTON, HOT PRESSED, < 1% POROSITY, GRAIN SIZE ~ 10 μm)</u>							
Span 2.54 cm, cross section 1.27 x 0.60 cm:							
35 \pm 4 (4)	240 \pm 27	100 \pm 80 (3)	1.1 \pm 0.2	44 \pm 6 (4)	304 \pm 40	60 \pm 40 (3)	1 \pm 0.5
Span 1.27 cm, cross section 0.62 x 0.24 cm:							
34 \pm 12 (7)	235 \pm 80	18 \pm 3 (3)	3 \pm 1	49 \pm 6 (7)	338 \pm 40	-	-
<u>B₄C (FIBER MATERIALS, HOT PRESSED, < 1% POROSITY, GRAIN SIZE ~ 2 μm)</u>							
Span 1.9 cm, cross section 0.51 x 0.25 cm:							
19 \pm 2 (5)	130 \pm 14	29 \pm 11 (4)	4 \pm 1	47 \pm 12 (5)	325 \pm 80	13 \pm 8 (3)	2 \pm 1.8

¹ Strengths measured at 23^oC in 3 point flexure with a head travel rate of ~ 1.27 mm/min.

² \perp and \parallel refer respectively to the direction of grinding relative to the bars' tensile axis. Lower numbers in parentheses give the number of values. The fewer number of values for flaw parameters than strengths reflect failure from processing defects or specimen edges.

³ a = flaw depth, b = flaw length along surface.

References

- [1] Rice, R. W., Panel Discussion, in The Science of Ceramic Machining and Surface Finishing, NBS Special Pub. 348, 407-408, S. J. Schneider and R. W. Rice, eds. (Govt. Printing Office, Wash., D.C. 20402, 1972).
- [2] Mecholsky, J. J., Freiman, S. W., and Rice, R. W., Effect of Grinding on Flaw Geometry and Fracture of Glass, J. Am. Ceram. Soc. [60] 3-4 (1977).
- [3] Mecholsky, J. J., Freiman, S. W., and Rice, R. W., Effect of Surface Finish on the Strength and Fracture of Glass, Proc. of the XIth Int. Congress on Glass, Prague, Czechoslovakia (1977).
- [4] Rice, R. W., Machining of Ceramics, in Ceramics for High-Performance Applications, 287-243, Proc. of 2nd Army Materials Technology Conf., Hyannis, Mass (1973).
- [5] Rice, R. W., Mecholsky, J. J., Freiman, S. W. and Morey, S. M., to be published in Proc. in Quantative NDE Conf. , Cornell Univ., Air Force Report #AFML-TR-77 (1977).
- [6] Rice, R. W., Processing Induced Sources of Mechanical Failure in Ceramics, in Proc. of Conf. on the Processing of Crystalline Materials, H. Palmour III, R. F. Davis, and T. M. Hare, eds., 303-319 (Plenum Press, 1978).
- [7] Rice, R. W., Microstructure Dependence of Mechanical Behavior of Ceramics, in Treatise on Materials Science and Technology, Vol. 11, Properties and Microstructure, 199-381 (Academic Press, N.Y., 1977).
- [8] Freiman, S. W., Mecholsky, J. J., Rice, R. W. and Wurst, J. C., Influence of Microstructure on Crack Propagation in ZnSe, J. Am. Ceram. Soc. [58] 9-10, 406-409 (1975).
- [9] Rice, R. W., Mecholsky, J. J. and Becher, P. F., The Effect of Grinding Direction on Flaw Character and Strength of Single Crystal and Polycrystalline Ceramics, to be submitted to J. Am. Ceram. Soc.
- [10] Rice, R. W., Machining, Surface Work Hardening, and Strength of MgO, J. Am. Ceram. Soc. [56] 10, 536-541 (1973).
- [11] Rice, R. W., The Effect of Grinding Direction on the Strength of Ceramics, in The Science of Ceramic Machining and Surface Finishing, NBS Special Pub. 348, 365-376, S. J. Schneider and R. W. Rice, eds., (Govt. Printing Office, Wash., D. C. 20402, 1972).
- [12] Rice, R. W., Fracture Topography of Ceramics, in Surfaces and Interfaces of Glass and Ceramics, 439-472, V. D. Frechette, W. C. LaCourse, and V. L. Burdick, eds. (Plenum Press, N. Y. 1974).
- [13] Kirchner, H. P., Gruver, R. M. and Walker, R. E. Strength Effects Resulting from Simple Surface Treatments, in The Science of Ceramic Machining and Surface Finishing, NBS Spec. Pub. 348, 353-363, S. J. Schneider and R. W. Rice, eds., (Govt. Printing Office, Wash., D. C. 20402, 1972).
- [14] Richerson, D. W., Schuldies, J. J., Yonushonis, T. M. and Johansen, K. M., ARPA/Navey Ceramic Engine Materials and Process Development Summary, in Proc. of 5th Army Materials Technology Conf. on Ceramics for High Performance Applications-II, J. J. Burke, E. N. Leno and R. N. Katz, eds. (Brook Hill Pub. Co., Mass. 1978).

- [15] Gielisse, P. J., Kim, T. J. and Choudry, A., Dynamic and Thermal Aspects of Ceramic Processing, Naval Air Systems Command Contract Report, 15 Nov 1970-15 Nov 1971, Univ. of Rhode Island, Ingston (Dec. 1971, AD 740 833).
- [16] Tressler, R. E., Langensiepen, R. A. and Bradt, R. C., Surface-Finish Effects on Strength-vs-Grain Size Relations in Polycrystalline Al_2O_3 , J. Am. Ceram. Soc. [57] 5, 226-227 (1974).
- [17] Bradt, R. C., Dulberg, J. L. and Tressler, R. E., Surface Finish Effects and the Strength-Grain Size Relationship in MgO, Acta Metallurgic [24] 529-534 (Pergamon Press, Great Britain, 1976).
- [18] Cranmer, D. C., Tressler, R. E. and Bradt, R. C., Surface Finish Effects and the Strength-Grain Size Relation in SiC, J. Am. Ceram. Soc. [60] 5, 230-237.
- [19] Bradt, R. C. and Tressler, R. E., Microstructure/Surface Finish Control of the Strength of Polycrystalline Ceramics, Proc. of 6th Int. Mat. Symposium on Ceramic Microstructures, 76, R. M. Fulrath and J. A. Pask, eds., 785-795 (Westview Press, Boulder, Colorado, 1976).
- [20] Rice, R. W., Freiman, S. W., Mecholsky, J. J., Ruh, R. and Harada, Y., Fractography of Si_3N_4 and SiC, in Ceramics for High Performance Applications-II, Proc. of 5th Army Materials Technology Conf., J. J. Burke E.N. Leno and R.N. Katz, eds. (Brook Hill Publishing Co., Chestnut Hill, MA, 1978).
- [21] Rice, R. W., Freiman, S. W. and Mecholsky, J. J., Fracture Sources in Si_3N_4 and SiC, Proc. of 1977 DARPA/NAVSEA Ceramic Gas Turbine Demonstration Engine Program Review, 665-688, J. W. Fairbanks and R. W. Rice, eds. Maine Maritime Academy, Castine, Maine, 1-4 Aug 1977 (MCIC 78-36).
- [22] Rice, R. W., Machining Flaws and the Strength-Grain Size of Ceramics, this conference.
- [23] McDonough, W. J., Flinn, D. R., Stern, K. H. and Rice, R. W., Hot Pressing and Physical Properties of Na Beta Alumina, J. Mat. Sci., 13, 2403-2412 (1978).
- [24] Richerson, D. and Yonushonis, T., in Ceramic Gas Turbine Engine Demonstration Program, Interim Report #4, 4-8 to 4-10, Airesearch Report #76-212188(4), Contract #N00024-76-C-5352 (1977).
- [25] Brüche, E. and Poppa, H., Zur Kenntnis der Glasoberfläche, Electron Microscopy, 336-338, F. S. Sjostrand and J. Rhodin, eds. (Academic Press, New York, 1956).
- [26] Imanaka, O., Lapping Mechanics of Glass-Especially on Roughness of Lapped Surface, Annals of the C.I.R.P., Vol. XIII, 227-233 (Pergamon Press, 1966).
- [27] Allgeyer, G. H. and Colwell, L. V., Aspects of Machining Glass-Ceramic Materials, in The Science of Ceramic Machining and Surface Finishing, NBS Special Pub. 348, 53-57, S. J. Schneider and R. W. Rice, eds (Govt. Printing Co., Wash., D.C. 20402, 1972).
- [28] Brian, L. and Wilshaw, R., Review Indentation Fracture: Principles and Applications, J. Mat. Sci. [10], 1049-1081 (1975).
- [29] Evans, A. G., Abrasive Wear Damage in Brittle Materials, this conference.

- [30] Doremus, R. H., Johnson, W. A., Depths of Fracture-Initiating Flaws and Initial Stages of Crack Propagation in Glass, *J. Mat. Sci.*, 13, 855-858 (1978).
- [31] Mecholsky, J. J. Fractographic Analysis of Delayed Failure in MgF_2 , submitted to *J. Am. Ceram. Soc.*
- [32] Dutta, S., Rice, R., Graham, H. and Mendiratta, M., Characterization and Properties of Controlled Nucleation Thermo Chemical (CNTD) Deposited Silicon Carbide, to be published.
- [33] Govila, R. K., Kinsman, K. R. and Beardmore, P., Fracture Phenomenology of a Lithium-Aluminum-Silicate Glass-Ceramics, *J. Mat. Sci.*, 13, 2081-2091 (1978).
- [34] Bansal, G. K., Duckworth, W. H. and Niesz, D. E., Strength-Size Relationships in Ceramic Materials: Investigation of a Commercial Glass-Ceramic, *J. Am. Ceram. Soc.* [55] 3, 289-308 (1976).
- [35] Bansal, G. K., Duckworth, W. H. and Niesz, D.E., Strength Size Relationships in Ceramic Materials: Investigation of an Alumina Ceramics, *J. Am. Ceram. Soc.* [59], 11-12, 472-478 (1976).
- [36] Rice, R. W., Pohanka, R. C. and McDonough, W. J., The Effect of Stresses from Thermal Expansion Anisotropy, Phase Transformations and Second Phases on the Strength of Ceramics, submitted for publication.
- [37] Richerson, D. and Yonushonis, T., in Ceramic Gas Turbine Engine Demonstration Program, Interim Report #5 , 3-9 to 3-11, Airesearch Report #76-212188(5), Contract #N00024-76-C-5352 (1977).

Note added in Proof

Two factors, slow crack growth and residual stresses, not addressed in the text should be briefly considered. While slow crack growth might increase flaw sizes by 50-100% in the extreme, this would not change the strength anisotropy unless the growth was significantly different for the two populations of flaws. The generally good agreement between measured strength anisotropy and that calculated from observed flaws argues against significant differences in flaw growth. Further, fracture energies calculated from observed flaw sizes generally agree with measured values [9,20-23,36] unless altered by other factors such as thermal expansion anisotropy [36], indicating flaw growth in most of these materials is limited, e.g. < 50%. If residual stresses in the surface from machining were compressive in nature, they would compensate, at least in part, for slow crack growth. On the other hand, if residual stresses are tensile, e.g. as indicated in recent indentation tests (private communication with Dr. Brian Lawn) then their effects would be additive to those of slow crack growth. Again, the above results indicate that any additive effects are limited. Thus, while further study of slow crack growth and residual stress are important to refine our understanding of machining flaw-mechanical property relations, they do not appear to require major changes in the results and conclusions of this study.

ACOUSTIC SURFACE WAVE MEASUREMENTS OF SURFACE CRACKS IN CERAMICS

B. T. Khuri-Yakub¹, A. G. Evans², and G. S. Kino²

¹Edward L. Ginzton Laboratory
Stanford University
Stanford, CA 94305

²Materials Department
University of California
Berkeley, CA 94720

Acoustic surface wave techniques for detecting and characterizing surface cracks in ceramics have been devised. The techniques have been demonstrated to detect cracks at least as small as 60 μm in depth, on polished samples. The crack detectability was diminished by surface grinding, because of a background effect attributed to the backscattering from surface microcracks. Preliminary experiments conducted on turbine blades indicated that the techniques can be applied to components of complex shape.

Key words: Acoustic surface wave; ceramic; surface characterization; surface crack; turbine blade.

1. Introduction

Surface cracks are an omnipresent source of fracture in structural ceramics [1-3]. The cracks are generated during finishing operations (such as grinding and machining) and usually consist of arrays of semi-elliptical cracks with an essentially random inclination to the surface but a preferred alignment parallel to the direction of motion of the abrading particles [4]. The characterization of these cracks is an essential constituent in an effective failure prediction procedure. The characterization techniques that have been conventionally applied to surface cracks are dye penetrants and fracture statistics [5]. The dye penetrant techniques are restricted to relatively large cracks because of inherent resolution limitations and are only viable in structural ceramic systems as preliminary inspection procedures. Statistical methods exhibit superior prospects [1,5]. But the statistical approach is not, by itself, capable of identifying components subject to anomalously severe surface damage on an individual basis. Alternative, or additional, surface crack characterization techniques must, therefore, be sought. An acoustic surface wave technique that has the basic pre-requisites for satisfying the failure prediction requirements is described in the present paper. The technique has been demonstrated to give good quantitative predictions of flaw size and fracture stress in glass samples. The experiments on hot pressed silicon nitride ceramics are at an earlier stage but indicate that surface cracks as small as 60 μm radius can be detected.

The scattering theory that provides the basis for pertinent acoustic measurements is firstly described, for both the short and long wavelength regimes. Then, the types of transducer designed to provide the requisite acoustic information are described. Thereafter, specific acoustic techniques for detecting and characterizing surface cracks on both plate samples and on turbine blades are presented: separate emphasis being afforded to the short and long wavelength regimes. Finally, the implications of the results for ultrasonic failure prediction are discussed.

II. Scattering Theory

An acoustic surface wave incident on a crack will be partially reflected. When the wavelength λ of the acoustic wave is comparable to the crack radius a , it will be demonstrated (eq. 2) that the scattered power P received at the transducer should be proportional to a^2 . Whereas when $a \ll \lambda$, $P \propto a^6/\lambda^4$ (eq. 7), and when $a \gg \lambda$, P should be independent of the wave-

length, (being roughly equal to its value when $a \approx \lambda$). Thus for maximum detectability, acoustic surface wave measurements should be made at a wavelength comparable to or smaller than the crack size. For example, on silicon nitride (surface wave velocity, 5.8×10^3 m/s), an acoustic surface wave with a frequency of the order of 100 MHz should optimize the detectability of a 60 μm crack. Thus it has been necessary to develop entirely new techniques for excitation of surface acoustic waves on ceramics, using frequencies much higher than those normally employed in nondestructive testing. Additionally, important information concerning surface cracks can be obtained in the long wavelength limit, $a \ll \lambda$, whenever the cracks are sufficiently large to yield detectable scattering. It is also of interest, therefore, to obtain information at the lower frequencies (10 - 20 MHz) pertinent to the long wavelength regimes.

Kino and Auld [6,7] have shown that the scattering coefficient S_{11} for a surface wave impinging at normal incidence onto a surface crack is;

$$S_{11} = \frac{j\omega}{4P} \int_{A_c} \Delta u_j \sigma_{ij} n_i dA_c \quad (1)$$

where S_{11} is defined as the ratio of the amplitude of the scattered signal at the terminals of the transducer to the incident signal; A_c is the crack area; σ_{ij} is the incident stress associated with the acoustic wave in the region of the crack, prior to the introduction of the crack; Δu_j is the displacement of the crack surface due to the incident acoustic surface wave, P is the power injected into the transducer and ω is the frequency. This relation will be used as a basis for predicting scattering characteristics at both short and long wavelengths. Note that the ratio of the scattered power to the incident power, P_s , is proportional at $|S_{11}|^2$.

II.1 Short Wavelength Scattering

When $a \gg \lambda$ and the width of the transducer $w \gg a$ (as would normally be the case), an approximate estimate of S_{11} can be made. It can be shown by analogy with plane wave scattering [6] that Δu_j has roughly twice the value of the displacement in the incident acoustic wave. It follows that

$$S_{11} \sim (\gamma\eta/w)a \quad (2a)$$

or,

$$P_s \sim (\gamma\eta/w)^2 a^2 \quad (2b)$$

where λ is a constant, equal to 2 for plane wave scattering, but < 2 for a crack; and η is an efficiency coefficient relating the input power at the transducer to the power incident on the crack. For a crack located on the central axis of the beam,

$$\eta = \eta_T \eta_D \quad (3)$$

where η_T is the transducer power lost upon converting the input electrical signal to an acoustic surface wave, and η_D is a diffraction loss term. For a flaw on the acoustic beam axis located in the Fraunhofer region, (i.e., in the far field where $z > w^2/\lambda$) at a distance z from the transducer, it can be shown that [8]

$$\eta_D = w^2/\lambda z \quad (4)$$

Combining equations (2), (3), and (4), the power loss becomes;

$$P_s = \left(\frac{\gamma\eta_T w}{z} \right)^2 \left(\frac{a}{\lambda} \right)^2 \quad (5)$$

A crude estimate of the crack detectability can be obtained from eq. (5). The reflection coefficient of a 90° corner for a material with a Poisson's ratio of 0.25 is 12 dB [19]: yielding a λ value of ~ 0.3 . Since η_T is typically ~ 0.1 for our transducer (see Section III), a frequency of 100 MHz and a 1 mm beam width (typical of high frequency transducers) requires that $z > 1.6$ cm. Hence for a flaw size of 50 μm , the power loss predicted by eq. (5) is ~ 54 dB. A 50 μm crack should thus be easily detected using an acoustic surface wave with a

wavelength comparable to the crack dimensions. It should also be noted that crack resonances can be excited, and observed, at short wavelengths [10]. The resonances of the cracks will change the amplitude of its reflection coefficient in a periodic manner; a fact which has been neglected in our rough calculation.

II.2 Long Wavelength Scattering

When $a \ll \lambda$, we might expect that the displacements in the neighborhood of a crack would be similar to the quasistatic displacement. The displacement Δu_z of the crack surface can be estimated from the quasistatic solution for a penny-shaped crack [7],

$$\Delta u_z = \sigma_{zz} \frac{4(1-\nu^2)}{\pi E} (a^2 - r^2)^{1/2} \quad (6)$$

where σ_{zz} is the stress normal to the crack, E is Young's modulus, r is the distance from the center of the crack, and ν is Poisson's ratio. Insertion of eq. (1) gives the scattering coefficient at the crack as;

$$S_{11} = \left[\frac{j\omega(1-\nu^2)\sigma_{zz}^2}{3EP} \right] a^3 \quad (7)$$

Furthermore, by writing σ_{zz}^2 in terms of p (7)

$$\frac{\sigma_{zz}^2}{P} = \frac{8E}{v_R^2} \left[1 - \left(\frac{v_s}{v_l} \right)^2 \right]^2 \frac{f_z}{(1+\nu)} \left(\frac{\omega}{w} \right), \quad (8)$$

and by invoking the transducer efficiency, η , it can be shown that the scattered signal at the transducer is;

$$|S_{11}| = \frac{8}{3} \pi^2 \left(\frac{a^3}{\lambda^2} \right) f_z \frac{\eta}{(1-\nu)w} \quad (9)$$

or,

$$P_s \propto a^6/\lambda^4 \quad (10)$$

where v_l , v_s and v_R are the longitudinal, shear and Rayleigh wave velocities respectively, and f_z is a normalized parameter tabulated by Auld [11]: for typical ceramics $f_z \sim 0.4$.

For a 10 MHz wave incident on a 100 μm crack located in the Fraunhofer zone ($z = 1.5$ cm), η_D for a beam width of 2 mm (typical for long wavelength transducers) is ~ 0.44 . Thus, for a transducer efficiency $\eta_T \sim 0.1$ eq. (9) yields a scattering coefficient $S_{11} \sim 9.18 \times 10^{-4}$. This corresponds to a 60 dB reduction from the input signal. This level should be discernable. However, the equivalent reduction for a 50 μm crack is 78 dB: a level which would be difficult to detect.

III. The Transducers

III.1 Calibration Procedures

The transducers used in this study were calibrated by firstly measuring the total loss L_0 between two closely spaced transducers, $L_1 + L_2$ (where $L_1 = 10 \log_{10} \eta_{T1}$, $L_2 = 10 \log_{10} \eta_{T2}$: the subscript T referring to transmission). The losses L_{C1} and L_{C2} associated with signals reflected from a closely spaced corner are then measured. These losses can be combined to yield values of L_1 or L_2 in accord with the following relations,

$$L_1 + L_2 = L_0 \quad (11a)$$

$$2L_1 + L_C = L_{C1} \quad (11b)$$

$$2L_2 + L_C = L_{C2} \quad (11c)$$

It follows that

$$L_1 = \frac{2L_0 - L_{C2} + L_{C1}}{4} \quad (12)$$

III.2 Transducers Designs

Schematics of three types of transducer configuration suitable for launching acoustic surface waves on ceramics and glass are shown in figures 1, 2, and 3. The first is a highly efficient type of wedge transducer for use at frequencies below 10 MHz. A pulsed rf signal is excited by means of a bulk wave transducer bonded to the wedge material; this bulk wave is incident at an angle θ to the normal at the surface such that

$$\sin \theta = v_w/v_s \quad (13)$$

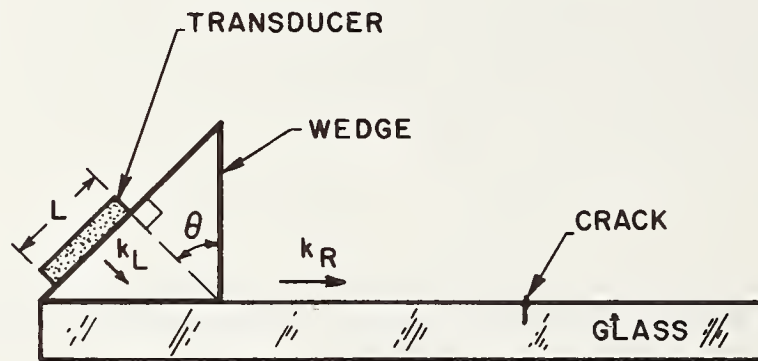


Fig. 1. Schematic diagram of surface crack and test set up with a wedge transducer.

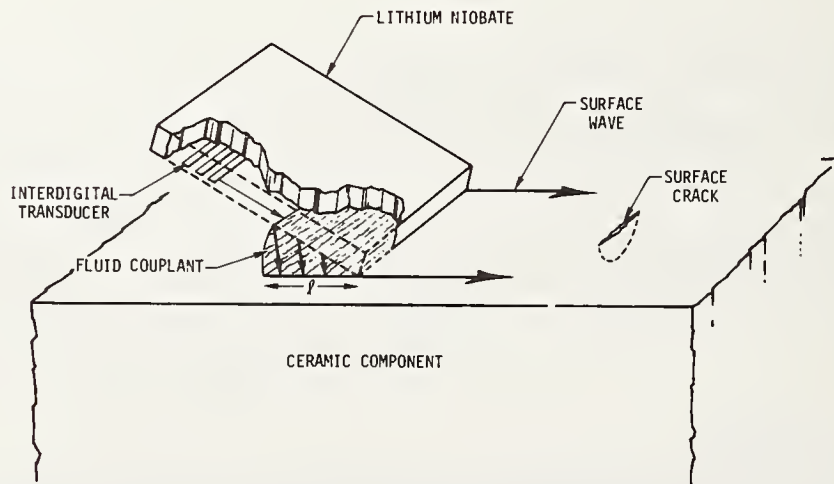


Fig. 2. A schematic of the surface to surface (STS) transducer.

where v_w is the wave velocity in the wedge material and v_s the surface wave velocity along the substrate. A new design procedure [12] for wedge transducers predicts that, for good conversion efficiency, it is necessary to have $\rho_w v_w / \rho_s v_s \sim 0.3$ (where ρ_w, ρ_s are the mass densities of wedge materials and substrate, respectively). Also, an optimum length of contact between the wedge and the substrate ($\sim 3 \times 10^{-3}$ m) is required to obtain a maximum theoretical conversion efficiency from bulk to surface waves of 0.81. The measured conversion efficiency of the current transducers approaches the theoretical value, being as high as 0.5 in the

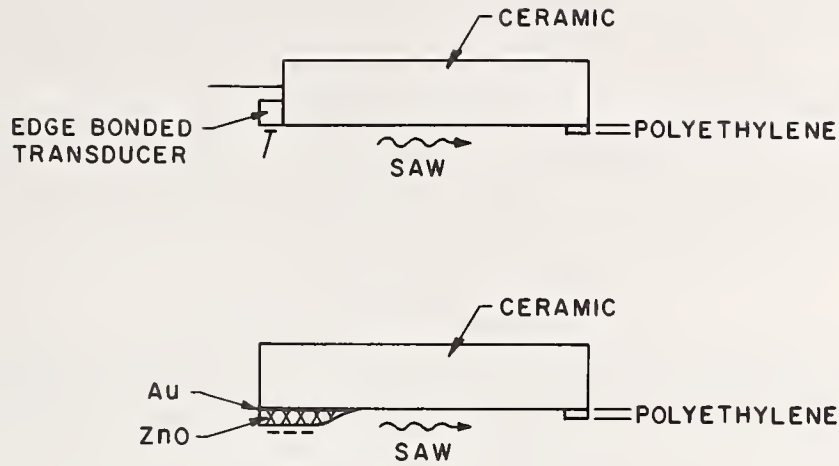


Fig. 3. A schematic of a surface to surface (STS) transducer using a ceramic substrate and excitation with an interdigital transducer on ZnO.

best cases. For example, the measured loss for an individual wedge transducer is typically 9 dB.

Normally, for the excitation of waves on glass or metals, the wedge material consists of a RTV silicone gel; this material has an extremely low wave impedance $Z_w (= \rho_w v_w)$. For excitation of surface waves on ceramics, which have a higher surface wave velocity, lucite is a superior wedge material. For reproducibility, it is usually convenient to use a liquid (such as water or ethylene glycol) between the wedge and the ceramic or glass substrate.

However, at higher frequencies it is difficult to construct suitable bulk wave transducers and to design a wedge that is sufficiently thin to ensure that acoustic losses in the wedge medium do not dominate the performance of the system. Thus, a new configuration, shown in figure 2, has been adopted for exciting very high frequency surface acoustic waves of ~ 100 MHz. A surface wave is first excited on a piezoelectric (LiNbO_3) delay line by an interdigital transducer. A fluid couplant is placed between the delay line (outside the transducer region) and the substrate on which an acoustic surface wave is to be excited. The surface wave becomes a leaky wave in the presence of the fluid and excites a bulk wave at an angle [13]

$$\theta_1 = \sin^{-1} \left(\frac{v_f}{v_{S1}} \right) \quad (14)$$

where v_f is the longitudinal wave velocity in the fluid and v_{S1} is the surface wave velocity on the LiNbO_3 . This longitudinal wave is, in turn, arranged to be incident on the sample at the critical angle θ_2 that permits surface wave excitation:

$$\theta_2 = \sin^{-1} \left(\frac{v_f}{v_{S2}} \right) \quad (15)$$

where v_{S2} is the surface wave velocity on the substrate of interest. The angle θ between the two solids is, therefore

$$\theta = \theta_1 - \theta_2 = \sin^{-1} \left(\frac{v_f}{v_{S1}} \right) - \sin^{-1} \left(\frac{v_f}{v_{S2}} \right) \quad (16)$$

The distance between the LiNbO_3 and the delay line is made as small as possible in order to minimize the propagation loss in the fluid couplant. For the case of a surface wave on the Y-Z cut LiNbO_3 delay line, coupled to Si_3N_4 ceramic, the calculated maximum efficiency (0.54) occurs for an overlay distance ℓ (fig. 2) of .5 mm, at a center frequency of 100 MHz. This constitutes a loss of about 2.7 dB for conversion of the surface wave from one material to the other. The current transducers yield a loss comparable to this predicted value. Ethylene glycol was used as the fluid couplant because it does not evaporate quickly and because it forms a good meniscus. The inclination θ for this couplant is 13° .

Although this type of transducer operates well at frequencies in the 30 to 100 MHz range, it is still not ideal for the present nondestructive testing application, because of the liquid medium. An alternate transducer, illustrated in figure 3, is thus under development. An interdigital transducer is deposited on a substrate material identical to that being tested. Piezoelectric ZnO is sputter deposited onto the transducer to give strong piezoelectric coupling. A polyethylene layer, a few micrometers thick, is then deposited onto the ZnO to form a compliant contact region. With this design, the component and wave guide, having identical wave velocities, can be parallel; thereby, permitting the polyethylene layer to be relatively thin and hence, allowing little acoustic loss.

IV. Low Frequency Measurements

The reflection coefficient for a surface crack obtained at low frequencies can be used to yield a direct prediction of the fracture strength of a brittle material. The requisite result can be derived from the scattering coefficient given in eq. (9). Firstly, the reflection coefficient is expressed in terms of a geometric stress intensity factor k_1 ($=2\sqrt{a}/\pi$ for a penny crack) as follows [14]:

$$k_1 = 2 \left(\frac{6(1-\nu)\lambda^2 |S_{11}| w}{\pi^5 f_z \eta} \right)^{1/6} \quad (17)$$

indicating that k_1 can be obtained immediately from a measurement of the scattering coefficient. It will be noted that the geometrical stress intensity factor k_1 is proportional to $|S_{11}|^{1/6}$, so that errors in the measurement have a very small influence on the predicted k_1 values. Then, since the fracture strength σ_c of a material is related to k_1 and the fracture toughness K_{1C} by

$$K_{1C} = \sigma_c k_1, \quad (18)$$

a determination of S_{11} and knowledge of K_{1C} yields a direct prediction of σ_c .

Pyrex discs 3 mm thick and 7.6 cm in diameter in the annealed condition were prepared for fracture testing by introducing small semi-elliptical surface cracks in the center of each disc. These pre-cracks were made in a controlled way by applying a bending moment of approximately 2 N.m to the disc and, on the side in tension, introducing a Knoop indentation with a force of 0.5 to 1N. This technique produces roughly half penny-shaped cracks with radii between 100 and 500 μm . Such small cracks were required to limit the crack size to less than the acoustic wavelength $\sim 9 \times 10^{-3}\text{m}$. Additionally, the half penny-shaped cracks may be coaxed to an extended semi-elliptical shape by applying a subsequent bending moment to the disc.

The strength of each disc was determined in biaxial flexure using the method of Wachtman, et al. [15]. The discs were loaded to fracture at a loading rate of approximately 60 MPas^{-1} . The loading rate was chosen to minimize possible slow crack growth effects [16]. To further insure against environmental influences, the specimens were subjected to a vacuum for one hour prior to strength testing, and exposed to a stream of dry nitrogen gas for three minutes prior to and during the flexure test.

Once the specimens were fractured, the geometry of the pre-cracks was studied by examining the fracture surface using reflected light. The aspect ratio (a/c) of the semi-elliptical surface pre-cracks could then be easily measured.

The stress intensity factor for the pre-crack was evaluated by the method of Shah and Kobayashi, [17],

$$K_I = \frac{M_B \sigma_B \sqrt{\pi a}}{E(k)} \quad (19)$$

where $E(k)$ is an elliptic integral of the second kind, M_B is a magnification factor which takes into account the aspect ratio and the proximity of the crack depth to the neutral axis, σ_B is the maximum bending stress at the surface of the specimen, and a is the length of the semi-minor axis (depth) of the pre-crack.

The ten samples tested gave a normally distributed set of fracture toughness measurements, and the mean value of fracture toughness, K_{IC} , at a confidence level of 90 percent was: $0.76 \pm 0.04 \text{ MPa m}^{1/2}$, comparable to the values obtained by Wiederhorn [18].

The experimental arrangement for measuring the acoustic surface wave reflection coefficient $|S_{11}|$ is shown schematically in figure 1. A wide band, high efficiency wedge transducer was used to excite and detect the surface acoustic waves. The transducer has a center frequency of 3.4 MHz, a bandwidth of 50 percent, and a one way insertion loss of 9.2 dB. Calibration of the transducer was conducted as described in Section III. All measurements were taken in the far field of the transducer ($z > x^2/\lambda$).

A set of acoustic measurements were taken with the front of the wedge, distance $z = 2.3$ cm from the crack and with the acoustic surface wave normal to the crack surface. The measurements were taken in the bending fixture, using a bending moment of approximately 2 N.m to ensure that the crack was open.

A series of reflection measurements was conducted on ten different cracks, and k_I calculated from eq. (17). In figure 4 the acoustic prediction of the fracture stress σ_C is plotted against the measured values of σ_C . A least squares fit of this data indicates a linear relationship between theoretical and experimental measurements with a slope of 0.85. We see that for larger, more irregular cracks (where the assumption of the theory that the diameter of the crack is less than 1/4 wavelength is not well satisfied), the error between theory and experiment increases. It is interesting to note that the effect of the ellipticity of some of the small surface pre-cracks appears not to affect the accuracy of the acoustic prediction of $k_{I\text{max}}$ to any appreciable degree. This confirms a prediction of Budiansky and Rice [19] that the effect, if any, should be less than 10 percent.

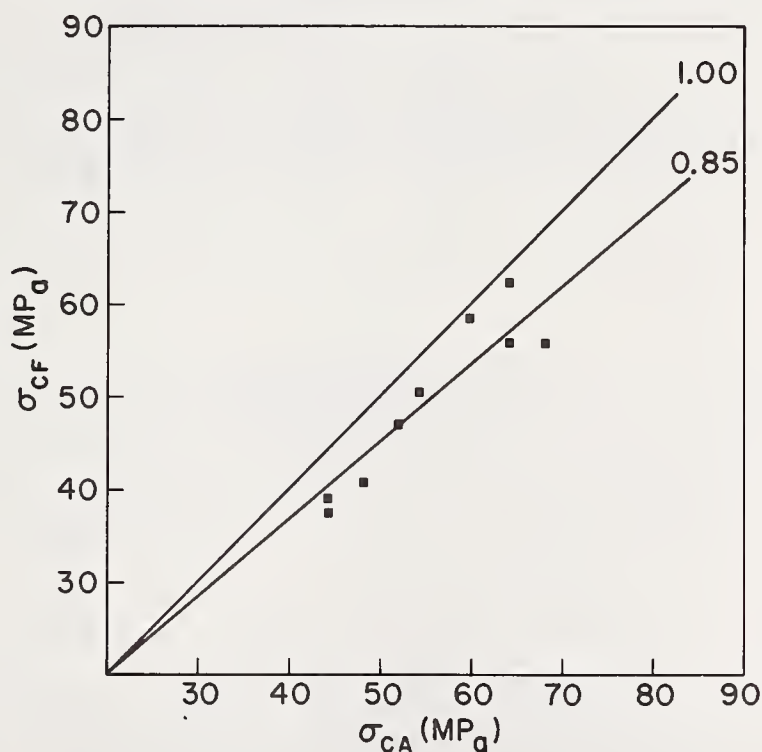


Fig. 4. Actual fracture stress versus predicted fracture stress.

V. High Frequency Defect Detection

V.1 Measurements on Flat Surfaces

The material selected for this study was a commercial, hot-pressed silicon nitride (NC 132). Plate specimens ($3 \times 3 \times 0.5$ cm) were machined from an as-pressed billet and one surface optically polished. Specific surface grinding treatments were then applied to each sample using 30 μm and 70 μm diamond abrasive pastes and a standard diamond wheel. Then,

three surface cracks were introduced using the Knoop indentation technique [13]. The sizes of the cracks were characterized using optical or scanning electron microscopy (fig. 5); the results are presented in figure 6. Subsequently, the plastic zones were removed by grinding¹ (the grinding condition corresponding to that applied prior to indentation). Thereafter, the cracks were not detectable, using either optical or electron microscopy, because the thin layer of surface plasticity that accompanies grinding tends to obscure the residual crack opening. It is assumed that all cracks are semicircular in shape, in accordance with observations of Petrovic and co-workers [20].

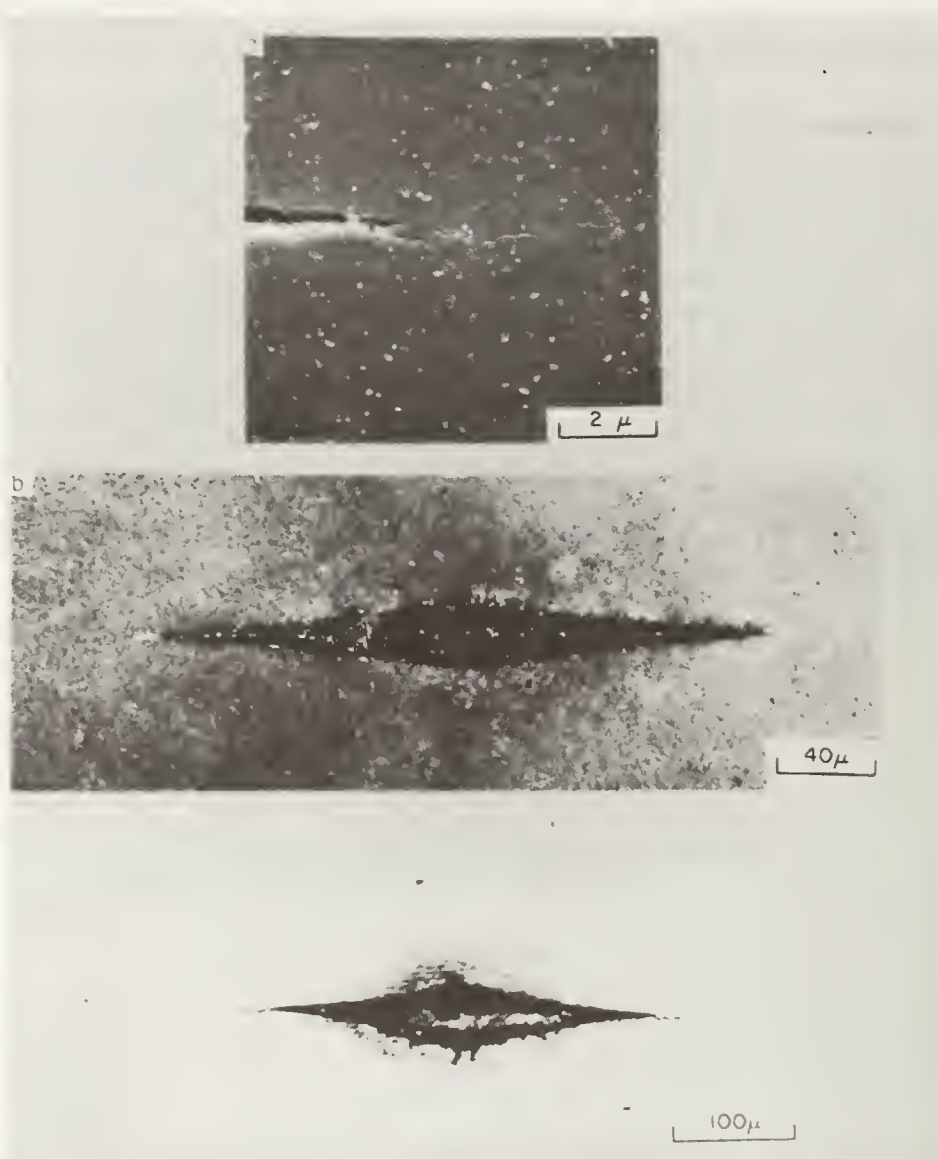


Fig. 5. Micrographs of surface cracks introduced by indentation:

- (a) scanning electron micrography, $P = 20 \text{ N}$,
- (b) polarized light reflected micrography, $P = 50 \text{ N}$,
- (c) reflected light optical micrograph, $P = 110 \text{ N}$.

The surface roughness of each sample was also measured using a Datatrak instrument. The results are summarized in figure 7. The expected increase in the amplitude of the surface irregularities with the grinding severity is apparent. It is also evident that uncharacteristically deep troughs exist in the sample subjected to a $30 \mu\text{m}$ grind (the consequence of a poorly sequenced grinding procedure) -- the significance of this feature will emerge later.

¹The plastic zone in Si_3N_4 is relatively shallow, and its removal does not effect a significant change in the dimensions of the surface cracks.

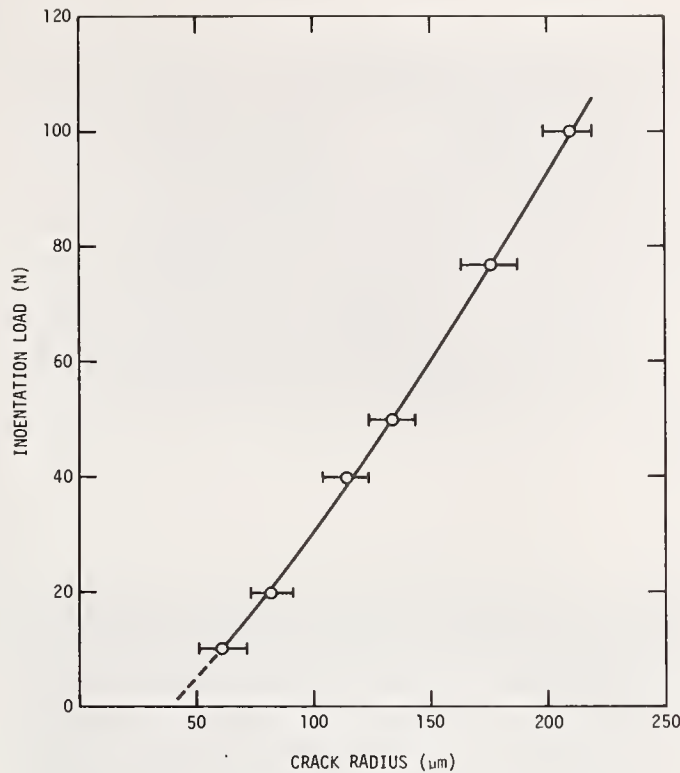


Fig. 6. The relation between indentation load and surface crack radius.

Cracks were introduced into each sample using indentation loads of 10, 20, and 40 N corresponding (fig. 6) to crack radii, a , of 60, 80, and 120 μm , respectively. The crack planes in each case were normal to the long axis of the sample; this coincides, in turn, with the incident direction of the acoustic surface wave. For the polished sample, the background scattering was minimal, and all cracks could be clearly distinguished, as illustrated in figure 8a, for the 60 μm crack.

For the sample with the 30 μm finish, the background level increased markedly (fig. 8b), and although distinct signals above the background were obtained for the 80 μm (fig. 8b) and 120 μm cracks, the 60 μm crack could not be discerned from the background scattering. Additional signals that could not be related to the deliberately introduced cracks were also apparent (fig. 8b). It is recalled that this sample contained unusually deep surface troughs (fig. 7b), which may signify the presence of relatively large underlying cracks introduced during a prior stage of the surface preparation sequence. The additional signals are thus almost certainly related to the presence of large cracks other than those introduced by indentation. This observation thus offers encouragement that the large size extreme of naturally occurring cracks will be distinguished by the present acoustic method.

For the sample with the 70 μm finish the even larger background level prevented the detection of both the 60 and 80 μm cracks, although a clear signal was obtained from the 120 μm crack (fig. 8c). On the rough ground sample, none of the deliberately introduced cracks could be isolated. However, distinct signals were apparent in other areas of the sample.

To ascertain the origin of the background (i.e., surface roughness and/or surface microcracks) each sample was polished to remove the surface irregularities, but to retain the sub-surface microcrack distribution. The acoustic measurements were repeated. No significant change in the signal amplitude or distribution could be detected. The backscattering is thus attributed, almost exclusively, to the arrays of surface microcracks introduced during the grinding process.

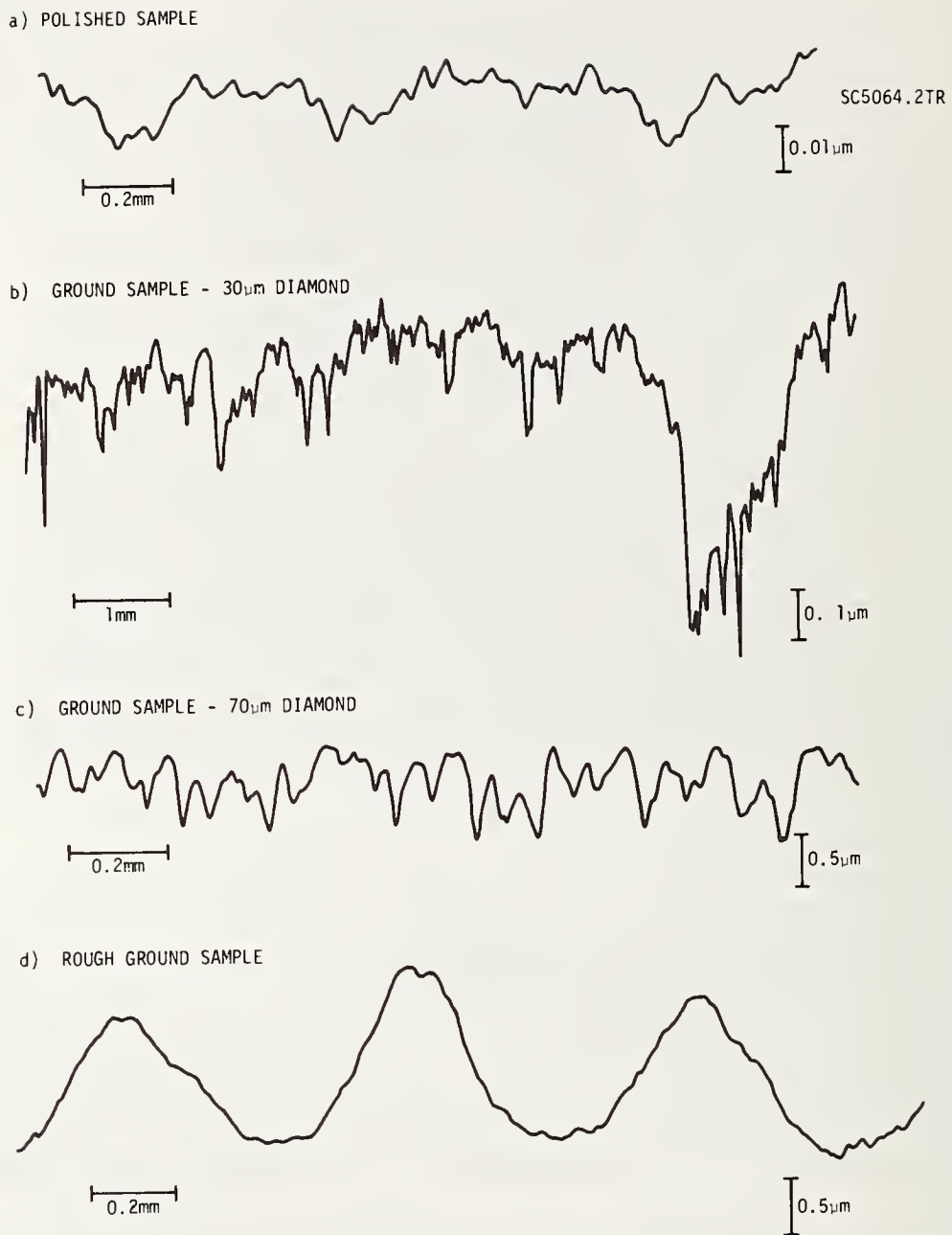


Fig. 7. Surface profiles of the various surfaces used in the present study, obtained using a Datatrak instrument.

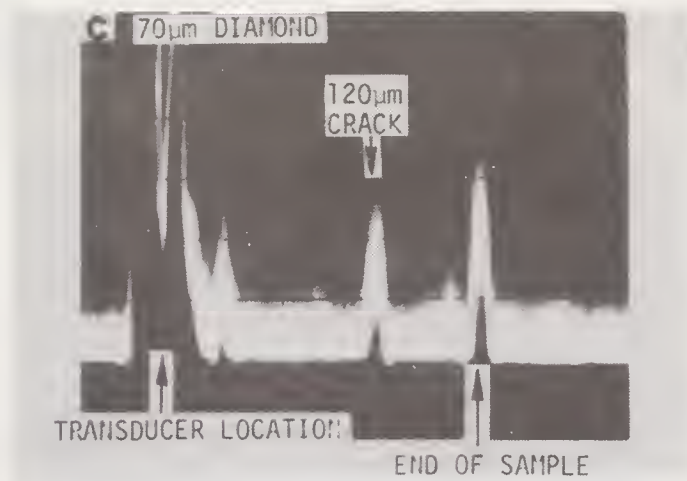
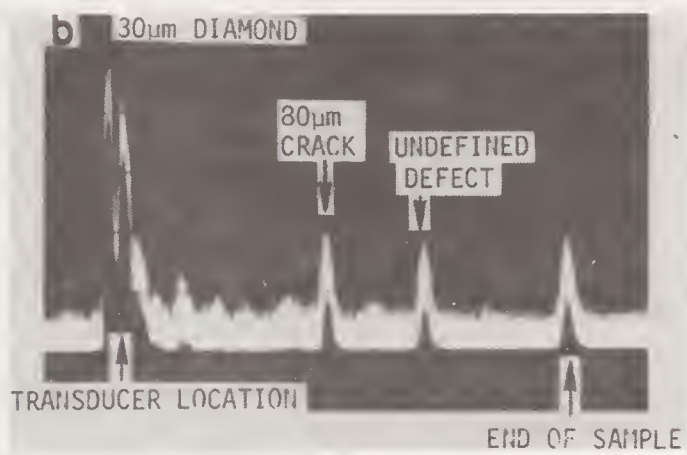
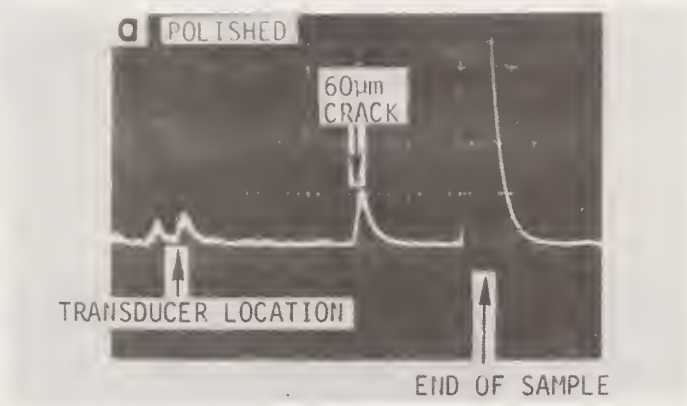


Fig. 8. Oscilloscope records of signals obtained from surface cracks.

V.2 Measurements on Turbine Blades

A schematic of the turbine blade configuration (NC 132 silicon nitride) and the transducer arrangement used for the study is shown in figure 9. The reduced section was afforded particular emphasis, since the highest stress obtains in this region during operation. A LiNbO_3 transducer was used as both transmitter and receiver. Experiments were conducted at 64 MHz or 100 MHz.

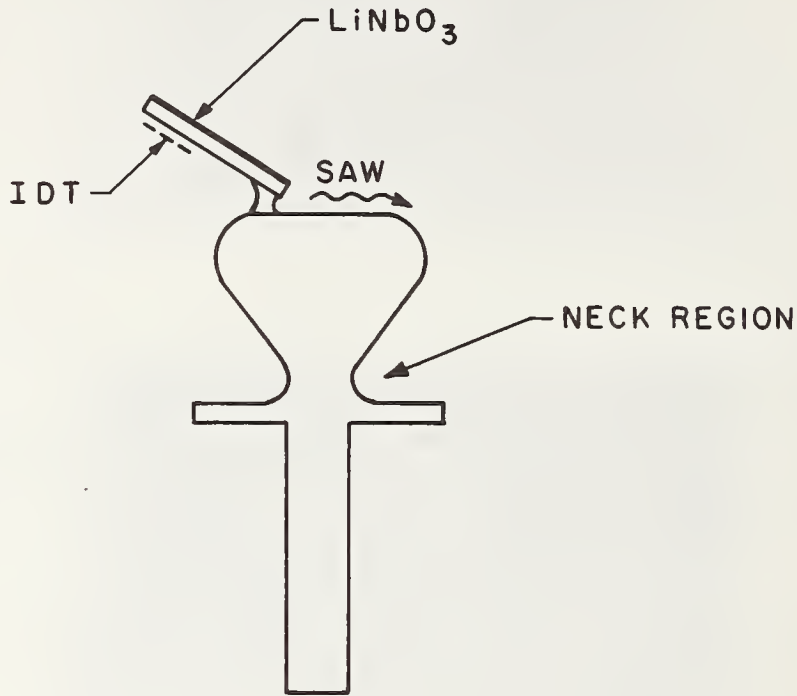


Fig. 9. Schematic of turbine blade and experimental set up.

The initial inspection of the turbine blade provided several indications from the reduced section. However, this section (in the blade examined) contained a series of parallel machining grooves $\sim 20 \mu\text{m}$ in wavelength and several microns on depth. To ascertain the relative contribution to the scattering from the groove and the underlying cracks, the surface in this region was finely polished to remove the macroscopic grooves. This procedure eliminated several signals, but the dominant ones, signifying the presence of the cracks, remained (fig. 10).

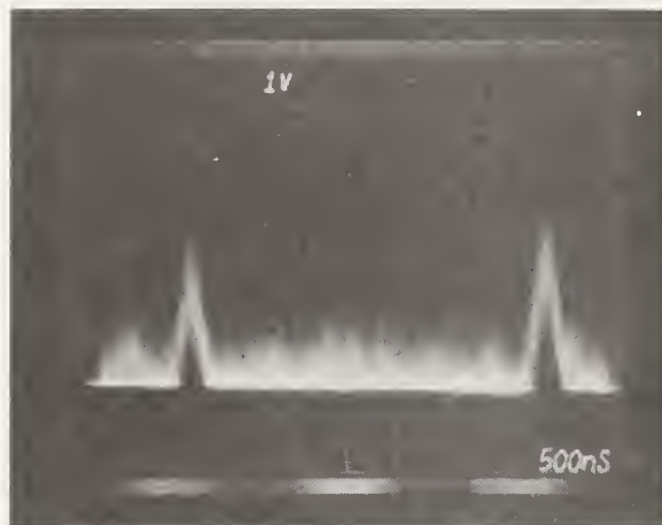


Fig. 10. Reflections obtained from surface cracks in the next region of a turbine blade.

Estimation of the magnitude of a crack in the reduced section of the blade differs from the analogous problem for flat plates by virtue of the presence of the curvilinear propagation surface and the concomitant propagation loss. The most convenient method for obtaining accurate crack size estimates is to calibrate the measurement system by obtaining the scattered amplitude for a well-defined crack located in the reduced section. Such a crack was generated by a 10 N Knoop indentation, followed by removal of the plastic zone. The signal amplitude obtained was then used as a reference for predicting the size of surface cracks in other blades with the same configuration.

VI. Discussion and Conclusion

The detectability of a crack is determined by the power scattered by the crack, relative to the insertion and propagation losses, and the input power, and is strongly dependent on the frequency employed. The detectability levels in the presence of microcracks are not yet theoretically predictable, but a theory analogous to that devised for grain scattering [21] could be developed. The present observations represent an upper bound for the smallest cracks that can be detected for each surface condition. There is an optimum frequency for crack detectability that depends on the size of the crack with respect to the large extreme of the background crack array; this frequency will be in the range $0.1 < ka < 1$ ($k = 2\pi/\lambda$ is the wave number), a range in which the scattering amplitude from the crack of interest approaches its maximum value ($ka \sim 1$) but varies less rapidly with frequency than the backscattering from the crack array ($ka < 0.1$). Subsequent studies will be concerned with the evaluation of optimum frequencies for detectability and crack size characterization. The transducer designs needed for this purpose have been established, as described in the present paper. Also, it is already apparent that cracks in the 50 - 200 μm range will be detectable: the specific level of detectability being governed by the characteristics of the background micro-crack arrays.

In instances where individual cracks cannot be detected, the backscattered amplitude may be an appropriate measure of the tendency for fracture [20]. The amplitude of the backscattering reflects the large extreme of the cracks that exist in that area element of surface, in a manner comparable to the attenuation caused by grain scattering [20]. This possibility is presently being explored.

Finally, it is emphasized that the method can be readily applied to components of complex shape, as demonstrated by the tests conducted on turbine blades.

Acknowledgment

We would like to thank J. Shyne and M. T. Resch who carried out the mechanical tests on the glass samples and some of the comparison calculations.

This work was supported by Office of Naval Research Contract No. N0014-78-C-0283, NSF Contract No. DMK-76-00726 through the Center for Materials Research at Stanford University, and NSF Contract No. ENG-75-18681.

References

- [1] Evans, A. G. and Jones, R. L., J. Amer. Ceram. Soc. **61**, 156 (1978).
- [2] Mecholsky, J. J., Freiman, S. W. and Rice, R. W., J. Mater. Sci. **11**, 1310 (1976).
- [3] Rice, R. W., Ceramics for High Performance Applications, J. J. Burke, ed. p. 287, (A. E. Gorum, and R. N. Katz, Brook Hill, 1974).
- [4] Mecholsky, J. J., Freiman, S. W. and R. W. Rice, J. Amer. Ceram. Soc. **60**, 116 (1977).
- [5] Evans, A. G., Kino, G. S., Khuri-Yakub, B. T. and Tittmann, B. R., Mater. Eval., April 1977, p. 85.
- [6] Kino, G. S., J. Appl. Phys. **49**, 6 (1978).
- [7] Auld, B. A., Wave Motion **1**, 1979.

- [8] Born, M. and Wolf, E., Principles of Optics, (Pergamon Press, New York, 1959).
- [9] Cuozzo, F., Cambiaggio, E. L., Damiano, J. and Rivier, E., IEEE Trans. Sonics Ultrason. SU-24 (1977).
- [10] Domarkas, V., Khuri-Yakub, B. T. and Kino, G. S., Appl. Phys. Lett. 33, 7 (1978).
- [11] Auld, B. A., Acoustic Fields and Waves in Solids, vols. I and II, (Wiley-Interscience, New York, 1973).
- [12] Fraser, J. D., Khuri-Yakub, B. T. and Kino, G. S., Appl. Phys. Lett. 32, 11 (1978).
- [13] Khuri-Yakub, B. T. and Kino, G. S., Appl. Phys. Lett. 32, 9 (1978).
- [14] M. T. Resch, B. T. Khuri-Yakub, G. S. Kino and J. C. Shune, "Stress Intensity Factor Measurement of Surface Cracks", presented at 1st International Symposium for Materials Characterization, 1978.
- [15] Wachtman, Jr., J. B., Capps, W. and Mandel, J., J. of Mater. 7, 188-194 (1972).
- [16] Evans, A. G. and Johnson, H., J. Mater. Sci. 10, 214-222 (1975).
- [17] Shah, R. C. and Kobayashi, A. S., Proc. of 1971 Nat. Symp. on Frac. Mech., Part 1 (ASTM STP 513, 1972).
- [18] Wiederhorn, S. M., J. Amer. Ceram. Soc. 52, 2 (1969).
- [19] Budiansky, B. and Rice, J. R., J. Appl. Mech. 45, 2 (1978).
- [20] Petrovic, J. J. and Mendiratta, M. G., J. Amer. Ceram. Soc. 59, 163 (1976).
- [21] Evans, A. G., Tittmann, B. R., Ahlberg, L., Khuri-Yakub, B. T. and Kino, G. S., J. Appl. Phys. 49, 2669 (1978).

Discussion

BENNETT

Does the ultrasonic technique for crack detection make it possible to detect cracks which reseal themselves and thus cannot be detected readily by other techniques?

EVANS

The surface acoustic wave technique certainly detects cracks which are not visible on the surface (even using the scanning electron microscope). This reflects the surface obscuration of the crack (effected by the plastic deformation at the surface), rather than a crack resealing.

I will speculate that partially resealed cracks will be detectable using ultrasonic waves, whenever the strain amplitude associated with the acoustic wave is large enough to overcome the 'resealing' crack surface force. These reopening requirements are not yet well understood.

BOWLES

1. How critical is the setting of the transducer on the substrate to generate the required surface waves?
2. Does the coupling medium affect the intensity of scattering from local flaws?

EVANS

1. With a LiNbO_5 wave guide the setting is critical ($\theta = 13^\circ$). However, if the wave guide is made from the same material as the material being investigated, this difficulty can be eliminated.

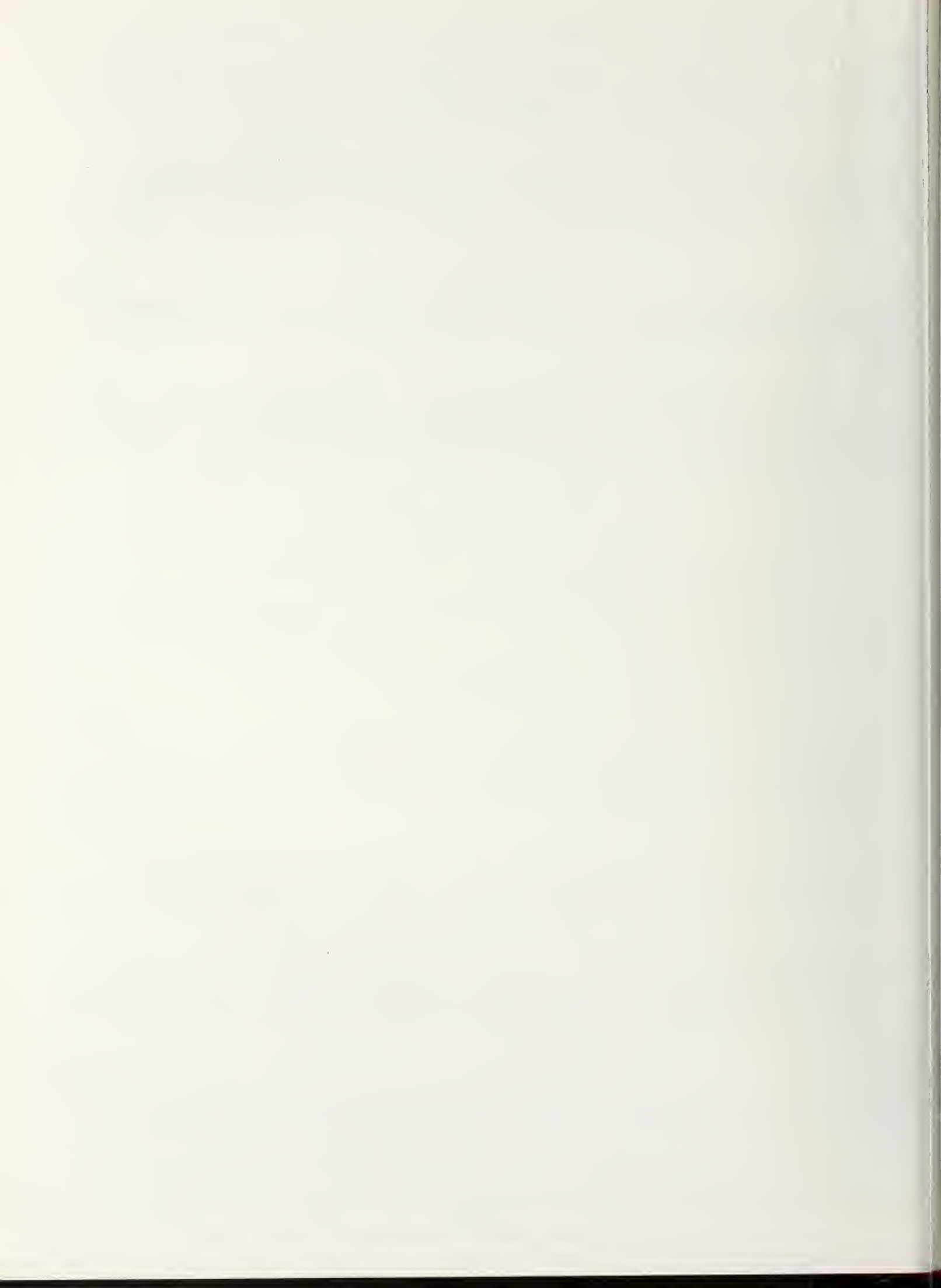
2. The penetration of the coupling medium into surface cracks can reduce the scattering amplitude. The effect has not been intensively explored; but should not cause difficulties if either the couplant is made from a polymer or if the transducer is remotely located from the region to be inspected.

WU

Can you comment on the orientation effect of the cracks on the detectability of this technique?

EVANS

We are now exploring orientation effects. I will speculate that, because of the relation between k and S_{11} , that the orientation dependence of the scattering will be similar to the dependence of the fracture stress on flaw orientation (see J. J. Petrovic, M. Mendiratta, J. Am. Ceram. Soc.)



CHARACTERIZATION OF SURFACE DAMAGE IN CERAMICS USING SELECTED AREA ELECTRON CHANNELING

J. Lankford and D.L. Davidson

Southwest Research Institute
San Antonio, Texas 78284

The technique of selected area electron channeling has been applied to the problem of characterizing subsurface plastic damage introduced during ceramic machining and polishing operations. The surfaces of ceramics spanning a wide range in hardness were prepared under controlled grinding and polishing conditions. Subsurface regions of sectioned specimens were subjected to electron channeling analysis, enabling the boundaries of the subsurface damage (plastic) zones to be mapped out. It was determined that under conditions of constant applied load, the depth of damage during polishing is inversely proportional to the square root of the hardness; this finding is in good agreement with predictions based on indentation theory.

Key Words: Electron channeling; plasticity; subsurface damage; surface damage.

1. Introduction

Damage produced in ceramic materials through conventional surface preparation techniques can manifest itself in at least two ways. First, a population of microflaws capable of degrading the mechanical properties may be introduced; Becher, for example, has shown [1]¹ that twins generated in alumina by surface grinding constitute failure initiation sites upon subsequent bend testing. Second, it is known that microplasticity attending mechanical surface preparation can be reflected in significant surface compressive stresses [2]. These likewise can exert an appreciable influence upon mechanical properties.

A consistent problem in dealing with these damage factors is the inherent difficulty in characterizing them. To a certain extent, topographically sensitive techniques such as scanning electron microscopy and profilometry can be used to characterize features such as surface cracks, pullouts, and surface roughness. However, the depth and severity of near subsurface microplastic damage is much more difficult to ascertain. In a few materials such as MgO, dislocation etch-pitting can be used to accurately map the subsurface plastic zone. However, the technique is not applicable in general, especially for materials of engineering interest such as Al₂O₃, SiC, etc. In these latter cases the only available data regarding the depth of machining damage has come from TEM studies such as those of Hockey, et al. [3,4], which because of the difficulty in knowing precisely the depth from which the foils are taken, provide rough estimates at best.

In this paper, a new technique is shown to be capable of providing hitherto unavailable information concerning near subsurface plastic damage layers in engineering ceramics. The technique of selected area electron channeling has been used primarily in the study of metal plasticity, but was recently applied by the authors to the study of indentation plasticity in SiC[5]. It is possible that the technique will prove helpful in other applications of ceramics where microplasticity is a consideration.

¹Figures in brackets indicate the literature references at the end of this paper.

2. Choice of Materials

The principal criteria for the selection of materials were a wide range in hardness, and that each material be available in single crystal form. The ceramics chosen, and their measured hardnesses, are indicated in table 1.² It was felt that statistical scatter could be reduced by using single crystals, since varying polycrystalline grain orientations would be expected to produce a non-uniform subsurface damage profile, reflecting crystallographic anisotropy in hardness. All crystals were approximately the same size.

Table 1.
Materials Chosen and Hardness Values

<u>Material</u>	<u>Hardness (GNm⁻²)</u>
SiC	34.0
Al ₂ O ₃	20.4
Si	11.0
GaAs	7.8

3. Experimental Procedure

For the surface finishing operations, two crystals of every specimen material were each mounted separately upon stainless steel right circular cylinders whose faces had been ground parallel. One set of four mounted specimens was then selected for diamond surface grinding, while the other set was used for metallographic surface polishing.

Grinding was carried out by gripping each cylinder in the chuck of a lathe, and making a pass across the face of the exposed specimen with an 800 grit, diamond bonded cup wheel. The three inch diameter wheel was turned at 3500 rpm, using a feed rate of 25 μ m/sec and a 25 μ m depth of cut; a steady stream of water soluble oil coolant was applied throughout the grinding pass.

For polishing, the other set of specimens was mounted in an automatic metallographic polishing apparatus. Wet polishing was performed using 600 grip SiC polishing compound and a pressure of about five pounds. Polishing was continued until an equilibrium situation was achieved with respect to apparent (optical) surface finish, i.e., with further polishing, no change in surface texture was evident.

Following characterization of these surfaces in the scanning electron microscope (using palladium to coat the non-conducting Al₂O₃), it was necessary to section the specimens to allow electron channeling characterization of subsurface damage. Since it was anticipated that the damage depth probably was not very deep, it appeared desirable to section the specimens on a taper. This "magnifies" depth inversely as the sine of the taper angle, thus increasing the damage zone dimension relative to the diameter of the probing scanning electron beam. The taper sectioning was performed as shown in figure 1. First, a cylindrical epoxy mount is machined so that one face (A-A') lies 15° from normal to the axis. Next, a ceramic specimen is cemented to this inclined surface with the ground/polished surface facing the mount. These are then placed in a mold, and epoxy is added to reform the cylindrical mount, sealing the specimen within. The mount is sectioned down to B-B' by sequential polishing, taking care to intersect the machined/

²MgO, with a hardness of ~3.5 GNm⁻², was also selected, but chipping of the taper edge during preparation unfortunately precluded damage depth measurements.

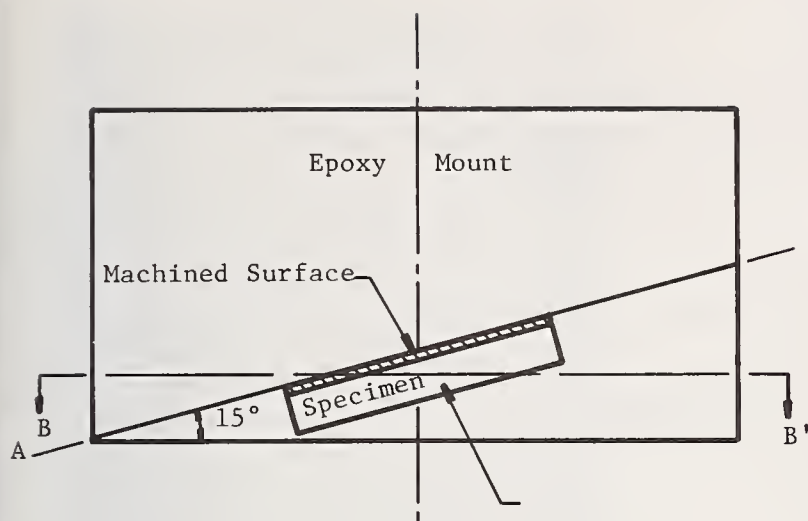


Fig. 1. Mounting scheme for taper section

polished surface of the ceramic, and finally the damage introduced into the ceramic along B-B' during sectioning is removed by ion milling. This process was carried out at the National Bureau of Standards by B. Hockey. Each specimen was argon-ion milled for a minimum of ten hours, so that flaw-free channeling patterns were produced in unground/unpolished areas of the specimens.

Selected area electron channeling has been applied extensively by the authors in the study of localized plasticity in metals [6] and ceramics [5]. The technique, generally described elsewhere [7], is as follows: The electron beam of an SEM is made to rock about a small area on the specimen surface, and the electrons backscattered from that surface are collected. Since electron backscattering is crystallographically specific, a pattern related to the orientation of the crystal is obtained. The acuity of lines within the pattern depends on instrument parameters and on the defect state of the crystal. As the defect density increases, the acuity of the lines on the channeling pattern is decreased. The sensitivity of the line acuity to defect density is material specific, but generally it has been found that very small amounts of crystallite damage may be detected. Suitable theoretical and experimental techniques are not now available to make quantification of this effect generally possible. Thus, while it is not difficult to define the extent of plasticity, a suitable technique has not been developed to quantify the magnitude of the plasticity determined, except in general terms.

The depth within the crystal from which information is being derived by the channeling technique depends on a combination of materials properties, accelerating voltage of the electron beam and detector characteristics. For the present work, an accelerating voltage of 20 keV was used for all the specimens and instrument parameters yielding a pattern of four degrees were obtained from an approximately $10\mu\text{m}$ diameter area of the surface. The same instrument parameters were used for all materials.

Since Al_2O_3 is an excellent insulator, it was necessary to vacuum deposit a very thin layer of amorphous graphite on the surfaces of the specimens studied. By carefully controlling the coating thickness, it is possible to obtain channeling patterns from Al_2O_3 which have the same line acuity as from conducting specimens.

The electron channeling data in the present circumstances were obtained from the ion-milled taper-section specimens as sketched in figure 2. Starting near the machined surface, a local region on the order of $10\mu\text{m}$ in diameter was interrogated by the electron beam, yielding a channeling pattern. This process was repeated as the beam was moved to other locations further from the surface, until a pattern of identical quality to that found at an "infinite" (large) distance was obtained, thus establishing the depth of plastic damage, d_p .

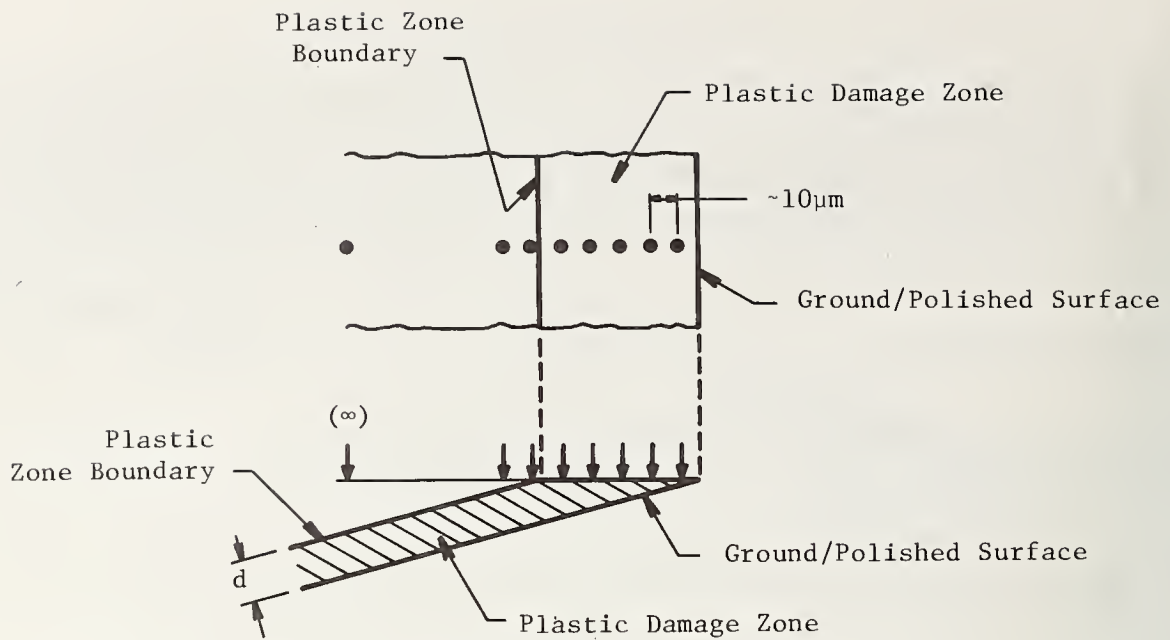


Fig. 2. Scheme for determining depth of subsurface plastic zone; arrows and spots indicate locations at which channeling patterns are taken; spot size $\sim 10\mu\text{m}$

4. Results

SEM views of the ground and polished surfaces are shown in figure 3, where hardness decreases moving from top to bottom. It is clear that despite the fact that both grinding and polishing were carried out under identical conditions for all four materials, there is no correlation between surface features and hardness. For example, ground SiC and Si exhibit chipping along with considerable plastic scoring, while ground Al_2O_3 and GaAs seem to be chipped and burnished. Polished alumina (fig. 3d) has an extremely smooth surface interspersed with microspalling, while harder SiC (fig. 3c) and softer GaAs (fig. 3h) are heavily scored by plastic gouges. In this case, surface appearance is obviously a poor parameter by which to rank ceramics with regard to abrasion resistance.

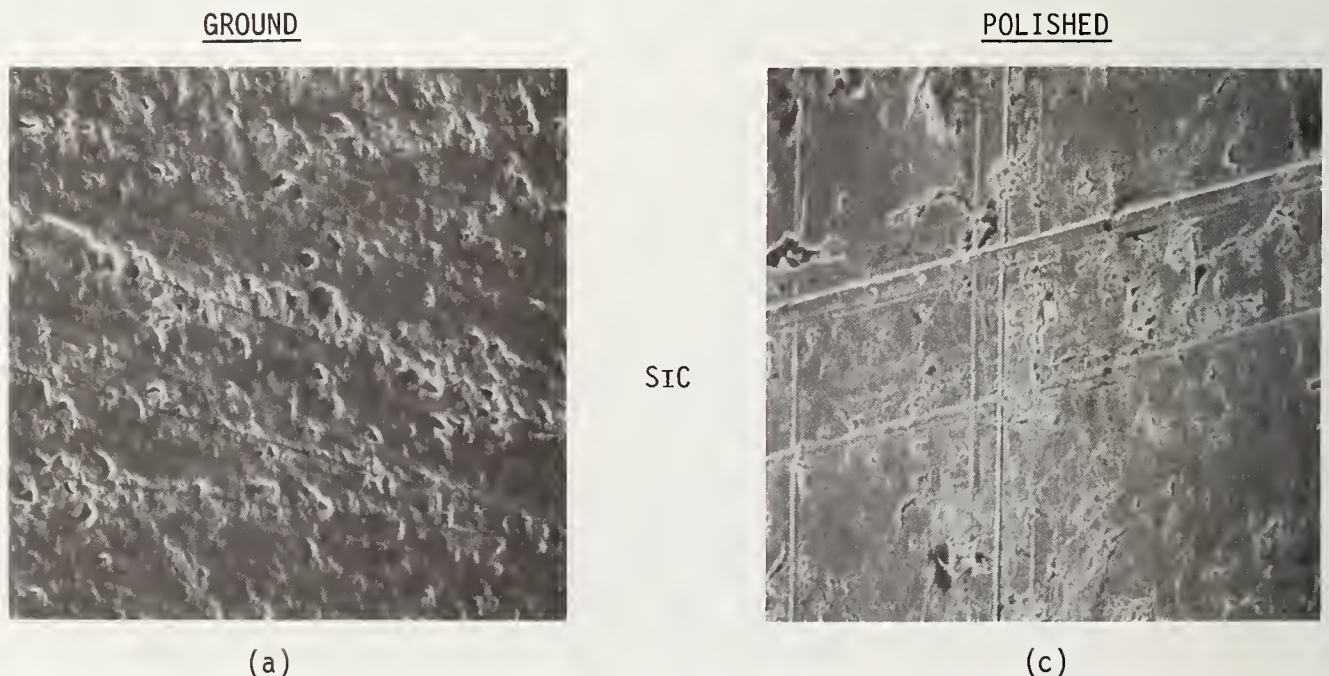


Fig. 3. High magnification views of ground and polished surfaces (700X).
(Continued on next page.)

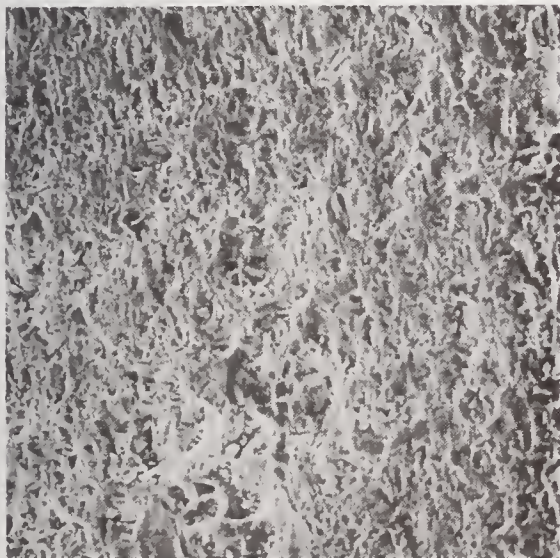
GROUND



(b)



(e)



(f)

POLISHED



(d)



(g)



(h)

AL₂O₃

SI

GAAS

Fig. 3.(Continued). High Magnification views of ground and polished surfaces (700X).

An example of subsurface damage characterization using electron channeling is shown for GaAs in figure 4. Five microns beneath the surface, damage is sufficiently extensive that the corresponding channeling pattern is nearly destroyed (fig. 4a). Somewhat deeper ($d = 12\mu\text{m}$, fig. 4b), the pattern begins to emerge, and is quite recognizable just inside the plastic zone ($d = 32\mu\text{m}$, fig. 4c). The difference between patterns obtained from just inside, versus anywhere outside, the plastic zone can be clearly discerned by comparing figures 5c and 5d.



(a) $d = 5\mu\text{m}$



(c) $d = 32\mu\text{m}$ (just inside plastic zone)



(b) $d = 12\mu\text{m}$



(d) $d = \infty$

Fig. 4. Typical channeling pattern results for polished GaAs.

Similar results were obtained for harder materials such as SiC, for which the extent of plasticity is confined to a region nearer the surface. (Table 2 summarizes the damage zone results for all four materials.) Figure 5a shows a distorted pattern $10\mu\text{m}$ below the surface, and figure 5b a much clearer version of the same pattern obtained right at the apparent plastic zone boundary. Close comparison between the latter photomicrograph and that corresponding to $d = 35\mu\text{m}$ (fig. 5c) show that a subtle but resolvable loss in clarity and fineness of detail characterizes the $d = 20\mu\text{m}$ pattern.

Table 2. Summary of damage zone results.

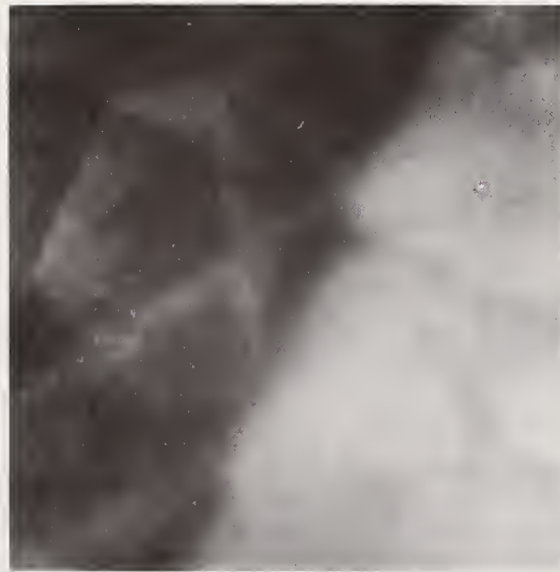
<u>Material</u>	<u>Plastic Zone Depth (μm)</u>	
	<u>Ground</u>	<u>Polished</u>
SiC	--	19.5
Al ₂ O ₃	32.0	21.0
Si	32.0	30.4
GaAs	46.5	38.5



(a) $d = 10\mu\text{m}$



(b) $d = 20\mu\text{m}$ (plastic zone boundary)



(c) $d = 35\mu\text{m}$

Fig. 5. Typical channeling pattern results for polished SiC

The effect of hardness upon the depth of equivalent damage is suggested in figure 6. At $d = 3\mu\text{m}$, polished silicon exhibits the pattern of figure 6a, and at $d = 9\mu\text{m}$, that of figure 6b. At approximately the latter depth, polished GaAs produces a pattern (fig. 6c) lower in quality than that of Si at $d = 3\mu\text{m}$. The lower hardness of the GaAs clearly exerts a major influence upon the damage gradient.



(a) Si, $d = 3\mu\text{m}$



(b) Si, $d = 9\mu\text{m}$



(c) GaAs, $d = 8\mu\text{m}$

Fig. 6. Comparison of effect of polishing damage upon channeling patterns for Si and GaAs, showing the influence of hardness.

This fact is emphasized in figure 7, a plot of the apparent plastic zone boundary d_p versus hardness H . Chipping of the specimen disallowed the determination of d_p for ground SiC, so that the slope of the ground specimen results is questionable. However, for the polished state, it seems reasonable to consider the potential significance of the observed relationship between d_p (polished) and H . As it turns out,

$$d_p \text{ (polished)} \propto \frac{1}{H^{1/2}} \quad (1)$$

which has interesting theoretical implications.

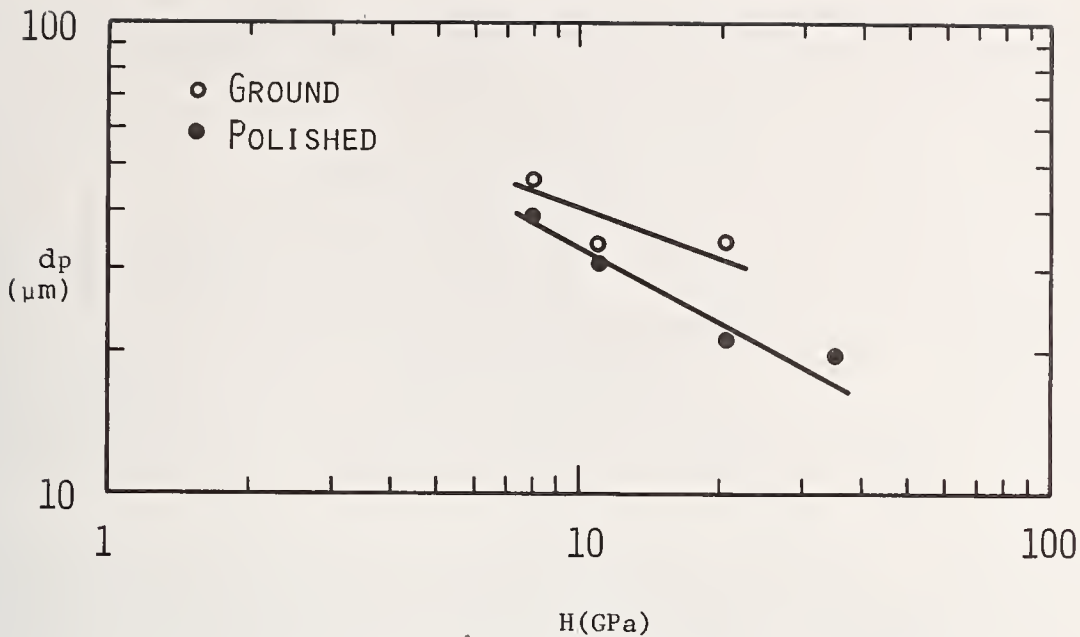


Fig. 7. Depth of plastic zone versus hardness.

5. Discussion

The preceding results indicate, as expected, that polishing introduces less subsurface damage, for approximately equivalent grit size, than does grinding. Moreover, the functional dependence of the polishing damage depth is controlled principally by hardness (under constant load conditions). This observation can be rationalized by appealing to the results of recent studies of the physics and mechanics of the elastic-plastic indentation process.

It is by now well known [8] that a sharp indenter under a load P produces a plastic impression of characteristic dimension a , which is related to hardness through

$$a = \left[\frac{P}{\alpha\pi H} \right]^{1/2} \quad (2)$$

where α is a geometric constant. If the load is constant, then

$$a \propto \frac{1}{H^{1/2}} \quad (3)$$

Recently, Lawn and Evans suggested [9] on the basis of geometrical similitude considerations that the depth of the plastic zone d_i beneath such an indent should be proportional to a . This prediction was borne out for SiC by recent work by the authors [5]. From equation (2), one would then expect

$$d_i \propto \frac{1}{H^{1/2}} \quad (4)$$

for indentations in materials of varying H under equal loads. This result also is predicted independently by the recent elastic-plastic analysis of Perrott [10]. The similarity between equations (1) and (4) is obvious.

From the preceding, it appears that the depth of the subsurface damage zone caused by polishing can be predicted on the basis of indentation theory, whereby a dynamic (sliding) indenter (i.e., a grit particle) behaves like a static indenter. This would

imply that if one could determine the depth of damage in a ceramic of a given hardness subject to prescribed polishing conditions, the damage zone in another ceramic polished under the same conditions could be predicted, based on its hardness alone. It is clear, in addition, that electron channeling recommends itself as a technique for obtaining information on plastic damage in materials which do not lend themselves to conventional damage assessment techniques (such as dislocation etchpitting).

The authors appreciate the support of the Office of Naval Research through Contract No. N00014-75-C-0668 during the course of this work. We are also very grateful for the kind help of Bernard Hockey at NBS, who performed the ion milling.

References

- [1] Becher, P. F., Fracture-strength anisotropy of sapphire, Jour. Am. Cer. Soc., 59, [1-2], 59-61 (Jan-Feb. 1976).
- [2] Rice, R.W., Panel discussion (Proc. Symposium Science of Ceramic Machining and Surface Finishing, National Bureau of Standards, Gaithersburg, Maryland, (Nov. 2-4, 1970), Book, The Science of Ceramic Machining and Surface Finishing, NBS Spec. Pub. 348, S. J. Schneider, Jr., and R. W. Rice, eds., pp 407-408 (National Bureau of Standards, Gaithersburg, Maryland, 1972).
- [3] Hockey, B. J., and Lawn, B. R., Electron microscopy of microcracking about indentations in aluminum oxide and silicon carbide, Jour. Mat. Sci., 10, [8] , 1275-1284 (August 1975).
- [4] Hockey, B. J., Wiederhorn, S. M., and Johnson, H. Erosion of brittle materials by solid particle impact (Proc. 2nd, Int. Conf. Frac. Mech. Ceramics, Pennsylvania State University, State College, Pennsylvania, July 27-29, 1977), Book, Fracture Mechanics of Ceramics, Vol. 3, R. C. Bradt, D.P.H. Hasselman, and F. F. Lange, eds., pp 379-401 (Plenum Press, New York, NY, 1978).
- [5] Lankford, J., and Davidson, D. L., Indentation plasticity and microfracture in silicon carbide, Jour. Mat. Sci. (in press).
- [6] Davidson, D. L. and Lankford, J., Plastic strain distribution at the tips of propagating fatigue cracks, Jour. Eng. Mat. and Tech., 98, [1] , 24-29 (Jan 1976).
- [7] Booker, G. R., Scanning electron microscopy-applications (electron channeling effects) in Modern Diffraction and Imaging Techniques in Materials Science, S. Amelinckx, R. Gevers, G. Remant, and J. van Landuyt, eds., pp 597-653 (North Holland, Amsterdam, 1970).
- [8] Lawn, B. R., Jensen, T., and Arora, A., Brittleness as an indentation size effect, Jour. Mat. Sci., 11, [3] , 573-575 (March 1976).
- [9] Lawn, B. R., and Evans, A. G., A model for crack initiation in elastic/plastic indentation fields, Jour. Mat. Sci., 12, [11] , 2195-2199 (Nov 1977).
- [10] Perrott, C. M., Elastic-plastic indentation: hardness and fracture, Wear 45, [3] , 293-309 (Dec. 1977).

Discussion

VAN GROENOU

1. Your results suggest that "the" force is constant, otherwise $d \sim 1 / \sqrt{H_u}$ would be difficult to understand. Our results on scratching on MgO_u crystals show etch pits at rather large depth, d being proportional to $\sqrt{F_n}$ (F_n = load).

2. Any plans for changing removal rates? Note that more particles become involved and that "the" force could well increase less than Z.

LANKFORD

1. We agree with the comments concerning the load dependency. Since d_i is shown to be proportional to a , it follows from Equation (2) that one would expect to see $d_i \propto \sqrt{F_n}/H$; our results were obtained for $F_n \sim$ constant.

2. We have no current plans for changing removal rates, although this is an obvious next step. The last statement is true. However, for materials polished under the same "increased force" conditions, one would still find $d_p \propto \sqrt{l}/H$, but with all of the d_p 's increased by $\sqrt{F_n}$.

NOVAK

1. How is the 15° angle sample generated?
2. Have you studied effects of heat treatments on the extent of work damage?

LANKFORD

1. The 15° angle is discussed in the paper.
2. No, not in ceramics. In metals, it has a very significant effect, reducing the extent and severity of damage.

Y-DEFLECTION MODULATED SECONDARY ELECTRON IMAGES IN THE EVALUATION OF CERAMIC SURFACE FINISH

L. P. Cook, E. N. Farabaugh, and C. D. Olson

National Bureau of Standards
Washington, D.C. 20234

Variations in secondary electron emission intensity as a function of surface topography have been examined for single crystal silicon surfaces of three different roughnesses. It is possible to calibrate absorbed current, and under carefully controlled conditions, to calibrate secondary emission for quantitative study of surface angular variation. Such data can be statistically processed to give information on surface slopes analogous to that obtained from profilometry. The agreement between profilometer and preliminary SEM data appears to be good for the roughest of the silicon surfaces. The utility of this as a general method for the examination of ceramic surfaces is suggested for instances where specimen charging can be properly eliminated.

Key Words: Ceramic; scanning electron microscope; secondary electron emission; silicon; surface roughness; y-deflection modulation

I. Previous Work

In an earlier symposium Sundahl and Berrin [1]¹ noted the difficulties encountered in interpreting the secondary electron signal produced by electron bombardment of machined surfaces of oxides such as Al_2O_3 , most of which are excellent electrical insulators in their pure state. While application of a conductive coat a few hundred nm thick is sometimes a solution, uniform coating of irregular surfaces is difficult. Possibly for these reasons, White, *et al* [2] did not derive quantitative data describing surface roughness from their image analysis system. It is the intent of this paper to explore the potential of secondary emission for use in the quantitative evaluation of surface finish by studying carefully prepared surfaces of silicon. Pure silicon has a resistance lower than most oxides at room temperature (e.g., 2.3×10^5 ohm cm for Si vs 10^{16} ohm cm for SiO_2) [3]. It does not charge sufficiently in the SEM to alter the secondary emission properties.

II. Signal Generation in the SEM

Because of the low energies involved (<50 eV), the bulk of the secondary electrons leaving the surface of a specimen originate in the top few nm where the probability of absorption is low [4] and the energy is sufficient to penetrate the surface potential barrier - hence the use of secondary emission for high resolution images. Both η [ratio of backscattered electron current to primary beam current] and δ [ratio of secondary electron current to primary current; or secondary electron yield] increase with increasing inclination. Production of secondaries is in part related to backscattering in that a high proportion of secondaries (up to 80%) are produced by exiting backscattered electrons [5] as opposed to those produced by entering primaries. Whereas the backscattered electrons leave the surface with a strong directional trend [6] secondaries do not. Efficient collection of secondaries is facilitated by application of positive bias to a collector in the vicinity of the sample. The ease with which secondaries are liberated depends upon the chemistry of the solids involved: insulators such as MgO and Al_2O_3 generally show a higher value of δ

¹Figures in brackets indicate the literature references at the end of this paper.

than metals, in spite of the increased backscattering in the latter [7]. Although a completely satisfactory theory of secondary emission has not been developed, a cosine relationship between δ and angle of incidence has been proposed [8]. One expression used for approximation of the secondary electron yield is [6,9]:

$$\delta = \frac{1}{\cos \theta} \int_0^{\infty} (f(o)e^{-z/x_s}) \left(\frac{1}{\epsilon} \cdot \frac{dE_o}{dx}\right) dx$$

where: θ is the angle of incidence, defined with respect to the normal of the specimen surface; $f(o)e^{-z/x_s}$ is the probability that an electron produced at depth z will escape to the surface if x_s is the mean free path of the secondary electron and $f(o)$ is a ratio of secondary current to primary current at the surface; $\left(\frac{1}{\epsilon} \cdot \frac{dE_o}{dx}\right)$ is a quantity relating to the number of secondaries produced in a given thickness dx if E_o is the energy of the incident electron beam, and ϵ is the excitation energy required to produce a secondary electron. In practice, quantities such as ϵ , $f(o)$ and x_s may not be known. If accurate values of emission as a function of surface orientation are required for a specific application the researcher is forced to rely upon empirically determined curves.

III. Experimental Approach

Total collection of electrons emitted from a sample surface in the SEM is experimentally difficult. On the other hand current absorbed by the specimen under conditions of constant incident current is perhaps the most unambiguous indication of surface beam/specimen interaction:

$$I_{\text{Absorbed}} = I_{\text{Beam}} - [I_{\text{Backscattered}} + I_{\text{Secondary}}].$$

If a combined coefficient of emission is defined as

$$\delta' = \delta + n,$$

then δ' as a function of angle of incidence can be derived from the absorbed current, since

$$\delta' = 1 - \frac{I_{\text{Absorbed}}}{I_{\text{Beam}}}.$$

Such a curve for a finely polished silicon wafer with a 20 KV incident beam is shown in figure 1. The resulting curve is quite smooth, and the increased sensitivity of the combined yield δ' to angular variation at values of $\theta > 60^\circ$ is apparent. Also, note that $\delta' > 1$ at high angles of inclination, in accordance with other results [4].

Figure 1 thus represents the basis for quantitative SEM study of surface roughness. In practice, compositional effects, noise and other electronic factors, electron beam spreading and surface contamination limit the utility of this approach. In the present study, the build-up of hydrocarbons due to pump oil polymerization in the electron beam which frequently occurs [10] has been eliminated by performing the experiments in a dry-pumped SEM. High purity single crystal Si cut normal to [111] was used, ensuring freedom from local compositional effects.

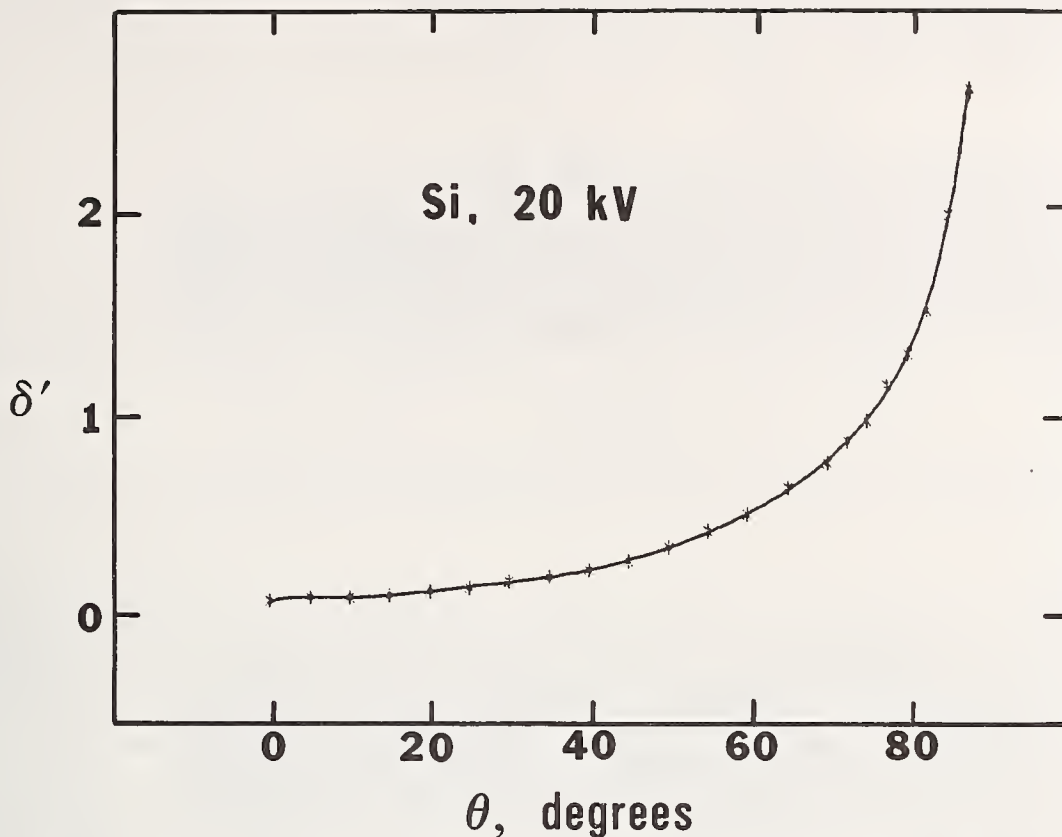


Figure 1. Variation in δ' with angle of inclination relative to incident beam for finely polished Si at 20 kV.

The absorbed current is the most reliable indicator of surface topography - yet the use of the secondary electron signal has certain advantages. Photomultiplier amplification of the secondary electron signal is highly efficient and rather straightforward when compared with the amplification procedures required for absorbed current. Furthermore, the secondary electron yield, δ , is more sensitive to variations in θ than is the backscattered yield, η . Therefore the absorbed current, which combines these effects, is as a whole a less sensitive indicator than secondary emission current. Finally, the secondary electron signal bears a more direct relation to the appearance of the sample surface, and secondary electron images are familiar to most researchers. Absorbed current signals must of course be electronically inverted to produce a similar effect. Most instruments are designed for easy manipulation of the secondary electron signal, but use of absorbed current is in general not as convenient.

The principle difficulties in the use of the secondary electron signal for quantitative study of surface roughness are geometrical in origin and have to do with signal collection factors. To study the effect of variation in surface position relative to the collector axis in our instrument, measurements of total signal were made while rotating the sample at 5° intervals away from the collector axis and keeping the angle of inclination relative to the electron beam constant. This experiment showed that a variation of a few tens of degrees in surface orientation relative to the collector axis produced only small changes in the collector signal which were well within the limits of error (1 to 5%) required for this preliminary study. We recognize that for other studies and other instruments, this condition may not hold. A second factor of equal importance is the differential contribution of backscattered electrons, via line-of-sight shadowing, to the signal. In our study, this effect has been minimized by use of high angles of incidence. Monte Carlo studies, such as those of Murata [6], have indicated a strongly peaked distribution of exiting backscattered electrons. At high angles of incidence, the great majority of backscattered electrons follow a trajectory close to the surface. Because of this, for a surface of high average inclination, relatively few backscattered electrons enter the secondary collector, and line-of-sight shadowing effects are minimized (refer to fig. 2 for a schematic of the geometrical arrangement in our system). The generation of additional secondaries as these

backscattered electrons impinge upon the sample chamber is an effect which can in large part be compensated by calibration.

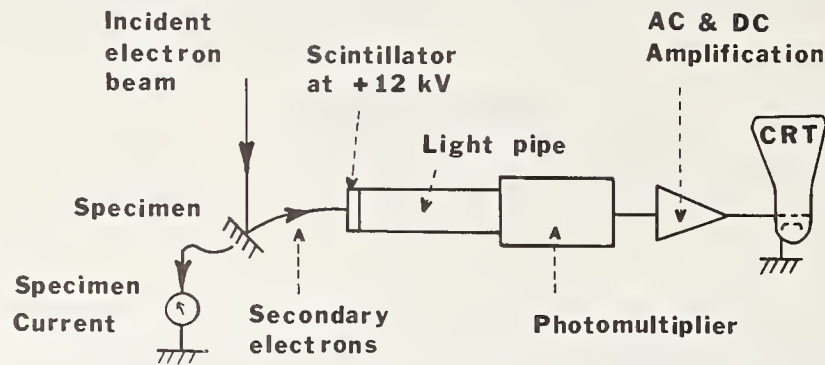


Figure 2. Signal collection process in the SEM (modified after ref. [11]).

With these restrictions in mind, we have studied variations in secondary emission for silicon surfaces. Operating conditions were kept constant by utilizing constant AC and DC gain (fig. 2), constant accelerating potential (calibrated with the continuum), and constant beam current (measured in a 200 μm aperture Faraday cup). For comparative work secondary collection geometry was optimized by use of $\theta = 70^\circ$, and a 12 mm working distance such that the scintillator (with collector at +300V) was positioned horizontally facing the area of observation. By utilizing such operating conditions, the secondary emission calibration micrograph in figure 3 was made. The 35° line scan differs only slightly in position from the zero degree scan (refer to fig. 1), and gives an indication of electronic noise, presumed nearly constant regardless of angle. The additional AC superimposed upon the DC level at higher angles in figure 3 is related to surface irregularities on the polished silicon wafer used for calibration. The electronic noise leads to estimated angular detection limits as follows for various angles of inclination: $\pm 10^\circ$ at 35° , $\pm 1.5^\circ$ at 70° and $\pm 0.5^\circ$ at 80° under typical operating conditions for our instrument. Comparison of figures 1 and 3 thus affirms, both at the signal generation and the signal collection steps in the signal processing train, the strong dependence of δ' on θ for $\theta > 60-70^\circ$. Because of play in the SEM stage, angles were always approached from the same direction (read to within $\pm 0.1^\circ$ or better). Calibration from the image at 90° was relatively easy; however additional calibration points were not available, and it is possible that a slight systematic error at lower angles was present.

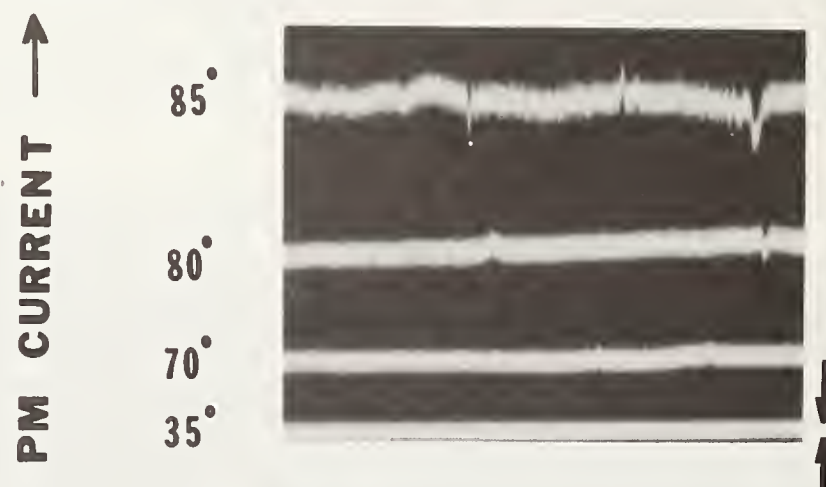


Figure 3. Calibration micrograph showing photomultiplier signal for scans across finely polished Si at four different values of θ . Arrows indicate estimated electronic noise.

For quantitative or semi-quantitative comparison (fig. 4), single secondary emission line scans are useful: these may be regarded as but one element of a y-deflection modulated image. Contrast (A.C. amplification) may then be adjusted for maximum response (for rapid

survey of a smooth surface for presence of irregularities, a complete y -deflection image is highly useful, as will be discussed in the ensuing section). Profilometry, for comparative purposes (fig. 4) was done using a diamond-tipped stylus of $\sim 3 \mu\text{m}$ radius. The instrumental set-up and data processing techniques used for profilometry have been described by Teague [12].

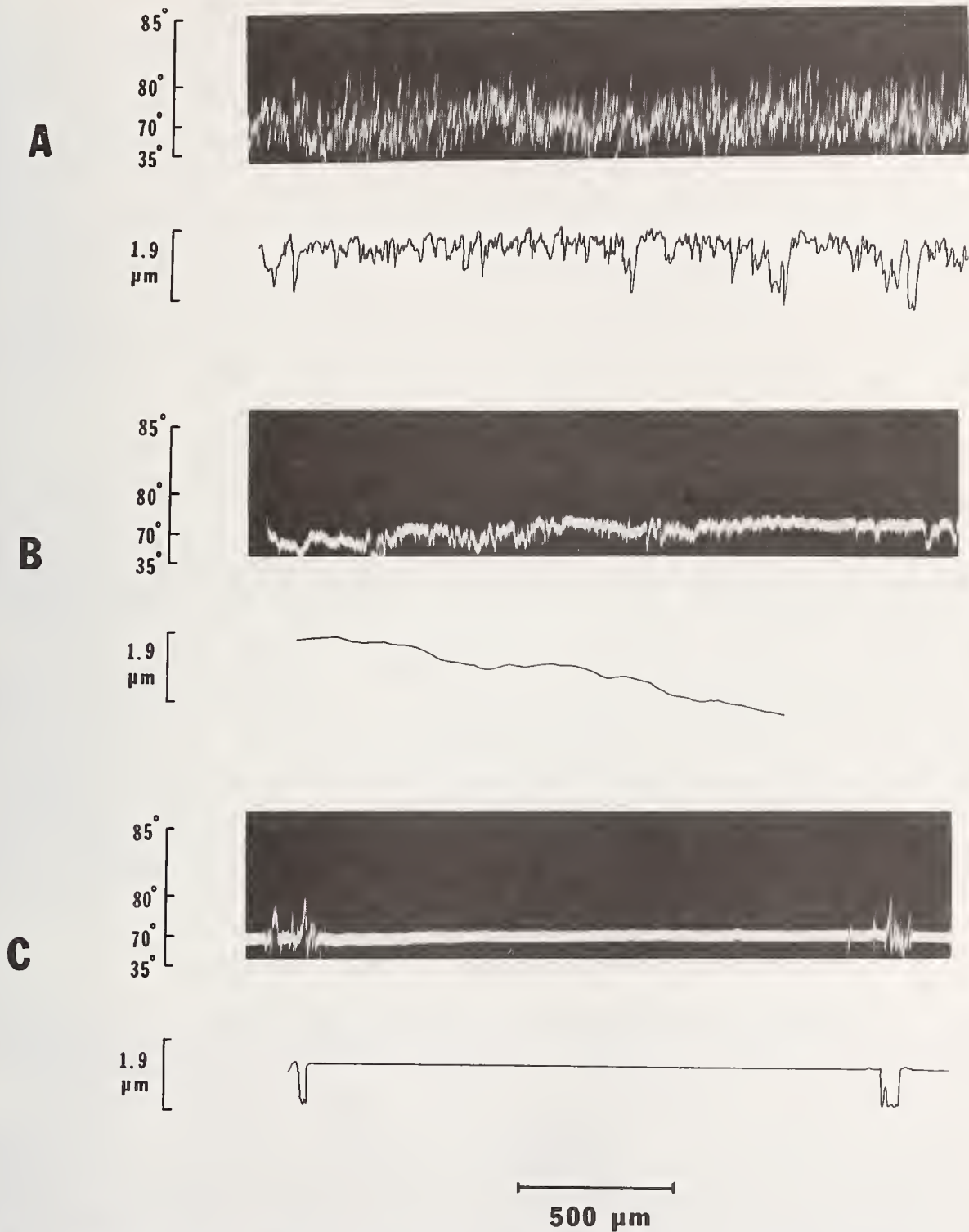


Figure 4. Comparison of secondary electron emission (upper) and profilometer scans (lower) for A) rough cut Si, B) chemically polished Si, C) finely polished Si.

In the present study, three specimens of single crystal Si cut normal to $[111]$ with the following surface preparations were used: rough-cut ($R_a = 0.57 \mu\text{m}$), chemically polished ($R_a = 0.17 \mu\text{m}$) finely polished ($R_a = 0.04 \mu\text{m}$).² Windowless energy dispersive x-ray spectrometry verified the relative cleanliness of the surfaces in that carbon and oxygen peaks were not detected (normally any very thin adsorbed layers would be vaporized

by local electron beam heating).

IV. Results

A. General Correlations

Results of comparative SEM and profilometer scans ~ 1.7 mm in length are shown in figure 4. The SEM profiles indicate surface inclination vs position on the surface. A detailed comparison of the two types of profiles is not possible because of the impossibility of positioning a stylus tip a few μm in diameter and an electron beam a few hundred nm in diameter in precisely the same fashion to traverse a surface of fine detail. The fluctuations in amplitude of the signals show a rather similar decrease in intensity from rough cut to finely polished. Coarse periodicities appear to correlate somewhat for both secondary emission and profilometer. The grooves of ~ 1.5 μm depth, visible on the profilometer scan of the rough cut Si (fig. 4a) are associated with cutting striations; the fine structure produced by the cutting action also varies in a periodic fashion, apparent in the coarse undulations of the secondary emission signal. Undulations are visible as well in both profilometer and secondary emission profiles of the chemically etched surface (fig. 4b). The finely polished surface (fig. 4c) is essentially "flat" with respect to both profilometer and secondary emission scans with the exception of a few undulations in the latter which may indicate local variations of a fraction of a degree in the surface uniformity.

B. Quantitative Comparison of SEM and Profilometer Data for Rough Cut Si

It is possible to gather quantitative angular information from secondary emission line scans analogous to that obtainable from profilometry. This has been done for the rough cut Si with the aid of a template constructed using a calibration scan (see fig. 3). Results are given in figure 5, a histogram which is a probability density distribution function in θ . It was obtained by integrating manually the portion of the sampled surface lying within each selected angular interval. The angle of surface inclination, θ , is different from the analogous parameter that would be measured by profilometry. In profilometry only the component of slope in the direction of travel is measured. In the SEM, θ is measured with respect to the direction of travel of the electron beam. An additional degree of freedom is thus present along a topographic traverse measured by the SEM, and the SEM-derived values should be thought of in terms of the relevant spherical coordinates. Since the average inclination of the surface with respect to the beam is 70° , the set of measured angles should be centered approximately around 70° . The SEM-derived average angle of inclination, $\bar{\theta}$, for the rough Si surface is indeed 70.6° , close to the specimen stage goniometer reading of 70.0° . The SEM-derived average slope, θ_{MD} , is 8.4° , in reasonable agreement with the profilometer average slope value of 9.7° (refer to Table 1 for description of the calculations).

C. Y-Deflection Modulated Images of Finely Polished Si

As figure 4c indicates, the finely polished surface shows few definable irregularities. It is in such cases that complete y-deflection modulated images can be employed to good advantage for examination of large areas of surface. The increased detail with which imperfections are visible on the surface in the image of figure 6b relative to the unmodulated image of figure 6a can be maximized by appropriate instrumental settings. Such increased clarity results from use of y-deflection as opposed to grey level as the contrast device. It is possible that some contribution from subsurface defects may be involved in the linear irregularities of figure 6b; the extent to which this is likely should perhaps be investigated further [13]. However, the potential of the method is emphasized when considering the sensitivity to very local variations of a fraction of a degree in surface orientation.

R_a is defined as $\frac{1}{L} \int_0^L |y| dx$ where y is the height of the surface with respect to the mean line; L is the traverse length of the surface profile.

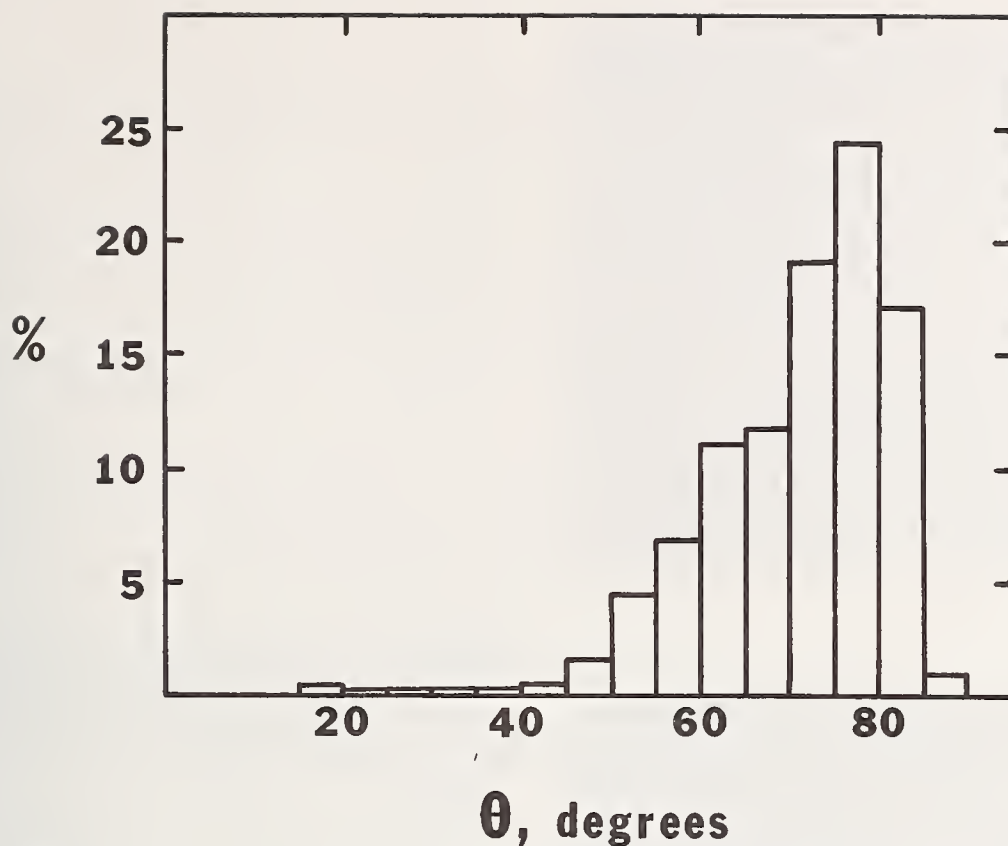


Figure 5. SEM-derived data for rough-cut Si (from 650 μm sample) showing the distribution of surface angular irregularities.

Table 1. Surface angular roughness parameters.^a

Angular arithmetic mean, $\bar{\theta}$

$$\bar{\theta} = \frac{\sum f_i \theta_i}{\sum f_i}$$

Angular mean deviation, θ_{MD}

$$\theta_{MD} = \frac{\sum f_i |\theta_i - \bar{\theta}|}{\sum f_i}$$

^a f_i is a weighting factor calculated from the histogram in figure 5.

V. Conclusions

Under appropriate operating conditions, quantitative information concerning surface angular roughness can be obtained for silicon surfaces from secondary emission. Suitable calibration can be obtained with minimal difficulty on most instruments. The sensitivity of secondary emission to variations in surface orientation is better than 0.5° for Si under typical operating conditions. Undoubtedly this could be improved by careful attention to the electronics involved.

Full y-deflection modulated images are useful primarily in examining very smooth surfaces for irregularities; this can be done quickly for large areas. For quantitative comparisons, line scans are needed. These can easily be correlated with normal SEM images and if desirable, in a general way with profilometer data. The use of absorbed current



A



B



2 μm

Figure 6. A - Secondary electron image of smooth Si surface with coarse scratch. B - Y-deflection modulated image of area in A. Note increased clarity with which minor surface flaws at left and right are visible.

rather than the secondary emission signal is advisable for improved accuracy- this is likely to result in decreased sensitivity, however.

Before the approach described here can be applied extensively to ceramic surfaces, it will be necessary to know if conductive coatings can be applied. If not, curves of total yield must be determined for each material; with these data operating conditions can be set such that $\delta' = 1$, hopefully suppressing the build-up of surface charge sufficiently that quantitative studies of surface roughness can be made. For efficient data collection, data processing equipment should be employed. Further work concerning accuracy and precision of this approach is desirable, especially studies elucidating the effect of electron beam spreading, and the possibility of reducing noise.

VI. Acknowledgements

We are grateful to E. Muth, who prepared the polished Si wafers used for calibration, and to F. Scire, who completed the profilometer scans. The manuscript has been improved through the suggestions of B. Hockey, A. Feldman, and D. Newbury, and particularly those of T. Vorbürger.

VII. References

- [1] Sundahl, R. C. and Berrin, L., Analysis and characterization of ceramic surfaces for electronic applications, NBS Spec. Publ. 348, 271-292 (1972).
- [2] White, E. W., McKinstry, H. A. and Diness, A., Quantitative surface finish characterization by CESEMI, NBS Spec. Publ. 348, 309-316 (1972).
- [3] Wolf, H. F., Silicon Semiconductor Data, pp. 1 and 602 (Pergamon, New York, 1969).
- [4] Bruining, H., The depth at which secondary electrons are liberated, *Physica* 3, 1046-1052 (1936).
- [5] Robinson, V. N. E., The origins of the secondary electron signal in scanning electron microscopy, *J. Phys. D* 7, 2169-2173 (1974).
- [6] Murata, K., Spatial distribution of backscattered electrons in the scanning electron microscope and electron microprobe, *J. Appl. Phys.* 45, 4110-4117 (1974).
- [7] Dekker, A. J., in Solid State Physics, pp. 422-426 (Prentice-Hall, Englewood Cliffs, New Jersey, 1957).
- [8] Oatley, C. W., The Scanning Electron Microscope, Part 1. The Instrument, pp. 156-165 (The University Press, Cambridge, 1972).
- [9] Ichinokawa, T., Iiyama, M., Onoguchi, A., and Kobayashi, T., Charging effect of specimen in scanning electron microscopy, *Jap. J. Appl. Phys.* 13, 1272-1277 (1974).
- [10] Conru, H. N., and Laberge, P. C., Oil contamination with the SEM operated in the spot scanning mode, *J. Phys. E* 8, 136-138 (1975).
- [11] Wells, O. C., Scanning Electron Microscopy, p. 25 (McGraw-Hill, New York, 1974).
- [12] Teague, E. C., Evaluation, revision and application of the NBS stylus/computer system for the measurement of surface roughness, NBS Tech. Note 902, 142 pp. (1976).
- [13] Baines, M., Clarke, D. R., and Howie, A., Backscattered images of dislocations and crystal defects, in Scanning Electron Microscopy: Systems and Applications 1973, pp. 443-335 (London, Institute of Physics, Conf. Series No. 18, 1973).



LATENT SCRATCHES ON OPTICAL GLASSES

THAT APPEAR AFTER CLEANING

T. Izumitani, E. Miyade, S. Adachi

Hoya Corporation
572, Miyazawa-cho, Akishima-shi, Tokyo, Japan

S. Harada

Hoya Electronics Co., Ltd.
3280, Nakamaru, Nagasaka-cho, Kitakoma-gun
Yamanashi-ken, Japan

The latent scratch which appears on polished optical glass surfaces was studied. The latent scratch, as the word implies, can be hardly detected in polishing process, but becomes evident after cleaning or after antireflection coating. The appearance of the latent scratch is affected by (1) the polisher, (2) the polishing grains, (3) the mechanical condition of the polishing, and (4) the glass property. And it is also affected by the corrosion power of the cleaning solution. It is concluded that the latent scratches are the scratches which are formed as undetectable fine scratches in the polishing process and grow to the detectable size in cleaning process. On the basis of this fact, a method of preventing latent scratches was suggested.

Key Word: Cleaning, chemical durability; glass surface; latent scratch; optical glass; polishing.

1. Introduction

Recently the latent scratch has become a serious problem to the lens makers who coat multilayer films on the lens surface, because antireflection multilayer coating makes it easier to recognize the presence of the abnormality (stain, contamination and scratch) on the glass surface. In addition the severe cleaning condition, which is necessary to get a completely clean surface, would accelerate the growth of the scratch. The latent scratch was experienced by the authors when the staining of optical glass in the polishing process was investigated. The latent scratch on the polished glass surface of BaCD 16 ($\text{SiO}_2\text{-B}_2\text{O}_3\text{RO}$) was recognized during electron-microscopic observation.

Photo 1(a) is the electron-micrograph of the polished glass surface of BaCD 16 before the cleaning, which shows the several spot-like Shiroyake (clouding). When at first BaCD 16 was immersed in trichloroethylene, the surface hardly changed as shown in Photo 1(b). Then this sample was immersed in water with ultrasonic agitation; the Shiroyake disappeared from the surface, as shown in Photo 1(c). Photo 1(d) shows the surface immersed in detergent solution with ultrasonic agitation. In this photograph, several scratches can be observed. These scratches were not detectable before the sample was immersed in detergent solution. It was necessary to make clear whether these scratches are formed in the cleaning process or in the polishing process.

The purpose of this paper is to make clear the nature of latent scratches and how they appear by studying the relationships: (1) between the polishing and the latent scratches, (2) between the cleaning and the latent scratches, and (3) between the glass properties and the latent scratches. We will also analyze the cleaning process and discuss detergents and the relationships between the detergent and the latent scratches. Then we will suggest how to prevent the formation of the latent scratches.

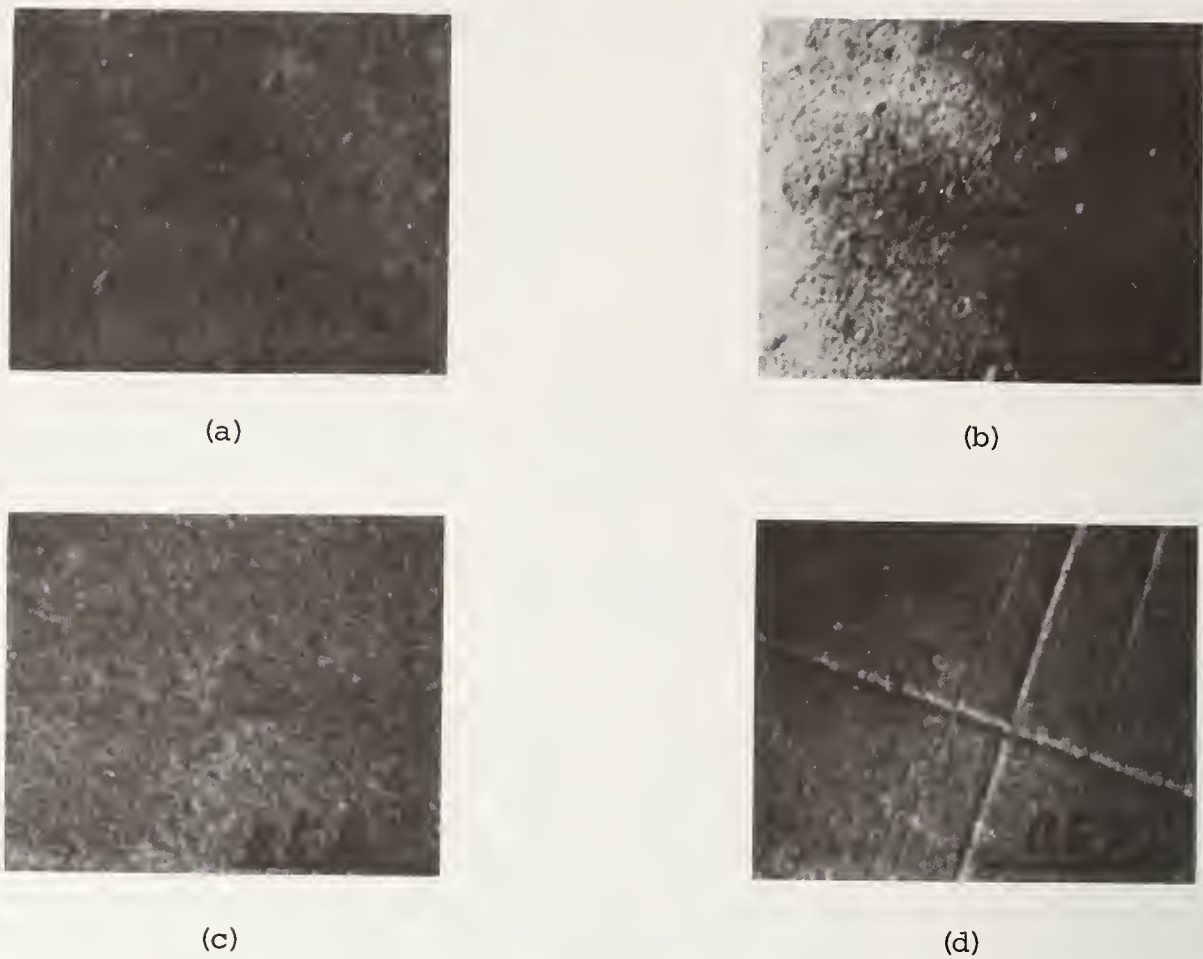


Photo 1. Appearance of latent scratch (BaCD 16)

- (a) After polishing
- (b) Cleaned in trichloroethylene with ultrasonic agitation
- (c) Cleaned in water with ultrasonic agitation
- (d) Cleaned in detergent with ultrasonic agitation

2. Latent scratch and polishing process

In order to study whether the latent scratch formation is correlated to the polishing process, the relationships between (1) the latent scratch and the polisher, (2) the latent scratch and the polishing grains (cerium oxide), and (3) the latent scratch and mechanical polishing condition were examined.

In this experiment, BaCED 4($\text{SiO}_2\text{-B}_2\text{O}_3\text{-RO}$) was used. The cleaning process is shown in Fig. (1). As the cleaning solution, (a) water, (b) detergent solution, and (3) 0.01N nitric acid were used, respectively.

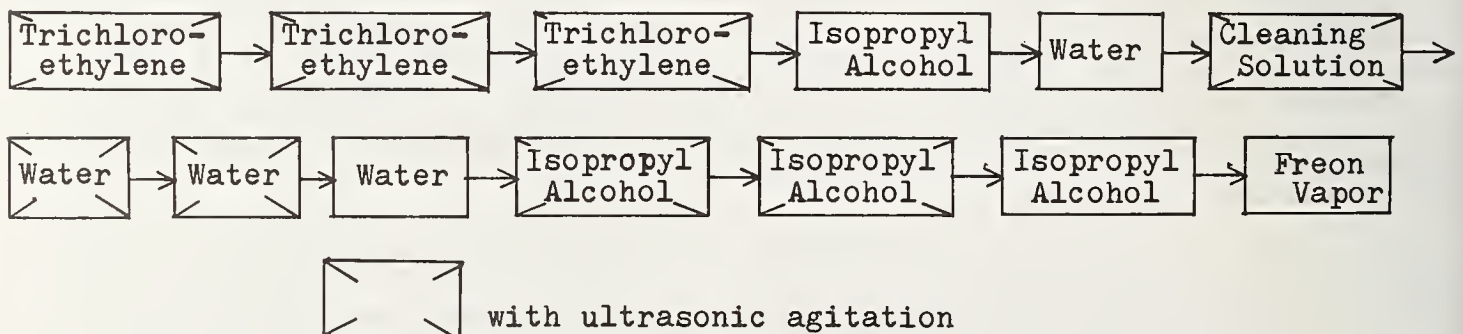


Fig. 1. Cleaning Process

2.1. Latent scratches and polisher

Photo 2(A) and Photo 2(B) show glass surfaces polished by Politex and Polyurethane, respectively. On the surface polished by Politex, no scratches are seen after cleaning in water or in the detergent solution. However, on the surface polished by Polyurethane, many scratches are seen after cleaning in water or in detergent solution.



(a) Cleaned in water for 120 sec. with ultrasonic agitation



(b) Cleaned in detergent for 40 sec. with ultrasonic agitation



(c) Cleaned in acid for 40 sec. with ultrasonic agitation

(A) Politex

(B) Polyurethane

Photo 2. Effect of the polisher on latent scratch formation (BaCED 4)

Especially when the surface was cleaned in acid, the difference between the surface polished by Politex and that polished by Polyurethane is remarkable. These results suggest that the formation of the latent scratches is affected by the polisher.

Politex is the elastic polisher and Polyurethane is the viscoelastic polisher. This may cause the considerable difference in the latent scratch formation even under the same polishing condition.

2.2. Latent scratch and polishing grains (cerium oxide)

The hardness of cerium oxide increases with the sintering temperature. Two kinds of cerium oxide were obtained from cerium hydroxide by sintering at 1200°C and 900°C. The former is harder than the latter. In this experiment, BSC 7 ($B_2O_3-SiO_2-R_2O$) was polished with the two kinds of cerium oxide. Photo 3(a) and Photo 3(b) show the surface of BSC 7, polished with softer cerium oxide and harder cerium oxide, respectively.



(a) Polished with soft grains



(b) Polished with hard grains

Photo 3. Effect of the hardness of the polishing grains on latent scratch formation (BSC 7 cleaned in detergent for 40 sec.)



(a) High polishing rate



(b) Low polishing rate

Photo 4. Effect of the polishing condition on latent scratch formation (BSC cleaned in detergent for 40 sec.)

The severe latent scratches are seen on the surface of the BSC 7 polished with harder cerium oxide. This indicates that harder polishing grains make the more latent scratches than softer grains.

2.3. Latent scratches and mechanical polishing conditions

The mechanical condition of the polishing can be changed by (a) pressure, (b) revolution speed and (c) the type of the polishing machine. Photo 4(a) shows the surface of BaCED 4 which was polished at higher pressure and higher revolution speed than that shown in Photo 4(b). The polishing rate was approximately four times faster. The result shows that the harder mechanical condition of polishing makes more latent scratches on the surface of the glass.

These results suggest that the latent scratches appearing after cleaning are affected by the polishing process. The latent scratches appear under the severe polishing conditions, i.e. the polishing the glass surface by the hard polisher with hard polishing grains under the hard mechanical condition.

From the fact that the number and size of latent scratches are affected by the polishing condition, it is concluded that the origin of the latent scratch is already made as a very fine scratch, which cannot be detected in the polishing process and that the fine

scratches will grow up to detectable size in a cleaning solution, such as water or especially detergent solution.

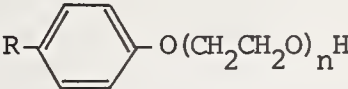
3. Latent scratch and cleaning process

Figure 1 shows a common automatic cleaning system for camera lenses. Pitch and the protective film on the polished glass surface is dissolved into trichloroethylene. Detergent is used for removing the polishing grains (cerium oxide, etc.) from the glass surface. Freon vapor is used to dry the lens. The latent scratch does not appear in the organic solvent. The latent scratch becomes visible in detergent solution.

3.1. Corrosion behaviour and cleaning power of cleaning solution

A synthetic detergent usually consists of surfactant and inorganic builder (table 1). The corrosive behaviour of the surfactant and the inorganic builder were examined. The cleaning power in removing polishing grains and finger marks adhering to the glass surface were also tested. The results are listed in tables 2 and 3.

Table 1. Main components of synthetic detergent

	Surface active agent	Inorganic builder	
Anion	ROSO_3Na 	NaHCO_3 Na_2CO_3 Na_3PO_4 $\text{Na}_4\text{P}_2\text{O}_7$ $\text{Na}_5\text{P}_3\text{O}_{10}$ Na_2SO_4	Powder
Nonion	$\text{RO}(\text{CH}_2\text{CH}_2\text{O})_n\text{H}$ 		Liquid

Corrosive power is measured as the percentage of weight loss after immersing the glass in the surfactant and inorganic builder solution for one hour at 50°C with stirring. All these data in Table 2 were normalized to the weight loss for water. Table 2 shows the surfactant itself cannot attack the glass but that water, which dissolves the surfactant, attacks the glass. Table 2 also shows the detergent exhibits almost the same corrosive power as the inorganic builder. This means that the corrosive power of the detergent is caused by the inorganic builder. Therefore, if the inorganic builder were eliminated, the corrosive power would be decreased and the latent scratch would hardly appear.

The cleaning powers of the surfactant, the inorganic builder and the detergent were compared qualitatively by judging whether the polishing grains or the finger mark adhered on the glass surface are removed by immersing in those solutions. As shown in Table 3, the surfactant and the detergent exhibit cleaning power against the finger mark, but does not have the cleaning capability against polishing grains. Only $\text{Na}_5\text{P}_3\text{O}_{10}$ which has the highest corrosion power among the inorganic builders can slightly remove the polishing grains. This suggests that in order to remove the polishing grains from the glass surface, the corrosion of the glass surface is inevitable. In other words, only high corrosive agents can remove the polishing grains from the glass surface.

3.2. Latent scratch and cleaning

The cleaning is considered to remove the contaminant from the glass surface. This is achieved by two methods, as illustrated in Fig. 2, (1) to dissolve the foreign matter or (2) to remove the foreign particles.

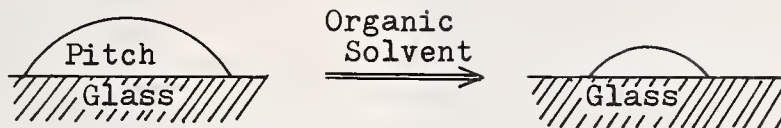
Table 2 Corrosion of glass by solutions

Solution	Glass pH	BaCED	BaCD	IaCL	IaC	IaFL	
		4	16	6	12	3	
Detergent A	9.6	4.6	4.5	4.1	6.6	3.3	anion
Detergent B	11.9	3.8	1.9	2.2	2.2	0.7	nonion
Surfactant A	6.5	1.9	1.7	1.7	2.1	1.2	nonion
Surfactant B	6.5	2.7	2.0	1.1	1.1	0.9	nonion
Surfactant C	6.5	1.6	2.9	-	-	-	anion
H ₂ O	6	1	1	1	1	1	
Na ₅ P ₃ O ₁₀	8.7	4.1	7.7	16.1	36.8	7.6	
NaHCO ₃	8	3.6	0.8	1.9	4.3	1.4	
Na ₄ P ₂ O ₇	11	5.8	2.7	-	-	-	
Na ₂ CO ₃	12	2.7	1.1	0.9	0.3	0.3	

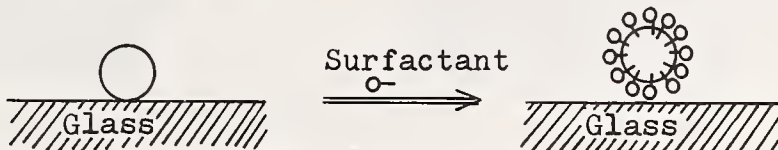
Table 3 Effectiveness of contaminant removal

Solution	Glass Contami- nant pH	BaCED 4		BaCD 16		Time	
		Cerium oxide	Finger mark	Cerium oxide	Finger mark		
Detergent A	9.6	-	+	-	+	3-5 min	1.0 wt%
Detergent B	11.9	-	+	-	+	"	1.0 vol%
Surfactant A	6.5	-	+	-	+	"	"
Surfactant B	6.5	-	+	-	+	"	"
Surfactant C	6.5	-	+	-	+	"	"
H ₂ O	6	-	-	-	-	"	
Na ₅ P ₃ O ₁₀	8.7	+	-	+	-	"	1.0 wt%
NaHCO ₃	9	-	-	-	-	"	"
Na ₄ P ₂ O ₇	11	-	-	-	-	"	"
Na ₂ CO ₃	12	-	-	-	-	"	"

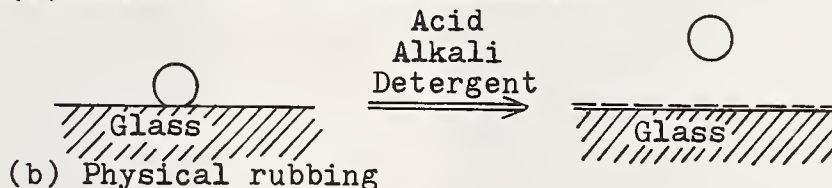
- (1) Dissolution of the foreign matter
 (I) Organic contaminant



- (2) Removal of the foreign particles
 (I) Organic contaminant



- (II) Inorganic contaminant
 (a) Dissolution of the interface



- (b) Physical rubbing



Fig. 2. Mechanism of Cleaning

It is an example of the former that the pitch is dissolved into trichloroethylene while the mechanism of removing the adhering polishing grains from the glass surface is rather the latter phenomenon. It is considered that the interface between the polishing grains and the glass surface is attacked by the corrosive cleaning solution, and as a result, the polishing grains are removed.

Because the detergent contains the inorganic builder which attacks the glass, it can slightly remove the adhering polishing grains. But at the same time, the inorganic builder attacks the glass surface and makes the latent scratches on the glass surface.

After all, these results indicate that in order to remove the adhering polishing grains from the glass surface, the formation of the latent scratch on the glass surface is inevitable. This means the polishing grains on the glass surface cannot be removed without the latent scratch formation. We cannot use the detergent to remove the polishing grains and avoid the appearance of the latent scratches.

The surfactant can not remove the polishing grains. As shown in Fig. (1), the surfactant can react with the organic contamination with its oleophilic group. But it can not react with the inorganic material such as the polishing grains, because it has no affinity for inorganic substance.

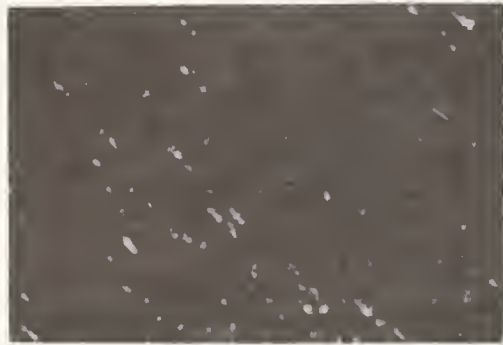
The conclusion is that the detergent can hardly remove the adhering polishing grains of cerium oxide without the appearance of the latent scratches. The adhering polishing grains on the glass surface should be removed by other methods, for example, by scrub off.

4. Latent scratch and the glass property

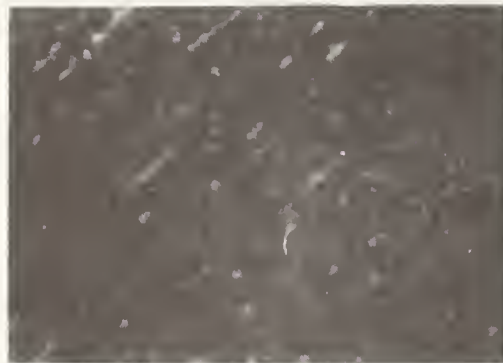
The mechanism of the appearance of the latent scratch was considered as follows. The glass surface is scratched by the polishing grains in the polishing process. The invisible, submicron scratches might be caused by some coarse polishing grains. These scratches will grow up to the extent of the detectable size in the cleaning process.



(a) Cleaned in water for 120 sec. with ultrasonic agitation



(b) Cleaned in detergent for 40 sec. with ultrasonic agitation



(c) Cleaned in acid for 40 sec. with ultrasonic agitation

(A) F2

(B) BaCD 16

Photo 5. Effect of glass property on latent scratch formation

Due to the mechanism, the relationship between the latent scratch and the glass property will be predicted. The tendency of generating the latent, fine scratches will be correlated to the glass hardness, and the tendency of the fine scratch to grow to a detectable size scratch and the glass properties were examined.

4.1. Latent scratch and glass hardness and chemical durability of glass

In this experiment, BaCED 4, F2 and BaCD 16 were polished. BaCED 4 and F2 have almost the same chemical durability, but F2 is softer than BaCED 4. Photo 5(A) shows the glass surface of F2. From the comparison of the surface of F2 (Photo 5A) with BaCED 4 (Photo 2B), it is evident that the more latent scratches can be seen on the surface of F2.

BaCED 4 and BaCD 16 have the same glass hardness, but BaCD 16 is less durable than BaCED 4. Photo 5(B) shows the glass surface of BaCD 16. From the comparison of the surface of BaCD 16 (Photo 5B) with BaCED 4 (Photo 2B), it is evident, too, that the more

latent scratches appear on the surface of less durable BaCD 16 and softer F2. This indicates that the latent scratch is correlated to the hardness and chemical durability of glass. The hard and high durable glass is desirable from the viewpoint of preventing the latent scratches.

5. Conclusion

The cause of the latent scratch is the scratches made in the polishing process. Relatively large, submicron scratches caused by the larger grains mixed in the polishing grains will grow up to the detectable size in the cleaning process. The size of the latent scratches detectable with unassisted eyes is considered about 3 - 4 μ and the latent scratch is essentially different from the substantial scratches (about 80Å) related to the polishing mechanism which can be observed with an electron-microscope after etching. The following three counterplans would be suggested for preventing the latent scratches.

1) Polishing condition

It is desirable that the glass should be polished with the soft polisher with the soft polishing grains under a mild mechanical condition.

2) Cleaning condition

The adhering polishing grains cannot be removed with the usual detergent without the formation of the latent scratches. It is desirable that the adhering cerium oxide be removed by physically rubbing the glass surface.

3) Improvement of the glass property

It is desirable that the hardness and the chemical durability of the glass are improved.

Discussion

BURKE

1. Is the groove that is revealed by the corrosive action of the detergent (the latent scratch) revealed prior to cleaning by observing a change in index of refraction of the glass at the site where the latent scratch would appear? This would be expected to be the case if the hard particle causing the latent scratch were to have caused compaction of the glass and thus decrease its corrosion resistance.

ADACHI

I think that the latent scratches are not recognized prior to cleaning by observing refractive index changes for two reasons:

1. Refractive index changes in the surface are complex. While polishing grains will cause compaction of the glass surface to increase the refractive index, leaching of soluble components of glass lowers the surface refractive index. Generally, refractive index of polished layer of optical glasses are lower than that of bulk glasses because of low chemical durability.

2. Because the size of the latent scratches is very fine (perhaps less than 1μ), we can hardly find them or measure the refractive index change at the latent scratch.

VAN GROENOU

Is the corrosion due to the grooves or possible cracks?

ADACHI

Grooves.

Session IV

Effects of Machining and Surface Finishing on Ceramic Properties

Session Chairman

R. C. Bradt, Pennsylvania State University



MACHINING FLAWS AND THE STRENGTH GRAIN SIZE BEHAVIOR OF CERAMICS

R. W. Rice

Naval Research Laboratory
Washington, D. C. 20375

A model for the strength-grain size dependence of ceramics failing from machining flaws is presented based on the observation that the size of machining flaws (C) shows little or no dependence on grain size. Two regimes of behavior are seen. At finer grain sizes, little or no strength dependence on grain size (G) exists because flaws are $> G$. For large G , the significant decrease of strength with increasing G is attributed to a transition from polycrystalline to either lower single crystal or grain boundary (i.e. bicrystal) fracture energies as the \sim constant (C) becomes significantly less than the G as G increases. The transition between the two regimes is when C and G are similar. Extensive analysis of strength-grain size data, and more limited directly correlated fractographic data support the proposed model. Spontaneous cracking in non-cubic materials is shown to support the model, but not be an alternate explanation for the transitions seen in machined Al_2O_3 or BeO . This analysis also further supports the observation that machining flaws do not vary greatly with typical variations in machining parameters.

Key Words: Strength; grain size dependence of strength; flaw sizes; brittle failure.

1. Introduction

Single phase as well as some multiphase ceramic polycrystalline bodies, especially those of limited to zero porosity, show a definitive and characteristic dependence of their brittle tensile failure on grain size (G) [1-4].¹ For most materials, such behavior occurs to temperatures of at least a few hundred $^{\circ}C$ and for many more refractory bodies to temperatures of $1000^{\circ}C$ or more. Typically, two regimes of such G dependence of brittle fracture are observed. At larger G , there is typically a significant increase in tensile (or flexure) strength(s) as G decreases. However, as G decreases below some intermediate level, e.g. below 10 to 50 μm , much less or possibly no, increase in S is observed with further decreasing G (fig. 1). The latter regime showing more limited or no increase in S with decreasing G typically gives a non-zero intercept on a Petch plot, i.e. a plot of S versus $G^{-1/2}$. In the past, such non-zero intercepts have often been interpreted as indicating strength control due to microplastic nucleation or growth of cracks [1-3]. However, recent fractographic information shows that this is commonly not the case, that flaws, commonly from machining, are typically the source of failure [2-4]. In the past, it was often assumed that the G dependence of S was due to the flaw size (C) being related to G , i.e. most commonly it was assumed that $C = G$. However, recent fractographic information shows that the size of flaws introduced by machining do not vary much, if at all, with G [5]. Thus, flaws are typically much smaller than large grains and typically much larger than fine grains. This extensive fractographic information thus invalidates

¹Figures in brackets indicate the literature references at the end of this paper.

the strength ranges for single crystals of the same material in their weaker orientations with the same set of finishing or testing parameters are indicated for the two sets of polycrystalline samples by 1) and 2) are shown respectively by X₁ and X₂.

the previous explanation for the grain size dependence of brittle failure of ceramics under tensile loading. The purpose of this paper is to review the pertinent fractographic observations on machining flaws and S-G data in order to relate the two together and to discuss the mechanisms of failure that they demonstrate or suggest.

2. Mechanisms of Failure

Before reviewing the fractographic and S-G data and their interrelation, it is appropriate to first briefly review the two basic mechanisms of failure. One mechanism is failure due to microplastic crack nucleation, due to blocking of slip bands or twins by other slip bands or other twins, or more commonly, by grain boundaries. Microplastic failure is typically represented by the equation:

$$S = \sigma_0 + KG^{-\frac{1}{2}} \quad (1)$$

where σ_0 is the stress to activate the slip or twinning phenomena that leads to failure, and K is a constant. The second mechanism, that of flaw failure, typically follows the relationship:

$$S = A \sqrt{\frac{E\gamma}{C}} \quad (2)$$

where A is a geometrical factor associated with the shape of the flaw, and may also be dependent on the size of the flaw relative to that of the specimen, as well as the location of the flaw in the specimen, E is Young's modulus, and γ is the fracture energy. As noted earlier, it has commonly been assumed in the past that C was related to G , commonly $C = G$, implying that one should be able to tell whether the mechanisms implied by eqs. (1) or (2) were operative by plotting S versus $G^{-\frac{1}{2}}$. Equation (1) would result in a straight line with a non-zero intercept at σ_0 while eq. (2) would result in a straight line with a zero intercept. However, as noted earlier and discussed in detail later, C is generally not related to G so this is not a valid method of separating the two mechanisms. Further, there are other complications such as the fact that the two mechanisms may interact, e.g. slip may aid the growth of pre-existing flaws to grow to a critical size. Also, there can be competition between the two processes such that one may dominate in one grain size region and the other in another grain size regime, with a transition between the two regimes shifting with such parameters as impurities, porosity, and surface finish, e.g. machining.

3. Proposed Mechanism of Failure

Any mechanism of brittle failure of polycrystalline ceramics must address the following factors:

1. Foremost is the fact that failure typically appears to initiate from machining flaws that have little or no dependence on G as noted earlier [5].

2. The observed dependence of strength on surface finish parameters such as grit size [6-9] and machining direction [5,10].

3. The possible dependence of strength on specimen size [5].

4. That strengths of polycrystalline specimens can often extend below

the strengths of single crystals of the same material given the same surface finishing which are tested in those orientations that give lower strength due to favorable orientation of lower fracture energy planes [2,4].

5. The expected interaction or competition between microplastic and brittle mechanisms of failure in materials such as MgO where the former mechanism can be operative [1,2].

The proposed mechanism of tensile (or flexural) failure is as follows. First consider the smaller G regime indicated by II in figure 1, i.e. where strength shows either limited or no dependence of G. Fractography has clearly shown that in this region flaws are typically many grains in size [2-5]. Since E does not depend on G, γ often does not depend significantly on G [2, 4, 11], and the flaws are multi-grained in size and show no relationship to the grain size, no significant dependence of S on G would thus be expected. This absence of any significant G dependence for failure with $C > G$ gives a non-zero intercept on a Petch plot, e.g. figure 1. This is now believed to be the predominant source of non-zero intercepts. The possible limited increase of strength with decreasing G in this region (II) can arise from either of at least two sources. The first source is some possible limited decrease of C with decreasing G [5], e.g. possibly following the limited increase of hardness with decreasing G. A second possible source is the effect of internal stresses, i.e. due to incompatible strains between grains in non-cubic materials or materials that have undergone a phase transformation. Since there are statistical variations of these stresses, as the number of grains encompassed by C decreases, internal stresses can increasingly aid failure. Such effects can begin to occur even when flaws encompass many grains [1,2,4,12]. With C nearly constant, the number of grains encompassed by the flaw increases with decreasing G, which would thus reduce the internal stress effect, and hence increase S.

This leaves the significant dependence of S on G in region I and the reason for the transition between regions I and II of figure 1 to be explained. A key observation is that the transition between these two different regimes of S-G behavior typically appears to occur when $C \sim G$ [2-4, 13]. Two explanations for the significant decrease in strength as G increases so the \sim constant C becomes progressively $< G$ have been considered. The first is that the machining flaws start propagating below the failure stress but are arrested when they encounter the adjacent grains. Failure would thus result when the stress increases to the level to propagate the flaw now the size of the grain in which it has grown, or the size of one or more grain boundary facets for intergranular flaws, into or around the surrounding grains. This mechanism provides a ready explanation for the G dependence of S in region I (fig. 1) since it gives the final flaw size $\sim G$. However, this mechanism leaves unexplained how cracks can grow several fold in size so their increase in stress intensity is greater than the change in fracture toughness on going from a single- to multi-grain crack can be arrested. Further, this mechanism does not explain how polycrystalline bodies with initial flaws similar to those in single crystals of the same material can have strengths similar to, or below, those of the weakest orientation of such crystals when polycrystalline fracture energies are several fold times those for common single- or bi-crystal fracture.

The second explanation for the significant G dependence of S in region I rests on the recognition that for C sufficiently smaller than G flaws would effectively see themselves in a single crystal environment for flaws within grains, or in a grain boundary environment for grain boundary flaws. In the extreme of such cases, failure would then be controlled by the single crystal fracture energy (γ_c) for failure on the easier cleaving or fracture surfaces of the single crystal or the fracture energy (γ_B) for crack propagation along a single grain boundary, e.g. bicrystal fracture energies. γ_c values vary from $\sim 1/3$ to $\sim 1/10$ of typical polycrystalline fracture energy (γ_{pc}) values. γ_B can be anywhere from a fraction, e.g. $1/2$, to 100% of γ_c . Thus, as previously suggested [2,4,14], it is proposed that the significant

increase in strength with decreasing grain size in region I arises from an effective transition from γ_C or γ_B to γ_{pc} as G of different specimens decrease relative to an \sim constant C.

Recent calculations indicate that unless the flaw is a sufficient fraction of G, e.g. 1/3 to 1/2, that propagation will become catastrophic before the crack reaches the grain boundary where a major, if not the total, increase of fracture energy towards γ_{pc} would occur [14]. This transition has been sketched out in some cubic materials based on calculations using the initial flaw size [4,14]. However, some crack growth may also occur [15]. There are also questions of whether the change from γ_C or γ_B to γ_{pc} values is really gradual or possibly a step function. The above noted transition could, in fact, be a result of different more abrupt transitions of individual flaws in different specimens due to varying grain-flaw parameters such as sizes and location [14]. In any event, it appears that the second mechanism, that of a γ transition, applies when C is sufficiently small relative to G, e.g. $C < G/3$, while the first is operative for C larger relative to G, e.g. $C > G/3$.

The above transition in γ is completed at different C/G ratios in different materials, e.g. ~ 1 to 3. This range depends upon a variety of factors such as texture and the orientation dependence of γ within a single grain [14]. The C/G ratio over which this transition occurs can also vary depending on the size, shape, and location of the flaw. Thus, for example, a flaw may be rather shallow but fairly elongated so it crosses into two or three grains, so it probably reached γ_{pc} sooner than a penny shaped flaw of the same depth located entirely within one grain or entirely along one grain boundary. Similarly, a flaw located entirely within a grain, but located adjacent to one grain boundary may have a different transition than a flaw whose ends are well away from the grain boundaries. Internal stresses from thermal expansion anisotropy (TEA) or phase transformation and redistribution of applied stresses due to elastic anisotropy (EA) may also effect the C/G ratios for completing this transition.

Note that the polycrystalline strength in region I can extend below the strengths for the weaker orientation of single crystals having the same surface finish as the polycrystalline materials for several reasons (fig. 1). There are extrinsic causes of this, such as impurities, and porosity. However, there are also intrinsic causes such as failure from grain boundary flaws in materials in which γ_B values are sufficiently below those of γ_C values. Also, internal stresses from phase transformation or TEA can contribute to failure either by adding to the applied stress or by allowing larger machining flaws to form, e.g. by machining flaws linking up with pre-existing cracks from the internal stresses or cracks forming from such stresses during machining operations. Stress concentrations due to EA, which also occurs in cubic materials, may also contribute to lower polycrystalline versus single crystal strengths.

The above model is clearly consistent with all of the observed effects of machining. Thus, for example, grinding perpendicular to the tensile axis of bars generally introduces more elongated and hence more severe flaws whether they are much larger or smaller than G [5]. They also lower the transition because, as noted above, elongated flaws should reach γ_{pc} values sooner because of their interaction with a greater number of grains. Similarly, effects of changing grit size would have the same effect. Again, in a similar fashion, if larger flaws occur in larger bodies, they will lower strengths in both large and fine G bodies and thus give transitions at larger G. Finally, the competition and trade-off between microplastic and flaw failure can also be anticipated. Since slip or twin nucleation of cracks is typically associated with slip bands and/or twins propagating across a single grain, a pre-existing flaw larger than that grain will dominate failure. Thus, entirely brittle failure of materials that can exhibit microplastic failure, such as MgO and CaO should occur for $C > G$.

However, as the C approaches G, the microplastic mechanisms can become competitive so that as flaws become smaller than the grain size, microplastic failure can begin to occur. When flaws are still a sufficient fraction of the G, slip assisted crack growth may be a dominant mechanism of failure.

Subsequent to the authors original discussion of this model, Bradt and colleagues also discussed a similar model in which the fine grain size region was also attributed to $C > G$ [6,]. They, however, attributed the transition and the subsequent larger G region where S depends more extensively on G to a change from machining to "intrinsic" flaws of unspecified character which they apparently felt depended upon G for an explanation of the G dependence of S. Several aspects of the model proposed by the present author were also independently proposed by Rhodes et al [16] who similarly attributed the transition in S-G behavior to $C \sim G$. Also, some aspects of the model were suggested in an earlier review of devitrified glasses by Emrich [17], i.e. a two branch S-G relation depending upon flaw size. Emrich attributes this model to Stookley [17], but the latter reference does not show a definite base for the model, so it appears that it is really more due to Emrich himself.

4. Comparison of the Strength Grain Size Model with Available Data

Considerable S-G data exists in the literature. Much of it lacks definitive characterization of either the surface finishing conditions or the strength test methods, and little fractography has been done. Much of the earlier data does not necessarily show a clear transition for several reasons. First, often only limited G ranges were investigated. Second, much of the data was not plotted in a fashion to clearly show such transitions, e.g. log-log plots which tend to obscure such transitions. Finally, there is also an important experimental difficulty in many materials; namely, variable grain sizes. Thus, for example, bodies such as Al_2O_3 which often readily exhibit exaggerated grain growth may have one large grain at or near the surface in which one or more machining flaws may form. If a flaw forms in or along such a large grain, that flaw is likely to be the source of failure which will then reflect a large, if not total, influence of the size of that large grain. In such cases, plotting S as a function of the average G can be quite misleading. Some have, therefore, plotted strength as a function of the largest G. While this author was one of the first to recognize such possible effects of large grains just inside the machined tensile surface, he has also clearly observed cases where large grains are present, but machining flaws did not form in them (e.g. fig. 2) and hence plotting their strength as a function of the large G is incorrect. This uncertainty of which G is controlling thus leads to substantial scatter in the data and must be considered. Despite these problems, there is still a substantial amount of data which either individually or collectively supports the proposed theory.

Figure 3 shows one of the more complete studies which, in fact, was one of the factors precipitating the development of the model of section 3. Note in figure 3 that the inserted fractographs of fracture initiating flaws clearly show an increase of the strength as G decreases as discussed in the model. Also, note since this is a cubic material in which internal stresses from TEA, or other complications such as those due to phase transformation are not present, one can calculate fracture energies from the indicated flaw sizes. Such calculated fracture energies do, in fact, show a transition from approximately 2 J/m^2 for $C \ll G$ in good agreement with DCB measurements of γ_c to $\sim 7 \text{ J/m}^2$ for $C \gg G$ in good agreement with DCB measurements of γ_{pc} .

The only other set of S-G data that has associated fractography with it are the more limited studies of B_4C (fig. 4). Evaluation of earlier B_4C data suggests a transition as shown in figure 4, and the more recent data of

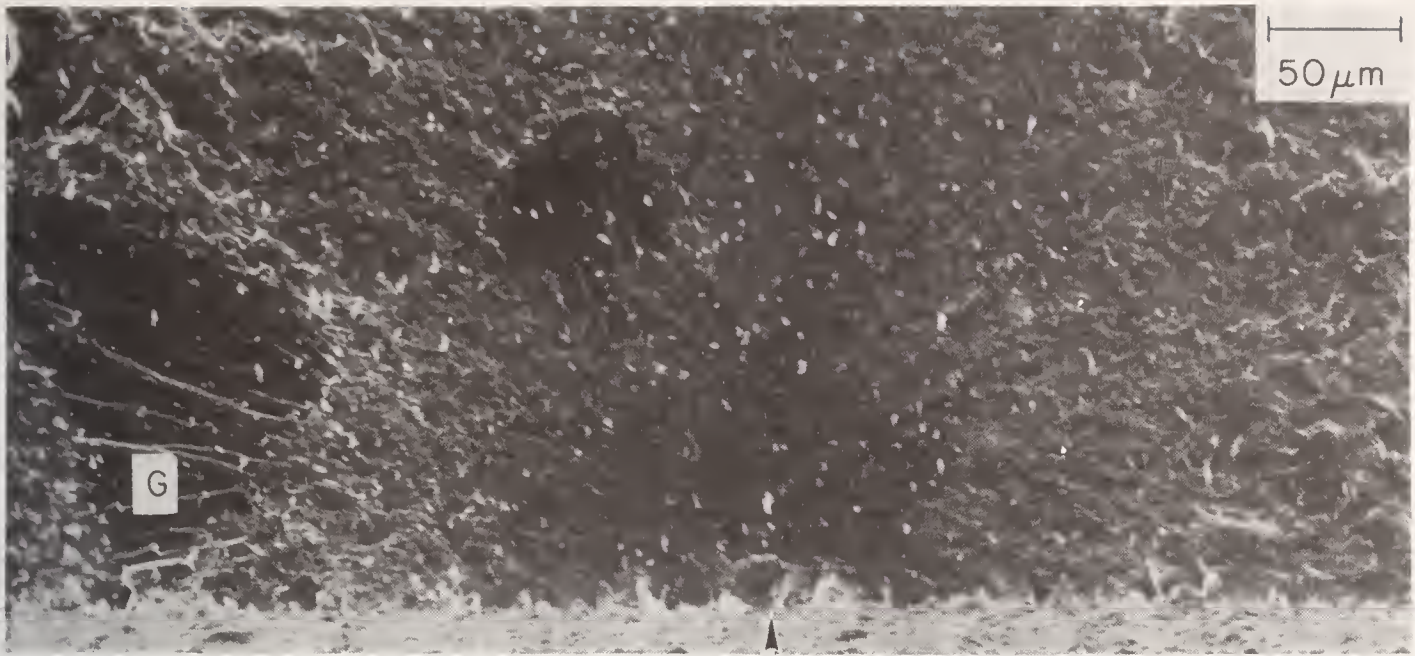


Figure 2, Example of fracture not initiating from larger grains. This lower magnification photo of B₄C (the same specimen shown at higher magnification in the right hand portion of figure 4) shows large grains to the left of the machining flaw origin (arrow). The largest grain (G) despite almost reaching the tensile surface is clearly not the source of failure showing that larger grains, while often sources of failure, are not always such sources.

the author is reasonably consistent with this, possibly suggesting a transition at somewhat larger G. Also, it shows a larger transition and lower strengths for specimens ground perpendicular in comparison to those ground parallel to the tensile axis. Because of possible differing compositions, and more generally because internal stresses may alter the apparent fracture energies calculated from the flaw sizes, such analysis is not attempted here.

Consider now Al₂O₃, one of the more extensively studied materials; i.e. see figures 5-7. Also note table 1 where much of the machining and mechanical testing parameters for these and other studies are given. Figure 5 shows earlier Al₂O₃ data of various investigators each indicating to various degrees, a S-G transition as expected. More recent flexural data of Al₂O₃ (fig. 5) again indicates various transitions, e.g. at larger G for specimens ground perpendicular than for those ground parallel to the tensile axis. Figure 7 represents various data from diametral compression tests of Al₂O₃ with indicated specimen compositions and sizes. While clearly significant less certain because of the limited data, these results are again consistent with a S-G transition. Note that all of the Al₂O₃ transitions are reasonably consistent, especially when one considers the uncertainty of the G values due to exaggerated grain growth. More specifically, they are also consistent with flaws observed in single and polycrystalline Al₂O₃, e.g. figure 9.

Consider next, BeO, one of the more extensively studied ceramics after Al₂O₃. Note that the extensive studies of carefully characterized material by Fryxell and Chandler [27] clearly suggest a transition at $G \sim 25 \mu\text{m}$ (fig.7). While this data is corrected to zero porosity (P), the individual sets of samples of \sim constant porosity each show similar trends. Also, this corrected data agrees well with the data of Bentle and Kniefel [28] for hot pressed BeO with $P \sim 0$. Note that Greenspan's incomplete data [30] would suggest a possible transition at finer G, which is consistent with the fact that his specimens were probably ground approximately parallel with the tensile axis while those of Fryxell and Chandler, and Bentle and Kniefel, were circumfer-

TABLE 1
MACHINING AND FLEXURE TEST DATA

Investigator	Machining	Flexure Test				
		Specimen (GM)		Type ²	Span(s) (cm)	LR ³ (mm/min)
		Cross Sect.	Length			
A. Al₂O₃:						
Spriggs & Vasilos	G (30 μ in)	0.38x 0.63	4.45	4	3.80 1.27	~ 0.15?
Passmore et al	G (ER ~ 0.4mm) then an. 24hr 900°C	0.38x 0.63	4.45	4	3.80 1.27	
Rice	G(320 grit) ER	0.25x	1.5	3	1.27	1.27
Evans & Tappin	G, ER	0.5 0.4 x 0.5	2.5	3	2.0	0.051
Tressler et al	G various grits, (ER ~ 1/16", ~ 1.6 mm)	0.63 x 0.63	5.1	3	3.05	0.5
B. BeO:						
Fryxell & Chandler	CG rods	0.58(dia)	8.88	4	7.61 2.54	1.52
Veevers	G rods	0.41(dia)	2.54	4	1.90 0.79	0.76
Bentle & Kniefel	Core drilled rods	0.25(dia)	2.54	3	1.90	0.051
Greenspan	G(25-35 rms)	~0.7 x 0.7	> 5	3	5.08	1-2 min to failure
O'Neill & Livey	G?	~0.43 x 0.43	2.54	3	2.0	unspecified
Hill et al	G?	~0.43 x 0.43	2.54	3	2.0	
C. MgO:						
Evans & Davidge	Sawn	0.35x 0.45	2.6	4	2.4 1.2	0.051
Bradt et al	D(C) G, ⊥ T.A. 100,220,400, or 600 grit	1.27x 1.27	3.8	3	3.05	0.51
Rice	G(320 grit), then DS (600 grit SiC) T.A., ER	0.25x 0.51		3	1.27 or 1.9	1.27
D. SiC:						
Gulden	3μ lapped (E.F.?)	.01x 0.1	< 0.63	4	0.43 .016	0.051
Cappola & Bradt	G?	0.64x 0.64	5.1	4	3.81 1.27	0.051
Prochazka & Charles	G(220 grit, 0.025mm per pass, 0.31 m/min EC)	0.254x 0.254	2.54	3	1.59	0.051

(continued)

TABLE 1

Investigator	Machining ¹	Flexure Test				
		Specimen (GM)		Type ²	Span(s) (cm)	LR ³ (mm/min)
Cross Sect.	Length					
Cranmer et al	D(C) G \perp T.A. 220,320,400 or 600 grit (0.005 mm pass)	0.3x 0.3	3.0	3	19	0.051

¹All machining with diamond abrasive unless otherwise specified. G = ground, D(C)G = down (climb) ground, \perp or \parallel T.A. = perpendicular or parallel to tensile axis (i.e. bar length), ER = edges radius or rounding, EC = edges chamfered, EF = edge finishing; DC = dry sanded, an = annealed.

²3 point or 4 point flexure.

³LR = loading rate.

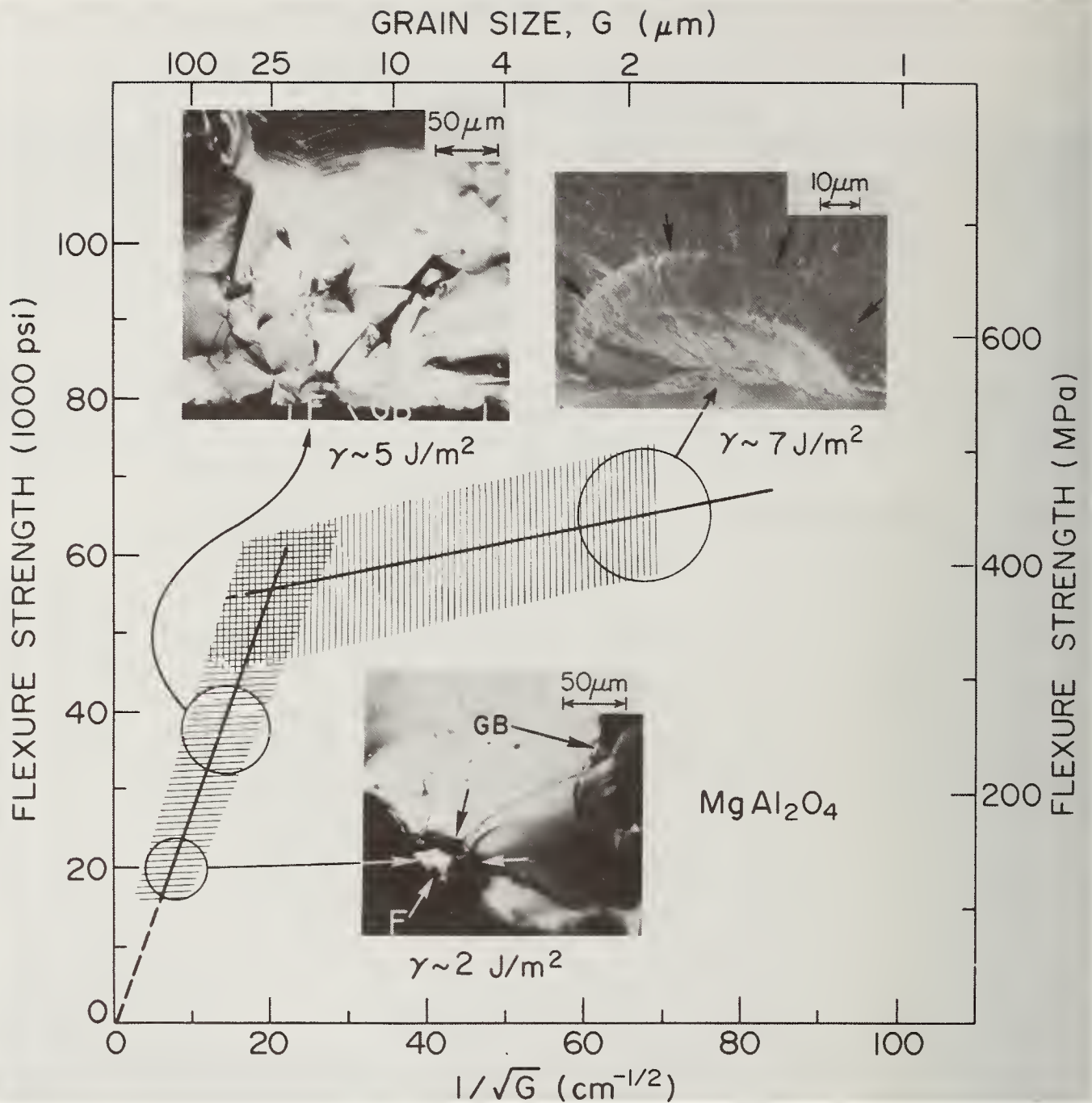


Figure 3. Strength-grain size behavior for MgAl₂O₄. The crossed hatch region shows the extensive strength-grain size data for near theoretical density MgAl₂O₄ of good purity, as reported by Rice and McDonough [13]. Note the inserted fractographs showing flaws found at fracture origins for the indicated levels of strength. Also note the fracture energies calculated from the observed flaws show the transition from single to polycrystalline values as discussed in the text. Note that the flaw for the insert of intermediate strength consists of both a transgranular machining flaw portion, marked F, as well as a portion along the adjacent grain boundary, marked GB. Also note that the weaker orientation of single crystal specimens of the same size and surface finish as for the polycrystalline specimens give typical strengths of ~ 210 MPa (30,000 psi). The strength of polycrystalline specimens extends below this level.

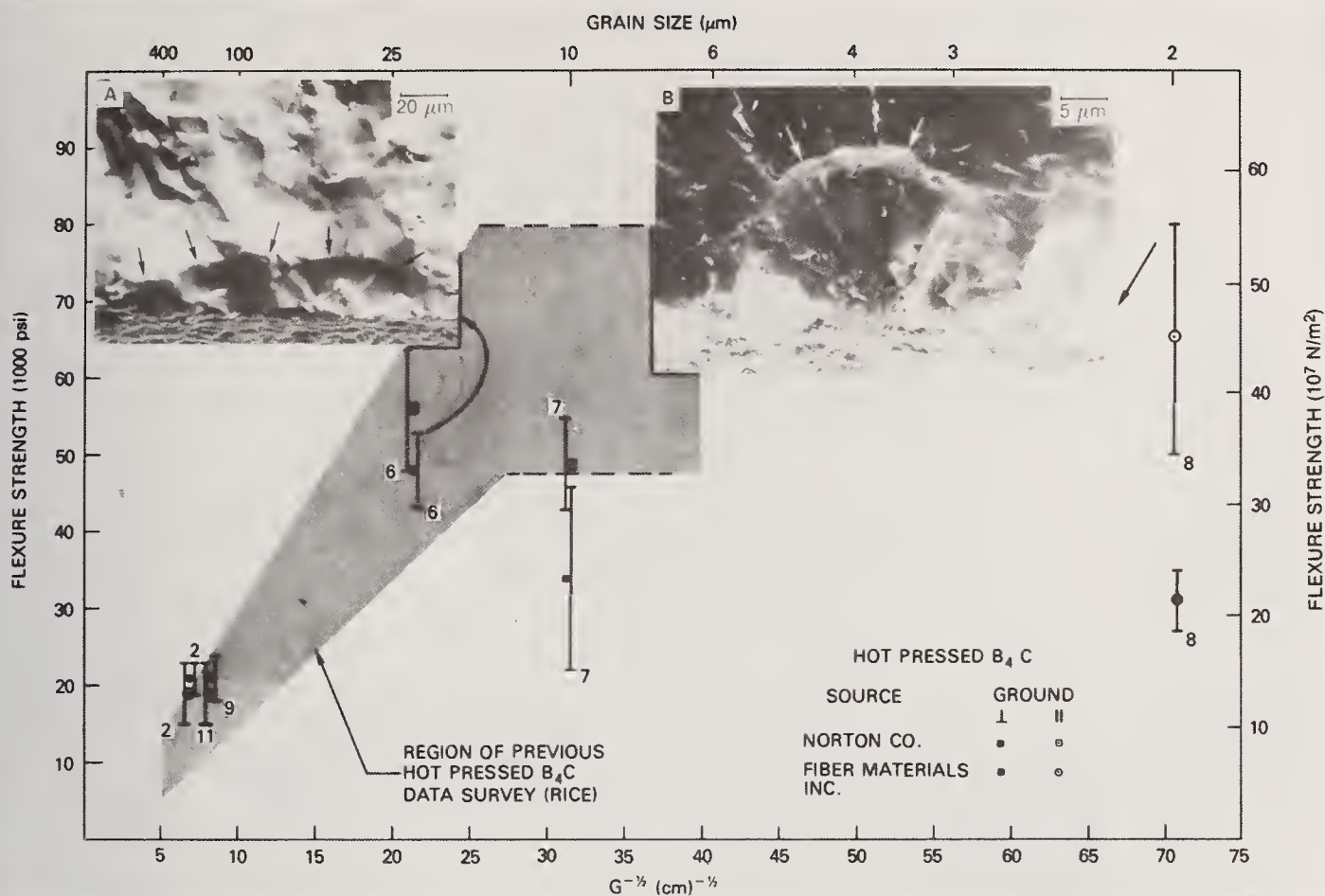


Figure 4. Strength-grain size data for hot pressed B_4C . Note the crossed hatch area representing analysis of an earlier survey of B_4C data [1], which gives a fair indication of S-G transition. More recent results of the author are shown by individual data points as well as the two fractograph inserts. The right insert shows a distinct fracture origin from a flaw much larger than the grain size in a fine grain body ground parallel with the tensile axis (see also fig. 2). The left insert shows a flaw whose depth is comparable to the intermediate grain size, but the flaw is fairly elongated perpendicular to the tensile axis. Internal stresses due to the non-cubic structure of B_4C as well as possible variations of stoichiometry in the different bodies makes fracture energy calculations from these flaw sizes and their interpretation in terms of the proposed fracture energy transition uncertain.

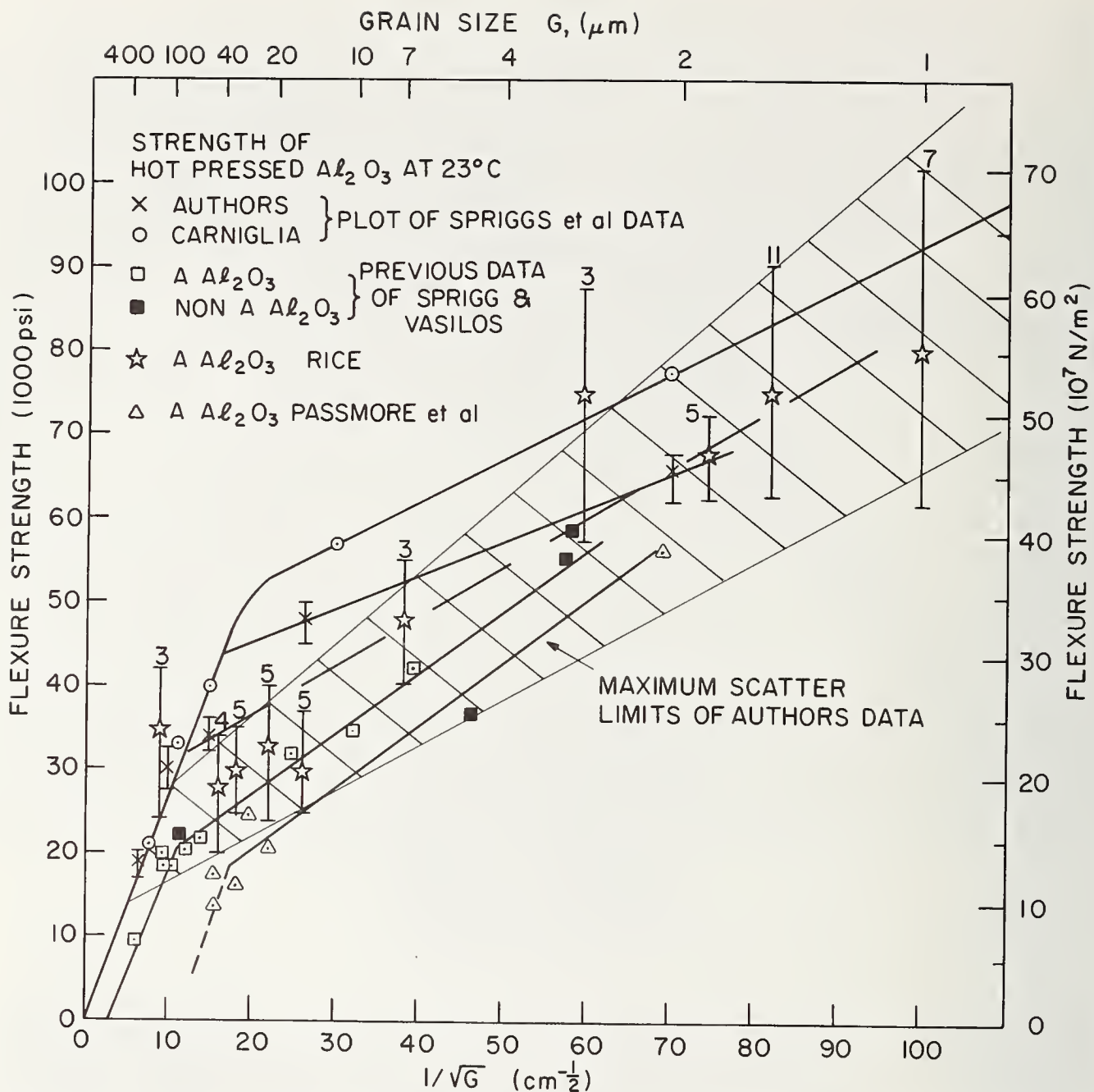


Figure 5. Earlier strength-grain size data for dense, machined Al_2O_3 . Note that while there are some differences in corrections for limited amounts of porosity, e.g. between Carniglia's and Rice's plot of Spriggs et al earlier data [1], all show strength-grain size transitions in the range of ~ 20 to $< 100 \mu\text{m}$. Note also that although specimens of Passmore et al [19] were annealed for 24 hours at 900°C after machining that both the fabrication temperature ($\geq 1400^\circ\text{C}$) as well as the temperature ($\sim 1700^\circ\text{C}$) for crack healing in larger grain Al_2O_3 [20] indicate that this annealing did not significantly effect the machining flaws.

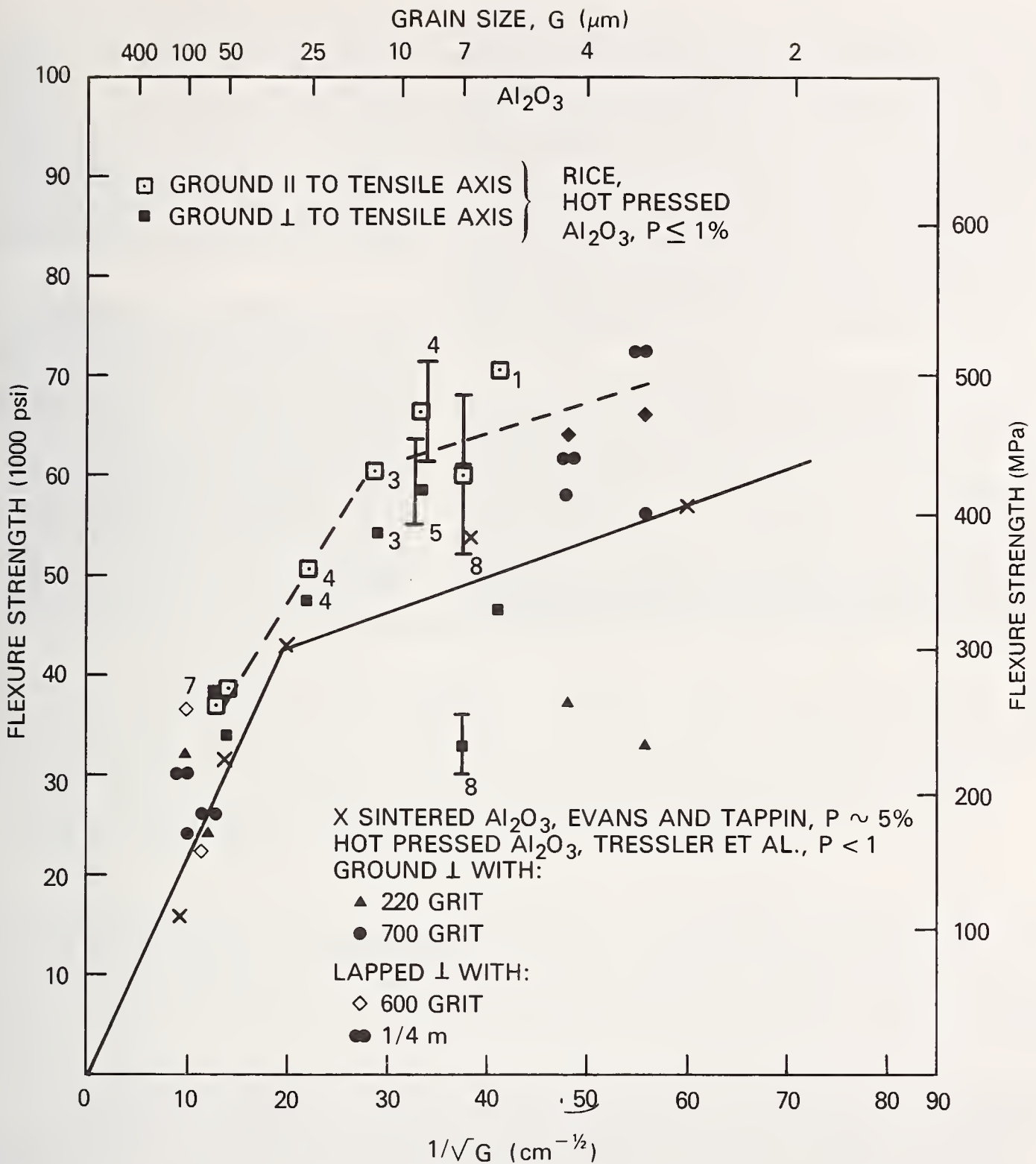


Figure 6. More recent strength-grain size data for Al_2O_3 . Limited data for parallel grinding, though scattered, shows a clear transition as does the limited data for perpendicular grinding, although this is more ill-defined [21]. Note that these transitions are reasonably consistent with the data of Evans and Tappin [22] for sintered alumina, especially when strengths are corrected for the $\sim 5\%$ porosity. Also note that the data for surface finishing of Tressler et al [7] with various grit sizes is consistent with the other data and the range of transitions that they indicate.

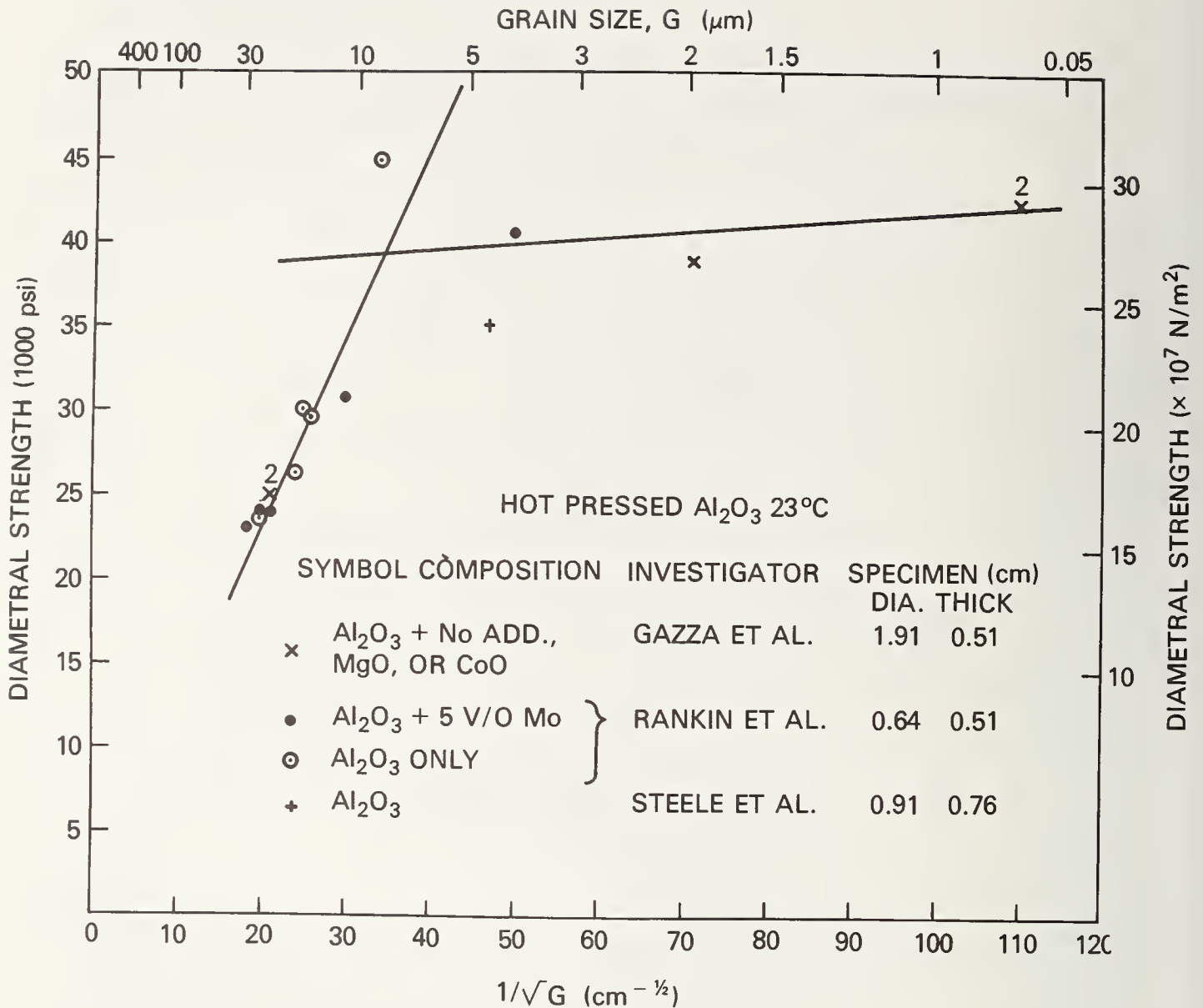


Figure 7. Strength-grain size data for diametral compression testing of Al_2O_3 . While the data [23-25] is limited, it is clearly consistent with a transition which would also for example be suggested by the data of Gazza et al [23] alone. Note that the use of Mo additions appears to have no significant affect on the strength other than controlling grain size, e.g. as shown by similar flexural studies of Al_2O_3 specimens with a range of Mo additions including those beyond the 5% level, by McHugh et al [26]. Note also that Rankin et al are the only ones to report a head travel rate (0.27 mm/min); however, Gazza (private communications) notes that they used the same head travel speed as Rankin et al. Steele et al's tests were conducted in a hand-operated press.

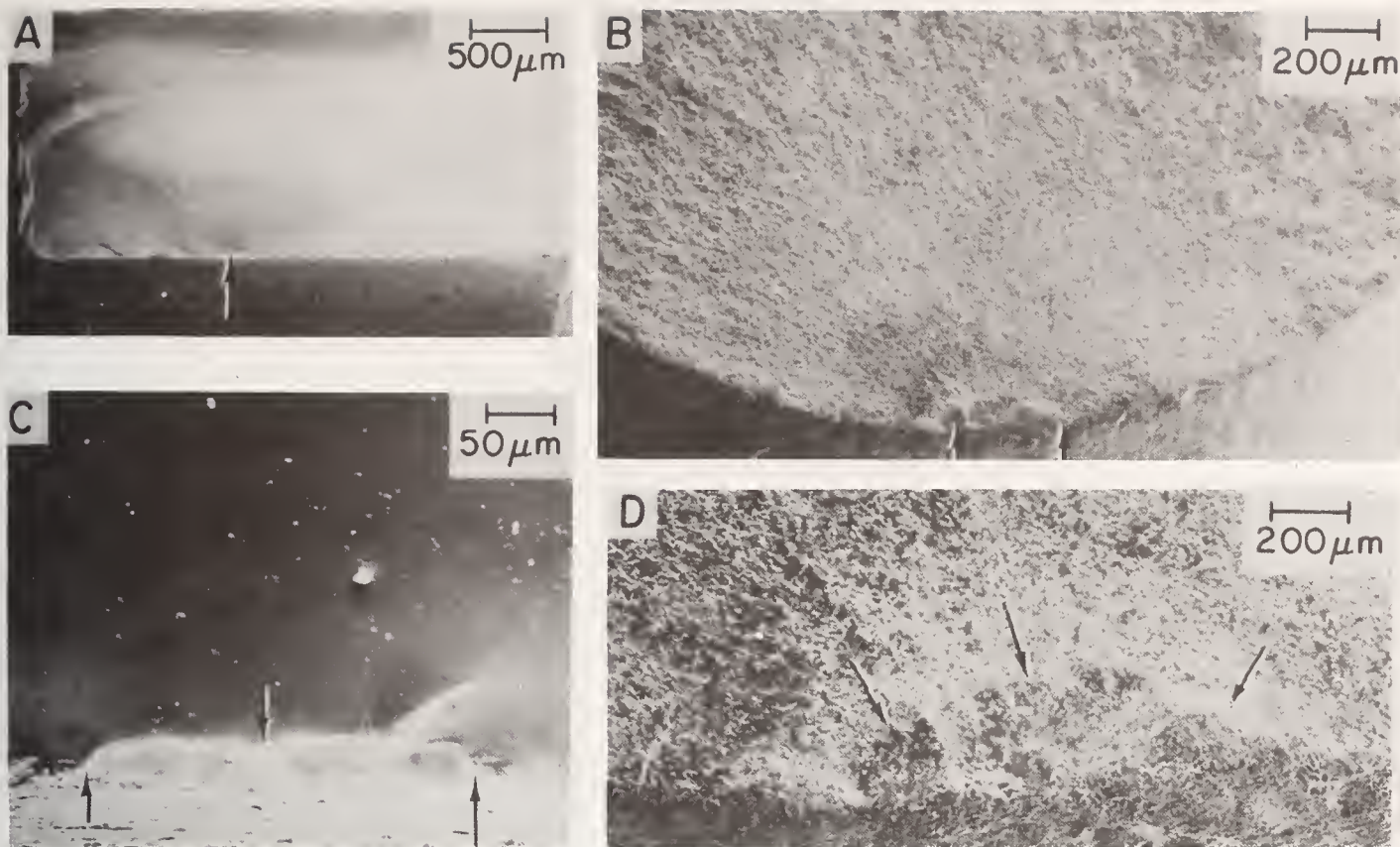


Figure 8. Example of machining flaws in Al_2O_3 . A and B) Machining flaw at the fracture origin of a sapphire laboratory test bar failing at 138 MPa (20,000 psi). C and D) Flaw at the fracture origin of a circumferentially machined large hot pressed Al_2O_3 tensile specimen having a gauge diameter of 14.4 mm, failure stress 275 MPa (40,000 psi). Note elongated flaws (arrows) due to machining perpendicular to the tensile axis in both samples.

entially machined. Also, Veavers' data [29], although low, in part due to its greater P , would also suggest a transition in the range observed for data of Fryxell and Chandler, and Bentle and Kniefel, were it corrected to $P = 0$. Figure 10 presents more recent BeO data that suggests a transition at finer grain sizes in comparison with those of Fryxell and Chandler, and Bentle and Kniefel. This is consistent with the data of figure 10 having higher strength expected from their probable grinding \sim parallel with the tensile axis.

An important question is whether the indicated C \sim G transitions for Al_2O_3 and BeO are due to machining or other flaws. In view of the densities and qualities of the bodies, dominance by processing flaws whose size is similar to machining flaws is unlikely. However, intrinsic flaws resulting from the TEA associated with their non-cubic crystal structures must also be considered. Data of Charles [33] on Lucalox rods with as-fired surfaces indicates a S-G transition at $G \geq 70 \mu\text{m}$. This is generally beyond the range of observed transitions for machined Al_2O_3 , but is in the G range for initiation of spontaneous cracks from TEA [34]. Similarly, Virkar and Gordon's S-G data on $\beta'' - \text{Al}_2\text{O}_3$ with as-annealed surfaces [35] shows a S-G transition at $G \geq 120 \mu\text{m}$. Though this value of G is probably somewhat high because of the tabular shape of the grains [4], the apparently similar thermal expansions and anisotropies of α and β aluminas again indicates that Al_2O_3 S-G transitions from intrinsic cracking are beyond those seen for the machined samples. This is also indicated by S-G data of as-annealed TiO_2 exhibiting spontaneous cracking and an associated S-G transition at $G \geq 50 \mu\text{m}$ [36],

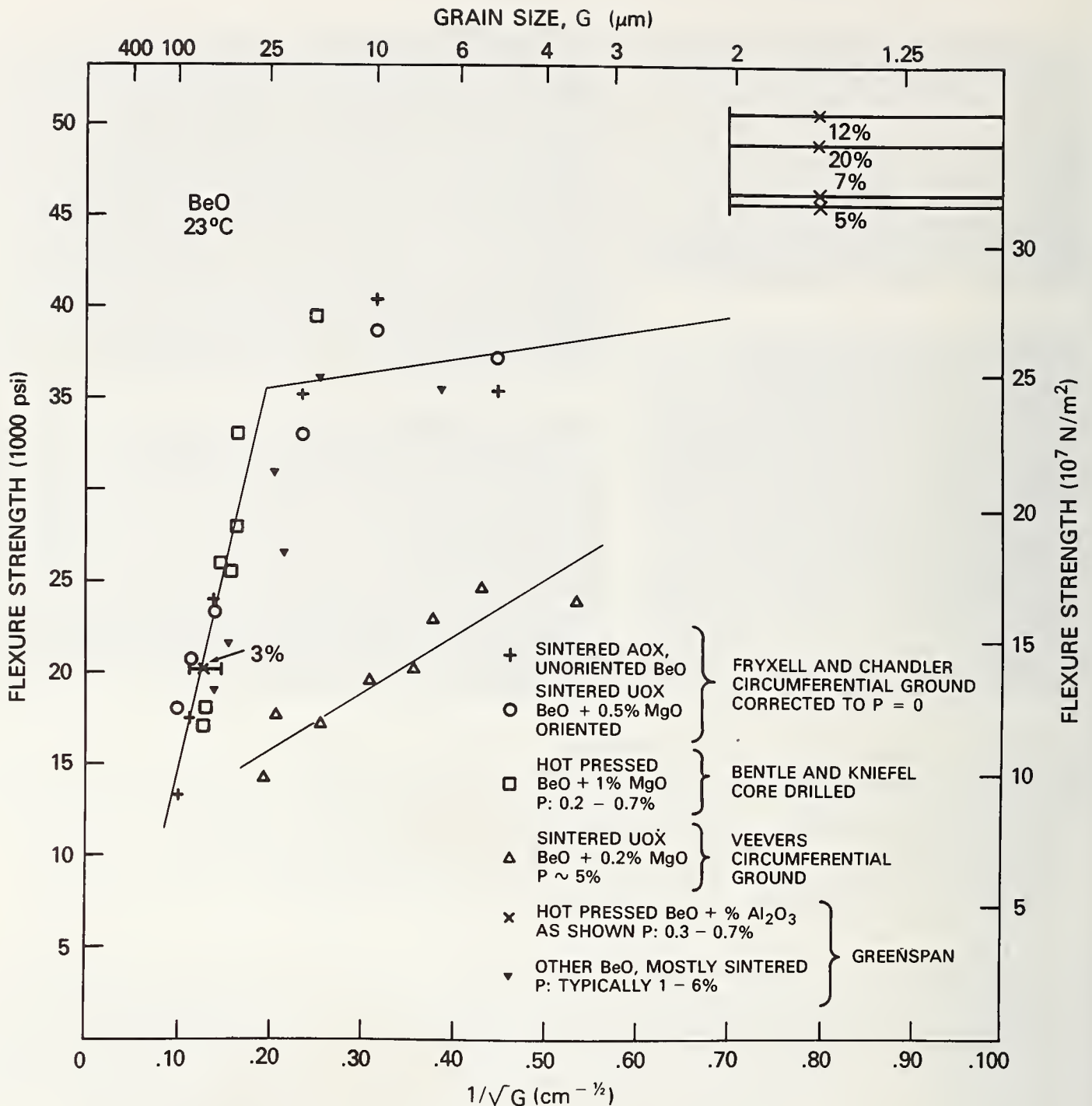


Figure 9. Strength-grain size data for earlier studies of BeO [27-30]. Note that the data of Fryxell and Chandler [27] is a compilation of their three sets of specimens having approximate constant porosities of 3.6, 8.6, and 13.6% all of which have been corrected to zero porosity using the porosity dependence determined by their study. Each of the individual sets of the specimens uncorrected for porosity would show approximately the same grain size transition. Note also that these corrected data agrees extremely well with hot pressed BeO of near zero porosity by Bentle and Kneifel [28].

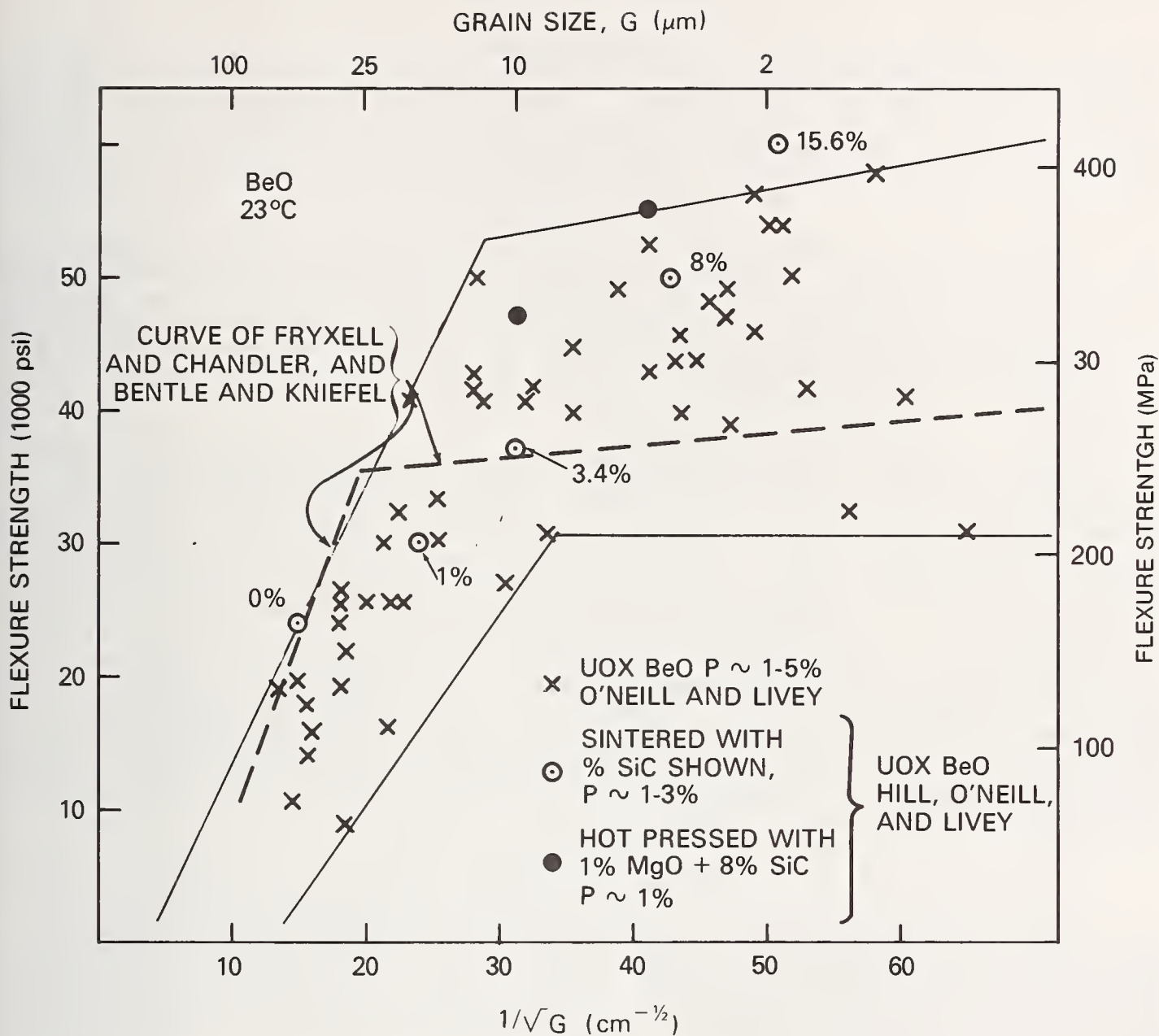


Figure 10. More recent strength-grain size data for BeO [31,32]. Note the distinct transition shown by the data of O'Neil and Livey [31] and that this transition is at a finer grain size than that indicated by data of Fryxell and Chandler, and Bentle and Kniefel. This is consistent with the proposed model since O'Neil and Livey's samples apparently were both smaller and were probably ground parallel with the tensile axis while those of all authors in figure 9, except probably Greenspan, were ground perpendicular to the tensile axis.

since TiO_2 exhibits such cracking at smaller G than Al_2O_3 [44]. BeO exhibits spontaneous cracking at similar grain sizes as Al_2O_3 [34], and hence the S-G transitions for machined BeO of this paper are below those expected for intrinsic cracks.

Thus, two factors should be noted. First the above S-G transitions associated with cracks from TEA significantly reinforce the model and the concept of S-G transitions at $C \sim G$. Second, the machined Al_2O_3 and BeO data is consistent with S-G transitions at $G \sim$ the size of machined flaws, not intrinsic cracks, e.g. from TEA. This latter fact is also consistent with observations on cubic materials, such as SiC and MgO below where such TEA and associated cracking does not occur.

Next consider the compilation of SiC data shown in figure 11. Note that both the small polished samples of CVD SiC suggests a S-G transition at smaller G than does the data of Cranmer et al [9], the latter indicating progressively larger G transitions for progressively coarser finishing. Correction for Cranmer's et al's use of the largest G would lower the G transition values, but not below that for the CVD SiC . Both of these sets of SiC data are consistent with the proposed model.

Finally, consider the data for MgO (fig. 12), which can exhibit microplastically induced or assisted failure. Note that the limited data for parallel ground specimens, at best, only faintly suggests transitions at somewhat small, but not necessarily unreasonable, grain sizes. However, perpendicular grinding results show a more definitive transition at quite reasonable grain sizes. Also, note that this data is quite consistent with earlier extensive studies [40] as well as more recent studies [42,8].

A summary of the tentative, as well as the fairly well established grain sizes for transitions in S-G behavior, are summarized in table 2. Table 2 also shows transitions suggested, or fairly well indicated, for other specimens based on re-evaluation of an earlier survey of strength grain size data [1]. Note that all of these are consistent with the typical flaw sizes observed for machining laboratory size specimens; the type of specimens tested in these studies.

5. Summary and Conclusions

A model has been presented for the grain size dependence of ceramic strengths controlled by machining flaws whose size has typically little or no relation to grain size. The model consists of two regimes. In the finer grain regime, flaws are substantially larger than the grain size so there is little or no decrease in strength with increasing grain size. Thus, strength-grain size curves are typically straight lines extrapolating to non-zero intercepts on a Petch ($S-G^{-1/2}$) plot.

In the larger grain regime, flaws are smaller than the grains and strengths decrease substantially with increasing grain size. When flaws are not too much smaller than G , e.g. $C > G/3$ subcritical growth to the grain size probably occurs. At small C/G ratios, e.g. $C/G < 1/3$ the fracture energies undergo a transition from grain boundary (for intergranular flaws) or single crystal (for transgranular flaws) to polycrystalline fracture energies as the flaw size to grain size ratio increases (mainly due to changing grain size). In any event, the transition between the finer and larger grain size regimes occurs when the flaw size (C) and grain size (G) are similar. Besides the smearing out of the transition in strength behavior due to C growing to G , the transition may not necessarily occur at $C = G$ for reasons such as flaw shape and location, as well as preferred grain orientation and the crystal orientation of fracture energy. Thus, an increase in flaw size shifts both the fine and large grain portions of the curves downward and increases the grain size of the transition between the two curves.

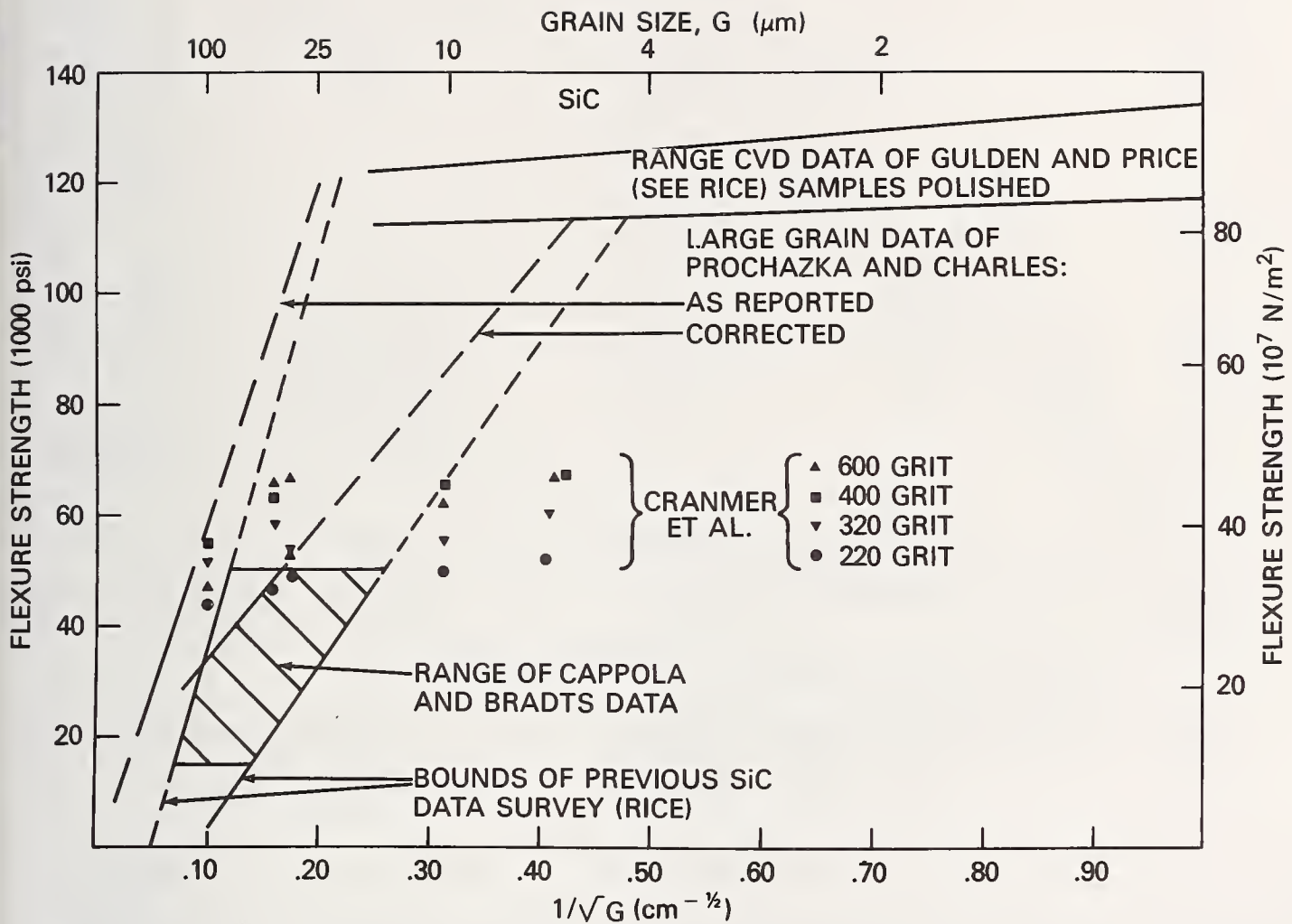


Figure 11. Strength-grain size data for SiC [1,4,6,9,37-39]. Note the consistency between the range of the previous data surveyed by Rice [1] and the more recent data of Coppola and Bradt [30]. Also note that these two ranges are more consistent with the correction of Prochazka and Charles [38] data as suggested by Rice et al [4]. These would suggest a transition for the small CVD SiC specimens of Gulden and Price from a few to ~ 20 microns. Note also the studies of hot pressed SiC ground or lapped perpendicular to the tensile axis with the various grit sizes [9] would indicate transitions at larger grain sizes. However, it should also be noted that Crammer et al plotted their data as a function of the largest grain size in the body. While larger grain sizes within a given body often mean the data should be represented by a somewhat larger grain size than the average, complete use of the largest grain size is probably an overcompensation (e.g. see fig. 2) so the G values for the transitions indicated by Crammer et al's data are probably somewhat high.

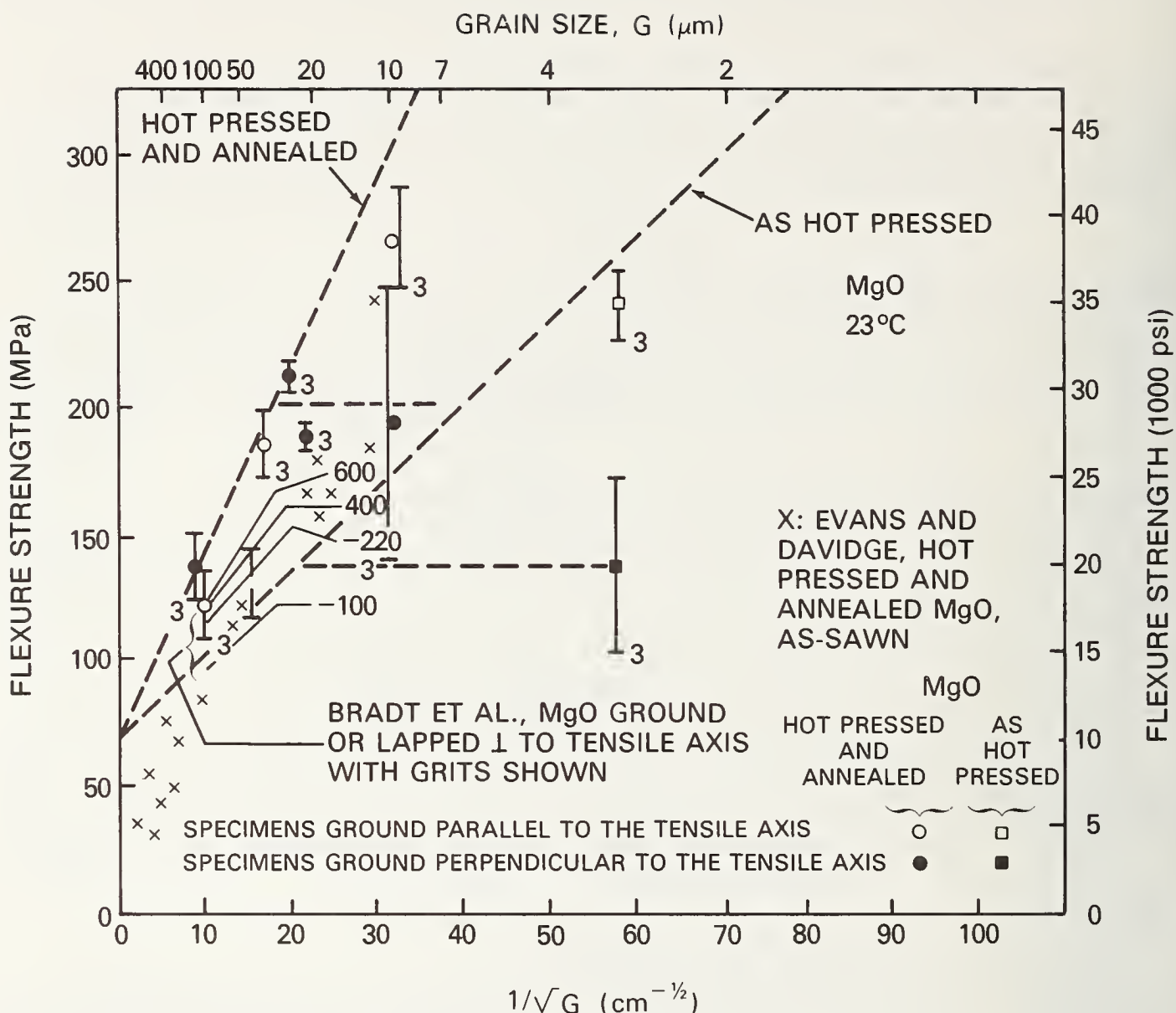


Figure 12. Strength-grain size data for MgO [8,21,40-42]. The dashed lines represent earlier extensive data of Rice [40]. Note that the more limited data for grinding parallel with the tensile axis [21,41] suggests that the transition for the as-hot pressed and hot-pressed, and annealed bodies at grain sizes from ~ 3 to $15 \mu\text{m}$. Note the earlier specimens of Rice [1] were tested with a 600 grit dry sanded surface for as-hot pressed samples while most of the hot pressed and annealed samples were tested with as-annealed surfaces. This more definitive indication of a transition in strength-grain size behavior for both types of samples ground perpendicular to the tensile axis and both of these transitions are clearly at larger grain sizes than those indicated for parallel ground samples. Note also the good agreement of the data of Bradt et al for samples ground or lapped perpendicular to the tensile axis with the various grit shown. Also, the data of Evans and Davidge [42] for hot pressed and annealed samples of MgO tested with as diamond-sawn surfaces, is also reasonably consistent with the other data, i.e. falling below the curve for hot pressed and annealed MgO tested with annealed or ground surfaces as expected.

TABLE 2
 "PETCH PLOT" BRANCHING¹

Material	Processing ²	Machining ³	Grain Size (μm) ⁴ of Branching
Al ₂ O ₃	Hot Pressing	} Various grinding and sanding grinding ⊥ grinding Grinding Grinding (500 grit?) Diamond Ground	30-90
Al ₂ O ₃	Hot Pressing		~ 20
Al ₂ O ₃	Hot Pressing		30-50
Al ₂ O ₃	Sintering P ~ 5%		20-25
Al ₂ O ₃	Hot Pressed		~ 8 ⁵
Al ₂ O ₃	Press Forged ⁶		~ 10
BeO	Sintered	Circumferential (i.e. ⊥) grinding	~ 25
BeO	Hot Pressed	Grinding (?)	~ 20
BeO	Sintered (P:1-5%)	Grinding (?)	10-25
BeO	Hot Pressed	Grinding (?)	~ 15?
MgO	Hot Pressed }	Grinding	~ 4??
		Grinding ⊥	~ 40
	Hot Pressed and annealed }	Grinding	~ 15?
		Grinding ⊥	~ 25
MgAl ₂ O ₄	Sintered and Hot Pressed }	P:0-2% Grinding	25 ± 10
TiB ₂	Hot Pressing	Unspecified machining	5 - 20
B ₄ C	Hot Pressing	Unspecified machining	15 - 20
B ₄ C	Hot Pressing	Grinding ⊥	~ 20
B ₄ C	Hot Pressing	Grinding ⊥	≥ 25?
SiC	CVD	Polishing	5 - 20
SiC	Hot Pressed	Grinding ⊥ (400 or 600 grit)	~ 35
SiC	Hot Pressed	Grinding ⊥ (320 grit)	> 35?
SiC	Hot Pressed	Grinding ⊥ (220 grit)	~ 50?

¹All data from flexure tests at room temperature except for two noted cases of Al₂O₃.

²Approximate % porosity P shown for some bodies. Typically hot pressed bodies had ~ 1% or less porosity.

³|| and ⊥ refer to direction of grinding relative to the tensile axis. ? indicates uncertainty in direction. Unspecified machining means samples were machined from larger pieces by unspecified processes which would most commonly be grinding, probably at or near || to the bar axis.

⁴Question marks indicate values indicated by limited data.

⁵From data for diametral compression at 23°C.

⁶From tests at - 196°C [1].

⁷Data corrected to zero porosity. Consideration of values at the different ~ constant levels of a few percent porosity would give similar results.

A survey of strength-grain size data shows good support for the model and the transition grain sizes most commonly $\sim 20-50 \mu\text{m}$, are typically consistent with commonly observed machining flaw sizes.

References

- [1] Rice, R. W., Strength/Grain-size Effects in Ceramics, Proc. British Ceramic Soc. [20], 205-257 (1972).
- [2] Rice, R. W., Microstructure Dependence of Mechanical Behavior of Ceramics, in Treatise on Materials Science and Technology, Vol. II, Properties and Microstructure, R. K. MacCrone, ed., 199-381 (Academic Press, Inc., New York, N.Y., 1977).
- [3] Rice, R. W., Fractographic Identification of Strength-Controlling Flaws and Microstructure, Fracture Mechanics of Ceramics, Vol. 1, R. C. Bradt, D.P.H. Hasselman, and F. F. Lange, eds., 323-345 (Plenum Pub. Corp., New York, N.Y., 1974).
- [4] Rice, R. W., Freiman, S. W., Pohanka, R. C., Mecholsky, Jr., J. J. and Wu, C. Cm., Microstructural Dependence of Fracture Mechanics Parameters in Ceramics, Fracture Mechanics of Ceramics, Vol. 4, R. C. Bradt, D.P.H. Hasselman, and F. F. Lange, eds, 849-876 (Plenum Pub. Corp., New York, N.Y., 1978).
- [5] Rice, R. W. and Mecholsky, Jr., J. J., The Nature of Strength Controlling Machining Flaws in Ceramics, this conference.
- [6] Bradt, R. C. and Tressler, R. E., Microstructure/Surface Finish Control of the Strength of Polycrystalline Ceramics, Proc. of 6th Int. Mat. Symp. Ceramic Microstructures-76, R. M. Fulrath and J. A. Pask, eds., 785-795 (Westview Press, Boulder, Colorado, 1976).
- [7] Tressler, R. E., Langensiepen, R. A., and Bradt, R. C., Surface-Finish Effects on Strength-vs-Grain Size Relations in Polycrystalline Al_2O_3 , J. Am. Ceram. Soc. [57] 5, 226-227 (1974).
- [8] Bradt, R. C., Dulberg, J. L., and Tressler, R. E., Surface Finish Effects and the Strength-Grain Size Relationship in MgO , Acta Metallurgica [24], 529-534 (Pergamon Press, Great Britain, 1976).
- [9] Cranmer, D. C., Tressler, R. E., and Bradt, R. C., Surface Finish Effects and the Strength-Grain Size Relation in Sic, J. Am. Ceram. Soc. [60] 5, 230-237.
- [10] Rice, R. W., The Effect of Grinding Direction on the Strength of Ceramics, The Science of Ceramic Machining and Surface Finishing, NBS Special Publication 348, S. J. Schneider and R. W. Rice, eds., 365-376 (Govt. Printing Office, Wash., D. C. 20402, 1972).
- [11] Rice, R. W. and Freiman, S. W., The Grain Size Dependence of Fracture Energy in Ceramics, submitted for publication.
- [12] Rice, R. W., Pohanka, R. C. and McDonough, W. J., The Effect of Stresses from Thermal Expansion Anisotropy, Phase Transformations and Second Phases on the Strength of Ceramics, submitted for publication.
- [13] Rice, R. W. and McDonough, W. J., Ambient Strength and Fracture Behavior of MgAl_2O_4 , in Mechanical Behavior of Materials, Proc. of 1971 Int. Conf. on Mechanical Behavior of Materials, Vol. 14, 422-431 (The Society of Materials Science, Japan, 1972).

- [14] Rice, R. W., Freiman, S. W. and Mecholsky, Jr., J. J., The Dependence of Strength Controlling Fracture Energy on the Flaw Size to Grain Size Ratio, submitted for publication.
- [15] Singh, J. P., Virkar, A. V., Shetty, D. K. and Gordon, R. W., On Strength-Grain Size Relationships in Polycrystalline Ceramics, submitted to J. Am. Ceram. Soc.
- [16] Rhodes, W. H., Berneburg, P. L., Cannon, R. M. and Steele, W. C., Microstructure Studies of Polycrystalline Refractory Oxides, Summary Report, 29 March 1972 to 28 April 1973, prepared for U.S. Naval Air Systems, Contract No. N00019-72-C-0298.
- [17] Emrich, B. R., Technology of New Devitrified Ceramics - A Literature Review, Technical Documentary Report No. ML-TDR-64-203, Air Force Materials Laboratory Research and Technology Division, Air Force Systems Command, Wright-Patterson Air Force Base, Ohio (1964).
- [18] Stookey, S. D., Ceramics Made by Nucleation of Glass-Comparison of Microstructure and Properties with Sintered Ceramics, in Proc. Am. Ceram. Soc. Symp. on Nucleation and Crystallization in Glasses and Melts, 1-4 (1962).
- [19] Passmore, E. M., Spriggs, R. M. and Vasilos, T., Strength-Grain Size-Porosity Relations in Alumina, J. Am. Ceram. Soc. [48] 1, 1-7 (1965).
- [20] Lange, F. F. and Radford, K. C., Healing of Surface Cracks in Polycrystalline Al_2O_3 , J. Am. Ceram. Soc. [53] 7, 420-421 (1970).
- [21] Rice, R. W., Machining of Ceramics, in Ceramics for High-Performance Applications, Proc. of Second Army Materials Technology Conference, J. J. Burke, A. E. Gorum, and R. N. Katz, eds, 287-343 (Brook Hill Pub. Co., Chestnut Hill, Mass., 1974).
- [22] Evans, A. G. and Tappin, G., Effects of Microstructure on the Stress to Propagate Inherent Flaws, Proc. British Ceramic Soc., No. 20, 275-297 (1972).
- [23] Gazza, G. E., Barfield, J. R. and Preas, D. L., Reactive Hot Pressing of Alumina with Additives, Am. Ceram. Soc. Bull. [48] 6, 605-610 (1969).
- [24] Rankin, D. T., Stiglich, J. J., Petrak, D. R. and Ruh, R., Hot-Pressing and Mechanical Properties of Al_2O_3 with an Mo-Dispersed Phase, J. Am. Ceram. Soc. [54] 6, 277-281 (1971).
- [25] Steele, B. R., Rigby, F. and Hesketh, M. C., Investigations on the Modulus of Rupture of Sintered Alumina Bodies, Proc. British Ceramic Soc., No. 6, 83-94 (1966).
- [26] McHugh, C. O., Whalen, T. J. and Humenik, Jr., M., Dispersion-Strengthened Aluminum Oxide, J. Am. Ceram. Soc. [49] 9, 486-491 (1966).
- [27] Fryxell, R. E. and Chandler, B. A., Creep, Strength, Expansion, and Elastic Moduli of Sintered BeO As a Function of Grain Size, Porosity, and Grain Orientation, J. Am. Ceram. Soc. [47] 6, 283-291 (1964).
- [28] Bentle, G. G. and Kniefel, R. N., Brittle and Plastic Behavior of Hot-Pressed BeO, J. Am. Ceram. Soc. [48] 11, 570-577 (1965).
- [29] Veevers, K., Recrystallization of Machined Surfaces of Beryllium Oxide, J. Australian Ceram. Soc. [5] 1, 16-20 (1969).

- [30] Greenspan, J., Development of a High-Strength Beryllia Material, Army Materials and Mechanics Research Center Report No. AMMRC-TR-72-16 (1972).
- [31] O'Neill, J. S. and Livey, D. T., Fabrication and Property Data for Two Samples of Beryllium Oxide, United Kingdom Atomic Energy Authority Research Group Report AERE-R4912 (1965).
- [32] Hill, N. A., O'Neill, J. S. and Livey, D. T., The Properties of BeO Containing up to 15 w/o SiC and up to 2 w/o MgO, Proc. British Ceramic Soc., No. 7, 221-232 (1967).
- [33] Charles, R. J., Static Fatigue: Delayed Fracture, in Studies of the Brittle Behavior of Ceramic Materials, Technical Report No. ASD-TR-628, 370-404, Aeronautical Systems Division, Wright Patterson AFB, Ohio (1962).
- [34] Rice, R. W. and Pohanka, R. C., The Grain Size Dependence of Spontaneous Cracking in Ceramics, accepted for publication in J. Am. Ceram. Soc (1978).
- [35] Virkar, A. V. and Gordon, R. S., Fracture Properties of Polycrystalline Lithia-Stabilized β'' -Alumina, J. Am. Ceram. Soc. [60] 1-2, 58-61 (1977).
- [36] Kirchner, H. P. and Gruver, R. M., Strength-Anisotropy-Grain Size Relations in Ceramic Oxides, J. Am. Ceram. Soc. [53] 6, 233-236 (1970).
- [37] Gulden, T. D., Mechanical Properties of Polycrystalline β -SiC, J. Am. Ceram. Soc. [52] 11, 585-590 (1969).
- [38] Prochazka, S. and Charles, R. J., Strength of Boron-Doped Hot-Pressed Silicon Carbide, Am. Ceram. Soc. Bull [52] 12, 885-891 (1973).
- [39] Coppola, J.A. and Bradt, R.C., Measurement of Fracture Surface Energy of SiC, J. Am. Ceram. Soc. [55] 9, 455-460 (1972).
- [40] Rice, R. W., Strength and Fracture of Hot-Pressed MgO, Proc. British Ceramic Soc., No. 20, 329-363 (1972).
- [41] Rice, R. W., The Effect of Grinding Direction on the Strength of Ceramics, in Proc. on the Science of Ceramics Machining and Surface Finishing, S. J. Schnieder, Jr. and R. W. Rice, eds., 365-376 (National Bureau of Standards Special Publication 348 (1972)).
- [42] Evans, A. G. and Davidge, R. W., The Strength and Fracture of Fully Dense Polycrystalline Magnesium Oxide, Phil. Mag. [20] 164, 373-388 (1969).

Discussion

RHODES

How general are these results? If the crack size is not related to the grain size, how do you explain the dependence of strength on grain size?

RICE

The results should be quite general based both on the breadth of materials already considered as well as on the principles involved. The concepts appear to have no restriction to any particular material class. The dependence of strength on grain size due to the initial flaw size not gen-

erally being related to the grain size is the subject of the paper "Machining Flaws and the strength Grain Size Behavior in Ceramics" by R. W. Rice elsewhere in the conference.

TRESSLER

I think it is important to emphasize that in the systematic studies of surface finish / grain size effects on strength of polycrystalline alumina and silicon carbide conducted at Penn State that in the fine grain high strength region the strength systematically increased with decreasing grit size with very slight dependence on grain size. This result is very important for machined high performance ceramics since one would like to machine fine enough to have the grain size control the strength. For fine grain ceramics one must use very fine polish to achieve this.

RICE

Although the effects of different grit sizes on the strengths of samples generally do not show up as being very pronounced on the scale of strengths and grain sizes considered in this survey, it is none-the-less agreed that grit size effects are quite important both in practice and from the standpoint of scientific understanding of the strength behavior of ceramics. Certainly the finishing studies at Penn State have been an important contribution in demonstrating and documenting the extent and details of such surface finish effects. However, I question whether or not one will commonly attempt to machine to a fine enough grit size to have grain size control strength for two reasons. First, in many fine grain bodies I expect that it will be fairly common that with finer finishing that internal processing defects will take over control of strength rather than the grain size itself. This is shown, for example, in the work of Wu and McKinney on machining of Si_3N_4 elsewhere in this conference. It is also indicated in your work on Al_2O_3 where the strengths of specimens ground to 600 grit finish and those to a quarter micron diamond polish cannot be distinguished and in your work on SiC where the strengths of your 400 and 600 grit ground bodies cannot be distinguished. There will also often be an economic constraint in limiting one to the degree of surface finish that is conducted. Since the improvement in strength with finer surface finishing commonly approaches a limit as indicated by the above three cited cases, and this limit is often approached asymptotically because of increasing competition between internal processing defects and machining flaws, one will have to consider the trade-off between decreasing improvement in strength vs continued increase in cost. However, I agree with what I believe is the general thrust of your comment, i.e. that one needs to know what the rate of increase is as a function of surface finishing procedures in order to make this judgment, and that this can have important practical results.

MALKIN

Can your results be explained alternatively in terms of the effect of grain size on the relative amounts of transgranular and intergranular fracture?

RICE

The results of different regimes of strength grain size behavior cannot be explained in terms of grain size dependence on the amount of transgranular-intergranular fracture. However, I am glad that you asked this question since it is a fair one and I failed to address it in the text. The reason that I state that the mode of fracture is not a cause of the strength change is based on three observations and also is supported by some simple theo-

retical considerations. First, if one considers the overall trends in fracture mode of the whole fracture surface, one observes the trend for changing from one mode of failure to another to typically occur over a greater grain size range than the transition in strength-grain size behavior shown in this paper, see for example data on MgO and Al_2O_3 . Second, Al_2O_3 and MgO show opposite trends of the mode of fracture with grain size, i.e. MgO shows increasing transgranular failure with increasing grain size while Al_2O_3 shows decreasing transgranular failure with increasing grain size, (1,2) yet they both show similar strength grain size trends. Third, $MgAl_2O_4$ and the B_4C materials typically tend to show very nearly if not total transgranular failure over the entire grain size range.

The question of the role of the mode of failure must, however, be considered further since the overall mode of crack propagation may not have a relationship to the mode of initial crack propagation. Thus, for example, the author has observed cases of intergranular fracture immediately at the fracture origin surrounded by 100% transgranular failure and more recently my colleagues have shown that cracks can propagate in an intergranular mode subcritically due to environmental, e.g. moisture, effects and then change to transgranular propagation when failure becomes catastrophic in materials such as $ZnSe$ and MgF_2 . However, focusing in on the question of the mode of failure at fracture origin in the materials of this study, the answer to your question still remains no.

$MgAl_2O_4$ is the only material of those studied here observed to indicate a change in the mode of fracture at the origin. $MgAl_2O_4$ fracture origins of fine grain bodies are all transgranular while the fracture origins of larger grain bodies were either inter-or transgranular or mixed with greater occurrence of intergranular failure origin in contrast to general transgranular fracture at all grain sizes. However, there is no strength difference observed between specimens with a transgranular initiating flaws and those with intergranular initiating flaws.

One can also ask what effect the mode of failure might have on the different properties controlling strength. Fracture energy is the primary candidate for this. However, in studies of MgO , fracture energy was constant over the broad range of grain sizes considered although there was a change from essentially complete intergranular failure at fine grain sizes to essentially completely to transgranular failure at large grain sizes, (2,3) Finally, some simple theoretical considerations support this lack of control by whether the failure mode is intergranular or transgranular. Both estimates based on surface energy measurements of fracture energy of grain boundaries show that typically they will range from ~ 50% to ~ 100% of the lower single crystal fracture energies. However, simple geometrical considerations show that the surface area created by intergranular failure vs transgranular failure varies from a factor of ~ 2 down to only slightly greater than 1. Thus, the differences in surface area between intergranular and transgranular failure approximately compensate for the potentially lower fracture energy of intergranular failure suggesting that one should not observe larger effects as previously discussed.

1) R. W. Rice, "Fracture Topography of Ceramics," Surfaces and Interfaces of Glass and Ceramics, Plenum Publishing Corp., New York, New York, 1974

2) R. W. Rice, "Microstructure Dependence of Mechanical Behavior of Ceramics," Treatise on Materials Science and Technology, Vol. II, Academic Press, New York, N.Y., 1977, pp. 199-381.

3) R. W. Rice, S. W. Freiman, & P. F. Becher, "Grain Size Dependence of Fracture Energy in Ceramics" submitted to Am. Ceram. Soc. for publication.

SURFACE MACHINING EFFECTS ON THE STRENGTH DISTRIBUTIONS OF ALUMINAS

T. E. Easler, T. A. Counter¹, R. E. Tressler and R. C. Bradt

Department of Materials Science and Engineering
The Pennsylvania State University
University Park, PA 16802

Three microstructurally different, dense polycrystalline aluminas were machined with 400-grit diamond at two different rates of surface removal. Flexural strengths were measured in four-point bending under toluene and the strength distributions analyzed by two-parameter Weibull statistics. Effects of edge-bevelling on the distributions were also examined. Machined surfaces and the bevelled and non-bevelled sample edges were examined by SEM. For all of the materials, the lesser rate of surface removal was less severe in edge chipping, and yielded higher average strengths and increased values of the Weibull parameters, m and σ_0 .

Key Words: Alumina; edge-bevelling; strength distributions; surface removal rate; Weibull function.

1. Introduction

Machining of the surface of ceramic materials dictates their strength in cases where machining induced surface flaws act as the failure origins. Surface flaws (features) resulting after a given machining process are related to several machining variables, such as the type of abrasive, the grit size of the abrasive, the direction of grinding, and the rate of surface removal [1-4]². Variations in the magnitudes of these effects from one material to another result from differences in the physical properties and/or microstructures of the machined materials. This paper reports the results of a study of the effects of the surface removal rate on the strength distributions of three polycrystalline aluminas. Although more general strength distributions can be applied, Weibull statistics were utilized because of their success in describing statistical distributions of the strength of ceramics [5-7].

The three-parameter form of the Weibull distribution can be expressed as:

$$F = 1 - \exp - \int_S \left(\frac{\sigma_f - \sigma_u}{\sigma_0} \right)^m dS, \quad (1)$$

where F is the probability of failure, σ_f is the observed fracture stress, σ_u is the lowest possible failure stress, σ_0 is a scaling parameter, m is the Weibull modulus, and S is the surface area of the specimen. If the lowest possible failure stress, σ_u , is assumed equal to zero, then the three-parameter form is reduced to the two-parameter form:

$$F = 1 - \exp - \left(\frac{\sigma_f}{\sigma_0} \right)^m S, \quad (2)$$

where S is the surface area in pure bending. In the four-point bend test when all of the specimens fail between the inner knife edges, S is the surface area subjected to uniform tensile stress.

¹ Present mailing address: 307 Gilbreath Hall, East Tennessee State Univ., Johnson City, TN 37601.

² Figures in brackets indicate the literature references at the end of this paper.

2. Experimental Procedure

2.1. Test materials

Three dense sintered polycrystalline aluminas were chosen for this study because they represent a range of interesting microstructures. Their physical properties are listed in table 1. The AL300 material has a rather large average grain size of 25 μ m, while the AL600 has a much finer average grain size, about 10 μ m. The AL995 has a bimodal grain size distribution consisting of large grains on the order of 25 μ m distributed in a finer grain size matrix of about 12 μ m. It appears that the fine grain matrix of AL995 is comparable to the microstructure of AL600. A semiquantitative spectrochemical analysis of these materials, reported elsewhere, has shown the major impurities to be Si, Mg, Ca, and Fe [4].

Table 1. Physical Properties of Aluminas

Materials*	ρ (gms/cc)	K_{IC} (MN/m ^{3/2}) [8]	E(MN/m ²)	Average G.S.(μ m)
AL300	3.74	2.53 \pm 0.27	3.3 x 10 ⁵	25
AL600	3.71	2.76 \pm 0.10	3.2 x 10 ⁵	10
AL995	3.85	2.48 \pm 0.12	3.6 x 10 ⁵	12 ,(25)

*Wesgo, Belmont, CA 94002.

2.2. Machining procedure

Specimens of the three alumina materials were finish machined at two different removal rates of down (climb) grinding [9], 2.5 x 10⁻⁴ and 2.5 x 10⁻⁵ inches/pass, to yield six combinations of surface finish and microstructure.

Between one hundred and one hundred and ten specimens were prepared and tested at each condition. Specimens were initially diamond sawed from 3/8 x 1-1/8 x 4-1/4" plates to approximate dimensions and then mounted on a steel plate using glycol phthallate. The surfaces were ground parallel, to size, with a 400-grit diamond wheel with the machining direction parallel to the subsequent direction of maximum tensile stress. The tensile surface was then finish machined, removing 2 x 10⁻³ inches with 400-grit diamond, perpendicular to the testing direction of maximum tensile stress. Thus, all specimens were initially sized by machining in the direction to create the least severe flaws, but finish machined in the direction yielding the most severe flaws. Machining was performed on a Brown and Sharpe surface grinder at a wheel speed of 2860 rpm and a table speed of 20 ft/min. using a water/water soluble oil coolant. The eight-inch diameter metal bonded wheel was a D400-L50M grading. Final specimen size was 1/8 x 1/8 x 1-1/8". After final finishing, specimens were cleaned in acetone and dried in air at 120°C. Edge bevelling was done manually on 600-grit SiC paper in the longitudinal orientation, the orientation for introduction of the least severe flaws.

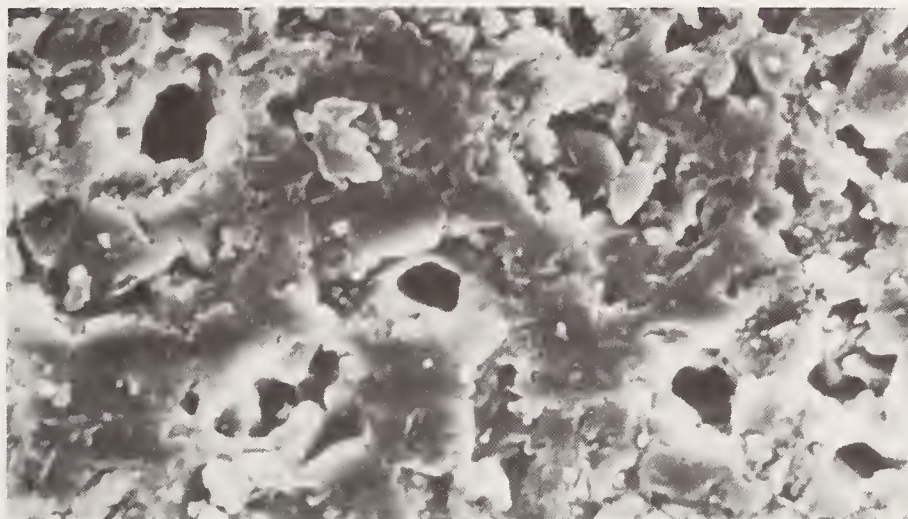
2.3. Testing procedure

After drying, the specimens were immersed in dry toluene prior to and during the testing, the objective being to actually measure failure from surface machining flaws and not extended flaws created by substantial subcritical crack growth. Dry toluene was used because it has been reported to act as an inert environment with regard to slow crack growth [10]. Actual testing was with 1/3-point loading in 4-point bending on an Instron Model TM commercial testing machine at a crosshead speed of 5 x 10⁻² inches per minute, a stressing rate of 1.7 x 10⁴ MN/m² min., or 2.5 x 10⁶ psi/min.

3. Results and Discussion

3.1. Examination of machined surfaces

Tensile surfaces were examined by scanning electron microscopy to compare the surface features of specimens finished at the different rates of surface removal, and to examine the bevelled edges. It was found that for the greater rate of removal, the surface generally appeared "cleaner". The microstructure was more readily discerned, in that grains, pores, grinding scratches, and some pullouts were more evident. In the case of the lesser rate of material removal, the surface appeared much smoother, with some evidence of plastic flow. There also appeared to be a large amount of small ($<1\mu\text{m}$) particle debris scattered across the tensile surface and within the pores open to the surface. Tensile surfaces of AL600 are compared in figure 1 for each of the surface removal rates. These general observations applied for each of the three materials.



(a)



(b)

Figure 1. Resultant surface features of AL600 after two rates of surface removal: a) 2.5×10^{-4} in/pass, b) 2.5×10^{-5} in/pass.

3.2. Data Analysis

A statistical analysis of the results was employed to evaluate the relative changes in the strength distributions. The two-parameter Weibull distribution function, eq. (2), was fitted to each of the six data sets so that the Weibull parameters could be directly compared. This method relates the range of strengths of a particular set of data to a probability of failure scale, which can be linearized by transforming eq. (2) to the following logarithmic form:

$$\ln \ln \left(\frac{1}{1-F} \right) = m \ln \sigma_f + [\ln S - m \ln \sigma_0], \quad (3)$$

$$y = ax + b. \quad (3-a)$$

The Weibull modulus, m , is then obtained from the slope, and the scaling parameter, σ_0 , is calculated from the intercept of the regression line.

3.3. Strength Data

Over one hundred data points for each set of conditions provided a good statistical population for a computer calculation of the least squares regression equations and Weibull parameters [11]. The data sets were also computer plotted so that the relative shapes and locations of the distributions could be visually compared. The strength distributions for the three aluminas are shown in figure 2, with the two removal rates for a specific material on the same plot. The pertinent descriptive statistical parameters are listed in table 2. From the R^2 values, it is evident that the two-parameter Weibull distribution is a quite satisfactory description of the data. However, the vertical drop-offs of the data at the lower strengths for AL300 and AL600 does indicate a tendency toward

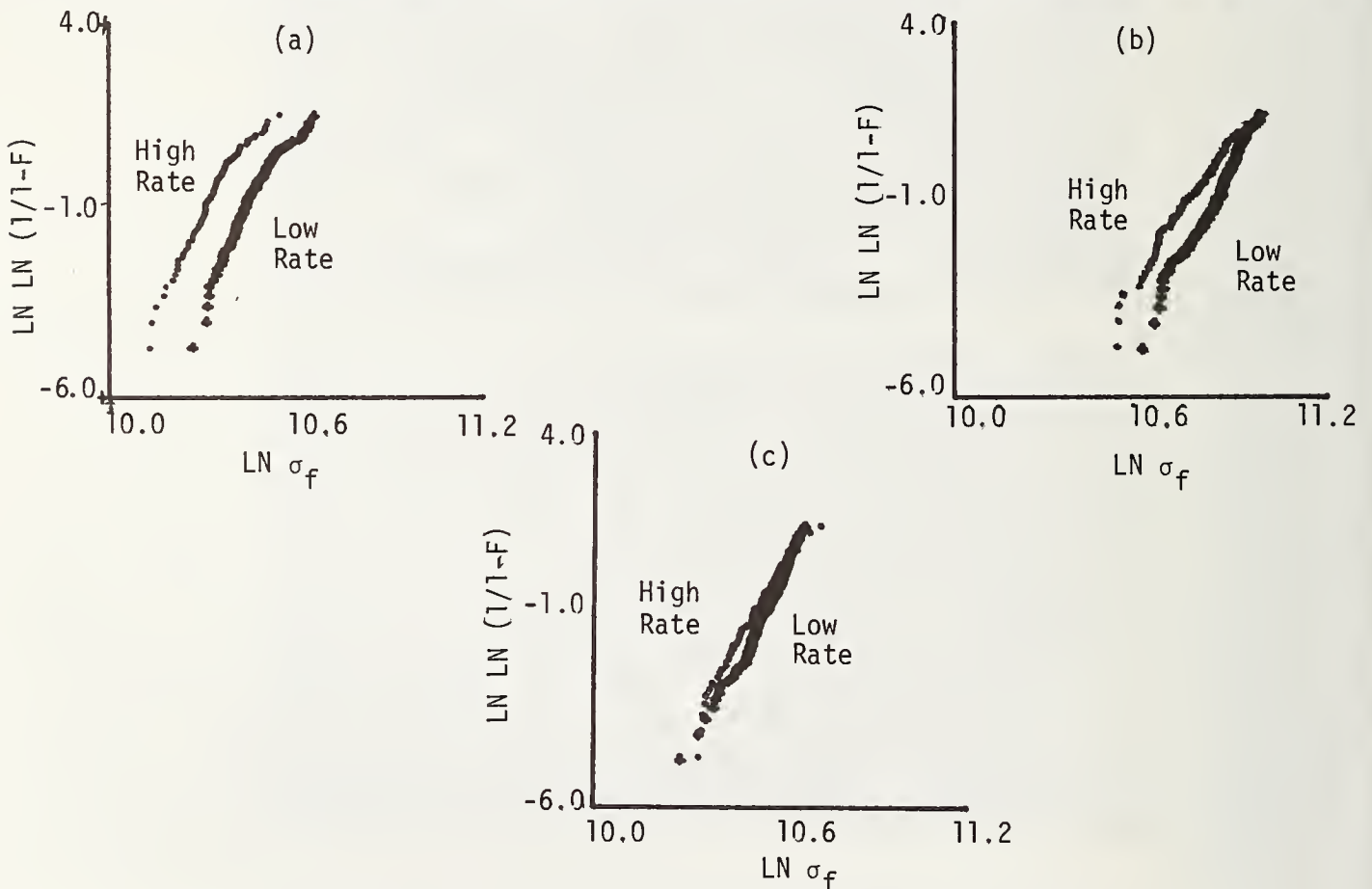


Figure 2. Comparisons of Weibull distribution for the three aluminas after two rates of surface removal. a) AL300, b) AL600, c) AL995.

a finite value of σ_u in eq. (1), so that a three-parameter Weibull may yield an improved fit for these data. The nonlinearity in the high strength region of the AL300 and the central region of the AL600 data also suggests the possibility of the existence of more than one flaw population as has been discussed by Johnson [12]. During SEM study of the fracture surfaces, flaw origins were sought but could not be conclusively identified as is often the case with polycrystalline alumina. Thus, multiple flaw populations could not be conclusively confirmed. From figure 2 and table 2, it is evident that the lesser rate of surface removal has a marked tendency to yield higher average strengths and a higher Weibull modulus, m . The trend is consistent throughout with the exception of the latter

for the AL300. From the differences that exist between the two different removal rates for the three materials, it is evident that some type of material/microstructure dependence exists, although the specific relationship is not obvious. The coarse grain size material, AL300, exhibits nearly parallel distributions over the entire range of strengths, including the low strength and the high strength tails. This indicates that the change in flaw severity due to surface removal rate is the same for all strength levels. On the other hand, the fine grain size AL600 material reveals a decreasing effect of the surface removal rate as the high strength region is approached. The high strength tails for both removal rates are nearly identical. Other than the low strength tail of the distribution for the higher removal rate, the shapes for AL600 are very similar. In the case of AL995, which contains some large 25 μ m grains, the strengths are comparable to those of AL300 (grain size \approx 25 μ m). This material is the least affected of the three by the surface removal rate during machining.

Table 2. Strength Distribution Parameters

Material	Parameters	Removal Rates (in/pass)	
		2.5×10^{-4}	2.5×10^{-5}
AL300	R^2 (%)	95.6	93.4
	m	13.5	13.3
	σ_0	25,850	29,650
	$\bar{\sigma}_f$ (psi)	32,200	36,900
AL600	R^2 (%)	97.6	98.3
	m	11.0	14.3
	σ_0	39,300	45,150
	$\bar{\sigma}_f$ (psi)	51,300	55,300
AL995	R^2 (%)	97.8	98.6
	m	13.4	15.5
	σ_0	31,800	33,550
	$\bar{\sigma}_f$ (psi)	39,500	40,400
AL600 (Bevelled)	R^2 (%)	97.7	94.4
	m	9.1	10.3
	σ_0	42,650	44,250
	$\bar{\sigma}_f$ (psi)	58,600	58,700

3.4. Effects of Edge-Bevelling

The AL600, the fine grain size, high strength material, was employed to determine the effects of edge-bevelling on the resultant strength distributions. The statistical parameters for this comparison are listed in table 2, the distributions are plotted in figure 3, and the bevelled vs. non-bevelled edges are compared in the micrographs of figure 4. The distributions in figure 3 and the parameters in table 2 clearly reveal that edge-bevelling yields an increase in average strength, an effect that is more pronounced for the higher rate of surface removal. Edge-bevelling also caused a slight decrease in the Weibull modulus, m, for both rates of surface removal. This effect probably results from not

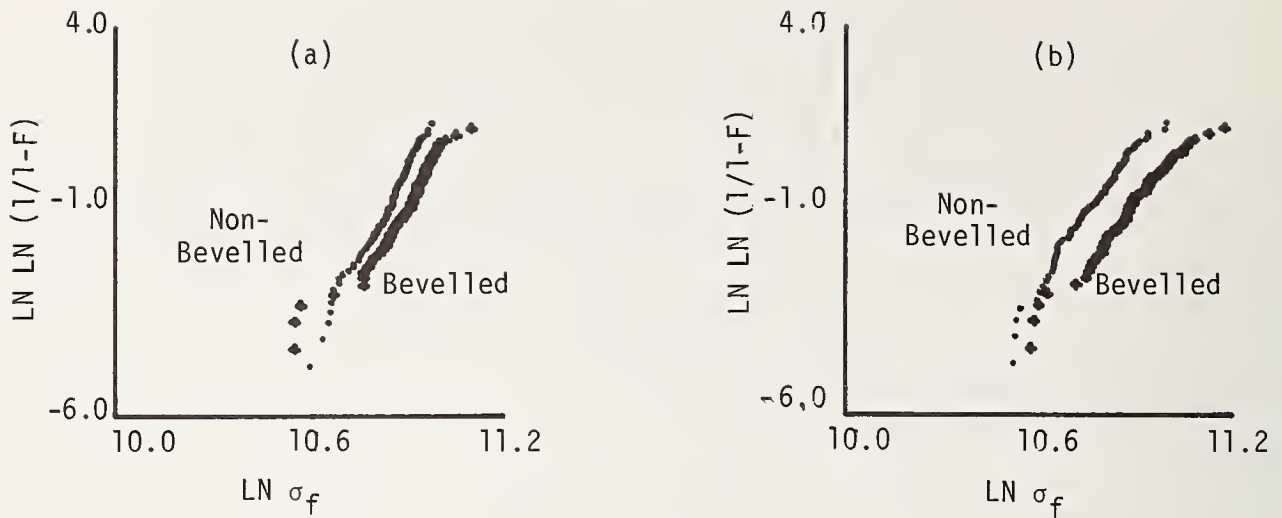


Figure 3. Weibull distributions comparing the strengths of bevelled and non-bevelled specimens of AL600 after a) the lesser surface removal rate, and b) the greater surface removal rate.

removing the most severe edge chipping flaws. As a result the low strength tail is little affected by bevelling, resulting in lower m -values but higher average strengths. Similarly, the bevelling process might be expected to tend toward a higher value of σ_u in a three-parameter fit.

Micrographs comparing bevelled and non-bevelled edges are shown in figure 4. It is evident that the bevelling process eliminated some of the edge chipping. It is likely that since the removal of edge flaws by the bevelling procedure results in increased strength for both removal rates, that the magnitude of the increase is probably related to the edge damage present before bevelling. The distributions for each removal rate are shown in figure 3. The wider separation in distributions seen for the high removal rate specimens indicates that more severe edge chipping occurred in this case than when the lesser removal rate was employed.

4. Conclusions

A less severe rate of material removal during surface grinding results in higher average strengths and an increased Weibull modulus. The differing shapes of the strength distributions for the three aluminas indicates that microstructure has a decided effect on the magnitudes of these increases. Specific details of this effect are not evident at this time.

The Weibull two-parameter equation fits the strength data rather well, although from the shapes of some of the distributions, such as for AL600, multiple flaw populations cannot be ruled out. Tendencies toward a finite value of σ_u , as evident with AL300, indicate that the three-parameter form may yield an improved fit over that of the two-parameter form.

Edge-bevelling can increase average strengths. Bevelling has a more pronounced effect on the strength of materials subjected to high rates of surface removal, since this surface finishing operation results in more severe edge chipping.

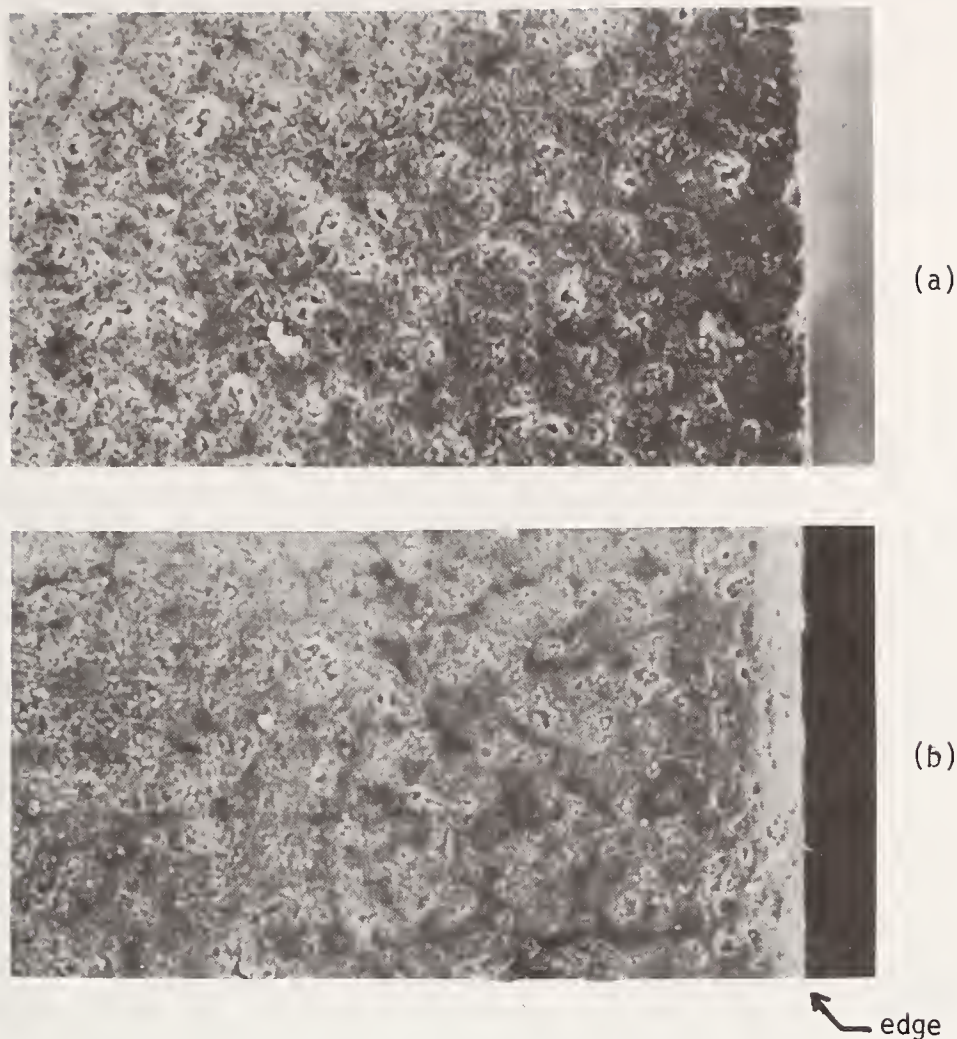


Figure 4. Comparison of a) non-bevelled and b) bevelled sample edges of AL600.

The authors express their thanks to the Alcoa Foundation for their support of this research, and also to Wesgo for supplying the alumina materials.

5. References

- [1] Busch, D. M., and Prins, J. F., A basic study of the diamond grinding of alumina (Proc. Sci. of Cer. Mach. and Surf. Fin., NBS, Gaithersburg, Maryland, Nov. 2-4, 1970), NBS Special Publication 348, p. 73-87.
- [2] Rice, R. W., The effect of grinding direction on the strength of ceramics (Proc. Sci. of Cer. Mach. and Surf. Fin., NBS, Gaithersburg, Maryland, Nov. 2-4, 1970), NBS Special Publication 348, p. 365-376.
- [3] Mueller, J. A., Grinding - a means of shaping and sizing ceramics (Proc. Sci. of Cer. Mach. and Surf. Fin., NBS, Gaithersburg, Maryland, Nov. 2-4, 1970), NBS Special Publication 348, p. 45-52.
- [4] Sedlacek, R., Halden, F. A., and Jorgensen, P. J., On the strength of ceramics as a function of microstructure, grinding parameters, surface finish, and environmental conditions (Proc. Sci. of Cer. Mach. and Surf. Fin., NBS, Gaithersburg, Maryland, Nov. 2-4, 1970), NBS Special Publication 348, p. 89-97.

- [5] McClintock, F. A., Statistics of brittle fracture, Fracture Mechanics of Ceramics 1, Eds. R. C. Bradt, D. P. H. Hasselman, and F. F. Lange, p. 93-114 (Plenum Press, New York, 1974).
- [6] Batdorf, S. B., Fundamentals of the statistical theory of fracture, Fracture Mechanics of Ceramics 3, Eds. R. C. Bradt, D. P. H. Hasselman, and F. F. Lange, p. 1-30 (Plenum Press, New York, 1978).
- [7] Evans, A. G., and Jones, R. L., Evaluation of a fundamental approach for the statistical analysis of fracture, J. Am. Cer. Soc., 61 [3-4] 156-160 (1978).
- [8] Easler, T. E., previously unpublished results.
- [9] Tressler, R. E., Langensiepen, R. A., and Bradt, R. C., Surface-finish effects on strength-vs-grain-size relations in polycrystalline Al_2O_3 , J. Am. Cer. Soc., 57 [5] 226-227 (1974).
- [10] Simpson, L. A., unpublished data, Atomic Energy of Canada, Whiteshell, Manitoba.
- [11] Jeryan, R. A., Use of statistics in ceramic design and evaluation, Technical Report X4-8515, Ford Motor Company, Dearborn, Michigan (1977).
- [12] Johnson, C. A., Fracture statistics of multiple flaw distributions (Presented at the Fall Meeting of the Basic Science Division of the American Ceramic Society, NBS, Gaithersburg, Maryland, Nov. 12-15, 1978).
- [13] Davies, D. G. S., The statistical approach to engineering design in ceramics (Proc. of Br. Cer. Soc., [22], June 1973, p. 429-452).
- [14] Weil, N. A., Bortz, S. A., and Firestone, R. F., Factors affecting the statistical strength of alumina, Materials Science Research 1, Eds., H. H. Stadelmeier, and W. W. Austin, p. 291-313 (Plenum Press, New York, 1963).

Discussion

FIRESTONE

Did you examine the specimens for fracture origins, specifically, the beveled specimens which broke at lower stresses than the non-beveled specimens from which it appears the specimens were damaged in bevelling?

BRADT

The fractures of specimens were examined. However, fracture origins were not sufficiently well defined to give definitive results.

EFFECT OF SURFACE FINISH ON THE STRENGTH OF HOT PRESSED SILICON NITRIDE

C. A. Andersson and R. J. Bratton

Westinghouse Research and Development Center
Pittsburgh, PA 15235

Statistical flexural strengths of hot pressed silicon nitride, Norton NC 132, were determined as functions of the stress axis to hot pressing direction, the coarseness of grinding and the stress axis to grinding orientation. The higher strengths of the material tested perpendicular to the hot pressing direction rather than parallel to it can be attributed to a proportional difference in the critical stress intensities between the directions. Coarser grinding media introduces larger flaws and reduces strength. Finally, transverse grinding produces stress concentrating grooves, effectively deeper cracks and possibly wider ones which reduce the applied stress necessary to cause propagation.

Key Words: Finishes; flexure; fracture; fracture mechanics; grinding, silicon nitride; strength; surface.

1. Introduction

The strength data reported in this paper were collected in support of a program¹ to develop ceramic blading for industrial size combustion turbines [1]². A major purpose of that program was to design, test and evaluate blade attachment concepts. In order to enable statistical failure predictions to be made of those blade forms, it was necessary to statistically determine the material strengths as functions of the orientation within the billets from which they were machined, and the diamond grinding procedures used. Two hot pressing orientations, three grinding meshes and two grinding directions, for a total of twelve combinations, were evaluated. These data, as well as their assessment, are presented herein.

2. Experimental

Test specimens measuring .125 x .250 x 1.125 in. (.32 x .64 x 2.86 cm) were cut from five billets of NC 132 hot pressed silicon nitride³, both parallel and perpendicular to the pressing direction and were diamond ground either parallel or perpendicular to the stress direction. Three diamond grit sizes were used: 325, 240, 80 mesh. Thirty 325 mesh ground specimens were prepared for each of the pressing directions and grinding direction orientations, and fifteen specimens were prepared for each of the other grinding mesh/orientation conditions.

The specimens were flexure tested at room temperature in an Instron Universal Test Machine using a steel fixture having inner and outer spans of 0.25 and 0.75 in. (0.64 and 1.91 cm), respectively. A crosshead speed of 0.05 cm/min (0.02 in/min) was used. Breaking loads were autographically recorded.

¹Electric Power Research Institute, Research Project No. 421-1.

²Figures in brackets indicate the literature references at the end of this paper.

³The Norton Company, Worcester, MA.

3. Results

The mean fracture strengths, $\bar{\sigma}_f$, variances, S^2 , standard deviations, S , and the coefficient of variance, C_{vm} , are presented in table 1. In agreement with previous investigators, the strength is dependent on orientation within the billet, i.e., for all conditions tested, the strength perpendicular to the hot pressing direction is 13 to 19 percent greater than that parallel to the pressing direction. The scatter is also greater in the strong direction as indicated by the coefficients of variation, C_{vm} . With one exception, C_{vm} perpendicular to the pressing direction ranges between 10 and 100 percent greater than the parallel orientation; in that exception, it is 15 percent lower.

Comparing the effects of grinding coarseness parallel to the stress direction: there is less than 5 percent difference between the 325 and 240 mesh surfaces, but a strength decrease of 30 percent occurs when 80 mesh grit is used. The grinding direction transverse to the stress axis orientation has a more profound effect: a strength decrease of 35 to 50 percent occurs for this grinding condition. For the worst cases tested (transverse grinding with 80 mesh grit) there is in excess of a 60 percent strength decrease when compared to the best cases tested (longitudinal grinding with 325 mesh grit).

In addition to the Gaussian distribution analyses, the data were also analyzed by two parameter Weibull statistical methods. All the data were assessed assuming that the failures were caused by flaws existing on the surface. In addition, the data for specimens whose surfaces were ground parallel to the stress axes were analyzed assuming that the defects were contained within their volumes.

For surface flaws the probability of failure, P_A , is given by:

$$P_A = 1 - \exp\left[-K_A A(\sigma/\sigma_{0A})^m\right], \quad (1)$$

where σ is the stress, m is the Weibull modulus, σ_{0A} is the Weibull characteristic strength for surface flaws, K_A is a constant dependent on specimen and loading geometries and A is the specimen surface area. The corresponding probability of failure for volume flaws, P_V , is

$$P_V = 1 - \exp\left[-K_V V(\sigma/\sigma_{0V})^m\right], \quad (2)$$

where K_V is the geometric constant, V the specimen volume and σ_{0V} the characteristic strength for volume flaws. Figure 1 contains plots of the data based on these equations. The Weibull parameters were determined statistically and the results are contained in tables 2 and 3. The lines in the figure represent the results of the analyses.

Comparing the data on figures 1(b) and 1(d) for the grinding directions transverse to the stress axes, the data with one exception seems to be reasonably well behaved. The exception is the 325 mesh ground data in which the stress axis is parallel to the pressing direction. These data (fig. 1(b)) have a lower Weibull modulus than the other two mesh sizes for this orientation. Thus, the probability of failure at stresses lower than 33 ksi (230 MPa) is greater for the 325 mesh than for the 80 mesh material. The physical cause for this is uncertain, but the fine grinding procedure seems to have put a wider dispersion of defect sizes on the surface.

4. Discussion

Brittle materials are known to fail from preexisting flaws within the body being loaded, and a fracture mechanics approach is generally accepted as the best criterion for failure. This criterion simply states that the applied stress, σ , at which a body fails is dependent not only on a property which is characteristic of the material (K_{IC} , the critical stress intensity parameter) but also on the flaw size ($2c$). Thus,

$$\sigma = Y K_{IC} / \sqrt{c} \quad (3)$$

where Y is a constant which accounts for the flaw shape and location, the geometry of the loaded body, the type of loading, etc.

Table 1. Room temperature flexural strengths and Gaussian distribution parameters of Norton NC 132 silicon nitride as functions of: 1) the orientation of the stress axis with respect to the hot pressing direction, 2) the surface grinding direction, and 3) the grinding mesh size.

Stress Axis to Pressing Direction Orientation	Grinding Direction Grinding Mesh Parameter:	Longitudinal with Stress Axis			Transverse to Stress Axis		
		325	240	80	325	240	80
Parallel	Mean Fracture Stress, $\bar{\sigma}_f$, ksi (MPa)	104.0 (717)	101.3 (698)	74.3 (512)	67.4 (465)	51.4 (354)	39.5 (272)
	Variance, S^2 , ksi ² (MPa ²)	100.2 (4763)	57.1 (2715)	190.1 (9038)	70.2 (3336)	9.1 (433)	2.8 (133)
	Standard Deviation, S, ksi (MPa)	10.0 (69)	7.6 (52)	13.8 (95)	8.4 (58)	3.0 (21)	1.7 (12)
	Coefficient of Variation, C_{vm}	.100	.075	.186	.124	.059	.043
	Number of Specimens, η	30	15	15	30	15	15
	Perpendicular	Mean Fracture Stress, $\bar{\sigma}_f$, ksi (MPa)	123.2 (849)	116.7 (805)	85.3 (588)	72.7 (501)	59.2 (408)
Variance, S^2 , ksi ² (MPa ²)		209.5 (9960)	95.0 (4516)	309.7 (14720)	58.6 (2785)	33.6 (1597)	16.9 (803)
Standard Deviation, S, ksi (MPa)		14.5 (100)	9.7 (67)	17.6 (121)	7.7 (53)	5.8 (40)	4.1 (28)
Coefficient of Variation, C_{vm}		.117	.083	.206	.105	.098	.087
Number of Specimens, η		30	15	15	30	15	14
Ratio: $\bar{\sigma}_f(\perp) : \bar{\sigma}_f(\parallel)$		1.18	1.15	1.15	1.13	1.15	1.19
Ratio: $C_{vm}(\perp) : C_{vm}(\parallel)$	1.17	1.11	1.11	.85	1.61	2.02	

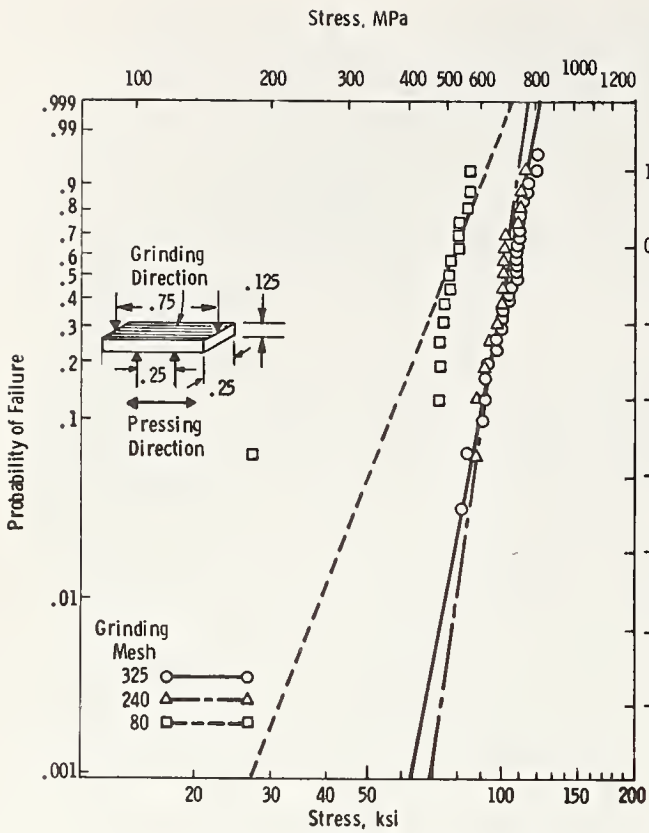
$$f(\sigma_f) = \frac{1}{(2\pi)^{1/2} S} \exp \left[-\frac{(\sigma_f - \bar{\sigma}_f)^2}{2S^2} \right]$$

$$\bar{\sigma}_f = \frac{1}{N} \sum_{i=1}^N \sigma_{fi}$$

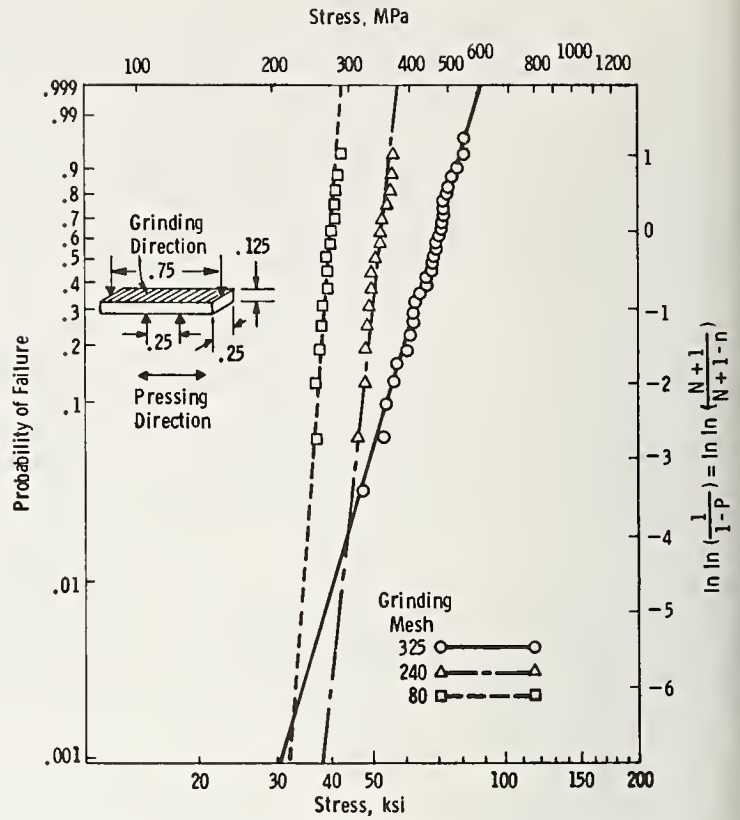
$$S^2 = \frac{1}{N-1} \sum_{i=1}^N (\sigma_{fi} - \bar{\sigma}_f)^2$$

$$C_{vm} = S / \bar{\sigma}_f$$

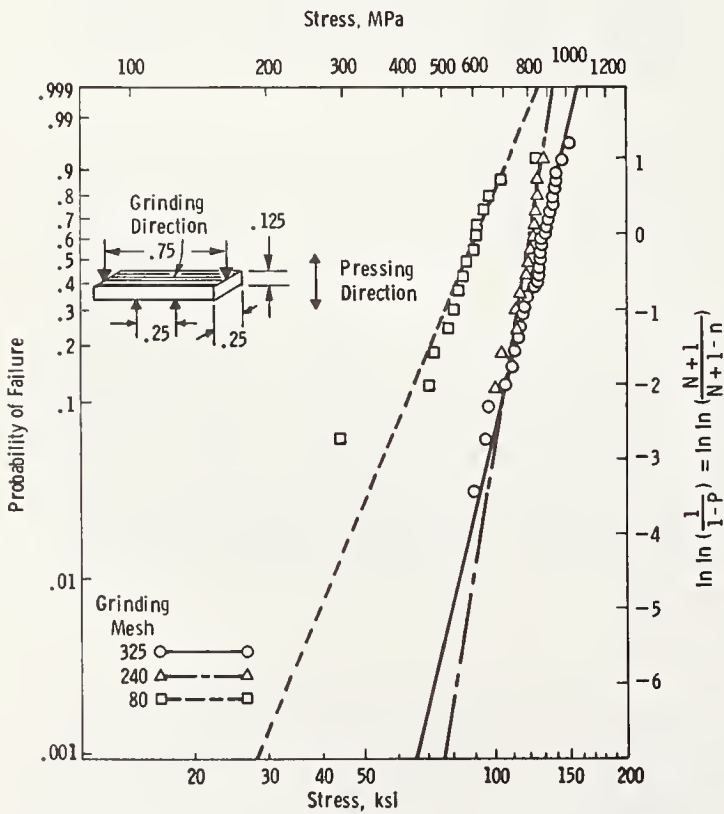
$$P_f = 1 - \frac{1}{(2\pi)^{1/2} S} \int_{\sigma}^{\infty} \exp \left[-\frac{(\sigma - \bar{\sigma}_f)^2}{2S^2} \right] d\sigma$$



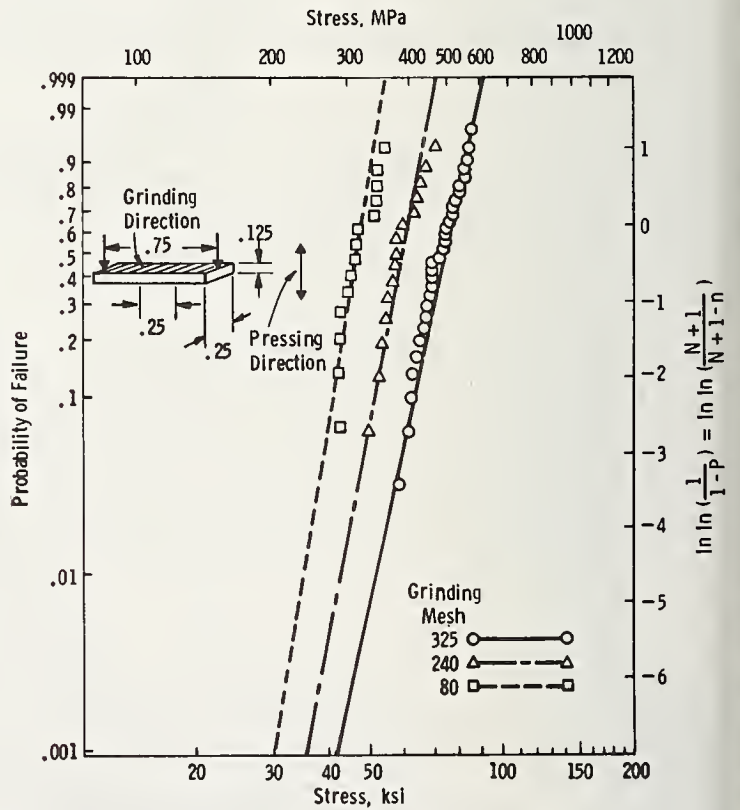
(a) Tensile axis oriented parallel to the pressing direction; grinding direction parallel to the tensile axis.



(b) Tensile axis oriented parallel to the pressing direction; grinding direction perpendicular to the tensile axis.



(c) Tensile axis oriented perpendicular to the pressing direction; grinding direction parallel to the tensile axis.



(d) Tensile axis oriented perpendicular to the pressing direction; grinding direction perpendicular to the tensile axis.

Figure 1. Probability of failure of Norton NC 132 as functions of flexural stress, hot pressing direction to stress axis orientation, grinding mesh size and grinding direction to stress axis orientation.

Table 2. Surface flaw Weibull distribution parameters for Norton NC 132 silicon nitride at room temperature as a function of: 1) the orientation of the tensile axis with respect to the hot pressing direction, 2) the surface grinding direction, and 3) the grinding mesh size.

Stress Axis to Pressing Direction Orientation	Grinding Direction: Grinding Mesh: Parameter:	Longitudinal with Stress Axis			Transverse to Stress Axis		
		325	240	80	325	240	80
Parallel	Weibull Modulus, m_A	12.9	17.1	6.7	9.8	22.0	30.5
	Characteristic Strength, σ_{oA} , ksi (MPa)	88.8 (612)	91.2 (629)	57.1 (394)	54.6 (376)	47.0 (324)	37.2 (256)
Perpendicular	Weibull Modulus, m_A	10.4	15.3	5.9	12.1	12.9	14.7
	Characteristic Strength, σ_{oA} , ksi (MPa)	99.8 (688)	104.1 (718)	62.8 (433)	63.3 (436)	50.6 (349)	41.7 (288)
$P_{fA} = 1 - \exp\left[-\int_A (\sigma/\sigma_{oA})^{m_A} dA\right]$							

Table 3. Volume flaw Weibull distribution parameters for Norton NC 132 silicon nitride at room temperature as a function of: 1) the orientation of the tensile axis with respect to the hot pressing direction, and 2) the grinding mesh size.

Stress Axis to Pressing Direction Orientation	Grinding Direction: Grinding Mesh: Parameter:	Longitudinal with Stress Axis	
		325	240
Parallel	Weibull Modulus, m_V	12.9	17.1
	Characteristic Strength, σ_{oV} , ksi (MPa)	58.3 (402)	65.4 (451)
Perpendicular	Weibull Modulus, m_V	10.4	15.3
	Characteristic Strength, σ_{oV} , ksi (MPa)	60.3 (416)	72.2 (498)
$P_{fA} = 1 - \exp\left[-\int_V (\sigma/\sigma_{oV})^{m_V} dV\right]$			

The effect on strength of stress axis to hot pressing direction for the silicon nitride tested can be attributed simply to the difference in the critical stress intensity factors between the orientations. Since the strengths perpendicular to the hot pressing direction range between 13-19 percent greater than those parallel to it for identical grinding mesh and grinding direction conditions, it can be assumed that the critical stress intensities differ proportionally for these pressing orientations. On the average, the K_{Ic} perpendicular to the hot pressing direction can be taken to be 16 percent greater than that parallel.

The effects of the coarseness of the grinding media and grinding direction with respect to the stress axis are more complicated. For example, it is expected that the size of the microcracks introduced during grinding, which will act as the sources of failure, will be dependent on the grinding mesh size. In addition, flaw shapes would be expected to be a function of the grinding direction; i.e., the cracks should be longer parallel to the grinding direction than perpendicular to it. Alternatively, parallel to the grinding direction, several closely spaced, uniformly shaped cracks could effectively act as a single long one. Finally, the grooves formed by the grinding process can act as additional stress concentrators when oriented perpendicular to the stress direction, thus changing the effective stress intensity factors.

The effect of grinding on the magnitude of flaw size is a complicated one beyond the scope of the present study. Other than noting that flaw size is expected to be somewhat proportional to grinding media size, it will not be discussed. However, grinding direction to stressing direction will be considered by assessing its effect on the proportionality constant in the fracture mechanics equation.

In the following discussion, it will be assumed that failure occurs from flaws at tensile surfaces of the bend specimens tested. Scanning electron micrographs of fracture surfaces such as those shown in figure 2 confirm this assumption⁴. Occasionally, failures can originate from defects contained within the volume of finely ground specimens, but these are exceptions to the rule in the present study. The procedure used will thus be to establish the stress intensity relationships for surface flaws in bending and then to determine the stress concentration effects of the grinding grooves on these relationships.

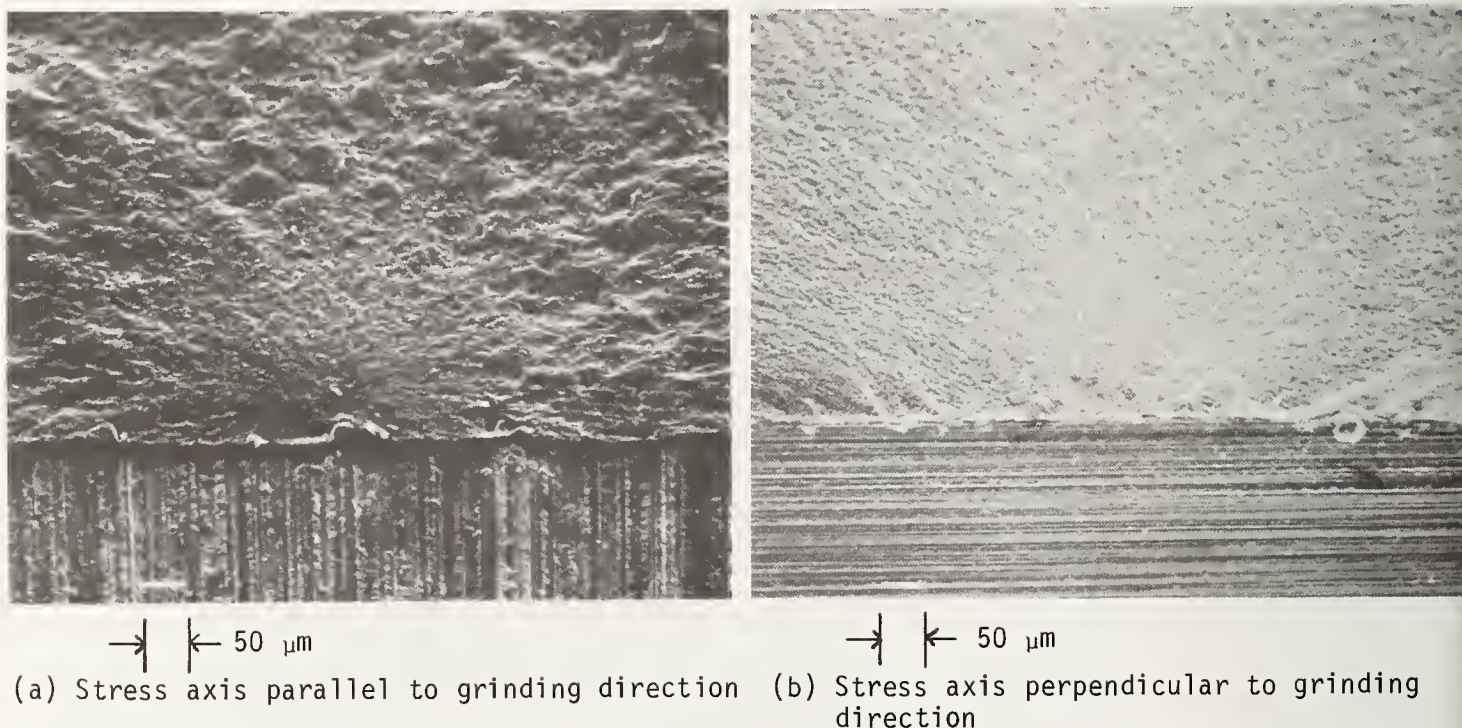


Figure 2. Typical flexural fracture surfaces of hot pressed silicon showing origins of failure. The bottom portion of each photo is the tensile surface of the flexure specimen.

⁴Note that the origin of failure for the stress axis parallel to the grinding direction is nearly semicircular, whereas it is spread parallel to the crack edge for the stress axis perpendicular to the grinding direction.

4.1. Stress intensity relationships for surface flaws in bending

The analysis of Kobayashi [2] for the stress intensity relationships in bending for semielliptic surface flaws oriented normal to the tensile axis was used. He graphically presents these as functions of the ratio of crack depth, b , to crack width, a , and of the ratio of crack depth to specimen thickness, h . It is assumed throughout the following, that the crack depth is small compared to the specimen thickness. Therefore, the values were extrapolated to b/h equal to zero and replotted in figure 3.

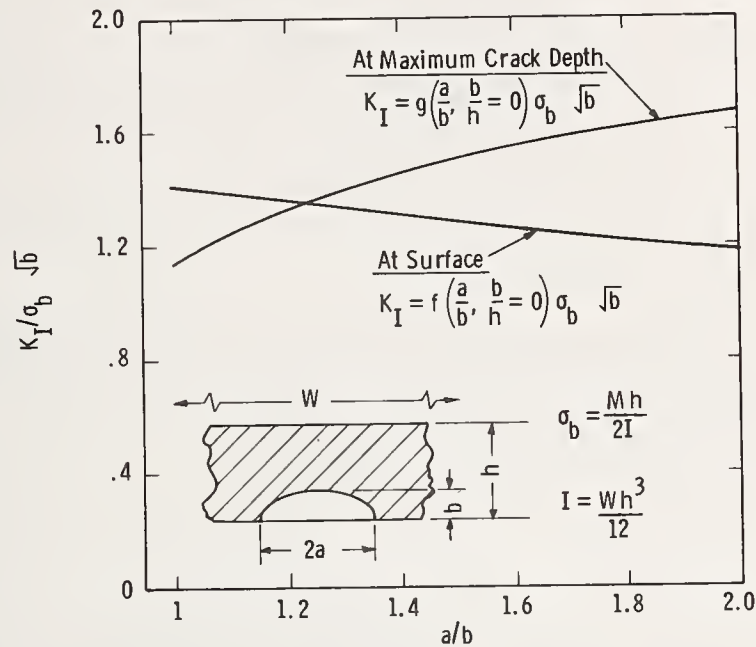


Figure 3. Stress intensity coefficients as a function of the crack width to crack depth ratio for shallow semielliptical surface cracks in bending [2].

In bending, the stress intensity relationship generally differs along the periphery of the crack. For example, for a semicircular crack ($a/b = 1$), the stress intensity coefficient in the direction of the a -axis is 1.41, whereas it is 1.14 at the maximum crack depth along the b -axis. Therefore, on loading, it would be expected that the critical stress intensity at the surface would be arrived at first and that the crack would first start growing in the direction parallel to the surface. As the crack grows, the a/b ratio changes, causing the stress intensity at the surface to decrease and that at the maximum depth to increase until a/b reaches a value of 1.23. At this ratio, the value of the coefficient is 1.35 for both orthogonal directions and crack propagation proceeds in both directions.

4.2. Stress intensity relationships for grinding direction parallel to the stress direction

Since the grinding grooves parallel to the stress direction do not contribute to the stress concentration, the stress intensity relationships given in figure 3 are applicable. Also, since the elliptical axes are usually nearly equal, the previous reasoning regarding crack growth can be applied and the relationship,

$$K_{Ic} = 1.35 \sigma_b \sqrt{b}, \quad (4)$$

can be used.

4.3. Stress intensity relationships for grinding direction perpendicular to the stress direction

Surface grooves such as would occur from grinding are known to cause stress concentrations which should affect the stress intensity relationships of surface cracks associated with them. A simple model based on some work that was done on two dimensional cracks [3] was devised to determine the stress intensity relationships as functions of groove and crack dimensions. In this model, a semielliptical crack is assumed to lie at the bottom of a semi-cylindrical groove. Using the previous notation, the a-axis of the crack is parallel to the axis of the semicylinder which, in turn, is perpendicular to the stress axis in bending. Both the groove radius, r , and the crack depth, b , are considered to be small compared with the specimen thickness, h , and the stress intensity relationships given in figure 3 can be used.

Parallel to the surface, at the bottom of the groove, the stress is multiplied by the stress concentration factor, k_t , of the groove ($k_t \approx 3$), and the relationship in the a-axis direction is:

$$K_I = f(a/b, b/h = 0) k_t \sigma_b \sqrt{b}. \quad (5)$$

An example of the function $f(a/b, b/h = 0) k_t$ for $a/b = 2$ has been plotted versus b/r in figure 4 as the long dashed/short dashed curve.

The stress concentration effect of the groove at the maximum crack depth is dependent on the relative size of the crack with respect to the groove. For very short crack depths, b , the crack will be influenced by the full stress concentration, k_t , and

$$K_I = g(a/b, b/h = 0) k_t \sigma_b \sqrt{b}. \quad (6)$$

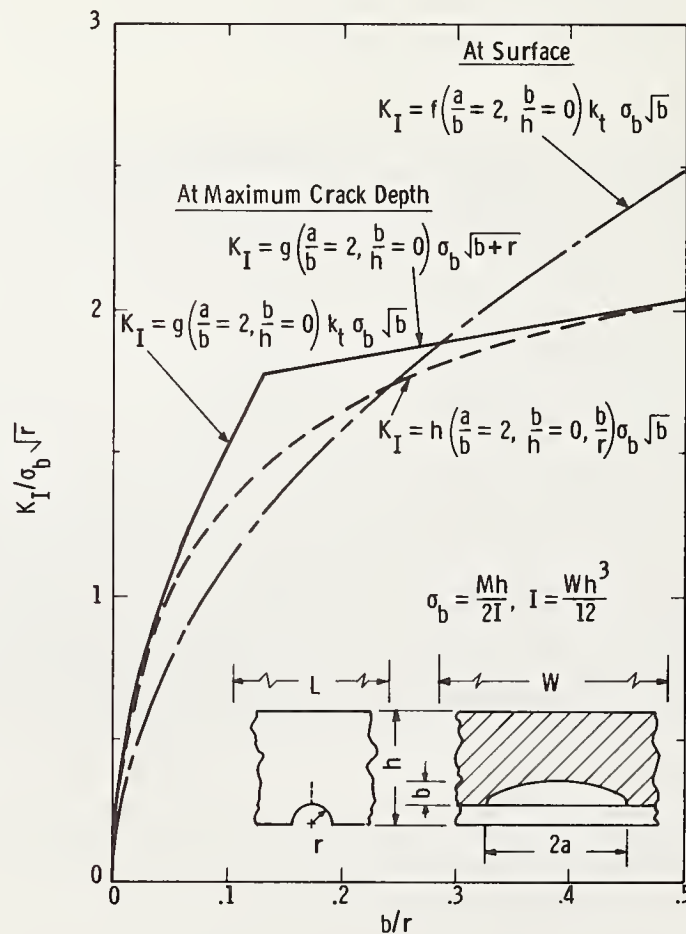


Figure 4. Stress intensity coefficients in bending as a function of the crack depth to groove radius for a shallow semielliptical crack at the bottom of a semi-cylindrical groove, and a crack width to depth ratio of 2.

For very deep cracks, with respect to groove radius, the stress concentration will be negligible and the only influence of the groove is to lengthen the crack by an amount equal to the groove radius, and:

$$K_I = g(a/b, b/h = 0) \sigma_b \sqrt{b + r}. \quad (7)$$

Equations (6) and (7) for $a/b = 2$ have been plotted as the solid line segments in figure 4. A smooth short dashed line representing the equation,

$$K_I = h(a/b, b/h = 0) \sigma_b \sqrt{b}, \quad (8)$$

has been drawn in this figure to represent intermediate crack depths.

Similar treatments for other a/b values were made to construct the stress intensity relationships given in figure 5. The long dashed/short dashed curve represents the stress intensity parallel to the bottom surface of the groove in the a -axis direction. The solid lines are the stress intensities, for various b/r values, at the maximum crack depth in the b -axis direction.

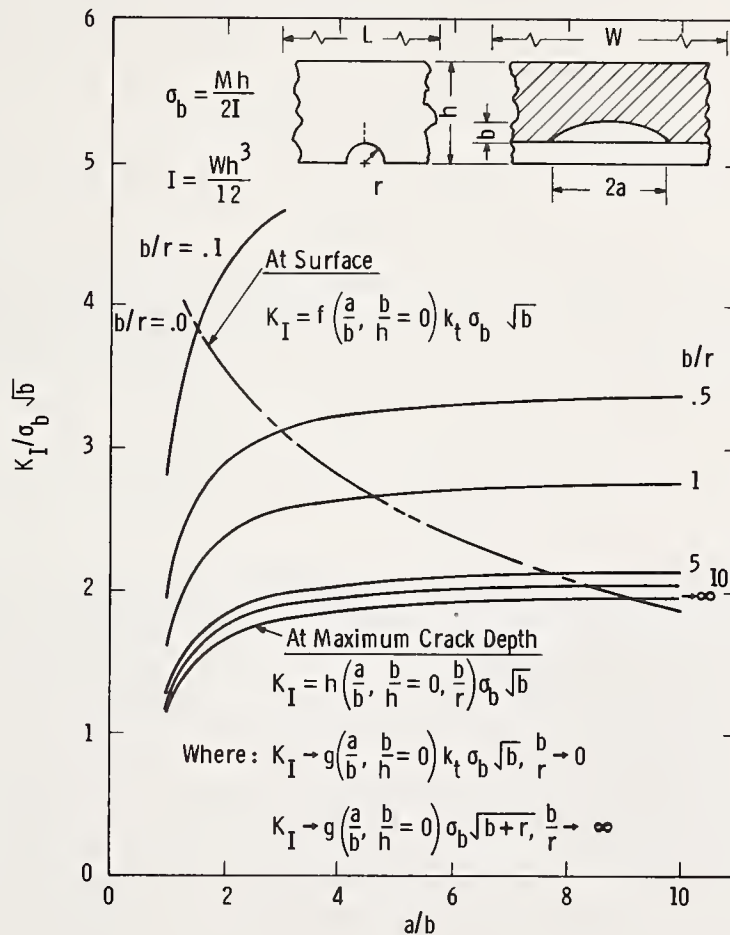


Figure 5. Stress intensity coefficients in bending as functions of the crack width to crack depth ratio and the crack depth to groove radius ratio for shallow semielliptical surface cracks at the bottom of semicylindrical grooves.

The consequences of figure 5 will now be examined. The stress concentration effect of transverse grooves is most pronounced at small b/r ratios and becomes negligible at large b/r .

Whether the K_I for a given applied stress is the greatest parallel to the surface or in the transverse direction at the maximum crack depth is dependent on both ratios, b/r and a/b . For example, for $b/r = 1$ and $a/b = 1$, the stress intensity at the surface is 2.5 times that at the maximum crack depth. On increasing the applied stress, the critical value would be reached at the surface first and the crack would grow laterally to an a/b ratio of 4.6 before fracturing transversely. On the other hand, for the same $b/r = 1$, and for elliptical crack axis ratios greater than 4.6, the K_I at the maximum crack depth would become critical first, and transverse fracture would proceed initially.

For reasonably large crack depth to groove radius ratios ($b/r > .5$), the shape of the crack does not have a significant effect on the stress intensity relationships. For example, consider two cracks, one having an initial $a/b = 1$ and the other an $a/b = \infty$, at the bottom of a groove with $b/r = 1$. The ratio of the stress intensities would be:

$$\frac{K_I(a/b = \infty)}{K_I(a/b = 1 \rightarrow 4.6)} = \frac{2.81}{2.65} = 1.06, \quad (9)$$

since the initial semicircular crack would be expected to grow laterally before transverse failure until a/b reaches 4.6. Thus an initially semicircular crack would be expected to sustain only six percent greater applied stress than one having an infinite a/b ratio for the same crack depth, b . In the absence of the groove, the stress intensity ratio would be:

$$\frac{K_I(a/b = \infty)}{K_I(a/b = 1 \rightarrow 1.23)} = \frac{1.99}{1.35} = 1.47, \quad (10)$$

and the initially semicircular crack could sustain 47 percent greater stress than the elongated one, if both cracks had the same depth.

The insensitivity of the stress intensity relationships to the shape of the cracks in the presence of grooves, is one factor that can contribute to the lower scatter in strength often observed for transversely ground materials. For example, in the present test series, the coefficients of variation for 80 mesh transversely ground specimens were .09 and .04, whereas for the parallel ground specimens they were .21 and .19.

4.4. Assessment of test results

In concurrence with previous investigations of hot pressed silicon nitride [4], the difference in strength parallel and perpendicular to the hot pressing direction is attributable to the difference in the stress intensity factors between the directions. The strength ratios parallel and perpendicular to the pressing direction ranged between .82 and .94 for six grinding directions averaging 0.86. It is reasonable to assume that this value can be used for the ratio of the critical stress intensities in the two directions. The K_{Ic} of this material was measured to be $4.6 \text{ MPa m}^{1/2}$ ($C_V = .09$) with the plane of the crack normal to the pressing direction [1]. The orthogonal K_{Ic} is estimated to be $5.4 \text{ MPa m}^{1/2}$.

The effect of the coarseness of the grinding mesh on the strengths of materials ground parallel to the stress axis is on the maximum flaw depth. Using the appropriate strengths and the K_{Ic} values above, the mean maximum crack depths, b , were calculated and the results presented in table 4.

The effect of the coarseness of the grinding mesh on the strengths of materials ground perpendicular to the stress axis is more complicated since the transverse grinding operation causes both cracks and grinding grooves to have affect. However, calculations show that the crack depth to groove radius, b/r , for each case tested was greater than unity. Therefore, the maximum crack depth is out of the stress concentration field of the groove, and the major contribution of the groove to the crack in the b -axis direction is to increase its depth. The effective depth is thus the sum of b and r . It has also been pointed out that for b/r greater than one, there is little difference in the stress intensity equations between the cases where the crack grew laterally to a maximum value at fracture or where a long crack preexisted. The effective crack depths were calculated for two extreme conditions: one for

Table 4. Calculated mean flaw depths of Norton NC 132 silicon nitride as functions of:
 1) the orientation of the stress axis with respect to the hot pressing direction,
 2) the surface grinding direction, and 3) the grinding mesh size.

Stress Axis to Pressing Direction Orientation	Grinding Direction: Mean Maximum Crack Depth, μm	Longitudinal with Stress Axis			Transverse to Stress Axis		
		Grinding Mesh: 325	240	80	325	240	80
Parallel	b^a	22	24	45			
	$b_{\text{eff}} = b+r, b/r = 1, a/b = 4.6^b$				28	48	81
	$b_{\text{eff}} = b+r, b/r = \infty, a/b = \infty^c$				25	43	72
Perpendicular	b^a	22	24	46			
	$b_{\text{eff}} = b+r, b/r = 1, a/b = 4.6^b$				33	50	78
	$b_{\text{eff}} = b+r, b/r = \infty, a/b = \infty^c$				29	44	69

$$^a K_I = 1.35 \sigma \sqrt{b}$$

$$^b K_I = 1.87 \sigma \sqrt{b_{\text{eff}}}$$

$$^c K_I = 1.99 \sigma \sqrt{b_{\text{eff}}}$$

which $b/r = 1$ and an initially semicircular crack grew at $a/b = 4.6$, and the other for which $b/r = \infty$ and the initial crack extended across the specimen width. These values are also given in table 4.

For longitudinal grinding, coarsening the grinding mesh from 325 to 240 to 80 mesh causes the mean maximum crack depth to increase from 22 to 24 to 46 μm , respectively. For transverse grinding the effective crack depths are considerably larger, averaging 29, 46 and 75 μm for the same respective mesh sizes. The transverse depths are thus approximately 30, 90 and 60 percent larger than their corresponding longitudinal grinding depths. A fraction of this difference can be attributed to the groove radius; however, both examination of the fracture surfaces and calculations show the transverse ground crack depths to be actually larger than the longitudinal ones after subtracting r . Thus, other factors related to the grinding techniques used must have contributed to the differences.

5. Summary

Flexural strengths of hot pressed silicon nitride, Norton NC 132, were determined as functions of the stress axis to the hot pressing direction, the coarseness of grinding media and the stress axis of grinding orientation. The strengths were statistically analyzed using both Gaussian and Weibull methods. Both the strengths and distributions were shown to be sensitive to each of the parameters. Strengths are the highest for materials finely ground parallel to the stress axis and tested perpendicular to the hot pressing direction. The best case tested was over 300 percent stronger than the worst case tested. The least amount of scatter occurred for the coarsest mesh specimens ground perpendicular to the stress axis.

The stress intensity relationships for surface flaws in bending were presented for conditions of both grinding parallel and perpendicular to the tensile axis. In bending, the

stress intensity is generally different around the crack periphery. When the stress intensity is greater at the surface than at the maximum crack depth, a crack will initially grow laterally, simultaneously decreasing the stress intensity at the surface and increasing the stress intensity at the maximum depth until its critical value is reached. If the stress intensity is greater at the maximum crack depth than at the surface, as in the case for wide cracks, transverse crack propagation will occur from the start.

Grinding perpendicular to the stress axis causes loss of strength for several possible reasons. Crack lengths parallel to the grinding grooves can be deeper and longer than those perpendicular. The groove depths can increase the effective crack depths. Grooves can act as stress concentrators, increasing the effective stress intensities. Each of the above effects reduce the applied stress necessary to reach the critical stress intensity and subsequent crack propagation.

The authors wish to thank Dr. A. Cohn and the Electric Power Research Institute for supporting the program for which the data presented herein was obtained. In addition, they wish to thank Mr. J. J. Nalevanko and Mr. W. J. Carmen for their experimental contributions.

References

- [1] Andersson, C. A., Bratton, R. J. and Booher, Jr., C. R., Ceramic turbine components research and development, part 1 - ceramic rotor blade development, Final Report, Electric Power Research Institute Research Project 421-1, (Dec. 1978).
- [2] Kobayashi, A. S., "Crack opening displacement in a surface flawed plate subjected to tension or plate bending, (Proc. 2nd International Conf. on Mechanical Behavior of Materials, Boston, Mass., August 1976), pp. 1073-1077.
- [3] Dowling, N. E., Fatigue at notches and the local strain and fracture mechanics approaches Paper presented at the 11th National Symposium on Fracture Mechanics, Blacksburg, VA, (June, 1978).
- [4] Miller, D. G., Andersson, C. A., Singhal, S. C., Lange, F. F., Diaz, E. S., Kossowski, R. and Bratton, R. J., Brittle materials design, high temperature gas turbine material technology, Final Report, Advanced Research Projects Agency, Contract No. DAAG-46-71-C-0162, AMMRC CTR 76-32, Vol. IV, (Dec. 1976).

Discussion

RICE:

First, I understand that you consider a semi-cylindrical gouge in the surface, i.e., a gouge with a width twice the depth. If this is correct, this leads to two questions. The first being what justification do you give for this in view of the extensive evidence shown in earlier work as well as quite extensively at this conference that groove width to depth ratios are typically ≥ 4 due to substantial fracturing along the path of the grit particles. The second related question is what effect would width to depth ratios of four-to-one and six-to-one have on your resultant calculations.

Secondly, I had concerns about your proposed failure criteria. As I understand it, you defined failure when the stress intensity for propagation of the flaw parallel with the surface equals the stress intensity for propagation inward from the surface. However, this appears to violate the normal failure criteria of the net stress intensity on the original flaw reaching the critical stress intensity value for the material. Thus, for example, if one had failure when the stress intensity was equal in two perpendicular directions, this would appear to imply that the propagating crack front would tend to preserve the shape of the flaw at the time of failure. This, however, is not observed since typically fracture mirror and related markings which outline the crack front characteristically approach a circular profile in a uniform stress field regardless of the shape of the original flaw. Your comments?

ANDERSSON:

With regard to your first question, as to the use of the semi-cylindrical gouge for my model, it was, of course, selected for the sake of simplicity in an attempt to explain observed trends. The model also assumes that fracture will occur from a single gouge or alternatively a gouge that is deeper than its neighbors since it ignores stress field interactions from neighboring gouges. However, the only change that would be required to account for different shaped gouges or gouge interactions is a change in the value of stress concentration factor, k_t , used in the equations. For example, using textbook values for k_t [1], it would change from 3.0 to 2.7 to 2.3 on increasing the groove width to depth ratio from 2 to 4 to 6, while maintaining the radius of curvature at the groove bottom. The major effect that this, in turn, would have would be to reduce the surface stress intensity coefficients (the dashed line in Fig. 5) by 10 and 25 percent, respectively. This, in turn, would reduce the intercept a/b ratio with the maximum crack depth stress intensity coefficients. The following table summarizes the effects for an exemplary case:

Parameter	Crack Width to Depth Ratio		
	2	4	6
k_t	3.0	2.7	2.3
b/r	1	1	1
a/b	4.6	3.7	2.4
$K_I/\sigma_b\sqrt{b}$	2.65	2.60	2.50

Thus, there is a two percent decrease in the stress intensity coefficient on using a width to depth ratio of 4 and a six percent decrease on using a ratio of 6. It can be concluded that the semi-cylindrical groove model is adequate, but may be adjusted if still more accurate calculations are desired.

The second question that you raised concerns the failure criteria that I use. In this paper, the failure stress has been defined as the stress at which the stress intensity factor orthogonal to the tensile surface (in the b -axis direction) reaches the critical value. For very wide cracks, the stress intensity in this direction is always the greatest and there exists no problem between definitions. However, for narrow cracks under the conditions described in this paper, the stress intensity is larger in the a -axis direction (parallel to the tensile surface) than in the b -axis direction, and other directions would be intermediate

to these. Therefore, on loading, subcritical crack propagation parallel to the surface would be expected to occur first with no propagation perpendicular to the surface. For example, assume the following initial parameters:

$$\begin{aligned} a &= 50 \text{ } \mu\text{m} \\ b &= 25 \text{ } \mu\text{m} \\ r &= 25 \text{ } \mu\text{m} \\ K_{Ic} &= 5 \text{ MPa m}^{1/2} \end{aligned}$$

From figure 5:

$$\begin{aligned} K_I \text{ (a-axis)} &= 3.54 \sigma \sqrt{b} \\ K_I \text{ (b-axis)} &= 2.37 \sigma \sqrt{b} \end{aligned}$$

On loading to a stress value of 282 MPa:

$$\begin{aligned} K_I \text{ (a-axis)} &= 5 \text{ (critical)} \\ K_I \text{ (b-axis)} &= 3.35 \end{aligned}$$

The crack would propagate in the a-direction. If it arrested at $a = 75 \text{ } \mu\text{m}$, at this stress value then:

$$\begin{aligned} K_I \text{ (a-axis)} &= 3.10 \sigma \sqrt{b} = 4.37 \text{ MPa m}^{1/2} \\ K_I \text{ (b-axis)} &= 2.56 \sigma \sqrt{b} = 3.60 \text{ MPa m}^{1/2}, \end{aligned}$$

both of which are below the critical value. Thus, the load must be increased to 323 MPa before the critical value is again reached in the a-axis direction. At 323 MPa:

$$\begin{aligned} K_I \text{ (a-axis)} &= 5 \text{ (critical)} \\ K_I \text{ (b-axis)} &= 4.13. \end{aligned}$$

This process will continue until the a-axis dimensions reach $115 \text{ } \mu\text{m}$ at which point

$$K_I \text{ (a-axis)} = K_I \text{ (b-axis)} = 2.65 \sigma \sqrt{b}$$

and at a stress of 377 MPa, the crack will catastrophically propagate in both orthogonal directions, since an increasing b value in the equations will maintain the criticality.

Finally, with regard to your comments on the shape of a propagating crack front, two points must be made. First the values presented in this paper were for small crack depths, b, with respect to the overall specimen thickness, h, and as such pertain to the shape of the crack at the time of initial propagation. As propagation proceeds b/h changes and must be accounted for in the stress intensity relationships (as has been done by Kobayashi in the paper used). These relationships would then dictate the crack front shape. Second, as the crack depth, b, to groove radius, r, ratio increases, the effectiveness of the stress concentration of the groove diminishes and the relationships presented break down. The stress intensity relationships of a propagating crack would be expected to revert to the usual form (fig. 3) and result in nearly semicircular fronts. Therefore, I find no contradiction between the present results and your observations.

Reference

- [1] Peterson, R. E., Stress concentration factors, Fig. 38, p. 57, John Wiley & Sons, New York, (1974).

THE EFFECT OF SURFACE FINISHING ON THE STRENGTH OF COMMERCIAL HOT PRESSED Si_3N_4

C. Cm. Wu and K. R. McKinney

Naval Research Laboratory
Washington, D. C. 20375

Effects of diamond grit size on the as-ground and oxidized strength of commercial hot-pressed Si_3N_4 were studied. Finer grit sizes gave higher as-ground strengths. Prolonged high temperature oxidation negates effect of machining on strength.

Key Words: Silicon-nitride; machining of ceramics; fracture strength; oxidation and degradation; and fracture origin.

1. Introduction

Hot-pressed Si_3N_4 is a promising candidate for ceramic heat engine parts [1,2]¹, but machining is needed to meet the close dimensional tolerances of some parts. Strengths can often be increased by finer finishing, but may be effected by subsequent oxidation. The purpose of this work was to investigate the machining and oxidation effects on the strength of commercial hot-pressed Si_3N_4 .

2. Experimental

Flexure bars were cut from hot pressed billets of Norton NC-132 Si_3N_4 such that the resultant fracture surface would be parallel to the hot pressing direction. The fracture would propagate perpendicular to the hot pressing direction, i. e. the bars were cut to reflect the possible greater strength of the billet if it had a preferred orientation of grain parallel with the hot press plunger surface. The bars were then diamond ground to a final cross section of ~ 2.5 mm x 7.5 mm with metal bonded grinding wheels of 180, 320, and 600 grit sizes. All surface grinding was parallel to the length of the bars. The 180 grit grinding was on a Boyar Schultz Hydraulic Surface Grinder with a 200 mm (8 inches) grinding wheel rotating at 1725 rpm and automatically translated at 760 mm/min with a feed rate of 0.025 mm per pass. The 320 and 600 grit grinding was on a Motor Appliance Corp's grinder with 100 mm (4 inches) wheel running at 3450 rpm translated manually at a speed of ~ 760 mm/min with a feed speed again of 0.025 mm per pass. After surface finishing, the edges were rounded off using a 600 grit bonded diamond grinding disk moving lengthwise along the bars to decrease the probability of failure initiating from the corners. Some ground samples were oxidized in an open end tube (Al_2O_3) furnace at 1430°C for 100 hrs. After oxidation, some of the specimens were refinished with the 180 grit grinding wheel until the surface appeared comparable to those attained before heat treatment. Flexure strengths for each were measured in an Instron machine with a 3-point flexure span of 12.7 mm (0.5 inches) and a cross head speed of 1.27 mm/min (0.05 in/min).

¹Figures in brackets indicate the literature references at the end of this paper.

3. Results and Discussions

The results of the strength measurements are summarized in table 1. Samples were from more than one billet, with billet-to-billet differences not significant in comparison to the finishing effects below. While there was no clear distinction between strengths of bars as ground with 180 or 320 grit diamond, there was a definite increase (e.g. 15%) in the bars as ground with the 600 grit wheel.

Table 1. Strength of NC-132 in various machining conditions.

Conditions	Grinding Wheel Grit Size	Strength		Standard Deviation		Typical Failure Origin
		MPa	ksi	MPa	ksi	
As Machined	180	884 (18) ^a	128	70	10	Machining flaws
	320	875 (5)	127	54	8	Machining flaws
	600	1032 (8)	150	74	11	Internal flaws or machining flaws
Oxidized at 1430°C for 100 hours after machining	180	470 (13)	68	68	10	Bubble-like reaction pits
	320	492 (7)	71	24	4	Bubble-like reaction pits
	600	508 (7)	73	44	7	Bubble-like reaction pits
Refinished after Oxidation	180	962 (11)	140	25	4	Machining flaws

^a Numbers in parentheses indicate number of specimens tested.

Fractographic studies of bars tested as ground with the 180 grit wheel showed fracture markings such as mirror and crack branching patterns indicating surface fracture origins associated with a deeper surface grinding groove, figure 1. Similar fracture origins were observed for 320 grit ground bars. While it was not possible to unequivocally define the specific flaws themselves, from all the indications, these failures clearly appeared to be from machining flaws introduced by and approximately perpendicular to the deeper grinding grooves, consistent with other observations [3,4]. On the other hand, 600 grit finished bars showed a mixture of fracture origins from either internal or surface flaws. The implication is that the hot-pressed material contains processing defects of comparable size to those introduced by 600 grit size diamond grinding, i.e. ~ 5 μm. From the economical point of view for machining of this material into final configurations, it is then obvious that any machining better than 600 grit size finishing is unnecessary as far as strength is concerned.

The flexure strength of specimens after 100 hours at 1430° heat treatment was about 485 MPa (70 ksi) for all three groups of specimens regardless of finishing prior to heat treatment. This was due to a thick porous layer that had formed on the specimen surface during the heat treatment. This layer contained numerous pits of different sizes that penetrated into the



Figure 1. Fracture origin in a 180 grit ground specimen as seen in SEM. The origin is beneath the surface under a deep machining groove. Arrows show boundary where crack branching began.

bulk of the material. Upon loading, these pits then acted as fracture origins as has been reported [5,6,7] and also shown in figure 2. Some pits have reached about 100 μ in size. No original machining introduced flaws were observable. One can see that the prolonged high temperature treatment has completely nullified the effect of machining on strength of the material.

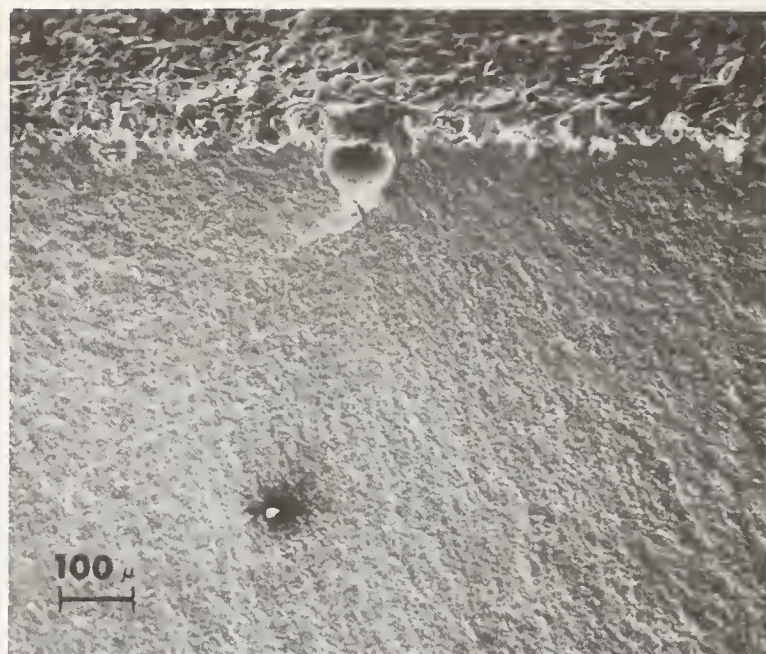


Figure 2. Oxidation pits become fracture origins in NC-132 Si_3N_4 specimens oxidized in air at 1430°C for 100 hrs regardless of finishing prior to oxidation.

In order to measure the strength level of the bulk of the oxidized material, the oxide layers were ground off with the 180 grit metal bonded wheel. The flexure strength measured reached slightly higher than the original at about 962 MPa (140 ksi) with smaller standard deviation. This perhaps is not surprising if we consider the fact that the impurities or second phases that were present may have dispersed more evenly or even diffused out of the body due to prolonged heat treatment at high temperature. At the same time, internal flaws may have also redistributed or shrunk in size and therefore higher strength could be obtained. Typically, fracture originated from cracks extending from the base of a deep machining groove.

One interesting question is: How far into the specimen does the damage extend due to the oxidation treatment? Although a definitive conclusion still cannot be drawn from the result presented here, from the fact that the strength has completely recovered to its original value after refinishing, it appears that the damage may be confined to as deep as the reaction pits have grown into the surface, i.e. on the order of 100 μm .

4. Summary

Flexure strength of 1200 MPa (160 ksi) for commercial hot-pressed Si_3N_4 is attainable through grinding with fine (600) grit metal bonded diamond wheels. Further increases will be limited since even at this stress level, internal processing defects were becoming frequent sources of failure. Therefore, grinding with finer grits does not appear productive. For specimens to be used in high temperature, fine machining is not needed since high temperature oxidation significantly degrades strength, e.g. by $\sim 50\%$ regardless of original grinding.

The authors would like to gratefully acknowledge R. W. Rice and P. F. Becher for their invaluable discussions.

References

- [1] Richerson, D. W., Materials characterization program overview, (Proc. of the 1977 DARPA/NAVSEA Ceramic Gas Turbine Demonstration Engine Program Review, Maine Maritime Academy, Castine, Maine, Aug. 1-4, 1977) pp. 187-91.
- [2] Richerson, D. W. and Yonushonis, T. M., Properties of silicon-nitride rotor blade materials, *ibid*, pp. 193-217.
- [3] Rice, R. W., Freiman, S. W., and Mecholsky, Jr., J. J., Fracture sources in Si_3N_4 and SiC , *ibid*, pp. 665-688.
- [4] Rice, R. W., Freiman, S. W., and Mecholsky, Jr., J. J., Fractography of Si_3N_4 and SiC (Ceramics for High Performance Applications-II, Proc. of the Fifth Army Mat. Tech. Conf., Newport, R.I., March 21-25, 1977), pp. 669-687.
- [5] Freiman, S. W., Mecholsky, J. J., McDonough, W. J., and Rice, R. W., Effect of oxidation on the room temperature strength of hot-pressed Si_3N_4 -MgO and ZrO_2 , *ibid*, pp. 1069-1076.
- [6] Richerson, D. W. and Yonushonis, T. M., Environmental effects on the strength of silicon-nitride, (Proc. of the 1977 DARPA/NAVSEA Ceramic Gas Turbine Demonstration Engine Program Review, Maine Maritime Academy, Castine, Maine, Aug. 1-4, 1977), pp. 247-271.
- [7] Freiman, S. W., Wu, C. Cm., McKinney, K. R., and McDonough, W. J., Effect of oxidation on the room temperature strength of silicon-nitride hot-pressed with MgO or ZrO_2 , *ibid*, pp. 655-663.

Discussion

GRAHAM

Is the improved strength (140 ksi) for the oxidized & machined (180 grit) as compared to the strength (128 ksi) for the machined (180 grit) unoxidized samples significant, and if so how do you explain the improvement? (If it isn't significant, is the 150 ksi for the 600 grit, unoxidized a significant difference from the 180 grit, unoxidized?)

WU & MCKINNEY

The improved strength for the oxidized and refinished specimens as compared to those only machined can be shown to be significant at the 1% level according to the Student t test. Two additional observations not mentioned in the paper should aid in supporting this. First, the appearance of the specimen surfaces after the same machining procedure is different for the two groups, i.e. the as machined specimens looked coarser than the re-finished specimens. Second, preliminary microhardness measurements showed higher hardness for the as machined group. This leads to the belief that an appreciable change may have taken place in the hulk during the oxidation treatment.

As to the difference between 180 grit and 600 grit as finished specimens, this also is significant at the 1% level. Reasons for this are explained in the paper.

SURFACE CONDITION AND STRENGTH OF SILICON CARBIDE - SILICON MATERIALS

T. J. Whalen and L. L. Terner
Research Staff, Ford Motor Company
Dearborn, Michigan 48121

The measured strength of SiC-Si materials with as-silicided, ground, and ground and polished surfaces was determined. The influence on strength of SiC and nickel coatings and the geometry of test specimens was studied.

Key Words: SiC, Surfaces, Coatings, Strength

1. Introduction

A process for molding and sintering silicon carbide materials has been developed and details are given in the literature [1,2]¹. Briefly, the process involves the formation of a SiC-filled, thermosetting plastic which can be injection or transfer molded into complex shapes. Subsequent steps include carbonizing the plastic at high temperature in an inert atmosphere to yield a carbon-SiC composite and siliciding the composite at high temperature in vacuum or controlled atmosphere to form a fully dense SiC-Si material. The final body has essentially the same dimensions as the initial molded shape within a tolerance of 1%.

Silicon carbide surfaces of high strength are difficult to form and maintain, and for this reason a study of the influence of coatings of chemically deposited materials such as nickel and SiC was initiated.

The purpose of this paper is to discuss the measured strength of SiC-Si composites as influenced by the surface condition, surface composition and geometry of the test specimens.

2. Testing Procedure

Sample bars 1/4" x 1/8" x 1 1/4" or 1/4" diameter x 1 1/4" were tested for flexural strength in 4-point bending upper span 3/8 in. (0.95 cm), lower span 3/4 in. (1.9 cm) at room temperature. Strengths are reported as "characteristic strength" which is defined as that strength at which the probability of failure is 62.3% of the tested population. Cross-head speed in the Instron tester was 0.05 in/min. The bars, were injection molded in preheated test bar molds at 155°C, except those bars for which thicknesses were varied and these were compression molded in a simple uniaxial preheated die.

Table I. Surface Conditions of Test Samples.

<u>Surface</u>	<u>Range of Surface Roughness (μin.)</u>
As Silicided	30 - 90
Ground	9 - 14
Polished	2 - 4
SiC Coated	28 - 57

3. Surface Conditions

Different Surfaces were generated by diamond grinding, polishing, hiping and coating with nickel or SiC. As-silicided surfaces were also evaluated. The maximum and minimum surface average roughness for typical samples as measured by a Gould Surfalyzer #150, is shown in table I.

4. Results and Discussion

The influence of surface condition on the measured strength of α -SiC test bars of rectangular cross section is shown in table II. The strength of as-silicided surfaces varies over a wide range, depending on the precise details of the siliciding operation. The presence of excess silicon on the surface makes transverse rupture testing a poor choice for evaluating the material since the maximum stress is generated at the test bar surface and silicon is brittle at room temperature and initiates fractures at low stresses. Grinding and polishing yield more reproducible surfaces and the values of strength tend to reflect the quality of these surface operations and of the SiC material itself. Much of our work has been done with hand-ground and polished samples with rectangular cross sections but good-quality surfaces free of edge chips were difficult to form with such brittle materials.

Table II. Surface Condition and Strength of α -SiC Rectangular Samples.

<u>Surface</u>	<u>Characteristic Strength</u>	
	<u>Kpsi</u>	<u>Mpa</u>
As Silicided	20-40	138-276
Ground and Polished	24	165
Nickel Plated	36	250

Round rods as samples were then investigated in an attempt to improve and simplify the flow of material in the mold during forming to reduce molding flaws. It was also anticipated that improved strengths could be attained by increasing the perfection of surfaces by machine grinding and polishing. The results shown in table III, compared with those listed in table II, indicate that the strengths increased significantly for the types of surfaces generated. Individual specimens with strengths in excess of 100 Kpsi were measured with both α -SiC and β -SiC compositions. It appears that the SiC-Si system has the potential to form high strength materials. The open issue that remains is how reproducibly and consistently can the high-strength SiC be fabricated and how well can the surfaces be protected against the formation of damaging flaws.

Table III. Surface Condition and Strength of α -SiC Round Samples.

<u>Surface</u>	<u>Characteristic Strength</u>	
	<u>Kpsi</u>	<u>Mpa</u>
As Silicided	49	340
Ground	61	420
Ground and Polished	75	520

Coating of the surface for strength improvement was attempted with a nickel coating and a SiC coating. Nickel was deposited electrolytically, and one can see from the data given in Table II that the strength increased significantly over the baseline data generated for comparable, ground and polished samples. For low and moderate temperature applications, a simple nickel coating may suffice to strengthen and perhaps protect these materials.

A dense SiC coating prepared by Chemetal Corporation with their Controlled Nucleation Thermochemical Deposition (CNTD) process was evaluated, and the strength data are listed in table IV. Although a significant increase in strength of coated samples was not realized, the coating appeared adherent and dense, as seen in the microstructures of figure 1.

An individual sample which underwent CNTD SiC coating had a porous surface layer beneath the coating which led to some strength degradation. (See figure 2). Heating of the SiC-Si specimens in a vacuum or inert atmosphere at high temperature prior to coating may have removed the Si phase near the surface which invariably leads to a strength reduction when tested in a flexure test.



Figure 1. Microstructure of CNTD SiC Coating on SiC-Si material.



Figure 2. Microstructure of Porous Surface Layer Beneath CNTD SiC Coating

Table IV. Influence of SiC (CNTD) Coating on Strength.

<u>Test Bars</u>	<u>Characteristic Strength</u>	
	<u>Kpsi</u>	<u>Mpa</u>
Round Cross Section		
Baseline - Ground and Polished	75	520
CNTD Coating	77	530
Rectangular Cross Section		
Baseline - Ground and Polished	32	220
CNTD Coating	35	240

The test bar geometry was varied to study the susceptibility of strength to area or volume under stress. Figure 3 shows the usual relationship observed for brittle materials as the test bar geometry changes. In figure 3 one sees that the strength of rectangular cross section specimens decreases as the thickness of the specimens increases. Preliminary data on stronger, round bars indicates that the effect of change in geometry has a less severe effect on strength.

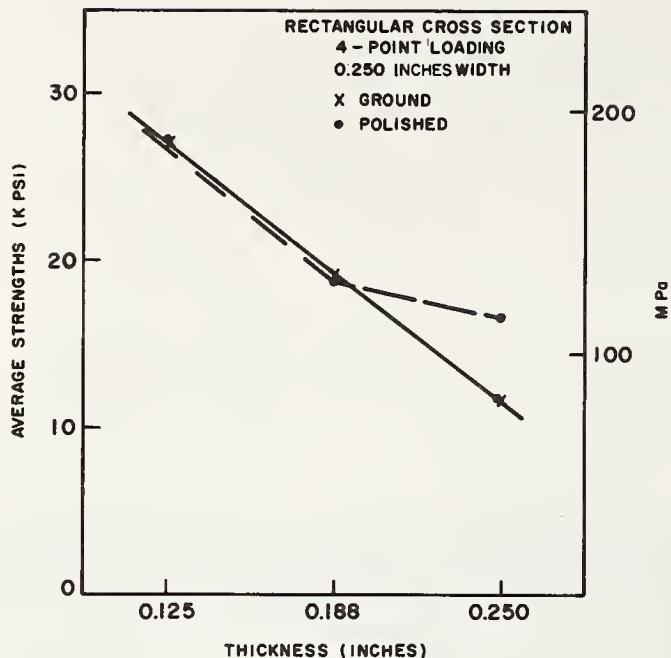


Figure 3. Influence of Sample Thickness on Strength of SiC-Si material.

As a first approximation, the quality of a ground and polished surface of a brittle material is proportional to the particle size of the brittle phase. When applied to SiC-Si composites, this approximation suggests that the strength, which is influenced by surface flaws, should decrease with increasing SiC particle size. Some data generated to investigate this assumption are given in figure 4. Each point on the graph represents 16 to 18 samples, and one can see that the strength peaks at a particle size about 16 μm . Samples of coarser particle size decrease in strength probably due to the increased flaw size generated on the surface by grinding and polishing of a phase (SiC) which tends to fracture by cleavage during these operations. Samples finer in particle size are difficult to silicide completely and, therefore, contain a pore phase which may behave as a stress concentrating flaw. The microstructures of the 8 μm and the 36 μm SiC materials are shown in figure 5. Exploring ways to silicide composites with finer SiC particles may be a fruitful avenue for future research.

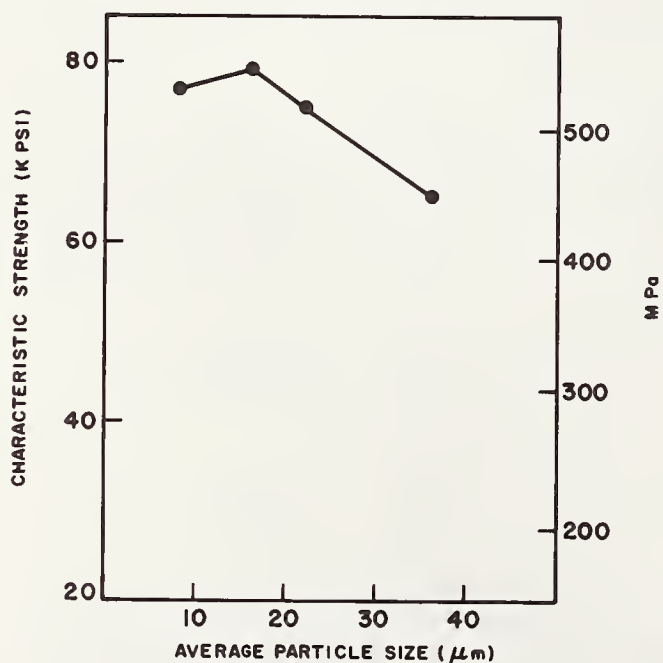


Figure 4. Strength as a function of Initial α -SiC Particle Size (round samples).

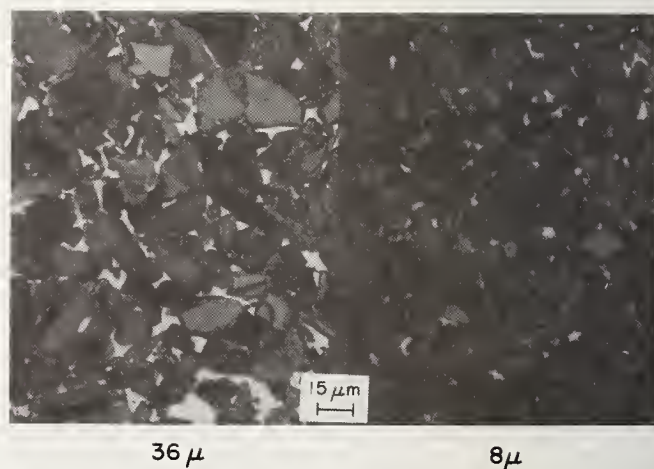


Figure 5. Microstructure of SiC-Si Samples.

Another process which can be brought to bear on altering the surface, and the interior of SiC-Si composites for improved mechanical properties is hot isostatic pressing (HIP). Examples of property improvement (strength and consistency) of brittle materials by HIP especially for WC cutting tools are well documented in the literature [3]. This process improves density by eliminating the pore phase. SiC-Si samples were subjected to HIP (30,000 psi argon at 1350°C for one hour) and the results are given in figure 6. The strength of the initial α -SiC and β -SiC were significantly increased by the HIP process, and further polishing of the samples increased the strength only slightly. Nickel-plated α -SiC of 22 μ m particle size was not altered by HIP.

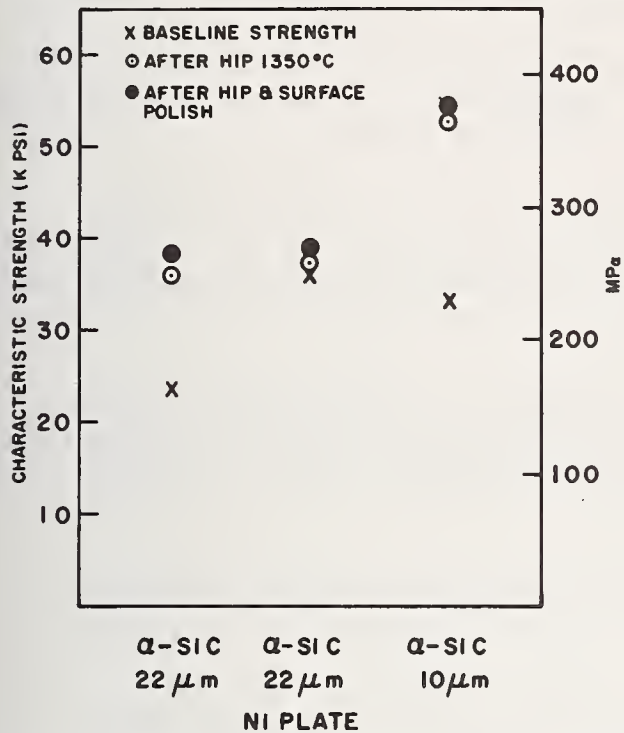


Figure 6. Strength of SiC-Si Samples After HIP at 1350°C for 1 hour.

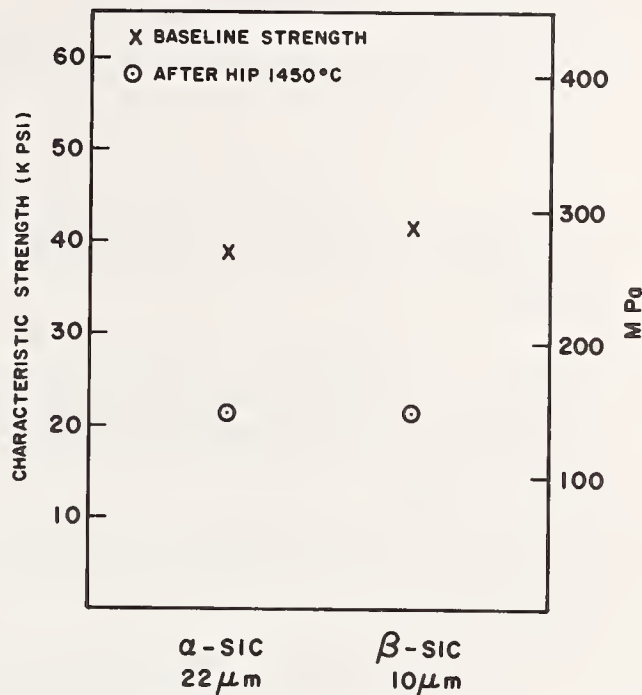


Figure 7. Strength of SiC-Si Samples After HIP at 1450°C for 1 hour.

Since significant improvement in strength was observed with the HIP process at 1350°C, which is below the melting point of silicon, it was logical to explore the effects of the process above the melting point of silicon, such as 1450°C. When this was done, the results are those given in figure 7. In both the α -SiC and in β -SiC, the strength decreased to nearly half of the original, baseline strength of these materials. This drastic decrease in strength could be understood when the microstructures of these treated materials were observed. The microstructure, shown in figure 8, clearly shows that the HIP process at 1450°C evaporated silicon from the surface of the specimens and produced a weak, porous layer at the surface.



Figure 8. Microstructure Near Surface of SiC-Si Sample After HIP at 1450°C for 1 hour.

Conclusions

1. SiC-Si Composites have the potential to attain strengths greater than 100 Kpsi, when used at room temperature.
2. SiC-Si materials with ground and polished surfaces yield greater strength when tested in flexure than do as-silicided materials.
3. Round test bars are easier to prepare and they give higher strengths than bars with rectangular cross sections.
4. HIP processing shows promise in increasing the strength of SiC-Si composites providing the migration of the Si phase near the surface can be controlled.

References

- [1] Willermet, P.A., Pett, R.A., and Whalen, T.J., Development and Processing of Injection-Moldable Reaction-Sintered SiC Compositions, Ceramic Bulletin 57 [8] 744-747 (August 1978).
- [2] Whalen, T.J., Noakes, J.E., and Turner, L.L., Progress on Injection-Molded, Reaction-Bonded SiC (Proc. 5th Army Materials Technology Conf. Newport, Rhode Island, March 21-25, 1977). Book, Ceramics for High Performance Applications - II J. L. Burke, E. N. Leno and R. N. Katz, eds., pp. 179-189 (Brook Hill Publishing Company, Chestnut Hill, Mass., 1978)
- [3] Van Cleave, D.A., Hipping Improves Properties in Castings and PM Parts, Iron Age, August 23, 1976.

Discussion

RICE

The negligible effect of SiC coatings is not surprising since this is not expected to fill in or bond cracks together. However, your Ni coating did increase strength. The question is whether this really "heals" cracks or alternatively alters, e.g. blunt cracks. Have you investigated this, e.g. by removing the Ni layer by polishing or etching?

WHALEN

We have polished the interfacial area to microscopically evaluate the continuity of the Ni coating. The adherence is good and it follows well the contours of the substrate. We do not know if the coating process alters the flaw geometry on a micro scale, but we are attempting to find out.

THE EFFECT OF GRINDING AND POLISHING ON THE STRENGTH OF ANNEALED SODA-LIME-SILICA GLASS

R. Bowles

British Glass Industry Research Association
Sheffield S10 2UA England

As part of the continuing studies sponsored by the Procurement Executive, Ministry of Defence (UK), recent work at British Glass Industry Research Association has aimed at assessing the defects generated in glass during its working under conventional grinding and polishing procedures.

The assessment has been mainly based upon mechanical strength property measurements of lath specimens typically 150 x 25 x 3.5 mm either at specific stages of processing or after a controlled sequence of operations designed to produce a state of minimum surface damage.

The strength of laths was determined under four point flexure test, at a nominal stress rate of 5 MPa/s under normal ambient conditions of temperature and humidity.

The resulting fracture stress data was calculated on simple bending theory after bonded strain gauge tests indicated its adequacy under observed deflections to fracture. Group statistics were largely calculated assuming normal distribution theory but tests on aggregated groups of specimens were also examined by Weibull distribution theory to determine the probability of fracture under relatively lower stresses.

Results show that by application of prior or inter-stage proof loading, that although a low fraction of weak specimens still emerges, a significant improvement of strength can be achieved in annealed glass specimens of reasonable size.

Key words: Defects; etching; glass; grinding; polishing; strength.

1. Literature Review

A review was made of some publications on polishing processes, methods of examining polished surfaces and of the effects of polishing on the strength of glass. A list of references is included herewith.

The mechanisms of grinding and polishing processes (1-12) in glass were comprehensively reviewed by Cornish (6) and he covered the period 1665-1961.

Surface examination techniques by electron microscope are numerous, references (1,2,4,6,7,9) illustrate the potentialities. Holland (13) considered optical microscopy using phase contrast and schlieren methods but concluded that it was not possible to differentiate between optical path differences due to refractive index gradient or topographical features. Holland (11) also reviewed the mechanisms of grinding and polishing in which surface flow is sometimes said to occur.

Levengood (3) showed that narrow deep cracks could be bridged at the surface by polishing glass with rouge on felt, and therefore the apparent absence of surface defects does not exclude their presence. Rawstron (4) illustrated the difference between surface polishing under high pressure and a heated slurry at 60°C that under low pressure and a cooler slurry at 15°C. From a microscope examination, it was concluded that surface flow predominated under the former condition whereas the slower, latter process produced general surface removal. Rawstron describes the use of a Talysurf instrument to measure the thickness of a polished layer ~100 nm deep on glass. Holland (13) described multiple beam interferometry to measure surface topography.

Ernsberger (14) used an ion-exchange process to examine the density of microcracks, and Levengood (13) used water vapour condensation to reveal microscopic scratches.

Stoll (8) measured the strength of fused silica discs 102 mm diameter 6.2 mm thick comparing a commercial surface preparation with a controlled grinding and polishing schedule set to remove at each stage, those defects remaining from previous work stages. Defects were estimated to be approximately 3 x abrasive particle diameters. The discs were tested under concentric rings and a strain gauge calibration had shown close agreement between measured stress and that calculated by an overhang corrected formula by Roark (15). The controlled schedule gave a 50% strength improvement over the commercial process, yielding 88 MPa compared with 59 MPa. Polished samples with light or severe scratches were found to be of similar strength ~48 MPa regardless of grinding history.

Shand (16) reported on a strength comparison using glass plates processed by one of five participant companies but he could not draw firm conclusions as to differences between processes because of large inherent variances within groups, typically ranging 40-110 MPa.

McKinney (12) tested fine grain alumina discs in different surface conditions, and measured rupture moduli by ball and ring test calibrated against strain gauge measurements. The strength was found to increase from 150 MPa to 250 MPa when the SiC grit used for surface grinding was reduced from 210 μm to 17 μm .

Mecholsky (17) tested several glass compositions, either as laths under three point bending or as discs to examine the effect of grinding in orthogonal directions of sample relative to a diamond grinding wheel, and found two differing flaw populations. He measured rupture moduli ~122 MPa after polishing and ~112 MPa for samples etched and containing known flaws in different orientations. He concluded defects in polished glass were ~23 μm deep. In an earlier paper, Mecholsky (18) examined the effects of sputtering on the strength of silicate glasses, and found that although a significant improvement obtained, sputtering introduced its own limiting constraint after removal of the original defect layer.

Shelyubskii (19) examined artificial defects produced in sheet glass by abrasion with electro-corundum grit sizes 1 to 1000 μm . He found a low dependence of minimum strength on grit size, and quoted a relation between defect layer depth (F) and grit size (D) as $F = 1.1D$. He differentiated between strengths resulting from grinding on a soft as opposed to a hard grinding table. He also commented on strength - sample size effect.

Orlova (20) reported on different glass compositions using discs, 30 mm diameter by 1.5 mm thick, which were ground through successive emery stages and then polished. Silicate glass in annealed condition was found to have a rupture modulus of 118 MPa.

Densienko (21) examined HF etched and chemically strengthened sheet glass using 44 mm square samples by 2 mm thick which were tested under central symmetric bending at 50 MPa/s. He observed an optimum etch removal of ~25 μm before ion-exchange and a subsequent light etch of ~2 μm to give a final strength ~700 MPa. Allowing for a quoted surface compression of ~300 MPa induced by the ion-exchange, the annealed glass strength could be construed to amount to the difference, i.e. 400 MPa for a commercial quality sheet glass after a surface etch of ~27 μm .

The question of interpretation of strength data as it relates to components of

different sizes, and under different stresses in service has been considered by several authors (22,23,24,25). Fracture mechanics theories have been used to calculate the probability of component lifetime from knowledge of original surface defect. Lenoë (23) advised caution in assumption of Weibull distributions and pointed out the possible variance of crack growth phenomena. Davidge (24) discussed strength-probability-time relationships for ceramic materials, and evaluated effective times to failure. Ritter (25) calculated the necessary proof stresses required to predict the probability of lifetime under particular stress, and in a later publication (26) he referred to the advantage of proof test in defining a threshold flaw size, whereas calculation of design data from typical stress distributions often yield low strength at low failure probabilities.

2. BGIRA experimental programme

The strength of annealed soda-lime-silica glass subjected to different surface finishing procedures, was measured under ambient conditions by flexure tests of lath and disc samples. Attempts were made to relate rupture moduli with corresponding surface finishes produced by diamond tool grinding, smoothing by free SiC grit, by ceria polishing and acid etching. Precautions were taken to avoid extraneous damage of the test surface during processing to try to obviate non-characteristic defects. Experiments were undertaken to assess the depth of surface flaws. The strength data distributions were assumed to be normal for purposes of comparison, and the results obtained from this programme were used to devise a process schedule so as to leave a minimum of defects on an adequately finished surface.

This schedule was tested on a group of lath samples to ascertain its effectiveness, and the consequent strength data were analysed by Weibull distribution theory.

3. Sample preparation

Two forms of sample were used, discs nominally 100 mm diameter by 5 mm thick, and laths nominally 150 x 25 x 3 mm. They were prepared from either white plate glass supplied as rough cast, 8 mm annealed strip, or from 4 mm float glass, both products of Pilkington Brothers Ltd.

The greater bulk of surface removal was necessary in the initial roughing stage for the as-cast glass by 8" diameter diamond cup wheel, grade 125-150 μ m grit size, metal bonded. Both surfaces of the glass were ground substantially to remove surface undulations and tonear-finish thickness. The discs were cut by diamond impregnated, thin-walled drill operated from both surfaces so as to reduce edge chipping. The roughing stage was not required for the 4 mm float glass stock which was basically worked on one surface only.

Both types of glass were smoothed by aqueous slurries using SiC grits of various grades, and polished by ceria slurry on felt pads.

Different edge finishes were investigated to seek to minimise edge failures which would otherwise introduce data non-characteristic of surface properties. Lath specimens required preferential edge treatments to reduce edge failure incidence.

Contact with the critical area of the test surface by measuring instruments was avoided, and progress through the various stages was monitored via known surface removal rates established on coupons.

The actual surface removal was measured between stages of working on the non-critical area of each sample, i.e. that for laths being outside the span of the four point test rig. In some instances, measurements were possible after fracture but not in the case of strong specimens which produced finely fragmented debris which also obscured the fracture origin.

Discs were processed in batches of five, being wax mounted on a block, and using

a controlled addition of SiC grit slurry against a steel lap. The discs were polished singly on an "Autosphere" polishing machine with a 150 mm felt pad and using a recirculating aqueous ceria slurry, they required usually 4 minutes but longer periods were set on occasion.

Laths were usually prepared by scoring the stock with a wheel cutter, using the scored side as the eventual compression test surface. The edges were worked in blocks of six laths to reduce them to a common width and the edges were arrissed by SiC grit, treating laths individually. After a selective edge etch applied whilst the main surfaces were protected by wax coating, the test surface was stripped and machined again in batches of six samples through smoothing and polishing stages. Working of laths in groups was preferred to achieve consistent process conditions.

For discs, typical surface removal rates measured in simultaneous grinding of five samples were as follows:-

Grade	SiC grit range (μm)	Mean (μm)	Average grinding rate ($\mu\text{m}/\text{hour}$)
320	18 - 46	32	342
400	14 - 34	24	284
600	8 - 25	16	135

Etching of samples was usually done by intermittent dip of groups of samples supported at their ends, in HF solution and then in water baths, thermostatically controlled. The problem of avoiding contact with test surfaces was most acute during this stage, and the process was again monitored by coupon specimens undergoing simultaneous treatment. The use of coupons also served to allow for diminishing etch rates with use of acid.

4. Test configurations

For disc samples, uniform pressure and concentric ring tests were applied and stresses were calculated according to formulae quoted in the appendix. In early studies of 110 mm diameter, 2 mm strengthened glass discs loaded under uniform pressure, bonded strain gauges showed that elementary theory (equation 3) in the appendix, did not apply. An empirical equation was derived and was of similar form to that allowing for the development of membrane stress component in addition to flexure stress but having different coefficients to the theoretical free edge condition. The stress analysis also indicated the differences between radial and tangential stress components off centre. From this study it was concluded that in certain cases, allowance should be made not only for fracture origin location, but also for original crack propagation direction when evaluating an appropriate fracture stress. However in the current tests of the weaker, annealed glass discs, much lower values of dimensionless stress (σ^*) resulted and therefore the elementary formula (equation 3) was deemed to be sufficiently accurate.

Concentric ring tests were applied to reduce the preponderance of edge failures experienced in the uniform pressure tests, and initially, different ring diameters were used to seek to minimise that tendency. Using concentric rings of 68 mm and 50 mm diameters, the incidence of edge failures decreased but there appeared to be a concentration of fracture origins near the inner ring radius which suggested an undesirable stress concentration in that region. Using elementary theory, (equation 7), fracture stresses were calculated and were compared with values obtained in uniform pressure tests. Although some degree of consistency was obtained, variance of test data was so large as to obscure potential differences between various groups of samples.

Tests on lath specimens were accordingly started with promising results in respect of statistical variance. Because these samples were easier to make, the subsequent

test programme was based upon such specimens which were tested under four point bending by a Monsanto-Tensometer 'E' test machine. Adjustment of the cross-head speed allowed the setting of a nominal stress rate of 5 MPa/s. This rate was calculated on assumption of elementary theory but it was found in other tests of chemically strengthened, 2mm thick glass laths, that a more comprehensive analysis may be required. For example, stress data as calculated from simple formula and as computed by numerical solution as per Ritter and Vrooman (27) was compared with data measured by bonded strain gauge up to fracture. A graph of stress versus load showed that non-linear stress-load relationships might become significant for stronger specimens withstanding greater deflections. Again however for annealed glass laths, elementary formulae were deemed adequate and a comparison between rupture moduli for discs under concentric ring tests, with laths under four point bend test gave agreement as illustrated.

It proved convenient to adopt a modified specimen preparation technique in which laths were given a pre-etch before applying surface machining stages. The purpose of this was to ensure the removal of significant defects before applying the final stage whose characteristic strength was to be evaluated. After pre-etch, samples were proof-loaded at 400 MPa for one minute, and survivors, usually about 90% of the original test batch, were then re-surfaced by different processes.

5. Assessment of surface defects

The defective region in a diamond ground glass surface was initially studied by forming a wedge shaped specimen in which ca 300 μm had been removed from one end whereas the other end was virtually untouched. The wedge was formed by using 600 SiC grit slurry, and this ground surface was polished by ceria. The specimen was then ion-exchanged in a $\text{LiNO}_3\text{-KNO}_3$ salt bath at 200°C for 2 hours, and the resulting crack pattern developed by HF dip for 2 minutes. Cracks were observed even at a depth of 300 μm and this observation was checked by repolishing the wedge surface to a further depth of 30 μm , and then subjecting the specimen to a second ion-exchange treatment. This had the effect of suppressing cracks except at the thick end of the wedge and down to a point corresponding to a total surface removal of ca 90 μm . This apparent discrepancy was attributed to the presence of defects introduced by the 600 SiC grit and not fully polished out before the first ion-exchange treatment. The second polishing stage eliminated much of this damage, and it was concluded that the defect layer due to diamond wheel grinding was approximately 90 μm deep.

Defective layer depths were also studied in etched and proof loaded laths which had been ground with particular grits. Groups of similarly processed laths were re-etched to different degrees and the corresponding rupture moduli measured. Pavelcheck (28) found that crack tips were relatively unaffected in early stages of HF etching of soda-lime glass, and he quoted a relationship between fracture stress (σ_0) for an original crack length (C_0) and fracture stress (σ) after etching a layer (δ) from the surface

$$(\sigma/\sigma_0)^2 = \frac{C_0}{C_0 - \delta} \quad (1)$$

This can be re-written as

$$(\sigma_0/\sigma)^2 = 1 - \delta/C_0 \quad (2)$$

and a plot of $(\sigma_0/\sigma)^2$ against δ should asymptotically reach zero when δ approximates to C_0 . Appropriate values for C_0 for different abrasive or polishing powders were evaluated for process conditions applying to this study. Those values were taken to represent minimum surface removal depths necessary to clear pre-existing flaws, and a schedule for progressive surfacing was evolved therefrom. The values ranged from 2 μm for a ceria polished surface ("Optipol 8G") to 22 μm for "Carborundum F400" SiC grit.

A group of 71 samples were processed from the etched, proof-loaded stage through 400, 600 SiC grits and ceria polish to a final light surface etch. After fracture, the fragmentation was almost always too fine to allow identification of fracture origin and it was not possible to distinguish between surface and edge fracture in all but 2 samples which failed unexpectedly at 117 and 148 MPa from the surface. The remaining 69 samples ranged from 464 MPa to 1310 MPa, having a mean of 976 MPa and a standard deviation of 185, i.e. a coefficient of variation of 0.19. These data are shown as a Weibull distribution and a comparison was made against a line of similar slope but equivalent to a characteristic time (τ) of 60s, i.e. the proof load duration. From that it appeared as if 4% of the population had failed at a stress equivalent to or less than proof test. It appeared therefore that some damage had been sustained in this fraction of the population and to this extent the controlled schedule had not resulted in the complete determination of a minimum strength level.

However whilst it is not known what process contributed defects to this weaker fraction of samples, it is clear that a final proof test could be used in practical components to establish a maximum defect intensity.

Acknowledgements

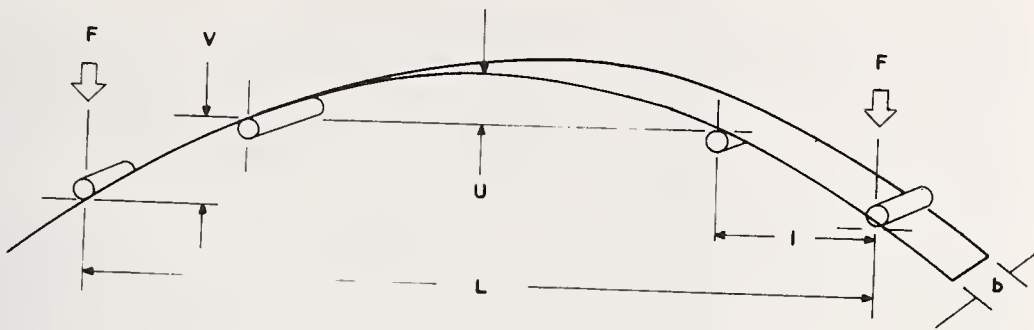
This work has been carried out with the support of the Procurement Executive, Ministry of Defence in the UK. The author wishes to thank the sponsor and the Council of the British Glass Industry Research Association for permission to publish this paper.

6. References

- (1) Brüche, E and Poppa, H., The polishing of glass. Part I - Optical polish, *Glastech. Ber.*, 28 (6) 232-242, (1955)
- (2) Brüche, E. and Poppa, H., The polishing of glass. Part II - Technical polishing of plate glass, *Glastech. Ber.*, 29,(5), 183-191, (1956)
- (3) Levengood, W.C. and Fowler, W.E., Morphology of fractures in polished glass surfaces, *J. Amer. Ceram. Soc.* 40, (1), 31-34, (1957)
- (4) Rawstron, G.O., The nature of polished glass surfaces. *J. Soc. Glass Technol.* 42, 253T-260T, (1958)
- (5) Brüche, E. et al. The polishing of glass (discussion). *Silikattechnik*, 10, (4), 213, (1959)
- (6) Cornish, D.C. The mechanism of glass polishing - a history and bibliography. BSIRA, Res. Rept. No. R 267, (1961)
- (7) Bound, U.M., Cornish, D.C. et al. The mechanism of glass polishing - II The effects of slurry concentration and temperature. BSIRA, Res. Rept. No. R 284, (1962)
- (8) Stoll, R., Forman, P.F., Edelman, J. The effect of different grinding procedures on the strength of scratched and unscratched fused silica. *Symp. Res. Mec. du Verre*, paper I-5, 377-392, (1962)
- (9) Cornish, D.C., Verrall, A.F.D., Watt, I.M. The mechanism of glass polishing. presented at Conference on the Physics of Optical Glass, 3rd-4th October 1963 Pilkington Bros. Ltd., Research Labs., Ormskirk, Lancashire.
- (10) Holland, L. The properties of glass surfaces. 15-73, (Chapman and Hall, 1964)
- (11) Holland, L. The properties of glass surfaces. 53-56, (Chapman and Hall, 1964)
- (12) Mc'Kinney, K.R. and Herbert, C.M. The effect of surface finish on structural ceramic failure. *J. Amer. Ceram. Soc.* 53, (9), 513-516, (1970)

- (13) Holland, L. The properties of glass surfaces, 107-120, (Chapman and Hall, 1964)
- (14) Ernsberger, F.M. A study of the origin and frequency of occurrence of Griffith's micro-cracks on glass surfaces. Advances in Glass Technology, Paper VI, 39, 511-524, (Plenum Press, New York 1962)
- (15) Roark, R.J. Formulas for stress and strain. p.195, (McGraw-Hill, 1954)
- (16) Shand, E.B. Weakening defects in glass. Amer. Ceram. Soc. Bull. 46, (11), 1111-1115, (1967)
- (17) Mecholsky, J.J., Freiman, S.W., Rice, R.W., The effects of surface finish on the strength and fracture of glass. 1977, Proc. XI ICG Conf. (11), 489-497, (Prague 1977)
- (18) Mecholsky, J.J., Rice, R.W. The effect of sputtering on the strength of silicate glass. J. Appld. Phys. 47, (7), 2972-2974, (1976)
- (19) Shelyubskii, V.I., Velikovskaya, N.A., Gutner, S.Kh. Effect of artificially applied surface defects on the strength of sheet glass. Steklo i Keram. 26, (11), 7-9, (1969). Glass and Ceramics 26, (11), 639-642, (1969)
- (20) Orlova, D.A., Kuznetsov, A. Ya., Mechanical strength of components made of various optical materials. Optikomekhanicheskaya promyshlennost (6), 79, (1975)
- (21) Densienko, O.N., Shchlegova, O.V., Soboliev, Ye. V. The effect of etching in HF on the strengthening of glass by means of low temperature ion-exchange 1976, Steklo i Keram. 33, (2), 13-14, (1976) Glass and Ceramics 33, (2), 92-93, (1976)
- (22) Wiederhorn, S.M., Strength of glass - fracture mechanics approach. Proc. X ICG Conf. (11), 1-13, (Kyoto 1974)
- (23) Lenoe, E.M., Neal, D.M. Assessment of strength-probability-time relationships in ceramics. AMMRC TR 75-13, pp. 22 (1975)
- (24) Davidge, R.W., McLaren, J.R., Tappin, G. Strength-probability-time relationships in ceramics. J. Mat. Sc., 8, 1699-1705, (1973)
- (25) Ritter, J.E., Laporte, R.P. Effect of test environment on stress-corrosion susceptibility of glass. J. Am. Ceram. Soc. 58, (7-8), 265-272, (1975)
- (26) Ritter, J.E., Meisel, J.A. Strength of failure predictions for glass and ceramics. J. Am. Ceram. Soc. 59, (11-12), 478-481, (1976)
- (27) Ritter, J.E., Vrooman, D.L., Rep. Themis-UM-69-4, Contract OWR-N00014-A-0146-3, (1969)
- (28) Pavelchek, E.K., Doremus, R.H. Fracture strength of soda-lime glass after etching. J. Mat. Sc. 9, 1803-1808, (1974)

Appendix 2. Bend test rig and formulae for lath samples



Where $M = F\ell$, $I = bt^3/12$, $2F = W$

Maximum deflection $(u + v) = \frac{M}{24EI} (3L^2 - 4\ell^2)$

$u = \frac{M}{8EI} (L - 2\ell)^2$, $v = \frac{M\ell}{6EI} (3L - 4\ell)$

max stress $\sigma = \frac{Mt}{2I}$, max strain $\epsilon = \frac{Mt}{2EI}$

substituting experimental parameters

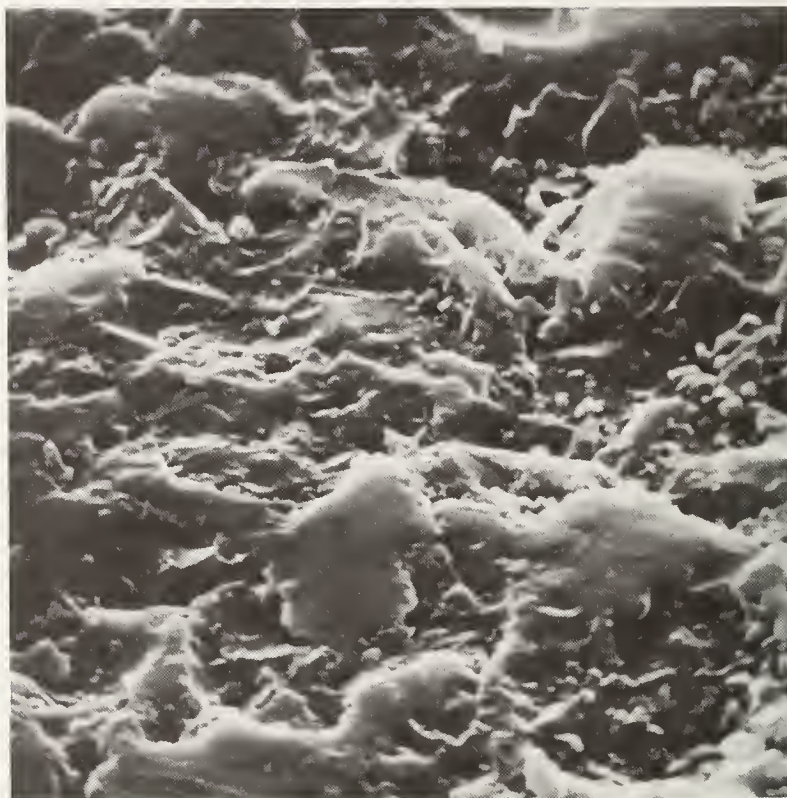
$L = 127 \text{ mm}$, $\ell = 44.5 \text{ mm}$, $E = 73 \text{ GPa}$

thickness $t = 3.5 \text{ mm}$, $\dot{v} = 3.5 \text{ mm/minute}$

stress rate $\dot{\sigma} = \frac{3Et\dot{v}}{\ell(3L-4\ell)} = 4.95 \text{ MPa/s}$

strain rate $\dot{\epsilon} = 68 \times 10^{-6}/\text{s}$

(a)

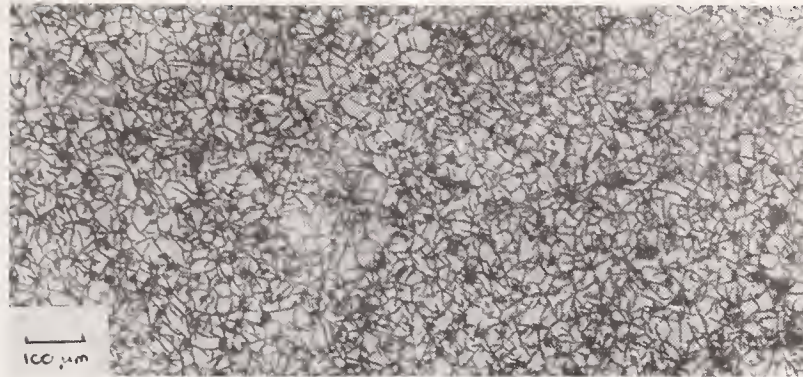


(b)

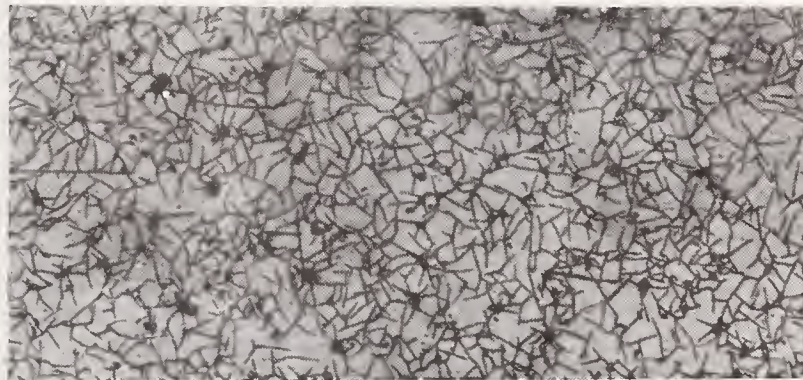


Figure 1. Photomicrographs by scanning electron microscope of a glass surface after diamond grinding (a) and 320 SiC smoothing (b) at 2400 x magnification.

(a)



(b)



(c)



Figure 2. Crack patterns after first ion-exchange of a glass specimen, wedge ground and polished after diamond grinding (a) at $60\ \mu\text{m}$ from original surface, (b) at $210\ \mu\text{m}$ and (c) at about $300\ \mu\text{m}$ depth.

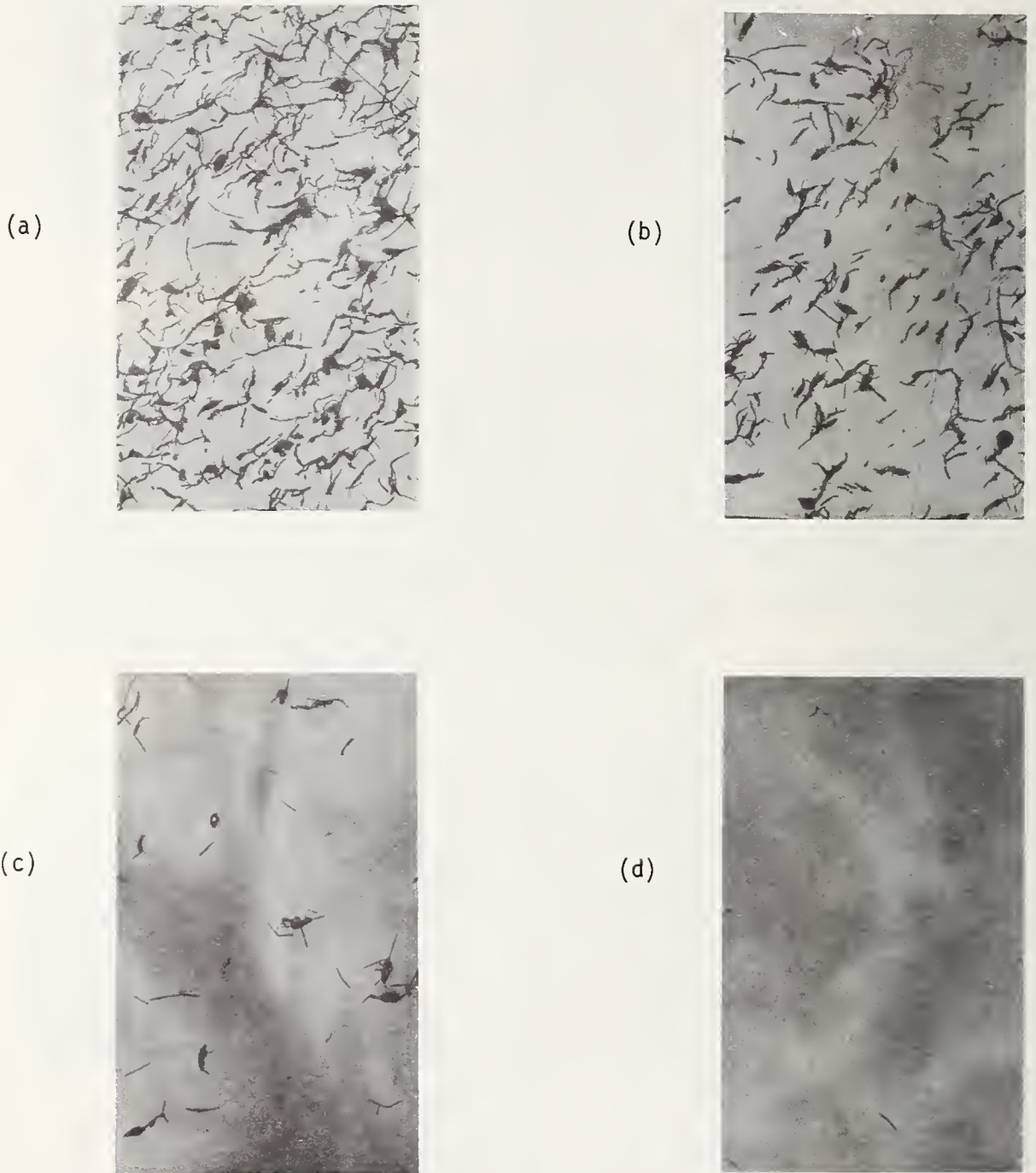


Figure 3. Crack patterns in wedged specimen as in figure 2 but after re-polishing and a second ion-exchange treatment; (a) at 20 μm from original surface, (b) at 40 μm , (c) at 65 μm and (d) at 90 μm depth.

SURFACE FLAW EFFECTS ON CRACK PROPAGATION FROM SUBSONIC WATER DROP IMPACT¹

Y. Marvin Ito and Martin Rosenblatt

California Research & Technology, Inc.
Woodland Hills, Ca. 91367

The effects of surface flaws on ceramic target damage from subsonic water drop impacts are investigated using numerical code simulations based on fundamental wave propagation and fracture mechanics concepts. The water drop impact generates a tensile stress wave with a steep near-surface gradient. As a consequence of this steep stress gradient, crack activation is dependent on the depth of surface flaws. In addition, a relatively large flaw can perturb the stress field such that crack activation in its vicinity is suppressed.

Key Words: Crack activation; numerical simulation; subsonic water drop impact; surface flaws.

1. Introduction

The damage of a ceramic target from a subsonic water drop impact is dependent on the tensile stresses generated by the impact and the criteria for the extension of flaws exposed to the tensile stress field. Since the target response is essentially elastic, the maximum tensile stresses are the radial stress components. Also, the tensile stress field has a steep near-surface gradient. Thus, these radial stresses tend to produce circumferential cracks which initiate at the surface and propagate into the target [1]².

As a consequence of the relatively steep near-surface stress gradient, it is expected [1] that crack activation is dependent on the depth of surface flaws (exposed to this stress gradient). It is the intent of this paper to analyze this effect for specified impact conditions.

2. Approach

A series of *numerical simulations* are performed in order to examine the effects of surface flaws on *zinc selenide* window damage from subsonic water drop impact. The normal impact conditions of a $2R_0$ diameter water drop onto the window target at velocity V_0 is shown in figure 1. A finite-difference computer code, WAVE-L, with an analytic pressure loading model is used to predict the target response.

WAVE-L is a two-dimensional (axial or plane symmetry), Lagrangian, explicit, finite-difference code based on the HEMP scheme [2] which integrates the governing partial differential equations of motion for arbitrary dynamic problems in solid and fluid mechanics. It has been applied in a number of particle impact investigations, including both subsonic [3] and hypersonic [4] erosion.

The analytic pressure loading model has been developed for simulating subsonic water drop impacts and is discussed elsewhere [5]. The impact model specifies the loading pressure on the target surface as a function of radius from the impact point and time, $P(r,t)$.

¹Research supported by Office of Naval Research under Contract No. N00014-77-C-0790.

²Figures in brackets indicate the literature references at the end of this paper.

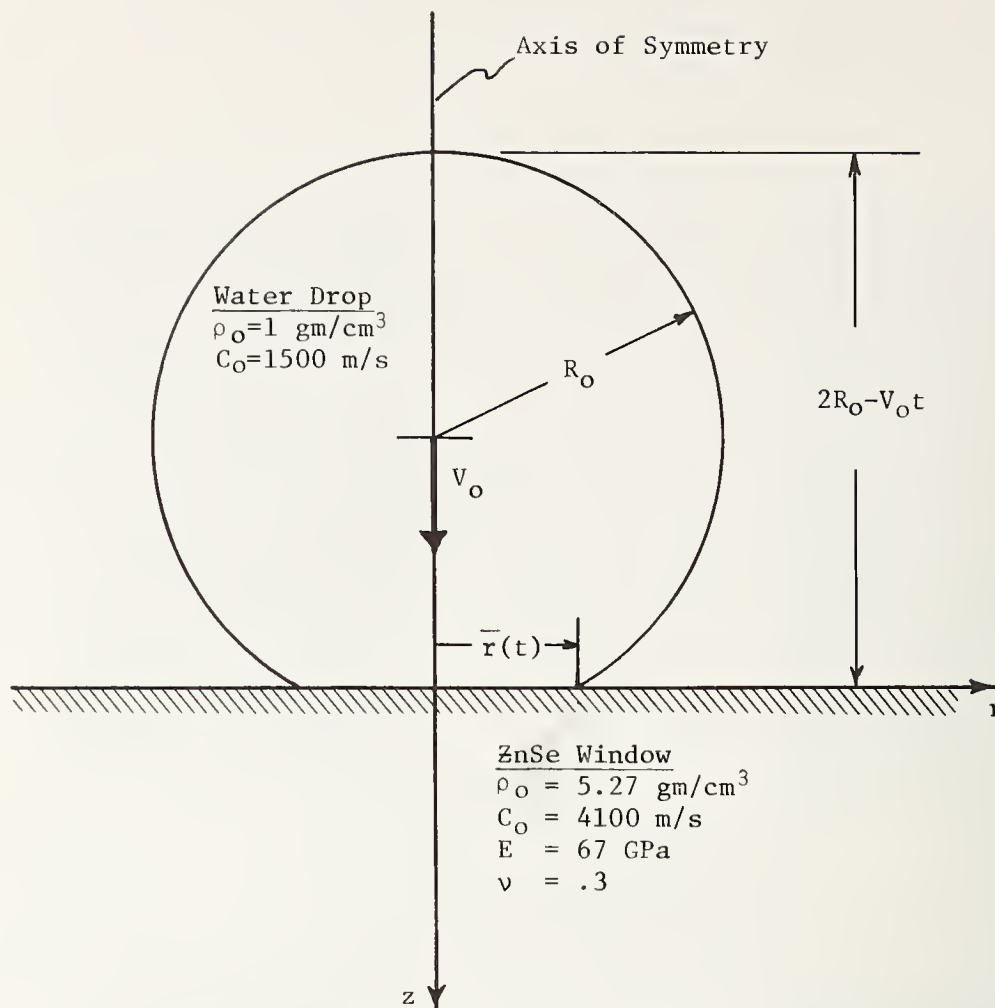


Figure 1. Normal impact conditions of $2R_0$ water drop onto zinc selenide (ZnSe) window at velocity V_0 .

The development of this analytic loading model was based on *detailed* WAVE-L numerical calculations [5] of spherical water drop impact onto a rigid surface. The rigid surface approximation is valid when the target surface deflection is negligible compared to the drop radius. For elastic materials, this condition is satisfied if the target material impedance (density times wave speed) is much greater than the water impedance. The zinc selenide targets described in this paper have an impedance which is 14 times greater than water. Hence, the *decoupled* approach is justified in the present case.

The loading pressure function, $P(r,t)$, for a water drop of 2-mm diameter ($2R_0$) impacting at 222 m/s (730 fps) velocity (V_0) onto a zinc selenide (ZnSe) window target has been determined [5]. Figure 2 gives the maximum impact pressure profile. Due to the spherical geometry and water material properties, an off-axis peak³ pressure occurs (at early times) which is about twice the Hugoniot value. This peak pressure occurs when the velocity of the radius of contact (\bar{r} in fig. 1) approximately equals the speed of sound (C_0) in water [5].

This impact pressure $P(r,t)$ is used as the loading boundary condition for the axisymmetric WAVE-L numerical calculation of the ZnSe target response. Figure 3 shows the initial computational grid for the target material using 80 cells per water drop diameter ($2R_0 = 2\text{mm}$). In the WAVE-L code, particle velocity is defined at the corners of the computational cells while the stress state is associated with the center of the cells.

³Note that this pressure peak will not occur for subsonic *solid* particle impacts, and observed differences in target response from solid versus liquid projectile impacts may be partially due to the presence of the off-axis pressure peak.

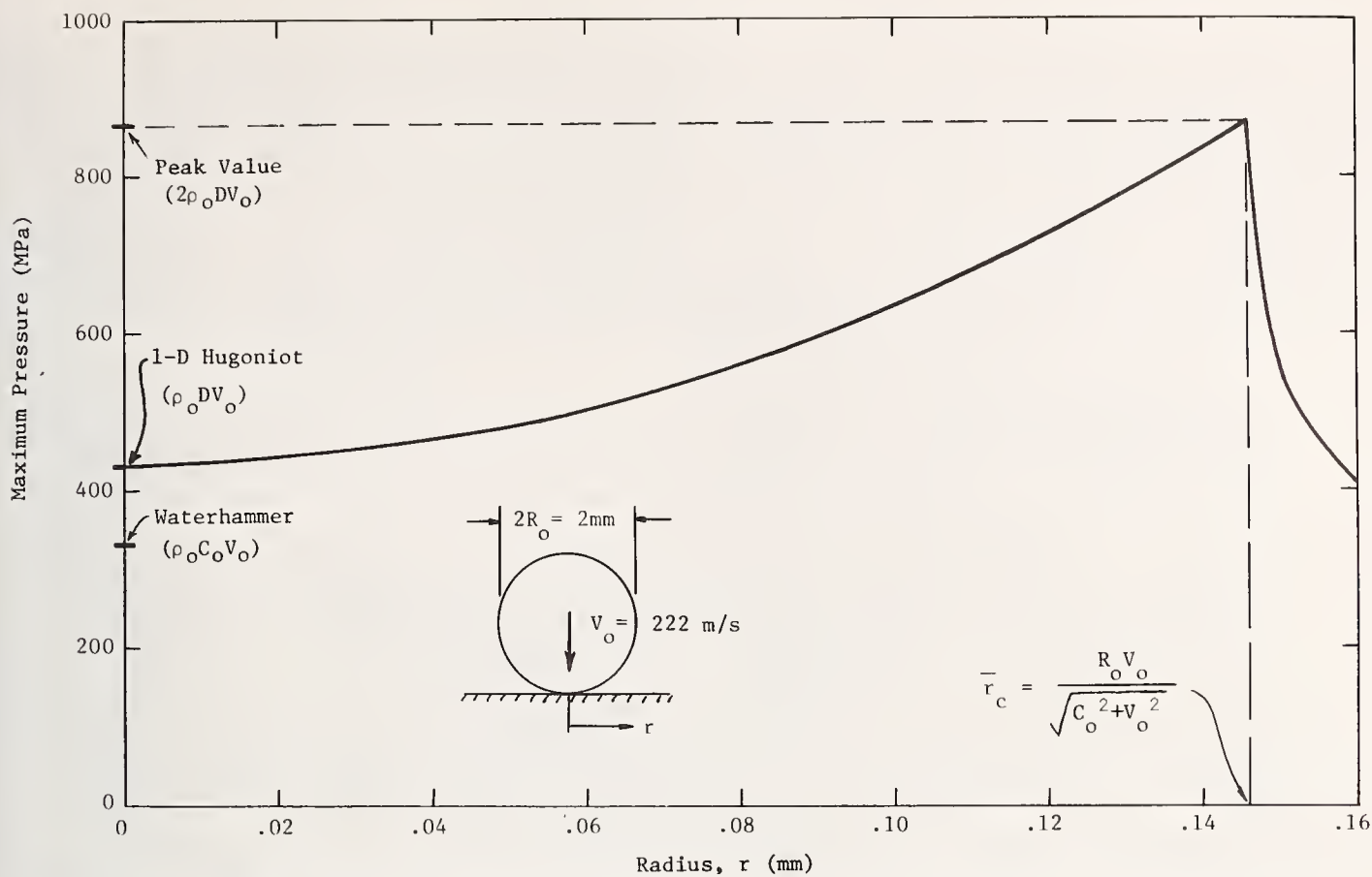


Figure 2. Maximum impact pressure as a function of radial distance from impact center for 222-m/s impact of 2-mm water drop onto ZnSe window.

CALIFORNIA RESEARCH AND TECHNOLOGY, INC.
ZNSE WINDOW IC

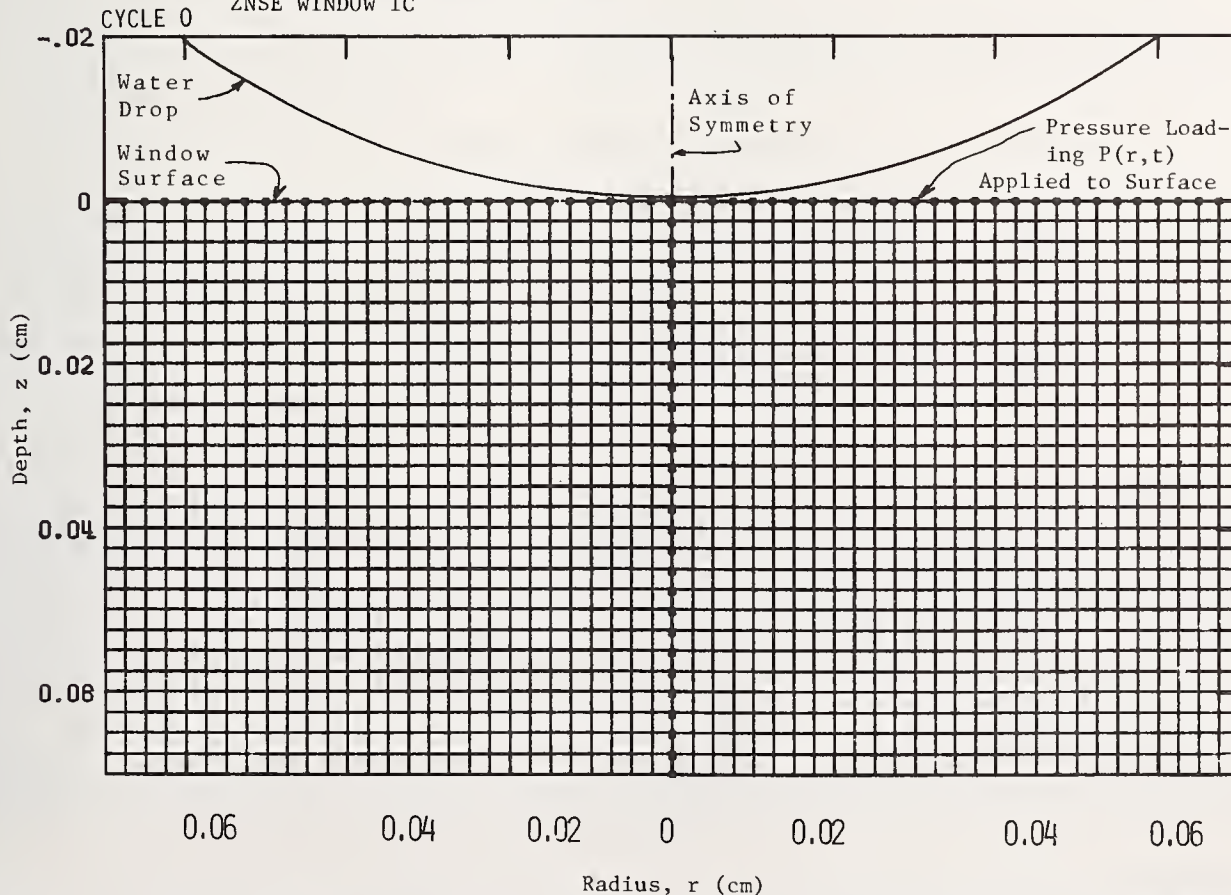


Figure 3. Initial computational grid in target material using cells per 2-mm water drop diameter.

Figure 4 indicates typical *elastic response* of a ZnSe window in terms of the particle velocity field and principal in-plane (r, z) *tensile* stress field at $0.1 \mu\text{s}$. The velocity vectors show the magnitude and direction of the velocity of the particle mass located at the tail of the vector. A 15-m/s (50-fps) scale bar is shown in the upper right corner of the figure. The principal tensile stresses are indicated by lines which show their magnitude and direction in the r - z plane. (Hoop tensile stresses are not indicated on these plots.) A 1-bar (14500-psi) scale bar is shown in the upper left corner of these plots. Thus, at $0.1 \mu\text{s}$ after the impact, the peak velocities are roughly 15 m/s (50 fps) in the target and the peak tensile stresses are about 2 kbar (30000 psi).

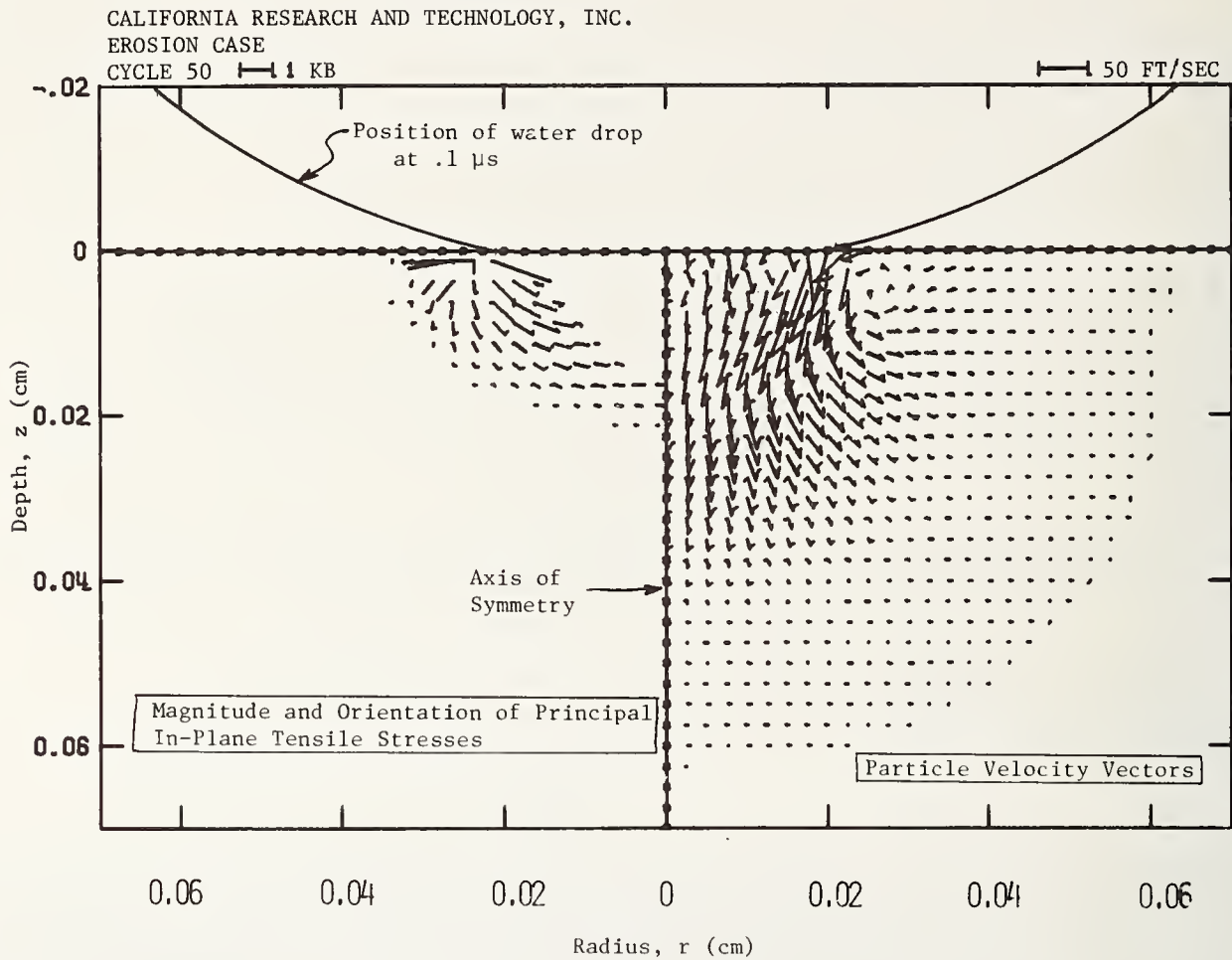


Figure 4. Elastic response of ZnSe window for 222-m/s impact of 2-mm water drop at $0.1 \mu\text{s}$ (80 computational cells per drop diameter).

It is seen that a region of high tensile stresses occurs *near* the surface, outside the contact area. The material directly under the contact area is in pure compression. Figure 5 shows the corresponding velocity and in-plane tensile stress fields at $0.2 \mu\text{s}$. The qualitative features are similar to the $0.1\text{-}\mu\text{s}$ plot; however, the peak velocities and peak tensile stresses have already decayed below the $0.1\text{-}\mu\text{s}$ values.

The specified impact conditions used in the present numerical simulations involve 222 m/s (730 fps) impact of 2-mm diameter water drop onto zinc selenide windows. These conditions are considered to be representative of subsonic liquid drop impact onto ceramic targets. In the following, Section 3 gives details of the near-surface stress gradient, Section 4 shows the effect of surface flaws and Section 5 has the concluding discussion.

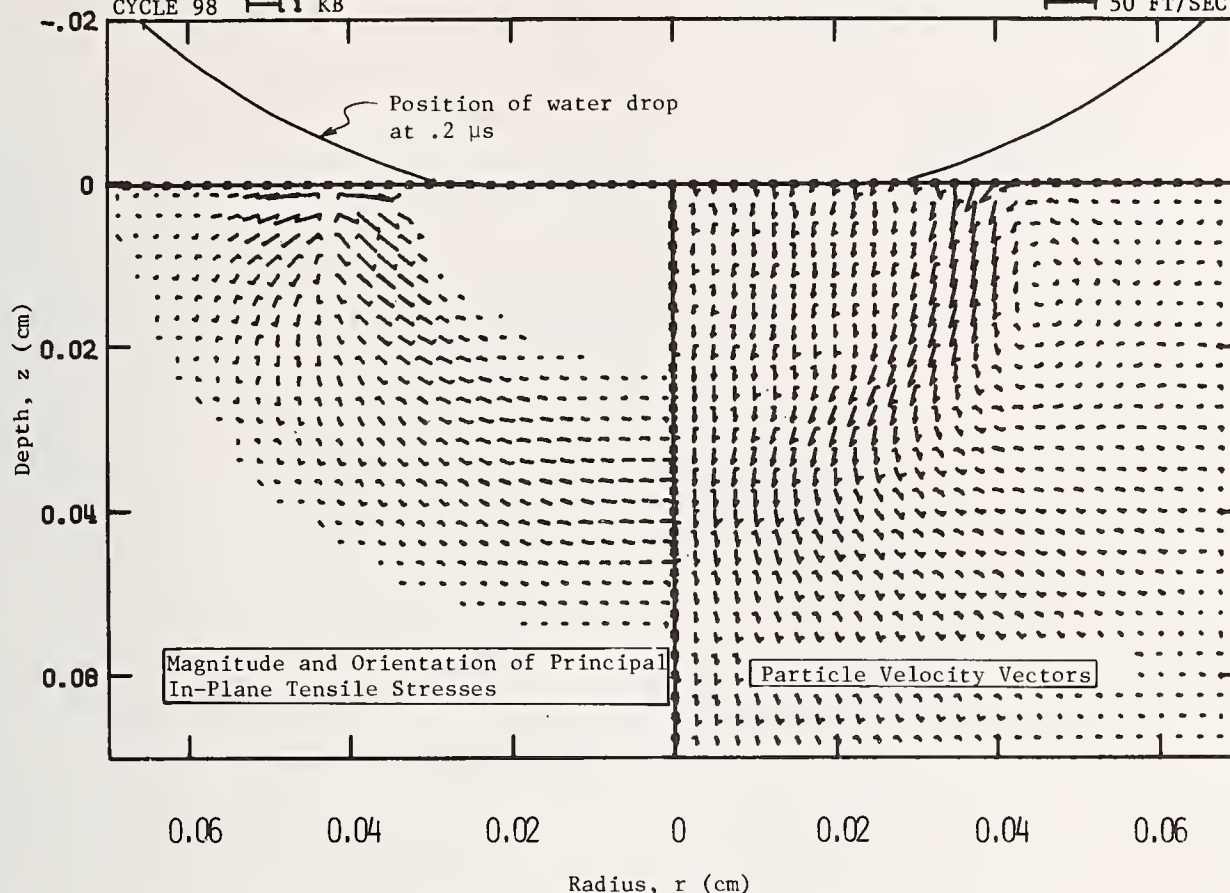


Figure 5. Elastic response of ZnSe window for 222-m/s impact of 2-mm water drop at 0.2 μ s (80 computational cells per drop diameter).

3. Near-Surface Stress Gradient

The formation of high tensile stresses near the surface of a ZnSe target impacted by a water drop is illustrated in figures 4 and 5 (Section 2). In this numerical simulation the initial computational grid (fig. 3 in Section 2) has 40 cells per water drop radius. Since the effective prediction of crack activation requires that these high tensile stresses be well characterized, an appropriate fine-zoned computational grid must be selected. Some calculations, employing selected fine-zoned computational grids in the near-surface impact region, provide a basis for selecting the grid structure for subsequent crack activation experiments.

Figure 6 shows the peak tensile stress versus depth in a ZnSe window impacted by a water drop at 222 m/s (730 fps) for three variations in computational cell size. Note the very steep stress gradient near the impact surface and its increased resolution⁴ with decreased cell size (where stress is defined at the cell center). For a water drop of 1-mm radius⁵ the finest-zoned (80 cells per drop radius) case is adequate to resolve peak tensile stress from 356 MPa (52000 psi) at a depth of about 6 μ m to 80 MPa (12000 psi) at 100 μ m depth.

⁴ In fact, an analytic solution by Blowers [6] predicts *infinite* peak tensile stress at the impact surface for purely elastic targets.

⁵ Note that these elastic solutions can be scaled linearly in dimensions and time for other drop radii as long as the impact velocity and material properties are not changed.

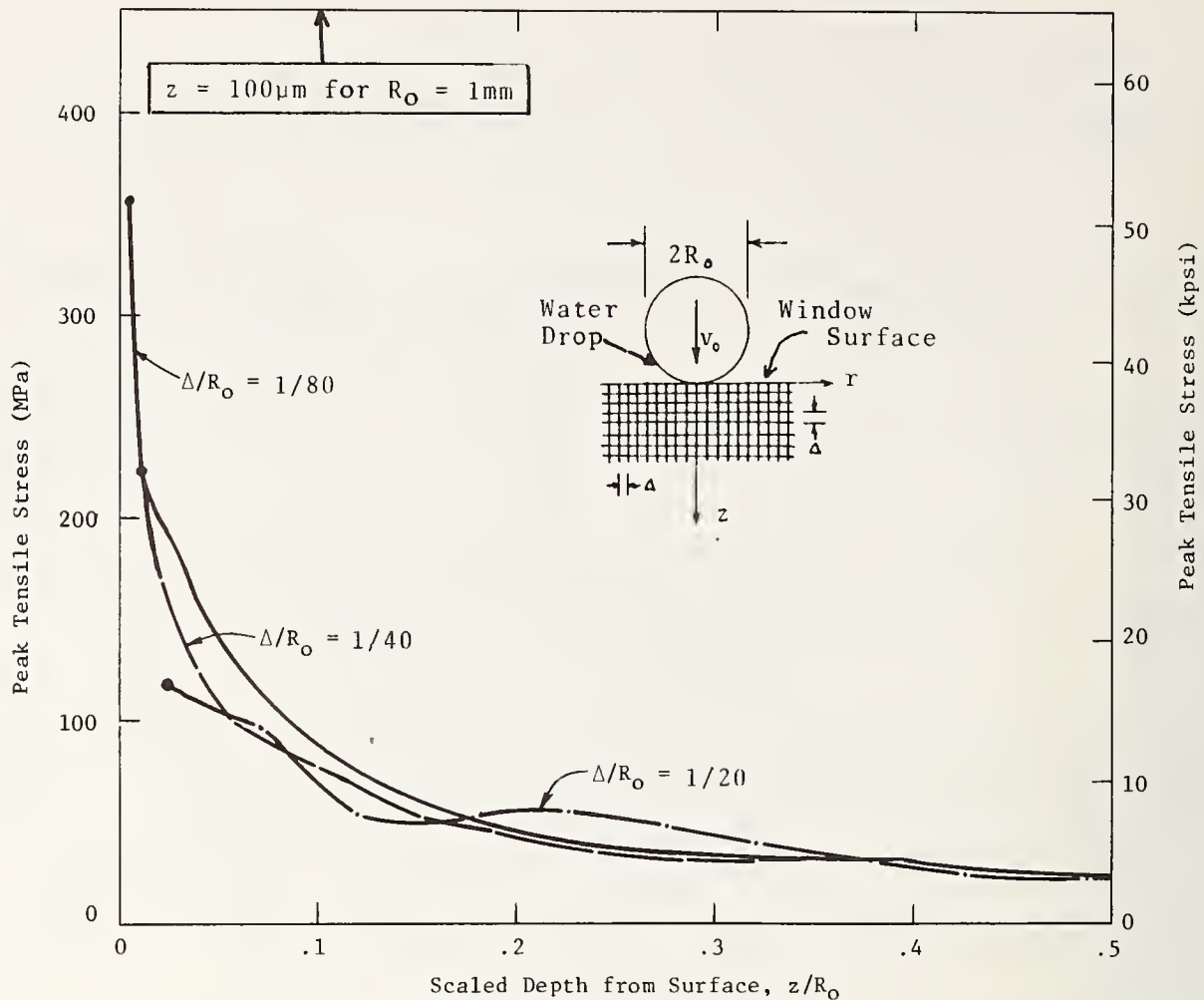


Figure 6. Peak tensile stress versus depth (for all radii) in a ZnSe window impacted by a water drop at 222 m/s for variations in computational cell size.

Figure 7 shows the peak tensile (radial) stress near the surface versus radius. The results are from the surface computational cells which have stress defined at the cell center depth of $z = R_0/160$ or $6.25 \mu\text{m}$. The maximum in the peak tension (356 MPa) occurs at radius $r_p \approx 0.2 R_0$ or $200 \mu\text{m}$. For $r < 0.1 R_0$ or $100 \mu\text{m}$ no tension develops in the target surface. At radius $2 r_p \approx 0.4 R_0$ or $400 \mu\text{m}$ the peak tension has dropped to only 200 MPa (30000 psi). The nominal static tensile strength of ZnSe is about 45 MPa (6500 psi).

The temporal development of the radial tensile stress at four radial locations ($3/4 r_p$, r_p , $3/2 r_p$ and $2 r_p$) near the target surface is given in figure 8. The pulse duration (which is about 30 ns at the maximum tension location r_p) increases with radial location (~ 60 ns at $3/2 r_p$ and ~ 75 ns at $2 r_p$).

The effect of a surface flaw of depth $R_0/80$ or $12.5 \mu\text{m}$ at radius $r_p \approx 0.2 R_0$ or $200 \mu\text{m}$ on the peak radial tensile stress is shown on figure 9. For this flaw, the stress gradient ahead of the crack tip is similar to that from the surface without a flaw, but the maximum in the peak radial tension is about 10 percent less.

It is concluded that the effects of surface flaws of depths from $10 \mu\text{m}$ and greater, which are exposed to these stress gradients, should be well characterized in subsequent crack activation experiments using the fine-zoned computational grid with 80 cells per drop radius.

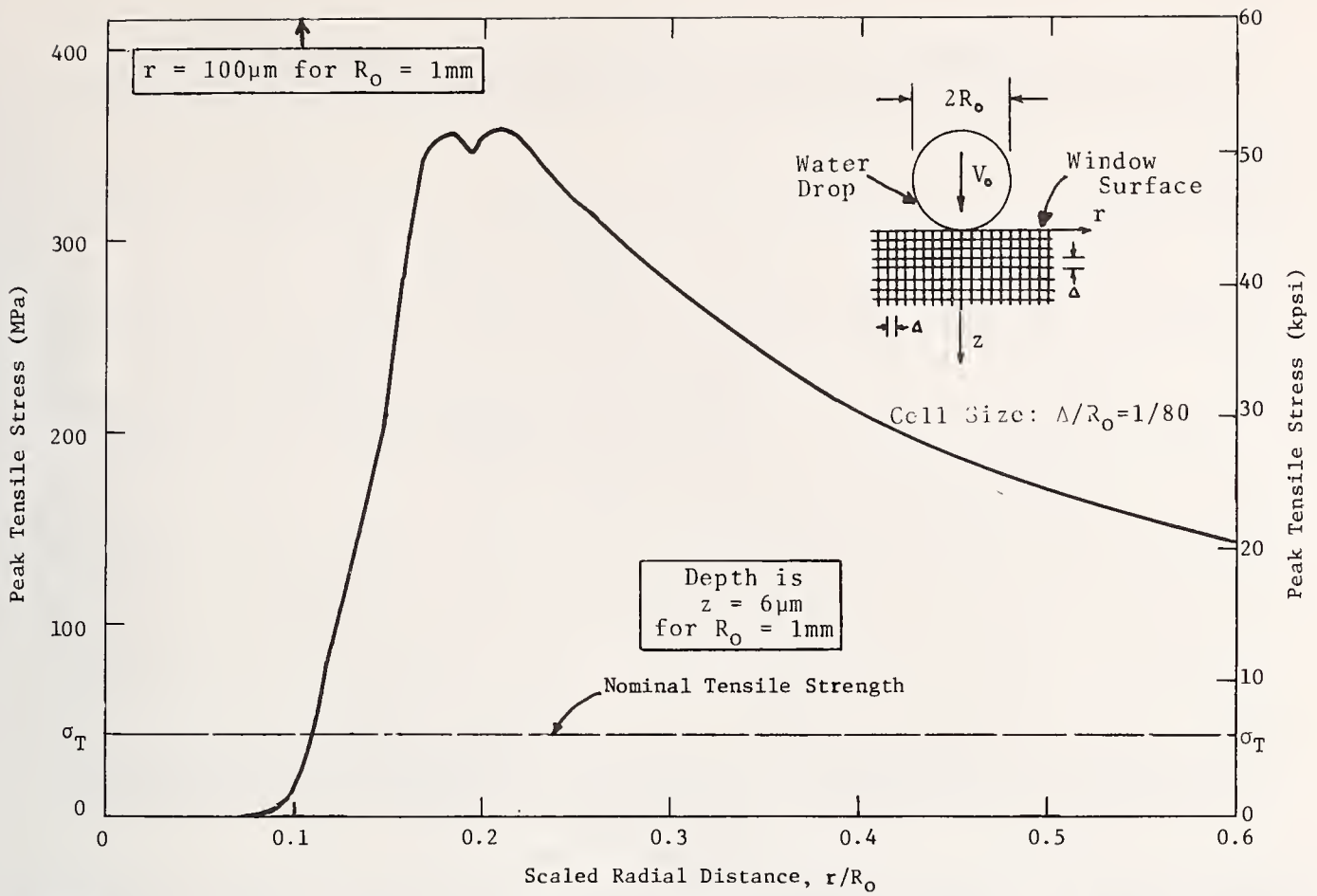


Figure 7. Peak tensile stress versus radius near the surface ($z=\Delta/2$) of a ZnSe window impacted by a water drop at 222 m/s.

CALIFORNIA RESEARCH AND TECHNOLOGY, INC.
 ONR HIGH STRESS GRADIENT CASE
 RADIAL TENSION TIME HISTORIES AT $Z = .000825$ cm for $R_0 = .1$ cm

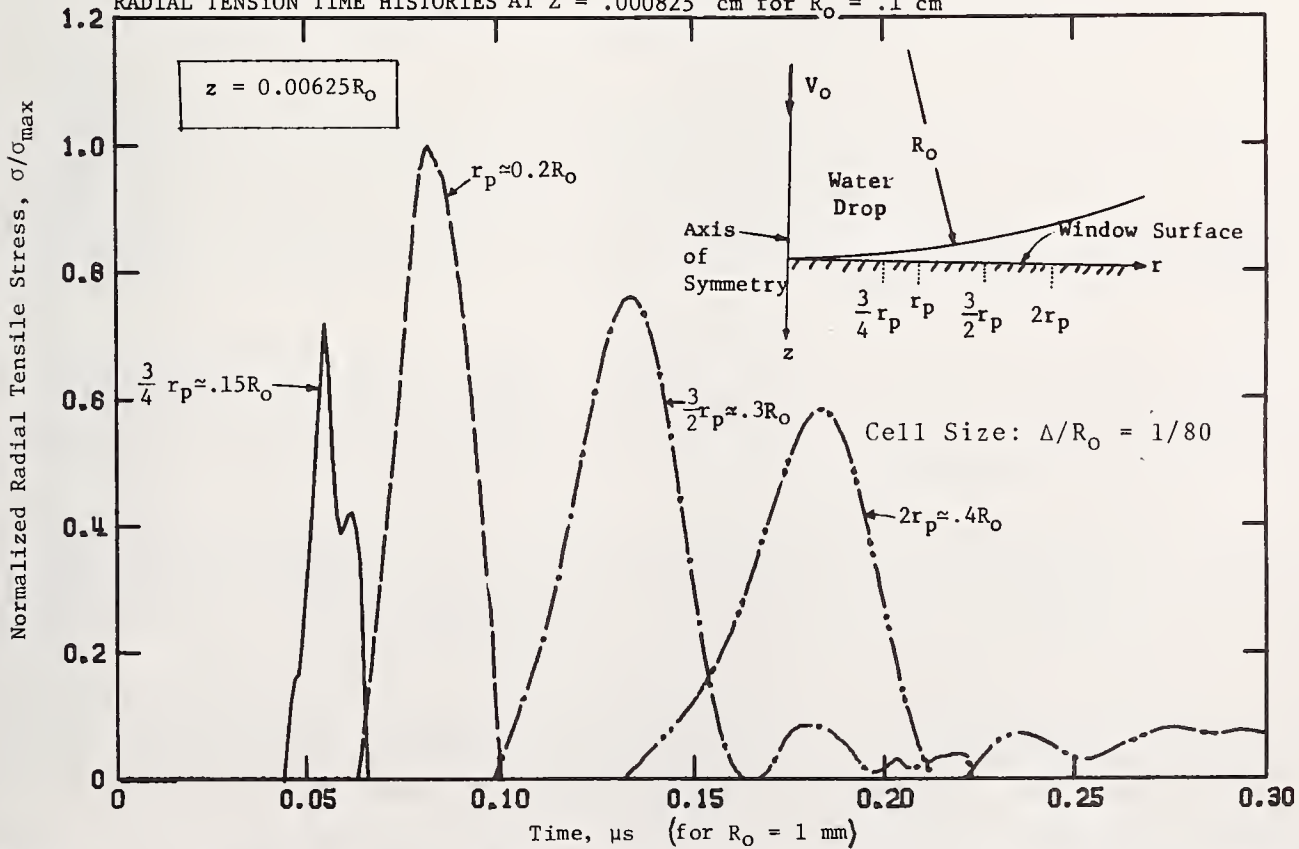


Figure 8. Normalized ($\sigma_{\max}=356$ MPa at $r=r_p$) radial tensile stress histories near surface ($z=\Delta/2$) for impact ($V_0=222$ m/s) of ZnSe window by a water drop ($R_0=1$ mm).

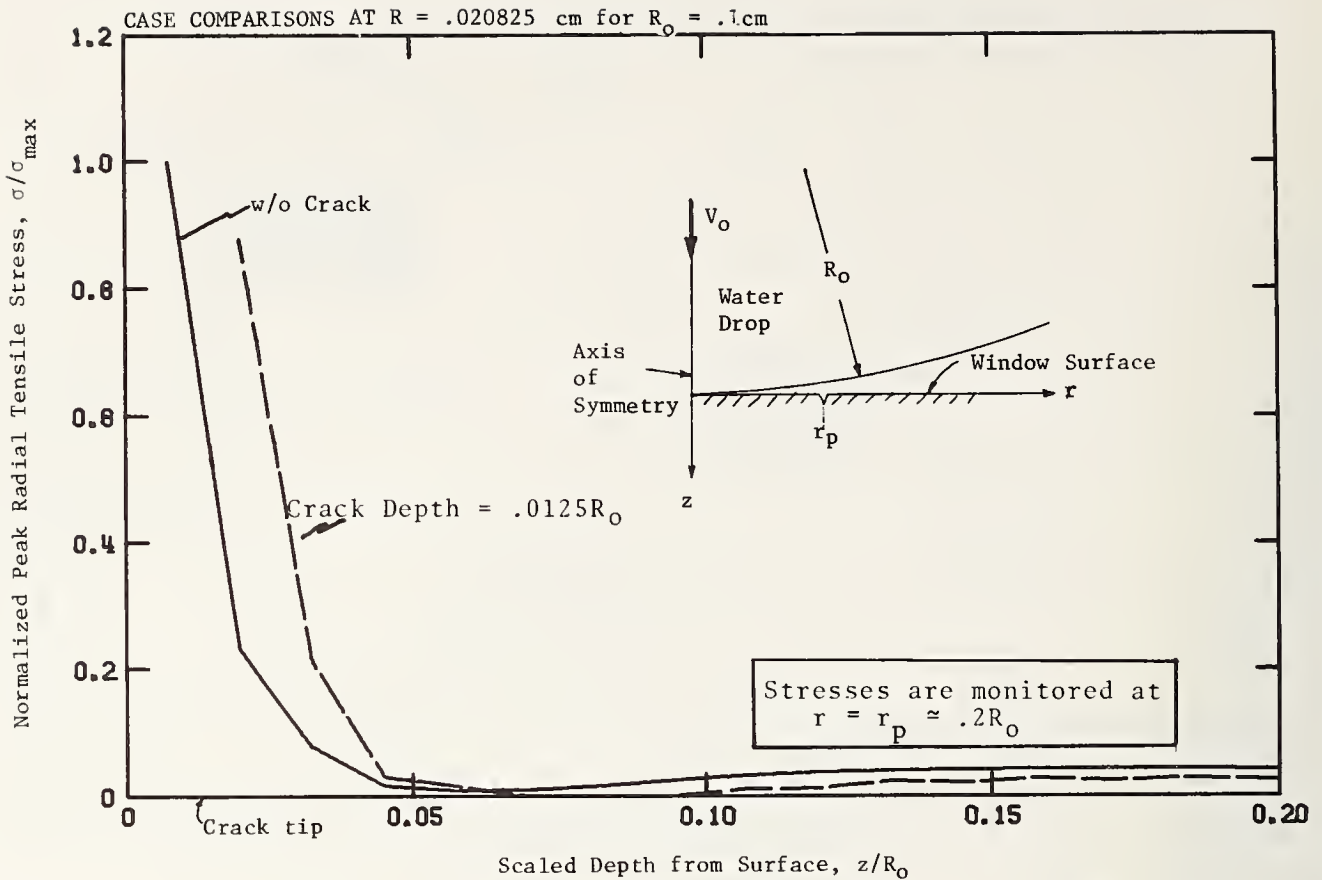


Figure 9. Effect of surface hoop crack at $r=r_p$ on normalized ($\sigma_{max}=356$ MPa) peak radial tensile stress versus scaled depth at $r=r_p$ for impact ($V_0=222$ m/s) on ZnSe window by a water drop ($R_0=1$ mm).

4. Surface Flaw Effects

In the numerical code a flaw is simulated as "tensile" cracks across computational cells near the surface. In a cell with an initial crack, no tensile stress across the crack is permitted, and no shear stress is permitted on the crack if the crack is open (the width of the crack is continuously monitored). These stress adjustments are important because a crack frequently alters the local stress field in such a way as to enhance its own growth. Thus, any realistic method of predicting crack growth must consider the altered stress field.

The crack activation experiments involve surface flaws of various depths located at radius $3/2 r_p \approx 0.3 R_0$ or $300 \mu\text{m}$. At this location, *without* a flaw, the maximum radial tensile stress is about 285 MPa and a tensile stress gradient develops to a depth of $z \approx 0.075 R_0$ or $75 \mu\text{m}$ (see fig. 10). Also, the tensile pulse duration near the surface is about 60 ns (see fig. 8 in Section 3).

Figure 10 shows the effect of surface hoop (circumferential) flaws on the radial tensile stress gradient ahead of the crack tip for crack depths of 25, 50, and $100 \mu\text{m}$ ($R_0=1$ mm). In each case, the peak radial tensile stress ahead (one-half a cell dimension) of the crack tip is enhanced, but decreases with increasing flaw depth.

Figure 11 shows the effect of the flaws at radius $3/2 r_p \approx 0.3 R_0$ or $300 \mu\text{m}$ on the peak radial tensile stress gradient monitored downstream at radius $2 r_p \approx 0.4 R_0$ or $400 \mu\text{m}$. A factor of four reduction (from the no flaw case) is observed near the surface for the $100 \mu\text{m}$ ($R_0=1$ mm) deep flaw. (Note that the stress profile upstream at $r_p \approx 0.2 R_0$ or $200 \mu\text{m}$ remains essentially unaffected by the flaws.)

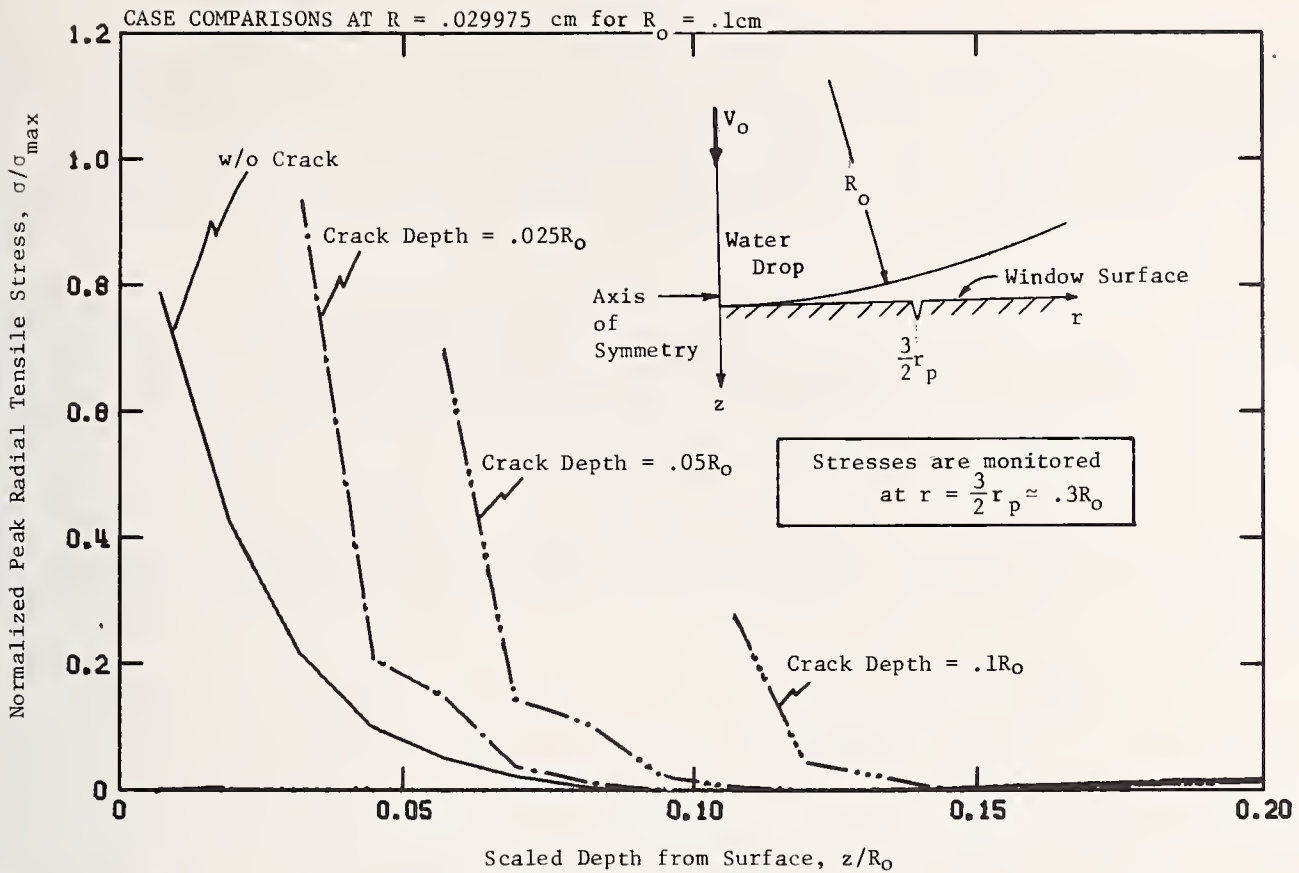


Figure 10. Effect of surface hoop cracks at $r=3/2r_p$ on normalized ($\sigma_{\max}=356$ MPa) peak radial tensile stress versus scaled depth at $r=3/2r_p$ for impact ($V_0=222$ m/s) of ZnSe window by a water drop ($R_0=1$ mm).

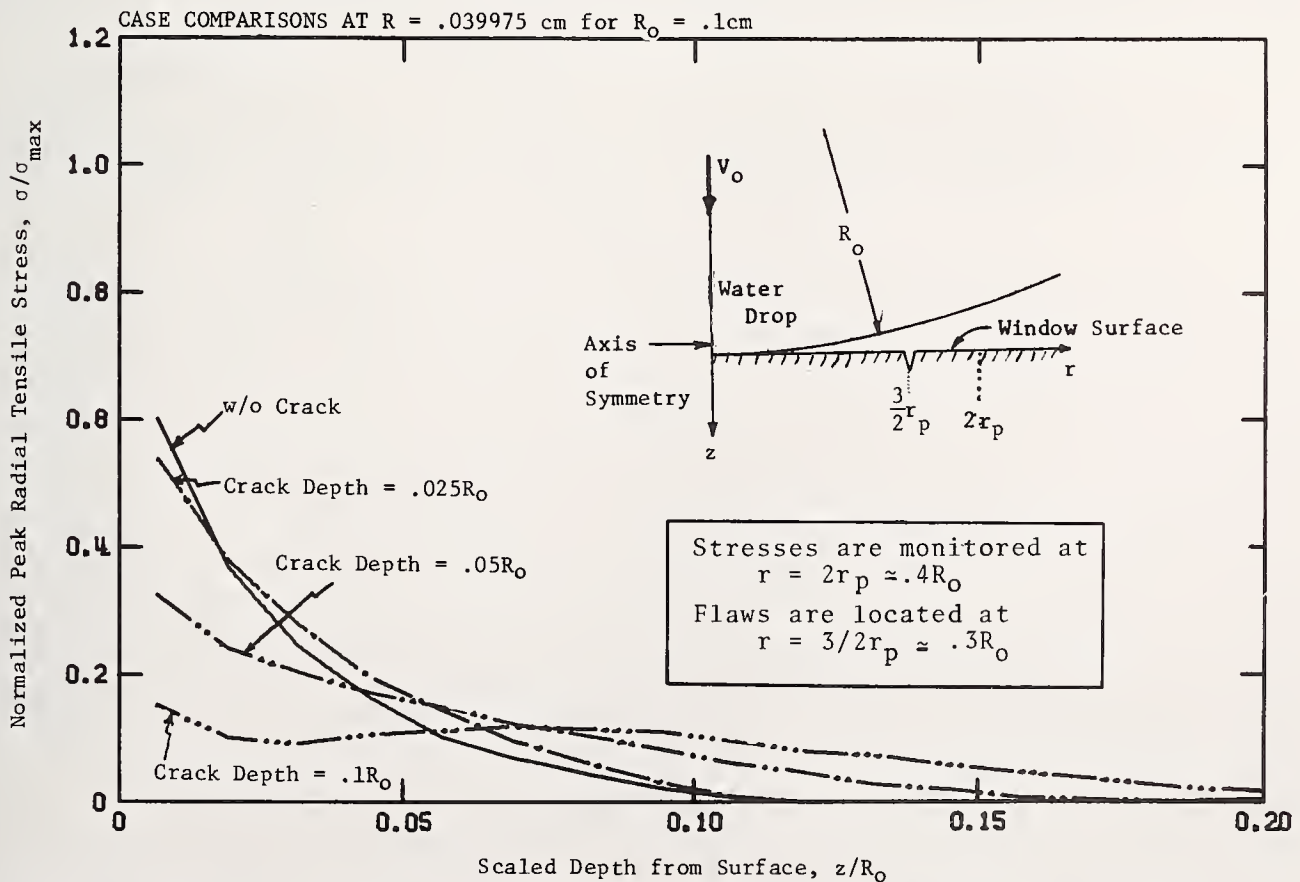


Figure 11. Effect of surface hoop cracks at $r=3/2r_p$ on normalized ($\sigma_{\max}=356$ MPa) peak radial tensile stress versus scaled depth at $r=2r_p$ for impact ($V_0=222$ m/s) of ZnSe window by a water drop ($R_0=1$ mm).

5. Discussion

The effects of surface flaws on ceramic target damage from subsonic water drop impacts are investigated using numerical code simulations. The pressure pulse due to water drop impact generates a tensile stress wave with a steep near-surface gradient. Figure 12 shows a schematic view of the effect of a surface flaw on the near-surface tensile stress profile. Upstream profiles remain essentially unchanged, while downstream profiles have reduced gradients and peak value at surface.

Using the stress intensity approach of fracture mechanics, the stress intensity factor, K_I , can be obtained⁶, as shown in figure 12, and crack activation is defined by the condition where $K_I \geq K_C$. Figure 13 shows the peak stress intensity factor for various surface flaws based on the results of the crack activation experiments from Section 4 (see fig. 10). For a toughness value of $K_C = 1 \text{ MPa}\sqrt{\text{m}}$, surface flaws of depth greater than $75 \text{ }\mu\text{m}$ will not propagate.

Thus, as a consequence of the steep stress gradient, surface crack activation under water drop impact is dependent on the depth of surface flaws. In addition, a relatively large surface flaw can perturb the stress field such that crack activation in its vicinity is suppressed.

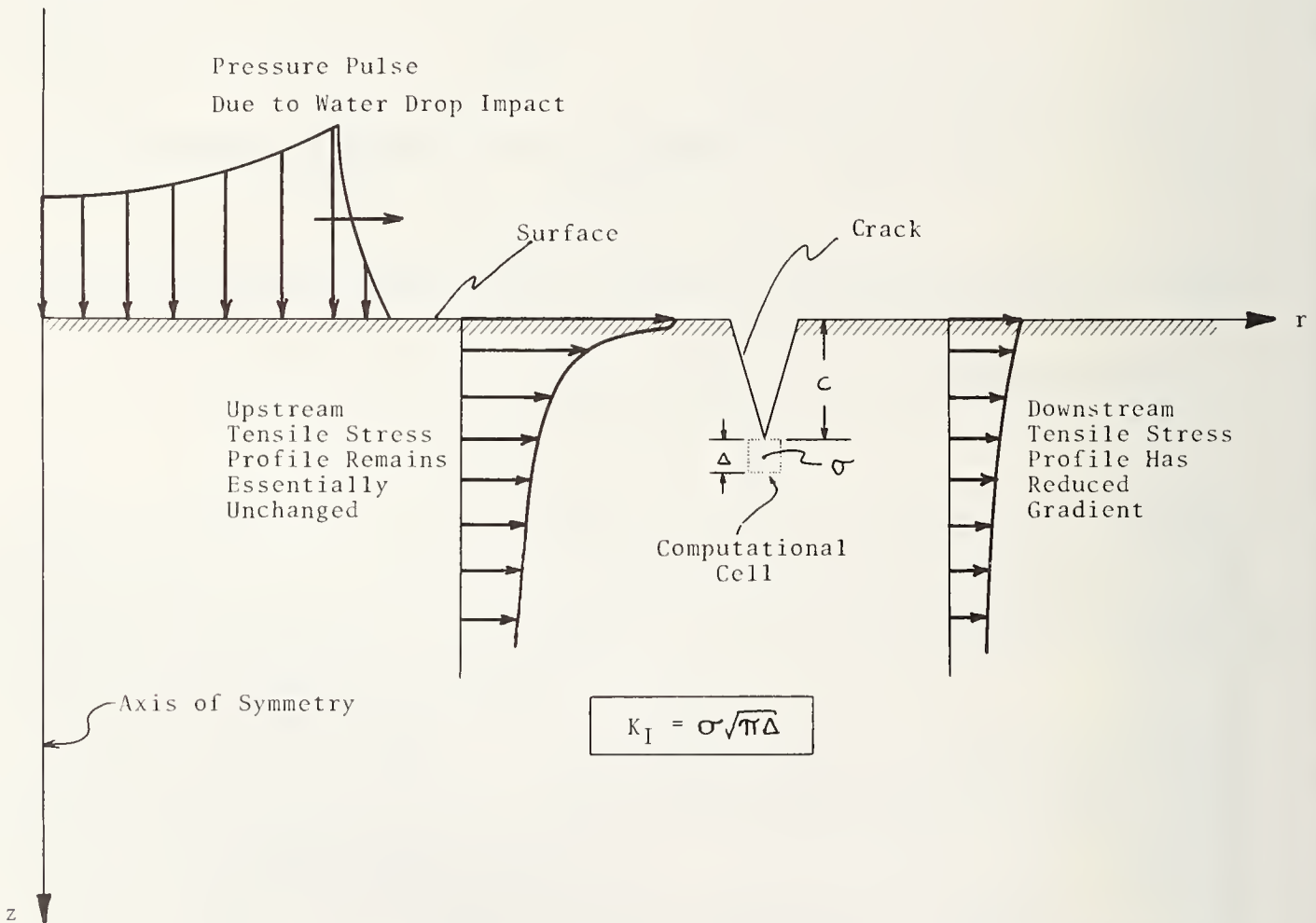


Figure 12. Schematic view of effect of a surface flaw on near surface tensile stress profile and associated stress intensity factor.

⁶ The stress intensity factor is calculated from

$$K_I = \sigma \sqrt{2\pi \frac{\Delta}{2}} = \sigma \sqrt{\pi \Delta}$$

where σ is the radial stress located one-half a cell dimension, $\Delta/2$, from the crack tip.

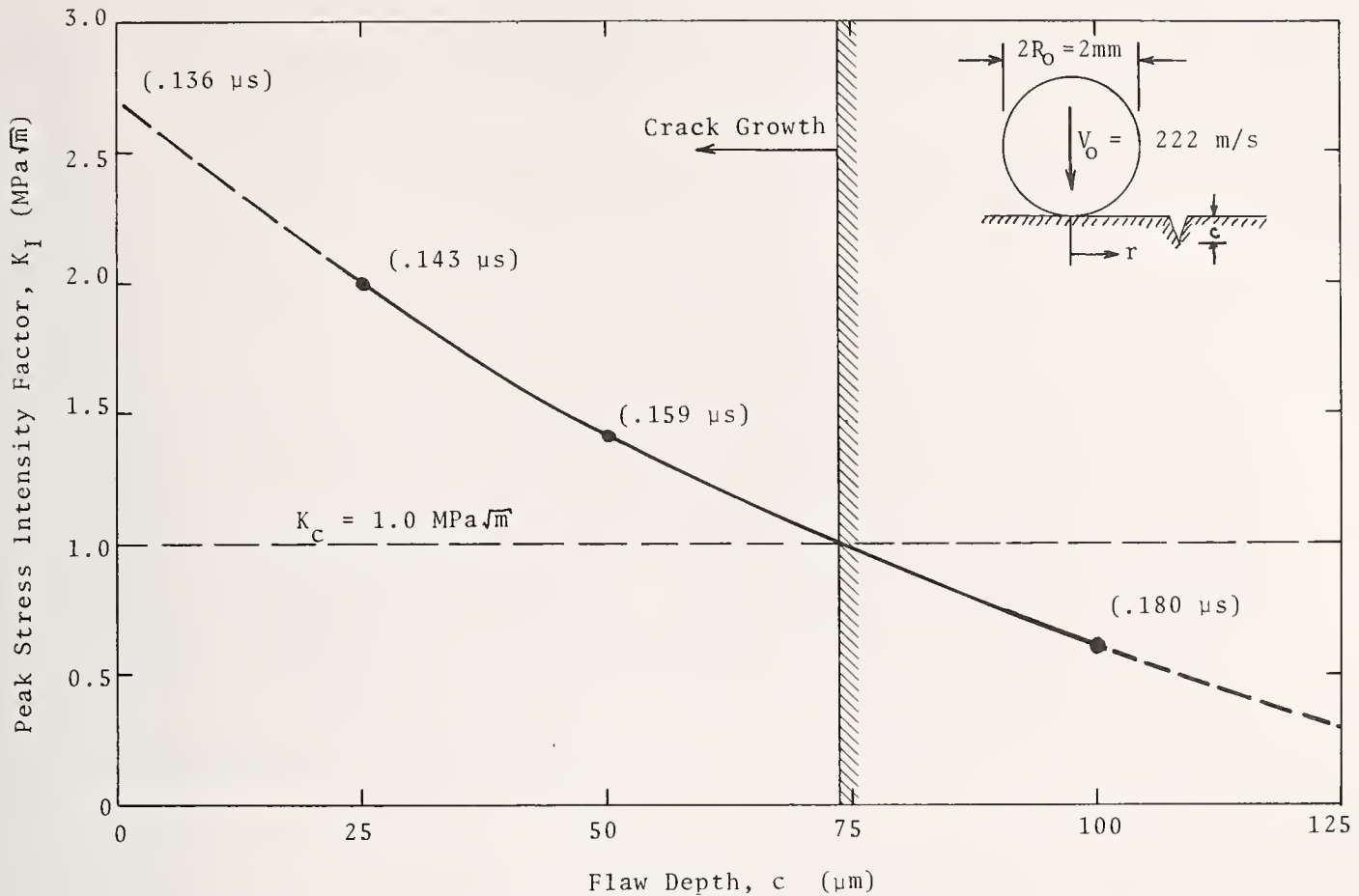


Figure 13. Peak stress intensity factor (and associated time) for various surface flaws located at $r=300 \mu\text{m}$ for 222m/s impact of a 2-mm water drop onto a ZnSe window.

The authors wish to acknowledge the useful discussions with A. G. Evans of the University of California, Berkeley (formerly at Rockwell International/Science Center).

References

- [1] Evans, A. G., Impact damage in ceramics, Report under Office of Naval Research Contract No. N00014-75-C-0609, Rockwell International/Science Center, Thousand Oaks, California (1977).
- [2] Wilkins, M. L., Calculation of elastic-plastic flow, Report UCRL-7322, Rev. I, Lawrence Radiation Laboratory, University of California, Livermore, California (1969).
- [3] Rosenblatt, M., Eggum, G. E., DeAngelo, L. A., and Kreyenhagen, K. N., Numerical investigation of water drop erosion mechanisms in infrared-transparent materials, Report AFML-TR-76-193, Air Force Materials Laboratory, Wright-Patterson Air Force Base, Ohio (1976).
- [4] Kreyenhagen, K. N., Rosenblatt, M., and Isabelle, T. R., Cratering, mass loss, and residual damage due to hypersonic particle impacts on ablative materials, Report AFML-TR-75-184, Air Force Weapons Laboratory, Kirtland Air Force Base, New Mexico (1976).
- [5] Ito, Y. M., Rosenblatt, M., Perry, F. W., and Eggum, G. E., Analysis of water drop erosion mechanisms in infrared-transparent materials using microphysical fracture models, Report AFML-TR-77-219, Air Force Materials Laboratory, Wright-Patterson Air Force Base, Ohio (1977).
- [6] Blowers, R. W., On the response of an elastic solid to droplet impact, J. Inst. Maths. Applics. 5, 167-193 (1969).



SURFACE CHARACTERISTICS OF DIAMOND-MACHINED CERAMIC SURFACES EVALUATED BY HIGH FLUENCE DIAGNOSTICS¹

M. J. Soileau, J. O. Porteus, and D. L. Decker

Michelson Laboratory, Physics Division
Naval Weapons Center, China Lake, CA 93555

Ceramic surfaces prepared by precision diamond-machining are compared with surfaces prepared by conventional polishing. Comparison is made on the basis of high fluence diagnostics. The results indicate that the diamond-machined surfaces have as high or higher failure resistance under high fluence loading as surfaces prepared using conventional techniques. Failure of both diamond-machined and polished surfaces are strongly dependent upon surface structure and surface contamination. These findings indicate that diamond-machining is an attractive alternative for generating optical surfaces on ceramic materials.

Key Words: Ceramic surfaces; diamond single-point machining; high fluence; laser irradiation

1. Introduction

Diamond-machining has been shown to be an attractive alternative to conventional polishing for producing high quality optical surfaces on metal mirrors [1]². This technique has also been applied to relatively soft dielectrics such as KCl and NaCl with promising results [2]. In this work ceramic surfaces prepared by precision diamond-machining are compared with surfaces prepared by conventional polishing. Comparison is made on the basis of visible effects produced by laser radiation. The thresholds for these effects indicate surface quality in terms of cleanliness and surface finish. The laser source is a single-pulsed commercial HF/DF laser with a maximum output of 200 mJ per pulse. The pulses are approximately 100 nsec in duration with wavelengths grouped at either 2.7 or 3.8 μm . The laser output is tightly focused on the sample surface by a 127-mm focal length ZnSe lens.

Diamond machined surfaces were produced on single-crystal CaF_2 (Irtran II). The details of the machining process are given elsewhere in these proceedings [3]. The results indicate that the diamond-machined surfaces have failure resistance under high fluence loading of the same order of magnitude as surfaces prepared using conventional techniques. In both types of surfaces, failure is initiated by surface defects and impurities.

2. Experimental

Disc-shaped samples of single-crystal CaF_2 and SrF_2 , and polycrystalline MgF_2 (Irtran II) were turned on-center with a single-point diamond tool to produce an optical surface. Part of the polished surface was left intact for comparison with the machined surfaces.

¹This work was performed under ONR Project No. RR02202, Task RR0220202, Dr. A. M. Diness, Program Manager.

²Figures in brackets indicate the literature references at the end of this paper.

The tightly focused output of a commercially available, single-pulsed HF/DF laser was used to probe the surfaces. The laser parameters are summarized in table 1. High fluence levels were obtained by focusing the laser output (20-mm diameter) with a 50-mm diameter, 127-mm focal length ZnSe lens. The focal spot diameter was approximately 55 μm , measured between the $1/e^2$ points of the Gaussian spatial intensity distribution. The pulse energy was monitored with a pyroelectric energy meter calibrated with a thermopile. Incident and transmitted waveforms were monitored with fast photon drag detectors. This facility is described in detail elsewhere [4].

Table 1. Laser parameters.

	Pulse energy (J)	Wavelength (μm)	Pulse width (nsec)	e^{-2} Focal spot diameter (μm)
HF	0.2	2.7	125	53
DF	0.2	3.8	95	57

The thresholds for visible spark, increased visible scatter, and/or truncation of the beam transmitted through the sample were measured in air. Changes in the surfaces were monitored with a 20-power microscope. The threshold for a particular effect was defined as that flux which produced the effect in 50% of the sites. Each site was irradiated only once; the thresholds determined under these conditions are called the one-on-one thresholds. Once the one-on-one thresholds were determined, an undamaged site was irradiated five times with a flux equal to 80% of the one-on-one threshold. After this conditioning the power was increased until a given effect was observed. Thresholds determined in this manner are referred to as N-on-one thresholds.

3. Results

The one-on-one thresholds for the diamond-machined and polished surfaces are summarized in table 2. The most significant features of these results are:

- A. The thresholds for the diamond-turned surfaces are of the same order as those of the polished surfaces.
- B. The thresholds for the polycrystalline MgF_2 (Irtran II) are of an order of magnitude lower than those of the single-crystal CaF_2 and SrF_2 surfaces.

Table 2. Summary of one-on-one damage thresholds.

Specimens	D-T low scatter	D-T high scatter	Polished
HF thresholds (10^9 W/cm^2)			
CaF_2	7.04	4.4	6.75
SrF_2 -4	2.86	3.86	6.74
SrF_2 -2	6.84	3.95	4.68
MgF_2 (poly)	0.32	---	0.34
DF thresholds (10^9 W/cm^2)			
CaF_2	10.6	7.99	9.37
SrF_2 -4	5.22	3.97	12.0
SrF_2 -2	8.20	---	6.34
MgF_2 (poly)	0.51	---	0.47

- C. For both polished and machined surfaces on all the materials studied, the HF (2.7 μm) thresholds are lower than the DF (3.8 μm) thresholds.
- D. The thresholds are dependent upon the surface quality of the materials.

The center-turned single-crystal samples showed alternating azimuthal regions of high and low visible scatter, which were apparently determined by the relationship of the cutting direction to the crystallographic axes. Thresholds were generally found to be 50% lower in the high-scatter regions. Figure 1 is a micrograph of a damage site in the low-scatter region and a damage site in the high-scatter region. Note that the damage in the high-scatter region is influenced by the scattering centers which are clustered along the machining marks.

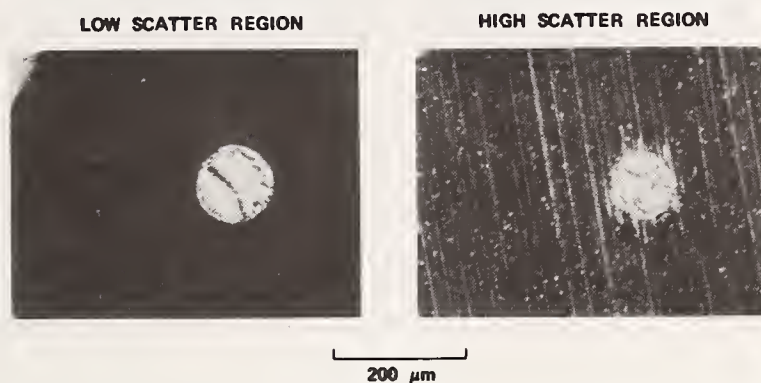


Figure 1. Surface damage on diamond-machined SrF_2 . In the low-scatter region, the damage region essentially maps the incident intensity distribution. In the high-scatter region, damage is seen to extend along the direction of the machining grooves where scattering centers are concentrated.

The lower thresholds measured at 2.7 μm as compared to 3.8 μm are suggestive that absorbed surface water is contributing to the failure for both the polished and diamond-machined surfaces. More evidence for suspecting that surface water plays an important role in the damage is seen in the results of the N-on-one experiments on these surfaces. These results are summarized in table 3. Note that for all cases where an N-on-one effect is seen, the effect (increase in damage threshold) is greater at 2.7 μm than at 3.8 μm .

Table 3. N-on-one effect (% increase).

Specimens	HF D-T	DF D-T	HF polished	DF polished
CaF_2	54	40	47	26
SrF_2 -4	0	--	--	--
SrF_2 -2	21	13	0	--
MgF_2 (poly)	21	14	0	--

These results suggest that for the N-on-one irradiations surface contaminants are being removed from the surface, and that the contaminants are selectively absorbing for the HF lines. The peak of the water absorption band corresponds to the strongest HF line (2.7 μm); thus, absorbed surface water is a likely contributor to surface damage at HF frequencies.

As can be seen from table 2, the damage thresholds for the Irtran II are an order of magnitude lower than for the single-crystal material. Near threshold the Irtran II failed by a change in visible scatter at the surface or

within the bulk near the surface. No truncation of the transmitted pulse was observed near threshold. This evidence and the micrographs in figures 2 and 3 indicate that failure is initiated by defects within the material or at the surface, and that the method of surface preparation has little or no effect. The mechanism of failure for the Irtran II is probably heating of absorbing defects within the focal volume.

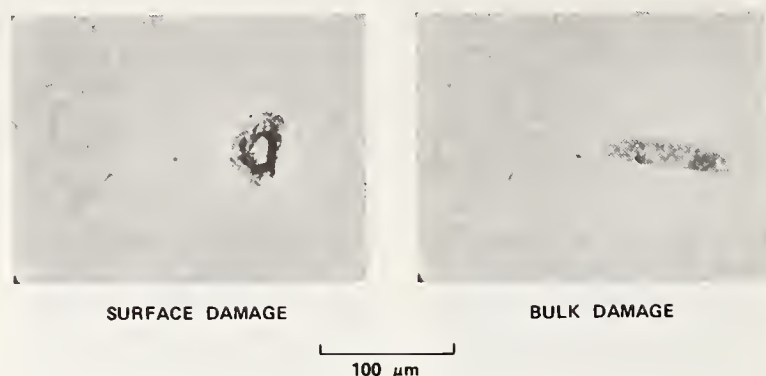


Figure 2. DF laser damage in polished Irtran II. Note that the damage site does not map the incident beam. In all cases the laser was focused on the surface. Note the high concentration of defects. These defects are uniformly distributed throughout the material.

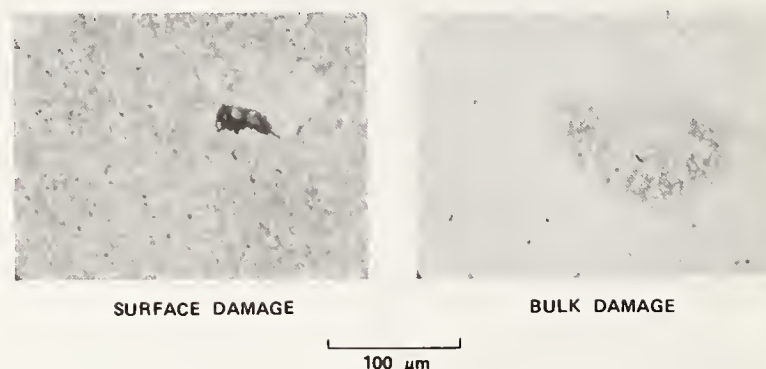


Figure 3. DF laser damage in diamond-turned Irtran II. Note the high concentration of defects. These defects are uniformly distributed throughout the specimen.

For the polished and diamond-turned surfaces on the single-crystal materials, laser damage was accompanied by a bright, visible spark, an increase in visible scattering, and an abrupt truncation of the beam transmitted through the specimen. An example of the truncation of the transmitted beam is seen in figure 4. Note that failure occurs at the peak of the pulse, and beam truncation occurs within the response time of the detector (less than 1.5 nsec). This type of behavior is strongly suggestive of electron avalanche breakdown. The probable mechanism of failure is avalanche breakdown initiated by surface defects and/or contaminants.

The effect of the orientation of the residual machining grooves with respect to the laser electric field was investigated. The one-on-one threshold was measured for the cases where the field was parallel to the perpendicular to the machining grooves. Polarizable defects perpendicular to the incident field should enhance the coupling of the laser energy to the surface and lower the threshold [5]. The threshold was found to be approximately 10% lower for the case of the field perpendicular to the grooves than for the case of the

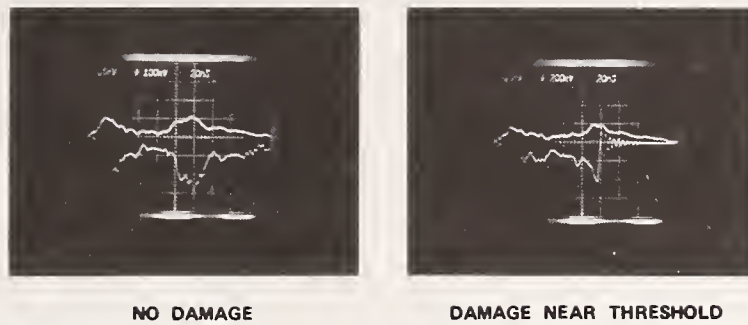


Figure 4. Transmitted waveform distortion. Note that near-threshold damage occurs at the peak of the pulse within the fall time of the detector (<1.5 nsec).

field parallel to the grooves. This decrease in threshold is as predicted by theory and is of little consequence for these low index materials. However, for high index materials such as GaAs, Si, ZnSe, and Ge, the effect could be significant since the induced polarization field caused by such defects is proportional to the index of refraction. In figure 5 one can see the effects of the interference of the induced polarization field and the incident laser field for the case of the incident laser field perpendicular to the residual machining grooves.

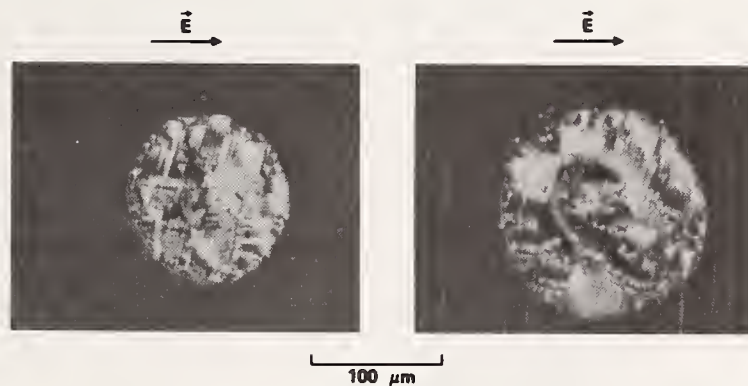


Figure 5. Effects of laser polarization in diamond-turned SrF_2 . Note the "ripples" in the figure on the right. These ripples are the result of interference between the impressed field and the local field due to polarization charges induced at surface defects by the incident field.

4. Summary and Conclusions

Diamond-machined surfaces on CaF_2 , SrF_2 , and Irtran II have HF/DF laser damage thresholds of the same order as polished surfaces on these materials. The mechanism of failure for single-crystal CaF_2 and SrF_2 appears to be electron avalanche breakdown initiated by defects and impurities in polished and diamond-machined surfaces. The mechanism of failure for Irtran II appears to be absorption by bulk defects and is thus independent of the method of surface preparation. The lower thresholds at HF frequencies compared to those at DF frequencies and the larger increase in thresholds (N-on-one effect) at HF compared to DF indicates that absorbed water has a significant effect on the damage thresholds of these surfaces at these frequencies.

References

- [1] The following review article summarizes the work on diamond-turned metal surfaces and is a good guide to work in this area; Porteus, J. O. and Decker, D. L., "Metal Mirror Damage and Precision Diamond-Turning," in Laser Damage of Optical Materials, A. J. Glass and A. H. Guenther, eds. (Academic Press, New York, 1979), in press.
- [2] Soileau, M. J., Bennett, J. M., Porteus, J. O., Faith, W. N., Jernigan, J. L., and Saito, T. T., "10.6 μm Pulsed Laser Studies of Diamond-Turned KCl Window Surfaces," in Laser Induced Damage in Optical Materials: 1976, A. J. Glass and A. H. Guenther, eds., National Bureau of Standards, Washington, DC (NBS Spec. Publ. 462, 1976), pp. 149-157.
- [3] Decker, D. L., Bennett, J. M., and Grandjean, D. J., "Optical and Surface Physical Characteristics of Diamond-Machined Infrared Windows," these proceedings.
- [4] Van Stryland, E. W., Bass, M., Soileau, M. J., and Tang, C. C., "Pulsed HF/DF Laser Damage in Window Materials," in Laser Induced Damage in Optical Materials: 1977, A. J. Glass and A. H. Guenther, eds., National Bureau of Standards, Washington, DC (NBS Spec. Publ. 509, 1977), pp. 118-125.
- [5] Temple, P. A., and Soileau, M. J., "Resonant Defect Enhancement of the Laser Electric Field," in Laser Induced Damage in Optical Materials: 1976, A. J. Glass and A. H. Guenther, eds., National Bureau of Standards, Washington, DC (NBS Spec. Publ. 462, 1976), pp. 371-378.

JOINT MEETING — ACS BASIC SCIENCE DIVISION AND SYMPOSIUM ON
THE SCIENCE OF CERAMIC MACHINING AND SURFACE FINISHING II

Conference Attendees

A

Scott J. Abel
Corning Glass Works
31501 Solon Road
Solon, OH 44139

S. Adachi
Hoya Optics USA, Inc.
2200 Sand Hill Road, Suite 200
Menlo Park, CA 94025

Marc A. Adams
Jet Propulsion Laboratory
4800 Oak Grove Drive
Pasadena, CA 91103

Art Ahlbrecht
3M Co.
251-2A
St. Paul, MN 55101

Rex Ashbrook
Kennametal Inc.
1011 Old Salem Road
Greensburg, PA 15601

Richard L. Ashbrook
NASA Lewis Research Center
Cleveland, OH 44017

B

Francis I. Baratta
Army Materials and Mech. Res. Ctr.
Watertown, MA 02172

Michael Baxter
Fair-Rite Products Corp.
One Commercial Row
Wallkill, NY 12589

Harold E. Bennett
Naval Weapons Center
Code 38101
China Lake, CA 93555

M. Berg
AC Spark Plug - GM
1300 N. Dort Highway
Flint, MI 48556

Philip L. Berneburg
GTE Sylvania, Inc./Chem. & Met. Div.
Hawes St.
Towanda, PA 18848

Charles F. Bersch
U.S. Navy
Air-52032
Washington, D. C. 20361

Howard D. Blair
Ford Motor Co.
P. O. Box 2053
Dearborn, MI 48121

Tim Bornemann
Libbey-Owens-Ford Company
1701 E. Broadway
Toledo, OH 43605

R. Bowles
British Glass Industry
Research Association
Northumberland Road
Sheffield, S10 2UA
ENGLAND

R. C. Bradt
Pennsylvania State Univ.
118 Mineral Industries Bldg.
University Park, PA 16802

Robert H. Bragg
Dept. of Matls. Science and
Mineral Engineering
Univ. of California
Berkeley, CA 94720

R. J. Bratton
Westinghouse R&D Center
1310 Beulah Road
Pittsburgh, PA 15235

R. Brehm
Philips Research Lab.
Proj. Holstlaan
Eindhoven, The Netherlands

John J. Brennan
United Technologies
Research Center
Silver Lane
E. Hartford, CT 06108

Leslie Bretland
Monsanto Research Corp.
Mound Facility, Mound Rd.
Miamisburg, OH 45342

A. Broese Van Groenou
Philips Research Laboratories
Eindhoven, 5600 MD
The Netherlands

S. D. Brown
Univ. of Illinois
Dept. of Ceramic Engineering
Urbana, IL 61801

Joseph E. Burke
General Electric Co.
P. O. Box 8
Schenectady, NY 12301

C

Rowland Cannon
Mass. Inst. of Tech.
77 Mass Ave.
Cambridge, MA 02139

H. W. Carpenter
Rockwell International
6633 Canoga Avenue
Canoga Park, CA 93104

David W. Chalkley
Trans-Tech, Inc.
12 Meem Avenue
Gaithersburg, MD 20760

C. P. Chen
Jet Propulsion Lab.
4800 Oak Grove Drive
Pasadena, CA 91103

Aleksandr S. Chizhov
Georgia Inst. of Technology
School of Mechanical Engineering
Atlanta, GA 30332

A. Choudry
Univ. of Rhode Island
Kingston, RI 02881

Richard C. Ciocci
Monsanto Research Corp.
Mound Facility
P. O. Box 32
Miamisburg, OH 45342

David R. Clarke
Rockwell International Sci. Ctr.
1049 Camino dos Rios
Thousand Oaks, CA 91360

Jay E. Comeforo
Accuratus Ceramic Corp.
Brass Castle Road, RD4
Washington, NJ 07882

L. P. Cook
National Bureau of Standards
B214, Materials Bldg.
Washington, D. C. 20234

G. A. Cooper
Institut Cerac S. A.
Chemin Des Larges Pieces
CH-1024 Ecublens, SWITZERLAND

S. M. Copley
Univ. of Southern Calif.
Materials Science Dept.
Los Angeles, CA 90007

Robert E. Cuthrell
Sandia Laboratories
5834
Albuquerque, NM 87185

Ivan B. Cutler
Univ. of Utah
Salt Lake City, UT 84112

D

Kiran H. Dalal
Cornell University
131 Bard Hall
Dept. of Materials Science & Eng.
Ithaca, NY 14850

D. L. Decker
Michelson Laboratory
Naval Weapons Center
China Lake, CA 93555

Arthur M. Diness
Office of Naval Research
Arlington, VA 22217

Steve Dole
General Electric Corp. Res. & Dev.
P. O. Box 8
Schenectady, NY 12301

Louis P. Domingues
Trans-Tech, Inc.
12 Meem Avenue
Gaithersburg, MD 20760

Alan L. Dragoo
National Bureau of Standards
Washington, DC 20234

Sunil Dutta
NASA - Lewis Res. Ctr.
21000 Brookpark Road
Cleveland, OH 44135

Ernest J. Duwell
3M Co. - Industrial Abrasives Div.
3M Center 251-2A
St. Paul, MN 55101

Ulf Dworak
Fa. Feldmuhhle AG
Fabrikstrasse 23 - 29
Plochingen, West Germany 7310

Hans P. R. Frederikse
National Bureau of Standards
Center for Materials Science
Washington, DC 20234

E

T. E. Easler
Pennsylvania State Univ.
118 Mineral Industries Bldg.
University Park, PA 16802

Steve Freiman
National Bureau of Standards
Fracture and Deformation Division
Washington, D. C. 20234

George O. Ellis, Sr.
Ellis Ceramtek, Inc.
Rt. #22, Salem Industrial Park
Lebanon, NJ 08833

George A. Fryburg
GTE Sylvania Inc.
Portsmouth Ave.
Exeter, NH 03833

A. G. Evans
Univ. of California
Matls. Dept.
Berkeley, CA 94720

E. R. Fuller
National Bureau of Standards
Bldg. 223, Rm. A355
Washington, D. C. 20234

G

Edward L. Exner
Kennametal, Inc.
1011 Old Salem Road
Greenburg, PA 15601

Jack T. Gardner
TRW Systems
One Space Park
Redondo Beach, CA 90278

F

Katherine T. Faber
The Carborundum Company
P. O. Box 1054
Niagara Falls, NY 14302

G. E. Gazza
Army Materials & Mech.
Research Center
Watertown, MA 02172

E. N. Farabaugh
National Bureau of Standards
Center for Materials Science
Washington, DC 20234

Richard L. Gentilman
Raytheon Res. Division
28 Seyon St.
Waltham, MA 02154

Mattison K. Ferber
Univ. of Illinois
204 Ceramics Bldg.
Urbana, IL 61801

Bhaskar B. Ghatge
Bell Telephone Lab., Inc.
555 Union Blvd.
Allentown, PA 18103

Ross Firestone
IIT Research Institute
10 West 35th Street
Chicago, IL 60616

Peter J. Gielisse
Univ. of Rhode Island
Crawford Hall
Kingston, RI 02881

A. D. Franklin
National Bureau of Standards
Center for Materials Science
Washington, DC 20234

M. N. Giovan
Jet Propulsion Lab.
23214 Osage Ridge Rd.
Valencia, CA 91355

Michael S. Franklin
TRW/Marlin Rockwell Div.
402 Chandler St.
Jamestown, NY 14701

Otto Goern
National Micronetics Inc.
Box 188
West Hurley, NY 12491

Robert J. Gottschall
U. S. Dept. of Energy
Div. of Matls. Sciences
Mail J309
Washington, DC 20545

Henry C. Graham
U. S. Air Force
WPAFB, OH 45433

Ken Green
Corps Porcelain Co.
600 9th St.
Golden, CO 80701

Albert V. Gress, Jr.
Monsanto Research Corp.
Box 32
Maimisburg, OH 45342

D. G. Grossman
Corning Glass Works
Sullivan Park
Corning, NY 14830

H

Joseph Thompson Hagan
University of Cambridge
Madingley Road
Cambridge CB3 0HE
Cambridge, ENGLAND

John W. Halloran
Pennsylvania State Univ.
119 Studle Bldg.
University Park, PA 16802

Barry L. Hammond
The David W. Taylor Naval
Ship R&D Center
Code 2812
Annapolis, MD 21402

Al Hare
Ellis Ceramtek, Inc.
Rt. #22, Salem Industrial Park
Lebanon, NJ 08833

D. P. H. Hasselman
Virginia Polytechnic Inst.
and State University
Dept. of Matls. Eng.
Blackburg, VA 24061

Kenneth A. Hatcher
Eaton Corp. - Engr. &
Research Center
26201 Northwestern Hwy
P. O. Box 766
Southfield, MI 48037

Irvin F. Havens
Bay State Abr. Div.
Dresser Corp.
10 Union St.
Westboro, MA 01581

J. D. Helfinstine
Corning Glass Works
Technical Staffs Division
Corning, NY 14830

Naim Hemmat
Allied Chemical
Morristown, NJ 07960

S. P. Hepburn
PPG Industries
153 Lingay Drive
Glenshaw, PA 15116

H. Herman
State Univ. of NY
Materials Science
Stony Brook, NY 11794

Arthur H. Heuer
Case Western Reserve Univ.
Olin 303, Univ. Circle
Cleveland, OH 44106

L. W. Hobbs
Case Western Reserve University
Cleveland, OH 44106

Michael Hoch
Univ. of Cincinnati, Loc 12
Dept. of Matls. Sci. and
Metallurgical Engineering
Cincinnati, OH 45221

Bernard Hockey
National Bureau of Standards
Center for Materials Science
Washington, D. C. 20234

H. Hohnke
Univ. of Michigan
600 Dartmoor
Ann Arbor, MI 48103

William D. Horn
Allied Chemical
1201 Continental Blvd.
Charlotte, NC 28210

Robert S. Houston
Norton Co.
New Bond St.
Worcester, MA 01601

I

Osamu Imanaka
Kanazawa Univ., Faculty of
Engineering
40-20, 2 Chome, Kodatsuno
Kanazawa, JAPAN 920

Moshe Ish-Shalom
Israel Ceramic & Silicate Inst.
Technion City
Haifa, ISRAEL 32000

Marvin Ito
California Research & Tech., Inc.
6269 Variel Ave., Suite 200
Woodland Hills, CA 91367

J

Karl Jakus
Univ. of Massachusetts
Mechanical Engineering
Amherst, MA 01993

B. E. Johnson
Owens - Illinois, Inc.
1700 N. Westwood Ave.
Toledo, OH 43666

Curtis A. Johnson
General Electric CR & D
P. O. Box 8
Schenectady, NY 12301

D. Lynn John
Northwestern Univ.
2145 Sheridan Road
Evanston, IL 60201

Virgil A. Johnson
Western Electric, Inc.
1600 Osgood Street
North Andover, MA 01845

Robin L. Jones
Electric Power Res. Inst.
3412 Hillview Ave.
P. O. Box 10412
Palo Alto, CA 94303

Choll K. Jun
Kennametal, Inc.
Research Lab.
P. O. Box 639
Greenburg, PA 15601

K

Hillard M. Kahan
Ampex Corporation
401 Broadway
Redwood City, CA 94063

William D. Kehr
IBM Corporation
67M/004
Tucson, AZ 85744

Thomas J. Kim
Univ. of Rhode Island
Dept. of Mechanical Eng.
Kingston, RI 02881

Randall R. Kinnick
Detroit Diesel Allison of
General Motors Corp. Matls.
P. O. Box 894 Speed Code W5
Indianapolis, IN 46206

Henry P. Kirchner
Ceramic Finishing Co.
P. O. Box 498
State College, PA 16801

Heinrich Knock
German Aerospace Res.
Establishment (DFVLR)
Linder Höhe
500 Koln 90, WEST GERMANY

Barry G. Koepke
Honeywell Inc.
10701 Lyndale Ave. S.
Bloomington, MN 55420

O. L. Krivanek
Univ. of California,
Berkeley
Berkeley, CA 94720

Vladimir Krstic
McMaster University
Hamilton, CANADA

H. Kuwamoto
Purdue University
West Lafayette, IN 47907

L

R. L. Landingham
Univ. of California
Lawrence Livermore Lab.
P. O. Box 808
Livermore, CA 94550

F. F. Lange
Rockwell Science Center
1049 Camino Dos Rios
Thousand Oaks, CA 91360

James Lankford
Southwest Res. Institute
8500 Culebra Road
San Antonio, TX 78284

D. C. Larsen
ITT Research Institute
10 West 35 Street
Chicago, IL 60616

Kai-Hung Lau
SRI International
G223, 333 Ravenswood Ave.
Menlo Park, CA 94025

D. William Lee
Arthur D. Little, Inc.
15 Acorn Park
Cambridge, MA 02140

Minydung Lee
General Electric Co.
Corp. R&D Center
Schenectady, NY 12345

David Lewis
NYS College of Ceramics
Alfred University
Alfred, NY 14802

Harold Lombard
DATA Materials
Div. Ferronics, Inc.
127 Main St.
Springfield, VT 05156

Victor Lou
General Electric
1219 Libby
Schenectady, NY 12307

M

R. K. MacCrone
R.P.I.
Troy, NY 12180

Howard McCollister
Owens-Illinois
Box 1035
Toledo, OH 43666

Edward J. McCormack
CS Draper Lab.
555 Tech Sq.
Cambridge, MA 02139

Larry G. McCoy
Battelle Columbus Lab.
505 King Ave.
Columbus, OH 43201

William J. McDonough
U. S. Naval Res. Laboratory
Washington, D. C. 20375

Kelly D. McHenry
Honeywell
10701 Lyndale Ave., South
Bloomington, MN 55420

Robert McKinley
Plessey/Frenchtown
8th & Harrison St.
Frenchtown, NJ 08825

K. R. McKinney
Naval Research Lab.
4555 Overlook Ave.
Washington, DC 20375

Edward A. Maguire
Raytheon Co.
28 Seyon St.
Waltham, MA 02154

Stephen Malkin
Faculty of Mechanical Eng.
Technion - Israel Inst. of
Technology
Haifa, ISRAEL

J. A. Mangels
Ford Motor Company
P. O. Box 2053
Dearborn, MI 48121

William R. Manning
Champion Spark Plug Co.
20,000 Conner Ave.
Detroit, MI 48234

R. H. Marion
Sandia Laboratories
Division 5846
Albuquerque, NM 87185

Jim Mathers
Univ. of Maryland
Chemical Engineering Dept.
College Park, MD 20742

Mel I. Mendelson
Pratt & Whitney Aircraft
P. O. Box 2691
W. Palm Beach, FL 33402

Gary L. Messing
Battelle Columbus Lab.
505 King Ave.
Columbus, OH 43201

Morton E. Milberg
Ford Motor Co.
Box 2053
Dearborn, MI 48121

A. J. Miller
Bell Laboratories, Inc.
555 Union Blvd.
Allentown, PA 18103

Alan D. Miller
University of Washington
Ceramic Engineering FB-10
Seattle, WA 98195

Drago Milovic
Western Gold and Platinum Co.
477 Harbor Boulevard
Belmont, CA 94002

T. E. Mitchell
Case Western Reserve Univ.
Cleveland, OH 44106

Takeshi Miyazaki
Kanazawa University
2-40-20, Kodatsuno
Kanazawa, JAPAN

Frank R. Monforte
Ampex Corporation
465 W. Maude Ave.
Sunnyvale, CA 94086

P. E. D. Morgan
Univ. of Pittsburgh
848 Benedum Hall
Pittsburgh, PA 15261

William Mosen
IBM
HY 52 North
Rochester, MN 55901

David Moskowitz
Ford Motor Co.
Eng. & Res. Staff
20,000 Rotunda Dr.
Dearborn, MI 48121

N

Ishverlal Naik
AiResearch Casting Co.
2525 W. 190th Street
Torrance, CA 90509

Takeo Nakazawa
Sumitomo Special Mtls. Co. LTD.
2-15-17 Egawa
Shimamoto-cho Mishima-gun
Osaka, JAPAN

Bernt Nariken
IBM
East Fishkill Facility
Route 52
Hopewell Junction, NY 12533

J. Noares
Vacuum Ornamental
11380 Harrison
Romulus, MI 48174

R. E. Novak
RCA Laboratories
Princeton, NJ 08540

O

Linus U. Ogbuji
Case Western Reserve Univ.
1589 Coventry Rd., #12
Cleveland, OH 44118

C. D. Olson
National Bureau of Standards
Center for Materials Science
Washington, DC 20234

Shinji Otsuki
Sumitoko Electronic Matls.
Co. LTD
282T-Ukumo Omachi-Machi
Saga, JAPAN

Peter Otten
Union Carbide Corp.
8888 Balboa Avenue
San Diego, CA 92123

P

John A. Palm
General Electric Co.
Corporate Res. & Dev. Ctr.
P. O. Box 8
Schenectady, NY 12301

Edward D. Parent
GTE Sylvania
Portsmouth Ave.
Exeter, NH 03833

Robert A. Penty
Hague International
3 Adams St.
South Portland, ME 04106

Harry Perry
Consolidated Beryllium Ltd.
Marble Hall Road, Milford Haven
Dyfed, UNITED KINGDOM

Ronald L. Peters
VR/Wesson Co. - A Division
of Fansteel
800 Market St.
Waukegan, IL 60085

Daniel R. Petrak
Harbison - Walker Ref. Co.
Div. Dresser Ind.
Garber Research Center
P. O. Box 98037
Pittsburgh, PA 15227

Bruce Pletka
Dept. of Metallurgical Eng.
Michigan Technological Univ.
Houghton, MI 49931

Robert Pohanka
Office of Naval Research
Code 471
Arlington, VA 22217

Q

CarrLane Quackenbush
GTE Labs.
40 Sylvan Road
Waltham, MA 02754

R

Bharat Rawal
AVX Ceramics Corp.
P. O. Box 867
Myrtle Beach, SC 29577

Dennis W. Readey
Ohio State Univ.
2041 College Road
Columbus, OH 43017

Robert R. Reeber
Dept. of Energy
20 Massachusetts Ave., N.W.
Washington, D. C. 20545

Gary M. Renlund
General Electric CRD
P. O. Box 8
Schenectady, NY 12301

William H. Rhodes
GTE Laboratories
40 Sylvan Road
Waltham, MA 02154

Paul E. Rempes
Champion Spark Plug Co.
Ceramic Division
20,000 Conner Ave.
Detroit, MI 48234

R. W. Rice
Naval Research Laboratory
Code 6360
Washington, DC 20375

Subhash Risbud
Lehigh Univ.
Coxe Lab. #32
Bethlehem, PA 18015

J. E. Ritter
Univ. of Massachusetts
Dept. of Mechanical Eng.
Amherst, MA 01003

M. W. Robare
AiResearch Manufacturing Co.
Phoenix, AZ 85034

Carl Robbins
National Bureau of Standards
Center for Materials Science
Washington, D. C. 20234

Jack A. Rubin
Kyocera International
8611 Balboa Ave.
San Diego, CA 92123

Robert Ruh
Air Force Matls. Lab.
Wright Patterson AFB, OH 45433

C. K. Russell
United States Steel Corp.
125 Jamison Lane
Monroeville, PA 15146

Ralph A. Russell
IBM Corp.
Hwy 52 No.
Rochester, MN 55901

S

H. Sato
Purdue University
West Lafayette, IN 47906

R. W. Scheidecker
Ames Laboratory, USDOE
Iowa State University
Ames, IA 50011

Frederick Schmid
Crystal Systems, Inc.
35 Congress St.
Salem, MA 01970

Lawrence R. Sparrow
COMSAT Laboratories
P. O. Box 115
Clarksburg, MD 20734

Detlev Schultz
Fair-Rite Products Corp.
One Commercial Row
Wallkill, NY 12589

Richard M. Spriggs
Lehigh University
c/o President's Office
Bldg. 27
Bethlehem, PA 18015

Susan R. Schuon
Michigan State Univ.
Dept. of Metallurgy Mech.
and Materials Science
East Lansing, MI 48824

M. Srinivasan
The Carborundum Co.
R&D Division
P. O. Box 1054
Niagara Falls, NY 14302

Nirmal Sharma
Univ. of Illinois
Dept. of Ceramic Engineering
204 Ceramics
Urbana, IL 61801

Read W. Steward
Eaton Corporation
26201 Northwestern Hwy
P. O. Box 766
Southfield, MI 48037

J. E. Sheehan
General Atomic Co.
P. O. Box 81608
San Diego, CA 92138

V. S. Sturican
The Pennsylvania State Univ.
328 MI Bldg.
University Park, PA 16802

L. B. Sibley
SKF Industries
1100 First Ave.
King of Prussia, PA 19406

Douglas L. Swanson
IBM
3605 Highway 52 North
Rochester, MN 55901

Wilbur G. Simmons
AF Office of Scientific Res.
Bldg. 410
BAFB, DC 20332

T

S. C. Singhal
Westinghouse Res. & Dev. Ctr.
1310 Beulah Road
Pittsburgh, PA 15235

Donna L. Taylor
Corning Glass Works
Sullivan Park
Corning, NY 14830

J. T. Smith
GTE Laboratories
40 Sylvan Rd.
Waltham, MA 02154

Leslie L. Terner
Ford Motor Co.
7400 Finnegan Dr.
West Bloomfield, MI 48033

R. H. Smoak
The Carborundum Co.
R&D Div., P. O. Box 1054
Niagara Falls, NY 14302

Bruce Thomson
United Technologies Res.
Silver Lane
E. Hartford, CT 06108

W. J. Smothers
Bethlehem Steel Corp.
Bethlehem, PA 18016

R. Thomson
National Bureau of Standards
Center for Materials Science
Washington, D. C. 20234

M. J. Soileu
Michelson Lab
Naval Weapons Ctr.
China Lake, CA 93555

Nancy S. Tighe
National Bureau of Standards
Center for Materials Science
Washington, D. C. 20234

R. E. Tressler
Pennsylvania State Univ.
118 Mineral Industries Bldg.
University Park, PA 16802

John V. White
Alberox Corp.
Industrial Park
New Bedford, MA 02745

Stuart Tuffs
Norton Co.,
Industrial Ceramics Div.
1 New Bond Street
Worcester, MA 01601

Sheldon M. Wiederhorn
National Bureau of Standards
Fracture and Deformation Div.
Washington, DC 20234

V

Ben A. Wilcox
National Science Foundation
1800 G St., NW
Washington, DC 20550

Jim Vagt
IBM
HY 52, North
Rochester, MN 55901

W. S. Williams
Univ. of Illinois
Matls. Res. Lab.
Urbana-Champaign, IL 61801

John D. Venables
Martin Marietta Labs.
1450 S. Rolling Road
Baltimore, MD 21227

Roger E. Wilson
Naval Surface Weapons Center
White Oak
Silver Spring, MD 20910

W

James M. Wimmer
Univ. of Dayton
300 College Park
Dayton, OH 45469

John B. Wachtman, Jr.
National Bureau of Standards
Center for Materials Science
Washington, D. C. 20234

T. W. Witkowski
Cast Western Reserve Univ.
Cleveland, OH 44106

Walter R. Wagner
IBM Corporation
P. O. Box 12195
Dept. E81-B101
Research Triangle Park, NC 27709

C. M. Wu
Naval Research Lab.
4555 Overlook Avenue
Washington, DC 20375

G. C. Walther
ITT Research Institute
10 West 35 Street
Chicago, IL 60616

Y

Gerald Q. Weaver
Norton Co., Industrial Ceramics Div.
1 New Bond Street
Worcester, MA 01606

Nobuo Yasunaga
Electrotechnical Laboratory
4-1, 5-chome, Mukodai-machi
Tanashi-shi, Tokyo
JAPAN 188

Francis H. Weikel
Corhart Refractories Co.
1600 W. Lee St.
Louisville, KY 40201

Hun C. Yeh
Cleveland State Univ.
1983 East 24 Street
Cleveland, OH 44115

Richard D. Weltzin
IBM GSD
3605 Hy 52 North
Rochester, MN 55901

C. F. Yen.
Oak Ridge National Lab.
Oak Ridge, TN 37830

Thomas J. Whalen
Ford Motor Co.
Box 2053
Dearborn, MI 48121

AUTHOR INDEX

- Andersson, C. A., 463
 Adachi, S., 417
- Bas, M., 283
 Bennett, H., 337
 Bowles, R., 489
 Bradt, R. C., 455
 Bratton, R. J., 463
 Brehm, R. 61
 Broese van Groenou, A., 61,43,147,191
- Casey, A. W., 231
 Cook, L. P., 407
 Cooke, F., 255
 Cooper, G. A., 115
 Copley, S. M., 283
 Countermine, T. A., 455
 Cuthrell, R. E., 139
- Davidson, D. L., 395
 Dean, S. K., 107
 Decker, D. L., 293, 315
 Doyle, E. D., 107
 Duwell, E. J., 201
- Easler, T. E., 455
 Evans, A. G., 1, 185, 379
- Farabaugh, E. N., 407
 Field, J. E., 15
 Firestone, R. F., 261
- Gentilman, R. 255
 Grandjean, D. J., 293
 Grossman, D. G., 221
 Gruver, R. M., 23
- Hagan, J. T., 15
 Harada, S., 417
 Hassler, C. R., 247
 Huerta, M., 93
- Ikeda, M., 325
 Imanaka, O., 157, 171, 317
 Ito, Y. M., 501
 Izumitani, T., 417
- Kawakami, S., 317
 Khuri-Yakub, B. T., 379
 Kimura, S., 325
- Kino, G. S., 379
 Kirchner, H. P., 23
 Koepke, B. G., 75
 Kokaji, Y., 325
- Landingham, R. L., 231
 Lankford, J., 395
 Levinger, R., 305
 Lindahl, R. O., 231
 Lokken, R. C., 201
 R. C., 201
- Maan, N., 43
 Malkin S., 93, 305
 McCoy, L. G., 247
 McKinney, K. R., 477
 Mecholsky, J. J., Jr., 351
 Messing, G. L., 247
 Miles, P., 255
 Miyade, E., 417
- Obara, A., 171
 Okutomi, M., 157
 Olson, C. D., 407
- Porteus, J. O., 315
- Rice, R. W., 185,351,429
 Richard, D. M., 23
 Richardson, D. W., 209
 Robare, M. W., 209
 Rosenblatt, M., 501
- Soileau, M. J., 315
 Stokes, R. J., 75
 Sugita, T., 317
 Swain, M. V., 15
- Tarumi, N., 171
 Taylor, D. L., 221
 Turner, L. L., 483
 Tressler, R. E., 455
- Veldkamp, J. B. D., 43
- Wallace, R. G., 283
 Whalen, T. J., 483
 Wu, C. Cm., 477
- Yamada, A., 325
 Yasunaga, N., 171

SUBJECT INDEX

A

Abrasionless machining, 262
 Abrasive machining, 1, 24, 210(Si), 216(Si₃N₄)
 damage, 457
 flaw distributions, 352
 models, 1, 71
 rates, 4, 61, 210, 216
 surface flaws, 351, 429
 two surface technique, 255
 Acoustic emission, 140, 142
 Acoustic surface waves, 379
 Al₂O₃, 75, 111, 142, 157, 171, 205, 247, 255,
 317, 325, 351, 395, 429, 455
 Auger spectroscopy, 345

B

Belt grinding, 202
 BeO, 429
 B₄C, 75, 351, 429

C

CaF₂, 293, 351, 513
 Cam grinding, 214
 Cemented carbides, 305
 Chemical milling, 266
 Chemomechanical effects, 115, 139, 162
 Coated abrasives, 202
 Contour grinding, 213
 Cracks,
 Hertzian cone, 23
 lateral, 5, 16, 24
 radial/median, 16, 24

D

Diamond sawing, 362
 surface flaws, 363-365
 Drilling, 116(quartz), 120(granite),
 121(marble), 142(glass, Al₂O₃, Si),
 224(glass ceramic)
 damage, 143
 effect of:
 additives, 122
 drill sharpness, 224
 environment, 140, 142
 lubrication, 224
 tool geometry, 228
 force, 225
 rates, 116, 120, 122, 124, 134, 135
 power, 226
 power dissipation, 133
 tool wear, 124
 Ductile-to-Brittle transition, 143

E

Elastic emission machining, 159
 apparatus, 160, 161
 model, 160
 Electric discharge machining, 266
 Electrochemical efficiency, 314
 Electrochemical grinding, 305
 rate, 306
 surface damage, 311
 Electron beam machining, 168, 267
 Electron channeling, 397
 Electron diffraction, 180, 320
 Electron spectroscopy for Chemical Analysis
 (ESCA), 180, 236, 332, 345
 Ellipsometry, 346
 Environmental effects, 44, 54, 115, 139, 186

F

Fracture mechanisms, 5, 16, 24, 158, 354, 431
 Fracture origins, 355-374, 435-443, 468, 479,
 480
 Fracture stress (see strength)
 Fracture toughness, 3, 25, 71, 84, 140, 384,
 469-471, 510
 Fractography, 351
 Ferrites, 44, 61, 75, 142, 147
 Friction, 46, 117
 Formed-wheel grinding, 214

G

GaAs, 395
 Glass, 15, 27, 48, 61, 93, 109, 140, 255,
 417, 489
 chemical durability, 424
 cleaning, 418
 Glass-Ceramic, 221
 Glass polishing,
 compounds, 234
 Granite, 120, 203
 Green machining, 209
 Grinding, (Al₂O₃) 79, 111, 205, 251;
 (ferrites) 66, 149; (fire brick) 205;
 (glass) 67, 93, 107, 192, 429; (granite)
 203; (quartz) 206; (Si₃N₄) 78, 216, 473,
 477
 correlation with material properties, 75
 crack size, 77, 351, 473, 479; (see also,
 fracture origins)
 damage 68, 80, 99, 109, 112, 192, 200, 251,
 398, 498-500.
 efficiency, 202
 forces, 62, 65, 68, 78, 85, 86, 99
 hardness, 66

SUBJECT INDEX (continued)

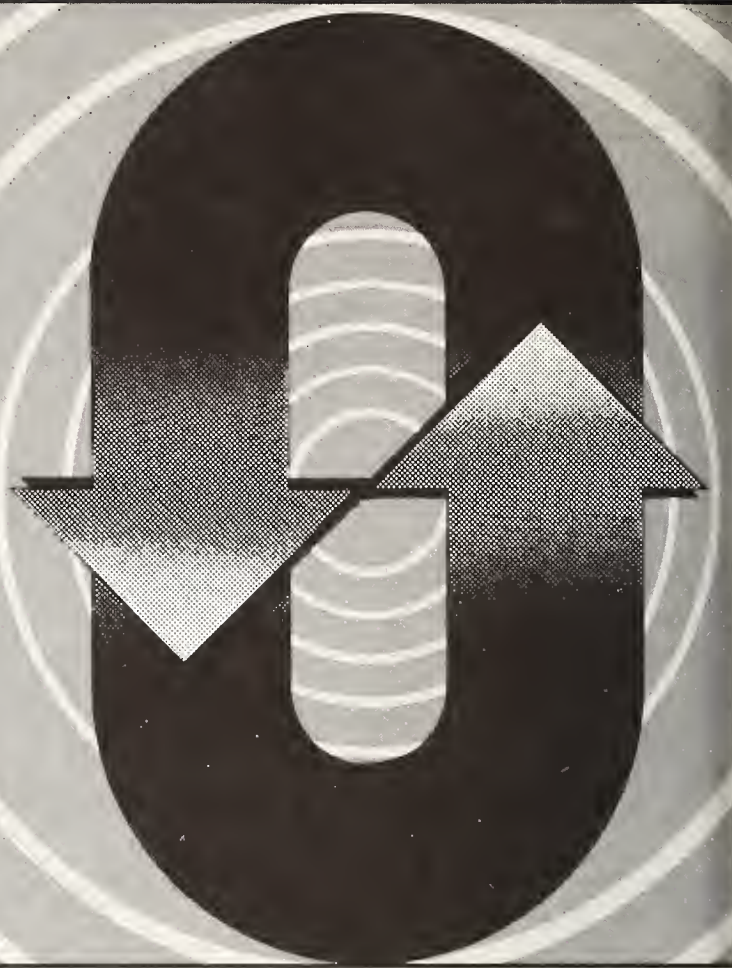
- models, 1, 71, 103, 191
 rates, 42, 192, 204-206, 216, 492
 size effect, 69
 specific energy, 309
 techniques, 209
 vibrations, 64
- H
- Hardness, 3, 49, 82, 185, 308, 402
 relation to machining, 187
 Hydrodynamic machining, 151, 263
 rates (fire brick), 265
 Hydrogen embrittlement, 141
- I
- Impact cracking, 5, 24, 501
 Indentation cracking, 5, 16, 24, 386
 Infrared domes, 255
 Infrared window materials, 293
 Ion-beam machining, 167, 261
 rates, 272
 Ion microprobe, 164, 372
 Interferometry, 259, 332, 339
- L
- Laser beam damage, 231, 348
 effect of surface finish, 514-516
 threshold, 302
 Laser beam machining, 268, 283
 groove depth, 285
 groove profile, 286
 specific cutting energy, 286
 removal rate, 289
 surface finish, 288
 Laser glass, 231
 Latent surface scratches, 417
- M
- Machining (see abrasive machining)
 Marble, 121
 MgAl₂O₄, 351, 429
 MgF₂, 293, 351, 513
 MgO, 48, 75, 118, 429
 Microstructure, 186, 222, 360, 486
 Mullite, 351
- N
- Numerical simulation, 501
- O
- Optical glass, 107
 Optical quality, 231, 259, 279, 343
- P
- Pantographic grinding, 215
 Plastic flow, 5, 16, 47, 103, 158, 398
 zone depth, 401, 403, 404
 Polishing, (Al₂O₃) 162, 173, 317, 325; (glass)
 231, 417; (Si) 178; (quartz) 181
 apparatus, 172, 173, 318
 damage, 166, 180, 238, 239, 331, 367, 398,
 418-420
 effect of environment, 163
 hydration, 165
 mechanochemical, 164, 171
 model, 159, 174
 rates, 165, 173, 242, 319, 330
 surface analysis, 320
 contamination, 231, 345
 finish, 166, 180, 331, 411
 Profile grinding, 214
 Prosthetic devices, 247
 PZT, 75
- Q
- Quartz, 115, 171
- R
- Raman spectroscopy, 167
 Reaction rates, 175
 Rehbinder effect, 115, 139
 Residual stresses, 2
 Rolling, 56
- S
- Sapphire (see Al₂O₃)
 Scanning electron microscopy (SEM), 80, 99,
 109, 112, 126, 143, 176, 233, 248, 251,
 285, 298, 386, 396, 407, 457, 498
 Scratch test, (ferrites) 46; (glass) 27, 50;
 (MgO) 52; (Si₃N₄) 28
 apparatus, 45, 326
 crack size, 28, 29, 51
 damage, 28, 29, 44, 46, 50, 53, 326
 environmental effects, 54
 hardness, 50
 size effect, 49
 Secondary electron emission, 407
 Secondary ion mass spectrometry (SIM), 236,
 346
 SiALON, 283
 Silicon, 142, 171, 325, 395
 Silicon carbide (SiC), 283, 395, 429, 483
 Silicon nitride (Si₃N₄) 28, 75, 209, 283,
 351, 385, 393, 463, 477
 Single point grinding, 29 (glass), 32 (Si₃N₄)
 crack size, 32, 34, 35, 37

SUBJECT INDEX (continued)

- damage, 33, 35
 forces, 31, 32, 35, 37
 groove depth, 30, 34
 Single-point diamond turning, 293, 513
 material removal, 296
 surface finish, 296
 Slow-crack growth, 372
 Specific energy, 48, 66, 96
 SrF₂, 293, 513
 Strength, (Al₂O₃) 250, 436, 441, 442, 458;
 (BeO) 436, 445; (B₄C) 358, 439; (CaF₂)
 358; (glass) 102, 358, 494; (MgAl₂O₄)
 358; 438; (MgF₂) 358, 362; (MgO) 436;
 (mullite) 358; (SiC) 429, 447, 484;
 (Si₃N₄) 211, 213, 219, 465, 478
 degradation 28, 29
 effect of:
 edge beveling, 459
 flaw geometry, 358
 grain size, 429
 grinding direction, 213, 250, 358, 459
 machining rate, 455, 459
 machining technique, 219
 oxidation, 478
 surface coating, 484, 485
 surface finish, 436, 459, 478, 484, 485,
 493
 ion beam machined, 273
 size effects, 367, 375, 486
 Surface characterization, 79, 99, 164, 180,
 236, 299, 320, 331, 337-350, 379, 395,
 407
 Surface flaws, 501
 Surface flaw detection, 379
 Surface melting, 68, 204
 Surface roughness, 228, 253, 300, 320, 340,
 388, 411, 483
- T
- TEM, 109, 110, 340
 Thermal stresses, 9
 Tool materials, 210
 Transducers, 381
 Tungsten carbide, 305
 Turbine components, 209, 390
- U
- Ultrasonic machining, 216
- W
- Water-drop impact, 501
 Wear,
 belt, 203
 debris, 98, 110, 113, 174, 328
 effect of additives, 132
 grinding wheel, 147, 152, 154
 profiles, 150
 tools, 124, 126, 137, 210, 227
 Weibull distribution, 455, 466
- X
- X-ray diffraction, 174, 176, 328
 X-ray topography, 48, 331
- Y
- Y-deflection modulation, 407
 Young's modulus, 185
 Yttraloz (Y₂O₃), 351
- Z
- Zeta potential, 117, 140
 Zinc selenide (ZnSe), 501

U.S. DEPT. OF COMM. BIBLIOGRAPHIC DATA SHEET	1. PUBLICATION OR REPORT NO. NBS SP 562	2. Gov't Accession No.	3. Recipient's Accession No.
4. TITLE AND SUBTITLE The Science of Ceramic Machining and Surface Finishing II		5. Publication Date October 1979	
7. AUTHOR(S) Bernard J. Hockey, National Bureau of Standards Roy W. Rice, Naval Research Laboratory, editors		8. Performing Organ. Report No.	
9. PERFORMING ORGANIZATION NAME AND ADDRESS NATIONAL BUREAU OF STANDARDS DEPARTMENT OF COMMERCE WASHINGTON, DC 20234		10. Project/Task/Work Unit No. 11. Contract/Grant No.	
12. SPONSORING ORGANIZATION NAME AND COMPLETE ADDRESS (Street, City, State, ZIP) Sponsored in part by: Office of Naval Research, 800 N. Quincy St., Arlington, VA 22217, Air Force Office of Scientific Research, Bolling AFB, Washington, DC 20332, and American Ceramic Society, 65 Ceramic Dr., Columbus, OH 43214		13. Type of Report & Period Covered N/A 14. Sponsoring Agency Code	
15. SUPPLEMENTARY NOTES Library of Congress Catalog Card Number: 79-600149 <input type="checkbox"/> Document describes a computer program; SF-185, FIPS Software Summary, is attached.			
16. ABSTRACT (A 200-word or less factual summary of most significant information. If document includes a significant bibliography or literature survey, mention it here.) <p>This volume presents the proceedings of the Second Symposium on the Science of Ceramic Machining and Surface Finishing held at the National Bureau of Standards in Gaithersburg, Maryland, on November 13-15, 1978. The symposium was jointly sponsored by the Air Force Office of Scientific Research, the American Ceramic Society, the Office of Naval Research, and the National Bureau of Standards. The purpose of the symposium was to review recent progress by discussion of current problems and research efforts. The proceedings contain forty of forty-three research papers, together with floor discussions, presented at the Symposium. Specific topics covered include: 1) mechanisms of abrasive machining and surface finishing; 2) technology of machining and surface finishing; 3) characterization of machined surfaces; and 4) effects of machining on the properties of ceramics. Also included is an edited discussion on hardness and its relation to machining.</p>			
17. KEY WORDS (six to twelve entries; alphabetical order; capitalize only the first letter of the first key word unless a proper name; separated by semicolons) Abrasion; ceramics; ceramic machining; effects of machining on ceramic properties; hardness; surface characterizations; surface finishing			
18. AVAILABILITY <input checked="" type="checkbox"/> Unlimited <input type="checkbox"/> For Official Distribution. Do Not Release to NTIS <input checked="" type="checkbox"/> Order From Sup. of Doc., U.S. Government Printing Office, Washington, DC 20402, SD Stock No. SN003-003-02122-9 <input type="checkbox"/> Order From National Technical Information Service (NTIS), Springfield, VA. 22161		19. SECURITY CLASS (THIS REPORT) UNCLASSIFIED	21. NO. OF PRINTED PAGES 524
		20. SECURITY CLASS (THIS PAGE) UNCLASSIFIED	22. Price \$9.00

Waste Heat Management Guidebook



A typical plant can save about 20 percent of its fuel—just by installing waste heat recovery equipment. But with so much equipment on the market, how do you decide what's right for you?

Find the answers to your problems in the *Waste Heat Management Guidebook*, a new handbook from the Commerce Department's National Bureau of Standards and the Federal Energy Administration.

The *Waste Heat Management Guidebook* is designed to help you, the cost-conscious engineer or manager, learn how to capture and recycle heat that is normally lost to the environment during industrial and commercial processes.

The heart of the guidebook is 14 case studies of companies that have recently installed waste heat recovery systems and profited. One of these applications may be right for you, but even if it doesn't fit exactly, you'll find helpful approaches to solving many waste heat recovery problems.

In addition to case studies, the guidebook contains information on:

- sources and uses of waste heat
- determining waste heat requirements
- economics of waste heat recovery
- commercial options in waste heat recovery equipment
- instrumentation
- engineering data for waste heat recovery
- assistance for designing and installing waste heat systems

To order your copy of the *Waste Heat Management Guidebook*, send \$2.75 per copy (check or money order) to Superintendent of Documents, U.S. Government Printing Office, Washington, D.C. 2040. A discount of 25 percent is given on orders of 10 copies or more mailed to one address.

The *Waste Heat Management Guidebook* is part of the EPIC industrial energy management program aimed at helping industry and commerce adjust to the increased cost and shortage of energy.

NBS TECHNICAL PUBLICATIONS

PERIODICALS

JOURNAL OF RESEARCH—The Journal of Research of the National Bureau of Standards reports NBS research and development in those disciplines of the physical and engineering sciences in which the Bureau is active. These include physics, chemistry, engineering, mathematics, and computer sciences. Papers cover a broad range of subjects, with major emphasis on measurement methodology, and the basic technology underlying standardization. Also included from time to time are survey articles on topics closely related to the Bureau's technical and scientific programs. As a special service to subscribers each issue contains complete citations to all recent NBS publications in NBS and non-NBS media. Issued six times a year. Annual subscription: domestic \$17.00; foreign \$21.25. Single copy, \$3.00 domestic; \$3.75 foreign.

Note: The Journal was formerly published in two sections: Section A "Physics and Chemistry" and Section B "Mathematical Sciences."

DIMENSIONS/NBS

This monthly magazine is published to inform scientists, engineers, businessmen, industry, teachers, students, and consumers of the latest advances in science and technology, with primary emphasis on the work at NBS. The magazine highlights and reviews such issues as energy research, fire protection, building technology, metric conversion, pollution abatement, health and safety, and consumer product performance. In addition, it reports the results of Bureau programs in measurement standards and techniques, properties of matter and materials, engineering standards and services, instrumentation, and automatic data processing.

Annual subscription: Domestic, \$11.00; Foreign \$13.75

NONPERIODICALS

Monographs—Major contributions to the technical literature on various subjects related to the Bureau's scientific and technical activities.

Handbooks—Recommended codes of engineering and industrial practice (including safety codes) developed in cooperation with interested industries, professional organizations, and regulatory bodies.

Special Publications—Include proceedings of conferences sponsored by NBS, NBS annual reports, and other special publications appropriate to this grouping such as wall charts, pocket cards, and bibliographies.

Applied Mathematics Series—Mathematical tables, manuals, and studies of special interest to physicists, engineers, chemists, biologists, mathematicians, computer programmers, and others engaged in scientific and technical work.

National Standard Reference Data Series—Provides quantitative data on the physical and chemical properties of materials, compiled from the world's literature and critically evaluated. Developed under a world-wide program coordinated by NBS. Program under authority of National Standard Data Act (Public Law 90-396).

NOTE: At present the principal publication outlet for these data is the Journal of Physical and Chemical Reference Data (JPCRD) published quarterly for NBS by the American Chemical Society (ACS) and the American Institute of Physics (AIP). Subscriptions, reprints, and supplements available from ACS, 1155 Sixteenth St. N.W., Wash., D.C. 20056.

Building Science Series—Disseminates technical information developed at the Bureau on building materials, components, systems, and whole structures. The series presents research results, test methods, and performance criteria related to the structural and environmental functions and the durability and safety characteristics of building elements and systems.

Technical Notes—Studies or reports which are complete in themselves but restrictive in their treatment of a subject. Analogous to monographs but not so comprehensive in scope or definitive in treatment of the subject area. Often serve as a vehicle for final reports of work performed at NBS under the sponsorship of other government agencies.

Voluntary Product Standards—Developed under procedures published by the Department of Commerce in Part 10, Title 15, of the Code of Federal Regulations. The purpose of the standards is to establish nationally recognized requirements for products, and to provide all concerned interests with a basis for common understanding of the characteristics of the products. NBS administers this program as a supplement to the activities of the private sector standardizing organizations.

Consumer Information Series—Practical information, based on NBS research and experience, covering areas of interest to the consumer. Easily understandable language and illustrations provide useful background knowledge for shopping in today's technological marketplace.

Order above NBS publications from: Superintendent of Documents, Government Printing Office, Washington, D.C. 20402.

Order following NBS publications—NBSIR's and FIPS from the National Technical Information Services, Springfield, Va. 22161.

Federal Information Processing Standards Publications (FIPS PUB)—Publications in this series collectively constitute the Federal Information Processing Standards Register. Register serves as the official source of information in the Federal Government regarding standards issued by NBS pursuant to the Federal Property and Administrative Services Act of 1949 as amended, Public Law 89-306 (79 Stat. 1127), and as implemented by Executive Order 11717 (38 FR 12315, dated May 11, 1973) and Part 6 of Title 15 CFR (Code of Federal Regulations).

NBS Interagency Reports (NBSIR)—A special series of interim or final reports on work performed by NBS for outside sponsors (both government and non-government). In general, initial distribution is handled by the sponsor; public distribution is by the National Technical Information Services (Springfield, Va. 22161) in paper copy or microfiche form.

BIBLIOGRAPHIC SUBSCRIPTION SERVICES

The following current-awareness and literature-survey bibliographies are issued periodically by the Bureau:

Cryogenic Data Center Current Awareness Service. A literature survey issued biweekly. Annual subscription: Domestic, \$25.00; Foreign, \$30.00.

Liquefied Natural Gas. A literature survey issued quarterly. Annual subscription: \$20.00.

Superconducting Devices and Materials. A literature survey issued quarterly. Annual subscription: \$30.00. Send subscription orders and remittances for the preceding bibliographic services to National Bureau of Standards, Cryogenic Data Center (736.00) Boulder, Colorado 80303.

U.S. DEPARTMENT OF COMMERCE
National Bureau of Standards
Washington, D.C. 20234

OFFICIAL BUSINESS

Penalty for Private Use, \$300

POSTAGE AND FEES PAID
U.S. DEPARTMENT OF COMMERCE
COM-215



SPECIAL FOURTH-CLASS RATE
BOOK
